

2015

BOOK OF PROCEEDINGS

ICENS

INTERNATIONAL CONFERENCE ON
ENGINEERING AND NATURAL SCIENCE

May 15 - 19 Skopje

www.icens2015.com

Organized by



Supported by



**BOOK OF PROCEEDINGS OF THE
I INTERNATIONAL CONFERENCE ON ENGINEERING
AND NATURAL SCIENCES (ICENS)**

15-19 MAY 2015, SKOPJE, MACEDONIA

Edited by

Prof. Dr. Özer Çınar
Hana Sarkinovic - Köse

© CNR Group, 2015

info@icens.eu
www.icens.eu
www.icens2015.com

Published by:

CNR Group Laboratuvar ve Arge Hizmetleri Sanayi Ticaret Limited Şirketi
Çifte Havuzlar Mah., Eski Londra Asfaltı Cad., Kuluçka Mrk., A1 Blok, 151/1C, İç Kapı No:1
B-20, Esenler / İstanbul, 34220
www.cnrgroup.eu

This work is subject to copyright. All rights are reserved, whether the whole or part of the material is concerned. Nothing from this publication may be translated, reproduced, stored in a computerized system or published in any form or in any manner, including, but not limited to electronic, mechanical, reprographic or photographic, without prior written permission from the publisher.

The individual contributions in this publication and any liabilities arising from them remain the responsibility of the authors. The publisher is not responsible for possible damages, which could be a result of content derived from this publication.

ISSN 2687-2447

Committees

SCIENTIFIC COMMITTEE

Prof. Dr. Abdulrezzak Memon, International University of Sarajevo
Prof. Dr. Adisa Parić, Faculty of Science Sarajevo
Prof. Dr. Aleksandar Dimitrov, Ss. Cyril and Methodius University
Prof. Dr. Anita Grozdanov, Ss. Cyril and Methodius University
Prof. Dr. Christos, Douligeris University of Erlangen-Nurnberg
Prof. Dr. Dragutin T. Mihailović, University of Novi Sad
Prof. Dr. Falko Dressler, University of Paderborn - Germany
Prof. Dr. Ian F. Akyıldız, Georgia Institute of Technology
Prof. Dr. İsmail B. Arpınar, University of Georgia
Prof. Dr. Liljana Gavrilovska, Ss Cyril and Methodius University
Prof. Dr. Lukman Thalib, Kuwait University
Prof. Dr. M. Asghar Fazel, University of Environment
Prof. Dr. Mehmet Akalin, Marmara University
Prof. Dr. Mehmet Karataş, Karamanoğlu Mehmet Bey University
Prof. Dr. Mehmet Kitiş, Süleyman Demirel University
Prof. Dr. Musa Hakan Asyalı, Yıldız Technical University
Prof. Dr. Özer Çınar, Yıldız Technical University
Prof. Dr. Perica Paunović, Ss. Cyril and Methodius University
Prof. Dr. Rifat Škrijelj, University of Sarajevo
Prof. Dr. Samir Đug, University of Sarajevo
Prof. Dr. Tanju Karanfil, Clemson University
Prof. Dr. Wolfgang Gerstacker, University of Erlangen-Nurnberg
Prof. Dr. Yılmaz Yıldırım, Bülent Ecevit University
Assoc. Prof. Dr. Ahmet Doğan, Yıldız Technical University
Assoc. Prof. Dr. Erkan Şahinkaya, İstanbul Medeniyet University
Assoc. Prof. Dr. Izudin Dzafic, International University of Sarajevo
Assoc. Prof. Dr. İsmail Usta, Marmara University
Assoc. Prof. Dr. Muhammet Uzun, RWTH Aachen University
Assoc. Prof. Dr. Mustafa Dolaz, Kahramanmaraş Sutcu Imam University
Assoc. Prof. Dr. Nusret Drešković, University of Sarajevo
Assoc. Prof. Dr. Senija Tahirović, International University of Sarajevo
Assist. Prof. Dr. Ševkija Okerić, University of Sarajevo
Assist. Prof. Dr. Haris Gavranović, International University of Sarajevo
Assist. Prof. Dr. Kevser Cırık, Kahramanmaraş Sutcu Imam University
Assist. Prof. Dr. Muhamed Hadziabdić, International University of Sarajevo
Assist. Prof. Dr. Murat Karakaya, Atılım University
Assist. Prof. Dr. Sasan Rabieh, Shahid Beheshti University

ORGANIZATION COMMITTEE

Prof. Dr. Özer Çınar, (Chairman) Yıldız Technical University
Prof. Dr. Ian F. Akyıldız, (Co-Chairman) Georgia Institute of Technology
Prof. Dr. Anita Grozdanov, Ss. Cyril and Methodius University
Prof. Dr. M. Asghar Fazel, University of Environment
Prof. Dr. Lukman Thalib, Kuwait University
Prof. Dr. Samir Đug, Faculty of Science Sarajevo
Assoc. Prof. Dr. İsmail Usta, Marmara University
Assoc. Prof. Dr. Nusret Drešković, University of Sarajevo
Assoc. Prof. Dr. Muhammet UZUN, RWTH Aachen University
Assist. Prof. Dr. Sasan Rabieh, Shahid Beheshti University
Assist. Prof. Dr. Kevser Cırık, Kahramanmaraş Sutcu Imam University
Hana Sarkinovic Köse, Zenith Group Sarajevo
Musa Köse, Zenith Group Sarajevo
İsmet Uzun, Zenith Group Sarajevo

Welcome to ICENS 2015

On behalf of the organizing committee, we are pleased to announce that the 1st International Conference on Engineering and Natural Sciences (ICENS 2015) is held from May 15 to 19, 2015 in Skopje, Macedonia. ICENS 2015 provides an ideal academic platform for researchers to present the latest research findings and describe emerging technologies, and directions in Engineering and Natural Sciences issues. The conference seeks to contribute to presenting novel research results in all aspects of Engineering and Natural Sciences.

The conference aims to bring together leading academic scientists, researchers and research scholars to exchange and share their experiences and research results about all aspects of Engineering and Natural Sciences. It also provides the premier interdisciplinary forum for scientists, engineers, and practitioners to present their latest research results, ideas, developments, and applications in all areas of Engineering and Natural Sciences. The conference will bring together leading academic scientists, researchers and scholars in the domain of interest from around the world .

ICENS 2015 is the oncoming event of the successful conference series focusing on Engineering and Natural Sciences. The scientific program focuses on current advances in the research, production and use of Engineering and Natural Sciences with particular focus on their role in maintaining academic level in Engineering and Applied Sciences and elevating the science level.

The conference's goals are to provide a scientific forum for all international prestige scholars around the world and enable the interactive exchange of state-of-the-art knowledge. The conference will focus on evidence-based benefits proven in clinical trials and scientific experiments.

Best regards,

Chairman of Conference

Prof. Dr. Özer ÇINAR

	SESSION A	SESSION B	SESSION C	SESSION D	SPECIAL SESSION
11:00	455 - Computational Hydrodynamic Analysis of Turbulent Duct Flow - Selcuk Selimli, Ziyaddin Recebli, Erol Arcaklioglu	338 - A Numerical Study on the Effects of Surface Roughness for a New Cyclone Filter - Fuat TAN, Irfan KARAGOZ, Atakan AVCI	374 - Detection of the weld damages by Lamb wave technique - Volkan Yusuf Şenyürek, Mustafa Demetgül	530 - A New Modified Shah Correlation on Condensation Heat Transfer in Plain Tubes Kemal Ermis, Yasar Sen	5G: Challenges and Innovative Solutions - Liljana Gavrilovska - Ss Cyril and Methodius University, Macedonia
11:15	531 - Towards Rotational Foam Molding Operations Based on Physical Blowing Agents - Remon Pop-Iliev	313 - Optimisation of Tool Edge Geometry and Cutting Parameters in Hard Turning Of AISI 52100 using Taguchi Method - Mehmet BOY, İbrahim ÇİFTÇİ, Mustafa GÜNAY, Halil DEMİR	400 - Numerical Investigation of Simultaneously Developing Laminar Flow And Conjugate Transient Heat Transfer in a Thick Walled Pipe - Selçuk Darıcı, Soner Şen	416 - A New Combined Method of Protein Extraction for Proteomic Studies - Can YILMAZ, Mesude İŞCAN	
11:30	457 - CFD Thermophysical Analysis of MHD Turbulent Pipe Flow - Ziyaddin Recebli, Selcuk Selimli, Erol Arcaklioglu	232 - Aerodynamic Simulation of a Traditional High-Speed Train with Different Head Angles - Gürhan Külahlı, Hilmi Yazıcı	169 - Gaussian and wavelet filtering methods for Michelson interferometric expansion measurement - Veysel Gökhan Böcekçi, Volkan Yusuf Şenyürek	266 - A Numerical Method To Find the Transient Temperature Distribution of Hollow Cylinders - Hakan Pekel and Vebil Yıldırım	Spectrum Sensing Approaches for Cognitive LTE-A Systems - Wolfgang Gerstacker - University of Erlangen-Nurnberg, Germany
11:45	499 - Jet formation and water pile-up in slamming of rigid bodies - Bulent Guzel, F. Cuneyt Korkmaz	331 - Comparison of linear and non-linear strain effects on an angled Timoshenko Beam FEM Model - Mustafa Taşkın, Özgür Demir, Hakan Paşahan	205 - Efficient Routing of Ambulances Aftermath of a Disaster - Hazan Daglayan, Nergiz Kilinc, Senem Aktas, Ibrahim Cerci, Murat Karakaya	507 - Numerical Analysis on Oxy-Fuel Combustion for Different Mixture Rate - Osman İPEK, Barış GÜREL, Mehmet KAN	
12:00	149 - Investigation of Aerodynamic Characteristics and Flow Visualization under Pitching Motion over Non-Slender Delta Wing - B. YANIKTEPE, C. OZALP, B. SAHIN and S. CAG	271 - Thermal Analysis of New Molten Salts Electrolyte for Medium Temperature Thermal Batteries - A.KOCA, Y.VAROL, H.F.ÖZTOP, F.YAKUPHANOĞLU, F.DAGDELEN, M.C.MENTES, G.PAKSOY, A.DERE	248 - Integrated Dynamic Analysis of a Six Axis Serial Robot - Şahin Yavuz, Hira Karagülle	167 - Alterations in the Activities of Chickpea Antioxidant Enzymes During the Progression of Drought Stress - Tuğçe Kalefetoğlu Macar, Oksal Macar	Cybersecurity: Recent Trends and Perspectives - Christos Douligeris - University of Piraeus, Greece
12:15	170 - Investigation of the Test Device Determining Characteristics of Automotive Brake Pads - Mustafa Timur, Hilmi Kuşçu, Sinan Savaş	237 - Effect of Magnet Materials on the Efficiency of Line Start Permanent Magnet Synchronous Motor - Seda Kül, Osman Bilgin	009 - The Concept of Urban Forest in Turkey, Situation Today and Targets - Atilla Atik, Füzün Aslan, Bülent Yılmaz	211 - The factors that effect the external patch repaired in laminated Composite Materials - Şükrü Çetinkaya, Haşim Pıhtılı, Hayri Yıldırım	
12:30	BREAK Lunch (Only for Blue, Green and Orange Package ID Holders)				
13:30	515 - Numerical Investigation of Al2O3-Water Nanofluid Flow And Heat Transfer in Sudden Expansion Channels - Engin GEDİK, Muhammed Atif TOPAL, Alper Ergün, Bahadır ACAR	240 - Design of Five Degrees of Freedom Bomb Loader - Ümit Koçer, Koray Kavlak	339 - A Study on Improving the Thermal Performance of the Solar Chimney System with Using Fresnel Lenses - Fuat TAN, Irfan KARAGOZ	532 - Automating Non-Destructive Product Disassembly Sequence Generation - İle Mircheski, Tatjana Kandikjan, Remon Pop-Iliev	Towards a more Safe and Green Driving Experience in Smart Cities using Vehicular Networking - Falko Dressler - University of Paderborn, Germany
13:45	188 - Determination of Failure Distribution Parameters for Welding Machines used in Ship Construction - Baha GÜNEY, Çağatay TEKE	289 - Optimization of Control Parameters of 2-DoF Twin-Rotor MIMO System - Gonca Ozmen Koca, Sengul Dogan	241 - The Correlation between CPU Core Temperatures of a Server under Specific Cooling Systems - Serhat Orkun TAN, Hüseyin DEMİREL	091 - Kinetics of fine dry grinding of barite in a laboratory steel ball mill - Ali ARAS, Alper OZKAN, Salih AYDOGAN	
14:00	458 - Evaluation and Modelling of Modified Hazelnut Shell in Pb2+ Removal From Aqueous Solution - Evren Gölge, Gülden Ova	309 - Modelling of Specific Cutting Resistance In Machining Of AISI P20 Plastic Mould Steel - Nafiz Yaşar, Mustafa Günay, Ulvi Şeker	336 - Analysis and Design of Passive and Active Interconnected Hydro-Pneumatic Suspension Systems in Roll Plane - Ferhat Saglam, Y. Samim Unlusoy	212 - Analysis of Laminated Composite Plates By Using Element-Free Galerkin Method - Özkan ÖZBEK, Ömer Yavuz BOZKURT	Transmission of warning messages and other reports through vehicular networks in Smart Cities - Monica Aguilar Igartua - Univ Politecnica de Catalunya, Spain
14:15	475 - Morphological Comparison of Transgenic and Non-Transgenic Corn (Zea mays L.) Lines Under Drought Stress - Oksal Macar, Tuğçe Kalefetoğlu Macar, Kültiğin Çavuşoğlu, Emine Yalçın	529 - The Parametric Study on Intercooler in Turbocharger Diesel Engine - Yasar Sen, Kemal Ermis	258 - Effects of heat treatment on abrasion properties of fir and beech wood - Hamiyet SAHIN KOL, Yusuf SEFIL, Sema AYSAL	295 - Monitoring of the Daily Global Solar Radiation in Eastern Turkey by Using Satellite Images - Selmin ENER RUSEN	
14:30	015 - Analysis of the Turkmen Tents that Provide Energy Efficiency by Use of Natural Material from the Socio-Economic and - GULSEN CENGİZ	369 - Design of Hydraulic Bulge Test Unit for Warm Forming - Emine Feyza Şükür, Hüseyin Selçuk Halkacı, Murat Dilmeç, Mevlüt Türköz	197 - A Genetic Algorithm for Safe and Rapid Transmission of Military Vehicles in a Minefield - Nergiz Kilinc, Ibrahim Cerci, Hazan Daglayan, Senem Aktas, Murat Karakaya	236 - E-Invoicing in Turkey and a Software-as-a-Service Solution - Ahmet Ozcan, Salim Eryigit	The social layer in Resource Competition - Ioannis Stavrakakis - University of Athens, Greece
14:45	238 - The Kinematic Analysis of the Eight Legged Scorpion Robot - Koray Kavlak, Hüseyin Sayman, Fatma Koç, Şakir Taşdemir, Kevser Dincer	511 - Determination of the Effects of Operating Parameters on the Supernatant Turbidity of Quartz Suspensions by Experimental Design - Adem Taşdemir, Tuba Taşdemir	224 - 8D Problem Solving Technique Case Studies in Industry for Metallic Materials Production - Yavuz Gezicioglu, Adnan Sozen	053 - Determination of Public Expectancy and Approach of Urban People Towards Urban Forest: Sample of Malatya-Turkey - Füzün Aslan, Atilla Atik, Bülent Yılmaz	
15:00	BREAK COFFEE / TEA				
15:15	207 - Numerical Investigation of Convective Heat Transfer Characteristics of TiO2/Water Nanofluid in a Trapezoidal Microchannel - Tuğçe İŞGÜZAR, Cüneyt UYSAL, Kamil ARSLAN, Hüseyin KURT	460 - Particle Swarm Optimization Approach to Solve Single Machine Total Weighted Tardiness Problem with Unequal Release Date - Serdar ÖZER, Tarık ÇAKAR	419 - Optimization of Surface Roughness in Wire-Cut EDM Of Aa6061/B4CP Using Response Surface Method - Şener Karabulut, Halil Karakoç, Ömür Kaya Kalkan, Ramazan Çıtak	376 - WDXRF Analysis and Determination of Effects in Cement Production Processes Sample Prepared with Pellet Method - Melike Arslanhan, Gökçe Borand, Zeynep Sır, Faruk Demir	
15:30	217 - Optimum Autofrettage Pressure for a High Pressure Cylinder of a Waterjet Intensifier Pump - Hakan Çandar, İmam Hüseyin Filiz	310 - Gender Determination from Regions of the Face - Betül AKKOÇ, Ahmet ARSLAN	417 - Controlling Temperature Rise in Mass Concrete Foundation of Folkart Towers - A. Atacan ÜTE	539 - Energy Efficiency Enhancement of A Household Refrigerator Using With Oil Cooling Condenser - Erdoğan Kılıçaslan, Alper Ergün, Engin Gedik, Bahadır Acar, Engin Özbaş	Mobile Health Solutions for Neurological Applications - Zaher Dawy - American University of Beirut, Lebanon
15:45	402 - Numerical Investigation of the Performance of Twisted and Untwisted Blades for Small Horizontal axis Wind Turbines - M.E. Abdelmoty, A. Osman, O.E. Abdellatif	329 - Identification of Normal and Abnormal Heart Sounds Using Neural Network - Fatma Zehra Göğüş, Bekir Karlık	018 - Analytical Investigation Of The Stress Distribution in the Beam End Connector in Storage Rack Systems - Yaşar PALA, Emre Çalış, Murat REİS	252 - UAV Route Planning for Avoiding Enemy Radars - Senem Aktas, Nergiz Kilinc, Hazan Daglayan, Ibrahim Cerci, Murat Karakaya	
16:00	191 - Vibration Control of an Onelink Flexible Manipulator with Harmonic Excitation - Şahin Yavuz, Hira Karagülle	130 - Research Data Management System Proposal having Confidentiality and Privacy - Feriştah Dalkılıç, Enis Karaarslan, Mehmet Beşir Eren	361 - Determination of the awareness level of individuals about the parks designed for the disabled - Füzün Aslan, Atilla Atik	454 - Salt Bath Nitriding of Fe72Al28 Intermetallic Alloy - İbrahim Çelikyürek	War on Faults - Ilir Capuni - Epoka University, Tirana, Albania
16:15	131 - Using Base Algorithms Combinatorially in Adaboost Ensemble for Intrusion Detection - Necati Demir, Gökhan Dalkılıç	497 - The Friction Welding of Feal Intermetallic Alloy And AISI 316 Stainless Steel - Ibrahim CELIKYUREK, Bedri BAKSAN, Osman TORUN, Akın OZCAN	044 - Providing Engineering Solutions to Forest Fire Access Problems Using Network Analysis Method - Abdullah E. AKAY, Hande E. KILIÇ	452 - Dry sliding wear behaviours of Fe3Al and Fe-32.5Al-15Ti alloys - O. Torun	
16:30	BREAK COFFEE / TEA				
16:45	End of the day	End of the day	End of the day	End of the day	End of the day

	SESSION A	SESSION B	SESSION C	SESSION D	SESSION E
9:00	023 - Utilization of Cryolite Based (Na3AlF6) Electro-Metallurgy Wastes in Fired Clay Brick Production - M.Serhat Başpınar, Uğur Karakaya, Akin Bozkurt and Emre Demir	155 - Identification of Waste Sources in Ready-Mixed Concrete Plants - Aynur Kazaz, Serdar Ulubeyli, Ahmet Arslan, Bayram Er, Murat Atıcı	352 - Removal of Phenol from Aqueous Solutions by Photo-Fenton Processes - Özlem TEPE, Arzu Y. DURSUN	364 - Determining the Risks in Maritime Container Terminals Operations: Health and Safety Applications - Gül EMECEN KARA, Ersoy KAÇMAZ	027 - Effect of Different Percentages of TENCEL® Fibres on Poly(lactic Acid) Fibres Based Nonwoven Structure Properties - M. Uzun, C. Bach, S. Jockenhoevel, I.Usta, M.Akalin
9:15	035 - Agricultural Waste Biomass Hydrolysis by Scytalidium thermophilum Xylanase - Didem SUTAY KOCABAS	146 - Effect of Catalyst Amount on Azo Dye (Basic Yellow 28) Oxidation Using Pr Doped TiO2-MMT Composite Photocatalyst - Başak Otsukarci, Yasemen Kalpaklı	301 - Proposals for the protection of water resources in the Prespa lake basin, Greece - Romanos - Vasileios Araviadis	371 - Determination of Hazard Effects of Truck Accident Carrying Hazardous Waste by Using Ranking System - Mehmet Emin ARGUN, Havva ATEŞ	063 - Glucose Concentrations in Blood Regarding to Different Physiological States of Holstein, Friesian Cattle - Nejra Hadzimusic
9:30	048 - Bioinformatics Application for the Detection of Pathogenic Bacteria by duplex real Time PCR - Ergün Şakalar, Ahmet Kaynak	186 - Removal Efficiency of The Herbicide Aclonifen by Soil Fungi - Gokhan Onder Erguven, Hurrem Bayhan, Bahar İkizoglu, Gurdal Kanat, Yasar Nuhoglu	328 - Removal Rate of Herbicide Aclonifen in Agricultural Sunflower Field in Natural Period - Hurrem Bayhan, Gokhan Onder Erguven, Gurdal Kanat, Sadullah Levent Kuzu	107 - Causes and Reasons of Soil Degradation Problems in Turkey - Taskin Oztas	257 - The Research of the Economic Impact of Granite Dust Remains Usage in Auto Brake Pads - Halil Kılıç, Mustafa Timur, İbrahim Mutlu, Sinan Savaş
9:45	038 - Foam Concrete Production with a Mineral Waste Addition - İsmail Demir, M.Serhat Başpınar, Erhan Kahraman, Volkan Atabey	486 - Physical Activity Prediction: Accelerometers or Gyroscopes - Musa Hakan Asyali, Ömer Kayaaltı	359 - The Impact of Climate Change on Maritime Transport Routes - Gökhan KARA	355 - Toxic and Hazardous Waste Management - Sakine UGURLU KARAAĞAÇ	280 - Comparative Assessment of Attributes and Ranking of Alternative Product Variants for Smart Running Shoes - Gülten Turhan
10:00	052 - Algae for Renewable Energy - Meltem CONK DALAY	251 - Natural Gas Consumption and Its Effect On Air Emissions in Turkey - Ali CAN, Halil EKMEKCI	332 - Removal of Color and COD from Wastewater of a Local Textile Factory by Coagulation - M. Sara TUNÇ, Özlem TEPE	005 - Slope Stability Analysis Method of Account Back And Examination of Tekke Landslide with Back Analysis Method - Mümin FİLİZ, Semiha GÖKCAN	034 - Detection of Human-Induced DNA Contamination Using Molecular Based Technique - Ergün ŞAKALAR, Şeyma ÖZÇIRAK ERGÜN, Cengiz ATASOĞLU, Emine AKAR, Cigdem PALA
10:15	065 - Application of Differential Evolution Algorithm for Interpretation of Magnetic Anomalies due to Dipping Dike-like Bodies - Ç. Balkaya, Y.L. Ekinci, G. Göktürkler	509 - Vehicle's On-Board Diagnostic(OBD) and Road Data Board Communication over Mobile Devices in Traffic - Gül Fatma TÜRKER, Akif KUTLU	187 - Removal Rate of Herbicide Trifluralin in Agricultural Sunflower Field in Natural Period - Gokhan Onder Erguven, Hurrem Bayhan, Bahar İkizoglu, Gurdal Kanat	250 - Animal Manure Effect on Climate Change and Usage As a Energy Sources in Turkey - Ali CAN	393 - Some example of mismanagement practices in natural vegetation İn Turkey - Mahmut DAŞCI, Binali ÇOMAKLI
10:30	070 - Evaluation of Presplit Blasting Operation in Apa-Hotamış Irrigation (AHI) Channel Construction - Bilgehan Kekeç, Niyazi Bilim, Mümin Yüce	302 - Groundwater Modelling of Afyonkarahisar Sinanpasa Plain - Murat KILIT	363 - Evaluation of Maritime Safety in Istanbul Strait Using Port State Control Inspections - Gül EMECEN KARA, Olgay OKŞAŞ	357 - Land use change detection in Turkish coastal zone by Corine database - Tuncay Kuleli	179 - Effect of Temperature on Copper Losses in Synthetic Matte-Slag System with Colemanite Addition - Aydın RÜŞEN, Ahmet GEVECI, Yavuz Ali TOPKAYA
10:45	BREAK COFFEE / TEA				
11:00	086 - Flocculation of wastewater from coal washing plant by polymers in Turkey - Selma Duzyol, Berk Eroç, Tevfik Ağacayak, Ali Aras	513 - A Doubly Fed Induction Generator Modelling and Controlling For Wind Turbine Applications - Huseyin AKDEMİR, Yavuz SEZER, Omer Faruk KARADA-VUT, Erkan MESE	372 - Use of Rainwater in Recreational Irrigation of a University Campus in Turkey - Ahmet Doğan	341 - Numerical Investigation of the Effect On Flow Characteristic of the Objects Placed Between Nozzle And Impinging Plate - M. Akçay, G. Külahlı, A. Akbıyık	308 - The Effects of Franchising System on International Marketing Strategies: Turkish Clothing Sector Case - Turan Atılğan, Seher Kanat
11:15	054 - Effects of Terebint (Pistacia terebinthus L) Oil Addition to Quail Diets on Growth Performance, Carcass Traits, Some Blood Parameters and Composition of Breast Meat Fatty Acid - Tuncay TUFAN*, Cavit ARSLAN, Aydın DAŞ	403 - Carnitine Levels in Milk And Milk Products - Rabia Serpil GÜNHAN, Suzan YALÇIN	378 - Investigation of Practical Design Approach for Circular Steel Base Plates - Mutlu Secer	330 - Near Surface Mounted CFRP Composites for Shear Strengthening of RC Beams - H.M. Tanarslan	476 - Stiffness Prediction of Bi-adhesive Single Lap Joints - Ozkan Oz, Halil Ozer
11:30	081 - Investigations into deep geological structure of Gulf of Antalya, Turkey by using airborne magnetic data - Abdullah Ateş	399 - Effect of Drying Conditions on Moisture Diffusivity in Thin Layer Drying of Apricot - Soner ŞEN, Selçuk DARICI	394 - Seismic behavior of mid-story buildings with base isolation system - Özgür Bozdağ	354 - Evaluation of Tank Container Logistics in Turkey - Olgay OKSAS, Gokhan KARA	TBA
11:45	032 - Quantification and Novel Duplex Identification of Escherichia coli O:157 H:7 and Listeria monocytogenes - Ahmet KAYNAK, Ergün ŞAKALAR	494 - Energy recovery potential of municipal sludge disposal and agricultural residuals - NEZAKET PARLAK, HÜSEYİN PEHLİVAN	528 - Human Resources Management and Relationship Horoscope - Erdoğan Adeviye, Adigüzel Orhan	030 - Natural Dyeing on Woollen Fabric Using Some Red Rose Petals - Emrah ÇİMEN, Mustafa DEMIRELLİ, Burcu YILMAZ ŞAHİNBAŞKAN, Mahmure ÜSTÜN ÖZGÜR	TBA
12:00	161 - A bacteriocinogenic lactic acid bacterium from Turkish traditional fermented sucuk and its molecular characterization - M.Gulluce, M.Kaya, G.Kaban, O.Baris, M.Karadayi, A.Kamiloglu, H.Genc, K.Fettahoglu, B.Alaylar	375 - Semi-quantitative analysis in WDXRF spectrometry of polyethylene materials used in food packaging - Gökçe Borand, Melike Arslanhan, Zeynep Sır, Fatih Dağdelen, Emine Alkin, Faruk Demir	316 - Prestressed near-surface mounted fibre reinforced polymer reinforcement for concrete structures - Gokhan SAKAR	031 - Dyeing Properties of Silk Fabric with Dactylopius Coccus Costa and Quercus Infectoria Olivier - B.Y. Şahinbaşkan, R. Karadağ, E. Torgan	TBA
12:15	156 - Evaluation of Current Recycling Facilities for RMC Plants in Turkey - Aynur Kazaz, Serdar Ulubeyli, Murat Atıcı, Bayram Er, Ahmet Arslan	502 - The microstructure and hardness analysis of decarburization followed by boronizing AISI 2080 tool steel - Arzum Uluköy, Yavuz Kaplan, Volkan Onar, Merve Yıldız, Emre Armağan, Okan Çarık	358 - Evaluation of Turkish Straits Vessel Traffic Services (TSVTS) Applications in the Istanbul Strait - Gökhan KARA	202 - Treatment of Dairy Wastewaters Using Anaerobic Baffled Bioreactor Started with Waste Activated Sludge - Erkan Sahinkaya, Adem Kılıç, Zaharia Marius, Bahadır Duygulu	TBA
12:30	BREAK Lunch (Only for Blue, Green and Orange Package ID Holders)				
13:30	043 - Propolis and Its Usage Opportunity - Sabire YERLIKAYA, Cemalettin SARIÇOBAN	TBA	049 - Model Development for the prediction of Prasinococcus sp. Growth - Esra Imamoglu, Zeliha Demirel, Meltem Conk Dalay	537 - Controlled Recirculation of Ventilating Air in Underground Coal Mining - Applications in Turkey and in the World - Cem SENSOGUT, İbrahim CINAR	TBA
13:45	103 - Synthesis and Characterization of Carbon nanotube supported PdAu formic acid electrooxidation anode catalysts - Dilan Atbas, Fazile Cicek, M. Mücahit Toprak, Hilal Kıvrak	176 - A New Statistical Approach to Assess Alternative Store Locations: Pugh Method - Mehmet Akalin, Gülten Turhan	305 - Employee Selection with Analytic Hierarchy Process in Clothing Sector: Turkish Case - Seher Kanat, Turan Atılğan	006 - An Investigation of The Effects of Chemical Additives on The Mortar Phase - Osman Ünal, Kadir Akyüz, Kadir Güçlüer	TBA
14:00	042 - An Early Warning System Design for Steel Frame Trusses - Yigit Mahmutoglu, Ali Gurbuz, Cemalettin Terzi	033 - Developing of a New Ionize Radiation Detection Method - Ergün ŞAKALAR, Emine AKAR, Şeyma ÖZÇIRAK ERGÜN, Ahmet KAYNAK	480 - Application of Digital Image Correlation in Uniaxial Tensile Test - Murat AYDIN, Kerim CETINKAYA	136 - Analysis and Back-Calculation Modelling of Snow Avalanche Event of 10th January 2015 in Uzuntarla (Trabzon-Turkey) - A. Aydın, R. Eker, Y.B. Odabaşı	TBA
14:15	120 - Non-enzymatic H2O2 sensor based on PtAu/C catalysts - Ozlem Sahin	122 - Astronomical aspects of the cult practice of the peak sanctuary Kokino - Olgica Kuzmanovska, Jovica Stankovski	129 - Distribution of Antibiotic and Antiseptic Resistance Genes in Isolated Staphylococci from Bovine Mastitis - Zafer CANTEKİN, Hasan SOLMAZ, Kemal Gurturk, İsmail Hakkı Ekin, Dilek Öztürk, Yasar ERGUN	126 - Is Plant Growth Promoting Rhizobacteria an Alternative to Mineral Phosphorus Fertilizer in Pea Seed Production? - M.K. GULLAP, H.I. ERKOVAN, K. HALILOĞLU, A. KOC	TBA
14:30	036 - Isolation and molecular characterization of bacterial strains with enrichment potential from Magnesite Mines in Kütahya - Selin Hundur, Medine Gulluce, Ceyda Bozoglu, Mehmet Karadayi	076 - Hydrogen Generation from Ammonia Borane by PVP-Protected Ruthenium-Rhodium Nanoparticles - Murat RAKAP	162 - Investigation the Effect of Connection Models on the Optimum Design of Semi-Rigid Steel Frames - Soner ŞEKER, Erkan DOĞAN, M. Polat SAKA, Celalettin KOZANOĞLU	373 - Determination of Oxygen Gain in Hydraulic Structures - Aslı SARI, Tuba BOSTAN, Saadetin TOPÇU, Ali COŞAR	TBA
14:45	245 - Application properties of groundnut hull/epoxy composites - Gulcihan Guzel, Huseyin Deveci	066 - Algorithm Analysis of Computer Games: 2048 Game Example - Ruya Samli	440 - Separation And Preconcentration Of Silver Ions On Activated Carbon From Vine Shoots - Harun Ciftci, Cigdem Er, Esin Kiray, Ergin Kariptas, Ahmet Cetin, Mehmet Erdem, Orhan Cakirer	438 - Determination of Lead by Flame Atomic Absorption Spectrometry After Separation/Preconcentration Process on Rhodococcus ruber - Ergin Kariptas, Esin Kiray, Cigdem Er, Harun Ciftci, Kıymet Kariptas	TBA
15:00	BREAK COFFEE / TEA				
15:15	253 - Synthesis of ethynyl-thiophenes as starting materials for the synthesis of biologically active compounds - Arif Kıvrak, Emrah Kavak, Aslı Köroğlu	367 - Cucurbit Viruses of Turkey - Serkan YEŞİL	165 - Optimization of Rapid DNA Extraction Protocol From Ancient Human Bones - Elif ÖZDEMİR-KAYNAK, Ozlem YESIL-CELİKAS	397 - Theoretical Approach for Modelling and Simulation of Electrical Passenger Car Powertrain System - Mustafa Umut KARAOĞLAN, Nusret Sefa KURALAY	TBA
15:30	092 - Effect of microwave pretreatment on nickel extraction from lateritic nickel ore in hydrochloric acid - Tevfik AGACAYAK, Merve KOSELER, Selma DUZYOL	055 - Synthesis and Characterization of Acid Activated Artvin Bentonite (AR) Designed as a Catalyst - O. Sungur, A. Tabak, B. Caglar	152 - Extracellular biosynthesis of biocompatible titanium dioxide nanoparticles by using fungus Aspergillus sp. - M. Sahin, A.Y. Demir, M. Gulluce, O. Baris, U. Demir, M. Karadayi, G. Karadayi	265 - Effect of carbon and nitrogen concentrations on PHB production by mixed culture submitted to aerobic dynamic feeding regime - Dilek AKMAN, Sebnem ÖZDEMİR, Kevsir CIRIK, Ozer CINAR	TBA
15:45	121 - Electrochemical Detection of Hydrogen Peroxide Based on Pt-MnO2/C Nanocomposite - Hilal Kıvrak, Orhan Alal, Dilan Atbas	430 - A Statistical Model for Predicting Yarn Evenness of Cotton Siropun Yarns - Tuba Bedez Ute, Huseyin Kadoglu	244 - A newly recorded mite species of the genus Storchia Oudemans (Acar: Stigmaeidae) for Turkey: S. hendersonae Fan and Zhang - S. DILKARAOĞLU, S. DOĞAN, O. ERMAN, S.SEVSAY, S. ADIL	192 - Hybridization of Electric Vehicle with Fuel Cell Based on Two Control Strategies - Mustafa Umut Karaoğlan, Nusret Sefa Kuralay	TBA
16:00	088 - Kinetic analysis of Zn(II) ions transport through a multi drop liquid membrane containing di-(2-ethylhexyl)phosphoric acid - Ramazan DONAT, Kadriye ESEN ERDEN	166 - Synthesis of β-Chloralose Derivative Via [3+2]-Cycloaddition of Aziridine with Acetonitrile - Emriye AY, Tamer KARAYILDIRIM, Kadir AY	150 - Ten lignocellulolytic fungal isolates from decaying woody materials and their ethanol production potentials - M. Karadayi, M. Gulluce, O. Baris, T.Y. Koc, S. Hundur, F. Sahin, M. Turan, H. Ozkan	TBA	TBA
16:15	114 - Effects of Cadmium on Metallothionein Gene Expression and Mineral Elements Uptake in Tomato (Lycopersicon esculentum) - Dursun KISA, Lokman ÖZTÜRK, Ali AYDIN, Şaban TEKİN	447 - Production of Alumix 13 Based Metallic Foams with Powder Metallurgy Method - Halil Karakoç, Görkem Kırmızı, Hanifi Çinici, Ramazan ÇITAK	446 - Experimental Investigation of Vertical Welded Connection Detail Between Precast RC Shear Wall Panels - Adem Solak, Yavuz Selim Tama, Salih Yilmaz, Hasan Kaplan	TBA	TBA
16:30	BREAK COFFEE / TEA				
16:45	End of the day	End of the day	End of the day	End of the day	End of the day

	SESSION 11:00:00	SESSION 13:30:00	SESSION 15:30:00
01A	297 - Optimization of GC-FID procedure for simultaneous determination of heroin and cocaine in real samples - Jeton Halili, Avni Berisha, Adelina N. Halili, Kaltrina Jusufi, Tahir Arbneshi	097 - Determination of Bacteriological, Physicochemical and Melissopallinological Properties of Some Pine Honeys in Mugla/TURKEY - N.N. Bozbeyoğlu, N. M.Doğan, S. Arslan, A. Güvensen	273 - Association between serum 25-hydroxyvitamin D and some inflammatory cytokines and angiogenic factors - F.B.S. Cinemre, H. Cinemre, B. Aydemir, C. Karacaer, A. Nalbant, T. Kaya, A. Tamer
01B	319 - Improvement of Laundering Durability of Polypyrrole Coated Cotton Fabrics - Zehra Yıldız, Onur Atak, İsmail Usta	098 - Calcium Carbonate Precipitation by Bacillus aerius strain U2 - Tuğba ŞENSOY, Nazime MERCAN DOĞAN, Ömer BOZKAYA, Erdal AKYOL	370 - The investigate of thermodynamic properties of the HLA-B*51 protein bound to different peptides which pathogenic role in Behcet' - Cenk DENKTAŞ
02A	113 - Comparison of Energy and Exergy Efficiency of the Refrigerants Instead of R22 in Air-to-Air Heat Pumps - Fadime Simsek, Kemal Comakli, Ömer Comakli	105 - Exopolysaccharide Production Potential of Bacillus pseudomycooides strain T1-11 in Molasses Medium - K. SOLMAZ, G. DOĞANLI, N. DOĞAN, Ö.ÇETİN, E. COŞKUN, T. BALGİR, B. ULUTÜRK	391 - Chemical Composition and in vitro Antimicrobial, Anticancer, Antioxidant Effects of the Essential Oil of Thymus convolutus - S. Çelen, A.D. Azaz, S. A.Türkoğlu, F. Köçkar, F.Z.Küçükbay
02B	327 - Investigation of Physical Properties of Woollen Fabrics on Thermal Comfort - Zehra Yıldız, Nuray Oz Ceviz, Vedat Dal, Engin Akcagun, Abdurrahim Yılmaz, Mustafa Atmaca, A. Berk Kurtulus	106 - Optimization of Cryopreservation of Neocholoris texensis Under Axenic and Non Axenic Culture Conditions - A.F. Sir, Ç. Demirkaya, Z. Demirel, E. Imamoğlu, M.C. Dalay	392 - Thymus pectinatus var pectinatus from Turkey essential oil: chemical composition and biological activities - S. Çelen, A.D. Azaz, S.A. Türkoğlu, F. Köçkar, F.Z. Küçükbay
03A	115 - Kinetic study of Cd2+ ions through a MDLM system using TNOA as a mobile carrier - R. DONAT , M.İ. EYİCE, H. CETİŞLİ	090 - The Synergetic Effects of Pesticides on Swimming Performance of Rainbow Trout (Oncorhynchus Mykiss) - Harun Arslan Muhammed ATAMANALP	395 - A Research on the Saprophytic Microfungi in Olive Fruit in Balıkesir Province - Berna Sanon, Ayşe Dilek Azaz, Selma Celen
03B	183 - The Production of Hexadecyltrimethylammonium bromide (HDTMA-Br) Modified Sepiolite for Heavy Metal Removal - Yasemen KALPAKLI, Hilal CANSEV	110 - The Effect of Environmental Conditions on Exopolysaccharide Production of Bacillus licheniformis strain B18 in Molasses Medium - Ö. Çetin, G. Doğanlı, N. Doğan, K. Solmaz, T. Balgır, E. Coşkun, B. Ulutürk	109 - Local Forage Ecotypes and Their Importance in Turkey - Mustafa TAN, Zeynep DURLU GUL
04A	234 - Porphyrin-Metal Complex Gold Nanorods - Ozgul Birel, Chenming Xue, Quan Li	143 - Genotoxic Effects of Anabolic Doping Steroid Nandrolone Decanoate in Human Peripheral Lymphocyte - Arif Ayar, Handan Uysal, Deniz Altun Çolak	171 - Milk Components from Native Cows versus Human Milk Components - Tolga İNAL, Murat ÇİMEN, Firat TOK
04B	235 - Production of Chitosan-Layered Silicate Nanocomposite Hydrogels and Investigation of Their Heavy Metal Adsorption Capacities - Seda Bozkurt, Sinan Şen	151 - Extracellular biosynthesis and characterization of ZnO nanoparticles using Rhodococcus K85 strain - A.Y. Demir, M. Sahin, M. Gulluce, O. Baris, T. Oznuluer, M. Karadayi, T. Arasoglu	204 - DNA Damage and Retrotransposon Polymorphism in Wheat Subjected to Drought Stress - Mahmut Sinan Taspınar, Seba Turhan, Burcu Sigmaz, Guleray Agar, Murat Aydın
05A	242 - Crosslink agent effect on Au/Poly(4-vinyl phenol):PMF (poly(melamine-coformaldehyde) methylated)/p-Si Schottky diode - Cem Tozlu	228 - Chemical composition of essential oil from Teucrium chamaedrys L. - Zuleyha Ozer Sagir, Turgut Kilic	227 - Analysis of the Essential Oil of Marrubium peregrinum L. - Zuleyha Ozer Sagir, Turgut Kilic
05B	277 - The Investigation of How the Methods, the Different Parts and Different Cultivars of Apples Effect on the Antioxidant Activity of - M. Yıldırım, F. Benzer, M. Çimen, D. Barış, H. Yıldırım	157 - Calcium Carbonate Precipitation induced by ureolytic Bacillus licheniformis B22 under some environmental conditions - T. ŞENSOY, M.C. AKDEMİR, K. KÖMÜR, M. ÖZÇANAK, N. MERCAN DOĞAN	239 - Effects of Different Bacterial Strains on Yield and Quality of Strawberry - Rafet ASLANTAS, Murat KOSE, Gursei OZKAN, Halil KARAKURT, Ramazan CAKMAKCI
06A	283 - Synthesis and characterization of novel poly(acrylamide-co-methacrylic acid) nanocomposite modified with organosmectite - A. Tabak, B. Caglar, F. Coldur, O. Sungur, S. Caglar	159 - Isolation of IAA producing bacteria from rocky areas in Gümüşhane-TURKEY - Ceyda Bozoglu, Mehmet Karadayi, Selin Hundur, Taha Yasin Koc, Selma Sezen, Burak Alaylar, Medine Gulluce	243 - The Effects of Modified Atmosphere Packaging with Ethylene Absorbers on Ascorbic Acid Contents in Red Bell Peppers - Omca DEMİRKOL, İnci CERİT
06B	414 - Investigation of Effects on Photodynamic Therapy by Synthesizing Novel Photosensitizers from Perylenedimide Derivatives - Furkan Özçil, Funda Yükrük	524 - Application of Ionic Liquids as Catalysts for the Synthesis of 3,4-Dihydropyrimidine-2(1h)-One Derivatives - .M.Abbasov, A.G.Talibov, G.N.Badalova, N.I.Mursalov, Sh.Z. Jabrailzadeh	288 - Influence of ultraviolet radiation on quality and microbial population in grape must - Kamila Mi-jowska, Ireneusz Ochmian, Paweł Nawrotek, Natalia Młodzik, Beata Zielińska
07A	294 - Comparing the analytical performance of the GC-FID and GC-MS for the determination of the drugs of abuse:Cocaine and heroin - J. Halili, A.N. Halili, K. Jusufi, A. Berisha, T. Arbneshi	198 - Determination of Effect of Manganese Toxicity on LTR RTs Polymorphism in Zea mays - Mahmut Sinan Taspınar, Esmayigider, Esra Arslan, Guleray Agar, Murat Aydın	315 - Plant Prebiotics for the Development of Fermented Dairy Products - Ozge Ozcan, Tulay Ozcan, Lutfiye Yilmaz-Ersan, Arzu Akpınar-Bayizit
07B	381 - Green synthesis of Ag - Au nanoparticles, attachment on the SiO2 microsphere surface and it's antibacterial activity - Süreyya Kadioğlu, Ahmet Balcı, Merve Girgin	200 - Effect of Picloram on DNA Methylation In Common Bean (Phaseolus vulgaris L.) - Esra Arslan, Murat Aydın, Mahmut Sinan Taspınar, Burcu Sigmaz, Semra Yagci, Guleray Agar	401 - Practicing Transhumance in Turkey: Examples of past and present - Binali ÇOMAKLI Mahmut DAŞCI
08A	104 - Enhanced Formic acid Electrooxidation Activity of Carbon nanotube Supported CoAuPd Catalysts - Orhan Alal, Hilal Kivrak	203 - Analyses of Somaclonal Variation in Endosperm-Supported Mature Embryo Culture of Rye (Secale cereale L.) - Murat Aydın, Esra Arslan, Mahmut Sinan Taspınar, Guleray Agar, Gokce Nardemir	132 - Plants Used for Folk Medicine in the Plateau Goller (Adana-Turkey) and Close Villages - Dilan Arslan, Serpil Demirci, Galip Akaydin
08B	299 - 2-((2/3/4-Hydroxybenzylidene)Amino)-6-Methyl-4,5,6,7-Tetrahydrothieno[2,3-C]Pyridine-3-Carbonitrile Synthesis and Investigation - Naki ÇOLAK, Saliha ALTINER, Nursabah SARIKAVAKLI	213 - Comparison of Different Variables on Aspergillus terreus in Different Fermentation Types - Nermin GUMUSTAS, Aytac KOCABAS	094 - Assessment of heavy metal contamination in the Golden Horn estuary sediments, Turkey - Bedri Alpar, Selma Ünlü
09A	300 - Chemical Constituents of Sideritis phrygia BORN. with Antimicrobial and Antioxidant Activities - Sema ÇARIKÇI, Zuleyha SAĞIR, Turgut KILIÇ	216 - Evaluation of Mycotoxin Content of Different Trademarks of Turkish Ravioli in Karaman Province of Turkey - S. GOKMEN, M.F. AYDIN, A. KOCABAS, A. SAYASLAN, H. YETİM, A. CAGLAR	249 - Plasma Paste Boriding of 21NiCrMo2 Steel Using Borax Paste for Multiple Gas Mixtures - Şükrü ÜLKER, Şükrü TAKTAK, İbrahim GÜNEŞ
09B	284 - The evaluation of the adsorption properties of the orange peels as a (bio)sorbent material: The removal of the Cu(II) and Ni(II) - A. Berisha, K. Jusufi, J. Halili, V. Mehmeti, F. Ferataj, J. Hasanaj, B. Korça	226 - Synthesis and Characterization of Novel Antimicrobial Active Benzoxanthene Carboxamide Derivatives - İbrahim Esirden, Pınar Sola, Erhan Başar, Muharrem Kaya	472 - The Effects of Feather Color on Hatchability Traits, Growth Performance, and Survival Rate in Japanese Quails - Kadir ÖNK, Mehmet SARI, Muammer TILKI, Serpil ADIGÜZEL İŞİK, Tuncay TUFAN
10A	324 - Determination of antioxidant activities of grape seed extracts by FRAP, HRSa and MCA methods - Ayşe SARIÇAM, Serap COŞANSU AKDEMİR, Omca DEMİRKOL	153 - Biosynthesis potential of Bacillus subtilis K101 for biocompatible and biodegradable CaCO3 nanoparticles - I. Akmayan, O. Baris, M. Gulluce, M. Karadayi, H. Akoguz, N. Hidiroglu	522 - The Examination of Viscosity Properties of Aluminum powder reinforced polypropylene - Abdulmecit GÜLDAŞ, Mehmet ALTUĞ, Servet TEMEL
10B	312 - Evaluation of the phenolic content of Sideritis trojana and S. athoa tea decoction and infusion - Sema ÇARIKÇI	508 - Polymer Modified Mortars Based on Fly Ash - Raman Aliti, Anita Grozdanov, Slobodan Bogoevski, Perica Paunovic, Goran Nacevski	024 - Nanoindentation study of CoCrMo alloys having different Pd additive - Osman Sahin, Suleyman Uzunoglu, Selma Ozarslan, Emine Sahin
11A	345 - Inhibition effect of the heterocyclic mercapto compounds on corrosion of copper in sulphuric acid solution - V. Mehmeti, K. Kalcher, A. Berisha, J. Halili, K. Jusufi, A.N. Halili, F. Podvorica	286 - Detection of Total Annual Rainfall Trends of Elazığ City, Turkey - Serkan ŞENOCAK, Muhammed Fatih EMEK, Reşat ACAR	102 - H-aggregates of Pyronin Y in aqueous solution containing graphene oxide sheets - Mehmet ŞİNOFOROĞLU, Bahri GÜR, Mustafa ARIK, Yavuz ONGANER, Kadem MERAL
11B	Evaluating water quality classes and trophic level for Lake Sapanca Basin - Seda Tünay, Temel Temiz, Osman Sönmez, Beytullah Eren, Mahnaz Gümrükçüoğlu, Rabia Köklü, Emrah Doğan, Bülent Şengörür	517 - PVC Membrane Electrode for The Potentiometric Determination of Iodide - Semra Muratoğlu, Ayça Demirel Özel	101 - Effect of Fish Manure and Nitrogen Fertilization on Growth and Yield of Radish (Raphanus sativus) - Raziye KUL, Ertan YILDIRIM, Melek EKİNCİ, Gonca ALAK, Muhammed ATAMANALP
12A	298 - The estimation of the sorption capacity of orange peels toward the analytical indicator - methyl orange - Kaltrina Jusufi, Avni Berisha, Jeton Halili, Bardha Korça, Valbonë Mehmeti	518 - Development Sensor Based System Software for the Control of Motor And Axis Motion on the CNC Turning Machine - Metin ZEYVELİ, Kürşat Mustafa KARAOĞLAN	512 - Functionalization of Polyester Knitted Fabrics by Dyeing with Multi-Walled Carbon Nanotubes - Nergis DEMİREL GÜLTEKİN, Cenkcut GÜLTEKİN, Ali BEYİT, İsmail USTA
12B	473 - Perchlorate-Selective Carbon Paste Electrode Based on A Calix[4]Arene Derivative - H. Elif Kormalı Ertürüna*, Ayça Demirel Özela, Özlem Şahinb, Mustafa Yılmazb, Esmayigider	519 - A Universal Machine Converting to Computer Numerical Control Machine with Microcontroller and Concurrent Control - Kürşat Mustafa KARAOĞLAN, Metin ZEYVELİ	
13A	029 - Molecular identification of Dunaliella sp. isolated from Ayvalık Saltern and Seyfe Lake - Zeliha Demirel, Esra Imamoğlu, Meltem Conk Dalay	470 - Web Server Security Scanner Application - Ali Buldu, Fuat Muminoglu, Resat Marzioglu, Kazim Yıldız, Volkan Yusuf Senyurek	
13B	071 - β-glucan Content and Antioxidant Activities of Boletus edulis - Özgür ÖZCAN, Figen ERTAN	269 - The LOX-1 3'UTR188C/T polymorphism in patients undergoing coronary artery bypass grafting - B. Aydemir, O. Baykara, İ. Onaran, T. Oner, C. Arslan, B.Cinemre, A.R. Kıziler, G. Kanigur	
14A	418 - Investigation of Roof and Terrace Gardens as an Alternative Green Area Model For Cities: A Case Study for Adana - Fűrüzan Aslan, Atilla Atik, Meltem Çetinman	270 - Variations in NFKB1, NFKBIA and pre-miR-499 Genes Contribute to Susceptibility to Atherosclerosis in Turkish Population - T. Oner, C. Arslan, B. Arapi, C. Tel, B. Aydemir, G. Kanigur	
14B	079 - Functional Liver Stress In Dairy Sheep During Summer Season - Amina Hrkovic-Porobija, Aida Hodzic	272 - Preliminary Report on Association of Anti-Saccharomyces Cerevisiae Antibodies with Vitamin D Deficiency - H. Cinemre, F.B.S. Cinemre, B. Aydemir, C. Karacaer, A. Nalbant, T. Kaya, A. Tamer	

	SESSION 09:00:00	SESSION 11:00:00	SESSION 13:30:00	SESSION 15:30:00
01A	100 - Polycyclic Aromatic Hydrocarbons (PAHs) in sediment as markers of contamination sources in the Sea of Marmara, Turkey - Selma Ünlü, Bedri Alpar, Koray Başeğmez	041 - Landslide Investigation Using Electrical Resistivity Imaging and Self-Potential Profiling - Sedat YILMAZ	404 - Investigation of Effect of Sewing Thread on Heating of Sewing Machine Needle - Vedat DAL, Mahmut KAYAR	385 - Evaluation of buildings strength from microtremor measurements: A case of Folkart Towers (Izmir/Turkey) - Emre Timur, Sinancan Öziçer
01B	181 - Application of the Environmental and Safety Integrated Management Systems in the Energy Sector - Bülent Şengörür, Rabia Köklü, Asude Ateş	082 - Investigation of Reinforcement Corrosion Effect on Concrete Strength by Seismic Velocities - Nevbahar Sabbağ, Osman Uyanık	061 - Effect of Nonionic and Anionic Surfactants on Endoglucanase - Saime Nur DEMİR, Selmihan SAHİN, İsmail OZMEN	450 - Recovery of copper and cobalt from copper slags as selective - Uyan YÜKSEL, İbrahim TEĞİN, Recep ZİYADANOĞULLARI
02A	489 - Investigation of a New Half Cloverleaf Intersection on the Regional Traffic by Vissim - O.Ü. BAYRAK, F. HATTATOĞLU, H.F. BAYATA, M.A. ÇOLAK, S. HINISLIOĞLU, N. TEPE	026 - The Synthesis of Novel Thiosubstituted 1,4-Naphthoquinone Compounds - Zeliha Özsoy-Güneş, Cemil İbiş	087 - Control of The Energy Flow with PLC for Battery Supported Hybrid Generation System in Case of a supplying to Local Area - Y.B. KOCA, A. YÖNETKEN, Y. OGUZ, T. ÖZER	453 - Syntheses of Potentially Active Triazoles from Carbohydrates and Nucleobases - Erkan HALAY, Emriye AY, Tamer KARAYILDIRIM, Kadir AY
02B	222 - Nanocomposite of cement paste/graphene composite and functionalized nanosilica - hydration kinetics and early stage response - Sylwia Mijowska, Ryszard J. Kalerćzuk	154 - The Investigation of Tribological Properties of Ceramic Filled Polypropylene Composites - Gürhan DENİZ, Ferhat YILDIRIM, Murat ÇOLAK, Salih Hakan YETGİN	095 - Load Frequency Control by PID, Fuzzy And Fuzzy - PID in a Three Areas Power System - Kadir Güler, Yüksel Oğuz, Ahmet Yönetken	459 - The Effect Of Fibre Characteristics On The Breaking Elongation Properties Of Cotton Siropun Yarns - Tuba Bedez Ute, Huseyin Kadoglu
03A	261 - A kinetic modeling study of phosphate removal onto modified bentonite clay - Mehtap Tanyol	072 - Edge detection applications of magnetic anomalies of Gölcük caldera, Isparta, SW Turkey - M.Nuri Dolmaz, Ezgi Erbek, Erdinc Oksum, H.Evrin Tutunsatar	127 - Input and Output Matching Circuits Design For Low Noise Amplifiers By Using Tapered Microstrip Lines - Mehmet Yerlikaya	461 - Investigating Mechanical Properties of Composites Prepared by Three Dimensional Hybrid Fibers - Yalçın BOZTOPRAK, Mustafa ÇAKIR, Mahmut KAYAR, Haluk DUGA, Vedat DAL
03B	275 - An adsorption study of methylene blue from aqueous solution with a low cost material - Nur Ayaz, Rabia Koklu, Cigdem Ozer	125 - Evaluation of gravity and magnetic imprints of the Eastern Anatolian Collision Zone - M.Nuri Dolmaz, Erdinc Oksum, U.Yalcin Kalyoncuoglu	134 - Self-organization of nanostructures using a buried square network of screw dislocations - Salah MADANI	466 - Optimization of physical and mechanical properties of the mealegris gallopova hydroxyapatite-magnesium oxide composites - Serdar PAZARLIOGLU, Selim HARTOMACIOGLU, Serdar SALMAN, Ayhan ONAT
04A	290 - Removal of organic molecules by bio-sorption process using activated banana peels as sorbents - A. Berisha, K. Jusufi, F. Podvorica, V. Mehmeti, T. Selimi, M. Sadiku	184 - Determination of Leakage Area in an Earth Dam Using Geo-Electrical Methods - Sedat YILMAZ	045 - New supported liquid membranes containing dioxime derivatives as ion carrier for facilitated transport of mercury ions - Fatma Karipcin, Esin Karamizrak, Esengül Kir, Hamza Korkmaz Alpoğuz	492 - A different Approach for the Prediction of Fabric Spreading Time in Cutting Department of Apparel Companies - Yelda KARATEPE MUMCU, Mahmut KAYAR
04B	296 - Removal of Heavy Metal Ions Cu(II) and Ni(II) from Aqueous Solutions Using Banana Peels As a (Bio) Adsorbent Material - K. Jusufi, A. Berisha, V. Mehmeti, B. Korça, J. Halili, J. Hasanaj, F. Ferataj	292 - Numerical Investigation of Pressure Drop of Al2O3 Nano-Dispersion in Water at Common Components of Pipe System - D.E. Alnak, B.Teymur, N.Tokgöz, B. Yaniktepe, C. Özalp	TBA	496 - Ship Financing Techniques in Turkey - Ersoy KACMAZ
05A	360 - Assessment of pollution at sea caused by vessel with nixous liquid substances and oil products - Ersoy KACMAZ, Gökhan KARA	325 - 3D Inversion of Airborne Magnetic Anomalies by Differential Evolution: a Case Study from the Biga Peninsula (NW Turkey) - Çağlayan Balkaya, Yunus Levent Ekinci, Gökhan Göktürkler	051 - The effects of TritonX-100 on the formation by using sol-gel grown of Cu2SnS3 - H. Ali Çetinkara, Samed Çetinkaya, Süleyman Kahraman, Sinan Yaşar, İsmail Bilican	037 - Protective effects of Coenzyme Q10 and Resveratrol on ZnO-TiO2 induced oxidative stress on D. Melanogaster - Deniz Altun Çolak, Handan Uysal
05B	007 - Production and Characterization of Al-Tic Composite Materials - A. Yonetken, A. Erol, M. Cakmakaya, Y. Oguz	448 - Cage Culture Potential of Rainbow Trout in Seyhan Dam Lake - Suat Dikel, Mustafa Öz, İlgin Özşahinoğlu, N.Burak Ünal	074 - Determination Of Cellulase Producing Thermophilic Bacteria Isolates - Selmihan SAHİN, İsmail OZMEN, Gamze BASBULBUL	008 - Parameter Estimation From Residual Gravity Anomalies of Subsurface Cavities Using Modeling Optimizations - Fikret Doğru
06A	021 - Characterization of Cu-Cr-Sic Composite Materials - A. Yonetken, A. Erol, H. Kaplan	523 - Structural investigation of Methyl 4'-[[3-methylphenyl] (phenyl) amino] biphenyl-4-carboxylate molecule for OLED - M. Kurt, E.B. Sas, M. Can, S. Okur, S. İçli, S. Demic	483 - An Experimental Investigation of the Effects of Runner Profiles on the Flows in the Plastic Injection Molds - Abdulkadir GÜLLÜ, Abdulmecit GÜLDAŞ, Resul TÜRK	016 - Energy analyse and management: A sample of milk factory in Turkey - Öznur Ö. Taner, Tolga Taner, Hüseyin Topal
06B	022 - Effect of Cobalt Doping on Nanostructured CuO Thin Films Deposited by SILAR Method - Fatih Bayansal, Turan Taşköprü, Bünyamin Şahin, Hacı Ali Çetinkara	490 - Modeling of Marshall Quotient of Hot Mix Asphalts by Artificial Neural Networks - Fatih HATTATOĞLU, H. Ferit BAYATA, Sinan HINISLIOĞLU, O. Ünsal BAYRAK, Neslihan TEPE	047 - Defluoridation from aqueous solutions by natural and acid activated Ignimbrite and Diatomite materials - Esengül Kir, Hatice Oruç, İsmail Kir	017 - Landscape Planning and Management for River Catchments of Hydroelectric Power Plants for Turkey - Havva Ülgen Yenil, Tolga Taner
07A	099 - Investigation of the diffusion kinetics of borided cold work tool steel - Salih KANAT, İbrahim GUNES	491 - Intermodality in Urban Transport: The Case of Istanbul - Olgay OKSAS	488 - Spectroscopic and Micro-chemical Analyses for the Characterization of a 15th Century Old-Slavonic Illuminated Manuscript - M. Kostadinovska, B. Minčeva-Sukarova, O. Grupče, Z. Jakovleska-Spirovska	124 - - Mathematical model to increase the sound absorption ability of textile floor coverings - M. Akdere, M. Uzun, G. Seide, T. Gries
07B	112 - Production of Al Based B4C Reinforced Foamable Composite Materials and Investigation of Their Mechanical Properties - Arif Uzun, Mehmet Turker	527 - Comparison of the house dust mites seen in living rooms and bedrooms in Erzurum (Turkey) - Erhan Zeytun, Salih Doğan, Fatih Özçiçek, Edhem Ünver, Sibel Dilkaraoğlu	177 - Noise Filtering on 3D Point Clouds Using Point Cloud Library - Murat Olcay Özcan, Deniz Taşkın, Kenan Baysal	172 - Investigation of Mechanical Properties of Chassis Profile Designed for Light Vehicles - Deniz Soyel Doğan, Ahmet Demirer
08A	144 - Materials Selection for Car Bumper with a Conventional Method As Well As CES Selector Software - Fehim FINDIK, Murat ÇOLAK	230 - Optimization of Structural Frame Sections for the Protection of Living Space for the Bus Rollover - M. Durat, F. Fiçici, M. Kapsız, E. Varol	195 - Testing a VHDL Design Using Open Source VHDL Verification Methodology - Kenan Baysal, Deniz Taşkın, Onur Bulut	456 - Investigation of different electrocatalysts (CCuZn, CCuZn-Ru) for production of hydrogen gas - Esra TELLİ, Coşkun ÖZALP, Gülfeza KARDAŞ
08B	145 - The Investigation of Wear Properties of Sıc Reinforced Polypropylene Composite - Salih HAKAN YETGİN, Murat ÇOLAK, Ferhat YILDIRIM, Gürhan DENİZ	175 - Modal analysis of a new electro-hydraulic dual axis solar tracking system prototype using the finite element method - Toufik OUTTAS and Fateh FERROUDI	220 - Convenience of Digital Design with FPGA - Onur BULUT, Deniz TAŞKIN, Murat Olcay ÖZCAN	303 - Isolation and Characterization of Bacterial Flora from Digestive System of Eusomus ovulum (Curculionidae) - H. ÖĞÜTCÜ, Y. ERBEY, M. ERBEY, S. SEZEN, M. KARADAYI, M. GÜLLÜCE
09A	040 - The effects of Cooking Conditions on the Total Polar Materials of Biodiesel Produced from Waste Frying Oils - Tuba Hatice DOĞAN	231 - Nutritional Composition of the Wild Edible Mushroom Agaricus lanipes Collected from the Gireniz Valley of Denizli - K. Gezer, O. Kaygusuz, M. Koizhaiganova, E.N. Herken, Y. Dodurga, M. Seçme, Y. Saldır	225 - Adaptive Filters for Speech Noise Cancellation - Motuma M.Abafoji, Ridvan Firat Cinar, Askin Demirkol, Zafer Demir	306 - Isolation and Identification of Rhizobium Strains of Wild Leguminous Species Collected from Kırşehir - Hatice ÖĞÜTCÜ, Ali BAŞYİĞİT
09B	096 - Fire Behavior and Compressing Strength of Cement Based Composites and Cellulosic Panels Produced for Thermal Insulation - Gülşah Torun, Özlem Korkut	206 - Gas Turbine Blade Leading Edge Cooling Effectiveness Based on the Distance of Turbulence Promoters - Azize AKCAYOGLU, Celal NAZLI, Fuat YILMAZ	276 - The Study on Effective Company Applications for Apparel Consumers' Online Buying Decisions - Mahmut KAYAR, Ayfer ÜNVER	067 - Investigation of dithiothreitol and sucrose in bull semen cryopreservation - Olga Büyükleblebici, Pürhan Barbaros Tuncer, Umur Taşdemir, Serhat Büyükleblebici, Emre Durmaz
10A	462 - Investigation of Ballistic Properties of Hybrid Composites - Yalçın BOZTOPRAK, Mustafa ÇAKIR, İlyas KARTAL, Halil DEMİNER	210 - Effect of dynamic stresses and geometric deformations on the fatigue strength - K. Lebcik, T. Outtas	380 - Estimation Of Effect Of Fabric Width And Assortment Distribution On Fabric Usage Efficiency By Neural Network Method - Mahmut Kayar, Yelda Karatepe Mumcu	068 - Comparison of Cryoprotective Effects of Trehalose and Cysteine in Different Cryoprotectants on Bull Semen - Serhat Büyükleblebici, Umur Taşdemir, Pürhan Barbaros Tuncer, Olga Büyükleblebici
10B	465 - Green synthesis of Ag/Au nanoparticles, attachment on the SiO2 microsphere surface and its antibacterial activity - Süreyya Kadioğlu*, Ahmet Balci, Merve Girgin	229 - Structural Analysis of the Wheel Vehicle's Suspension Carrier - M. Durat, F. Fiçici, S. Karakulak, Z. Ayparçası	425 - Effect of Black Cumin Oil (Nigella sativa) on the Growth Performance, Body Composition and fatty acid profile of Rainbow Trout - Mustafa ÖZ, Suat DİKEL, Mustafa DURMUŞ	386 - Geophysical investigation of Gülbahçe geothermal area (Urla/Izmir) using VLF-R method - Emre Timur
11A	215 - Available and Toxic Heavy Metal Concentrations in Soil and Compost - Emine Elmaslar Özbaş, H. Kurtuluş Özcan, Göksel Demir	138 - A New Species of Zercon C. L. Koch, 1836 (Acari, Zerconidae) for Turkish Fauna: Zercon juvarae Çalugar, 2004 - Raşit URHAN, Mehmet KARACA, Elif Hilal DURAN	429 - Detection of Neuraminidase Activities in Bovine and Human Group B Streptococci - İsmail Hakkı EKİN, Kemal GURTURK, Suat EKİN, Ziya İLHAN, Ozgul GULAYDIN, Cigdem ARABACI, Hasan SOLMAZ	084 - Investigation of Building Foundation Type By Microtremor Method - Osman Uyanık, Sinancan Öziçer, Emre Timur, Nevbahar Sabbağ
11B	182 - Sapanca Lake Air Pollution Originating from transportation- Investigation of Heavy Metal Emissions - Hülya Demirel, Asude Ateş, Seref Soyulu	247 - Investigation of the Tribological Performance of Doped Semi-Synthetic Engine Oil - Murat KAPSIZ, Ferit FIÇICI, Ramazan ŞENER	432 - Development and Validation of a Multiresidue Method for the Determination of Pesticide Residues in Water by GC-NPD - Bahar Bayrak	020 - Examination of Tensile Rupture Testing on ADSS Cable - İbrahim Güneş
12A	214 - Effect of Municipal Solid Waste (MSW) Compost on Growth of Phaseolus vulgaris - Emine Elmaslar Özbaş, V. Zülal Kiremitci, Nüket Sivri	046 - Preparation and characterization of magnetic polysulfone /thiourea microspheres and its application for the removal of Cr (III) - Esengül Kir, Tuğba Yiğit, Fatma Karipcin, Tuğba Sardohan Köseoğlu	139 - A New Record of Mesostigmatid Mites for Turkish Fauna from Kırklareli - Mehmet KARACA, Raşit URHAN, Elif Hilal DURAN	321 - A Comparative Study on Target Density Functions - Ridvan Firat Cinar, Askin Demirkol, Motuma M. Abafoji, Zafer Demir
12B	274 - Foraminiferal Biostratigraphy of the middle Eocene in the Eastern Part of the Malatya Basin, Eastern Anatolia - M. Kaya, D. İbilioğlu, G. Gülmez, A.Ö. Önal	307 - Performance Analysis of Turbocharged Two-Stroke Diesel Engine - Yasin Ust, Umit Gunes, Asim Sinan Karakurt	434 - Antimicrobial Activities of Four Perylenediimides - Şafak Yağan, Funda Yükrük, Gülhan Vardar Ünlü	
13A	267 - Effect of Wax and Polytetrafluoroethylene on Tribological Properties of Fibre Glass Filled Polyphenylene Sulfide Composites - F. YILDIRIM, S.H. YETGİN, M. ÇOLAK, G. DENİZ	311 - Effects of Piston Motion on Specific Surfaces of the Cylinder Liner in a Compression Ignition Engine - Mehmet Cakir, İsmail Hakkı Akcay	435 - Development A Solid-Phase Extraction Method For Separation And Preconcentration Of Nickel Ions Using Rhodococcus ruber Biomass - Esin Kiray, Ergin Kariptas, Cigdem Er, Harun Ciftci	
13B	085 - Comparison of Laboratory and In-Situ Concrete Strength Results - Osman Uyanık, Nevbahar Sabbağ, Sinancan Öziçer	349 - Experimental and theoretical studies on corrosion behavior of some mono and polyhydroxy aromatic derivatives on mild steel - Valbonë Mehmeti, Kurt Kalcher, Avni Berisha, Kaltrina Jusufi	439 - An Analytical Method For Separation And Preconcentration Of Indium Ions On Activated Carbon From Vine Shoots - Harun Ciftci, Cigdem Er, Esin Kiray, Ergin Kariptas, Esen Ciftci, Mehmet Erdem	
14A	083 - The Importance of Using Seismic Ultrasonic Velocities Together In Determining of Concrete Strength - Osman Uyanık, Nevbahar Sabbağ, Buket Ekinci, Ziya Öncü	356 - Investigation of Effect of Ultrasonic Sewing Speed on Ultrasonic Seam Tensile Properties - Mahmut KAYAR, S. İlker MİSTİK, Sinem GÖK	443 - Recovery of Copper And Cobalt From Converter Slag By A Novel Flotation Method - İbrahim Tegin, Recep Ziyadanoğulları	
14B	039 - MBDEPX4: An interactive tool for Curie Point Depth (CPD) estimation from spectral analyzes of magnetic data - Erdinc OKSUM, M. Nuri DOLMAZ, Z. Mümtaz HISARLI	389 - Experimental Performance Analysis of a Desiccant Cooling System - Osman KARA, Ertaç HÜRDOĞAN, Orhan BÜYÜKALACA, Tuncay YILMAZ	073 - Investigation of Industrial Applications of Cellulase - Selmihan Sahin, İsmail Ozmen, Hacı Halil Byık	

TABLE OF CONTENTS

- 1-6 **Determining the awareness level of the use of parks for the handicapped in the example of Malatya**
Atilla ATIK, Fűrüzan ASLAN
- 7-14 **Physical Activity Prediction: Accelerometers or Gyroscopes?**
Musa Hakan Asyalı, Ömer Kayaaltı
- 15-20 **Determining the Risks in Maritime Container Terminal Operations: Health and Safety Applications**
E. GülEmecen Kara, Ersoy Kaçmaz
- 21-25 **Removal efficiency of the herbicide aclonifen by soil fungi**
Gokhan Onder Erguven, Hurrem Bayhan, Bahar Ikizoglu, S. Levent Kuzu, Gurdal Kanat, Yasar Nuhoglu
- 26-31 **Natural Gas Consumption and Its Effect on Air Emissions In Turkey**
Ali CAN, Halil EKMEKCI
- 32-39 **Carnitine levels in milk and milk products**
Rabia Serpil GÜNHAN, Suzan YALÇIN
- 40-49 **Investigation of the diffusion kinetics of borided cold work tool steel**
Salih KANAT, Ibrahim GUNES
- 50-55 **The Impact of Climate Change on Maritime Transport Routes**
Gökhan Kara
- 56-60 **Effect of Magnet Materials on the Efficiency of Line Start Permanent Magnet Synchronous Motor**
Seda Kül, Osman Bilgin
- 61-69 **Analytical Investigation of the Stress Distribution in the Beam end Connector in Storage Rack Systems**
Yaşar Pala, Emre Çalış, Murat Reis
- 70-78 **Integrated Dynamic Analysis of a Six Axis Serial Robot**
Şahin Yavuz, Hira Karagülle
- 79-86 **A Statistical Model for Predicting Yarn Evenness of Cotton Sirospun Yarns**
Tuba Bedez Üte, Hüseyin Kadoğlu

TABLE OF CONTENTS

- 87-93 **Evaluation of Maritime Safety in Istanbul Strait Using Port State Control Inspections**
E. Gül Emecen Kara, Olgay Okşaş
- 94-99 **Animal Manure Effect on Climate Change and Usage as a Energy Sources in Turkey**
Ali CAN
- 100-107 **Evaluation of Turkish Straits Vessel Traffic Services (TSVTS) Applications in the Istanbul Strait**
Gökhan KARA
- 108-114 **Vibration Control of an Onelink Flexible Manipulator with Harmonic Excitation**
Şahin YAVUZ, Hira KARAGÜLLE
- 115-120 **The Effect of Fibre Characteristics on the Breaking Elongation Properties of Cotton Sirospun Yarns**
Tuba Bedez ÜTE, Hüseyin KADOĞLU
- 121-133 **Slope Stability Analys Method Of Account Back And Examination Of Tekke Landslide With Back Analysis Method**
Mümin FILİZ, Semiha GÖKCAN
- 134-143 **An investigation of the effects of additive type and amount on mortar phase**
Osman ÜNAL, Kadir AKYÜZ, Kadir GÜÇLÜER
- 144-151 **Parameter Estimation From Residual Gravity Anomalies Of Subsurface Cavities Using Modelling Optimizations**
Fikret DOĞRU
- 152-158 **Providing Engineering Solutions to Forest Fire Access Problems Using Network Analysis Method**
Abdullah E. AKAY, Hande E. KILIÇ
- 159-163 **Flocculation of Waste Water from Coal Washing Plant by Polymers in Turkey**
Selma DÜZYOL, Berk ERÖZ, Tevfik AĞAÇAYAK, Ali ARAS
- 164-168 **Kinetics of Fine Dry Grinding of Barite in a Laboratory Steel Ball Mill**
Ali ARAS, Salih AYDOĞAN, Alper ÖZKAN
- 169-172 **Assessment of Heavy Metal Contamination in the Golden Horn Estuary Sediments, Turkey**
Bedri ALPAR, Selma ÜNLÜ

TABLE OF CONTENTS

- 173-181 **Production of B4C Reinforced AlSi7 Foamable Composite Materials and Investigation of Their Mechanical Properties**
Arif UZUN, Mehmet TÜRKER
- 182-190 **Astronomical Aspects of the Cult Practise of the Peak Sanctuary Kokino**
Olgica KUZMANOVSKA, Jovica STANKOVSKI
- 191-198 **Using Base Algorithms Combinatorially in Adaboost Ensemble for Intrusion Detection**
Necati DEMIR, Gökhan DALKILIÇ
- 199-208 **Materials Selection for car Bumper with a Conventional Method as well as CES Selector Software**
Murat ÇOLAK, Fehim FINDIK, Salim ASLANLAR
- 209-215 **Identification of Waste Sources in Ready-Mixed Concrete Plants**
Aynur KAZAZ, Serdar ULUBEYLI, Ahmet ARSLAN, Bayram ER, Murat ATICI
- 216-220 **Evaluation of Current Recycling Facilities for RMC Plants in Turkey**
Aynur KAZAZ, Serdar ULUBEYLI, Ahmet ARSLA
- 221-225 **Gaussian And Wavelet Filtering Methods For Michelson Interferometric Expansion Measurement**
Veysel Gökhan BÖCEKÇİ, Volkan Yusuf SENYUREK
- 226-233 **Determination of Failure Distribution Parameters for Welding Machines Used in Ship Construction**
Baha GÜNEY, Çağatay TEKE
- 234-242 **Numerical Investigation of Convective Heat Transfer Characteristics of TiO₂/Water Nanofluid in a Trapezoidal Microchannel**
Tuğçe İŞGÜZAR, Kamil ARSLAN, Cüneyt UYSAL, Hüseyin KURT
- 243-248 **Adaptive Filters for Speech Noise Cancellation**
Motuma ABAFOGI, Askin DEMIRKOL, Ridvan Firat CINAR, Zafer DEMIR
- 249-254 **Aerodynamic Simulation of a Traditional High-Speed Train with Different Head Angles**
Gürhan KÜLAHLI, Hilmi YAZICI, Mehmet AKÇAY
- 255-261 **E-invoicing in turkey and a software-as-a-service solution**
Ahmet OZCAN, Salim ERYIGIT
- 262-268 **The Correlation between Cpu Core Temperatures of a Server under Specific Cooling Systems**
Serhat Orkun TAN, Hüseyin DEMİREL

TABLE OF CONTENTS

- 269-275 **Application properties of groundnut hull/epoxy composites**
Gülcihan GÜZEL, Hüseyin DEVECI
- 276-282 **Plasma paste boriding of 21nicrmo2 steel using borax paste for multiple gas mixtures**
Şükrü ÜLKER, Şükrü TAKTAK, İbrahim GÜNEŞ
- 283-291 **The effect of wax and polytetrafluoroethylene on tribological properties of fibre glass (gf) filled polyphenylene sulfide composites**
Ferhat YILDIRIM, Murat ÇOLAK, Salih Hakan YETGIN, Gürhan DENİZ
- 292-297 **Thermal Analysis of New Molten Salts Electrolyte for Medium Temperature Thermal Batteries**
Ahmet KOCA, Fethi DAGDELEN, Hakan F.ÖZTOP, Gamze Pelin AKSOY, Yasin VAROL
Mehmet Cem MENTES, Fahrettin YAKUPHANOĞLU, Aysegul DERE
- 298-303 **Detection of Total Annual Rainfall Trends of Elazığ City, Turkey**
Serkan ŞENOCAK, Reşat ACAR, Muhammed Fatih EMEK
- 304-313 **Proposals for the Protection of Water Resources in the Prespa Lake Basin, Greece**
Romanos – Vasileios ARAVIADIS
- 314-320 **Employee Selection with Analytic Hierarchy Process in Clothing Sector: Turkish Case**
Seher KANAT, Turan ATILGAN
- 321-326 **The Effects of Franchising System on International Marketing Strategies: Turkish Clothing Sector Case**
Turan ATILGAN, Seher KANAT
- 327-333 **Modelling of Specific Cutting Resistance in Machining of AISI P20 Plastic Mould Steel**
Nafiz YAŞAR, Mustafa GÜNAY, M. Erdi KORKMAZ, Ulvi ŞEKER
- 334-342 **Optimisation of Tool Edge Geometry and Cutting Parameters in Hard Turning of AISI 52100 Using Taguchi Method**
Mehmet BOY, Mustafa GÜNAY, Halil DEMİ, İbrahim ÇİFTÇİ
- 343-347 **Improvement of Laundering Durability of Polypyrrole Coated Cotton Fabrics**
Zehra YILDIZ, İsmail USTA, Onur ATAĞ
- 348-356 **A Comparative Study on Target Density Functions**
Ridvan Firat CINAR, Motuma M. ABAFOĞI, Zafer DEMİR, Askin DEMİRKOL
- 357-362 **Investigation of Physical Properties of Woolen Fabrics on Thermal Comfort**
Zehra YILDIZ, Vedat DAL, Ahmet Berk KURTULUS, Abdurrahim YILMAZ, Engin AKCAGUN
Nuray Oz CEVİZ, Mustafa ATMACA

TABLE OF CONTENTS

- 363-369 **Removal of Color and COD from Wastewater of a Local Textile Factory by Coagulation**
Müslün Sara TUNÇ, Özlem TEPE
- 370-378 **Analysis and Design of Passive and Active Interconnected Hydro-Pneumatic Suspension Systems in Roll Plane**
Ferhat SAĞLAM, Y. Samim ÜNLÜSOY
- 379-386 **Numerical Investigation of the Effect of Objects with Different Profiles on Flow Characteristics**
Mehmet AKÇAY, Gürhan KÜLAHLI, Hilmi YAZICI
- 387-392 **Removal of Phenol from Aqueous Solutions by Photo-Fenton Process**
Özlem TEPE, Arzu Y. DURSUN
- 393-397 **Evaluation of Tank Container Logistics in Turkey**
Olgay OKŞAŞ, Gökhan KARA
- 398-405 **Detection of the weld damages by lamb wave technique**
Volkan Yusuf ŞENYÜREK, Mustafa DEMETGÜL, Hüseyin YÜCE
- 406-410 **Investigation of Practical Design Approach for Circular Steel Base Plates**
Mutlu SEÇER
- 411-415 **Production of Alumix 13 Based Metal Foams Using Powder Metallurgy**
Halil KARAKOÇ, Hanifi ÇINICI, Ramazan ÇITAK
- 416-420 **Computational Hydrodynamic Analysis of Turbulent Duct Flow**
Selcuk SELIMLI, Ziyaddin RECEBLI, Erol ARCAKLIOGLU
- 421-424 **CFD Thermophysical Analysis of MHD Turbulent Pipe Flow**
Ziyaddin RECEBLI, Selcuk SELIMLI, Erol ARCAKLIOGLU
- 425-431 **Web Server Security Scanner Application**
Ali BULDU, Fuat MUNINOGLU, Kazim YILDIZ, Resat MARZIOGLU, Volkan Yusuf SENYUREK
- 432-437 **Application of Digital Image Correlation in Uniaxial Tensile Test**
Murat AYDIN, Xin WU, İbrahim KADI, Kerim ÇETINKAYA, Mustafa YAŞAR
- 438-445 **The Microstructure and Hardness Analysis of Decarburization Followed by Boronizing AISI D3 Tool Steel**
Arzum ULUKÖY, Yavuz KAPLAN, Merve YILDIZ, Okan ÇARIK, Volkan ONAR, Emre ARMAĞAN, Ahmet Çetin CAN

TABLE OF CONTENTS

- 446-454 **Determination of The Effects of Operating Parameters on The Residual Turbidity of Quartz Suspensions by Design of Experiments**
Adem TAŞDEMİR, Tuba TAŞDEMİR
- 455-463 **The Parametric Study on Intercooler in Turbocharger Diesel Engine**
Yasar SEN, Kemal ERMIS
- 464-471 **A New Modified Shah Correlation on Condensation Heat Transfer in Plain Tubes**
Yasar SEN, Kemal ERMIS
- 472-483 **Controlled Recirculation in Ventilation of Underground Mines- Applications in Turkey and in the World**
İbrahim ÇINAR, Cem ŞENSÖĞÜT
- 484-487 **Dry Sliding Wear Behaviors of Cast Fe₃Al and Fe_{32.5}Al₁₅Ti**
Osman TORUN
- 488-495 **Energy Efficiency Enhancement of a Household Refrigerator Using With Oil Cooling Condenser**
Erdoğan KILIÇASLAN, Alper ERGÜN, Engin GEDIK, Bahadır ACAR, Engin ÖZBAŞ
- 496-503 **Evaluating Water Quality Classes And Trophic Level For Lake Sapanca Basin**
Seda TÜNAY, Temel TEMİZ, Osman SÖNMEZ, Rabia KÖKLÜ, Beytullah EREN, Emrah DOĞAN Mahnaz GÜMRÜKÇÜOĞLU, Bülent ŞENGÖRÜR
- 504-509 **Application of the Environmental and Safety Integrated Management Systems in the Energy Sector**
Asude ATEŞ, Bülent ŞENGÖRÜR, Rabia KÖKLÜ
- 510-513 **The concept of urban forest in Turkey, situation today and targets**
Atilla ATIK, Fürüzan ASLAN
- 514-519 **Determination of public expectancy and approach of urban people towards urban forest: sample of Malatya-Turkey**
Atilla ATIK, Fürüzan ASLAN
- 520-527 **Numerical Analysis on Oxy-Fuel Combustion for Different Mixture Rate**
Barış GÜREL, Mehmet KAN, Osman İPEK
- 528-532 **Converting a universal machine to computer numerical controlled machine with microcontroller and concurrent control**
Metin ZEYVELİ, Kürşat Mustafa KARAOĞLAN

TABLE OF CONTENTS

- 533-540 **Effect of Microwave Pretreatment on Nickel Extraction from Lateritic Nickel Ore in Hydrochloric Acid**
Merve KÖSELER, Selma DÜZYOL, Tevfik AĞAÇAYAK
- 541-548 **Numerical investigation of al₂o₃-water nanofluid flow and heat transfer in sudden expansion channels**
Muhammed Atif TOPAL, Alper ERGÜN, Bahadır ACAR, Engin GEDİK
- 549-556 **Optimization of Control Parameters of 2-DoF Twin-Rotor MIMO System**
Sengul DOGAN, Gonca Ozmen KOCA
- 557-563 **Research Data Management System Proposal Having Confidentiality and Privacy**
Enis KARAARSLAN, Feriştah DALKILIÇ
- 564-571 **Hybridization Of Electric Vehicle With Fuel Cell Based On Two Control Strategies**
Nusret Sefa KURALAY, Mustafa Umut KARAOĞLAN
- 572-580 **Theoretical Approach For Modeling And Simulation Of Electrical Passenger Car Power train System**
Nusret Sefa KURALAY, Mustafa Umut KARAOĞLAN
- 581-586 **Development sensor based system software for the control of motor and axis motion on the cnc turning machine**
Kürşat Mustafa KARAOĞLAN, Metin ZEYVELI
- 687-592 **Control of the energy flow with plc for battery supported hybrid generation system in case of a supplying to local area**
Ahmet YÖNETKEN, Tolga ÖZER, Yavuz KOCA, Yüksel OĞUZ
- 593-597 **Toxic and Hazardous Waste Management**
Sakine UGURLU KARAAĞAÇI
- 598-609 **Structural analysis of the wheel vehicle's suspension conveyor**
Mesut DURAT, Ferit FICIÇI, Selçuk KARAKULAK, Zekeriya AYPARÇASI
- 610-616 **Effects of Heat Treatment on Abrasion Properties of Fir and Beech Wood**
Hamiyet ŞAHİN KOL, Yusuf SEFİL, Sema AYSAL KESKİN
- 617-626 **Comparison of energy and exergy efficiency of the refrigerants instead of r22 in air-to-air heat pumps** Fadime ŞİMŞEK, Kemal ÇOMAKLI, Ömer ÇOMAKLI
- 627-631 **Practicing Transhumance in Turkey: Examples of Past and Present**
Binali ÇOMAKLI, Mahmut DAŞCI

TABLE OF CONTENTS

- 632-639 **Analysis and Back-Calculation Modelling of the 10 January 2015 Uzuntarla (Trabzon-Turkey Snow Avalanche Event)**
Abdurrahim AYDIN, Remzi EKER, Yunus BARIŞ ODABAŞI
- 640-647 **The factors effect the external bonded patch repaired in laminated composite materials**
Şükrü ÇETİNKAYA, Haşim PIHTILI, Hayri YILDIRIM
- 648-655 **Some Example of Mismanagement Practices in Natural Vegetation in Turkey**
Mahmut DAŞCI, Binali ÇOMAKLI
- 656-664 **Performance Analysis of Turbocharged 2-Stroke Diesel Engine**
Ümit GÜNEŞ, Yasin ÜST, A. Sinan KARAKURT
- 665-673 **Analysis of the Turkmen Tents that Provide Energy Efficiency by Use of Natural Material from the Socio-Economic and Environmental Point of View**
Gülşen CENGİZ
- 674-678 **Particle swarm optimization approach to solve single machine total weighted tardiness problem with unequal release date**
Serdar ÖZER, Tarik ÇAKAR
- 679-685 **Sapanca Lake Air Pollution Originating from Transportation-Investigation of Heavy Metal Emissions**
Hülya DEMİREL, Asude ATEŞ, Şeref SOYLU
- 786-692 **An Adsorption Study of Methylene Blue from Aqueous Solution with a Low Cost Material**
Nur AYAZ, Rabia KOKLU, Cigdem OZER
- 693-700 **A Numerical Method to Find the Transient Temperature Distribution of Hollow Cylinders**
Hakan PEKEL, Vebil YILDIRIM
- 701-704 **Removal rate of herbicide trifluralin in agrucultural sunflower field in natural period**
Gokhan ONDER ERGUVEN, Bahar IKIZOGLU, Hurrem BAYHAN, Levent KUZU, Gurdal KANAT
- 705-711 **Evaluation of Presplitting Blasting Operation in Apa-HotamI Irrigation (Ahi) Channel Construction**
Bilgehan KEKEC, Niyazi BILIM, Mumin YUCE
- 712-716 **Removal rate of herbicide aclonifen in agrucultural sunflower field in natural period**
Gokhan ONDER ERGUVEN, Bahar IKIZOGLU, Hurrem BAYHAN, Levent KUZU, Gurdal KANAT
- 717-724 **Load Frequency Control Of Three Area Power System By Using PID, FUZZY And FUZZY-PID Controller**
Kadir GÜLER, Ahmet YÖNETKEN, Yüksek OĞUZ

TABLE OF CONTENTS

- 725-729 **Salt Bath Nitriding of Fe₇₂Al₂₈ Intermetallic Alloy**
İbrahim ÇELIKYÜREK
- 730-734 **The Research of the Economic Impact of Granite Dust Remains Usage in Auto Brake Pads**
Halil KILIÇ, Mustafa TİMUR, İbrahim MUTLU, Sinan SAVAŞ
- 735-742 **Optimization of Surface Roughness in Wire-cut EDM of AA6061/B4CP Using Response Surface Method**
Şener KARABULUT, Halil KARAKOÇ, Ömür Kaya KALKAN, Ramazan ÇITAK
- 743-748 **The Friction Welding of FeAl Intermetallic Alloy and AISI 316 Stainless Steel**
İbrahim ÇELIKYÜREK, Osman TORUN, Bedri BAKSAN, Akın OZCAN
- 749-755 **Investigation of the Test Device Determining Characteristics of Automotive Brake Pads**
Mustafa TIMUR, Hilmi KUŞÇU, Sinan SAVAŞ
- 756-760 **Effects of Piston Motion On Specific Surfaces of the Cylinder Liner in a Compression Ignition Engine**
Mehmet ÇAKIR, İsmail Hakkı AKÇAY
- 761-768 **Analysis of Laminated Composite Plates Using Element-Free Galerkin Method**
Özkan ÖZBEK, Ömer Yavuz BOZKURT
- 769-781 **Optimum Autofrettage Pressure for a High Pressure Cylinder of a Waterjet Intensifier Pump**
Hakan ÇANDAR, Hüseyin FİLİZ
- 782-793 **The Effects of Feather Color on Hatchability Traits, Growth Performance, and Survival Rate in Japanese Quails (*Coturnix coturnix japonica*)**
Kadir ÖNK, Mehmet SARI, Muammer TİLKİ, Serpil ADIGÜZEL IŞIK, Tuncay TUFAN
- 794-802 **Determination of Oxygen Gain in Hydraulic Structures**
Asli SARI, Tuba BOSTAN, Ali COŞAR
- 803-815 **Use of Rainwater in Recreational Irrigation of a University Campus in Turkey**
Assoc. Prof. Dr. Ahmet Doğan
- 816-824 **Investigation of the Tribological Performance of a Doped Semi-Synthetic Engine Oil**
Murat KAPSIZ, Ferit FIÇICI, Ramazan ŞENER
- 825-832 **Investigation of Mechanical Properties of Chassis Profile Designed for Light Vehicles**
Deniz SOYEL DOĞAN, Ahmet DEMİRER
- 833-846 **Effects of Terebint (*Pistacia Terebinthus* L) Oil Addition to Quail I on Growth Performance, Carcass Traits, Some Blood Parameters and Composition of Breast Meat Fatty Acid**
Cavit ARSLAN, Tuncay TUFAN, Aydın DAŞ

DETERMINING THE AWARENESS LEVEL OF THE USE OF PARKS FOR THE HANDICAPPED IN THE EXAMPLE OF MALATYA

Fürüzan ASLAN

İnönü University Faculty of Fine Arts and Design Department of Landscape Architecture, 44280, Malatya, Turkey.
furuzan.aslan@inonu.edu.tr

Atilla ATIK

İnönü University Faculty of Fine Arts and Design Department of Landscape Architecture, 44280, Malatya, Turkey.
atikatilla@hotmail.com

Abstract

According to "World Report on Disability (2010)" of World Health Organisation (WHO), more than a billion people are estimated to live with some form of disability, or about 15% of the world's population. In Turkey, according to TurkStat, ratio of the disabled to total population is 12.29% which makes nearly 10 million people all over the country. Disability may be innate or caused during some unfavourable events. From this point of view, any individual is a candidate for being disabled. Due to the impossibilities in their physical functions, the disabled have limited access in their living area to urban areas and opportunities to use them. However, basic duty of civilisations and states is to deliver services equally to whole sides of society. In order for the disabled to participate in social life, civilisations should have priory aim to set up various activity areas in urban for such groups. Required designs and regulations are beginning to be implemented in parks in order to meet the disabled's recreational needs. Extension of the designs for the disabled within parks is a good practice example. In addition, the number of specially designed parks for the disabled to perform their all kinds of activities in these parks by considering their physical disabilities is increasing more and more. City centre of Malatya shelters totally 105 city parks serving actively in 2015, among which only one was designed especially for the disabled and so-called "Disabled Park". A questionnaire survey was conducted to determine the disabled's awareness level about the Disabled Park and their use frequency of the park in Malatya city. It was determined according to data obtained from questionnaire survey that 63.8% of the disabled living in Malatya city centre are not aware of a Disabled Park specially designed park serving for themselves. Among the participants, those aware of the presence of such a park (36.2% of all participants), 76.3% reported to visit the park at least once. When the visiting frequency of the participants who replied "yes" to the question "Which often have you visit the Disabled Park?" was asked, 20.8% of the participants stated that they visit the park less than once a month, 44.8% once a month, 17.2% once a week and 17.2% everyday. According to the results above, it was found that great majority of the disabled living in Malatya city centre are not well aware of the presence of a park specially designed for their own needs. Various suggestions were proposed for the use of the Disabled Park in Malatya more actively.

Keywords: *Open green area, City, Disabled people, City park, Malatya.*

1. Introduction

Being handicapped, disabled, crippled and similar terms have been defined in various ways by different institutions and people. With the broadest sense, being handicapped is defined as a loss in body functions or body structure[1]. Besides this definition, the definition of being handicapped has been defined in Turkey in the Paragraph "C" of the Social Services and Protection of Children Institution Law with the number 2828, Item 3. According to this item, the handicapped individual is "a person in the need of protection, care, rehabilitation, consultancy and support services due to losing his/her bodily, mental psychological, emotional and social skills because of an accident or a disease after birth and due to not being able to cover the requirements of normal life".

Turkish Standards Institution (TSE) has defined the state of being handicapped as the limitation or the loss in using the bodily and mental functions [2].

The International Labor Organization (ILO) defines a handicapped person as "an individual whose expectations on finding, keeping and improving a job that is suitable for him/her has decreased considerably due to an accepted physical or mental disability"[3].

According to the United Nations (UN), the definition of being handicapped is being 'crippled', and the UN defines this term as "an individual who cannot fulfil the individual or social activities, which normally are expected to be done by himself/herself, due to an inherited or later-acquired deficiency in his/her bodily or mental skills".

The World Health Organization (WHO) has demonstrated a professional approach which is in accordance with its area of medical expertise and defined it as a disease, and defined the relevant concepts by classifying them under various titles.

The Rights of the Disabled has encountered various handicaps in history until today. Turkey has intensified the activities in policy-making, legal regulations and institutional infrastructures from the second half of 1990s. The Administration of the Handicapped was established in 1997, and the council meeting was held in 1999 for the first time and in 2005, and the legal regulation, which is shortly known as "The Law of the Handicapped" was accepted. These activities constitute the basic display and the efforts in the field for the handicapped[4].

According to the "World Report on Disability (2010)" of the World Health Organization (WHO), more than a billion people are estimated to live with some form of disability, or about 15% of the world's population. In Turkey, according to TurkStat, the ratio of the disabled to total population is 12.29% which makes nearly 10 million people all over the country. Disability may be innate or caused during some unfavorable events. From this point of view, any individual is a candidate for being disabled[5].

In our country, where the number of the handicapped is high, there are various problems for the handicapped who have many different types of disabilities, especially in terms of transportation from the areas where they live to the urban areas, and using the urban areas freely. The handicapped individuals cannot cover their daily needs due to the negative obstacles in the urban areas. Not providing the handicapped with the mobility that will enable them to act in the urban areas without having difficulties leave them unaided in covering their own social needs.

The biggest obstacles that prevent the handicapped from joining the society are related with transportation and physical environment. The physical environment in which the handicapped live is extremely important in that they lead to limitations in the lives of the handicapped due to their physical dysfunctions/deficiencies. Roads, pavements, public buildings, parks and gardens, schools, houses, transportation vehicles and similar physical environmental issues are serious obstacles preventing the handicapped from joining the society [6]. In order for the handicapped to cover their needs within the society without being excluded from the social life, they must make use of city parks which are among the public areas and which are important elements in enhancing the life quality of the urban life.

Cities must not consist of mere buildings and transportation, and have several facilities that are available for all the people living in them. Green areas are among the most important ones of these facilities [7]. Because in these areas, the aim is to balance all the conditions for the benefit of the society. For this reason, green area designs must be cared for among the most important functions in physical design of the settlements which are the residential areas of the people [8].

Green areas are the areas that are designed and planted by local administrations to cover the recreational needs like having a walk, having fun, bodily activities and leisure activities of the people other than the accommodation and working. These areas are the common cultural or natural areas in which the people living in the city use in mutual consent. These areas are also the places that constitute or must constitute the important parts of the city in terms of public areas. These areas may be within the functional areas and may cover trees and plants and other natural elements [9].

The benefits of open green areas in a city for the society have been revealed by many researchers from various disciplines. Among the benefits of such areas, there are the effect of decreasing the stress and psychological disorders of the people living in cities [10, 11], the effect of decreasing the obesity [12, 13], the effect of increasing physical activity [14], the effect of protecting health [15], the effect of increasing life quality [16] and the effect of positive influences on people in terms of psycho-social aspects [17].

In this context, to cover the recreational needs of the handicapped, necessary designs are made in parks which are among the most important elements of green area systems in cities. The designs which are made specifically for the handicapped individuals becoming widespread is one of the examples in this context. In addition, to cover the needs of the handicapped in a park with all the recreational activities, the whole of the design process must be made by taking the needs and limitations of the handicapped into consideration. The number of such recreational areas increase day by day.

2. Materials and Methods

According to the figures of 2015, there are 94 active parks in the city center of Malatya. Among these parks, there is only one park which is called as "the Park of the Handicapped" and which is specially designed for the handicapped people. The Park of the Handicapped in Malatya is located in the city center, in Cengiz Topel Avenue, Başharık Neighborhood, 5th Street. The park is established on an area of 2500 m². In the scope of the study, a questionnaire has been prepared to arouse the user awareness on "the Park of the Handicapped" that is established specially for the handicapped in the city of Malatya, and to determine the use of the park by the handicapped. In determining the exemplification volume, the Proportional Approach determined with the help of the formula was made use of [18].

$$n = \frac{Np(1-p)}{(N-1)\sigma_{px}^2 + p(1-p)}$$

In the formula; n shows the size of the exemplification, N is the size of the universe; σ_{px}^2 is the variance¹; p is the rate of the handicapped visiting the park².

There are no previous studies dealing with the rates of the handicapped visiting the city parks in the city center of Malatya. Since a pre-questionnaire study has not been performed to determine the p value, the $p=0.5$ value that would give the highest value from the $p(1-p)$ multiplication was taken to ensure that the exemplification size is as large as possible [19].

3. Results and Discussion

According to the 2011 Registry of Births and Housing data from the TurkStat, there are 420 227 people with at least one disability in the Eastern Anatolia region, and 69 376 in Malatya. According to the result obtained with the formula given above, the size of the exemplification is at least 96. By adding 10% to the exemplification volume calculated, the size of the exemplification has been defined as 105 people in total. The data and some statistical information based on these data are given in the table.

In determining the highest exemplification volume; ¹This value is accepted as $1.645 s_p^2=0.05 s_p^2 = 0.03$; ² and calculated as $p=0.5$.

Table 1. The results of the questionnaire.

Socio-demographic characteristics	Name of characteristics	Label	Number	%	Sdt. Dev.	Scale
Gender	Female (1)	FEML	34	32.4	0.470	1-2
	Male (2)	MALE	71	67.6		
	TOTAL		105	100		
Marital Status	Single (1)	SING	66	62.9	0.486	1-2
	Married (2)	MAR	39	37.1		
	TOTAL		105	100		
Age	≤20 (1)	YONG	25	23.8	0.852	1-4
	21-40 (2)	MYNG	45	42.9		
	41-60 (3)	MDDL	29	27.6		
	≥61 (4)	ELDRL	6	5.7		
	TOTAL		105	100		
Education Level	Illiterate (1)	ILTRT	20	19.0	1.451	1-6
	Primary School (2)	PRIM	27	25.7		
	Secondary school (3)	SCND	34	32.4		
	High school (4)	HIGH	7	6.7		
	Vocational school (5)	VOCS	9	8.6		
	University graduate (6)	UNIG	8	7.6		
	TOTAL		105	100		
Occupation	Housewife (1)	HWIF	11	10.5	2.455	1-6
	Public officer (2)	OFCR	10	9.5		
	Worker (3)	WRKR	14	13.3		
	Retired (4)	RTRD	5	4.8		
	Self-employed (5)	SELF	18	17.1		
	Unemployed (6)	UNEM	47	44.8		
	TOTAL		105	100		
Income Level	≤1000 TL (1)	IL1	78	74.3	0.697	1-4
	1000-2000 TL (2)	IL2	16	15.2		
	2000-3000 TL (3)	IL3	10	9.5		
	≥3000 TL (4)	IL4	1	1.0		
	TOTAL		105	100		
Disability Group	Orthopedic (1)	ORTP	43	41.0	1.746	1-5
	Hearing (2)	HEAR	5	4.8		
	Mental (3)	MENT	33	31.4		
	Visually impaired (4)	VISL	19	18.1		
	Speech and language (5)	SPEC	5	4.8		
	TOTAL		105	100		
Do you have any social insurance?	Yes (1)	INSY	67	63.8	0.483	1-2
	No (2)	INSN	38	36.2		
	TOTAL		105	100		
The Ownership Status of your House	It belongs to me and/or to my spouse (1)	OWN	26	24.8	0.794	1-3
	It belongs to my family and/or relatives (2)	FML	37	35.2		
	Rent (3)	RNT	42	40.0		
	TOTAL		105	100		

Do you know about the park of the handicapped in Malatya?	Yes (1)	PINY	38	36.2		
	No (2)	PINN	67	63.8		
	TOTAL		105	100	0.483	1-2
Have you ever visited the park of the handicapped in Malatya?	Yes (1)	PVSY	29	27.6		
	No (2)	PVSN	76	72.4		
	TOTAL		105	100	0.449	1-2
How often do you visit the park of the handicapped in?	Never(1)	POFN	76	72.4		
	Everyday(2)	POFD	5	4.8		
	Once a week (3)	POFW	5	4.8		
	Once a month (4)	POFM	13	12.4		
	Less than once a month (5)	POFM ⁺	6	5.7		
	TOTAL		105	100	1.316	1-5

According to the data obtained from the questionnaire, it has been determined that 63.8% of the handicapped people living in the city center of the city of Malatya were not aware of the existence of a park for the handicapped in the city. In this context, it has become clear that the majority of the handicapped living in the city center of Malatya were not aware of a park that was designed for their use. It is necessary that the local administrations organize informative activities and introduce the park for its potential users.

27.6% (29 people) who participated in the questionnaire stated that they had visited the park at least once.

5.7% of the participants visit the park less than once a month; 12.4% once a month; 4.8% once a week; and 4.8% everyday.

In the light of the data obtained in the study, it has become clear that the rate and frequency of the usage of the park of the handicapped is extremely low. The reasons of this rate being low must be determined with new questionnaire studies and interviews must be made with the handicapped to eliminate the reasons.

In addition, the population of the city center of Malatya is 498 588 according to the 2011 data, and about 13.9% of this is handicapped. Although the rate of the handicapped in the city center is so high, the number of the parks designed especially for the use of the handicapped is only one. The handicapped must make use of the parks, which are among the public areas and which increase the quality of life in the city, without being excluded from the social life together with the whole of the society in an independent manner. In the 61st Item of the 1982 Constitution it is stated that "The State takes the precautions that will ensure that the handicapped are protected and oriented with the social life". This Item has been in the Constitution as a direct regulation for the handicapped. In addition, in the 60th Item, which is under the title of Social Security, in the 1982 Constitution it is stated that "Everybody has the right of social security. The State takes the necessary precautions to ensure this security and establishes the relevant institutions". This item gives the duty of performing the relevant regulations for the handicapped being oriented in the social life [20]. For this reason, it is suggested that the number of the parks that are designed especially for the handicapped in the city center is increased to at least 15% of the existing parks under the title of equality and positive discrimination for the handicapped by taking the population of the handicapped people in the city into consideration.

References

1. Erdoğan, H.N. (2010). *The disabled and problems their families face*. Öz-Veri, 7(2):1635-1650.
2. TSE (1991). *TS 9111 Özürlü İnsanların Kamet Edeceği Binaların Düzenlenmesi*. Ankara: Türk Standartları Enstitüsü Matbaası.
3. ILO (1983). *ILO 159 No'lu Sakatların Mesleki Rehabilitasyon ve İstihdamı Hakkındaki Sözleşme*. <http://www.csgb.gov.tr/csgbPortal/cgm.portal?page=oz&id=4>.

4. Özgökçeler, S. and Alper, Y. (2010). Özürlüler Kanunu'nun Sosyal Model Açısından Değerlendirilmesi, İşletme ve Ekonomi Araştırmaları Dergisi (BERJ), 1(1):33-54.
5. WHO (2010). http://www.who.int/disabilities/world_report/2011/accessible_en.pdf.
6. Karataş, K. (1998). The disabled want to live in cities free. Ufkun Ötesi (monthly journal, publication of Disabled Confederation), 2(4):10-13.
7. Pamay, B. (1978). İstanbul Halkının Rekreasyon Gereksinimi ve Eğilimleri ile Yeşillik İlişkisi. Ibid, pp. 161-6.
8. Atabay, S. (1988). Yeşillik Planlaması ve Peyzaj Tasarım Kolları İlişkisi. Yıldız Üniversitesi Matbaası, İstanbul.
9. Dil, M. (2004). İstanbul'un yeşillik sisteminin, planlama kriterleri açısından değerlendirilmesi. Yüksek Lisans Tezi, İstanbul Teknik Üniversitesi, Fen Bilimleri Enstitüsü, İstanbul.
10. Annerstedt, M., Ostergren, P., Bjork, J., Grahn, P., Skarback, E., Wahrborg, P. (2012), "Green qualities in the neighbourhood and mental health - results from a longitudinal cohort study in Southern Sweden", BMC Public Health, 12, 337.
11. Ward Thompson, C., Roe, J., Aspinall, P., Mitchell, R., Clow, A., Miller, D. (2012), "More green space is linked to less stress in deprived communities: evidence from salivary cortisol patterns", Landscape and Urban Planning, 105(3), 221-229.
12. Nielsen, T.S., Hansen, K.B. (2007). Do green areas affect health? Results from a Danish survey on the use of green areas and health indicators, Health and Place, 13, 839-850.
13. Bell, J., Wilson, J., Liu, G. (2008). Neighborhood greenness and 2-year changes in body mass index of children and youth, American Journal of Preventive Medicine, 35, 547.
14. Mitchell, R. (2012). Is physical activity in natural environments better for mental health than physical activity in other environments?, Social Science & Medicine, 2012, 1-5.
15. Mitchell, R., Popham, F. (2008). Effect of exposure to natural environment on health inequalities: an observational population study, The Lancet, 372, 1655-1660.
16. Stigsdotter, U., Ekholm, O., Schipperijn, J., Toftager, M., Kamper-Jorgensen, F., Randrup, T. (2010). Health promoting outdoor environments - Associations between green space, and health, health-related quality of life and stress based on a Danish national representative survey, Scandinavian Journal of Public Health, 38, 411-417.
17. Hung, K., Crompton, J. (2006). Benefits and constraints associated with the use of an urban park reported by a sample of elderly in Hong Kong, Leisure Studies, 25, 291-311.
18. Newbold, P. (1995). Statistics for Business and Economics. Prentice-Hall, New Jersey, USA. 867 p.
19. Miran, B. (2003). Basic Statistics. Aegean University Printing Office, İzmir, pp. 24-50.
20. Çınarlı, S. (2010). Engellilere Yönelik Kamu Hizmetleri, Kazancı Hukuk Yayınevi, İstanbul.

PHYSICAL ACTIVITY PREDICTION: ACCELEROMETERS OR GYROSCOPES?

Musa HAKAN ASYALI

Corresponding author: Yildiz Technical University, Dept. of Biomedical Engineering, 34220, Esenler/İstanbul, Turkey.
asyali@yildiz.edu.tr

Ömer KAYAALTI

Erciyes University, Develi Hüseyin Şahin Vocational School, Dept. of Computer Technologies, Kayseri, Turkey,
kayaalti@erciyes.edu.tr

Abstract

The aim of activity recognition is to recognize the type of physical movements, i.e. walking, running, sitting, staircase climbing etc. Nowadays, physical activity recognition is an important research area because of its potential use in health and emergency care. There are several different sensory devices to determine the orientation and position of an object. Gyroscopes and accelerometers are commonly used for this purpose. The main difference between accelerometer and gyroscope sensors is that gyroscope sensor can sense angular rotational velocity whereas accelerometer can sense linear velocity change of movement. In this study, we aimed at comparing efficacy of accelerometer and gyroscope sensor data for activity prediction. We have first extracted some basic statistical features and autoregressive model coefficients from accelerometer and gyroscope sensor values separately and then we have evaluated the performance of classifiers designed to predict the type of physical activity using these features. Our results indicate that, one can predict the type physical activity using features obtained from accelerometer and gyroscope data equally well, as there are no significant differences among the performance of the classifiers using the features obtained from accelerometer and gyroscope data.

Keywords: Physical activity prediction; wearable sensors; first order statistics; autoregressive model; pattern recognition.

1. INTRODUCTION

Physical activity recognition is an important tool with many potential applications in healthcare. There are several motivations behind physical activity monitoring and its automatic recognition using machine learning algorithms. Firstly, there has been a dramatic increase in average life expectancy during the last several decades. For instance, in Japan life expectancy at birth now exceeds 83 years [1]. Due to achievements of mankind, in technology in general and in healthcare in particular, relative portion of the aged population has been increasing steadily recently. According to statistics on European Union (EU) demographics, median age is also increasing [2]. The median age in EU countries rose from 38.3 years in 2001 to 41.9 years in 2013, which corresponds to an average increase of 0.3 years per year. These indicators underline the fact that home healthcare and telemedicine applications will become a relatively more important component of the healthcare system. Detection of the physical activity of elderly people at home, which will provide valuable information about their health status, is of crucial importance.

Another motivation has to do with the advancement of technology again, but relatively indirectly this time. Due to comfort increasing features of the technology, people are less mobile, especially in developed countries. People walk less (drive more) and even do their grocery shopping while sitting in front of their computers. Healthcare providers (public healthcare systems, etc.) are looking for ways to motivate relatively less mobile people of today's world to carry out more physical activity to improve their health. Essentially, this is a preventive medicine strike in protecting public health against mass diseases like obesity and diabetes. In this context, we need to first measure, record and analyze daily activity of people and make suggestions to them, based on their data. For these reasons, measurement and analysis and/or interpretation of physical activity is of great importance.

There are several different sensory devices to determine the orientation and position of an object. Gyroscopes and accelerometers are commonly used for this purpose. An accelerometer is a sensory device that measures proper acceleration. A gyroscope is a sensory device that measures rotational motion. The main difference between accelerometer and gyroscope sensors is that gyroscope sensor can sense angular rotational velocity whereas accelerometer can sense linear velocity changes of movement.

There are numerous studies for physical activity recognition in literature. Khan et al., classified 15 different types of physical activity using artificial-neural-networks that used autoregressive (AR) model coefficients of acceleration signals as discriminative features, i.e. as inputs [3]. He and Jin also used AR model parameters of acceleration data in activity recognition [4]. In order to predict children's energy expenditure, Puyau et al. measured their physical activity by using accelerometer based activity monitors [5]. Kwapisz et al. tried to classify or predict to 6 different types of physical activity (coming downstairs, jogging, sitting, standing, climbing upstairs, and walking) using first order statistical features obtained from cell phone accelerometer recordings [6].

Activity information can easily be recorded by using miniature (light-weight) sensors (mostly accelerometers) to be connected to the body at several appropriate places, mostly at extremities. Nowadays smart phones include many advanced sensors including position sensors (geo-magnetic field sensor and the orientation sensor) and motion sensors (the accelerometer and gyroscope) etc. which can sense and record physical activity with great ease. There are even application software developed to run on these smart devices that analyze and report daily physical activities of its user.

In this study, using a publicly available dataset, we have tried to find which sensory devices (accelerometer or gyroscope) are more useful or meaningful in physical activity recognition. Using a publicly available dataset whose details are given in the next section, we have tested the performance of classifiers based on these two types of inertial measurement units. In the following *Experimental* section, we have outlined the features that we have extracted from both families of inertia measurements (linear versus rotational inertia sensors, or accelerometer versus gyroscope) in activity classification. We have also described the classification or machine learning algorithm and the experimental design that we have applied in the study. As shown in the *Results and Discussion* and discussed in the *Conclusions* sections, our results have revealed that the use of either family of signals (accelerometer or gyroscope) provides equally well prediction accuracies in physical activity recognition.

2. 2. EXPERIMENTAL

An easy way to comply with the symposium paper formatting requirements is to use this document as a template and simply type your text into it.

2.1. Materials

2.1.1. Dataset

In this study, we have used the University of Southern California, Signal and Image Processing Institute's (USC-SIPI) Human Activity Dataset (HAD), which is available at <http://sipi.usc.edu/HAD/>. This dataset contains 3-axis accelerometer and 3-axis gyroscope sensor recordings that have been collected from 14 subjects (Gender: 7 male, 7 female; Age: range 21-49, mean \pm SD: 30.1 \pm 7.2; Height (cm): range: 160-185, mean \pm SD: 170.0 \pm 6.8, Weight (kg): range: 43-80, mean \pm SD: 64.6 \pm 12.1; where SD stands for standard deviation). For detailed information about the dataset, please see [7].

The USC-SIPI HAD includes 12 different types of activity: walking forward, walking left, walking right, walking upstairs, walking downstairs, running forward, jumping up, sitting, standing, sleeping, elevator up, and elevator down. Each subject tried or repeated each activity 5 times, as such there are $12 \times 5 = 60$ trials/recordings (6-channels of time series data) or data files per subject. There are total of $14 \times 60 = 840$ data files, trials or activity samples. While the subjects were carrying out the planned physical activity, accelerometer and gyroscope data with 3 degrees of freedom (i.e. along X, Y, and Z axes) are collected simultaneously using wearable sensors (MotionNode USB, by Motion Workshop, Seattle, WA). The specifications of the recording device can be found at [8]. The range of capturable acceleration and rotation rates were $\pm 6g$ and ± 500 degrees per second (dps) respectively. Here, g is the acceleration due to gravity, which is approximately 9.81 m/s² on the surface of the Earth. Sampling rate is 100 Hz, i.e. 100 samples per second, for each of the 6 channels (3 accelerometer + 3 gyroscope).

Our inspection of the data files revealed that the durations of activity recording trials were not the same. For each subject, there were variations within the 5 trials of each activity type. There were also across subjects as well. Table 1 reports the average data length (in seconds) for each subject and activity type. We notice that the range of recording durations is from 7.00 to 132.80 seconds and overall (across both subjects and activity types) average mean recording length is 33.47 seconds.

Table 1. Average data length (in seconds) for each subject and activity type

Subject #	Walk Forward	Walk Left	Walk Right	Walk Upstairs	Walk Downstairs	Run Forward	Jump Up	Sit	Stand	Sleep	Elevator Up	Elevator Down
1	24.60	32.80	37.40	61.40	57.40	16.40	14.00	40.00	19.00	50.00	19.37	18.37
2	25.20	31.00	34.40	43.40	44.40	17.80	14.00	20.00	19.00	50.00	20.63	24.43
3	26.80	21.80	20.20	7.60	7.00	19.00	15.80	29.00	30.00	50.00	22.40	22.60
4	28.00	28.40	34.20	8.80	8.40	19.20	12.80	40.00	40.00	50.00	24.21	23.93
5	26.60	35.60	35.40	10.40	8.20	17.80	8.20	20.00	20.00	50.00	23.43	24.13
6	25.80	33.20	44.00	8.20	7.80	19.40	8.60	40.00	40.00	50.00	20.38	20.18
7	21.20	23.20	32.80	8.40	8.00	11.00	15.40	28.00	30.00	50.00	19.06	22.23
8	30.00	51.40	55.80	42.60	42.40	30.00	14.30	30.00	30.00	50.00	18.19	19.02
9	85.00	45.00	41.60	69.00	62.80	29.80	16.40	32.00	28.00	50.00	30.89	31.05
10	85.40	33.60	35.40	61.80	56.00	30.20	9.90	40.00	40.00	50.00	29.81	26.56
11	97.00	41.40	40.20	37.20	32.20	42.60	20.20	54.00	54.00	50.00	29.37	27.91
12	132.80	53.80	45.60	25.80	22.60	18.00	26.80	50.00	52.00	50.00	29.27	31.70
13	99.20	33.40	31.80	23.60	22.80	45.40	16.60	50.00	50.00	100.00	21.96	18.07
14	55.20	53.00	62.20	15.40	14.80	36.40	21.20	50.00	20.00	50.00	22.03	19.83

In Figure 1, we show sample data from trials of Subject #4 for all 12 different types of physical activity. Left and right panels respectively show accelerometer and gyroscope recordings for X, Y, and Z channels or axes. As different activities have different recording durations, we have depicted only first 6 seconds of each channel of data. If we examine the data given in the figure, we observe that accelerometer values portray very similar values for "elevator up" and "elevator down" activities (two bottom left panels in Figure 1). When we separately plot the X-channel accelerometer signals for these two activities (see Figure 2) for the whole duration of the recordings, we observe that there are significant changes in the signals during the aforementioned activities, however action (i.e. major changes in the signals) start up right after 7th second. This is why we missed these changes in Figure 1, as we have only plotted only first 6 seconds of the signals.

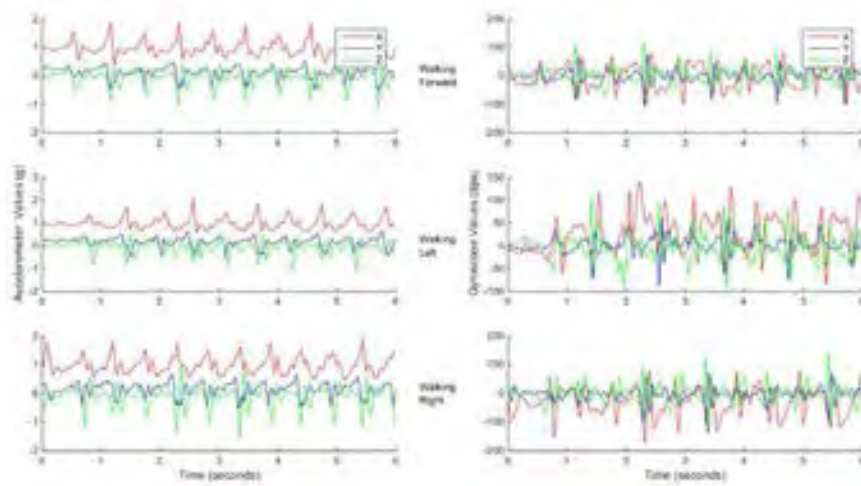
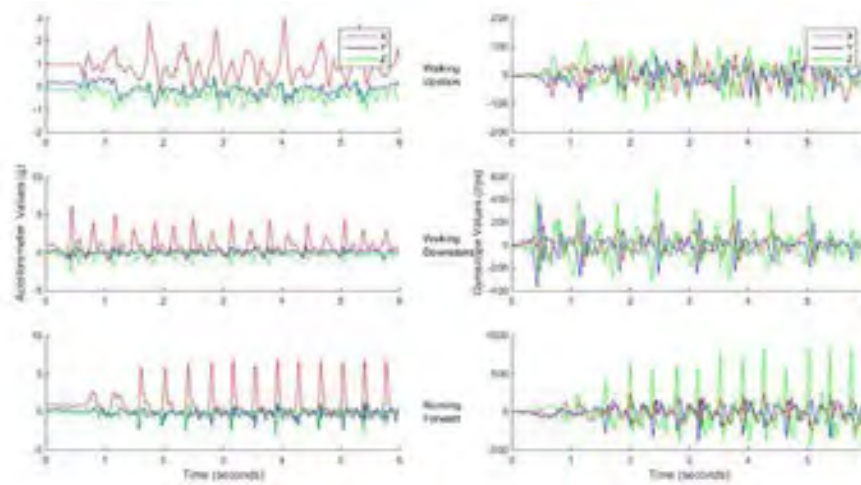


Figure 1. Sample data from trials of Subject #4 for all 12 different types of activity. Left and right panels respectively show accelerometer and gyroscope recordings for X, Y, and Z axes



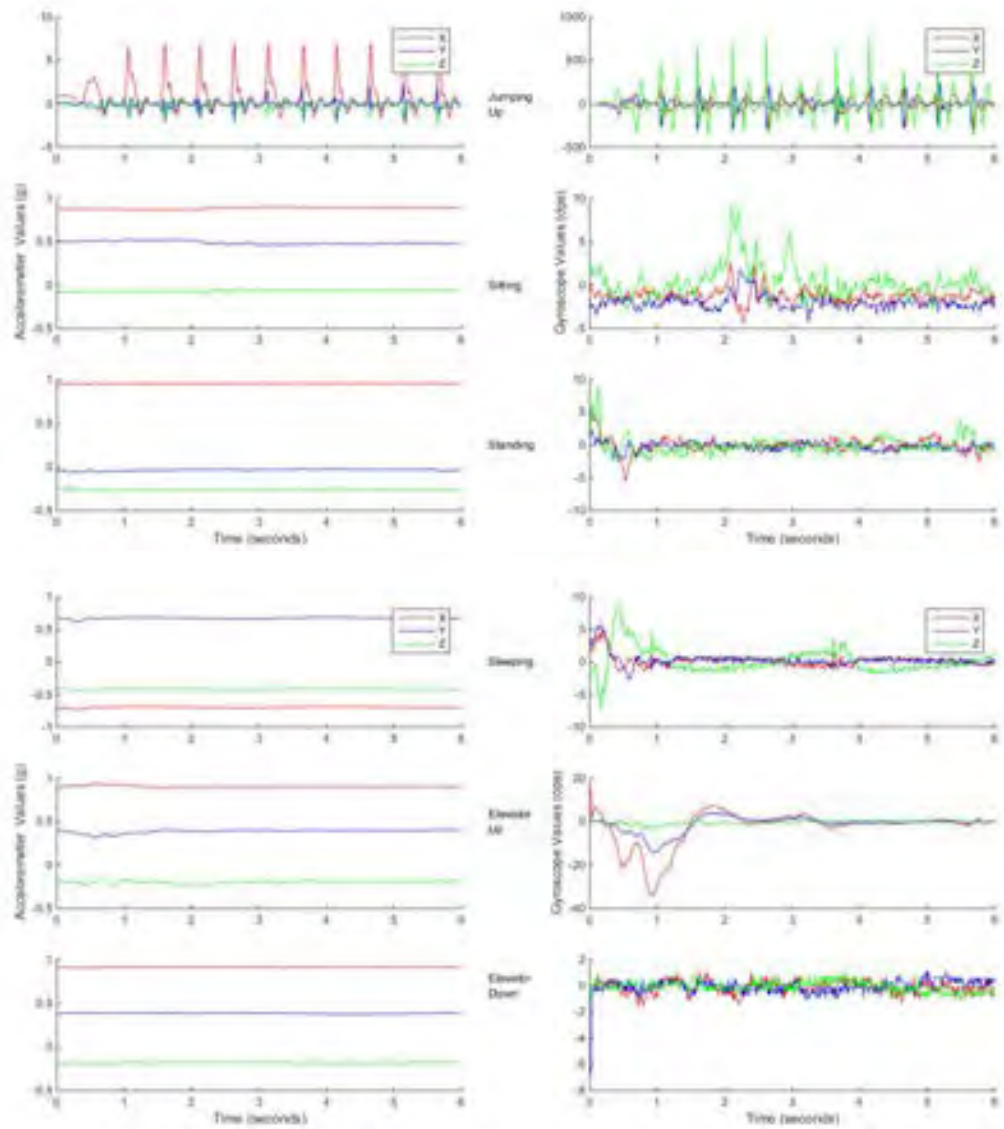


Figure 1. (Continued from previous page.)

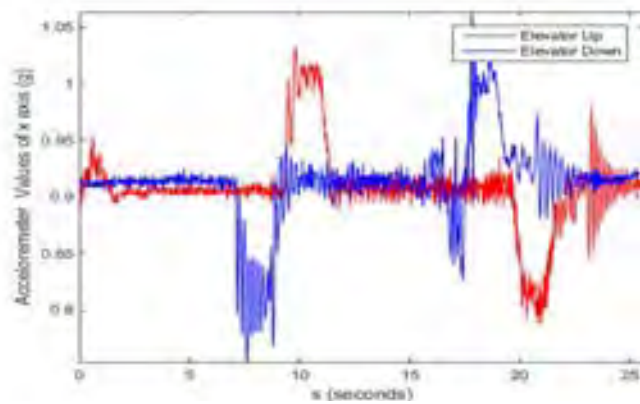


Figure 2. The X-axis accelerometer signal corresponding to Subject #4's elevator up and elevator down activities in Figure 1 is redrawn for the whole duration of the recordings

2.1.2. First Order Statistics

Mean, variance, skewness and kurtosis are the fundamental statistical features of a time series. The mean is the average or expected value of the time series. The variance is a measure of the spread or distribution of the time series around the mean value. Skewness is a measure of the asymmetry of the time series around the mean value. Kurtosis is a measure of the flatness of the distribution of the time series. A percentile is a measure of what percent of the total frequency scored below that measure. For example, n th percentile is the value for which there are $n\%$ of the signal values below it. As such, the median is the same value with the 50th percentile.

In this study, for each activity trial and for each signal channel (3 accelerometer + 3 gyroscope, total of 6 channels) we have obtained *mean, variance, skewness and kurtosis* and *25, 50 and 75th percentile values* (total of 7 parameters) that we collectively call as FOS (first order statistical) features. There are total of 7 parameters per channel \times 6 channels = 42 FOS features per trial; half (21) of these FOS features are from accelerometer and the other half (21) are from gyroscope signals. We have later used these FOS features (along with AR features) in automatic recognition of the type of physical activity.

2.1.3. Autoregressive Model

A model which assumes that current value of a time series can be predicted using some number of its previous values is called an autoregressive (AR) model. AR model is a simple and useful method for describing stochastic behavior of a time series. AR model's structure is given by Equation 1:

$$x(t) = \sum_{i=1}^M a_i x(t-i) + e(t) \quad (1)$$

where $x(t)$ is the signal or time series to be modeled, a_1, a_2, \dots, a_m are the autoregression coefficients; M is the order of the model and $e(t)$ is the error or residue term [8]. In estimation of AR model parameters, we have utilized *armcov* function of MATLAB (Mathworks Inc. Natick, MA). This function uses the modified covariance method which estimates model parameters by minimizing the forward and backward prediction errors in the least squares sense [9].

Some studies on physical activity classification recognition in the literature have utilized AR model parameters as signal features to be used by classification methods and obtained successful results. By this motivation, we have estimated an AR model of order 15 for each signal of activity trials. While selecting the model order as 15, we have considered the following points: i) dynamics of the underlying physical mechanisms, ii) the length of the accelerometer and gyroscope signals (at least 7 seconds or 700 data points), and iii) typical values used in the literature. With this selection of model order we have extracted total of $3 \times 15 = 45$ features for both accelerometer and gyroscope signals, as each of these sensor family has 3 signal channels (X, Y, and Z axes).

2.1.4. Classification

The k -Nearest Neighbors algorithm (k -NN; k is an odd integer) is a simple non-parametric classification method [10-11]. Although k -NN does not exhibit any modeling capability (hence the name, non-parametric) it is typically used in classification settings as a benchmark or reference method due to its relatively good prediction performance almost in any case. In this study, as we have aimed at comparing the usefulness or value of *accelerometer and gyroscope signals* in activity recognition, we have used only one classification method and selected it to be the k -NN method due its simplicity and good prediction performance.

Let \mathbf{x} be a sample (or test data) point in the feature space to be classified. In k -NN method, first \mathbf{x} 's all k nearest neighbors are found in the training dataset and their class labels are noted. Then, \mathbf{x} is assigned to the class of the samples/neighbors that appear most frequently among those k neighbors. If there is a tie, then \mathbf{x} is randomly assigned to any of those tied classes.

Using too many features in classifier design causes a serious problem known as the *curse of dimensionality*. The number of features should be a few times less than the number of samples in the training set. In order to cope with this problem, feature reduction or selection methods are used. The goal of feature selection is to find feature subsets (of the original feature set) which can yield acceptable classification performance. In this study, we have utilized the Sequential Forward Selection (SFS) method [11] for feature selection.

In measuring prediction accuracy rate of classifiers, we have used the well-known m -fold Cross-Validation (CV) method, where m is either 5 or 10. In this method, we divide the training set into $m > 2$ parts and form m sub-blocks of data. Then, we take a sub-block in turn and use it for testing of the classifier that is trained on the remaining $m-1$ sub-blocks of data. We note the resulting prediction accuracy rate and repeat the whole classification trial with a different sub-block used as test data until all sub-blocks are processed. After m

iterations, we obtain m prediction accuracy rates and we finally average these to find the overall classification performance, i.e. the overall prediction accuracy rate [10-11].

2.2. Methods

In our study, for each activity trial (14 subjects with 70 trials each) we have obtained FOS and AR features as described earlier. For each family of inertial sensors (linear vs. rotational or accelerometer vs. gyroscope signals) we have obtained total of 21 (FOS) + 45 (AR) = 66 features. We have then used SFS method to select a fewer number of features that may yield acceptable classification performance. We have used k -NN classifiers with $k = 3$ and $k = 5$, in our classification trials with SFS method and measured the classification performance (i.e. prediction accuracy) with 5- and 10-fold CV. In these trials, we have observed that increasing the number features beyond 10 did not provide any further increase in the classification performance. Therefore, we have set the number of features to be used in the classification trials as 10.

3. RESULTS AND DISCUSSION

In Table 2, we present the classification results based solely on features obtained from accelerometer and gyroscope signals. As we have tried 2 k values (3 and 5) for the k -NN classifier and two fold values (5 and 10) for the CV method we have reported total of 4 prediction accuracy rates for each type of signal family in Table 2. We observe that prediction accuracy rates obtained using features from either signal family (accelerometer or gyroscope) are very close. We further notice that k -NN classifier with $k=3$ and 10-fold CV performance estimation method, provide slightly better prediction accuracy rates.

Table 2. Comparison of classification performance of accelerometer and gyroscopes sensors

Feature Family	k -NN ($k = 3$)		k -NN ($k = 5$)	
	CV = 5	CV = 10	CV = 5	CV = 10
<i>Accelerometer</i>	79.17	82.50	77.98	78.93
<i>Gyroscope</i>	79.76	80.60	77.86	79.17

In Table 3, we present the confusion matrix, for the classification of physical activity trials into 12 categories, corresponding to the best classification result, i.e. k -NN classifier with $k=3$ and 10-fold CV using accelerometer features. Here we observe that the sum of correctly classified cases, which are the diagonal entries of the matrix, is $62 + 55 + 61 + 58 + 59 + 69 + 67 + 59 + 61 + 70 + 33 + 39 = 693$, and when we divide this by the total of number of trials (840), we obtain and confirm the %82.50 best accuracy rate that appears in Table 2. Upon examining the confusion matrix given in Table 3, we notice that the sleep activity is fully recognized with no error for 70 trials. Whereas elevator up and elevator down are recognized or predicted with high error (33/70 and 39/70 respectively). We further notice that these two activities are confused among themselves mostly.

Table 3. Confusion matrix corresponding to the best classification result

		Real Activity											Total	
		Walk Forward	Walk Left	Walk Right	Walk Upstairs	Walk Downstairs	Run Forward	Jump Up	Sit	Stand	Sleep	Elevator Up		Elevator Down
Predicted Activity	Walk Forward	62	8	3	6	4	0	0	0	0	0	0	83	
	Walk Left	1	55	6	0	1	0	0	0	0	0	0	63	
	Walk Right	3	7	61	4	1	0	0	0	0	0	0	76	
	Walk Upstairs	2	0	0	58	3	0	0	1	0	0	0	64	
	Walk Downstairs	2	0	0	2	59	0	0	0	0	0	0	63	
	Run Forward	0	0	0	0	2	69	3	0	0	0	0	74	
	Jump Up	0	0	0	0	0	1	67	0	0	0	0	68	
	Sit	0	0	0	0	0	0	0	59	3	0	1	63	
	Stand	0	0	0	0	0	0	0	8	61	0	7	83	
	Sleep	0	0	0	0	0	0	0	0	0	70	0	70	
	Elevator Up	0	0	0	0	0	0	0	0	2	0	33	24	59
	Elevator Down	0	0	0	0	0	0	0	2	4	0	29	39	74
	Total	70	70	70	70	70	70	70	70	70	70	70	70	840

4. CONCLUSIONS

In this study, we have designed and compared performance of classifiers based on features obtained from accelerometer and gyroscope sensors for physical activity recognition. Our results indicate that the performance even simple classifiers like *k*-NN using first order statistical and autoregressive model features from these two family of sensors/signals are both very high and very close each other. This point underlines the value of both accelerometer and gyroscope sensors/signals in detecting or recognizing type of physical activity.

REFERENCES

- [1]. (2014) Health: Key tables from OECD - ISSN 2075-8480, Life expectancy at birth, total population.[Online]. Available:http://www.oecd-ilibrary.org/social-issues-migration-health/life-expectancy-at-birth-total-population_20758480-table8
- [2]. (2014) Eurostat, Population structure and ageing.[Online]. Available:http://ec.europa.eu/eurostat/statistics-explained/index.php/Population_structure_and_ageing
- [3]. A. M. Khan, Y. K. Lee, S. Y. Lee, and T. S. Kim, "A triaxial accelerometer-based physical-activity recognition via augmented-signal features and a hierarchical recognizer," *Information Technology in Biomedicine, IEEE Transactions on*, vol. 14, pp. 1166-1172, 2010.
- [4]. Z. Y. He and L. W. Jin, "Activity recognition from acceleration data using AR model representation and SVM", in *Proc. Machine Learning and Cybernetics International Conference*, 2008, pp. 2245-2250.
- [5]. M. R Puyau, A. L. Adolph, F. A. Vohra, I. Zakeri, and N. F. Butte, "Prediction of activity energy expenditure using accelerometers in children", *Med Sci Sports Exerc.*, vol. 36(9), pp. 1625-31, Sep. 2004.
- [6]. J. R. Kwapisz, G. M. Weiss, and S. A. Moore, "Activity recognition using cell phone accelerometers", *ACM SigKDD Explorations Newsletter*, vol. 12, pp. 74-82, 2011.
- [7]. M. I. Zhang and A. A. Sawchuk, "USC-HAD: A Daily Activity Dataset for Ubiquitous Activity Recognition Using Wearable Sensors", *ACM International Conference on Ubiquitous Computing (UbiComp) Workshop on Situation, Activity and Goal Awareness (SAGAware)*, Pittsburgh, Pennsylvania, USA, Sep. 2012.
- [8]. (2015) MotionNode Bus Specification onMotionNodeWebsite. [Online]. Available:http://www.motionnode.com/MotionNode_Bus_Specification.pdf
- [9]. S. Kay, *Modern spectral estimation: theory and application*, Englewood Cliffs, NJ, 1988.
- [10]. M. H. Asyali, D. Colak, O. Demirkaya, and M. S. Inan, "Gene expression profile classification: a review", *Current Bioinformatics*, vol. 1, pp. 55-73, 2006.
- [11]. A. K. Jain, R. P. W. Duin, J. Mao, "Statistical pattern recognition: A review", *IEEE Trans. Pattern Anal. Mach. Intell.*, vol. 22(1), pp. 4-37, 2000.

DETERMINING THE RISKS IN MARITIME CONTAINER TERMINAL OPERATIONS: HEALTH AND SAFETY APPLICATIONS

E. GülEmecen Kara

*Istanbul University, Department of Maritime Transportation Management Engineering, 34320, Avcılar/Istanbul, Turkey.
emeceng@istanbul.edu.tr*

Ersoy Kaçmaz

Istanbul University, Department of Maritime Transportation Management Engineering, 34320, Avcılar/Istanbul, Turkey.

Abstract

The maritime container terminal is the physical link between ocean and land modes of transportation. It fulfils functions of the transshipment and the temporary storage of containers. Container terminal system is composed of two components. The first is the quayside with loading and unloading of ships. The second is the landside. It comprises container yard where containers are stacked and gate side where containers are transferred to other modes of transportation. Container terminal is a dynamic system in which many operations together. Container terminal operations contain a variety of dangers, because of operation rate, job multiplicity of machines, machines and people working in the same environment and vertically stacking. In this study, container terminal structure, handling equipment and terminal operations are described. Terminal operations risks are analyzed by divided into two subsystems: quayside operation and landside operation. Measures to be taken and health and safety practices are discussed.

Keywords: *Container Terminal, Quayside Operation, Landside Operation, Operational Risk, Safety*

1. INTRODUCTION

Maritime container terminals play an important role in the container transportation process. They are not passive points of interface between sea and land transport. They have become logistic centers acting as the natural points of intermodal interchange. Today's container terminals need a significant amount of investment in order to develop and maintain both their infrastructure and superstructure. At the same time, they face much fiercer competition than ever before [1]. They need to exhibit management competency to increase container turnover, and to success a fast transshipment process combined with reduced costs in the allocation of scarce resources.

The basic function of a container terminal is transshipment and the temporary storage of containers. Container terminal system has complex structure. It comprises several components which interact with each other. Many operations are done at the same time and with accordance together. There are many moving handling machines in the terminal area. Handling machines and terminal workers work in the same environment.

Operations at container terminals take place throughout 24 hours and in all types of weather. There are often pressures to load or unload a ship's cargo quickly to free up a wharf. At the same time external truck drivers want to receive or discharge of their cargo as quickly as possible and get back on the road. These factors make it a potentially high-risk industry to work in. Occupational accidents occurring in the ports compose an important part of all work-related accidents. Ever-changing circumstances lead to ever-changing risks. Terminal managements must put appropriate health and safety measures in place to manage these risks properly [2].

The accident occurring in the terminal threatens the human and environmental health. At the same time it is one of the most important factors affecting the efficiency of terminal operations [3].

In this study, container terminal structure, handling equipment and terminal operations are described. Terminal operations risks are analyzed by divided into two subsystems: quayside operation and landside operation. In this context measures to be taken and health and safety practices are determined.

2. MARITIME CONTAINER TERMINAL SYSTEM

The maritime container terminal is the physical link between ocean and land modes of transportation. That is, it is an intermodal storage, transfer and distribution center. It fulfils functions of the transshipment and the temporary storage of containers. Container terminal system that has entries such as human, machine, and field is a functional integrity. Container terminal system is composed of two components. The first is the quayside with loading and unloading of ships. The second is the land side. It comprises container yard where containers are stacked and gate side where containers are transferred to other modes of transportation. Container terminals have different types of handling equipment and the terminal layouts [4].

2.1. Handling Equipment

Handling equipment used at container terminals can be classified into three groups which are explained below.

Quay Cranes (QC)

The loading and unloading at a container ship are performed by Quay Cranes. Quay cranes have two types: Mobil Crane (MHC) and Gantry Crane (SSC – ship to shore crane). SSC is fixed quay crane. It moves on a particular rail. Operation the performance of this cranes is in the range of 22–30 boxes/h. MHC moves on wheels. It rotates about its axis. It may go to any place on the quay.

Yard Cranes (YC)

Yard cranes are used for stacking and handling of containers in the container yard. The most common types of these cranes are Rail-Mounted Gantry (RMG) cranes, Rubber-Tired Gantry (RTG) cranes, Forklifts and Reach stackers (CRS).

RTGs and RMGs are used for stack containers. A RTG runs on rubber tires. It carries a container on its spreader which can move both horizontally and vertically. By combining the movement of the spreader and the RTG itself, containers can be placed in any storage location of a block. A block usually consists of six rows and four tiers of containers. At busy time, a block can be worked on by two RTGs. RMGs are similar to RTGs except that they run on rail. They are taller and wider than RTGs, allowing 12 rows and 5 tiers. They also run faster, since a container rides more stable on it.

CRS and Forklift are used to move and stack containers in the container yard. Forklift is a heavy-duty forklift which holds a container by spanning the forks on the two holes at the bottom of a container. It is more suitable for empty containers. CRS is mobile vehicles with an extensible spreader. It holds container from above. The raising spreader enables eight tiers (high) for empty containers and six tiers for loaded containers.

Transport Vehicles (Yard Support Vehicles)

These vehicles are used to transport containers between container yard and other locations inside of container terminal. The most common types of these vehicles are Yard Trucks (YTT), Multi Trailers, and Straddle Carriers (SC).

YTT is a tractor with a detachable chassis. It is one of the most convenience means to transport containers on land for a short distance. There are twist locks on a chassis which lock the container on chassis in its position. They are usually used to transport containers between storage locations and the berths. SC can be regarded as a reduced version of RTG. It is used for transportation between the stack and other locations such as a quay crane, the area for external trucks, or the train area. SC not only transport containers, but are also able to stack containers in the yard. SC exist in numerous variants [5].

2.2. Container Terminal Operations

Container terminal operations can be divided into two subsystems: quayside operation, landside operations which comprise yard operation and hinterland operation.

Quayside Operations: These operations comprise ship operations and the transportation of containers between quay and stack. Ship operations include the discharging operation and the loading operation. During the discharging operations, quay cranes unload containers from the ship to a transport vehicle. Then, this vehicle delivers the inbound container to a yard crane. For the loading operation, the process is carried out in the opposite direction.

Landside Operations: These operations comprise yard operations and hinterland operations. Yard operations are related to container handling and storage operations in a yard. The yard crane picks up the inbound container from transport vehicle and then this crane stacks it into a position in storage area separated into blocks. Later it is delivered out of storage for transfer to other modes. For the import container, the process is carried out in the opposite direction. Hinterland Operations comprise receiving and delivery operations. When a container arrives at a container terminal by an external truck, the container is inspected at a gate to check whether all documents are ready and check for damages to the container. Also, at the gate, information regarding where an export container is to be stored and where an import container is located is provided to the external truck. When the external truck arrives at a transfer point of the yard, yard equipment, which can be a yard crane or straddle carrier, either receives a container from the truck, which is called the receiving operation, or delivers a container to the truck, which is called the delivery operation [6].

3. THE RISKS IN CONTAINER TERMINAL OPERATIONS: HEALTH AND SAFETY

Terminal operations risks and rules that must be followed are analyzed by divided into two subsystems: quayside operation and landside operation.

3.1. Risks in Quayside Operations and Safety

Operations carried out in the quay side impose various risks based on the characteristics of quay cranes and transport vehicles used in the handling of containers and the nature of operation.

Danger in ship operations starts while ship berthing. During berthing rope of ship can stretch or break. The breaking of the ship's rope is very damaging event as an uncontrolled force. Therefore to approach the rope and available in the study area is dangerous and prohibited.

Getting on and off board the vessels must be done by using a ship boarding ladder, entry-exit to the ship must not be done from the ship railing and over the pulpits absolutely. Personnel who are boarding on the vessel must wear shoes whose soles are not slippery and must be careful against slipping and falling by considering that there may be slippery materials like ice and oil, etc. on the vessel ground. There must be sufficient illumination provided on the vessel.

The quay cranes give warning signals when they are moving and inform the persons around them. Getting on the equipment which are moving and being present on the outbound route is prohibited. Likewise, vehicle approach route must be determined for each crane. Entry of third persons to the area where vessel operation is carried out by a vehicle or on foot is not allowed.

The equipment for lashing of containers located on the deck one on the top of the other is called "twistlock". There are three types of twistlocks, namely automatic, semi-automatic and manual. It is prohibited that the twistlocks that are taken out are placed in the working area, on the vehicle routes, SSG rails, empty sides and corners.

There is a falling risk for containers during ship and loading and unloading operations because of reasons including incorrect locking of twistlocks, and defective twistlock. Moreover, containers may move beyond the control of the operator during both loading on the vessel and within the hold as a result of the vibration and wobbling of the containers and bumping to fixed places on the vessel. Therefore during loading operation it must not be approached the containers and the required safety distance must always be kept.

There are some rules which must be followed in the handling of containers out of the standards. In the unloading operation of reefer containers, container unloading must be started after making sure that reefer plugs are not connected and are bundled. Electric shock must be considered as well. The equipment such as a sling, lock and hook used during the operation of out of gauge (OOG) container must be according to the weight of the load that is to be lifted. IMO labels placed on the containers show that the load carried in the container is hazardous material. Care must be taken during handling of such containers and security rules must be obeyed maximally.

After the completion of ship loading operation, containers must be fixed to each other and proper places of the ship by special equipment against slipping and falling risk. It is necessary that this process, called lashing, must be done in the places that are found necessary and carefully and it must be controlled. Wrong lashing applications may cause various accidents such as slipping and falling of the containers to the sea.

While the ship berthing, the booms of the SSG crane that extend to the sea are erected in the air. After the completion of ship berthing and maneuvering, the booms of the cranes are lowered on to the hold of the ship again. The cranes located on or next to the ship must be removed for preventing bumping during the leave of the ship.

Terminal transport vehicles move on lanes that are drawn on the quay. The drivers who are to use the terminal transport vehicles must obey defined speed limits. Reverse maneuvering without seeing the back, and turning and changing lanes on the quay are dangerous. In the other hand, when the hatch of the ship are opened, the hatch must be placed in a proper place not to prevent the traffic on the quay.

3.2. Risks in Landside Operations and Safety

Many operations are carried out in the container field simultaneously and there are many working machines in the field. The nature of land operations contains dangers because of reasons including the characteristic of the container yard and equipment, working of machines and people in the same setting, and stowing vertically. There are rules that need to be followed during container stacking and container shifting in the field, their transportation and transfer to terminal vehicles and other transportation modes, and process of filling and emptying the container.

The ground where container stacking will be made must be flat. The containers which are stacked on an uneven ground may be damaged, bent and lose their shape because the load is not distributed evenly. Moreover, the containers which are stacked on an uneven ground will lean and their tumbling risk will increase. Containers are weak against the forces to be applied from the ceiling and side walls because of their structure. A steel framework bears the weight in the containers. Therefore, as the containers are stacked one on top of the other, the upper corners of the container below must be joined with the base corners of the upper container, and contact must be made between the upper surface and lower surfaces.

The equipment are used in the container yard, designed specifically for stacking containers. Stacking style and plans in the container yard change depending on the properties of these equipment. Container stacking more than the defined row and tier must not be made. The precautions that need to be taken and the rules that need to be followed show differences according to the properties of the crane used in the container yard. In the container delivery operations made by RTG, the container taken from the stacking must be kept on the stacking not on the vehicle way until the vehicle shows up to take the container. However, after the vehicle which comes to take the container takes its place, the container must be loaded in the vehicle by passing over

the truck bed and it should not be passed over the cabin. In the container receiving operations, before the vehicle which brings the container stops completely, the operation must not be started.

In the operation made by CRS, proper maneuvering area must be reserved for placing the containers to the stacking or taking them from the stacking. There must not be persons between CRS and the terminal transport vehicle during the operation. The first move must be slow and careful by considering the possibility that the containers taken from the terminal transport vehicle may be unbalanced in some cases. Carriage of the containers to long distances within the terminal by both CRS and RTG is prohibited.

The containers which carry dangerous load must be stored in certain divisions reserved for them in the field and stored as a single line preferentially. These areas must be isolated as much as possible; fire extinguishers may be placed in locations close to these areas and a drainage system and a fire extinguisher station can be established around the stowing field against possible leakages.

Container transportation is done by terminal transport vehicles in the terminals between the quay, container storage field and terminal door. There are some rules and security precautions that need to be obeyed as these transportation operations are made. A crucial part of the accidents occurring in the terminal takes place in these areas. The door and terminal traffic generated by external truck which bring export containers or take over import containers affects land and ship operation processes of the terminal and in addition it brings along significant risks within the terminal. Different door and terminal traffic arrangements must be developed to reduce these effects. The roads within the terminal must be supported by traffic signs and direction signs.

The drivers who are to use the terminal transport vehicles must pay attention to the written instructions and warnings, writings and signs in the field. The vehicles should not be driven faster than traffic allow. Moreover, as the containers are carried by the terminal transport vehicles, loads more than the carriage capacity that is determined by the manufacturer company must not be loaded on the truck beds.

Adverse weather conditions create important risks in the storage yard. Strong winds have the risk to move the containers in high stacking. Especially, it is dangerous for the empty containers which are stowed one on top of other as a single line. Attention should be paid that their doors are closed. Weather conditions must be followed up and in conditions when frost and icing is expected, precaution must be taken against icing on the roads with salt and defroster in advance.

4. CONCLUSIONS

The container terminals are a complex system where many operations are carried out simultaneously. Various handling equipment and people work in the same field. The operational risks in the container terminals occur depending on reasons such as the operation type, characteristics of the terminal field, properties of the used equipment, competency of terminal workers, environmental conditions and lack of security rules.

The risks that are faced during quayside operations and land operations show differences from each other. The risks in quayside operations occur depending on handling errors in general. In land operations on the other hand, a large part of the risks occur during transportation of the containers by terminal transportation vehicles and during stacking of the containers in the field. The accident types encountered during the operations are falling, slipping, jamming of the containers and hitting to some place in general. Such events can cause material damage and operation delay with the best possibility and can cause serious results for the health of the workers and environment.

In this context, it is necessary that the terminal administration determines the risks according to the technical properties of their own terminals and carry out works to prevent these. At the same time the terminal administration must provide the most appropriate environment for the health of their workers and inspect regularly whether the determined rules are followed up or not. It is necessary that work health and security trainings are offered to all personnel working in the terminal and their awareness must be raised on this matter. Especially the crane operators who have the training and ability to do the work and act according to the determined security rules will enable minimizing the risks in the terminal.

REFERENCES

- [1]. K.P.B Cullinane and M.Khanna, "Economies of Scale in Large Containerships: Optimal Size and Geographical Implications", *Journal of Transport Geography*, Vol. 8, pp. 181-195, 2000.
 - [2]. HSE, A Quick Guide to Health and Safety in Ports, [Online]. Available: <http://www.hse.gov.uk/>, 2011.
 - [3]. E.G.Emecen Kara, G.Kara and M.Bamyacı, "Productivity Measurement of Maritime Container Terminals", 6th International Logistics Supply Chain Congress, Istanbul, Turkey, November 6-7, pp.453-457, 2008.
 - [4]. E.G.Emecen Kara and F.Heydarova, "Container Terminal Operations and Operations Planning", 6th International Logistics Supply Chain Congress, Istanbul, Turkey, November 6-7, pp.433-439, 2008.
 - [5]. D.Steenken, S.Voß, and R.Stahlbock, Container Terminal Operation and Operations Research—a classification and literature review, *OR Spectrum*, Volume 26, pp 3–49, 2004.
 - [6]. K.H.Kim, Y.M.Park and M.J.Jin, An Optimal Layout of Container Yards, *OR Spectrum*, Volume 30, pp 675–695, 2007.
-

REMOVAL EFFICIENCY OF THE HERBICIDE ACLONIFEN BY SOIL FUNGI

Gokhan Onder Erguven

*Yildiz Technical University, Department of Environmental Engineering, 34220, Esenler/Istanbul, Turkey.
gokhanondererguven@gmail.com*

Hurrem Bayhan

Bahar Ikizoglu

S. Levent Kuzu

Gurdal Kanat

Yasar Nuhoglu

Abstract

In this study, laboratory campaigns were done to determine the removal efficiency of Aclonifen (2-chloro-6-nitro-3-phenoxyaniline). This compound is widely used during weed activity in Thrace Region and Anatolia.. The fungi isolated from these lands were used in the study. Monitoring were mostly conducted by chemical oxygen demand (COD) with all isolated fungi and mix of them. Total Organic Carbon (TOC) experiments were done only with mix of the fungi. Isolation of fungi from the soils, where aclonifen was not applied, were made through seeding to standard plate count agar. Fungi acquired from this isolation procedure were identified by 16s RNA gene technique. Herbicide including liquid of 100 ml was prepared and fungi culture was added in this liquid. This mixture was held in a shaker at a standard temperature of 200C. Monitoring took 5 days at aerobic condition. Daily culture sample was taken and COD and TOC analysis were made with this culture. According to the COD results, highest and lowest removal efficiencies were obtained by Metacordycepschlamydosporia and Penicilliumtalaromyces, from 15600mg/L to 1040 mg/L and 6390mg/L, respectively. Additionally, experiments were done by the isolated fungi culture (Penicilliumthrichoderma, Stachybotryschartarum, Penicilliumsimplicissimum, and Alterniaalternata), in parallel. Experimental studies were completed by adding the analysis of total organic carbon. According to the COD and TOC experiment results with fungi mix, the degradation rate was 88%, from 7150mg/L to 870mg/L as TOC and removal efficiency as COD was 91%, from 15600mg/l to 1360mg/L in 5 days.

Keywords: *Aclonifen, Chemical Oxygen Demand, Total Organic Carbon, Degredation Rate*

1. INTRODUCTION

Aclonifen is a diphenylether herbicide in which one ring is unsubstituted and the other is NH₂-1, Cl-2, NO₂-6 substituted. This substitution, especially NH₂-1, is a particular feature in the diphenylether herbicidal family. In contrast with other herbicides of the same family (acifluorfen, oxyfluorfen, bifenox), this compound is not only acting through a phytotoxic protoporphyrin IX accumulation but also through an inhibition of carotenoid biosynthesis [1].

The metabolism pathways of the microbial degradation of several diphenyl ethers have been studied. [2] reported that the main degradation pathway of oxyfluorfen by *A. chroococcum* was reduction of nitro group to amino compound, further acetylation of a amino derivative, O-dealkylation and dechlorination. The experiments were performed to study the degradation of chlornitrofen [3] and diphenyl ethers [4] using *Phlebiabrevispora* and *Lentinustigrinus*, respectively.

However, there are no reports on the degradation of Aclonifen using fungi cultures. In this study, microbial degradation of Aclonifen were studied with fungi isolated from an agricultural area previously unexposed to Aclonifen. Soil samples from sunflower field with known history of no pesticide usage, located in Kirklareli City, Turkey were also collected as source of pesticide degrading microbes. In the experiments 6 species of fungus were isolated from the soil samples using different media plates and Aclonifen degradation was investigated.

2. MATERIAL and METHOD

2.1. Chemicals and Reagents

Aclonifen herbicide, under the trade name "Chekic 600", was supplied by an agricultural products shop. This herbicide contains 600 gr L⁻¹ of Aclonifen active ingredient. All media for the isolation and enrichment of fungi were obtained from Sigma Aldrich.

2.2. Soil Sample Collection

Experiments were done on soil samples obtained from farming areas around the Kirklareli City. The majority of the farms selected in the area have been cultivating sunflower and wheat for several years. Soil with no background of Aclonifen concentration was collected from an organic farm. All samples were collected randomly from the top 0–20 cm of soil following the standard procedure and stored in glass vessels at an ambient temperature [5].

2.3. Media Preparation

Dextrose Casein Peptone Agar, Potato Dextrose Agar, Dichloran Rose Bengal Chlorinated Agar, Sabouraud Dextrose Agar, Malt Extract media were prepared according to manufacturer's instructions (Sigma Aldrich-USA) and were autoclaved at 121°C for 15 min. to ensure that the solution was sterilized. After cooling, diluted agricultural soil (containing no trace of Aclonifen) in an isotonic solution was added into petri dishes.

2.4. Isolation and Enrichment Studies

Fungi were isolated from the soil samples using serial dilution on different media plates. Fungi incubation took about one week at 20°C. After growing, the plates were screened for any colonies that were visually different from the others. The colonies were selected at random and denoted F1 to F6 for fungi. After incubation, the cultures were placed carefully in an enrichment media for seven days to grow at 20°C, and were shaken continuously.

2.5. Molecular Characterization Studies

The fungi marked on the petri dishes were sown in PDA petri dishes by streak plate to ensure the reproduction from sport fungi. The fungi that were grown at room temperature and from single colony isolation were transferred to other PDA petri dishes and were kept at room temperature until they reached the appropriate size for DNA isolation. Growing fungi were scratched using a sterile blade and crushed with liquid nitrogen in sterile conditions, after which, DNA was isolated from the powder hypes.

An ordinary Taq polymerase was conducted for PCR using many combinations of ITS (Internal transcribed spacer) region primers, which are often used in the definition of DNA. In PCR, the expected length of bands were obtained only for F1 (*Penicilliumthrichoderma*), F4 (*Metacordycepschlamydosporia*) and F6 (*Alternariaalternata*). For the other fungi, F2 (*Penicilliumsimplicissimum*), F3 (*PenicilliumTalaromyces*) and F5 (*Stachybotryschartarum*), One-Taq polymerase was used. The three primers designed by [6] gave two results. These tapes, which were cut from the agarose gel and cleaned (in the case of multiple bands) or as a single band, PCR reaction were sent directly to the sequence analysis. A Thermo-Scientific GeneJET Gel

Extraction Kit was used in the cleaning of the bands cut from the agarose gel. In cases of a sequence reaction on the bands (cut from the agarose gel) not performing well, re-amplification was made (by One Taq polymerase).

2.6. Microbial Biodegradation Studies

In the liquid media study, the Aclonifen active ingredient and microcosm were added to 100 ml of 0.8% isotonic saline water. The Aclonifen was prepared from Chekic 600 (trade name of the herbicide) in the same concentration as used in the field (200ml/1000m²). The growing media used in the experiments were the previously isolated and the enriched fungi, with 1 ml of the solutions obtained from of all kinds from the separately enriched solution used in the experiments.

In this phase, solution samples were monitored at 24-hour intervals on the basis of the Chemical Oxygen Demand (COD) and Total Organic Carbon(TOC) parameter. 100 ml of sample (includes 98 ml of 0.08% NaCl and 1 ml of enriched culture solution of fungi and 1 ml of herbicide) was used in the experiments. The samples were filtered through 45µm filter paper then analysed through the Standard Methods 5220C: Closed reflux titrimetric method and Standard Methods 5310B: Total organic carbon by High-Temperature Combustion Method.

3. RESULTS andDISCUSSION

The results of identification of species isolated from studied soils are given in Table 1. The COD removal efficiencies of the isolated and identified fungi are given in figure 1. According to the results, it is clear that the best performance was obtained from the mixed cultures. As seen from the figure, isolated fungi consortia showed the highest degradation of 91% in the COD parameter in five days. The initial COD and TOC value 15600mg/l and 7150mg/l respectively. The degradation rate for TOC is 88% in same time period for fungi mix (Figure2).

Table 1.The primers, sequence and references used to identify the fungi

Fungi code and approximate species identity	First primer 5'-3' sequence and reference	Second primer 5'-3' sequence and reference
<i>Penicilliumthrichoderma</i> (F1)	ITS3 GCATCGATGAAGAACGCAGC [7].	ITS _{env} ATCCCTACCTGATCCGAGGTC [6].
<i>Penicilliumsimplicissimum</i> (F2)	ITS6 GAAGGTGAAGTCGTAACAAGG [8].	ITS _{env} ATCCCTACCTGATCCGAGGTC [6].
<i>Penicilliumtalaromyces</i> (F3)	ITS4 TCCCTCCGCTTATTGATATGC [7].	ITS6 GAAGGTGAAGTCGTAACAAGG [8].
<i>Metacordycepschlamyosporia</i> (F4)	ITSTRfw GAGACCGCCACTGTATTTTCG [6].	ITS3 GCATCGATGAAGAACGCAGC [7].
<i>Stachybotryschartarum</i> (F5)	ITS1 TCCGTAGGTGAACCTGCGG [7].	ITS _{env} ATCCCTACCTGATCCGAGGTC [6].
<i>Alternariaalternata</i> (F6)	ITS3 GCATCGATGAAGAACGCAGC [7].	ITS _{env} ATCCCTACCTGATCCGAGGTC [6].

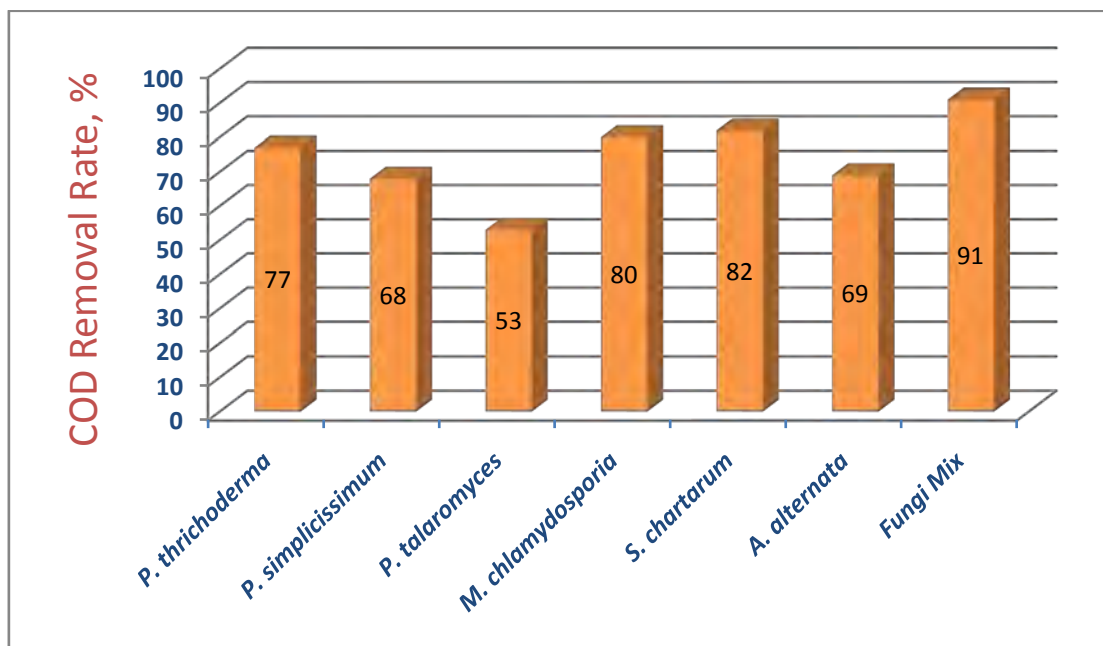


Figure 1. Removal rate of Aclonifen as COD

It was observed that COD removal efficiencies of the systems vary according to the microbial differences in the liquid medium. The best removal was achieved by *Stachybotryschartarum* in five days as 82%. The lowest removal efficiency 53% by *Penicilliumtalaromyces* in 5 days. Removal efficiency of the fungi, separately for *Penicilliumtrichoderma*, *Penicilliumsimplicissimum*, *Metacordycepschlamydosporia*, and *Alterniaalternata* species, were 77%, 68%, 80%, and 69% respectively in 5 days, whereas it was increased to 91% for fungal mixture during the same period. The ratio was 88% for the Total Organic Carbon parameter during the same time in mixed cultures.

4. CONCLUSION

This study showed that biodegradation ratios of Aclonifen were found sufficiently high, especially for the mixed fungi cultures. In the liquid medium, COD removal efficiency of the systems vary according to microbial differences. The best removal could be achieved by *Stachybotryschartarum* in 5 days as 82%. For Total Organic Carbon studies results, removal rate was 88% in same time period for mixed cultures of Fungi.

Biography:

GokhanOnderErguven was born in Kırklareli, Turkey on November 2, 1982. He received the engineering degree in environmental engineering from the “Trakya” University, Tekirdag, Turkey, in 2007. He received the M.Sc degree in the department of Agricultural structures and irrigation of natural sciences institute, “Namık Kemal” University, in 2010. Since 2011, He is academic at environmental engineering department of, Yildiz Technical University, Istanbul, Turkey. His research interests pesticides, natural treatment, environmental pollution, bioremediation

ACKNOWLEDGMENT

This research has been supported by Yildiz Technical University Scientific Research Projects Coordination Department. Number: 2012-05-02-KAP07

REFERENCES

- [1]. Kilinc, O., Grassetb, R., Reynaud, S., 2011. The herbicide Aclonifen: The complex theoretical bases of sunflower tolerance. *Pesticide Biochemistry and Physiology*. 100(2), 193–198.FLEXChip Signal Processor (MC68175/D), Motorola, 1996.
 - [2]. Chakraborty, S.K., Bhattacharyya, A., Chowdhury, A., 2002. Degradation of oxyfluorfen by *Azotobacterchroococcum* (Beijerinck). *Bulletin of Environmental Contamination and Toxicology*. 69, 203–209.
 - [3]. Kamei, I., Kondo, R., 2006. Simultaneous degradation of commercially produced CNP herbicide and of contaminated dioxin by treatment using the white–rot fungus *Phlebiabrevispora*. *Chemosphere* 65, 1221–1227.
 - [4]. Federici, E., Giubilei, M.A., Cajthaml, T., Petruccioli, M., Annibale, A.D., 2011. *Lentinus* (*Panus*) *tigrinus* augmentation of a historically contaminated soil: Matrix decontamination and structure and function of the resident bacterial community. *Journal of Hazardous Materials*. 186, 1263–1270.
 - [5]. Carter, M.R., Gregorich, E.G., 2006. *Soil Sampling and Methods of Analysis*, Second Edition by Taylor & Francis Group, LLC. International Standard Book Number -13, 978-0-8493-3586-0 (Hardcover)
 - [6]. Avcioglu-Dundar, B. 2014. Unpublished results.
 - [7]. White, T.J., Bruns, T., Lee, S., Taylor, J. 1990. Amplification and Direct Sequencing of Fungal Ribosomal Rna Genes for Phylogenetics. in: *PCR Protocols: A Guide to Methods and Applications*. Academic Press New York, p: 315–322.
 - [8]. Cooke, D.E., Drenth, A., Duncan, J.M., Wagels, G., Brasier, C.M., 2000 A molecular phylogeny of phytophthora and related oomycetes. *Fungal Genetics and Biology* 30, 17-32.
-

NATURAL GAS CONSUMPTION AND ITS EFFECT ON AIR EMISSIONS IN TURKEY

Ali CAN

Karabük University, Faculty of Engineering, Mechanical Engineering Department, 78050, Karabük, Turkey,
alican@karabuk.edu.tr

Halil EKMEKÇİ

Karabük University, Faculty of Engineering, Mechanical Engineering Department Ms. student, 78050, Karabük, Turkey,
h.ekmekci_78@hotmail.com

Abstract

Air is polluted and it is one of the biggest problems of earth environment. There is some agreement for the reduction of air emissions and almost all countries signed the Kyoto Protocol to decrease emissions for the future. However, this is not the case, the world still emits CO₂ and its concentration reaches approximately 380 ppm in the atmosphere. This gas, as a direct greenhouse gas, is important because it is responsible for approximately 60% of the earth's climate change. The other direct greenhouse gases such as CH₄, N₂O and F-gases are the responsible for remaining part. At the beginning of the 1970s, the natural gases are firstly used in industries in Turkey, with a value of 15 million m³/year, but it was reaches 45 600 million m³/year in 2013. This quantity is important because it is producing 33.9 million tones of oil equivalent (TOE) energy. The same quantity of energy could be produced by approximately 158 million tones lignite or 60 million tones of hard coal. In 2013, with the consumption of natural gas totally produce 88.2 million tones of CO₂ equivalent emissions. If hard coal was used instead of natural gas, the total emission would be 152 million tones of CO₂ equivalent emissions which is 72% more than natural gas consumption's emissions. If lignite was used, the total CO₂ equivalent emission would be 160 million tones. This quantity is 81% more. Therefore, using natural gas is one of the ways to tackle with climate change in Turkey in short time.

Keywords: *Climate Change, Greenhouse Effect, CO₂ Equivalent, CH₄ and N₂O Emissions, IPCC Methodology*

According to the IPCC [5], the most important greenhouse gases are carbon dioxide (CO₂), methane (CH₄), nitrous oxide (N₂O), hydrofluoro carbons (HFCs), perfluoro carbons (PFCs), and sulfur hexafluoride (SF₆). With the burning of coal, the first three gases are highly emitted to the atmosphere. The traditional solid fuels (such as coal, hard coal, lignite and etc.) emit gases, containing harmful effects on the environment and human beings, into the atmosphere during combustion; while pollutant effects of natural gas on the atmosphere are very low ([6]). Although, Turkey signed United Nations Climate Framework Convention on Climate Change and Kyoto Protocol without any commitment, it has to change their dirty fuels to clean fuels to tackle with climate change and to decrease the emissions in the future [9].

The purpose of this study was to investigate the effect of natural gas consumption on air emission of Turkey by using IPCC methodology and the consumption data of natural gases. The necessary data were obtained from the emission inventories of the State Institute of Statistics and energy balance tables of Ministry of Energy and Natural Resources. The CO₂, CH₄ and N₂O emissions were calculated by using the IPCC-Tier 1 method [4], [5].

2. METHODOLOGY

The method (IPCC - Tier 1) was used to estimate the CO₂, CH₄ and N₂O emissions. The estimation process can be divided into some steps that lead to figures for CO₂ and non-CO₂ emissions from fuel consumption. The general formula (1) for the CO₂ emission is given as [5].

$$\text{CO}_2 \text{ emissions} = \sum (U_n + I_n - HI_n - IB \pm SC) * EF * CF * E * C\text{-CO}_2 \quad (1)$$

U _n	: The fuel production quantity
I _n	: Imported fuel quantity
HI _n	: Exported fuel quantity
IB	: International Bunkers
SC	: Stock changes
CF	: Conversion Factor
n	: Fuel type
EF	: Emission Factor
E	: Efficiency (Coal 95% and Natural Gas 99%)
C-CO ₂	: Carbon to CO ₂ emission

And the general formula (2) for the CH₄ and N₂O emissions are given by IPCC Guidelines [5].

$$\text{Non-CO}_2 \text{ emissions} = \sum (U_n + I_n - HI_n - IB \pm SC) * EF * CF \quad (2)$$

According to IPCC Guidelines, the energy units are converted into Net Calorific Values (NCV). The international bunkers are subtracted from the calculations. And, for natural gas, the carbon emission factor depends on the composition of the gas which, in its delivered state, is primarily methane, but can include small quantities of ethane, propane, butane, and heavier hydrocarbons. Natural gas flared at the production site will usually be "wet", i.e., containing far larger amounts of non-methane hydrocarbons. The carbon emission factor will be correspondingly different for different fuel types.

The emission factors (EF) for different types of coal and natural gas for the direct greenhouse gases are given below Tables 1 and 2. The calorific values of coal are changing considerably between 1970 and 2013. For calculating the TOE values of coal annual conversion factors are used for each year. For lignite the minimum value is 6.90 TJ/Gg and maximum value is 25.98 TJ/Gg. The values for hard coal are changing between 25.35 TJ/Gg and 31.43 TJ/Gg.

Table 1. CO₂ Factors (IPCC)

Fuel Types	CO ₂		
	EF	Efficiency	C-CO ₂
Unit: tC/TJ			
Hard Coal	25,8	0,980	3,6667
Lignite	27,6	0,980	3,6667
Asphalt	25,8	0,980	3,6667
Second Fuel Coal	25,8	0,980	3,6667
Natural Gas	15,3	0,995	3,6667

Source: [5]

Table 2. Non-CO₂ Factors (IPCC)

CH₄ Factors				
Fuel Types	Electricity	Industry	Other	Transport
	EF	EF	EF	EF
	(Kg/TJ)	(Kg/TJ)	(Kg/TJ)	(Kg/TJ)
Hard Coal	1	10	300	10
Lignite	1	10	300	10
Asphalt	1	10	300	10
Second Fuel Coal	1	10	300	10
Natural Gas	1	5	5	50
N₂O Factors				
Fuel Types	Electricity	Industry	Other	Transport
	EF	EF	EF	EF
	(Kg/TJ)	(Kg/TJ)	(Kg/TJ)	(Kg/TJ)
Hard Coal	1,4	1,4	1,4	1,4
Lignite	1,4	1,4	1,4	1,4
Asphalt	1,4	1,4	1,4	1,4
Second Fuel Coal	1,4	1,4	1,4	1,4
Natural Gas	0,1	0,1	0,1	0,1

Source: [5]

3. RESULT AND DISCUSSION

The result of this study showed that the natural gases consumption over Turkey has been increasing throughout the years. In order to emphasize, in year 2013, the total consumption was reached approximately $45.610 \cdot 10^6 \text{ Sm}^3$ in Turkey (Figure 1). In this year, 53.65 % of natural gas was used for 105 116 GWh electricity production. And the remaining parts are used to supply of energy for residential households, industry, transport, and agricultural activities with the values 27.57%, 17.83%, 0.81% and 0.13% respectively. The consumption of the natural gases emits 88.07 million tones CO₂, 5.20 ktone CH₄ and 0.16 ktone N₂O. The emissions are equal to 88.24 million tones of CO₂ eq. The shares of direct greenhouse gases as CO₂ eq. in sectors, however, are a little different from the usage and are equal to 53.52% from electricity production, 27.54% from household, 17.82% from industry, 0.99% from transport and 0.13% from agricultural activities (Table 3).

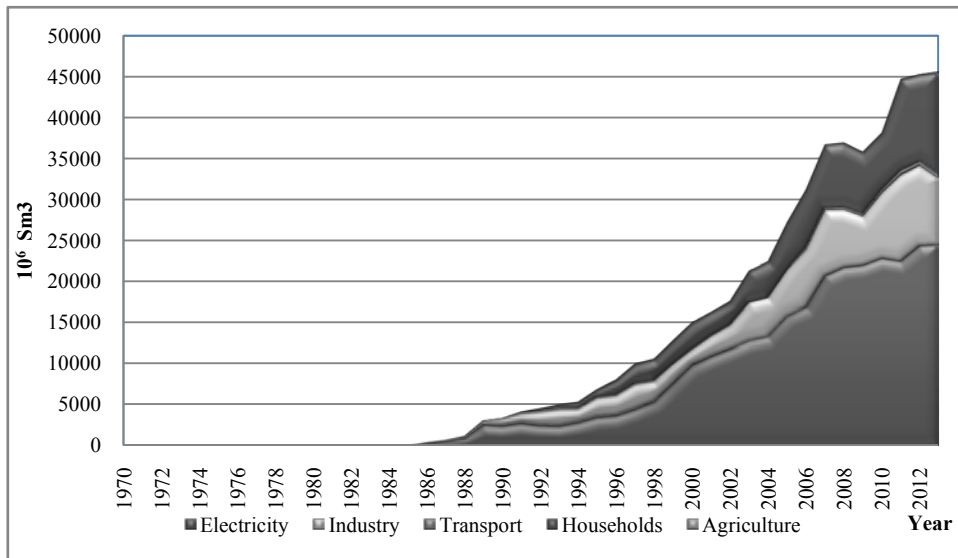


Figure 1. Total Natural Gas Consumption by different sources in Turkey between 1970-2013

Table 3. Emissions in 2013 (Gg)

	CO ₂	CH ₄	N ₂ O
Electricity	47180.3821	0.8452	0.0845
Industry	15681.6110	1.4047	0.0281
Other	24361.4178	2.1822	0.0436
Household	24245.4417	2.1718	0.0434
Agriculture	115.6840	0.0104	0.0002
Transport	855.3606	0.7662	0.0015
Total	88078.7715	5.1982	0.1578

As given in Table 3, the highest methane (CH₄) emission in 2013 was seen from households with a value of 2.17 ktone (Gg). The highest CO₂ and N₂O emission were observed in electricity production with respective values of 47 million tones and 0.08 ktone. Throughout the years, the emissions are increasing considerably especially in electricity production, industry and households. The Figure 2. is showing that the CO₂, CH₄ and N₂O emissions are reaching 88.08 million tones, 5.20 ktone and 0,16 ktone, respectively. In order to get CO₂ equivalent values as seen in Figure 3, the CH₄ are multiplied by 21 and N₂O is multiplied by 310 and the obtained values are added to CO₂ emissions (IPCC 1996).

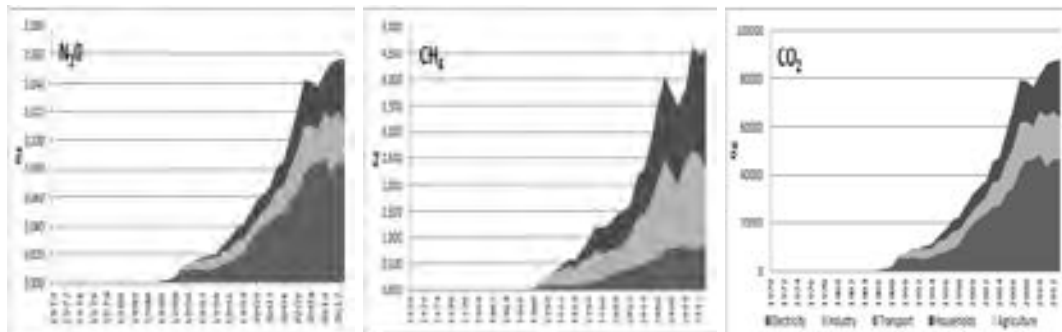


Figure 2. CO₂, CH₄ and N₂O emissions between 1970-2013

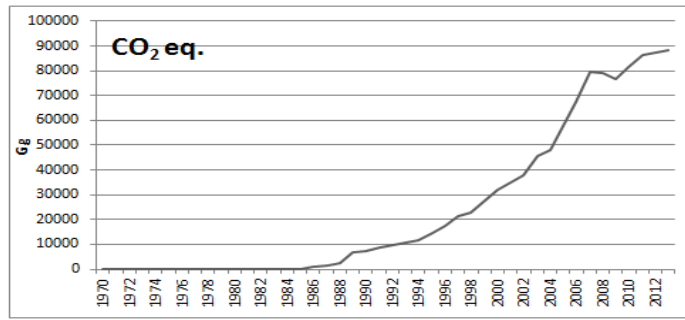


Figure 3. CO₂ eq. emissions between 1970-2013

In Turkey, the natural gas is used instead of coal. Therefore, if the natural gas was not used, then the emissions from coal will be more than present situation (Figure 4). After the 1988, the effect of using natural gas was considerably decreased the total emissions to the atmosphere. In this year, the total emission was decreased around 2 million tones CO₂ eq. If the same quantity energy (i.e., 37.63 million TOE coal in 2013) is used by burning coal for electricity production, industry, households, transport and agriculture, there will be needed 60 million tones lignite or 158 million tones hard coal.

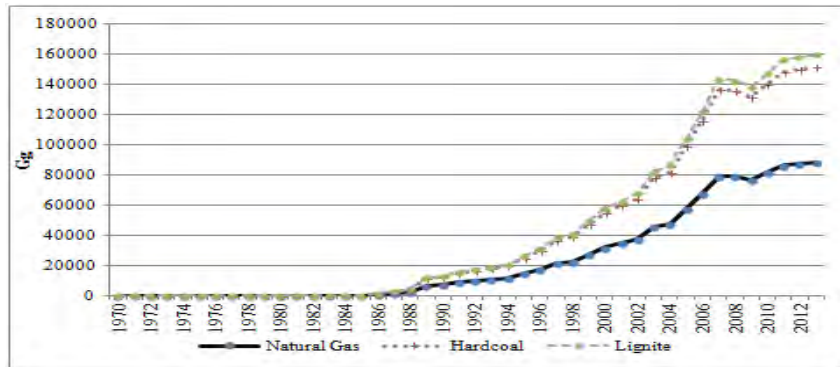


Figure 4. CO₂ eq. emissions from different fuels between 1970-2013

The CO₂ eq. emission difference is 70 million tones in 2013. According to the usage of lignite or hardcoal or both, the emission value can be changed. The minimum difference will be obtained if natural gas is used instead of hardcoal or maximum difference will be obtained if entire natural gas is used instead of lignite or other types of coal. The following figure explains the minimum and maximum differences according to the usage of different types of coal (Figure 5).

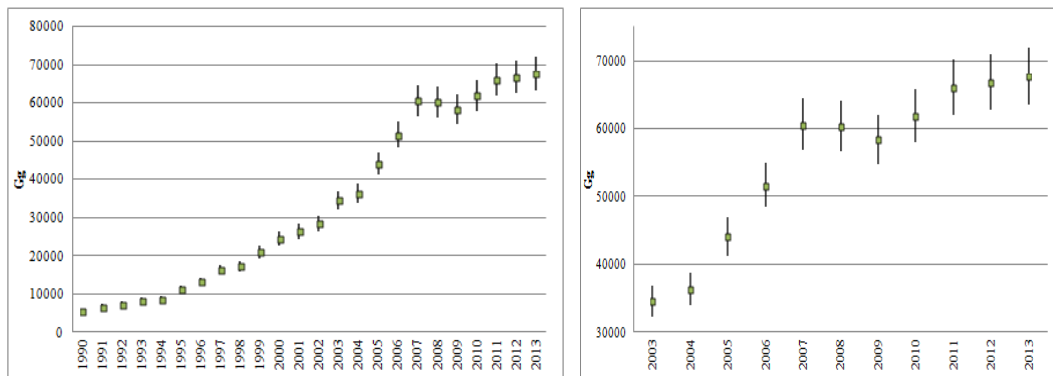


Figure 5. The minimum and maximum CO₂ eq. emissions in case coal used between 1970 – 2013.

4. CONCLUSION

This study has shown that the natural gases usage in Turkey decrease 70 million tones CO₂ eq. emissions in Turkey according to the IPCC Guidelines. Each category is considered and calculated according to the Guidelines. Using natural gas is one of the ways to tackle with climate change for Turkey in short time. However, the limited reserve will prohibit Turkey for future plans. At the beginning of the 1970s, the natural gases are firstly used in industries in Turkey, with a value of 15 million m³/year, but it was reaches 45 600 million m³/year in 2013. This quantity is important because it is approximately produce 33.9 million tones of oil equivalent (TOE) energy. The same quantity of energy could be produced by approximately 158 million tones lignite or 60 million tones of hard coal. And this quantity energy by burning coal could create minimum 63.7 million tones CO₂ eq. extra emissions by using only hardcoal or maximum 71.7 million tones CO₂ eq. extra emissions by using only lignite or other types of coal. So the different percentage usage of different coal instead of natural gas could give extra emissions. Therefore, using natural gases as a fuel is one way to tackle with climate change for Turkey.

REFERENCES

- [1]. Amponsah N.Y., Trolborg M., Kington B., Aalders I., Hough R.L.; Greenhouse Gas Emissions from Renewable Energy Sources, ScienceDirect journal, 2014.
 - [2]. Greb S.F., Eble C.F., Peters D.C., Papp A.R.; Coal and The Environmental (7-11; 15-32p), 2006.
 - [3]. IPCC Summaries for Policymakers and Other Summaries – Intergovernmental Panel on Climate Change. 1-22, 43p, 1994.
 - [4]. IPCC Greenhouse Gas Inventory Reference Manual – Revised 1996 IPCC Guidelines for National Greenhouse Gas Inventories – Volume 3 – Intergovernmental Panel on Climate Change – Edited by Houghton J.T., et al. 1996.
 - [5]. IPCC Greenhouse Gas Inventory Reference Manual – IPCC Guidelines for National Greenhouse Gas Inventories - Intergovernmental Panel on Climate Change, 2006.
 - [6]. Kakaee A. H., Paykani A., Ghajar M. The influence of fuel composition on the combustion and emission characteristics of natural gas fueled engines. Renewable and sustainable Energy reviews 38.p.64-78, 2014.
 - [7]. MENR - The annual Energy and Petroleum Balance Sheets 1970-2013, Ministry of Energy and Natural Resources, 2013.
 - [8]. Thorin E., Basics of Energy - Energy Sources, Energy Conversion Energy Use , References - 2014 Elsevier Inc., 2014.
 - [9]. TurkStat, National Greenhouse Gas Inventory Report, 1990-2011. Annual Report submission under the “Framework Convention on Climate Change, 2013.
 - [10]. Vivoda V. Natural gas in Asia: Trade, markets and regional institutions. Energy Policy-p.80-90, 2014.
 - [11]. Westphal K., Institutional change in European natural gas markets and implications for energy security: Lessons from the German case - Energy Policy-p.35-43, 2014, 2014.
-

CARNITINE LEVELS IN MILK AND MILK PRODUCTS

Rabia Serpil GÜNHAN

*1 Selçuk University, Department of Food Technology, Vocational High School of Technical Sciences, Konya, Turkey.
rsgunhan@selcuk.edu.tr*

Suzan YALÇIN

Selçuk University, Department of Food Hygiene and Technology, Faculty of Veterinary Medicine, Konya, Turkey

Abstract

In this study the aim was to determine the levels of L-carnitine in milk and milk products consumed in Turkey. For this purpose, each of the 15 different of the UHT milk, pasteurized milk, plain yoghurt, strained yoghurt, white cheese, kashar cheese, totally 90 samples were taken from markets. L-carnitine concentrations were measured by HPLC-fluorescence detector. According to the analysis' results, the mean level of free carnitine in UHT milk as 1,57 mg /100g, total carnitine as 2,19 mg /100g, the mean level of free carnitine in pasteurized milk as 1,07 mg /100g and the total karnitin as 1,45 mg /100g were determined. As for the mean level of free carnitine in white cheese as 0,32 mg /100 g, total carnitine as 0,57 mg /100g and the mean level of free in kashar cheese as 0,46 mg/100 g, total carnitine as 0.65 mg/100 g were determined. Furthermore, the mean level of free carnitine in plain yoghurt and in strained yoghurt were respectively determined as 0,47 mg/100g, 0,70 mg /100 g and also for the mean level of total carnitine as 0,80 mg /100g , 1,15 mg /100g. In statistical evaluation, the difference between the groups of white and kashar cheese in terms of free carnitine was found to be significant ($p < 0.001$). While the difference between plain and strained yoghurt for free carnitine was not important, the difference in terms of total carnitine was significant ($p = 0.013$). As for between pasteurized and UHT milk, the difference in terms of free and total carnitine was significant ($p < 0.001$). In addition, differences in terms of free and total carnitine were determined to be significant ($p < 0.05$) in product groups and in some types of products. Consequently, it was concluded that milk and milk products having a great place in nutrition have different concentrations of carnitine and the carnitine levels detected were found to be important for meeting the individuals' needs of daily carnitine.

Keywords: Carnitine, milk, milk products, HPLC, fluorescence dedector

1. INTRODUCTION

In recent years, L-carnitine has become one of the prominent bioactive compounds. L-carnitine is present endogenously in all mammals and it is a non-protein amino acid derivative which has a low molecular weight (161.2 g/mole), contains quaternary nitrogen and can be dissolved in water. ([11]-[31]). Although it is similar to vitamin in a functional manner, it doesn't have the full characteristics of vitamin because of its synthesizing in the body. Carnitine has the D- and L- forms. "L" form is defined as the physiological form of carnitine and it is important in human and animal nutrition ([21]). L-carnitine plays an important role in lipid metabolism and energy production acting as a carrier by transporting the long chain fatty acids into the mitochondria for β -oxidation ([4]-[17]). Also many studies have proved that L-carnitine is used as an auxiliary in reinforcing muscles, in the treatment of neurodegenerative diseases, hypertension and diabetes. ([16]). Carnitine deficiency or disorder in the body causes diseases such as degradation in fatty acid metabolism ([31]-[32]), hyperlipemia, hyperammonemia, hypoglycemia, skeletal muscle diseases and myasthenia ([18]).

L-carnitine is synthesized endogenously from lysine and methionine amino acid ([15]). Micro nutrients such as vitamin C, iron, pyridoxine and niacin are necessary for the biosynthesis of carnitine. Overall quality of the diet is important ([30]). Under normal conditions, healthy people can synthesize adequate amounts of carnitine. However, the specified daily need amount of carnitine has been increasing for pregnant women and newborn babies ([27]). In the case of infancy or high energy requirements as pregnancy and lactation endogenous synthesis is not enough because of increasing carnitine requirement ([5]).

L-carnitine is present as acyl carnitine and free carnitine in cells and tissues ([14]). Daily requirement of carnitine (15 mg) is provided by endogenous biosynthesis and exogenous sources ([1]). The amount of carnitine taken with food is variable. Intake of carnitine varies between 23-135 mg/day and 2-12 μ mol/kg/day in individuals consumed variety food ([8]-[25]). Regular daily nutrition provides 472 μ mol (76.5 mg) carnitine. The 77.8% of this comes from meat products and 14.4% of it from dairy products and eggs ([7]). Bioavailability of carnitine taken from foods and food supplements is between 57-87 %, 14-18% respectively ([27]-[3]).

Enzymatic, spectrophotometric, chromatographic and electrophoretic techniques are used in determining the detection and quantification of carnitine. Studies have been developed by using radio-enzymatic methods, HPLC / UV, HPLC / fluorescence, flow injection analysis, tandem MS, HPLC / tandem MS ([21]-[6]).

In this paper, free and total carnitine levels were studied in pasteurized milk, UHT milk, plain yoghurt, strained yoghurt, white cheese and kashar cheese and those levels of carnitine were compared among the groups of milk products.

2. MATERIAL and METHODS

2.1. Materials

15 different samples of each UHT milk, pasteurized milk, plain yoghurt, strained yoghurt, white cheese and kashar cheese were taken from markets which makes a total of 90 samples. These samples were kept at -18°C until the carnitine levels were determined.

2.2. Reagents and Apparatus

L-carnitine (Sigma CO283), (3-carboxypropyl) trimethylammonium chloride (γ -butyrobetaine hydrochloride), 1-Aminoanthracene (Aldrich, A28606), 1-ethyl-3-(3-dimethylaminopropyl)carbodiimide hydrochloride (EDAC) (Fluka, 03450), Ammonium acetate (Merck, 101115.1000), Acetic acid (Merck, 100063), Chloroform (Merck, 102431), Acetone (Merck, 100014), Sodium phosphate monobasic monohydrate (Sigma, S9638), Disodium hydrogen phosphate dihydrate, Acetonitrile (Merck, 100030), perchloric acid, hydrochloric acid. All other chemicals were used without further purification.

HPLC analyses were conducted using a Shimadzu brand equipped with autosampler (AIL-20ACHT), column oven (CTO-20A), fluorescence detector (Shimadzu Model RF-20A), pump (LG-20AT), HPLC column (HIC-ACE-121-1546 ACE 5 C18) (150*4,6mm).

2.3. Optimal HPLC Conditions

The HPLC mobile phase was prepared by mixing 700ml of 0.1 M ammonium acetate in water (pH 3.5 adjusted with acetic acid) with 300 mL of acetonitrile. Chromatographic separation was performed at a flow rate of 1.5mL/min, using HIC-ACE C18, 150 × 4.6 mm I.D., particle size 5 μ m column. The excitation and emission wavelengths of the spectrofluorimeter were 248 and 418 nm, respectively. The amount injection of the sample into the HPLC system was 20 μ L. The peak area ratios of L-carnitine and internal standard (2 μ g/mL γ -butyrobetaine hydrochloride) were used to measure L-carnitine concentration. Retention times of L-carnitine and IS were 4.0 and 4.9 min, respectively.

2.4. Preparation of calibration Standards

A stock solution of L-carnitine was prepared by dissolving approximately 10 mg in 10ml deionized Milli-Q filter water. Further standard solutions were obtained by applying serial dilutions of the stock solution with 0,1, 2, 10 and 20 ppm L-carnitine. 2 μ g/ml of γ - butyrobetaine was prepared for internal standard and calibration curve was drawn ([2]).

2.5. Sample Preparation, Extraction and Precipitation

After 2 g of both white cheese and kashar samples were weighed, they were homogenized three times with 5 ml of saline solution by using the homogenizer. 5 ml of cheese solution was taken from the obtained amount of 15 ml. After plain yoghurt and strained yoghurt were weighed as 2 g, 5 ml of distilled water was added and homogenized. 5 ml of milk was taken directly from the milk samples. Sample preparation was carried out according to the method of Reference [9]-[33] with minor modifications. 5 ml 0,25 M HClO₄ was added into 5 ml samples and 500 μ l internal standard and mixed. Then it was left at room temperature about 60 min. and filtrated. Deproteinized 10 ml samples were divided in two parts for determining the level of free and total carnitine. For free carnitine it was arranged to pH 6,5. For total concentration, 5 ml sample was hydrolyzed with 6 M KOH. Then it was left at 40°C for one hour in water bath. HClO₄ (70% w/v) was added to pH 6,5. For each free and total carnitine, 1 ml of supernatant was taken and passed through 0,45 μ m membrane and used for the derivatization reaction.

2.6. Derivatization Procedure

Derivatization procedure was carried out according to the method of Ref [2]. The 1-Aminoanthracene (fluorescent reagent) was dissolved in acetone (16 mg/mL) and 1-ethyl-3-(3-dimethylaminopropyl) carbodiimide (EDC) in 0.01 M NaH₂PO₄-H₂O pH 3.5 (160 mg/mL). The 500 μ l of the supernatant was mixed with 500 μ l of 0.01 M NaH₂PO₄-H₂O (pH 3.5). The 20 μ l of 1M HCl, 100 μ l of 1-aminoanthracene solution and 100 μ l of EDC solution were then sequentially added to the sample with continuous vortex mixing. The mixture was incubated at 25°C for 20 min and the excess reagent was removed by washing the sample with 5 mL of diethyl ether. A 300 μ l aliquot of the aqueous phase was then transferred into another tube, and 700 μ l of 0.01 M NaH₂PO₄-2H₂O, pH 9.1 was added to adjust the pH of the samples to about 7 and the mixture was washed with 5 mL of chloroform. The 500 μ l aliquots of the final aqueous phase were diluted with 500 μ l of 0.01 M NaH₂PO₄-H₂O, pH 3.5 and 20 μ l of this solution was injected into the high performance liquid chromatography (HPLC) system.

2.7. Chromatographic Analyses

The linearity of the calibration standard curve of L-carnitine is shown in Fig.1. Regression coefficient (r^2) of calibration was found as 0.9918. L-carnitine concentration of samples was calculated by utilizing the calibration curve. The retention times for L-carnitine and internal standard were 4.044 and 4.866 min respectively in Fig 2.

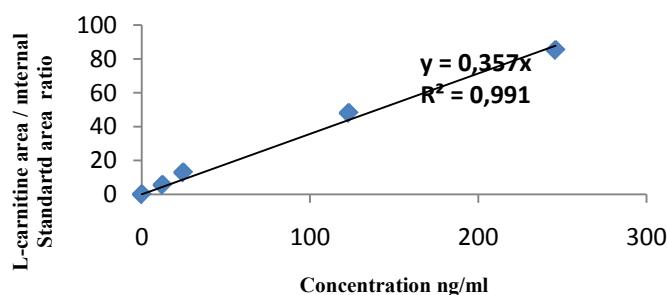


Fig.1. Standard calibration curve of L-carnitine

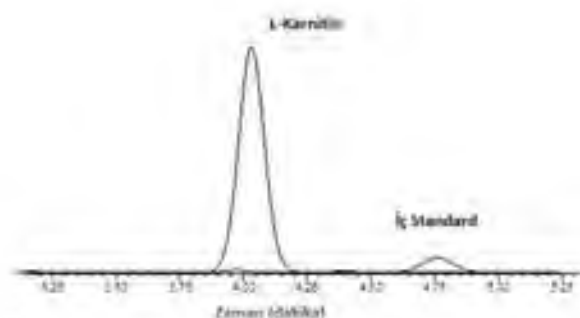


Fig.2. HPLC chromatograms of L-carnitine and internal standard

2.8. Statistical Analyses

The statistical analyses were performed with SPSS 21.0. The mean and standard error of data were calculated. The differences between parameters in cheese, in yoghurt and in milk were analyzed through the significance test of the difference between two groups. The differences of carnitine content among a variety of milk and milk products were analyzed by using one-way ANOVA test. Homogeneity of variances was assessed by using Levene test. As variance is not homogenous, Welch ANOVA was used and if the difference between groups is found to be significant, Tamhane T2 test was performed in paired comparison. Differences were considered as significant if $p < 0.05$ ([12]).

3.RESULTS andDISCUSSION

In this study, statistical evaluations were made between two groups in cheese, in yoghurt and in milk samples. Statistical evaluations were presented for white cheese and kashar in table 1, for plain yoghurt and strained yoghurt in table 2 and for pasteurized milk and UHT milk in table 3. In addition, the evaluation between dairy products was shown in table 4.

Table 1. Comparison of white cheese and kashar in terms of L-carnitine

		Mean ± std.error	t	p
Free carnitine (mg/100g)	White cheese	0,32 ± 0,03	-4,636	<0,001
	Kashar cheese	0,46 ± 0,02		
Total carnitine (mg/100g)	White cheese	0,57 ± 0,05	-1,451	0,158
	Kashar cheese	0,65 ± 0,03		
Acyl carnitine (mg/100g)	White cheese	0,25 ± 0,03	1,644	0,111
	Kashar cheese	0,19 ± 0,03		

n=15

While the amount of free carnitine in white cheese was determined as 0,32 mg/100g, the one in kashar cheese was determined as 0,46 mg/100g. Differences between the two groups were found to be significant (p<0,001). No difference was observed in terms of total carnitine.

Table 2. Comparison of plain yoghurt and strained yoghurt in terms of L-carnitine

		Mean ± stderror	t	P
Free carnitine (mg/100g)	Plain yoghurt	0,47 ± 0,06	-2,043	0,053
	Strained yoghurt	0,70 ± 0,10		
Total carnitine (mg/100g)	Plain yoghurt	0,80 ± 0,05	-2,728	0,013
	Strained yoghurt	1,15 ± 0,12		
Acyl carnitine (mg/100g)	Plain yoghurt	0,33 ± 0,05	-1,849	0,075
	Strained yoghurt	0,45 ± 0,04		

n=15

While the level of free carnitine of plain yoghurt was found as 0,47 mg/100g, the one in strained yoghurt was found as 0,70 mg/100g. Differences between the two groups were found to be significant (p = 0,013) in terms of total carnitine.

Table 3. Comparison of pasteurized milk and UHT milk in terms of L-carnitine

		Mean ± stderror	t	P
Free carnitine (mg/100g)	UHT milk	1,57 ± 0,02	16,924	<0,001
	Pasteurized milk	1,07 ± 0,02		
Total carnitine (mg/100g)	UHT milk	2,19 ± 0,07	9,024	<0,001
	Pasteurized milk	1,45 ± 0,05		
Acyl carnitine (mg/100g)	UHT milk	0,62 ± 0,07	3,028	0,006
	Pasteurized milk	0,38 ± 0,04		

n=15

The differences between the pasteurized milk and UHT milk are crucial in terms of free (p<0,001) and total carnitine (p<0,001).

Table 4. Comparison of milk and milk products in terms of L-carnitine

		n	Mean ± stderror	F	P
Free carnitine (mg/100g)	Cheese	30	0,39a ±0,02	112,71	<0,001
	Yoghurt	30	0,58b ±0,06		
	Milk	30	1,32c ±0,05		
	Total	90	0,76 ±0,05		
Total carnitine (mg/100g)	Cheese	30	0,61a ±0,03	93,46	<0,001
	Yoghurt	30	0,97b ±0,07		
	Milk	30	1,82c ±0,08		
	Total	90	1,13 ±0,06		

*the parameters shown by different letters are different.

The differences among the groups of cheese, yoghurt and milk were found to be significant in terms of free carnitine (p<0,001) and total carnitine (p<0,001).

The levels of mean free carnitine and total carnitine of dairy products offered for consumption by different brands are indicated in Fig 3.

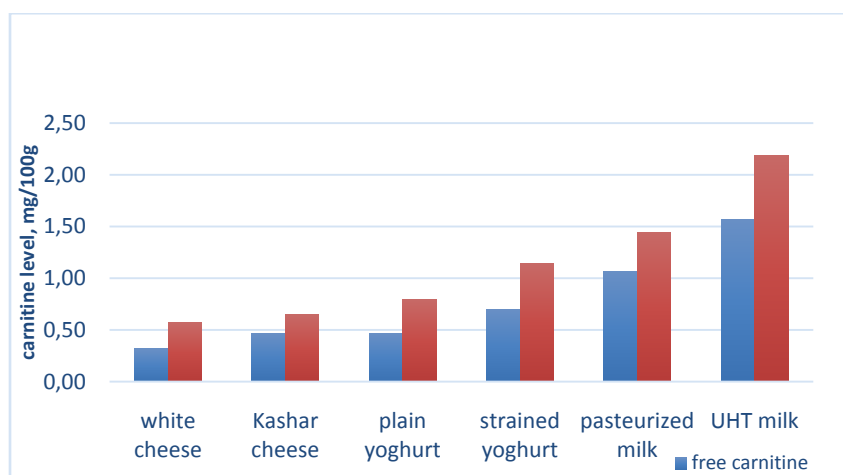


Figure 3. The level of mean free and total carnitine of dairy products

After carnitine was discovered, a series of methods had been developed for quantitation. Mostly, these methods have been used in order to determine carnitine levels in blood plasma and urine ([19], [20], [14], [23], [28]-[22]). Identity and quantity studies of carnitine are also present in food and food supplement ([24], [27], [26], [29], [23]-[1]).

In the study the mean level of free carnitine in UHT milk as 1.57 mg /100g, total carnitine as 2.19 mg /100g, the mean level of free carnitine in pasteurized milk as 1,07 mg /100g and the total carnitine as 1.45 mg /100g were determined. Similar results were obtained: free carnitine as 1.34 mg/100g, total carnitine as 2.56 mg/100g in UHT milk and free carnitine as 1.27 mg/100g, total carnitine as 2.64 mg/100g in pasteurized milk ([10]). In the study of ref [33], the levels of free and total carnitine in milk were determined as 1.65 mg/100g, 2.85 mg/100g, respectively by using enzymatic method. In other studies, the amounts of total carnitine in milk were indicated as between 2.1 and 5.8 mg/100g ([17]-[33]).

Reference [13] measured the level of free carnitine content in raw milk to be 1,9 mg/100g and in milk as 1,8 mg/100g. Ref [7] determined carnitine in milk as 2,3 mg/100ml and ref [23] rather discretely measured as 10,1±1,1 mg/100g. In this study, the levels of carnitine found in milk are similar compared to the results of

the past studies. the differences could be due to the use of different analytical methods, sample preparations and preprocessing procedures like homogenization, standardization and some processes are applied in producing pasteurized and UHT milk. And also milk may be produced by using milk powder. For these reasons, carnitine levels in milk vary.

The mean level of free carnitine in white cheese as 0,32 mg /100 g, total carnitine as 0,57 mg /100g and the mean level of free in kashar cheese as 0,46 mg/100 g, total carnitine as 0.65 mg/100 g were determined. Ref [7] determined carnitine level in cheese as 1,8 mg/100 g and Ref [10] indicated the level of free carnitine as 0,16 mg/100g, total carnitine as 0,79 mg/100g in natural cheese. Ref [27] found free carnitine level as 2,89 mg/100g, total carnitine level as 3,46 mg/100g in white cheese. The data obtained in this study are determined as lower than the literature data. As can be seen in the study of Ref [27]), this difference could be due to cheese variety, difference of production, using microbial cultures and maturation process. During storage of cheese, dry matter and carnitine concentration of cheese increase because of the evaporation of water. The difference of carnitine concentrations between white and kashal cheese might be due to different manufactory processes.

Furthermore, the mean levels of free carnitine in plain yoghurt and in strained yoghurt were respectively determined as 0.47 mg/100g, 0.70 mg /100 g and also for the mean level of total carnitine as 0.80 mg /100g , 1.15 mg /100g. Ref [10] detected free carnitine level as 1.48 mg/100g, total carnitine level as 3.03 mg/100g in plain yoghurt. In the study of ref [27] free and total carnitine levels in yoghurt were indicated as 2.30 mg/100g, 3.46 mg/100g respectively. However, the level of carnitine in yoghurt was found to be lower than the literature data. It can be resulted from adulteration made in yoghurt production, separation of milk fat and addition of margarine. Separation process has damaged the structure of carnitine in milk. On the other hand, adding milk powder and microbial cultures have affected the level of carnitine ([27]). The difference of carnitine levels in the plain yoghurt and strained yoghurt can be due to differences in manufacturing processes.

The carnitine levels compared among the dairy products were found to be significant ($p < 0,001$). Cheese contains less carnitine than milk because during cheese manufacturing milk was curdled and strained and removed whey from cheese products. Removing whey affects the carnitine content in cheese because of the hydrophilic characteristics of carnitine ([27]). The carnitine levels in milk may vary even though the same manufacturing processes applied to the samples. The carnitine concentrations of milk and milk products also change according to product types, fat content, animal species, metabolism, lactation durations and numbers. The amount of carnitine decreases as lactation period progresses ([34]- [27]).

4.CONCLUSION

As a result, detailed knowledge was obtained about the level of carnitine in milk and milk products. Carnitine content in milk, yoghurt and cheese varied due to the different samples, analytical methods, preparation of samples and process steps. Milk and milk products are important for humans in meeting the proposed Daily need for carnitine (0.3-1.9 mg/kg). It should also be noted that L-carnitine is sold as food supplement. But bioavailability of carnitine taken from food is higher. In this regard, detailed studies are required for determination of carnitine levels in various foods, especially in processed food.

ACKNOWLEDGMENT

This article was prepared from the No.10202030 doctoral thesis project. The authors thank the Scientific Research Projects Coordination Unit of Selçuk University for providing financial support.

REFERENCES

- [1]. Bodkowski R, Pekala J, Patkowska-Sokola B, Jamroz D, Steininger M, Lochynski S, Dobrzanski Z, Nowakowski P. Applications of enzymatic methods and liquid chromatography (HPLC) for determination of carnitine content in milk and meat. In: Szoltysik M, Dabrowska A, ed. *New Trends in Food Analytics*. Wroclaw. pp. 63-73, 2011.
 - [2]. Cao Q-R, Ren S, Park M-J, Choi Y-J, Lee B-J. "Determination of High Soluble L-Carnitine in Biological Samples by Reverse Phase High Performance Liquid Chromatography with Fluorescent Derivatization." *Arch Pharm Res.*, vol. 30(8), pp.1041-1046, 2007.
 - [3]. Cao Y, Hao C, Wang C, Li P, Wang L, Guan H, Li H. "Urinary excretion of L-carnitine, acetyl-L-carnitine, propionyl-L-carnitine and their antioxidant activities after single dose administration of L-carnitine in healthy subjects." *Braz J Pharm Sci.*, vol. 49, pp. 185-191, 2013.
 - [4]. Cao Y, Wang Y, Liu C, Wang L, Han Z, Wang C. "Comparison of pharmacokinetics of L-carnitine, acetyl-L-carnitine and propionyl-L-carnitine after single oral administration of L-carnitine in healthy volunteers." *Clin Invest Med.*, vol. 32 (1), pp. 13-19, 2009.
 - [5]. Cho SW, Cha YS. "Pregnancy increases urinary loss of carnitine and reduces plasma carnitine in Korean women" *Br J Nutr.*, vol. 93, pp. 685-691, 2005.
 - [6]. Dabrowska M, Starek M. "Analytical approaches to determination of carnitine in biological materials, foods and dietary supplements", *Food Chemistry.*, vol.142, pp. 220-232, 2014.
-

- [7]. Demarquoy J, Georges B, Rigault C, Royer MC, Clairet A, Soty M, Lekounougou S, Borgne FL. "Radioisotopic determination of l-carnitine content in foods commonly eaten in Western countries." *Food Chemistry*, vol. 86, pp. 137-142, 2014.
- [8]. Evans AM, Fornasini G. "Pharmacokinetics of L-carnitine." *ClinPharmacokinet*. 2003; 42(11): 941-967.
- [9]. Hamamoto M, Shimoda K, Matsuura N, Matsuura H. "A method for the fractionation and determination of carnitines in milk and milk products." *J JpnSocNutr Food Sci.*, vol. 41, pp. 389- 395, 1988a.
- [10]. Hamamoto M, Shimoda K, Matsuura N, Matsuura H. "Determination of free, short-chain acyl and long-chain carnitines in milk and milk products." *J JpnSocNutr Food Sci.*, vol. 41, pp. 397- 404, 1988b.
- [11]. Harmeyer J. The Physiological role of L-carnitine. Lohmann Information. 2002, vol. 27.
- [12]. Hayran M, Hayran M. *Sağlık Araştırmaları için Temel İstatistik*. Ankara, Art Ofset Matbaacılık Yayıncılık Organizasyon Ltd Şti. 2011, vol. 421.
- [13]. Indyk HE, Woollard DC. "Enzymatic determination of free carnitine in milk and infant formulas" *Journal of AOAC International*, vol. 78, pp. 69-74, 1995.
- [14]. Jones LL, McDonald DA, Borum PR. "Acylcarnitines: Role in brain". *Prog in Lipid Res.*, vol. 49, pp. 61-75, 2010.
- [15]. Krasovicova-Kudlackova M, Simoncic R, Bederova A, Babinska K, Beder I. "Correlation of carnitine levels to methionine and lysine intake" *Physiol Res.*, vol. 49, pp. 399-402, 2000.
- [16]. Kurt Ö, El SN. "Biyoaktif bir gıda bileşeni L-karnitin: beslenme ve sağlığı açısından önemi ve biyoyararlılığı." *Tıbbi Bilim Dergisi*, vol. 4 (2), pp. 97-102, 2011.
- [17]. La Count DW, Drackley JK, Weigel DJ. "Responses of dairy cows during early lactation to ruminal or abomasal administration of L-carnitine" *J Dairy Sci.*, vol. 78, pp. 1824-1836, 1995.
- [18]. Li K, Sun Q. Simultaneous determination of free and total carnitine in human serum by HPLC with UV detection. *J Chromatogr Sci.*, vol. 48 pp. 371-374, 2010.
- [19]. Longo A, Bruno G, Curti S, Mancinelli A, Miotto G. "Determination of L-carnitine, acetyl-L-carnitine and propionyl-L-carnitine in human plasma by high-performance liquid chromatography after pre-column derivatization with 1-aminoanthracene" *J Chromatogr B.*, vol. 686, pp. 129-139, 1996.
- [20]. McEntry CJ, Lever M, Storer MK. "A high performance liquid chromatographic method for the measurement of total carnitine in human plasma and urine". *Clinica Chimica Acta.*, vol. 344, pp. 123-130, 2004.
- [21]. Minkler PE, Ingalls ST, Hoppel CL. "Strategy for the isolation, derivatization, chromatographic separation, and detection of carnitine and acylcarnitines". *Anal Chem.*, vol. 77, pp. 1448-1457, 2005.
- [22]. Peng M, Liu L, Jiang M, Liang C, Zhao X, Cai Y, Sheng H, Ou Z, Luo H. "Measurement of free carnitine and acylcarnitine in plasma by HILIC-ESI-MS/MS without derivatization" *J Chromatogr B.*, vol. 932, pp. 12-18, 2013.
- [23]. Pormsila W, Krahenbühl S, Hauser PC. "Determination of carnitine in food and food supplements by capillary electrophoresis with contactless conductivity detection" *Electrophoresis*, vol. 31, pp. 2186-2191, 2010.
- [24]. Prokoratova V, Kvasnicka F, Seccik R, Voldrich M. "Capillary electrophoresis determination of carnitine in food supplements" *J Chromatogr A.*, vol. 1081, pp. 60-64, 2005.
- [25]. Rebouche CJ. "Kinetics, pharmacokinetics and regulation of L-carnitine and acetyl-L-carnitine metabolism" *Ann. N.Y. Acad. Sci.*, vol. 1033, pp. 30-41, 2004.
- [26]. Rigault C, Mazue F, Bernard A, Demarquoy J, Le Borgne F. "Changes in L-carnitine content of fish and meat during domestic cooking" *Meat Science*, vol. 78, pp. 331-335, 2008.
- [27]. Seline KG, Johein H. "The determination of l-carnitine in several food samples" *Food Chemistry*, vol. 105, pp. 793-804, 2007.
- [28]. Sowell J, Fuqua M, Wood T. "Quantification of total and free carnitine in human plasma by hydrophilic interaction liquid chromatography tandem mass spectrometry" *J Chromatogr Sci.*, vol. 49, pp. 463-468, 2011.
- [29]. Starkey DE, Denison JE, Seipelt CT, Jacobs WA. "Single-Laboratory Validation of a liquid Chromatographic/Tandem Mass Spectrometric method for the determination of free and total carnitine in infant formula and raw ingredients" *Journal of AOAC International*, vol. 91, pp. 130-142, 2008.
- [30]. Steiber A, Kerner J, Hoppel CL. "Carnitine: a nutritional, biosynthetic and functional perspective" *Mol Aspects Med.*, vol. 25, pp. 455-473, 2004.
- [31]. Tanphaichitr V, Pakpeankitvatana R. "Effects of dietary protein intake on carnitine status in Thai men" *Nut Res.*, vol. 21, pp. 31-39, 2001.
- [32]. Thangasamy T, Subathra m, Sittadjody S, Jeyakumar P, Joyee AG, Mendoza E, Chinnakkanu P. "Role of L-carnitine in the modulation of immune response in aged rat" *Clinica Chimica Acta.*, vol. 389, pp. 19-24, 2008.
- [33]. Woollard DC, Indyk HE, Woollard GA. "Enzymatic determination of carnitine in milk and infant formula" *Food Chemistry*, vol. 59 (3), pp. 325-332, 1997.
- [34]. Woollard DC, Indyk HE, Woollard GA. "Carnitine in milk: a survey of content, distribution and temporal variation" *Food Chemistry*, vol. 66, pp. 121-127, 1996.

BIOGRAPHY

Rabia Serpil Günhan was born in Konya, Turkey on April 4, 1971. She received the engineering degree in food engineering from the "Hacettepe" University, Ankara, Turkey, in 1996. She received the M.Sc and Ph.D. degree in the department of food hygiene and technology of veterinary faculty, "Selçuk" University, in 2006 and 2014, respectively. Since 2011, She is academic at food technology department of vocational high school, Selçuk University, Konya, Turkey. Her research interests food chemistry and functional food.

INVESTIGATION OF THE DIFFUSION KINETICS OF BORIDED COLD WORK TOOL STEEL

Salih KANAT

Department of Metallurgical and Materials Engineering, Institute of Natural and Applied Sciences, Afyon Kocatepe University, 03200 Afyonkarahisar, Turkey. salih.kanat@hotmail.com

Ibrahim GUNES

Department of Metallurgical and Materials Engineering, Faculty of Technology, Afyon Kocatepe University, 03200, Afyonkarahisar, Turkey.

Abstract

In this study, the case properties and diffusion kinetics of cold work tool steel (X210CrW12) borided in Ekabor-II powder were investigated by conducting a series of experiments at temperatures of 1123, 1223 and 1323K for 2, 4 and 8 h. The boride layer was characterized by optical microscopy, X-ray diffraction technique and micro-Vickers hardness tester. X-ray diffraction analysis of boride layers on the surface of the steels revealed the existence of FeB, Fe₂B, CrB and Cr₂B compounds. Depending on the chemical composition of substrates and boriding time, the boride layer thickness on the surface of the steel ranged from 13.54 μm and 164.42 μm . The hardness of the boride compounds formed on the surface of the steels ranged from 1672 to 2118 HV_{0,05}, whereas Vickers hardness values of the untreated the steels was 584 HV_{0,05}. The activation energies (Q) of the borided steel were 180.359 kJ/mol. The growth kinetics of the boride layers forming on the cold work tool steel and the thickness of boride layers were also investigated.

Keywords: *Activation energy, Boride layer, Cold work tool steel, Kinetics, Micro-hardness.*

1. INTRODUCTION

Boriding is a diffusion surface treatment, which is defined as the enrichment of the surface of a workpiece with boron by means of thermo-chemical treatment. It is well known that the boronized layer has high hardness, high hot hardness and good wear resistance, corrosion resistance and oxidation resistance [1-20]. Thermal diffusion treatments of boron compounds used to form iron borides typically require process temperatures of 973K and 1323K for 1 to 12 hours. The process can be carried out in solid powder (boronizing compound), liquid, gaseous, electrochemical or plasma medium [6-12]. In this technique the boriding (pack) agent in powder form is placed into a heat resistant stainless steel box and samples are embedded into this powder under inert gas atmosphere. At the end of boriding time, the stainless steel box is cooled at room temperature and then, dust over the samples is removed [2].

Boron atoms due to their relatively small size (atomic radius of 0.9 Å) and very mobile nature can diffuse easily into ferrous alloys (atomic radius of 1.24 Å) and the boriding of ferrous materials results in the formation of either a single layer (Fe₂B) or double-layer (FeB/Fe₂B) with definite composition. The phase equilibrium diagram of the binary system iron-boron shows the existence of two iron borides: Fe₂B with 8.8 wt. % B approximately, and FeB with 16.2 wt. % B approximately [3-13]. For practical applications, the formation of a single-phase (Fe₂B) is more desirable than a dual-phase layer comprising FeB and Fe₂B. This is because, although the boron rich FeB phase is harder, it is more brittle than the iron sub-boride, Fe₂B phase. Furthermore, crack formation is often observed at the FeB/Fe₂B interface of a dual-phase layer, as FeB and Fe₂B phases exhibit substantially different coefficients of thermal expansion. These cracks often lead to flaking and spalling when a mechanical load is applied. One of the important properties of a borided layer is that it keeps its hardness in subsequent heat treatment [9-14].

The primary objective of present study is to investigate characterization and kinetics of borided cold work tool steel that is the one of the most well-known cold work tool steels. Moreover, this study was to investigate the effect of process parameters, such as temperature, time and chemical composition, on the boride layers formed on the cold work tool steel after powder pack boriding at different processing temperatures and times.

2. EXPERIMENTAL DETAILS

2.1. Boriding and characterization

The cold work tool (X210CrW12) contained 2.08 wt.% C, 12.3wt.% Cr, 0.6 wt.% W, 0.16 wt.% Ni, 0.36 wt.% Mn and 0.25 wt.% Si. The test specimens were cut into Ø28x10mm dimensions, ground up to 1200G and polished using diamond solution. The boriding heat treatment was carried out in a solid medium containing an Ekabor-II powder mixture placed in (stainless steel box) an electrical resistance furnace operated at the temperature of 1123K, 1223K and 1323K for 2, 4 and 8 h under atmospheric pressure. At the end of boriding time, the box is cooled at room temperature and then, dust over the samples is removed. After the surfaces of the boronized specimens were ground, polished and etched with a 3% Nital solution, their microstructures were observed by Nikon MA100 optical microscope. The presence of borides formed in the coating layer was confirmed by means of X-ray diffraction equipment (Shimadzu XRD 6000) using Cu K α radiation. The hardness measurements of the boride layer on each steel and untreated steel substrate were made on the cross-sections using a Shimadzu HMV-2 Vickers indenter with a 50 g load.

2.2. Evaluation of the activation energy of the boron diffusion

In order to study the diffusion mechanism, borided cold work tool steel was used for this purpose. It is assumed that the boride layers grow parabolically in the direction of diffusion flux and perpendicular to the substrate surface. So, the time dependence of boride layer thickness can be described by Eq. (1):

$$x^2 = Dt \quad (1)$$

Where x is the depth of the boride layer (mm), t the boriding time (s), D the boron diffusion coefficient through the boride layer. It is a well-known fact that the main factor limiting the growth of a layer is the diffusion of boron into the substrate. It is possible to argue that the relationship between growth rate constant,

D , activation energy, Q , and the temperature in Kelvin, T , can be expressed as an Arrhenius equation (Eq. (2)):

$$D = D_0 \exp\left(-\frac{Q}{RT}\right)$$

(2)

Where D_0 is a pre-exponential constant, Q the activation energy (J/mol), T the absolute temperature in Kelvin and R is the ideal gas constant (J/mol K).

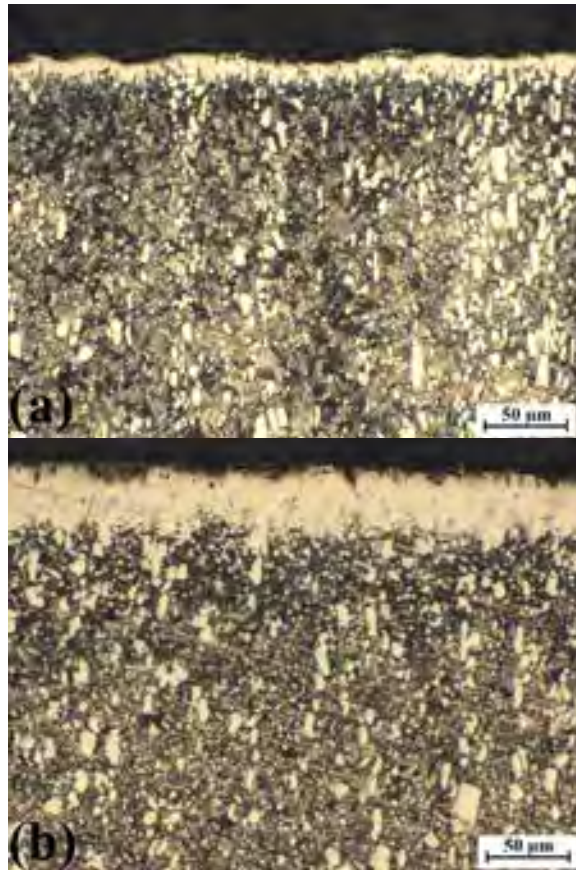
The activation energy for the boron diffusion in the boride layer is determined by the slope obtained in the plot of $\ln D$ vs. $\frac{1}{T}$, using Eq. (3):

$$\ln D = \ln D_0 - \frac{Q}{RT} \quad (3)$$

3. RESULTS AND DISCUSSION

3.1. Characterization of boride coatings

The cross-section of the optical micrographs of the borided cold work tool steel at the temperature of 1123K and 1323K for 2 and 8 h are shown in Figure 1. As can be seen the borides formed on the cold work tool steel substrate have a saw tooth morphology. It was found that the coating/matrix interface and matrix could be significantly distinguished and the boride layer had a columnar structure. Depending on the chemical composition of substrates, boriding time and temperature the boride layer thickness on the surface of the cold work tool steel ranged from 13.54 μm and 164.42 μm in Figure 2.



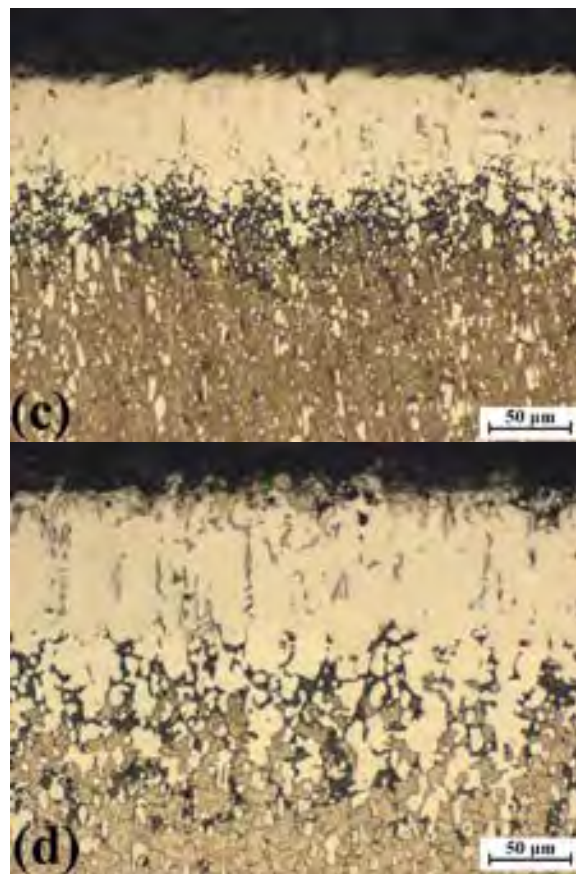


Figure 1: The cross-section of borided cold work tool steel; a) 1123K - 2h, b) 1123K - 8h, c) 1323K - 2h, d) 1323K - 8h.

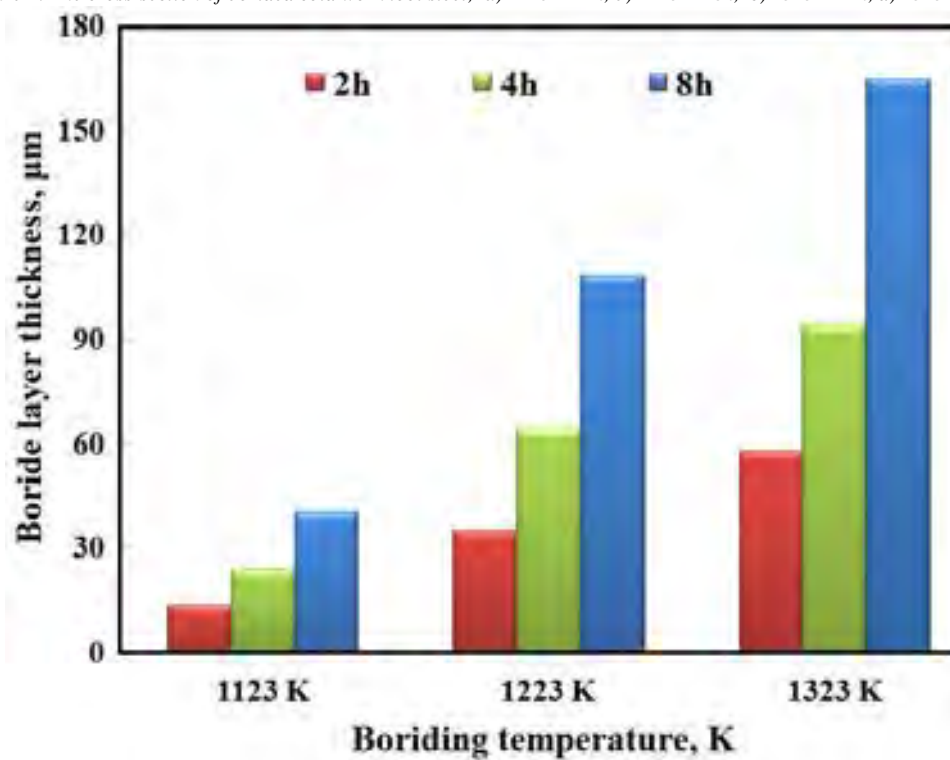


Figure 2: The thickness values of boride layers with respect to boriding time and temperatures.

Figure 3 gives the XRD pattern obtained at the surface of borided cold work tool steel at 1123K and 1323K for treatment time 2 and 8 h. XRD patterns show that the boride layer consists of borides such as SB and S₂B (S=Metal; Fe, Cr). XRD results showed that boride layers formed on the cold work tool steel contained the FeB, Fe₂B, CrB and Cr₂B phases in Fig. 3.

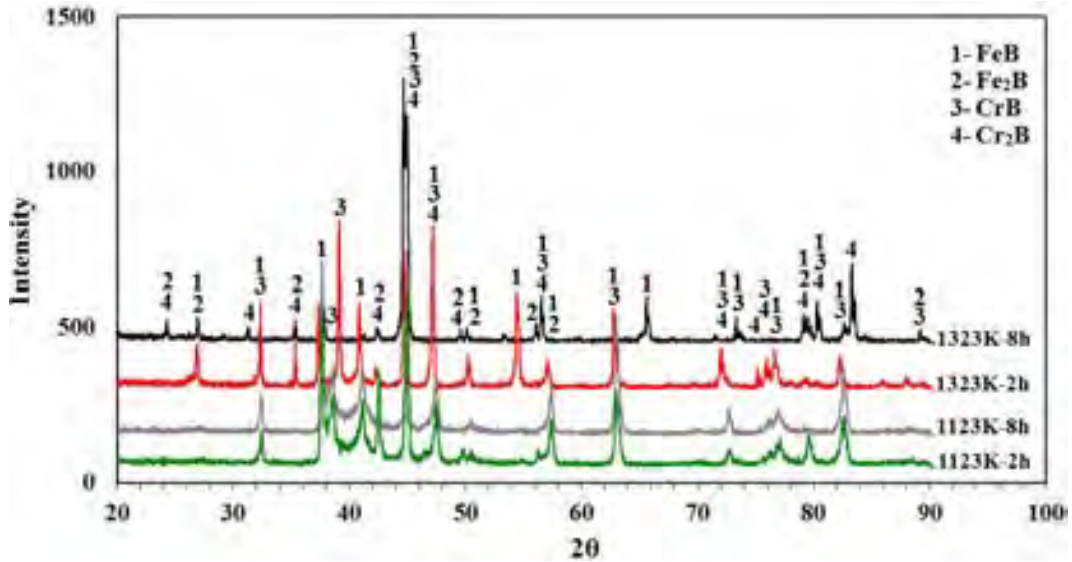


Figure 3: X-ray diffraction patterns of borided cold work tool steel.

Micro-hardness measurements were carried out from the surface to the interior along a line in order to see the variations in the boride layer hardness, transition zone and matrix, respectively. Micro-hardness of the boride layers was measured at 10 different locations at the same distance from the surface and the average value was taken as the hardness. Micro-hardness measurements were carried out on the cross-sections from the surface to the interior along a line; see Figure 4.

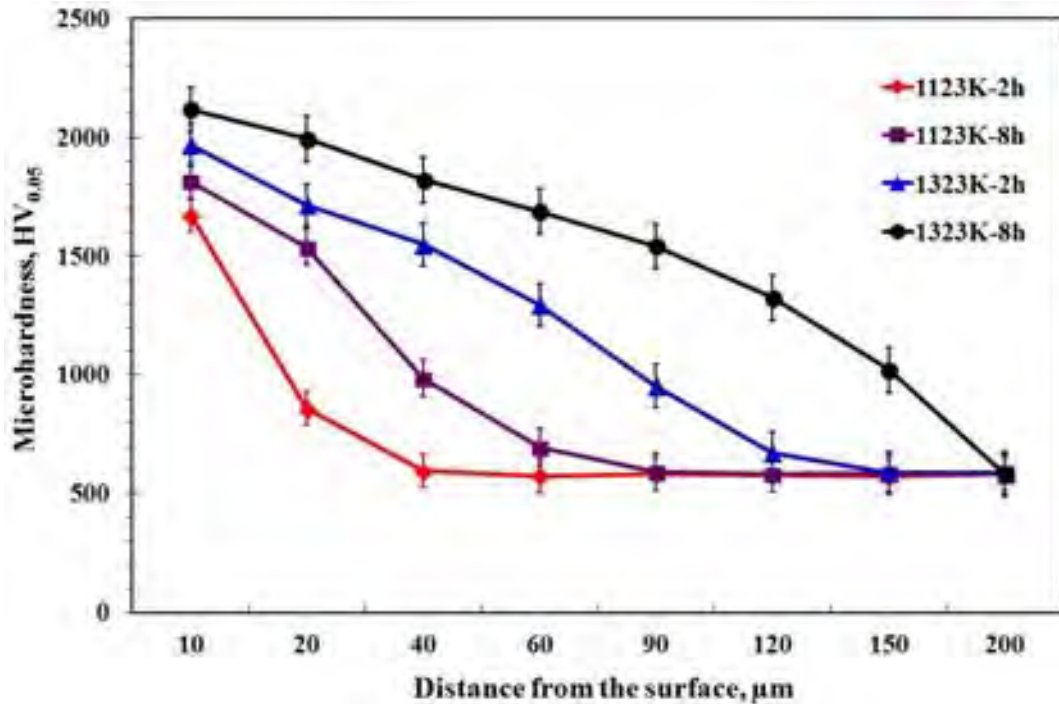


Figure 4: The variation of hardness depth in the borided cold work tool steel.

The hardness of the boride layer formed on the cold work tool steel varied between 1672 and 2118 HV_{0.05}. On the other hand, Vickers hardness values were 584 HV_{0.05}, for the untreated cold work tool steel. The micro-hardness of the boride layer also depends strongly on the composition and structure of the boride layer and composition of the material. When the hardness of the boride layer is compared with the matrix, boride layer hardness is approximately four times greater than that of the matrix.

3.2 Kinetics

In this study, the effects of the processing temperature and boriding time on the growth kinetics of the boride layer were also investigated. Kinetic parameters such as processing temperature and time must be known for the control of the boriding treatment. Figure 5 shows the time dependence of the squared value of boride layer thickness at increasing temperatures. This evolution followed a parabolic growth law where the diffusion of boron atoms is a thermally activated phenomenon. The growth rate constant D at each boriding temperature can be easily calculated from Eq. (1).

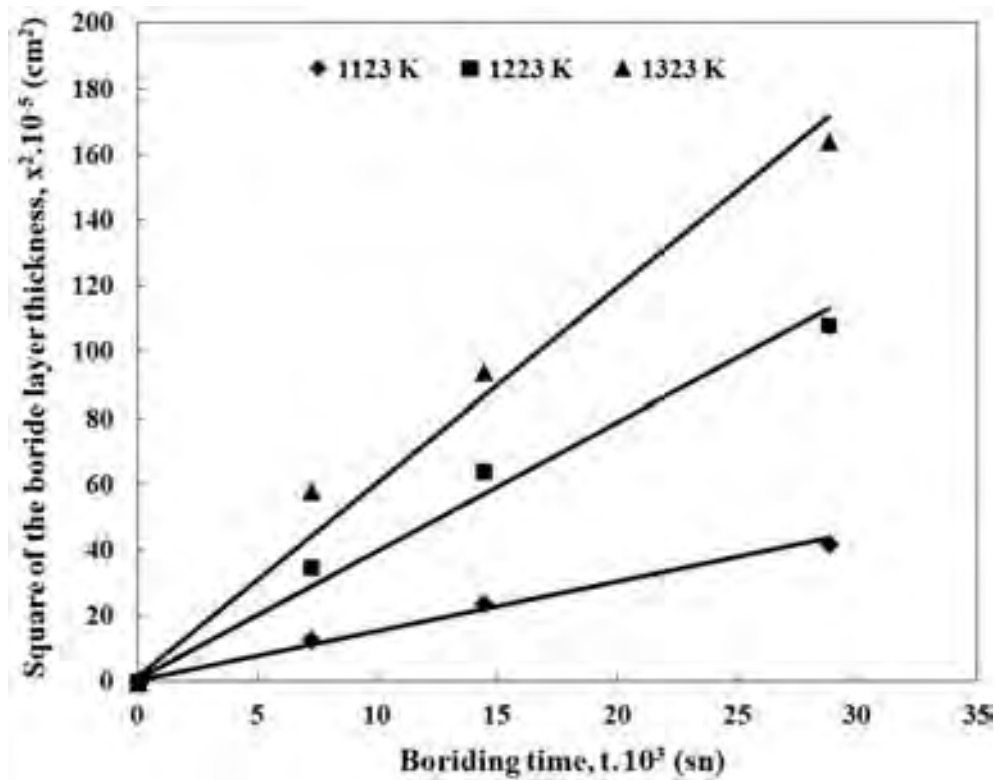


Figure 5: The time dependence of squared boride layer thickness at increasing temperatures.

As a result, the calculated growth rate constants at the three temperatures: 1123, 1223 and 1323 K are the following: 0.244×10^{-9} , 1.187×10^{-9} , and 4.539×10^{-9} cm² s⁻¹ for the borided cold work tool steel. Table 1 lists the calculated values of growth constant at each boriding temperature.

Table 1. The growth rate constant (D) as a function of boriding temperature.

Material	Growth rate constant ($\text{cm}^2 \text{s}^{-1}$)		
	Temperature, K		
	1123 K	1223 K	1323 K
X210CrW12	0.244×10^{-9}	1.187×10^{-9}	4.539×10^{-9}

Figure 6 describes the temperature dependence of the growth rate constant. The plot of $\ln D$ as a function of the reciprocal temperature exhibits a linear relationship according to the Arrhenius equation. The boron activation energy can be easily obtained from the slop of the straight line presented on Figure 6. The value of boron activation energy was then determined as equal to 180.359 kJ/mol for the borided cold work tool steel.

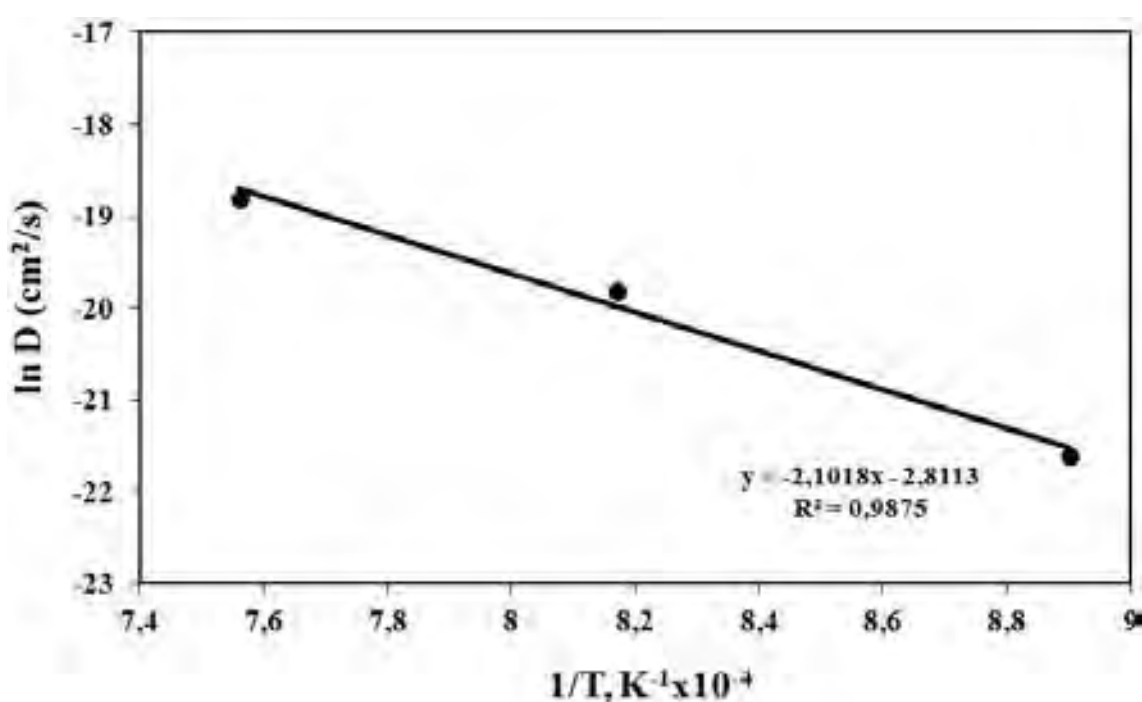


Figure 6: The temperature dependence of the growth rate constant according to the Arrhenius equation.

Table 2 compares the obtained value of energy (180.359 kJ/mol) with the data found in the literature. It is seen the reported values of boron activation energy depended on the chemical composition of the substrate and on the used boriding method. The calculated value in this study is compatible with the values reported in the literature as seen in Table 2 [17-19].

Table 2. The comparison of activation energy for diffusion of boron with respect to the different boriding medium

Steel	Temperature range (K)	Boriding medium	Activation energy (kJ/mol)	References

AISI 8620	973-1073	Plasma paste	99.77	[17]
AISI 316	1073-1223	Pack	199	[4]
AISI H13	1073-1273	Powder	186.2	[21]
AISI D2	1123-1273	Electrochemical	137.8	[18]
AISI D2	1073-1223	Salt bath	170	[16]
AISI D2	1123-1273	Pack	201.5	[19]
X210CrW12	1123-1323	Pack	180.539	Present study

A contour diagram describing the evolution of boride layer thickness as a function of the boriding parameters (time and temperature) is shown in Figure 7.

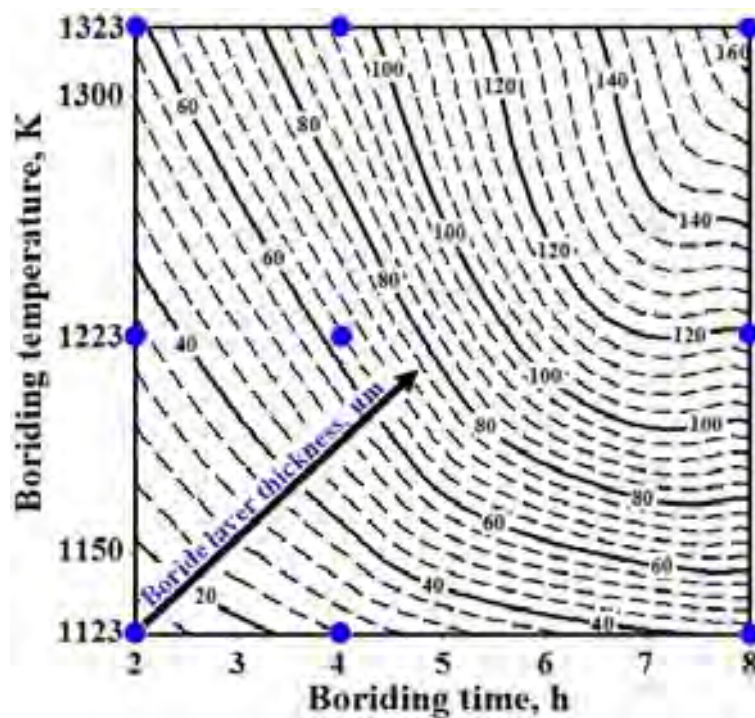


Figure 7: Contour diagram describing the evolution of boride layer thickness as a function of boriding parameters.

This contour diagram can be used for two purposes: (1) to predict the coating layer thickness with respect to the process parameters, namely time and temperature; (2) to determine the value of process time and temperature for obtaining a predetermined coating layer thickness [23]. The boride layer increased with the increase in boriding time and temperature in the borided cold work tool steel.

4. CONCLUSIONS

In this study, wear behavior and some of the mechanical properties of borides on the surface of borided cold work tool steel were investigated. Some of the conclusions can be drawn as follows.

- The boride layer thickness on the surface of the cold work tool steel was obtained, depending on the chemical composition of substrates, 13.54-164.42 μm .
- The multiphase boride coatings that were thermo chemically grown on the cold work tool steel were constituted by the FeB, Fe₂B, CrB and Cr₂B phases.
- The surface hardness of the borided steel was in the range of 1672-2118 HV_{0.05}, while for the untreated the steel substrate it was 584 HV_{0.05}.
- The boron activation energy was estimated as 180.359 kJ/mol for the borided cold work tool steel.
- A contour diagram relating the boride layer thickness to the boriding parameters (time and temperature) was proposed. It can be used a simple tool to select the optimum boriding layer according to the practical utilization of this kind of material.

ACKNOWLEDGEMENT

The authors are grateful to the Scientific Research Project (14.FEN.BİL.49) Council of Afyon Kocatepe University. This article was written based on Salih Kanat's master thesis.

5. REFERENCES

- [1]. Bindal, C., Ucisik, A. H., (1999). Characterization of borides formed on impurity-controlled chromium-based low alloy steels. *Surface and Coatings Technology*, No. 122, 208-213.
 - [2]. Campos-Silva, I., Ortiz-Dominguez, M., Lopez-Perrusquia, N., Meneses-Amador, A., Escobar-Galindo, R., and Martinez-Trinidad, (2010). Characterization of AISI 4140 borided steels. *J., Appl. Surf. Sci.*, vol 256, p. 2372-2379.
 - [3]. Culha, O., Toparli, M., Sahin, S., and Aksoy, T., (2008). Characterization and determination of Fe₃B layers' mechanical properties. *J. Mater. Process. Technol.*, vol. 206(1-3), p. 231-240.
 - [4]. Genel, K., (2006). Boriding kinetics of H13 steel. *Vacuum*, No. 80, 451-457.
 - [5]. Gunes, I., (2013). Kinetics of borided gear steels. *Sadhana*, No.38, 527-541.
 - [6]. Gunes, I., Taktak, S., (2012). Surface characterization of pack and plasma paste boronized of 21NiCrMo2 steel. *Journal of the Faculty of Engineering and Architecture of Gazi University*, v. 27, pp. 99-108.
 - [7]. Gunes, I., Erdogan, M., and Çelik, A.G., (2014). Corrosion behavior and characterization of plasma nitrided and borided AISI M2 Steel. *Materials Research*, vol. 17(3), p. 612-618.
 - [8]. Gunes, I., Dalar, A., (2013). Effect of sliding speed on friction and wear behaviour of borided gear steels. *Journal of the Balkan Tribological Association*, No. 19 (3), 325-339.
 - [9]. Gunes, I., Ulker, S., Taktak, S., et al. (2013). Kinetics of plasma paste boronized AISI 8620 steel in borax paste mixtures. *Protection of Metals and Physical Chemistry of Surfaces*, No. 49, 567-573.
 - [10]. Gunes, I., (2014). Tribological Properties and Characterisation of Plasma Paste Borided AISI 5120 Steel. *Journal of the Balkan Tribological Association*, v. 20, pp. 351-361.
 - [11]. Hudakova, M., Kusy, M., Sedlicka, V., Grgac, P., (2007). Analysis of the boronized layer on K190PM tool steel. *Materials and Technology*, 41, 81-84 (WOS:000255055400004 (ISSN: 1580-2949).
 - [12]. Keddam, M., Chegroune, R., (2010). A model for studying the kinetics of the formation of Fe₂B boride layers at the surface of a gray cast iron. *Applied Surface Science*, No. 256, 5025-5030.
 - [13]. Keddam, M., (2004). A kinetic model for the borided layers by the paste-boriding process. *Applied Surface Science*, No. 236, 451-455.
 - [14]. Martini, C., Palombarini, G., Poli, G., and Prandstraller, D., (2004). Sliding and abrasive wear behaviour of boride coatings. *Wear*, vol. 256(6), p. 608-613.
 - [15]. Matuschka, A.G.V., (1980). Boronizing, Heyden and Son Inc., Philadelphia, vol.1, p. 11.
 - [16]. Ortiz-Dominguez, M., Keddam, M., Elias-Espinosa, M., Damian-Mejia, O., Flores-Renteria, M.A., Arenas-Flores, A., Hernandez-Avila, J., (2014). Investigation of boriding kinetics of AISI D2 steel. *Surface Engineering*, vol. 30(7), p. 490-497.
 - [17]. Ozdemir, O., Omar, M. A., Usta, M., Zeytin, S., Bindal, C., Ucisik, A. H., et al. (2009). An investigation on boriding kinetics of AISI 316 stainless steel. *Vacuum*, No. 83, 175-179.
 - [18]. Sen, S., Sen, U., and Bindal, C., (2005). An approach to kinetic study of borided steels. *Surf. Coat. Technol.*, vol. 191(2-3), p. 274-285.
 - [19]. Sen, S., Sen, U., Bindal, C., (2005). The growth kinetics of borides formed on boronized AISI 4140 steel. *Vacuum*, vol. 77(2), p. 195-202.
 - [20]. Sinha, A.K., (1991). Boriding. *ASM Handbook. Journal of Heat Treating*, vol. 4, p. 437.
-

- [21]. Sista, V., Kahvecioglu, O., Eryilmaz, O.L., Erdemir, A., and Timur, S., (2011). Electrochemical boriding and characterization of AISI D2 tool steel. *Thin Solid Films*, vol. 520(5), p. 1582-1588.
- [22]. Uslu, I., Comert, H., Ipek, M., Ozdemir, O., and Bindal, C., (2007). *Materials and Design*, vol. 28(1), p. 55.
- [23]. Venkataraman, B., and Sundararajan, G., (1995). The high speed sliding wear behaviour of boronized medium carbon steel. *Surf. Coat. Technol.* vol. 73(3), p. 177-184.

THE IMPACT OF CLIMATE CHANGE ON MARITIME TRANSPORT ROUTES

Gökhan Kara

Istanbul University, Department of Maritime Transport Management Engineering, 34320, Avcılar/İstanbul, Turkey.
karagok@istanbul.edu.tr

Abstract

The large part of the international trade is carried out by maritime lines transport. Most commonly used in maritime routes, there are certain routes. Main shipping lanes are those supporting the most important commercial shipping flows servicing major markets. One of the most vital sea routes between the Far East and Europe is the Southern Sea Route, which threads through the Straits of Malacca and across the Indian Ocean to pass through the Suez Canal. A northern passage, crossing the Bering Sea into the Barents Sea of Russia's far north and hugging Russia's Arctic shore, would constitute a mere 60% of the distance of its southern counterpart. The temperature is expected to rise as a result of climate changing. Meteorologists sea ice in the arctic ocean in the next fifty years, they estimate will withdraw quickly further north due to the temperature rise. Northern sea route will become more favorable for maritime transport in Arctic Ocean. In this study, the new maritime lines routes that may occur due to climate change impact on maritime transport are discussed. Ever made studies on this subject are evaluated briefly.

Keywords: *Climate Change, Meteorology, Northern Sea Route, Maritime Transport, Arctic Ocean*

1. INTRODUCTION

The main transport lines in the maritime transport in the world is determined based on the amount of import and export cargo. Today, the most important point of this line is emerging as the Far East. A large part of international trade is conducted in Europe, Asia and America. As is known, transportation costs constitute approximately 30-40% of the total cost of a product. Therefore, the easiest way to reduce the cost of a product, transport costs are minimum to make. Available maritime transport routes are the most appropriate line in today's climate. However, depending on the changes occurring in the climatic conditions may arise new routes. In particular, the northward withdrawal of glaciers due to global warming in the Arctic Ocean, here it will provide favorable conditions for maritime transport.

The Arctic's physical geography is mainly characterized by the sea ice, permafrost, glaciers, ice sheets, and river and lake ice [1]. Arctic seaways provide a definitely shorter route between Europe and Asia than routes through Panama or the Suez. The summer melting of sea ice has fuelled scenarios of an impending explosion in transit traffic through the Northeast and Northwest Passages, as ship owners desperately try to reduce fuel costs and increase their rotations [2]. Under the effect of climate change, the Polar ice cap has lost 40% of its thickness in only 40 years.

2. MAIN MARITIME SHIPPING ROUTES

There is a certain number of maritime shipping routes that can be used for maritime transport. The main axis is a circum-equatorial corridor linking North America, Europe and Pacific Asia through the Suez Canal, the Strait of Malacca and the Panama Canal. Maritime routes are a function of obligatory points of passage, which are strategic locations, of physical constraints (coasts, winds, marine currents, depth, reefs, and ice) and of political borders. As a result, maritime routes draw arcs on the earth water surface as intercontinental maritime transportation tries to follow the great circle distance. Main shipping lanes are those supporting the most important commercial shipping flows servicing major markets (Figure 1). Secondary shipping lanes are mostly connectors between smaller markets. In part due to physiography, geopolitics and trade specific locations play a strategic role in the global maritime network. They are labeled as strategic passages and can be classified into two main categories:

Primary passages are the most important since without them there would be limited cost effective maritime shipping alternatives which would seriously impair global trade. Among those are the Panama Canal, the Suez Canal, the Strait of Hormuz and the Strait of Malacca, which are key locations in the global trade of goods and commodities.

Secondary passages support maritime routes that have alternatives, but would still involve a notable detour. These include the Magellan Passage, the Dover Strait, the Sunda Strait and the Taiwan Strait [3]. In a novel approach, meteorologist's sea ice in the arctic ocean in the next fifty years, they estimate will withdraw quickly further north due to the temperature rise. Northern sea route will become more favorable for maritime transport in Arctic Ocean.



Figure 1. Main maritime shipping routes [3].

3. NORTHERN SEA ROUTE (NSR)

The NSR is a shipping lane between the Atlantic Ocean and the Pacific Ocean along the Russian coast of Siberia and the Far East, crossing five Arctic Seas: the Barents Sea, the Kara Sea, the Laptev Sea, the East Siberian Sea and the Chukchi Sea [4]. The Northern Sea Route, or NSR, is the modern-day designation for the Arctic marine route that extends from the Russian islands of Novaya Zemlya to the Bering Strait, which separates the State of Alaska from Russia. It extends a distance of between 2200 and 2900 nautical miles (ran) along Russia's northern coastline, where encounters with bitter cold temperatures, ice-choked seas, shallow straits, blinding fog, and isolation are routine. The route extends across or into four seas of the Arctic Basin: the Kara, the Laptev, the East Siberian, and the Chukchi. It is the most challenging segment of the historic Northeast Passage from Europe to the Far East, offering a shorter distance between seaports in the North Atlantic and the North Pacific relative to the Suez and Panama Canal routes that are currently used (Figure 2). Transit distances between North Pacific and European ports are 35-60% less than the traditional southerly routes [5].



Figure 2. The NSR and current (Southern sea route) shipping routes.

4. IMPACT OF CLIMATE CHANGE IN THE NORTH SEA ROUTE

The history of Arctic temperature anomalies from 1880 to 2006 is shown in Fig. 3. The zero line represents the average temperature for the time period 1961–1990. In the late 1800s, the Arctic was relatively cold but the temperature has warmed by about 0.7 °C over the 20th century. There was a warm period from the 1920s to the 1940s and cold periods in the early 1900s and in the 1960s. Over the last decade the temperatures were consistently more than 1.0 °C above the 20th century average [4].

Figure 3 demonstrates historical records of Arctic temperature anomalies between 1880 and 2000. It is clearly shown that the Arctic was relatively cold in the late 1800, and temperatures started to warm by about 0.7 °C over the 20th century. It is also worth noting that warm periods existed between the 1920s and 1940s, and cold periods in the early 1900s and 1960s. As for the last decade it is apparent that temperatures were constantly more than 1.0 °C above the 20th century average value [4]. Other observations also confirm that air temperature has increased at a rate that is double the global average over the last hundred years [7]. Therefore, Arctic temperature trends are essentially worth tracking, as they represent a solid indicator for the impacts of climate change. This is a significant issue for predicting the future of Arctic shipping routes [4].

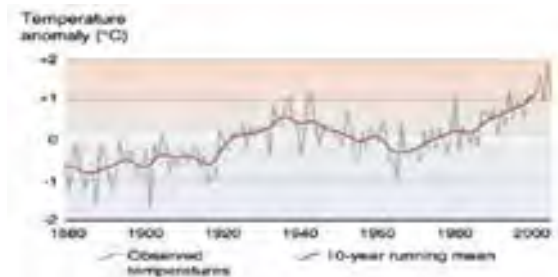


Figure 3. Trends in Arctic temperature, 1880–2006. [4].

The projected reduction in sea ice is likely to improve access along the NSR as shown in Fig. 4. The navigation season is often defined as the number of days per year with navigable conditions, generally meaning days with less than 50% sea ice cover. For the NSR, the navigation season was in 2004 projected to

increase from 20–30 days per year to 90–100 days per year by 2080. This estimate might however be too conservative since the melting of the sea ice has increased dramatically from 2004 to 2007 [4].



Figure 4. Projected increase in days of the navigation season through the NSR [9].

5. SHIPPING ADVANTAGE IN THE NORTH SEA ROUTE

A look at the map shows the savings in distance that can be achieved with the Arctic routes: for example, a trip between London and Yokohama through the Northwest Passage is 15,700 km and 13,841 km through the Northeast Passage, which is significantly shorter than the route through Suez (21,200 km) or Panama (23,300 km). The sailing distance between Yokohama and Rotterdam via the NSR is approximately 6920 miles, compared to the traditional route via Suez Canal which is 11460 miles. Table 1 shows the general relation between ice thickness/ weather conditions and average speed along the NSR. The average speed drops dramatically from 12–13 knots during the summer period to around 6–7 knots during winter [2]. There are relation between ice thickness/ weather conditions and average speed along the NSR. Expected speeds in different months are indicated in Table 1. The average speed drops dramatically from 12–13 knots during the summer period to around 6–7 knots during winter [4].

Table 1. Assumed speed along NSR and ice thickness and weather conditions [3].

Ice thickness/weather conditions	Speed in knots
0/clear	18
0/fog	15
0.25	13
0.5	10
1	8
1.5	6
2.5	6

Research results that have been published over the last 10-15 years have consistently shown that the Arctic sea ice has been gradually shrinking and thinning over the last few decades. There are however uncertainties regarding the pace and pattern of the melting, and predictions of future sea ice cover differ greatly. The scenario chosen for the Arctic Climate Impact Assessment (ACIA) in 2004, predicted a largely ice-free Arctic Ocean in late summers in 100 years. More recent and more radical scenarios see the Arctic Ocean ice free in summers already in 30-50 years – but then again there are others models which predict a longer process [7].

The diminishing Arctic sea ice cover is a fact, while the pace of the process is still uncertain. But the Arctic Ocean is gradually becoming more accessible, and shipping in the region is bound to increase. We are already seeing more regional traffic, mostly related to the development and export of petroleum resources. Other export cargoes, imports to the Arctic settlements and cruise activities may also increase. Later, when the ‘summer window of opportunity’ widens, occasional transits may be seen. Under the most radical climate change scenarios, it will probably still take around 20-30 years from now until conditions have become suitable for such occasional transits. Large-scale, year-round transit operations are hardly possible before the ice cover has disappeared for most of the year, and this does not seem realistic in at least 40-60 years from now [8].

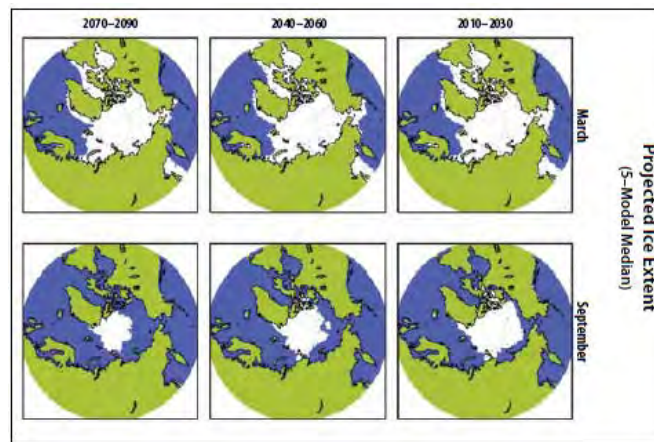


Figure 5. Arctic sea ice simulations for the 21st century. [8].

The assessment confirmed, using a wealth of current Arctic research, that declining Arctic sea ice is a key climate change indicator. During the past five decades the observed extent of Arctic sea ice has declined in all seasons, with the most prominent retreat in summer. While the ACIA models have now been surpassed by more capable Global Climate Model (GCM), each of the five GCMs used in the ACIA did project a continuous decline in Arctic sea ice coverage throughout the 21st century (Figure 5). From a strategic planning perspective, this is a key factor for evaluating future Arctic marine transport systems. As noted previously, one of the models simulates a summer ice-free Arctic Ocean by 2050, a future scenario of great significance for Arctic shipping and offshore development. Such a physical occurrence would mean that multi-year ice could possibly disappear in the Arctic Ocean. All of the next winter's ice would be first-year: no ice will have survived a winter season (and be able to gain strength and thickness). GCM projections to 2100 suggest that in the summer the Arctic sea ice will retreat further and further away from most Arctic coasts, potentially increasing marine access and extending the season of navigation in nearly all Arctic regional seas. One critical limitation of the GCMs is that they are not useful for determining the state of sea ice in the Northwest Passage region [8].

6. CONTENT

The large part of the international trade is carried out by maritime lines transport. Most commonly used in maritime routes, there are certain routes. Main shipping lanes are those supporting the most important commercial shipping flows servicing major markets. The temperature is expected to rise as a result of climate changing. Increase in the average temperature of the world, depending on the climate change causes temperatures to rise in the north and South Pole. Meteorologists sea ice in the arctic ocean in the next fifty years, they estimate will withdraw quickly further north due to the temperature rise. Therefore, the northern sea ice will melt in time and is expected to retreat further north. Northern sea route will become more favorable for maritime transport (for about four months in summer) in Arctic Ocean. As a result, significant cost advantages will be obtained maritime transport.

REFERENCES

- [1]. ACIA, "Arctic Climate Impact Assessment (ACIA)", Cambridge University Press, Cambridge 2005.
- [2]. Lasserre, F., Pelletier, S., "Polar super seaways? Maritime transport in the Arctic: an analysis of shipowners' intentions", Journal of Transport Geography, Vol 19, 1465-1473, 2011.
- [3]. Rodrige, JP, "The Geography of transport system". 05.03.2015. Web site: http://people.hofstra.edu/geotrans/eng/ch3en/conc3en/main_maritime_shipping_routes.html, 2009.
- [4]. Liu, M., Kronbak, J., "The potential economic viability of using the Northern Sea Route (NSR) as an alternative route between Asia and Europe". Journal of Transport Geography, Vol 18, 434-444, 2010.

- [5]. Nathan D. Mulherin, Duane T. Eppler, Tatiana O. Proshutinsky, Andrey Yu. Proshutinsky, L. Dennis Farmer and Orson P. Smith., "Development and Results of a Northern Sea Route Transit Model". CRREL Report 96-5. US Army Corps of Engineers Cold Regions Research & Engineering Laboratory.(A), 1996.
 - [6]. Bobylev LP, Kondratyev KY, Johannessen OM. "Arctic environment variability in the context of global change". New York: Springer-Praxis; p. 470, 2004.
 - [7]. Ragner, C.L., "Den norrasjövägen'.In Hallberg, Torsten (ed), Barents – ettgränslandiNorden". Stockholm, Arena Norden,pp. 114-127, 2008.
 - [8]. Arctic Council Arctic Marine Shipping Assessment 2009 Report, PAME.
 - [9]. Based on ACIA. "Impacts of a warming Arctic: Arctic Climate Impact Assessment". Cambridge University Press, 2004.
-

EFFECT OF MAGNET MATERIALS ON THE EFFICIENCY OF LINE START PERMANENT MAGNET SYNCHRONOUS MOTOR

Seda Kül

*Selcuk University, Department of Electric and Electronical Engineering, 42250, Konya, Turkey.
sedakul@selcuk.edu.tr*

Osman Bilgin

*Selcuk University, Department of Electric and Electronical Engineering, 42250, Konya, Turkey.
obilgin@selcuk.edu.tr*

Abstract

In this paper, the effect of the magnet materials on a LSPMSM is investigated. Using NdFe and SmCo magnets low power LSPMSM are designed by helping RMxpert software and the differences of the efficiency curves have been obtained. The results demonstrated that maximum efficiency can be achieved with properly chosen materials and optimization of the motor dimension in the analyses. End of the analysis, the connection between type of the materials and the shape of the geometry are directly related with the efficiency of the LSPMSM are revealed.

Keywords: *line start, permanent magnet synchronous motor*

1. INTRODUCTION

On the last decades, high efficiency electrical motors gradually come into prominence with increasing energy consumption especially in the industrial area. Therefore, the optimization of the electric motor efficiency has an importance for energy saving. Induction motors have been generally used in constant speed motor-pump applications. Permanent magnet synchronous motors (PMSM) are more efficient than induction motors, but they need to uneconomical inverters for starting.

In this situation, line start permanent magnet motor (LSPMSM) is a superior alternative to induction motor and permanent magnet motor.

LSPMSM is a hybrid machine and its permanent magnets are buried beneath the squirrel cage. It is also a combination of PMSM and induction motor (IM). PMSM provides higher efficiency during synchronous operation while IM ensure the motor for starting directly without any power electronic devices. A better efficiency can be achieved with lower stator copper losses at steady state [1]. About this situation there is some studies. Richter and Neumann [2] examine ferrite and SmCo magnet materials effect to motor performance. Kurihara [3] used NdFeB magnet to attain high efficiency have adequate starting ability. The other studies generally intend to get high efficiency with other methods like different rotor structure, changeable electromagnetic parameters

2. Modeling LSPMSM

LSPMSM model have been designed by using RMXprt and Maxwell 2D/3D software programmes. Interior permanent magnet structure is used for the analyzed. It is shown the motor model which is attained from the Maxwell 3D in Figure 1.

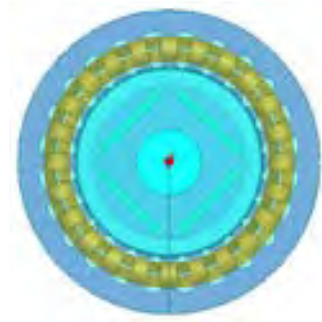


Figure 1. LSPMSM model

Motor characteristic features are given in Table 1:

Table 1. Motor parameters

Name	Rating value	Unit
Rated power	1.1	kW
Rated voltage	220	V
Rated speed	1500	rpm
Number of poles	4	
Phase	3	
Air gap	0.4	mm
Outer diameter of the stator	120	mm
Inner diameter of stator	75	mm
Shaft diameter	25	mm

Two motor which have been embedded different magnet materials are designed and simulated. Table. 2 shows general differences NdFeB and SmCo magnet materials.

Table 2. Comparison of NdFeB and SmCo

Material	Energy Product (MGOe)	Density (lbs/in3-gm/cm3)	Cost	Coercivity (MA/m)	Remanence (T)
NdFeB	10-48	0.275-7.5	Lower	0.875-1.99	1-1.3
SmCo	15-32	0.300-8.3	Higher	0.493-1.59	0.82-1.16

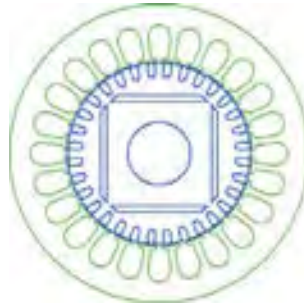


Figure 2. RMXPRT model of the LSPMSM

3. Analysis of the LSPMSM

After motor design is completed with Rmxprt, efficiency, power factor and magnetization curves of the motor are attained.

First design SmCo magnet is used and simulation in full load operating. As follow efficiency and power factor curves respectively are shown below.

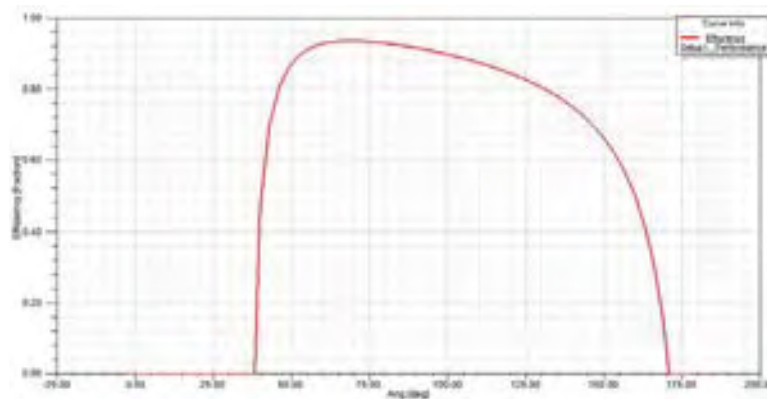


Figure 3. Efficiency curve versus torque angle

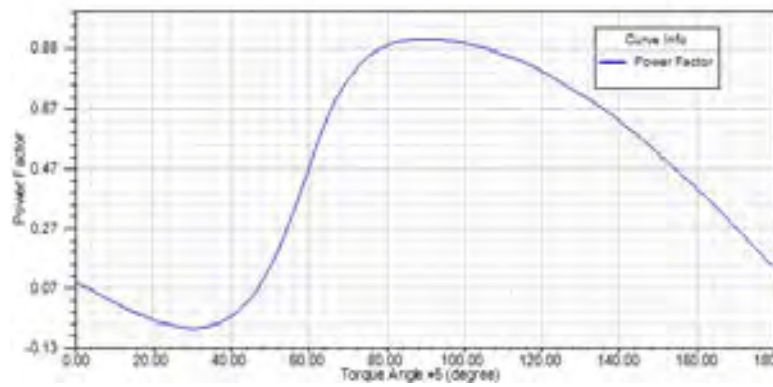


Figure 4. Power Factor curve versus torque angle

In the second design magnet material is changed with NdFeB. Simulating result in full load operating is acquired again.

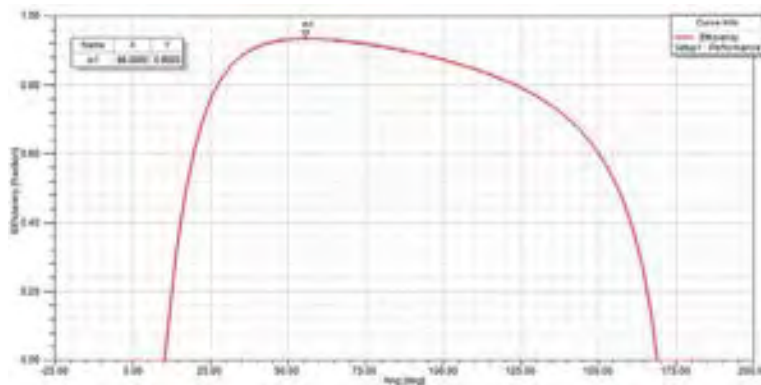


Figure 5. Efficiency curve versus torque angle

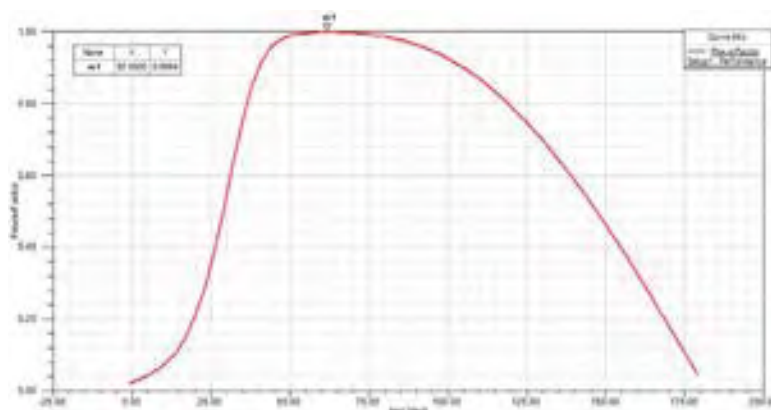


Figure 6. Power Factor curve versus torque angle

4. Conclusion

Two motors designs were completed and simulated. At first it is said that the magnet material effects the performance of the motors. The magnet type is effect the motor performances like efficiency, power factor, torque. It is seen the differences of the efficiency and power factor from the motor curves which have been acquired with full load operation. Table 3 is shown the power factor and efficiency values which have analyzed motors.

Table 3. Efficiency and power factor values

Motor type	Efficiency	Powerfactor
Embedded SmComagnet	90.83	0.96
Embedded NdFeBmagnet	93.41	0.99

REFERENCES

- [1]. Kurihara, Kazumi, and M. Azizur Rahman. "High-efficiency line-start interior permanent-magnet synchronous motors." *Industry Applications, IEEE Transactions on* 40.3,2004,page 789-796.
 - [2]. Libert, F., J. Soulard, and J. Engstrom. "Design of a 4-pole line start permanent magnet synchronous motor." *ICEM*, 2002.
 - [3]. Richter, E., and T. W. Neumann. "Line start permanent magnet motors with different materials." *Magnetics, IEEE Transactions on* 20.5, pp.1762-1764, 1984
-

ANALYTICAL INVESTIGATION OF THE STRESS DISTRIBUTION IN THE BEAM END CONNECTOR IN STORAGE RACK SYSTEMS

Yaşar Pala

Uludağ University, 16059, Nilüfer/Bursa, Turkey.
mypala@uludag.edu.tr

Emre Çalış

Uludağ University, 16059, Nilüfer/Bursa, Turkey.
emrecalis@ucge.com

Murat Reis

Uludağ University, 16059, Nilüfer/Bursa, Turkey.
reis@uludag.edu.tr

Abstract

In this study, beam end connector system connecting upright column and pallet beam is investigated for mechanical refinement and optimum dimensions depending upon the stress distribution in the pallet beam and connector parts. An analytical method is developed and design provisions are provided such that the stability strength of the frame structure constructed by means of beam connector system becomes maximum. Results indicate that a nearly intermediate position of the beam connector with respect to the pallet beam must be preferred instead of top-level or bottom level connections of the connector- pallet beam connection.

Keywords: *Beam end connector, stiffness, steel rack systems, analytical method, cantilever, portal*

1. INTRODUCTION

Boltless semi-rigid connections are widely used in the storage rack industry to connect the uprights and pallet beams. There are several commercially available beam end connectors and they are categorized as torque and slot design, blanking design, stud-incorporated design and dual integrated tab design [1]. Other types of connectors are also designed by combining these classes. Most of the research on these systems has rather been experimental [2], [3] and computational [4], due to the complexity of the system's behavior [5]-[8]. Therefore, numerous research papers, most of which involve experimental results, have been published on the behavior of beam end connectors. Bajoria and Talikoti used different ways to find the flexibility of an end connector. The results of double cantilever test were found to match well with the full scale frame test. The experimental results and the finite element results were also compared [9]. The experimental analysis of semi-rigid boltless connectors was carried out by Markazi, et al. [1]. They attempted to classify the connectors based on their special features. The comparison of the results from a pushover analysis of a single story frame using a moment-rotation relation of beam-to-column connections obtained from cantilever tests and the experimental results from portal tests was made by Asawasongkram, et al. [10]. Kozlowski and Slecicka used to assess main joint properties and they compared them with test results [11]. Aguirre investigated the structural properties of c onnections for ra ck structures and showed that the failure is controlled by the connection elements [12].

It is evident from the previous studies that load carrying capacity, buckling load and failure of the storage rack systems are intimately related to the behavior of beam end connector. So, it is inevitable to design a beam end connector that has as large rotational stiffness value as possible. A beam end connector consists of a perforated plate bent into L-shape. There are several parameters that determine the strength of the hook-in end connector. Among these are the number of tabs, geometry of tabs, thickness of the end plate, welding length and type, relative position of the end plate and the pallet beam and the positions of tabs on the end plate. Experiments indicate that the relative position of the end plate and the pallet beam (r) and the positions of the tabs on the end plate are extremely important on the rotational stiffness of the connector. In the present study, the optimum value of the distance between the top side of the pallet beam (r in Fig.2(b)) is determined via an analytical method so as to obtain a more rigid connector type. Until now, any satisfactory analytical model used to determine true behavior of the beam end connector and the optimum relative position of the pallet beam and connector part has not been obtained. Therefore, an analytical method that helps to appreciate design parameters, needs to be developed.

In the present study, an analytical method is developed to find the stress distributions in the end plate, tabs and the pallet beam. First, the mid-point deflection of the elastically restrained pallet beam is obtained in terms of rotational stiffness of the beam connector obtained by means of portal tests. Second, stresses in the end plate are obtained. In the formulation, in order to assess the relative positioning effects of the end connector and pallet beam on the rotational stiffness of the beam end connector, plate position with respect to the top level of the pallet beam can be changed. In this way, it is aimed to explain the effect of the relative position of the pallet beam and the end connector on the rotational stiffness of the semi-rigid end connector. Third, using the results of stresses in the end plate, tab forces are obtained to see the relative positioning effects on tab forces. In order not to exceed the yield point in loaded tabs on the end plate, the relative positions of tabs with respect to the bottom side of the end plate can be changed so that the stress values on them can be decreased. This surely increases the total strength of the beam end connector deformed in elastic or plastic regions. It is one of the objectives of the present study.

2. METHOD OF SOLUTION

2.1. Deflection Analysis of the Beam with Elastic Ends

Let us consider a beam subjected to a force $2F$ at the middle point $x=L/2$ (Fig.1). Since the ends of the beam are assumed to have elastic nature, the end moments at the points A and B are $M_A=k_A\theta_A$ and $M_B=k_B\theta_B$, respectively ($k_A=k_B=k$). The present problem is statically indeterminate. That is, both M and k are unknown. Therefore, these values of stiffness are to be found from experiments so that end moments $M_A=M_B$ can be obtained by means of the following method. The equation of equilibrium for a beam can be written as

$$EI \frac{d^4 y}{dx^4} + P \frac{d^2 y}{dx^2} = q \quad (1)$$

where P is the axial force and q is the distributed load. In the present problem, it can be assumed that the axial force is negligibly small (so $d^4 y/dx^4=0$). The integration of this equation has the forms

$$y_1(x) = A_1 + A_2x + A_3x^2 + A_4x^3, \quad 0 \leq x \leq L/2 \quad (2a)$$

$$y_2(x) = B_1 + B_2x + B_3x^2 + B_4x^3, \quad L/2 \leq x \leq L \quad (2b)$$

The constants (A_n, B_n) will be obtained from the boundary conditions. These conditions can be written as

$$y_1(0) = 0, \quad y_2(L) = 0, \quad y_1\left(\frac{L}{2}\right) = y_2\left(\frac{L}{2}\right), y_1'\left(\frac{L}{2}\right) = y_2'\left(\frac{L}{2}\right), y_1''\left(\frac{L}{2}\right) = y_2''\left(\frac{L}{2}\right) \quad (3a)$$

$$Iy_2''''\left(\frac{L}{2}\right) - EIy_1''''\left(\frac{L}{2}\right) = 2FEIy_1''_1 = ky_1'|_{x=0}, \quad EIy_2''_2 = -ky_2'|_{x=L} \quad (3b)$$

The condition given by Eq.(3a) yields $A_1 = 0$. Utilizing the other conditions results in

$$A_3 = \frac{k}{2EI}A_2, \quad B_1 + B_2L + B_3L^2 + B_4L^3 = 0kB_2 + (2EI + 2Lk)B_3 + (6EIL + 3kL^2)B_4 = 0 \quad (4)$$

$$A_2 + u_4A_3 + u_5A_4 - B_2 - u_4B_3 - u_5B_4 = 0, \quad 2A_3 + u_6A_4 - 2B_3 - u_6B_4 = 0 \quad (5)$$

$$B_4 - A_4 = \frac{F}{3EI}u_1A_2 + u_2A_3 + u_3A_4 + B_1 - u_1B_2 - u_2B_3 - u_3B_4 = 0 \quad (6)$$

where $u_1 = L/2, u_2 = (L/2)^2, u_3 = (L/2)^3, u_4 = L, u_5 = 3(L/2)^2, u_6 = 3L$.

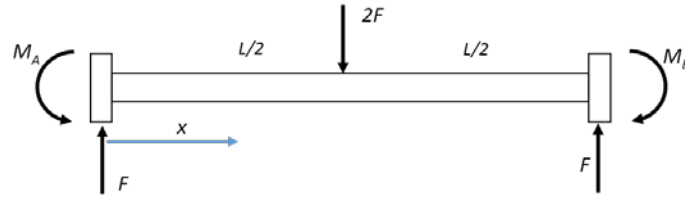


Figure 1. Beam and the beam forces

In matrix form, Eqs.(4-5-6) can be written as

$$\begin{bmatrix} \frac{k}{2EI} & -1 & 0 & 0 & 0 & 0 & 0 \\ 0 & 0 & 0 & 1 & L & L^2 & L^3 \\ 0 & 0 & 0 & 0 & k & (2EI + 2Lk) & (6EIL + 3kL^2) \\ u_1 & u_2 & u_3 & -1 & -u_1 & -u_2 & -u_3 \\ 1 & u_4 & u_5 & 0 & -1 & -u_4 & -u_5 \\ 0 & 2 & u_6 & 0 & 0 & -2 & -u_6 \\ 0 & 0 & -1 & 0 & 0 & 0 & 1 \end{bmatrix} \begin{bmatrix} A_2 \\ A_3 \\ A_4 \\ B_1 \\ B_2 \\ B_3 \\ B_4 \end{bmatrix} = \begin{bmatrix} 0 \\ 0 \\ 0 \\ 0 \\ 0 \\ \frac{F}{3EI} \\ 1 \end{bmatrix} \quad (7)$$

or

$$[A][X] = [Y] \quad (8)$$

The solution of the matrix equation is in the form[13]

$$[X] = [A]^{-1}[Y] \quad (9)$$

After matrix $[X]$ is obtained, deflections can be found by means of Eqs.(2a) and (2b).

2.2. Stress Distribution in the Beam End Connector

To determine the forces and stresses in the tabs, the stress distribution in the end plate must be obtained. Since the beam is subjected to bending, end plate will also be subjected to bending and thus must have a neutral axis. If the stress change in the plate is assumed to be linear along the y axis, the neutral axis can be found. But, whatever the relative position of the end plate and the pallet beam is, this value always becomes $y=H/2$, the mid-point of the plate (Fig.2b). It is obvious that neutral axis cannot be the mid-point of the plate for varying values of r. Here, $r=H-h-u$ (Fig.2b). Thus, bi-linear stress distribution on the end plate must be accepted (Fig.3). This bi-linear change of the stress on the end plate results in two unknowns, namely the slopes k_1 and k_2 . But, the position of the neutral axis is also not known and this inserts a third unknown into the problem. To determine the stresses, only two static equilibrium equations can be written. Therefore, using the experimental results, the possible correct position of the neutral axis needs to be obtained. Test results clearly indicate that neutral axis passes from the bottom side of the pallet beam in all cases. Indeed, due to the rigid nature of the welded region, the end plate is forced to rotate around this axis. As a result, the position of neutral axis is assumed in advance. Meanwhile, u must always be greater than $u>0$ since the assumption of bi-linear change of stresses are failed in this case.

Let us write the static equilibrium condition for the stresses of the end plate in the x direction:

$$+\rightarrow \Sigma F_x = 0, \quad -\left(k_1 t \frac{y^2}{2}\right)\Big|_0^u + \left(k_2 t \frac{y^2}{2}\right)\Big|_0^{H_0-u} = 0$$

from which the following result is obtained:

$$\frac{k_1}{k_2} = \frac{(H_0-u)^2}{u^2} \quad (10)$$

In a similar manner, moment equation about the point O yields

$$\zeta + \Sigma M_o = 0, \quad -M_0 = \left(\frac{k_1 t}{3} u^3\right) + \left(\frac{k_2 t}{3} (H_0 - u)^3\right), \quad (11)$$

where k_1 and k_2 are unknowns and t is the thickness of the end plate and $y=u$ shows the position of the neutral axis. Solving Eqs.(10) and (11) simultaneously gives

$$k_1 = \frac{-3M_0}{t(H_0 u^2)}, \quad k_2 = \frac{-3M_0}{tH_0(H_0-u)^2}, \quad (12)$$

Thus, stresses on the end plate are obtained as follows (Fig.3):

$$\sigma_1 = k_1 y = \frac{3M_0(u-y)}{t(H_0 u^2)}, \quad 0 < y < u, \quad \sigma_2 = k_2 y = \frac{-3M_0(y-u)}{tH_0(H_0-u)^2}, \quad u < y < H_0 \quad (13)$$

It is better to write Eqs.(13) in the dimensionless forms:

$$\frac{tH^2\sigma_1}{M_0} = \frac{3\left(1 - \frac{r}{H} - \frac{h}{H} - \frac{y}{H}\right)}{\left(1 - \frac{r}{H} - \frac{h}{H}\right)^2}, \quad 0 < y < u, \quad \frac{tH^2\sigma_2}{M_0} = \frac{3\left(1 - \frac{r}{H} - \frac{h}{H} - \frac{y}{H}\right)}{\left(\frac{r}{H} + \frac{h}{H}\right)^2}, \quad u < y < H_0 \quad (14)$$

It is observed from the experiments that the critical stress is σ_2 since the beam is forced downward. To see the relative positioning effect on the stresses, it is assumed that $H = 250 \text{ mm}$, $h = 150 \text{ mm}$, $r = 0,40,70 \text{ mm}$, $t = 4 \text{ mm}$, respectively. On the top side of the end plate, dimensionless values of σ_2 are obtained as $\sigma_2 = 3.116$ ($r = 0 \text{ mm}$), $\sigma_2 = 1.038$ ($r = 40 \text{ mm}$), $\sigma_2 = 0.83$ ($r = 70 \text{ mm}$), respectively. It is clearly seen that shifting the pallet beam downward with respect to the end plate decreases the dimensionless stress σ_2 . As a result, beam end connector becomes more rigid with downward shifting of the pallet beam with respect to the end plate since, in the new case, each tab takes on more load well below the yield point in the horizontal direction. However, on the other hand, our second limit criteria is that the maximum deflection must be smaller than $\delta < L/200$. When this criteria is taken into account, it can be concluded that the configuration where $r=40 \text{ mm}$ is the more suitable one to be chosen since the maximum deflection of the mid-point measured is $11,78 \text{ mm} < 13,5 \text{ mm}$. The value of mid-point deflection continues to decrease after $r > 40 \text{ mm}$. However, local buckling formation is observed on the lateral surfaces of the pallet beam after this value and therefore, the greater values of r are excluded. Tab Forces

Figure 4 shows tab forces and the stress distribution in the end plate. The number of tabs are chosen as 5. The distance between two tabs is d . The bottom tab has a distance e from $y=0$. It is assumed that the forces in the tabs are bi-linearly varied as in the case of end plate. The equations of force and moment equilibrium for the end plate and tabs can be determined as follows:

$$+\rightarrow \Sigma F_x = 0, \quad -\int_0^u k_1 t y dy + \int_0^{H_0-u} k_2 t y dy + F_1 + F_2 + F_3 + F_4 + F_5 = 0 \quad (15)$$

$$\zeta + \Sigma M_o = 0$$

$$-\int_0^u (k_1 y) t y dy + \int_0^{H_0-u} (k_2 y) t y dy + |F_1(u - e)| + |F_2[u - (e + d)]| + |F_2[u - (e + 2d)]| + |F_2[u - (e + 3d)]| + |F_2[u - (e + 4d)]| = 0 \quad (16)$$

or, after carrying out the integrations,

$$Q_1 + F_1 + F_2 + F_3 + F_4 + F_5 = 0, \quad P_1 + |F_1(u - e)| + |F_2[u - (e + d)]| + |F_2[u - (e + 2d)]| + |F_2[u - (e + 3d)]| + |F_2[u - (e + 4d)]| = 0 \quad (17)$$

Here, Q_1, P_2 are given as

$$Q_1 = -\int_0^u k_1 t y dy + \int_0^{H_0-u} k_2 t y dy = \frac{-k_1 t u^2}{2} + \frac{k_2 t (H_0 - u)^2}{2}$$

$$P_1 = -\int_0^u (k_1 y) t y dy + \int_0^{H_0-u} (k_2 y) t y dy = \frac{-k_1 t u^3}{3} + \frac{k_2 t (H_0 - u)^3}{3} \quad (18)$$

For the case of $u < e + d$,

$$Q_1 + c_1(u - e) + c_2[u - (e + d)] + c_2[u - (e + 2d)] + c_2[u - (e + 3d)] + c_2[u - (e + 4d)] = 0$$

$$P_1 + c_1(u - e)^2 + c_2[u - (e + d)]^2 + c_2[u - (e + 2d)]^2 + c_2[u - (e + 3d)]^2 + c_2[u - (e + 4d)]^2 = 0 \quad (19)$$

or

$$Q_1 + c_1(u - e) + c_2(4u - 4e - 10d) = 0,$$

$$P_1 + c_1(u - e)^2$$

$$+ c_2 \left[(u - (e + d))^2 + (u - (e + 2d))^2 + (u - (e + 3d))^2 + (u - (e + 4d))^2 \right] = 0 \quad (20)$$

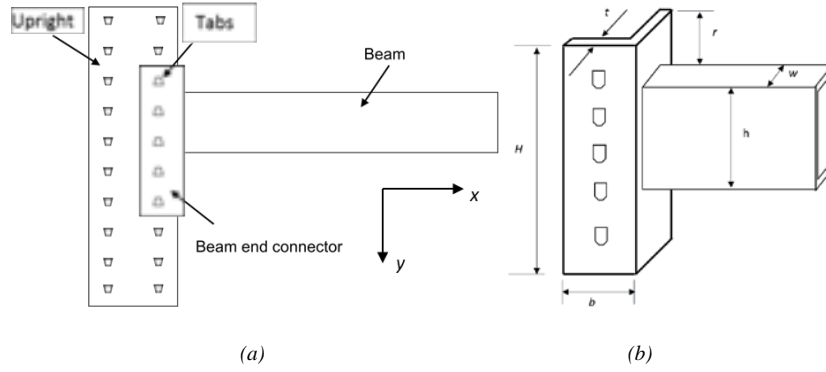


Figure 2. Beam end connector and the column

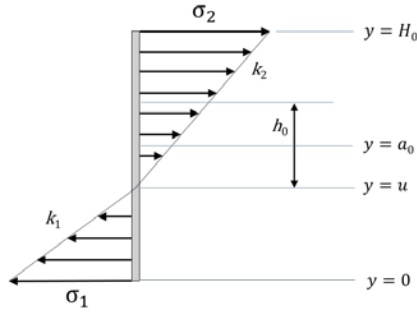


Figure 3. Bi-linear stress distribution on the end plate

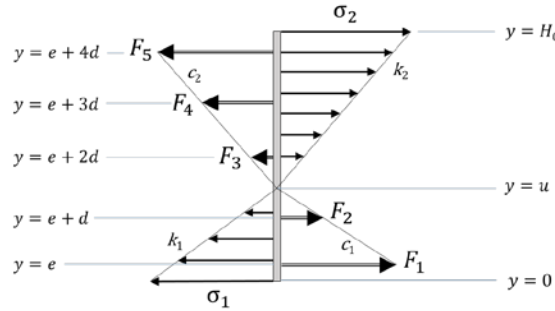


Figure 4. Tab forces and stress distribution in the beam end connector

Letting

$$Q_2 = (u - e), \quad Q_3 = (4u - 4e - 10d), \quad P_2 = (u - e)^2$$

$$P_3 = [u - (e + d)]^2 + [u - (e + 2d)]^2 + [u - (e + 3d)]^2 + [u - (e + 4d)]^2$$

Eq.20 can be expressed as

$$c_1 = \frac{Q_3 P_1 - Q_1 P_3}{Q_2 P_3 - Q_3 P_2}, \quad c_2 = \frac{Q_2 P_1 - Q_1 P_2}{Q_3 P_2 - Q_2 P_3} \quad (21)$$

Tab forces for this case are given by

$$F_1 = c_1 R_1, F_2 = c_2 R_2, F_3 = c_2 R_3, F_4 = c_2 R_4, F_5 = c_2 R_5 \quad (22)$$

where

$$R_1 = (u - e), R_2 = [u - (e + d)], R_3 = [u - (e + 2d)], R_4 = [u - (e + 3d)], R_5 = [u - (e + 4d)] \quad (23)$$

For the case of $e + d < u < e + 2d$, Q_2, Q_3, P_2, P_3 are

$$Q_2 = (2u - 2e - d), \quad Q_3 = (3u - 3e - 9d), \quad P_2 = (u - e)^2 + [u - (e + d)]^2$$

$$P_3 = [u - (e + 2d)]^2 + [u - (e + 3d)]^2 + [u - (e + 4d)]^2 \quad (24)$$

Tab forces in this case are

$$F_1 = c_1 R_1, F_2 = c_1 R_2, F_3 = c_2 R_3, F_4 = c_2 R_4, F_5 = c_2 R_5 \quad (25)$$

For the case of $e + 2d < u < e + 3d$, Q_2, Q_3, P_2, P_3 are given as

$$Q_2 = (3u - 3e - 3d), \quad Q_3 = (3u - 3e - 7d), \quad P_2 = (u - e)^2 + [u - (e + d)]^2 + [u - (e + 2d)]^2$$

$$P_3 = [u - (e + 3d)]^2 + [u - (e + 4d)]^2 \quad (26)$$

Tab forces in this case are

$$F_1 = c_1 R_1, F_2 = c_1 R_2, F_3 = c_1 R_3, F_4 = c_2 R_4, F_5 = c_2 R_5$$

For the case of $e + 2d < u < e + 3d$, Q_2, Q_3, P_2, P_3 are given as

$$Q_2 = (4u - 4e - 6d), \quad Q_3 = (u - e - 4d), \quad P_3 = [u - (e + 4d)]^2$$

$$P_2 = (u - e)^2 + [u - (e + d)]^2 + [u - (e + 2d)]^2 + [u - (e + 3d)]^2 \quad (27)$$

Tab forces in this case are

$$F_1 = c_1 R_1, F_2 = c_1 R_2, F_3 = c_1 R_3, F_4 = c_1 R_4, F_5 = c_2 R_5 \quad (28)$$

The thickness and the width of the tab is taken as 4 mm and 11 mm, respectively. The material is St37 ($\sigma_{yield} = 240\text{MPa}$). The change of forces in each of the tabs with u is plotted in Fig.5. u is started from $y=26$ mm (1 mm above the bottom tab). Therefore, no extension of the curves to the left is seen in Figs.5 and 6. If it was assumed $u=25$ mm, the assumption of bi-linear change of both stresses and tab forces would be failed. It is seen from Figs.(5) and (6) that tab forces decreases with increasing values of u , as expected. For the smallest value of u , the stress in tab 1 is maximum. This is also satisfied by the first of Eq.(13). Indeed, σ_1 goes to infinity for $u \rightarrow 0$, and decreases for smaller values of u . When $u=H-h$, It must be reminded that u must change between $e < u < H-h$.

3. COMPARISON OF EXPERIMENTAL AND THEORETICAL RESULTS

To determine the rotational stiffness of the beam end connector and compare the mid-point deflection with that obtained by the theoretical approach, several experiments were carried out. While the beam deflects under the applied load P , the uprights are assumed to be stationary. The rotational stiffness was obtained by connecting the end connectors at both ends of the beam to the uprights as in a frame structure (Fig.8). In the present case, the end moment is $M=k\theta$. Thus, the value of the rotational stiffness can be found by simply dividing this moment by the angle θ . Table 1 gives the experimental and theoretical values of mid-point deflections for a beam with the length $L=2700$ mm, the modulus of elasticity $E=210000$ N/mm², plate thickness $t=1.2$ mm, width $w=50$ mm, height $h=150$ mm, and the applied load $P=30000$ N. Experimental values for the deflections for each configuration determined by the variable r depicted in Table 1 were recorded at times $t=0$, $t=30$ minutes and $t=4$ hours for each beam. It was found that the mid-point deflection was not changed after $t=4$ hours. Depending on these values and the maximum stresses that the connector can stand in the linear region, an optimum end connector is to be chosen as the best configuration. It must be observed from Table 1 that both analytical and experimental values decrease above k_{40} , where $r=40$ mm. The standard maximum value of deflection proposed by the specifications is $L/200=13.5$ mm. This value is satisfied by all experimental values while analytical results stay around the standard value proposed by the specifications. It should be pointed out that the axial force in the beam has been omitted in the formulation. It is clear that the inclusion of the axial force will slightly reduce the deflection of the beam, and analytical and experimental results will become closer. It is concluded from Table 1 that the stiffness reduces with increasing values of r while the mid-point deflections increase up to the value of $r=40$ mm. Thus, although the stiffness k decreases with increasing value of r up to $r=40$ mm, the maximum load that the pallet beam can carry increases, as seen in Table 2. The reason for the increase in load-carrying capacity with increasing values of r is that tabs, which carry less loads for small r values, take more loads with increasing r . In order to see the deflection curve, using Eqs.(2a,2b) and (9), Figs.7 have been plotted for the values $L=2700$ mm, $E=210000$ N/mm², $t=1.2$ mm, $w=50$ mm, $h=150$ mm, $H=250$ mm, $P=30000$ N, $\sigma_y=350$ N/mm². The maximum deflection for $k_{70}=2.467 \times 10^9$ and $k_{40}=2.356 \times 10^9$ are 13.7613 and 13.8723 mm, respectively

Cantilever tests were also conducted to see the physical behavior and the total strength capacity of the beam end connectors. The results for rotational stiffness k in portal test can be different than those obtained from cantilever tests. The cantilever test set up consists of a short cantilever connected to the center of the column of's hort length. Both ends of t he column are rigidly supported. The load is applied monotonically by a hydraulic jack placed on a load cell. The free end of the cantilever beam is constrained by a vertical guide to prevent an undesirable out-of plane movement of the beam. The applied loads are recorded at each increment of loading until the failure occurred at the connection. Displacement transducer is mounted to measure beam deflections. $M - \theta$ curve is plotted for each type of beam end connector and the rotational stiffness of each connector is determined in accordance with FEM standards (Table 1). Table 2 yields the maximum loads for the cantilever beam depending on the value r . The maximum loads, that the tabs and beam end connector can stand up to the yield point, were obtained as 6589 N, 8499 N, 9636 N, 10646 N for corresponding values of $r=0,20,40$ and 60 re spectively. Although the maximum loads increase with increasing values of r , maximum deflections also increase up to $r=40$ mm. When the maximum deflection and the corresponding loads are evaluated together, it can be concluded that the configuration for $r=40$ mm is the most suitable one to be chosen in commercial production. After $r>40$ mm for this configuration, undesired local buckling effects start to occur. Therefore, the configurations where $r>40$ mm must be excluded in commercial productions. [8], [13].

In order to see the mid-point deflection and the rotational stiffness of the end connectors in actual field conditions, portal test setup has also been set. In the portal test, the beam end connector is subjected to shear, bending and axial force. So, the rotational stiffness in these conditions must be expected to be different than those obtained in cantilever tests [14]. The horizontal distance between the column centerlines is 2700 mm. Vertical displacements of the mid-point of the pallet beam have been recorded by means of a LVDT. Vertical load was taken as 30000 N.

Table 1. Experimental and Theoretical Values of the Mid-Point deflection of Elastically Restrained Pallet Beam

Stiffness, k_r (Nmm/rad)	Exp. values, δ_{max} (mm) (after 30 minutes)	Exp. values, δ_{max} (mm) (after 4 hours)	Theoretical values, δ_{max} (mm)
$k_0=2.818 \times 10^9$	9.9	10	13.4639
$k_{20}=2.654 \times 10^9$	10.3	10.55	13.5937
$k_{40}=2.356 \times 10^9$	11.78	11.80	13.8722
$k_{60}=2.432 \times 10^9$	11.33	11.40	13.7952

Table 2. Maximum loads corresponding to yielding in the cantilever test. Moment arm $l=50$ mm.

	$r=0$	$r=20$	$r=40$	$r=60$
Max. load at yielding (N)	6584	8499	9686	10646
Stiffness $\times (10^{-8})$	$k_0=1.3765$	$k_{20}=1.4753$	$k_{40}=1.4082$	$k_{60}=1.6891$

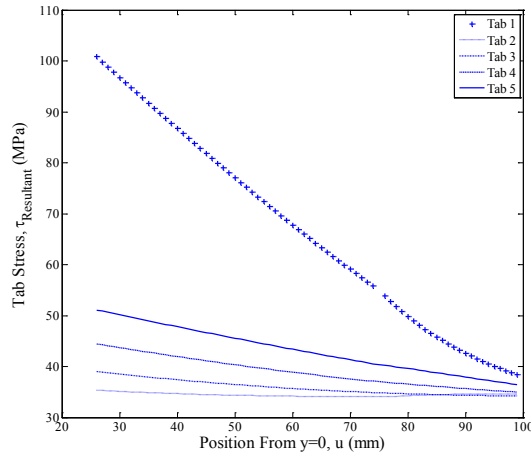


Figure 5. The variation of normalized tab stresses versus position (u)

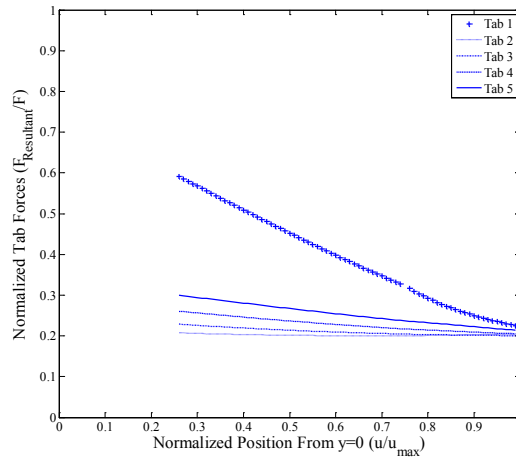


Figure 6. The variation of normalized tab forces versus normalized position (u/u_{max})

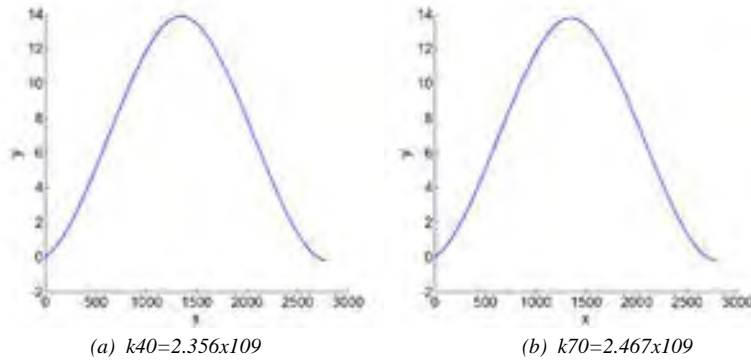


Figure 7. Deflection Curve. $L=2700mm$, $E=2.1 \times 10^5 N/mm^2$, $t=1.2mm$, $w=50mm$, $h=150mm$, $P=30000N$, $\sigma_y=350 N/mm^2$.

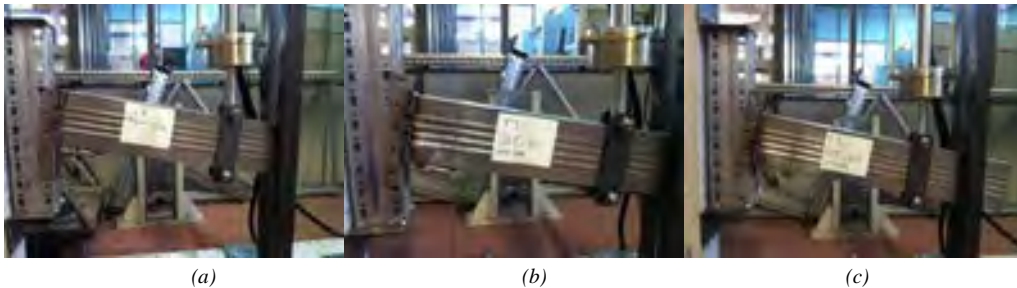


Figure 8. Cantilever test setup designed for different values of r . a) $r=0$, b) $r=40 mm$, c) $r=60 mm$.

4. RESULTS AND CONCLUSIONS

In this study, an analytical method has been developed to obtain the optimum selection of the beam end connector under two restrictions, namely the specified maximum value of the mid-point deflection of the pallet beam and the maximum stresses in the tabs and end plate. First, deflection analysis involving the rotational stiffness coefficient was made. Both cantilever tests and portal tests were carried out to find the rotational stiffness k for each case. Portal test results were used in the formulation. Second, stresses in the tabs and end plate were obtained. The relative position (r) of the end plate and the pallet beam was obtained such that the maximum value of the stresses don't exceed the yielding point of the materials. The results obtained were found to be compatible with those in commercial productions.

ACKNOWLEDGMENT

This research was supported by Ministry of Science, Industry and Technology (Turkey) under the code 0310-STZ-2023-2. This study has also been supported by steel rack system manufacturer UCGE DRS Company, Bursa, Turkey.

REFERENCES

- [1]. F.D. Markazi, R.G. Beale, M.H.R. Godley, "Experimental analysis of semi-rigid boltless connectors", *Thin-Walled Structures*, 28(1), 57-87, 1997.
 - [2]. F. Roure, M.M. Pastor, M. Casafont, M.R. Somalo, "Stub column tests for racking design: Experimental testing, FE analysis and EC3", *Thin-Walled Structures*, 49(1), 167-184, 2011.
 - [3]. A. Crisan, V. Ungureanu, D. Dubina, "a-Behaviour of cold-formed steel perforated sections in compression. Part 1- Experimental investigations", *Thin-Walled Structures*, 61, 86-96, 2012.
 - [4]. A. Crisan, V. Ungureanu, D. Dubina, "b-Behaviour of cold-formed steel perforated sections in compression: Part 2- numerical investigations and design considerations", *Thin-Walled Structures*, 61, 97-105, 2012.
 - [5]. N. Baldassino, C. Bernuzzi, "Analysis and behavior of steel storage pallet racks", *Thin Walled Structures*, 37: 277-304, 2000.
 - [6]. S.W. Jones, P.A. Kirby, D.A. Nethercot, "The analysis of frames with semi-rigid connections - A State-of-the-Art Report", *Journal of Constructional Steel Research*, 3, 2-13, 1983.
 - [7]. S.M. Maxwell, W.M. Jenkins, J.N. Howlett, "A Theoretical Approach to the Analysis of Connection Behavior", *Proc. of Conference on Joints in Steel Work*, England, 45-269, 1981.
 - [8]. Mecalux, 2014, webpage, www.mecalux.com
 - [9]. K.M. Bajoria, R.S. Talikoti, "Determination of Flexibility of Beam-to-Column Connectors used in thin walled cold-formed steel pallet racking systems", *Thin Walled Structures*, 44, 372-380, 2006.
 - [10]. N. Asawasongkram, P. Chomchuen, P. Premthamkorn. "Experimental Analysis of beam-to-column connection in steel storage racks using cantilever test and portal test method", *Hokkaido University Reports*, 1-8, 2013.
 - [11]. A. Kozłowski, L. Słeczka. "Preliminary Component Method Model of Storage Rack Joint", *Connections in Steel Structures V-Amsterdam*, June 3-4 2004.
 - [12]. A. Carlos Aguirre, "Structural properties of connections for rack structures", *Connections in Steel Structures V-Amsterdam*, June 3-4 2004.
 - [13]. Shaffer, 2014, webpage, www.ssi-schaefer.com
 - [14]. N. Baldasaroni, C. Bernuzzi, R. Zandonini, *Performance of Joints in Steel Storage Pallet Racks*, 382-392, 2001.
-

INTEGRATED DYNAMIC ANALYSIS OF A SIX AXIS SERIAL ROBOT

Şahin Yavuz

Dokuz Eylül University, Department of Mechanical Engineering, 35397, Buca/İzmir, Turkey.

sahin.yavuz@deu.edu.tr

Hira Karagülle

Dokuz Eylül University, Department of Mechanical Engineering, 35397, Buca/İzmir, Turkey.

hira.karagulle@deu.edu.tr

Abstract

Serial robots are by far the most common robots used in industrial applications such as welding, pick and place, and various processes. Computers and engineering programs play important role to constitute motion analysis and design process. These days, engineers can analyze all parameters to produce the generous robots which are required for the process and find effective solutions quickly by using computer programs with the development of the technology. In this study, a six axis serial robot is produced by using integrated approaches with parallel analysis in SolidWorks, CosmosMotion, VisualBasic and Adlink Motion Control Card. The parts of the robot are modeled in SolidWorks and produced the real model of the robot. Kinematic analysis is studied in CosmosMotion by defining the velocity profile to the end effector point through the software algorithm developed in VisualBasic, which uses the application programming interface (API) capabilities. Different tasks are given to the robot in this study. The kinematic workspace and maximum motor velocities are evaluated by inverse kinematic analysis for each task. The kinetic workspace and maximum motor torques are evaluated by forward kinetic analysis. The optimum trajectory is chosen after reviewing dynamic analysis and the same trajectory is generated using ADLINK motion control card. Velocity mode is used. The maximum deviation for each motor is determined which is between the sending velocity profile data and the receiving feedback velocity profile data and compared whether the deviation values are in acceptable ranges.

Keywords: *Robot programming, dynamic analysis, trajectory planning*

1. INTRODUCTION

Mechanic, electronic and computer technologies are used in mechatronic systems. The creation and analysis of the mechanical model are done with computer aided programs [1]. Servo motors are widely used in mechatronic systems. There are two main types of control in servo motors. These are PC-based or stand-alone control systems [3].

One of the major objects of the research in the robotic systems is to evaluate dynamic analysis and to control the motion of the robot by using different methods. Some researchers carried out an adoptive learning strategy using neural an artificial network algorithm to control the motion of a 6 D.O.F manipulator robot and to overcome the inverse kinematics problem [4]. Two researchers studied on the systematic derivation of the $n \times n$ generalized inertia matrix of a general n -axis manipulator. They developed two methods to compute the joint accelerations from the governing equations of motion, which are based on the Cholesky decomposition of the generalized inertia matrix and a combination of minimum-norm and least-squares approximations of under determined and over determined linear algebraic systems. These two researchers developed also an algorithm based on Kane's dynamical equations for the numerical solution of the inverse dynamics of robotic manipulators of the serial type which produces the time histories of the n torques or forces required to drive the manipulator through the prescribed trajectory [5].

Nguyen and Poorandealed with the design of the end effector and showed the effects of system parameters on the end-effector dynamics. The emphasis in their some researches is to employ Lagrangian approach to derive a set of equations of motion and Newton-Raphson method to solve forward kinematic [6].

Examining the studies in literatur, the lack of integrated software which performs the modeling, dynamic analysis and the motion of the robot is observed. An integrated design process presented by Karagülle and applied to a hexapod robot which can be used for medical operations[2].

2. MODELING OF SIX AXIS ROBOT

In this study, a six-axis robot, which may extend to 1.5m and have 5kg tip load is discussed as shown in Figure 1. Robot is modeled in Solidworks [7]. The modeling software developed in Visual Basic reads the data from the databases and models the parts, sub-assemblies, members and the robot automatically, using the Application Programming Interface (API) capabilities of SolidWorks. SolidWorks + CosmosMotion package is used in this study. The robot model developed in SolidWorks is used automatically in CosmosMotion. Solid modeling of parts and assembly can also be done using the Graphical User Interface (GUI) capabilities of SolidWorks without the modeling software.

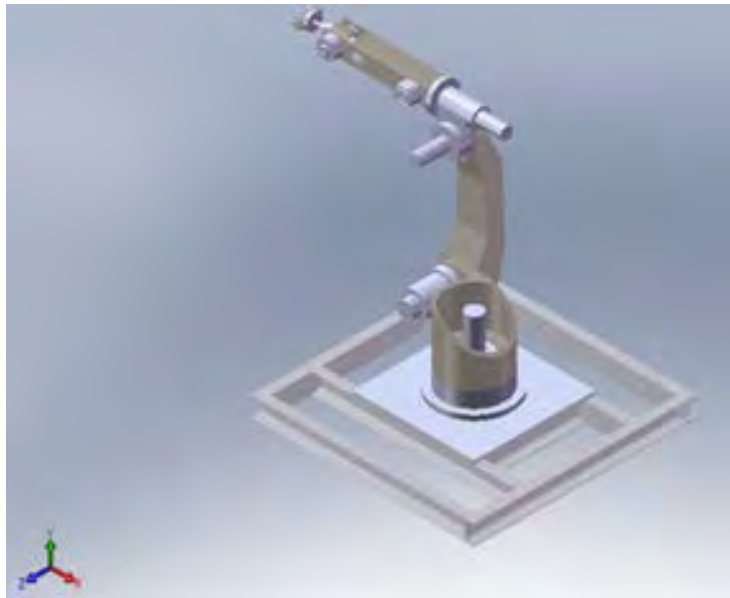


Figure 1. Model of the robot with undetailed parts

The model of the six axis robot assembly consists of motion sub-assemblies which are called as members as shown in Figure 2. Each member consists of models of parts or sub-assemblies which have a common rigid body motion. Members are connected by revolute joints.



Figure 2. Members of the robot

3. MOTION ANALYSIS

The position of the robot is defined by the position of the moving end-point. The incremental position vector of the end-point is defined as $\mathbf{q}_{ei} = [x_i, y_i, z_i, \theta_{xi}, \theta_{yi}, \theta_{zi}]^T$. $x_i, y_i,$ and z_i are the incremental displacements and θ_{xi}, θ_{yi} and θ_{zi} are the incremental rotation angles of the end-point from its previous position in the $x, y,$ and z directions, respectively. The time interval for an incremental displacement is defined as $t_i = [t_1, t_2]$, where t_1 is the starting time and t_2 is the ending time for the incremental motion. The distances are given in mm, times are given in seconds, unless otherwise stated.

The motor rotation vector is defined as $\dot{\mathbf{q}}_{mi}(t) = [\dot{\theta}_{1i}(t), \dot{\theta}_{2i}(t), \dot{\theta}_{3i}(t), \dot{\theta}_{4i}(t), \dot{\theta}_{5i}(t), \dot{\theta}_{6i}(t)]^T$. $\dot{\theta}_{1i}(t), \dot{\theta}_{2i}(t), \dot{\theta}_{3i}(t), \dot{\theta}_{4i}(t), \dot{\theta}_{5i}(t)$ and $\dot{\theta}_{6i}(t)$ are time histories of the motor velocities for the axes 1, 2, 3, 4, 5 and 6, respectively. The starting position of the end-point is defined as $\mathbf{q}_{es} = \mathbf{q}_{ea} + \mathbf{q}_{is}$, where the first term is the assembly position vector. The second term is the incremental displacement vector for the starting position, which is defined as $\mathbf{q}_{is} = [x_{is}, y_{is}, z_{is}]^T$. The assembly position is given as $\mathbf{q}_{ea} = [-944.44, 1003.52, -163.74]^T$.

The database for a planned task contains the information for the end point, $\mathbf{q}_{es}, \mathbf{q}_{ei}$ and t_i for motion steps. An example motion input may be given as

$$0, 4, -400, -800, 0, 0, 0, 0$$

Here, $t_1=0s$ starting time, $t_2=4s$ ending time, $x_1=-400mm, y_1=-800mm, z_1=0mm, \theta_{x1}=0^\circ, \theta_{y1}=0^\circ$ and $\theta_{z1}=0^\circ$. The end-point motion follows the trapezoidal velocity profile by the integration software (IS) which is created in VisualBasic, given in Figure 3.

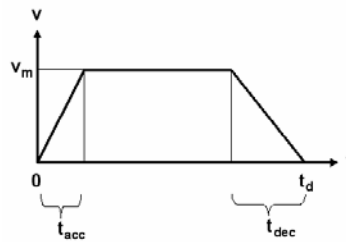


Figure 3. Trapezoidal velocity profile

3.1. Inverse Kinematic Analysis

In the inverse kinematics analysis, the incremental position vector \mathbf{q}_{ei} is given and the time histories of motor velocities $\dot{\mathbf{q}}_{mi}(t)$ are found. The RotateZ components of all motors are set to “Free” for the inverse kinematic analysis. A motion object is assigned to the end point. The location of the object is at the end-point, and the variable name “motione” is assigned to the motion object. motione has 6 degrees of freedom titled as TranslateX, TranslateY, TranslateZ, RotateX, RotateY, and RotateZ. The TranslateX, TranslateY, TranslateZ, RotateX, RotateY, and RotateZ components are set to the “Velocity” mode in motion type and “Spline”

function to enter the data points of velocity profile. An example time history of the velocity profile which is created in IS, is given below.

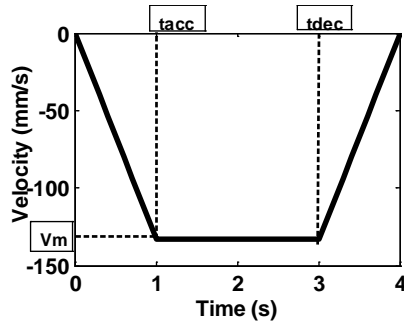


Figure 4. Trapezoidal velocity profile for displacement x

Table 1. Example motion input

q_{es}	Step-1	
	t_i	q_{ei}
$[172.84, 1010.26, -164.14]^T$	$[0, 4]$	$[-400, -800, 0, 0, 0, 0]$

Plot objects for the motor rotations are defined to observe the results. The results can be exported to the files and can be read. The time histories of motor angles and velocities are transferred to Visual Basic after the inverse kinematic analysis in CosmosMotion. Motor-3 angle and velocity time histories are shown in Figure 5 for the path given in Table 1.

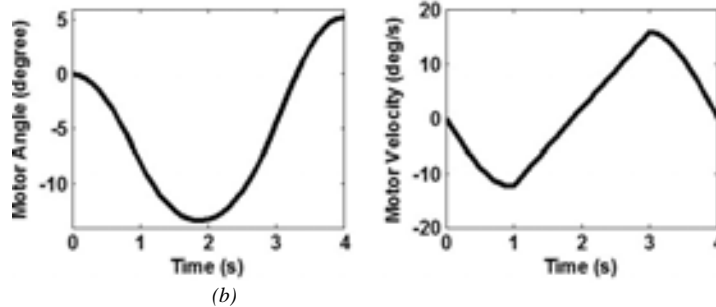


Figure 5. Motor-3 a) angle and b) velocity time histories (for path in Table 1)

The maximum motor angles are determined and evaluated by the IS whether they exceed the limits for the real robot. If the motor angles are within the limits, it means the robot is in the workspace, and the reachability button turns to green color in the kinematic evaluation chart shown in Figure 6. The motor velocities are checked whether they exceed the limits. Similarly, these buttons turn to the green or red colors. The percentages of the maximum motor velocities to the motor velocity limits are indicated in the chart. They must be below 100.

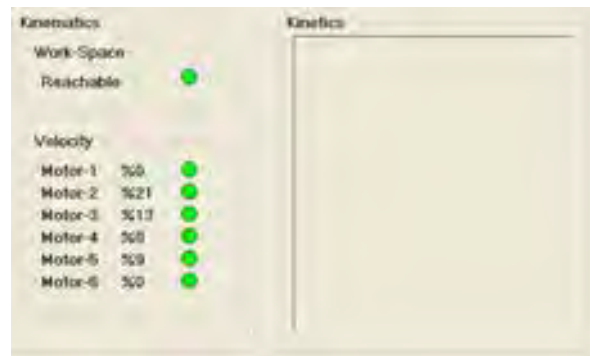


Figure 6. Results chart for evaluating kinematic parameters in IS

3.2. Forward Kinetic Analysis

All the components of the end-point motion (motion) are set to “Free” and the RotateZ components of Motor-1, Motor-2, Motor-3, Motor-4, Motor-5 and Motor-6 are set to the “Velocity” mode in motion type and “Spline” function to enter the data points of velocity profile in the forward kinetic analysis. The time histories of $\dot{\theta}_{1i}$, $\dot{\theta}_{2i}$, $\dot{\theta}_{3i}$, $\dot{\theta}_{4i}$, $\dot{\theta}_{5i}$ and $\dot{\theta}_{6i}$ found in the inverse kinematic analysis are assigned to the corresponding RotateZ components. Plot objects are defined to observe the kinetic outputs such as motor torques and reaction forces. An example time history of Motor-3 torque is shown in Figure for the path given in Table 1.

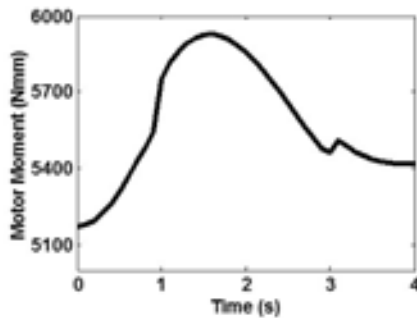


Figure 7. Motor-3 torque time history

The percentages of the maximum reaction forces and motor torques to the corresponding limit values are shown in Figure 8. The results are shown with vertical colored lines. The line is shown in green color if the percentage is less than 50. The brown color is used if the percentage is between 50.1 -100. The red color is used if the percentage is above 100, which indicates that the task is out of kinetic workspace.



Figure 8. Results chart for evaluating kinetic parameters in IS

4. MOTION CONTROL

ADLINK PCI 8366 motion control card is used for sending the created path from SolidWorks to actual robot [10]. Drive and control system include 6 Mitsubishi servo motors given in Table 2 and a personal computer. PCI-8366 is a PCI bus interface card designed for personal computer or industrial computer accompanied with a Mitsubishi MR-J2S-B type or SSCNET type servo amplifier. PCI-8366 can control up to 6 servo amplifiers. The connection between the motion control board and the amplifier is done via high-speed serial communication of the SSCNet II protocol.

Table 2. Drive system

Axis	Servo motor ^a /Driver ^a	Moment (Nm)	Gear unit ^b /Gear ratio
1	HC-KFS73B/MR-J2S-100B	2.4	HFUC-40-80/ 80
2	HC-SFS102B/MR-J2S-70B	4.78	HFUC-40-100/ 100
3	HC-KFS43B/ MR-J2S-40B	1.3	HFUC-32-100/ 100
4	HC-KFS23B/ MR-J2S-20B	0.64	HFUC-20-80/ 80
5	HC-KFS13B/ MR-J2S-10B	0.32	HFUC-20-80/ 80
6	HC-KFS50B/ MR-J2S-10B	0.16	HFUC-14-80/ 80

^a Mitsubishi Electric [8], ^bHarmonic Drive [9]

After performing the desired motion in CosmosMotion by integrated software, the inverse kinematic analysis and forward kinetic analysis are evaluated respectively and time based velocity profile data for all motors are written to the file using the following code.

Call `elem.ExportCSVFile (fl)`

Time based velocity profile graphics are seen as degree/sec in GUI, but the velocity data are saving as rad/sec while exporting data from SolidWorks. Therefore, all data are converted to degree/sec by software automatically. Next step is changing interface in IS by clicking “Motion” button to communicate the software with ADLINK motion control card. After clicking “Motion” button, all servo motor drivers are on and ready to drive. On the “Motion” interface, there are many buttons to move the actual robot such as manual motion commands for each motor, demo motion and trajectory moving for following the planned path by getting the data from SolidWorks. For manual motion, we can move specified axis with a specified speed and acceleration/deceleration time by clicking “move-a” button. Manual motion uses “start_tr_move” function.



Figure 9. “Motion” interface on the IS

“save abs pos.” button in the program interface, saves the pulse information of current position from the encoders on the motors and also writes the values on a file. By this program if the robot loses its current position for whatever reason, it can go back to its set position by clicking “Rest pos.” button. During robot’s movement if the motor torques are exceeded because of an obstacle or if an error occurs in any of the drivers, “Alarm Status” screen shows which driver is faulty and why.

In this section, it is described how to send velocity commands to motion control card by IS. For trajectory motion, “single axis velocity motion” and “change velocity on the fly” functions are used. Single axis velocity motion function uses “tv_move” command to accelerate the axis from a starting velocity to a specified maximum velocity (Figure 10).

`tv_move (Axis, StrVel, MaxVel, Tacc)`

Here;

Axis: Axis number

StrVel: Starting velocity

MaxVel: Maximum velocity

Tacc: Acceleration time

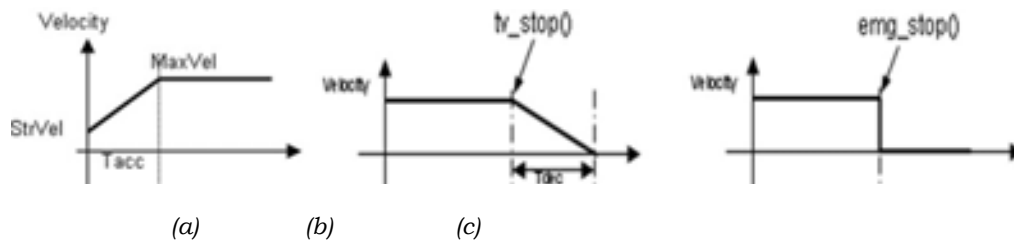


Figure 10. (a)tv_move, (b)tv_stop and (c)emg_stop commands

Change velocity on the fly function uses the following commands as shown below.

tv_change (Axis, SpeedFactor, Tacc)

tv_stop (Axis, Tdec)

emg_stop (Axis)

“tv_stop” command stops the specified axis with a deceleration time period (Tdec) and a trapezoidal velocity profile during deceleration. “emg_stop” command stops the specified axis instantly (Figure 10).

“tv_change” command changes the moving speed of a specified axis with acceleration time period (Tacc) and a trapezoidal velocity profile during acceleration. The second parameter “Speed- Factor” is used to define the new speed. For example, if the specified axis starts its motion using tv_move command and the “MaxVel” is set to be 10 mm/sec. Then tv_change is applied with “Speed- Factor” = 1.5. The new speed is $1.5 * 10 = 15$ mm/sec (Figure 11).

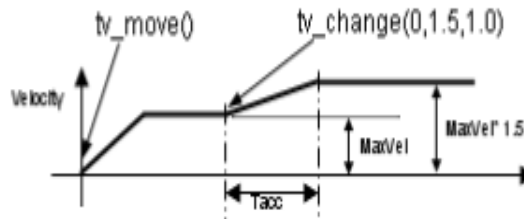


Figure 11. tv_change command

“Move Traj.” button on the IS applies the developed algorithm with the following order:

1- IS reads the velocity data of all axis from the text files and finds the maximum velocity value of each axis and checks whether the maximum velocity value given by SolidWorks is smaller than the maximum velocity of the actual motor. If the maximum velocity value in simulation is higher than the maximum velocity of the actual motor, the message box appears on the screen and gives a warning “Max. Velocity!” Program stops running and doesn’t continue applying the algorithm.

2- Speed-Factor needs the ratio of new velocity to starting velocity. For example, motor starts the motion with the speed of 100 mm/sec and the new velocity is wanted to be 200 m m/sec. Then Speed-Factor must be $200/100=2$. It is given in motion input data that the time intervals in simulation are 0.1 second. So that, total simulation time is 9 seconds and 91 velocity data for each axis are exported from SolidWorks. IS calculates all the speed factor values of each axis to use it in tv_change command.

3- All motor velocity data are taken from motor from the first step ($t=0$ s) to the end motion with 0.1s time interval simultaneously and written to text file. Example code is given below.

```
For naxis = 0 To 5
a = get_velocity(naxisa(naxis), vel_enc, vel_com)
Print #naxis + 1, t(naxis, 1), Round((vel_enc / kpuls(naxis)), 5), Round((vel_com / kpuls(naxis)), 5), vel(naxis, 1)
Next naxis
```

Figure 12. Reading velocities from motor

All time based velocity feedback data for each axis are written to the text file and compared the velocity data given by SolidWorks. Both velocity profile data are graphed by MATLAB. Experimental and simulation velocity profiles for motor-3 are shown in Figure 13.

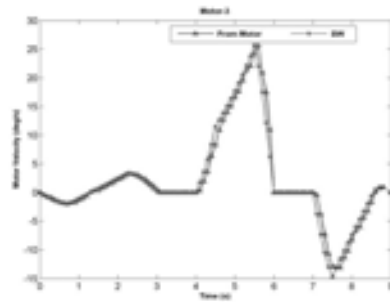


Figure 13. Velocity profile for actual motors and motors in simulation (Motor-3)

Maximum deviations between reference data (taken by SolidWorks) and receiving data (taken by actual motor) are calculated for all motors given in Table 3.

Table 3. The ratio of the maximum deviation between reference data (by SolidWorks) and receiving data (by actual motor)

The ratio of maximum deviation (%)	
Motor-1	0.0134
Motor-2	0.1285
Motor-3	0.0639
Motor-4	0.0005
Motor-5	0.115
Motor-6	0.0279

5. CONCLUSIONS

Mechatronic systems can be designed and analyzed by the VisualBASIC API of computer aided design and analysis software. The data that is obtained from inverse kinematic analysis is used for motor control in motion analysis. Motor control system software which can be controlled by the VisualBASIC API is integrated with motion analysis.

In this study, a 6-axis robot is modeled in SolidWorks, and kinematic and kinetic workspaces are evaluated by defining a task to the end effector.

With the inverse kinematic analysis velocity data of each servo motor are obtained and sent to the real system through the Adlink PCI-8366 motion control card. During the motion, velocity data is obtained simultaneously with the simulation time-step from each motor and simulation data is compared with the velocity data obtained from the motors in the real system. The results showed that robot's end effector moved to the targeted position with a maximum deflection of %0.1285 and followed the velocity curve with high sensitivity.

The integration software which is developed for modeling in SolidWorks, performing motion simulation, evaluating simulation results in terms of kinematic and kinetic workspaces and moving the real system, can be used for other custom designed industrial robots or systems.

ACKNOWLEDGEMENTS

We are grateful for the support of *International Conference on Engineering and Natural Science* for helping make this conference possible.

REFERENCES

- [1]. Ş. Yavuz, "Trajectory planning of a six axis serial robot based on dynamic analysis", M.Sc Thesis, Graduate School of Natural and Applied Sciences of DokuzEylül University, July 2012.
- [2]. M. Akdağ, H. Karagülle, L. Malgaca, "An integrated approach for simulation of mechatronic systems applied to a hexapod robot", *Mathematics and Computers in Simulation*, 82(5), s.818-835,2011.
- [3]. (2011)Sensoray website. [Online] Available:http://www.sensoray.com/support/appnotes/pc-based_machine_control.htm/
- [4]. A. T. Hasan, A. M. S. Hamouda, N. Ismail, H. M. A. A. Al-Assadi, "An adaptive-learning algorithm to solve the inverse kinematics problem of a 6 D.O.F serial robot manipulator", *Advances in Engineering Software*, 37, s.432-438, 2006.

- [5]. J. Angeles, O. Ma, “An algorithm for the inverse dynamics of n -axis general manipulators using Kane's equations”, *Computers & Mathematics with Applications*, 17(12), s.1545–1561, 1989.
- [6]. C. C. Nguyen, F. J. Pooran, “Kinematic analysis and workspace determination of a 6 dof robot end-effector”, *Journal of Mechanical Working Technology*, 20, s.283–294, 2003.
- [7]. (2007) SolidWorks Corporation website. [Online]. Available: <http://www.solidworks.com/>
- [8]. (2011) Mitsubishi Electric Automotion Inc. website. [Online]. Available: <http://www.mitsubishi-automation.com/>
- [9]. (2012) Harmonic Drive AG website. [Online]. Available: <http://www.harmonicdrive.de/>
- [10]. (2012) Adlink Technology Inc. website. [Online]. Available: <http://www.adlinktech.com/>

BIOGRAPHY

. ahinYavuz was born in Izmir, Turkey in 1986. He received the B.E. and M.E. degrees from DokuzEylul University, Izmir, Turkey, in 2009 and 2012, respectively.

Since 2010, he is a research assistant at DokuzEylul University and since 2012, he is pursuing his PhD.

His main areas of research interest are robotics, vibration control, integrated softwares, PLC and servo applications.



A STATISTICAL MODEL FOR PREDICTING YARN EVENNESS OF COTTON SIROSPUN YARNS

Tuba Bedez Üte

Ege University, Department of Textile Engineering, 35040, Bornova/İzmir, Turkey.

tuba.bedeز@ege.edu.tr

Hüseyin Kadođlu

Ege University, Department of Textile Engineering, 35040, Bornova/İzmir, Turkey.

huseyin.kadodlu@ege.edu.tr

Abstract

Raw material costs constitute the majority of the yarn production costs, therefore it is critically important to select the suitable cotton blend and to know required fibre characteristics for spinning. This article is a part of a comprehensive work including the experimental research and the modeling of the physical and mechanical properties of the cotton sirospun yarns. In this paper, a model for estimating sirospun yarn evenness from cotton fibre properties was investigated. For this purpose, different cotton blends were selected from different spinning mills in Turkey and their properties were measured with AFIS (Advanced Fibre Information System). Besides some yarn production parameters were also selected as independent variable (predictor) due to their significant effect. Sirospun yarns were produced at Ege University Textile Engineering Department's spinning mill under the same conditions. Linear multiple regression method were performed and statistical evaluation showed that generated equations for predicting yarn evenness had a large R^2 and adjusted R^2 values.

Keywords: *Estimation, AFIS, multiple regression analysis, prediction, sirospun, yarn evenness*

1. INTRODUCTION

Yarn production is a sequence of processes that convert fibres into yarn, which will be used in various end products. Basic interest of every spinner is to reduce costs and to optimize the spinning process as well as to reach the desirable yarn quality. Raw material costs are more than half of the total manufacturing costs in a spinning mill, therefore knowing and monitoring the quality characteristics of the fibers, with the purpose of reducing costs and optimizing the spinning process, have great importance for the spinners.

For many years, the spinning machinery manufacturers enhanced the spinning process and reduced the mass variation of yarns, rovings and slivers thanks to precise measurement. This improvement provides an opportunity to increase productivity and to reduce considerably the raw material costs [1].

As much as spinners would like to produce an absolutely regular yarn, it is unachievable because of cross sectional fibre variation and the mechanical constraints. Accordingly, there are limits to achievable yarn evenness. According to Martindale, in the best possible conditions, the following evenness limit could be achieved for ring-spun yarns:

$$U_{lim} \frac{80}{\sqrt{n}} < \sqrt{1 + 0.0004 CV_D^2} \quad \text{or} \quad CV_{lim} \frac{100}{\sqrt{n}} < \sqrt{1 + 0.0004 CV_D^2} \quad (1)$$

n is the number of fibers in the yarn cross section

CV_D is the coefficient of variation of the fiber diameter

Since the variation of the fibre diameter is small enough to be ignored in industrial use, the equations reduce to:

$$U_{lim} \frac{80}{\sqrt{n}} \quad \text{or} \quad CV_{lim} \frac{100}{\sqrt{n}} \quad (2)$$

This can be expressed approximately as $CV \approx 1.25U$. In the evaluation of the achieved evenness, the unevenness index I is commonly used which is defined as [2]:

$$I = \frac{CV_{normal}}{CV_{lim}}$$

In recent years, prediction of the yarn quality characteristics from process parameters and fibre properties is one of the favorite research subjects for the engineers. Consequently researchers have been developed various mathematical, statistical and empirical models which are considerably important for the spinners in terms of raw material selection [3-9]. Especially, Hunter [8] and Ethridge et. al. [9] has investigated models for predicting yarn irregularity by using fibre parameters. Most of the researchers are focused on modeling of ring spun and rotor spun yarn properties but there is a few study on modeling sirospun yarn characteristics.

It is authenticated that, yarn properties are particularly influenced from fibre properties and this effect becomes more influential in the case of finer yarns. This paper is a part of a work concerning the experimental research and determination of the equations and models for estimating the sirospun yarn quality characteristics from the yarn production parameters and cotton fiber properties which are measured by the HVI and AFIS systems. As a result, equations were derived for the prediction of yarn tenacity, breaking elongation, unevenness and hairiness by using fiber and yarn properties. Some of the results are given in previous papers [10-13]. Regressional estimation of cotton sirospun yarn properties from fibre properties measured with HVI [11], regressive estimation of yarn hairiness of cotton sirospun yarns from AFIS fiber properties [12] and the prediction of yarn strength of cotton sirospun yarns from AFIS fiber properties by using linear regression analysis [13] were investigated previously.

2. EXPERIMENTAL

2.1. Materials

As the raw material represents about 50-75% of the manufacturing cost of a short-staple yarn and it has a significant effect on productivity and quality, yarn producers focus on the suitable blend [14].

In order to investigate the effect of fibre properties, various cotton blends were supplied from spinning mills in different regions of Turkey. Cotton fibres properties were analyzed with Advanced Fibre Information

System (AFIS) which is developed for the measurement of individual fibres. The features provided with the USTER are given in Table 1 [15].

Table 1. Fibre properties that can be measured with AFIS.

Nep Classification:	Fiber and seed coat nep count per gram and size (μ m) distribution.
Length:	Fiber length by number and by weight distributions, short fiber content by number and by weight (%).
Maturity:	Maturity, immature fiber content (%) and fineness (mtex) distribution.
Trash:	Dust and trash count per gram and size (μ m) distribution; visible foreign matter content (%).

AFIS can be used for blend composition, analysis of changes in fibre properties during processing, optimization of the process parameters and predicting the produced yarn quality [16]. Different blends are coded from B1 to B11 and fibre properties measured with AFIS are given in Table 2.

Table 2. Fibre properties of different blends measured with AFIS.

Fibre properties	Abbreviation	B1	B2	B3	B4	B5	B6	B7	B8	B9	B10	B11
Fiber nep count per gram	Nep Cnt/g	4	19	24	8	5	7	152	12	19	25	17
Mean length by weight	L(W) (mm)	29,5	28,1	25	30,3	26,8	27	24,8	26,1	26,3	28	25,5
Upper Quartile Length by weight	UQL (w)	35,2	33,9	30,7	36,6	32	32,6	30,9	31	31,2	33,9	30,6
Short fibre content by weight	SFC (w) %	2,3	3,7	6,2	2,4	3,8	4,6	9,9	3,7	4,6	3,9	5,1
Mean length by number	L(n) (mm)	25,8	24,2	21,5	26,4	23	23,3	20,2	22,9	22,7	24,3	22,2
Length variation by number	L(n) %cv	37,6	40,3	40,3	38,9	38,4	40	48,5	37,8	39,6	39,2	38,7
Short fibre content by number	SFC (n) %	8,5	11,6	15,1	9	11,3	13,2	25,5	11	12,8	11,4	14,2
5% Length by number	5.0% (mm)	40,9	39,9	36,7	42,4	37,3	38,2	35,6	36,1	36,9	39,1	35
Total trash count per gram*	Total Cnt/g	8	11	14	7	29	16	84	5	14	9	9
Trash count per gram	Trash Cnt/g	0	0	0	0	0	0	11	0	2	0	2

* dust particles included

Upper quartile length by weight and 5% length by number values of the different blends are given in Figure 1. B4 blend has the highest values, whereas B11 has the lowest length values.

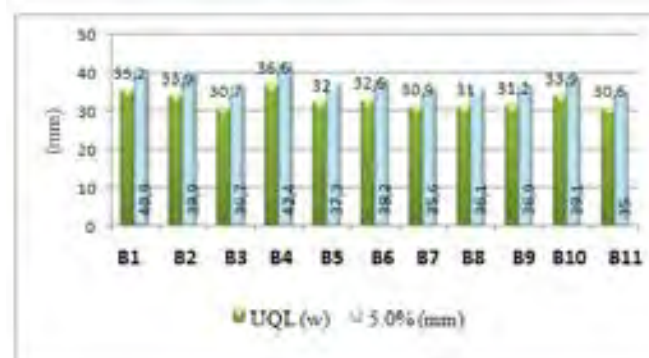


Figure 1. UQL (w) and 5.0% (mm) values of the different blends

Short fibre content by number and by weight values of the different blends are given in Figure 2. B1 and B4 blends have the lowest short fibre content while B3 and B7 blends have the highest ratios.

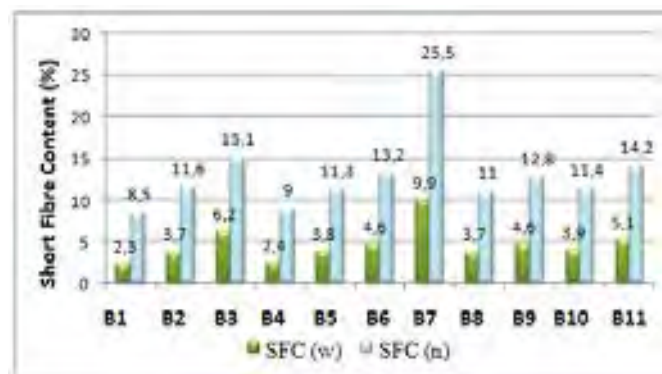


Figure 2. Short fibre content by weight and short fibre content by number values of the different blends

2.2. Methods

Yarn production parameters, as is known, have significant effect on yarn properties. Accordingly, yarn count, twist coefficient and strand spacing, which is defined as the distance between the two parallel roving strands fed through the drafting system, were also selected as predictors. As the sirospun yarns are produced with two rovings, spinners have to produce finer rovings and increase the creel capacity of the spinning frame. Besides, a double roving sirospun guides and condensers must be used in siro-spinning, which is mounted on the rail and disconnected from the traverse mechanism.

According to experimental design, it is planned to spun in four yarn counts (11.81, 14.77, 19.69 and 29.53 tex), at three twist coefficients and three strand spacing values, for each blend. More clearly, each linear density was spun at 3, 6 and 9 mm strand spacing, and at three different twist multipliers (α_{T1} 3831, α_{T1} 4310 and α_{T1} 4789). Cotton sirospun yarns were produced on a Rieter Model G30 ring spinning machine by keeping the spinning conditions constant. Some samples cannot be produced because of the raw material quality and drafting limits of the machine. For each yarn type, ten samples were produced and tested. Comparison was made between the yarns of different linear density, different twist factor and strand spacing. Experimental plan for each blend and yarn codes are given in Figure 3 and Table 3, respectively.

Subsequently yarn quality characteristics was measured and Uster Tester 5 was used for determining of the yarn unevenness, number of thin places, number of thick places, number of nep.

Final step is determining the equations and models for estimating the sirospun yarn unevenness from the yarn production parameters and cotton fiber properties which are measured by AFIS instrument. For this purpose, multivariate linear regression methods were performed. Statistical analyses were performed using Gretl (GNU Regression, Econometrics and Time-series Library) software.

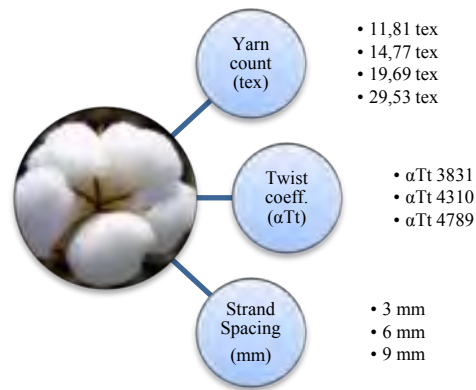


Figure 3. Experimental plan.

Table 3. Yarn code matrix.

Twist coeff.	Strand spacing	Yarn count			
		11,81 tex	14,77 tex	19,69 tex	29,53 tex
α_{Tt} 3831	3 mm	28	1	10	19
	6 mm	29	2	11	20
	9 mm	30	3	12	21
α_{Tt} 4310	3 mm	31	4	13	22
	6 mm	32	5	14	23
	9 mm	33	6	15	24
α_{Tt} 4789	3 mm	34	7	16	25
	6 mm	35	8	17	26
	9 mm	36	9	18	27

3. RESULTS AND DISCUSSION

Yarn unevenness, number of thin places, number of thick places, number of nep were measured with Uster Tester 5. According to the Figure 4, it is found that yarn unevenness is higher for finer yarns and increases with the increasing of the twist coefficient and strand spacing. For some blends, some yarn types cannot be produced because of poor spinning stability depending on the fibre quality, strand spacing and yarn count.

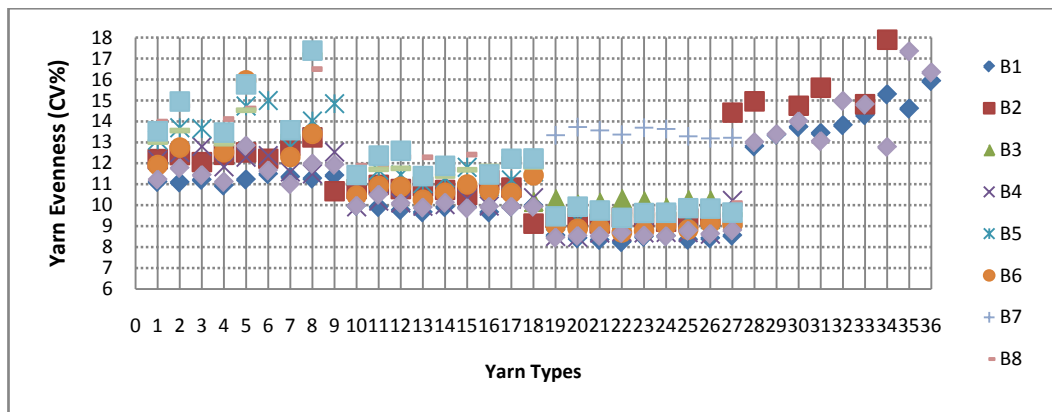


Figure 4. Yarn unevenness values (CV%).

Regression analysis is used for the investigation of relationships between two groups of variables. The obtained model can be used to describe the relationship between dependent and independent variables and to predict new values. As the yarn characteristics are influenced by fibre properties, production parameters, the spinning conditions, etc. the multiple regression analysis and ordinary least-squares methods were selected.

The types of relationship between selected parameters and yarn properties were checked by curve estimation and correlation analysis. Based on statistical analysis, a nearly linear relationship between fibre properties measured with AFIS and yarn properties was found, therefore, the linear multiple regression analysis method was chosen for this study [7].

Table 4. Pearson correlation coefficients between fibre properties measured with AFIS.

	Nep	L _w	SFC _w	UQL _w	L _n	SFC _n	%5L _n	Total	Trash
Nep	1	-0,366**	0,788**	-0,256**	-0,493**	0,838**	-0,283**	0,778**	0,901**
L _w	-0,366**	1	-0,804**	0,986**	0,986**	-0,739**	0,973**	-0,386**	-0,451**
SFC _w	0,788**	-0,804**	1	-0,709**	-0,885**	0,989**	-0,706**	0,706**	0,786**
UQL _w	-0,256**	0,986**	-0,709**	1	0,953**	-0,640**	0,985**	-0,309**	-0,383**
L _n	-0,493**	0,986**	-0,885**	0,953**	1	-0,833**	0,935**	-0,489**	-0,556**
SFC _n	0,838**	-0,739**	0,989**	-0,640**	-0,833**	1	-0,645**	0,754**	0,843**
%5L _n	-0,283**	0,973**	-0,706**	0,985**	0,935**	-0,645**	1	-0,314**	-0,420**
Total	0,778**	-0,386**	0,706**	-0,309**	-0,489**	0,754**	-0,314**	1	0,783**
Trash	0,901**	-0,451**	0,786**	-0,383**	-0,556**	0,843**	-0,420**	0,783**	1

**Correlation is significant at 0.01 level (two-tailed).

According to Pearson correlation coefficients, there is high correlation between number based and weight based measurements ($r > 0,98$). Besides, correlation between fibre length measurements (UQL(w)-L(w)) were also high (Table 4). As a result, for regression analysis, fibre properties that have a higher correlation with yarn unevenness were used: nep /gr, L(w), SFC(w), Total cnt, Trash cnt. Besides these, yarn count, twist coefficient and strand spacing were also chosen as independent variables.

A polynomial relation was found between short fibre content and yarn unevenness, due to curve estimation. Apart from that, there is a linear relationship between fibre properties and yarn properties. Following the curve estimation and collinearity tests, Best Subsets Regression method was used for determining which independent variables should be included in the model. To analyze the model in details, Stepwise regression was used. Models with higher adjusted R2, but lower Akaike and Schwarz values were determined. Finally, heteroskedasticity is tested with White test, it is found and a new model was established. Otherwise, it can invalidate statistical tests of significance that assume that the modelling errors are uncorrelated and normally distributed and that their variances do not vary with the effects being modelled.

Regression coefficients of variables, t-values and significance level of each variable of the final model are given in Table 5. Regression coefficients, which are constants, represent the rate of change of the yarn unevenness as a function of changes in the fibre properties and yarn parameters. Signs (+ or -) of regression coefficients of variables indicate the direction of influence P-value indicate the statistical significance. If the p-value is less than the significance level α , the null hypothesis is rejected and the result is statistically significant.

Table 5. Regression coefficients, t-values and significance level of t-values of linear regression model for yarn unevenness.

	Coefficient	Std. error	t-ratio	p-value
Constant	19.977	0.505	39.556	<0.00001***
Strand spacing (mm)	0.028	0.004	7.932	<0.00001***
Yarn count (Ne)	0.181	0.001	151.054	<0.00001***
Twist coefficient (α_c)	0.058	0.019	3.036	0.00242**
L _w	-0.529	0.013	-39.271	<0.00001***

SFC_w	0.378	0.117	3.228	0.00126***
SFC_w^2	-0.191	0.021	-8.964	<0.00001***
SFC_w^3	0.018	0.001	15.025	<0.00001***
Trash cnt	0.023	0.011	2.084	0.0373**
R^2	0.9272	Adjusted R^2	0.9269	
Yarn unevenness (CV%) = 19,977 + 0,028 F.A.M. + 0,181 Yarn count (Ne) + 0,058 (α_c) - 0,529 L_w + 0,378 SFC_w - 0,191 SFC_w^2 + 0,018 SFC_w^3 + 0.023 Trash cnt				

** is significant for $\alpha=0.05$.

*** is significant for $\alpha=0.01$.

All of the regression coefficients in the model are statistically significant. According to the equation, yarn unevenness increases with the increase of yarn fineness, twist coefficient and strand spacing. Among fibre properties, fibre length and short fibre content have greater influence on yarn evenness. As fibre length increases and trash count decreases, yarn unevenness decreases. Short fibre content has a polynomial relation, yarn unevenness increase with the increase of short fibre content, up to a limit, after that decrease and increase again.

Figure 5 shows the scatter plot of predicted yarn unevenness values versus actual yarn unevenness values and regression line of the models. A high correlation ($r=0,95$) was found between actual and predicted values.

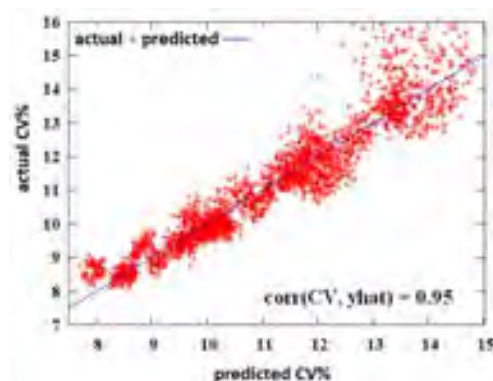


Figure 5. Predicted versus actual values of yarn evenness.

4. CONCLUSION

As the raw material costs are more than half of the total manufacturing costs in a short staple spinning mill, therefore knowing and monitoring the quality characteristics of the fibers, have great importance for the spinners. In this paper, a model for estimating sirospun yarn evenness from cotton fibre properties was investigated. This article is a part of a comprehensive work and some of the results are given in previous papers. Cotton fibre properties, measured with AFIS and some yarn production parameters such as yarn count, twist coefficient and strand spacing were selected as predictors. Linear multiple regression method were performed and statistical evaluation showed that generated equations for predicting yarn evenness had a large R^2 and adjusted R^2 values. Prediction ability of our model is very high as shown in Figure 5. Yarn unevenness increases with the increase of yarn fineness, twist coefficient and strand spacing. Fibre length and short fibre content are most important fibre properties for yarn unevenness. As fibre length increases and trash count decreases, yarn unevenness decreases.

ACKNOWLEDGEMENT

The authors express their thanks to the **Republic of Turkey, Ministry of Science, Industry and Technology and SÖKTAŞ**, which is a designer and producer of cotton and cotton blended fabrics, for supporting this research.

REFERENCES

- [1]. Rupp, J., 2008, Efficient Yarn Production, September-October, 2008, <http://www.textileworld.com>, http://www.textileworld.com/Issues/2008/September-October/Features/Efficient_Yarn_Production
 - [2]. *The Unevenness Limit*, www.rieter.com, <http://www.rieter.com/cz/rikipedia/articles/technology-ofshort-staple-spinning/reducing-the-unevenness-of-yarn-mass/unevenness-of-yarn-mass/the-unevenness-limit/> (Date Accessed: April 2015)
 - [3]. El Mogahzy Y., Broughton R. M., Lynch W. K.; Statistical Approach for Determining the Technological Value of Cotton Using HVI Fiber Properties, *Textile Res. J.* Vol. 60 (1990) pp. 495-500.
 - [4]. Majumdar P. K., Majumdar A.; Predicting the Breaking Elongation of Ring Spun Cotton Yarns Using Mathematical, Statistical, and Artificial Neural Network Models, *Textile Res. J.*, Vol. 74 (2004) pp. 652-655.
 - [5]. Frydrych I. and MatusakM., 2002, Predicting the Nep Number in Cotton Yarn Determining the Critical Nep Size, *Textile Research Journal*, 72: 917-923.
 - [6]. Majumdar A., Majumdar P. K. and Sarkar B., 2005, Application of linear regression, artificial neural network and neuro-fuzzy algorithms to predict the breaking elongation of rotor-spun yarns, *Indian Journal of Fibre&Texile Research*, 30: 19-25.
 - [7]. Üreyen M.E. and Kadoğlu H, "Interactions Between AFIS Fibre Properties and Ring Cotton Yarn Properties", *Tekstil ve Konfeksiyon*, 18 (1), p.8-14., 2008.
 - [8]. Hunter L., 2004, Predicting cotton yarn properties from fibre properties in practice, 27th International Cotton Conference, Bremen, Germany, 62-70.
 - [9]. Ethridge M. D., Zhu R.; Prediction of Rotor Spun Cotton Yarn Quality: A C omparison of Neural Network and Regression Algorithms, *Proceedings of the Beltwide Cotton Conference Vol. 2*, 1996, pp.1314-1317.
 - [10]. Bedez Ute T., *Research On Spinning of Short Staple Fibres by Sirospun System*, Ege University Graduate School of Natural and Applied Sciences, Master of Science Thesis, 2007.
 - [11]. Bedez Üte T., Kadoğlu H., 2014, *Regression estimation of Cotton Sirospun Yarn Properties From Fibre propertiers*, *AUTEX Research Journal*, Vol. 14, No:3, September 2014, p.161-167.
 - [12]. Bedez Ute T., Kadoğlu H., 2012, "Regression Estimation of Yarn Hairiness of Cotton Sirospun Yarns From Afis Fiber Properties", 6th International Textile, Clothing & Design Conference - Magic World of Textiles, October 07-10, Dubrovnik, Croatia.
 - [13]. Bedez Ute T., Kadoğlu H., 2012, "The Prediction of Yarn Strength of Cotton Sirospun Yarns From AFIS Fiber Properties By Using Linear Regression Analysis", *The Inter-Regional Research Network On Cotton For The Mediterranean& Middle East Regions*, November 05-07, Antalya.
 - [14]. *Characteristics of the Raw Material*, www.rieter.com, <http://www.rieter.com/tr/rikipedia/articles/technology-ofshort-staple-spinning/raw-material-as-a-factor-influencing-spinning/characteristics-of-the-raw-material/>, (Date Accessed: April 2015)
 - [15]. *Uster AFIS Pro Brochures*, www.uster.com, Uster Technologies, <http://www.uster.com/en/instruments/fiber-testing/uster-afis-pro/>(Date Accessed: 27 Temmuz 2012)
 - [16]. Frydrych I. and Matusiak M., 2002, "Trends of AFIS Application in Research and Industry", *FIBRES & TEXTILES in Eastern Europe*, July/September,: 35-39.
 - [17]. Ureyen M.E. & Kadoğlu H, 2006, *Regression Estimation of Ring Cotton Yarn Properties from HVI Fiber Properties*, *Textile Research Journal*, Vol 76, 2006, p360.
-

EVALUATION OF MARITIME SAFETY IN ISTANBUL STRAIT USING PORT STATE CONTROL INSPECTIONS

E. Gül Emecen Kara

*Istanbul University, Department of Maritime Transportation Management Engineering, 34320, Avcılar/Istanbul, Turkey.
emeceng@istanbul.edu.tr*

Olgay Okşaş

Istanbul University, Department of Maritime Transportation Management Engineering, 34320, Avcılar/Istanbul, Turkey

Abstract

Istanbul Strait is one of the heaviest maritime traffic of the seaways in the world. On the other hand, it has significant navigational challenges. In addition to these factors, sub-standards ships threat the lives as well as the marine environment. However, high risk arising from maritime shipping in this region may be reduced and safely navigation may be enhanced by means of Port State Control inspections. Especially, inspections of Black Sea MOU are very important for maritime safely in Istanbul Strait. In this context, in this study, Black Sea MOU inspections data are investigated for general an evaluation during 2004-2013 periods. And later, performance of Flag States of the most passing from Strait region is determined by using Black Sea MOU inspections and other regional MOUs inspections. Thus, an assessment of maritime safety is done for this region.

Keywords: *Istanbul Strait, Port State Control, Black Sea MOU, Safety*

1. INTRODUCTION

Istanbul Strait has become important link between Black Sea which is a closed sea and the rest of the world for centuries. It is one of the heaviest maritime traffic of the seaways in the world. On the other hand, it, as related to its twisting path and powerful currents, presents significant navigational challenges. In addition to these factors, sub-standard ships which are navigating in an unsafe condition threaten the lives as well as the marine environment. Therefore, there is always high risk arising from maritime shipping in this region. However, risk may be reduced and safely navigation in this region may be enhanced by means of Port State Control inspections.

Port State Control (PSC) mechanism has been established for the purpose of confirming that condition of the ship and its equipment comply with the requirements of international conventions and that the ship is manned and operated in compliance with applicable international laws. Regional agreements on port state control have been established in order to exchange information on ships inspected, and to unify the standards for inspection, ship detention and training of officers conducting inspections under Port State Control [1].

The first regional agreement, including Europe and North Atlantic region, was created in Western Europe in 1982 by means of Paris MOU (Memorandum of Understanding on Port State Control). Since then setup other regional agreements are Acuerdo de Vina del Mar Agreement (Latin American region), Tokyo MOU (Asia-Pacific region), Caribbean MOU (Caribbean region), Mediterranean MOU (Mediterranean region), Indian Ocean MOU (Indian Ocean region) Abuja MOU (West and Central African region), and Black Sea MOU (Black Sea region).

Although these PSC regimes are same, there are differences in the applications such as target inspections rate of ships, assessment of performance of flag states and selecting priority flags and ships for inspection. Paris MOU and Tokyo MOU generate a black/grey list of flags based on the statistics of inspections and detentions conducted during previous 3 years. This black list aims to identify ships that pose a very high risk. There aren't the black/gray lists in Black Sea MOU. However, Flag States whose number of detention exceeds the average detention rate, exceeding 10 numbers of inspections, are listed. Although United States are not a member of any regional agreement, they conduct port state control inspections, adding to their own rules. United States use The Port State Control Safety and Environmental Protection Compliance Targeting Matrix to better target ships that pose the most risk to their ports. The larger and stringent inspections are conducted in Paris MOU, Tokyo MOU and United States [2].

Especially inspections of Black Sea MOU are very important for maritime safety in Istanbul Strait, because it demonstrates performance of ships passing through this region. In this context, in this study, Black Sea MOU inspections are investigated for evaluating detention rates and types of deficiencies detected in inspections during the period of 2004- 2013. Performance of Flag States of the most passing from Strait region is determined by using Black Sea MOU inspections and other regional MOUs inspections. And as related to this performance an assessment of maritime safety is done for this region.

2. PORT STATE CONTROL INSPECTIONS IN THE BLACK SEA MOU REGION

In 2000 the Black Sea Memorandum of Understanding on Port State Control was signed by 6 Black Sea countries with the common understanding of main principles for PSC. Target inspection rate in Black Sea MOU is at least 15 % per country within a period of 3 years. A port State control visit on board will normally start with verification of certificates and documents. When deficiencies are found or the ship is reportedly not complying with the regulations, a more detailed inspection is carried out. When serious deficiencies are found, the ship shall be detained. The captain is instructed to rectify the deficiencies before departure. Only internationally accepted conventions shall be enforced during port State control inspections. These conventions are the so-called "relevant instruments" [3].

Black Sea MOU inspection statistics over the period of 2004-2013 are summarized in Figure 1. Percentage of inspections with deficiencies and detentions are given in Figure 2. These inspection data were obtained from Black Sea MOU Web Site [4]. It is seen that over 60 % deficiencies are detected in inspections and that detentions rate is subsequently decrease.

*Evaluation of Maritime Safety in Istanbul Strait Using Port State Control Inspections,
E. Gül EmecenKara, OlgayOktaş*

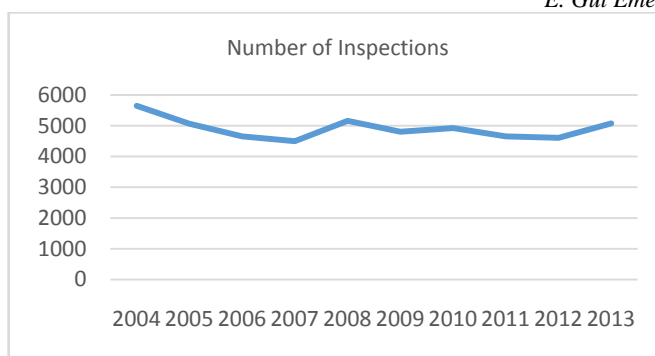


Figure 1. PSC Inspection Data (2004-2013).

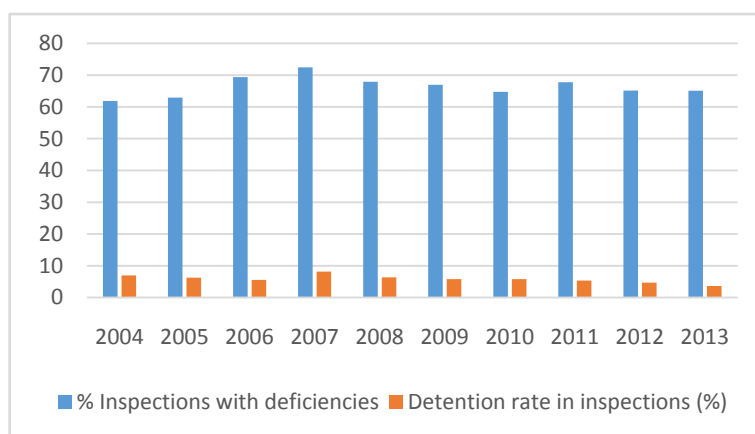


Figure 2. Percentage of Deficiencies and Detentions (2004-2013).

Percentage of deficiencies by categories over the period of 2004-2013 are shown in Figure 3. It is seen that safety of navigation, lifesaving appliances, stability- structure and related equipment and fire safety measures are top four deficiency categories.

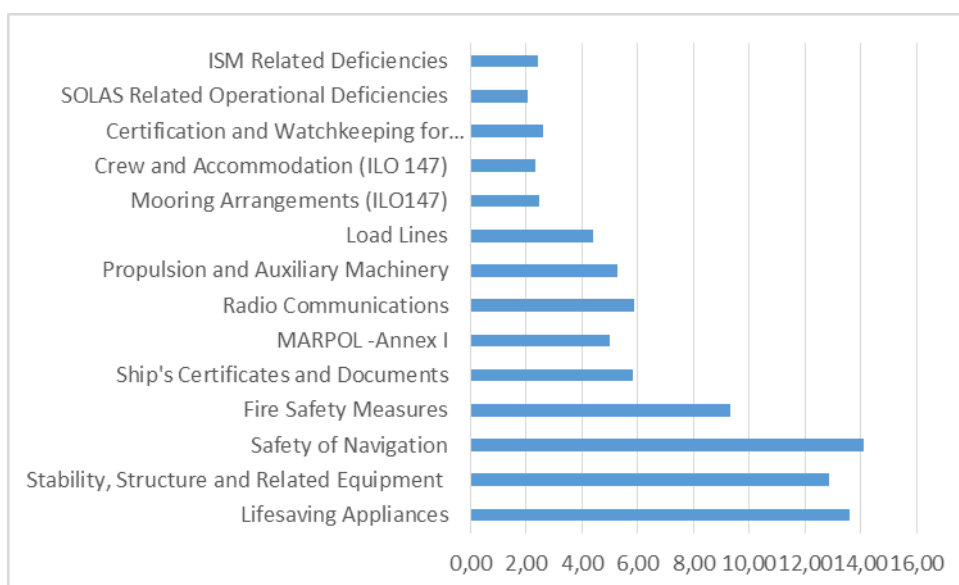


Figure 3. Percentage of major deficiencies by categories.

3. MARITIME SAFETY IN ISTANBUL STRAIT

3.1. Vessel Traffic in Istanbul Strait

The numbers of vessels that passing through Istanbul Strait between 1997-2013 years are shown in Figure 4. In addition to this figure, approximately more than two million people pass through the Istanbul Strait daily by small crafts. This value is four times higher than Suez Channel and tree times than Panama Channel [5]. Percentage of ships passing through Istanbul Strait per Flags are given in the Figure 5.

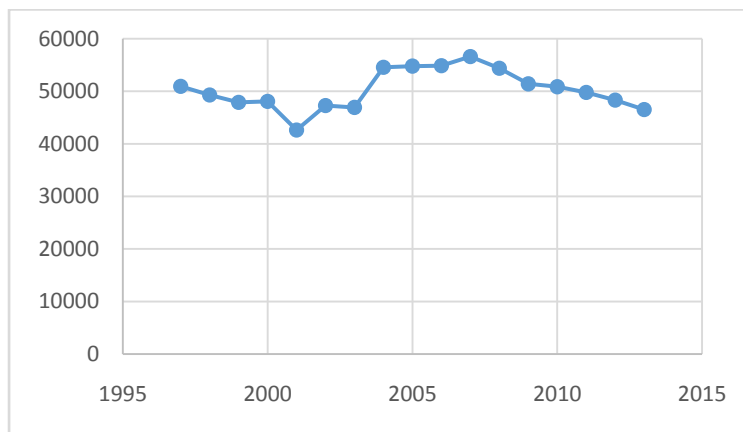


Figure 4. The number of ships that passing through Istanbul Strait between 1997-2013.

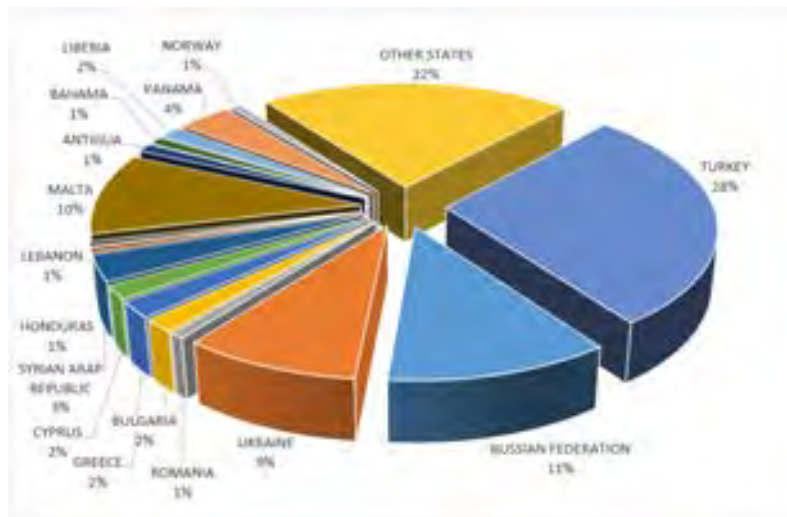


Figure 5. Ships passing through Istanbul Strait per flags.

3.2. Flag State Performance of Ships Passing through Istanbul Strait

In this study, performances of top 16 Flag states of the most passing from region are considered for evaluation. Because Flag state performance reflects to risks that arise from marine transportation in the region. Used PSC data were obtained from annual reports of all regional MOU.

Detention rates of these flag states which are calculated from PSC data for the period of 2004-2013 are given in Figure 6 and Figure 7. Most of these countries have larger detention rates in inspections.

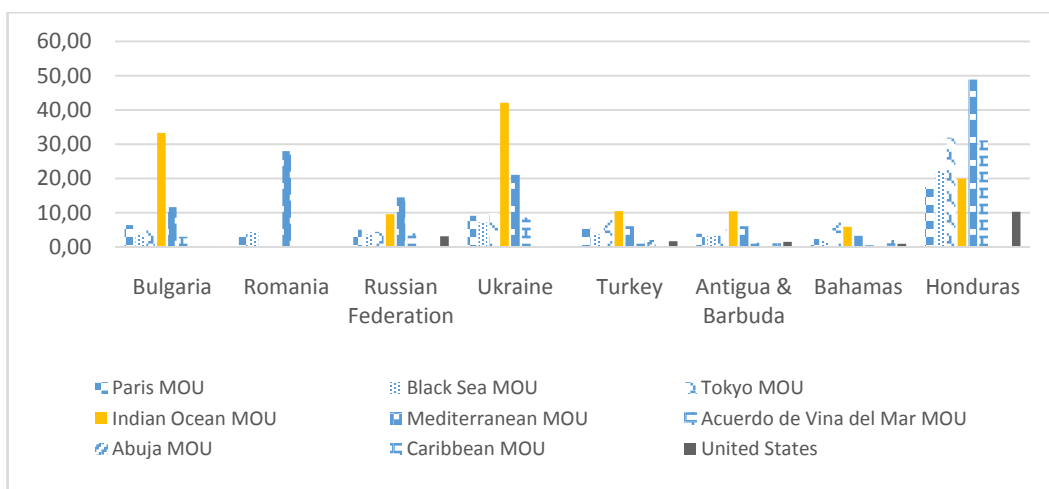


Figure 6. Detention rates of ships passing through Istanbul Strait by flags in each MOU (%).

Honduras, Syrian Arab Republic, Ukraine, Panama and Lebanon from these flag states have been a maximum detention percentage (Over % 5) in the Black Sea MOU for investigated periods. Also these flag states have a maximum detention percentage in the Paris MOU.

It is seen that Honduras has a maximum detention percentage in all Regional MOUs except Indian Ocean MOU over this period. Panama and Ukraine have a maximum detention percentage (42 % around) in the Indian Ocean MOU.

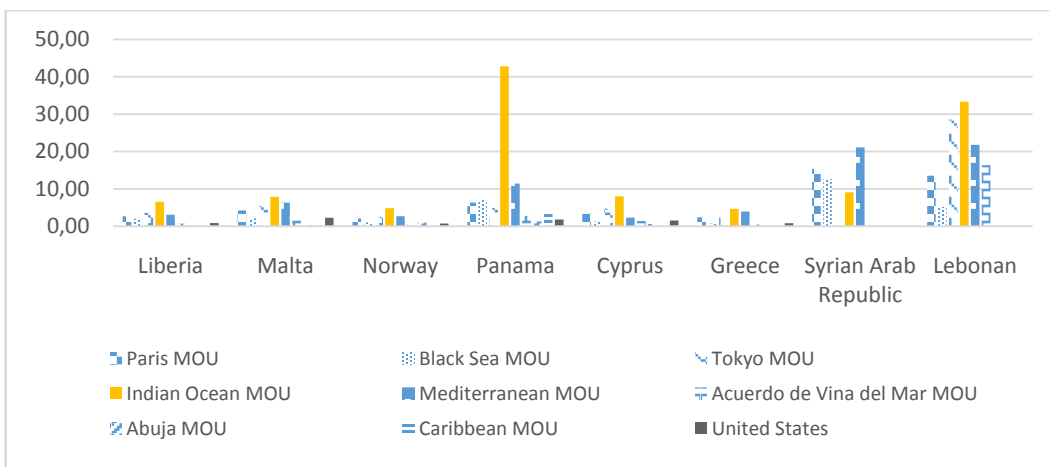


Figure 7. Detention rates of ships passing through Istanbul Strait by flags in each MOU (%).

Calculated deficiency rates of the most passing flag states from this region for the period of 2004-2013 are given in Figure 8 and Figure 9. These states have over % 50 deficiency percentage in the Paris MOU, the Black Sea MOU, the Tokyo MOU, the Indian MOU, and the Mediterranean MOU. Honduras, Syrian Arab Republic, Romania, Ukraine and Lebanon have a maximum deficiency percentage (Over % 75) in the Black Sea MOU respectively.

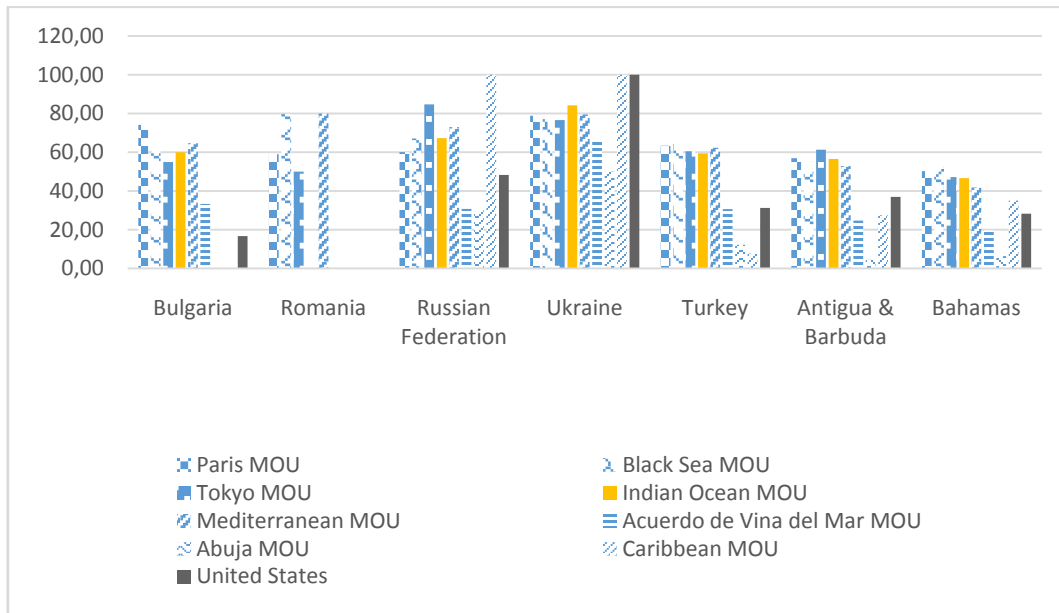


Figure 8. Deficiency rates (%).

Besides this profile Ukraine, Bulgaria, Syrian Arab Republic and Lebanon are in the Gray List in Paris MOU in 2013. Turkey is in the Flag State Safety Compliance targeted list in United States in the same year. Panama and Ukraine are in the list of 2013 Flag states exceeding average detention percentage in Black Sea MOU. Panama is also in the Flag State Safety Compliance targeted list in United States.

Honduras is in the Black List in Paris MOU and it is in the Flag State Safety Compliance targeted list in United States. Antigua& Barbuda is in the Gray List in Tokyo MOU, Cyprus and Malta are in the Flag State Safety Compliance targeted list in United States in 2013 year. The Black list, The Grey list, targeted list and Flag states exceeding average detention percentage list demonstrate flag states with high risk.

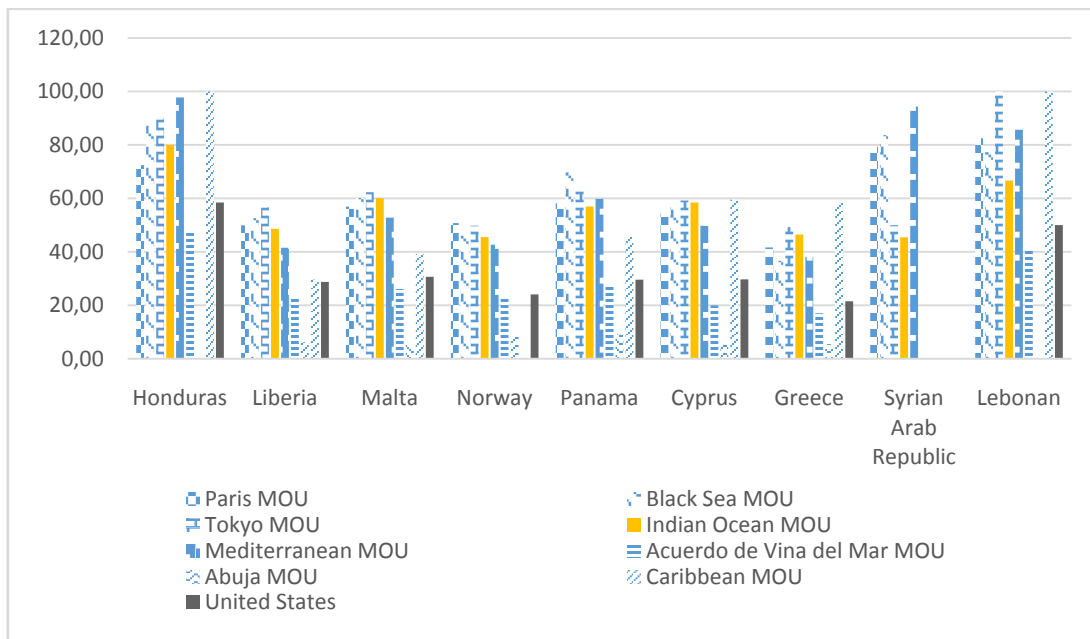


Figure 9. Deficiency rates (%).

4. CONCLUSIONS

In this study, performance of the most passing flag states from Istanbul strait region has been taken into the consideration for evaluation of risks. Honduras and Syrian Arab Republic from these flag states have over 10% detention rate in the Black Sea MOU during the period of 2004-2013. Ukraine, Panama and Lebanon have between 5% and10 % detention rates and Antigua& Barbuda, Turkey, Russia Federation and Bulgaria have over 3% detention rate in the same period. In addition to this profile Honduras, Syrian Arab Republic, Romania, Ukraine and Lebanon have larger deficiency percentage (Over 75 %) i n the Black Sea MOU respectively. Most of these flag States have larger detention rate and deficiency rate in other MOUs.

In some of t he regional MOUs, Ukraine, Bulgaria, Syrian Arap Republic, Lebanon, Panama, Honduras, Antigua& Barbuda, Cyprus and Malta are in the risk lists (the Black list, the Grey list, targeted list, Flag states exceeding average detention percentage list) in 2013 year.

It is seen that safety of navigation, lifesaving appliances, stability- structure and related equipment and fire safety measures are top four deficiency categories in the Black Sea MOU during the period of 2004 - 2013.

Flag state performance found in PSC inspections reflects to risks that arise from maritime transportation in the region. If re gional MOU inspections carry out stringent and effective, substandard ships may be eliminated over time. By this way, navigation safety is enhanced and risks arising from maritime transportation may be reduced in this region.

REFERENCES

- [1]. E.G.Emecen Karaand M.Yıldız, *LimanelarımızdaLimanDevletiKontrolüUygulamaları,TürkiyeKıyıveDenizAlanları VI UlusalKonferansı, Muğla, Turkey, 7-11 November 2006, ss.661-670, 2006.*
- [2]. E.G. Emecen Kara andM. Karaoğlu, *LimanDevletiKontrolüİncelemelerive Risk Değerlendirmesi, TürkiyeKıyıveDenizAlanları VII UlusalKongresi, Ankara, Turkey, 27-30 May 2008, ss.581-588, 2008.*
- [3]. (2015), About us.BS MOU website. [Online]. Available: <http://www.bsmou.org/>
- [4]. (2015), Annual Reports, BS MOU website. [Online]. Available:<http://www.bsmou.org/>
- [5]. DTO, 2006 DenizSektörüRaporu, Yayın No 71, İstanbul, 2007.

ANIMAL MANURE EFFECT ON CLIMATE CHANGE AND USAGE AS A ENERGY SOURCES IN TURKEY

Ali CAN

Karabük University, Faculty of Engineering, Mechanical Engineering Department, 78050, Karabük, Turkey,
alican@karabuk.edu.tr

Abstract

Climate is changing with the increasing number of population. Since the people wealth is mostly depended on economy and economical growth is explained by the high energy usage, there will always be high energy needed. The energy demand is mostly supplied by non-renewable energy sources for human beings wealth and economy. The investigators are searching new energy sources due to the possible end of non-renewable energy sources. The renewable energy sources such as wind, solar radiation, water, biogas production from the wastes and livestock manure are becoming more and more important due to consideration of positive environmental effect. The livestock manure is one of the new valuable energy sources for the people. Within this study, the livestock manure's CH₄ and N₂O emissions and the energy potential from manure as biogases will be considered. The highest energy could be produced in Balıkesir, Konya and Erzurum provinces, because 12% of Turkey's livestock's (cattle, buffalo and dairy cattle) are in these cities. The CH₄ and N₂O emissions from these provinces are 88.4 Gg and 0.85 Gg, respectively. These emissions are 2120.29 Gg CO₂ equivalents. According to the 2013's energy balance tables, 1564 ktonnes of Oil Equivalent (TOE) was produced from the animal and plant wastes. The total CH₄ and N₂O emission from this energy source are around 2.03 Gg CH₄ and 0.27 Gg N₂O. These emissions are just 42.67 Gg CO₂ equivalents. It was only 1.83% of total animal wastes in Turkey. Therefore, producing energy from animal wastes will not only result emission reduction, but also produce clean energy which decreases total consumption of non-renewable energy.

Keywords: Climate Change, Greenhouse Effect, CO₂ Equivalent, CH₄ and N₂O Emissions, IPCC Methodology

1. INTRODUCTION

The livestock manure was considered under agricultural activities of IPCC Guidelines [6], [7]. The most important direct greenhouse gases are CO₂, CH₄ and N₂O [4]. Methane emissions from manure management are usually smaller than enteric fermentation emissions, and are principally associated with confined animal management facilities where manure is handled as a liquid. Livestock manure is principally composed of organic material. When this organic material decomposes in an anaerobic environment (i.e., in the absence of oxygen), methanogenic bacteria, as part of an interrelated population of micro-organisms, produce methane [2], [5]. During storage of manure, some manure nitrogen is converted to N₂O. Emissions of N₂O related to manure handling before the manure is added to soils are included in this source category. Nitrous oxide is formed when manure nitrogen is nitrified or denitrified. The amount of N₂O released depends on the system and duration of waste management [1], [4]. The CH₄ from animal manure can be used as a clean energy. The energy production from manure saves emissions from fossil fuel combustion, resulting in a positive environmental impact and resulting in fewer emissions in case climate change consideration. Moreover, as manure contains a large amount of ammoniacal N, and due to nitrification and denitrification processes, land spreading of poultry manure causes larger emissions of N₂O than combustion [3].

Turkey signed United Nations Climate Framework Convention on Climate Change and Kyoto Protocol without any commitment [10]. In Turkey, total 1.6 million tones of oil equivalent (TOE) energy were obtained from animal and plant wastes [9]. In order to tackle with climate change and to decrease the emissions in the future, Turkey could use animal wastes as a fuel to obtain a clean energy.

The purpose of this study was to investigate the effect of livestock manure on air emission in Turkey by using IPCC methodology. The numbers of livestock's data were obtained on the web site of State Institute of Statistics [11] and the energy balance tables are gathered from Ministry of Energy and Natural Resources [9]. The CH₄ and N₂O emissions were calculated by using the IPCC-Tier 1 method [7].

2. METHODOLOGY

The method (IPCC - Tier 1) was used to estimate the CH₄ and N₂O emissions. And the general CH₄ production capacity and its energy as biogases are also calculated according to the IPCC Methodology and Turkish energy conversion factors obtained from energy balance tables.

The general formula (1) for the CH₄ emission from Enteric Fermentation is given as [6]:

$$\text{CH}_4 \text{ emission} = \sum A_n * EF * CF \quad (1)$$

A_n : The number of livestock
CF : Conversion Factor
EF : Emission Factor
n : Type of livestock (Cattle, Buffalo, Sheep, Goats, Camel, horse, mules, swine, poultry)

And the general formula (2) for the CH₄ emission from manure management is given as:

$$\text{CH}_4 \text{ emission} = \sum A_n * EF_c \quad (2)$$

A_n : The number of livestock
EF : Emission Factor
n : Type of livestock (Cattle, Buffalo, Sheep, Goats, Camel, horse, mules, swine, poultry)
c : Temperate or cool emission factor

The general formula (3) used for the N₂O emission for Manure Management is;

$$\text{N}_2\text{O emission} = \sum A_n * EF * CF * N\text{-N}_2\text{O} \quad (3)$$

A_n : The number of livestock
CF : Conversion Factor
EF : Emission Factor
N-N₂O : Molecular weight of N₂O/N - (44/28)

n : Type of livestock (Cattle, Buffalo, Sheep, Goats, Camel, horse, mules, swine, poultry)

According to the IPCC (1996) Guidelines, The method for estimating methane emission from enteric fermentation and manure management requires three basic steps:

- a) Divide the livestock population into subgroups,
- b) Estimate emission factors for each subgroup in terms of kilograms of methane per animal per year – separate emission factors are required for enteric fermentation and manure (Table 1).
- c) Multiply the subgroup emission factors by the subgroup populations to estimate subgroup emission

Table 1. CH₄ emission Factor for Enteric fermentation and Manure Management

Livestocks type	Enteric Fermentation		Manure Management	
	Emission	Conversion	Emission	Emission
	Factor	Factor	Factor	Factor
			Cool	Temperate
Dairy Cattle (avg)	68,5	0,001	7	16
Dairy Cattle	56	0,001	7	16
Other Cattle	44	0,001	1	1
Buffalo	55	0,001	1	2
Sheep	5	0,001	0,1	0,16
Sheep	6,5	0,001	0,11	0,17
Goats	5	0,001	0,11	0,17
Camels	46	0,001	1,3	1,9
Horse	18	0,001	1,1	1,6
Swine	1	0,001	1	4
Mules&Dankeys	10	0,001	0,6	0,9
Poultry	-	-	0,012	0,018

Source: [6]

Table 2. N₂O emission Factors

Livestock Type	Direct N ₂ O		Indirect N ₂ O		Fraction of Total N used as fertilizer
	N	Waste	Fraction of	N ₂ O	
	Excretion/animal kg N/head/year	Management Type (%)	Total N lost	Emission factor	
Dairy Cattle	82,58125	0,0027875	0,2096	0,01	0,8
Other Cattle	45,08845	0,006305	0,15975	0,01	0,5
Buffalo	44,384	0,00705	0,132	0,01	0,5
Sheep (domestic)	13,5022625	-	-	0,01	-
Sheep (merinos)	13,5022625	-	-	0,01	-
Goats	16,49435	0,002	-	0,01	-
Camels	33,2661	-	-	0,01	-
Horse	37,86875	0,002	0,05	0,01	0,1
Swine	6,79995	0,0068925	0,150225	0,01	0
Mules&Dankeys	37,86875	0,002	0,05	0,01	0,1

Poultry	-	-	-	-	-
Chicken	0,4089825	0,0005	0,2375	0,01	0,2
Duck & Geese	0,817965	-	-	0,01	0
Turkey	1,83668	0,0005	0,2375	0,01	0,2

Source: [6]

For the consideration, the CH₄ and N₂O are converted to CO₂ equivalent emissions. The CH₄ is multiplied by 21 and N₂O is multiplied by 310 and the obtained values are gathered to reach CO₂ equivalent emissions. In order to draw maps, Geographic Information System is used [8].

3. RESULT AND DISCUSSION

The result of this study showed that the livestock wastes could be an alternative energy sources over Turkey. This energy is clean and eco-friendly, therefore producing energy from livestock wastes will decrease the adverse affect of non-renewable fuel usage in the environment. Turkey has a great potential for producing CH₄ from livestock wastes. Approximately, quarter of the livestock could be gathered in the specially designed animal farms. The following maps, seen on Figure 1, just show the last 10 year livestock average numbers in Turkey Provinces. According to these graphs, the highest cattle livestock population was seen in Erzurum, Konya and Balıkesir.

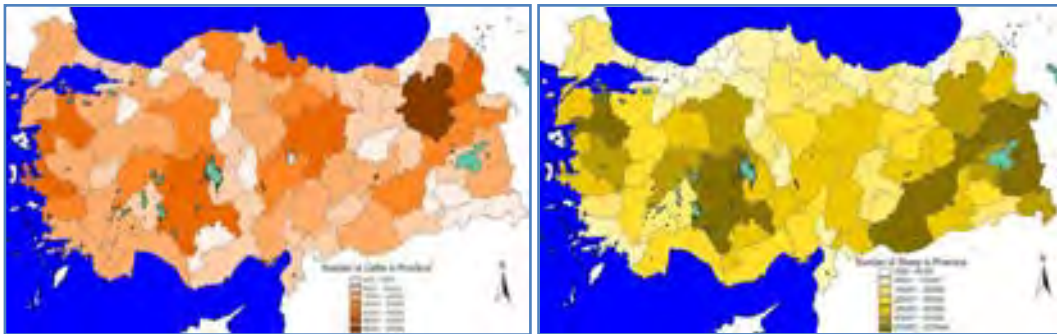


Figure 1. 2003-2014 (10 year) averages of cattle and sheep population in Turkey province.

By using 10 year averages of livestock population and IPCC methodology, the potential CH₄ emission was calculated. According to the CH₄ emissions resulted from enteric fermentation of livestock's and manure management, 2367.6 GW electricity could be produced from the animal wastes. The distributions of potential electricity capacity of provinces are given in Figure 2.

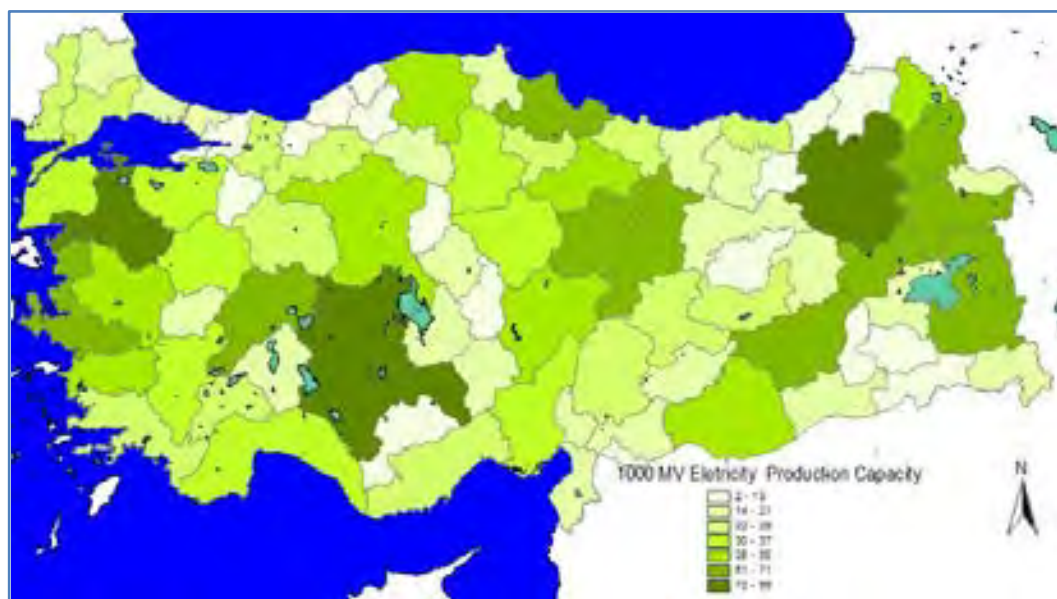


Figure 2. The distributions of potential electricity capacity of provinces

The highest portion electricity could be produced from cattle. It was approximately 77.79% (Table 3). In practical, turning all wastes into energy was not possible because the livestock population is distributed entire area of the provinces. However, such as Erzurum, Konya and Balıkesir which form 12% capacity of total probable energy production provinces can be organized or just cattle can be collected in animal farms. In case, the produced energy will decrease 2.5 million tones of CO₂ equivalent emissions annually. If the number of organized animal farms is increased, the decreased CO₂ equivalent emissions could be reached approximately 20 million tones of CO₂ equivalent emissions annually. The produced biogases will also emit CH₄ and N₂O into the atmosphere. However, the quantity is just 0.5 ktone/year. If the manure was not collected and just let it free to emit emissions into the atmosphere, then the total CO₂ equivalent emissions would be around 18.85 million tones as given in Table 3.

Table 3. The emission from livestock (10 year averages)

Animal Type	Enteric	Manure	Direct	Indirect	CO ₂ Eq. (Gg)
	CH ₄ (Gg)	CH ₄ (Gg)	N ₂ O (Gg)	N ₂ O (Gg)	
Cattle	564,87	49,01	4,45	1,91	14863
Buffalo	3,25	0,08	0,03	0,01	81
Sheep	124,38	2,91	0,00	0,00	2673
Goats	31,95	0,91	0,33	0,00	793
Camels and Llamas	0,05	0,00	0,00	0,00	1
Horses	3,50	0,26	0,02	0,01	88
Mules and Asses	3,77	0,27	0,04	0,01	102
Swine	0,00	0,01	0,00	0,00	0
Poultry	0,00	3,98	0,09	0,43	246
TOTAL	731,78	57,41	4,9676	2,3670	18847

According to the Energy balance tables of Turkey, in 2013, just a 1.83% of livestock manure (including also plant wastes) is used as energy. The following Figure 3. gives CO₂ eq. emissions from the annual usage of livestock manure as fuel according to the energy balance tables.

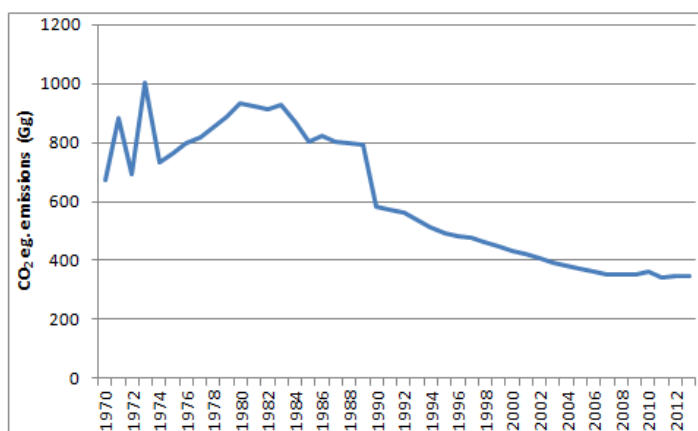


Figure 3. CO₂ eq. emissions from the annual usage of livestock manure as fuel

Between the years 1970 and 1988, the livestock manure is highly used as fuel by farmers in the rural areas. After 1990's, the usage of livestock manure is considerably decreased. And finally, it reached the lowest value in 2013. It was only 4.7 million tones of livestock wastes. Compared to the total livestock numbers in Turkey, it was very low.

4. CONCLUSION

According to this study, there is a big potential in the provinces to produce energy from livestock wastes. The livestock manure is one of the new valuable energy sources for the people. From this source, the potential electrical energy, which is around 2367.6 GW, could be produced. And this value energy from animals, decreases, annually, approximately 20 million tones of CO₂ equivalent emissions. According to the Energy balance tables of Turkey, in 2013, just a 1.83% of livestock manure (including also plant wastes) was used as energy. Therefore, producing energy from animal wastes will not only result emission reduction, but also produce clean energy which decreases total consumption of renewable energy. Moreover, obtaining biogases energy from animal manure is one way to tackle with climate change for Turkey.

REFERENCES

- [1]. Carran, R.A., Theobald, P.W. and Evans, J.P.; Emission of nitrous oxide from some grazed pasture soils in New Zealand. Australian Journal of Soil Research V.33-p.341-352, 1995.
- [2]. Crutzen P.J., Aselmann I., Seiler W. Methane production by domestic animals, wild ruminants, other herbivorous fauna, and humans. p.271-284, 1986.
- [3]. Billena P., Costab J., Aab L. V., Caneghem J. V., Vandecasteelea C. Electricity from poultry manure: a cleaner alternative to direct land application, Journal of cleaner production, Vol 96. p. 467-475, 2015.
- [4]. Duxbury, J.M. and A.R. Mosier. Status and issues concerning agricultural emissions of greenhouse gases. In: Agricultural Dimensions of Global Climate Change H.M. Kaiser and T.E. Drennen (eds.). St. Lucie Press, Delray Beach, Florida, U.S.A, p.229-258, 1993.
- [5]. Gibbs, M.J. and D.E. Johnson; Livestock Emissions. In: International Methane Emissions, US Environmental Protection Agency, Climate Change Division, Washington, D.C., U.S.A., 1993.
- [6]. IPCC Greenhouse Gas Inventory Reference Manual – Revised 1996 IPCC Guidelines for National Greenhouse Gas Inventories – Volume 3 – Intergovernmental Panel on Climate Change – Edited by Houghton J.T., et al., 1996.
- [7]. IPCC Greenhouse Gas Inventory Reference Manual – IPCC Guidelines for National Greenhouse Gas Inventories - Intergovernmental Panel on Climate Change, 2006.
- [8]. Martin D. ; Geographic Information Systems – Second Edition – Socio economic applications.p.71-161., 1996.
- [9]. MENR, The annual Energy and Petroleum Balance Sheets 1970-2013, Ministry of Energy and Natural Resources, 2013.
- [10]. TurkStat, National Greenhouse Gas Inventory Report, 1990-2011. Annual Report submission under the “Framework Convention on Climate Change, 2013.
- [11]. TurkStat, - TÜİK - Agricultural Statistics Databases (2003-2013). <http://tuikapp.tuik.gov.tr/hayvancilikapp/hayvancilik.zul>. date:01.04.2015.

EVALUATION OF TURKISH STRAITS VESSEL TRAFFIC SERVICES (TSVTS) APPLICATIONS IN THE ISTANBUL STRAIT

Gökhan KARA

Istanbul University, Department of Maritime Transport Management Engineering, 34320, Avcılar/Istanbul, Turkey.
karagok@istanbul.edu.tr

Abstract

The region consisting of the Turkish Straits, called Istanbul and Çanakkale Straits and the Sea of Marmara, is one of the regions that have the highest concentration of maritime traffic in the World. In the year 2012, 45.529 ships in total have passed through Istanbul Strait with a monthly average of 4028 ships. Daily averages are 140 ships for Istanbul Strait. In the year 2014, 150.000.000 tons of dangerous cargoes shipped through Istanbul Strait. In addition to these figures, approximately more than two million people pass across the Istanbul Strait daily by small passenger vessels. Turkish Straits Vessel Traffic Services (TSVTS) was put into service with the purpose of lessening the risks of maritime accidents which may happen and directing the maritime traffic in the area with continuous observations made and increasing the safety of life, properties and the environment in the Turkish Straits and in the Sea of Marmara. This study will assess situation from when establishment of VTS. Istanbul Strait ship accidents that may occur, the effect of VTS applications were examined. This analysis allowed us to investigate the impact of various factors on the risk profile of the Istanbul Strait.

Keywords: *Turkish Straits, Vessel Traffic Services, Istanbul Strait, TSVTS, Maritime accidents*

1. INTRODUCTION

Istanbul Strait in terms of ship traffic is very dense transition center. Each year, approximately 45,000 ships pass. The Istanbul Strait is about 31 km long, an average 22 of 1.5 km wide and with its narrowest place of just 698 meters (Figure 1). All of these vessels on both sides of the passage in which a densely population constitutes a potential threat to Istanbul. For example, 20% of the ships are carrying dangerous cargo in 2014. In case of any accident that might occur, the people who live there and the sea life will be affected as seriously negatively. Istanbul Strait in the past year; collision, grounding, explosion and fire as many accidents have occurred. The largest of these accidents, crude oil loaded "Independent" at the ship have collided with another vessel in 1979 and has caused the oil spill into the sea. Turkish Straits Vessel Traffic Services (TSVTS) was put into service with the purpose of lessening the risks of maritime accidents which may happen and directing the maritime traffic in the area with continuous observations made and increasing the safety of life, properties and the environment in the Turkish Straits and in the Sea of Marmara. The vessels arriving at the North or South entrance of the Strait of Istanbul enter the Strait according to the directions of VTS, which uses strict and well defined regulations, rules and all other data that are received by radars, sensors and stations [1]. The TSVTS does not simply enhance the safety of navigation but it also serves an important function in coordinating emergency teams in case of an emergency. The TSVTS also makes risk assessments by using information received from vessels, tugs, SAR, and medical boats etc. It also issues warnings to other vessels and strives to prevent or minimize the risk of an accident or of an unexpected situation from taking place [2].



Figure 1. The strait of Istanbul.

2. SERVICES AND PURPOSE OF THE TSVTS

Information service provided by a VTS is the case that VTS is enabling essential or necessary information provided to the users i.e. those on-board subject to make navigational decision. Second service provided by a VTS is navigational assistance. Navigational assistance is a higher level service comparing the previous one and it is the case that VTS is involving decision making process regarding the ship's navigation and providing navigational advice to those on-board and consequently monitor its effects. Other service provided by VTS is traffic organization service [3].

2.1. Task and Responsibilities

Traffic organization is a service to prevent the development of dangerous maritime traffic situations of an early stage and in fact it regulates the traffic within the VTS area [3].

Information service is a service for providing information about maritime traffic, the position of vessels in relation with order vessels, intended movements of other vessels, notices to marines, meteorological information and any other information deemed to be necessary by the VTS Operators.

Traffic organization service is a service for providing operational information before vessels enter the Straits to assist vessel traffic organization in accordance with the Turkish Straits Maritime Traffic regulations [2]. Improvement of Efficiency of Traffic; by achieving an appropriate planning and execution delays can be avoided and optimum traffic flow can be obtained. This capability also depends on the quality of the VTS

elements as well as VTS objectives. Similarly through the service provided this benefit can be shared by the service providers, allied services and the users.

Improvement of Safety of Environment by achieving safer navigable waters VTS does serve to reduce the environmental risks simultaneously in fact. Nevertheless, there are some other facilities provided by the VTS for the environmental protection in the following areas: Improvement of Safety of Traffic by foresighted prevention of situations of likely to be endangering either the vessel concerned or any other encounters in the vicinity or the environment. Optimized traffic flow and additional navigational assistance (if provided) for ships carrying dangerous and/or noxious cargo can decrease the possibility of casualties involved these type of vessels, In case of emergency of a pollution incident early detection can be performed and co-operation can be done with the emergency clean-up services and other official bodies. Consequently by regulating the traffic further problems can be prevented in advance. By continuous monitoring illegal and deliberate spills and other source of pollution events can be prevented [3].

2.2. Services Provided

Services provided by TSVTS has been defined by considering the regulations and recommendation of IALA related with VTS and TSVTS has been providing Information, Navigational Assistance and Traffic Organization Services in accordance with A.857(20) and A.827(19) numbered regulation of IMO.

Information Service

- Marine Traffic information.
- Information about the position of a vessel in relation with other vessels.
- Information about positions of other vessels by means of distances from own vessel, course and speed over the ground.
- Information about intended movements of other vessels.
- Notice to Mariners.
- Meteorological information and current situation.
- Information about the reported status of aids to navigation.
- Any other information when deemed necessary by the TSVTS.

Navigational Assistance Service

Navigational assistance is a service for providing information in order to ensure the safe navigation of vessels experiencing difficulties due to navigational equipment failure or bad weather. Navigational Assistance Service will be provided when severe meteorological situations have been observed, deficiencies or breakdowns have occurred during the passage of the participants, when required by the master or when deemed necessary by the TSVTS. With regard to the safety of navigation, decision making process on the bridge of the participant vessels may be assisted by providing the following information.

- Position information in order to ensure safe navigation of vessels sailing within the TSS
- Information about movements of other vessels in the vicinity
- Warnings with regard to dangerous situations that might develop

The beginning and ending time of the navigational assistance service must be clearly agreed and recorded by the Master and TSVTS operator.

Traffic Organization Service

- Vessel Sailing Plan and its entry permission, time and date to the Istanbul and Çanakkale Straits.
 - Any changes in the Sailing Plan.
 - Necessary operational information to the vessels before entering the Straits related to the traffic organization.
 - Operational information to all vessels in Straits according to the Turkish Straits Maritime Traffic Regulations.
 - The SP 1 and SP 2 Reports constitute the primary sources for traffic organization service to be provided by the TSVTS. Sending all these reports timely and accurately will increase the efficiency of traffic organization.
-

As vessels not providing timely and accurate information will disrupt the regular flow of maritime traffic may expose to delays and penalty procedure. After all, vessels not providing timely and accurate information may create risk in terms of safety of life, property and navigation by endangering not only their own vessels but also the others. All these services above are provided on request of Vessels or by TSVTS as deemed necessary. TSVTS cannot be hold as responsible related with services unclaimed [6].

In addition, the TSVTS, provides important services for security measures in accordance with the IMO (International Maritime Organization) adopted International Ship and Port Security Code (ISPS) was adopted by the IMO, and for search and rescue operations. The TSVTS is the first contact point in the case of any emergency in the VTS area and it distributes all related information to the concerned organization [2].

3. VESSEL TRAFFIC SERVICES IN ISTANBUL STRAIT

The competent authority of Turkish Straits Vessel Traffic Service (TSVTS) is the Minister of Transportation, and the General Director of Coastal Safety and Salvage Administration, appointed by the Turkish Government, is the TSVTS Authority. In addition to the safety of navigation, the TSVTS applies the emergency plans, and coordinates all the means to be used in accordance with these plans (towing, firefighting, antipollution, S.A.R., medical care). But its domain of responsibility is limited by “the fact that the ultimate decision relating to the safety of navigation is given by the Master, and that any information, any warning, any instruction or recommendation given by the VTS does not affect in any way the responsibility of managing the vessel, the professional ability and the knowledge of the Master”. All the VTS operators are Captains with at least two years of command experience, and received a specific formation in conformity with the IALA standards. There are currently three VTS areas in the Turkish straits: the Istanbul VTS (55Nm), the Çanakkale VTS (78Nm), and The Marmara Sea TSS (71 Nm). Istanbul VTS is divided into 4 sectors, each one controlled by an operator [5].

Information on the vessel traffic situation is obtained from 8 towers on the Istanbul strait (Figure 2). Each tower is fitted with a X band radar and a remote-controlled TV camera sending data to the area's VTS center. Three towers in each VTS area are equipped with VHF devices. Six AIS base stations are established in the Turkish straits, and the straits pilot station has 50 portable AIS transponders units, enabling each pilot to obtain a whole image of the vessels proceeding through the straits.

The sectors of Istanbul VTS; sector Türkeli, sector Kavak, sector Kandilli, sector Kadıköy and sector Marmara (Figure 2).

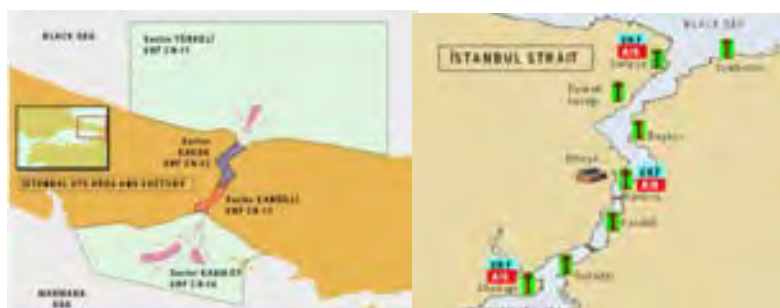


Figure 2. VTS areas and vessel traffic stations in the strait of Istanbul [6].

3.1. Pilotage in the Turkish Straits

There is a well-established system of Pilotage in the Turkish Straits, operated by Turkish Maritime Incorporated. The service employs 140 pilots from two stations in the Strait of Istanbul and two stations in the Strait of Çanakkale. Pilotage within the Turkish Straits is compulsory only for vessels bound for or leaving Turkish ports, and/or for LNG vessels transiting the Strait of Çanakkale. Pilotage is recommended by IMO and the Turkish Authorities for all vessels transiting the Turkish Straits. Although almost all large tankers adhere to the recommendations of the IMO Resolution and employ a pilot [7].

4. RISK ASSESSMENT OF ISTANBUL STRAIT

Narrower sea passage having areas such as the straits, they differ from each other depending on the structural, physical, oceanographic and meteorological factors. Risk in narrow straits varies according to channel dimensions, configurations, and length, hydrodynamics, commodity types and flows, vessel types, hull forms, sizes, propulsion and steering systems, vessel loading, traffic types, patterns, density, times of movement, tides etc. All of these factors are not identical at every narrow strait. A general statement cannot be taken custom-made for every narrow strait. But, it gives an idea to make a strait -specific assessment [3]. Hazards in a narrow strait often come along with the following risk factors at the (Table 1).

The primary mission of the regulations and the VTS is to reduce the maritime transportation risks in the Strait [6]. The risk assessment studies identified that many casualties originated from equipment or human failures on vessels carrying non-dangerous cargo, registered with Flag States associated with lower safety standards. Consequently, efforts to improve the quality of vessels that transit the Turkish Straits would reduce overall casualty risk in the Straits. This suggests that a robust regional inspection regime to enforce international Conventions and regulations would be of benefit. Increased use of tankers of under 200 meters in length, which are not affected by the current implementation of the rules for 'Restricted Vessels', is undesirable because, for a given volume of cargo, it will have the unwanted effect of increasing the density of traffic in the Straits and therefore the risk. The current system requires that 'Restricted Vessels' and other vessels carrying hazardous goods must clear specific points in the respective Straits - i.e. substantially complete the transit – before similar vessels can enter from the opposite direction. Further obstruction to consistent traffic scheduling and transit direction flow is caused by the priority given to Restricted Vessels bound for Turkish ports. While LNG vessels bound for Marmara ports have a stated priority in the Turkish Rules, other vessels do not [7].

Table 1. General risk factors in the transition narrow strait [4].

Risk Factors		
Physical Factors	Vessel Factors	Economic Factors
- Strait geometry and configurations	- Types	- Ship scheduling
- Hydraulic and hydrologic conditions	- Sizes	- Cargo transfer operations
- Hydrography Environmental Conditions (E.g. Currents, Wind, etc.)	- Propulsion and steering systems	
	- Hydrodynamics	
	- Maneuvering behavior	
	- Vessel status/Maintenance condition	
Transit Considerations	Potential Consequences to	Human Systems
- Cargoes	- Vessel	- Decision making
- Marine traffic	- Human life	- Suitability, qualifications and proficiency of
- Duration of exposure	- Environment	- Vessel operators
- Navigational aids and support systems,	- Economics	- Bridge team
- Waterway management/Traffic systems	- Property	- Support system personnel
- Subsystem support (Such as tugboats)		- Work environment

4.1. Statistical Analysis

Until now Istanbul strait has undergone large number of marine accidents. These accidents are occurred as collision (touching, rubbing, aging), grounding, sinking and capsizing, fire and explosion, crash ashore (lean land) and a machine malfunction. The causes of the accident in the Strait describes as follows:

- Lack of Pilotage
- The nature of the strait
- Surface currents
- Restricted visibility
- Local conditions
- Onboard mechanical failures and technical failures

The above reasons are generally the risk of accidents in the narrow waterway at different locations and conditions. They are affected to varying degrees. In other words, accident locations and for some time,

It cannot be estimated as deterministic. The statistical analysis was used to analysis the accidents occurred in Strait of Istanbul in the period of 1995-2014. These statistics show the total number of vessels, number of ships proceeding with a pilot, accidents and the total number of vessels carrying dangerous cargo that passed through Istanbul strait during the this years. They are compared with each other.

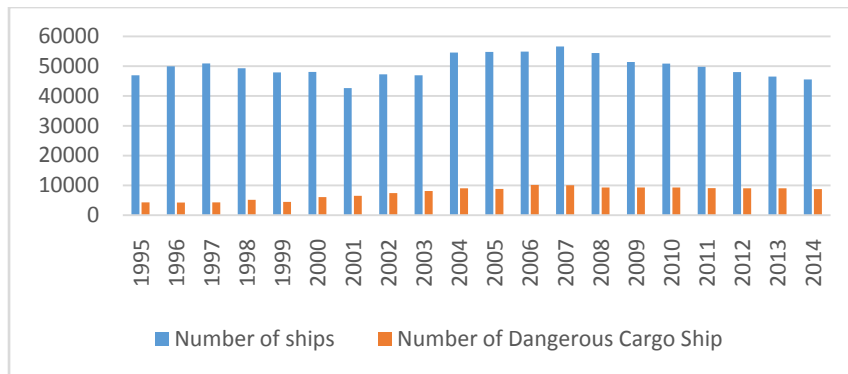


Fig 3. The total number of vessels and the number of dangerous cargo ship in Istanbul strait (1995-2014).

One of the most important reason for this improvement can be attributed to the efficient and proper traffic organization provided by the VTS, which began providing these services at the and of 2003. According to this statistics, almost 20 percent of these vessels carry dangerous cargo [2].

As seen in Figure 3, despite of the total number of vessels decreased after 2004, remained almost the same as the number of ships carrying dangerous cargo. In 2008, due to the economic crisis that occurred in the world, Istanbul has been a reduction in the number of ships passing through the strait.

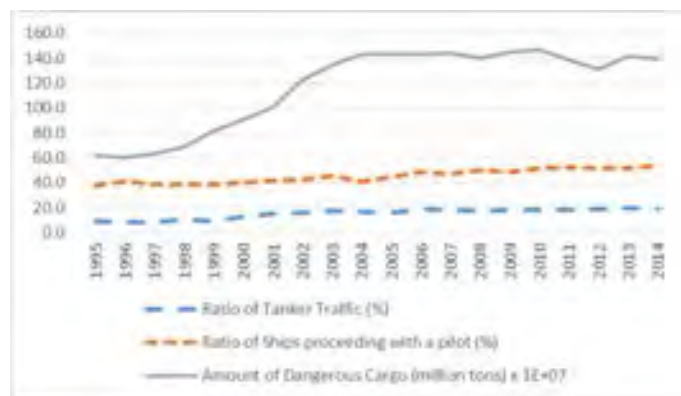


Fig 4. The amount of dangerous cargo, ratio of tanker traffic and ratio of vessels proceeding with a pilot in Istanbul strait are compared with each other (1995-2014).

In Figure 4, the amount of dangerous cargo, the ratio of dangerous cargo traffic and ration of vessels proceeding with a pilot in Istanbul strait between the years 1995-2014 are compared with each other. As shown in Figure 4, after the start of process VTS in 2004, the proportion of ship pilots who demand increased by 50 percent. However, the amount of dangerous goods transported increased by almost two times.

After starting the process VTS, a significant reduction in the number of accidents occurred in response to the increasing number of tankers. It increased the number of ships that pilots assigned according to the VTS

regulations and rules are determined as a result of the significant decrease in the number of accidents (Figure 5).

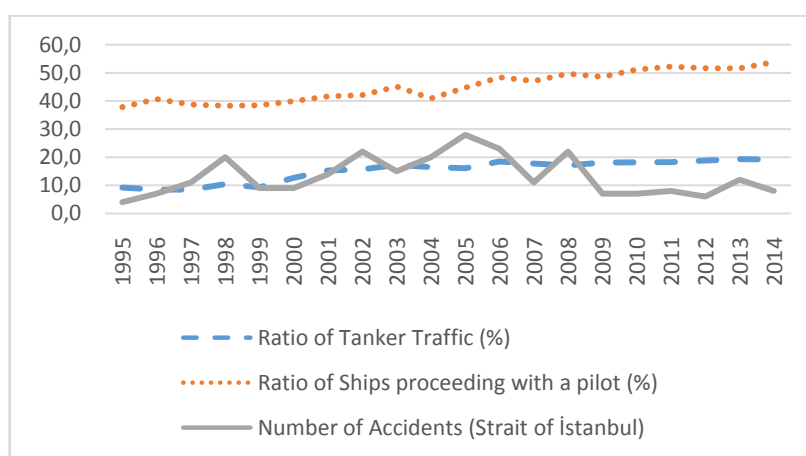


Fig 5. The number of accidents, ratio of tanker traffic and ratio of vessels proceeding with a pilot in Istanbul strait are compared with each other (1995-2014).

5. RESULTS AND DISCUSSIONS

Tankers carrying dangerous cargo have become a serious threat to safety of navigation, human life and environment in the İstanbul Strait. Accidents, which may occur, especially from dangerous cargo traffic, could create hazard such as oil spill and closes of the Strait of İstanbul traffic. In addition to the VTS, the use of a pilot during passage provides another important means for enhancing the safety of navigation. Although engaging a pilot in the İstanbul Strait is strongly recommended by IMO resolution A.827 the percentage of vessels engaging a pilot is only 51 percent in total for all vessels in Istanbul Strait in 2014 of which only 35.4 percent was comprised non-stopover vessels [2]. After the entry into Vessel Traffic Services (VTS-2004), there has been a significance improvement in safety of vessel traffic and marine environment. Although the total number of ships carrying dangerous cargoes with the increasing number of ships, VTS applications in particular has led to a reduction in accidents that may occur as a result of human error. 70% of the accidents occurred in the Istanbul strait by ships that do not demand maritime pilots. The collision was the most accident type occurred in the Bosphorus and respectively grounding, fire/explosion, stranding, contact, foundering/capsizing and breakdown. After the implementation of The Maritime Traffic Regulations and introduction of Traffic Separation Schemes (TSS) in 1994 and implementation of VTS in 31 December 2003 there has been a significance decrease the number of accidents in the Strait.

6. CONTENT

After the Turkish Straits VTS is established, the last ten years, the Bosphorus and the Dardanelles has an effective and efficient services. Depending on the growing energy needs in the world has caused to an increase in the amount transported, also ships with carrying oil and its derivatives. Sea accidents occur in the very narrow channel and passage in maritime transport. The Istanbul strait waterways having the most traffic after from Gate Malacca in the world. In addition, the city of Istanbul has been established on both sides of the strait. Therefore, the effect of accidents occur will be important. The human error is the major cause of accidents and respectively current and bad weather conditions and local traffic density. The vessels should be promoted to appoint maritime pilot in bad weather conditions.

REFERENCES

- [1]. Almaz, Ö.A., Or, İ., Özbaş, B., "Investigation of Transit Maritime Traffic in The Strait of Istanbul Through Simulation Modeling and Scenario Analysis. International Journal of Simulation", Vol 7, No 7, 2006.
- [2]. Oral, N. and Öztürk, B., "The Turkish Straits, maritime safety, legal and environmental aspects. Turkish Marine Research Foundation". İstanbul. Publication Number 25, 2006.
- [3]. Öztürk, B. and Özkan, R. (Eds.), "The Proceedings of the Symposium on the Straits used for International Navigation". Turkish Marine Research Foundation. İstanbul, Turkey, Publication Number: 11, 2002.

- [4]. Minding The Helm, National Academy Press, p.57, 1984.
- [5]. Pizon, F.X., "Turkish Marine Research Foundation publication. Turkish Straits Vessels Traffic Service". 2015. Web site: http://www.afcan.org/dossiers_techniques/tsvts_gb.html.
- [6]. VTS Users Guide, Turkish Straits Vessel Traffic Service, "General Management of Coastal Safety and Salvage Administrations", 3rd edition, May 2004, Istanbul, 2004.
- [7]. Guidelines for Transiting the Turkish Straits, Briefing Paper for OCIMF Member Companies, OCIMF, August 2007.

VIBRATION CONTROL OF ANONELINK FLEXIBLE MANIPULATOR WITH HARMONIC EXCITATION

Şahin YAVUZ

Dokuz Eylul University, Department of Mechanical Engineering, 35397, Buca/İzmir, Turkey.
sahin.yavuz@deu.edu.tr

Hira KARAGÜLLE

Dokuz Eylul University, Department of Mechanical Engineering, 35397, Buca/İzmir, Turkey.
hira.karagulle@deu.edu.tr

Abstract

Flexible manipulators are more desirable than rigid manipulator due to lightweight arm, higher motion speed and better energy efficiency. The flexibility causes residual vibrations at the end point after motion. Therefore, controlling residual vibration of flexible manipulators is important. In this study the residual vibration of a flexible beam is studied in ANSYS. The trapezoidal velocity profile is applied in the transient analysis. The residual vibrations are observed for the control-off case. A high frequency harmonic velocity excitation is applied after the end of the trapezoidal velocity profile to control the residual vibration. An exponential decaying is added to the harmonic excitation after a certain time. It is known that the vibration amplitudes of a system decrease when the system is excited at higher frequency than the natural frequencies. The effect of the amplitude, frequency, the duration of the application and the exponential decaying factor on the suppression of the residual vibration is analyzed.

Keywords: *flexible manipulators, harmonic excitation, vibration control*

1. INTRODUCTION

Flexibility of robot manipulators depends on the parameters such as the weight, the dimension, the payload and speed of manipulators. The effect of flexibility in manipulators is observed as vibrations both during the motion and after the motion has finished. Vibrations caused after finishing the motion are called as residual vibrations. Residual vibrations also affect the accuracy and settling time at the end point. The performance of such manipulators or repeatability decreases in high speed engineering applications. Suppressing residual vibrations are important and possible by applying different control strategies such as passive or active.

Active control requires actuator, sensor and a control system. Many researchers have examined feedback approaches to the control of flexible systems such as the use of endpoint position feedback and feedback of strain gage measurements [1-4].

Another approach for vibration control is passive control such as input shaping. Command shaping is a method of reducing vibration that does not require additional sensors or actuators. The earliest form of command shaping was the use of high-speed cam profiles as motion templates. Cam profiles were shaped to decrease energy at system resonances [5].

Input shaping has been investigated and extended by many researchers [6,7]. Input shapers containing negative impulses were shown to improve response time [8]. Some researchers used input shaping on a long-reach manipulators [9,10]. Input shaping was used to control a flexible pointing mechanism on a recent space shuttle mission [11].

In this paper, exponential harmonic input is applied to the system to reduce the residual vibration of the end point of the link. Exponential harmonic input consists of different parameters such as decaying factor, excitation frequency and initial angle. The effect of these parameters is analyzed.

2. MODELING OF THE SYSTEM

In this study, onelink flexible beam model is considered as shown in Figure 1. Flexible beam is modeled in ANSYS by using APDL (ANSYS Parametric Design Language) which allows you typing commands in text file and running analysis without using graphical interface. In graphical interface study, it is very difficult to fix when there is a mistake on the model. Therefore, APDL is much easier and faster way to create a model and make changes on the model. BEAM3 element is used as a flexible beam. BEAM3 is a uniaxial element with tension, compression, and bending capabilities. The element has three degrees of freedom at each node: translations in the nodal x and y directions and rotation about the nodal z-axis. The element is defined by two nodes, the cross-sectional area, the area moment of inertia, the height, and the material properties. The material of the beam is aluminum and the properties of the beam are given in Table 1.



Figure 1. Model of the robot flexible beam

Table 1. Properties of the aluminum beam

Properties	Values
Modulus of Elasticity, E (N/m^2)	68×10^9
Density, ρ (kg/m^3)	2800
Length, L (mm)	500
Height of the cross-section, h (mm)	0.8
Width of the cross-section, b (mm)	20

The other element type used in APDL is MPC184 element to define revolute joint. The MPC184 family of elements serves to connect the flexible and rigid component to each other in a multibody mechanism. An

MPC184 joint element is defined by two nodes with six degrees of freedom at each node. The relative motion between the two nodes is characterized by six relative degrees of freedom. Depending on application, different kinds of joint elements can be configured by imposing appropriate kinematic constraints on any or some of these six relative degrees of freedom. For example, to simulate a revolute joint, the three relative displacement degrees of freedom and two relative rotational degrees of freedom are constrained, leaving only one relative rotational degree of freedom available. Some joint types of MPC184 elements are given in Table2.

Table 2. Drive system

Joint Element Type	Keyoption (1)	Keyoption (4)	Constraints
Revolute	6	-	5
Z-axis Revolute	6	1	5
Universal	7	-	4
Translational	10	-	5
Spherical	5	-	3
Cylindrical	11	-	4
Z-axis Cylindrical	11	1	4

In Figure 1, the motor is connected to the beam at point O. Defining MPC184 element as a revolute joint with keyoption(1) as 6 and keyoption(4) as 1 allows to rotate the beam on the axis-z. Due to having joint flexibility of the motor, motor rotational spring constant is defined as 16000 N m/rad. Example codes for defining element types in APDL are given below:

```

et,1,beam3          !first element type is beam3
r,1,A,Izz,ymax      !r,1,area,cross sectional area, height
uimp,1,ex,dens,,E,rho,0 !material properties such as density and modulus of elasticity
et,2,mpc184         !second element type is mpc184
keyopt,3,1,6        !revolute joint between rigid and flexible beam
keyopt,3,4,1        !z axis is revolute axis
TB,JOIN,3,,STIF     !defining joint stiffness
TBDATA,21,16000     !value of the joint stiffness
    
```

Modal analysis is performed in ANSYS and first three natural frequencies are identified as $f_1 = 2.5474$ Hz, $f_2 = 15.965$ Hz and $f_3 = 44.701$ Hz, respectively. Natural frequencies can be calculated for the cantilever beam analytically as follows:

$$\omega_n = \frac{\beta_n}{L^2} \sqrt{\frac{EI}{\rho A}} (\text{rad/s}) \quad (1)$$

Here, β_n , L , E , I , ρ and A is frequency parameter, length of the beam, modulus of elasticity, inertia of cross section and cross sectional area, β_n frequency parameter for first three frequency is 3.516, 22.03 and 61.7, respectively.

3. VIBRATION CONTROL WITH HARMONIC INPUT

In flexible systems, the vibration occurs major problem after the motion. Suppressing residual vibration after the motion is a large research area for the researchers. In this study, exponential harmonic input is applied after the end of the trapezoidal velocity profile to control the residual vibration. The harmonic input can be written in the form as follows:

$$\theta = \theta_0 \cos \omega_0 t \quad (2)$$

$$\omega = \omega_0 \theta_0 \sin \omega_0 t \quad (3)$$

Here, θ_0 and ω_0 are initial angle in degree and excitation frequency in degree/s, respectively. θ and ω are angular displacement and angular velocity based on time. Transient analysis is used in ANSYS to obtain response spectrum of the system. An arbitrary trapezoidal velocity profile is applied to the system during 1.5s and residual vibration of the end point of the flexible beam is observed after the motion. The Rayleigh damping is used in transient analysis to take effect the damping of the system and considered as $\eta=0$, $\beta=3.8e-4$, where, η and β are damping coefficients [12]. Total time duration is given 4s. Velocity profile input and system response are given in Figure 2.

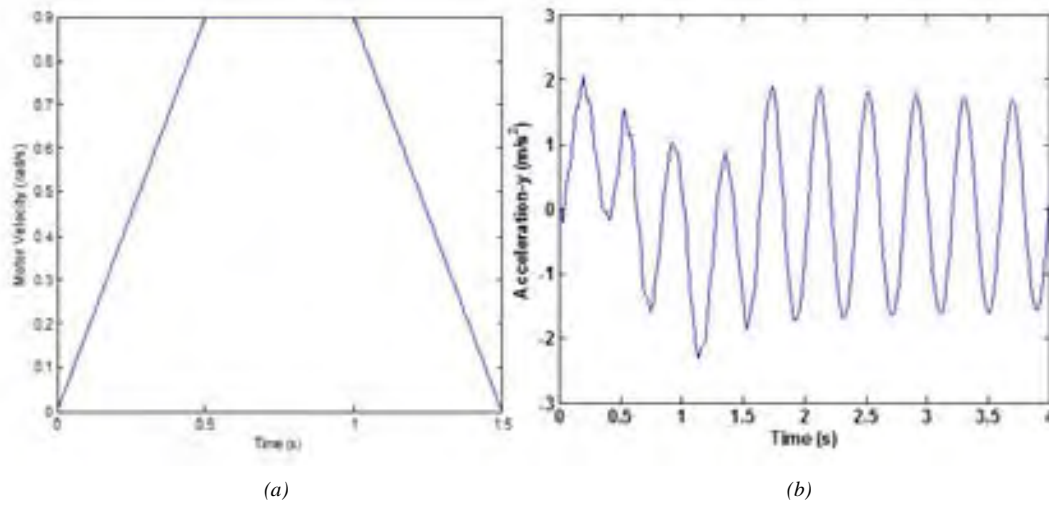


Figure 2. (a) Velocity profile input, (b) system response

It is shown that the amplitudes of residual vibration are extremely high and the end point of the flexible beam reaches the steady state value in a long time. The harmonic input given in Equation 3 is applied after the end point of the velocity profile. The excitation frequency ω_0 and initial angle θ_0 are chosen as two times of the first natural frequency and 1 degree, respectively. The control-off and control-on results are given in Figure 3.

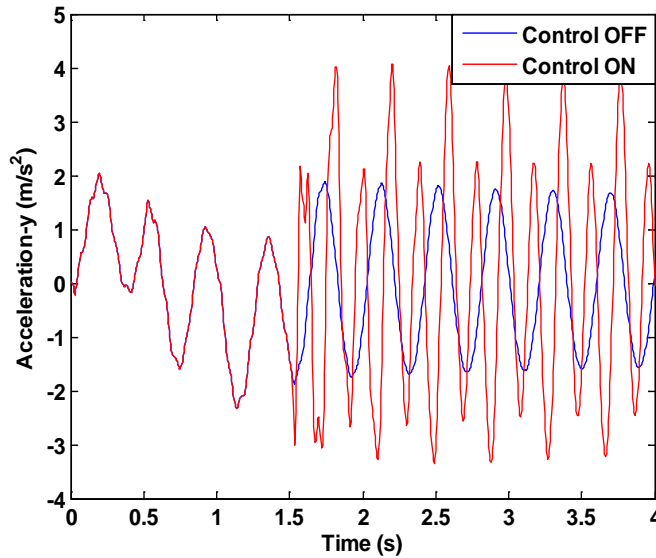


Figure 3. Response spectrum of the end point

The amplitudes of the end-points acceleration are increased. An exponential decaying factor is added to the harmonic input to decrease the residual vibration. The exponential harmonic input parameters given in Equation 4, initial angle, excitation frequency and decaying factor are chosen by trial. Different parameters are applied at the end point of the velocity profile and response spectrums are given in Figure 4-8.

$$\omega = \omega_0 \theta_0 e^{-at} \sin \omega_0 t \quad (4)$$

Here, a is the decaying factor.

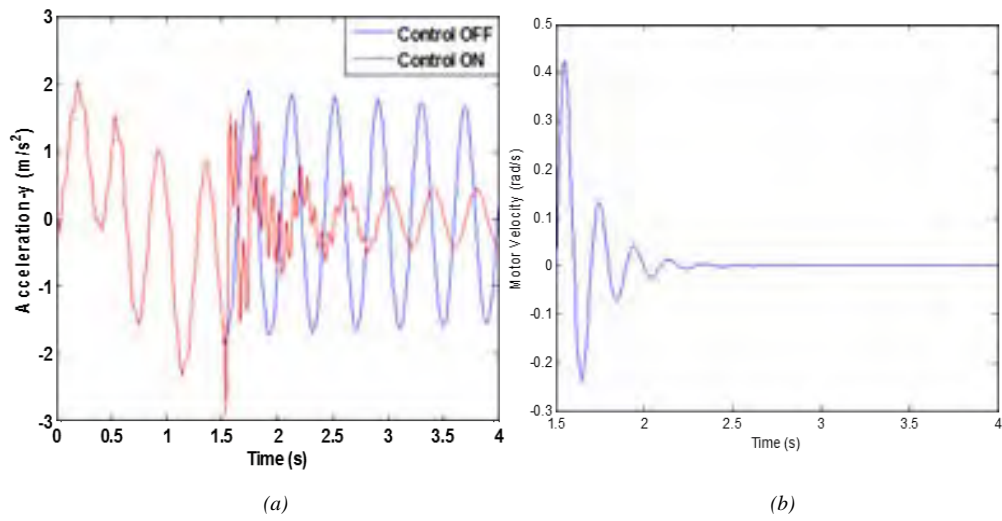


Figure 4. (a) Response spectrum of the end point, (b) exponential harmonic input ($\theta_0=1$ degree, $\omega_0=2f_1$, $a=-6$)

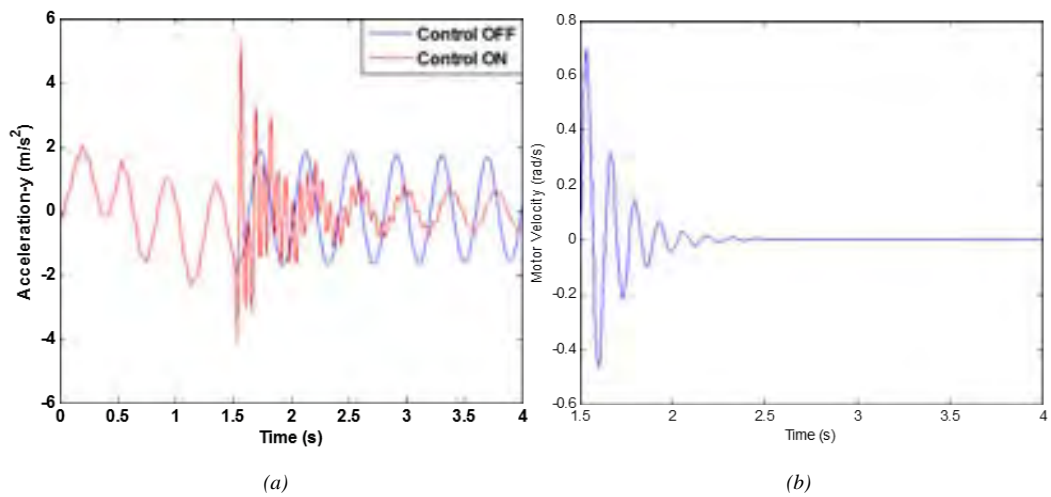


Figure 5. (a) Response spectrum of the end point, (b) exponential harmonic input ($\theta_0=1$ degree, $\omega_0=3f_1$, $a=-6$)

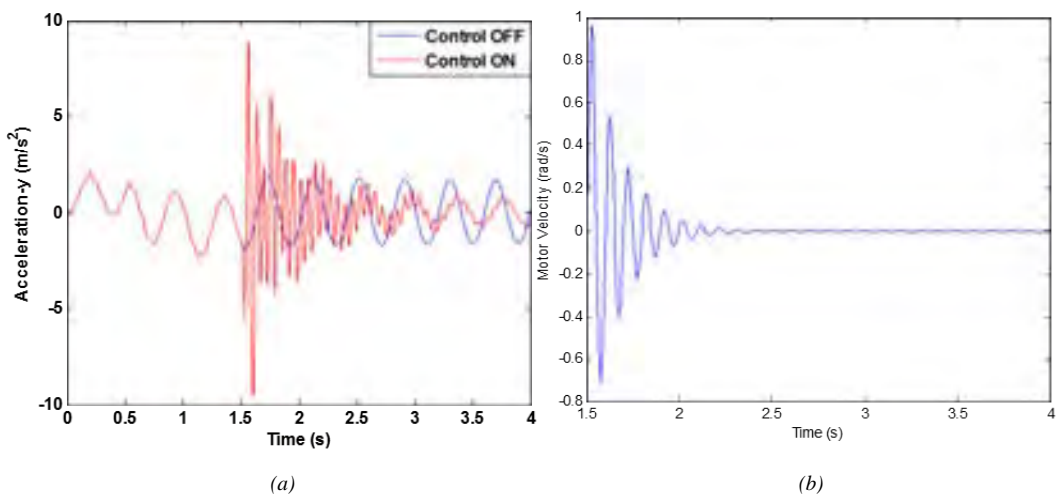


Figure 6. (a) Response spectrum of the end point, (b) exponential harmonic input ($\theta_0=1$ degree, $\omega_0=4f_1$, $a=-6$)

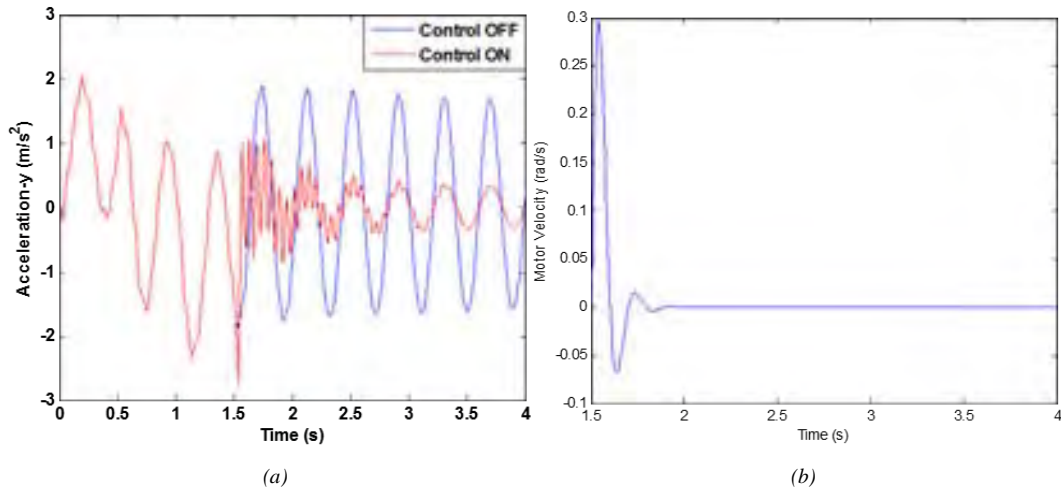


Figure 7. (a) Response spectrum of the end point, (b) exponential harmonic input ($\theta_0=1$ degree, $\omega_0=2f$, $a=-15$)

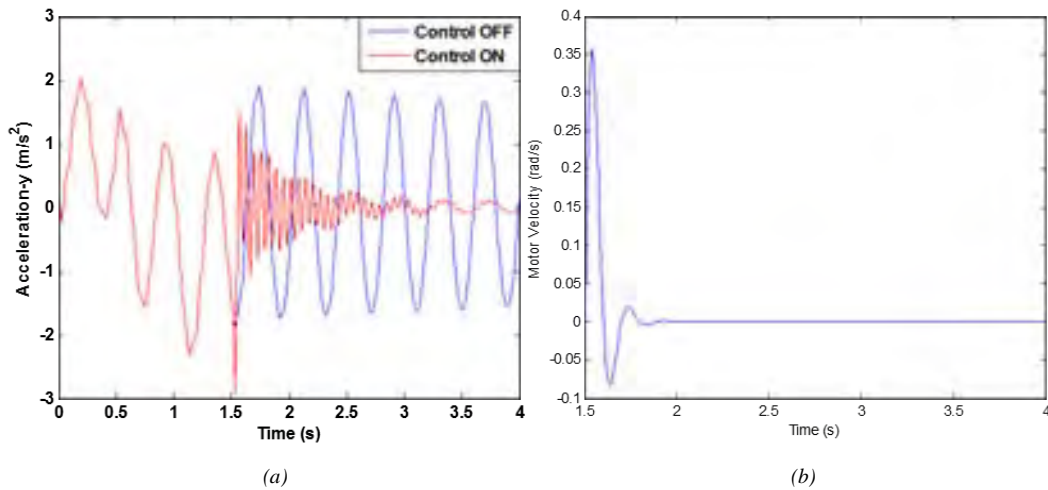


Figure 8. (a) Response spectrum of the end point, (b) exponential harmonic input ($\theta_0=1.2$ degree, $\omega_0=2f$, $a=-15$)

4. CONCLUSIONS

In this paper, vibration control of an onelink flexible manipulator with harmonic excitation is presented. The flexible beam is modeled in ANSYS. Modal analysis and transient analysis are used to determine natural frequencies of the system and to obtain the residual vibration after the motion. An arbitrary velocity profile is applied to the flexible beam and different exponential harmonic inputs are applied to suppress the residual vibration of the end point of the beam. The effect of the parameters of exponential harmonic input is analyzed and it was observed that exponential harmonic input parameters are important to suppress the residual vibration of the flexible beam.

ACKNOWLEDGEMENTS

We are grateful for the support of *International Conference on Engineering and Natural Science* for helping make this conference possible.

REFERENCES

- [1]. Alberts, T.E., et al., "Experiments in Optimal Control of a Flexible Arm with Passive Damping", Fifth VPISSU/AIAA Symposium on Dynamics and Control of Large Structures, Blacksburg, VA, 1985. Science. 1973, Boca Raton, FL: CRC Press, Inc., pp.1071.
- [2]. W. J. Book and S. Cetinkunt, "Near Optimal Control of Flexible Robot Arms on Fixed Paths," IEEE International Conference on Robotics and Automation, St. Louis, MO, 1985.

- [3]. R. H. Cannon and E. Schmitz, "Initial Experiments on the End-Point Control of a Flexible One Link Robot," *The International Journal of Robotics Research*, Vol. 3(No. 3), 1984.



- [4]. M. G. Hollars and R.H. Cannon, "Experiments on the End-Point Control of a Two-Link Robot with Elastic Drives," *Proceedings of the AIAA Guidance, Navigation and Control Conference*, Williamsburg, VA, pp. 19-27, August, 1986.
- [5]. J. L. Wiederrich and B. Roth, "Design of Low Vibration Cam Profiles," *Conference on Cams and Cam Mechanisms*, Liverpool, England, Vol. 1, 1974.
- [6]. N. C. Singer, "Residual Vibration Reduction in Computer Controlled Machines," *MIT Artificial Intelligence Lab Technical Report No. AITR-1030*, 1989.
- [7]. N. C. Singer and W.P. Seering, "Preshaping Command Inputs to Reduce System Vibration," *ASME Journal of Dynamic Systems, Measurement, and Control*, 112(March): pp. 76-82, 1990.
- [8]. W. Singhose, N. Singer, and W. Seering, "Design and Implementation of Time-Optimal Negative Input Shapers," *ASME Winter Annual Meeting*, Chicago, IL, 1994.
- [9]. J. F. Jansen, "Control and Analysis of a Single-Link Flexible Beam with Experimental Verification," *ORNLTM-12198*, Oak Ridge National Laboratory, 1992.
- [10]. D. P. Magee and W.J. Book, "Filtering Schilling Manipulator Commands to Prevent Flexible Structure Vibration," *American Control Conference*, Baltimore, MD, 1994.
- [11]. T. D. Tuttle and W.P. Seering, "Vibration Reduction in 0-g Using Input Shaping on the MIT Middeck Active Control Experiment," *American Control Conference*, Seattle, WA, 1995.
- [12]. W. T. Thomson and M. D. Dahleh, *Theory of Vibration with Applications*, 3rd edition. Englewood Cliffs: Prentice-Hall, 1988.

BIOGRAPHY

ŞahinYavuz was born in Izmir, Turkey in 1986. He received the B.E. and M.E. degrees from DokuzEylul University, Izmir, Turkey, in 2009 and 2012, respectively. Since 2010, he is a research assistant at DokuzEylul University and since 2012, he is pursuing his PhD. His main areas of research interest are robotic, vibration control, integrated softwares, PLC and servo applications.

THE EFFECT OF FIBRE CHARACTERISTICS ON THE BREAKING ELONGATION PROPERTIES OF COTTON SIROSPUN YARNS

Tuba Bedez ÜTE

*Ege University, Department of Textile Engineering, 35040, Bornova/İzmir, Turkey.
tuba.bede@ege.edu.tr*

Hüseyin KADOĞLU

*Ege University, Department of Textile Engineering, 35040, Bornova/İzmir, Turkey.
huseyin.kadoglu@ege.edu.tr*

Abstract

Among measurable yarn characteristics, yarn elongation has significant effect on weaving performance, particularly for high speed looms. However, it has not received much attention of researchers. Yarn elongation is affected by fibre properties and basic spinning parameters such as yarn twist and yarn count. This study has been performed to investigate the effects of cotton fibre characteristics and spinning process variables on the breaking elongation properties of 100% cotton sirospun yarns. Sirospun yarns were spun at Ege University, Textile Engineering Department under the same conditions from different cotton blends. Fibre properties were measured by AFIS Instrument and the breaking elongation of the sirospun yarns were measured by Tensorapid. Additionally, for prediction of yarn elongation, a statistical model has been developed with linear multiple regression method.

Keywords: *breaking elongation, cotton, estimation, fibre characteristics, sirospun yarns, prediction.*

1. INTRODUCTION

Main objectives of the spinners are keeping the process parameters under control via optimization of the production costs, machine settings, production rates etc. and meeting the customer demands. Therefore, analyzing the raw material characteristics, that represents the largest cost item, is very important. These approaches enhance the desired yarn quality and provide competitive advantages.

Physical and mechanical fiber parameters like length, tenacity, strain, fineness, maturity, stickiness, color, trash and nep content can be measured with modern instrumental methods on the basis of bundle or individual fiber measurements [1]. Advanced Fibre Information System (AFIS) is based on single fiber testing and used for controlling and optimizing the process parameters as well as predicting the produced yarn quality. [2].

Previous researches showed that, yarn properties are particularly influenced from fibre properties and this effect becomes more influential in the case of finer yarns. Among measurable yarn characteristics, yarn breaking elongation has significant effect on weaving and knitting performance, for the high-efficiency machines. However, it has not received much attention of researchers. Yarn elongation is affected by fibre properties and basic spinning parameters such as yarn twist and yarn count. Figure 1 shows the degree of influence of the fibre characteristics on the breaking force of ring-spun yarn [3].

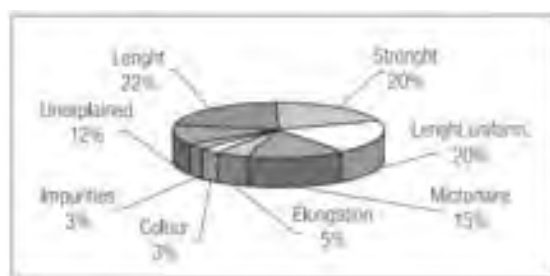


Figure 1. Dependence of ring spun yarn's breaking force on fibre characteristics.

Majumdar et al (2004), compared mathematical, statistical, and artificial neural network models for predicting the breaking elongation of ring spun cotton yarns. They used cotton fiber properties (fiber bundle tenacity, elongation, UHML, uniformity index, micronaire, reflectance degree, and yellowness), measured with HVI, as inputs. They have reported that the breaking elongation of cotton ring spun yarns is influenced by fiber properties, particularly, fiber elongation, fiber length uniformity and yellowness. They have found that ANN model's prediction performance is better than the statistical and mathematical models, respectively [4].

In another study, they have developed linear regression, artificial neural network and neuro-fuzzy models for prediction of the breaking elongation of rotor-spun yarns. Again they've used fiber properties measured with HVI and yarn count as predictors. They've find out that yarn count and cotton fibre fineness are the most efficient estimators, and, artificial neural network and neuro-fuzzy models' prediction accuracy is better than regression models [5].

Baykal et al, have used blend ratios and yarn count as independent variables in regression models to predict the strength and elongation properties of cotton/polyester blended rotor yarns. They've showed that breaking elongation values of the blended yarns are decreased with the increase of metric yarn count and decrease of polyester ratio in the blended yarn [6].

The breaking elongation and strength properties of spliced ring spun yarns were predicted with response surface methodology by using splicing parameters, fiber properties measured with HVI and yarn production properties as predictors. They've presented that fiber fineness, fiber length, short fiber index, fiber elongation, yarn count, yarn twist and opening air have significant effect on the breaking elongation of spliced yarns. [7].

The performance of neural network during the prediction of cotton ring spun yarn breaking elongation was investigated. It is reported that, yarn twist, yarn count, fiber elongation, length, length uniformity and spindle speed are the most influential factors for yarn breaking elongation [8].

As is seen from the literature survey, most of the studies on prediction of yarn properties were carried out for ring spun yarns. There are very few studies on prediction of yarn properties of sirospun yarns. This paper is a part of a work concerning the experimental research and determination of the equations and models for estimating the sirospun yarn quality characteristics from the yarn production parameters and cotton fiber properties which are measured by the HVI and AFIS systems. As a result, equations were derived for the prediction of yarn tenacity, breaking elongation, unevenness and hairiness by using fiber and yarn properties.

Some of the results are given in previous papers [9-12]. Regressional estimation of cotton sirospun yarn properties from fibre properties measured with HVI [10], regressional estimation of yarn hairiness of cotton sirospun yarns from AFIS fiber properties [11] and the prediction of yarn strength of cotton sirospun yarns from AFIS fiber properties by using linear regression analysis [12] were investigated previously.

2. EXPERIMENTAL

2.1. Materials

In this study, eleven different cotton blends were supplied from spinning mills in different regions of Turkey. In order to eliminate the effects of process parameters, fibre properties were measured from rovings by using an Advanced Fibre Information System (AFIS). The main test results of fibre properties are given in Table 1. B1 to B11 represents different blends.

Table 1. Fibre properties of different blends measured with AFIS.

	Fiber nep count per gram	Mean length by weight	Upper Quartile Length by weight	Short fibre content by weight	Mean length by number	Length variation by number	Short fibre content by number	5% Length by number-	Total trash count per gram*	Trash count per gram
	Nep Cnt/g	L(w) (mm)	UQL (w)	SFC (w) %	L(n) (mm)	L(n) %cv	SFC (n) %	5.0% (mm)	Total Cnt/g	Trash Cnt/g
B1	4	29,5	35,2	2,3	25,8	37,6	8,5	40,9	8	0
B2	19	28,1	33,9	3,7	24,2	40,3	11,6	39,9	11	0
B3	24	25	30,7	6,2	21,5	40,3	15,1	36,7	14	0
B4	8	30,3	36,6	2,4	26,4	38,9	9	42,4	7	0
B5	5	26,8	32	3,8	23	38,4	11,3	37,3	29	0
B6	7	27	32,6	4,6	23,3	40	13,2	38,2	16	0
B7	152	24,8	30,9	9,9	20,2	48,5	25,5	35,6	84	11
B8	12	26,1	31	3,7	22,9	37,8	11	36,1	5	0
B9	19	26,3	31,2	4,6	22,7	39,6	12,8	36,9	14	2
B10	25	28	33,9	3,9	24,3	39,2	11,4	39,1	9	0
B11	17	25,5	30,6	5,1	22,2	38,7	14,2	35	9	2

* dust particles included

2.2. Methods

Fibre properties measured by AFIS are predictive factors of our study. Yarn count, twist coefficient and strand spacing, which is defined as the distance between the two parallel roving strands fed through the drafting system, were also selected as predictors because of their significant effects on yarn properties. According to experimental design, it is planned to spun in four yarn counts (Ne 20, Ne 30, Ne 40 and Ne 50), at three twist multipliers (α_e 4, α_e 4,5 and α_e 5) and three strand spacing values (3, 6 and 9 mm), for each blend. Cotton sirospun yarns were produced on a Rieter Model G30 ring spinning machine by keeping the spinning conditions constant. Some samples cannot be produced because of the raw material quality and drafting limits of the machine. Experimental plan for each blend with yarn sample codes is given in Table 2.

Table 2. Experimental plan for one cotton blend and yarn sample code matrix.

Twist coefficient		α_e 4			α_e 4,5			α_e 5			
Strand spacing		3 mm	6 mm	9 mm	3 mm	6 mm	9 mm	3 mm	6 mm	9 mm	
B1	Yarn count	Ne 40	1	2	3	4	5	6	7	8	9
		Ne 30	10	11	12	13	14	15	16	17	18

Ne 20	19	20	21	22	23	24	25	26	27
Ne 50	28	29	30	31	32	33	34	35	36

Yarn sample codes

Subsequently the breaking elongation values of the yarns were measured with Uster Tensorapid. Final step is determining the equations and models for estimating the sirospun yarn breaking elongation from the yarn production parameters and cotton fiber properties which are measured by AFIS instrument. For this purpose, multivariate linear regression methods were performed. Statistical analyses were performed using Gretl (GNU Regression, Econometrics and Time-series Library) software.

3. RESULT AND DISCUSSION

Yarn strength and breaking elongation were measured with Uster Tensorapid. Breaking elongation values of the cotton sirospun yarns are given, all together in Figure 2.

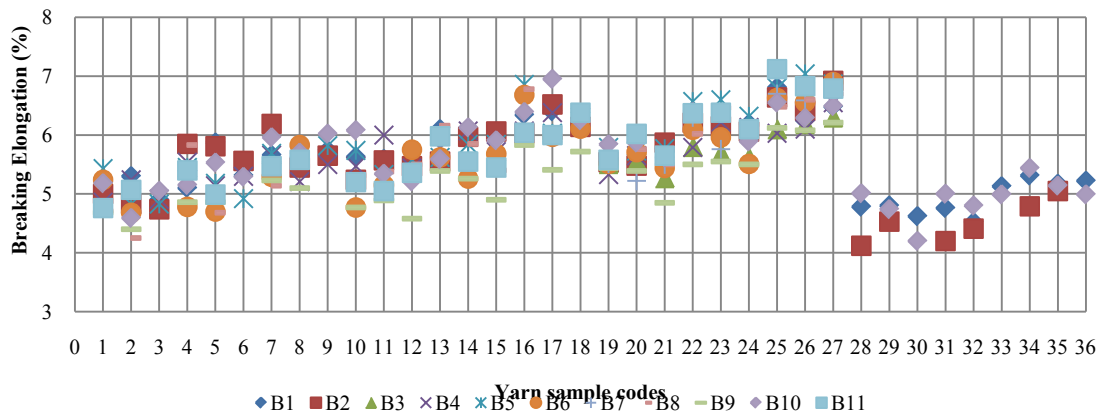


Figure 2. Breaking elongation values (%) of cotton sirospun yarns.

For some blends, some yarn types cannot be produced due to fibre quality, wide strand spacing and fine yarn counts. Experimental plan can be completely produced for only B1 and B10 blends. For this reason, comparison between the yarns of different linear density, different twist factor and strand spacing, for these blends is shown in Figure 3.

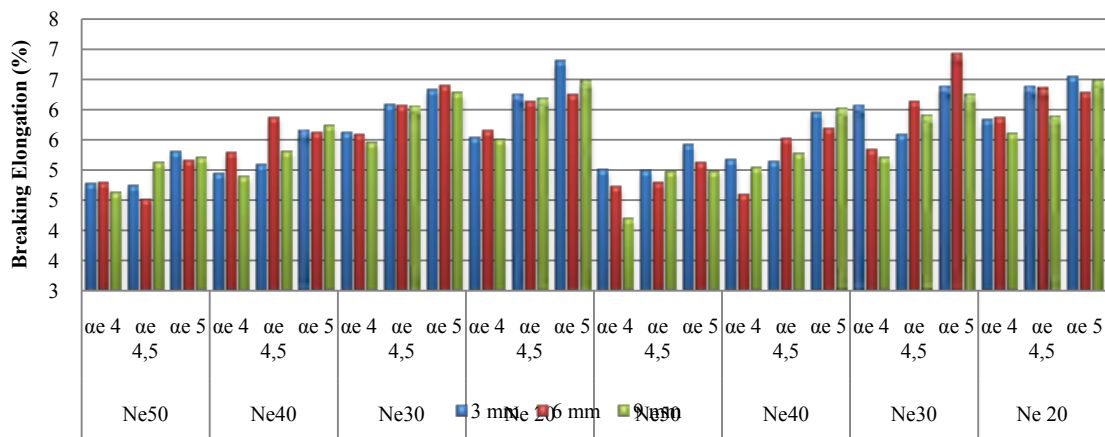


Figure 3. The breaking elongation values of the yarns of different linear density, different twist factor and strand spacing (for B1 and B10).

As is seen from the figure, breaking elongation increases with the increasing of twist coefficient and yarn thickness.

Regression analysis is used to investigate the relationships between parameters and to predict breaking elongation characteristics of the cotton sirospun yarns. The types of relationship between selected parameters and yarn breaking elongation values were checked by curve estimation and correlation analysis. The linear multiple linear regression and ordinary least-squares methods were selected depending on the to multiple factors and nearly linear relationship between fibre properties and yarn properties [13]. Based on the Pearson correlation coefficients, some of the independent variables were omitted due to high correlation with other variables. Weight based measurements have higher correlation with yarn breaking elongation, in brief fibre properties used for regression models were; nep /gr, L(w), SFC(w), UQL (w), total count, Trash count. Yarn count, twist coefficient and strand spacing were also chosen as independent variables. A linear relationship between fibre properties and yarn properties was found with the curve estimation and collinearity tests. Best Subsets regression and stepwise regression was used and heteroskedasticity is tested. In conclusion, an equation is developed for the prediction of breaking elongation of cotton sirospun yarns.

Yarn breaking elongation (%) = 17,087 + 0,011 Strand spacing - 0,033 Yarn count (Ne) + 0,758 α e - 1,744 Lw + 1,119 UQLw - 0,762 SFCw + 0,011 TotalCnt + 0,149 Trash Cnt	R² = 0.68	Adj. R² = 0.69
---	-----------------------------	----------------------------------

Regression coefficients of variables, t-values and significance level of each variable of the model are given in Table 3. Regression coefficients represent the rate of change of the yarn breaking elongation as a function of changes in the fibre properties and yarn parameters. Signs (+ or -) of regression coefficients of variables indicate the direction of influence.

Table 3. Regression coefficients, t-values and significance level of t-values of linear regression model for breaking elongation.

	Constant	Strand spacing (mm)	Yarn count (Ne)	Twist coefficient (α_e)	L_Wmm	UQLw	SFCw	TotalCnt	TrasgCnt
Coefficient	17.087	0.011	-0.035	0.758	-1.744	1.119	-0.762	0.011	0.149
Std. error	0.811	0.003	0.001	0.016	0.104	0.067	0.042	0.001	0.012
t-ratio	21.079	3.874	-43.315	46.519	-16.847	16.606	-18.014	11.689	12.376
Sig.	0.000*	0.000*	0.000*	0.000*	0.000*	0.000*	0.000*	0.000*	0.000*

*** is significant for $\alpha=0,01$.

All of the regression coefficients in the model are statistically significant. According to the equation, breaking elongation increases with the increase of yarn thickness, twist coefficient and strand spacing. Among fibre properties, fibre length is the most efficient estimator. As fibre length and short fibers content increase, breaking elongation decreases.

Figure 5 shows the scatter plot of predicted yarn unevenness values versus actual yarn unevenness values and regression line of the models. A high correlation ($r=0,95$) was found between actual and predicted values.

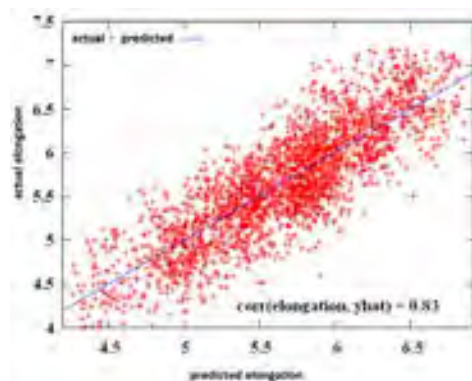


Figure 4. Predicted versus actual values of breaking elongation (%).

4. CONCLUSION

Even though the yarn elongation has significant effect on weaving and knitting performance, particularly for high speed machines, it has not received much attention of researchers. This study has been performed to investigate the effects of cotton fibre characteristics and spinning process variables on the breaking elongation properties of 100% cotton sirospun yarns. Eleven different cotton blends were supplied from different spinning mills. In order to eliminate the effects of process parameters, fibre properties were measured from rovings by using an Advanced Fibre Information System (AFIS). Cotton sirospun yarns were spun in four yarn counts (Ne 20, Ne 30, Ne 40 and Ne 50), at three twist multipliers (α 4, α 4,5 and α 5) and three strand spacing values (3, 6 and 9 mm) on a Rieter Model G30 ring spinning machine at Ege University, Textile Engineering Department, by keeping the spinning conditions constant. The breaking elongation of the sirospun yarns were measured by Uster Tensorapid. Additionally, for prediction of yarn elongation, a statistical model has been developed with linear multiple regression method. The goodness of fit statistics showed that the equation had a large coefficient of multiple determination (R^2) and adjusted R^2 values. According to the model, breaking elongation increases with the increase of yarn thickness, twist coefficient and strand spacing. Among fibre properties, fibre length is the most efficient estimator. As fibre length and short fibers content increase, breaking elongation decreases.

ACKNOWLEDGMENT

The authors express their thanks to the **Republic of Turkey, Ministry of Science, Industry and Technology and SÖKTAŞ**, which is a designer and producer of cotton and cotton blended fabrics, for supporting this research.

REFERENCES

- [1]. Frydrych, I., Matusiak, M. Challenges for Fiber Quality Measurement, https://www.icac.org/Meetings/Plenary/61cairo/documents/tis/frydrych_1.pdf
 - [2]. Uster AFIS Pro Brochures, www.uster.com, Uster Technologies, <http://www.uster.com/en/instruments/fiber-testing/uster-afis-pro/> (Date Accessed: July 2012)
 - [3]. Jackowski, T., Chylewska, B., Cyniak, D., Influence of the Spinning Process Parameters on Strength Characteristics of Cotton Yarns, *FIBRES & TEXTILES in Eastern Europe* July/September 2002
 - [4]. Majumdar K. and Majumdar A., 2004, Predicting the breaking elongation of ring spun cotton yarns using Mathematical, Statistical and Artificial Neural Network Models, *Textile Research Journal*, 74 (7): 652-655.
 - [5]. Majumdar A., Majumdar P. K. and Sarkar B., 2005, Application of linear regression, artificial neural network and neuro-fuzzy algorithms to predict the breaking elongation of rotor-spun yarns, *Indian Journal of Fibre & Textile Research*, 30: 19-25.
 - [6]. Baykal P.D. and Babaarslan O., Erol R., 2006, Prediction of strength and elongation properties of Cotton/Polyester- Blended OE rotor yarns, *FIBRES & TEXTILES in Eastern Europe*, 14, 1(55): 18-21.
 - [7]. Gürkan P., Özdi N., Taşkın C., Şenol M.F., "Farklı Harmanlardan Üretilen Pamuk İpliklerinde Uç Birleştirme Bölgesinin Mukavemet ve Uzama Özelliklerinin Tahminlenmesi", - *Tekstil ve Konfeksiyon*, Cilt 20, Sayı 2, 109-114.
 - [8]. Mwasiagi, J.I., Huang, X., Wang, X., 2008, Performance of neural network algorithms during the prediction of yarn breaking elongation, *Fibers and Polymers*, Volume 9, Issue 1, pp 80-86]
 - [9]. Bedez Ute T., Research On Spinning of Short Staple Fibres by Sirospun System, Ege University Graduate School of Natural and Applied Sciences, Master of Science Thesis, 2007.
 - [10]. Bedez Ute T., Kadoğlu H., 2014, Regression estimation of Cotton Sirospun Yarn Properties From Fibre properties, *AUTEX Research Journal*, Vol. 14, No:3, September 2014, p.161-167.
 - [11]. Bedez Ute T., Kadoğlu H., 2012, "Regression Estimation of Yarn Hairiness of Cotton Sirospun Yarns From Afis Fiber Properties", 6th International Textile, Clothing & Design Conference - Magic World of Textiles, October 07-10, Dubrovnik, Croatia.
 - [12]. Bedez Ute T., Kadoğlu H., 2012, "The Prediction of Yarn Strength of Cotton Sirospun Yarns From AFIS Fiber Properties By Using Linear Regression Analysis", The Inter-Regional Research Network On Cotton For The Mediterranean & Middle East Regions, November 05-07, Antalya.
 - [13]. Üreyen M.E. and Kadoğlu H., "Interactions between AFIS Fibre Properties and Ring Cotton Yarn Properties", *Tekstil ve Konfeksiyon*, 18 (1), p.8-14., 2008.
-

SLOPE STABILITY ANALYSIS METHOD OF ACCOUNT BACK AND EXAMINATION OF TEKKE LANDSLIDE WITH BACK ANALYSIS METHOD

Mümin FILIZ

Suleyman Demirel University, Isparta and 32000, Turkey.
mfiliz@tef.sdu.edu.tr

Semiha GÖKCAN

Bilecik Seyh Edebali University, Bilecik and 11000, Turkey.
semiha.gokcan@bilecik.edu.tr

Abstract

One of the methods used in slope stability analysis is the method of back accounts. In the method provides the detection of unknown parameters from the parameters are known. In this study, which is one of slope stability methods back calculation method by including information about the method applied Tekke Landslide was investigated. There are the characteristics of the soil profile among the factors that control the slope stability. In addition; there are additional loads can be located on the slope with topographic, geological, hydrological, climatic conditions and vibration forces. Ground material condition of Tekke Landslide on Antalya-Burdur highway were investigated and improvement works were carried out for path to enhance the existing standards. As a result of the assessment and accounts; the most appropriate solution is found to be the fore-piling applications for area available protect from landslides an increasing size. This situation has been deducted around the landslide area as to be properly drained. This situation was designed and implemented will not be allowed to the water inlets the bottom of the slope in landslide area.

Keywords: *Slope, Stability, Tekke Landslide*

1. INTRODUCTION

The loss due to the mass movements (landslides) in Turkey, because of which the number of the dead and premises is numerous, are of great significance. Champer movements cause to the champer corruptions on highways as well as constructional damage in urban areas and harvest losses in rural regions on account of rippled surface structure of our country. These movements might occur due to human acts however they might as well come out by themselves. The measurements to be applied for these movements in Turkey are practised by various ways, one of which is Back Measurement Method. This method provides to determine the way that the earth would conduct in future, and thus designate proper precautions to be taken.

On the highway between Antalya and Burdur, in Tekke passage, a landslide occured as a result of a stability problem due to the weakness of geological units and existence of underground water. For this reason on this route were drillings constructed in order to gain data for back measurement method to get a local betterment by means of geological-geotechnical studies. The data obtained from Tekke Landslide has been analysed through PLAXIS, an alaysisprgram with an ending element, and thus attempted to strenghten the earth to realize precautions not to have a future occurance of the same event.

2. EXPERIMENTAL

On the highway between Antalya and Burdur, in Tekke passage, a champer movement occured resulting in the deformity of existing quality of the highwa. The higway route is shown in Pic. 5.1. In order to meet the increasing traffic current due to the development of our country the Burdur-Antalya highway has been reconstrated by warm mixture method. In this betterment project the starting point is the existing champer movement and thus the reasons for the corruption is analysed. The surface parameters analysed and for that the scurity factor is taken as. By means of the usage od Back Measurement Method the model is applied in Plaxis program and parameters giving the slide condition are determied. These parameters are used in the betterment project applied later on.

Within these the studies, in order to determine the geometrics of t he landslide geological-geotechnical surveys are realized by means of several drilling applications on the highway between Antalya and Burdur, in Tekke passage. Several essential tests are applied then on the samples taken from these drillings, which are then used for geological and geotechnical mapping of the route. The findings are put into the usage for proper betterment process in case of a repetition of the landslide.

2.1. Materials

The place of 2.1.1. Landslide: Highway between Antalya and Burdur, Tekkekoy region.

The geology of 2.1.2. Survey Area: The structure of the land of the city area has a complex texture because of the combinations occured in various geological eras. Prior to the second geological era the region was within TETIS geocenklnal era, and through second, third and fouth eras the land have passed the Alpine orogeny having its shape today.

The formations commonly seen in the region belong to vairouspeoriodes of mesozoic and tesierpeirods. Quaternary storages take place in the lower areas of the region. (Figure. 1)



Figure 1. 1/25000 scale Geology Map of the project area and the environment

2.1.3. Tectonical Evolution

Burdur city and its environment is within 1st degree earthquake zone, and in the past century numerous earthquakes occurred, 11 of which were either medium or high level earthquakes. As a result because of the numerous deaths and loss of land premises people started to abandon the place, which then affected the economical and social life blocking the development of the whole area.

The city of Burdur is located over Burdur plate zone which is one of the most active plates in the West Anatolia. (Figure 2). Within the years of 1914, 1957 and 1971 various major earthquakes between the sizes of 6.1 – 7.1 occurred in the area. The distance of the underground water from the surface is of a great importance within the areas enjoying first degree earthquake risk because of the deflation of the surface.



Figure 2. The constructional map of the area

2.1.4. Geomorphology

The area has two parts geomorphologically, one of which is Burdur reservoir involving Burdur and Yarışlı Lakes, and the other is Tefenni reservoir in the southwest of Burdur reservoir between Karamanlı-Tefenni and Kemer. These young reservoirs which occurred in different durations in lengths and developments connect with a passage.

2.1.5. Seismicity

According to the data obtained from “Turkey Earthquake Regions Map” studied by T.C. Bayındırlık ve İskan Bakanlığı (Ministry of Public Settlements) the project area is in a first degree earthquake area. The horizontal earthquake acceleration to be used in slope stability analysis is to be taken as $a_h \approx 0.2 g$.

2.1.6. Land Studies

As a result of drilling applications organized by Highways 13. Region, on the highway between Antalya and Burdur, in Tekke passage, a landslide occurred as a result of a stability problem due to the weakness of geological units and existence of underground water. For this reason on this route were drillings constructed in order to gain data for back measurement method to get a local betterment by means of geological-geotechnical studies. As a consequence of these results the structure of the ground is Silty sand and Clay sand, and this info is then used in the designs.

The sieve analysis results in accordance with the samples obtained from the drillings: The percentage majority of the ground particles goes through sieve 200, and for this reason Atterberg Limits tests are required.

Atterberg Limits tests results for the drillings samples taken from the area involved in the reports are;

Liquid Limit LL (%)=31-44

Plastic Limit PL (%)= 15-17

Plasticity Index PI (%)= 15,5-27,5

Natural Water content between (%): 10-11

Table 1. Tekke Landslide area Laboratory test results

TEST RESULT TABLE											
SAMPLE			Atterberg Limits				Sieve Analysis Over %				USCS Ground Class
Drill No	Depth (m)	Sample No	Wa (%)	LL	PL	PI	4 %	10 %	40 %	200 %	
SK-5	9,00-9,07	SPT-6	6,8		N-P		52,0	39,5	24,5	3,2	SP
SK-5	10,50-10,95	SPT-7	19,0	36,3	15,2	21,1	72,5	66,9	55,2	40,0	SC
SK-5	13,50-13,67	SPT-9	9,4	43,7	16,2	27,5	75,5	72,3	61,7	47,8	SC
SK-6	1,50-1,95	SPT-1	7,4		N-P		61,7	51,8	39,2	18,6	SM
SK-6	4,50-4,85	SPT-3	12,0		N-P		76,1	62,5	38,3	23,0	SM
SK-6	9,00-9,28	SPT-6	4,2		N-P		69,8	59,1	45,0	20,9	SM
SK-6	15,00-15,35	SPT-10	10,9	31,8	16,1	15,7	62,1	54,4	45,0	35,1	SC
SK-6	19,50-19,60	SPT-13	13,3		N-P		63,2	49,5	32,4	12,1	SM
SK-7	4,50-4,70	SPT-3	11,2	37,3	17,0	20,3	97,0	88,7	65,4	46,3	SC
SK-7	10,50-10,60	SPT-7	9,5		N-P		65,3	54,3	44,1	25,5	SM

Table 1. Drilling list

No	Drill No	Depth (m)	YASS. (m)
1	SK-5	34,00	-
2	SK-6	30,00	15,50m
3	SK-7	20,00	-

2.1.7. Research area geology and Tekke Landslide size

During the construction of the existing highway Dutluderelimestones located in a massive and steep slope on the right handside (TRjd) are constructed with mixed filling and some part of the way with filling (Qm). The reason why there is a noncontinuous surface between the old slope (Qc) and the filling is that the cullival (Qc) and Kızılcadağmelange and contact of the filling are not constructed in a squeezed way from the bottom towards the top along with its high and steep slope structure.

Besides there is a water canal taken from the small river running towards Tekke village in 1050-1053 elevages, which goes through the landslide area (probably in the area of the filling before the land slide). This water canal is still running without coating and control through the landslide. Some part of the canal disappears in the landslide. It is thought that this canal weakens the filling and activates the landslide. Moreover the rainfalls leak through the filling+cullivion-surface contact which results in a noncontinuous surface. This, with the addition of gravity creates stability problem. In addition the the upper parts of melanges (Kkzm) in the basis are very weak-non durable, a lot-totally seperated, fragmental and in the form of clay.

In the skirts of the landslide area is a retaining wall constructed before. The wall itself and the dilatations have lost their stability due to openings towards outside and drawdowns, which depend on two reasons:

First; the wall cannot bear the filling on top of it. Second; the leaking water at the base charges the grounds. Consequently, Tekke landslide; is a filling landslide with 70 metres in width, and 80-90 metres in length. All told 3 drillings (SK-5, SK-6 and SK-7 drillings) have been applied in the area. In accordance with the drillings the section of the landslide area is shown in Figure. 3

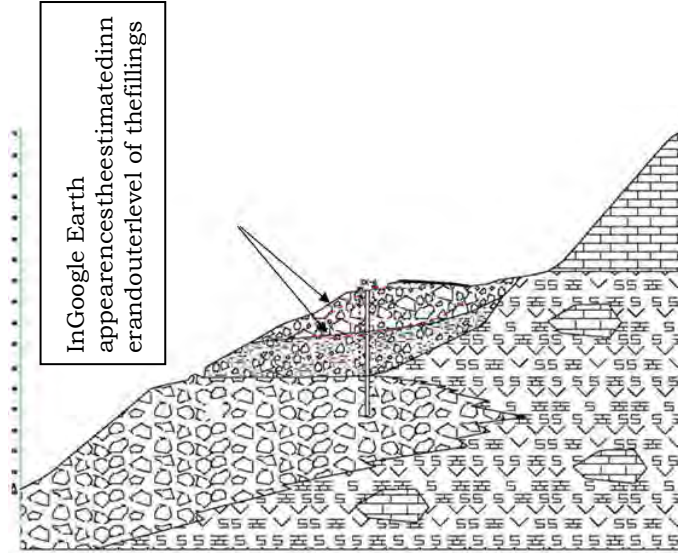


Figure 3. landslide zone section

2.1.8. The Susceptibility of the units against water

When the permeability of the units are taken into consideration the existing way fillings is constructed with sand, blocked pebbles and blocks which are permeable, and colluvials, depending on the pebbles and clay they involve, are permeable and half permeable. The Recrystallized limestones involved in Dutderelimestones (TRjd) and conglomerate and limestone blocks in Kızılcadağ melange (Kkzm) are half permeable and impermeable depending on the leaks and gaps within themselves.

3. GEOMETRICAL PROJECTS

The target of this project studies is to find a permanent solution for the landslides occurred in Turkey Antalya-Burdur Highway km 99+200. In order to have an idea of the occurrence and mechanism of the landslides for the mentioned solution analysis in the land of the occurrence has been done along with several detailed geological and geotechnical researches have been applied concerning the landslide area. In accordance with these studies the tests and assumptions determined some geotechnical parameters which are then used in designing. Google earth provided the existing and past chamber and highways conditions. This data provided useful info for the design of the landslide along with what kind of stability problems might occur in future.

As a result of the evaluations, the way to protect the existing Antalya-Burdur highway in part 99+200 from a bigger landslide is the fore-pile application. While analysing fore-piles the method used is basic ground mechanics principals. PLAXIS program is for the design. The concrete design of the Fore-piles is applied/resulted according to the The principals of design and Constructions of Concrete Structures (TS500) along with the regulations for the structures to be constructed in disaster areas.

Besides various suggestions have been taken into consideration in order to support the fore-piles and to decrease the amount of the load likely to come on the fore-piles.

3.1. The conditions of the environment during the landslide

Tekke landslide occurred in Burdur-Antalya highway KM: 99+200. As it can be seen from the photographs and the section of the landslide chamber slope is about 30 degrees (Figure. 4). The chamber angles that have

slided and settled on the filling are below 30 degrees. In the geotechnical department these materials have been named as colluvial and way fillings. The angle of the chamfer slopes from the wall that has moved towards the valley grounds go until 35 degrees. This material has been defined as Bresh. On the other side of the highway there is a steep drop-off with 40-45 degrees structured with limestone (Figure.5). The existing chamfer slopes provides useful data about the endurance of the material.



Figure 4. The Landslide and the deformations



Figure5. The steep drop-off on the other side of the landslide

The satellite photographs of the landslide provides important ideas about the shape and the reasons of the landslide. In the photo in year 2003 (Figure 6) we understand that the highway has three lines and there is a landslide in the 15-20 mt of the chamfer towards the valley grounds moving the fillings. In the photograph that belongs to year 2006 (Figure 7) we see that the part that slided has been repaired with a 30 degree filling. The 2010 (Figure8) photograph shows we can see that the repaired filling slipped. In Figure11 the the borders of the estimated filling is shown with red lines. Upon analysing the photographs we can clearly see that the 2-3 mt high wall underneath the chamfer has started to lose its stability in the 2003 landslide. When comparing 2006 and 2010 photographs the filling and the wall side of the filling has moved clearly. All these datas indicate that the sliding mechanism occurred in complex (mix) surface.



Figure 6.The satellite photo of the landslide in 2003.



Figure 7. The satellite photo of the landslide in 2006.



Photo 8. The satellite photo of the landslide in 2010.

4. BACK ACCOUNT ANALYSIS

The analysis of Tekke Landslide has been realized by PLAXIS, a program with elements with ends. The model of element with ends is shown in Figure 9. The highway is represented with a 10kPa regular spread load.

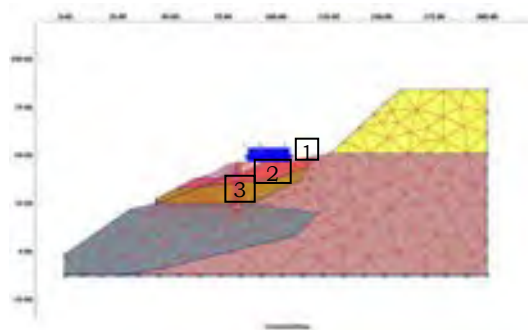


Figure 9. The realized PLAXIS model

According to the observations of the landslide area and the laboratory experiment results analysis has been resulted and the model slide surface of the landslide and the shape of the slide has been drawn. (Figure 10). Table 5.11 shows that the landslide is 60 m long. Accordingly the simplest solution to protect the highway from a growing landslide was to locate piles that are connected with bent cap method 15 m behind the beginning of the landslide. The piling application has been determined in the duration of construction.

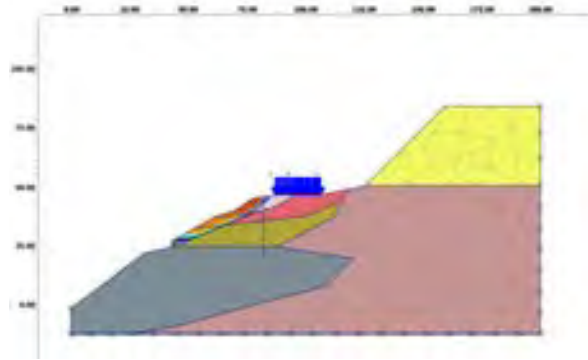


Figure 10. The existing material parameters along with a probable landslide situation in the area



Figure 11. The size of the landslide

The Material parameters used in analysis are shown in Table 3.

Table 3. Material parameters used in analysis

ID	Name	Type	γ_{unsat} [kN/m ³]	γ_{sat} [kN/m ³]	k_x [m/day]	k_y [m/day]	u [-]	E_{ref} [kN/m ²]	C_{ref} [kN/m ²]	Φ (°)	Ψ (°)	E_{incr} [kN/m ³]	C_{incr} [kN/m ³]	γ_{ref} [m]	τ - Strength [kN/m ²]	R_{inter} [-]
1	RoadFilling	Dranied	19.0	19.0	0.0000	0.0000	0.30	35000.0	4.0	27.00	0.00	0.0	0.0	0.00	0.0	0.60
2	RoadFilling	Dranied	19.0	19.0	0.0000	0.0000	0.30	40000.0	4.0	28.00	0.00	0.0	0.0	0.01	1E10	0.65
3	Colluvial	Dranied	19.0	19.0	0.0000	0.0000	0.30	45000.0	4.0	29.00	0.00	0.0	0.0	0.00	0.0	0.70
4	Bres	Dranied	22.0	22.0	0.0000	0.0000	0.30	2E5	100.0	37.00	0.00	0.0	0.0	0.01	100	0.90
5	Melange	Dranied	22.0	22.0	0.0000	0.0000	0.30	3E5	250.0	38.00	0.00	0.0	0.0	0.05	50	0.90
6	Limestone	Dranied	22.0	22.0	0.0000	0.0000	0.30	4E5	350.0	40.00	0.00	0.0	0.0	0.05	500	0.90
7	Wall	Dranied	24.0	24.0	0.0000	0.0000	0.20	2.8E7	5E3	55.00	0.00	0.0	0.0	0.02	2000	1.00

The 80 cm fore-Piles have been designed to socket to the strong Brash layer by 3 mts, 1 mt away from center to center all told 25 mts in length. When measuring the piles 3 loading methods have been used.

The situation of the filling conducted in 2006 that lost all its passive endurance by sliding totally (Table 2)

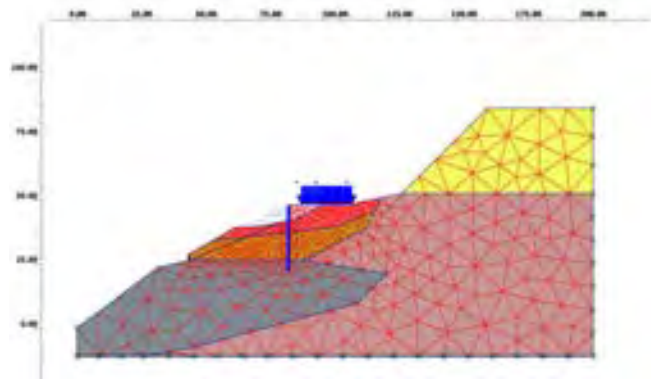


Table 12. First loading situation

The situation of the wall under the chamfer that loses its endurance and falls down (Table13)

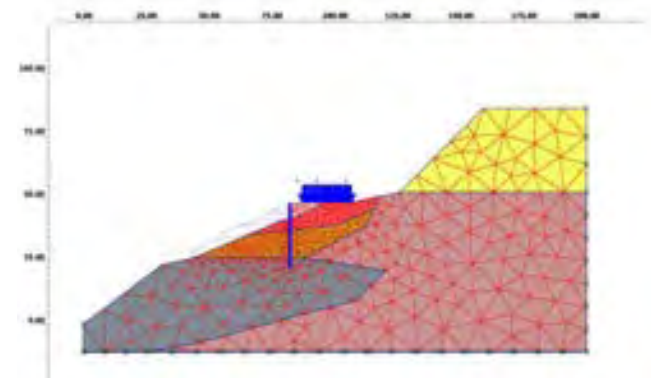


Table 13. Second loading situation

Earthquake situation (horizontal earthquake acceleration taken as 0.2g)

5. Concrete Calculations

The section effect currency obtained from analysis and the currency used in the design are shown in Table 4. The design values for 1st and 2nd situations have been enlarged by 1.6 factor and the design has been realized, and for the earthquake situation the currencies are taken the way they are.

Table 4. The currency used analysis results and Fore-pile design










	Analysis Results		
	N (kN/m)	V(kN/m)	M (kN.m/m)
1. Situation	83	89	290
2. Situation	63	91	335
3. Situation	148	154	364

	Currencies Used in Design		
	N (kN/m)	V(kN/m)	M (kN.m/m)
1. Situation	132,8	142,4	464
2. Situation	100,8	145,6	536
3. Situation	148	154	364

The concrete design of fore-piles are constructed by taking The Rules of Construction and Design of Concrete Structures (TS500) and The Regulations for Structures to be Built in Disaster Areas into consideration by the Administration of 13. Region.

The analysis results conducted in PLAXIS program are as below:

The factor for 1.And 2.Situations is designed as 1.6 in order to keep the situations safe and for the 3. Situation, the earthquake situation, the currencies remain the same.

1.Situation PLAXIS results	 <p>AxialStrength Diagram</p>	 <p>DiscontinuationStrength Diagram</p>	 <p>Moment Diagram</p>
2.Situation PLAXIS results	 <p>AxialStrength Diagram</p>	 <p>DiscontinuationStrength Diagram</p>	 <p>Moment Diagram</p>
3.Situation PLAXIS results	 <p>AxialStrength Diagram</p>	 <p>DiscontinuationStrength Diagram</p>	 <p>Moment Diagram</p>

Fore Pile Concrete Analysis Results (The existing factors of fore-piles and beams applied in the landslide area)

Discontinual Outfit Calculation

CALCULATIONS

Pile Diameter	800 mm
Clear Concrete Cover	75 mm
Concrete Class	C20
Shear Reinforcement Steel Grade	S420
Longitudinal Reinforcement	Ø25
Shear Reinforcement	Ø8
V_x (kN)	150

INPUT

V_{red} (kN)	160.227
V_{ed} (kN)	380.7627

If $V_{red} < V_d$ increase pile diameter
If $V_d > V_{red}$ we need to calculate shear reinforcement, use minimum shear reinforcement and maximum steel usage

s_{min}	143.4 mm
-----------	----------

check if $s_{min} > d$ and use $s = d$ if $s > 3 \times d$, use envelope SMA, LDF

s_{max}	143.4 mm
-----------	----------

OUTPUT

USE 125 mm

SHEAR REINFORCEMENT DESIGN FOR PILES

Pile Diameter, d	800 mm
Clear Concrete Cover, c_c	75 mm
Concrete Class	C20
Shear Reinforcement Steel Grade	S420
Longitudinal Reinforcement	Ø25
Shear Reinforcement	Ø8
Design Shear Force, V_x (kN/pile)	150

INPUT

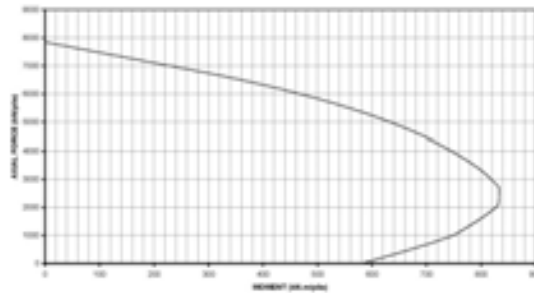
USE Ø8 @ 125 AS SHEAR REINFORCEMENT

Lengthwise outfit Calculation

MOMENT INTERACTION DIAGRAM FOR PILE REINFORCEMENT DESIGN

pile diameter	=	800 mm	concrete grade	=	C20
Ø long. reinforcement	=	25 mm	Ø spiral	=	8 mm
# of reinforcement	=	12	clear concrete cover	=	75 mm
steel grade	=	S420			
steel ratio	=	0.0117	dist. from axis of long. reinf. to top conc. fiber	=	95 mm

INTERACTION DIAGRAM FOR CIRCULAR PILES D=800mm WITH 12Ø25



Caping Beam Calculation

KAZIK BAŞLIK KIRIŞI HESABI

Donatı Hesabı (TS 500)

Malzeme : B5 20 . S 420

$f_{td} = 365 \text{ MPa}$ $f_{td} = 365 \text{ MPa}$

Kiriş boyutları :

$f_{td} = 13.33 \text{ MPa}$

$f_{td} = 1.07 \text{ MPa}$

$b_w = 1000 \text{ mm}$, $h = 1000 \text{ mm}$, paspayı = 75 mm , $d = 925 \text{ mm}$

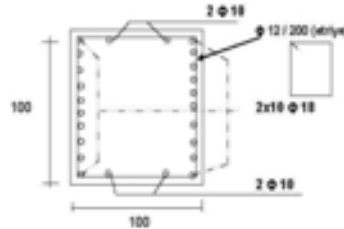
$A_{s,req} = 0.87 f_{td} / f_{td} \cdot b_w \cdot d = 2163.2 \text{ mm}^2 \rightarrow 10 \phi 18 \text{ (iç, dış)}$

Malzeme : B5 20 . S 420

$s = 200 \text{ mm}$ için

minimum etriye :

$A_s = 0.30 / 2 \cdot b_w \cdot s \cdot f_{td} / f_{td} = 87.70 \text{ mm}^2 \rightarrow \phi 12 / 200 \text{ (etriye)}$



6. RESULTS

We determine the conditions in case of a chamfer reconstruction and an appropriate model for chamfer now. Thus upon applying a model, the way to determine an unknown parameter is to enter the known parameters and get a result through it. The back calculation method is one of the most effective methods in our country where it contributes a great deal to complete the betterment projects economically and safely in chamfer conditions in which a landslide occurred. Also PLAXIS program for which the method make use practically and safely has been a source to apply within this study. PLAXIS program indicates the geometrical model that it creates within itself appropriate to the real condition in a detailed way.

To be able to examine the landslide occurred on Antalya-Burdur highway in 99+200 and to make use of the highway safely the problem has been approached in a safe way by means of Back Calculation method. Accordingly the area has been examined for several ways like geological, geotechnical and for earthquakes. The geological units determined in the landslide area; Existing road filling (Qm), Cullivion (Qc), Recriticalized Limestone Dutdere limestone (TRjd), Serpantit, Limestone and KızılcadagMelange and Olistostrom that constitute Conglomerates (Kkzm). The Tekke landslide is within the 1st degree earthquake zone in Turkey Earthquake Map (1996). Three drills the depth of which vary between 20-30 mt were organized in the area to examine the existing landslide mechanism. As a result of the laboratory examinations and analysis of the samples taken from the drills along with the studies and the examinations applied in the landslide area, the data that determined the size and type of the landslide has been modelled by means of PLAXIS program. This model has been subject to certain loads within parameters. Upon entering the loads 3 different situations have been defined and these situations have been then analysed. The 1st situation is that the filling applied in 2006 loses its passive endurance by sliding totally, the 2nd is the situation that the wall underneath the chamfer loses its endurance and falls down and the 3rd situation is where the loads applied by taking the horizontal earthquake acceleration 0.2 g. As a result of the analysis for 1st and 2nd situations the N, V, M values are close, and for 3rd situation the value is pretty high. The reason for this is tension created by a probable earthquake situation. The values obtained in the designing process according to the results: For 1st and 2nd situations the 1.6 factor is multiplied and obtained, and the 3rd (earthquake situation) is kept the same. All these standards and the concrete design of the Fore-piles are applied/resulted according to the The principals of design and Constructions of Concrete Structures (TS500) along with the regulations for the structures to be constructed in disaster areas.

The position of the landslide is exactly in 99+175-99+235 km which is determined along with the studies conducted with Higways 15. Region Administration. In order not to give damage during the deep foundation diggings the fore piling system which is one of the chamfer supporting systems has been conducted. Fore piling system presents a high safety preference depending on the depth of the digging, the conditions of the ground and surcharge (environmental) loads as well as economical solutions. Accordingly in order to prevent the landslides in the area the 80 cm fore-Piles have been designed to socket to the strong Brash layer by 3 mts, 1 mt away from center to center all told 25 mts in length. When measuring the piles 3 loading methods have been used. In addition the simplest solution to protect the highway from a growing landslide was to locate piles that are connected with bent cap method 15 mts behind the beginning of the landslide. The piling application has been determined in the duration of construction. The application cot was determined in the duration of construction. The concrete used in the piles is Concrete C20, Steel S420 class, ϕ 25iron, and in the entries ϕ 8 iron in addition of spacer 75 mm distance has been left. The concrete used in the beams is Concrete C20, Steel S420 class, ϕ 25iron, and in the entries ϕ 8 iron in addition of spacer 75 mm distance has been left. In beam connection ϕ 25 iron is used and the links are determined as ϕ 8. The link slope is in 1000x1000 mm measurements. In addition to the fore piling applications for strengthening the broken chamfer some precautions are also planned for the water that has an accelerating effect for the landslides. The surrounding area of the landslide has been drained properly and the leaking parts underneath the chamfer have been blocked. In order not to have any repetitions of some identical problems several precautions have been taken. As a result of this study we understand how important it is to take precautions for such occasions like preventing from the landslides because of the rough topographical structure of our country and as well as our country being in the earthquake zone. The factors causing landslides (e.g. slope, rain, type of land, gravity, various natural disasters, various construction activities etc.) according to the place of the region and the condition of it should be analysed, examined and determined one by one, and studies and examinations should be done in order to prevent the repetitions of the same events. In addition to this

Necessary precautions should be taken. The experiments applied and conducted in labrotary and in the land represent the limited part of the region. Also the analysis that the back calculation method provides us indicates more precise data of the section edurence information. Within the application of back calculating method which is applied through the geotechnical data in such occasions, the usage of PLAXIS program (Ended Elements Method) reveals that the betterment of sliding chamfers might as well be provided in a short time.

ACKNOWLEDGMENT

I hereby present my deepest appreciations to 13. Region Highway Administration staff and Civil Engineer Suat Erol.

REFERENCES

- [1]. Akçakal, Ö., A Case Study By Using Back-Calculation Method In Slope Stability Analysis, Istanbul Technical University, Institute of Science, M.Sc., 85S, Istanbul. 2009.
 - [2]. Durgunoğlu, H. T., Kulaç F., Karadayılar T. veBaştürk, G., 1990. Back calculation method in the stability of the soil behavior: BuğrularEtut, İstanbul.
 - [3]. Mining Technical Exploration 100 000'lik Geological Map of Antalya. <http://www.mta.gov.tr/v2.0/daire-baskanliklari/jed/index.php?id=100cd>
 - [4]. Yıldız, L. (2005). Bearing Capacity Of Shallow Foundation OnGeogrid – Reinforced Slope, Department of Civil EngineeringInstitute Of Natural And Applied SciencesUniversity Of Çukurova
 - [5]. About Construction in Disaster Zones Regulations, 1998. The Ministry of Public Works and Settlement, Ankara.<http://www.mevzuat.gov.tr/metin.aspx?Mevzuatkod=7.5.11445&sourcexmlsearch=&mevzuatilistat=0>
-

AN INVESTIGATION OF THE EFFECTS OF ADDITIVE TYPE AND AMOUNT ON MORTAR PHASE

Osman ÜNAL

AfyonKocatepeUniversity, Department of Civil Engineering, 03200, Afyonkarahisar, Turkey.
unal@aku.edu.tr

Kadir AKYÜZ

Kolsan A.Ş., Ankara, Turkey,
k.akyuz@yandex.com.tr

Kadir GÜÇLÜER

Corresponding author:Adiyaman University, Vocational School of Technical Science, 02340, Adiyaman, Turkey,
kgucluer@hotmail.com

Abstract

In concrete production the use of chemical and mineral contribution today is increasing rapidly in order to improve of strength, durability and viscosity properties. In this respect, in this study it is investigated that the effect on strength and viscosity properties of used mineral and chemical additive in normal mortar. Thus, both the fresh and hardened properties of a worksheet that provides surveys were conducted. As aggregate 0-2 mm grain size of crushed sand, binding as CEM I 42.5 R cement used in the mortar mixture which three different chemical additives with fly ash mineral additive used. Water / Cement ratio of 0.5 and the amount of binder 500 kg / m³ in the mixture taken as constant, chemical contribution rate must be selected as %0.5 to %1 and %1.5, fly ash %10 in rates has been substituted with cement. Viscosity of the the mortar was measured to determine the workability and consistencies characteristics. In general, the angular speed increases in viscosity of mortar is reduced and chemical additives mortars viscosity values higher than spending out of control mortars. By making 28 day compressive and bending tests for mechanical properties have been determined amount and type of additives on properties of the mortar. As a result, the mortar will be produced at different temperatures effect of super plasticizer additive for chemical additives both fluidity and strength according to the score from the other additives has been given to the most appropriate

Keywords: *Viscosity of Mortar, Chemical Additives, Fly Ash, Crush Sand.*

1. INTRODUCTION

Concrete is known as a construction material that is produced by the mixture of aggregates of mineral essence such as sand, gravel or crushed stone, which make up 70% of its total volume, together with water and cement and some chemical or mineral admixtures when needed; it has a plastic consistency at the beginning, but solidifies and gains strength over time through the hydration of the cement. Today, it can be observed that there is an increase in the consumption of ready-mixed concrete in the construction industry as a result of rapid constructions. It is inevitable for a material, which is so widely used, not to display an improvement parallel to technology. Concrete, which used to be made up of only those ingredients as water, cement and aggregates, has gained several favorable features through the addition of chemical and mineral admixtures into its composition. It has become almost impossible for the modern concrete technology of our day to produce concrete without employing chemical or mineral admixtures. (Felekoğlu et al., 2004).

The types of mineral admixtures used in concrete are fly ash, blast furnace slag and silica fume. Although these materials do not display a cementitious feature on their own, they might gain a binding feature when used together with cement. Thus, they can fill in the macro-gaps microstructure and affect some qualities of the concrete, such as its compressive strength or fluidity positively. Fly ash is a type of artificial pozzolana, which is a by-product having pozzolanic properties derived by burning pulverized coal in coal-fired power plants (Güçlüer and Ünal, 2010).

Fly ash is a valuable concrete admixture of pozzolanic quality which affects many features of the concrete positively. Owing to its global structure, it improves the workability of the concrete, reduces bleeding (surface water) of fresh concrete, contributes to long-term strength of the concrete, decreases its permeability and increases its resistance to internal and external abrasion (Yiğiter et al. 2004).

Rheological properties of cement paste are the critical performance values for its slump value, consistency and workability. The reology of cement paste is affected by the proportion of the mixture and characteristics of materials, the water-cement proportion, admixture of cement and thinness of powder material. Those changes mentioned may or may not lead to provide advantages (Bentz et al, 2012). That's why, the reology of cement paste can be affected by several variables (Turk, 2012).

Viscosity, on the other hand, is the measurement of the resistance which a fluid shows against deformation under surface tension. It can also be defined as the internal resistance of the fluid against flowing. All of the real fluids, except superfluids, resist surface tension. However, a fluid that does not resist surface tension is called 'ideal fluid'. Viscosity is independent from pressure and increases in parallel with temperature (Internet Source 1).

Reology of concrete of higher fluidity can be explained by the yield point describing its behavior and plastic viscosity parameters. The strength required for the concrete to be triggered is defined as yield point, and the resistance it puts against flowing under external tensions is called plastic viscosity (Karataş et al., 2010).

Concrete which has a high yield point is harsh and resistant to movement, whereas one having a high viscosity is flowable, yet very slow in movement. If the plastic viscosity is very low, it is rather flowable; however, it is quite difficult to keep together the cement and sand particles in the suspension and concrete is prone to severe dissolution and bleeding (Karataş et al., 2010).

Yazıcı Ş. (2003), stated in his study that super plasticizer admixtures increased workability and at the same time could cause the water amount in the mixture to decrease, and thus, would contribute to increase the compressive strength. Chemical components of the cement type and their features are the most important parameters affecting the performance of plasticizers. Different mortar samples produced in different proportions and with various cement types and plasticizer admixtures differ in their rheological behaviors (Golazewski and Szwabowski, 2004).

In their experimental study, Subaşı et al. (2008) increased the amount of fly ash gradually and reached conclusions based on compressive strength, through evaluating the physical qualities of wet mixtures, such as setting time and slump value and mechanical qualities of harsh mixtures. According to the results, setting time of the sample with 5% fly ash addition was observed to decrease, whereas for the ones with 10%-20% and 30% fly ash addition, the setting time increased. Compressive strength of samples was found to decrease with the increase in fly ash.

Montes et al.,(2013), produced cement pastes with 10%-30% and 50% limestone and fly ash admixtures and employed plasticizers of melamine-naphthaline-polycarboxylate base in the mixtures in their study. As a result, they indicate an increase in the efficacy of the plasticizers owing to the mineral admixtures they added.

For a fresh concrete mixture to have a self-compacting property, it needs to have low threshold shear stress and optimum viscosity. Viscosity is the measurement of the resistance which a fluid shows against deformation under surface tension. Increase in viscosity is important as it prevents segregation. (Açıkgenç et al. 2013).

In this study, the aim is to determine the effects of the mortars produced by addition of chemical admixtures like super plasticizer, air entraining and retarder admixtures and by binding cement with a 10% fly ash substitute, on viscosity features and strength.

2. EXPERIMENTAL

This study investigates the effects of chemical admixture usage upon strength and viscosity features of fresh and hardened mortars. During the study, cement and fly ash were used as binding materials and crushed sand of 0-2mm grain size as aggregate, and three different kinds of chemicals were added in order to provide workability.

2.1. Materials

In mortar mixtures, CEM I-42.5/R type Portland cement in conformity to TS EN 197-1 standard was fixed at 500 kg/m³ as the binding material TS EN 197-1/A3 (2008). Specific gravity of the cement is 3,07 and total alkali content is 65%. Fly ash was supplied by KütahyaTunçbilek thermal plant and the chemical and physical properties of the cement and fly ash are shown in Table 1. 10% of the cement was substituted by fly ash in mixtures except the control mixture.

Table 1. Properties of the cement and fly ash

Component, %	Fly Ash	Cement
CaO	6.66	63.6
SiO ₂	47.4	16.6
Al ₂ O ₃	19.8	4.72
Fe ₂ O ₃	11.8	3.27
S+A+F	79.0	-
MgO	4.76	1.91
Na ₂ O	0.57	0.34
K ₂ O	2.62	1.06
SO ₃	1.86	4.72
Cr ₂ O ₃	0.13	0.04
TiO ₂	0.88	0.41
K.K.	2.76	2.69
Specific Gravity	1.99	3.07
(Specific surface area), cm ² /g	3126	3312

The effects of three different chemical admixtures on determining the viscosity of mixtures were investigated and the properties of admixtures that were added, according to the statement of the manufacturer company, are given in Table 2.

Table 2. Properties of chemical admixtures

	FLUICON 274W	AERMIX	RETARDEX
Technical Properties	Superplast.	Air Entraining	Retarder

Appearance	No segregation	No segregation	No segregation
Color	Dark Brown	Lightcolor, Amber	Brown
RelativeDensity(gr/cm3)	1,204	1,01	1,194
PH Value	6,73	7,1	7,38
Chloride Content	< 0,1	< 0,1	0,0021
Alkali Amount(Na₂O)%	< 5	< 0,5	< 5
Solid Content	39,23	---	38,03

2.2. Methods

Superplasticizers, retarders and air entraining admixtures were preferred as chemical admixtures since they are used more commonly in the sector. Too much or too little addition of the chemical admixture affects the usage, durability and fluidity of the mortar. Chemical admixtures, which are generally recommended for use between 0,5% to 2%, differ according to the type of the chemical binder and the amount of water used in the mortar (TS EN 934- 2, 2002). Thus, the mixtures we used in our study were produced by adding admixtures at rates of 0%-0,5%-1%-1,5%. As for the mixtures prepared with an admixture inclusion of 2%, too much fluidity, bleeding of admixture and water, too late setting time and disintegration at the course of curing were observed. Crushed sand of 0-2mm grain size was added to the mixtures. The physical properties of crushed sand are given in Table 3. and sieve analysis in Figure 1.

Table 3. Physical properties of crushed sand

Bulk Specific Gravity -dry-	2,659
Bulk specific gravity –saturated surface, dry-	2,688
Apparent Specific Gravity	2,740
Absorption Amount gr	5,5
Absorption Percentage	1,112

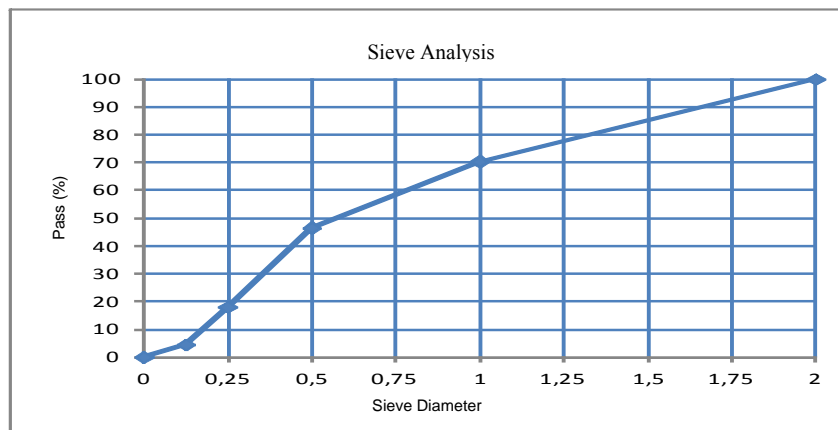


Figure 1. Sieve analysis of crushed sand

For all of the mortar productions, water/binder (cement) ratio was fixed at 0,50. In the control samples and all of the mixtures with a fly ash substitute of 10% of cement weight, the total amount of binder employed was 500 kg/m³. Superplasticizer, air entraining and retarder admixtures were used at 3 different ratios as 0,5%, 1% and 1,5% of the amount of binder in the mixtures. FA stands for fly ash, SP for superplasticizer, R for retarder, AE for air entraining and WA for without additive in the series produced.

Brookfield DV-II+ PRO Series viscosimeter was utilized for viscosimeter measurements. The container used for viscosimeter measurement has a volume of 1000 ml and is made of hard plastic (Figure 2).



Figure 2. Brookfield DV-II+ PRO Series Viscosimeter, measurement container and spindle number RV 7.

Spindle number RV 7 was used for measurement. Spindle number RV 7 is a means of measurement which can be employed for measuring semi-fluid materials like concrete mortar. Thus, it is easier to conduct the processes taking into consideration the fluidity of fresh mortar, its pumpability, ability to settle into the mould and easiness/difficulty in flowing. Besides, the greatest factor that may have an influence on that fluidity is the ratio of chemical admixture, mineral admixture and water added into the mortar. The mortar mixtures produced were poured into 40*40*160mm prismatic steel moulds and after keeping it for 24 hours, they were extracted from moulds and were cured in lime-saturated water of 20 ± 2 oC. (Figure 3).



Figure 3. Moulds used and samples produced

By carrying out experiments of flexure and compression upon the samples, the effects of chemical admixtures on their mechanical features were assessed.

3. RESULTS AND DISCUSSION

Today, the application of chemical admixtures is increasing rapidly in order to improve the strength, durability and viscosity properties in concrete production. This study investigates the effects of using chemical admixtures in mortar upon strength and viscosity.

Viscosity of the mortars were measured at 10, 20, 30, 40, 50, 60, 70, 80, 90 and 100 rpm angular velocities and immediately after puddling. Thus, viscosity values of each mixture at different angular velocities (cP) were obtained and viscosity-angular velocity diagrams were drawn (Figure 4-9).

When the viscosity diagrams of mortars with the three chemical admixtures—together with the control mortar of FA0—were examined, it was observed that viscosity curves of mortars with each of three admixtures, which were added at 0.5% rate to the mixtures, were above that of control mortar. The situation is the same for mortar samples of 1.5%. In this case, it is possible to say chemical admixtures increase viscosity.

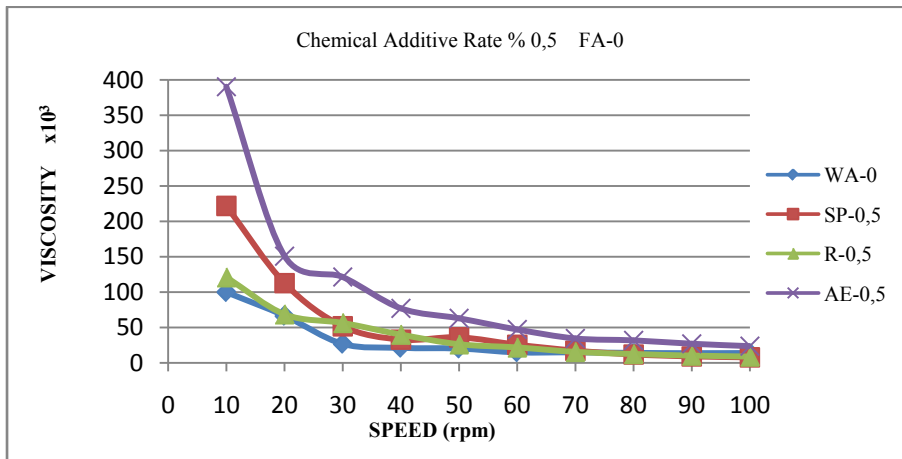


Figure 4. Viscosity measurement diagram of mortars without FA

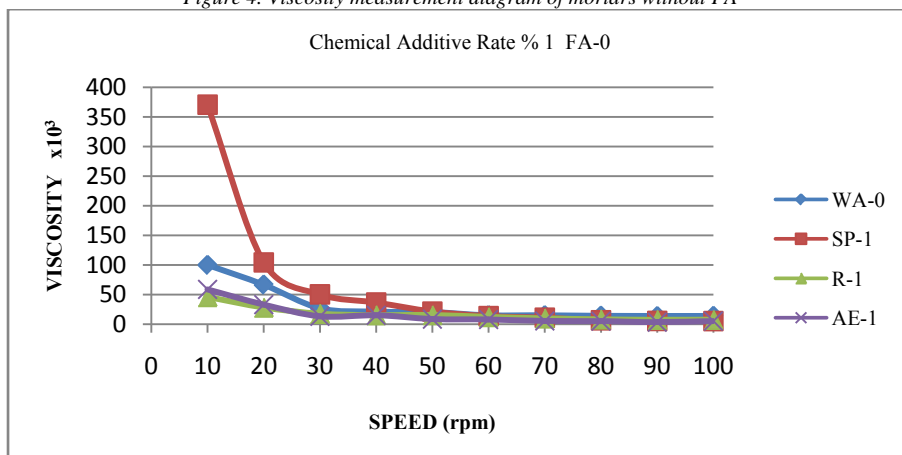


Figure 5. Viscosity measurement diagram of mortars without FA

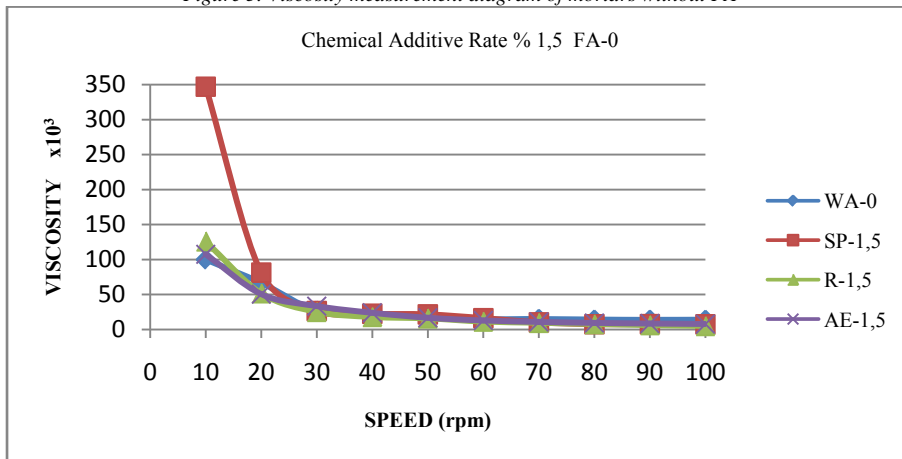


Figure 6. Viscosity measurement diagram of mortars without FA

Viscosity is the measurement of the resistance which a fluid shows against deformation under surface tension. Increase in viscosity is important in that it prevents segregation. For all of the mortars, viscosity value was decreased when the angular velocity increased and curves exhibited an asymptotic approach towards X axis.

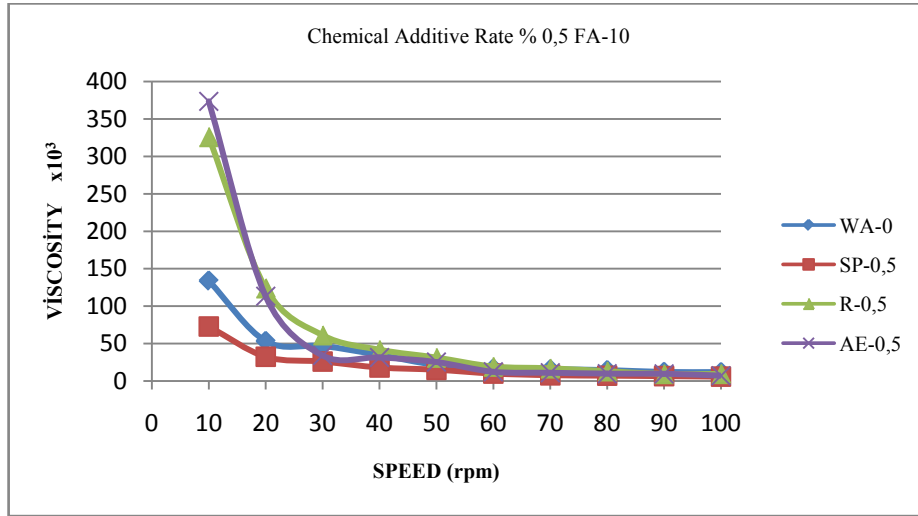


Figure 7. Viscosity measurement diagram of mortars with 10% FA

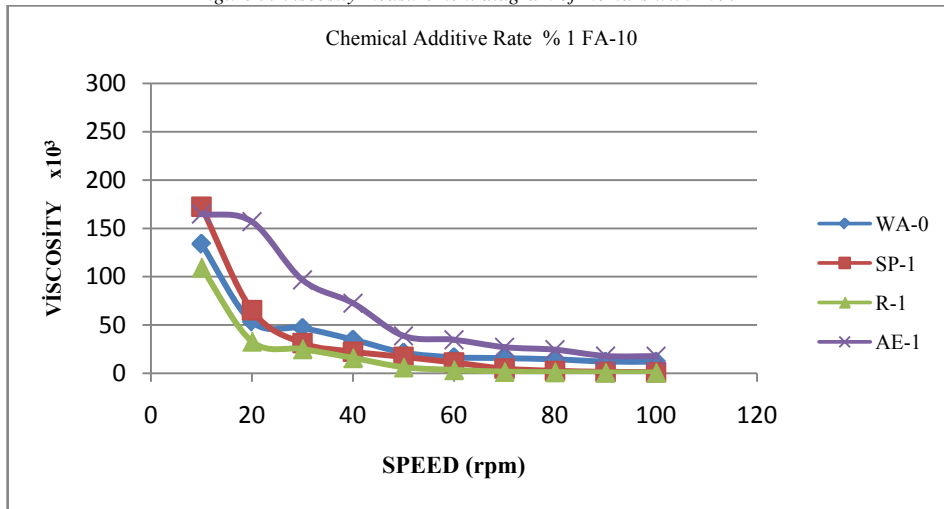


Figure 8. Viscosity measurement diagram of mortars with 10% FA

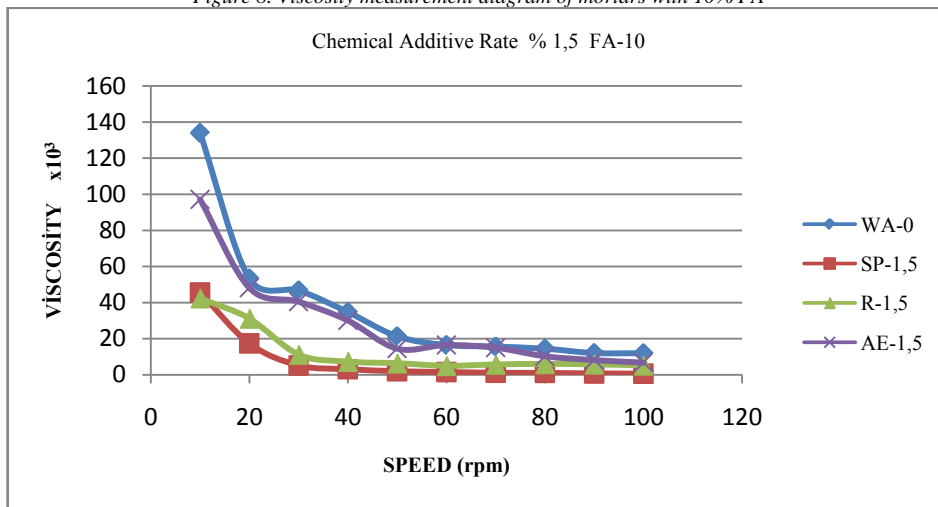


Figure 9. Viscosity measurement diagram of mortars with 10% FA

Application of 10% FA in mortars changed the operating levels of chemical admixtures and rendered a higher viscosity to R and AE admixtures. As for the mortar with SP admixture, the viscosity value decreased at a level even below that of control mortar and its fluidity increased. However, for the mortars produced with R and AE admixtures, fluidity increased as more amount of admixture was used, and thus, viscosity value also increased.

When the amount of admixture was increased, whereas there was an increase in viscosity value of AE admixture, a dramatic decrease was observed in that of SP admixture, and a more flowable mortar was attained compared to the one without admixtures and with AE admixture. Besides, fly ash that was used has also got an effect on mortar. As a consequence of substituting cement with 10% fly ash, the need for water grew, but fluidity was attained through chemical admixtures since no extra water was added. Experiments carried out previously put forth that FA, whose grain size is smaller than that of cement, affects workability positively.

Results that were obtained during the study were given in Table 4 and effects of admixture type and amount on strength were assessed in diagrams (Figure 10-11).

Table 4. Compressive and Flexural Strengths (MPa)

Admixture Type	Compressive Strength (MPa)			Flexural Strength (MPa)		
	0,50%	1%	1,50%	0,50%	1%	1,50%
WA FA-0	21,9	21,9	21,9	6,2	6,2	6,2
SP FA-0	31,8	34,5	36	7,3	8	8,3
AE FA-0	12,2	10,8	11,8	5,6	4,2	4,9
WA FA-10	23,1	23,1	23,1	6,5	6,5	6,5
SP FA-10	33,1	34,4	36,4	7,2	8	8,7
AE FA-10	12,7	11,4	12,2	5,8	4,3	5,3

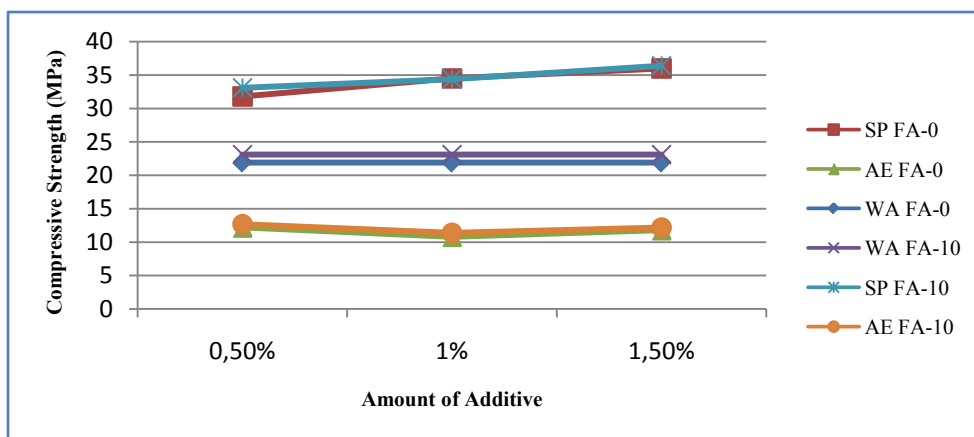


Figure 10. Compressive strength of samples produced

Comparing FA10 mixtures to FA0 control samples, when the amount of admixture was raised, strength of samples with SP admixture tends to increase, whereas it tends to decrease in samples produced with AE admixture. Strength of samples with AE admixture reached a value below that of control mortar.

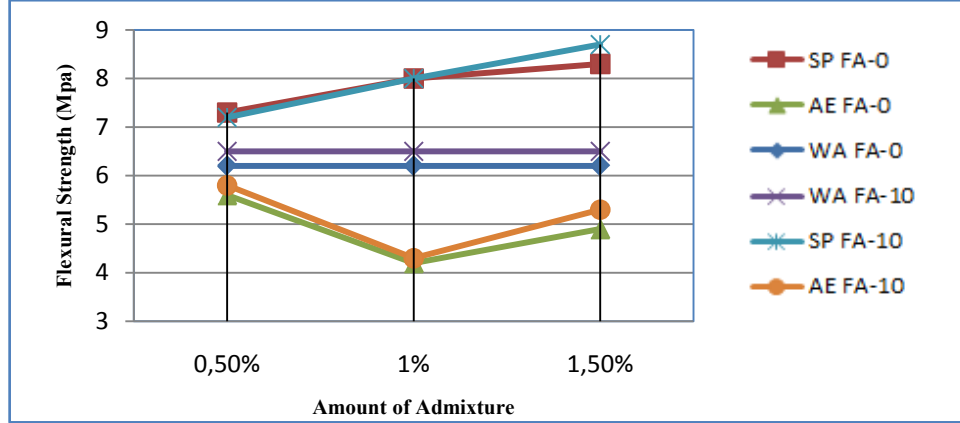


Figure 11. Flexural strength of samples produced

When the effect of chemical admixture on flexural strengths of samples produced, it can be stated that it shows similar behavior to compressive strength. The effect of SP admixture was higher than control samples in area as well. Hence, it is possible to say that SP admixture facilitates workability of mixtures and as it enables them to settle homogeneously, it reduces void space and improves strength. When the amount of SP admixture was increased from 0.5% to 1.5%, strength improved at a rate of 20-25%.

4. CONCLUSIONS

Increase in the amount of retarder chemical admixture causes the fluidity to decrease which, in turn, makes it difficult to settle in the mould, and thus void space in internal structure grows; so it is possible to say it leads to compressive strength to decrease.

Air entraining chemical admixtures, on the other hand, yield rather favorable results compared to retarder admixtures; yet, they are left behind by superplasticizer admixtures in terms of flexural and compressive strength.

Flexural and compressive strength of samples produced using superplasticizers showed 30-40% increase compared to that of control samples.

To sum up, it is convenient to conclude that, among chemical admixtures, superplasticizers, when employed with mineral admixtures, show the best performance compared to other types, in terms of both fluidity and strength—for mortars that will be applied under appropriate weather conditions. Hence, they can contribute to production of mortar and concrete of higher quality.

REFERENCES

- [1]. Açıkgöç, M., Karataş, M., Ulucan, Z., Ç. (2013). Elazığ Yöresine ait Atık Tuğla ve Kireç Taşı Tozunun Kendiliğinden Yerleşen Harcın Mühendislik Özelliklerine Etkisi. Pamukkale Üniversitesi Mühendislik Bilimleri Dergisi, Cilt 19, Sayı 6, Sayfalar 249-255.
- [2]. Bentz, P., D., Ferraris, F., C., Galler, M., A., Hansen, A., S., Guynn, J., M., (2012). Influence of particle size distributions on yield stress and viscosity of cement-fly ash pastes. Cement and Concrete Research 42 (2012) 404-409.
- [3]. Felekoğlu B., Türkel S., Baradan B. (2004). Kendiliğinden Yerleşen Beton: Bölüm 1 Genel Tanıtım, Kullanım Alanları, TMMOB, İnşaat Mühendisleri Odası İzmir Şubesi, Haber Bülteni, 05 Haziran, Cilt 19 Sayı: 117, s. 20-24.
- [4]. Golaszewski, J., Szwabowski, J., (2004). Influence Of Superplasticizers On Rheological Behaviour Of Fresh Cement Mortars. Cement and Concrete Research 34 (2004) 235-248.
- [5]. Güçlüer, K., Ünal, O. (2010) Uçucu Küllü Çeriğinin Beton Dayanımına Geçirirliğin Üzerine Etkisi, Yapı Teknolojileri Elektronik Dergisi, 6 (1) 11-18.
- [6]. Karataş E., Aykan G., Magarotto R. (2010). Akıllı Dinamik Beton: Yenilikçi Viskozite Düzenleyici Katkı İle Kendiliğinden Sıkışan Betonlara Yeni Bir Bakış, BASF Yapı Kimyasalları San. Tic. A.Ş.

[7]. Montes, B., O., Alonso, M., M., Puertas, F., (2013). Viscosity And Water Demand Of Limestone- And Fly Ash- Blended Cement Pastes In The Presence Of Superplasticisers. *Construction and Building Materials* 48 (2013) 417–423.

[8]. Subaşı S., Kap, T. ve Beycioğlu A., Çullu M. (2008). Uçucu Kül Katkı Miktarının Beton İşlenebilirliğine Sertleşme Sürelerine Olan Etkisi, Uluslararası Hazır Beton Kongresi, 438-448, İstanbul/Türkiye.

[9]. Turk, K., (2012). Viscosity And Hardened Properties Of Self-Compacting Mortars With Binary and Ternary Cementitious Blends Of Fly Ash And Silica Fume. *Construction and Building Materials* 37 (2012) 326–334.

[10]. TS EN 197-1/A3 (2008). Çimento- Bölüm 1: Genel Çimentolar- Bileşim, Özellikler ve Uygunluk Kriterleri, Türk Standartları Enstitüsü, Ankara.

[11]. TS EN 934- 2 (2002). Kimyasal Katkılar – Beton, Harç ve Şerbetçin – Bölüm: 2 Beton Katkıları – Tarifler, Özellikler, Uygunluk, İşaretleme ve Etiketleme, Türk Standartları Enstitüsü, Ankara.

[12]. Yazıcı Ş. (2003). Süper Akışkanlaştırıcıların Betondaki Bazı Fiziksel ve Mekanik Özelliklere Etkileri, DEÜ Mühendislik Fakültesi, Fen ve Mühendislik Dergisi Cilt:5 Sayı: 1 Sh: 03-114 Ocak.

[13]. Yiğiter, H., Aydın, S., Yazıcı, H., Baradan, B. (2004). C Tipi Uçucu Kül Katkılı Betonların Bazı Fiziksel, Mekanik ve Durabilite Özelliklerinin Araştırılması, THBB Beton 2004 Kongresi, 58-66, İstanbul.

Internet Resources

[1]. www.viskozimetre.com/viskozite_nedir.html , 8.02.2014

PARAMETER ESTIMATION FROM RESIDUAL GRAVITY ANOMALIES OF SUBSURFACE CAVITIES USING MODELLING OPTIMIZATIONS

Fikret DOĞRU

Dokuz Eylul University, Department of Geophysical Engineering, 35160, Buca /İzmir, Turkey.
fikret.dogru@deu.edu.tr

Abstract

In addition to the global method and the traditional method which are commonly used in geophysics artificial neural networks methods were used to estimate the cavity parameters of residual gravity anomalies. Feed Forward Backpropagation neural network is a technique commonly used for inversion problems, recently. In addition to this method, the Cascade Forward Backpropagation and the Nonlinear Autoregressive Network were used for parameter estimation and the results of errors were compared. Also Genetic Algorithm and Levenberg-Marquardt algorithm were used for estimation of depth and radius parameters from residual anomaly and the results of errors compared. In the theoretical study, horizontal cylinder model representing the underground cavity was used. The effectiveness of the method was investigated by adding noise to the horizontal cylinder gravity anomalies. After calculating the error values, it was determined that Levenberg-Marquardt algorithm and Nonlinear Autoregressive Neural Network seem to be the least affected methods from noise. Residual gravity data of Medford (USA) cavity site was used for field investigations. When the results of field data were analyzed, it is seen that Feed Forward Backpropagation and Nonlinear Autoregressive Neural Network gave the closest result to known structure depth value from the drilling. Among the applied methods in the field application, although the lowest error value of inversion results obtained by the Levenberg-Marquardt algorithm, the depth value obtained from this method is the most different known from the drilling value.

Keywords: Gravity, Artificial Neural Network, Genetic Algorithm, Geophysics, FFBP, NARX.

1. INTRODUCTION

The determination change of the physical properties of the causative sources in horizontal and vertical directions is the goal of the evaluation of the gravity data. One of the most important problems in interpreting gravity data, the result is not the only and definitive. In other words, an infinite number of model design can produce the same symptom ([17]). However, a unique solution may be obtained by incorporating certain prior information, such as assigning a simple geometry to the causative source ([18]). Various methods have been presented for the interpretation of residual gravity anomaly. Such methods include least squares approaches ([5]; [11]; [19]; [1]), neural networks ([4]; [15]; [6]), continuous wavelet transform ([3]), 3D analytic signal amplitude ([16]).

2. METHODS

2.1. Artificial Neural Network

Neural networks is the algorithm that developed to simulate the principle of operation of the human brain ([14]). In the neural networks, the cells contains neurons and the neurons connect to each other in different ways by links as in the human brain. These networks has a capacity of learning, data storing and reveal the relationship between data.

A schematic diagram of a FFBP neural network is shown in figure 1.

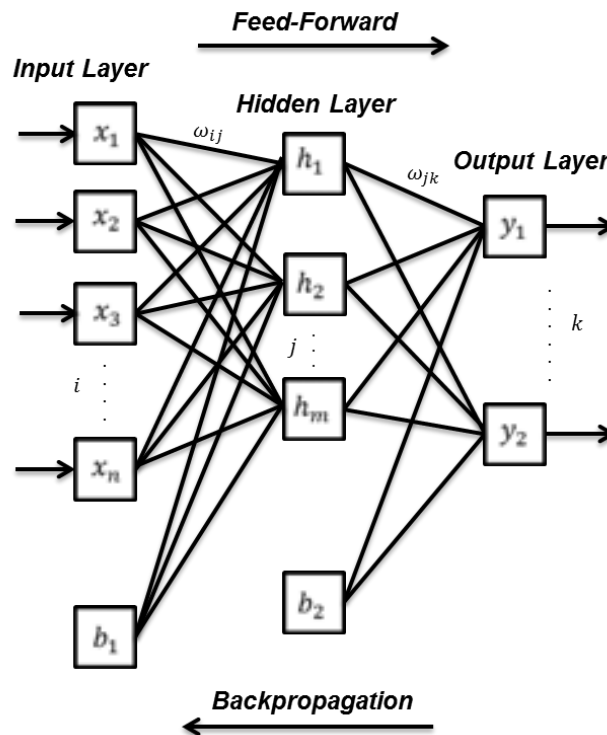


Figure 1. Schematic diagram of an FFBP neural network structure.

In this notation the residual gravity values are the inputs, the radius and depth are the outputs. To solve the problem, all inputs and nodes are collected at each hidden node after being multiplied by weights. Then, a bias is attached to this sum, and it is transformed through a certain function and transferred to the next layer. Mathematically, the output of network y_k is computed by the equation 1.

$$y_k = \tilde{f} \left\{ \sum_{j=1}^m w_{jk} f \left[\sum_{i=1}^n (w_{ij} x_i + b_1) + b_2 \right] \right\}, \quad k = 1, 2, \dots, \dots, l \quad (1)$$

In this equation; n is the number of neurons in the input layer, m is the number of neurons in the hidden layer and l is the number of neurons in the output layer. b_1 is the bias values of the first layer and b_2 is the bias value of the second layer. f is the activation function among input and hidden layer and \tilde{f} is the activation function among hidden and output layer.

In this study, two parameters is desired in the neural network (depth and radius) so the neuron number of outputs is $l = 2$. In this case, the equation (1) can be expressed in the following way:

$$R = \tilde{f} \left\{ \sum_{j=1}^m w_{j1} f \left[\sum_{i=1}^n (w_{ij} g_i + b_1) + b_2 \right] \right\}, \quad (2)$$

$$z = \tilde{f} \left\{ \sum_{j=1}^m w_{j2} f \left[\sum_{i=1}^n (w_{ij} g_i + b_1) + b_2 \right] \right\}, \quad (3)$$

In these equations; g_i values are the residual gravity values, R is the radius and z is the depth.

CFBP neural network operates similarly to the FFBP neural network. In this neural network, all the input values are linked to the all layers, unlike FFBP neural network. CFBP neural network also has capacity of learning as in the same FFBP neural network. Using two or more layers and sufficient number of neurons can be provided the relationship between output and input (Figure 2).

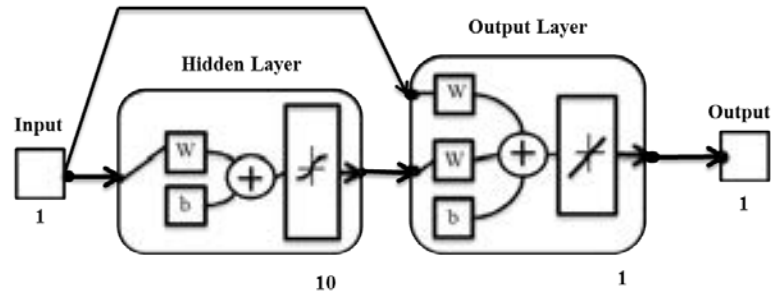


Figure 2. Schematic diagram of Cascade Forward Backpropagation neural network.

NARX networks can learn to predict one time series given past values of the same time series, the feedback input, and another time series. This learning ability is able to forecasting another time series. In this neural network, the delay time is given for feedback and input unlike other networks (Figure 3).

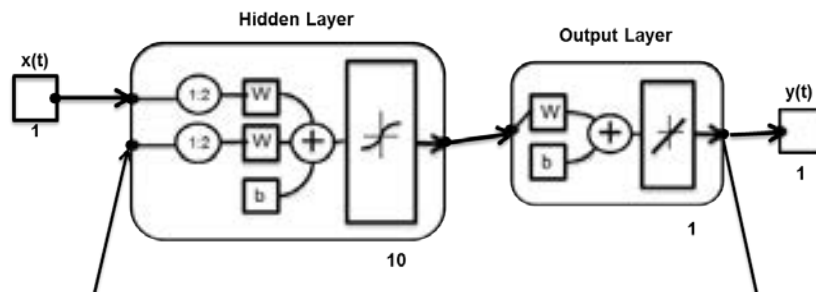


Figure 3. Schematic diagram of The Nonlinear Autoregressive Network.

2.2. Genetic Algorithm

Genetic algorithm is a metaheuristic global optimization method that inspired by the natural evolution and firstly developed by Holland ([8]). This method produces constantly improving solutions. Objective of genetic algorithm is made the maximum of the fitness function. The minimization of objective function or error function are carried out by taking the inverse of the fitness function.

Genetic algorithm has three operators which are selection, crossover and mutation. These operators are used to obtain new populations with better fitness value from the initial population. Algorithm searches for the best results by changing numerous times the solutions of the individuals in the population. Each step select new individuals within the population and crossed them to produce new individuals for the next generation. The algorithm ends with the end of the generation number. In this process, the best fitness value is accepted as a solution ([12]; [9]).

2.3. Levenberg-Marquardt Algorithm

There is no linear relationship between the observational values and model parameters in geophysical problems so problem is solved by linearized most times.

Generalized least squares solution for non-linear equation systems are given following formula;

$$\Delta p = (A^T A)^{-1} A^T \Delta d \quad (4)$$

In this equation, A is the matrix containing the partial derivatives, Δd is the difference between the calculated values with observed values and Δp is the correction parameter vector.

If data does not contain complete information for the solution of some parameter, column of data resolution matrix corresponding of this parameter is close to zero. Eigenvalues of these parameters can also be close to zero. Oscillations caused by small eigenvalues must be damped during iteration. The following formula is obtained by adding a numerical value to diagonals of $A^T A$ matrix according to the matrix property ([11]).

$$\Delta p = (A^T A + \varepsilon^2 I)^{-1} A^T \Delta d \quad (5)$$

This solution is known Levenberg-Marquardt inversion or damped least-squares. In this equation, I is the unit matrix, ε^2 is the real number and is called the damping factor ([10]; [13]).

3. THEORETICAL MODEL STUDIES

Residual gravity anomaly of horizontal cylinder is used as the theoretical data. Radius and depth values are respectively 1.5595 m and 3.119 m. In addition, %5 random noise is added to this data (Figure 4). After the training stage of each ANN method is completed, radius and depth values were obtained by entering noise-free, noise-corrupted data to the network. 1409 theoretical data is used for training the network and each data has 141 values.

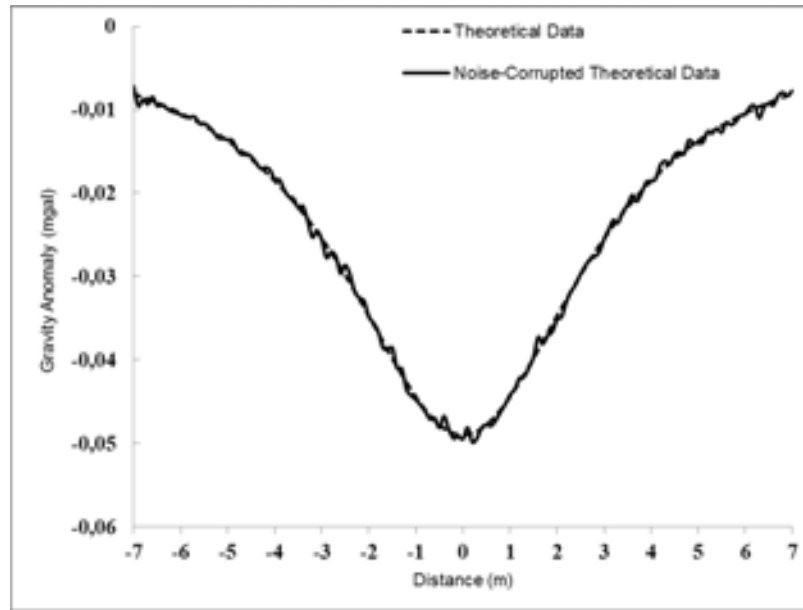


Figure 4. Noisy and free-noisy theoretical residual gravity anomalies.

In each ANN method, a momentum and adaptive learning rate backpropagation gradient descent (traingdx) training function is used. Bias and weight in the training function is updated according to the gradient descent momentum and adaptive learning rate. Learning rate and momentum coefficient are respectively 0.01 and 0.9 in the ANN training stage. One hidden layer is used, and the number of neurons is taken 10. The 10000 iterations for ANN method was considered adequate. The 100 iterations is given for LM algorithm. However, a change parameter or error was not observed after 4 iterations. The number of population for GA is 100, and crossover parameters are taken 0.8. Results are given in table 1 and 2.

Table 1. The application results for noise-free data.

METHOD	Radius (m)	Depth (m)	Rmse (%)	Iteration Number
FFBP	1,5586	3,1173	0,003	10000
CFBP	1,5578	3,1173	0,064	10000
NARX	1,5578	3,1176	0,065	10000
GA	1,56	3,119	0,00019	51
LM	1,5563	3,1193	0,00025	100

Table 2. The application results for noisy-corrupted data.

METHOD	Radius (m)	Depth (m)	Rmse (%)	Iteration Number
FFBP	1,5685	3,0765	0,0068	10000
CFBP	1,6214	3,139	0,026	10000
NARX	1,5959	3,1398	0,014	10000
GA	1,559	3,111	0,0064	51
LM	1,557	3,12	0,6	100

4. FIELD STUDY

Figure 5 shows the residual gravity profile for a cavity anomaly located at the Medford site, Florida, USA ([2]). Florida site is cavity site with limestone geological structures. In a study conducted by Hajian et al. ([7]), the shape of the cavity in the Medford area has been identified as a horizontal cylinder. The values obtained from the drilling depth was obtained as 3.57 m. The same parameters are used both the inversion of field and theoretical data. The results of the methods are shown in table 3.

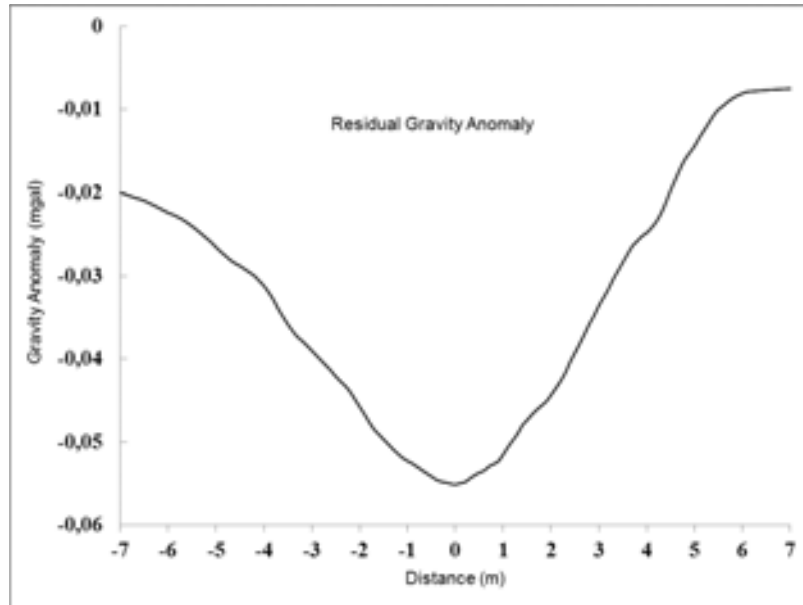


Figure 5. Residual gravity profile over a cavity at the Medford test site ([2]).

The same iteration number, NARX and FFBP approximately gave the same results. The depth values obtained from the drilling and obtained from NARX and FFBP are seen to be close. In the results, acceptable errors obtained from the CFBP method. When looking at the parameter and the error value obtained on the results of GA are in compliance with the results of known values from drilling.

Table 3. The application results for field data.

METHOD	Radius (m)	Depth (m)	Rmse (%)	Iteration Number
FFBP	1,8504	3,5241	5,9	10000
CFBP	1,979	3,8045	8,1	10000
NARX	1,8501	3,526	5,9	10000
GA	1,829	3,656	5,4	51
LM	1,851	3,8373	5,3	100

5. CONCLUSIONS

In this study, the current neural network method (CFBP, NARX) were tested for estimation the radius and depth parameter from residual gravity anomalies. In addition to these methods, FFBP neural network, GA and LM algorithm were used and the results were compared. The effectiveness of these methods tried and tested in a noise-corrupted and noise-free theoretical data. Although working principle of FFBP neural network is different from the NARX neural network, obtained inversion results values were too close each other. CFBP neural network method provided the highest error values in both theoretical and field data application but the

results are acceptable. Even though the lowest root mean square error value was calculated from the inversion of field data using by Levenberg-Marquardt algorithm, computed depth is much more distant comparing with present one which was obtained from drilling. Also the ANN method has been shown to give good results in the inversion of geophysical problems as the traditional method LM and the global method GA which is commonly used in geophysics. This study shows that CFBP, NARX neural network methods could be effectively used for solution of problems in geophysics in addition to FFBP neural network.

6. REFERENCES

- [1] Abdelrahman, E.M., Bayoumi, A.I., and El-Araby, H.M., 1991. A least-squares minimization approach to invert gravity data, *Geophysics*, 56, 1, 115-118.
 - [2] Butler, D.K., 1984. Microgravimetric and gravity gradient techniques for detection of subsurface cavities, *Geophysics*, 49, 7, 1084-1096.
 - [3] Chamoli, A., Srivastava, R.P. and Dimri, V.P., 2006. Source depth characterization of potential field data of Bay of Bengal by continuous wavelet transform, *Indian Journal of Marine Sciences*, 35, 3, 195-204.
 - [4] Elawadi, E., Salem, A., and Ushijima, K., 2001. Detection of cavities and tunnels from gravity data using a neural network, *Exploration Geophysics*, 32, 4, 204-208.
 - [5] Gupta, O.P., 1983. A least-squares approach to depth determination from gravity data, *Geophysics*, 48, 3, 357-360.
 - [6] Hajian, A., 2004. Depth Estimation of Gravity Anomalies by Neural Network, M.Sc. Thesis, Tehran University, Iran (in Persian).
 - [7] Hajian, A., Zomorrodian, H., and Styles, P., 2012. Simultaneous Estimation of Shape Factor and Depth of Subsurface Cavities from Residual Gravity Anomalies using Feed-Forward Back-Propagation Neural Networks, *Acta Geophysica*, 60, 1043-1075.
 - [8] Holland, J., 1975. *Adaptation in Natural and Artificial Systems*, University of Michigan Press.
 - [9] Lee, K. Y., and Mohamed, P. S., 2002. A real-coded genetic algorithm involving a hybrid crossover method for power plant control system design, in *Proceedings of the 2002 Congress on Evolutionary Computation*, pp. 1069-1074.
 - [10] Levenberg, K., 1944. A Method for the solution of certain nonlinear problems in least squares. *The Quarterly of Applied Mathematics*, 2, 164-168.
 - [11] Lines, L.R. and Treitel, S., 1984. A review of least-squares inversion and its application to geophysical problems, *Geophysical Prospecting*, 32, 2, 159-186.
 - [12] Luke, S., 2009. *Essentials of metaheuristics*. Lulu, Retrieved January 20th, 2012, from <http://cs.gmu.edu/~sean/book/metaheuristics/>.
 - [13] Marquardt, D.W., 1963. An algorithm for least-squares estimation of nonlinear parameters, *Journal of the Society for Industrial and Applied Mathematics*, 11(2): 431-441.
-

- [14] McCulloch, W.S., and Pitts, W., 1943. A logical calculus of the ideas immanent in nervous activity, *Bulletin of Mathematical Biology*, 5, 4, 115-133.
 - [15] Osman, O., Alhora, A.M., and Ucan O.N., 2007. Forward modeling with forced neural networks for gravity anomaly profile, *Mathematical Geology*, 39, 6, 593-605.
 - [16] Roest, W. R., Verhoef, J., and Pilkington, M., 1992. Magnetic interpretation using 3-D analytic signal: *Geophysics*, 57, 116–125.
 - [17] Roy, A., 1962. Ambiguity in geophysical interpretation, *Geophysics*, 27, 1, 90-99.
 - [18] Roy, L., Agarwal, N.P., and Shaw, R.K., 2000. A new concept in Euler deconvolution of isolated gravity anomalies, *Geophysical Prospecting*, 48, 3, 559-575.
 - [19] Salem, A., Elawadi, E., and Ushijima, K., 2003. Short note: Depth determination from residual gravity anomaly data using a simple formula, *Computer and Geoscience*, 29, 6, 801-804.
-

PROVIDING ENGINEERING SOLUTIONS TO FOREST FIRE ACCESS PROBLEMS USING NETWORK ANALYSIS METHOD

Abdullah E. AKAY

Corresponding author: Bursa Technical University, Department of Forest Engineering, 16200 Bursa, Turkey.
abdullahakay@btu.edu.tr

Hande E. KILIÇ

Abstract

The forest fires are the greatest environmental disaster on forest resources. In order to effectively fight against forest fires, ground team should access fire areas by fire trucks in short time through road network. In this study, Geographical Information System (GIS) based network analysis method was used to decide the optimum route with minimum fire access time. The study area consisted of Paşalar, Sarnıç and Turfal Forest Enterprise Chiefs, located in Mustafakemalpaşa Forest Enterprise Directorate of Bursa, Turkey. These Enterprises are classified as the 2nd degree fire sensitive areas where there was headquarter for the firefighting team. In the application, firstly, the road network, location of the firefighting headquarters and potential fire sites were digitized by using ArcGIS 10 software. Then, the optimum route, providing the fastest transportation from headquarter to possible fire sites, was determined by using Closest Facility tool of Network Analyst extension of ArcMap module under ArcGIS 10. Also, inaccessible areas due to fire risk were marked in the network database and disregarded in network analysis to ensure safety during the process. Finally, the location of the firefighting headquarter was evaluated using Service Area tool of Network Analyst by considering the critical response time to the possible fire areas. The results indicated that new firefighting headquarters should be established in the study area in order to access the forested areas on time. Building new roads and increasing the design speed on the current roads by improving their standards can be also considered to address the forest fire access problem.

Keywords: Forest Fires, Firefighting Headquarters, Shortest path, GIS, Network Analyst

1. INTRODUCTION

The forested areas (5.5 million ha) located along the coastline from the Mediterranean to the Marmara region are highly sensitive to forest fires in Turkey [4]. According to forest fire statistics, about 10,000 ha of forested areas had been burned annually [2]. In order to effectively fight against forest fires, fire fighting team must arrive to the scene in critical response time. The arrival time of fire fighting team at a fire area should not exceed critical response time when the probability of controlling forest fires rises markedly [7]. Therefore, it is very important to determine the areas that can be reached by fire fighting team in critical response time. The critical response time are computed based on fire sensitivity level of the forested areas (Table 1).

Table 1. Critical response time to forest fires by fire sensitivity levels (minutes) [7]

	Fire Sensitivity Levels				
	I	II	III	IV	V
Critical Response Time (min)	20	30	40	50	50

The engineering solutions can be provided to determine the areas that can be reached in a specific time period based on a road network data including length and travel speed [1]. A network analysis method is usually used to solve such transportation problems. Besides, GIS tools with network analysis based modules are capable of solving transportation problems [2].

A GIS tool was developed in a previous study [5] to determine efficiency of fire trucks in responding forest fires. The vehicle travel speed on different road types and the critical response time were used as decision variables. Bonazountas et al. [3] also studied access time of vehicles to a fire using GIS network analysis tools for managing forest damages.

A decision support system was developed by Keramitsoglou et al. [7] for fire management purposes within Greece. The several variables were considered such as road type, road condition, and population density.

In this study, location of a fire fighting team serving for three Forest Enterprise Chiefs in the city of Bursa were evaluated by using Network Analysis tool of GIS. The forested areas that can be reached by fire fighting team in critical response time were determined in the study area. The optimal travel route and associated response times of fire fighting team to potential fire areas were generated in evaluation process. Besides, inaccessible areas due to fire risk were disregarded in network analysis to ensure safety during the fire fighting activities.

2. MATERIAL AND METHODS

2.1. Study Area

The study area covers three Forestry Enterprise Chiefs (FECs) of Paşalar, Sarıç and Turfâl located in northwestern region of Turkey. These Enterprises are classified as the 2nd degree fire sensitive areas [7]. There is a fire fighting team located in the north boarder of the study area (Figure 1). The locations of potential fire areas were determined based on the information obtained from the Bursa Forest Regional Directorate and used to generate fire map.

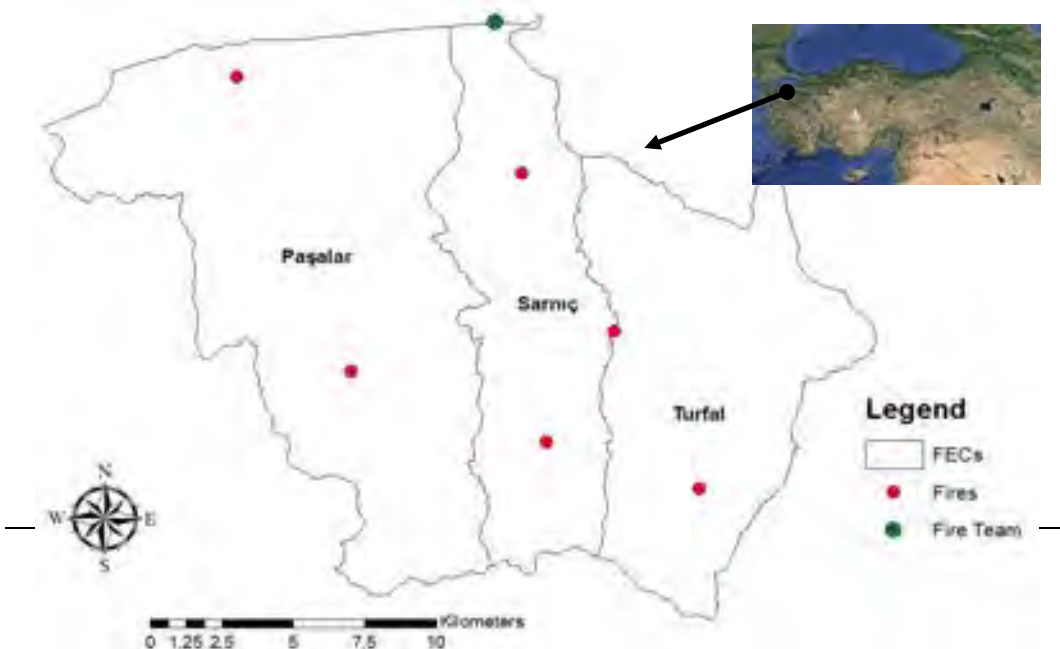


Figure 1. Fire fighting teams and potential fires located in the selected Forest Enterprise Chiefs (FECs)

2.2. GIS Analysis

In order to perform GIS analysis, firstly, road map was developed based on topographic maps. The average travel time of fire truck for each road section was added into the attribute table of road network layer. The travel time was computed based on road length and average speed of a fire truck using the following formula:

$$t_i = \frac{l_i}{v_i} \cdot 60 \quad (1)$$

t_i : travel time for road section i (minutes)

l_i : length of road section i (km)

v_i : average speed of fire truck for road section i (km/hour)

60: used to convert the unit of travel time from hour to minute

Vehicle speed varies depending on road types including asphalt, gravel, and forest roads (Table 2). Forest map within the study area was generated based on stand type maps provided by Bursa Forest Regional Directorate.

Table 2. Average vehicle speeds for road types

Road Type	Speed
	(km/hour)
Asphalt	60
Gravel	40
Forest Road	20

Network Analyst extension of ArcGIS 10 was used to determine forested areas that can be reached by fire fighting teams in critical response time. Network Analyst extension provides several methods to solve routing problems: New Route, New Service Area, New Closest Facility, New OD Cost Matrix, New Vehicle Routing Problem, and New Location-Allocation (Figure 2). In this study, New Service Area and New Closest Facility methods were used based on network database where travel times were assigned to the links representing the road sections in the study area.

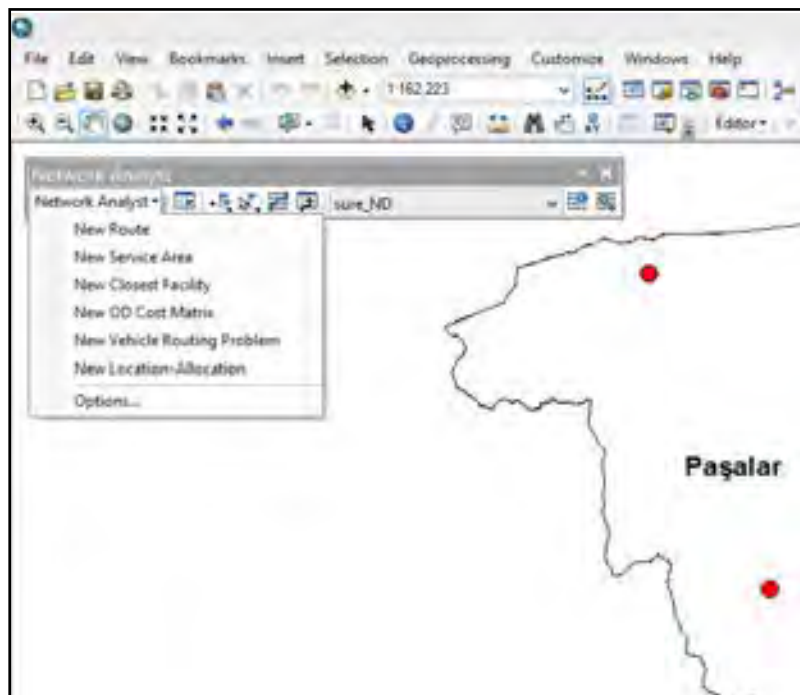


Figure 2. The methods under Network Analyst

The New Service Area method works similar to a GIS buffer analysis. A service area point represents a center point from which other portions of the network can be reached in a given total link value. In this study, the locations of the fire fighting teams are considered as service area points while service areas are the forest areas that can be reached within the critical response time.

The New Closest Facility method was implemented to determine the fastest access routes from the initial response team to the potential fire areas in the study area. Then, some of the road sections with fire risk were excluded from the network system by locating polygon barriers on those links. Finally, New Closest Facility method was implemented again to find not only the fastest but also the safest travel route to the potential fire areas.

3. RESULTS AND DISCUSSION

Results indicated that total length of the road network was 525.02 km (Figure 3). Most of the road section was classified as forest road (70.83%), followed by asphalt road (17.51%), and gravel road (11.67%). The results indicated that the total area of forest land was 21410 ha in which the proportion of high forest and coppice forest were 84.96 % and 15.04 %, respectively (Figure 4).

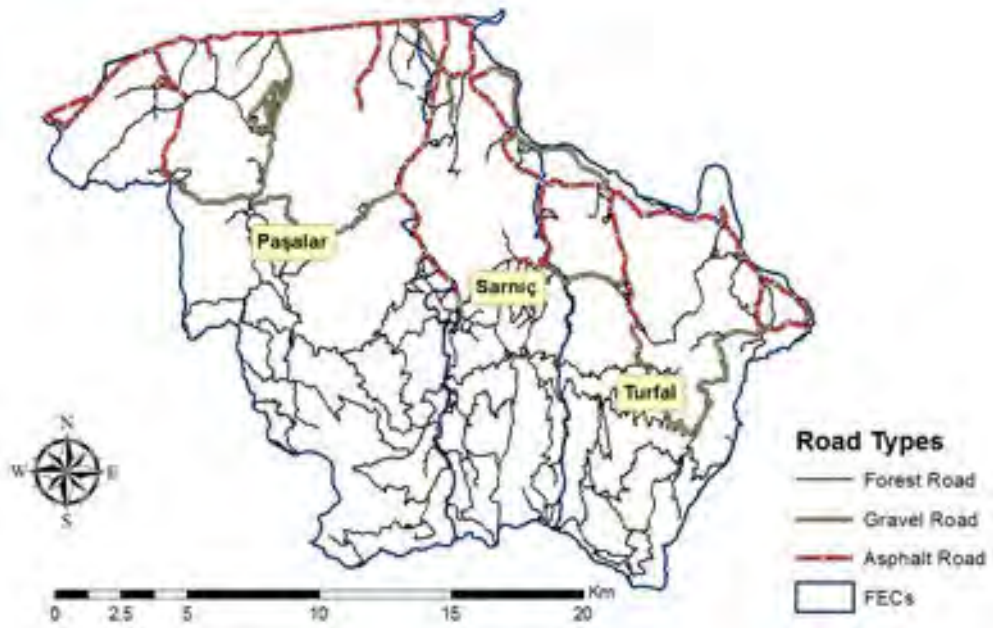


Figure 3. Road network map

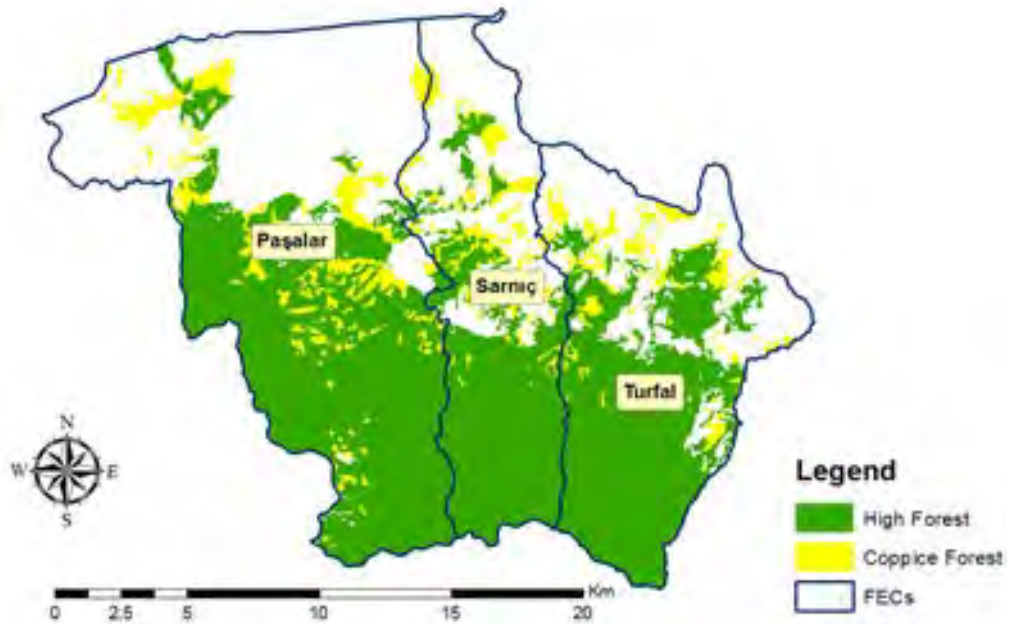


Figure 4. The map of the forest land in the study are

New Service Area method was used to determine the areas that can be reached by initial response teams within a critical response time. In GIS analysis, the buffer area that can be reached by fire trucks through the road network within critical response time of 30 minutes were investigated for forest lands sensitive to fire at the second degree. It was found that 31.28% of the forest land can be reached by initial response teams within a critical response time. Considering high and coppice forest lands, 26.18% and 60.29% of the forest lands can be reached within a critical response time, respectively (Figure 5).

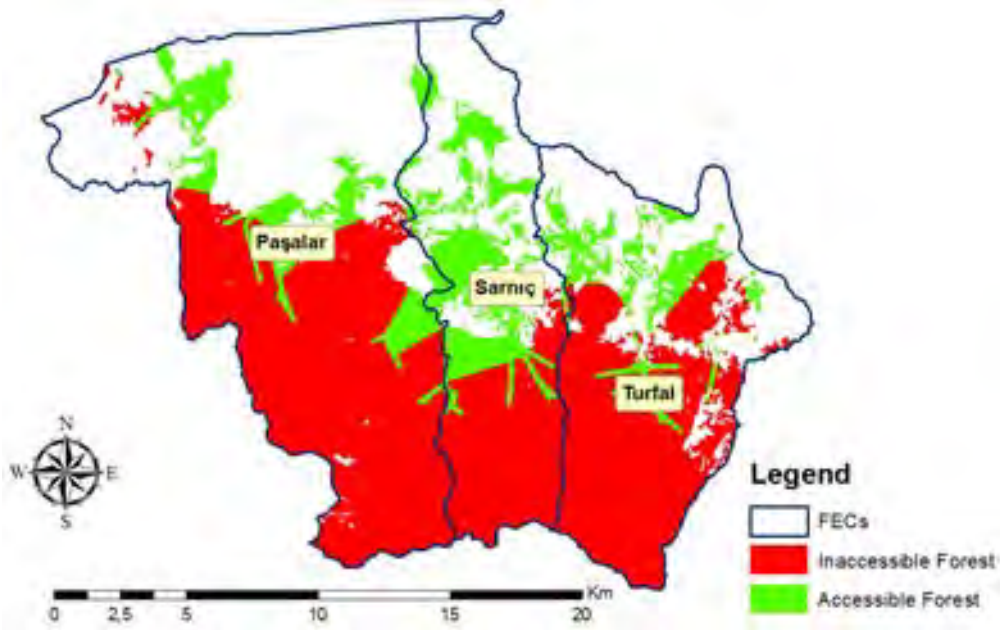


Figure 5. The accessibility of the forest land

The fastest access routes for the initial response team to the potential fire areas in the study area were determined using the New Closest Facility method. Results indicated that there is a relationship between travel time and road length, as well as between travel time and road types. Initial response teams that reached potential fire areas within the minimum arrival time were identified considering two cases: 1) fastest access route and 2) safest access route. Figure 6 indicates the fastest access routes to the six potential fire areas. It was found that three of these fires (1, 2, and 3) were not accessible by the ground teams within the critical response time, while other three fires were accessed in less than 20 minutes (Table 3).

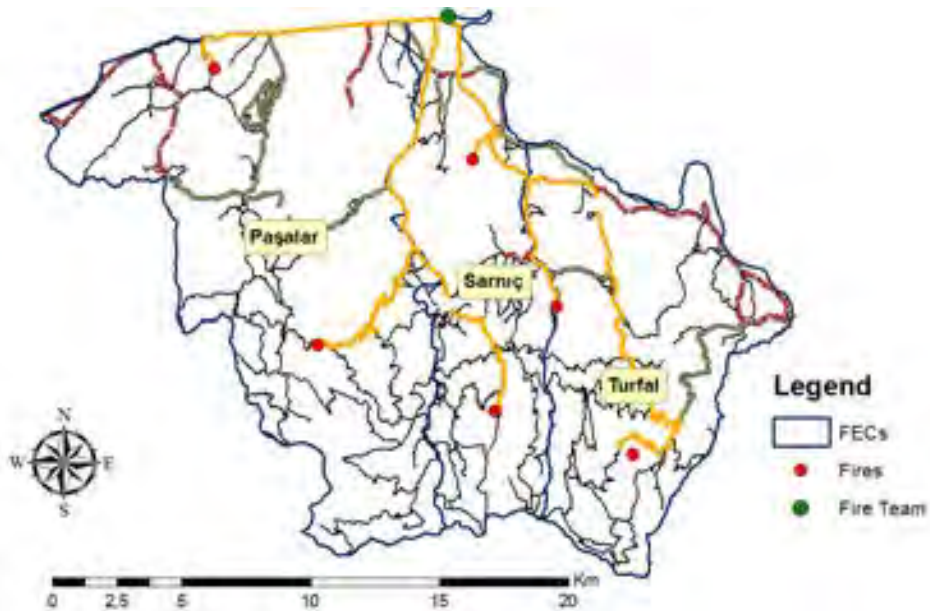


Figure 6. The fastest access routes to the potential fire areas

Table 3. Response time to potential fire areas

Cases	Potential Fire Areas					
	1	2	3	4	5	6
No Barriers	31,33	38,35	45,25	11,00	10,14	17,12
With Barriers	31,33	41,30	63,30	19,47	10,14	17,12

For the second case, polygon barriers were placed in the network system to determine the safest or most reliable access routes to the potential fire areas (Figure 7). It was found that the response team that reached the potential fire areas within the critical response time was the same as in the first case. However, routes from response team to fire areas were changed for three fire areas (2, 3, and 4). The results from both cases indicated that new response teams should be considered by the in order to reach potential fire areas within the critical response time.

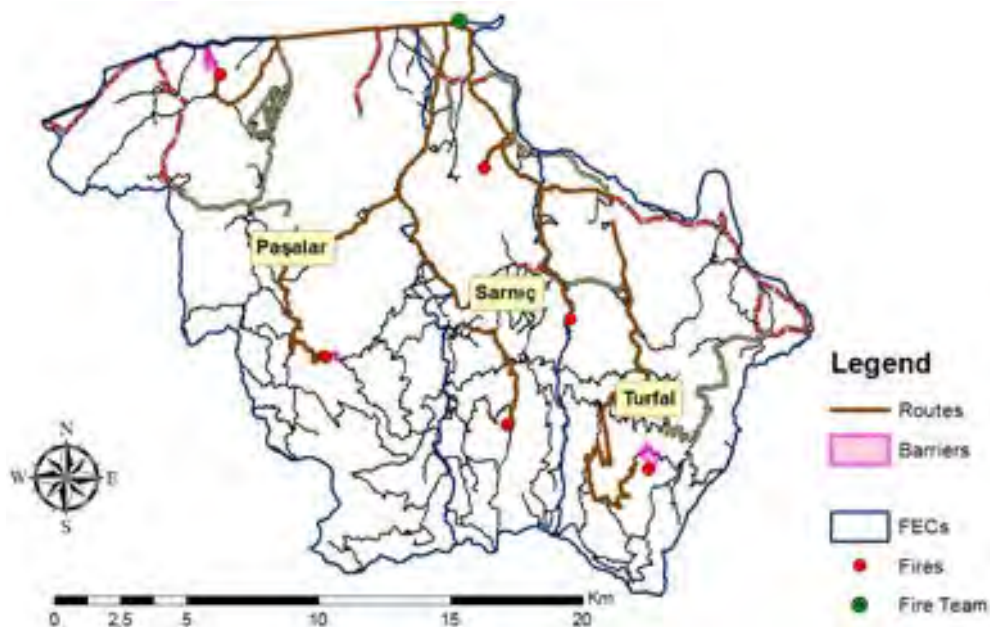


Figure 7. The safest access routes to the potential fire areas

4. CONCLUSIONS

The findings indicated that 68.72% of the forested areas could not be reached within the critical response time. The results also revealed that fire fighting teams could not reach 73.82% and 39.71% of high forest and coppice forest, respectively. Therefore, the results suggested that additional fire fighting teams are necessary in the region. Besides, new roads should be built or existing roads should be improved considering design speed.

The results showed that a GIS-based systems can be effectively used to assist fire managers in directing mobile fire fighting teams to potential fire areas in real-time. The polygon barriers located in one of scenarios to simulate the influence of potential road closures demonstrated that the decision support system can be used to not only determine the fastest access route but also to identify a safer and more reliable route.

5. REFERENCES

- [1]. Akay, A.E., Erdas, O., Karas, I.R. (2006). Using GIS and optimization techniques in selecting forest road alignment with minimum sediment yield. First Remote Sensing and GIS Symposium, 27-29 November, ITU, Istanbul. 10 p.
- [2]. Akay, A.E., Sakar, D. (2009). Using GIS Based Decision Supporting System in Determining Optimum Path that Provides the Transportation to Fire Zone at the Shortest Time. The Chamber of Turkish Engineers and Architects. The Congress of Geographic Information Systems. 02-06 November. Izmir, Turkey.
- [3]. Bonazountas, M., Kallidromitou, D., Kassomenos, P., Passas, N. (2007). A decision support system for managing forest fire casualties. *Journal of Environmental Management* 84(4), 412-418.
- [4]. CFE, (2008). The Chamber of Forest Engineers' Commission Report on Forest Fire in Serik and Tasagil Forest Enterprise Directorates of Antalya Forest Regional Directorate on July 31st-August 4th 2008. The Chamber of Forest Engineers. Ankara. 9 p.
- [5]. Dimopoulou, M., Giannikos, I. (2004). Towards an integrated framework for forest fire control. *Eur. J. Oper. Res.* 152, 476-486.
- [6]. GDF, (2008). *Fire Action Plan*. General Directorate of Forestry. 106 p.
- [7]. Keramitsoglou, I., Kiranoudis, C.T., Sarimveis, H., Sifakis, N. (2004). A multidisciplinary decision support system for forest fire crisis management. *Environmental Management*, 33(2), 212-225.

FLOCCULATION OF WASTE WATER FROM COAL WASHING PLANT BY POLYMERS IN TURKEY

Selma DÜZYOL

Selcuk University, Department of Mining Engineering, 42075, Konya, Turkey.
selmad@selcuk.edu.tr

Berk ERÖZ

Tevfik AĞAÇAYAK
Ali ARAS

Abstract

Fine and ultrafine particles come into existence in consequence of the size reduction operations during the preparation for industrial requirement and causing the environmental problems if not evaluated as raw material. These fines are difficult to separate from the recycled plant water by gravity methods. Some chemicals called polymers are used in the size enlargement of fine particles to settle quicker by increasing gravity forces on the flocculated larger particles. In this study, the flocculation behaviour of waste water from the coal washing plant was investigated. The flocculation tests were performed in the presence of different types of polymers at different polymer dosages. Flocculation time and pH of suspension were also studied. Flocculation of suspensions was ascertained by turbidity (nephelometric turbidity unit, NTU) measurements. After flocculation experiments, the residual turbidity of suspension was measured and the best results at optimum conditions were obtained as 12.3 NTU, 15.1 NTU and 8.9 NTU for A-150 (anionic), FLOC 27 AS (anionic) and N-100 (non-ionic) polymers, respectively.

Keywords: *Flocculation, polymer, waste water, turbidity*

1. INTRODUCTION

Coal is an important fossil fuel used as a main source of energy in Turkey. However, it is required to clean from the inorganic impurities by washing due to its heterogeneous structure. Also, one of the important problems is to get rid of the ultra-fine particles occurring as the consequence of size reduction operations from the recirculating plant water after the beneficiation operations. Flocculation enables both recycling of plant water without these impurities and fast settling of fine and ultrafine particles. Flocculation method has also been applied in several industries such as mineral processing, water treatment, processing of industrial wastes for instance paper, textile, sugar etc. either to produce pure water or dewatering of concentrate. The turbidity value of suspension implies the suspended particulate matters in the suspension. Therefore, turbidity is the simple way to measure the performance of flocculation.

The aggregation of fine particles using polymers having high molecule weight and dissolubility in water is known as flocculation. Polymeric flocculants are long-chain molecules with high molecular weights and are characterized by their ionic nature as cationic, anionic and non-ionic. They may be classified as natural, synthetic or modified. The polymer adsorption onto the mineral surfaces is occurred by either charge neutralization or bridging [1]. Charge neutralization is usually weak and reversible and ensured from electrostatic and van der Waals forces [2]. Bridging which in consequence of chemical adsorption is usually strong and irreversibly occurs through covalent bonding between the adsorbate and the surface species on the solid [1].

The adsorption of anionic polymers on the negative mineral surface is commonly attributed to cation bridging [3,4]. The non-ionic polymers adsorb on coal and mineral particles mainly by means of hydrogen bonding or hydrophobic interactions [5,6]. For a successful flocculation, some parameters such as pH, ionic strength, type of flocculants and its properties including molecular weight, charge density, and molecular structure are counted as significant variables [4,7-11].

In this study, flocculation of waste water from a coal washing plant was studied by the use of three types of polymers. The effects of some parameters such as pH, stirring speed, polymer dosage and flocculation time were investigated. The flocculation performance was evaluated by means of turbidity measurements.

2. EXPERIMENTAL

2.1. Materials

The waste water from coal washing plant was used in the flocculation experiments. The waste water brought as slurry in a closed vessel was stirred continuously to prevent the settling of solid particles in the suspension. The solid ratio of waste water was determined as 4.4% (w/w).

Three types of polymers as A-150, FLOC 27-AS and, N-100 flocculants were prepared as 0.1% (w/w) solutions in the present work. The pH adjustment of suspension was executed by using sodium hydroxide and hydrochloric acid (Merck) and measured by a Jenco 6230 digital pH meter. All chemicals were analytical grade and distilled water was also employed for the preparation of the solutions throughout the experimental works.

2.2. Flocculation

The 250 cm³ volume of suspension was agitated for 1 min to realize dispersion thoroughly at a rotating speed of 500 rpm in a cylindrical cell of 400 cm³ with four baffles. These baffles were attached to the interior surfaces of cell in order to increase the collision efficiency. After 5 min of conditioning time for pH adjustment, the polymer was moderately added into the suspension. The suspension was then stirred for another 3 min to allow the flocculation. At the end of the flocculation time, the stirring speed was decreased to 180 rpm so as to let floc growth for 3 min. After the system was stopped, the suspension was taken in to the volume of 250 ml of the graduated measure and allowed for 20 min to floc settling. At the end of the settling time, certain amount of supernatant was taken from the certain part of the suspension by using a special syringe for turbidity measurements.

The residual turbidity of suspension was measured to be 345 NTU by Velp TB1 turbidimeter after sedimentation time of 20 min without addition of polymer. The initial turbidity of suspension was also measured at the beginning of the experiments as to be 1410 NTU.

3. RESULTS AND DISCUSSIONS

3.1. The Effect of pH

The effect of pH on the turbidity of waste water of coal suspension in the presence of 4 mg/L polymer is given in Fig. 1. The stirring speed and flocculation time were kept constant as 500 rpm and 3 min, respectively. The anionic polymers A-150 and 27-AS showed similar behaviour and minimum turbidity of suspension was reached at pH=10.5. For non-ionic polymer (N-100) the pH of suspension did not affect the turbidity of suspension except from the acidic medium. Therefore, the pH of the suspension was kept constant as 10.5 for A-150 and 27-AS and 8 which is the natural pH of the suspension for N-100 polymers.

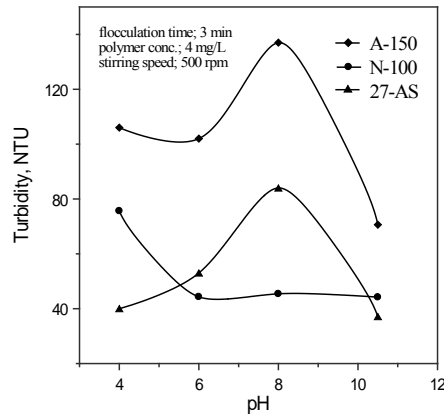


Figure 1. Effect of pH on the turbidity of waste water of coal suspension

3.2. The Effect of Stirring Speed

The influence of stirring speed on turbidity was also investigated and the obtained results are given in Fig. 2. The turbidity of suspension was decreased with the increasing of stirring speed as seen from the Fig. 2. However, intense agitation was led to an increase of the turbidity value of suspension. As it is known that the increase in the stirring speed promotes the adsorption rate of polymers [12]. However, large flocs with high settling rates occur in low stirring speeds, while very high stirring speed during flocculation results in irreversible floc degradation leading to much reduced settling rates [13]. Hence, the turbidity of suspension rather depends on the stirring speed. Consequently, 350 rpm were determined to be appropriate stirring speed for all polymer types.

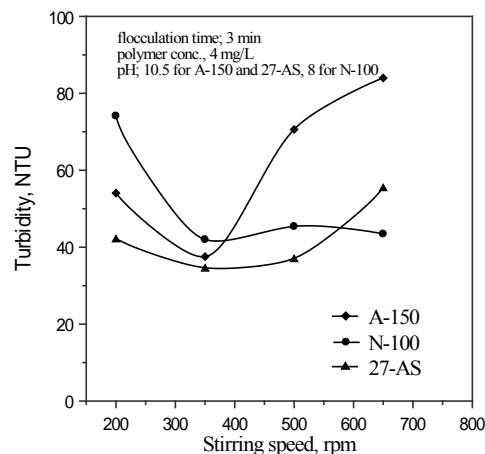


Figure 2. Effect of stirring speed on the turbidity of waste water of coal suspension

3.3. The Effect of Polymer Dosage

Fig. 3 shows the effect of polymer dosages on the residual turbidity of waste water of coal suspensions. The turbidity value of suspension was 345 NTU in the absence of polymer. The ability of polymers on the turbidity removal was clearly seen from the Fig. 3. Three types of polymers were influential for flocculation of suspension in small quantities. However, the best turbidity results were obtained for N-100 and 27-AS at

20 mg/L as to be 8.9 NTU and 15.1 NTU, respectively. As the polymer concentration was increased, more particles were brought together and the size of composed flocs became larger. Therefore, these flocs settled more quickly causing a decrease in the turbidity of suspension. Although the increase in A-150 dosage did not dramatic change the turbidity. Also, the turbidity of suspension was 37.5 NTU in the presence of 4 mg/L of A-150 polymer. The optimum polymer dosage was determined for A-150 as 4 mg/L and 20 mg/L for the others.

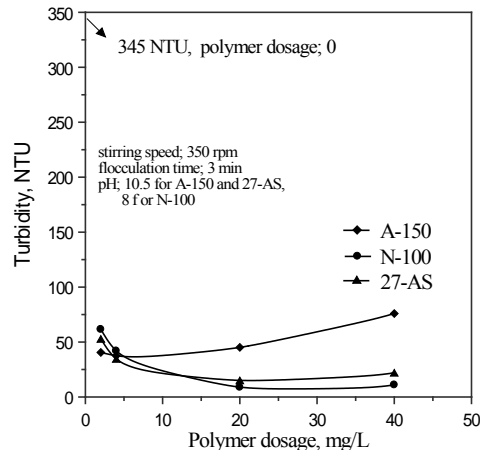


Figure 3. Effect of polymer dosage on the turbidity of waste water of coal suspension

3.4. The Effect of Flocculation Time

The extent of surface coverage is significantly affected the conditioning time for the mineral with the polymer. Extended conditioning may possibly result in re-dispersion due to the saturation coverage of the particle surface by the polymer molecules [14,15]. The variation of turbidity of suspension depending on flocculation time is shown in Fig. 4. The optimum flocculation time for N-100 and 27-AS was determined to be 3 min and was 10 min for A-150. The best turbidity results were reached as 12.3 NTU, 15.1 NTU and 8.9 NTU for A-150, 27-AS and N-100 polymers, respectively.

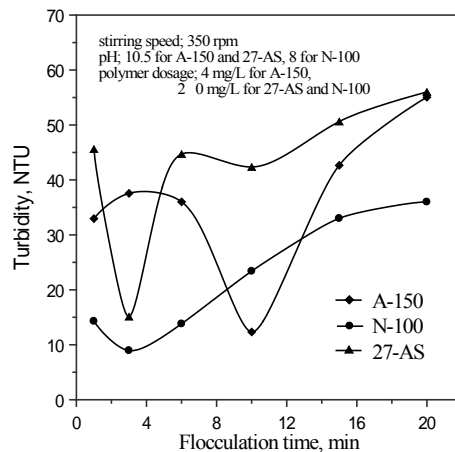


Figure 4. Effect of flocculation time on the turbidity of waste water of coal suspension

4. CONCLUSIONS

Both anionic and non-ionic polymers were flocculated well the waste water of coal suspension. Optimum pH values of suspensions were determined as 10.5 and 8 for A-150 and 27-AS and N-100 polymers, respectively.

The turbidity of suspension was very depended on stirring speed. The best results were obtained at 350 rpm of stirring speed for three types of polymers.

The optimum polymer dosages were specified as 20 mg/L for N-100 and 27-AS. In addition, 4 mg/L of dosage was favorable for A-150.

The flocculation time was also rather effective on the turbidity of suspension. The minimum turbidity values were reached at 3 m in for N-100 and 27-AS and 10 m in for A-150 polymers. The measured minimum turbidity values were 8.9, 12.3 and 15.1 for N-100, A-150 and 27-AS polymers, respectively.

ACKNOWLEDGMENT

The financial support given by the Scientific Research Project Fund of Selcuk University on the present work is greatly acknowledged.

REFERENCES

- [1]. Y. A. Attia, *Flocculation*, in: *Colloid Chemistry in Mineral Processing*, New York: Elsevier, 277–308, 1992.
 - [2]. G. D. Parfitt and C. H. Rochester, *Adsorption of small molecules*, in: *Adsorption from Solution at the Solid/Liquid Interface*, Academic Press, New York 3–48, 1983.
 - [3]. A. Sworska, J. S. Laskowski and G. Cymmerman, “Flocculation of the Syncrude fine tailings Part I. Effect of pH, polymer dosage and Mg^{2+} and Ca^{2+} cations”. *International Journal of Mineral Processing*, vol. 60, pp. 143–152, 2000.
 - [4]. B. Yarar, “Evaluation of Flocculation and Filtration Procedures Applied to WSRC Sludge”, Colorado School of Mines, Report no: DE-AC09-96SR18500, 34, 2001.
 - [5]. M. J. Littlefair and N. R. S. Lowe, “On the selective flocculation of coal using polystyrene latex”. *International Journal of Mineral Processing*, vol. 17, pp. 187–203, 1986.
 - [6]. E. Sabah and I. Cengiz, “An evaluation procedure for flocculation of coal preparation plant tailings”. *Water Research*, vol. 38, pp. 1542–1549, 2004.
 - [7]. M. F. Werneke, “Application of synthetic polymers in coal preparation”. *Soc. Min. Eng. IME*, pp. 79–106, 1979.
 - [8]. G. Atesok, “Adsorption of polymers”. *Bull. Tech. Univ. Istanbul*, vol. 41, pp. 13–32, 1988.
 - [9]. R. Hogg, “Flocculation and dewatering”. *International Journal of Mineral Processing*, vol. 58, pp. 223–236, 2000.
 - [10]. A. R. Karbassi, S. S. Bassam and M. Ardestani, “Flocculation of Cu, Mn, Ni, Pb, and Zn during Estuarine Mixing (Caspian Sea)”. *International Journal of Environmental Research*, vol. 7(4), pp. 917–924, 2013.
 - [11]. S. Duzyol, “Evaluation of flocculation behavior of marble powder suspensions”. *Physicochemical Problems of Mineral Processing*, vol. 51(1), pp. 5–14, 2015.
 - [12]. R. R. Stromberg and G. M. Kline, “Adsorption of polymers on glass and other substances”. *Mod. Plast.*, 38(8) 123; 38(9) 241, 1961.
 - [13]. P. Oforia, A. V. Nguyen, B. Firth, C. McNally and O. Ozdemir, “Shear-induced floc structure changes for enhanced dewatering of coal preparation plant tailings”. *Chemical Engineering Journal*, vol. 172, pp. 914–923, 2011.
 - [14]. A. S. Michaels, “Aggregation of suspensions by polyelectrolytes”. *Ind. Eng. Chem.*, vol. 46, pp. 1485, 1954.
 - [15]. J. A. Kitchener, “Principles of action of polymeric flocculants”, *Br. Polym. S.*, vol. 4, pp. 217, 1972.
-

KINETICS OF FINE DRY GRINDING OF BARITE IN A LABORATORY STEEL BALL MILL

Ali ARAS

Selçuk University, Department of Mining Engineering, Konya, Turkey.
aliaras@selcuk.edu.tr

Salih AYDOĞAN

Selçuk University, Department of Mining Engineering, Konya, Turkey.
saydogan@selcuk.edu.tr

Alper ÖZKAN

Selçuk University, Department of Mining Engineering, Konya, Turkey.
alpozkan@selcuk.edu.tr

Abstract

Dry grinding properties of barite were investigated with the emphasis on a kinetic study in a laboratory ball mill. The S_i (specific rate of breakage) and $B_{i,j}$ (primary breakage distribution) values were determined by using the single sized feed fractions of $-850+600\ \mu\text{m}$, $-600+425\ \mu\text{m}$ and $-425+300\ \mu\text{m}$. Dry grinding of single size intervals showed that this material followed the first-order breakage law. The $B_{i,j}$ values obtained for the sample were $\gamma=0.80$, $\phi=0.43$ and $\beta=3.69$. The breakage parameters of barite in terms of the S_i , aT , \dot{q} and Y values were also compared to some materials reported previously.

Keywords: Ball milling, barite, breakage, grinding kinetics

1. INTRODUCTION

Breaking and especially grinding are important processes that are used for the size reduction of materials, production of large surface area and liberation of valuable minerals from their matrices. This processes increase costs in mineral processing. In fact, a very little amount of the energy that is consumed in comminution can be used effectively and a large amount of energy is wasted in various ways (noise, heat, etc.). Production of an excessive amount of fine material will both increase the grinding cost and prevent obtaining the required product.

The kinetics of grinding in ball mills can be analyzed using two major models: the energy-size relationship and the population-balance models. The latter has eclipsed the energy-size relationship because it can explain grinding rates in greater detail. By describing the evolution of the entire size distribution with time in batch grinding, the population-balance model uses two primary kinetic functions; these are the breakage-rate function and the breakage-distribution function ([1], [2]).

This study reports on the kinetics of dry grinding of barite obtained from Huyuk and compares the results of dry grinding of barite to those of different brittle materials.

2. MATERIALS AND METHODS

High purity barite sample was obtained from Huyuk district of Konya. The density of the sample, measured by a pycnometer, was determined as 4.35. The sample was crushed and prepared to $-850+600 \mu\text{m}$, $-600+425 \mu\text{m}$, and $-425+300 \mu\text{m}$ feed size fractions for the grinding experiments. These fractions were batch ground in a steel laboratory ball mill for 0.4, 1, 2, 4, 8, 16, 32 and 64 min of grinding times.

After each grinding period the balls were cleaned and removed from the mill. Then, a sample of approximately 45 g was taken from the ground material for screen analysis. The sample was transferred to a set of sieves arranged in $\sqrt{2}$ sequence. Each screen was washed with water for at least 5 minutes starting from the top size and then each screen was put into the oven to dry. The dried material remaining on each screen was dry sieved with a shaker. Then, each remaining fraction on the screen was weighed. Thereafter, the balls and screened material were returned to the mill for further grinding test. The properties of the ball mill used and grinding conditions are given in Table 1.

Table 1. Ball mill properties and grinding conditions

Mill	Inner diameter, mm	200
	Length, mm	191
	Volume, cm^3	6000
	Critical speed, rpm	101.1
	Operational speed, rpm	76
Media (Balls)	Material	alloy steel
	Diameter, mm	25
	Number	92
	Specific gravity, g/cm^3	7.8
	Fractional ball filling	0.2
	Powder-ball loading ratio	0.5
	Fractional powder filling	0.04

3. RESULTS AND DISCUSSION

3.1. Determination of the Specific Rates of Breakage

The first-order plots obtained for dry grinding of barite of $-850+600 \mu\text{m}$, $-600+425 \mu\text{m}$ and $-425+300 \mu\text{m}$ feeds were shown in Figure 1. As seen from Figure 1, S_i values increased as the feed sizes became coarser. That is, while the highest S_i value obtained was 1.18 min^{-1} for $-850+600 \mu\text{m}$, the lowest S_i value was 0.68 min^{-1} for $-425+300 \mu\text{m}$ feed. The initial grinding results obey the first-order breakage form;

$$w_i(t) = w_i(0) \exp(-S_i t) \quad (1)$$

Figure 2 shows the variation of the specific rates of breakage (S_i) against particle feed sizes, which is obtained from the first-order plots data as in Figure 1. The values of S_i can be fitted to the Eq. (2):

$$S_i = a_T (x_i / x_0)^\alpha \quad (2)$$

which gave an a_T value of 1.35 min^{-1} using $\alpha=0.80$, $x_i=850 \text{ }\mu\text{m}$ and $x_0=1000 \text{ }\mu\text{m}$.

3.2. The Primary Breakage Distribution Function Values

The equation for calculation of $B_{i,1}$ by the BII calculation method [2] is as following:

$$B_{i,1} \cong \frac{\log[(1 - P_i(0))/(1 - P_i(t))]}{\log[(1 - P_2(0))/(1 - P_2(t))]}, \quad i > 1 \quad (3)$$

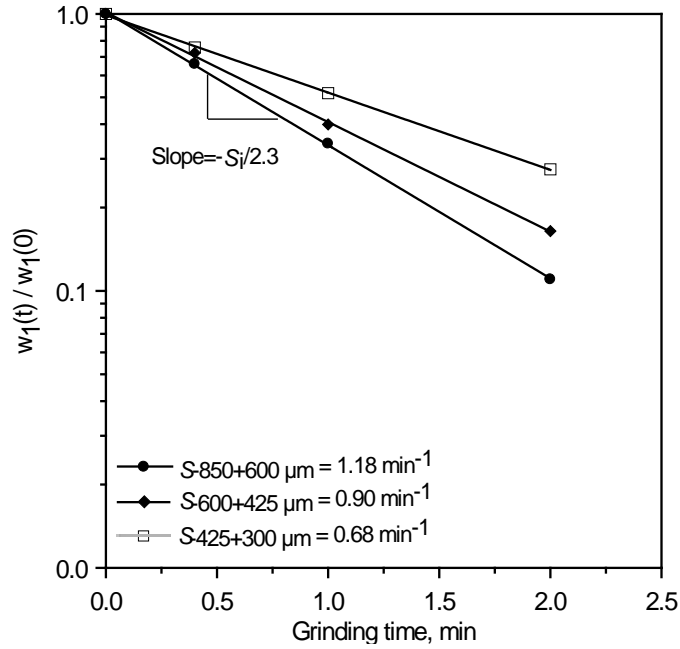


Figure 1. First-order plots for various feed sizes of barite

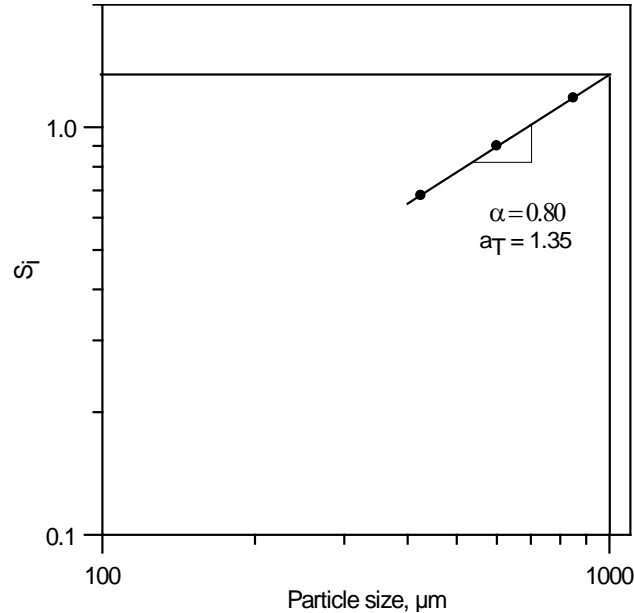


Figure 2. Variation of the S_i values of barite with particle size

where $P_i(0)$ = cumulative weight fraction at time 0 for size interval i , $P_i(t)$ = cumulative weight fraction at time t for interval i . The cumulative primary breakage distribution function determined using the BII calculation method is shown in Figure 3. The γ , ϕ , and β values of cumulative primary breakage distribution can be closely fitted by an empirical function;

$$B_{i,1} = \phi \left(\frac{x_{i-1}}{x_1} \right)^\gamma + (1-\phi) \left(\frac{x_{i-1}}{x_1} \right)^\beta, i > 1 \tag{4}$$

where x_i is the top size of the size interval indexed by i . The parameters γ , ϕ and β are characteristic of the barite sample being ground.

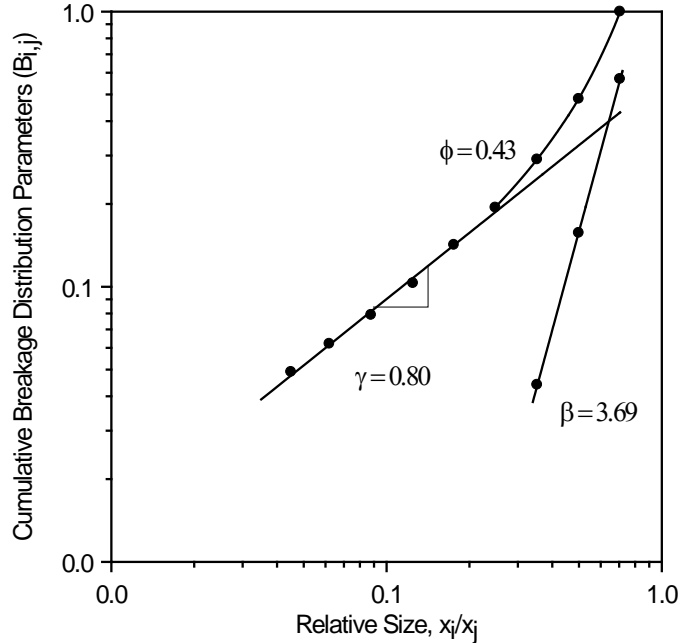


Figure 3. Primary breakage distribution function for barite

As seen from Figure 3, the breakage distribution parameters of barite were determined to be $\gamma=0.80$, $\phi=0.43$ and $\beta=3.69$. The comparison of the breakage parameters of barite in terms of the S_i , a_T , α and γ values to the other brittle materials (quartz, calcite and colemanite) reported previously in the literature [3], [4], [5] under similar experimental conditions is given in Table 2. From the Table 2, it is seen that barite is broken faster than quartz, calcite and colemanite in terms of the a_T and S_i values. On the other hand, barite produces finer material, compared to quartz, calcite and colemanite, by considering the γ value of $B_{i,j}$.

The dry grinding kinetics of barite obtained from Kahramanmaraş region was also studied ([4]). The researchers used a laboratory ball mill and studied under similar experimental conditions with this study. The characteristic breakage parameters determined for the barite used in their study were determined as follows: $a_T=1.10 \text{ min}^{-1}$, $\alpha=0.60$, $\gamma=0.80$, $\phi=0.70$ and $\beta=3.81$. These values are close to the data found in this study.

Table 2. Breakage parameters of barite, quartz, calcite and colemanite

Feed size, μm	Barite				Quartz*			
	S_i, min^{-1}	a_T, min^{-1}	α	γ	S_i, min^{-1}	a_T, min^{-1}	α	γ
-850+600	1.18				0.51			
-600+425	0.90	1.35	0.80	0.80	0.40	0.60	0.80	1.20
-425+300	0.68				0.32			
		Calcite**			Colemanite***			
-850+600	0.86				0.82			
-600+425	0.72	1.00	0.73	0.94	0.64	0.96	0.87	1.21
-425+300	0.53				0.45			

* [3]

** [4]

*** [5]

Figure 4 shows the particle size distributions obtained at various times of dry grinding of -600+425 μm barite feed in the ball mill. As can be seen, the 80% passing size of the material ground in the mill reached approximately 100 μm at a grinding time of 8 min.

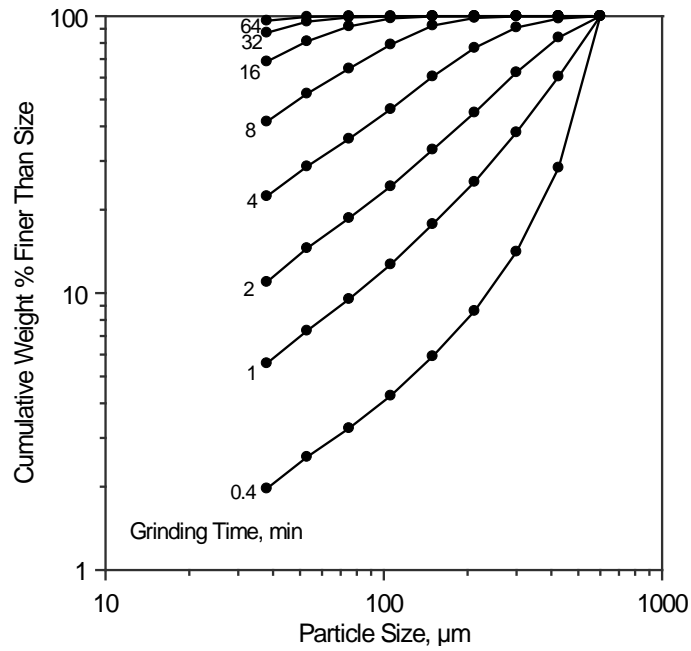


Figure 4. Product size distributions from dry grinding of $-600+425 \mu\text{m}$ barite

4. CONCLUSIONS

Dry grinding of single size intervals of barite followed the first-order breakage law. As the top sizes fed to the mill increase, the specific rate of breakage (S_i) values increase as well, indicating a more rapid breakage of the top sizes. It was found that the characteristic breakage parameters of barite were $a_T=1.35 \text{ min}^{-1}$, $\alpha=0.80$, $\gamma=0.80$, $\phi=0.43$ and $\beta=3.69$. When the breakage parameters of barite were compared to the other materials (such as quartz, calcite and colemanite) under similar experimental conditions, it can be said that barite is broken faster than quartz, calcite and colemanite in terms of the a_T and S_i values. Also, barite produces fine material compared to quartz, calcite and colemanite, in terms of the γ value of $B_{i,j}$.

ACKNOWLEDGMENT

The authors acknowledge the financial support of this study provided by Selcuk University Scientific Research Project Fund for project numbers: 06101010 and 15701192.

REFERENCES

- [1]. R.K. Rajamani, D. Guo, "Acceleration and deceleration of breakage rates in wet ball mills", *Int. J. Miner. Proc.*, 34, 103-118, 1992.
- [2]. L.G. Austin, R.R. Klimpel, P.T. Luckie, "Process Engineering of Size Reduction: Ball Milling", SME/AIME, New York, 1984.
- [3]. L.G. Austin, M. Yekeler, T.F. Dumm, R. Hogg, "The kinetics and shape factors of ultrafine dry grinding in a laboratory tumbling ball mill", *Part. Part. Syst. Charact.*, 7, 242-247, 1990.
- [4]. E. Teke, M. Yekeler, U. Ulusoy, M. Canbazoglu, "Kinetics of dry grinding of industrial minerals: Calcite and barite", *Int. J. Miner. Proc.*, 67, 29-42, 2002.
- [5]. A. Aras, A. Özkan, S. Aydoğan, "Kinetics of fine dry grinding of colemanite", *Proceedings of the 11. International Mineral Processing Symposium*, 2008, 57-62, Belek-Antalya, Turkey.

ASSESSMENT OF HEAVY METAL CONTAMINATION IN THE GOLDEN HORN ESTUARY SEDIMENTS, TURKEY

Bedri ALPAR

*Istanbul University, Department of Marine Geology and Geophysics, 34116, Fatih/İstanbul, Turkey.
bedrialpar@gmail.com*

Selma ÜNLÜ

Istanbul University, Institute of Marine Sciences and Management, Department of Physical Oceanography and Marine Biology, 34116, Fatih/İstanbul, Turkey, su@istanbul.edu.tr

Abstract

The Golden Horn is an urban estuary in the hearth of ancient Istanbul, Turkey. Rapid urban growth and uncontrolled industrial development (1950-1985) led to a severe increase in pollution levels of its water and cohesive sediments. The last mitigation solution was to bring the Black Sea's clean, but more saline, water into the Golden Horn through the Kağıthane stream which is started at the end of 2012. In order to assess the sediment quality and to highlight the anthropogenic contributions to heavy metal distributions, selected heavy metals in the surficial anoxic sediments were studied before (December-2012) and after (August-2013) the sea water pumped into the Golden Horn. Multiple chemometric approaches, geo-accumulation index and principal component analysis, indicated three different regions characterized by different heavy metal concentrations along the estuary, implying the possible effects of natural and anthropogenic sources. In August 2013, the metal concentrations show slight increments if compared to those measured before the pumping of sea water. The data sets were compared with Interim Sediment Quality Guideline and Probable Effect Level values. The ecotoxicological significance of Pb and Zn also increased at some specific places. Although it is early to evaluate that these findings are caused by the new hydrodynamic regime of the estuary, it is highly possible that flocculation have an impact on the large-scale events such as pollutant transport, deposition, and sedimentation in the estuary. Therefore, considering flocculation of cohesive sediments, sediment quality monitoring in the estuary must be continued regularly.

Keywords: *ecological risk, estuaries, guidelines, heavy metals, pollution, flocculation, sediment quality*

1. INTRODUCTION

Rapid urban growth and uncontrolled industrial development between 1950 and 1985 led to a severe pollution increment in the Golden Horn estuary (Figure 1). The siltation due to waste dump by streams caused anaerobic decomposition problems in this urban estuary. After many mitigation efforts the last one was to pump the Black Sea's clean, but more saline, water into the estuary through the Kağıthane stream. It started at the end of 2012.

The main scope of this study is to assess the sediment quality and highlight anthropogenic contributions of heavy metals in the bottom surficial anoxic and cohesive sediments of the Golden Horn estuary. In this context an assessment has been carried out for the selected heavy metals in the bottom sediment of the Golden Horn by comparing the samples collected before (December-2012) and after (August-2013) the sea water pumped into the Golden Horn.



Figure 1. The Golden Horn estuary is located at the junction of the Bosphorus Strait and the Sea of Marmara, Turkey. Rapid urban growth and uncontrolled industrial development (1950-1985) led to tremendous pollution at this historical recreational region.

2. METODOLOGY

Seasonal sediment samples were taken from the same stations in December 2012 and August 2013 (Figure 2). The sampling stations determined by Magellan ProFlex TM500 global position system. Top surface of the grabs, approximately 50 g, was removed using a plastic spoon and placed in a numbered plastic bag. The sampling depth was 3 cm to represent the same time interval required for accumulation of the sediment trend. The samples recovered were then kept frozen prior to chemical and granulometric analyses. In the laboratory, the samples were defrosted at room temperature, dried at 40°C to constant weight, then grounded in agate mortar and screened through a nylon sieve.

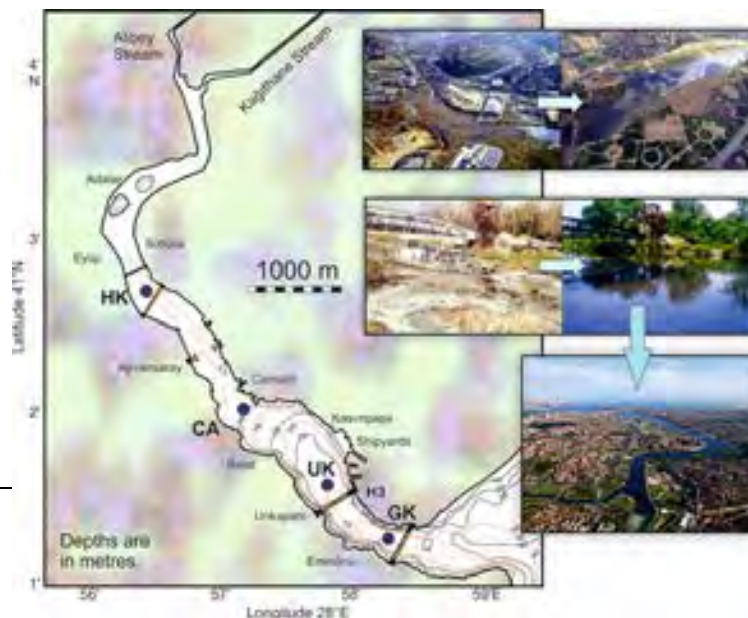


Figure 2. Many small and comprehensive projects were done to heal the ecologically unlivable conditions in the Golden Horn. Organic matter entrance has been limited by sediment dredging operations at the stream's mouth. They remained, however, far from initiating a large-scale transformation, especially for the bottom sediments. The last effort was to pump the Black Sea water via the Kağıthane stream. Figure shows the sediment stations visited in Dec. 2012 and Aug. 2013, before and after this pumping.

Grain-size analysis and classification followed Folk's (1974) methodology [1]. Coarser grained sediments ($<4\phi$ or 0.063 mm) were dry sieved, whilst fine-grained material ($>4\phi$) were analyzed using the hydrometer method. The dry percentages of sand ($>63\mu\text{m}$), silt ($2\mu\text{m}<\phi<63\mu\text{m}$), and clay ($<2\mu\text{m}$) were determined.

Element concentrations in the sediment samples were determined in the digested phase by Inductively coupled plasma mass spectrometry (ICP-MS) analysis at ACME Analytical Labs, Vancouver-Canada. All samples and blanks were analyzed in duplicates for quality assurance/quality control of laboratory analyses. OREAS24P and OREAS45E were used as the standard sediment sample for quality control of metal analyses. The measured concentrations of all metal analyzed were within the published metal contents given by Ore Research and Exploration Pty. Ltd. in 2012. Minimum detection limits for 0.25 g sediment were 0.01% for Al and Fe; 0.1 ppm for Ni, Cu, Cd and Pb; 0.2 ppm for Co; and 1 ppm for V, Cr, Mn, Zn and As. All the reagents and chemicals used were of analytical reagent grade suitable for ultratrace analysis.

3. RESULTS AND DISCUSSION

The adsorption and sedimentation processes of metals are usually related with grain size [2]. Grain size analysis demonstrated that the samples were mainly composed of fine-grained and cohesive sediments. The mud ratios of the sediments were always higher than 92%.

Cu, Pb, Zn and As indicated moderate to-significant enrichments while others minimal (Figure 3a). The metal concentrations were higher after the sea water pumping (Figure 3b). The highest increments were for As (average 8.6%), Fe (5.2%), Cr (4.6%) and Zn (4.0%). Unexpectedly Pb decreased slightly (10-20%) at the inner estuary (# CA and HK) while it increased 1.12-1.14 times at the outer estuary (# UK and GK) (Figure 3b). This explains the increment of the PLI for UK and GK (Figure 3c).

To evaluate ecotoxicological significance of heavy metal contamination, data sets were compared with the NOAA sediment quality guideline [3]. According to Interim Sediment Quality Guideline and Probable Effect Level values, the ecotoxicological significance of Pb and Zn increased at UK (Figure 3d). Even it needs further observations, we may suggest that these changes might be related with salinization of the surface water layer of the estuary (Figure 3e).

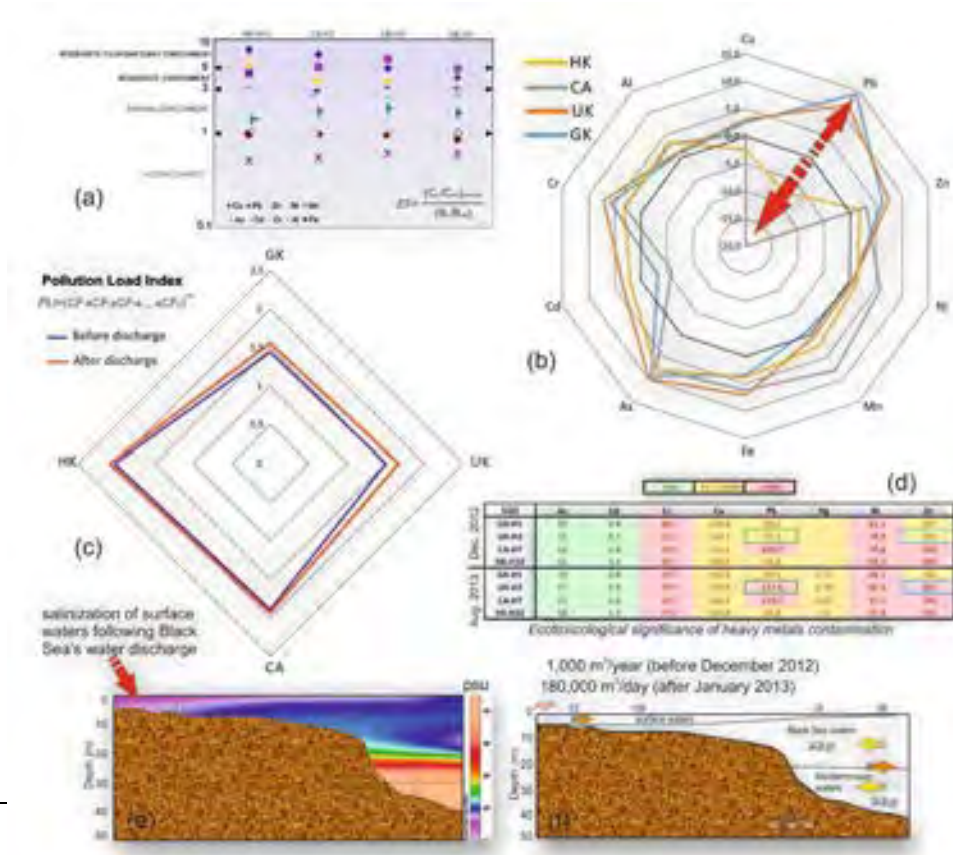


Figure 3. At the end of 2012, the municipality started to pump the Black Sea's clean but more saline (17 psu) water into the Golden Horn estuary (260,000 cubic meters per day) through the Kağıthane Stream. In August 2013 a slight increment in metal concentrations were measured as compared to those measured before the Black Sea water discharge. This figure shows how were the changes in the enrichment factors, pollution load indexes, ecological significance and salinization of surface waters after the sea water pumping process.

Before the sea water discharge, the riverine sediments had been transported by the stream's lower flow-rate fresh waters and then met with the brackish surface waters of the inner estuary. Following the Black Sea water discharge, however, riverine sediments are came in contact with saline water well before they are discharged into the estuary. Cohesive sediments tend to flocculate at moderate salinities if the physical conditions are appropriate [4]. Increased pollution load in the stream and flocculation are believed to be the main causes of the slight deterioration we assessed (Figure 3f).

4. CONCLUSIONS

In the late 2012 the Black Sea's clean and saline (17 psu) water was started to be pumped into the Golden Horn estuary through the Kağıthane stream. Naturally this process caused estuary's thin and fresh surface water to be denser, therefore to gain ability to carry the suspended particles farther, possibly up to the outer estuary where salinity increases to normal level. In fact, salinity affects sediment flocculation. Already at moderate salinities, cohesive sediments tend to flocculate if the physical conditions are appropriate. Increasing flocculation might have impact on the large-scale events such as pollutant transport, deposition, and sedimentation in the estuary.

As sedimentation is a continuous process, the sediment bed is probably the best medium to store records about the pollution history of a given water body. Although it is too early to make a final conclusion, we propose that the new hydrodynamic conditions in the estuary modulates metal transportation in water and deposition in sediment. Therefore, on the basis of our preliminary observations, we strongly suggest that sediment quality monitoring in the Golden Horn estuary must be continued regularly in the near future.

ACKNOWLEDGMENT

This study have been supported by the Research Fund of Istanbul University, the project UDP-52527 allocated to BA. The authors gratefully thank to the scientific crew and technicians for their help during field data collection.

REFERENCES

- [1]. R.L. Folk, *Petrology of sedimentary rocks*, Hemphill Publishing Co., Austin, TX, 182pp, 1974.
- [2]. M.P. Jonathan and V. Ram-Mohan, "Heavy metals in sediments of the inner shelf off the Gulf of Mannar, southeast coast of India", *Mar. Pollut. Bull.*, vol. 46 (2), pp. 258-268, 2003.
- [3]. D.D. MacDonald, C.G. Ingersoll and T.A. Berger, "Development and evaluation of consensus-based sediment quality guidelines for freshwater ecosystems", *Arch Environ Contam. Toxicol.*, vol. 39, pp. 20-31, 2000.
- [4]. A.J. Mehta, "Characterization of cohesive sediment properties and transport processes in estuaries" in *Lecture notes on Coastal and Estuarine Studies, Estuarine Cohesive Sediment Dynamics, Proceedings of a Workshop on Cohesive Sediment Dynamics with Special Reference to Physical Processes in Estuaries* (ed: A.J. Mehta), vol 14, pp. 290-325, 1986.

BIOGRAPHY

Bedri Alpar is Full Professor of Marine Sciences at the Istanbul University (IU). He was raised in Pendik, a village of Istanbul, Turkey. Then he attended the Geophysical Engineering Faculty of IU where he received his BSc in 1974 and MSc two years later. He went on to work for the Turkish Petroleum Corporation, the General Directorate of Mineral Research and Exploration, and the Department of Navigation, Hydrography and Oceanography of the Turkish Navy. Meanwhile he conducted academic research in Japan, UK and Italy. In 1993 he completed a Doctorate of Marine Science in the Institute of Marine Sciences and Geography at IU. In 1996 he joined the Institute of Marine Sciences and Management at IU as an associate professor and became a full professor of marine sciences in 2003. His skills are in marine geology and geophysics, seismic exploration, natural hazards, oceanography, and sediment pollution. He is author or co-author of +45 articles published in leading ISI journals, +180 peer-reviewed scientific manuscripts in international refereed journals and conferences, with +800 Web of Science and +1600 in Google Scholar citations.

PRODUCTION OF B4C REINFORCED ALSI7 FOAMABLE COMPOSITE MATERIALS AND INVESTIGATION OF THEIR MECHANICAL PROPERTIES

Arif UZUN

Kastamonu University, Department of Mechanical Engineering, 37100, Kastamonu, Turkey.
auzun@kastamonu.edu.tr

Mehmet TÜRKER

Gazi University, Department of Metallurgy and Materials Engineering, Ankara, Turkey,
mturker@gazi.edu.tr

Abstract

In this study, foamable composite materials were produced by powder metallurgy method. Experimental study, 1 wt. % foaming agent (TiH₂), 7 wt. % Si and 2, 4 and 6 wt. % B₄C with aluminum powder was mixed. Then mixed powders were pressed, extruded and rolled for the production of foamable materials. According to the experimental results, the relative densities of foamable materials increased by secondary operations and over 98% relative density were obtained. In addition the tensile strength of the composites increased with increase in the rate of B₄C.

Keywords: *Foamable material; Mechanical properties; B₄C; Aluminum*

1. INTRODUCTION

Many manufacturing methods can be applied depending on the matrix and the reinforcing element in the production of aluminum matrix composites. The most commonly used production methods are solid-state and liquid-state production methods. Powder metallurgy (PM), which is among solid-state production methods, enables the serial production and production of the direct net shaped parts thanks to mold cavities. In general, the method comprises mixing, pressing and sintering of the matrix alloy and the reinforcing element powders. But today, the condensation processes can be applied in addition to manufacturing processes in order to achieve high performance PM parts. The condensation processes are performed by applying the stress and temperature at the same time for the removal of residual pores. The condensation can be performed by processes such as hot isostatic pressing, powder forging, explosive compression, rolling and extrusion [1].

B₄C, used as the reinforcing element in Al matrix composite (AMC) materials, is a light weight material. In particular, its properties such as the modulus of elasticity, corrosion resistance, wear resistance, hardness, and thermal stability are high [2]-[4]. The lack of studies conducted on Al/B₄C powder metal materials compared to the liquid-state production methods is noteworthy in the literature. Most of the studies conducted on Al/B₄C composite materials produced by PM method aim to determine the mechanical properties of the produced materials. It is indicated that the wear resistance significantly increases with the increase in the amount of particles in B₄C reinforced Al matrix composites produced by hot isostatic pressing using PM method [5]. The study which was conducted by Zhang et al., revealed that the strength of Al6092/B₄C composites produced by the two different processes such as extrusion and hot pressing increased with increasing volume rate of particles [6]. Similar results have been stated in studies conducted by other researchers [7]. Meanwhile, there have been studies conducted regarding the optimization of production parameters in the production of Al/B₄C systems with similar production methods mevcuttur [8]. Onoro et al., investigated the effect of reinforcing element on the mechanical properties of composite materials, produced by hot extrusion, at high temperatures [9].

Foamable materials are precursor materials used prior to foaming in the production of metallic foam. The most important feature which distinguishes this material from other composite materials, is foaming agent it contains and the final shape. It is converted as metallic foam with heat treatments applied after the production. Therefore, mechanical and physical properties of the produced foams varies depending on the characteristics of the materials prior to foaming. Foamable materials can be produced by using powder metallurgy, semi-solid melt method, accumulated roll bonding, and friction stir welding methods [10]-[14]. Researchers have carried out not only production of foamable material but also foam production by using these methods. Foamable material production by powder metallurgy method is firstly started with mixture of the metal powders (alloy powders, reinforcing elements) and foaming agent powders [10], [15], [16]. Then, the mixture powders are compacted by using different techniques such as extrusion, pressing, or rolling for the production of foamable material [17]-[19]. Since these processes directly affect the density and foamability of the foam which is final product, it should be quite careful during the production process. Any residue or other errors in the structure can negatively affect a subsequent process. For example, the porosity rate at foamable materials produced without the use of adequate compression pressure increases. In this case, the non-homogeneous pore structures in the samples after foaming (metal foams) are obtained. The study conducted by Young and Kang emphasized that uniform foams can be obtained from the foamable Al6061 alloy containing pores less than 1% depending on the compression pressure and the heating temperature [20]. Ceramic particles such as SiC, Al₂O₃, TiB₂, and TiC are widely added in order to improve the stability of Al foams in this method [21]-[25].

In this study, B₄C reinforced AlSi7 foamable materials were produced by using powder metallurgy method and their mechanical properties were investigated. The mechanical properties of precursor material also affects the mechanical properties of foam structure in the metallic foam production by powder metallurgy method. The production of the precursor materials which have a perfect structure positively affects the quality of the foam. This study determined the effect of production processes on the physical and mechanical properties of B₄C reinforced foamable precursor materials which were produced before foaming.

2. EXPERIMENTAL

2.1. Materials

In experimental studies, Al (as the matrix material), TiH₂, (as the foaming agent), Si (as an alloying element) and B₄C powders (as reinforcement elements) were used for the production of B₄C reinforced foamable AlSi7 materials. Detailed physical properties of powders used in the experimental studies are given in Table 1.

Table 1. Detailed physical properties of powders

Powder	Supplier	Particle size (µm)	Particle shape	Purity (%)
Al	Ecka Granules	<160	Irregular	99,0
TiH ₂	Sigma-Aldrich	<44	Irregular and angular	98,0
Si	Atlantic Equipment Engineers	<10	Sharp edged and smooth	99,9
B ₄ C	NurolTeknology	<10	Angular	-

2.2. Production of foamable materials

The starting materials (7 wt. % Si, 1 wt. % TiH₂, 2, 4 and 6 wt. % B₄C) were blended with the base aluminum powder in a three-dimensional mixer for 30 minutes. The mixture powders were cold compacted under 400 MPa in a steel die. These samples were pre-sintered to facilitate extrusion process at the temperature of 550 °C for 60 min. The extrusion process was carried out at 550 °C before rolling in order to produce foamable precursor samples. After extrusion, the rolling process were applied to the powder metal block samples in order to make the plate thickness of 5 mm. Figure 1 illustrates schematically the production process.

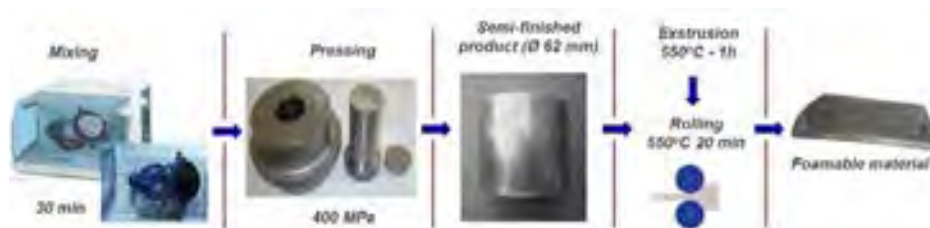


Figure 1. Schematic view of the production process

2.3. Characterizations

Tensile tests on a universal tensile testing machine were carried out to measure the tensile strength of the foamable materials, according to ASTM-E8. Vickers micro hardness was measured with 200 g load and a dwell period of 10 s. Several measurements were done for each hardness value. Microstructure examinations were done using scanning electron microscope (SEM). The specimens, which were taken from the middle zone, were prepared by standard metallographic techniques.

3. RESULT AND DISCUSSIONS

3.1. Change of Density

Secondary operations such as extrusion, rolling, and forging in addition to the compression processes can be applied in order to obtain PM products with high density and low porosity in the production of Al-based composite materials [26]. However, the deformation occurring in pre-formed materials produced during these process brings problems such as the cracking. Abdel-Rahman and El-Sheikh tried to explain the effect of the relative density on deformation feature at PM components. According to the researchers, there is a need for high stresses for deformation of materials with high relative density [27].

Figure 2 illustrates graphic of the density variation of B₄C reinforced foamable composite materials depending on secondary operations. When the graphic was examined, the increase in the amount of particles reduced the relative density of the samples from approximately 94 % to 90 % after pressing. However, this density difference (4 %) reduced to about 2% with extrusion and to 1% with rolling. In all three stages, the increase in the amount of B₄C had a reducing effect on the relative density of the samples. It was observed that as a result of rolling process, the values of the relative density in B₄C-free samples increased at the rate of 5 %. This difference increased to 8 % with the increase in the amount of B₄C (6 %). Therefore, it could be asserted that secondary operations had a positive effect on the relative density values of the foamable material containing B₄C.

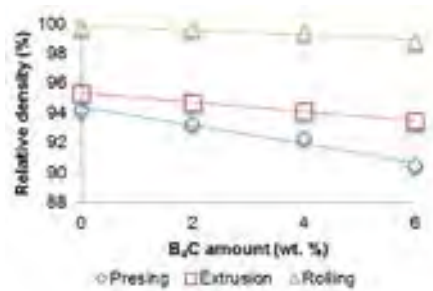


Figure 2. The relative density variation of B₄C reinforced foamable composite materials depending on secondary operations

Table 2 illustrates the average density variations obtained in the samples as a result of applied secondary operations. The increase occurring in the deformation of the foamable materials based on extrusion and rolling processes applied after pressing led to an increase in the relative density.

Table 2. The average density variations obtained in the samples as a result of applied secondary operations

PM block samples	Sample Code	Compaction processes	Bulk density (g cm ⁻³)	Relative density (%)	Theoretical density (g cm ⁻³)
Al	B ₀	Presing	2.53	94.19	2.686
		Extrusion	2.56	95.30	
		Rolling	2.68	99.78	
2 % B ₄ C reinforced Al	B ₂	Presing	2.50	93.21	2.682
		Extrusion	2.54	94.70	
		Rolling	2.67	99.65	
4 % B ₄ C reinforced Al	B ₄	Presing	2.47	92.23	2.678
		Extrusion	2.52	94.10	
		Rolling	2.66	99.42	
6 % B ₄ C reinforced Al	B ₆	Presing	2.42	90.46	2.675
		Extrusion	2.50	93.45	
		Rolling	2.64	98.80	

3.2. Examination of Microstructure

Figure 3 shows SEM images and EDS analysis values of 6% B₄C reinforced/unreinforced pressed samples. When the images were examined, the pores around TiH₂ and Si particles in B₄C-free samples were observed (Figure 3a). A similar situation was also observed in samples containing 6% B₄C. In particular, it was observed that the interface compatibility between the matrix and B₄C particles, which were detected by EDS analysis, was not sufficient (Figure 3b-c).

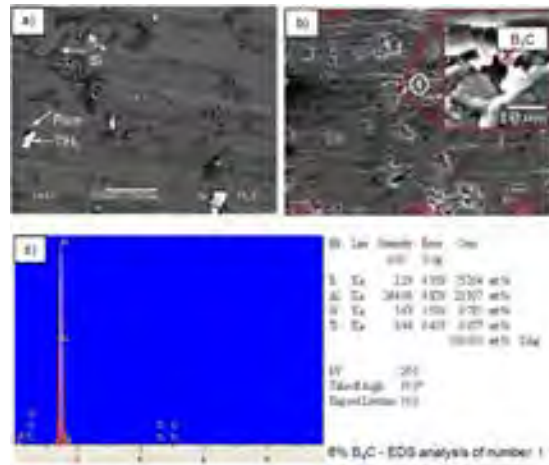


Figure 3. SEM images and EDS analysis of the pressed 6% B₄C reinforced/unreinforced samples a) Unreinforced, b) 6% B₄C reinforced, c) 6% B₄C reinforced-EDS analysis of number 1

Figure 4 illustrates SEM images and EDS analysis of 6% B₄C reinforced/unreinforced extruded samples. When the images were examined, the pores as the pressed samples around TiH₂ and Si particles in the structure of B₄C-free samples were not found (Figure 4a). Especially, it could be asserted that the interface compatibility between the matrix and Si particles was sufficient. It was observed that the interfacial compatibility of particles with matrix developed compared to the pressing process in 6% B₄C reinforced samples (Figure 4b, c). This situation had an effect increasing the relative density.

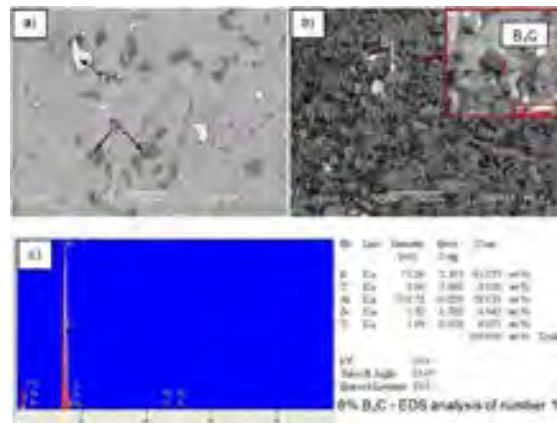


Figure 4. SEM images and EDS analysis of the extruded 6% B₄C reinforced/unreinforced samples a) Unreinforced, b) 6% B₄C reinforced, c) 6% B₄C reinforced-EDS analysis of number 1

Figure 5 illustrates SEM images and EDS analysis of 6% B₄C reinforced/unreinforced rolled samples. The pores in the pressed and extruded samples, were eliminated by rolling and particles were directed toward the rolling direction (Figure 5a,c,d). Microstructure images of 6% B₄C reinforced samples after the rolling, it was observed that the interfacial compatibility of particles with matrix developed compared to pressing and extrusion in these samples (Figure 5b, e).

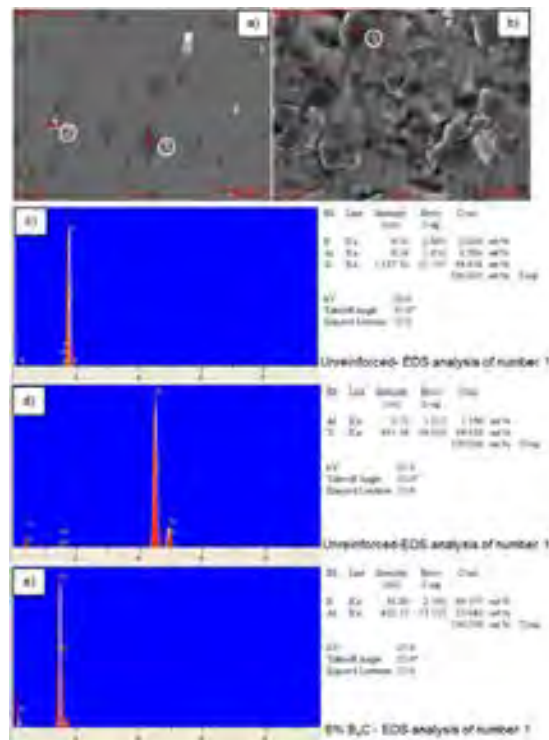


Figure 5. SEM images and EDS analysis of the rolled 6% B₄C reinforced/unreinforced samples a) Unreinforced, b) 6 % B₄C reinforced, c,d) Unreinforced-EDS analysis of numbers 1 and 2, e) 6 % B₄C reinforced-EDS analysis of number 1

Figure 6 shows the variance of color distribution of each element in elemental mapping on SEM-EDS images of samples. Accordingly, it could be asserted that the particles generally had homogenous distribution in the Al matrix with the increase in the amount of B₄C. However, the particles were oriented and approached to each other due to reduction in cross-sectional area of the samples during the rolling process (Figure 5a). This situation occurred by radial forces generated during the deformation. Furthermore, the radial forces caused a significant reduction in the number of pores in the structure of the foamable material. Banhart indicated that a significant pores or cracks were removed by making foamable materials to be exposed to rolling and foaming agent could be more retained in the matrix [28]. In the study conducted by Lee et al., the cold rolling process after the extrusion led to the breakage of the interfacial bond between particles and the matrix and the breakage of the TiH₂ particles. Therefore, this reduced the foaming capability of the foamable materials [29]. In this study, the significant particle breaking by rolling was not observed. Furthermore, the interface between the particles with the matrix developed. This is thought to be associated with the fact that the rolling process was performed at 550°C and the particles were easily replaced in the ductile matrix with increasing formability. The relative densities of foamable materials after the rolling was over 98 %. In their study, Paulin et al., reported that the relative density was at least 98% in terms of foa mability at compression of t he foamable materials [30]. Even a single compression technique applied to the foamable materials may affect the foaming behavior [31]. On the other hand, the secondary operations such as extrusion and rolling were used for compression of the foamable materials in this study. In the line of purpose of this study, especially the necessity of these operations is understood considering the dimensional limitations in foamable material production by using powder metallurgy method.

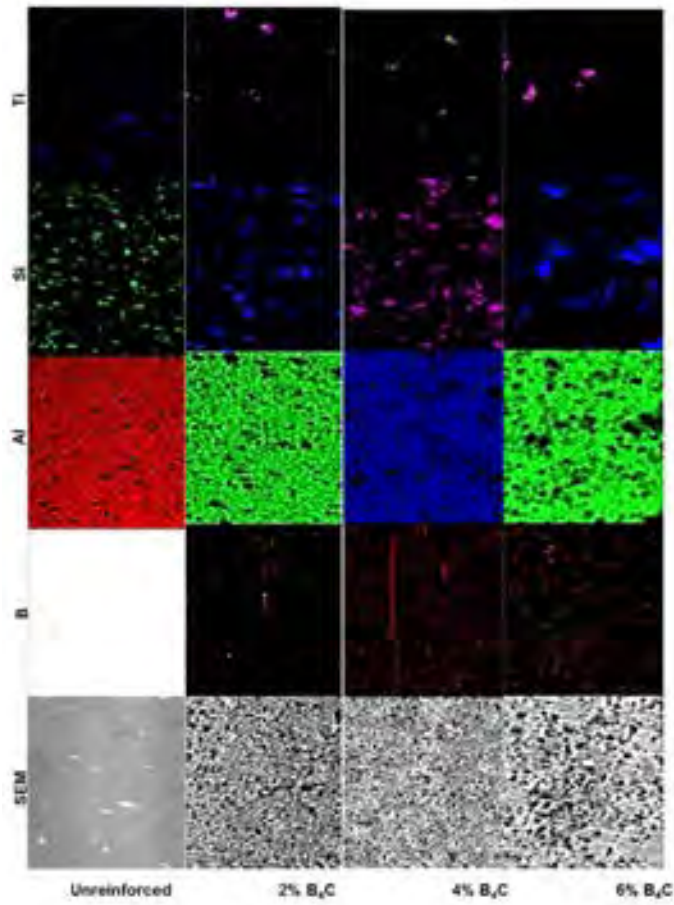


Figure 6. The variance of color distribution of each element in elemental mapping on SEM-EDS images of rolled samples (Fast Map images)

3.3. Tensile Properties

Table 3 illustrates tensile test results of B₄C reinforced foamable AlSi7 materials. When the table was examined, the maximum tensile strength was obtained with 216 MPa at 6% B₄C reinforced samples. On the other hand, the minimum tensile strength was obtained with 193 MPa at B₄C unreinforced samples. In foamable materials, the tensile strength increased with increase in the amount of B₄C; whereas, the ductility decreased. It is thought to be associated with the fact that B₄C particles in the structure caused strain hardening during the plastic deformation [32]. This case is strengthened by hardness values increased with the addition of B₄C in AlSi7 foamable material (Figure 7). Moreover, the cracks, voids or pores in the structure can cause similar effects. Thus, the graphic in Figure 1 shows that the relative density reduced with increase in the amount of B₄C before.

Table 3. Tensile test results of B₄C reinforced/unreinforced foamable AlSi7 materials

Samples	UTS* (MPa)	Elongation _{UTS} (%)	Breaking elongation (%)
0% B ₄ C	193	10,43	13,43
2% B ₄ C	193	8,19	11,61
4% B ₄ C	208	8,27	10,04
6% B ₄ C	216	7,24	8,62

UTS*: Ultimate tensile strength

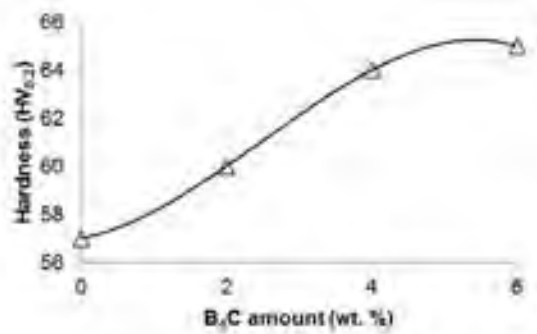


Figure 7. Variations of hardness value of the samples as a function of B₄C content

4. CONCLUSION

In this study, production of B₄C reinforced AlSi7 foamable composite materials and their mechanical properties were investigated. The relative densities of foamable materials increased by secondary operations and over 98% relative density were obtained. The tensile strength and hardness of the composites increased with B₄C addition.

ACKNOWLEDGMENT

The authors wish to thank The Scientific Research Project Unit of the Gazi University (Project number - 07/2012-44) for support.

REFERENCES

- [1]. R.M. German, *Powder Metallurgy and Particulate Materials Processing*, S.Saritas, M.Turker, N. Jr., Ed. Ankara, Turkey: Turkish powder metallurgy association, 2005.
- [2]. J. Jung, and S. Kang, "Advances in manufacturing boron carbide-aluminum composites," *Journal of the American Ceramic Society*, vol. 87(1), pp. 47-54, 2004.
- [3]. A.R. Kennedy, "The microstructure and mechanical properties of Al-Si- B₄C metal matrix composites," *Journal of Materials Science*, vol. 37, pp. 317-323, 2002.
- [4]. K.B. Khan, T.R.G.Kutty, and M.K. Surappa, "Hot hardness and indentation creep study on Al-5% Mg alloy matrix-B₄C particle reinforced composites," *Materials Science and Engineering A*, vol. 427, pp. 76-82, 2006.
- [5]. F. Tang, X. Wu, S. Ge, J. Ye, H. Zhu, et al. "Dry sliding friction and wear properties of B₄C particulate-reinforced Al-5083 matrix composites," *Wear*, vol. 264, pp. 555-561, 2008.
- [6]. H. Zhang, K. T. Ramesh, and E.S.C. Chin, "High strain rate response of aluminum 6092/B₄C composites," *Materials Science and Engineering A*, vol. 384, pp. 26-34, 2004.
- [7]. L.E.G.Cambronero, E. Sanchez, J.M. Ruiz-Roman, and J.M. Ruiz-Prieto, "Mechanical characterization of AA7015 aluminum alloy reinforced with ceramics," *Journal of Materials Processing Technology*, vol. 143-144, pp. 378-383, 2003.
- [8]. J.Abenojar, F. Velasco, and M.A. Martinez, "Optimization of processing parameters for the Al+10%B₄C system obtained by mechanical alloying," *Journal of Materials Processing Technology*, vol. 184, pp. 441-446, 2007.
- [9]. J. Onoro, M.D. Salvador, and L.E.G. Cambronero, "High-temperature mechanical properties of aluminum alloys reinforced with boron carbide particles," *Materials Science and Engineering A*, vol. 499(1-2), pp. 421-426, 2009.
- [10]. J. Banhart, "Manufacturing routes for metallic foams," *Journals of Materials*, vol. 52, pp. 22-27, 2000.
- [11]. V.Gergely, and B. Clyne, "The FORMGRIP Process: Foaming of reinforced metals by gas release in precursors," *Advanced Engineering Materials*, vol. 2, pp. 175-178, 2000.
- [12]. Y.Hangai, and T. Utsunomiya, "Fabrication of porous aluminum by friction stir processing," *Metallurgical and Materials Transactions A*, vol. 40, pp. 275-277, 2009.
- [13]. K.Kitazono, Y. Kikuchi, E. Sato, and K. Kuribayashi, "Anisotropic compressive behavior of Al-Mg alloy foams manufactured through accumulative roll-bonding process," *Materials Letters*, vol. 61, pp. 1771-1774, 2007.
- [14]. N.Li, S.Xing, P.Bao, and Z. Liu, "A research on fabrication of aluminum foam precursor using semi-solid melt," in *Proc. 2nd International Conference on Mechanical and Electronics Engineering*, 2010, pp.49-54.
- [15]. J. Banhart, "Manufacture, characterization and application of cellular metals and metal foams," *Progress in Materials Science*, vol. 46, pp. 559-632, 2001.
- [16]. J. Banhart, "Aluminium Foams: On the road to read to read applications," *Mrs Bulletin*, pp. 290-295, 2003.
- [17]. F. Baumgärtner, I. Duarte, and J. Banhart, "Industrialization of powder compact foaming process," *Advanced Engineering Materials*, vol. 2, pp. 168-174, 2000.
- [18]. J. Banhart, "Metallic foams: challenges and opportunities," in *Proc. Eurofoam2000*, MIT-Verlag Bremen, 2000, pp. 13-20.
- [19]. H.P.Degischer, B. Kriszt, "Handbook of Cellular Metals: Production, Processing and Applications," Wiley-VCH, Weinheim, 2002.
- [20]. S.W. Young, and C.G. Kang, "Fabrication of foamable precursors by powder compression and induction heating process," *Metallurgical and Materials Transactions B*, vol. 35, pp. 769-776, 2004.

-
- [21]. S.Asavavisithchai, and A. Opa, "Effect of TiC particles on foamability and compressive properties of aluminium foams," *Chiang Mai Journal of Science*, vol. 37(2), pp. 213-221, 2010.
- [22]. U.Gokmen, and M. Turker, "Effect of Al₂O₃ addition on the foamability behavior of aluminum and alumix 231 based metallic foam," *Journal of the Faculty of Engineering & Architecture of Gazi University*, vol. 27(3), pp. 651-658, 2012.
- [23]. M.Guden, and S. Yuksel, "SiC-particulate aluminum composite foams produced from powder compacts: foaming and compression behavior," *Journal of Materials Science*, vol. 41, pp. 4075-4084, 2006.
- [24]. A. R. Kennedy, and S. Asavavisithchai, "Effect of ceramic particle additions on foam expansion and stability in compacted Al-TiH₂ povde precursors," *Advanced Engineering Materials*, vol. 6, pp. 400-402, 2004.
- [25]. A.R. Kennedy, and S. Asavavisithchai, "Effects of TiB₂ particle addition on the expansion, structure and mechanical properties of PM Al foams," *Scripta Materialia*, vol. 50, pp. 115-119, 2004.
- [26]. M.K. Surappa, "Aluminum matrix composites: Challenges and opportunities," *Sadhana*, vol. 28, pp. 319-334, 2003.
- [27]. M. Abdel-Rahman, and M.N. El-Sheikh, "Workability in forging of powder metallurgy compacts," *Journal of Materials Processing Technology*, vol. 54, pp. 97-102, 1995.
- [28]. J. Banhart, "Aluminium Foams for lighter vehicles," *International Journal of Vehicle Design*, vol. 37, pp. 114-125, 2005.
- [29]. H. J. Lee, S. H. Eom, Y. K. Song, and S. S. Cho, "Effects of aluminum powder content and cold rolling on foaming behavior of Al_p/Al₅Si₄Cu₄Mg/0.8TiH₂ composites," *Materials Science and Technology*, vol. 19, pp. 819-825, 2003.
- [30]. I. Paulin, B.Sustarsic, V.Kevorkijan, S. D.Skapin, and M. Jenko, "Synthesis of Aluminium Foams by the Powder-Metallurgy Process: Compacting of Pecursors," *Materials and Technology*, vol. 45, pp. 13-19, 2011.
- [31]. B.L.Bonaccorsi, and E. Proverbio, "Powder compaction effect on foaming behavior of uni-axial pressed PM precursors," *Advanced Engineering Materials*, vol. 9, pp. 864-869, 2006.
- [32]. A.Mazahery, and M.O. Shabani, "Mechanical Properties of Squeeze-Cast A356 Composites Reinforced with B₄C Particulates," *Journal of Materials Engineering and Performance*, vol. 21, pp. 247-252, 2012.
-

ASTRONOMICAL ASPECTS OF THE CULT PRACTISE OF THE PEAK SANCTUARY KOKINO

Olgica KUZMANOVSKA

*Ss Cyril & Methodius University, Faculty of Natural Sciences and Mathematics, Department of Physics,
Arhimedova 3, P.O. Box 162, Skopje, Macedonia olgicak@pmf.ukim.mk*

Jovica STANKOVSKI

*National Museum Kumanovo, Macedonia,
jovicastankovski@yahoo.com*

Abstract

The latest astronomical research of the site known as “Tatikev Kamen” (or peak sanctuary Kokino) casts light on the cult practice of the local population of the Bronze Age in this region in northeast Macedonia. The newly-discovered astronomical platform has been used to observe the heliacal appearance of the star Aldebaran in a period of approximately 500 years, as well as the sunrise at the equinox. In 21 century BC, Aldebaran has been much nearer to the point of equinox. Therefore, the stone notch that marked the spring equinox has been used in the same time as a marker for the heliacal rising of Aldebaran, an event which has happened two months after the spring equinox. In the morning of the heliacal rising of the star, the appearance of the sun on the “mutual” marker has been visible from the platform with the stone thrones. In this article we express the view that the period from the spring equinox to the appearance of the Sun at the “mutual marker” (from the platform with the thrones) is a period in which, even nowadays, according to the local culture and folklore tradition, the local population celebrates different holidays which still encapsulate visible elements from pagan cults. Those are folklore customs related to the celebrations of the so-called Agrarian and Stock Breeding New Year, as well as holidays related to the cosmological concepts of the Bronze Age people in the region.

Keywords: *Archaeoastronomy, heliacal rising, solar calendars, stone markers*

1. INTRODUCTION

The ancient observatory Kokino (also known as “Megalithic observatory Kokino”) is a part of the archeoastronomical locality Tatihev Kamen (Tatic Rock), located 30 km northeast from the town of Kumanovo, Macedonia. Its geographical coordinates are $\varphi = 42^{\circ} 15' 48''$ north latitude, and $\lambda = 21^{\circ} 57' 10''$ east longitude. The locality has been discovered on an upper part of a hill with volcanic origin. Having a height of 1013 m, the hill dominates the surrounding area and the village of Kokino at its foothill (Figure 1). The site contains several artificially carved and flattened surfaces (platforms) and objects cut in the rocks, such as stone seats, astronomical and ritual markers, paths, etc (Figure 2).

The most fascinating part of the locality is the lower, western platform (A) which contains monumental stone seats (or “thrones”) carved in the rock terrain (Figure 3). Their construction, as well as the construction of the platform, was naturally predisposed by the geological system of fractures and fissures. The fractures in the rocks are limited in almost ideal cube blocks which could be moved relatively easy [9]. The thrones are lined in south-north direction and in such a manner that a person who sits on them faces the eastern horizon. A second platform (C) that strictly had astronomical purpose is positioned around 30 m southwest from the thrones’ platform. A separate side path (I) that starts from the bottom of the hill leads to it. On the north slope of the locality there is another platform made for astronomical observations (E). It is a part of the northern terrace (D). Around 70 m to east and 15 m higher than platform “A” there is one more artificially flattened surface (platform B) with the main path (approach) to the archeoastronomical locality - constructed on the rocks.

The role of the locality as mountain, extra urban sanctuary (i.e. peak sanctuary) for the Bronze Age people in the region during the whole period of the second millennium BC, was confirmed by its topographic characteristics (its dominant position on the hill, the large radius of visibility for the top that can be approached by the slope lit by the morning sun), as well as the large number of excavated artifacts discovered in the archeological context (e.g. [20],[21]). The archeological campaigns started at 2001. Its use as megalithic astronomical observatory was additionally proved.



Figure 1. Panoramic view of the archeoastronomical locality “Tatihev kamen”

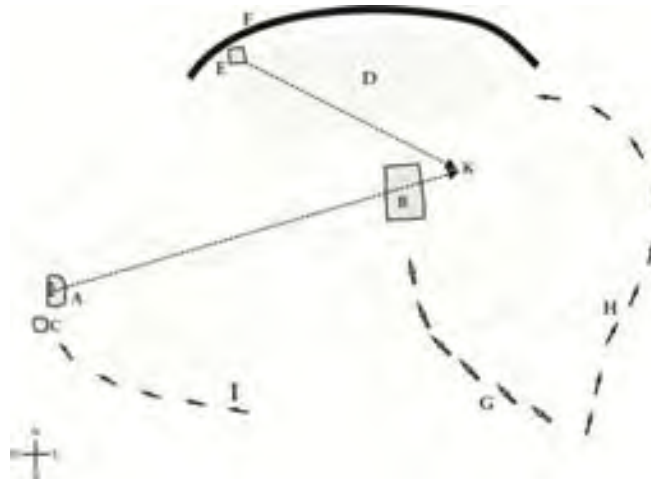


Figure 2. Map of the locality “Tatičev kamen”. **A** – first platform with the stone seats. **B** – upper eastern platform. **C** – astronomic platform (second platform). **E** - astronomic platform (third platform). **D** – northern terrace. **F** – sanctuary wall. **G** – main access path. **H** - access to the northern terrace. **I** - side path. **K** – mutual marker

2. ARCHAEOASTRONOMICAL RESEARCH

Most part of the archeological material was found on the highest part of the site and on the north slope of the hill (the so called northern terrace). It dates from the three phases of the Bronze Age: the early Bronze Age (21st-17th c. BC), see Figure 7 and Figure 8, middle Bronze Age (17th-14th c. BC) and late Bronze Age (14th-11th c. BC), according to the modified Reinecke chronology of the Bronze Age for central Europe. This sacred enclosure or “temenos” was enclosed by a 80 m long wall (Figure 4), noted with “F” on the map of the locality (see Figure 2). In the archeological research of the “temenos” area two types of religious structures were revealed; the ritual pits (Figure 5) and the circular stone constructions (Figure 6). The ritual pits had been formed around natural fissures of the rocks and delimited with stones mixed with earth and sometimes of clay. They were filled with ceramic vessels or their fragments, as well as ceramic votive figurines, pyramidal weights, moulds for casting bronze objects, stone axes, etc. The deposit was then covered with earth and small stones. So far, the most similar to the Kokino ritual pits are the pits of the Bronze Age sanctuary discovered at the locality Gradiste near village Pelince, around 8 km west of Kokino. It dates from almost the same chronological period [22].



Figure 3. The western platform with the stone seats (thrones)

Very fascinating is the discovery of the small ceramic figurines: a female torso, a small figurine of a bovine and several representations of a human leg (Figure 7). Almost identical figurines were found in a similar context on the mountain sanctuary Traostalos on the island Crete. According to most authors they probably had a function of providing fertility

and good health of people and livestock (e.g. [2], [5], [6], [15], [16], [20], [21]). The figurines were had been deposited on the mountain sanctuaries of Crete during most of the Middle Minoan period (22nd-17th c. BC). In the Late Minoan I period (16th-15th c. BC) most of these sanctuaries were no longer used (e.g. [4], [17]). The similarity of the archaeological artefacts (i.e. the clay figurines) and the archaeological context in which they were found emphasize the same aspects of the religious cults of the Kokino sanctuary and the sanctuaries on Crete, regardless of the geographical distance of their Bronze Age communities. Recent ethnographic, linguistic and archaeological researches confirm the relation of the Greek and Cretan religious beliefs, as well as of the other Aegean communities with those of the Eastern peoples of Anatolia, Syria and Egypt since the Neolithic times. The relations were even stronger during the Bronze Age (e.g. [3],[7]). Breaking the ceramic vessels and scattering their parts after the ritual was practiced by the early Neolithic communities. In Kokino sanctuary, the fragments of a same vessel burned by fire are discovered even 20 m apart from each other.



Figure 4. Sanctuary wall

Another ritual practise identified in Kokino has similar parallels on the Mediterranean basin. It is connected with the so called circular stone constructions, composed of big stones arranged in circles with diameters of 1-2m. The deposit put in the circles or around them is similar with the one from the pits. At the end of the ritual which probably included libations, the deposits were covered with earth and small stones forming a shape of small tumulus. Figure 8 shows a completely preserved cup and funnel discovered in one of the pits.



Figure 5. Ritual pit

Figure 6. Circular stone constructions

A similar ritual was performed around 60 km southeast of Kokino, at the locality Saint Atanasie near the town Kocani. The locality contains three circular (with radius 2-4 m) and two rectangular (with area 2×2.5m) platforms constructed on natural rock which was previously covered with layer of stones coated with clay. At these platforms the researchers discovered fragmented ceramic vessels, anthropomorphic and zoomorphic clay and terracotta figurines, stone hand mills, stone axes etc. Saint Atanasie sanctuary was built at the end of 5th and the beginning of 4th c. BC (e.g. [1], [14]). According to the archeological findings it was related with the eneolithic settlement discovered near it.

In early mountain sanctuaries on Crete dating from Middle Minoan (MMII) period, circular constructions made from layers of pebbles were made, with votive figurines placed inside or near them [17].

The thrones' platform and the small platforms "C" and "E" on Figure 2 contain astronomical alignments which provide unambiguous evidence that some of the religious rituals at Kokino were performed according to the motion of the sun and several other celestial objects. In the astronomical research, we measured the position of these alignments in order to identify the motives and estimate the period of the year the ritual celebrations had been most probably arranged. The markers that point to the rising positions of the sun, other stars and probably the full moon on particular calendar dates are presented by small notches in the rocks which are artificially carved and distinguishable from the natural cracks. There are indications that the notches are remains of apertures, i. e. they were covered on top with horizontally placed stones in order to create narrow "windows" through which the astronomical event was observed. We calculated the declination δ (the latitude above the celestial equator) of this marker using the formula:

$$\sin \delta = \cos A \cos \varphi \cos h + \sin \varphi \sin h \quad (1)$$

and taking into account the small correction due to astronomical refraction. The azimuth A , estimated from the north horizontal point and the altitude over the horizon h , were measured by a geodetic instrument with laser, while φ is the geographical latitude of the locality. We also used the Red Shift 4 computer program to reconstruct the sky map of the locality in different periods of the Bronze Age.

The most distinguishable astronomical marker, the so called "ritual marker", is constructed for the observer sitting on the thrones. It has a form of aperture placed just below the highest part of the locality through which the sun rises on certain dates of the year. The sun's rays pass through the right edge of the artificially cut trench on the eastern platform (noted with 'B' on Fig. 2) and then through another artificial notch below. As a result they illuminate just one of the thrones in the centre of the platform. The declination δ of the marker (see Table 1) defined as the altitude above the celestial equator - coincides with the positions of the rising sun in the middle of May (14th or 15th of May) and in the end of July (30th or 31st of July). In the early Bronze Age, i.e. around 2000 BC when the observatory was constructed (according to the archaeological evidence), the sun rose through the marker in the third week of May and at the beginning of August, due to change in obliquity of the Earth's rotational axis [16].



Figure 7. Ceramic votive figurines Figure 8. Cup and funnel from the early Bronze Age

The astronomical observations of the motion of the rising sun throughout the year were made from a narrow platform composed of a n artificially flattened stone blocks (noted with 'C' on Figure 2). Considering the period of one millennium the locality was used as an observatory and its main religious purpose, we guess that the observations were made on a daily basis by the local priests. They were probably accessing it from an additional side path (noted with 'I' on Figure 2). The platform satisfies one of the basic criteria that Hawkins laid out for a site to be considered as a megalithic observatory as a homogeneous group of markers can be observed from a single central point [10]. Having the magnitude of the solar disk, three of the markers point to the extreme positions of the rising sun on winter and

summer solstices and to the point of equinox, in spring and autumn [16]. Namely, moving apparently on the celestial circle – the ecliptic, the sun changes its daily motion on the sky, too. As a result, it rises precisely on east just on two dates, in the end of March and end of September (i.e. in the point of equinox). On the other days throughout the year the sunrise position is relocated from the equinox point and has extreme positions on summer (end of July) and winter solstice (end of December). The existence of markers of the extreme positions and the equinoxes indicates that the Kokino people had a simple solar calendar based on the observations of the daily motion of the rising sun. The calendar was used for performing religious rituals that were undoubtedly related with arranging agricultural work of the community (e.g. [15], [16], [20]). The stone markers for solstices and equinoxes and the rising sun through them on particular calendar dates are shown on Figure 9.



Figure 9. The stone markers of summer solstice –S1, autumnal and vernal equinox – S2 and winter solstice – S3, and the rising sun on the particular days (photos above), observed from the platform “C”

The existence of a marker for the equinoxes indicates the sophisticated observational skills of the Kokino “astronomers”. The sun’s declination δ at these two dates (around 21st of March and 22nd of September) is about zero degrees. For the Bronze Age communities, the equinox point in the sun’s yearly motion on the sky, indicated the turning point between the two extremes and divided the solar cycle into a warm and a hot season (e.g. [11],[19]). Additional confirmation that the builders of the megalithic observatory Kokino were familiar with the concept of equinox is the existence of a second equinox marker. It can be observed from the platform “E” on the northern terrace. Additionally to this marker, few other prominent notches were carved on the rock that covers the eastern horizon of an observer standing on platform “E”. Their declinations match almost exactly with the theoretical declinations of the bright star Aldebaran in the constellation Taurus, in the course of the half of the second millennium BC (e.g. [15], [16]). Additionally, the equinox marker was also Aldebaran’s marker in the years when the sanctuary was constructed because the Aldebaran’s position was in the equinox point in the 21st century BC (see Table 1). More precisely, the year of the exact match of the Aldebaran’s position and the equinox marker is 2083 BC, according to the Red Shift 4 computer program. Just like most of the stars, Aldebaran’s position changed due to its proper motion and the precession of the Earth’s axes. That was the reason for carving the other four of its markers in the course of several centuries.

Table 1. Horizontal azimuth and altitude, astronomical refraction corrections and declinations of the three markers that relate the astronomical platforms

Marker	Azimuth	Altitude	Refraction correction (')	Declination (°)
Ritual marker on platform “A”	76°05'10"	12°01'40"	4.67	18.26
Equinox marker on platform “C”	89°43'27"	-1'23"	34	-0.19
Equinox marker on platform “E” (also Aldebaran’s marker)	106°58'13"	18°02'42"	2.7	0.14



Figure 10. The stone block with the “mutual” marker, seen from the highest part of the locality (bottom), the rising sun in the middle of May, observed from the thrones’ platform (upper left) and the rising sun on vernal equinox, which was also Aldebaran’s rising position around 2000 BC, observed from platform “E” (upper right)

We estimate that the heliacal rising of Aldebaran and the near star cluster Pleiades, which happened around 60 days after the spring equinox, was the astronomical event related with the religious cults of Kokino. The heliacal rising of a star is defined by its appearance in the eastern horizon of the observer just before sunrise and, after a period of invisibility. The heliacal rising of different bright stars marked the beginning of new seasons in many ancient calendars [19]. The error of several days when determining the heliacal rising of a star is inevitable due to the change in visibility, climate conditions and the observational criteria of the ancient sky-watchers. For the case of Kokino observatory, there is one very important coincidence; the equinox marker on the platform “E” (which was also Aldebaran’s marker around 2000 BC), is constructed on a same stone block as the ritual marker through which the sun rises on two mornings (in middle of May and late July). In other words, in the beginning of the second millennium BC, the heliacal rising of Aldebaran in the second half May through the equinox marker seen from platform “E” and the sunrise through the ritual marker seen from the thrones’ platform happened in the same morning (see Figure 10). As the equinox marker and the ritual marker are built on the same stone block, they are “mutual” for the both platforms, the one with the thrones and platform “E” (noted with “K” on Figure 2).

In the next chapter we will discuss the most possible relation between the astronomical alignments and the rituals arranged in Kokino sanctuary during the Bronze Age.

3. CONCLUSIONS AND DISCUSSION

The latest archeoastronomical research of the astronomical alignments of the northern terrace of the peak sanctuary Kokino enables better insight on the cult practice of the Bronze Age communities of the north part of Macedonia. It also indicates its influence on the present-day rituals related with the so called spring cycle of holidays in the folklore of the surrounding area.

The period between the spring equinox and the day of the heliacal rising of the star Aldebaran on the “mutual” marker (i.e. the morning when the sun lights just one stone seat on the lower throne platform), which happens in the second half of May, is a season of spring holidays in the local folklore. Most of them have had pagan origin and were later incorporated in the new Christian beliefs. Also, the mythological representations and practices of the old solar calendars were coordinated with the Julian calendar (which is also solar).

However, it is still an open question what was the exact event (natural or astronomical) that marked the beginning of the pagan New Year in the Bronze Age. In the Macedonian tradition there are several closed cycles that contain mythical, religious and social characteristics which can be useful for the determination [18]. For example, the agricultural New Year begins with sowing and plowing the fields. The activities were beginning with the Orthodox Christian holiday Krstovden on September 27th. On this day the sower was on the field before sunrise saying a prayer

and then starting the work. According to some researchers, these magical practices were marking the beginning of the agricultural New Year [18]. In Kokino, the illumination of one of the stone thrones by the morning sun occurred in May, but also in late July or beginning of August. We hypothesize that the rituals arranged on the second date were celebrating the successful harvest, as one of the most important events of the agricultural communities in the area. The person who had the principal role in the execution of the mountain ritual probably sat on the illuminated seat, most likely - the tribal leader in a role of head priest. The scene described the concept of uniting the Heavens and Earth which ensured the cyclic renewal of nature. The ritual was known in antiquity as 'hieros gamos' i.e. the "sacred marriage" or union of the fertility Goddess and her divine male consort [8].

A variety of sources suggest that people in the Aegean believed in similar myths and had practiced corresponding rituals since the Bronze Age period with the divine couple having different names in different mythological concepts. In the region of the Near East the sacred union was made between Innana and Dumuzi, or Ishtar and Tammuz. In Greek mythology there is a divine couple in each generation of gods; Gaia and Uranos, Rhea and Cronos, Hera and Zeus, etc. All of the myths suggest the annual death of the male at the end of spring or early summer, and his rebirth in the autumn when he reunites with the goddess. In Near East the sacred marriage was one of the main rituals in the celebrations that marked the beginning of the New Year. On Crete in the historical period - the New Year, was starting near the autumn equinox marking the rainy season [13].

Motives of the cosmic hierogamy between the Heavens and the Earth and the sacred marriage are also present in the Macedonian ethnical tradition. The main element of these cosmological concepts is the water, i.e. the heavenly rain. This was not ordinary, but divine rain that marked the sacred union between Heavens and Earth if it occurred on strictly determined time periods and under certain conditions. Thus, most of the spring holidays are related with special activities, such as picking special plants or collecting the morning dew [18]. In western part of Macedonia the dominant activity was stockbreeding. In this region the beginning of the New Year was related with the holiday called Letnik in mid March. The activities arranged around this holiday had magic meaning and were performed for a purpose of providing the fertility and prosperity of the community. The holiday was related with other spring holidays (Gjurgjovden, Eremija, etc.) that celebrated the awakening and renewal of nature.

The most important in the spring cycle was a Christian holiday with archaic, pagan origin, called Gjurgjovden (May 6th). It is also celebrated by non-Christian communities in Macedonia and had a basic meaning of celebration of life and the nature reborn [12]. The rituals performed on Gjurgjovden are similar to those of some Roman holidays, as Palilija on April 21th, when people ornamented the live stock with green branches and sacrifices were given to the gods for the sake of protecting the people and live stock from accidents. The celebrations in honor of the god Dionysus performed by the ancient Greeks and Thracians, according to many ancient authors, have similar elements with the rituals performed by Macedonians that all culminated around Gjurgjovden and marked the beginning of the warm (summer) half of the year.

We suggest that the beginning of the New Year for the Bronze Age community that built the sanctuary and the megalithic observatory Kokino coincided with the heliacal rising of Aldebaran in the second half of May. Then, the star was visible in dawn, before sunrise, for the first time after many months of invisibility. The event was symbolically marked by the notch seen from platform "E", which was also the marker for the sunrise on spring (vernal) equinox in the period the sanctuary was built. We guess that Aldebaran, among other bright stars, was chosen to be observed because its appearance coincided with the position of the sun in equinoxes. As the Aldebaran's marker is "mutual" for platforms "E" and the one with the thrones, the sunrise through the ritual marker on the thrones' platform happened in the morning of the heliacal rising of the star on platform "E". According to the archaeological evidences the two astronomical events were the main cause for arranging the celebrations and rituals. They marked the beginning of the new season, the renewal of the nature and starting the agricultural work cycles on which the whole community depended of.

REFERENCES

- [1]. Atanasova, I. (2011). *The results of the excavations of the early eneolithic sanctuary St. Atanasie, near village Spancevo - Kocani*, Macedoniae Acta Archaeologica, 20, 185-203
- [2]. Chryssoulaki, S. (2001). *The Traostalos Peak Sanctuary: Aspects of Spatila Organisation*, Aegaeum 22, 57-66.
- [3]. Dietrich, B.C. (1967). *Some light from the East on Cretan Cult Practice*, Historia: Zeitschrift für Alte Geschichte, 16 (4), 385-413.
- [4]. Dietrich, B.C. (1969). *Peak Cults and Their Place in Minoan Religion*, Historia: Zeitschrift für Alte Geschichte, 18 (3), 257-275.
- [5]. Faure, P. (1963). *Cultes de sommets et cultes de caverns en Crète*, Bulletin de Correspondance Hellenique, 87, 493-508.
- [6]. Faure, P. (1967). *Nouvelles recherches sur trois sortes de sanctuaires crétois*, Bulletin de Correspondance Hellenique, 1967-II, 114-150.
- [7]. Frankfort, H. (1948). *Kingship and the Gods. A study of Ancient Near Eastern Religion as the Integration of Society*. Nature, 314-316.
- [8]. Graves, R. (1972). *The Greek Myths, Olympic Myth of the Creation of the World*, Penguin Books (Harmondsworth, Middlesex)
- [9]. Gjurdjevic, N. (2003). *Geological reconnaissance of the terrain on the archaeological localities around Kumanovo during year 2002*, Pyraichmes, II, 289-298.

- [10]. Hawkins, G.S. (1966). Astro – archaeology, SAO Special Report, No 26.
- [11]. Hughes, D.W. (2005). Neolithic and Early Bronze Age skywatchers and the precession of the equinox, *Journal of the British Astronomical Association*, 115 (1), 29-35.
- [12]. Kitevski, M. (2013). Македонски празници и празнични обичаи, Скопје, 112-161.
- [13]. Koehl, B.R. (2001). The “Sacred Marriage” in Minoan Religion and Ritual, *Aegaeum*, 22, 237-243.
- [14]. Kolistrkoska Nasteva, I. (2011). St. Atanasie, eneolithic sanctuary and a part of the discovered material, *Macedoniae Acta Archaeologica*, 20, 171-184.
- [15]. Kuzmanovska, O., *Stankovski, J. (2014)*. The astronomical relation of the ritual platforms of the peak sanctuary Kokino, *SEAC 2013 Athens, ASTRONOMY: Mother of Civilization and Guide to the Future Mediterranean Archaeology and Archaeometry*, 14 (3), 259-269.
- [16]. *Kuzmanovska-Barandovska O., Stankovski, J. (2011)*. The role of the astronomical alignments in the rituals on the peak sanctuary at Kokino, Macedonia, *Journal of Astronomical History and Heritage*, 14 (3), 221-229. Link: <http://adsabs.harvard.edu/abs/2011JAHH...14..221K>
- [17]. Nowicki, K. (1994). Some remarks on the Pre- and Protopalatial peak sanctuaries in Crete, *Aegean Archaeology*, 1, 31-48.
- [18]. Risteski, Lj. S. (2005). Категориите простор и време во народната култура на Македонците, 364-369
- [19]. Ruggles, C.L.N. (2005). *Ancient Astronomy: An Encyclopedia of Cosmologies and Myth*, Oxford.
- [20]. Stankovski, J. (2007). The Peak Sanctuary Taticev kamen at the Village of Kokino and Two of its Cults, *Thracia*, 17, 259-268.
- [21]. Stankovski, J. (2010). A Contribution to the study of the Ritual Activities at the site Taticev Kamen, Vilagge of Kokino, *Macedoniae Acta Archaeologica*, 19, 115-125.
- [22]. *Trajkovska, L. (2003)*. *Shrine from the early Bronze Age of Gradiste in the village of Pelince, near Kumanovo, Pyraichmes, II*, 263-279.

BIOGRAPHY

Dr Olgica Kuzmanovska is an Assistant Professor in the Department of Physics, Faculty of Natural Sciences and Mathematics in Skopje, Republic of Macedonia. Her main research interests lie in theoretical astrophysics, mainly in the theory of spectral line formation and radiative transfer in stellar atmospheres and modeling of stellar structure. She is also interested in the history of astronomy and archaeoastronomy in Macedonia. She is the Secretary of the Astronomical Society of the Republic of Macedonia.

USING BASE ALGORITHMS COMBINATORIALLY IN ADABOOST ENSEMBLE FOR INTRUSION DETECTION

Necati DEMİR

okuzEylul University, Department of Computer Engineering, 35390, Tınaztepe, Buca/İzmir, Turkey.
ndemir@demir.web.tr

Gökhan DALKILIÇ

Corresponding author: DokuzEylul University, Department of Computer Engineering, 35390, Tınaztepe, Buca/İzmir, Turkey. dalkilic@cs.deu.edu.tr

Abstract

With the increased bandwidth thereby wider usage of the Internet, the risk of attacks has raised dramatically. To prevent these attacks, intrusion detection tools are being used. Conventional intrusion detection tools are signature-based which can detect only known type of attacks. The aim of the researchers, who are developing machine learning based intrusion detection methods, is to detect the previously unknown attacks. The main objective of this study is to use an ensemble method for intrusion detection. This ensemble method, unlike other similar methods, combines the multiple prediction models of different base classification algorithms. As a methodological approach, we run experiments by combining several combinations of different base classification algorithms in ensemble method. We used 5 different algorithms that produced 15 different combinations. KDD99 dataset, which is a widely used dataset for intrusion detection studies, is used in the experiments. We trained our ensemble methods with 2%, 10% and 14% of KDD99 dataset which produced 45 different experiments. In every experiment we assigned a label to each row of KDD99 testing dataset and measured accuracy of each label as metric. KDD99 dataset contains 5 different labels and at the end we calculated 225 metric values. We found that; for different types of traffic, different portions of the dataset give the best results. And also, different algorithm combinations detect different labeled traffic more accurately.

Keywords: *Ensemble, KDD, KDD99, Machine learning*

1. INTRODUCTION

The Internet has become one of the essential tools of our life today. Not just business operations are heavily operated on the Internet, but also ordinary users using Internet have increased much more than ever. Besides regular usage, there has been remarkable increase in the number of incidents reported to the United States Computer Emergency Response Team (US-CERT) by Federal Agencies according to the reports [11]-[14], presented to the US Congress. Figure 1 shows the increase of the reported incidents. In 2014, 640,222 total incidents were reported to US_CERT and that number was 218,886 in the year 2013. This makes an annual increase of 192.50%. These numbers highlight the ineffectiveness of the solutions against the incidents.

Therefore, information security needs to be concerned carefully. Intrusion detection systems (IDS) are major tools to detect attacks. Most IDS use signature based techniques. These signatures are extracted from the attacks and stored in the IDS database, to be compared against network traffic. But this kind of technique does not have an ability to detect unknown type of attacks.

To detect unknown type of attacks, there are studies for IDS techniques using anomaly detection based on machine learning algorithms. Machine learning techniques have the ability to learn from existing dataset and to classify the new type of traffic as normal or a anomaly/attack by previous learnings. Some of them use classification algorithms such as neural networks, genetic algorithms, support vector machines or clustering algorithms such as self-organizing maps, k-nearest neighbors. On the other hand, some of the studies use combination of these algorithms. There are two techniques mainly used to combine several algorithms; hybrid techniques and ensemble techniques.

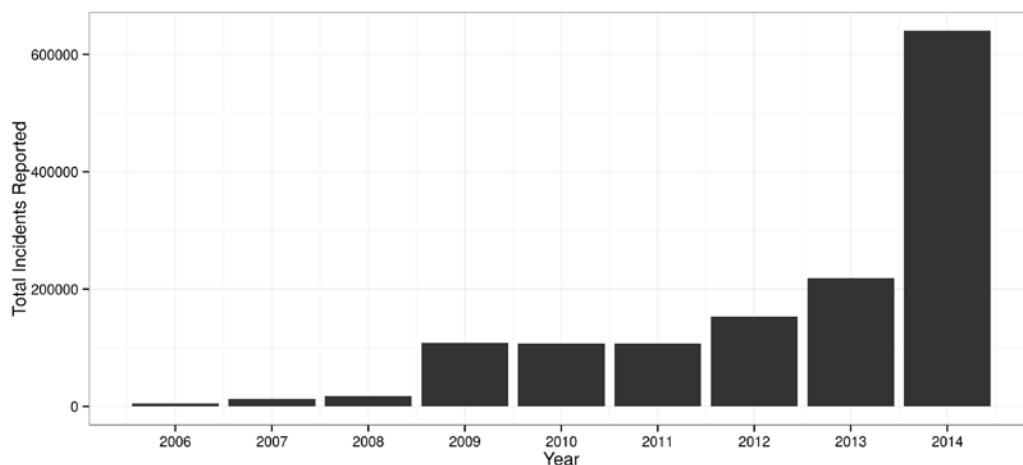


Figure 1. Incidents reported to US-CERT by federal agencies between 2006 and 2014

Hybrid techniques (also referred as hybrid classifiers) typically consist of two functional components. The first one takes raw data as input and generates intermediate results. The second one will then take the intermediate results as the input and produce the final results [6]. Ensemble techniques (also referred as ensemble classifiers or ensemble learners) use multiple algorithms to obtain better performance. Section 3 describes ensemble techniques in detail. In this study, an ensemble technique is used for intrusion detection.

2. PREVIOUS WORKS

Various machine learning techniques have been used for intrusion detection since the dataset formed when the Fifth International Conference on Knowledge Discovery and Data Mining (KDD99) was held. Some of the studies use single classification algorithms and some of them use hybrid methods. In the following paragraphs, firstly a study which uses single classification algorithms is introduced and followed by the study which improves the technique by using a hybrid method.

Reference [15] uses J48 and Naïve Bayes classification algorithms by using various data reduction techniques which can be shown as examples of single classification algorithms. References [4] and [19] use Support Vector Machines (SVM). Reference [4] also uses Random Forest (RF) and compares these studies where he finds that SVM classification produces more accurate results than RF and RF takes less time to train the classifier than SVM. Li and Guo [10] use Transductive Confidence Machines for K-Nearest Neighbors (TCM-KNN) algorithm with different K values. Tsai and Lin [16] propose a hybrid learning model based on the Triangle Area based Nearest Neighbors (TANN).

Self Organizing Maps (SOM) is another approach for anomaly detection. References [3] and [5] use SOM for anomaly detection. Reference [7] uses a hybrid method which includes the SOM and Resilient Propagation Neural Network (RPROP). SVM is a classification algorithm used in various studies. Wang and Stolfo [17] use SVM for intrusion detection. Khan et al. [8] use SVM and hierarchical clustering forming a hybrid method. Lee [9] uses Apriori for rule extraction and uses these rules for classification. Zhang et al. [18] use Rough Set Classification (RCS) which is also a technique for rule extraction and proposes a hybrid genetic algorithm to increase the convergence speed and decrease the training time of RSC.

3. OUR STUDY

3.1. Motivation

Up to now, so many studies using machine learning techniques, have been published for IDS. It is obvious that none of the studies alone has the capacity to identify all types of intrusion when it comes to detection and false alarm rate. Therefore, hybrid or ensemble classifiers should be used to improve the detection rates. In this study, we decided to use an ensemble classifier, Adaboost. Adaboost implementations take one base classification algorithm and the dataset as input and re-samples the dataset to create multiple classification models. Our main motivation in this study is to use more than one base classification algorithm as input.

3.2. Ensemble Classifier

Ensemble classifiers are meta-classifiers which combine the output of the classification models by different techniques. In this context, the term “classification model” is the output of the training classification algorithm with data, which is also used for prediction. Figure 2 shows how classification model is created and how it is used.

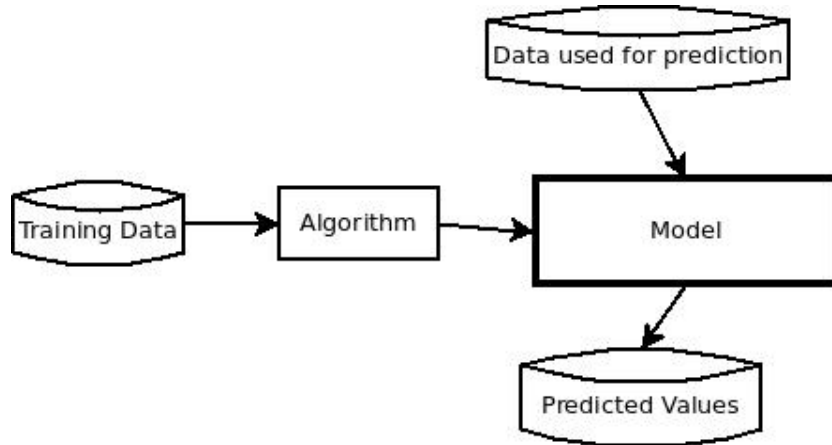


Figure 2. Classification model

There are two widely used techniques in ensemble classifiers; bagging (also referred as bootstrap aggregating) [1] and boosting [2]. Bagging trains the classification algorithms by using a randomly selected subset of the training set. On the other hand, boosting trains each classification model to emphasize the training dataset that previous models mis-classified. Adaboost uses boosting technique.

3.3. Adaboost

AdaBoost, short for “Adaptive Boosting”, is an ensemble algorithm created by Yoav Freund and Robert Schapire who won the “Gödel Prize” in 2003 for their work. As an ensemble classifier, Adaboost uses many other types of classification algorithms to improve their performance. Adaboost combines the outputs of classification models into a weighted sum that represents the final output as shown in Equation 1. Adaboost works with weak models. In this context, “weak model” is a model which predicts slightly better than random guessing.

$$H(x) = \sum_{t=1}^T w_t f_t(x) \tag{1}$$

where f is the weak model and w is the weight calculated.

To our best knowledge, the implementations of Adaboost use one classification algorithm, select random subsets of training dataset, create classification models, and then combine the outputs by using boosting. Figure 3 shows this process.

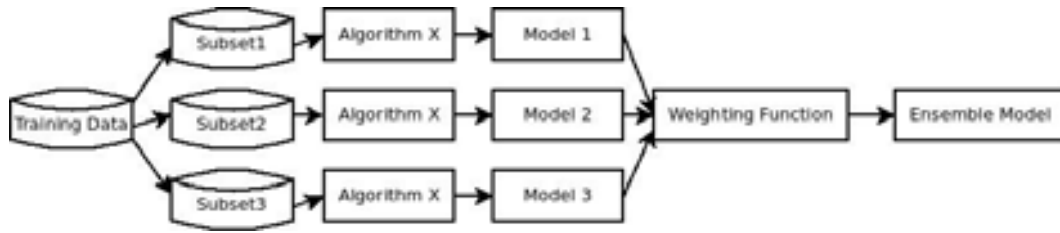


Figure 3. Adaboost

Our study uses more than one classification algorithm.

3.4. Methodology

We used different combinations of four classification algorithms, SVM, Random Forest (RF), Stochastic Gradient Descent (SGD) and Naïve Bayes which results in 15 different combinations. The combinations are listed in Table 1. The first four rows contain only one classification algorithm. As a result of combinations and using these four algorithms solely in Adaboost, gives the same result as running the classification algorithm alone.

Table 1. Combination of classification algorithms

Combination Number	Algorithms Used
1	SVN
2	RF
3	SGD
4	NB
5	SVM+RF
6	SVM+SGD
7	SVM+NB
8	RF+SGD
9	RF+NB
10	SGD+NB
11	SVM+RF+SGD
12	SVM+RF+NB
13	SVM+SGD+NB
14	RF+SGD+NB
15	SVM+RF+SGD+NB

We also trained ensemble classifier by using all these combinations, with different percentages of KDD data set; 2%, 10% and 14%. For the 2% training set, 20% of *kddcup.data_10_percent* (http://kdd.ics.uci.edu/databases/kddcup99/kddcup.data_10_percent.gz) was selected randomly. For the 10% training set, *kddcup.data_10_percent* (http://kdd.ics.uci.edu/databases/kddcup99/kddcup.data_10_percent.gz) was completely used. For the 14% training dataset, 14% of the *kddcup.data* (<http://kdd.ics.uci.edu/databases/kddcup99/kddcup.data.gz>) was randomly selected.

3.5. Performance Metrics

Each classifier produces a confusion matrix as shown in Table 2. Confusion matrix is a table layout which is used to visualize the performance of a classification model. In Table 2, columns describes the predicted classes and rows describes the actual classes.

Table 2. Example of confusion matrix

	Normal	Probe	DoS	U2R	R2L
Normal	X ₀₀	X ₀₁	X ₀₂	X ₀₃	X ₀₄
Probe	X ₁₀	X ₁₁	X ₁₂	X ₁₃	X ₁₄
DoS	X ₂₀	X ₂₁	X ₂₂	X ₂₃	X ₂₄
U2R	X ₃₀	X ₃₁	X ₃₂	X ₃₃	X ₃₄
R2L	X ₄₀	X ₄₁	X ₄₂	X ₄₃	X ₄₄

Performance of the classifier is evaluated in two ways: performance of each category and overall performance. Equations 2, 3, 4, 5, and 6 show the calculation of detection rates obtained for each category.

$$DetectionRate_{Normal} = \frac{X_{00}}{\sum X_{0i}} \tag{2}$$

$$DetectionRate_{Probe} = \frac{X_{11}}{\sum X_{1i}} \tag{3}$$

$$DetectionRate_{DoS} = \frac{X_{22}}{\sum X_{2i}} \quad (4)$$

$$DetectionRate_{U2R} = \frac{X_{33}}{\sum X_{3i}} \quad (5)$$

$$DetectionRate_{R2L} = \frac{X_{44}}{\sum X_{4i}} \quad (6)$$

4. RESULTS

As discussed earlier, running all combinations of selected algorithms with Adaboost produces 15 confusion matrices. By using Equations 2, 3, 4, 5 and 6, we obtained 5 values for each matrix: $DetectionRate_{Normal}$, $DetectionRate_{Probe}$, $DetectionRate_{DoS}$, $DetectionRate_{U2R}$ and $DetectionRate_{R2L}$. We iterated three times for each training dataset. As a result, we obtained 180 different values. Figures 4, 5, and 6 show the graphs of detection rates for each category after training with 2%, 10% and 14% of the dataset respectively.

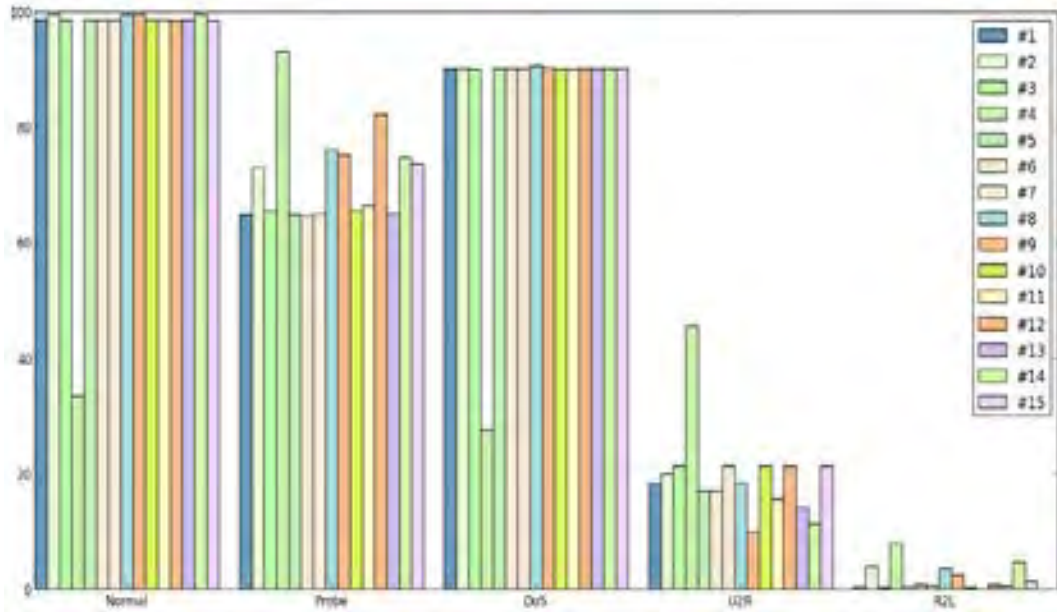


Figure 4. Detection rate of each combination after training with 2% of the dataset

From Figure 4, Naïve Bayes (#4) has the highest accuracy ratio for detecting Probe, U2R and R2L, but it is the worst for DoS. For the normal traffic, combination #14 is the best. For U2R and R2L, detection ratios are below 50%.

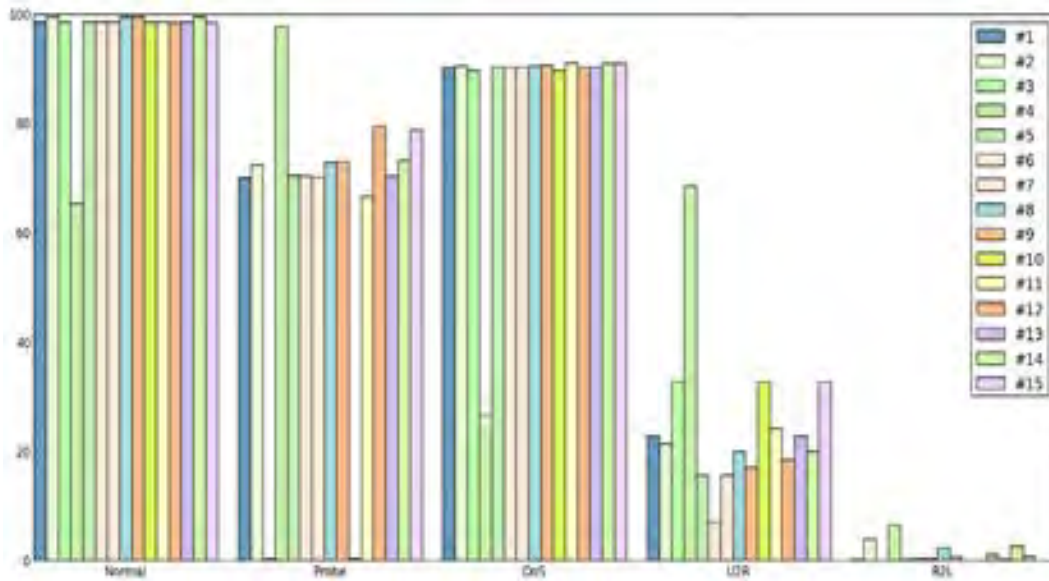


Figure 5. Detection rate of each combination after training with 10% of the dataset

Like the previous figure, in Figure 5 Naïve Bayes (#4) has the highest accuracy ratio for detecting Probe, U2R and R2L, but in this figure for DoS, combination #11 outperforms the others. Again U2R and R2L ratios are not satisfactory, but now combination #4 has a ratio greater than 50% (68.57%).

In Figure 6, combination #4 is the best for Probe, U2R and R2L like the previous two figures. For R2L, combination #4 has much higher accuracy rate compared to the 2% and 10% of the datasets used in previous tests. For the normal traffic the ranking changes and combination #2 is better than the others.

Table 3 gives a summary of the results by listing only the best three combinations for each category and for each dataset. For Normal category; combination #14 shows up in three datasets, ranking first in two datasets and ranking third in the last dataset. For Probe category; combination #4 shows up in three datasets and ranks first every time. For DoS category; combinations #8 and #15 show up twice while others once. For U2R category; combination #4 ranks first every time. For R2L category; combination #4 ranks first every time. The highest ratios are marked bold in the table.

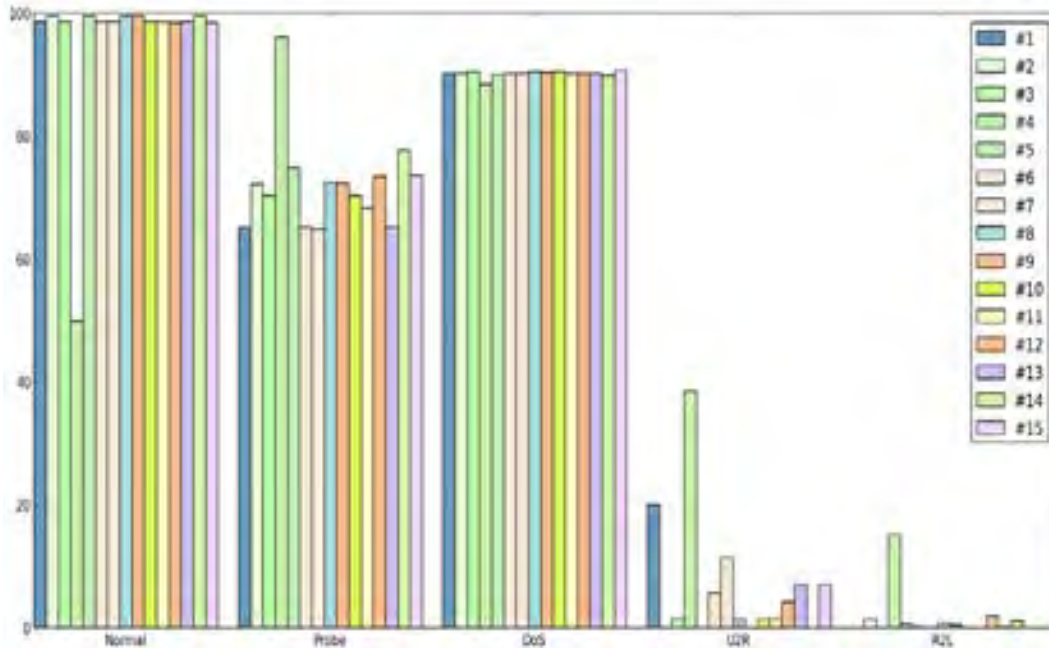


Figure 6. Detection rate of each combination after training with 14% of the dataset

Table 3. Summary of the results

	Normal		Probe		DoS		U2R		R2L	
	Rank	%	Rank	%	Rank	%	Rank	%	Rank	%
2% of Dataset	#14	99.57	#4	93.27	#8	90.66	#4	45.71	#4	7.98
	#8	99.55	#12	82.33	#9	90.32	#7	21.43	#14	4.80
	#9	99.55	#8	76.15	#2	90.26	#3	21.43	#2	4.05
	#14	99.59	#4	97.90	#11	91.22	#4	68.57	#4	6.62
10% of Dataset	#9	99.58	#12	79.56	#14	91.03	#3	32.86	#2	4.03
	#2	99.56	#15	78.80	#15	90.96	#15	32.86	#14	2.78
	#2	99.59	#4	96.11	#15	90.66	#4	38.57	#4	15.16
12% of Dataset	#5	99.58	#14	77.70	#8	90.55	#1	20.00	#12	1.90
	#14	99.57	#5	74.85	#3	90.48	#7	11.43	#2	1.43

5. CONCLUSIONS

In this study, Naïve Bayes (combination #4) performs best for the *Probe*, *U2R* and *R2L* categories while using Random Forest, Stochastic Gradient Descent and Naïve Bayes as base the classifiers in Adaboost (combination #14) has the highest score for the *Normal* category. The combination of Support Vector Machines, Random Forest and Stochastic Gradient Descent as the base classifiers in Adaboost (combination #11) performs best for the *DoS* category.

Although boosting and bagging are widely used methods in ensemble classifiers, other methods like Bayesian model averaging and stacking can be used. Other types of ensemble methods, using the same combinations, can be analyzed and compared for the future work.

ACKNOWLEDGMENT

This project is partially supported by DEU Scientific Research Project 2015.KB.FEN.013.

REFERENCES

- [1]. L. Breiman, "Bagging predictors," *Machine learning*, Springer-Verlag, vol. 24, no. 2, pp. 123-140, Aug. 1996.
- [2]. Y. Freund, R. Schapire, "A short introduction to boosting," *Journal-Japanese Society for Artificial Intelligence*, vol. 14, no. 5, pp. 771-780, Sep. 1999.
- [3]. L. Girardin, "An eye on network intruder-administrator shootouts," in *Proc. of the Workshop on Intrusion Detection and Network Monitoring*, 1999, pp. 19-28.
- [4]. M. A. M.Hasan, B. Pal, and S. Ahmad, "Support vector machine and random forest modeling for intrusion detection system (IDS)," *Journal of Intelligent Learning Systems and Applications*, vol. 6, no. 1, pp. 45-52, Feb. 2014.
- [5]. A. J.Hoglund, K. Hatonen, and A. S. Sorvari, "A computer host-based user anomaly detection system using the self-organizing map," in *Proc. IJCNN*, 2000, pp. 411-416.
- [6]. J. S. R. Jang, and C. T. Sun, *Neuro-fuzzy and soft computing: a computational approach to learning and machine intelligence*, Upper Saddle River, NJ, USA: Prentice-Hall, 1996.
- [7]. C. Jirapummin, N. Wattanapongsakorn, and P.Kanthamanon, "Hybrid neural networks for intrusion detection system," in *Proc. ITC-CSCC*, 2002, pp. 928-931.
- [8]. L. Khan, MAwad, and B.Thuraisingham, "A new intrusion detection system using support vector machines and hierarchical clustering," *The VLDB Journal—The International Journal on Very Large Data Bases*, vol. 16, no. 4, pp. 507-521, Oct. 2007.
- [9]. W. Lee, "A data mining framework for constructing features and models for intrusion detection systems," Doctoral dissertation, Columbia University, New York, NY, USA, 1999.
- [10]. Y. Li, and L. Guo, "An active learning based TCM-KNN algorithm for supervised network intrusion detection," *Computers & Security*, vol. 26, no. 7-8, pp. 459-467, Dec. 2007.
- [11]. (2008) Office of Management and Budget, Fiscal Year 2006, 2007 Reports to Congress on Implementation of The Federal Information Security Management Act of 2002. [Online]. Available: https://www.whitehouse.gov/sites/default/files/omb/inforeg/reports/2006_fisma_report.pdf https://www.whitehouse.gov/sites/default/files/omb/inforeg/reports/2007_fisma_report.pdf
- [12]. (2009) Office of Management and Budget, Fiscal Year 2008 Report to Congress on Implementation of the Federal Information Security Management Act of 2002. [Online]. Available: https://www.whitehouse.gov/sites/default/files/omb/assets/reports/fy2008_fisma.pdf
- [13]. (2013) Office of Management and Budget, Fiscal Year 2009, 2010, 2011, 2012 Reports to Congress on Implementation of The Federal Information Security Management Act of 2002. [Online]. Available: https://www.whitehouse.gov/sites/default/files/omb/assets/egov_docs/FY09_FISMA.pdf, https://www.whitehouse.gov/sites/default/files/omb/assets/egov_docs/FY10_FISMA.pdf https://www.whitehouse.gov/sites/default/files/omb/assets/egov_docs/fy11_fisma.pdf https://www.whitehouse.gov/sites/default/files/omb/assets/egov_docs/fy12_fisma.pdf
- [14]. (2014) Office of Management and Budget, Annual Report to Congress: Federal Information Security Management Act, [Online]. Available: https://www.whitehouse.gov/sites/default/files/omb/assets/egov_docs/fy_2013_fisma_report_05.01.2014.pdf https://www.whitehouse.gov/sites/default/files/omb/assets/egov_docs/final_fy14_fisma_report_02_27_2015.pdf

- [15]. S. S. Panwar, and Y. P. Raiwani, "Data reduction techniques to analyze NSL-KDD Dataset," *Journal Impact Factor*, vol. 5, no. 10, pp. 21-31, 2014.
 - [16]. C. F. Tsai, and C. Y. Lin, "A triangle area based nearest neighbors approach to intrusion detection," *Pattern Recognition*, vol. 43, no. 1, pp. 222-229, Jan. 2010.
 - [17]. K. Wang, and S. Stolfo, "One-class training for masquerade detection," 2003.
 - [18]. L. Zhang, G. Zhang, L. Yu, J. Zhang, and Y. Bai, "Intrusion detection using rough set classification," *Journal of Zhejiang University Science*, vol. 5, no. 9, pp. 1076-1086, Sep. 2004.
 - [19]. J. Zhang, M. Zulkernine, and A. Haque, "Random-forests-based network intrusion detection systems," *IEEE Transactions on Systems, Man, and Cybernetics, Part C: Applications and Reviews*, vol. 38, no. 5, pp. 649-659, Sep. 2008.
-

MATERIALS SELECTION FOR CAR BUMPER WITH A CONVENTIONAL METHOD AS WELL AS CES SELECTOR SOFTWARE

Murat ÇOLAK

*Bayburt University, Faculty of Engineering, Material Science and Nanotechnology Department, Bayburt, TURKEY,
Tel: +904582111177 (3262) fax:+904582111178, mcolak@bayburt.edu.tr,*

Fehim FINDIK

Sakarya University, Faculty of Technology, Metallurgy and Material Engineering Department, Sakarya, TURKEY,

Salim ASLANLAR

Sakarya University, Faculty of Technology, Metallurgy and Material Engineering Department, Sakarya, TURKEY,

Abstract

In engineering design, selecting the suitable materials is known as an important step for the design process. Nowadays, selecting the suitable material from the 160 thousands industrial material is important as well as difficult issue to meet the different design requests and having the properties of designer will promote. In order to select the suitable materials, the technical personnel should have enough knowledge such as materials structure, density, melting point, thermal expansion coefficient, tensile and yield strength, elongation percentage, modulus of elasticity, hardness and other properties. In order to select the most suitable material, there are a lot of selection systems assisting to the design engineer. The simplest one of these methods is to use the tables for materials properties in design engineers' handbooks. Besides, computer systems are increasingly being used. In the current study, selection materials for car bumper will be done using a classical selection method as well as computer aided selection software and advantages and disadvantages for both methods will be compared to each other according to the obtained results. During the materials selection, the evaluations are done considering mechanical, physical, chemical properties as well as economical and production processes. The selected materials are consistent with the related studies as well as recent trends in sector. In case of comparing materials selection methods, it is concluded that the most practical selection can be done via computer aided software in the light of recent data.

Keywords: *Materials selection, computer aided CES software, computer aided design, car bumper.*

1. INTRODUCTION

Design is done to meet the projected needs in the light of scientific data considering the previous experience of the producers and consumers in the current technological level in the direction for the consumers' requirements. In the direction of the mentioned targets, the analysis is prepared for the intended problem solving follows synthesis, materials selection, measuring and control methods for design issue. In general, engineering design contains the all activities such as indicating the duty for any of the technical system, determining the physical principles, selecting the suitable elements consistent with those principles, and preparing part and assembly technical drawings [1,2].

Choosing the appropriate materials for engineering design is known the important step for materials selection process. Using all materials requires several choosing elements and this step is considered as problem solving activity [3-5]. Problem solving involves an extensive information flow. Considering the used parts in several recent vehicles such as tractor (15-20 thousands), car (25-30 thousands), military tank (40 thousands), submarine (120 thousands) and aircraft (5-6 millions), the importance and the difficulty of materials selection problem can be well understood [1, 2, 6-12]. Selecting the suitable materials is one of the main factors for any of the products has stable and low fabrication cost performing the functions successfully. Design engineers must balance between functional needs and costs. The economy for materials is really important due to costs for materials compose 50% of product price for many artifacts. However, occurring of materials in minimum cost is not sufficient for lowest total cost; since beside the starting price of the materials, product and assembly costs, costs for the other materials in products, guarantee and service costs for products are also important [1, 13-16].

Nowadays, there are a wide range of materials group including metals, ceramics, glasses, polymers, elastomers and composites having suitable mechanical, physical and environmental properties for using designers to meet the various design needs such as performance and economics. Currently designers can choose materials from those resources for different engineering applications. Novel materials such as new alloys and coatings can be considered within the selected materials. But this situation brings the optimum materials selection to the more difficult case [1,16-19]. In this place, it is needed for an information management system. For the last years, some systems are developed in mechanical design for the needs in design engineers in the area of computer aided materials and production method. This development is done in the area for organizing the data bases for materials and production methods from selecting many factors and developing the systematic methods comparing the materials and production techniques. Classical (conventional) materials selection method is the oldest and simplest method can be applied in the light of standards as well as the data about physical properties and performance taken from the producers and suppliers. Recently, computer aided materials selection methods are developed adding to the classical (conventional) design procedure [12, 20-23]. Using the computer systems in which stored the materials properties provides faster and wide capacity of materials data for designers [2,24,25]. These methods are quite useful for designers to decide them for the optimum material selection considering the cost issue [1].

Materials selection can be done with different methods. As a first issue, Ashby [6,26,27] and Dargie [28] have investigated several studies about the screening method. For the screening method, Ashby [2,29] presented a Granta Design software having a graphic interface. By means of Ashby diagrams, it is possible to draw a graph between two properties and to see the place of materials group where placed in the graph. For the second method, there are knowledge based systems, but its usability is limited due to their complexity and needing to the very wide information requirement [19]. Shanian and Savadogo [15,18,22,23] have developed various methods, however these methods cannot permit the weighting for gradual materials properties. In addition, many researchers presented different materials selection methods [1-34]. But, the quantitative and logical based selection methods, reliability of the selection, repeatability and experience of the designers are required for the other steps outside the initial materials preliminary screening issue. Qualitative materials selection methods are separated into various categories. The "cost per unit property method" (CPUPM) and the "limits on properties method" (LOPM) have a pre-screening purpose within these methods, and "weighted properties method" (WPM) can be used as a decision mechanism [26]. CPUPM method is suitable for a pre-screening process combining with a materials cost issue and here one property is openly ahead comparing to others. Thus, low cost materials are chosen and target materials group can be constricted [28].

Despite many researchers suggested many methods about materials selection, it is difficult to mention an optimum selection method accepted for everybody about the issue. Each method has advantages as well as disadvantages. Hence, materials selection will be done for car bumper and flywheel via classical materials selection method as well as using computer aided materials selection software following preliminary screening, limited properties and decision mechanism. During the materials selection process mechanical, physical and chemical properties as well as cost and formability will be taken into account. Thus, evaluating the results for materials selection categories will be investigated all together comparing the differences and the advantages for both materials selection methods.

Materials assortment for the car bumper and flywheel are given as examples for the conventional materials selection method.

2. MATERIALS SELECTION BY CONVENTIONAL (CLASSICAL) METHOD

The old and the simplest materials selection method in design is done using the data and standards taken from the materials producers, suppliers about materials' physical properties and performance characteristics. The process steps are summarized as follows:

- Analysis of the required properties of the materials: Working and environmental conditions are evaluated in the production area for the targeted artifact.
- Selection of the candidate materials: Alternative materials are listed in resisting to the conditions and variations during the service life.
- Developing the candidates: Desired properties are compared with the engineering properties for the candidates in the wide materials spectrum.
- Selection of the optimum materials matching to the required properties: Optimum material selection is done in the light of perception, experience and judgment obeying the best agreement.

2.1. Materials selection for car bumpers

Bumper is a sheet existing in front and back of the car and absorbing the impact and shock energy [26,35,36]. Let us examine the steps for the materials selection as follows:

1- Analysis for the required properties of the materials: the required or requested properties from the car bumpers are arranged in order as follows:

- impact resistance must be elevated (high fracture toughness)
- mass must be light (low density)
- formability must be easy
- corrosion resistance must be high (no rusting)
- price must be cheap

2- Selection for candidate materials:

Evaluating the required properties for car bumpers, it is possible to suggest the following materials as candidates:

- polymers [(polymethyl metacrilate (PMMA), polypropylene (PP)]
- metals (stainless steels, Al-alloys)
- composites [carbon fiber reinforced plastics (CFRP), glass fiber reinforced plastics (GFRP)]

3- Developing the candidates:

Let us evaluate the candidate materials for car bumpers and give points in the light of the requested properties. In this method; a ranking system is applied to the candidate materials according to their potential performance for the required properties. Then, a grading process is applied to the candidates among 1 to 10. If the candidate fully obeys the rule, 10 scores is given, otherwise 1 score can be consistent for the mentioned nominee. During the grading process for the materials selection issue, the designers' experiences as well as the general materials data taken from the handbooks are used. The candidate materials are written into the columns and the required properties into the rows, and then materials properties are read from the Ashby's [26] selection graphs and written into the related rows for the correct candidates (Table 1).

Table 1. Car bumpers candidate materials and grading [26].

Property/Materials	PMMA	PP	Stainless steel	Al alloy	CFRP	GFRP
Fracture toughness (MPa m ^{1/2})	1.5 (1p)	1 (1p)	50 (10p)	25 (7p)	20 (6p)	30 (8p)
Density (Mg/m ³)	1.2 (10p)	0.9 (10p)	7.8 (2p)	2.7 (5p)	1.7 (8p)	1.8 (8p)
Formability	+++ (10p)	+++ (10p)	++ (8p)	++ (8p)	+ (6p)	+ (6p)

Corrosion resistance	Excellent	Excellent	Good (7p)	Good (7p)	Good (7p)	Good (7p)
Cost (USD/kg)	15 (7p)	2.5 (10p)	60 (4p)	15 (8p)	400 (1p)	35 (6p)
Total grading	38p	41p	31p	35p	28p	35p

4- Selection of the optimum materials matching to the required properties

It is seen from Table 1 that two polymeric materials can supply the optimum properties for the car bumper and therefore they have the highest grades, and they are PP (41 points) and PMMA (38 points). The mentioned polymeric materials are the optimum candidates due to their lower cost and density, easy formability and excellent corrosion resistance. Then the GFRP and Al-alloy have taken the part as candidates having 35 points each, respectively. However, these two candidates are placed behind the polymers due to their higher cost and unsuccessful properties for the requirement. After that, stainless steel comes with 31 points as candidate materials. Nevertheless, stainless steel stays in the back about the material selection problem due to its high density (ie heavy material) and elevated cost issues despite its positive properties in ranking such as corrosion resistance and high fracture toughness. As a summary, PP and PMMA polymeric materials are selected for the optimum materials for a car bumper.

3. COMPUTER AIDED MATERIALS SELECTION APPLICATIONS

In the current study, CES Selector 2014 software is used for the computer aided materials selection method developed by Granta Design group heading by Ashby. In the previous literature, there are a number of materials selection papers reported by several investigators [2,6,13] successfully using the CES Selector software. Useful information can be found in the system using search button, such as current investigation about the selected materials, properties for the alternative materials, and production processes. It is possible to find the data and their properties about alternative materials using the search button, if it is desired alternative materials can be developed using the available data base. Clicking selection button and using these data in the software, an assortment can be done according to the materials group

For the materials selection, first tabbing for “selection” and then materials database is determined in software. Using the determined materials database, graphs are drawn depending on the properties and firm boundary conditions, thus materials selection process can be continued. For screening method, Ashby’s team Granta Design offered a software named as Granta Design as a graphic interfaced program [2,29]. It is possible to see the place of the materials group in the Ashby’s graphs shown for the relationship between two properties. In Figure 1, steps are seen for a graphical drawn for a sample selection.

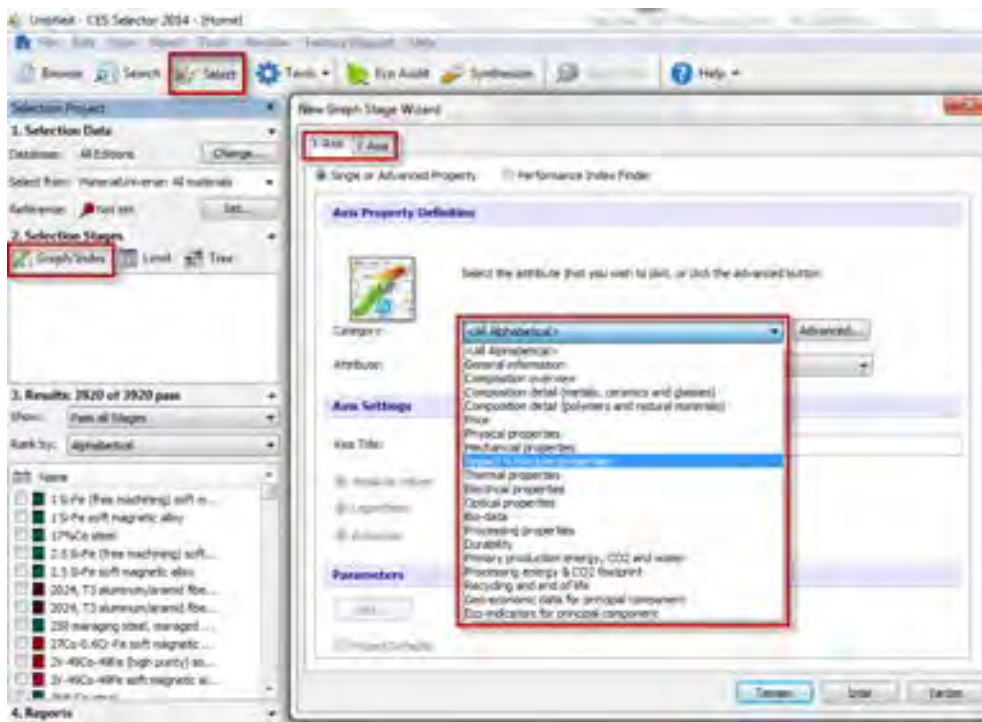


Figure 1. Materials selection for a graphical drawn for application steps

The other materials selection application is that the required boundary conditions are selected from the limit values in the software and selection process is finished. In this part, the selection is done determining for all required minimum and maximum boundary conditions taking into account of the material will be used in a place and the alternative materials are arranged accordingly in order. According to the given boundary conditions, the user can compare the alternative materials and then makes the materials choice for the selection problem.

3.1. A case study for car bumpers using CES selector software

For the materials selection, first it is possible and beneficial to discover the data about the used materials, processes and properties from the software using the search button and this data will facilitate the selection issue. In Figure 2, the materials selection results are seen for the car bumper using search button in software.

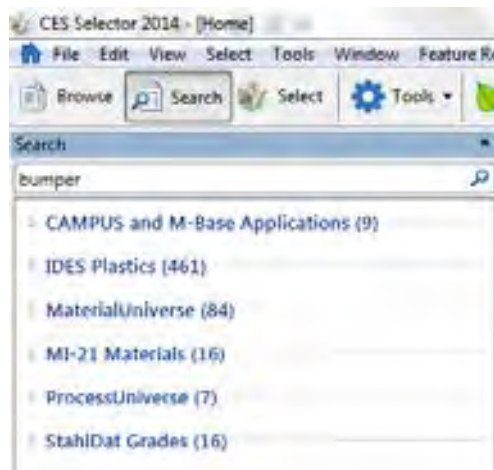


Figure 2. Search results in CES Selector for car bumper.

In Figure 2 within the software, the alternative materials for car bumper within the different data base and forming methods for those materials are determined. In this section, if it is desired selection issue can be completed taking into account of the materials properties previously used. This part is especially quite beneficial for the partly inexperienced users who has no idea about the materials will be selected. In this study, the selection process is continued in detailed evaluating the materials properties obtained after the searching. As a result of the evaluating the required properties and investigating the current materials for bumper materials, polymers, metals and composites are present as alternatives. Therefore, the choice of “all materials” within the “materials universe” database will be the best process due to giving the assortment facility for all materials in selection tag within the software.

After the assortment for suitable database, the selection process will be continued via giving the required boundary conditions. Within this part, firstly the selection for suitable materials group is done among the 3920 candidates. It is seen the selection process for materials group in Figure 3.

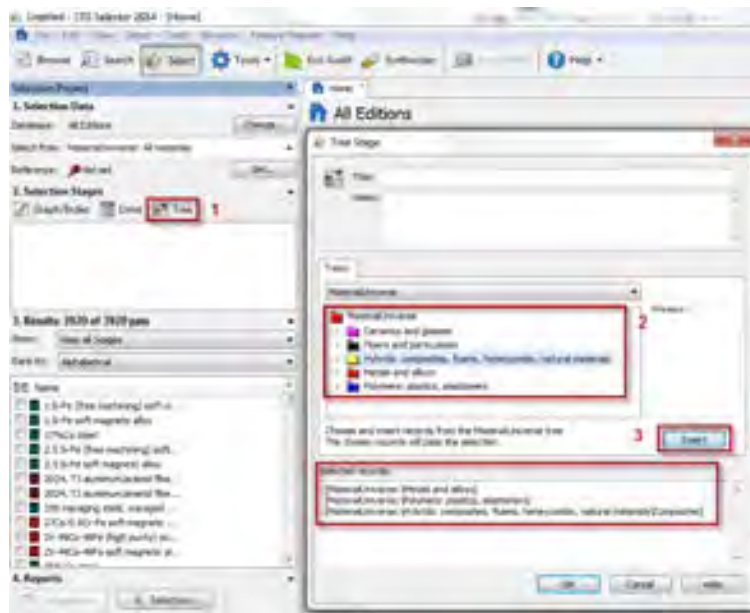


Figure 3. Selection process steps for materials group.

From the “materials universe” database, 2851 materials are remained suitable for the selection of metals and alloys, polymers, plastics, elastomers and composites. From the required properties, it is possible to show the two properties comparatively inside a graph within the selection steps. For the bumper materials, due to the most significant property is fracture toughness, therefore the relationship between fracture toughness against density and corrosion resistance are given in Figure 4 and Figure 5, respectively.

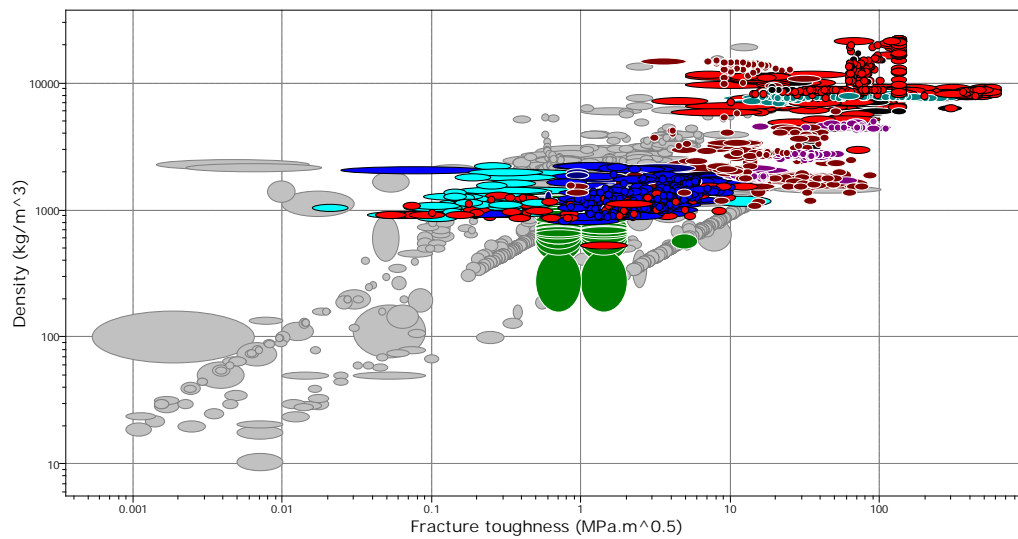


Figure 4. Comparison for density properties depending on fracture toughness.

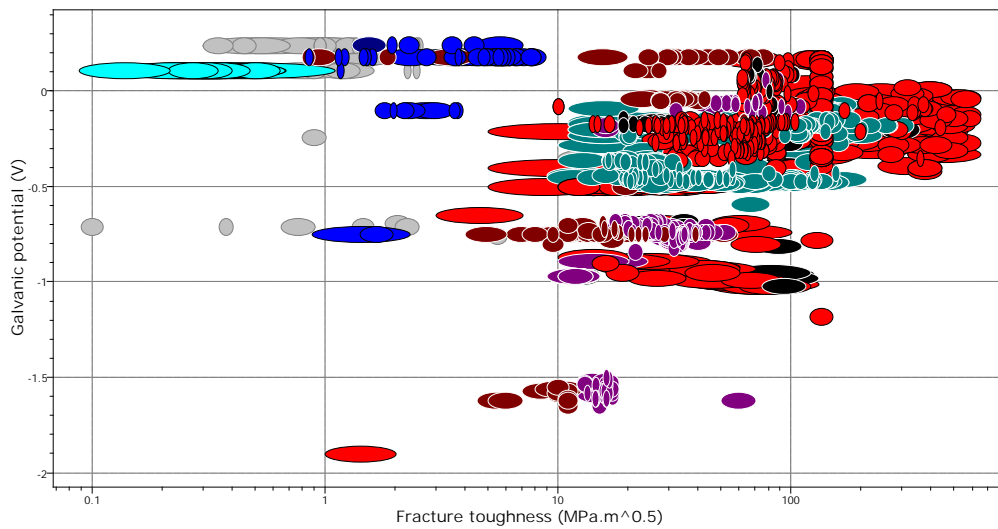


Figure 5. Comparison for corrosion resistance (galvanic potential) depending on fracture toughness

The materials groups are seen as different colors in graphs. The passive materials in gray color are presented in eliminated materials depending on the boundary conditions entered in database. In this step, if it is desired, selection is done from the materials groups in the graphs, or for the more sensitive selection, the process can be continued via concentrating on this material group. In this study, the selection process will be continued via entering the required minimum and maximum limit values for the materials. The determined and used boundary conditions for the materials are tabulated in Table 3.

Table 3. The property and boundary condition used for car bumper materials selection

Attribute	Constraints
Price (USD/kg)	≤ 5
Density (kg/m^3)	$\leq 3e3$
Fracture toughness ($\text{MPa}\cdot\text{m}^{0.5}$)	≥ 1
Galvanic potential (V)	≥ -0.6

For the materials properties, if it is necessary a value span can be determined, or writing the required minimum or maximum values will be sufficient as seen in Table 3. For the selection step, entering the boundary conditions are seen in Figure 6 via deciding the limits within the software.

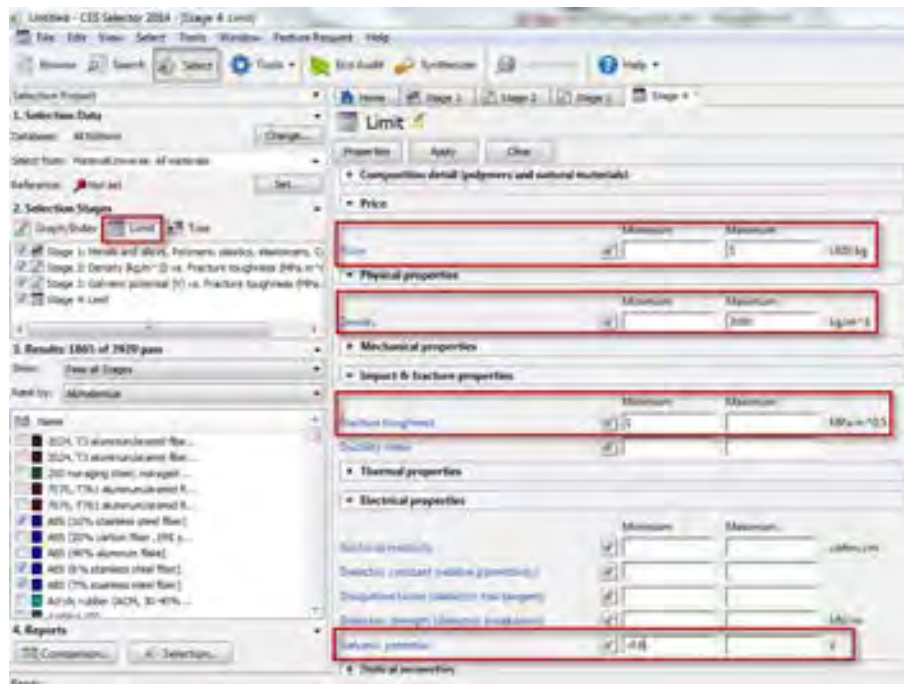


Figure 6. Definition of materials limit values in software.

As a result of entering the limit values, only 5 materials are stayed on suitable for the selection conditions. The remained materials are compared to each other and selection process is continued. In Table 4, there are a comparative table for the materials obtained from the software considering them to have suitable properties for bumpers after the screening process. Finally, the most suitable material selection is done evaluating the properties of formability from the comparative table. In the light of the mentioned assessment, the most appropriate material is selected as PP (copolymer, conductive, 5% carbon powder) for car bumper. The current conclusion is consistent with the previous used materials and determined by the conventional (classical) method.

4. EVALUATION FOR THE MATERIALS SELECTION METHODS AND CONCLUSIONS

In the current study, the selection process is done in a practical way using a classical method as well as computer aided CES Selector software. In both methods, there are several selection steps such as prescreening, evaluating limit values, considering optimum properties, cost and formability criteria, and assessing the properties and deciding to the candidates depending on the required properties. Due to the similar materials selection approaches within the classical method and computer aided software; consistent results are obtained in the examined case study.

Due to the characteristic properties for the car bumper are fracture toughness, corrosion resistance, lower density and cost, depending on the determined properties and boundary conditions, the best suitable material is found as PP from the polymeric materials. However, as a result of the selection by computer aided software, a PP (copolymer, conductive, 5% carbon powder) material can be directly and clearly selected. On the other hand, after the selection for candidates the material is clarified inside the group, if it is necessary a suitable database can be used for the more reliable and clear selection from the more alternatives related to the materials group such as (IDES Plastics).

For classical materials choice method, the selecting personnel should have wide knowledge, skill and experience in detail. The technical personnel should recognize the materials and have idea about the materials properties. Furthermore, the mentioned personnel can follow the fast developing materials such as metallic materials, polymers, elastomers, ceramics, composites as well as the new processes due to the forcing market and science. This situation is quite difficult considering especially current 160 thousands and continuously updating materials spectrum. However, there is no need to intense knowledge for the users due to updating the related data by software firms in computer aided software. The user can determine the optimum material very fast and more accurately comparing among the obtained results via studying the selection alternatives and entering the materials limits into the software. Moreover, the obtained results can be repeatable, and this can remove the mistakes originating from the wrong knowledge of the user.

Table 4. Comparison of outgoing materials according to boundary conditions for car bumper materials.

	ABS (10% stainless steel fiber)	PP (10-12% stainless steel fiber)	PP (copolymer, conductive, 5% carbon powder)
Composition overview			
Base	Polymer	Polymer	Polymer
Polymer type	ABS	PP	PP-copolymer
Polymer type full name	Acrylonitrile butadiene styrene	Polypropylene	Polypropylene copolymer
% filler (by weight) (%)	10	10 - 12	5
Filler type	Stainless steel fiber	Stainless steel fiber	Carbon powder
Composition detail (polymers and natural materials)			
Polymer (%)	90	88 - 90	95
Carbon (powder) (%)	0	0	5
Stainless steel (fiber) (%)	10	10 - 12	0
Price			
Price (USD/kg)	3.95 - 4.35	3.02 - 3.32	2.78 - 3.19
Physical properties			
Density (kg/m ³)	1130 - 1150	991 - 1020	947 - 976
Impact & fracture properties			
Fracture toughness (MPa.m ^{0.5})	1.99 - 2.39	1.9 - 2	1.12 - 1.18
Ductility index	0.51 - 0.62	1.98 - 2.43	9.34 - 11.4
Impact strength, notched 23 °C (kJ/m ²)	7 - 7.8	15.3 - 24.2	62 - 82.3
Impact strength, notched -30 °C (kJ/m ²)		13.1 - 13.8	48.7 - 51.2
Impact strength, unnotched 23 °C (kJ/m ²)		82.2 - 86.4	113 - 200
Impact strength, unnotched -30 °C (kJ/m ²)		67.7 - 71.1	93 - 200
Electrical properties			
Galvanic potential (V)	-0.14 - -0.06	-0.14 - -0.06	0.07 - 0.15
Processing properties			
Polymer injection molding	Limited use	Limited use	Excellent
Polymer extrusion	Unsuitable	Unsuitable	Limited use
Polymer thermoforming	Acceptable	Unsuitable	Limited use

REFERENCES

- [1]. Fındık F. Materials Selection and Applications (in Turkish), Sakarya Yayıncılık, Sakarya 2008.
- [2]. Ashby MF, Shercliff H, Cebon D. Materials engineering, science, processing and design. Oxford: Elsevier; 2007.
- [3]. Sapuan SM. A knowledge-based system for materials selection in mechanical engineering design. Mater Des 2001;22:687-895.
- [4]. Sapuan SM, Jacob MSD, Mustapha F, Ismail N. A prototype knowledge-based system for material selection of ceramic matrix composites of automotive engine components. Mater Des 2002;23:701-8.
- [5]. Amen R, Vomacka P. Case-based reasoning as a tool for materials selection. Mater Des 2001;22:353-8.
- [6]. Ashby MF, Bréchet YJM, Cebon D, Salvo DL. Selection strategies for materials and processes, Materials & Design, Volume 25, Issue 1, Pages 51-67, February 2004.
- [7]. Farag MM. Quantitative methods of materials selection. In: Kutz M, editor. Handbook of materials selection; 2002.
- [8]. Goldsberry C. Computer modeling and how it helps drive material selection. Mod Plast Worldwide 2006;83:150-2.
- [9]. Jurkowski B, Olkhov YA, Kelar K, Olkhova OM. Thermomechanical study of low-density polyethylene, polyamide 6 and its blends. Eur Polym J 2002;38:1229-36.
- [10]. Balakrishna A, Rao DN, Srinivas J, Satish P. Computer aided material selection processes in concurrent engineering using neural networks. J Inst Eng (India): Mech Eng Div 2007;88:20-3.
- [11]. Karana E, Hekkert P, Kandachar P. Material considerations in product design: a survey on crucial material aspects used by product designers. Mater Des 2008;29:1081-9.
- [12]. Jalham IS. Computer-aided quality function deployment method for material selection. Int J Comput Appl Technol 2006;26:190-6.
- [13]. Cebon D, Ashby M. Datasystems for optimal material selection. Adv Mater Process 2003;161:51-4.

- [14]. Pham DT, Pham PT. Computational intelligence for manufacturing. LLC: CRC Press; 2001.
 - [15]. Giudice F, La Rosa G, Risitano A. Materials selection in the life cycle design process: a method to integrate mechanical and environmental performances in optimal choice. *Mater Des* 2005;26:9–20.
 - [16]. Kumar S, Singh R. An intelligent system for modeling and material selection for progressive die components. *Key Eng Mater* 2007;344:873–80.
 - [17]. Ramalhete PS, Senos AMR, Aguiar C. Digital tools for material selection in product design. *Materials and Design* 31 (2010) 2275–2287
 - [18]. Bovea MD, Vidal R. Materials selection for sustainable product design: a case study of wood based furniture eco-design. *Mater Des* 2004;25:111–6.
 - [19]. Abeyundara UGY, Sandhya B, Shabbir G. A matrix in life cycle perspective for selecting sustainable materials for buildings in Sri Lanka. *Build Environ* 2009;44:997–1004. <http://dx.doi.org/10.1016/j.buildenv.2008.07.005>.
 - [20]. Ashby MF. Materials selection in conceptual design. *Mater Sci Technol* 1989;5:517–25.
 - [21]. Kromm FX, Quenisset JM, Lorriot T, et al. Definition of multi materials design method. *Mater Des* 2007;28:2641–6.
 - [22]. Vezzoli C, Manzini E. *Design for environmental sustainability*. New York: Springer; 2008.
 - [23]. Pilani R, Narasimhan K, Maiti SK, Singh UP, Date PP. A hybrid intelligent systems approach for die design in sheet metal forming. *Int J Adv Manuf Technol* 2000;16:370–5.
 - [24]. Shackelford FJ. *Introduction to materials science for engineers*. London:Pearson; 2009.
 - [25]. Askeland DR. *The science and engineering of materials*. 5th ed. London:Thomson; 2009.
 - [26]. Ashby MF. *Materials selection in mechanical design*. New York: Pergamon Press; 1995.
 - [27]. Rao RV, Patel BK. A subjective and objective integrated multiple attribute decision making method for material selection. *Mater Des* 2010;31:4738–47.
 - [28]. Kutz Myer, editor. *Handbook of materials selection*. New York: John Wiley & Sons; 2002.
 - [29]. Zha XF. A web-based advisory system for process and material selection in concurrent product design for a manufacturing environment. *Int J Adv Manuf Technol* 2005;25(3–4):233–43.
 - [30]. Findik F, Turan K. Materials selection for lighter wagon design with a weighted property index method. *Materials and Design* 37 (2012) 470–477
 - [31]. Ashby MF, Johnson K. *Materials and design: the art and science of materials selection in product design*. Oxford: Butterworth Heinemann; 2002.
 - [32]. Edwards KL. Selecting materials for optimum use in engineering components. *Mater Des* 2005;26:469–73.
 - [33]. Manshadi BD, Mahmudi H, Abedian A, Mahmudi R. A novel method for materials selection in mechanical design: combination of non-linear normalization and a modified digital logic method. *Mater Des* 2007;28:8–15.
 - [34]. Rao RV. *Decision making in the manufacturing environment using graph theory and fuzzy multiple attribute decision making methods*. London: Springer-Verlag; 2007.
 - [35]. Crane FAA, Charles JA. “Selection and Use of Engineering Materials”, The Garden City Press Ltd. 1984.
 - [36]. *Metals Handbook, ASM Handbook, v. 20, ASM International, 1992.*
-

IDENTIFICATION OF WASTE SOURCES IN READY-MIXED CONCRETE PLANTS

Aynur KAZAZ

Akdeniz University, Department of Civil Engineering, 07058, Antalya, Turkey.
akazaz@akdeniz.edu.tr

Serdar ULUBEYLI

Bulent Ecevit University, Department of Civil Engineering, 67100, Zonguldak, Turkey.
ulubeyli@beun.edu.tr

Bayram ER

Akdeniz University, Department of Civil Engineering, 07058, Antalya, Turkey.
bayramer@akdeniz.edu.tr

Ahmet ARSLAN

Akdeniz University, Department of Civil Engineering, 07058, Antalya, Turkey.
arslnahmt07@hotmail.com

Murat ATICI

Akdeniz University, Department of Civil Engineering, 07058, Antalya, Turkey.
aticimurat@yandex.com

Abstract

In today's highly industrialized world, an enormous amount of wastes is originated from the construction industry. This type of wastes conversely affects both macro-economic conditions and environment of a country or a region. Therefore, waste management is an important aspect of project management. Although there is a wide variety of construction materials, concrete is still the mostly used one in the construction industry and thus has a big impact on the amount of construction-based wastes. Reducing such wastes is among the objectives of the waste management issue in construction projects. Accordingly, the determination of waste sources is the first step to deal with them. Based on these arguments, the current paper presents a study that aims to identify the sources of fresh concrete wastes in ready-mixed concrete (RMC) plants as a part of an on-going research project. Toward this aim, production and delivery processes of RMC were reported and discussed in a detailed manner from the perspective of waste management. As a result, four sources were identified for such wastes. It was also found out that only two types of these sources (i.e., over-order and residual RMC in the truck-mixer drum) are quantifiable.

Keywords: *construction waste, fresh concrete waste, ready-mixed concrete, waste sources.*

1. INTRODUCTION

Today, construction wastes constitute approximately 20–40% of the area occupied by wastes in a country ([16], [5], [10]). Construction wastes produced per year in England [8] and US [20] are estimated as 91 and 164 million tons, respectively. Especially in developing countries such as Turkey where the construction industry is in a rapid development process (Figure 1), the rate of construction wastes is expected to be higher [19]. Therefore, minimizing or recycling construction wastes is a crucial activity for using the limited natural resources efficiently for a long term.

Although there are different construction systems, reinforced-concrete structures are still common. Easy supply and low cost of raw materials, easy forming, and low know-how requirement in the production process are main reasons of using concrete in construction projects. In a concrete building, the cost of concrete may rise up to 10% of the total project cost [3]. In addition, according to Turkish Ready Mixed Concrete Association [18], Turkey has an annual ready-mixed concrete (RMC) production amount of 102 million m³ (Figure 2).

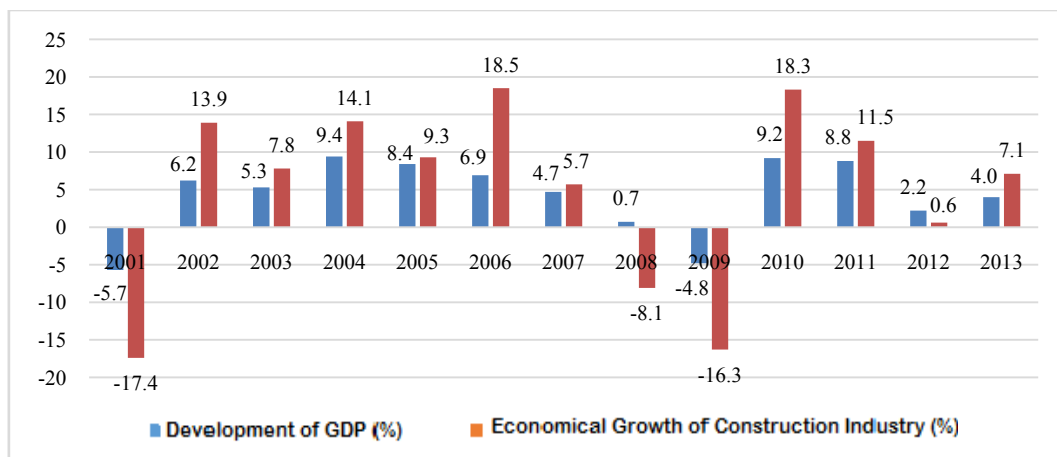


Figure 1. Comparison of the economic role of the construction industry with the development of GDP in Turkey

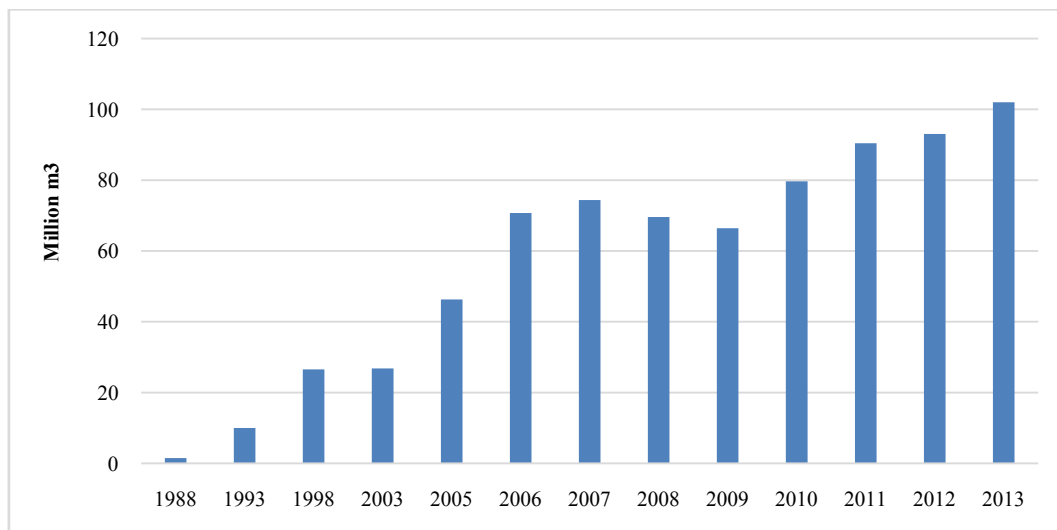


Figure 2. The annual production amount of RMC

This production amount places Turkey in the first rank in Europe and the third rank in the world (Table 1). Therefore, it can be argued that concrete wastes have a big impact on construction-based wastes, and reducing them will improve both macro-economic conditions and the built environment in Turkey.

Waste management encompasses preventing, collecting, transporting, and disposal of wastes. Main principles of waste management are reducing, reusing, and recycling of wastes. Therefore, for an effective waste management procedure in a construction site, it is important to determine which kinds of wastes can be reduced, reused, or recycled. Concrete wastes appear in two ways during the whole lifecycle of a construction project: (i) as the fresh concrete waste during the implementation phase and (ii) as the demolition waste during the destruction of the structure.

Demolition wastes are generated as hardened concrete after the building completes its economic life. Therefore, reducing demolition wastes or recycling them to their raw materials seems impossible in the current technological conditions. However, reusing crushed demolition wastes as filling materials or aggregate for fresh concrete are common practices in the construction industry ([1], [11], [14], [15], [21], [2], [6], [13]).

Fresh concrete wastes occur both in construction sites and in RMC plants at the start of the economic life of a project before concrete gets hardened. There are recycling facilities which separate the fresh concrete to its raw materials. Therefore, identifying the sources of fresh concrete wastes can be helpful both for determining preventive measures and for calculating the amount of this waste that can be recycled. In this context, the current paper presents a study that aims to identify the sources of fresh concrete wastes in RMC plants as a part of an on-going research project.

Table 1. The RMC production amount of ERMCO countries in 2013

Country	Amount of Production (million m ³)	RMC per Person (m ³ /person)
Spain	16.3	0.3
Italy	31.7	0.5
Turkey (2013)	102	1.3
Germany	45.6	0.6
France	38.6	0.6
England (UK)	19.6	0.3
Portugal	2.7	0.3
Belgium	12.5	1.1
Poland	18	0.5
Ireland	2.4	0.5
Netherland	6.6	0.4
Norway	3.8	0.8
Sweden	3.3	0.3
Total of Europe	218.1	0.5
Russia	44	0.3
USA	230	0.8
Japan	99	0.8

2. LIFECYCLE OF THE FRESH CONCRETE

Concrete is mainly used to produce the bearing elements of a structure. Therefore, the quality of the fresh concrete has a big impact on the strength of a structure. This quality depends on the mixing ratios of raw materials used in the fresh concrete production. For example, an increase of 20% and 30% of the water content will decrease the strength of concrete by %30 and 50%, respectively [17]. Although the concrete quality is determined by internationally and nationally accepted standards, the fresh concrete produced in site by unskilled workers will likely have a high risk for quality. In addition, since the amount of concrete produced in site is limited, every production may also have different qualities. In order to overcome these problems, the fresh concrete is produced in RCM plants where the production is supported by automation systems and the product is transported by truck mixers to construction sites.

The production process in RMC plants starts with laboratory tests. In these tests, the quality of raw materials and their compatibilities are evaluated. In fact, these tests are conducted when new raw materials arrive to the batching plant. Therefore, each RMC plant has also a quality control department. After these tests are completed, for each concrete class a specific mixing ratio is determined and saved into the automation system.

In RMC plants, concrete is produced in two ways: (i) dry system and (ii) wet system (Figure 3). In the dry system, cement and aggregate are mixed in truck mixers without adding water and admixture. The water and admixture are added at the construction site before concrete is poured. Nevertheless, this system seems to be logical when the transport distance is too long. If the transport time exceeds two hours, there will be some quality problems. If the moisture content of the truck mixer is too high, the chemical reaction between cement and aggregate will start before the necessary water is added. In addition, admixtures and water may be added by unskilled workers in site and the necessary mixing for a homogenous concrete production may not be waited. Therefore, in RMC plants, the wet system is more common than the dry system. In the wet system, all of raw materials stored in different places are weighed separately and put into the mixing drum of the plant by means of the automation system. Since over-mixing will lead to segregation in the fresh concrete, the mixing process is continued for a specific duration in mixing drums, and then, the mixed concrete is poured into truck mixers where the mixing process will continue until it arrives to the construction site [9]. Finally, in construction sites, the fresh concrete transported by truck mixers is poured into formworks by concrete pumps, and residual concrete is transported back to RMC plants.

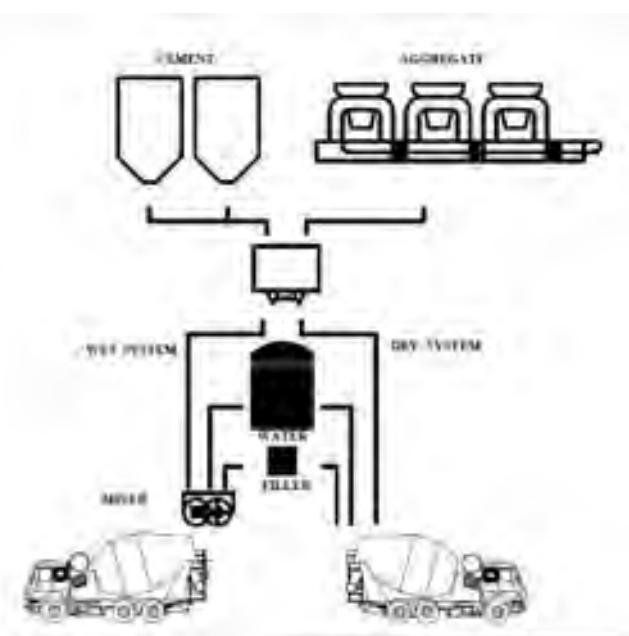


Figure 3. The operation schema of RMC plants

3. SOURCES OF FRESH CONCRETE WASTES

In order to identify the sources of fresh concrete wastes, three different RMC plants operating in different cities in Turkey were investigated as a part of an on-going research project. Each RMC plant was visited once a week for 12 months. After detailed observations, four sources for fresh concrete wastes were identified as follows.

3.1. During the Filling Process of Truck Mixers

Since the hopper of a truck mixer is at the back side, truck mixers have to draw close backwards to the mixing drum's discharging part. In this situation, depending on drivers' abilities, sometimes the hopper and discharging parts do not match exactly, and as a result, some fresh concrete is unintentionally poured outside of the truck mixer. In addition, if the production stops for a while or the concrete class changes, then the mixing drums should be washed up. In this process, some fresh concrete waste is generated. Although the amount of waste generated by each filling or washing up effort seems to be negligible, the sum of this waste in RMC plants with high production amounts becomes remarkable. For example, the waste amount shown in Figure 4 was produced within two hours in an RMC plant with an average daily concrete production of 750

m³. However, it is very difficult to measure the amount of this waste due to the intensive vehicle traffic. In practice, when the production stops, this waste is collected and stored by loaders in the debris area.

3.2. Quality Control Laboratory

In RMC plants, besides the quality control of raw materials, the quality of the fresh concrete has to be controlled. In practice, for this purpose, some fresh concrete from each production is taken and filled up into cube formworks in the laboratory of the RMC plant. In general, this exceeds the needed amount, and hence, some fresh concrete waste is also generated in this process.

3.3. The Adhesive Concrete in a Truck Mixer's Drum

Although truck mixers try to pour all of the fresh concrete content in construction sites, there always remains some adhesive concrete in their drums. Therefore, after truck mixers return to RMC plants, their drums are washed up by adding about 200-300 liter water. In the context of the ongoing research project, in each visit of RMC plants, 10 truck mixers were washed and the waste content was measured. The preliminary statistical analysis revealed that approximately 500 kg aggregate comes out as waste in the 100 m³ fresh concrete production.



Figure 4. The waste generation during the filling process

3.4. The Over-Order Concrete

In construction projects, wastes are inevitable. Therefore, the planned material amount rarely matches with the actual material need. Especially in concreting works, this difference can be observed more clearly due to some reasons such as the content of filler blocks and reinforcement and poor workmanship. In order to overcome this problem, many planning engineers have the tendency of over-ordering materials. For this purpose, they determine a coefficient based on their own personal experience and multiply it with the planned amount [[12], [7], [4)]. Nevertheless, since these coefficients are based on experience and are not exact values, almost in every order the residual fresh concrete occurs because of over ordering. However, in practice, this residual concrete is not stored in the debris area. Instead, if the transport duration does not exceed two hours, it is mixed with lower class concrete of another order and used in other projects. For example, if the residual concrete class is C30, it is mixed with C25. Therefore, this type of wastes is mostly encountered at the end of the working day. Since this type of wastes is documented, the amount is measurable.

The aforementioned types of wastes are a part of the production and are inevitable. In addition to these waste sources, it was also observed that fresh concrete wastes are also generated from a problem in production, such as the breakdown of some machines. Although the amount of this waste can be huge when compared with

other types of concrete wastes, it occurs rarely and randomly. For example, during on-plant observations, 3 m³ fresh concrete was produced only once.

Similar to other enterprises, the aim of RMC plants is to make some profits. In this respect, many RMC plants neglect the environmental impact of fresh concrete wastes and do not strive to reduce or recycle these wastes. Interviews with plant managers revealed that the low cost and easy supply of raw materials are main obstacles for taking countermeasures.

4. CONCLUSIONS

In today's highly industrialized world, an enormous amount of wastes is originated from the construction industry. Since wastes are unused materials that do not have an economic value, they conversely affect both macro-economic conditions and the built environment of a country or a region. In this context, waste management becomes an important aspect of project management.

For an effective waste management procedure, it is important to determine which kinds of wastes can be reduced, reused, or recycled. In this regard, the first step of waste management should be the determination of waste sources. In this study, it was aimed to identify the sources of fresh concrete wastes in RMC plants. Toward this aim, three different RMC plants were observed in every week for a year. The results revealed that fresh concrete wastes are generated in four different sources in an RMC plant (i.e., during the filling process of truck mixers, quality control laboratory, the adhesive concrete in the truck mixer's drum, and over-ordering). Because of the operation process of the batching plants, only adhesive concrete in the truck mixer's drum and the over-order concrete are quantifiable.

ACKNOWLEDGMENT

The authors gratefully acknowledge the managers and employees of the batching plants for their generous collaboration and contributions. The authors also thank the financial supports provided by Committees on Research Grants of Akdeniz University and Bulent Ecevit University. This study is based on an on-going research project which is financially supported by the Scientific and Technological Research Council of Turkey (TUBITAK) under the grant number MAG-113M428.

REFERENCES

- [1]. Y. H. Cho, and S. H. Yeo, "Application of recycled waste aggregate to lean concrete subbase in highway pavement", *Canadian Journal of Civil Engineering*, vol. 31, pp. 1101-1108, 2004.
- [2]. R. Herrador, P. Perez, L. Garach, and J. Ordonez, "Use of recycled construction and demolition waste aggregate for road course surfacing", *Journal of Transportation Engineering*, vol. 138, pp. 182-190, 2012.
- [3]. A. Kazaz, S. Ulubeyli, and F. Turker, "The quality perspective of the ready-mixed concrete industry in Turkey", *Building and Environment*, vol. 39, pp. 1349-1357, 2004.
- [4]. H. Kerzner, *Project Management: A Systems Approach to Planning, Scheduling and Controlling*, 10th ed., New Jersey, USA: John Wiley and Sons, 2009.
- [5]. C. J. Kibert, "Deconstruction as an essential component of sustainable construction", in *Proc. Second Southern African Conference on Sustainable Development in the Built Environment*, 2000, p. 1-5.
- [6]. S. Kou, B. Zhan, and C. Poon, "Feasibility study of using recycled fresh concrete waste as coarse aggregates in concrete", *Construction and Building Materials*, vol. 28, pp. 549-556, 2012.
- [7]. J. P. Lewis, *Project Planning, Scheduling, and Control: A Hands-On Guide to Bringing Projects in on Time and on Budget*, 3rd ed., New York, USA: McGraw-Hill, 2001.
- [8]. M. Osmani, J. Glass, A. D. F. Price, "Architects' perspectives on construction waste reduction by design", *Waste Management*, vol. 28, pp. 1147-1158, 2008.
- [9]. L. S. Pheng, *Theory and Practice of Construction Export Marketing*, Burlington, UK: Ashgate Publishing Company, 1996.
- [10]. C. S. Poon, "Reducing construction waste", *Waste Management*, vol. 27, pp. 1715-1716, 2007.
- [11]. A. Rao, K. N. Jha, and S. Misra, "Use of aggregates from recycled construction and demolition waste in concrete", *Resources, Conservation and Recycling*, vol. 50, pp. 71-81, 2007.
- [12]. G. J. Ritz, *Total Construction Project Management*, New York, USA: McGraw-Hill, 1994.
- [13]. R. V. Silva, J. de Brito, and N. Saikia, "Influence of curing conditions on the durability-related performance of concrete made with selected plastic waste aggregates", *Cement and Concrete Composites*, vol. 35, pp. 23-31, 2013.
- [14]. M. A. Sobhan, S. A. Mofiz, and H. M. Rasel, "Effect of gradation and compactive effort on the properties of bituminous mixes with waste concrete aggregates", *International Journal of Civil and Environmental Engineering*, vol. 11, pp. 18-21, 2011.
- [15]. M. S. Sobri, S. H. Hamzah, and A. R. M. Ridzuan, "Ultimate strength of steel fabric reinforced concrete short wall panel using crushed concrete waste aggregate (CCwA)", *International Journal of Civil and Environmental Engineering*, vol. 11, pp. 64-80, 2011.
- [16]. M. J. Stokoe, P. Y. Kwong, and M. M. Lau, "Waste reduction: a tool for sustainable waste management for Hong Kong", in *Proc. R'99 World Congress*, 1999, p. 165-170.
- [17]. M. Şimşek, *Construction Materials - I*, Istanbul, Turkey: Seçkin Publisher, 2013. (in Turkish)
- [18]. TRMCA (Turkish Ready Mixed Concrete Association). (2014) Statistics. [Online]. Available: <http://www.thbb.org/en/industry>

- [19]. T. Tuy, Y. Cheny, L. Hwang, "Properties of HPC with recycled aggregates", *Cement and Concrete Research*, vol. 36, pp. 943–950, 2006.
- [20]. G. Winkler, *Recycling Construction and Demolition Waste*, New York, USA: McGraw-Hill, 2010.
- [21]. C. J. Zega, and A. A. D. Maio, "Recycled concretes made with waste ready-mix concrete as coarse aggregate", *Journal of Materials in Civil Engineering*, vol. 23, pp. 281–286, 2011.

EVALUATION OF CURRENT RECYCLING FACILITIES FOR RMC PLANTS IN TURKEY

Aynur KAZAZ

Akdeniz University, Department of Civil Engineering, 07058, Antalya, Turkey.
akazaz@akdeniz.edu.tr

Serdar ULUBEYLI

Bulent Ecevit University, Department of Civil Engineering, 67100, Zonguldak, Turkey.
ulubeyli@beun.edu.tr

Bayram ER

Akdeniz University, Department of Civil Engineering, 07058, Antalya, Turkey.
bayramer@akdeniz.edu.tr

Murat ATICI

Akdeniz University, Department of Civil Engineering, 07058, Antalya, Turkey.
aticimurat@yandex.com

Ahmet ARSLAN

Akdeniz University, Department of Civil Engineering, 07058, Antalya, Turkey.
arslnahmt07@hotmail.com

Abstract

Construction wastes are mostly generated during implementation and demolition phases of a project. Since these wastes are inevitable, waste management focuses on reducing, reusing, and recycling of wastes instead of eliminating them. As the largest part of construction wastes, concrete is one of the mostly used materials in construction projects. Three raw materials of concrete (i.e., gravel, cement, and water) are natural resources, and over consumption can negatively affect the economy and environment of a country. In this regard, recycling of fresh concrete wastes is an important issue for waste management in the domain of construction. Although there are different recycling facilities for fresh concrete wastes, ready-mixed concrete (RMC) plants in Turkey do not have to build them. In the current study, it was aimed to present the benefits of the recycling facilities for RMC plants in Turkey as a part of an on-going research project. To this aim, different recycling facilities were compared with each other, and then, operation processes of these facilities were investigated by visiting some RMC plants. The results revealed that most of managers in these plants are aware of potential benefits of the recycling facilities. However, they find managing these facilities difficult, and thus, most of them do not build these facilities in their plants.

Keywords: *construction waste, fresh concrete waste, ready-mixed concrete, recycling facilities.*

1. INTRODUCTION

The construction industry generates enormous amounts of wastes. Since these wastes are not used in the production process, they do not add any value to the project. Therefore, this kind of wastes conversely affects both macro-economic conditions and the built environment of a country. It is estimated that in England [7] and in the US [14] approximately 91 and 164 million tons construction waste are produced, respectively. Although the estimated total annual amount of solid wastes in Turkey is 38 million tons [8], there is no a scientific research that clearly addresses how much of these originates from the construction industry. However, according to Baytan [1] who estimated a concrete waste ratio of 6.1%, it can be assumed that the total construction waste in Turkey varies between 2 and 2.5 million tons.

Due to the variety of materials used in construction projects, the type of wastes also varies. However, concrete wastes have the highest share of 50-55% by weight among other types of wastes ([6], [3]). In the concrete production, natural resources, such as water, gravel, and cement, are used. Therefore, the excessive consumption of concrete can cause environmental issues as well as economic problems. In this regard, minimizing or recycling concrete wastes has become a crucial issue for the construction industry to date.

Concrete wastes are generated both during the implementation phase as the fresh concrete waste and during the demolition phase as the demolition waste. In the related literature, some studies demonstrated that the crushed demolition wastes can be reused as filling materials or aggregate for the fresh concrete production ([2], [9], [11], [12], [16], [4], [5], [10]). Similarly, in practice, if a recycling facility is not used, the fresh concrete waste is stored in the debris area of the RMC plant and used as a filling material after it hardens.

In Turkey, RMC plants have to build a sedimentation pond for fresh concrete wastes. In this sedimentation pond, only water can be recycled for the fresh concrete production and other raw materials are stored as waste in the debris area. On the other hand, although there are different recycling facilities for fresh concrete wastes, in Turkey the reuse of these raw materials is not common among RMC plants. In this study, it was aimed to present the benefits of the recycling facilities for RMC plants in Turkey as a part of an on-going research project. To this aim, different recycling facilities were compared with each other, and then, the operation processes of these facilities was investigated by visiting some RMC plants.

2. THE CONCEPTUAL BACKGROUND

In developing countries such as Turkey, the construction industry is in a rapid development and thereby has a significant impact on the national economy. Since 2009, Turkey has been ranked first in Europe and third in the world with an approximate annual fresh concrete production amount of 100 million m³. Therefore, it is evident that an enormous amount of the fresh concrete waste is generated in Turkey.

Although there are different recycling facilities for fresh concrete wastes, in Turkey the RMC plants do not have to use them. Especially, the low cost of raw materials is the main obstacle for the installation of these facilities [15]. In order to determine the utilization ratio of the recycling facilities, 284 RMC plants which are members of Turkish Ready Mixed Concrete Association [13] were contacted. Interviews conducted with plant managers via phones revealed that only 28% of these plants have a recycling facility and only 22% of them use these facilities in an active manner, as presented in Table 1. The difficulty in managing the operation process is the main obstacle of using a recycling facility. In fact, the result of these interviews showed that although most of managers are aware of benefits of utilizing the recycling facilities, they do not give adequate importance to this issue. In this context, the main goal of this study is to extend the utilization rate of the recycling facilities among RMC plants by introducing potential saving costs.

Table 1. The utilization ratio of the recycling facilities among members of TRMCA

	Existing	Existing but not actively used	Not existing	Total
Number of the Recycling Facilities	63	16	205	284
Percentage (%)	22.18%	5.63%	72.18%	100.00%

3. THE WORKING PRINCIPLES OF THE RECYCLING FACILITIES

Fresh concrete recycling facilities mainly allows reusing the waste water and aggregate of unhardened concrete by separating it to its raw materials by means of some physical methods. In this context, although there are different types of recycling facilities, their working principles are almost the same. A typical recycling facility consists of five different parts such as hopper, the clean water supply unit, the washing

drum, the aggregate discharge unit and the contaminated water discharge unit, as shown in Figure 1. First, the fresh concrete waste poured into the hopper is transmitted to the washing drum by a sieve which also has an inbuilt vibrator. After the preliminary separation performed by the sieve, the fresh concrete is concurrently washed and rotated in the washing drum. By this way, aggregates of the fresh concrete are separated and discharged from the washing drum. The contaminated water produced during the recycling process is transmitted to sedimentation ponds for further reuse. Since the contaminated water contains small cement and aggregate particles, an agitator is built into the contaminated water discharge unit.

Recycling facilities used in RMC plants may have different capacities, engine powers, or productivity values. However, basically, recycling facilities differs from each other due to two main features. The first feature is the existence of the discharge sieve. The discharge sieve is located in the aggregate discharge unit and used to separate wet aggregates from their water and small particle contents. Therefore, besides obtaining drier recycled aggregates, recycling facilities with discharge sieves can also increase the amount of the recycled water.

The second feature is the operation method of the recycling facilities. In this context, these facilities are grouped as manual and automatic systems. In manual systems, the recycling facility has to be started manually after the hopper is filled with the fresh concrete and switched off manually after the recycling process ends. In other words, an additional worker has to be employed for such recycling facilities. In automatic systems, the recycling process starts automatically after the weight of the fresh concrete poured into the hopper exceeds a certain value and stops automatically after the recycled aggregates are discharged from the facility. Therefore, in such systems, there is no need to employ an additional worker.

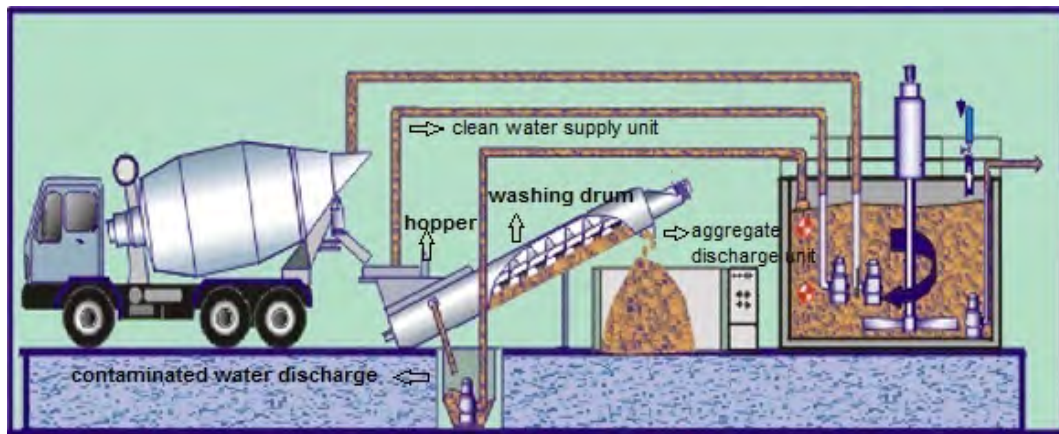


Figure 1. Parts of a typical recycling facility

4. SAVING COSTS OF THE RECYCLING FACILITIES

According to RMC plants' managers, the main obstacle of using a recycling facility in the batching plants is the difficulty in managing the operation process. In this respect, to most of the managers, as the recycling process is a time consuming activity, truck mixer drivers do not want to wait this process, and hence, an additional worker has to be employed. However, as mentioned before, automatic recycling facilities do not require to follow the recycling process. In other words, the utilization of automatic systems can eliminate the aforementioned reasons. In this study, as a part of an ongoing research project, it was aimed to determine benefit costs of an automatic recycling facility. For this purpose, document records of an RMC plant which utilizes a recycling facility and has a monthly fresh concrete production amount of 10,000 m³ were investigated, and an interview was conducted face-to-face with the manager of this plant.

Utilizing a recycling facility not only allows reusing the waste water and aggregate but also reduces the disposal cost of the waste material. In this regard, an RMC plant that utilizes a recycling facility can save costs in three different items. According to document records, it was calculated that the investigated RMC plant saves approximately 1,080 tons of water and 300 tons of aggregates by recycling the fresh concrete waste in a month. In addition, in the context of the on-going research project, it was estimated that, in the 100 m³ fresh concrete production, 500 kg aggregates come up as residual from truck mixers' drums. Therefore, the total amount of recyclable aggregates can increase up to 350 tons for the investigated RMC plant by taking into account its monthly production. Similarly, assuming that 75% of the fresh concrete ingredient is formed by aggregates, the investigated RMC plant can also save from the disposal cost of 467 tons of the concrete waste. The unit cost of each cost item was taken from the TRMCA databank, and hence, saving costs for the investigated RMC plant was calculated as \$5,092 per month, as given in Table 2.

Table 2. Saving cost items of the investigated RMC plant

Benefits	Monthly Quantity (Ton)	Unit cost per Ton (\$)	Monthly Sum (\$)
Water	1,080,000 lt	0.5	540
Aggregate	350 t	5	1,750
Disposal	467 t	6	2,802
Total			5,092

5. CONCLUSIONS

Concrete is one of the widely used materials in the construction industry. Therefore, an enormous part of the construction waste is originated from concrete. The reduction, re-use, and recycling of this waste can positively contribute to the economy and built environment of a country. In this respect, crushed demolition wastes are used as filling materials or aggregates in the fresh concrete production. Similarly, by using recycling facilities, fresh concrete wastes are recycled to its raw materials, and water and aggregates obtained from this recycling activity are reused in the new fresh concrete production.

Although there are different recycling systems available in the market, they are not common among RMC plants operating in Turkey. In addition to the fact that there is no a legal obligation for using them, the difficulty in managing the recycling process seems to be the main obstacle. In this study, it was aimed to introduce the benefits of the recycling facilities to RMC plants from a cost-based perspective. For this purpose, operation principles of the recycling facilities were explained, different recycling facilities were compared, and potential saving costs of an RMC plant that uses a recycling facility were calculated. The results revealed that managing automatic recycling facilities is not as difficult as assumed and that the investigated RMC plant can save about \$5,092 per month by using a recycling facility.

This study is a part of an ongoing research project and has not been completed yet. In this context, in the future, more RMC plants using recycling facilities can be investigated in order to estimate the statistically acceptable values of saving costs. In addition, the establishment and maintenance costs of these recycling facilities can be determined by contacting with the related manufacturers of the recycling facilities. Finally, the profitability analysis can also be conducted for such facilities.

ACKNOWLEDGMENT

The authors gratefully acknowledge the managers and employees of the batching plants for their generous collaboration and contributions. The authors also thank the financial supports provided by Committees on Research Grants of Akdeniz University and Bulent Ecevit University. This study is based on an on-going research project which is financially supported by the Scientific and Technological Research Council of Turkey (TUBITAK) under the grant number MAG-113M428.

REFERENCES

- [1]. M. Baytan, "Origins and magnitude of waste in the Turkish construction industry", MSc. thesis, Middle East Technical University, Ankara, Turkey, 2007.
- [2]. Y. H. Cho, and S. H. Yeo, "Application of recycled waste aggregate to lean concrete subbase in highway pavement", *Canadian Journal of Civil Engineering*, vol. 31, pp. 1101-1108, 2004.
- [3]. C. F. Hendriks, and H. S. Pietersen, "Sustainable raw materials: construction and demolition waste", RILEM Publications, France, Report 22, p. 201, 2000.
- [4]. R. Herrador, P. Perez, L. Garach, and J. Ordonez, "Use of recycled construction and demolition waste aggregate for road course surfacing", *Journal of Transportation Engineering*, vol. 138, p. 182-190, 2012.
- [5]. S. Kou, B. Zhan, and C. Poon, "Feasibility study of using recycled fresh concrete waste as coarse aggregates in concrete", *Construction and Building Materials*, vol. 28, pp. 549-556, 2012.
- [6]. M. Mulheron, "The recycling of demolition debris, current practice, products and standards in the United Kingdom", in *Proc. the Second International RILEM Symposium*, Tokyo, Japan, 1988, p. 510-519.
- [7]. M. Osmani, J. Glass, and A. D. F. Price, "Architects' perspectives on construction waste reduction by design", *Waste Management*, vol. 28, pp. 1147-1158, 2008.
- [8]. M. Öztürk, "Construction/demolition waste management", Ministry of Environment and Forestry, Ankara, Turkey, 2005. (in Turkish)
- [9]. A. Rao, K. N. Jha, and S. Misra, "Use of aggregates from recycled construction and demolition waste in concrete", *Resources, Conservation and Recycling*, vol. 50, pp. 71-81, 2007.

- [10]. R. V. Silva, J. de Brito, and N. Saikia, "Influence of curing conditions on the durability-related performance of concrete made with selected plastic waste aggregates", *Cement and Concrete Composites*, vol. 35, pp. 23-31, 2013.
 - [11]. M. A. Sobhan, S. A. Mofiz, and H. M. Rasel, "Effect of gradation and compactive effort on the properties of bituminous mixes with waste concrete aggregates", *International Journal of Civil and Environmental Engineering*, vol. 11, pp. 18-21, 2011.
 - [12]. M. S. Sobri, S. H. Hamzah, and A. R. M. Ridzuan, "Ultimate strength of steel fabric reinforced concrete short wall panel using crushed concrete waste aggregate (CCWA)", *International Journal of Civil and Environmental Engineering*, vol. 11, pp. 64-80, 2011.
 - [13]. TRMCA (Turkish Ready Mixed Concrete Association). (2014) Statistics. [Online]. Available: <http://www.thbb.org/en/industry>
 - [14]. G. Winkler, *Recycling Construction and Demolition Waste*, New York, USA: McGraw-Hill, 2010.
 - [15]. R. H. Zaharieva, E. Dimitrova, and F. B. Bodin, "Building waste management in Bulgaria: challenges and opportunities", *Waste Management*, vol. 23, pp. 749-761, 2003.
 - [16]. C. J. Zega, and A. A. D. Maio, "Recycled concretes made with waste ready-mix concrete as coarse aggregate", *Journal of Materials in Civil Engineering*, vol. 23, pp. 281-286, 2011.
-

GAUSSIAN AND WAVELET FILTERING METHODS FOR MICHELSON INTERFEROMETRIC EXPANSION MEASUREMENT

Veysel Gökhan BÖCEKÇİ

Volkan Yusuf SENYUREK

Abstract

In this study, the extension of metals was measured using a Michelson interferometric measuring system. The resulting signal was analyzed using video processing. In order to improve the measurement performance noisy signal were filtered. For filtering, standard Gaussian filtration, which commonly used for such applications and a new approach wavelet filtering method is used. Gaussian filtering relative error obtained as %3.3 and Wavelet filtering relative error obtained as %2.1. The results show that the wavelet filtering method is more successful for interferometric video signals.

Keywords: *Expansion Measurement, Wavelet Filtering, Interferometry, Video Processing*

1. INTRODUCTION

Nowadays interferometric systems, that uses the interference property of the light, have an important application area in optoelectronics. Interferometric displacement measurement systems are one of the commonly used systems in the precision displacement measurements [1].

Masuda, has carried out a thermal expansion measurement of Corundum (Al_2O_3) with a differential laser interferometer system that using He-Ne laser up to temperature of 1000K [2].

Suska, has measured the linear thermal expansion coefficients of rod-shaped materials having the dimensions of $60 \text{ mm}^2 \times 40 \text{ mm}^2$ and size of 100 mm-1300 mm by using the laser interferometric method, between 10°C - 40°C [3].

Zagar, has measured the amounts of heat expansion of copper samples at 4 different temperatures using laser interferometer separately, and then has tested the linearity of the system [4].

Demarest has described an electronic interferometric measuring system with high-resolution, high speed and reduced amount of uncertainty in laser measuring systems. In his study, he has evaluated the relationship between the structure of interferometric measuring system and measurement performance of laser displacement sensor [5].

Zhang, has measured the surface roughness and amount of displacement using an optical sensor, simultaneously. As a result of the experiments using 10 different surfaces, 100% reliable surface classification has been made [6].

Neubert and his colleagues have designed a high-speed dilatometer to test expansion and contraction of solid subjects. They have achieved a 0.3 nm resolution by using the differential interference measurement method. Induction furnace for used in the system was working with induction heating and gas cooling system and was heated to 1600°C [7].

James and his team have investigated the determination of thermal expansion coefficients of materials in the process of expansion and contraction of materials at high temperatures of metallurgical processes by computer-based process modeling of thermal deformation resulting from stress and strain of materials. They have introduced the dilatometer for measurements at high temperatures, mechanical, optical imaging and interference systems, x-ray diffraction methods and electrical pulse injection techniques [8].

Schödel, by taking into account the significantly growing demand for information on dimensional stability and thermal expansion properties of high-tech materials, has investigated the recent developments in elongation and thermal expansion measurements using PTB sensitive interferometers. It was found that, for samples of uncertainty of thermal expansion measurement is constant and being 10^{-9} K^{-1} or less [9].

In this study gauss and wavelet filters examined to increase measurement performance on the interferometric systems. This filters were realized by using MATLAB platform. The results that obtained via wavelet filter, which proposed as a new method, were analyzed.

2. EXPERIMENTAL SETUP

Main parts of the experimental setup are shown in figure 1.



Figure 1. Experimental setup

Experimental setup consist of interferometric system, video hardware and software.

2.1. Hardware Implementation

The hardware structure of the measurement system consist of Michelson interferometer, video camera and computer. Thermal expansion test device (LETI-1), which produced by Lambda Scientific Pty. Ltd., used for Michelson interferometer system. Video was recorded by Samsung VP-D351 digital camera via IEEE 1394 port.

2.2. Software Implementation

Software part of measurement system shown in figure 1. The interference video signal was processed by a programme written in MATLAB/Simulink software. The process steps are signal reduction, filtering, thresholding, labeling and fringe counting.

Signal Reduction

The frame dimension of the interferogram video signals are 736x576. one video signal composed of many frame, so matrix based processing is not easy for in this big frames. This process increases the computational load. The frame dimensions of video were reduced to 21x154 by using sub-matrix block in Simulink.

Filtering

There are many parasites in interferogram video signals that caused from laser intensity variation over time, quality of camera sensor and ambient. At this point, the filter types play an important role to prevent possible deviation that may be occur in the results. For this aim, gauss and wavelet filters were used.

Wavelet Filter

The wavelet transform (WT) is a method of converting a function (or signal) into another form which either makes certain features of the original signal more amenable to study or enables the original data set to be described more succinctly. To perform a wavelet transform it needed a wavelet which, as the name suggests. In fact, a wavelet is a function which satisfies certain mathematical criteria. A wavelet is compared to a section at the beginning of a signal to calculate the time-scale wavelet coefficient that shows the degree of correlation between the wavelet and signal section. The wavelet is translated in time and the process is repeated until the whole signal is covered. The wavelet is scaled again and the previous process is repeated for all scales.

The denoising procedure consists of the following steps,

- Choose a wavelet and choose decomposition level, Compute the wavelet coefficients of a signal. A large number of wavelets to be chosen for denoising. The best one depends on signal and application.
- For each level, select a threshold and apply soft or hard thresholding to the detail coefficients. Setting the thresholds is essential part of denoising. There are many thresholding selection rules (universal threshold, Stein's Unbiased Risk Estimate method, minimax method, hybrid method etc.).
- From the modified wavelet coefficients of the details the denoised signal is reconstructed.

Thresholding

The thresholding phase is used to convert the video signal from the former phase into dual images with automatic threshold values. Determination of threshold value is made by threshold phase, using the method developed by Otsu. The contrast of minimized pixel groups in the first image was separated in a histogram and a threshold value was determined. According to pixel brightness value (either below or above the threshold value), the image frame was formed as a dual image containing a binary number set

Labelling

The block tags connected elements in the image frame of the video signal which was transformed into dual image form and the reference number of the elements were transferred to an output. A tagging matrix was developed, within which a pixel equal to 0 represents base, a pixel equal to 1 represents the first connected element and a pixel equal to 2 represents the second connected element.

Fringe Counting

The binary number value was converted into the decimal system and transferred to fringe counting phase. After the number of sliding interference fringes due to displacement were detected, the amount of extension in the experimental material was calculated with equation 1.

$$\Delta L = \frac{\lambda}{2} N \quad (1)$$

In this equation, ΔL corresponds to the extension amount; λ ; He-Ne corresponds to laser wavelength laser and N corresponds to the number of fringes. The sub-system of the result phase allows the amount of expansion to be calculated in units of μm .
be calculated in units of μm .

3. RESULTS AND DISCUSSION

In the experiment, a copper bar which expansion coefficient is was used. The temperature changed from 20°C to 50°C and interferometry system counted 302 fringes when gauss filter was used. This number correspond to expansion of 95.75 μm . When wavelet filter used, system counted 299 fringes and that value correspond to expansion of 94.64 μm . In this temperature range, theoretical expansion is 92.7 μm . Relative error is calculated for Gauss and wavelet filters %3.3 and %2.1 respectively.

4. CONCLUSION

Gaussian and wavelet filters were used separately for interferogram video signals. Filter performances were compared by observing expansion results. Gaussian filtering relative error obtained as %3.3 and Wavelet filtering relative error obtained as %2.1. The results show that the wavelet filtering method is more successful for interferometric video signals.

REFERENCES

- [1]. D. Lin, X. Jiang and F. Xie, "High stability multiplexed fibre interferometer and its application on absolute displacement measurement and on-line surface metrology", *Optical Society of America*, Vol. 12, pp. 5729-5734,2004.
 - [2]. K. Masuda, "Differential Laser-interferometer Thermal Expansion Measurements", *American Metalurgist*, Vol. 85, pp. 279-282,2000.
 - [3]. J. Suska and J. Tschirmich, "An Interferometric Device for Precise Thermal Expansion Measurement on Bar-shaped Materials", *Measurement Science and Technology*, Vol. 10, pp. 211-217,1999.
 - [4]. B. Zagar, "A Laser Interferometer measuring Displacement with Nanometer Resolution", *IEEE Transaction on Instrumentation and Measurement*, Vol. 43, pp. 332-336,1994.
 - [5]. A. Demarest, "High-resolution, high-speed, low data age uncertainty, heterodyne displacement measuring interferometer electronics", *Measurement Science and Technology*, Vol. 9, pp. 1024-1030,1998.
 - [6]. K. Zhang and C. Butler, "A fiber optic Sensor for the Measurement of Surface Roughness and Displacement Using Artificial Neural Networks", *IEEE Transaction on Instrumentation and Measurement*, Vol. 46, pp. 899-902,1997.
 - [7]. Neubert, E. Bindl, M. Mehnert, H. Rädcl and C. Linseis, "A high-speed interferometric dilatometer based on the inductive heating of a specimen", *Measurement Science and Technology*, Vol. 20, pp. 101-108,2009.
 - [8]. J. James, J. Spittle, S. Brown and R. Evans, "A review of measurement techniques for the thermal expansion coefficient of metals and alloys at elevated temperatures", *Measurement Science and Technology*, Vol. 12, pp. 153-161,2001.
 - [9]. R. Schödel, "Ultra-high accuracy thermal expansion measurements with PTB's precision interferometer", *Measurement Science and Technology*, Vol. 19, pp. 1-11, 2008.
-

DETERMINATION OF FAILURE DISTRIBUTION PARAMETERS FOR WELDING MACHINES USED IN SHIP CONSTRUCTION

Baha GÜNEY

Sakarya University, Department of Industrial Engineering, 54187, Serdivan/Sakarya, Turkey.
bguney@sakarya.edu.tr

Çağatay TEKE

Sakarya University, Department of Industrial Engineering, 54187, Serdivan/Sakarya, Turkey.
cteke@sakarya.edu.tr

Abstract

Planning, conducting and control of maintenance activities enable to the highest level of availability of transport vehicles in the fleet is one of the most important aspects of transportation. Maintenance is a set of activities that carry out to keep a system or equipment in operation. Maintenance activities are basically divided into two types as preventive maintenance and corrective maintenance. Failure distribution of machines and equipment has to be known for planning spare parts, labor and tools. This can be determined by using failure data and suitable statistical method. In this study, failure distribution parameters of welding machines which is used in ship construction were determined by using real failure data. Applied method was shown for the equipment which is vitally important.

Keywords: *Failure distribution parameters, ship construction, maintenance, welding machine.*

1. INTRODUCTION

One of the most important problems of people in our day is construction. It has become a real problem especially in transportation system such as ship construction. (MEB, 2014: 1).

Ship construction process should be formed and managed properly in order to ensure completion of the process in time. The maintenance planning of welding machines used in ship construction should be arranged such that availability is always at a maximum level. In addition, spare part, labor and equipment planning should also be carried out properly so that maintenance activities can be carried out as planned. It is possible to do this for preventive maintenance activities since the times have already been scheduled. However, the same is not true for corrective maintenance activities. Because it is not known when there will be a failure. If the past failure data are available for the system or component for which corrective maintenance activities will be carried out, this uncertainty can be decreased significantly. Since past failure data will fit a certain statistical distribution and if the parameter values for this distribution are determined then it is possible to carry out spare part, labor and equipment planning based on the failure time estimations.

2. MAINTENANCE

Maintenance covers all the actions carried out to repair or to ensure that a unit, part or equipment continues to work under certain conditions (Dhillon, 2002). With regard to production systems, maintenance activities are those that are carried out so that all production systems or certain equipment are in working order. This definition shows that maintenance function covers not only intervention to a failure but also proactive tasks such as routine inspection, preventive maintenance, replacement and condition monitoring.

Various decisions related with specifications, purchasing, planning, operating, performance evaluation, development, replacement and scrapping are made for every stage of the life curves of various technical systems such as factories, machinery, equipment or plants within the scope of maintenance management. Maintenance management is thus the management of physical assets based on this wide perspective (Köksal, 2007: 13).

2.1. Corrective Maintenance

It would be wiser to explain the concept of failure prior to corrective maintenance. Failure is the stopping of a system or the decrease in production rate and/or quality due to an unpreventable reason. In this method, intervention or repair is carried out after the failure. The machine or machines stop until repair. Maintenance crew and maintenance workshop strive to start the production system in the shortest possible time. Spare machines or spare parts are put into use if any so that the line continues working.

In corrective maintenance, a machine does not go through maintenance unless there is a failure. Other maintenance works are carried out with the repair when there is a failure. Most of the repairs are quick-fixes that are made to ensure that the failed part is repaired and that the machine continues to operate. These companies operate as minimum repair and work with professional maintenance companies for large maintenance-overhaul works. This is a management approach that minimizes maintenance crew and material costs (Köksal, 2007: 54).

Corrective maintenance is observed most frequently in the following cases (Köksal, 2007: 54):

- Small workshops with general purpose universal workbenches,
- Facilities that are planned to be sold out because they have become outdated or idle due to the changes in the market,
- In cases when there is more than one spare equipment in the facility (e.g. when there are three parallel connected equipment and one of them fails)
- Activities that support main production (forklift, compressor and similar equipment)

2.2. Preventive Maintenance

In this method, the machinery equipment, buildings or facilities go through inspection at certain periods and before any failure arises and protective activities such as machinery adjustment, cleaning, part replacement, painting and other minor repairs are carried out if necessary. It is a preventive activity (Köksal, 2007: 54-55).

Preventive maintenance should have the following properties (Köksal, 2007: 54-55):

- Oiling: An oiling program should be included in all preventive maintenance policies. It should be carried out with trained personnel.
- Inspection: The condition of machinery equipment is under constant control with regular inspections. It should be decided to stop the machine for maintenance prior to the arising of any changes due to heat, vibration or wear.
- Programmed power off or maintenance: It is the planning of short or long term general maintenance or power off maintenance work. Transfer workbenches, heat treatment ovens, presses and reactors for short term.

The preventive maintenance activities listed above are generally carried out outside the production hours so that the operation is not stopped.

3. FAILURE DISTRIBUTIONS

When the failures in a system or component are recorded, it will be observed that the failure data fit a certain statistical distribution. When the current failure data are evaluated statistically, it will fit a distribution and the parameters of that distribution will take on values. The parameter values of the distribution will yield the failure distribution of the related system or component. Based on this information, failure times will be estimated and maintenance planning will be made.

Even though there are many models used for failure distribution, the most widely used are weibull distribution, exponential distribution and normal distribution.

3.1. Weibull Distribution

Weibull distribution was put forth by Waloddi Weibull in 1951 in order to estimate the life times of machines. Today, it is used in the statistical models that are part of the science of engineering as well as in life data analysis. Weibull distribution is widely used in models that will be set up for the data set related with failure ratios which in some cases has a Rayleigh or exponential distribution based on the values that the shape parameter takes.

In general, the Weibull distribution is one that has a scale and shape parameter. The two parameter weibull probability density function is given below:

$$f(T) = \frac{\beta}{\eta} \left(\frac{T}{\eta}\right)^{\beta-1} \exp\left[-\left(\frac{T}{\eta}\right)^{\beta}\right] \quad (1)$$

Here, $f(T) \geq 0$, $T \geq 0$, $\beta > 0$, $\eta > 0$ and β is the shape parameter, η is the scale parameter. The two parameter weibull cumulative distribution is given below:

$$F(T) = 1 - \exp\left[-\left(\frac{T}{\eta}\right)^{\beta}\right] \quad (2)$$

One of the parameters of the Weibull distribution is the shape parameter and the reason for various different distributions is the value that the shape parameter takes. Failure rates increase over time when the slope value ranges between 0 and 1, that is when $0 < \beta < 1$. As a special case, when $\beta = 1$, " $f(T) = 1/\eta \exp(-T/\eta)$ " distribution is an exponential distribution. Here, " $1/\eta = \lambda$ " represents the failure rate. When $\beta = 2$, it becomes the rayleigh distribution (Zeytinoglu, 2009: 74).

4. DETERMINING THE PARAMETER VALUES OF THE DISTRIBUTION

Statistical models mostly depend on data for estimations. The accuracy of any estimation depends on the completeness and quality of the data to be used. A good estimation can be made when a good data set is combined with the right model. The data that we will use when determining the parameter values of failure distribution may not be complete, they may include some uncertainties. Thus, we can classify the data used for analysis as complete data and censored data.

4.1. Complete Data

Complete data means that every sample unit has been observed and is known. For example, if we are testing five units and if all five of these units have failed during testing then it means we have complete data (http://reliawiki.org/index.php/Life_Data_Classification, 03.06.2013:

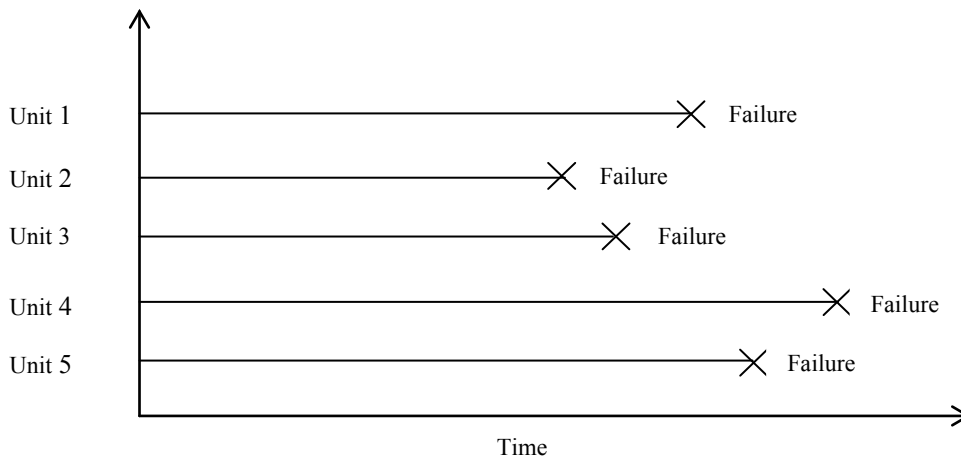


Figure 1. Complete data

4.2. Censored Data

In many cases, not all sample units fail during testing or there may be instances when we cannot detect the exact time of failure. Such data are known as censored data. There are three types of censored data: right censored, interval censored and left censored(http://reliawiki.org/index.php/Life_Data_Classification, 03.06.2013:1).

4.2.1 Right Censored Data

It is the most common among censored data. For example, if we have tested five units and if only three of these units have failed until the end of the test, it means we have two right censored data(http://reliawiki.org/index.php/Life_Data_Classification, 03.06.2013:1).

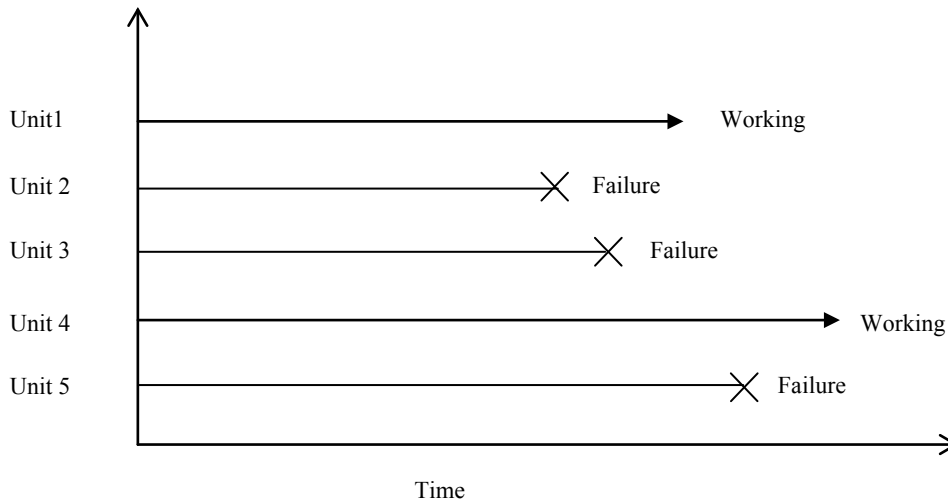


Figure 2. Right censored data

4.2.2 Interval Censored Data

Interval censored data represents the uncertainty regarding the time of failure of the tested unit. Thus, it is not certain when the unit has failed. This is observed in cases when the related unit is not under constant monitoring. For example, if we are testing 5 units and we observe these units every 100 hours, we can only know if the units failed between the observation times. If we are to give a more detailed explanation; if we observe that the unit is functioning at the end of the first 100 hours and that it has failed at the end of the second 100 hours, we can state that this unit has failed during 100-200 hours(http://reliawiki.org/index.php/Life_Data_Classification, 03.06.2013:1).

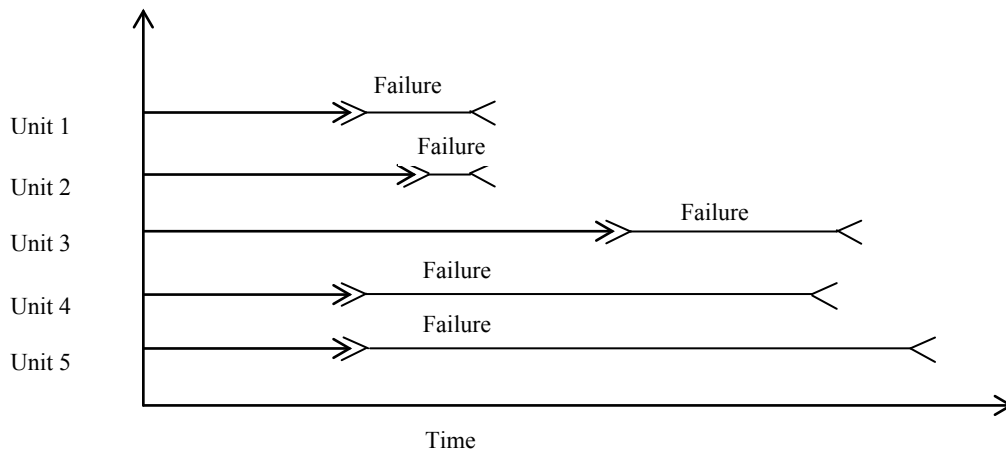


Figure 3. Interval censored data

4.2.3 Left Censored Data

It is known as "left censored data" in English. For left censored data, we can know if the tested units have failed before a certain time or not. For example, we can state that the unit has failed before 100 hours, however we cannot give an exact time. In other words, this means that the unit has failed at some point in the 0-100 hour interval (http://reliawiki.org/index.php/Life_Data_Classification, 03.06.2013:1).

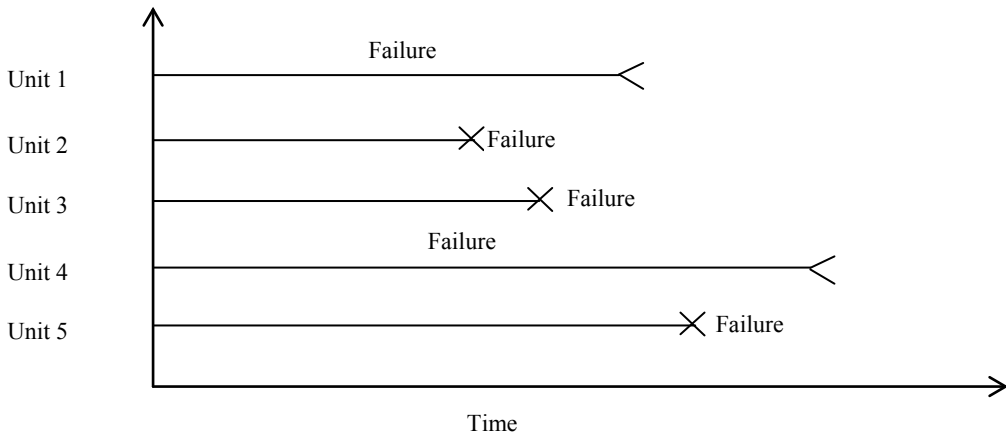


Figure 4. Left censored data

5. APPLICATION

Failures of welding machines used in ship construction have been handled in the application. Welding machines play an important role for ship construction process. Indeed, welding machines failures significantly effect it.

Maximum likelihood estimation method, probability plotting, least squares method and moment method can be listed as methods used to estimate the parameter values of failure distribution. In this study, welding machines failure data were used to calculate the weibull distribution parameter values using Weibull++ software in accordance with the maximum likelihood estimation method.

5.1. Maximum Likelihood Estimation Method

k and c are shape and scale parameters respectively in Weibull distribution. Maximum likelihood estimation is one of the methods used to calculate these parameters. Failure data comprise a set of n elements such as

v_1, v_2, \dots, v_n when using this method. The probability of $V = v_i$ in the observation is proportional with $f(v_i; k, c)$. Similarly, the probability of events occurring can be expressed as $V = v_1 \dots V = v_n$. Since the events are independent of each other, the probability of events $L = \prod_1^n, \dots, V = v_n$ occurring can be written as such:

$$L = \prod_1^n f(v_i; k, c) \quad (3)$$

Scale parameter;

$$c = \left[\frac{\sum_{i=1}^n (v_i)^k}{n} \right]^{\frac{1}{k}} \quad (4)$$

Shape parameter;

$$k = \left[\frac{\sum_{i=1}^n v_i^k \ln(v_i)}{\sum_{i=1}^n v_i^k} - \frac{\sum_{i=1}^n \ln(v_i)}{n} \right]^{-1} \quad (5)$$

is obtained with these equations.

It is difficult to solve the equation since it is iterative. Hence, it is not a method used before modern technology.

5.2. Determination of Failure Distribution Parameters

The analysis was conducted with torch failure data of welding machines which is used in ship construction. Failures of torches are of crucial importance for welding machine because they affect running of the system substantially. Welding machines have 198 torches totally. Failure data of the torches was recorded for 3963 days. 165 torches failed during the analysis period and the remaining 15 torches have not had any failures. Thus, we have 165 complete data and 15 right censored data.

Failure data of the torches have been entered in the Weibull++ software and the weibull distribution parameters for it have been determined. "Failure" expression was used for complete data while entering the failure data into the software, whereas "Suspension" expression was used for censored data. The time value for censored data covers the time period from the starting time of the related torch to the end of the analysis process. Parameter values for the two parameter weibull distribution have been determined as $\beta=1,852$ and $\eta=19951,916$ in hours. In addition, the mean time to failure value for the torches has been determined approximately as 17720 hours. In other words, the average life of them is 17720 hours. The screenshots of the software used for analysis have been given below:

Determination of Failure Distribution Parameters for Welding Machines Used in Ship Construction

Baha Güney - ÇağatayTeke

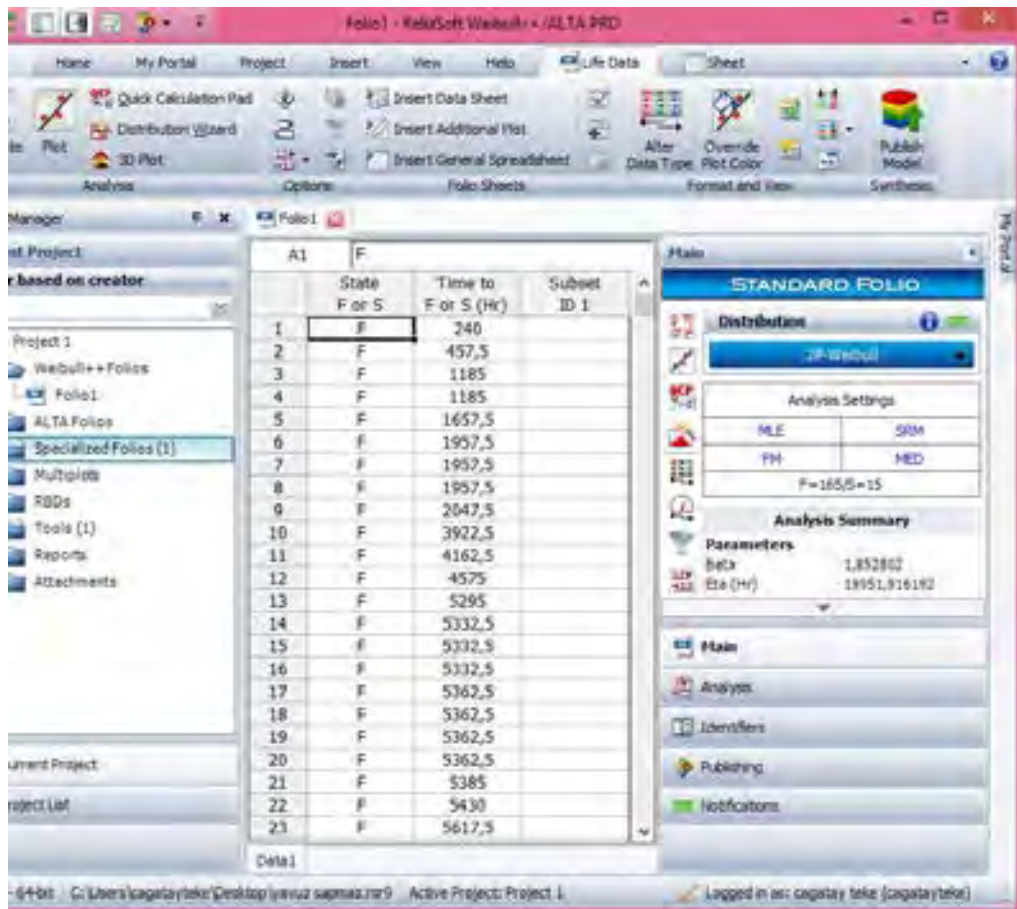


Figure 5. Screenshot of analysis

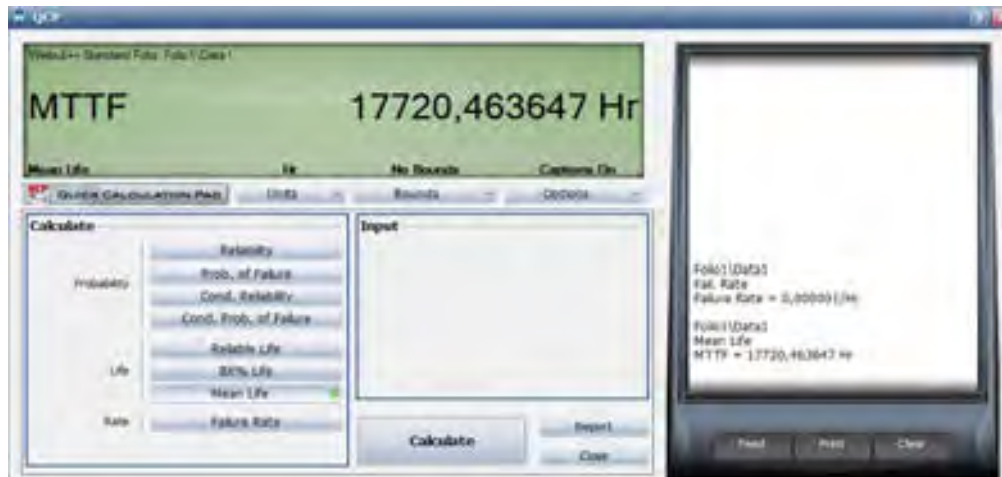


Figure 6. Screenshot of analysis

6. CONCLUSION

Planning of spare parts, labor and equipment to be used in maintenance activities has to be carried out accurately in order to ensure that the planning activities are executed in a planned manner. It is possible to do this for preventive maintenances, because the maintenance times are predetermined. However, the maintenance time is not certain for corrective maintenance activities since it is not known beforehand when a failure will arise.

In this study, failure data of welding machines used in ship construction have been used to determine the failure distribution parameters via Weibull++ software in accordance with the maximum likelihood estimation method. In this way, failure times will be estimated and corrective maintenances will be carried out in proper manner. Since the spare part, labor and equipment planning will be carried out in accordance with this estimated value.

REFERENCES

- [1]. Dhillon, B.S. (2002), *Engineering Maintenance, A Modern Approach*, CRC Press.
- [2]. Köksal, M. (2007), *Bakım Planlaması*, Seçkin Yayıncılık.
- [3]. MEB (2012), *Raylı Sistemler Alanı*, <http://mebk12.meb.gov.tr/meb_iys_dosyalar/54/01/194077/icerikler/rayli-sistemler-alani_145801.html>, Date:21.03.2014.
- [4]. Zeytinoğlu, F.Ç. (2009), "Weibull Dağılımının Ölçek ve Biçim Parametreleri İçin İstatistiksel Tahmin Yöntemlerinin Karşılaştırılması", İstanbul Ticaret Üniversitesi Sosyal Bilimler Dergisi, Yıl 8, Sayı 15, 73-87.
- [5]. *Life Data Classification*, <http://reliawiki.org/index.php/Life_Data_Classification>, Date:03.06.2013.

NUMERICAL INVESTIGATION OF CONVECTIVE HEAT TRANSFER CHARACTERISTICS OF TiO₂/WATER NANOFLUID IN A TRAPEZOIDAL MICROCHANNEL

Tuğçe İŞGÜZAR

Mechanical Engineering Department, Faculty of Engineering, Karabuk University, 78050, Karabuk, Turkey.
tugceisguzar@gmail.com

Cüneyt UYSAL

Mechanical Engineering Department, Faculty of Engineering, Karabuk University, 78050, Karabuk, Turkey.
cuneytuysal@karabuk.edu.tr

Kamil ARSLAN

Mechanical Engineering Department, Faculty of Engineering, Karabuk University, 78050, Karabuk, Turkey.
kamilarslan@karabuk.edu.tr

Hüseyin KURT

Mechanical Engineering Department, Faculty of Engineering, Karabuk University, 78050, Karabuk, Turkey.
hkurt@karabuk.edu.tr

Abstract

In this study, the forced convective heat transfer and fluid flow of TiO₂/water nanofluid through the trapezoidal cross-sectioned microchannel having corner angle of 45° was numerically investigated. The flow was considered as three-dimensional steady-state thermally and hydrodynamically developing laminar flow condition ($100 \leq Re \leq 1000$). The constant heat flux was applied at the bottom and side surfaces of the microchannel. Top surface of the microchannel was insulated. The hydraulic diameter and the length of the trapezoidal microchannel were considered as 150 μm and 5 cm, respectively. The numerical analyses were performed for different nanoparticle volume concentrations ($\phi = 1-4$ vol.%) of TiO₂/water nanofluid. The convection heat transfer coefficient and the Darcy friction factor values were obtained from numerical calculations. As a result, it is observed that the convective heat transfer coefficient increases with increasing in nanoparticle volume concentration. The maximum convective heat transfer enhancement was obtained to be 14.87% for TiO₂ nanoparticle addition of 4.0 vol.%. However, the Darcy friction factor is not affected by the increasing in nanoparticle volume concentration.

Keywords: Convection heat transfer coefficient, Darcy friction factor, Forced convection, TiO₂/water nanofluid, Trapezoidal microchannel.

1. INTRODUCTION

Nanofluids are new class of fluids which consist of a base fluid with nano-sized particles (1–100 nm) suspended within them. Using nanofluids are very important topic for heat transfer applications recently because of the fact that their higher heat transfer performance compared to that of their base fluids. They are prepared through addition of metallic or non-metallic nanoparticles to conventional fluids such as water, ethylene glycol (EG) and engine oil. In recent years, nanofluids have been considered as a next generation heat transport fluid for a wide application areas, which microelectronic cooling is one of them. The micro tube heat exchangers were used for cooling microelectronic equipment. Using the nanofluids in micro tube heat exchangers enhance the convective heat transfer ratios. Hence, heat transfer and fluid flow characteristics of nanofluid flow in microchannels is becoming important issue for heating and cooling applications of microelectronic equipment.

Choi [1] first proposed in 1995, nanofluid as a new type of fluid that consists of uniformly dispersed and suspended nanometersized particles. A number of studies have been performed on the thermal conductivity of nanofluids, and considerable thermal conductivity enhancement has been consistently achieved at very low concentrations of nanoparticles as compared with that of base liquid [2–5]. Kayhani et al. [6] experimentally analyzed the heat transfer and pressure drop of TiO₂/water nanofluid flow in circular cross-sectioned duct. The study was performed under turbulent flow condition. Different volume concentration of nanofluids (0.1, 0.5, 1.0, 1.5 and 2.0%) was used in the experiments. It was obtained that heat transfer coefficients increased with increasing nanofluid volume fractions. Zhang et al. [7] performed the experimental study for TiO₂/water nanofluid flow in a multiport minichannel flat tube. The nominal diameters of TiO₂ nanoparticles of 10, 30, and 50 nm were dispersed in water at various volume concentrations ranging from 0.005% to 1%. The study was carried out for 100<Re<6100. Nusselt numbers obtained from experimental analysis did not increase with increasing volume concentration and decreased with increasing particle diameter. The forced convective heat transfer of nanofluids, made of TiO₂ nanoparticles and water or (ethylene glycol/water mixture) were used for the experimental study performed by Vakili et al. [8]. The experiments were conducted in a straight vertical pipe under laminar and turbulence forced flow conditions. The nanofluid convective heat transfer of water and ethylene glycol/water mixture was compared with base fluids. It was obtained in this study that, the mixture consisting of 60 wt.% ethylene glycol and 40 wt.% distilled water has more convective heat transfer coefficient rates than the nanofluid of distilled water. The enhancement of convective heat transfer for addition of TiO₂ nanoparticles with increasing particle concentration was also observed. Another experimental study, Arani and Amani [9] investigated the effect of nanoparticle volume fraction on the convection heat transfer characteristics and pressure drop of TiO₂/water nanofluids with nanoparticle volume fraction between 0.002 and 0.02 in a horizontal double tube counter-flow heat exchanger under turbulent flow condition. It is observed that the Nusselt number increases with increasing the Reynolds number or nanoparticle volume fraction. The heat transfer and friction characteristics of turbulent forced flow of TiO₂/water nanofluids in elliptical tube were numerically investigated by Hussein et al. [10]. Four different volume concentrations (0.25%-1%) and different TiO₂ nanoparticle diameters (27 nm - 50 nm) was used. The constant surface heat flux was applied at the tube surface. The results showed that the Nusselt number and friction factor increased with decreasing TiO₂ nanoparticle diameters but increasing volume concentrations of TiO₂ nanoparticles. Nitiapiruk et al. [11] investigated the convective heat transfer performance of a microchannel heat sink using TiO₂/water nanofluid. It is observed from the experimental study that the use of the model which is based on experimental data is very important to estimate the friction factor, while the use of different models to calculate of thermal conductivity has no considerable effect on the prediction of Nusselt number. An experimental work was carried out on the TiO₂/R600a nano-refrigerants used in a domestic refrigerator by Bi et al. [12]. The refrigerator performance was investigated using energy consumption and freeze capacity tests. It was obtained the refrigerator performance was better than the pure R600a system. Also, it was suggested that using TiO₂/R600a nano-refrigerant in domestic refrigerators was feasible.

It is obtained from literature review that the heat transfer characteristics of base fluids increase with adding nanoparticles. Nevertheless, there is no detailed investigation about TiO₂/water nanofluid flow in trapezoidal cross-sectioned microchannel. It is aimed to close this gap in the literature in this study. In this study, the forced convective heat transfer and fluid flow of TiO₂/water nanofluid through the trapezoidal cross-sectioned microchannel having corner angle of 45 ° was numerically investigated. The numerical analyses were performed for different nanoparticle volume concentrations (ϕ=1-4 vol.%) of TiO₂/water nanofluid. The flow was under hydrodynamically and thermally developing laminar flow condition (100≤Re≤1000). The constant heat flux was applied at the bottom and side surfaces of the microchannel. The average convection heat transfer coefficient and the average Darcy friction factor values were obtained from numerical calculations.

2. NUMERICAL PROCEDURES

Laminar forced flow and heat transfer of TiO₂/water nanofluid in a trapezoidal cross-sectioned microchannel was investigated numerically. Since the flow field is symmetric, only one half of the channel has been considered in the numerical calculations for reducing the computational time. The constant heat flux of $q_w^* = 10000 \text{ W/m}^2$ was supplied at the top and side surfaces of the microchannel. The hydraulic diameter and the length of the trapezoidal microchannel were considered as $150 \mu\text{m}$ and 5 cm , respectively. Schematic diagram depicting the cross-section of the computational domain was presented in Figure 1. The geometrical dimensions of the trapezoidal cross-sectioned microchannel were also given in Table 1.

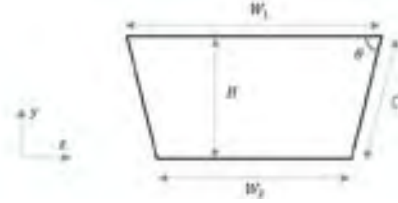


Figure 1. The cross-section of the trapezoidal microchannel

Table 1. The geometrical dimensions of trapezoidal microchannel

θ	$H (\mu\text{m})$	$W_1 (\mu\text{m})$	$W_2 (\mu\text{m})$	$C (\mu\text{m})$
45°	100	522.76	322.76	141.42

Infinitesimal (less than 100 nm) solid particles are considered to be able using single phase approach, so single phase approach was adopted for nanofluid modeling and the fluid phase was assumed to be as a continuous. The following assumptions were adopted for this study: (i) Both heat transfer and fluid flow in microchannel were in three dimensional and steady-state; (ii) fluid flow was incompressible and laminar flow; (iii) the physical properties of nanofluid, such as density, specific heat, thermal conductivity were taken as temperature independent; and (iv) negligible buoyancy effect, viscous dissipation and radiation heat transfer. With mentioned above assumptions, governing equations; continuity, momentum and energy are given, respectively:

$$\text{Continuity Equation: } \frac{\partial U}{\partial X} + \frac{\partial V}{\partial Y} + \frac{\partial W}{\partial Z} = 0 \quad (1)$$

$$\text{x-Momentum Equation: } \left(U \frac{\partial U}{\partial X} + V \frac{\partial U}{\partial Y} + W \frac{\partial U}{\partial Z} \right) = -\frac{dP}{dX} + \frac{1}{Re} \left(\frac{\partial^2 U}{\partial X^2} + \frac{\partial^2 U}{\partial Y^2} + \frac{\partial^2 U}{\partial Z^2} \right) \quad (2)$$

$$\text{y-Momentum Equation: } \left(U \frac{\partial V}{\partial X} + V \frac{\partial V}{\partial Y} + W \frac{\partial V}{\partial Z} \right) = -\frac{dP}{dY} + \frac{1}{Re} \left(\frac{\partial^2 V}{\partial X^2} + \frac{\partial^2 V}{\partial Y^2} + \frac{\partial^2 V}{\partial Z^2} \right) \quad (3)$$

$$\text{z-Momentum Equation: } \left(U \frac{\partial W}{\partial X} + V \frac{\partial W}{\partial Y} + W \frac{\partial W}{\partial Z} \right) = -\frac{dP}{dZ} + \frac{1}{Re} \left(\frac{\partial^2 W}{\partial X^2} + \frac{\partial^2 W}{\partial Y^2} + \frac{\partial^2 W}{\partial Z^2} \right) \quad (4)$$

$$\text{Energy Equation: } \left(U \frac{\partial \theta}{\partial X} + V \frac{\partial \theta}{\partial Y} + W \frac{\partial \theta}{\partial Z} \right) = \frac{1}{Re \cdot Pr} \left(\frac{\partial^2 \theta}{\partial X^2} + \frac{\partial^2 \theta}{\partial Y^2} + \frac{\partial^2 \theta}{\partial Z^2} \right) \quad (5)$$

where, U , V , and W are the dimensionless velocity components, Re is the Reynolds number, Pr is the Prandtl number, P is the dimensionless pressure and θ is the dimensionless temperature.

In the above equations, the following dimensionless parameters are used:

$$X = \frac{x}{D_h}, Y = \frac{y}{D_h}, Z = \frac{z}{D_h}, U = \frac{u}{u_{in}}, V = \frac{v}{u_{in}}, W = \frac{w}{u_{in}}, \text{ and } \theta = \frac{T - T_{in}}{T_w - T_{in}}$$

where, u , v , and w [m/s] are the velocity components, x , y and z [m] are Cartesian coordinates, D_h [m] is the hydraulic diameter of the microchannel, T_w [K] is the surface temperature of the heated section of the microchannel, u_{in} [m/s] and T_{in} [K] are the average velocity and average temperature at the inlet of the microchannel, respectively.

The boundary conditions were used for solving the continuity, momentum and energy equations. The no-slip conditions were imposed at the surfaces of the microchannel. The uniform wall heat flux was applied at the bottom and side surfaces of the microchannel with a value of $q_w''=10000$ W/m². The insulated boundary condition was taken at the top surface. Pressure outlet boundary condition was used at the exit of the microchannel. The boundary conditions used in this study were given below in detail:

Boundary conditions at the inlet: $U = 1$, $\theta = 1$

At the outlet: $P = P_{out}$

At the fluid-solid interface: $U = 0$, $\theta = \theta_s$, $-k_s \frac{\partial \theta_s}{\partial n} = -k \frac{\partial \theta}{\partial n}$

At the bottom and side surfaces: $q_w = -k_s \frac{\partial \theta_s}{\partial n}$

At the top surface: $q_w = 0$

To calculate the heat transfer coefficient for nanofluid, it is necessary to apply the thermophysical property models. The necessary thermophysical properties in this study are density, viscosity, specific heat and thermal conductivity. In the following equations, the subscripts 'np', 'f' and 'nf' refer to the nanoparticles, the fluid and the nanofluid, respectively.

The density and the specific heat of the TiO₂/water nanofluid are determined, respectively [13]:

$$\rho_{nf} = (1 - \phi) \rho_f + \phi \rho_{np} \quad (6)$$

$$(\rho C_p)_{nf} = (1 - \phi) (\rho C_p)_f + \phi (\rho C_p)_{np} \quad (7)$$

where ρ [kg/m³] is the density and C_p [kJ/kg.K] is the specific heat.

For determining the thermal conductivity of TiO₂/water nanofluid, the following correlation for thermal conductivity k [W/m.K] and viscosity μ [N.s/m²] proposed by [14] was used, respectively:

$$k_{nf} = k_f 0.8938 \left(1 + \frac{\phi}{100}\right)^{1.37} \left(1 + \frac{T_{nf}}{70}\right)^{0.2777} \left(1 + \frac{d_p}{150}\right)^{-0.0336} \left(\frac{\alpha_p}{\alpha_f}\right)^{0.01737} \quad (8)$$

$$\mu_{nf} = \mu_f \left(1 + \frac{\phi}{100}\right)^{11.3} \left(1 + \frac{T_{nf}}{70}\right)^{-0.038} \left(1 + \frac{d_p}{170}\right)^{-0.061} \quad (9)$$

where, α [m²/s] is thermal diffusivity at constant pressure [15].

The purpose of this study is to calculate the average Nusselt number and Reynolds number along with average Darcy friction factor. The hydraulic diameter ($D_h=4A_c/P$) is chosen as the characteristic length.

The Reynolds number is given by,

$$Re = \frac{UD_h}{\nu} \quad (10)$$

The Nusselt number is defined as,

$$Nu = \frac{hD_h}{k} \quad (11)$$

The Darcy friction factor is calculated by,

$$f = \frac{\Delta P(D_h / L)}{(\rho U^2 / 2)} \quad (12)$$

where, U [m/s] is the mean velocity of the air flow in the trapezoidal cross-sectioned microchannel and ν [m²/s] is the kinematic viscosity of TiO₂/water nanofluid. ΔP [Pa] is the pressure drop along the microchannel and L [m] is the axial length of the microchannel. In addition, h [W/m².K] is the average heat transfer coefficient is obtained by:

$$h = \frac{\dot{m}c_p(T_{bo} - T_{bi})}{A_s(T_w - T_b)} \quad (13)$$

where, \dot{m} [kg/s] is the mass flow rate, T_{bi} [K] and T_{bo} [K] are bulk temperatures of the TiO₂/water nanofluid at the inlet and outlet of the microchannel, respectively. All nanofluid properties in the microchannel were evaluated at the bulk temperature; $T_b = (T_{bi} + T_{bo}) / 2$. A_s [m²] and T_w [K] are the surface area and the surface temperature of the heated section of the microchannel.

In the computations, the finite-volume method based commercial CFD software Ansys Fluent 15.0 was used to perform the numerical calculations by solving the governing equations along with the boundary conditions. The convection terms in mass, momentum and energy equations were discretized using a second order upwind scheme, respectively. The standard scheme was employed for discretization of pressure and the SIMPLE algorithm was used to resolve the coupling between velocity and pressure [16]. SIMPLE-code family is based on the spatial integration of the conservation equations over finite control volumes. The Green-Gauss cell based method was applied for discretization of the momentum and energy equations. To obtain convergence, each equation for mass, momentum, and energy was iterated until the residual falls below 1×10^{-6} . No convergence problems were observed during the calculations.

The hexahedral mesh distribution was used for trapezoidal cross-sectioned microchannel. The number of grid points or control volumes is increased close to wall of the microchannel to enhance the resolution and accuracy as given in Figure 2.



Figure 2. The mesh distribution of the microchannel geometry

The grid independence study was performed by refining the grid size until the variation in both average Nusselt number and average Darcy friction factor are less than 0.3% and 0.6%, respectively. To obtain the optimum mesh size, a grid independence study was conducted using six different grid sizes changing from 2.2×10^4 to 9.4×10^5 for $Re = 1 \times 10^3$ given in Figure 3. It was observed that a further refinement of grid size from 5.76×10^5 to 9.4×10^5 , the changing of average Nusselt number and average Darcy friction is negligible. Thus, grid size of 5.76×10^5 points was considered as optimum grid size. Same procedure was used for other nanofluid volume fractions, and optimum grid size was obtained for each calculation.

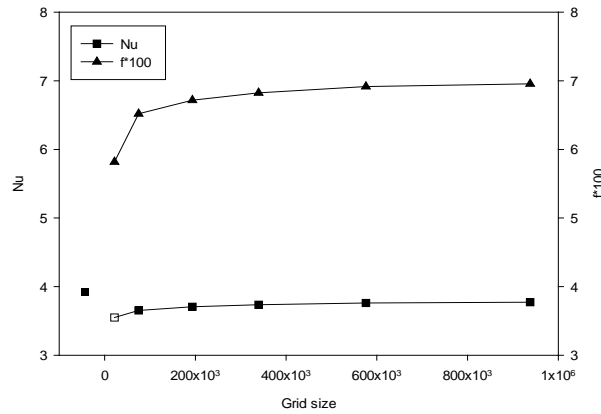


Figure 3. The change of average Nusselt number and average Darcy friction with grid size.

The code was further validated by comparing the present results with the experimental results of Sieder and Tate [17] as shown in Figure 4a. It is seen that the average Nusselt number values fall between the accepted ranges. Moreover, for the validation of the code, the average Darcy friction factor values obtained by present study were compared with the experimental results of Wu and Cheng [18] for the trapezoidal microchannel as shown in Figure 4b. The results obtained by present study are good agreement with the correlation proposed by Wu and Cheng [18].

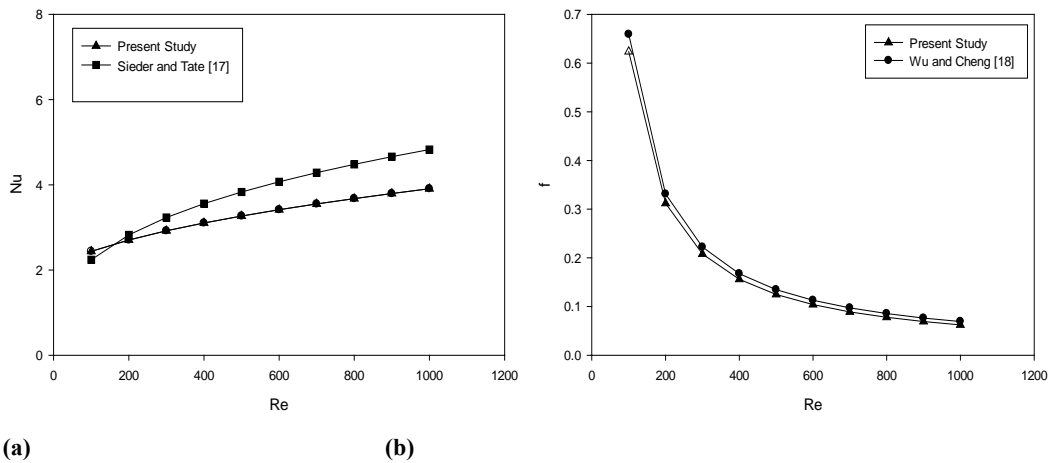


Figure 4. Comparison of numerical results with literature: (a) average Nusselt number, (b) average Darcy friction factor.

3. RESULTS AND DISCUSSION

The thermal and hydrodynamic performances of TiO_2 /water nanofluid flow through the trapezoidal microchannel were numerically investigated. The numerical calculations have been performed under thermally developing laminar flow conditions ($100 \leq Re \leq 1000$). Numerical results were presented in non-dimensional Nusselt number and Darcy friction factor. Average Nusselt numbers were calculated using the temperature fields of the nanofluid flow in the microchannel. In addition, average Darcy friction factor was estimated by determination of pressure drop in the microchannel.

The thermal performance of trapezoidal cross-sectioned microchannel by using TiO_2 /water nanofluid having different nanoparticle volume fractions was examined by presenting the results of average convective heat transfer coefficient for each nanoparticle volume fraction. The change of average convective heat transfer coefficient with the Reynolds number for different nanoparticle volume fractions of TiO_2 /water nanofluid is shown in Figure 5a.

As can be seen from Figure 5a, the average convective heat transfer coefficients increase with increasing Reynolds numbers for whole nanoparticle volume fractions. Also, increasing nanoparticle volume fraction in base fluid increases the average convective heat transfer in microchannel. The maximum average convective heat transfer enhancement is obtained from TiO₂/water nanofluid having nanoparticle volume fraction of 4.0 vol.%. When the value of average convective heat transfer obtained for 4.0 vol.%TiO₂/water in comparison to that of pure water for Re=100, 500 and 1000, the average convective heat transfer enhancements are obtained as 11.35, 13.95 and 14.87%, respectively. Therefore, the effect of TiO₂ nanoparticle addition in water on the average convective heat transfer coefficient increases with increasing in the Reynolds number. The average Darcy friction factor variation for the different nanoparticle volume fraction of TiO₂/water nanofluid versus the Reynolds number is shown in Figure 5b. As can be seen from Figure 5b, the effect of TiO₂ nanoparticle addition in water on the average Darcy friction factor is negligible for TiO₂/water nanofluid flow.

It is clear that usage of TiO₂/water nanofluid as a heat transfer fluid provides a significant advantage because of their increasing effect the convective heat transfer and remaining unresponsive for the Darcy friction factor.

The velocity and temperature distributions of TiO₂/water nanofluid flow at the outlet of the trapezoidal microchannel for different nanoparticle volume fractions and Re=1000 are shown in Figure 6 and Figure 7, respectively. It is seen that the velocity and temperature distribution changes with increase in nanoparticle volume fraction. The velocity in the center of the microchannel increases with increase in nanoparticle volume fraction of TiO₂/water nanofluid.

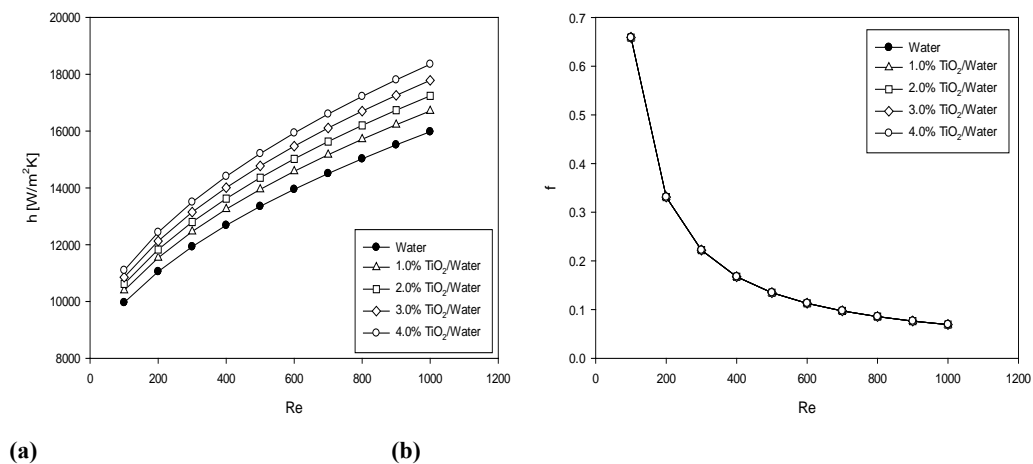


Figure 5. Numerical results for different nanoparticle volume fractions of TiO₂/water nanofluid: (a) convective heat transfer coefficient, (b) Darcy friction factor.

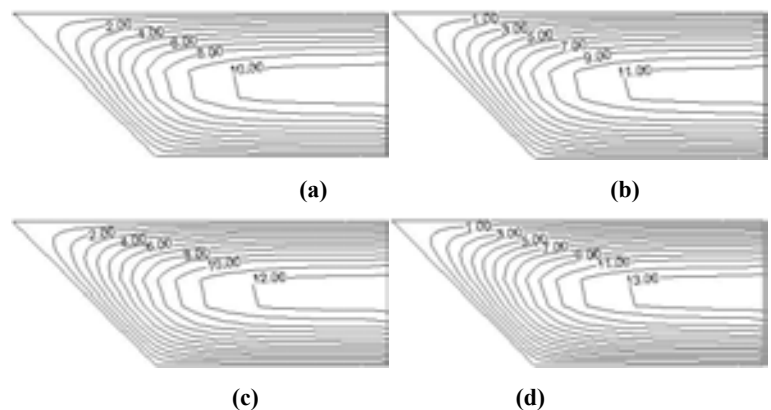


Figure 6. Velocity distribution at the outlet of the microchannel for different nanoparticle volume fractions: (a) $\phi=1.0\%$; (b) $\phi=2.0\%$; (c) $\phi=3.0\%$; (d) $\phi=4.0\%$

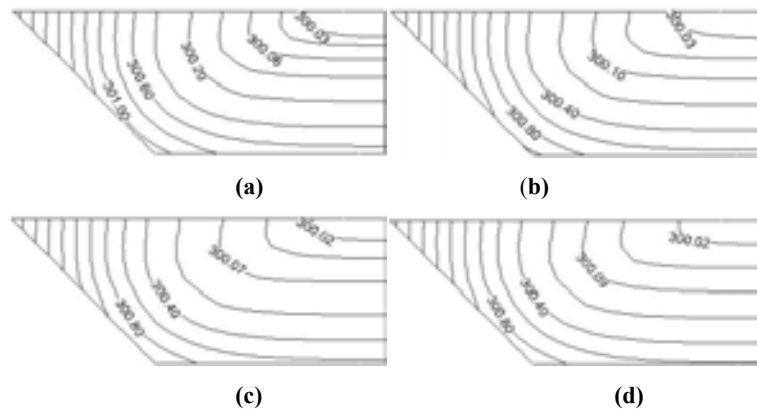


Figure 7. Temperature distribution at the outlet of the microchannel for different nanoparticle volume fractions; (a) $\phi=1.0\%$; (b) $\phi=2.0\%$; (c) $\phi=3.0\%$; (d) $\phi=4.0\%$

4. CONCLUSIONS

In this study, the forced convective heat transfer and fluid flow of $\text{TiO}_2/\text{water}$ nanofluid through the trapezoidal cross-sectioned microchannel was investigated numerically. The numerical analyses were performed for different nanoparticle volume concentrations ($\phi=1-4$ vol.%) of $\text{TiO}_2/\text{water}$ nanofluid under thermally and hydrodynamically developing laminar flow condition ($100 \leq \text{Re} \leq 1000$). While the constant heat flux was applied at the bottom and side surfaces of the microchannel, top surface of the microchannel was insulated. It is observed from the numerical calculations that the convective heat transfer coefficient increases with increasing in nanoparticle volume concentration. The maximum convective heat transfer enhancement was obtained to be 14.87% for TiO_2 nanoparticle addition of 4.0 vol.%. However, the Darcy friction factor is not affected by the increasing in nanoparticle volume concentration.

ACKNOWLEDGMENT

The authors would like to thank to The Scientific and Technological Research Council of Turkey (TUBITAK) for supporting this project.

REFERENCES

- [1]. S.U.S.Choi, *Enhancing Thermal Conductivity of Fluids with Nanoparticles*, in: D.A. Singer, H.P. Wang (Eds.), Development and Applications of Non-Newtonian Flows, ASME, New York, 1995, pp. 99–106.
- [2]. S.Lee, S.U.S.Choi, S.Li, J.A. Eastman, Measuring Thermal Conductivity of Fluids Containing Oxide Nanoparticles. *J. Heat Transfer*, vol.121, pp. 280–289, 1999.
- [3]. J.A.Eastman, S.U.S.Choi, W. Yu, L.J. Thompson, Anomalous Increased Effective Thermal Conductivity of Ethylene Glycol-Based Nanofluids Containing Copper Nanoparticles, *Appl. Phys. Lett.*, vol. 78, pp. 718–720, 2001.
- [4]. X. Wang, X.Xu, S.U.S. Choi, Thermal Conductivity of Nanoparticle-Fluid Mixture, *J. Thermophys. Heat Transfer*, vol. 13, pp. 474–480, 1999.
- [5]. S.K.Das, N. Putra, P.Thiesen, W.Roetzel, Temperature Dependence of Thermal Conductivity Enhancement for Nanofluids, *J. Heat Transfer*, vol. 125, pp. 567–574, 2003.
- [6]. M.H.Kayhani, H.Soltanzadeh, M.M.Heyhat, M.Nazari, F.Kowsary, Experimental Study of Convective Heat Transfer and Pressure Drop of $\text{TiO}_2/\text{water}$ Nanofluid, *International Communications in Heat and Mass Transfer*, vol. 39, pp. 456–462, 2012.
- [7]. J. Zhang, Y.Diao, Y. Zhao, Y. Zhang, Experimental Study of $\text{TiO}_2/\text{Water}$ Nanofluid Flow and Heat Transfer Characteristics in a Multiport Minichannel Flat Tube. *International Journal of Heat and Mass Transfer*, vol. 79, pp. 628–638, 2014.
- [8]. M. Vakili, A.Mohebbi, H.Hashemipour, Experimental Study on Convective Heat Transfer of TiO_2 Nanofluids, vol. 49, pp. 1159–1165, 2013.
- [9]. A.A.A. Arani, J. Amani, Experimental Study on The Effect of $\text{TiO}_2/\text{Water}$ Nanofluid on Heat Transfer and Pressure Drop, *Experimental Thermal and Fluid Science*, vol. 42, pp. 107–115, 2012.
- [10]. A.M. Hussein, R.A. Bakar, K. Kadirgama, K.V. Sharma, Heat Transfer Enhancement With Elliptical Tube Under Turbulent Flow TiO_2 -Water Nanofluid. doi:10.2298/TSCI130204003H.
- [11]. P. Nitiapiruk, O. Mahian, A.S. Dalkilic, S. Wongwises, Performance Characteristics of a Microchannel Heat Sink Using $\text{TiO}_2/\text{Water}$ Nanofluid and Different Thermophysical Models, *International Communications in Heat and Mass Transfer*, vol. 47, pp. 98–104, 2013.
- [12]. S. Bi, K. Guo, Z. Liu, J. Wu, Performance of a Domestic Refrigerator Using TiO_2 -R600a Nano-Refrigerants Working Fluid, *Energy Conversion and Management*, vol. 52, pp. 733–737, 2011.
- [13]. V. Bianco, O. Manca, S. Nardini, Numerical Investigation on Nanofluids Turbulent Convection Heat Transfer Inside a Circular Tube, *International Journal of Thermal Sciences*, vol. 50, pp. 341–349, 2011.

- [14]. A.M. Hussein, K.V. Sharma, R.A. Bakar, K. Kadirgama, The Effect of Cross Sectional Area of Tube on Friction Factor and Heat Transfer Nanofluid Turbulent Flow, *International Communications in Heat and Mass Transfer*, vol. 47, pp. 49-55, 2013.
- [15]. S.K. Das, S.U.S Choi, W. Yu, T. Pradeep, *Conduction Heat Transfer in Nanofluids*, Nanofluids Science and Technology. New Jersey: John Wiley & Sons, Inc., 2008.
- [16]. S.V. Patankar, *Numerical Heat Transfer and Fluid Flow*. Washington: Hemisphere Publishing Corporation, 1980.
- [17]. E.N. Sieder, G.E. Tate, Heat Transfer and Pressure Drop of Liquids in Tubes, *Ind. Eng. Chem.*, vol. 28, pp. 1429–1435, 1936.
- [18]. H.Y. Wu, P. Cheng, Friction Factors in Smooth Trapezoidal Silicon Microchannels with Different Aspect Ratios, *International Journal of Heat and Mass Transfer*, vol. 46, pp. 2519-2525, 2003.

BIOGRAPHY

Kamil ARSLAN is an Associate Professor of Mechanical Engineering Department at Karabük University, Turkey. He received his Ph.D. from Mechanical Engineering Department, Gazi University, Turkey, in 2010. He is active in both teaching and research in the area of thermal sciences. Also, he is interested in computational fluid dynamics, experimental methods in heat transfer and nanofluids.

ADAPTIVE FILTERS FOR SPEECH NOISE CANCELLATION

Motuma ABAFOGI

Sakarya University, Faculty of Engineering, Dept. of Electrical & Electronics, Sakarya/TURKEY

Ridvan Firat CINAR

Sakarya University, Faculty of Engineering, Dept. of Electrical & Electronics, Sakarya/TURKEY
Batman University, Technology Faculty, Dept. of Electronics & Communications Eng., Batman/TURKEY

Askin DEMIRKOL

Batman University, Technology Faculty, Dept. of Electronics & Communications Eng., Batman/TURKEY

Zafer DEMIR

Anadolu University, Porsuk Vocational School, Department of Electricity and Energy, Eskisehir/TURKEY

Abstract

Audio signal is corrupted by noise from the surrounding environment which might be a moving car, train, factory, or a noisy telephone channel. Since noise is random and varying continuously, we need to estimate the noise at every instant to remove it from the desired signal. There are many schemes for noise reduction but the most efficient scheme to accomplish noise cancellation is to employ adaptive filters. In speech signal enhancement there are two categories of algorithms in which either a single microphone or multiple microphones are employed to clean up the noisy signal. In this paper, MATLAB simulations of different adaptive algorithms and comparison of their performances for noise cancellation in a noisy environment, specifically industrial noise, is carried out. A comparative analysis of different adaptive filters in the presence of a single and dual microphone is provided. A robust voice activity detector (VAD) is incorporated in the single channel speech enhancement.

Keywords: *Speech Enhancement, Kalman Filter, Least Mean Square, Spectral Subtraction, VAD*

1. INTRODUCTION

Noisy environments usually constitute most part of our daily lives. The noise in automobiles, trains, or work areas like factories, which for the most part is unavoidable, makes communication between two individuals quite difficult. In order to improve the poor voice quality, speech enhancement becomes a necessity in these kinds of noisy environments. Some of the application areas of noise cancellation products are hearing aids, mobile phones, teleconferencing etc. [1]. In this paper, the comparative analysis of some of the adaptive filtering techniques used in speech signal enhancement where a single and multiple input signals are available in a heavy noise industry is described.

2. SINGLE MICROPHONE NOISE CANCELLATION

The only available signal in a single microphone system is a noisy speech signal. In this kind of environment, the same microphone captures both voice and noise. From among the various techniques used to suppress the noise in the signal, the spectral subtraction technique employing the robust multiple observation likelihood ratio test (MO-LRT) voice activity detection (VAD) is used.

2.1. Voice Activity Detection

From among the different VAD techniques mentioned in [2], the multiple observation likelihood ratio test (MO-LRT) which was described in [3] and [4] is employed so as to enhance the output signal quality of the single microphone. For $2m+1, \{y_{l-m}, \dots, y_{l-1}, y_l, \dots, y_{l+m}\}$ observation vectors, the MO-LRT is given as [4]:

$$l_{l,m} = \sum_{l-m}^{l+m} \ln \frac{P_{y_k/w_1}(y_k/w_1)}{P_{y_k/w_0}(y_k/w_0)} \quad (1)$$

Where $p(w_i/y)$ is the posterior probability, l represents the frame being classified as speech (w_1) or non-speech (w_0) which is in fact the pure noise. The likelihood ratio test (LRT) can be computed recursively as follows.

$$l_{l+1,m} = l_{l,m} - \phi(l-m) + \phi(l+m+1) \quad (2)$$

where,

$$\phi(k) = \ln \frac{P_{y_k/w_1}(y_k/w_1)}{P_{y_k/w_0}(y_k/w_0)} \quad (3)$$

The classification is made by comparing $l_{l,m}$ with the decision threshold η which is experimentally determined. For $l_{l,m} \geq \eta$ (4) frame contains speech and otherwise non-speech. The graph below shows a typical output of a VAD system employing MO-LRT technique where a voice recorded in a noisy industrial environment is used as an input.

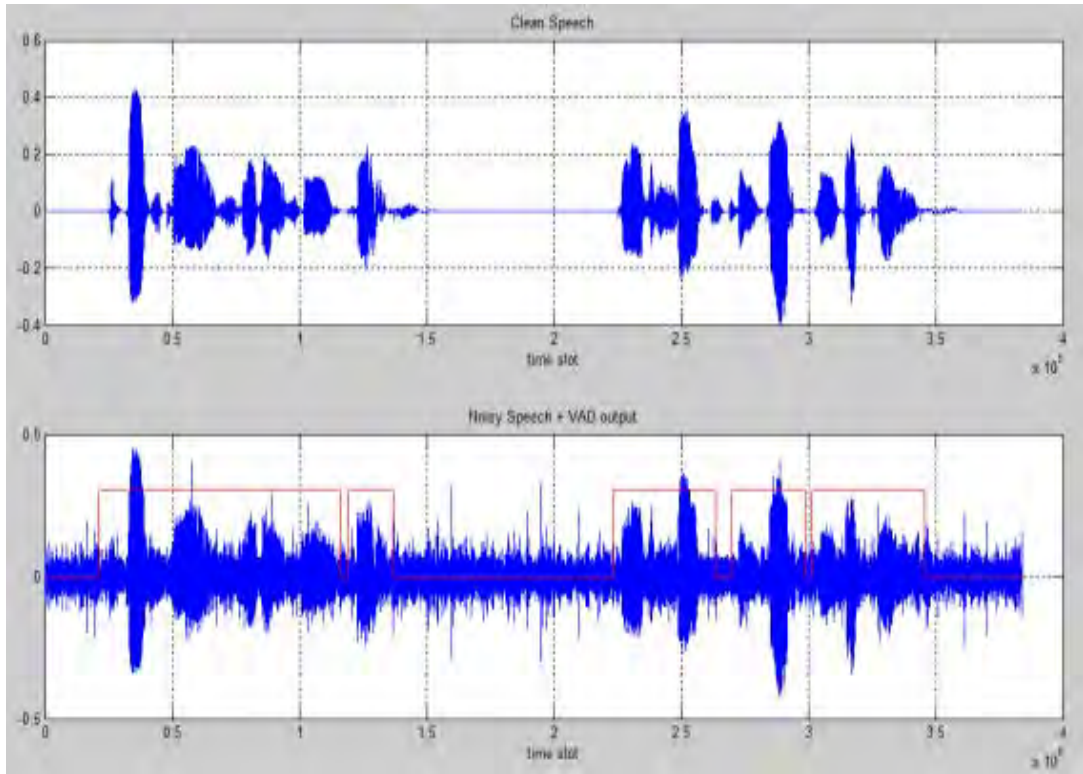


Figure 1. A typical output of a VAD system employing MO-LRT technique

2.2. Spectral Subtraction

The frequency domain representation of a noisy speech signal $y(m)$ can be expressed as [1] $Y(k) = X(k) + N(k)$, $k=0,1,\dots,M-1$ (5) where $Y(k)$, $X(k)$ and $N(k)$ are the short time discrete Fourier transforms of the noisy speech, clean speech and noise respectively. The complex polar form representation is given as: $Y_k e^{j\theta_{Y_k}} = X_k e^{j\theta_{X_k}} + N_k e^{j\theta_{N_k}}$, $k=0,1,\dots,M-1$ (6) where X_k , Y_k and N_k are the magnitudes of the frequency spectrums $X(k)$, $Y(k)$ and $N(k)$ while θ_{Y_k} , θ_{X_k} , θ_{N_k} represent their corresponding phases. Spectral subtraction is a technique used to restore the power or magnitude spectrum of a signal by subtracting an estimate of the average noise spectrum from the noisy signal spectrum [5]. The incoming signal $y(m)$ is buffered and divided into segments of M samples length. These samples will be transformed into M spectral samples via Discrete Fourier transform (DFT) after the samples are windowed using Hamming window. [5] The spectral subtraction carried out in order to estimate the original clean speech spectrum is expressed as: [5][6][7][8]

$$|X_w(f)|^b = |Y_w(f)|^b - \alpha |N_w(f)|^b \quad (7)$$

Where $N(f)$ is the time averaged noise spectra. The parameter α is 1 for full noise subtraction and greater than 1 for over subtraction while b is 1 for magnitude spectral subtraction and 2 for power spectral subtraction. In this paper the magnitude spectral subtraction with the MO-LRT voice activity detection technique described above is used. In Figure 3, a voice recorded in a noisy industrial environment is used as an input to the developed MO-LRT based Spectral Subtraction method.

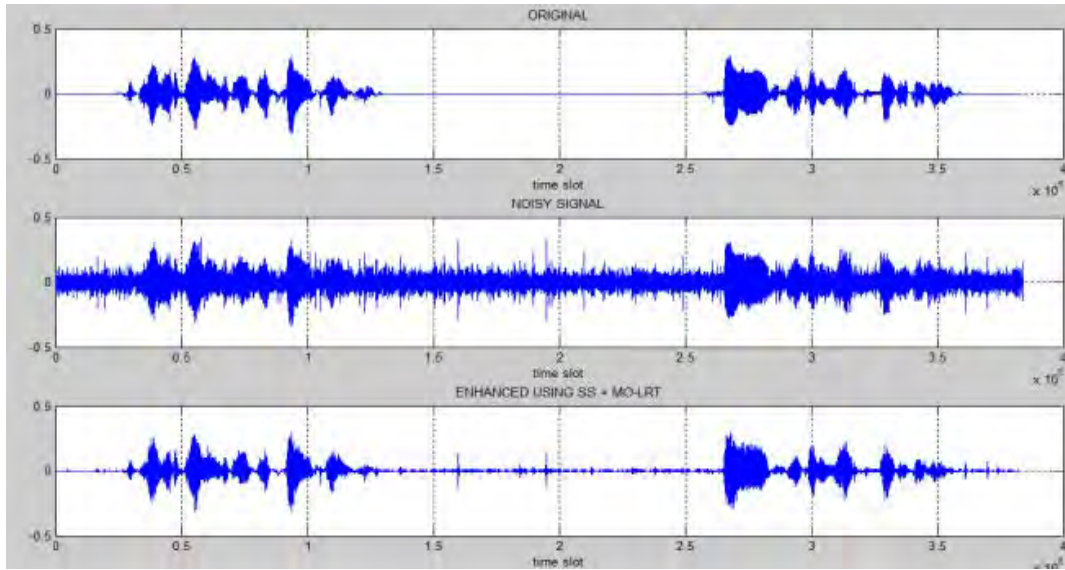


Figure 2. Output of a MO-LRT based SS technique

3. DUAL MICROPHONE NOISE CANCELLATION

In a dual microphone system, the primary and reference microphones should be placed properly in such a way that the speech level at the primary microphone is higher than the level at the reference microphone. In this paper, the least mean square (LMS), Kalman filter and Kalman filter based LMS filter will be used for the case of a dual microphone.

3.1. Least Mean Square (LMS)

The least mean square algorithm is one of the most widely used and computationally simple noise reduction algorithms. The basic steps involved in LMS technique are [9][10]:

- i. Computation of the output $y(n)$ as:

$$y(n) = w^T(n)x(n) \quad (8)$$

Where $x(n)$ and $w(n)$ are the input and weight vectors respectively

- ii. Estimation of error $e(n)$ as:

$$e(n) = d(n) - y(n) \quad (9)$$

Where $d(n)$ is the desired signal

- iii. Update the weight vector as:

$$w(n+1) = w(n) + 2\mu e(n)x(n) \quad (10)$$

3.2. Kalman Filter

The Kalman filter which was developed by R.E. Kalman in 1960 has a wide range of applications. It is based on the state space formulation of a discrete or continuous time systems. Kalman filtering technique using only a single microphone has been discussed in [11]. However in this paper, we consider a situation where there is an additional reference microphone. For a system described by:

$$\left. \begin{aligned} x(k+1) &= F(k)x(k) + n(k) \\ y(k) &= H^T(k)x(k) + v(k) \end{aligned} \right\} \quad (11)$$

The autocorrelation of the state noise $Q(k)$ and the measurement noise $R(k)$ is expressed as:

$$\begin{aligned} Q(k) &= E[n(k)n^T(k)] \\ R(k) &= E[v(k)v^T(k)] \end{aligned} \quad (12)$$

3.3. Kalman Based LMS

Since the stability of the LMS algorithm depends on the step size μ , a more efficient version of LMS which is the normalized LMS is widely used. In this case the weight update in the LMS is modified as:

$$w(k+1) = w(k) + \frac{\alpha e(k)x(k)}{x^T(k)x(k) + q} \quad (13)$$

Where $0 < \alpha < 2$ and q is small as compared to $x^T(k)x(k)$. In the combined Kalman based normalized LMS the weight is updated as

$$[12] \quad w(k+1) = w(k) + \frac{e(k)x(k)}{P(k) + R(k) / \delta_w^2(k)} \quad (14)$$

Where

$$\delta_w^2(k+1) = \delta_w^2(k) \left[1 - \frac{P(k) / N}{P(k) + R(k) / \delta_w^2(k)} \right] + Q(k) \quad (15)$$

Figure 4 below shows the enhancement of a noisy speech in an industrial environment using these various methods.

4. COMPARATIVE ANALYSIS

At this stage, we examine the performance of MO-LRT based spectral subtraction technique that employs a single microphone and the other adaptive filtering techniques mentioned above where there exists an additional reference microphone. From the mean square error (MSE) comparison it is evident that in spite of a single microphone used in the MO-LRT based spectral subtraction technique, the MSE obtained is very much closer to the dual microphone case. The spectrogram of these results clearly indicates that the performance of LMS has improved when combined with the Kalman filter.

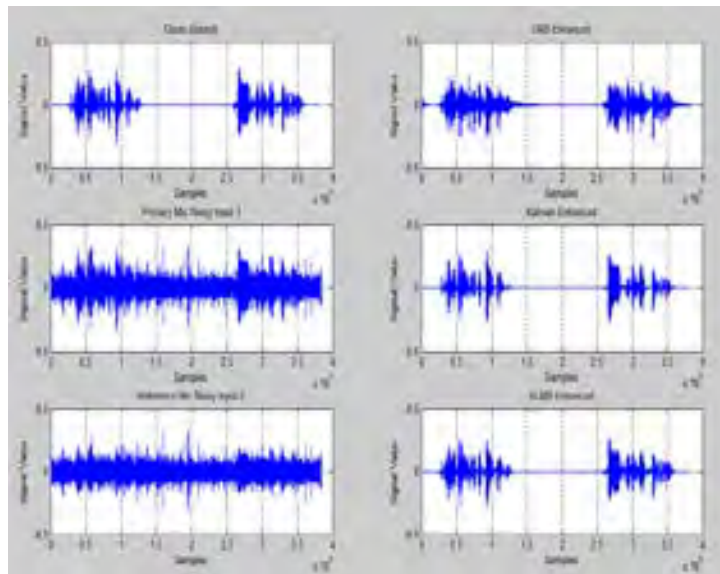


Figure 3. Output of the various methods (dual Mic)

REFERENCES

- [1]. Saeed V. Vaseghi, "Multimedia Signal Processing: Theory and Applications in Speech, Music and Communications", 2007 John Wiley & Sons Ltd.
 - [2]. Michael Grimm and Kristian Kroschel, "Robust Speech Recognition and Understanding", June 2007.
 - [3]. Lee Ngee Tan, Bengt J. Borgstrom and Abeer Alwan, "Voice Activity Detection Using Harmonic Frequency Components in Likelihood Ratio Test", ICASSP 2010.
 - [4]. Javier Ramirez, Jose C. Segura, "Statistical Voice Activity Detection Using a Multiple Observation Likelihood Ratio Test", IEEE Signal Processing Letters, VOL 12, No. 10, October 2005.
 - [5]. Saeed V. Vaseghi, "Advanced Digital Signal Processing and Noise Reduction", John Wiley & Sons Ltd, 2000.
 - [6]. Poruba J., "Speech Enhancement Based on Non Linear Spectral Subtraction", IEEE Devices, Circuits and Systems 2002.
 - [7]. Boll S.F., "Suppression of Acoustic Noise in Speech Using Spectral Subtraction", IEEE Trans ASSP 1979.
 - [8]. Kamath S. and Loizon P., "A Multiband Spectral Subtraction Method for Enhancing Speech Corrupted by Colored Noise", Proc. IEEE conference on Acoustics, Speech, Signal Processing, 2002.
 - [9]. Sambur M.I., Nutley N.J., "LMS Adaptive Filtering for Enhancing the Quality of Noisy Speech", IEEE Conference on ICASSP 1978.
 - [10]. Sayed A. Hadei, M. Lotfizad, "A Family of Adaptive Filter Algorithms in Noise Cancellation for Speech Enhancement", IJCEE 2010.
 - [11]. Paliwal K.K., "A Speech Enhancement Method Based on Kalman Filtering", IEEE Conference on ICASSP 1987.
 - [12]. Mahmoodzaadeh A., "Speech Enhancement Using a Kalman Based Normalized LMS Algorithm", Telecommunications, 2008, IST symposium.
-

AERODYNAMIC SIMULATION OF A TRADITIONAL HIGH-SPEED TRAIN WITH DIFFERENT HEAD ANGLES

Gürhan KÜLAHLI

Pamukkale University, Department of Automotive Engineering, 20070, Denizli, Turkey,
gkulahli@pau.edu.tr

Hilmi YAZICI

Corresponding author: Pamukkale University, Faculty of Technology, Department of Automotive Engineering,
Denizli, Turkey. hyazici@pau.edu.tr

Mehmet AKÇAY

Pamukkale University, Department of Mechanical Education, 20070, Denizli, Turkey.
makcay@pau.edu.tr

Abstract

The shapes of traditional high speed trains (THST) which are becoming more widespread every other day are important in terms of the pressure they are exposed to and velocity distribution. This study examined the effect of different head angles of a traditional high speed train on aerodynamic characteristics. The aerodynamic analysis was conducted by taking five different models of train head angles which were 10, 15, 20, 25 and 30 degrees, and considering that the train was travelling at a speed of 50 m/s in clear weather. The simulation was created by using ANSYS/Fluent program based on the mechanical theory of viscous flow and 3D incompressible viscous flow model. By the final of this study; maximum speed of air flow was revealed between 61.7- 71.6 m/s. The maximum pressure differences value of the train surface was revealed between 1294.9 - 2723.6 Pa. The minimum value of coefficient drag was obtained 0.3090 at the 15°.

Keywords: Train head shape, aerodynamic characteristic, numerical calculation, head angle

1. INTRODUCTION

Energy needs and rapid transportation are rising each passing day. In this context, energy and time come to forth as two important concepts. While vehicles are aimed to quickly reach their destination to save time, they are also wanted to be energy-efficient.

One way to reduce energy consumption values of vehicles and enhance road handling and safety is through reducing the drag force they are exposed to. Vehicles consume less energy with a better aerodynamic design. The noise level is decreased and stable driving is ensured [1].

The shapes of traditional high speed trains which are becoming more widespread every other day are important in terms of the pressure they are exposed to and velocity distribution. Kwon et al. states that the head of trains should also be considered while examining the aerodynamic shape [2]. When the micro-pressure waves that the trains are exposed to are taken into account, there are important tendencies towards the aerodynamic shape [3]. Studies have been conducted on the aerodynamic characteristics of traditional speed trains [4-6], underground trains [7], and head, tail and other parts of magnetic trains [8,9].

Chen et al. (2012) determined the aerodynamic forces on a magnetic train travelling through an evacuated tunnel based on different evacuation pressures, blockage rates, and head and tail shapes using ANSYS/Flotran program. The pressure areas on the train were analyzed in different evacuation pressures and blockage rates. It was found that the train was least exposed to aerodynamic forces in an environmental

pressure of 1000 Pa in the tunnel. There were not significant differences between different head shapes in reducing aerodynamic drag forces. In a tunnel pressure of 1000 Pa, a blunt-shaped tail and a blockage rate of 0.25 were found to be more effective in reducing drag forces [10].

Tao (2011) analyzed the formation of pressure waves in a tunnel. The simulation model of the pressure waves was structured on two-equation k-epsilon model using the dynamic gridded finite volume model based on three-dimensional viscous variable equation. The pressure distribution on trains with variant sizes and travelling at differed speeds in the tunnel was numerically obtained. The result of the simulation was compared with other experimental studies. It was observed that the result of the study was consistent with those of previous experimental studies [11].

Kulahlı and Yılmaz (2014) conducted a 2D aerodynamic analysis of a light commercial vehicle using the ANSYS/Fluent software, and examined the distributions of air flow, air flow vectors and pressure. They investigated the effect of front bumper area and front window angle of the vehicle on its aerodynamic characteristics. The study revealed that the curvature of the front bumper did not have any significant effect on the aerodynamic characteristics of the vehicle. They examined front window angles in 30-40-50 degrees and found that there was pressure intensity in 40-50 degree angles, and an angle between 30-40 degrees would be suitable [12].

Yang et al. (2010) numerically calculated the aerodynamic characteristics of the head part of an underground train, and obtained the calculated models of its contour design. They analysed and compared the flow distributions and the difference of aerodynamic parameters between these models by using 3D turbulent Navier-Stokes equations and variable grid technology. The numeric calculation of the aerodynamic characteristics of the head part of the underground train provided the theoretical base necessary for improving the head angles of an underground train [13].

Kim and Kim (2007), are conducted three-dimensional experimental and numeric analyses of variable airflow induced by an underground train in a tunnel. In the experimental analysis, a modelled tunnel at a scale of 1/20 was used, and time dependent pressure and airspeeds were obtained. Three-dimensional variable numeric analysis was done by using sharp interface method for the same geometrical configuration used in the experimental analysis. It was found that the numeric model results were consistent with the experimental analysis results [13].

Choi and Kim (2014) investigated the effects of nose shape of a train and tunnel section area on aerodynamic drag. They calculated aerodynamic drag by using Computational Fluid Dynamics (CFD). The train speeds were taken as 100 km/h and 200 km/h. As the train speed increased from 100 km/h to 200 km/h, aerodynamic drag increased nearly four times. As the nose shape changed from a blunt to a streamlined shape, aerodynamic drag are decreased nearly 50%. As the tunnel section area increased, aerodynamic drag decreased nearly 50% [15].

The current study examined the effect of different head angles of a traditional high speed train on aerodynamic characteristics. The airflow and pressure distributions between the surfaces in the operating area of the train were investigated. The pressure distributions in the head part of the train were examined. The aerodynamic analysis was conducted by taking five different models of train head angles which were 10, 15,

20, 25 and 30 degrees, and considering that the train was travelling at a speed of 50 m/s in clear weather. Although the analyzed head and tail lengths were the same, they varied depending on the angles. The simulation was created by using ANSYS/Fluent program based on the mechanical theory of viscous flow and 3D incompressible viscous flow model

2. MATERIAL AND METHOD

In this study, the aerodynamic analysis of a traditional high-speed train (THST) having different head and tail angles was conducted using ANSYS/Fluent program and creating a virtual wind tunnel. It was assumed that the THST was travelling in clear weather. Five different train head angles including 10, 15, 20, 25 and 30 degrees were examined. The head and the tail had the same angle. The 3D models shown in Figure 1 were created using the Solidworks software. The created models were transferred to the ANSYS/Workbench software in which meshing was carefully done in accordance with the analysis of the train. Following the meshing step, the boundary conditions of the analysis area of the train were indicated and the virtual wind tunnel was created

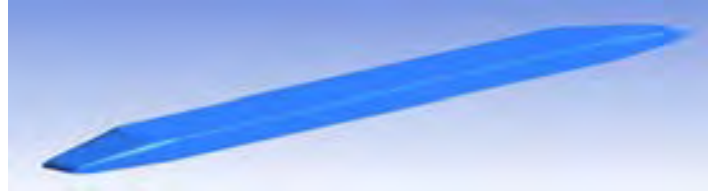


Figure 1 3D model of the THST

The body of the THST examined was 30-meter long, 4-meter wide and 3-meter high. However, the head and tail lengths varied depending on the angles. Table 1 presents the dimensional information of the THST.

Table 1 THST analysis parameters

Head and tail angle (Degree)	Model	Body length (m)	Head length (m)	Node	Elements	Velocity (m/s)
10°	D10	30	11.3	163328	839425	50
15°	D15	30	7.5	152736	840376	50
20°	D20	30	5.5	143589	789232	50
25°	D25	30	4.2	136779	751047	50
30°	D30	30	3.5	135765	745232	50

The aerodynamic analysis was conducted considering the THST was travelling at a speed of 50 m/s (180 km/h) in an area that was open to atmosphere. The Reynolds number of the airflow that came into contact with the THST during the travel was higher than 105 and turbulent. 3D standard k-ε model was used to simulate the airflow. Various assumptions were made during the simulation work. The estimated calculation time, degree of convergence and the calculation for the change in pressure waves were done with compressible gas assumption. In addition, it was also assumed that the air temperature was 20°C and the outside surfaces of the THST were smooth. The rail wheels were omitted in geometrical drawing. To shorten the analysis time for the finite element simulation, the analysis was conducted by scaling down the THST dimensions to 1/1000. Nevertheless, the medium-scaled numeric analysis was completed in one hour.

The maximum drag force was found from the train cross sectional area in the vertical plane by using ANSYS/Fluent software. Drag coefficient (C_d) was calculated by using the formula below [16];

$$C_d = \frac{F_d}{0.5\rho AU^2} \quad (1)$$

where F_d is drag force, ρ is the density of air (1.204 kg/m³) and U is the velocity of air. The area (A) is the cross sectional area vertical to the air flow direction. Analysis was performed considering value that pressure and temperatures is 101,325 Pa, 20 ° C respectively.

3. RESULTS AND DISCUSSION

The air flowing on the train in high speeds is an important factor affecting energy consumption and driving stability. The aerodynamic characteristics of vehicles change depending on the head shape of trains. Therefore, it is of significance to examine the head shape of trains in terms of aerodynamics.

In this section, the simulation of a THST having different head angles (10, 15, 20, 25 and 30 degrees) was made with the ANSYS/Fluent software. The relationship between aerodynamic drag and head shape was examined, and the results for the drag force, coefficient drag, pressure and speed distribution are presented in this section. Drag force in the vertical sectional area of the train was found and drag force was calculated using the formula No 1. Drag force and drag coefficient value are given table 2. As shown in Table 2, drag force and drag coefficient were observed changing the directly proportional with nose angle, excluding the 10 ° nose angle. Minimum and maximum value of drag coefficient was performed 15°, 0.3090 and 30°, 0.3861 respectively. Drag coefficient of 10 ° was estimated little more than 15 ° because of the length of the nose.

Table 2 Value of drag forces and drag coefficients

Nose angle (degree)	Area (m ²)	Drag force (N)	Density (kg/m ³)	Drag coefficient
10	0.0012	0.5844	1.204	0.3235
15	0.0012	0.5581	1.204	0.3090
20	0.0012	0.5906	1.204	0.3270
25	0.0012	0.6524	1.204	0.3612
30	0.0012	0.6973	1.204	0.3861

The speed distributions of the models examined are shown in Figure 2. The analysis revealed that the maximum speeds on the D10, D15 and D20 models were 61.7 m/s, 64.5 m/s, and 68.4 m/s, respectively. The maximum speed on the D25 model was found to be 70.4 m/s while the maximum speed on the D30 model which had the highest speed was 71.6 m/s.

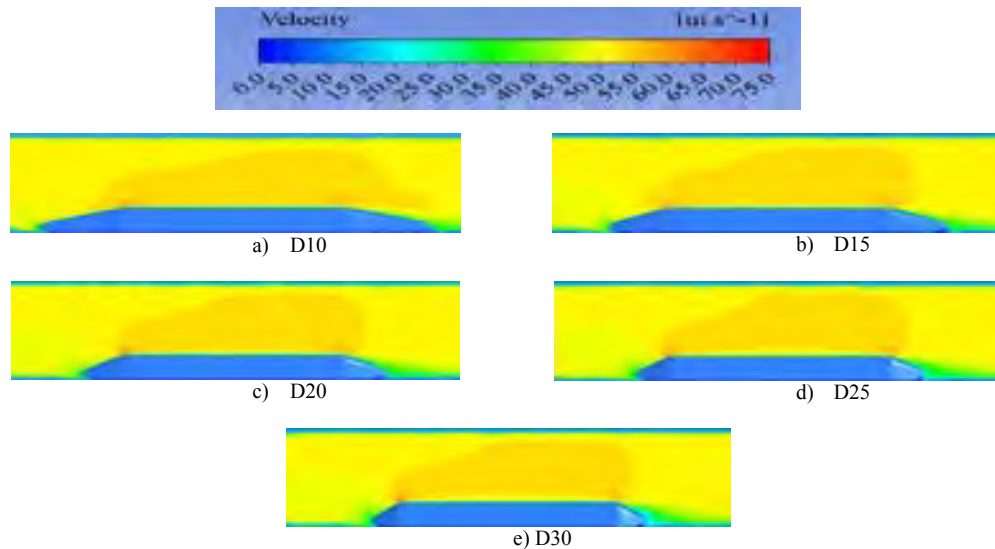


Figure 2 Speed distributions

The analysis showed that as the nose angle increased, the maximum speed increased too. The minimum speed was obtained in the D10 model and the maximum speed in the D30 model. The reason for the minimum speed could be due to the nose angle and the drag coefficient being low.

The pressure distributions of the models examined are shown in Figure 3. The analysis revealed that the maximum negative pressures on the D10, D15 and D20 models were 1294.9 Pa, 1432.9 Pa and 1881.2 Pa,

respectively. The maximum negative pressure on the D25 model was found to be 2440 Pa while the maximum negative pressure on the D20 model which had the highest speed was 2723.6 Pa.

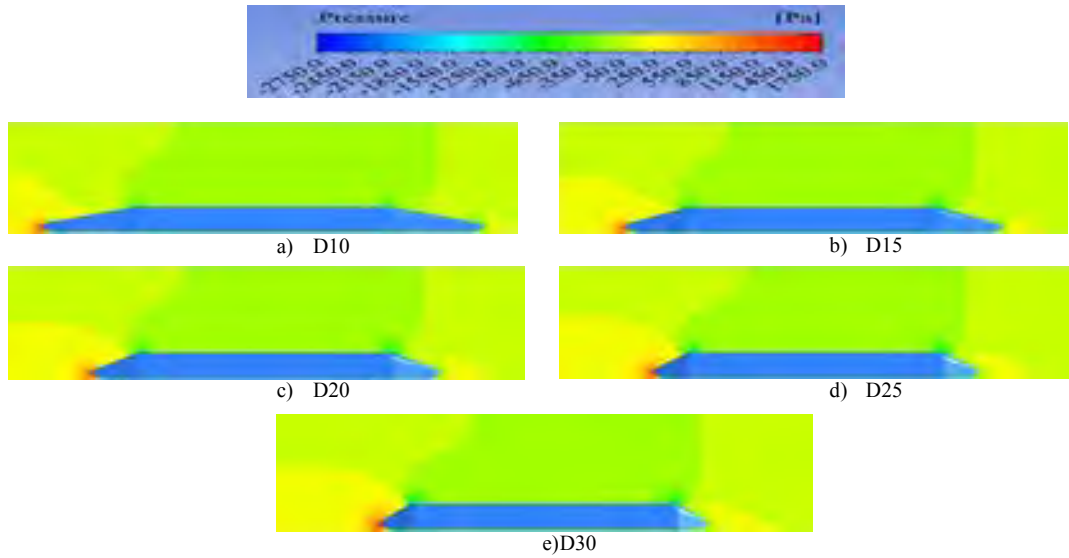


Figure 3 Pressure distributions

The distributions of pressure flowing to the head part of the train are presented in Figure 4. As shown in Figure 4, the positive pressure applied on the train intensified in the nose area. Since the nose shapes of the trains were the same, the maximum positive pressures were close in the analysis results. The pressure intensity on the head parts of the trains was found to increase as the head angle increased, which also caused the drag coefficient on the train to increase.

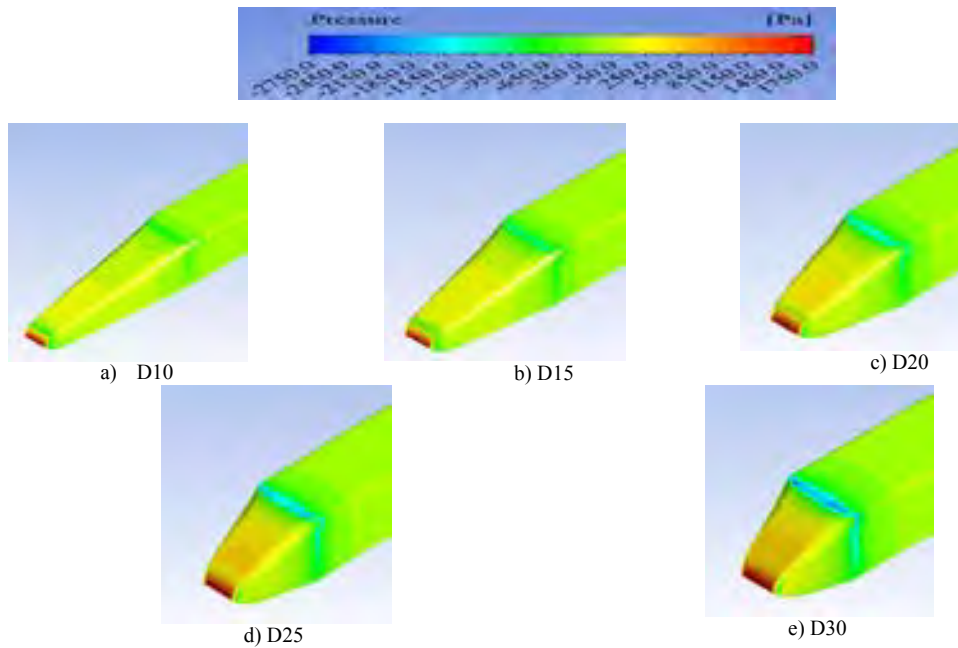


Figure 4 Distributions of pressure on the head part

4. CONCLUSION

The pressure intensity on the head parts of the trains was found to increase as the head angle increased. This also caused the drag coefficient on the train to increase. The minimum speed obtained was 61.7 m/s while maximum speed was 71.6 m/s. For the pressure differences, the minimum value was 1294.9 Pa, and the maximum was 2723.6 Pa. The pressure and speed distribution results revealed using linearly changing angles are thought to be useful for similar models to be created in the future. Drag force and drag coefficient were observed changing the directly proportional with nose angle, excluding the 10 ° nose angle. Minimum and maximum value of drag coefficient was performed 15°, 0.3090 and 30°, 0.3861 respectively. Drag coefficient of 10 ° was estimated little more than 15 ° because of the length of the nose. In conclusion, the optimum train nose angle is determined to be around 15°.

ACKNOWLEDGMENT

This work was financially supported by the BAP, Pamukkale University in Turkey.

REFERENCES

- [1]. Y.A Çengel and J.M., Cimbal, *Fluids Mechanics*, 1nd ed., Izmir, Turkey: Güven Press,2008
- [2]. H.B. Kwon, K.H. Y.S. Kim, et al. "Nose shape optimization of high-speed train for minimization of tunnel sonic boom," *JSME International Journal Series C Mechanical Systems, Machine Elements and Manufacturing*, vol. 44(3), pp. 890-899, 2001.
- [3]. J.S. Lee J.S., J.H. Kim, "Approximate optimization of high-speed train nose shape for reducing micro pressure wave." *Structural and Multidisciplinary Optimization*, vol.35(1),pp 79-87,2008
- [4]. J. Zhang, "Research on optimum nose and tail shapes of foreign high-speed trains.", *Electric Drive for Locomotive*, vol.35(2), pp. 16-18,2000.
- [5]. R.L. Chen, Q.Y. Zeng, J. Xiang, et al., "Study on the performance of aerodynamics of high-speed train with different nose shapes." *Journal of Hunan University of Science and Technology (Natural Science Edition)*, vol. 24(1), pp. 45-48, 2009.
- [6]. Y. Yan, W.N. Fang, "Analysis of head shape design of high-speed train", In: Proceedings of The 2006 International Conference On Industrial Design "the 11th China Industrial Design Annual Meeting" Hangzhou, China, pp 152-156, 2006.
- [7]. J.R. Zhang, L. Zhou, Q.H. Sun, et al., "Simulated calculation of distributing of air flow around metro train head and its design analysis", *Railway Locomotive and Car*, vol. 28(2), pp.43-47, 2008.
- [8]. H.Q. Tian, D. Zhou, P. Xu. "Aerodynamic performance and streamlined head shape of train", *China Railway Science*, vol. 27(3), pp.47-55, 2006.
- [9]. S.G. Yao, P. Xu. "Aerodynamic shape optimization of domestic maglev train", *Railway Locomotive and Car*, vol. 27(3), pp33-34, 2007.
- [10]. R.L. Chen, Q.Y. Zeng, J. Xiang, et al. "Study on the performance of aerodynamics of high-speed train with different nose shapes", *Journal of Human University of Science and Technology (Natural Science Edition)*, vol. 24(1), pp.45-48, 2009.
- [11]. B.H. Tao, "Numerical analysis on the pressure waves in tunnels", *The 6th Int. Conference on Computer Science & Education (ICCSE 2011)*, Superstar Virgo, Singapore, August 3-5, 2011.
- [12]. G. Kılahlı, Y. Yılmaz. "Effect to aerodynamic shape for front bumper type and windshield angle on a light commercial vehicle", *7th Automotive Technologies Conference (OTOKON'14)*, Bursa, Turkey, 26-27 May, 2014.
- [13]. B. Yang, M. Wan, Q. Sun., "Numerical calculation of aerodynamic characteristics of metro train head", *2nd International Conference on Future Computer and Communication*, Wuhan, China, 21-24 May,2010, vol. 1 pp 419-422.
- [14]. J.Y. Kim, K.Y. Kim. "Experimental and numerical analyses of train-induced unsteady tunnel flow in subway" *Tunneling and Underground Space Technology*, vol. 22: pp. 166-172, 2007.
- [15]. J.K. Choi, K.H. Kim, "Effects of nose shape and tunnel cross-sectional area on aerodynamic drag of train travelling in tunnels", *Tunneling and Underground Space Technology*, vol. 41, pp.62-73, 2014.
- [16]. S. Kırmacı, M. Pakdemirli, "Flow analysis and determination of drag forces for spikes of crops", *Mathematical and Computational Applications*, vol. 17(1), pp. 83-91, 2012.

E-INVOICING IN TURKEY AND A SOFTWARE-AS-A-SERVICE SOLUTION

Ahmet OZCAN

Idea TeknolojiÇözümleri, Research and Development, Istanbul, Sun Plaza BBDO Blok Dereboyu Cd. BilimSk No:5 34398
Maslak, Istanbul, TURKEY. Phone: (+90) 212 276 56 76, Fax: (+90) 212 276 58 88, ahmet.ozcan@ideateknoloji.com.tr

Salim ERYIGIT

Idea TeknolojiÇözümleri, Research and Development, Istanbul, Sun Plaza BBDO Blok Dereboyu Cd. BilimSk No:5 34398
Maslak, Istanbul, TURKEY. Phone: (+90) 212 276 56 76, Fax: (+90) 212 276 58 88, salimeryigit@ideateknoloji.com.tr

Abstract

E-invoicing is becoming the standard way of billing globally thanks to its efficiency, cost and auditing convenience. Turkey is one of the countries that standardized its e-invoicing procedures and e-invoice is now mandatory for certain companies and optional for others. The companies have two options for e-invoicing: they may implement their own software, which should meet the imposed specifications; or they may lean to eligible integrator companies that provide software-as-a-service solutions. In this paper, we first discuss the e-invoicing procedure in general. Then, we move on to the standard that is used in Turkey, and its differences from the other countries. We then discuss the platform-independent software solution that is used by one of the leading integrator companies. In particular, we describe the database, web and web service structures employed in detail. Finally, we give statistics about the usage and penetration of e-invoicing solutions.

Keywords: *e-invoice, web design, web service, database.*

1. INTRODUCTION

Electronic invoicing is a B2B/B2C paradigm that allows billing between two companies without the need for printed material. Although the definition of e-invoicing vary between regions, the definition by the EU legislation can be stated as: “The issuing and receipt of VAT compliant invoices in an electronic format” [1]. The main requirements for e-invoice can be listed as:

- The electronic document should have a simple to form, technology independent format and standard. For this task, Universal Business Language (UBL) standard is widely used in Europe.
- The source and integrity of the document should be guaranteed. Timestamps and electronic signatures are usually employed for achieving these requirements.
- It should be possible to store the electronic document for long periods of time for accountability. Since these documents tend to be small, storing them is no longer a big issue.

The benefit of e-invoicing are [2]:

- Reduced cost,
- Quick payment and access,
- Easy to process and control workflow,
- Enhanced consistency and productivity,
- Less disputes between parties,
- Easy to manage cash flow,
- Green and environment friendly.



Figure 1: E-invoicing in Europe [3]

The e-invoicing procedure in Europe can be seen in Figure 1. The suppliers send e-invoices to the buyer in one of the formats that have been agreed in advance. These invoices should adhere to the aforementioned requirements. Upon receipt of an e-invoice, the buyer assures the authenticity and integrity of the document. Then he/she converts it into desired format for archiving and stores at least for the legally required time duration.

The rest of the paper is organized as follows: In Section 2, we discuss the e-invoicing in Turkey and its differences from European counterparts. Section 3 explains a software-as-a-service solution together with some usage statistics. Finally, Section 4 concludes this paper.

2. THE CASE OF TURKEY

With a recent legislation in Turkey, all companies with a turnover greater than some threshold are mandated to use e-invoicing. Like in South American countries, the system in Turkey is controlled and provided by a centralized authority, Turkish Revenue Administration (TRA). The main differences between Europe and Turkey can be found in Table 1.

Table 1: E-invoicing differences between Turkey and Europe

	<i>Europe</i>	<i>Turkey</i>
<i>Format:</i>	<i>Various</i>	<i>Only UBL-TR</i>
<i>Control:</i>	<i>Independent agencies</i>	<i>Centralized-government agency</i>
<i>Messaging:</i>	<i>Various messaging protocols: Electronic data interchange, XML, etc.</i>	<i>All messages are relayed in UBL-TR format through TRA</i>
<i>Methods for e-invoicing:</i>	<i>Through service providers, Direct integration.</i>	<i>Through service providers, Direct integration, Through TRA web portal.</i>
<i>Main goal:</i>	<i>Reduced operational costs and shorter process times.</i>	<i>Tax control.</i>

As can be seen in the table above, companies have three alternative methods for e-invoicing. They can develop their own software solutions, or use solutions provided by integrator companies that are deemed eligible by TRA, or use TRA portal. Among these alternatives, TRA portal is the least preferred method, especially for big companies, due to the following reasons:

- There is a monthly limit, beyond which the portal cannot be used.
- In a single session, only a limited number of e-invoices can be uploaded.
- The e-invoices are only archived for 6 months.
- The responses to the e-invoices cannot be observed.

The details of e-invoicing process in Turkey can be seen in Figure 2. Among the three alternative methods, using the system through an authorized integrator company is the most viable and employed one among companies due to requiring no initial investment, no maintenance overhead and support for automated procedures.



Figure 1: E-invoicing in Turkey

3. A SOFTWARE-AS-A-SERVICE SOLUTION

In this section, we discuss the software architecture of the leading e-invoicing integrator company in Turkey. The company provides a software-as-a-service solution to its customers using a subscription business model. The utilized software architecture is shown in Figure 3. This figure covers the supplier point of view. The case for the consumer is very similar, thus, omitted.

In the first step, the supplier -through either direct integration or integrator provided web portal- sends the generated invoice in desired format (CSV, txt, xml, xls/xlsx). The received invoice is transformed to UBL-TR following the steps that are shown in Figure 4. This transformation takes place at either integration web service or e-invoice web service depending on the access strategy of the company. The received document is converted to UBL-TR format by XSL transformation using the company specific XSLT file. UBL-TR is a modified version of UBL that is designed by TRA in order to meet country and culture specific needs.

Continuing with Figure 3, the resulting UBL-TR file is stored in the database. Integration window service periodically checks the database for new records by utilizing e-invoice web service. These new records are first checked for structural accuracy using XML schema definition, then they are checked for semantic accuracy using schematron validation. This schematron file meets the standards imposed by the TRA and the integrator company. If these checks are successful, integration windows service calls the signature service in order to sign the new e-invoice using the signature of the integrator. Subsequently, integration windows service puts the signed e-invoices into envelopes and sends them to TRA. Furthermore, integration windows service also periodically checks TRA web service for incoming envelopes to the supplier. These received envelopes are stored in the database (through e-invoice web service). They are also opened for classifying the contents of the

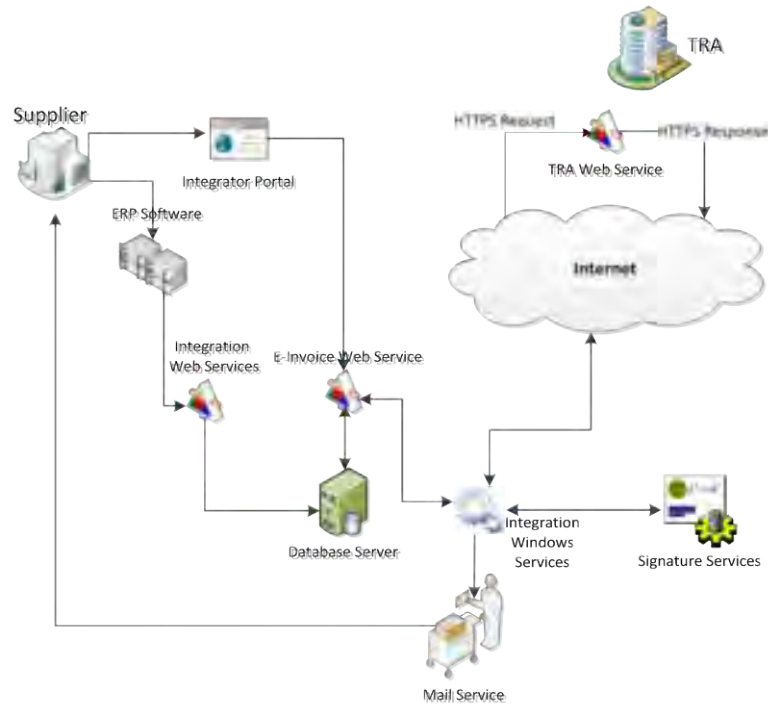


Figure 2: Software architecture of the described system

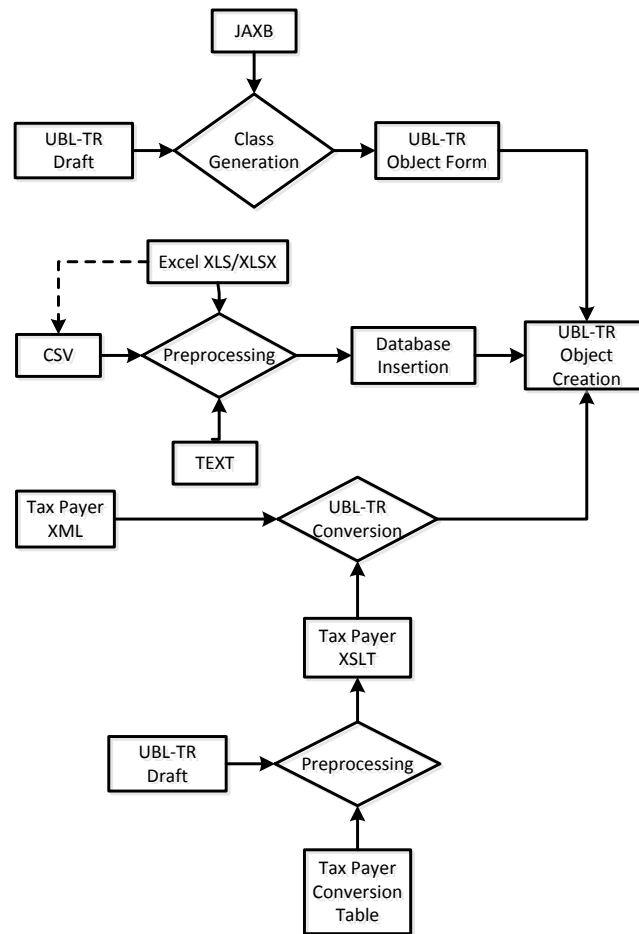


Figure 3: UBL-TR Conversion

envelope such as incoming invoices, system responses and application responses. The envelopes used in the e-invoice system of Turkey adhere to the standard business document header format. If the content of the envelope requires the notification of the supplier (e.g. received e-invoice), the supplier is notified by integration windows service through mail service.

All of the described steps/actions are logged for future accountability. Furthermore, all e-invoices are stored in the system for at least 10 years, which is in compliance with the legislation.

Since the architecture utilizes web services that conform to the SOAP standard, the system can be used by any operating system and ERP application. Moreover, the web portal also provides platform independent access to the system.

After discussing the system, we now give a couple of usage statistics. In Figure 5, we show the percentage of used currencies in the number of e-invoices. On the other hand, Figure 6 shows the percentage of total amount each currency has within the gross total of e-invoice amounts. We observe that most of the e-invoices use the local currency TL (also referred as TRY) with the other currencies having very little share. However, we observe that these low shares for USD and EUR translate to relatively higher percentages when looking at Figure 6. This suggests that although the foreign currencies are infrequently used in e-invoices, the amounts of these e-invoices are usually large.

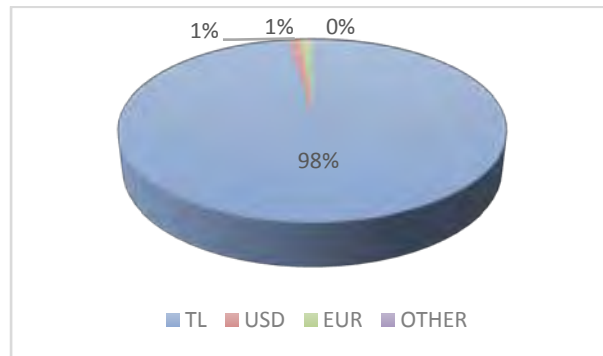


Figure 4: Percentage of used currencies

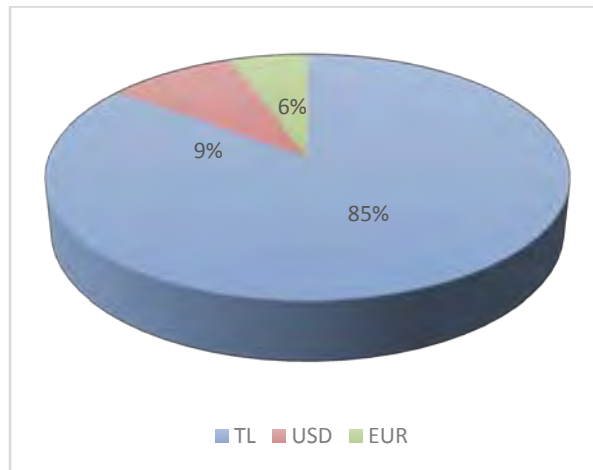


Figure 5: Percentage of total amount for each currency in the gross total of e-invoices

Finally, we observe the distribution of the TL e-invoices in Figure 7. As can be seen in this figure, most of the TL e-invoices have a low amount. That is to say, 40 % percent of the e-invoices have amounts lower than 500 TL. This observation is also in accordance with our previous claim.

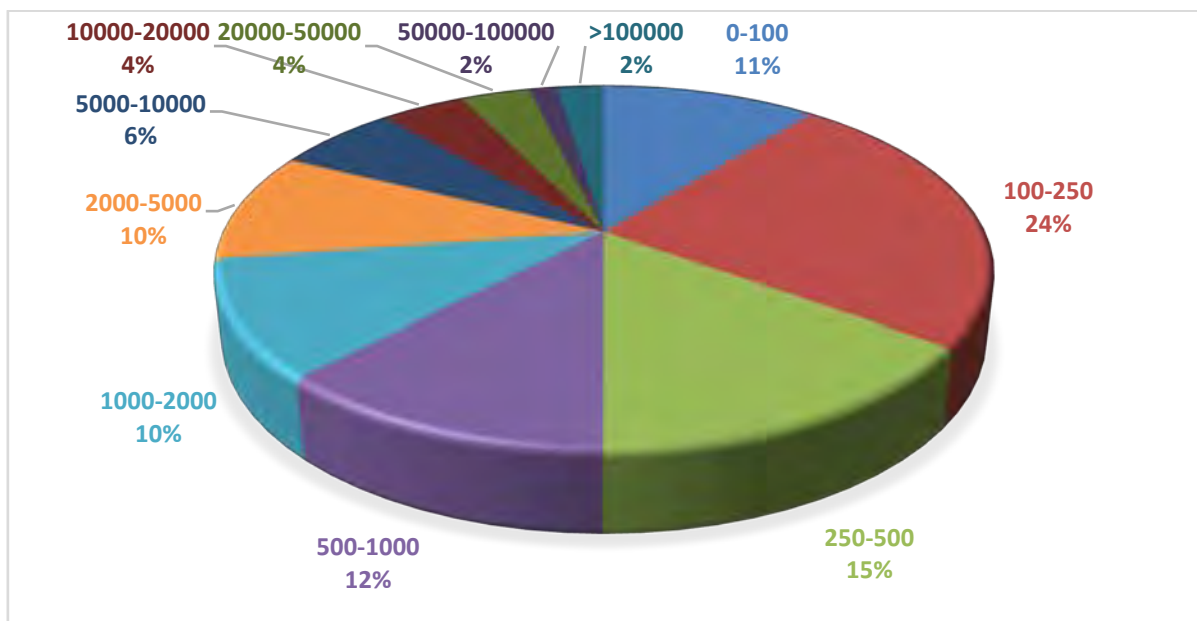


Figure 6: Distribution of e-invoice amounts in TL

4. CONCLUSION

In this paper, we describe the e-invoicing system that is utilized in Turkey, together with comparisons with the system in Europe. We also discuss the software architecture of the leading e-invoice integrator company in Turkey. Usage statistics about the system are also provided. For future work, we plan to employ data mining and big data techniques to achieve more semantic and deep inferences.

REFERENCES

- [1]. Koch B., (2014), E-invoicing/E-billing, Billentis Technical Report.
- [2]. Bayar S., Ulkar G., Dogan U. (2015), Turkiye'deAvrupa'da E-faturaUygulaması, AkademikBilisim, Eskisehir.
- [3]. <http://www.einvoicingbasics.co.uk>

THE CORRELATION BETWEEN CPU CORE TEMPERATURES OF A SERVER UNDER SPECIFIC COOLING SYSTEMS

Serhat Orkun TAN

Karabük University, Karabük Vocational School, Department of Electric and Energy, 78050, Karabük, Turkey.
serhatorkuntan@karabuk.edu.tr

Hüseyin DEMİREL

Karabuk University, Departments of Electrical and Electronics Engineering, 78050, Karabük, Turkey,
hdemirel@karabuk.edu.tr

Abstract

The improvements in the computer world have promoted faster and ergonomic systems in recent years. Although the speed and the ergonomics are desirable for users, they introduce some issues to the computer systems such as the control of increased temperature. Since servers continuously provide services to many clients, they are chiefly affected by this temperature increment. In this study, thermoelectric cooler was applied on the CPU of the server and the effect of this application was investigated on the CPU and the CPU cores in short time intervals in the perspective of cooling. We also made an approach to uncover the correlations between whole CPU temperature and each CPU core temperatures.

Keywords: *Thermoelectric module, Heatsink, CPU, Cooling Systems, Server, Quad Core CPUs.*

1. INTRODUCTION

Computers, indispensable parts of our daily lives, are now providing services at high speed under intensive operation loads through the evolving technology. The reflection of this fast and intensive working character on computer hardware has remarkable and provoking results in terms of temperature increment. Thus, this temperature increase may cause a malfunction or an irreversible error on critical hardware of computers. This situation should be handled most seriously on server systems because of their permanent and intensive working structures. Including memory and control units in its structure and also carrying out the arithmetic and logic operations, CPU is the most critical hardware among the server hardware [1]. In ten years' time it is envisaged that the power dissipation will increase linearly on high performance CPUs of servers [2].

High power density and thermal throttling for cooling limitations can be obtained by adding Cores to CPU chip [3]. Servers have multi-core CPUs and other extra sophisticated hardware in order to manage many clients connected to it. Recently, server overheating has become a familiar problem in comprehensive data centres. Therefore, cooling server hardware should be dealt with severely on behalf of the prevention of undesirable situations that arise due to temperature [4].

Consequently, in order to avoid exposure to high temperatures different cooling systems have been developed for CPUs and other computer components. Among these cooling systems, heatsink is generally used by PC manufacturers. In this system the cooling block absorbs the heat and the fan is mounted on the block to zoom out the heat. Some disadvantages as noise, vibration and high power consumption, have forced the users to choose different cooling systems [5]

One of these preferred systems is heat pipe which has an operating principle based on deploying high amount of heat from the substance while its state change from liquid to gas. Considering its affordable prices, high performance heat pipe systems are mostly preferred. When some disadvantages at high speeds as noise, vibration, etc., are ignored the heat sink model is preferable at high speeds. However, the heat pipe cooling method has better thermal performance than heat sink at specific low fan speeds [6].

Rather complex but high efficient water cooling systems have been designed for cooling the computer hardware. When compared to air systems, water cooling systems have higher heat transfer coefficients so the heat transfer through the water block into a liquid is carried out in a very efficient manner [7]. Size of the heat exchanger channels, flow rate of the liquid, surface area of radiator fins and airflow for heat rejection are four important parameters to identify the water cooling system efficiency [8]. On the other hand, this cooling system could not find wide application area in the high performance computer system due to its large size, high cost and less reliability [9].

Environmentally friendly thermoelectric modules have some advantages such as quiet and vibration-free working, very light and compact size, temperature control ability, longevity lasting, etc., which make it superior to other cooling systems [7]. As they are suitable for working together with coolers, applications with thermoelectric devices are generally used in our daily lives such as fridges for hotel-use, home-bar and so on [10]. Thermoelectric cooler, generally named as Peltier, is formed by the serial connection of P-type and N-type elements. One side of thermoelectric module cools while the other side is hot via the direct current passed through Peltier. This situation is illustrated by the Peltier effect [11]. Considering peltier effect, server hardware can be cooled by the peltier modules. The important point here is the heat on the hot side of the Peltier module which needs to be eliminated in order to prevent damages at hardware. This undesirable heat on the hot side of Peltier element can be disposed by applying heatsink or water cooling on to that side [12].

In order to reveal the performance of the thermoelectric module, an investigation was performed with thermoelectric cooler for cooling the water in a tank. Heatsinks were used to remove the heat that causes extreme temperatures on thermoelectric cooler's hot side. As a result of tests carried out at various time intervals, it was observed that the temperature on water tank decreased in time by the thermoelectric module application. In order to make a comparison to ensure these results, the system was connected to a computer for taking measurements, and it was observed that the results were very close to each other [13]. In another research, the thermoelectric cooler and heat pipe were cooperated for cooling the CPU of a PC as another approach. The temperature of thermoelectrically cooled CPU and the coolant temperature as nanofluids used in heatpipe were examined. The results obtained from this study remarked that the cooperation of two cooling systems was seen to be relatively effective compared to others [14]. In a nother study, embedded thermoelectric coolers were attentively designed and implemented in accordance to decrease CPU core temperatures. Consequently, core temperatures were decreased between 5 °C and 6 °C with the aid of this system [15].

Many studies like mentioned above had proven the advantages of thermoelectric modules, but economic reasons have prevented these systems to diverge. However, from now on, there are expectations about the widespread use of the thermoelectric technology in the future as the area of microelectronics [16].

2. SYSTEM OVERVIEW

The water cooling system was collaborated with a peltier module within a server system which has a quad-core CPU structure as shown in below Fig. 1.

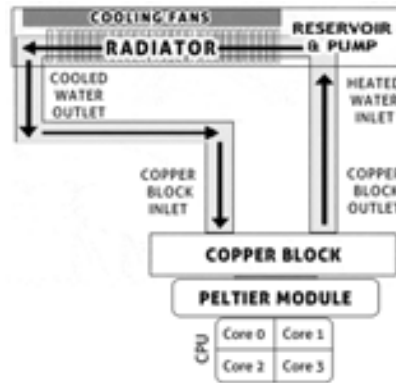


Figure 1. The block diagram of the CPU cooling system

Here, water cooling system was cascaded with peltier module to protect the hardware from overheating on the hot surface of module. TEC1-12706 model type with 90 W power and 4*4*0,5 cm size Peltier module, was used under 12 V DC voltage to cool CPU cores. Here, TEC symbolizes thermoelectric cooler.

The properties of server which has a 64 bit operating system are shown as Table 1.

Table 1. The properties of the server

Server Hardware	Property
Processor	Intel ® Xeon ® Quadcore, CPU E3-1220 V2 @ 3.10 GHZ
Motherboard	Intel C202 Chipset Server
RAM	4 GB DDR3 ECC 1333 MHZ Memory
HDD	500 GB Seagate 7200 Rpm 32 MB Cache NCQ
System type	64 bit operating system

Software benchmarks and performance testing are the best techniques to compare the efficiency of emerging parallel architectures with the built-in support for parallelism at different levels. Two different software programs were used to run the server under varying workloads and to evaluate the temperature data on the CPU. One of these is CPU BurnIn benchmark program which was used to stimulate the operation of the server under %100 workload. This program forced CPU by installing consecutive work procedures in order to acquire the possible highest temperatures [17]. The program runtime was set up to ten minutes time interval to force the CPU to full workload. And the other is, Speed Fan Program, generally used for monitoring voltage, fan speed and temperature values of server hardware. The program's statistics and logging characteristics are available to achieve temperature values desired at each time slot [18]. MS Excel program was also embedded to save the obtained temperature data. PASW Statistics program was also used for linear and multi linear regression analyzes to apply on the four core CPU, and the temperature visualizations were made in Matlab.

3. CONTROL & ANALYZE

In this study, the rationale of the experiments can briefly described as, the temperature values on CPU cores are interpreted by applying two cooling systems: heatsink and thermoelectric cooler. To this end, while CPU BurnIn program is running under full (%100) workload for ten minutes interval, the CPU core temperatures

of the server system, can be monitorized with Speed Fan program. This provides us to make a comparison between core temperature values and also to calculate the correlation coefficients for linear and multi linear regression analyzes method. The experiments were made at room temperature at 25 °C before and after mounting the thermoelectric module on the CPU. First of all we started to take temperature data from CPU which was cooled by commercially available heatsink system.

3.1. Heatsink

The temperature-time graph shown in Fig. 2 for CPU and each CPU cores was obtained while using the heatsink available on server.

The average temperature of the CPU was calculated as 48.52 °C from the data in Fig.2 and the maximum and the minimum values of the temperature for CPU were remarked as 54.5 °C and 35 °C respectively.

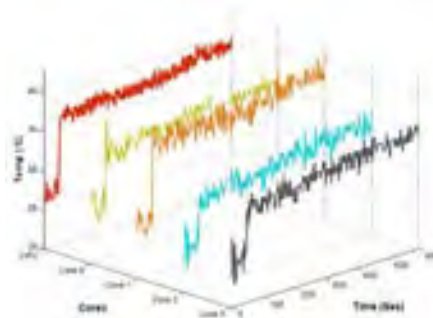


Figure 2. The temperature graph of the heat-sink application

Analysing the core temperatures, it is seen that Core1 has the highest value with 58 °C and Core0 has the lowest value with 53 °C at maximum temperature values. The nearest maximum temperature value to the CPU is Core 2 temperature with 54 °C in this category.

Table 2. Cpu temperatures obtained with heatsink.

	Max. Temp.(°C)	Min. Temp. (°C)	Average Temp. (°C)
Core0	53	35	44.80
Core1	58	38	48.59
Core2	54	33	43.65
Core3	56	34	44.74
CPU	54.5	35	48.52

Considering the minimum temperatures of cores, Core1 has again the highest temperature value with 38 °C. Although the temperatures are very close to each other Core2 has the lowest temperature value with 33 °C and Core0 has the same temperature value with CPU in this category.

The average temperature values show that Core 1 has not only the maximum average temperature but also the nearest average temperature to the CPU temperature.

Linear and multi linear regression analyzes were made to interpret these data more clearly. In case of using one variable, the highest correlation coefficient was obtained with Core0 and the lowest one was obtained with Core1.

$$CPU = 11,859 + 0,818.Core0 \quad r = 0,845 \quad (1)$$

$$CPU = 13,212 + 0,727.Core1 \quad r = 0,807 \quad (2)$$

By using two variables the highest correlation coefficient was obtained with Core0 and Core3. Core1 and Core2 gave the lowest coefficient values.

$$Q = 9,699 + 0,498.Core0 + 0,369.Core3 \quad r = 0,891 \quad (3)$$

$$Q = 11,883 + 0,347.Core1 + 0,454.Core2 \quad r = 0,859 \quad (4)$$

Three variables usage showed that Core0, Core2 and Core3 had maximum and Core1, Core2 and Core3 had minimum coefficient values respectively.

$$Q = 9,379 + 0,396.Core0 + 0,215.Core2 + 0,268.Core3 \quad r = 0,900 \quad (5)$$

$$Q = 10,757 + 0,254.Core1 + 0,263.Core2 + 0,311.Core3 \quad r = 0,883 \quad (6)$$

As it is expected when all variables were used, the correlation coefficient was higher than the other situations.

$$Q = 8,646 + 0,347.Core0 + 0,110.Core1 + 0,175.Core2 + 0,253.Core3 \quad r = 0,902 \quad (7)$$

3.2. Thermoelectric Cooler

First of all the hot and cold surfaces of the TEC1-12706 Peltier module were identified by the 12 V DC supplied from the power supply of the server. Cold surfaces of Peltier modules were mounted on the CPU and then as shown in Fig.1 the copper block of water cooling system was mounted on the hot surfaces of Peltier modules to compensate the heat on that side. The graph below was obtained by using the thermoelectric cooler on CPU of the server.

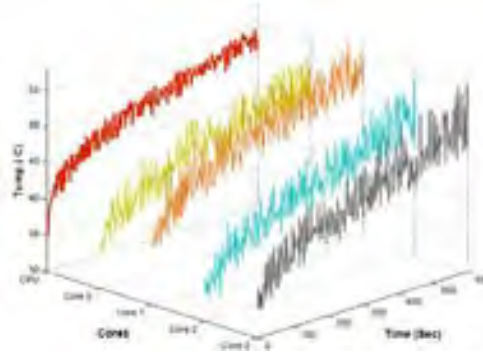


Figure 3. The temperature graph of the thermoelectric cooler application

In case of making a general assessment for the table below, the CPU temperatures are mostly converge to Core1 temperatures at all maximum, minimum and average temperatures categories.

Table 3. Cpu temperatures obtained with thermoelectric cooler

	Max. Temp.(°C)	Min. Temp. (°C)	Average Temp. (°C)
Core0	38	25	34.12
Core1	41	25	35.64
Core2	36	23	32.3
Core3	36	23	33
CPU	40	26	36.42

The equations (8) and (9) indicated that the highest correlation coefficient was obtained with Core1 and the lowest one was obtained with Core2.

$$CPU = 2,989 + 0,913.Core1 \quad r = 0,943 \quad (8)$$

$$CPU = - 0,581 + 1,143.Core2 \quad r = 0,878 \quad (9)$$

Core0 and Core1 had the highest correlation coefficient when using two variables. Core2 and Core3 were given the lowest coefficient values.

$$Q = - 1,388 + 0,408.Core0 + 0,652.Core1 \quad r = 0,953 \quad (10)$$

$$Q = - 1,852 + 0,499.Core2 + 0,670.Core3 \quad r = 0,910 \quad (11)$$

As the formulations below show; when three variables were used, Core0, Core1 and Core3 had maximum and Core0, Core2 and Core3 had minimum coefficient values respectively.

$$Q = - 2,367 + 0,332.Core0 + 0,525.Core1 + 0,249.Core3 \quad r = 0,957 \quad (12)$$

$$Q = - 6,206 + 0,616.Core0 + 0,264.Core2 + 0,396.Core3 \quad r = 0,938 \quad (13)$$

In the case where all the four variables used the highest correlation coefficient was obtained as shown in below equation.

$$Q = - 2,712 + 0,318.Core0 + 0,504.Core1 + 0,104.Core2 + 0,195.Core3 \quad r = 0,958 \quad (14)$$

4. CONCLUSIONS

Alike which of the cooling system is more efficient on CPU cooling, and which core of the CPU has the greatest impact on general CPU temperature can both be revealed as a result of the data obtained from experiments.

The experimentally achieved thermoelectric cooling system's average CPU temperatures are approximately 10 °C and 15 °C lower than the heatsink cooling system. According to these results when compared with thermoelectric cooling system heatsink cooling system is not a sufficient system in the perspective of cooling.

In the meaning of preventing the system from the destructive temperatures, thermoelectric cooler system is a superior system which reduces the maximum temperatures that CPU can reach. However, there are some factors that can convert this advantage to a disadvantage. These factors can be listed as; the formation of ice or moisture around the peltier module, water leakages on the water cooling system, and the increase in power demand. The smooth operation of the system should be provided by removing these factors from the system.

The other phenomenon that was handled in this study is the correlation between core temperatures of the CPU. This case was discussed individually for two different cooling systems.

Firstly, when analyzing the heatsink cooling system, average CPU temperature is closest to the Core 1 temperature. Here the main point to be emphasized is, although the minimum and maximum temperature values of Core 1 are not so close to the average CPU temperature, it directly affects the average CPU temperature due to its working character.

The thermoelectric cooler application implied that the Core 1 temperature values are very similar to the CPU temperature values according to the conclusions drawn from Table 3 and Figure 3. As thermoelectric cooler application decreases the general CPU temperature, it should be noted that, at lower temperatures maximum and minimum temperature values of CPU also varied in parallel with Core1. This means that Core1 explicitly showed its influence over CPU at lower temperatures in contrast to the heatsink cooling system.

As the work intensity is thought to increase the temperature in all electronic circuits, here Core1 is conspicuous as the hardest working and most effective unit among CPU units.

The system can also be developed with various designs by increasing the effectiveness of the thermoelectric module. A control unit can be designed to stop the cycle of the water cooling part, while the level of the temperature on the hot side of the peltier module has not enough capacity to influence the cold side. Another proposal is that to disable the peltier module for power consumption, while CPU is working under inadequate workloads. When the need arises, these control mechanisms should be formed by processing the control signals with any external port of the server and controlling the CPU temperatures by software. These suggestions can be improved to achieve less power consumption and more effective cooling of the system.

REFERENCES

- [1]. Bates, M. P., *An Introduction to Microelectronics PIC Microcontrollers*, 3rd Edition Elsevier Ltd., pp. 3-26, 2011.
 - [2]. Copeland D., "64-bit Server Cooling Requirements", *21st IEEE Semi-Therm Symposium*, 2005.
 - [3]. Elsayaf M. A., Fahmy H. A., and Elshafei, A. L., "CPU Dynamic Thermal Management via Thermal Spare Cores", *25th IEEE Semi-Therm Symposium*, 2009.
 - [4]. Wang, X., Xing, G., and Lin, C. X., "Maximizing the detection probability of overheating server components with sensor placement based on thermal dynamics", *Sustainable Computing: Informatics and Systems*, vol. 3, pp. 148–160, Jan. 2013.
 - [5]. Choi, J., Jeong, M., Yoo, J., Seo, M., "A new CPU cooler design based on an active cooling heatsink combined with heat pipes" *Applied Thermal Engineering*, Volume 44, pp. 50–56, November 2012.
 - [6]. Kim, K. S., Won, M. H., Kim, J. W., Back, B. J., "Heat pipe cooling technology for desktop PC CPU", *Applied Thermal Engineering*, Jan 2003
 - [7]. Davis, M., Weymouth, R. and Clarke, P., "Thermoelectric CPU Cooling using High Efficiency Liquid Flow Heat Exchangers", Hydrocool Pty Ltd, Fremantle, Australia. (2005)
 - [8]. Upadhya, G., Munch M., Zhou, P., Hom, J., Werner, D., and Cooligy, M. M., "Micro-Scale Liquid Cooling System for High Heat Flux Processor Cooling Applications", *22nd IEEE Semi-Therm Symposium*, 2006
 - [9]. Yang, C. Y., Yeh, C. T., Wang, P. K., Liu, W. C. and Kung, E. Y. C., "An In-situ Performance Test of Liquid Cooling for a Server Computer System", *Microsystems Packaging Assembly and Circuits Technology Conference (IMPACT)*, 5th International, pp. 1–4, 2010.
 - [10]. Nishihata, H., Kido, O., Ueno, T., Peltier Cooling System Utilizing Liquid Heat Exchanger Combined with Pump, *IEEE 21st International Conference on Thermoelectronics*, 2002
 - [11]. D. M. Rowe, *Application of thermoelectric cooling*, *CRC Handbook of Thermoelectrics*, CRC Press Inc., Boca Raton, pp. 617–683, (1995).
 - [12]. Tan, S. O., Demirel, H. and Turker, I., "The Efficiency of using a Thermoelectric Module on CPU Systems in the Perspective of Cooling", *AWER Procedia Information Technology and Computer Science*, WCIT-2012, pp. 1069–1073, Antalya, 2012.
 - [13]. Chein, R., Chen, Y. "Performances of thermoelectric cooler integrated with microchannel heat sinks", *International Journal of Refrigeration*, Taiwan, 28: 829-830 (2005).
-

- [14]. N. Putra, Yanuar, F. N. Iskandar, "Application of nanofluids to a heat pipe liquid-block and the thermoelectric cooling of electronic equipment" *Experimental Thermal and Fluid Science*, Volume 35, Issue 7, pp. 1274–1281, October 2011.
- [15]. Alley, R., Soto, M., Kwark, L., Crocco, P. and Koester, D., "Modeling and Validation of On-Die Cooling of Dual-Core CPU using Embedded Thermoelectric Devices", *24th IEEE Semi-Therm Symposium*, 2008.
- [16]. Stockholm, J. G., Current state of peltier cooling, *IEEE 16th International Conference on Thermoelectrics*, Germany, pp 37–46, 1997.
- [17]. *BurnIn Test V 7.1 Users Guide*, Passmark Software Pty Ltd., Sydney, Australia, 2013.
- [18]. (2012) SpeedFan Access Temperature Sensor, "What is SpeedFan", Available: <http://www.almico.com/speedfan.php>

Serhat Orkun TAN, graduated from Gaziantep University, Electrical & Electronics Engineering Department in 2005, got master degree from Karabük University in 2013 and continues his education as a PhD student in Karabuk University. Now, he is a lecturer in Karabuk University Vocational School and is engaged in semiconductor devices and thermoelectric modules.

Hüseyin DEMİREL, graduated from Gazi University Electronic and Computer Education Department in 1997. After that he got MS and PhD from Gazi University in 1999 & 2010 respectively. As an assistant professor in Karabuk University Electrical and Electronic Engineering Department, he is also the assistant director in Institute of Science and Technology in Karabuk University, working in digital electronics and thermoelectric modules.

APPLICATION PROPERTIES OF GROUNDNUT HULL/EPOXY COMPOSITES

Gülcihan GÜZEL

Selçuk University, Department of Chemical Engineering, 42035, Selçuklu/Konya, Turkey.

Hüseyin DEVECİ

Selçuk University, Department of Chemical Engineering, 42035, Selçuklu/Konya, Turkey.

hdeveci@selcuk.edu.tr

Abstract

Polymeric composites are developed with polymeric matrix/convenient filler; much better interactions between matrix and filler. And also biodegradability of natural fibers is significant factor in polymeric materials. Polymeric composites have many using areas such as buildings, automotive, aerospace, and packing industries. Some parameters as microstructure and dimensions have an effect on polymer composite properties. Epoxy resins (ER) are one of the most important classes of thermoset polymers that harden with heat effect. They are used in high-performance composites on a large scale due to their great mechanical, thermal and chemical properties such as good resistance to chemicals, high tensile and compressive strength, and high heat distortion temperature. In this study, groundnut hull/epoxy resin composites were prepared. Groundnut hull as filler, epoxy resin (NPEL 128), polyethylene glycol (PEG), and 25 wt % hardener based on aliphatic amines for epoxy resins (EPAMINE PC 17) were used. Commercially available epoxy resin was a bisphenol A-type resin modified with aromatic diluents. Hardness, adhesion, corrosion, water sorption, freezing tests and thermal analysis were carried out to determine composite properties. According to experimental results, the hardness of the composite materials reduced with the addition of groundnut hull and PEG. The water sorption of the composites increased when the amount of filler rose. And also the highest residue at 600 °C was obtained as 12,66% by the neat epoxy resin.

Keywords: epoxy, groundnut hull, composite, thermal properties

1. INTRODUCTION

Recently, polymers have become remarkable materials owing to better modulus and flexibility, high specific strength, good resistance to corrosion and low density [1, 2]. Polymer composite/nanocomposites have received great attention due to the high mechanical properties to weight ratio, thermal stability and chemical improvements when compared with neat polymers [3, 4, 5]. They are commonly used in many industrial areas such as transportation, construction, electronics [6], aerospace [7] and weight sensitive applications [2]. Epoxy resins are one of the most substantial thermoset polymers [8, 9]. Utility of epoxy resins has shown great increase [10] with several benefits including absence of byproducts through curing, lower shrinkage [11], usage of different temperature range [4], environmental stability [12]. Moreover epoxy resins exhibit lower specific weight than metals, good corrosion resistance [13] and high adhesion properties. Epoxy resins are usually focused to use as adhesives, coatings and matrix for composite production [12, 14]. With various hardeners or curing agents based on aliphatic amines, aromatic amines and anhydrides, epoxy resins are crosslinked at room temperature or at high temperature interval. Curing reactions improve not only mechanical properties but also thermal properties like decomposition temperature [4, 12]. In spite of a lot of advantages, the main drawback of epoxy resins is to be brittle polymers that brings about crack formation and restricts their usage in many applications [11]. Addition of natural or synthetic materials/fibers and metals as reinforcement to epoxy resins enhance their mechanical, thermal, physicochemical, barrier properties and also provides cost reduction [3, 15].

There are many studies interested in composites with bio-based fillers [17, 18] especially organic waste materials. Wheat straw and husk, sugarcane bagasse, coconut shell, cotton stalk [19], walnut shell [17], barley husk [20] as filler have been widely used for the preparation of various composites because waste materials are abundant and cheap. Furthermore they are environmental friendly materials and using biological waste provides to avoid of environmental pollution [7, 21, 22]. Groundnut hull is one of the agricultural organic wastes which have not been widely used as filler up to now [22]. With the addition of groundnut hull to different polymers, composites that have low density, improved mechanical, thermal properties can be obtained [19].

2. EXPERIMENTAL

2.1. Materials

In this work NPEL 128, bisphenol A-type resin modified with aromatic diluents, was used as a matrix system. NPEL 128 has 184-190 g/eq epoxy equivalent weight and 12000-15000 cps at 25 °C viscosity. Filler utilized in preparing composites was groundnut hull that is organic waste material. EPAMINE PC17 hardener based on aliphatic amines was used in curing process. And also PEG (polyethylene glycol) was utilized to bring flexibility to composite materials.

2.2. Methods

Groundnut hull in different proportions (0, 5, 10, 15, 20 wt %) was added to NPEL 128 and the mixtures were stirred mechanically for an hour. After stirring, they were mixed in an ultrasonication bath to obtain well-dispersed suspension at room temperature for half an hour. EPAMINE PC17 hardener was added to the mixtures at a ratio of 25 % by weight. Later, the mixtures were poured into stainless-steel moulds according to ASTM D 638 standard and cured in an oven for 4 h at 40 °C followed by postcuring for 4 h at 80 °C. With the remaining mixture from each specimen, aluminum metals were coated and dried at between 40-80 °C. The same process was carried out by adding 5 % PEG to obtain other composites.

2.3. Characterization

2.3.1. Mechanical properties

For determining the hardness of composites, Shore Durometer TH 210 tester is used. To obtain the most accurate values of composite hardness, measurements were taken at different points on each specimen and arithmetic values of hardness were calculated.

2.3.2. Thermal properties

Thermogravimetric analysis was carried out by Lab. METTLER STAR SW thermal analyzer under a flowing nitrogen atmosphere. The groundnut hull/epoxy composites were equilibrated at certain temperature and then heated at a rate of 10 °C/min from 25 to 650 °C.

2.3.3. Adhesion properties

“Lattice notch method” [23] was used to investigate adhesion properties of the composites. Firstly, aluminum surface was blasted and cleaned. Later, groundnut hull/epoxy mixture was applied to metal surface as a thin layer. All specimens were dried for 8 h at between 40-80 °C. After curing process, the layers were divided into squares which have 1 mm x 1mm dimension with a razor blade. These squares were pulled suddenly by a kind of tape. Some part of the squares was removed from the surface whereas the other squares were on the metal surface. The % adhesion was calculated with this equation:

$$\text{Adhesion \%} = \frac{(a - b)}{a} \times 100$$

where a is the total square number and b is the square removed from the surface number.

2.3.4. Corrosion properties

Different solutions that are 3% NaCl, 10% H₂SO₄, 10% NaOH and water were chosen to determine corrosion properties of the groundnut hull/epoxy composites [24]. Small part of the composites were immersed in the these solutions at room temperature for two weeks and then corrosion resistance of the composites was interpreted by observing any defects like color change, swelling.

2.3.5. Water sorption properties

Epoxy resins are vulnerable thermoset materials to water sorption. Even if small amount of water, it affects many properties of epoxy composites such as chemical decomposition, swelling, weakening mechanical properties and decreasing glass transition temperature (T_g) [25]. In order to obtain water sorption properties of the epoxy composites, small part of the specimens were plunged into distilled water at room temperature for 15 days. Specimens were removed from water once in two days. After specimens were wiped up, they were weighted with analytical balance [26]. The % water sorption values were calculated by following equation:

$$\text{Water sorption, \%} = \frac{(m_1 - m_2)}{m_2} \times 100$$

where m₁ is the weight of the specimen at the time of measurement and m₂ is the weight of the specimen at first.

2.3.6. Cold resisting properties

Not only is heat resistance of the epoxy composites important factor but also cold resisting properties are remarkable point in their applications. According to TSE K 86, cold resisting properties of the composites were specified. The specimens were kept in a fridge for 24 h at -25 °C. Whether such changes as cracks, fractions occurred on the specimens or not were observed by naked eye.

3. RESULTS AND DISCUSSION

3.1. Mechanical properties

Fillers added to polymer matrix can have an effect on cross-linkage so composite hardness can be enhanced or reduced depend on filler structure. The hardness values of all the epoxy composites were shown in Table 1. It can be seen that the hardness of the composites decreased with the increase in groundnut hull content from 0 wt% to 20 wt% even if just a drop. The highest hardness was obtained at neat epoxy resin as 86 Shore D. When the groundnut hull was compared with epoxy resin, the groundnut hull has ductile structure thus composite hardness decreased with organic filler loading as expected.

Table 1. Hardness values of the composites

Composite	Filler, %	Hardness, Shore D	Hardness with 5% PEG
ER1F1	0	86,00	83,33
ER1F2	5	84,33	83,00

ER1F3	10	83,00	81,83
ER1F4	15	80,67	78,17
ER1F5	20	78,00	74,33

Moreover composite hardness showed a decline with the addition of 5% P EG because PEG possesses plasticizing property. Interfacial bond strength between matrix and filler may be weakened by PEG.

3.2. Thermal properties

TGA analysis was applied to composite materials to investigate thermal degradation of the epoxy composites. The TGA results were indicated in Table 2. Initial decomposition temperature, T_5 , T_{10} , T_{50} which are respectively %5, %10, %50 degradation occurs were shown in this table. And also residue that remains at 600 °C namely char was determined from TGA thermograms.

Table 2. TGA analysis data of the composites

Composite	Filler, %	IDT °C	T_5 °C	T_{10} °C	T_{50} °C	600 °C, % residue
ER1F1	0	121,5	264,17	339,17	379,67	12,66
ER1F2	5	103,5	251,5	330,67	380,17	11,87
ER1F3	10	97,83	234,5	326,17	379,17	11,27
ER1F5	20	99,33	222	289,17	403,33	10,35

The initial decomposition temperature, T_5 and T_{10} were decreased with the addition of groundnut hull to epoxy resin. There was not significant change at mid-point temperatures except composite which has 20% organic waste loading. Furthermore the residue value was changed slightly compared to epoxy resin. The char composition is substantial factor which restricts combustible gases formation. According to results, any remarkable increment was not observed because the groundnut hull has lower thermal stability than the epoxy resin.

3.3. Adhesion properties

Adhesion properties of the epoxy composites are taken into consideration in a lot of industry applications especially metal surface coating. The layer that is composite mixture applied to metal surface such as aluminum, steel can enhance some properties. The layer can not only retard flammability but increase resistance to corrosion as well. As it can be seen from Table 3, % adhesion values were given depend on the filler material and PEG addition. The best result was obtained by neat epoxy resin and the others had % adhesion values above 90%. The small difference between results may arise from nonhomogeneous layer and partial agglomeration of groundnut hull on the aluminum metal surface. While the PEG was added to groundnut hull/epoxy composites, there were hardly changes in the adhesion properties.

Table 3. Adhesion properties data of the composites

Composite	Filler, %	Adhesion, %	Adhesion with 5% PEG, %
ER1F1	0	100	100
ER1F2	5	96	95
ER1F3	10	93	94
ER1F4	15	96	95
ER1F5	20	92	93

3.4. Corrosion properties

Corrosion resistance of epoxy composites to saline, acidic, alkaline and water environments is important parameter in the usage area of the composites. The corrosion resistance can be raised by supplement of filler materials. To determine corrosion tolerance of the composite specimens, small parts of them were exposed to 3% NaCl, 10% H₂SO₄, 10% NaOH and water solutions. It was observed that whether there was any difference or in appearance of the composites or color change of solutions for two weeks. The interaction between the composite parts and the solutions did not occur; therefore there was not any change on the composite parts and the color of the solutions. The corrosion resistance properties were indicated in Table 4.

The groundnut hull added to epoxy resin at various content did not affect the corrosion resistance on a large scale. Moreover the addition of the PEG did not alter the resistance of the composites to corrosion.

Table 4. Corrosion resistance of the composites

Composite	Filler, %	PEG, %	NaCl, 3%	NaOH, 10%	H ₂ SO ₄ , 10%	Water
ER1F1	0	0	++	++	++	++
ER1F2	5	0	++	++	++	++
ER1F3	10	0	++	++	++	++
ER1F4	15	0	++	++	++	++
ER1F5	20	0	++	++	++	++
ER1PF1	0	5	++	++	++	++
ER1PF2	5	5	++	++	++	++
ER1PF3	10	5	++	++	++	++
ER1PF4	15	5	++	++	++	++
ER1PF5	20	5	++	++	++	++

Positive, +

3.5. Water sorption properties

Water sorption plays a substantial role in the evaluation of the composite material properties. Besides, the chemical composition is the other factor that affected water sorption. Many natural fillers are tend to absorb water because of hydrophilic hydroxyl groups [17]. The absorbed excessive water may weaken interfacial bonding, so increase delamination. The water uptake as a function of time was indicated in Figure 1. The amount of water absorbed increased with the rise in groundnut hull content at room temperature. In other words, the epoxy composite filled with 0% had lower water absorption than the others. The water sorption values varied between %0,19 and %0,73 after one day. After 8 days, water sorption almost remained stable for all composites. The PEG influence was presented in Figure 2 for 15 d ays. The water sorption of groundnut hull based epoxy composites was raised by the addition of the PEG similarly the composites without the PEG. The amount of absorbed water increased from %0,71 to %3,87. The epoxy composites with PEG exhibited more water sorption than the composites without the PEG. This can be due to –OH groups in the PEG, because –OH groups interact with hydrogen in the water.

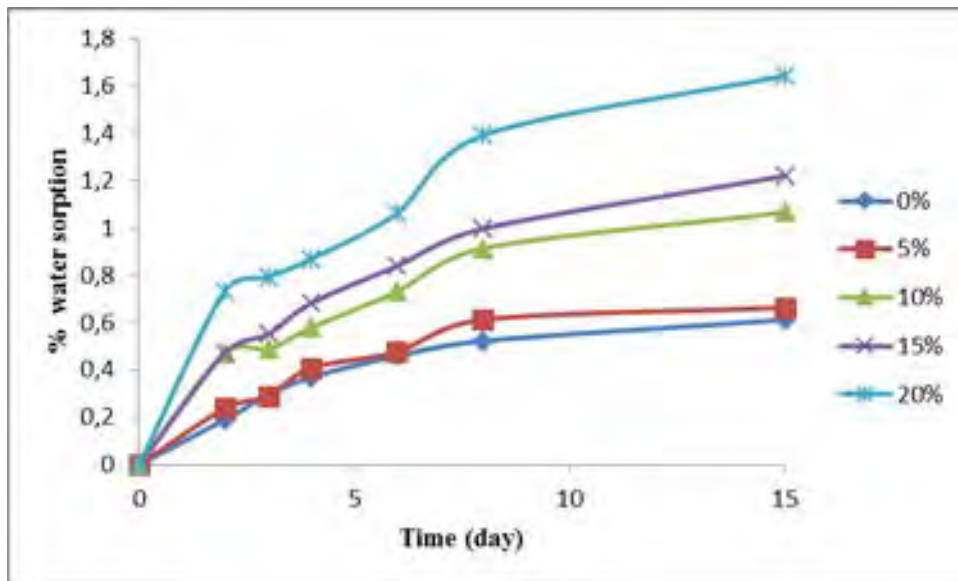


Figure 1. % water sorption of the composites without PEG

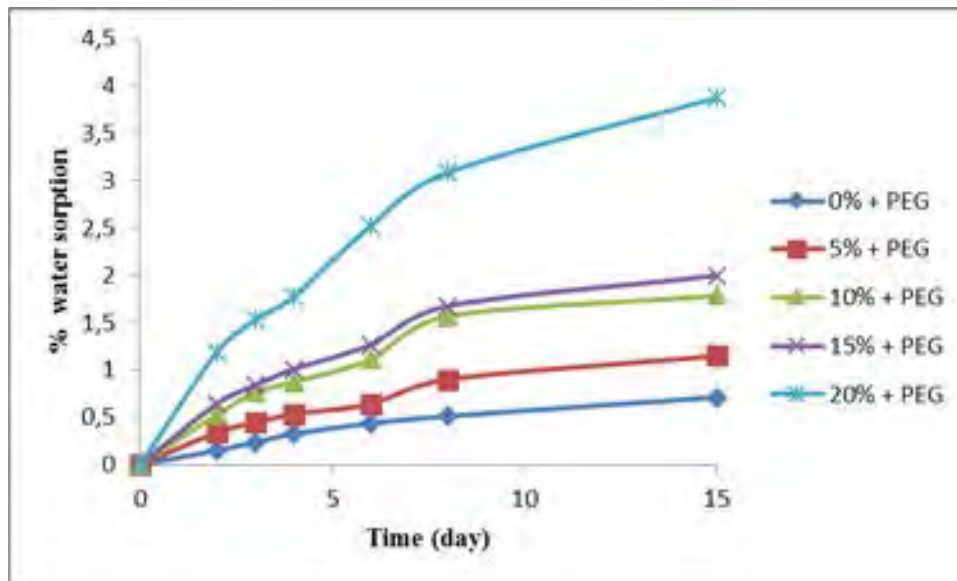


Figure 2. % water sorption of the composites with PEG

3.6. Cold resisting properties

The polymeric composite materials are used in environments that require both temperature and cold resistance. Hence resistance of the composites to low temperatures has an importance in many applications. The cold resisting properties of the epoxy composites were specified by TSE K 86 in this study. The specimens were kept in a fridge for 24 h at $-25\text{ }^{\circ}\text{C}$ and then physical appearance of the specimens was observed by naked eye. There were not any defects for instance cracks and fractions.

4. CONCLUSIONS

In this experimental study, main object was to prepare groundnut hull/epoxy composite materials and investigate some properties such as mechanical, thermal, corrosion resistance, water sorption, adhesion and cold resisting. According to the results obtained, the hardness values decreased partially due to chemical structure of the natural filler and PEG. The initial decomposition temperature and the temperatures that occurs %5, %10 degradation reduced with increasing the filler content. However the mid-point temperature and residue at $600\text{ }^{\circ}\text{C}$ showed similar values in all composites. The adhesion properties of the epoxy composites changed negligibly with the addition of the filler as compared to neat epoxy resin. Moreover these composites were found to have favorable corrosion resistance to 3% NaCl, 10% H_2SO_4 , 10% NaOH and water solutions. The water sorption of the composites without PEG merely rose when compared to the composites with PEG. While the former varied from %0,19 to 0,73, the latter changed between %0,71 and %3,87. In addition to what is mentioned above the epoxy composites have a capacity for cold resistance. The most important point of this study is that agricultural waste groundnut hull can be utilized to prepare epoxy composites and utilization of groundnut hull provides to avoid from environmental pollution. And also using this filler, the cost can be reduced successfully in the composite preparation.

REFERENCES

1. Shivamurthy, B., Murthy, K., Joseph, P. C., Rishi, K., Bhat, K. U. and Anandhan, S., Mechanical properties and sliding wear behavior of jatropha seed cake waste/epoxy composites, *J Mater Cycles Waste Manag.* 17:144-156, 2014.
2. Rout, A. K. and Satapathy, A., Study on mechanical and tribo-performance of rice-husk filled glass-epoxy hybrid composites, *Materials and Design*, 41, 131-141, 2012.
3. Shokrieh, M. M., Kefayati, A., R. and Chitsazzadeh, M., Fabrication and mechanical properties of clay/epoxy nanocomposite and its polymer concrete, *Materials and Design*, 40, 443-452, 2012.
4. Azeez, A. A., Rhee, K. Y., Park, S. J. and Hui D., Epoxy clay nanocomposite-processing, properties and applications: A review, *Composites: Part B*, 2012.

5. Yilmazer U. and Ozden, G., Polystyrene-Organoclay Nanocomposites Prepared by Melt Intercalation, In Situ, and Masterbatch Methods, *Polymer Composites*, 2006.
 6. Meneghetti, P. and Qutubuddin, S., Synthesis, thermal properties and applications of polymer-clay nanocomposites, *Thermochimica Acta*, 442, 74-77, 2006.
 7. Khalil, H.P.S., A., Fizree, H.M., Bhat, A.H., Jawaid, M. and Abdullah C.K., Development and characterization of epoxy nanocomposites based on nano-structured oil palm ash, *Composites: Part B*, 53, 324-333, 2013.
 8. Hepworth, D. G., Bruce, D. M., Vincent, J. F. V. and Jeronimidis, G., The manufacture and mechanical testing of thermosetting natural fibre composites, *Journal Of Materials Science*, 35, 293-298, 2000.
 9. Fard, M., Y., Raji, B. and Chattopadhyay, A., The ratio of flexural strength to uniaxial tensile strength in bulk epoxy resin polymeric materials, *Polymer Testing*, 40, 156-162, 2014.
 10. Tripathi, M., Kumar, D., Rajagopal, C. and Roy, P. K., Curing kinetics of self-healing epoxy thermosets, *J Therm Anal Calorim*, 119:547-555, 2015.
 11. Işık, I., Yilmazer, U. and Bayram, G., Impact modified epoxy/montmorillonite nanocomposites: synthesis and characterization, *Polymer*, 44, 6371-6377, 2003.
 12. Li, X., Kang, H., Shen, J., Zhang, L., Nishi, T. and Ito, K., Miscibility, Intramolecular Specific Interactions and Mechanical Properties of a DGEBA based Epoxy Resin Toughened with a Sliding Graft Copolymer, *Chinese Journal of Polymer Science*, Vol. 33, No. 3, 433-443, 2015.
 13. Zotti, A., Borriello, A., Martone, A., Antonucci, V., Giordano, M. and Zarrelli, M., Effect of sepiolite filler on mechanical behavior of a bisphenol A-based epoxy system, *Composite: Part B*, 67, 400-409, 2014.
 14. Shih, Y., Mechanical and thermal properties of waste water bamboo husk fiber reinforced epoxy composites, *Materials Science and Engineering A*, 445-446, 289-295, 2007.
 15. Mavani, S. I., Mehta, N. M. and Parsania, P. H., Synthesis, Fabrication, Mechanical, Electrical, and Moisture Absorption Study of Epoxy Polyurethane-Jute and Epoxy Polyurethane-Jute-Rice/Wheat Husk Composites, *Journal of Applied Polymer Science*, Vol. 106, 1228-1233, 2007.
 16. Cai, G., Feng, J., Zhu, J. and Wilkie C. A., Polystyrene-and poly (methyl methacrylate)-organoclay nanocomposites using a one-chain benzimidazolium surfactant, *Polymer Degradation and Stability*, 99, 204-210, 2014.
 17. Datta, J. and Wloch, M., Selected biotrends in development of epoxy resins and their composites, *Polym. Bull.*, 71:3035-3049, 2014.
 18. Raju, G. U. and Kumarappa, S., Experimental study on mechanical properties of groundnut shell particle-reinforced epoxy composites, *Journal of Reinforced Plastics and Composites*, 30, 1029-1037, 2012.
 19. Bledzki, A. K., Mamun, A. A. and Volk, J., Barley husk and coconut shell reinforced polypropylene composites: The effect of fibre physical, chemical and surface properties, *Composites Science and Technology*, 70, 840-846, 2010.
 20. Mishra, S. C., Nayak, N. B. and Satapathy, A., Investigation on Bio-waste Reinforced Epoxy Composites, *Journal of Reinforced Plastics and Composites*, Vol. 29, No.19, 3016-3020, 2010.
 21. Oksman, K., Wallstrom, L., Berglund, L. A. and Filho, R. D. T., Morphology and Mechanical Properties of Unidirectional Sisal-Epoxy Composites, *Journal of Applied Polymer Science*, Vol. 84, 2358-2365, 2002.
 22. Ishidi, E. Y., Adamu, I.K., Kolawale, E. G., Sunmonu, K. O. and Yakubu, M. K., Flammability and Thermal Characteristics of Alkaline Aqueous Solution Treated Groundnut Shell-HDPE Composites, *Journal of Thermoplastic Composite Materials*, Vol. 24, 875-888, 2011.
 23. Deveci, H., Ahmetli, G., Ersoz, M. and Kurbanli, R., Modified polystyrenes: Corrosion, physicomechanical and thermal properties evaluation, *Progress in Organic Coatings*, 73, 1-7, 2012.
 24. Qaiser, S., Saleemi, A. R. and Umar, M., Biosorption of lead(II) and chromium(VI) on groundnut hull: Equilibrium, kinetics and thermodynamics study, *Electronic Journal of Biotechnology* ISSN:0717-3458, Vol. 12, No. 4, 1-17, 2009.
 25. Olmos, D., Lopez-Moron, R. and Gonzalez-Benito, J., The nature of the glass fibre surface and its effect in the water absorption of glass fibre/epoxy composites. The use of fluorescence to obtain information at the interface, *Composite Science and Technology*, 66, 2758-2768.
 26. Abdelkader, A. F. and White, J. R., Water Absorption in Epoxy Resins: The Effects of the Crosslinking Agent and Curing Temperature, *Journal of Applied Polymer Science*, Vol. 98, 2544-2549.
-

PLASMA PASTE BORIDING OF 21NICRMO2 STEEL USING BORAX PASTE FOR MULTIPLE GAS MIXTURES

Şükrü ÜLKER

Afyon Kocatepe University, Department of Mechanical Engineering, 03200, Afyonkarahisar, Turkey.

Şükrü TAKTAK

Afyon Kocatepe University, Department of Metallurgy and Material Engineering, 03200, Afyonkarahisar, Turkey.

taktak@aku.edu.tr

İbrahim GÜNEŞ

Afyon Kocatepe University, Department of Metallurgy and Material Engineering, 03200, Afyonkarahisar, Turkey.

Abstract

Plasma paste boriding is a thermo-chemical diffusion process in which boron is diffused into the steel in plasma environment at high temperatures. The paste used having environmentally friendly boron raw materials and gases which have inert characteristics make this process more advantageous when compared with plasma boriding.

In this study, 21NiCrMo2 steel was borided using borax paste in plasma environment at temperatures of 700 and 800oC for duration of 2 and 5 h and for gas mixtures of 60%N2+20%H2+20%Ar and 20%N2+60%H2+20%Ar. The properties of the boride layer were evaluated by optical microscopy, X-ray diffraction (CuK α radiation, $\lambda=1,5418 \text{ \AA}$), the micro-Vickers hardness tester (for 50 g load). The results revealed that X-ray diffraction analysis of boride layers on the surface of the boronized steel exhibited FeB and Fe2B phases and intensity of FeB and Fe2B phases changed depending on the plasma gas mixtures. The thickness and hardness of boride layer increased with the increase in temperature and time of plasma paste boriding process.

Keywords:

1. INTRODUCTION

Boriding is a process in which the surfaces of metals and alloys are saturated with boron. This process is performed to increase the hardness and the wear and corrosion resistances of these materials for engineering components for industrial applications that require such properties. The thickness of the formed boride layer affects the mechanical and chemical properties of borided materials, and it depends on the boriding temperature, the treatment time and the boron potential that surrounds the surface sample [1],[2],[3],[4]. Therefore, it is important to select the optimum process parameters to obtain boride layers with adequate thicknesses for their intended practical applications. Boriding can be carried out in solid, liquid, or gaseous medium [5]. The process is normally carried out by heating the substrate materials at a temperature between 700 to 1100 °C for a specific time (1-12 hours) and in the appropriate chemical environment. At present, several kinds of boriding methods are available for the production of hard boride layers such as, pack boriding, paste boriding salt-bath boriding (electroless and electrolytic including ultrafast boriding), fluidized-bed boriding, gas-phase and plasma boriding, plasma paste boriding and superplastic boriding [6],[7],[8], [9], [10], [11]. In order to decrease the boriding temperature and time, ion implantation boriding [12], and plasma-assisted boriding [13] have been studied over the past 40 years [14],[15]. Although the plasma boriding process has a superior advantage when compared to conventional boriding processes, the gases (B_2H_6 , BCl_3) used in plasma boriding, which have expensive, poisonous and explosive characteristics, constitute its disadvantages. The disadvantages in the plasma boriding process can be eliminated through the plasma paste boriding surface process. The fact that the paste used has environmentally friendly boron raw materials and that the gases used are generally hydrogen, argon and nitrogen, which have inert characteristics, make this process advantageous [16]. Plasma paste boriding caused lower activation energy for the formation of boride layer than that for the conventional boriding process. It is possible that the formation of boride layer at lower temperatures in plasma is more effective than the conventional processes. Boriding temperatures and times decrease for plasma system and boride layers form at lower temperatures [17].

Argon and Hydrogen are important gases for plasma paste boriding process. Ar is used to change the plasma parameters such as electron temperature and electron density which influence the production of active species by inelastic collisions, plasma reactions and plasma surface interactions. During plasma paste boronizing, borax reacts with active hydrogen (H^+) in glow discharge. Atomic boron was produced through the decomposition of the boron hydride (B_xH_y) from the paste, and this atomic boron became the active boron, B^+ within the molten borax or in the glow discharge. Finally, this active boron, B^+ , diffused and reacted with Fe to form the boride layer. Nitrogen is diatomic gas like hydrogen (two atoms to every molecule). Nitrogen containing plasmas have higher energy contents for a given temperature than the atomic gases of argon and helium because of the energy associated with dissociation of molecules. In addition, nitrogen tends to form compounds with iron and can change the structure of boride layer [11], [23],[24],[25].

The characterization of borided steels by using various boriding processes has been evaluated by a number of investigators [18],[19],[20],[21],[22]. However, the literature on characterization of plasma paste borided steels in three gas plasma environment is scarce. In this study, low alloyed 21NiCrMo2 steel was plasma paste borided for the gas mixtures of Ar, H_2 and N_2 . The phase structure and microhardness of the boride layers were investigated using optical microscopy, X-ray diffraction (XRD), microhardness tester.

2. EXPERIMENTAL

2.1. Materials

21NiCrMo2 steel which contained 0.19% C, 0.4% Cr, 0.7% Mn and 0.4% Ni was used for the investigation. The samples had a cylindrical shape and were 18 mm in diameter and 6 mm in length.

2.2. Methods

The samples were ground using up to 1000 mesh SiC paper and polished with 0.1 alumina suspension to obtain a smooth surface. Borax powder was accumulated on the steel that was immersed in a powder-alcohol suspension. A plasma paste boronizing treatment was performed in a dc plasma system, which is shown in Fig.1. The prepared samples were placed in the vacuum container and the container pressure was set to 2×10^{-2} mbar of vacuum. The samples were plasma paste boronized at 700 and 800 °C for 2 and 5 h in a gas mixture of 60% N_2 +20% H_2 +20%Ar (6N) and 20% N_2 +60% H_2 +20%Ar (6H) under a constant pressure of 5 mbar. The temperature of the samples was measured by using a chromel-alumel thermocouple that was placed at the bottom of the treated samples.

Cross-sections of plasma paste boronized steels were prepared metallographically to observe morphological details using the BX60 Olympus microscope. The X-ray diffractograms were obtained by using a copper tube source as dictated by the conventional bragg-brentano (θ - 2θ) technique having symmetric geometry with monochromatized radiation ($\text{Cu K}\alpha$, $\lambda=0.15418$ nm). The thickness of the layers formed on the steels was measured by an optical micrometer attached to the optical microscope. The hardness of the boride layers was measured on the cross-sections using the Micro-Vickers indenter (Shimadzu HMV-2) with 50 g loads.

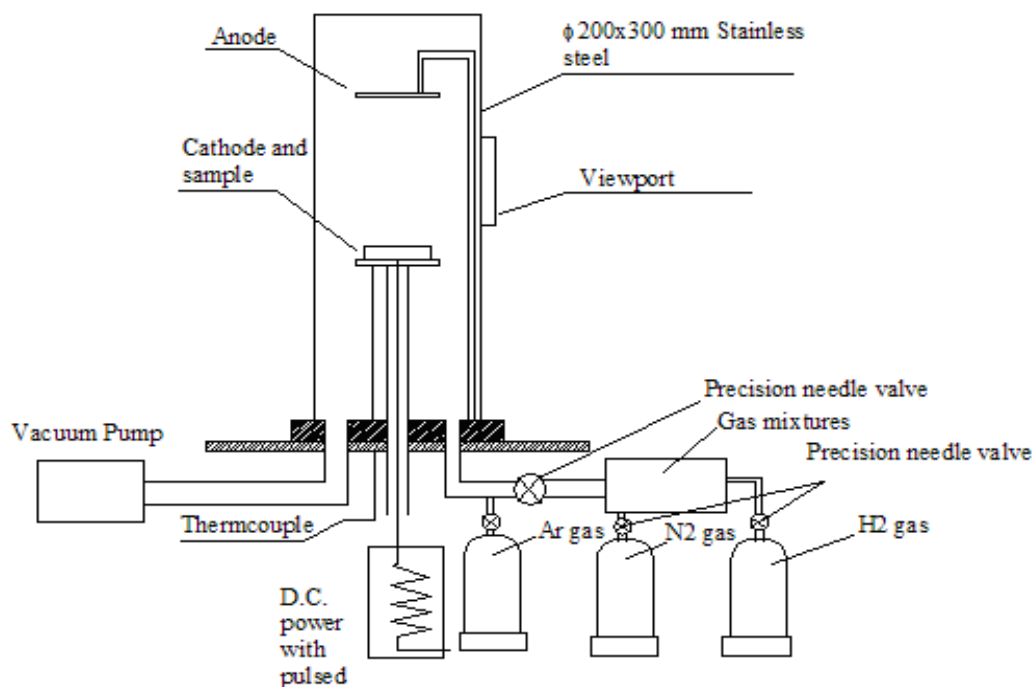


Figure 1. Schematic illustration of plasma paste boriding system.

3. Results and Discussions

3.1. Surface Characterization

The cross section optical micrographs of the plasma paste borided 21NiCrMo2 steel at temperature of 800 °C for 5 h in a gas mixture of 60%N₂+20%H₂+20%Ar and 20%N₂+60%H₂+20%Ar are indicated in Fig. 2. The saw-tooth morphology was developed on the cross-sections of the borided steel in relation to the chemical composition of the substrate composed of pearlite and netlike ferrite. This columnar shape of the boride layers was observed in borided iron and carbon steels with low carbon contents [26],[27]. This experimental fact is due to an anisotropic diffusion of boron atoms where the boride needles grow rapidly along the [001] direction that minimizes the growth stress [28],[29].

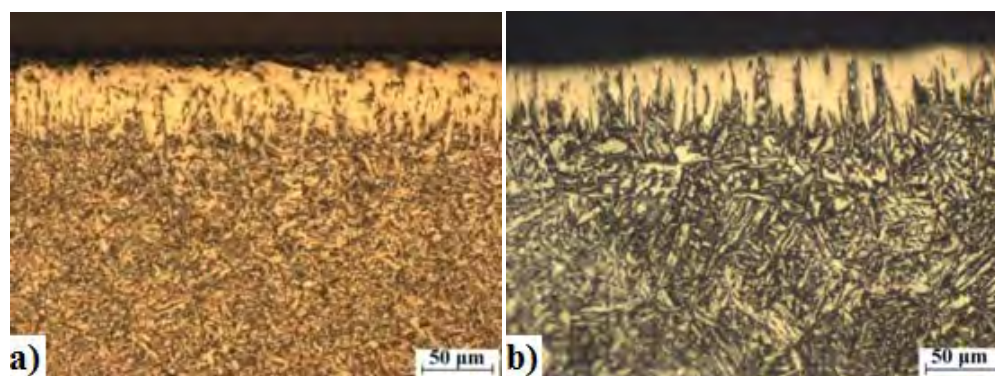


Figure 2. Cross section optical micrographs of the plasma paste borided steel at 800 °C for 5 h in a gas mixture of a) 60%N₂+20%H₂+20%Ar and b) 20%N₂+60%H₂+20%Ar.

Table 1 shows boride layer thickness of plasma paste borided samples. As can be seen in Table 1, thickness of boride layers increased with increasing boriding temperature and time due to the high mobility of boron in the borided layer at high temperatures. This finding is in agreement with literature [28],[29],[30]. Boride layer thickness reached a value of 48 μm for 700 °C, while it was only 50 μm for 800 °C and 5h in the gas mixture of 20%N₂+60%H₂+20%Ar. For 60%N₂+20%H₂+20%Ar gas mixture, thickness of boride layer was found 50 μm at 700 °C, whereas it was 60 μm at 800 °C and 5h. This result showed that boride layer thickness increased with the increase in nitrogen amount of gas mixtures.

Table 1. Boride layer thickness of plasma paste borided steel in gas mixture of 60%N₂+20%H₂+20%Ar and 20%N₂+60%H₂+20%Ar

Plasma Gas Mixture	Plasma Temperature (°C) and holding time (h)			
	700		800	
	2	5	2	5
	Boride layer thicknesses (μm)			
20%N ₂ +60%H ₂ +20%Ar	16	48	30	50
60%N ₂ +20%H ₂ +20%Ar	20	50	43	60

Figure 3 indicates the XRD patterns of plasma paste borided steel for two different gas mixtures. The diffracted intensities of the boride phases depended on the boriding temperature, time and plasma gas mixture. As shown in Figure 3, boride layer consisted of FeB and Fe₂B phases. FeB contribution (2θ≈38°) to the pattern was increased in the gas mixture of 60%N₂+20%H₂+20%Ar at 800 °C. The intensity of Fe₂B phase also decreased in the same gas mixture. This is due to the fact that diffusion of boron atom decreases inwards to the steel as a result of diffusion of nitrogen into the steel.

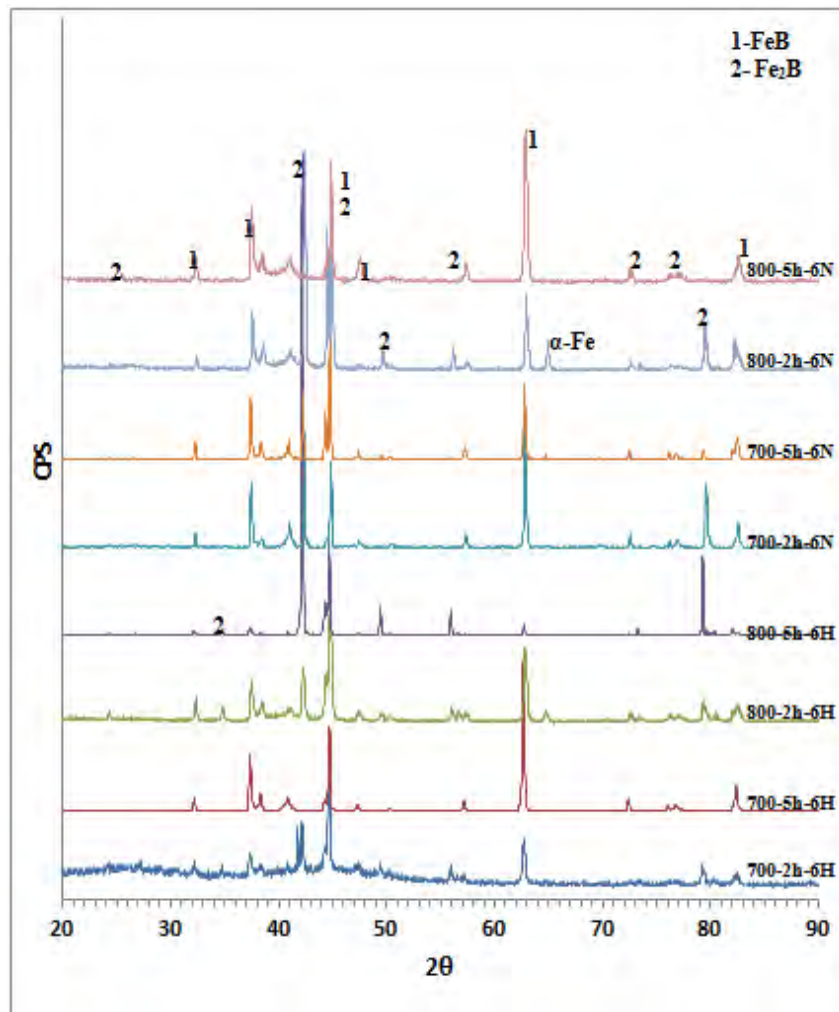


Figure 3. XRD patterns of the surfaces of the plasma paste borided steel at increasing temperatures and times for 20%N₂+60%H₂+20%Ar (6H) and 60%N₂+20%H₂+20%Ar (6N).

3.2. Microhardness Measurement

Microhardness measurements were made on the cross-sections of the borided samples from the surface to the interior as a function of depth. Figure 4 shows the microhardness profiles obtained on the cross-sections of plasma paste borided samples at 700 and 800 °C for duration of 2 and 5 h in gas mixtures of 20%N₂+60%H₂+20%Ar (6H) and 60%N₂+20%H₂+20%Ar (6N). It is seen that the shape of the microhardness profiles is affected by the boriding temperature. These profiles can be correlated with the variation of boron concentration through the boride layer. The diffusion front due to the formation of iron borides varies in the same direction as the hardness gradient. The hardness of boride layers on plasma paste borided steel at 800 °C was higher than that at 700 °C. It was also noticed that the longer boriding time results in higher surface hardness values due to the formation of a harder FeB phase [18],[30]. As can be seen in Fig. 4, while a maximum surface hardness of 1765 HV_{0.05} was obtained for the steel borided at 800 °C for 5 h, the lowest surface hardness of 1685 HV_{0.05} was found for the sample borided at 700 °C for 2 h in the gas mixture of 20%N₂+60%H₂+20%Ar. However, for the case of 60%N₂+20%H₂+20%Ar gas mixture, the surface hardness values of 1743 and 1673 HV_{0.05} were obtained for the samples borided at 800 and 700 °C for 5 h and 2 h, respectively. The results of micro-hardness measurement pointed out that plasma paste boriding enhanced the surface hardness of 21NiCrMo2 steel surfaces and hardness value in gas mixture of 20%N₂+60%H₂+20%Ar is slightly higher than that of 60%N₂+20%H₂+20%Ar gas mixture. In thermo-chemical boriding treatments, high hardness is attained directly through formation of borides during boriding and does not require quenching [2], [5], [31], [32].

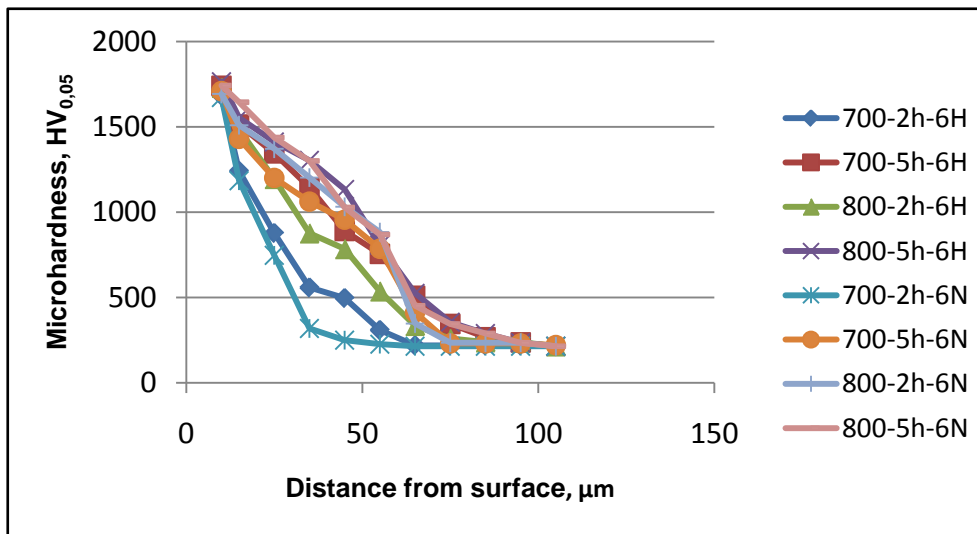


Figure 4. Microhardness profiles obtained on the polished cross-sections of plasma paste borided at 700 and 800°C for duration of 2 and 5 h in gas mixtures of 20%N₂+60%H₂+20%Ar (6H) and 60%N₂+20%H₂+20%Ar (6N).

4. CONCLUSIONS

In this study, plasma paste boriding process, which consists of borax paste, was successfully performed on 21NiCrMo2 steel. Since the plasma activates the chemical reaction more, a thicker boride layer is formed than conventional boriding methods at similar temperatures. It is possible to establish boride layer with the same thickness at lower temperatures in plasma environment. The saw-tooth morphology was formed on the cross-sections of the borided steel for both gas mixtures. Thickness of boride layers increased with increasing boriding temperature, time and nitrogen amount of gas mixtures. Boride layer consisted of FeB and Fe₂B phases and FeB intensity in the pattern was increased in the gas mixture with high nitrogen content. Plasma paste boriding promoted the surface hardness of 21NiCrMo2 steel surfaces and hardness value in gas mixture with low nitrogen is slightly higher than that of gas mixture with high nitrogen content.

ACKNOWLEDGEMENT

This research was carried out under Project Number 10.TEF.02 in the framework of the Coordinatorship of Scientific Research Projects (BAPK) of Afyon Kocatepe University.

REFERENCES

- [1]. A. Matuschka, *Boronizing*, Philadelphia, PA. Heyden Publications 1980.
- [2]. A.K. Sinha, *Boriding (Boronizing) of Steels. ASM Handbook. Heat Treating*. Ohio, US: 10th ed. ASM International: Materials Park, 1991, vol 4.
- [3]. R. Chatterjee-Fischer, *Boriding and Diffusion Metallizing*. In: Sudarshan TS, editor. *Surface Modification Technologies: An Engineer's Guide*. New York, United States of America: Marcel Dekker, 1989.
- [4]. B. Bhushan, and B.K. Gupta, *Handbook of tribology: materials, coatings, and surface treatments*. New York, United States of America: McGraw-Hill, 1991.
- [5]. G. Palombarini, and M. Carbucicchio, "Growth of Boride Coatings on Iron," *Journal of Materials Science Letters*, vol. 6 (4), pp. 415-416, April 1987.
- [6]. S. Sahin, and C. Meric, "Investigation of the effect of boronizing on cast irons," *Materials Research Bulletin*, vol.37 (5), pp. 971-979, April 2002.
- [7]. E.R. Cabeo, G. Laudien, S. Biemer, K.T. Rie, and S. Hoppe, "Plasma-assisted boriding of industrial components in a pulsed d.c. glow discharge," *Surface & Coatings Technology*, vol. 116, pp. 229-233, September 1999.
- [8]. A. Erdemir, O.L. Eryilmaz, G. Kartal, and S. Timur, "Boriding surface of metal (e.g. ferrous) by providing molten electrolyte having boron components, providing electrochemical boriding system, operating furnace to establish high temperature for molten electrolyte, and boriding metal surface," U.S. Patent 2010018611-A1, 2010.
- [9]. K.G. Anthymidis, P. Zinoviadis, D. Roussos, and D.N. Tsipas, "Boriding of nickel in a fluidized bed reactor," *Materials Research Bulletin*, vol. 37 (3), pp. 515-522, March 2002.
- [10]. O. Kahvecioglu, V. Sista, O. L. Eryilmaz, A. Erdemir, and S. Timur, "Ultra-fast boriding of nickel aluminate," *Thin Solid Films*, vol. 520 (5), pp. 1575-1581, December 2011.
- [11]. I. Gunes, S. Ulker, and S. Taktak, "Plasma paste boronizing of AISI 8620, 52100 and 440C steels," *Materials and Design*, vol. 32(4), pp. 2380-2386, April 2011.

- [12]. J. G. Buijnsters, P. Shankar, P. Gopalakrishnan, W. J. P. Van, Enckevort, J. J. Schermer, S. S. Ramakrishnan, and J. J. Ter, Meulen, "Diffusion-modified boride interlayers for chemical vapour deposition of low-residual-stress diamond films on steel substrates," *Thin Solid Films*, vol. 426, pp. 85-93, December 2003.
- [13]. K. A. Khor, L. G. Yu, and G. Sundararajan, "Formation of hard tungsten boride layer by spark plasma sintering boriding," *Thin Solid Films*, vol. 478, pp. 232-237, May 2005.
- [14]. J. A. Davis, P. J. Wilbur, D. L. Williamson, R. Wei, and J. J. Vajo, "Ion implantation boriding of iron and AISI M2 steel using a high-current density, low energy, broad-beam ion source," *Surf. Coat. Technol.*, vol. 103-104, pp. 52-57, May 1998.
- [15]. P. X. Yan, Z. Q. Wei, X. L. Wen, Z. G. Wu, J. W. Xu, W. M. Liu, and J. Tian, "Post boronizing ion implantation of C45 steel," *Appl. Surf. Sci.*, vol. 195, pp. 74-79, July 2002.
- [16]. J. H. Yoon, Y. K. Jee, and S. Y. Lee, "Plasma paste boronizing treatment of the stainless steel AISI 304," *Surf. Coat. Technol.*, vol. 112, pp. 71-75, February 1999.
- [17]. I. Gunes, and S. Taktak, "Surface characterization of pack and plasma paste boronized of 21NiCrMo2 steel," *Journal of the Faculty of Engineering and Architecture of Gazi University*, vol. 27 (1), pp. 99-108, 2012.
- [18]. S. Sen, U. Sen, and C. Bindal, "The growth kinetics of borides formed on boronized AISI 4140 steel," *Vacuum*, vol. 77 (2), pp. 195-202, January 2005.
- [19]. I. Uslu, H. Comert, M. Ipek, F.G. Celebi, O. Ozdemir, and C. Bindal, "A comparison of borides formed on AISI 1040 and AISI P20 steels," *Materials & Design*, vol. 28 (6), pp. 1819-1826, July 2007.
- [20]. I. Ozbek, H. Akbulut, S. Zeytin, C. Bindal, and A.H. Ucisik, "The characterization of borided 99.5% purity nickel," *Surface & Coatings Technology*, vol. 126 (2-3), pp. 166-170, April 2000.
- [21]. S. Taktak, "Characterization of pack borided AISI 4140 steel after nickel electroplating," *Kovove Mater.*, vol. 45, pp. 215-222, 2007.
- [22]. N. Suwattananont, and R. Petrova, (2012). "Formation of multi-component boronization by adding transition metal group VIB," *Solid State Sciences*, vol. 14 (11-12), pp. 1669-1672, Nov. 2012.
- [23]. P.A. Dearnley, T., Farrell, and T. Bell, "Current developments in plasma boriding," *IPAT 85. 5th International Conference on Ion and Plasma Assisted Techniques*, 1985, p.359.
- [24]. A. Kuper, "Plasma-assisted boronizing," *Advanced Materials & Processes*, vol. 161 (3), pp. 20- 22, 2003.
- [25]. K.T. Rie, "Recent advances in plasma diffusion processes," *Surface & Coatings Technology*, vol. 112 (1-3), pp. 56-62, 1999.
- [26]. P. Goerriot, R. Fillit, F. Thevenot, J.H. Driver, and H. Bruyas, "The influence of alloying element additions on the boriding of steel," *Materials Science and Engineering*, vol. 55 (1), pp. 9-19, August 1982.
- [27]. O. Ozdemir, M. Usta, C. Bindal, and A. H. Ucisik, "Hard iron boride (Fe₂B) on 99.97wt% pure iron," *Vacuum*, vol. 80 (11-12), pp. 1391-1395, September 2006.
- [28]. C.M. Brakman, A.W.J. Gommers, and E.J. Mittemeijer, "Boriding of Fe and Fe-C, Fe-Cr, and Fe- Ni alloys - Boride-layer growth-kinetics," *Journal of Materials Research*, vol. 4 (6), pp. 1354-1370, June 1989.
- [29]. G. Palombarini, and M. Carbucicchio, "On the morphology of thermochemically produced Fe₂B/Fe interfaces," *Journal of Materials Science Letters*, vol. 3 (9), pp. 791-794, 1984.
- [30]. S. Sen, I. Ozbek, U. Sen, and C. Bindal, "Mechanical behavior of borides formed on borided cold work tool steel," *Surf. Coat. Technol.*, vol. 135, pp. 173-177, January 2001.
- [31]. K. Genel, "Boriding kinetics of H13 steel," *Vacuum*, vol. 80 (5), pp.451-457, January 2006.
- [32]. S. Taktak, "Some mechanical properties of borided AISI H13 and 304 steels," *Materials & Design*, vol. 28 (6), pp. 1836-1843, 2007.

BIOGRAPHY

Dr. Taktak received his PdD in Metallurgical and Materials Engineering from institute of natural and applied science, Sakarya, Turkey in 2002. He is a Professor at Afyon Kocatepe University, Afyonkarahisar, Turkey, since 2007. His area of interest is surface engineering for tribological applications such as oxidative and high temperature at unlubricated conditions. He has published around 30 papers in international peer reviewed journals.

THE EFFECT OF WAX AND POLYTETRAFLUOROETHYLENE ON TRIBOLOGICAL PROPERTIES OF FIBRE GLASS (GF) FILLED POLYPHENYLENE SULFIDE COMPOSITES

Ferhat YILDIRIM

Dumlupınar University, Faculty of Technical Education, Department of Machine Education, 43500 Simav, Kütahya,
ferhat.yildirim@dpu.edu.tr,

Salih Hakan YETGIN

Dumlupınar University, Faculty of Technical Education, Department of Machine Education, 43500 Simav, Kütahya,

Murat ÇOLAK

Bayburt University, Faculty of Engineering, Material Science and Nanotechnology Department, Bayburt, TURKEY,

Gürhan DENİZ

Sakarya University, Faculty of Technical Education, Department of Metal Education, Sakarya, TURKEY

Abstract

In this experimental research, the tribological performance of 40%wt fibre glass (GF) filled polyphenylene sulfide (PPS-GF), 4wt% wax filled PPS-GF, 10wt% polytetrafluoroethylene (PTFE) filled PPS-GF and 4wt% wax/10wt% PTFE filled PPS-GF sliding against X40CrMoV5-1 steel under dry sliding conditions were studied using a pin-on-disc tribometer. The influences of applied load and sliding speed on tribological properties were investigated. All the materials were dried at 140 oC for 4 hour before compounding. PPS-GF composites were fabricated on twin screw extruder. The temperatures from the feed zone to the die of the extruder were 275, 280, 288, 295 and 300 oC, respectively. Thereafter, the specimens for tribological tests were produced using injection-molding machine, with an injection pressure of 500 bar and temperature profile of 275, 285, 295, 300 and 300 oC. The screw speed was fixed at 80 cm³/s and the mould temperature was 30 oC. Tribological tests were carried out at sliding speeds of 0.5, 1.0, and 1.5m/s and applied load values of 60, 90 and 120N. The results show that the coefficient of friction for PPS-GF and its composites were decreased while specific wear rate increased with increased applied load and sliding speed values. The coefficient of friction and specific wear rate of the PPS-GF polymer decreased with the addition of wax and PTFE. The specific wear rate for PPS-GF and its composites are in the order of 10–14 and 10–15 m² / m.

Keywords: PPS, Wax, PTFE, Friction, Wear

1. INTRODUCTION

Poly(p-phenylensulfide) (PPS) is an excellent crystalline thermoplastic with heat and chemical resistance, and it is used broadly as an alternative material of metal in car parts, electricity and electronic products, and precision parts. As a new type of engineering plastic, poly(phenylene sulfide) [1]. PPS shows high mechanical strength as well as dual properties of thermoplastic and thermoset. Those outstanding properties of PPS are attributed to its chemical structure composed of phenyl groups linked by a sulphur atom, and hence, PPS has been used in a variety of market segments including industrial and consumer goods sectors. However, the low glass transition temperature and the brittleness with low elongational strain also restrict its further applications. Several techniques hence have been applied to overcome the marginal properties of PPS [2]-[5].

A solid lubricant is defined as a material that provides lubrication to two surfaces moving relatively to each other. The solid lubricants often lead to decrease of coefficient of friction and specific wear rate through the reduction in adhesion with the counterface or the creation of a transfer film at the interface [6]. The solid lubricants such as ultra-high molecular weight polyethylene (UHMWPE) [7-9], polytetrafluoroethylene (PTFE) [7]-[11], molybdenum disulfide (MoS_2) [6,7,11], graphite [9,12,13] and carbon [11] have been thus widely used to enhance the friction and wear properties of polymers [7]. There have been numerous investigations effect of the influence of solid lubricant on the friction and wear behaviour of different polymers. Yi-Lan et al. [7] investigated the tribological properties of $\text{TiO}_2/\text{PA6}$ nanocomposites filled with MoS_2 , UHMWPE, PTFE and their combinations. Mehmet and Hayrettin [10] examined the effect of sliding velocity, bearing pressure and temperature on friction and wear of PA66, PA66+18%PTFE and PA66+20%GFR+25%PTFE journal bearings at ambient conditions. Laigui et al. [11] investigated the friction and wear behaviour properties of graphite (C), molybdenum disulfide (MoS_2), and polytetrafluoroethylene (PTFE) filled polyphenylene sulfide (PPS) composites. Suck and Dae-Won [12], investigated nylon composite with graphite and oil for anti-static sliding applications. In this study, the influence of load, sliding speed and lubrications on the friction and wear behaviour of PPS-GF polymers have been studied and compared.

2. EXPERIMENTAL DETAILS

The matrix material 40%wt fibre glass (GF) filled polyphenylene sulfide with 1.65g/cm^3 density was obtained from Royal DSM in Hollanda. In sample preparation process, the PTFE and wax were added to 40%wt fibre glass (GF) filled polyphenylene sulfide with 4wt% and 10 wt% ratios. The composite granules were prepared using twin screw extruder AYSA Lab-30 at temperatures ranging from 275 to 300 °C. The specimens of 40%wt fibre glass (GF) filled polyphenylene sulfide and its composites were moulded by using an injection moulding machine at temperatures from 275 to 300 °C. Wear tests were carried out on a pin-on-disc wear test configuration at room temperature under dry conditions. The cylindrical pin flat ended specimens of size 6 mm in diameter and 50 mm length were tested against X40CrMoV5-1 steel disc. Figure 1 represents a schematic diagram of the pin-on-disc wear test configuration that was designed and used for this work. Sliding wear data reported here is the average of at least three runs. The average mass loss was used to calculate the specific wear rate (K_o) as

$$K_o = \Delta m / L \cdot F \cdot \rho \quad (\text{m}^2/\text{N}) \quad (1)$$

where Δm is average mass loss (g), L is sliding distance (m), F is the applied load (N) and ρ is density of the materials (g cm^{-3}).



Figure 1. Schematic diagram of wear test rig.

3. PRESENT AND DISCUSSIONS

Table 1 present coefficients of friction and wear rate values for P PS-GF, PPS-GF+4%Wax, PPS-GF+10%PTFE and PPS-GF+4wt%wax+10wt%PTFE composite against steel counterface, tested at room temperature, dry condition, 0.5, 1.0 and 1.5m/s sliding velocity and at 60, 900, 120N load values. Figure. 2 and 3 show the variation of friction coefficient of PPS-GF, PPS-GF+4%Wax, PPS-GF+10%PTFE and PPS-GF+4wt%wax+10wt%PTFE composite with applied load at 0.5m/s and 1.5m/s sliding speeds respectively. It is clear from these figures that the coefficient of friction of tested PPS-GF polymers decrease linearly with the increase in load value. Similar results obtained by Mehmet and Hayrettin [10]. There is an average decrease of 20% in friction coefficient value from 60N to 90N increase in load value. For all combination of materials used in this investigation, the average coefficient of friction value for 4wt%wax filled PPS-GF, 10wt%PTFE filled PPS-GF and 4wt%wax/10wt%PTFE filled PPS-GF polymers are 37%, 26% and 41% lower values than that of the PPS-GF composite, respectively.

Table 1. Tribological properties for PPS-GF, PPS-GF+4%Wax, PPS-GF+10%PTFE and PPS-GF+4wt%wax+10wt%PTFE composites against steel disc tested at different sliding speed and load.

Materials	Load (N)	Sliding speed (m/s)					
		0.5			1.0		
		0.5	1.0	1.5	0.5	1.0	1.5
Coefficient of friction (μ)			Specific wear rate (m^2/N)				
PPS-GF	60N	0,285	0,260	0,249	9,02E-15	1,00E-14	1,11E-14
	90N	0,278	0,224	0,195	1,09E-14	1,48E-14	1,73E-14
	120N	0,256	0,201	0,182	1,16E-14	1,61E-14	1,88E-14
PPS-GF+4%Wax	60N	0,176	0,162	0,160	6,07E-15	7,17E-15	8,27E-15
	90N	0,165	0,150	0,144	8,46E-15	8,83E-15	9,93E-15
	120N	0,152	0,139	0,131	9,65E-15	1,02E-14	1,21E-14
PPS-GF+10%PTFE	60N	0,217	0,191	0,181	7,04E-15	8,80E-15	9,97E-15
	90N	0,194	0,171	0,164	9,38E-15	9,78E-15	1,29E-14
	120N	0,175	0,153	0,145	1,02E-14	1,20E-14	1,70E-14
PPS-GF+4wt%wax+10wt%PTFE	60N	0,158	0,151	0,148	4,35E-15	5,59E-15	7,46E-15
	90N	0,149	0,140	0,134	6,63E-15	7,04E-15	8,29E-15
	120N	0,142	0,131	0,124	7,46E-15	8,08E-15	9,95E-15

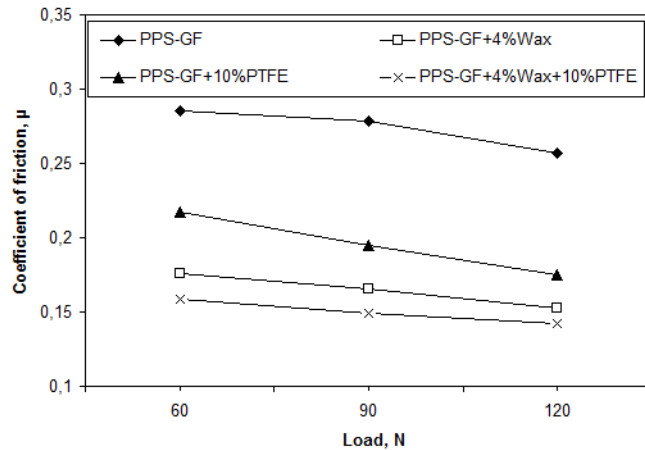


Figure 2. Variation of coefficient of friction with load for PPS-GF, PPS-GF+4%Wax, PPS-GF+10%PTFE, PPS-GF+4%Wax+10%PTFE composites tested against steel (Sliding speed; 0.5m/s).

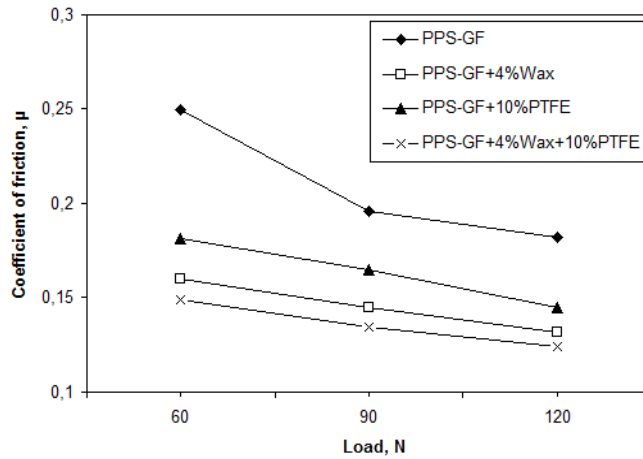


Figure 3. Variation of coefficient of friction with load for PPS-GF, PPS-GF+4%Wax, PPS-GF+10%PTFE, PPS-GF+4%Wax+10%PTFE composites tested against steel (Sliding speed; 1.5m/s).

Figure 4 and 5 show the variation of friction coefficient of PPS-GF, PPS-GF+4%Wax, PPS-GF+10%PTFE and PPS-GF+4wt%wax+10wt%PTFE composite materials with sliding speed values under 60N and 120N loads values, respectively. The coefficient of friction of tested all materials decreases linearly with the increase in sliding speed. In the case of PPS-GF, there is an average 30% decrease with the increase sliding speed. For PPS-GF+4%Wax, PPS-GF+10%PTFE and PPS-GF+4wt%wax+10wt%PTFE composite materials there is an average decrease of 12%, 15% and 10% in friction coefficient value for a 100% increase in sliding speed, respectively. The tribological behaviors of polymers and polymer-based composites are closely related to the transfer film characteristics. The decreasing of friction with increasing of load and sliding speed results from transfer film formation. And, it provide to increase of film thickness and increase the holding ability of the film on the counter surfaces [14-16].

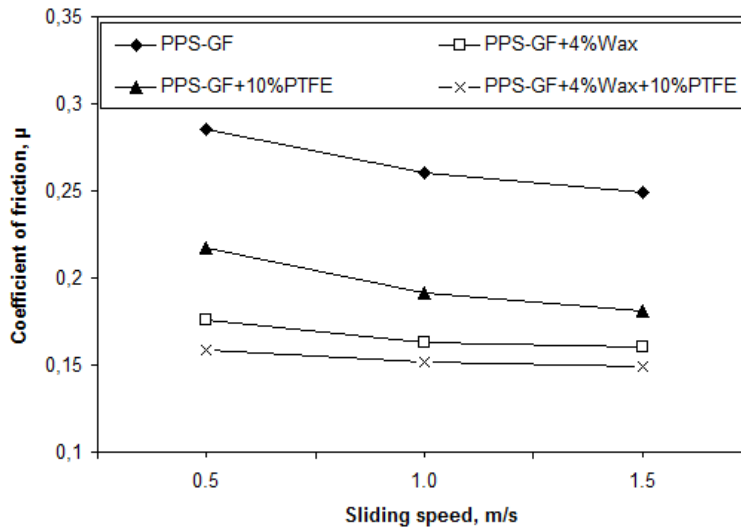


Figure 4. Variation of coefficient of friction with sliding speed for PPS-GF, PPS-GF+4%Wax, PPS-GF+10%PTFE, PPS-GF+4%Wax+10%PTFE composites tested against steel (Load; 60N).

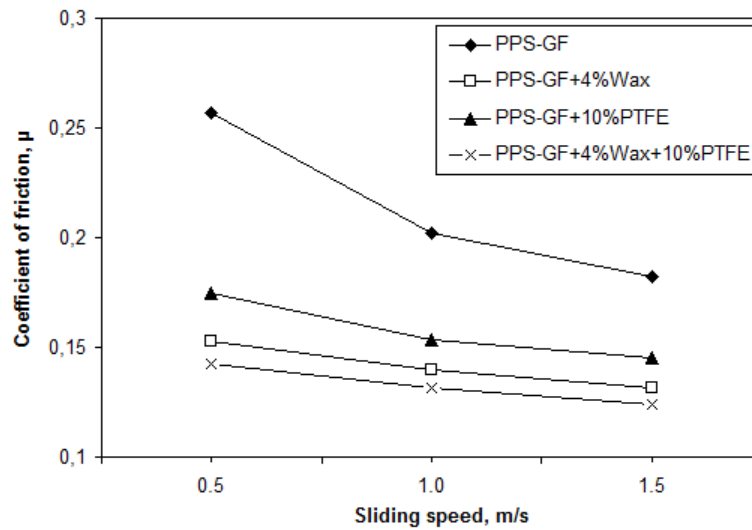


Figure 5. Variation of coefficient of friction with sliding speed for PPS-GF, PPS-GF+4%Wax, PPS-GF+10%PTFE, PPS-GF+4%Wax+10%PTFE composites tested against steel (Load; 120N).

Figure 6 and 7 show the variation of specific wear rate versus load for PPS-GF, PPS-GF+4%Wax, PPS-GF+10%PTFE, PPS-GF+4%Wax+10%PTFE composites. It is clear from these figures that the wear rate for all tested materials is increases with the increment of load values. In general the specific wear rate for PPS-GF is in the order of 10^{-15} while PPS-GF+4%Wax, PPS-GF+10%PTFE, PPS-GF+4%Wax+10%PTFE composites are in the order 10^{-14} m^2/N . It is seen that among tested PPS-GF and its composite materials, the lowest wear rate is for PPS-GF+4%Wax+10%PTFE with a value of 4.35×10^{-15} m^2/N followed by PPS-GF+4%Wax with 6.07×10^{-15} m^2/N and PPS-GF+10%PTFE with 7.04×10^{-15} m^2/N and the highest value is 1.88×10^{-14} m^2/N for PPS-GF. This means that wax and PTFE presence in the composite presents 35% lower wear rate of PPS-GF material.

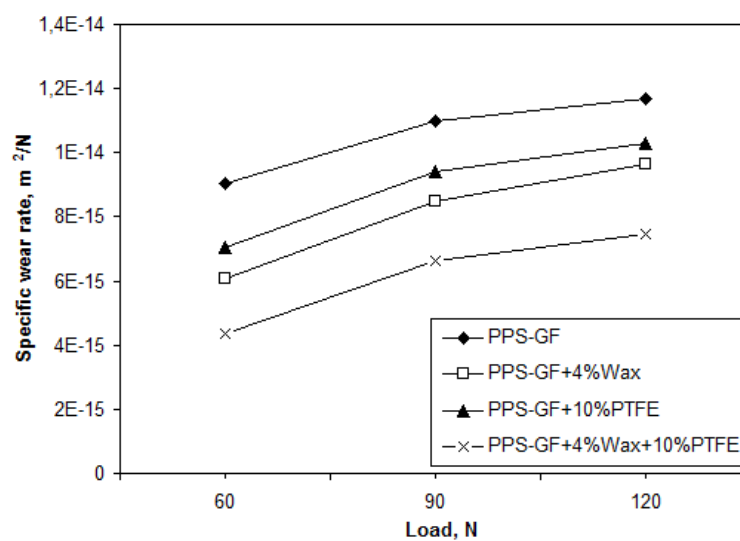


Figure 6. Variation of specific wear rate with load for PPS-GF, PPS-GF+4%Wax, PPS-GF+10%PTFE, PPS-GF+4%Wax+10%PTFE composites tested against steel (Sliding speed; 0.5m/s).

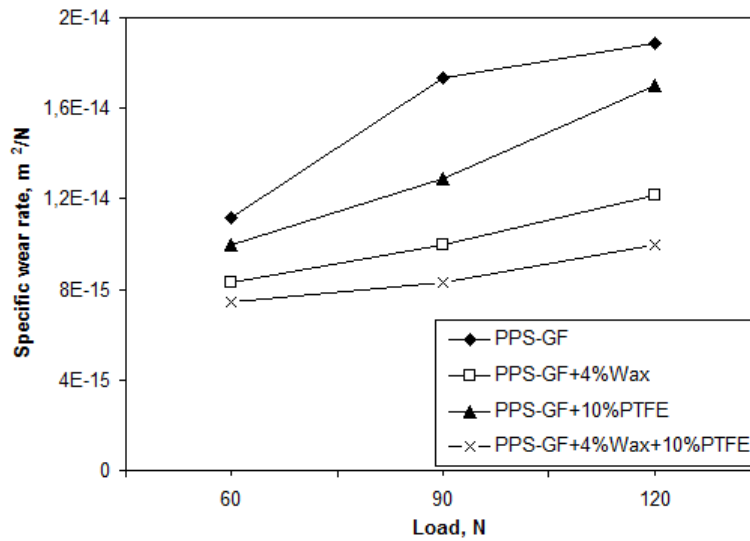


Figure 7. Variation of specific wear rate with load for PPS-GF, PPS-GF+4%Wax, PPS-GF+10%PTFE, PPS-GF+4%Wax+10%PTFE composites tested against steel (Sliding speed; 1.5m/s).

Figure 8 and 9 present the variation of specific wear rate with sliding velocity under 60 and 120 N load values respectively. It is clear from these figures that the specific wear rate values increase with the increase in sliding speed values. The addition of graphite and wax resulted in large improvement in lowering friction coefficient and wear rate of PPS-GF polymer. The PPS composite showed the highest specific wear rate value. This result could be explained by the brittleness of the PPS composite from the higher amount of reinforcing glass fibres and due to weak bonding between the fibres and the matrix [17].

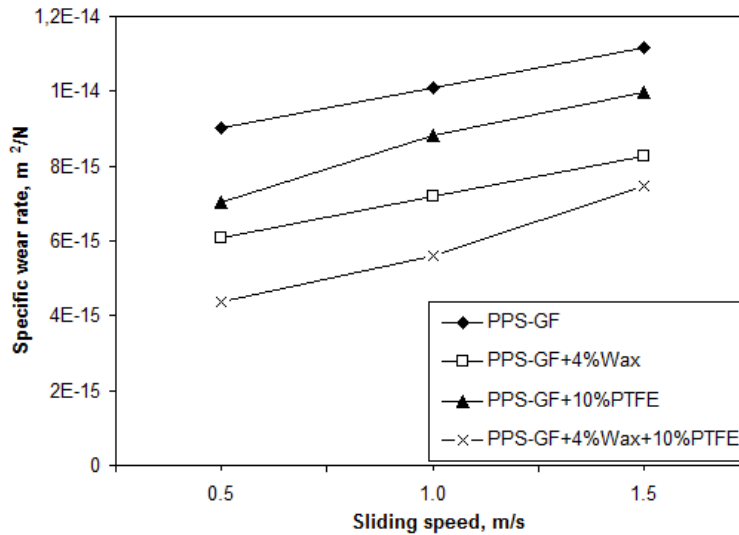


Figure 8. Variation of specific wear rate with sliding speed for PPS-GF, PPS-GF+4%Wax, PPS-GF+10%PTFE, PPS-GF+4%Wax+10%PTFE composites tested against steel (Load; 60N).

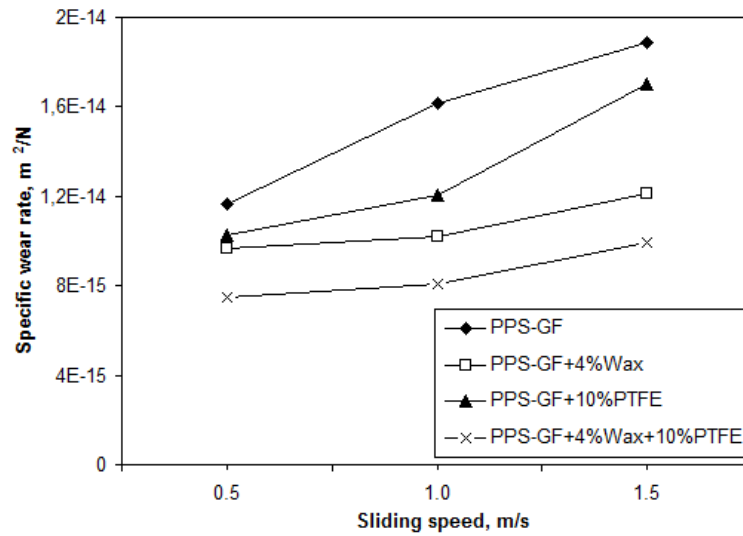
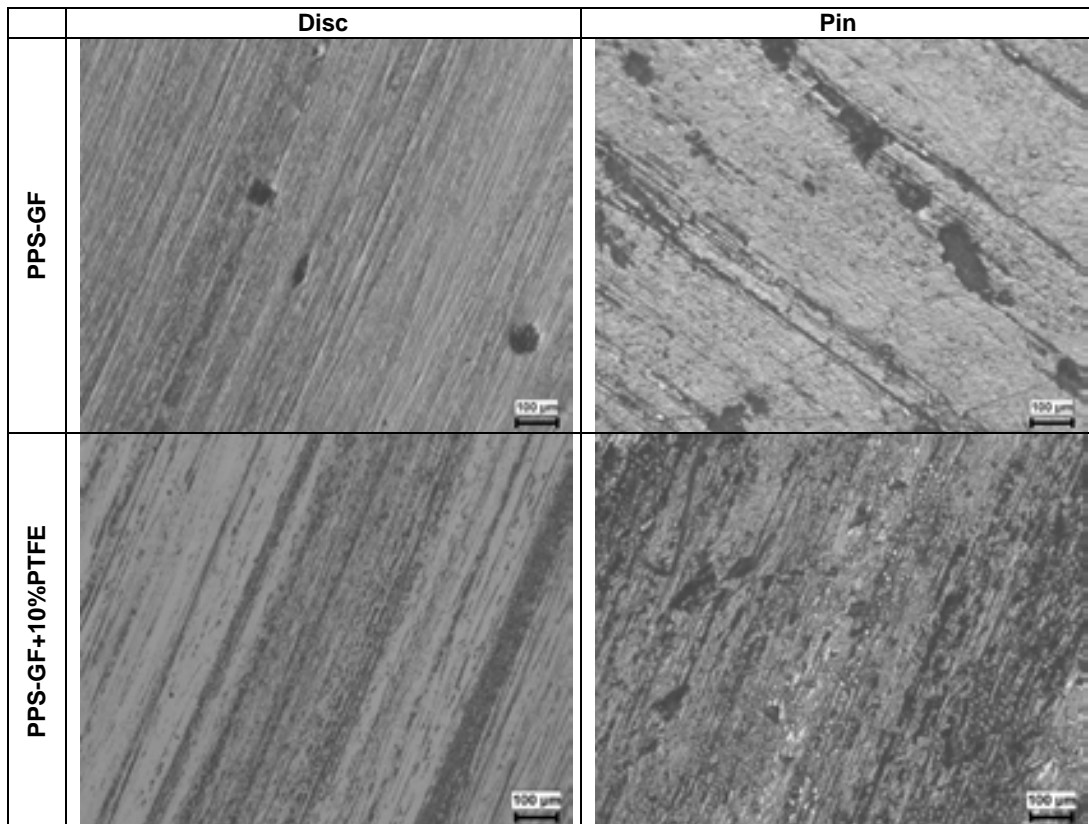


Figure 9. Variation of specific wear rate with sliding speed for PPS-GF, PPS-GF+4%Wax, PPS-GF+10%PTFE, PPS-GF+4%Wax+10%PTFE composites tested against steel (Load; 120N).

Figure 10 show the microscopy examination of pin and disc surfaces for PPS-GF, PPS-GF+4%Wax, PPS-GF+10%PTFE, PPS-GF+4%Wax+10%PTFE composites under 90N load value and at 0.5 sliding speed conditions. For PPS-GF polymer pin materials, worn surface showed sliding with wider and deeper grooves, which is resulted from removed brittle GFR. For PPS-GF disc surface, transfer film was thin and discontinuous, which correspond to its high friction coefficient and wear rate. In case of wax and PTFE filler, the formation of transfer film is more active and stable. This transfer film protects the surfaces and has lubricant behaviors. This process caused to much lower coefficient of friction and specific wear rate values.



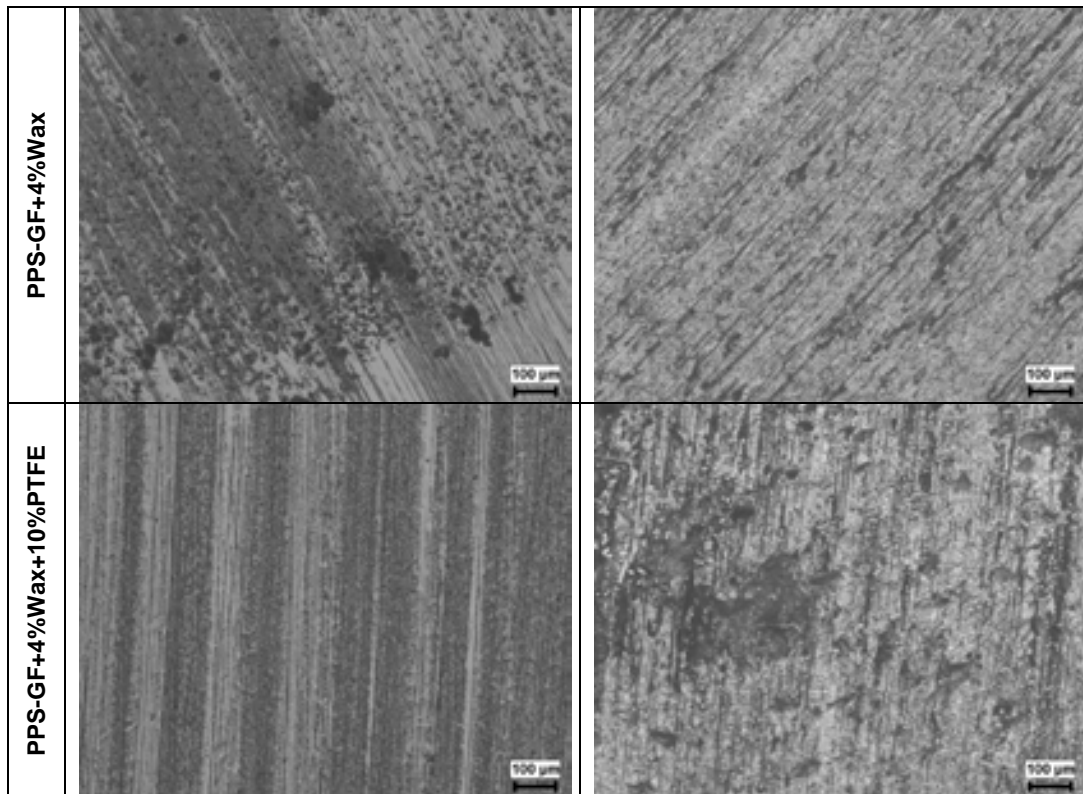


Figure 10. Pin and disc worn surface microscopy at 90N load and 0.5m/s sliding speed for PPS-GF, PPS-GF+4%Wax, PPS-GF+10%PTFE, PPS-GF+4%Wax+10%PTFE composites.

4. CONCLUSIONS

1. The coefficient of friction of tested PPS-GF polymers decrease linearly with the increase in load and sliding speed value.
2. In general the specific wear rate for PPS-GF is in the order of 10^{-15} while PPS-GF+4%Wax, PPS-GF+10%PTFE, PPS-GF+4%Wax+10%PTFE composites are in the order 10^{-14} m^2/N .
3. The specific wear rate values increase with the increase in load and sliding speed values.
4. The addition of wax and PTFE fillers into PPS-GF decreases the friction coefficient and specific wear rate of PPS-GF composites.
5. Transfer film to the steel disc that leads to increased wear resistance.

REFERENCES

- [1]. R. Hiroi, H. Tanaka, "A New Nano filler to Improve the Friction and Wear Properties of PPS," in International Conference on Science of Friction, 2010.
- [2]. J.R. Fried, *Polymer Science and Technology*, 2nd ed, Pearson Education Inc, New York, 2003.
- [3]. D. Wu, L. Wu, J. Wang, Y. Sun, M. Zhang, "Effect of epoxy resin on the thermal behaviors and visco elastic properties of poly (Phenylene sulfide)," *Materials Chemistry and Physics*, vol.128, pp. 274–282, 2011.
- [4]. J. Masamoto, K. Kudo, "Elastomer toughened Polyphenylene Sulfide," *Memoirs of Fukui University of Technology*, vol. 34:1, 2004.
- [5]. Y. Haribabu, K. Ajay, B. Ravikiran, "Fabrication and Characterization of PPS/40%GF/nano-CaCo₃ Hybrid Composites," *Int. Journal of Modern Engineering Research*, vol. 3(4), pp. 2262-2266, 2013.
- [6]. E. Basavaraj, B. Ramaraj, J. H. Lee, "Polyamide 6/carbon black/molybdenum disulphide composites: Friction, wear and morphological characteristics," *Materials Chemistry and Physics*, vol. 138, pp. 658-665, 2013.
- [7]. Y. Yi-Lan, L. Du-Xin, S. Gao-Jie, D. Xin, "Investigation of the influence of solid lubricants on the tribological properties of polyamide6 nanocomposite," *Wear*, vol. 311, pp. 57–64, 2014.
- [8]. L. Du-Xin, Y. Yi-Lan, D. Xin, L. Wen-Juan, X. Ying, "Tribological properties of solid lubricants filled glass fiber reinforced polyamide 6 composites," *Materials and Design*, vol. 46, pp. 809–815, 2013.

- [9]. X. Li Du, J. Li Wen, Y. Xie, X. Li Xiang, "Effects of Solid Lubricants on Friction and Wear Behaviors of Polyamide 6," *Journal of Applied Polymer Science*, vol. 124, pp. 4239–4248, 2012.
- [10]. D. Mehmet T, D. Hayrettin, "Wear behaviors of Polytetrafluoroethylene and glass fiber reinforced Polyamide 66 journal bearings," *Materials and Design*, vol. 57, pp. 560–567, 2014.
- [11]. W. Laigui, Y. Shengrong, L. Weimin, X. Qunji, "An Investigation of the Friction and Wear Behaviors of Polyphenylene Sulfide Filled With Solid Lubricants," *Polymer Engineering and Science*, vol. 40-8, pp. 1825-1832, 2000.
- [12]. C.K. Suck, C. Dae-Won, "Improvement of frictional properties and abrasive wear resistance of nylon/graphite composite by oil impregnation," *Wear*, vol. 254, pp. 103–110, 2003.
- [13]. X.R. Zhang, X.Q. Pei, Q.H. Wang, "Effect of Solid Lubricant on the Tribological Properties of Polyimide Composites Reinforced with Carbon Fibers," *Journal of Reinforced Plastics and Composites*, pp. 1-8, 2008.
- [14]. J. Khedkar, J. Nagulescu, E. Meletis, "Sliding wear behavior of PTFE composites," *Wear*, vol. 252, pp. 361–369, 2002.
- [15]. T. Tevruz, "Tribological behavior of carbon filled Polytetrafluoroethylene (PTFE) dry journal bearings," *Wear*, vol. 221, pp. 61–8, 1998.
- [16]. J. Wang, M. Gu, B. Songlo, S. Ge, "Investigation of the influence of MoS₂ filler on the tribological properties of carbon filler reinforced nylon 1010 composites," *Wear*, vol. 255, pp. 774–779, 2003.
- [17]. H. Unal, A. Mimaroglu, V. Serdar, "Dry sliding performance of thermoplastics against reinforced unsaturated polyester (BMC): In use in electrical contact breakers components," *Wear*, vol. 261, pp. 841–847, 2006.
-

THERMAL ANALYSIS OF NEW MOLTEN SALTS ELECTROLYTE FOR MEDIUM TEMPERATURE THERMAL BATTERIES

Ahmet KOCA

dr.koca.ahmet@gmail.comFirat University, Technology Faculty, Mechatronics Eng. Dep. TURKEY

Yasin VAROL

Firat University, Technology Faculty, Automotive Eng. Dep. TURKEY

Hakan F.ÖZTOP

Firat University, Technology Faculty, Mechanics Eng. Dep. TURKEY

Fahrettin YAKUPHANOĞLU

Firat University, Faculty of Science, Physics Dep. TURKEY

Fethi DAGDELEN

Firat University, Faculty of Science, Physics Dep. TURKEY

Mehmet Cem MENTES

Firat University, Technology Faculty, Automotive Eng. Dep. TURKEY

Gamze Pelin AKSOY

Firat University, Technology Faculty, Mechatronics Eng. Dep. TURKEY

Aysegul DERE

Firat University, Faculty of Science, Physics Dep. TURKEY

Abstract

Thermal batteries have generally three sections; anode, cathode and electrolyte. We developed a new molten salts electrolyte with binary mixture. Its thermal conductivity and DSC analysis were evaluated and compared with mixture components. It was concluded that the new molten salts electrolyte with binary mixture can improve thermal and electrical capacity in medium temperature thermal batteries.

Keywords: *binary mixture, thermal analysis, electrolyte, thermal battery*

1. INTRODUCTION

Thermal activated (also known thermal) batteries are used as the primary power sources for ordnance applications. Their inherent advantages such as reliable, robust, rugged and longtime storage, made them primary power sources for the military applications. First time the Germans developed this technology for a power source of their V2 rockets during WWII [1]. Dr. Georg Otto Erb is credited with developing the molten-salt battery that used the heat of the rocket to keep the salt liquid during its processing [2]. In 1946 thermal battery technology was used and developed by the Americans.

The thermal battery cell basically has three elements; anode, cathode and electrolyte. It uses a molten, ionically conducting electrolyte as a separator between the anode and cathode [3]. Until the electrolyte becomes molten, the battery is essentially inert. Once activated the thermal battery, power can be delivered at extremely high rates. The desired battery power voltage is obtained by stacking the required number of cells.

The convectional LiCl-KCl molten salt systems, which has been used as an electrolyte in thermal batteries, has a melting point 350oC [4]. For high temperature molten salts batteries, there are a lot of works to obtained better thermal and ionic conductivity [5-8].

There has been interest in recent years to adopt thermal “activated” battery for some domestic applications such as power sources for borehole drilling application [9]. However, this would require the use of electrolytes lower melting points ($\leq 300^{\circ}\text{C}$). Lithium based eutectic mixtures as electrolyte were studied by the authors to obtained lower melting points with better thermal and ionic conductivity [10-15].

We developed a new molten salts electrolyte with binary mixture. We mixed the salt hydrates in several mixture ratio and finally found proper ratio for better thermal and electrical capacity.

2. EXPERIMENTATION

The experimental work consists of synthesis of the mixture of proper salt hydrates as electrolyte and their mixture ratio. We used Potassium thiocyanate (KSCN) and Butanaminium iodide (C₄H₁₂IN) as salt hydrates as binary mixture materials. Their and binary mixture thermal and chemical properties were shown in Table 1.

Table 1. Salt hydrates properties

SaltHydrate	Chemical Formula	MolarMass (g/mol)	Density (g/cm ³)	Melting Point (°C)	Boiling Point (°C)	Entalphy (mJ/mg)	Appearance
Potassiumthiocyanate	KSCN	97.181	1.886	173.2	500	137	Colorless
Tetramethylammoniumiodide	C ₄ H ₁₂ 4NI	201.05	1.840	300	-	893	White solid
New Molten Salt Electrolyte	50% KSCN +50% C ₄ H ₁₂ IN			248.3		433	colorless

Hot plate magnetic mixer was used to homogenies binary mixture (Fig 1). KSCN and C₄H₁₂IN were mixed different ratio. Also Omega® high temperature heater tape was used with PID Temperature controller for more sensitive heat control (Fig 2). We made thermal analysis with Differential Scanning Calorimetry (DSC) and found that 50% KSCN and 50% C₄H₁₂IN mixed homogenously (Figure 3).



Figure 1. Hot Plate Magnetic Mixer



Figure 1. PID Temperature controller

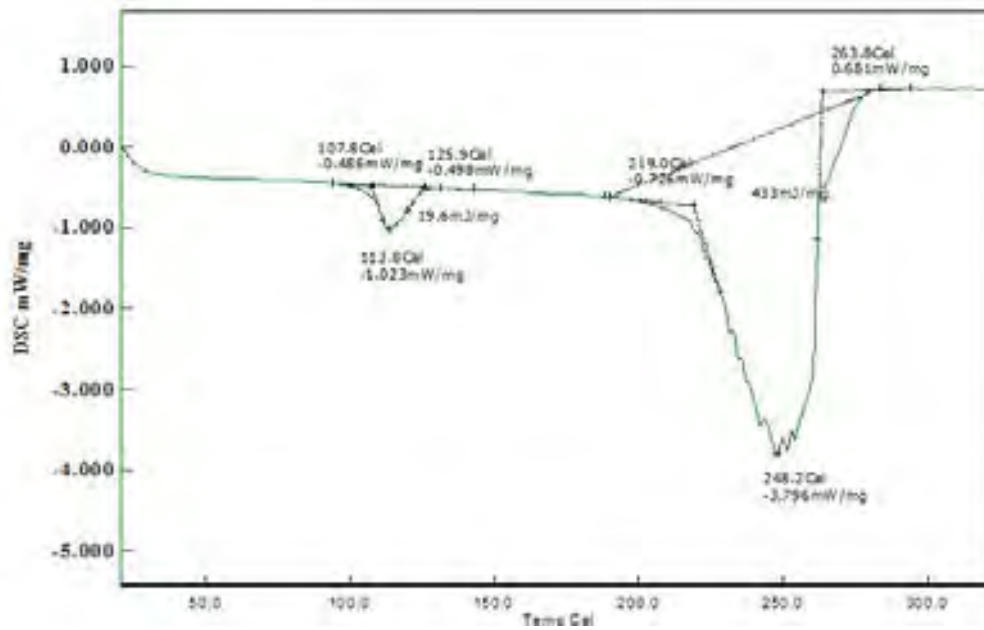
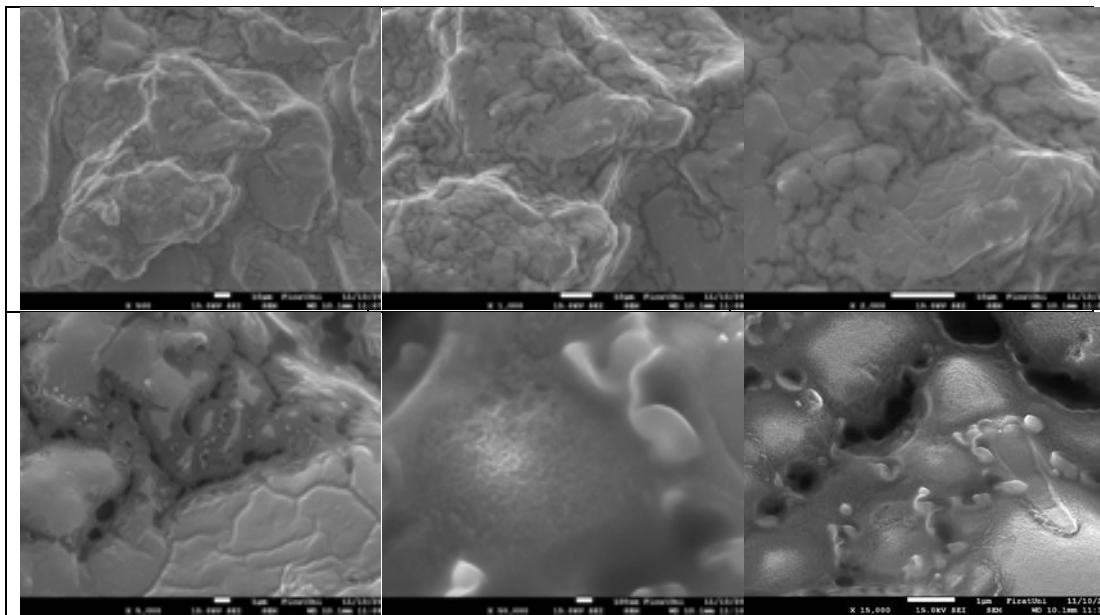


Figure 3. DSC measurements of 50% KSCN and 50% C4H12IN mixture

3. RESULTS

50% KSCN and 50% C4H12IN mixture molecular structure was investigated by Field Emission Scanning Electron Microscope (FESEM). Figure 4 shows FESEM images 10 μ m x 2.000 scale. Distribution of small particles was clearly shown in FESEM results. The results show that small particles in mixture covered homogenous by the other materials. Particles distribution is randomly formed and they are clustering certainly areas.



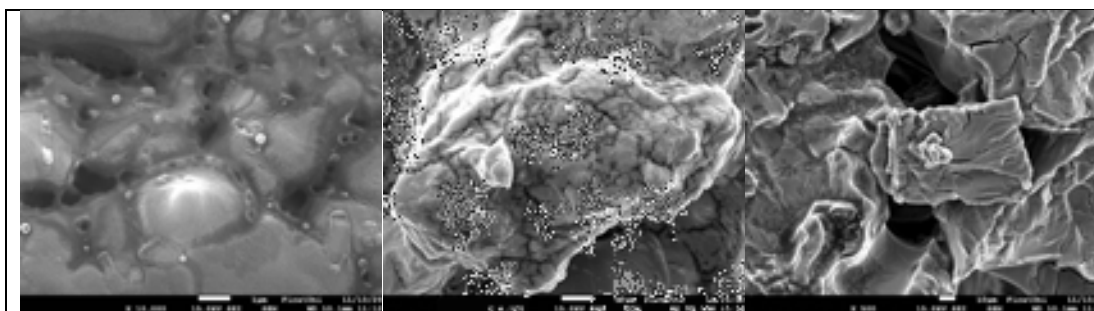


Figure 4. FESEM images of 50% KSCN and 50% C₄H₁₂IN mixture

Thermal conductivity is made for pure salt hydrates and mixture, separately. Table 2 shows thermal conductivity results. It shows that mixture thermal conductivity (0.103W/mK) is almost same with pure materials. However melting point of new material (248.3oC) is more suitable for medium range thermal battery. Also enthalpy of new molten salt electrolyte is 433mJ/mg. It is one of the higher value of molten salts materials which have melting point between 200-250oC.

Table 2. Thermal conductivity of materials

Salt Hydrate	Chemical Formula	Thermal Conductivity (W/mK)	Volumetric Heat Capacity (Mj/m ³ K)	Thermal Diffusivity (mm ² /s)	Measurement Temperature (°C)	Measurement Duration (min.)
Potassiumthiocyanate	KSCN	0.129	1.054	0.139	26.827	2
Tetramethylammoniumiodide	C ₄ H ₁₂ NI	0.112	1.084	0.124	25.847	2
New Molten Salt Electrolyte	50% KSCN +50% C ₄ H ₁₂ IN	0.103	0.875	0.109	25.117	2

It was concluded that the new molten salts electrolyte with binary mixture can improve thermal and electrical capacity in medium range temperature thermal batteries.

ACKNOWLEDGMENT

This study is carried out in scope of 112M411 numbered research project supported by The Scientific and Technological Research Council of Turkey (TUBITAK). The authors would like to thank to TUBITAK for their financial support.

REFERENCES

- [1]. W. E. Kuper, "A Brief history of thermal battery," in *Proc. 36th Power Sources Conf.*, 1994, p. 300-309.
- [2]. R.A. Guidotti, "Thermal Batteries: A Tehnology Review and Future Directions," in *27th International SAMPE Technical Conference, Albuquerque, New Mexico, USA*, 1995.
- [3]. R. A. Gidotti and P. Massaet, *Thermally activated ("thermal") battery technology Part I: An overview (Review)*, Journal of Power Sources 161, 2006, pp. 1443-1449.
- [4]. S. Fujiwara, F. Kato, S. Watanabe, M. Inaba, A. Tasaka, *New iodide-based molten salt systems for high temperature batteries*, J. Power Sources, vol.194 (2), 2009, pp. 1180-1183.
- [5]. Fujiwara, M. Inaba, A. Tasaka, *New molten salt systems for high-temperature molten salt batteries: LiF-LiCl-LiBr-based quaternary systems*, J. Power Sources, vol.195 (22), 2010, pp. 7691-7700
- [6]. G.J. Janz, F.W. Dampier, G.R. Lakshminarayanan, P.K. Lorenz, R.P.T. Tomkins, *New molten salt systems for high-temperature molten salt batteries: LiF-LiCl-LiBr-based quaternary systems*, Molten Salts: Volume 1, Electrical Conductance, Density, and Viscosity Data National Standard Reference Data Series (NSRDS), National Bureau of Standards (NBS) vol.15, 1968, pp. 114-119

- [7]. G.J. Janz, R.P.T. Tomkins, C.B. Allen, J.R. Downey Jr., G.L. Gardner, U. Krebs, S.K. Singer, *Molten salts: volume 4, part 2, chlorides and mixtures, electrical conductance, density, viscosity, and surface tension data* JPCRD, 1975, pp. 871–1178
 - [8]. S. Fujiwara, M. Inaba, A. Tasaka, *New molten salt systems for high temperature molten salt batteries: Ternary and quaternary molten salt systems based on LiF-LiCl, LiF-LiBr, and LiCl-LiBr*, Journal of power Sources, vol.196, 2011, pp. 4102-4018.
 - [9]. P. Masset, R.A. Guidotti, *Thermal activated (thermal) battery technology Part II. Molten Salt electrolytes (Review)*, Journal of Power Sources, vol.164,2007, pp. 397-414.
 - [10]. B. Codd, Proceedings of the 33rd Power Sources Conference, 1988, p.359
 - [11]. R.A. Guidotti, F.W. Reinhardt, Proceedings of the Electrochemical Society, 2002-19 (Molten Salts XIII), 2002, p. 63.
 - [12]. R.A. Guidotti, F.W. Reinhardt, Proceedings of the International Symposium on Molten Salts XII, vol. 99-41, 2000, p. 451.
 - [13]. R.A. Guidotti, F.W. Reinhardt, Proceedings of the International Symposium on Molten Salts XII, vol. 99-41, 2006, p. 701.
 - [14]. R.A. Guidotti, F.W. Reinhardt, Proceedings of the 36th IECEC, vol. 1,200, p. 905
 - [15]. R.A. Guidotti, F.W. Reinhardt, Proceedings of the 39th Power Sources Conference, 2000, p. 470
-

DETECTION OF TOTAL ANNUAL RAINFALL TRENDS OF ELAZIĞ CITY, TURKEY

Serkan ŞENOCAK

Atatürk University, Department of Civil Engineering, 25240, Erzurum, Turkey.
ssenocak@atauni.edu.tr

Muhammed Fatih EMEK

Author: 12th Regional Directorate of Highways, 25070, Erzurum, Turkey.
mfemek@gmail.com

Reşat ACAR

Atatürk University, Department of Civil Engineering, 25240, Erzurum, Turkey.
racar@atauni.edu.tr

Abstract

In this study, a possible trend is investigated for total annual rainfalls fall to Elazığ city in Turkey. For this purpose, Mann-Kendall test, Spearman's Rho test and Sen's slope method is applied to total annual rainfall data of 8 rainfall observation stations that is obtained from General Directorate of Meteorology (GDM), changing from 1960 to 2013. The run test (Swed and Eisenharth) and Pettitt tests are used in determine the homogeneity of total annual rainfall data series. According to trend analysis results; decreasing significant trend existence is observed at one rainfall observation station being as Sivrice, for are 95% confidence level. For 90% confidence level, Ağın and Elazığ have also decreasing trends in addition to them. According to Sen's slope method a decreasing direction tendency at all 8 observation stations. These results could be associated with regional climate changes and are consistent with projections related to global changing phenomena.

Keywords: *Elazığ; trend analysis, Mann-Kendall test, Spearman's rho test, Sen's slope method*

1. INTRODUCTION

Due to its importance, climate change has been an active area of research in the last decades. Precipitation is perhaps the most important component of the complex hydrologic cycle because of its impact on our daily life. Therefore, precipitation is often taken as a starting point towards the understanding of changes of the governing processes of climate. Point precipitation data is extensively recorded over the land surface and constitutes an important element for monitoring the hydrological cycle. The study of precipitation variability is very relevant, mainly because of its impact on society, economic activities (e.g. agriculture), land use and water resources. Actually, temperature has the main effect on climatic change, so both precipitation and temperature trend research may be considered together, especially at the interpretation stages [1].

The parameter that shows the greatest variety among the climate elements in terms of time and space is the amount of precipitation and the systematical increases and decreases during this process have the property of being most significant evidence of climate change [2].

How the trend analysis of the rainfalls is well known, defining the future of the water will be just as well known. In this study, the trend of the rainfalls have been determined by using Mann-Kendall test and Spearman's rho test which are nonparametric methods and the trend slopes have been determined by using the Sen's slope test, with the data obtained from the precipitation stations in Elazığ.

2. REGION AND DATA

Elazığ which has rich surface water resources is located in the Eastern Anatolia Region. Euphrates and Dicle Rivers collect all waters of the rivers of the province. The point where Murat and Karasu Rivers join and Murat River and its tributary Peru are now inundated by the Keban Dam Lake. The Karakaya Dam Lake, on the other hand, is located in the bend of Euphrates River Baskilmass. The major tributaries of Murat River located within the province are Haringet and Cip streams.

Hazar Lake is most important natural lake. The lake which is 1248 meters above the sea level is now discharging its water into the Euphrates Basin through a tunnel constructed to operate hydro- power plant in 1957 while it discharged its water only to Tigris River Basin in previous years. Keban Dam Lake is second artificial lake of the Turkey and it has 675 kilometres square area. The area of the Karakaya dam lake is 298 kilometres square. Cip River is a tributary of Murat River. There is a little artificial dam lake back of the Cip Dam which constructed on the Cip River.

In the central and northern parts of Elazığ region, cold-continental climate is dominant, while vicinity of the Keban dam lake is characterised with mild-continental climate.

Elazığ has a continental climate (Köppen climate classification: Dsa) with cold and snowy winters and hot and dry summers. However, due to the natural and artificial lakes around the city, some partial variations from this climate is experienced.

The data of minimum 31 years and maximum 54 years of the 8 precipitation stations, between the years 1960 and 2013 are present. Keban Precipitation Station with 808 m height and Sivrice Precipitation Station with 1300 m height draw attention, when the 8 precipitation stations are considered according to their height from the sea level. In the Figure 1 the station numbers of the 8 stations that are used to be evaluated in this study, the years that the data are obtained and the locations of the stations are shown in Table 1.



Figure 1. Locations of stations

Table 1. Station locations and record duration

Stations	Longitude (E)	Latitude (N)	Elevation (m)	Record Duration
Ağın	38,72	38,94	900	1979–2013 (35)
Baskil	38,83	38,57	1300	1979–2013 (35)
Elazığ	39,26	38,64	989	1960–2013 (54)
Karakoçan	40,04	38,94	1090	1980–2013 (34)
Keban	38,74	38,79	808	1963–2013 (51)
Maden	39,40	38,23	1100	1980–2010 (31)
Palu	39,93	38,69	869	1966–2013 (48)
Sivrice	39,31	38,45	1240	1979–2013 (35)

3. METHODS

Trend, which can also be defined as the long-term movement, is the development or the inclination which a time series shows towards a direction in long-term. Since the trend analysis is a long-term examination, obtaining the data on a monthly or a seasonal basis will not affect the result of the analysis. The trend of a series can be linear or curvilinear. However, the most significant characteristic of the trend is being consistent in both conditions [3].

It can be researched with the statistical tests whether a considerable decrease or an increment (trend) occur in the measured values of a magnitude in the course of time. Since the hydrological magnitudes (precipitation, flow) have a characteristic that changes randomly in time, researching a continuous decreasing or increasing inclination requires the use one of specific methods [4].

3.1. Mann–Kendall Test

Mann-Kendall test is a statistical testing method that is commonly used in defining the trend in time series in hydrology and climatology fields and that is also suggested by World Meteorological Organization (WMO). Mann-Kendall test pulled its rank in trend analysis in several studies. Non-parametric tests are usually more robust compared with parametric ones, among which the Mann–Kendall test is the most used in hydrology and climatology. Therefore, to detect any monotonic trends in the precipitation time series at all considered grid points, the Mann–Kendall test was used. This test consists of comparing each value of the time series with the remaining in a sequential order. The Mann-Kendall statistic S is given as

$$S = \sum_{k=1}^{n-1} \sum_{j=k+1}^n \text{sgn}(x_j - x_k) \quad (1)$$

The application of trend test is done to a time series x_i that is ranked from $i=1, \dots, n-1$ and x_j , which is ranked from $j=i+1, \dots, n$. Each of the data point x_i is taken as a reference point which is compared with the rest of the data points x_j so that,

$$\text{sgn}(x_i - x_j) = \begin{cases} +1 & \text{if } (x_i - x_j) > 0 \\ 0 & \text{if } (x_i - x_j) = 0 \\ -1 & \text{if } (x_i - x_j) < 0 \end{cases} \quad (2)$$

It has been documented that when $n \geq 8$, the statistic S is approximately normally distributed with the mean.

The variance statistic is given as

$$\text{Var}(S) = \frac{n \cdot (n-1) \cdot (2n+5)}{18} \quad (3)$$

The test statistics Z is computed as has been

$$Z = \begin{cases} \frac{S-1}{\sqrt{\text{Var}(S)}} & S > 0 \\ 0 & S = 0 \\ \frac{S-1}{\sqrt{\text{Var}(S)}} & S < 0 \end{cases} \quad (4)$$

Z here follows a standard normal distribution. A positive (negative) value of Z signifies an upward (downward) trend. A significance level α is also utilized for testing either an upward or downward monotone trend (a two-tailed test). If Z appears greater than $Z_{(\alpha/2)}$ where α depicts the significance level, then the trend is considered as significant.

3.2. Spearman's Rho Test

A quick and simple test to determine whether correlation exists between two classifications of the same series of observations is the Spearman's rank correlations test. In this test, there is a significant trend only if the correlation between time steps and rainfall observations are found to be significant. Account of the test statistic Z based on r_s was not presented here, since it can easily be found in statistical books.

The test statistics r_s is computed as

$$r_s = 1 - 6 \cdot [\sum_{i=1}^n (R(x_i) - i)^2] / (n^3 - n) \quad (5)$$

For $n > 30$, the distribution of r_s will be normal, so that the normal distribution tables can be used. In this case, the test statistic r_s is computed by

$$Z = r_s \cdot \sqrt{n - 1} \quad (6)$$

If $|Z| > Z_\alpha$ at a significance level of α ; then the null hypothesis of no trend (on the other word, values of observations are identically distributed) is rejected.

3.3. Sen's Estimator of Slope

If a linear trend is present, the true slope (change per unit time) can be estimated by using a simple non-parametric procedure developed. In computational procedures, the slope estimates of N pairs of data are first computed by

$$Q_i = \frac{x_j - x_k}{j - k} \quad (7)$$

For $i=1, \dots, N$; where x_j and x_k are data values at times j and k ($j > k$); respectively. The median of these N values of Q_i is Sen's estimator of slope. If there is only one datum in each time period, then

$$N = n(n - 1) / 2 \quad (8)$$

where n is the number of time periods. If N is odd, then Sen's estimator is computed by

$$Q_{\text{median}} = Q_{(N+1)/2} \quad (9)$$

and if is even, then Sen's estimator is computed by

$$Q_{\text{median}} = [Q_{N/2} + Q_{(N+2)/2}] / 2 \quad (10)$$

The detected value of Q_{median} is tested by a two-sided test at the $100(1-\alpha)\%$ confidence interval and true slope may be obtained by the non-parametric test.

4. RESULTS

There are several statistical methods to analyze the trend of precipitations. As being used in the trend analyses of several climatic parameters, the nonparametric methods, Mann Kendall test, Spearman's rho test for

analyzing the trend of precipitations and Sen's inclination method for defining the inclination of the trend are preferred. In this trend analysis, it is aimed to evaluate the monthly and annual areal precipitation amounts on the basis of the stations. The annual areal precipitations of each station have been analyzed with Mann-Kendall test, Spearman's Rho test and the Sen's inclination method and the results in Table 2 were obtained.

Table 2. Results of trend analysis

Stations	Mann - Kendall			Spearman's Rho			Sen's Slope
	Z	$\alpha=0,05$	$\alpha=0,1$	Z	$\alpha=0,05$	$\alpha=0,1$	Q
Ağın	-1,704	-	↓	-1,717	-	↓	-3,49
Baskil	-2,073	↓	↓	-1,984	↓	↓	-3,58
Elazığ	-1,895	-	↓	-1,790	↓	↓	-1,66
Karakoçan	0,000	-	-	-0,189	-	-	-0,07
Keban	-1,267	-	-	-1,361	-	-	-1,48
Maden	-1,360	-	-	-1,500	-	-	-5,57
Palu	-1,467	-	-	-1,450	-	-	-2,17
Sivrice	-2,031	↓	↓	-1,998	↓	↓	-4,48

According to Mann-Kendall and Spearman's Rho trend analysis results; significant trend existence is observed at 2 of 8 units rainfall observation stations being as Baskil and Sivrice, annual total rainfalls are 95% confidence level, in addition to these Ağın and Elazığ being as observation stations at 4 units rainfall observation stations annual total rainfalls are 90% confidence level to decreasing direction. Results of trend analysis are shown in the Figure 2.



Figure 2. Results of Mann-Kendall and Spearman's Rho trend analysis

The inclination of the trend in these stations becomes significant following the search of a considerable trend. Sen's inclination method have been used in order to define of the inclination of the trend. As a result of the analyses carried out with Sen's inclination method with the data of 8 precipitation stations; only decrease is observed all 8 stations.

5. CONCLUSION

Since the precipitation is the source of water which is necessary for the life of all living creatures, it is the most important environmental factor that affects the structural properties, species diversity and biotic rhythm of animal and plant associations. Actually following the variations that are observed or expected in precipitations is significant especially for the regions where the drought pose a threat.

In Elazığ, which has the highest potential of water in the Eastern Anatolia Region, the precipitations being in the form of snow and irregular, causes the flow regime to become irregular..

When the data that are obtained from the General Directorate of Meteorology, in order to be used in this study are examined, it has been determined that the station that receives the highest precipitation with average of 840,4 mm is Maden, and the lowest is Keban with the average of 377,6 mm. In addition, when the maximal precipitation was observed in Maden with total of 1293,9 mm in 1987, the minimal was observed in Keban station with 152,8 mm in 2013. When it is evaluated annually in average, between the years 1960 and

2013, 1988 is the year that the maximal precipitation with average of 782,9 mm was received and 2013 is the year that the minimal precipitation with average of 239,0 mm was received.

According to Mann–Kendall trend analysis results; significant trend existence is observed at 2 of 8 units rainfall observation stations being as Baskil and Sivrice, annual total rainfalls are 95% confidence level, in addition to these Ağın and Elazığ being as observation stations at 6 units rainfall observation stations annual total rainfalls are 90% confidence level to decreasing direction.

According to Spearman's Rho trend analysis results; significant trend existence is observed at 2 of 8 units rainfall observation stations being as Baskil and Sivrice, annual total rainfalls are 95% confidence level, in addition to these Ağın and Elazığ being as observation stations at 4 units rainfall observation stations annual total rainfalls are 90% confidence level to decreasing direction. According to Sen's slope method a decreasing direction tendency at 8 units observation stations, and there is no increasing direction is determined.

The results of the analyses that are performed with Mann–Kendall test and Spearman's rho test for the total annual precipitations have showed that there occurred significant decrease in the trend of the same stations, with the confidence interval between 90% and 95%. According to these results, the province of Elazığ and its surroundings is under risk, since it shows a significant decreasing tendency.

In this study, the trend is analyzed by using only the precipitation data. Carrying out similar studies on other meteorological parameters will form a basis both for the confidentiality of this study and also for the studies on climate change. Similarly, evaluating these results with different climate scripts will provide contribution to the determination of the water potential in the future of the region [5].

REFERENCES

- [1]. R. Acar and S. Senocak, *Detection of statistically significant trends in the short duration rainfalls (SDR) of Adana city*, EGU General Assembly 2008: 1522-H52.1 Session on "Climate, Water and Health", 2008.
- [2]. M. Karabulut and F. Cosun, *Kahramanmaraş ilinde yağışların trend analizi*, Coğrafi Bilimler Dergisi, Vol.7(1), 2009, pp.65-83.
- [3]. B.A. Köksal, *İstatistik Analiz Metodları*, Çağlayan Kitabevi, 1998.
- [4]. D.R. Helsel and R.M. Hirsch, *Statistical methods in water resources*, Studies in Environmental Science, Vol.49, 1992.
- [5]. M.F. Emek, *Doğu Anadolu Bölgesi Yıllık ve Aylık Toplam Yağışların Trend Analizi*, Atatürk Üniversitesi Fen Bilimleri Enstitüsü, 2014

PROPOSALS FOR THE PROTECTION OF WATER RESOURCES IN THE PRESPA LAKE BASIN, GREECE

Romanos – Vasileios ARAVIADIS

Araviadis Romanos - Vasileios, 53100, Florina, Greece.

romanosar@yahoo.gr

Abstract

The present paper focuses on the region of Prespa in northwestern Greece, a disadvantaged mountainous region, whose natural environment is protected by numerous international treaties (Ramsar, Natura2000) and which depends heavily on its surface water resources for most of its socio-economical activities. The study area's primary surface water bodies are the trans-border lakes Small and Great Prespa, which, over the years, have witnessed a decline in both the quality and the quantity of their waters. Therefore, the paper's main objectives are to investigate the pressures that the water resources are under and to propose ways to counteract the current negative quantity and quality trends. The research methods employed in the present research include: review of relevant literature and the implementation of a set of methodological tools, namely SWOT Analysis, Stakeholder Analysis and the Logical Framework Approach (LFA). The literature review showed that activities of the primary sector are responsible for the largest percentage of water use in the study area, agriculture being the top consumer of water. Therefore, the paper discusses new irrigation-related technologies, aimed at achieving higher water efficiency and lower levels of agrochemical pollution of the aquifer. The implementation of the methodological tools results in an overall schematization of the factors that can affect water resources in the study area and in probable policy making axes. The research concludes, among others, that the region can exploit several developmental and financial programs in order to achieve the goals of enhancing water quality and quantity and achieving sustainable economic development.

Keywords: *Irrigation, Prespa lakes, Water resources*

1. INTRODUCTION

The protection of the environment and the establishment of a global framework of sustainable development has been a permanent topic in the sector of policy making in recent decades. Indeed, both the continuation of life in general, and the vast majority of modern human activities heavily depend on the condition and availability of natural resources.

Water is one of those natural resources because of its importance both for the continuation of life and for many activities of economic nature, i.e. industry, agriculture, tourism etc.. The importance of water resources is further highlighted in small remote regions where agriculture is usually the main economic activity and the primary source of income.

The Greek part of the Prespa region, which is the focal point of the present paper, belongs to the type of regions described above. It is located in northwestern Greece, on the borders between Greece, Albania and the Former Yugoslav Republic of Macedonia (F.Y.R.O.M.) and gets its name from the two trans-border lakes that are found in it, namely Lakes Small and Great Prespa. Great Prespa Lake is divided between the F.Y.R.O.M., Albania and Greece, whereas lake Small Prespa is divided between Greece and Albania.

It is calculated that 65% of the active population is occupied in the primary sector, the main economic activities - in order of population occupied in them - being: agriculture, stock raising, fishing and forestry. An interesting fact is that about 58% of the crops in the study area are bean cultivations, so that beans can be characterized as a monoculture for the study region [9]. During the last years, activities of the tertiary sector, such as tourism and commerce have also witnessed a development, accounting for the occupation of 23% of the population [10].

The study area also has a unique environmental and ecological value mainly due to its rich biodiversity centered around the Prespa Lakes. Specifically, in the region one can find circa 1500 plant species, 60 mammal species, 33 species of reptiles and amphibians, 23 species of fish – of which 9 are endemic – and 273 bird species, among which the most populous colony of the globally rare Dalmatian pelican in the world [14]. It is calculated that the region of Prespa gathers over 50% of the bird, amphibian and mammal species that can be found overall in Greece [4].

The study area's aforementioned ecological value is reflected on the legal protection regime that exists in the area. As far as national legislation is concerned, the Prespa National Forest was declared in the Greek part of Prespa in 1974 and was extended and renamed to Prespa National Park in 2009, covering 32,700 hectares. As for international legislation, two areas within the Prespa basin, Lake Small Prespa or Micro Prespa and Mount Varnous, have been designated as Special Areas of Conservation (SACs) and Special Protection Areas (SPAs) under Directives 92/43/EC ("Habitats/NATURA Directive") and 79/409/EEC ("Wild Birds Directive") respectively. According to these designations they have been included within the NATURA 2000 network sites, under the codes GR1340001 (Lake Small Prespa) and GR1340003 (Mount Varnous) [6].

Lake Micro Prespa is also one of the 10 sites in Greece designated under the Ramsar Convention on Wetlands, an intergovernmental treaty that provides the framework for national action and international cooperation for the conservation and wise use of wetlands and their resources, as a contribution towards achieving sustainable development throughout the world [6].

For all the reasons described above, it is obvious that the natural environment of the region of Prespa is considered highly valuable. Furthermore, it is obvious that the area's water resources are important both for environmental and for economic and developmental reasons. Therefore, the present paper focuses on investigating the pressures that the study area's water resources are under, on assessing whether corrective plans should be implemented and if so, what those corrective plans should be.

2. MATERIALS AND METHODS

The methods and techniques used in the present research are: the review of the relevant literature and the implementation of methodological tools.

The review of the relevant literature is a standard method used to record the current knowledge and theoretical and methodological contributions on a certain topic. As such, it is not described further in the present paper, as its characteristics can be accessed fairly easily on various sources.

The methodological tools employed in the research are described below.

2.1. SWOT Analysis

SWOT Analysis is a standard tool used in various types of cases and consists in the recording of the Strengths and Weaknesses of an idea or project, in other words, its internal environment, as well as the Opportunities and Threats that can affect its course or development, which, in turn, constitute its external environment. The initial letters of the words Strengths, Weaknesses, Opportunities and Threats make up the name of the method.

After the recording of the various characteristics of the issue under question as described above, Strengths can be combined with Opportunities in order to neutralize Weaknesses and prevent the manifestation of Threats.

In the present paper, the SWOT Analysis was implemented on the study area aiming to form proposals for the protection of water resources.

2.2. The Stakeholder Analysis

The Stakeholder analysis consists in the identification of the implicated parts in a project, proposal or situation, of their interests and their needs in relation with the project under question, as well as the implications-pressures that they cause or that can be caused to them by the implementation of the aforementioned project, proposal or situation [3].

In issues regarding water resources management, the Stakeholder analysis has to include all users of the water resources of the region under question who exercise pressure on said water resources and who would be affected by potential proposals for the improvement in the management of the water potential.

2.3. The Logical Framework Approach

The Logical Framework Approach (LFA) is a method developed by USAID at the end of the 60s and at 1990 by a Norwegian working group supported by Samset & Stokkeland. It is promoted by the OECD and the Directorate General for Development of the Committee of the European Communities [12].

It is a detailed tool, which consists of a series of phases and analyses, designed to cover the stages of planning, implementation and management of projects, management plans and other actions.

Its main component is the Logical Framework Matrix or Logframe Matrix, which summarizes the key elements of a project plan as well as how the main goals of the plan will be achieved. In the present research, it is implemented in order to analyze the strategy axes that are proposed for the improvement of the water resources management as well as for the achievement of sustainable economic development in the study area.

3. RESULTS AND DISCUSSION

All paragraphs must be justified, i.e. both left-justified and right-justified.

3.1. Literature Review on the Pressures on Water Resources

3.1.1. Definition and distinction of pressures

In the framework of the present research, pressures on the water resources of the study region were identified following the definitions and categorization of pressures on the aquatic environment, as defined in the European Union Water Framework Directive, or Directive 2000/60/EC.

According to the latter, pressures on water resources are distinguished, on the basis of the spatial dimension of the activity that causes them, in point pressures and non-point (diffuse) pressures, each one related to various pollution sources [2].

Furthermore, pressures on water resources are distinguished between surface water bodies and groundwater bodies, on the basis of the recipient of the pressure and between pollution pressures, quantitative pressures (abstractions) and other pressures, on the basis of the type of the pressure [9].

3.1.2. Pollution Pressures

- 1) Point pressure sources:
 - Urban waste

The collection of urban waste in all Regional Districts of the Municipality of Prespa is carried out through a sewage network, except for the community of Psarades, where the waste management is done in individual systems, which are examined later on in the part that concerns non-point pressures [9].

In the basin of the Prespa lakes, there are no settlements with more than 2000 inhabitants and therefore, the construction of an Urban Waste Treatment Plant is not required, according to Directive 91/271/EEC. However, in the study area there are two Urban Waste Treatment Plants, which use the method of Constructed Wetlands but are currently under repair works [9].

- Overflows from rainwater pipes

Due to the lack of sufficient data for the assessment of the overflows from rainwater pipes as a point pressure, according to the provisions of Guidance document No21: Guidance for Reporting under the Water Framework Directive, they are elaborated together with diffuse runoff from urban areas later on.

- Industry

There is no remarkable industrial unit operating in the study area.

- Stabled livestock

Stock raising is an important traditional economic activity in the study region. However, only the breeding of swine can be included in the category of activities that cause point pressure because swine raising units, due to the nature of these animals, require special constructions in a designated space, excluding the possibility of free farming [9].

- Fishfarming

No fisheries are found in the study area.

- Landfill sites

Solid waste in the Municipality of Prespa and the regional district of Kristallopigi is gathered and transferred to the Waste Transshipment Stations of the neighboring cities of Florina Kastoria and from there they are transhipped to the regional landfill of Kozani. In any case, there is no pressure caused by landfill sites in the study area [9].

- Extractive activity

The operation of quarries or other extractive activities is not permitted within the Prespa National Park, hence there is no pressure caused by extractive activities [9].

2) Non-point pressure sources

- Urban runoff and overflows from rainwater pipes

Rainwater is the runoff that goes through built areas and often carries a large variety of pollutants, in quantities that can negatively influence the environment, the surface water recipients but also the underground aquifers. Due to the lack of data on the management of the overflows of rainwater in the settlements of the study area, the assessment of the pressure under question is considered related primarily to the surface area and the use of its built areas [9].

According to the relevant literature, a percentage of urban coverage lower than 3% advocates for an urban runoff and rainwater pipe overflow pressure of low intensity. Urban areas in the study region cover an area of 1.66 km², which correspond to about 0.5% of the total surface area of the study region. In conclusion, it can be estimated that the pressure on the surface water bodies of the study area which is caused by urban runoff and overflows from rainwater pipes is of low intensity [9].

- Transportation networks

The road network within the study area is mostly provincial, forestal or rural and the regional network has small length and a low daily traffic load. Therefore, runoff from the road network is not a significant pressure on the quality of the surface water resources [9].

- Urban liquid waste not treated by a Waste Treatment Plant

The disposal of waste in individual sewage systems is considered a non point pollution. In the study area, this practice is in use only in the Regional district of Psarades of the Municipality of Prespa, which has a population of 83 inhabitants [9]. The estimation of the pollutant loads that end up in Lake Great Prespa are shown on table 3.

- Outflows from agricultural activity
-

Pollutant loads which come from agricultural activities include nitrogen loads, phosphorus loads and pesticide residues. A percentage of the outflowing loads corresponds to the runoff, which burdens the surface waters and a part of them leaches towards deeper ground layers and may burden the waters of the aquifer. The measure of the pollutant load that ends up in the aquatic system depends on its type, on its quantity, on the way and the time of application, on the position and the morphology of the land parcel, on the presence and density of a drainage system and on a large number of ground-related factors [9].

- Livestock raising

The sector of livestock raising, except for swine breeding, is included in the activities causing non point pollution on the basis of several criteria concerning the nature of this activity. The basic pollutants produced by livestock are: organic load, nitrogen and phosphorus. According to the relevant literature, the percentage of the produced load that is a runoff to the aquatic systems is 15% for nitrogen and 3% for phosphorus. Furthermore, deep leaching is considered to account for 17% of the nitrogen runoff and for 1% of the phosphorus runoff [9].

- Spaces of uncontrolled waste disposal

Uncontrolled waste disposal is a practice which has been abandoned in the study region, hence there is no pollutant load produced by sites of uncontrolled waste disposal [9].

- Outflow from other land uses

According to Guidance Document 3 for the Directive 2000/60/EU, “Analysis of pressures and impacts”, the primary land uses that are calculated as pressures are urban, forest, herbaceous and bushy areas and agricultural uses. The pressures caused by these uses can be quantified in Total Nitrogen (TN) and Total Phosphorus (TP) [9].

3.1.3. Quantitative Pressures (Abstractions)

Quantitative pressures in the study area’s water resources are reported herein according to the main use which they stem from.

1) Abstractions for irrigation

According to the relevant literature, the total abstractions for irrigation are estimated at around 5.9 hm³/year, of which 5.02 hm³/year are abstracted from surface waters – most of them from Lake Small Prespa- and 0.32 hm³/year are abstracted from ground waters [9].

2) Abstractions for water supply

According to the same source, abstractions for the area’s water supply are estimated at around 0.37 hm³/year, of which 0.24 hm³/year are abstracted from surface waters and 0.13 hm³/year from ground waters [9].

3) Abstractions for livestock breeding

On the same logic, abstractions for livestock are estimated at around 0.2 hm³/year and are abstracted from ground waters [9].

From the data presented above, it becomes obvious that irrigation is the largest consumer of water in the study area and also that the largest quantity of water is abstracted from surface waters, and from the Lake Small Prespa specifically.

3.1.4. Other pressures

The types of “other pressures” defined by the Directive 2000/60/EC are:

- flow regulations – hydromorphological alterations
- artificial recharge of aquifers
- desalination
- sand extractions

For the study region, the relevant literature records that none of the types of pressures mentioned above have an impact on the water resources of the study area [9].

3.1.5. Status of water resources

According to the literature, Directive 2000/60/EC characterizes the ecological and chemical status of surface water resources and quantitative and qualitative status of ground water resources.

For the study area, all groundwater systems are given a Good quantitative and qualitative status [9].

The area's fluvial water bodies are characterized by a "Good" chemical status, whereas their ecological status is unknown [9].

As for the lacustrine water bodies, Lake Great Prespa's ecological condition is characterized as "Moderate" and Lake Small Prespa's as "Poor". However, the most remarkable fact is that the chemical status of both Lakes is characterized as "Bad" [9].

3.2. Implementation of methodological tools

3.2.1. The SWOT Analysis

In order to form proposals for the protection of the water resources in the study area, a SWOT analysis was performed with the aim to record the strengths, weaknesses, opportunities and threats that are present in the region of Prespa. They are recorded as follows:

- 1) Strengths
 - Existence of rare biodiversity, protected by the Ramsar Convention
 - Area with a remarkable natural environment, included in the Natura 2000 network
 - Existence of a large number of studies for the area, that have been executed in the framework of developmental programs and programs of trans-border cooperation (Interreg, Life 2014-2020, Horizon, OEMN etc.)
 - Presence of environmental organizations in the area
 - Existence of the monoculture of beans, characterised as product of Protected Geographical Indication (PGI)
 - Existence of organic farming, mainly of Prespa beans
 - Progress of the study for the installation of a drip-irrigation network in the study area
 - 2) Weaknesses
 - Old existing irrigation network, causing remarkable water losses and low irrigation water efficiency
 - Drawdown of Great Prespa Lake, primarily from the 80s onward
 - Lack of a common Management Plan for the Prespa Basin in transnational level between the countries which share the Prespa Lakes
 - 3) Opportunities
 - Application of Directive 2000/60/EU via the publication of the Management Plan for the river basins of the River basin District of Western Macedonia and that of the Special Management Plan of the basin of Prespa.
 - New Common Agricultural Policy for the period 2014-2020, including financial aids like: coupled payments for Natura 2000 areas, for bean cultivation, for disadvantaged/mountainous regions, for organic farming etc.
 - New national Rural Development plan for the period 2014-2020
 - Increase in eco-tourism and agro-tourism
 - Possibility of certification of agricultural products
 - 4) Threats
 - Non-global confrontation of problems in a trans-boundary river basin level because of the lack of a common Management Plan
 - Quantitative and qualitative degradation of the water resources caused by human activities
-

- Difficult economic period
- Intense weather phenomena – climatic change
- Possible proposals for the protection of water resources can arise from the combination of points from the above recorded SWOT analysis, so that strengths can attract opportunities to prevent the manifestation of threats.

As it was mentioned beforehand, specifically in section 2.1, the points of the SWOT analysis that can be combined on the basis of the previous reasoning can be summarized as following:

For starters, the rich faunal and floral biodiversity of the study area – which is under numerous protection regimes – and the intense presence of a virgin natural environment are elements that can create opportunities for the growth of tourism, especially environmental tourism, agro-tourism etc.

Secondly, the presence of the bean monoculture creates opportunities for the certification of this product and the creation of a stronger “brand-name” for the area.

Also, organic farming can spread further with the financial aids for organic farming provided by the new Common Agricultural Policy.

In addition, the perspective of the installation of a new drip-irrigation network for the crops of the study area is an opportunity to solve the problems caused by the existing irrigation network and to avoid the threat of the qualitative and quantitative degradation of the water resources.

Finally, the lack of a common trans-border-level Management Plan for the basin of Prespes is a weakness of the study area, which can allow for the manifestation of the threat of a non global confrontation of environmental problems. However, there is a variety of developmental trans-border programs that have taken place and are in progress, which can help prevent the threat under question.

3.2.2. The Stakeholder Analysis

The second methodological tool that was used in the process of forming proposals for the protection of the water resources in the study region is the Stakeholder analysis. A brief description of this analysis can be found on sub-section 2.2. of the present paper.

The Stakeholder Analysis as it was implemented for the issue under question is presented on table 1, further down.

3.2.3. The Logical Framework Approach

The last methodological tool that was used in the process of forming proposals for the protection of the water resources in the study region is the Logical Framework Approach. A brief description of this method can be found on sub-section 2.3. of the present paper.

The Logframe matrix for the issue at hand is shown in table 2.

Table 1. Stakeholder Analysis for the region of the Prespa Lake basin

Stakeholder	Interests	Needs	Implications/Pressures they can cause	Implications/Pressures they may suffer
Farmers	The water resources' good quality is important for the good quality of the crops produced	Water of certain quantity and good quality - Efficient irrigation network	Degradation of water resources' quality due to agrochemicals	Loss of income due to water losses from irrigation network
Livestock breeders	The water resources' good quality is important for the health of the stock	Water of certain quantity and good quality	Degradation of water resources' quality due to livestock waste	Negative implications on health of their stock due to pollution of water resources
Fishers	The water resources' good quality and quantity are important for the reproduction and health of the fish	Good quality and, if possible, ceasing of the drawdown in lake waters	Imbalance in the lakes' ecosystems due to overfishing	Reduction of fish population due to pollution and drawdown of lake waters
Residents	The water resources' quality affects their health	Potable water of good quality	Degradation of the lakes' waters due to littering – Over	Negative effect on their health due to pollution of the aquifer

	via drinking water – The less polluted the water is, the lower the treatment costs will be The better the state that the Lakes’ environment is in, the more they feel satisfied with their destination choice - The water resources’ quality affects their health via drinking water The better the state that the Lakes’ environment is in, the more satisfied their customers will be	Potable water of good quality – Good state of the natural environment	consumption of potable water Degradation of the lakes’ waters due to littering - Wasting of potable water	Negative effect on their health due to pollution of the aquifer – Negative impression by the state of the destination they chose
Tourists				
Touristic facility owners		Potable water of good quality – Good state of the natural environment	Overuse of water supplies	Loss of customers due to unattractive state of the natural environment

Table 2. Logical Framework Matrix for the study area

Goal: The protection of water resources in the study area and the achievement of sustainable development

Description	Indexes	Means of Verification	Assumptions and risks
1. Improvement of qualitative state of the water resources	Pollution Indexes - Characterization of qualitative status of aquatic systems	Measurements – Monitoring of physicochemical parameters and of special pollutants in the river basin	Active commitment of the three neighbouring countries in the control and monitoring of the quality of waters – Implementation of national and community legislation – Implementation of Directive 2000/60/EU – Implementation of river basin management plan – Low increase of population
1.1. Actions for the concentration of hazardous pollutants in the water bodies	Concentrations of hazardous pollutants and physicochemical variables, according to directives – Characterization of the water bodies’ ecological and chemical situation	Field measurements	Approval of necessary funds – Implementation of the appropriate regulations
1.2. Establishment – reinforcement of monitoring mechanisms	Staffing of municipal, regional and national authorities	Reports by said authorities – Posting of work position notices	Approval of necessary funds – Active commitment by authorities Implementation of Directive 2000/60/EU - Implementation of river basin management plan -
2. Quantitative improvement of water resources	Water Exploitation Index (WEI) – Basin water balance – Levels of the basins water bodies	Measurement of abstractions per use of water – Measurement of rainfall/precipitation	Active commitment of the three neighbouring countries in the control and monitoring of the quantity of waters - Low increase of population – Installation of drip irrigation network in the Greek part of the basin
2.1 Promotion of the installation of irrigation systems	Implementation studies – Inclusion of actions in financial programs	On the spot research/autopsy – Implementation studies	Approval of necessary funds
2.2. Pricing actions	Review – Modification of legislation	Publication of law review	Prioritization of the present issue by appropriate authorities
3. Achievement of conditions of economic development	Inhabitants’ income pro capita – Increase of population – Increase in work positions	Population census – Regional reports on economy and occupation	Confrontation of difficult economic situation – Diffusion of agricultural products within the basin area – Turn towards

3.1. Actions for the reinforcement of agriculture	Quantities of produce – Producers' income	Records by agricultural cooperatives - Regional reports on agricultural production	alternative tourism – Touristic growth Prioritization of the present issue by appropriate authorities - Confrontation of difficult economic situation – Use of the new CAP
3.2. Actions for the reinforcement of commerce	Quantities of purchased/sold products - Income	Records by the appropriate authorities - Regional reports on commerce	Prioritization of the present issue by appropriate authorities - Confrontation of difficult economic situation – Use of the new CAP
3.3. Actions for the reinforcement of tourism	Arrivals/Visits by tourists	Records by the Hotel owners' Association of Florina	Prioritization of the present issue by appropriate authorities – Promotional campaigns

3.3. Discussion

As it has been pointed out beforehand, irrigation is the primary consumer of water in the study area. Furthermore, as demonstrated by the results of the implementation of the LFA in the area, the installation of irrigation-related systems is one of the actions proposed towards achieving the goal of the quantitative improvement of the water resources. Therefore, the present research proposes a set of irrigation-related systems that can assist in the achievement of the aforementioned goal.

1) Installation of a drip irrigation network

The advantages of drip irrigation are widely known. For the study area, the function of a drip irrigation system is expected to lead to the irrigation of a more extended area with the same amount of water. Furthermore, it is expected to lead to a considerable reduction in the washout of the terrains and a consequent need to use less fertilizer. This, in combination with the more effective application of water in the root region of the plants will result in less diffuse development of parasitic weeds and consequently, to the use of inferior quantities of herbicides. The lower cost that the producers will have to incur and the expected higher productivity are expected to lead to a better living standard. Finally, the lower expected use of fertilizers and herbicides is expected to lead in the reduction of the concentration of hazardous substances in the aquifer, as these substances end up in the aquifer or the lakes either through the ground or via surface runoff.

2) Reuse of treated wastewater in irrigation

The use of treated wastewater for irrigation is a popular practice in many countries, especially arid and semi-arid ones [13]. Many studies have tested its effects on fruit yield and quality [8, 7, 14] and it has also been tested in combination with drip-irrigation systems and Waste Treatments Plants using the method of Constructed Wetlands, a method which is being used in the Waste Treatment Plants of the study area [1].

3) Automated Water-intake Device for irrigation

The following system focuses on the economical use of water resources. With the aid of an electronic card, a farmer can purchase water quantity units. Subsequently, he/she has the ability to pump the quantity of water he wishes to apply to his parcel. After the quantity has been applied, the pump is automatically switched off, thus avoiding potential waste of water and higher water costs for the farmer. After the end of the irrigation session, the appropriate amount of water quantity units is subtracted from the quantity that the farmer has paid for beforehand.

4) Precision agriculture

Precision agriculture is a new agricultural practice, which utilizes specific information, defined in space and time, to assess the right amount of water or fertilizer needed in a specific area of the crop's surface [5]. In that way, it takes potential variabilities within the same parcel into account.

Precision agriculture utilizes technologies, such as productivity maps, GPS systems, laboratory analyses, GIS and systems of variated application (of fertilizer or water), in order to accurately apply the correct quantities of substances to a particular area of the parcel, depending on the needs of the area under question.

4. CONCLUSIONS

In conclusion, the present paper focuses on the region of the Prespa basin, in northwestern Greece, a tri-state trans-border region with valuable ecosystems and virgin natural environment, which is protected by national and international environmental treaties and legislation. Lakes Small and Great Prespa are the center of this region and take part in most of its socio-economic activities.

According to the literature review that was conducted during the present research, it was found that the quality and quantity of the water resources of the study region have both witnessed a decline. Therefore, the paper analyzed the various kinds of pressure that the water resources are under and subsequently applied a set of methodological tools in order to schematize the study area's environment and to discover ways that the current negative quality and quantity trends can be reversed.

The SWOT Analysis recorded the basic characteristics of the study area and combined them with one another in order to discover ways to create opportunities for economic development and protection of the water resources. The Stakeholder Analysis recorded all the users of water resources in the area along with their interests and needs from using water and the pressures-impacts they can cause or that can be caused to them. Finally, the Logical Framework Approach set the improvement of the qualitative and quantitative state of the water resources in the study area as the main strategy axes and subsequently described actions through which they can be achieved. It can be concluded that with the use of financial aid provided by the new Common Agricultural Policy as well as by programs of developmental nature (Horizon 2020, Interreg etc.), the study region can implement the actions proposed by the present paper towards the goal of protecting the water resources, like the installation of new irrigation-related systems.

ACKNOWLEDGMENT

The present research has been executed with the sponsorship of the fellowship program "IKY FELLOWSHIPS OF EXCELLENCE FOR POSTGRADUATE STUDIES IN GREECE – SIEMENS PROGRAM", to which I wish to express my gratitude.

Furthermore, I would like to thank the organizing committee of the International Conference on Engineering and Natural Sciences 2015 (ICENS 2015) for accepting the present paper for presentation.

REFERENCES

- [1]. Cirelli, G.L. et al., (2012). Treated municipal wastewater reuse in vegetable production. *Agricultural Water Management*, vol. 104, pp. 163– 170.
 - [2]. Directive 2000/60/EC of the European parliament and of the council of 23 October 2000 establishing a framework for Community action in the field of water policy [2000] OJ L327/1
 - [3]. European Training Foundation (1996). *Tempus Tacis Project Management handbook* [Online]. Office for Official Publications of the European Communities, Luxembourg. Retrieved 29 April 2015. Available: http://eacea.ec.europa.eu/tempus/doc/tacishandbook_en.pdf
 - [4]. JunEx. Biodiversity and habitat types [Online]. Retrieved 27 April, 2015. Available: <http://www.junex.gr>
 - [5]. Karydas, C., Silleos, N., Silleos, G. A new precision farming technique, for use on a wheat crop under Mediterranean agronomic conditions. *6th Balkan Conference on Operational Research*, 22-25 May 2002, Thessaloniki, Greece.
 - [6]. Koutseri, I. (2012). Saving fish biodiversity in the Prespa basin. LIFE09 INF/GR/319 project. Society for the Protection of Prespa
 - [7]. Manas, P. et al. (2002). Aptitud agronomica del agua residual depurada procedente de la E.D.A.R. de Albacete. *Invest. Agr.: Prod. Prot.Veg*, vol. 17 (1).
 - [8]. Mavrogianopoulos, G. and Kyritsis, S. (1995). Use of municipal wastewater for biomass production. Project report of Agricultural University of Athens.
 - [9]. Ministry of the Environment and Climatic Change (2014). Special Management Plan for the Sub-basin of Prespa of the River basin of Prespa (GR01) of the River basin District of Western Macedonia (GR09). Annex to the "Management Plan for the River basins of the River basin District of Western Macedonia"
 - [10]. Municipality of Prespes. Economy – The secondary sector [Online]. Retrieved 20 April, 2015. Available: <http://www.prespes.gr>
 - [11]. Municipality of Prespes. Economy - The tertiary sector – Current situation of services [Online]. Retrieved 1 May, 2015. Available: <http://www.prespes.gr>
 - [12]. Norwegian Agency for Development Cooperation (NORAD) (1999). The Logical Framework Approach (LFA). Handbook for objectives-oriented planning.
 - [13]. Pedrero, F. et al. (2010). Use of treated municipal wastewater in irrigated agriculture – Review of some practices in Spain and Greece. *Agricultural Water Management*. vol. 97. pp. 1233-1241.
 - [14]. Pedrero, F. and Alarcon, J.J. (2009). Effects of treated wastewater irrigation on lemon trees. *Desalination*, vol. 246, pp. 631–639.
 - [15]. Society for the protection of Prespa. Habitats and endangered species. Retrieved 30 April, 2015. Web site: <http://www.spp.gr>
-

EMPLOYEE SELECTION WITH ANALYTIC HIERARCHY PROCESS IN CLOTHING SECTOR: TURKISH CASE

Seher KANAT

Dr., Ege University, Department of Textile Engineering, Bornova, İzmir, Turkey,
seher.kanat@ege.edu.tr

Turan ATILGAN

AProf. Dr., Ege University, Department of Textile Engineering, Bornova, İzmir, Turkey,
turan.atilgan@ege.edu.tr

Abstract

Competition is increased day by day in clothing sector which has a significant place in Turkish economy with its export potential and employment. The enterprises, which desire success under intense rivalry, must give great importance to labor which is a classic production factor. When the labor intensive structure of clothing sector is taken into consideration, the importance of labor can be understood better. At this point, the enterprises confront with the employment of qualified, well educated and knowledgeable employees as an important factor which increases their competitiveness. Therefore, the clothing enterprises must select their qualified employees correctly. Analytic hierarchy process is one of these methods which can be used in accordance with this purpose. Analytic hierarchy process is one of the multi criteria decision making methods and it provides a selection from among alternatives. Analytic hierarchy process is a fast, effective and easy applicable method in cases where the number of criteria and alternatives are surplus just as employee selection in clothing sector. The managers of clothing enterprises can manage the qualified employee selection process effectively and successfully by using this method. Within the scope of this study, the blue-collar employee selection of a clothing enterprise, which operates in İzmir province and takes place within the 500 biggest industrial enterprises of Turkey, will be performed with analytic hierarchy process and suggestions will be made related to blue-collar employee selection criteria.

Keywords: *Employee selection, analytic hierarchy process, Turkish clothing sector*

1. EMPLOYEE SELECTION PROCESS

Employee selection is the evaluation of worker candidates, who apply for any job within the organization, according to the criteria like knowledge, skill, ability and attitude and states a decision situation which is concluded in acceptance or rejection [7]. The main purpose of the employee selection process is to find the workers who are most appropriate to the job requirements [3]. An employee selection process, which depends on objective criteria, creates a trust towards the enterprise and also provides an efficient work environment due to the selection of the best candidates [7]. In this context, the employee selection process involves the curriculum vitae (CV) applications, application forms, examinations (psychology and ability tests), interviews, getting information about candidates, employee selection decision, physical examination report, recruitment and orientation [3,7].

The techniques which are used in employee selection process can be listed as; the evaluation of CVs and application forms, research about the candidates' past, written and oral examinations, tests (intelligence, ability, personality, attention, creativity, knowledge, memory and perception), interview and physical examination [5,8,11].

Most common reasons for elimination can be summarized as; lack of adequate educational and performance record, obvious misfit from outward appearance and conduct, failure to meet minimum standards, failure to have minimum necessary aptitude, negative aspects of personality, unfavorable or negative reports on past performance, lack of necessary innate ability, ambition or other qualities, physically unfit for job, remaining candidate placed in available position [4].

There are many researches within the literature which use analytic hierarchy process (AHP) for employee selection. These researches generally focus on white-collar employee selection. The main criteria that are determined within these researches can be summarized as; before the interview, the interview, after the interview, general abilities, general culture, personality, foreign language level, creative thinking, research skills, graduation level, professional experience, pre-assessment process, technical evaluation, references, main characteristics, core competencies and complementary characteristics. The sub-criteria can be listed as; curriculum vitae, education level, work experience, foreign language, personality, references, verbal skills, mathematical skills, visual skills, general culture, dynamism, strength, sociality, self-confidence, computer knowledge, adaptation to organizational culture, eagerness to learn, team leadership, communication, planning and organization, stress endurance, predisposition towards shift working, earning expectation, technical information, customer orientation, job appropriation, team awareness, analytic thinking, follow and control abilities, problem solving abilities, reporting abilities, appearance, talking abilities, expression abilities, consistency and willingness to work [2, 5, 8, 10,11].

At the research which is conducted by Göklüberk Özlü (2006), employee selection process in clothing sector is investigated. According to the research results, blue-collar employee selection techniques in the clothing sector can be summarized as; written examination, oral examination, interview, practice examination, tests, evaluation of the application forms and references. The properties which will be searched in production employees (sewing, cutting, ironing, quality control and preparation employees) are determined as; machine and equipment utilization knowledge, technical information and skills, education level, work experience and pattern knowledge [6].

At another research which is conducted by Şener (2011), employee selection process of an integrated textile enterprise is fulfilled by analytic hierarchy process. The selection is performed for clothing quality control employee candidates. The main criteria are determined as; expected main properties, expected core competencies (social and technical) and expected complementary characteristics. The sub-criteria can be listed as; technical information, work experience, education level, job appropriation, aptitude for team work, flexibility, willingness to novelty and alteration, color separation, attention, hand-eye coordination, manual skill, reporting ability, self-expression ability, consistency, willingness to work and communication skill [12].

2. MATERIAL AND METHOD

The aim of the research is to perform the blue-collar employee selection of a clothing enterprise with analytic hierarchy process, which operates in İzmir province and takes place within the 500 biggest industrial enterprises of Turkey. In this context, an interview is made with human resources manager and production manager of the enterprise. The enterprise uses curriculum vitae and application form evaluation, interview, technical oral examination, technical practice examination, physical examination report evaluation and two months testing period techniques in blue-collar employee selection process.

The blue-collar employee selection criteria, which are determined with the help of literature, are updated according to the criteria that are significant for the enterprise during the interview. The blue-collar employee criteria are altered according to the production processes in which employees are involved. In our study,

sewing and quality control processes, which are the significant and critical points of the production, are taken into consideration. Therefore, the criteria are determined separately for sewing and quality control employees. After that, the managers give points to the employee candidates according to these criteria via the survey. The obtained points are evaluated separately for sewing and quality control employee candidates via analytic hierarchy process which is a mathematical modeling technique.

Table 1. Evaluation scale of analytic hierarchy process [1]

Numerical Value	Definition
1	Equal importance
3	Moderate importance
5	Strong importance
7	Very strong importance
9	Extreme importance
2,4,6,8	Intermediate values

Analytic hierarchy process is one of the multi-criteria decision-making techniques and it is defined by Professor Thomas L. Saaty. It possesses a wide application area and it is efficiently used in many decision-making problems. The analytic hierarchy process model starts with aim. The aim is followed by main criteria, sub-criteria and alternatives respectively. The basic problem of the multi-criteria decision process is the importance determination for alternatives by taking the criteria into consideration. Decision-maker gives points to the alternatives according to the criteria, which are found at the higher level within the hierarchy, in order to determine the relative importance levels. The points are given according to the scale which is shown in Table 1 and the paired comparison matrixes are constituted [1].

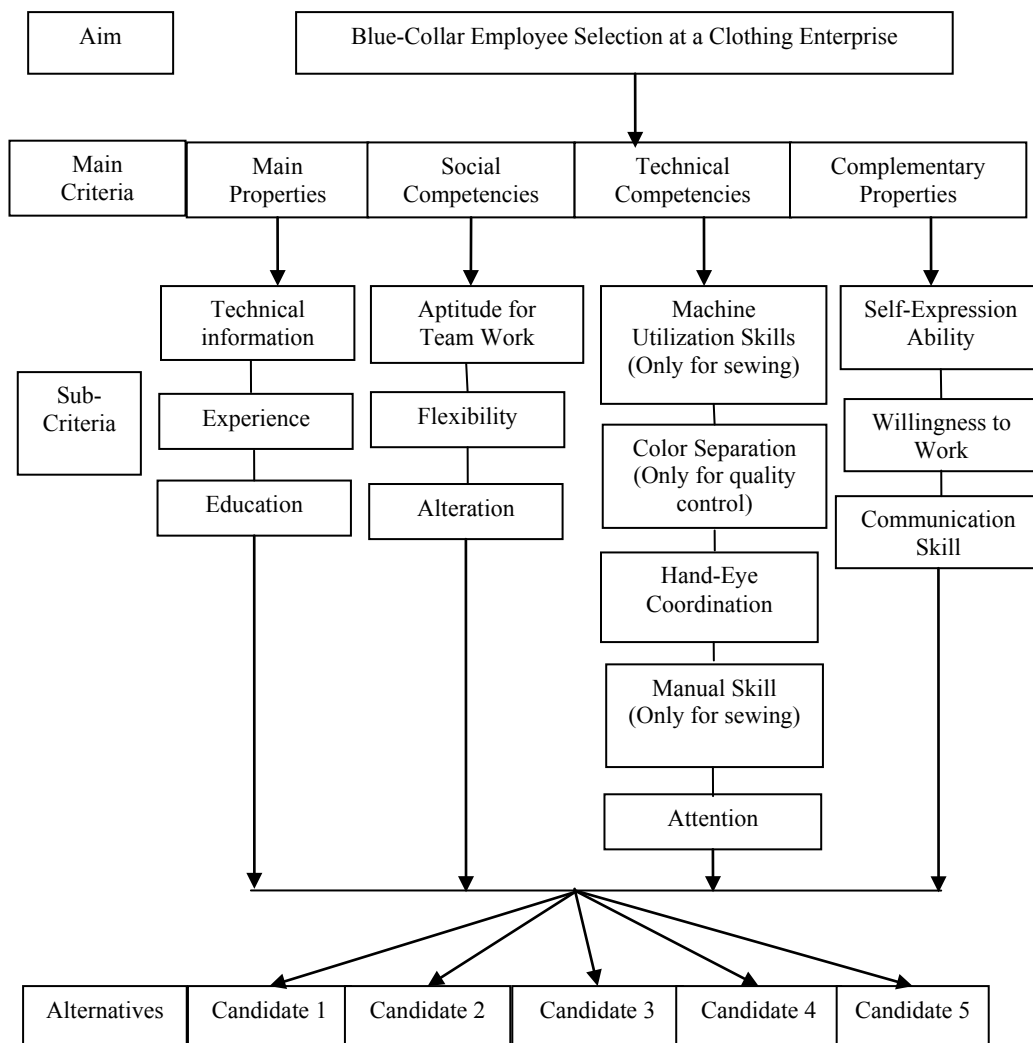


Figure 1. The model constituted within the scope of the research

Within the scope of the research a model is constituted (Figure 1) and survey questions are prepared via this model. The main criteria and sub-criteria within the model are determined with the help of the literature [6,12] and the interview which is made at the enterprise. According to these, 4 main criteria and 13 sub-criteria are determined for sewing employees whereas 4 main criteria and 12 sub-criteria are specified for quality control employees. Main properties, social competencies, technical competencies and complementary properties are determined as main criteria for both groups. Sub-criteria for both groups are specified as; technical information (professional knowledge), work experience (professional experience), education level, aptitude for team work, flexibility (easy orientation to different processes and technologies), willingness to novelty and alteration, self-expression ability, willingness to work, communication skill, attention and hand-eye coordination. In addition to these properties, manual skill (grasp, curling and twisting abilities of the fingers, hand and wrist) and machine and equipment utilization skills are expected from sewing employees. On the other hand, the color separation ability (non color blindness diagnosis with physical examination) is expected from quality control employees. The sewing and quality control employee candidates constitute the alternatives of the model.

The survey involves 13 main, 65 sub questions for sewing employees whereas 12 main, 60 sub questions for quality control employees. An example from survey questions is shown in Table 2. The obtained data are transferred to paired comparison matrixes (130 matrixes for sewing employees and 120 matrixes for quality control employees) via the original method [9]. After that, the paired comparison matrixes are transferred to the 2.2.6.0 version of Super Decisions program.

Table 2. An example from survey questions

Attention Please: The points of the candidates are increased from 2 to 9 within the options. 2 represent the minimum point whereas 9 represent the maximum point. 1 point shows that all candidates are at the same advantage (point) level. In each line only one number can be chosen. The same point (in an example 8) can be chosen for all candidates.

1. Give points to the sewing employee candidates according to their technical information (professional knowledge).

Candidate 1	1	2	3	4	5	6	7	8	9
Candidate 2	1	2	3	4	5	6	7	8	9
Candidate 3	1	2	3	4	5	6	7	8	9
Candidate 4	1	2	3	4	5	6	7	8	9
Candidate 5	1	2	3	4	5	6	7	8	9

Table 3. An example from paired comparison matrixes

1. Compare the sewing employee candidates dually according to their technical information (professional knowledge). The figures which are located in the left part of 1 indicate that the left candidate is more advantageous according to the right candidate whereas the figures that are located in the right part of 1 indicate that the right candidate is more advantageous according to the left candidate. Number 1 shows that both candidates are at the same advantage (point) level.

Candidate 1	9	8	7	6	5	4	3	2	1	2	3	4	5	6	7	8	9	Candidate 2
Candidate 1	9	8	7	6	5	4	3	2	1	2	3	4	5	6	7	8	9	Candidate 3
Candidate 1	9	8	7	6	5	4	3	2	1	2	3	4	5	6	7	8	9	Candidate 4
Candidate 1	9	8	7	6	5	4	3	2	1	2	3	4	5	6	7	8	9	Candidate 5
Candidate 2	9	8	7	6	5	4	3	2	1	2	3	4	5	6	7	8	9	Candidate 3
Candidate 2	9	8	7	6	5	4	3	2	1	2	3	4	5	6	7	8	9	Candidate 4
Candidate 2	9	8	7	6	5	4	3	2	1	2	3	4	5	6	7	8	9	Candidate 5
Candidate 3	9	8	7	6	5	4	3	2	1	2	3	4	5	6	7	8	9	Candidate 4
Candidate 3	9	8	7	6	5	4	3	2	1	2	3	4	5	6	7	8	9	Candidate 5
Candidate 4	9	8	7	6	5	4	3	2	1	2	3	4	5	6	7	8	9	Candidate 5

3. FINDINGS OF THE RESEARCH

Table 4 and 5 are obtained via Super Decisions program which show the priority values of alternatives. Besides, Table 6 and 7 show the limit super matrix forms which are also obtained via the program.

Table 4. The priority values of alternatives for sewing employee candidates

Alternatives	Normalized by cluster	Limiting values
Candidate 1	0,30578	0,305780
Candidate 2	0,27081	0,270814
Candidate 3	0,20352	0,203516
Candidate 4	0,11222	0,112216
Candidate 5	0,10767	0,107674

Table 5. The priority values of alternatives for quality control employee candidates

Alternatives	Normalized by cluster	Limiting values
Candidate 1	0,29062	0,290619
Candidate 2	0,18077	0,180768
Candidate 3	0,24086	0,240861
Candidate 4	0,18721	0,187214
Candidate 5	0,10054	0,100538

Table 6. Limit super matrix for sewing employee candidates

	Candidate 1	Candidate 2	Candidate 3	Candidate 4	Candidate 5
Technical information (Professional knowledge)	0,414680	0,257293	0,152895	0,087566	0,087566
Work experience (Professional experience)	0,285714	0,142857	0,285714	0,142857	0,142857
Education level	0,166667	0,166667	0,333333	0,166667	0,166667
Aptitude for team work	0,303106	0,303106	0,064870	0,164459	0,164459
Flexibility (Easy orientation to different processes and technologies)	0,327608	0,327608	0,193835	0,075475	0,075475
Willingness to novelty and alteration	0,327608	0,327608	0,193835	0,075475	0,075475
Machine and equipment utilization skills	0,250000	0,250000	0,250000	0,125000	0,125000
Attention	0,431846	0,277525	0,178847	0,055891	0,055891
Hand-eye coordination	0,359466	0,359466	0,153473	0,063798	0,063798
Manual skill (Grasp, curling and twisting abilities of the fingers, hand and wrist)	0,259932	0,259932	0,259932	0,138155	0,082048
Self-expression ability	0,267509	0,267509	0,267509	0,148398	0,148398
Willingness to work	0,230769	0,230769	0,230769	0,076923	0,230769
Communication skill	0,350237	0,350237	0,080688	0,138150	0,080688

Table 7. Limit super matrix for quality control employee candidates

	Candidate 1	Candidate 2	Candidate 3	Candidate 4	Candidate 5
Technical information (Professional knowledge)	0,368940	0,109265	0,206265	0,206265	0,109265
Work experience (Professional experience)	0,111111	0,111111	0,333333	0,333333	0,111111
Education level	0,500000	0,125000	0,125000	0,125000	0,125000

Aptitude for team work	0,222222	0,222222	0,222222	0,222222	0,111111
Flexibility (easy orientation to different processes and technologies)	0,297834	0,157772	0,297834	0,157772	0,088788
Willingness to novelty and alteration	0,297834	0,157772	0,297834	0,157772	0,088788
Color separation ability (Non color blindness diagnosis with physical examination)	0,222222	0,222222	0,222222	0,222222	0,111111
Attention	0,439655	0,158013	0,158013	0,158013	0,086305
Hand-eye coordination	0,259932	0,138155	0,259932	0,259932	0,082048
Self-expression ability	0,272727	0,272727	0,272727	0,090909	0,090909
Willingness to work	0,222222	0,222222	0,222222	0,222222	0,111111
Communication skill	0,272727	0,272727	0,272727	0,090909	0,090909

The research model achieves its aim with the last calculation and evaluation process and the blue-collar employee selection for sewing and quality control departments of a clothing enterprise is occurred. According to the obtained results, the most appropriate candidate for sewing is Candidate 1 (30,57%). This candidate is followed by Candidate 2 (27%), Candidate 3 (20,35%), Candidate 4 (11,22%) and Candidate 5 (10,76%) respectively. On the other hand, Candidate 1 (29%) is the most appropriate candidate for quality control. This candidate is followed by Candidate 3 (24%), Candidate 4 (18,72%), Candidate 2 (18%) and Candidate 5 (10%) respectively.

4. CONCLUSIONS AND GENERAL EVALUATION

The clothing sector, which possesses high employment and export potential, has an importance place within the Turkish economy. The enterprises which operate in the sector must increase their competitiveness in order to be successful in national and international markets. At this point, the enterprises confront with the employment of qualified, well educated and knowledgeable employees as an important factor which increases their competitiveness. When the labor intensive structure of clothing sector is taken into consideration, the importance of successful and qualified blue-collar employment can be understood better. Therefore, the sector must perform the blue-collar employee selection accurately.

According to our research results, analytic hierarchy process is a method which can be used successfully in clothing enterprises for blue-collar employee selection. The method compares the blue collar employee candidates between each other and even the candidates are too close to each other it provides an accurate selection process which ends up with the selection of best candidate. Besides, the method brings many employee selection techniques (curriculum vitae evaluation, written and oral examinations, interview etc.) together and gives single evaluation result. In this context, it is a technique which eases and shortens the evaluation process for managers.

As it can be seen from our research, the blue-collar employees must possess different properties according to the clothing departments in which they work. However, the common expected properties of blue-collar employees can be listed as; education level, experience, technical information, communication skill, willingness to work, aptitude for team work, flexibility (easy orientation to different processes and technologies), willingness to novelty and alteration. Turkish clothing sector is a labor intensive sector and generally its production is based on orders. Therefore, especially the production employees must have more technical information, must be skilled at team work, must be open to alteration, must be easily adapted to different methods and techniques and must possess good communication skills. It is very hard for an employee, who is lack of these properties, to be successful and provide contribution to the enterprise.

According to another result of our study, the technical properties of blue-collar employees differ according to the clothing departments in which they work. Sewing department, which is one of the most significant departments of clothing production and which employs the maximum personnel within the enterprise, must hire careful and attentive employees whose hand-eye coordination, manual skills, machine and equipment utilization skills are good. Especially the clothing enterprises, which produce lots of orders in small quantities just like the investigated enterprise, look for sewing employees who can utilize different sewing machines. The mistakes of the sewing employees directly affect and decrease the quality of the products. Therefore, the sewing employees must possess talent, expertise, and manual skills. On the other hand, the quality control, which is also another significant department, must hire careful and attentive employees who can separate colors accurately. The employees must not possess manual skills and machine utilization skills. However, they must easily and accurately determine the faults in the dark colored fabrics and stitches.

As it can be seen from our research results, there are many technical and social criteria which affect the blue-collar employee selection in clothing sector. Analytic hierarchy process is a selection process which evaluates and brings many employee selection techniques together. It specifies the best candidate by comparing candidates between each other according to the determined criteria. In this context, the method is a successful technique which can be used for accurate employee selection process.

REFERENCES

- [1] Bamyacı M., 2008, Modern logistics management: a site selection model for organized logistics centers, İstanbul University, Institute of Sciences, Department of Maritime Transportation and Management Engineering, PhD Thesis, 204 p. (in Turkish)
 - [2] Baykal İ.Ö., 2007, Implementation of multi-criteria decision making methods to employee selection problem, Galatasaray University, Institute of Sciences, Department of Industrial Engineering, Master Thesis, 104 p. (in French)
 - [3] Can H., Güney S., General Business: Criteria, Concepts, Institutions, 2007, Arıkan Printing House, 567 p. (in Turkish)
 - [4] Certo S.C., Certo S.T., Modern Management, 2006, 10th Edition, Pearson Prentice Hall, 621 p.
 - [5] Çoban M., 2012, Using analytic hierarchy process in personnel selection and a research on manufacturing industry, Balıkesir University, Institute of Social Sciences, Department of Business Administration, Master Thesis, 123 p. (in Turkish)
 - [6] Göklüberk Özlü P., 2006, A research study on personnel selection process in ready-to-wear sector, Tekstil ve Konfeksiyon, Volume 3, p: 200-205 (in Turkish)
 - [7] Gürüz D., Gürel E., Management and Organization: From Individuals to Organization, From Idea to Act, 2006, Nobel Printing House, 455 p. (in Turkish)
 - [8] İstemi J., 2006, Use of Analytic hierarchy process method in personnel selection, İstanbul Technical University, Institute of Sciences, Department of Industrial Engineering, Master Thesis, 194 p. (in Turkish)
 - [9] Kanat S., 2012, The effects of knowledge management on supply chain management in clothing sector, Ege University, Institute of Sciences, Department of Textile Engineering, PhD Thesis, 121 p. (in Turkish)
 - [10] Özcan M., 2012, Comparison of effectiveness of AHP and Topsis methods in personnel selection process: an empirical study at a production company, Hacettepe University, Institute of Social Sciences, Department of Business Administration, Master Thesis, 130 p. (in Turkish)
 - [11] Özkan Ö., 2007, The study of decision making methods used for personnel selection: AHP, Electre and Topsis Sample, Dokuz Eylül University, Institute of Social Sciences, Department of Labor Economics and Industrial Relations, Master Thesis, 200p. (in Turkish)
 - [12] Şener T., 2011, Analytic hierarchy process in personnel selection problem: a sample application for the textile sector, Selçuk University, Institute of Social Sciences, Department of Business Administration, PhD Thesis, 208 p. (in Turkish)
-

THE EFFECTS OF FRANCHISING SYSTEM ON INTERNATIONAL MARKETING STRATEGIES: TURKISH CLOTHING SECTOR CASE

Turan ATILGAN

Prof. Dr., Ege University, Department of Textile Engineering, Bornova, İzmir, Turkey,
turan.atilgan@ege.edu.tr

Seher KANAT

Dr., Ege University, Department of Textile Engineering, Bornova, İzmir, Turkey,
seher.kanat@ege.edu.tr

Abstract

The enterprises must think globally instead of locally due to the today's rapidly globalizing business world. Enterprises, especially the ones that operate in international markets, struggle with compelling rivalry conditions in order to survive and accommodate to new circumstances. Within this context, rapidly globalizing business world, which is parallel to the globalizing world, intensively affects the marketing strategies and implementations of enterprises. Turkish clothing sector, which rapidly penetrates into the international markets since 1980s, is intensively affected from this globalization and alteration movement. Turkish clothing enterprises use different techniques and methods in order to penetrate into the international markets effectively and successfully. Franchising, which is the exclusivity of definite privileges for a certain time in a specific area from the main enterprise to another enterprise, is one of these methods which can be used with this purpose. Franchising system is generally used by Turkish clothing enterprises during the international market penetration. Enterprises benefit from this strategy during the penetration to the countries, which possess different political, judicial, economical and cultural structure, in order to be able to reduce the risk. When they get used to the market, they eliminate franchising system and establish their own retailing systems. However, franchising system is an effective and successful method especially for the first international market penetration of an enterprise with its own brand. In this study, the franchising systems of successful Turkish clothing enterprises, which use this strategy as an international marketing strategy and possess their own brands, will be analyzed. Also the effects of franchising systems on the enterprises' marketing success will be investigated.

Keywords: *Employee selection, analytic hierarchy process, Turkish clothing sector*

1. FRANCHISING SYSTEM AS A MARKETING STRATEGY

Worldwide, franchising constitutes the fastest growing retail format in history. In the past decade thousands of European and United States franchise chains have been seduced into international expansion [11].

Franchising is an arrangement of organizations whereby a manufacturer or marketer of a product or service grants exclusive rights to independent entrepreneurs in return for royalties and often conformance to certain operating procedures. A franchise system promises the franchisor rapid market penetration at a relatively low cost, compared with establishing company-owned units. For the franchisee, it provides an opportunity to enter a business with a proven product/service or brand name [7].

Franchisors typically develop product or service ideas and offer these ideas to franchisees for marketing in prescribed territories. In return, franchisees pay initial fees and royalties to franchisors. Franchisors formulate overall business strategies and expect franchisees to function as integral parts of a system by implementing these strategies. However, franchisees may enjoy relative freedom in recruiting personnel, managing routine operations and running local marketing programs. Franchising provides the flexibility required implementing hybrid strategies in which some elements of the marketing mix are standardized by the franchisor across global markets and other elements are locally determined by franchisees. It serves as a significant alternative to both non-integration and full vertical integration. This combination features are likely to make franchising an attractive organizational form for competing in global markets [9].

The term franchising can describe a wide variety of business activities but the contemporary franchise system commonly in use is referred to as business format franchising [8]. Business format franchising may be defined as the granting of a license for a predetermined financial return by a franchising company (the franchisor) to its franchisees, entitling them to make use of a complete business package, including training, support and the corporate name, thus enabling them to operate their own businesses to exactly the same standards and format as the other units in the franchised chain [1,3,5,8].

Business format franchising can be viewed as a distribution system. Essentially, it is the process of licensing rights and obligations to copy a unique market positioning using a packaged, configured system. It may include an entire business format covering a marketing strategy and plan, operating manuals and standards, quality control, ongoing two-way communication and assistance designed to have the franchisee replicate, in different locations, the entire master franchisor's business concept [10].

Franchising is fast becoming one of the most popular entry mode strategies for international retail companies when moving into international markets [3]. In terms of market entry mode strategies available to international retail companies, franchising has proved an increasingly popular mode of operation in recent times [8]. The internationalization of retail operations through franchising has been recognized as an increasingly important entry mode strategy during the past decade as the internationalization of retailing has reached a more mature phase in its development [4]. Over one-third of all United Kingdom retailers operating in international markets are fashion retailers. Due to the prevalence of fashion retailers on the international scene, many firms such as Benetton, Marks & Spencer, Mothercare, Gap and more recently Mango and Zara are offered as examples of retailer internationalization [2,3].

Table 1. Implementing a business franchise system into a new international market [10]

<p>Stage One: Descriptive: An international marketing research process is applied to international business franchise relationships</p> <p>1. Franchise company conducts two information searches: International country analysis in terms of economic, demographic (identifiable consumer segment), distance, political risk, competitive and other environmental variables. International partner criteria selection in terms of financial capability, experience and managerial factors, demographic factors, attitudes and personality and others such as health and reputation.</p> <p>2. International partner conducts two information searches: Franchise company and business franchise system selection in terms of financial capability, experience and managerial factors, demographic factors, attitudes and personality and others such as business success and reputation.</p> <p>Within the context of the international country analysis, the franchisee (the customer) also end-consumer in terms of economic, demographic, distance, political risk and others such as competition. Also, demographic information on the target market and consumer attitudes and perceptions about franchise and others such as reputation of business and other international partners.</p>
<p>Stage Two: Diagnostic: Domestic franchising-core-periphery concepts are applied to international business franchising</p> <p>1. Information exchange: The international business franchise relationship determines the appropriate level of standardization and adaptations (in terms of mandatory and voluntary adaptations) via the exchange process</p>

<p>of business plans and disclosure statements.</p> <p>2. Core-periphery concepts: Core-periphery concepts applied to management practices and marketing strategies in the international franchise system.</p> <p>3. Arrangement: The international business franchising system configures its features and strategies. A hybrid configuration with the strategy of standardization and mandatory/voluntary adaptations emerges.</p> <p>4. Favorable contract: The development of a favorable contract by all parties-An efficient (explicit with codes of conduct and clauses) contract setting performance standards and mechanisms for monitoring and controlling.</p>
<p>Stage Three: Predictive: Implementing the business franchising contract into an international market: Favorable contract is predetermined and predictive with ongoing open communication for flexibility for changes in the market and each party's needs.</p>

In international retail franchising, retail firms franchise their brand and store concept to franchisees in return for a franchise fee and margin on the product sold [2]. We may understand franchising as a low commitment/investment entry mode compared to own store openings. The wholly owned entry mode requires a greater involvement (level of market-specific managerial and financial resources committed to a foreign firm), allowing for greater control (authority to affect or direct the activities of a foreign firm) and returns than does the franchising option. For its part franchising is beneficial because it reduces the amount of franchisor investment [6]. Motives for franchising internationally can be summarized as; fortuitous franchisee interest from third parties, exploit potential markets, increase sales and profits, market expansion, domestic market saturation, desire to be known as an international firm, perceived favorability of the external environment, desire for growth, operating experience, top management's international experience, tolerance for risk, perception of the firm's competitive advantage, external change agent influence [2]. Table 1 indicates the way for implementing a business franchise system into a new international market [10]

2. INTERNATIONAL FRANCHISING SYSTEMS OF TURKISH CLOTHING ENTERPRISES

Franchising system is generally used by Turkish clothing enterprises during the international market penetration. Enterprises benefit from this strategy during the penetration to the countries, which possess different political, judicial, economical and cultural structure, in order to be able to reduce the risk. When they get used to the market, they eliminate franchising system and establish their own retailing systems. However, franchising system is an effective and successful method especially for the first international market penetration of an enterprise with its own brand.

In this study the franchising systems of successful Turkish clothing enterprises, which use this strategy as an international marketing strategy and possess their own brands, and their effects on enterprises' marketing successes are analyzed. For this purpose, interviews are made with marketing managers.

2.1. LC Waikiki

LC Waikiki is established in 1985 as a French brand. Since 1997 it proceeds on its way as a Turkish brand. It produces women, men, children, teenagers and baby clothes. The brand possesses 515 physical stores in 23 countries. The enterprise aims to become one of the best European clothing retailers, which possess their own brands, since 2023.

The enterprise benefits from franchising system during international market penetration. The enterprise has used the franchising system during Saudi Arabia market penetration in 2012 for the first time. The enterprise penetrated into Iran, Saudi Arabia and United Arab Emirates by using franchising system. The brand still grows with franchising system in these countries. The enterprise considers for penetrating into Algeria, Tunisia, Uzbekistan and Lebanon.

The 13% of the enterprise's abroad stores work with franchising system. The enterprise defines the franchising system as a useful strategy for penetrating into international markets. The enterprise prefers the franchising system due to the legal regulations within the penetrated markets. The franchisees don't make any payment under the name of franchising fee. However, the enterprise considers for receiving an initial payment. The franchisees must provide the necessary conditions such as; store location, being experienced in the sector and having financial power. Also the franchisees' stores are managed by the main office in Turkey.

2.2. Mavi Jeans

Mavi, which is established in 1991, produces denim wear and non-denim sportswear for women and men. Mavi has been the leading jeans brand in Turkey since the last 18 years with 11 % market share. The brand possesses 352 stores in 50 countries. The enterprise aims to create a Mediterranean brand around blue jean culture and perfect fitting jeans.

The enterprise benefits from franchising system during international market penetration. The enterprise has used the franchising system for international market penetration since 1996. The enterprise penetrated into Iran, Saudi Arabia, United Arab Emirates, Egypt, Libya, Oman, Iraq, Ukraine, Albania, Azerbaijan, Armenia, Georgia, Kazakhstan, Kyrgyzstan, Turkmenistan and Kosovo by using franchising system. The brand still grows with franchising system in these countries except Kazakhstan. At the present time, the enterprise possesses its own stores in Kazakhstan.

The 30% of the enterprise's abroad stores work with franchising system. The enterprise defines the franchising system as a useful strategy for penetrating into international markets. The enterprise prefers the franchising system for minimizing risks, penetrating into the markets easily, growing, being a known brand in international markets and managers' experiences. The franchisees don't make any payment under the name of franchising fee. However, the franchisees must provide the necessary conditions. The store is located due to the mutual research of Mavi and franchisee. Mavi draws the architectural project of the store. Unmovable decoration materials are produced by Mavi and the payment is made by franchisee. The store employees are educated by Mavi. Franchisee buys the products from Mavi with a defined discount ratio which is determined in the contract. For example, if the sale price of a product is 100\$ according to the global price list, the franchisee pays 36 \$ for the product. Besides, the franchisee must buy opening stock from the products according to the store size (m²) and market requirements. Franchisee can participate in the seasonal collection meetings and gives its own orders or buys the recommended products. The franchisee must perform the marketing activities which are determined by the contract. The marketing activities alter due to the buying amount and Mavi's approval.

2.3. Defacto

Defacto, which is established in 2003, produces women, men, children and teenager clothes. The brand possesses 274 stores in 15 countries. The enterprise aims to become a world brand in 10 countries within 10 years.

The enterprise benefits from franchising system during international market penetration. The enterprise has used the franchising system for international market penetration since 2015. The enterprise penetrated into Bahrain, Kuwait, Oman, Qatar, Saudi Arabia, Jordan, Lebanon, Yemen, Algeria and Tunisia by using franchising system. The brand still grows with franchising system in these countries. In the future, the enterprise plans to possess its own stores in these countries.

The 31% of the enterprise's abroad stores work with franchising system. The enterprise defines the franchising system as a useful strategy for penetrating into international markets. The enterprise prefers the franchising system for minimizing risks, penetrating into the markets easily, growing and legal regulations. The franchisees don't make any payment under the name of franchising fee. However, the franchisees must provide the necessary conditions. Franchisees decide to the store locations, marketing strategies, education of store employees, store layout and employee selection process together with Defacto. However, the payments are made by franchisees.

2.4. Colin's

Colin's, which is established in 1983, produces denim wear and non-denim sportswear for women and men. The brand possesses approximately 600 stores in 37 countries.

The enterprise benefits from franchising system during international market penetration. The enterprise has used the franchising system for international market penetration since 1983. The enterprise penetrated into Russia, Ukraine, Kazakhstan, Balkan countries and Arabian countries by using franchising system. The brand still grows with franchising system in these countries.

The 60% of the enterprise's abroad stores work with franchising system. The enterprise defines the franchising system as a useful strategy for penetrating into international markets. The enterprise prefers the franchising system for minimizing risks, penetrating into the markets easily, growing and being a known brand in international markets. The franchisees must provide the necessary conditions. Store locations, store sizes (m²), visual appearance of the stores, store layout and education of the store employees are managed by Colin's.

2.5. Damat - Tween

Damat - Tween, which is established in 1986, produces suits, shirts, jackets, pants and sportswear for men. The brand possesses 99 stores in 28 countries. The brand aims to become one of the world's top five men brands that lead the men fashion.

The enterprise benefits from franchising system during international market penetration. The enterprise has used the franchising system for international market penetration since 1995. The enterprise penetrated into

Morocco, Egypt and Nigeria by using franchising system. The brand still grows with franchising system in Egypt. The enterprise has started to open its own stores or corner shops in Morocco and Nigeria.

The 20% of the enterprise's abroad stores work with franchising system. The enterprise defines the franchising system as a useful strategy for penetrating into international markets. The enterprise prefers the franchising system for minimizing risks, penetrating into the markets easily and being a known brand in international markets. The franchisees make 10.000 Euro payments under the name of franchising fee. Also, the franchisees must provide the necessary conditions. The store must be located in shopping malls or in thoroughfare. The store size must be at least 150 m² and the shop window's width must be at least 6 meters. The payments must be guaranteed by the banks. Damat-Tween gives education to the store employees about products and sales techniques.

2.6. Koton

Koton, which is established in 1988, produces women, men, children and teenager clothes. The enterprise possesses 392 stores in 25 countries. The enterprise aims to become a fast fashion brand, which owns the favorite and richest collections, throughout the five continents since 2023.

The enterprise benefits from franchising system during international market penetration. The enterprise has used the franchising system for international market penetration since 2004. The enterprise penetrated into Saudi Arabia, Albania, Azerbaijan, Bahrain, United Arab Emirates, Iraq, Iran, Kyrgyzstan, Kosovo, Libya, Uzbekistan and Jordan by using franchising system. The brand still grows with franchising system in these countries.

The 56% of the enterprise's abroad stores work with franchising system. The enterprise defines the franchising system as a useful strategy for penetrating into international markets. The enterprise prefers the franchising system for minimizing risks, penetrating into the markets easily, growing and being a known brand in international markets. The franchisees must provide the necessary conditions. Franchisees must determine the store location according to the sales amount. The sales efficiency must be protected. The store size must be at least 1500 m². Franchisees must provide and protect the store standards (layout, furniture etc.). Franchisees must obey the annual purchase budgets and make the payments on time.

2.7. İpekyol

İpekyol, which is established in 1986, produces skirts, blouses, jackets, trousers and casual wear for women. The enterprise possesses 120 stores in 5 countries.

The enterprise benefits from franchising system during international market penetration. The enterprise has used the franchising system for international market penetration since 2011. The enterprise penetrated into Egypt, United Arab Emirates, Iraq and Azerbaijan by using franchising system. The brand still grows with franchising system in these countries.

The 100% of the enterprise's abroad stores work with franchising system. The enterprise defines the franchising system as a useful strategy for penetrating into international markets. The enterprise prefers the franchising system for minimizing risks, penetrating into the markets easily, growing and being a known brand in international markets. The franchisees make payments under the name of franchising fee. Franchising fees alter according to the countries. Also the franchisees must provide the necessary conditions. The store size must be at least 180 m². The store must have a storage which minimally equals to the 10% of the store size. The store must be located in most popular shopping mall or in the fashion street of the city. The architectural concept of the store is specified by İpekyol. Franchisees must purchase products from two collections per year. At least 80% of the collection products must be ordered. Franchisees must have budgets for marketing activities. The franchising privilege is given for three years. Mono-brand policy is required.

3. CONCLUSIONS AND GENERAL EVALUATION

Rapidly globalizing business world, which is parallel to the globalizing world, almost obligates the enterprises to penetrate into international markets. Therefore, the clothing sector which is intensively affected by alteration and global culture, motives the enterprises for operating in international markets. Within this context, Turkish clothing enterprises, which have operated in international markets since 1980s, nowadays continue to their ways with their own brands. Today the branded clothing products take a 25% share from Turkey's total clothing export. As the sector's branded clothing export continues to increase, the marketing strategies that are used during international market penetration differentiate. Franchising system is one of these marketing strategies.

According to our research results, Turkish clothing enterprises benefit from franchising system during international market penetration. Our enterprises prefer the franchising system for minimizing risks, penetrating into the markets easily, legal regulations, growing and being a known brand in international

markets. 13%-100% of our enterprises' abroad stores work with franchising system. Our enterprises are acquainted with this system in different years but they have benefited from franchising system since 1983.

According to another result of our research, Turkish clothing enterprises use the franchising system during the initial international market penetration. After promotion and recognition activities, the enterprises turn towards retailing (they start to open their own stores). However, if they are pleased with system's operations and profitability, they continue with franchising system. In some countries, they continue to grow with franchising system due to the legal regulations. However, at this point, franchising system turns into a very important strategy which eliminates the barriers.

As it can be seen from our research results, our clothing enterprises penetrated into Kosovo, Albania, Ukraine, Russia, Azerbaijan, Armenia, Georgia, Kazakhstan, Kyrgyzstan, Turkmenistan, Uzbekistan, Iraq, Iran, Bahrain, Kuwait, Saudi Arabia, United Arab Emirates, Egypt, Libya, Oman, Qatar, Jordan, Yemen, Algeria, Tunisia, Morocco and Nigeria by using franchising system. Turkish clothing brands prefer to penetrate into Balkan, Middle East, Asia, Arab and North Africa countries by using franchising system. As it can be seen, most of these countries haven't reached to intended development levels in terms of social, economical, political and legal. Therefore, these countries can be classified as risky and troublesome markets for foreign investments. At this point, franchising system turns into a useful strategy which removes the obstacles.

According to another result of our research, Turkish clothing enterprises generally don't receive any payment under the name of franchising fee. However, the franchisees must provide the necessary conditions such as; store location, store size, store decoration, education of store employees, marketing activities, sold collection amounts and properties.

As it can be seen, franchising system is a marketing strategy which is preferred by Turkish clothing enterprises during international market penetration. Turkish clothing enterprises, which are successful both in national and international markets and possess their own brands, intensively benefit from franchising system.

REFERENCES

- [1] Altinay L, Roper A., 2005, The entrepreneurial role of organizational members in the internationalization of a franchise system, *International Journal of Entrepreneurial Behavior & Research*, V.11, No.3, p:222-240
 - [2] Doherty A.M., 2007, The internationalization of retailing: factors influencing the choice of franchising as a market entry strategy, *International Journal of Service Industry Management*, V.18, No.2, p: 184-205
 - [3] Doherty A.M., Alexander N., 2004, Relationship development in international retail franchising: case study evidence from the UK fashion sector, *European Journal of Marketing*, V.38, No.9/10, p:1215-1235
 - [4] Doherty A.M., Alexander N., 2006, Power and control in international retail franchising, *European Journal of Marketing*, V.40, No.11/12, p:1292-1316
 - [5] Doherty A.M., Quinn B., 1999, International retail franchising: an agency theory perspective, *International Journal of Retail & Distribution Management*, V.27, No.6, p:224-236
 - [6] Forte R., Carvalho J., 2013, Internationalization through franchising: the Parfois case study, *International Journal of Retail & Distribution Management*, V.41, No.5, p:380-395
 - [7] Preble J.F., Hoffman R. C., 1998, Competitive advantage through specialty franchising, *Journal of Consumer Marketing*, V.15, No.1, p:64-77
 - [8] Quinn B., Doherty A.M., 2000, Power and control in international retail franchising: evidence from theory and practice, *International Marketing Review*, V.17, No.4/5, p:354-372
 - [9] Sashi C.M., Karuppur D.P., 2002, Franchising in global markets: towards a conceptual framework, *International Marketing Review*, V.19, No.5, p: 499-524
 - [10] Thompson M., Stanton J., 2010, A framework for implementing retail franchises internationally, *Marketing Intelligence & Planning*, V.28, No.6, p:689-705
 - [11] White D.W., 2010, The impact of marketing strategy creation style on the formation of a climate of trust in a retail franchise setting, *European Journal of Marketing*, V.44, No.1/2, p:162-179
-

MODELLING OF SPECIFIC CUTTING RESISTANCE IN MACHINING OF AISI P20 PLASTIC MOULD STEEL

Nafiz YAŞAR

Karabuk University, Vocational College, 78050, Karabuk, Turkey.
nafizyasar@karabuk.edu.tr

M. Erdi KORKMAZ

Karabuk University, Faculty of Engineering, 78050, Karabuk, Turkey.
merdikorkmaz@karabuk.edu.tr

Mustafa GÜNAY

Karabuk University, Faculty of Engineering, 78050, Karabuk, Turkey.
mgunay@karabuk.edu.tr

Ulvi ŞEKER

Gazi University, Faculty of Technology, 06500, Ankara, Turkey.
useker@gazi.edu.tr

Abstract

AISI P20 plastic mould steels are frequently used where wear and corrosion resistance is needed in the industry. This study was performed in two stages whose first is to measure the cutting forces occurred in machining of AISI P20 plastic mold steel and second is to model of specific cutting resistance (k_s). The machining experiments were performed on CNC lathe for AISI P20 plastic mold steel. The uncoated cemented carbide cutting tools which have SNMG 120408-QM form with a 75° approaching angle according to ISO 1832 were used in the experiments. Three different levels of cutting speed, feed rate and depth of cut as cutting parameters were selected and experiments were performed according to Taguchi L27 orthogonal array. In first stage, cutting forces were measured by using Kistler 9257B type dynamometer. In second stage, specific cutting resistance was calculated by using data of main cutting force. The effects of cutting parameters on specific cutting resistance were evaluated with the analysis of variance (ANOVA). The feed rate is the most important factor on k_s value with %61.32 PCR. Mathematical model were developed using the artificial neural nets (ANN) in order to predict the specific cutting resistance.

Keywords: *Specific cutting resistance, AISI P20, Analysis of variance, Artificial Neural Networks (ANN)*

1. INTRODUCTION

Plastic mould steels are extensively used in locations which desire heat, corrosion and abrasion resistance in the industry. It is required that resistance to chemical interaction, surface hardening and [processability](#) must be considered as well as plastic raw material to be injected, hardness of steel material and corrosion resistance [1]. In addition, parameters such as mold design dimensions, surface burnishability and weldability must be considered. Increase of plastic product sizes cause increase of mould dimensions, so requirement of high toughness is revealed. Heating processes to be applied may cause deformation problems such as distortion and crack in hardening. Therefore, existing of pre-hardened mould steels such as AISI P20 is an important factor [2]. These steels does not require due to its hardness of 30-36 HRC and have capability of easy machining due to having sulphur. On the other hand, it is emphasized that cost analysis efficiency of plastic injection market must be increased. Mould steel production cost and mould machining cost affect total cost of plastic material produced with injection. In this regard, rough and finish machining are the most expensive two machining processes between mould machining processes depending on machinability of mould steel [3]. Therefore, in order to decrease of the machining cost in plastic moulding, modeling of machining outputs such as cutting forces and surface roughness as well as optimization of cutting conditions will contribute to increase of efficiency.

Cutting forces occurring during metal removing operation have a significant role on heat generation, tool life, and quality of machined surface and sizes of workpiece. Cutting forces are also used in the design of machined tools, cutting tools and required jigs [4]. In addition, independent variables such as tool material and geometry, workpiece material, cutting parameters (cutting speed, feed rate and depth of cut), cutting fluid and machine tool and dependent variables such as tool life, energy consumption and surface integrity must be associated for efficiency of machining process [5]. In this regard, modeling of cutting forces has become one of the work spaces of metal cutting theory. Existing of lots of variables interrelated affecting cutting forces makes the development of mathematical model difficult. In recent years with the transfer of developing computer technology to machining, analysis and modeling studies such as analysis of variance, multiple regression analysis, artificial neural networks (ANN), and fuzzy expert system have been performed in order to minimize or eliminate difficulties in machining process [6]-[12].

In this study, variation of specific cutting resistance during machining of AISI P20 plastic mould steel with different levels of cutting speed, feed rate and depth of cut has been analyzed. Effects of cutting parameters on specific cutting resistance (k_s) have been investigated by analysis of variance. In addition, mathematical model of k_s with artificial neural networks has been developed.

2. MATERIALS AND METHOD

The experimental samples were made of AISI P20 plastic mould steel with dimensions $\text{Ø}60 \times 400$ mm. Prior the experiments, the samples were turned with a depth of cut of 0.5 mm in order to remove the outer layer which might have been hardened by rolling process in production stage. In Table 1, chemical composition of the workpiece materials has been demonstrated.

Table 1- Chemical composition of the workpiece materials

Material	% C	% Si	% Mn	% Cr	% S	% Mo	% Ni	% P	BHN
DIN 1.2312	0.40	0,30	1.49	1.89	0.1	0.19	-	0,024	333-335

All machining tests were conducted in TC-35 JOHNFORD CNC turning center. The cutting tool was a commercial product available from Sandvik, consisting of a tool holder and indexable inserts suited to ISO 5608 and ISO 1832, respectively. Product no. of the tool holder is PSBNR 2525M12. The uncoated carbide inserts were SNMG 120408-QM H13A. Cutting parameters, i.e. cutting speed (V), depth of cut (a), and feed rate (f) were selected. The experiments were carried out with using three different cutting speed, feed rate and depth of cut. Cutting forces were measured with a Kistler 9257 B type piezoelectric dynamometer and an associated 5019 B130 charge amplifier connected to PC employing Kistler Dynoware software.

Design of experiments and statistical analysis was performed by using MINITAB statistical software. The factors and factor levels are summarized in Table 2. These factor levels result in a total of 27 unique factor level combinations. Using analysis of variance (ANOVA) and full factorial design of experiment, the effectiveness on the specific cutting resistance of cutting parameters were investigated. The ANOVA output and the calculated F-ratios are shown in Table 3. It was selected the 0.05 level for testing the significance of the main effects.

Table 2- Factors and factor levels

Symbol	Factors	Level		
		1	2	3
V	Cutting speed (m/min)	125	175	225
f	Feed rate (mm/rev)	0.1	0.25	0.4
a	Depth of cut (mm)	1	1.75	2.5

3. RESULTS AND DISCUSSION

Figure1 showing interaction between cutting parameters (V,f,a) and specific cutting resistance (k_s) have been drawn in order to analyze k_s values obtained from experiments. Specific cutting resistance (k_s) has been calculated using the equation of Kienzle [1].

$$F_c = [A_0 \cdot k_2] \cdot k_V \cdot k_f \cdot k_a \cdot k_r \quad (1)$$

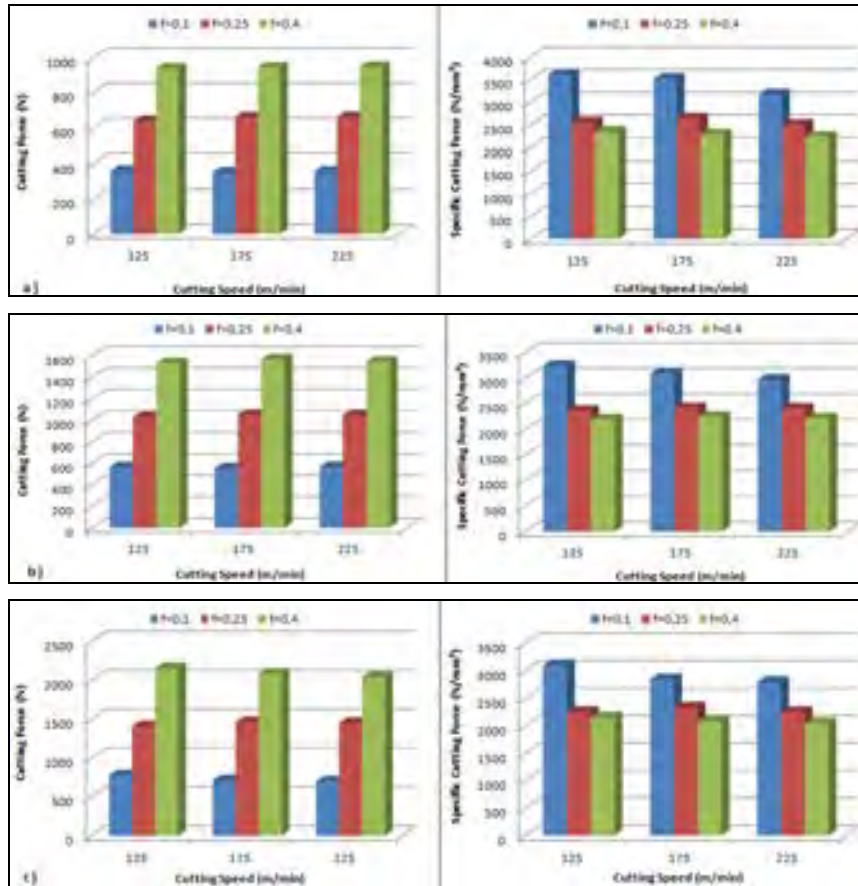


Fig.1 – Variation of k_s depends on cutting parameters, a) $a=1$ mm; b) $a=1.75$ mm; c) $a=2.5$ mm

In experiments performed using uncoated cutting tool, it is obvious that increase of cutting speed decrease specific cutting resistance insensibly but increase of feed rate, depth of cut decrease specific cutting resistance distinctly (Fig.1). It was determined that cutting forces measured especially for 1 mm of depth of cut and 0.1 mm/rev feed rate are higher than that of 2 mm of depth of cut and 0.4mm/rev feed rate. The reason is that the higher feed rate and depth of cut, the higher chip cross-section. In the machining of A ISI P20 steel, the highest k_s value has been calculated as 3610 N/mm² in 1 mm depth of cut, 0.1 mm/rev feed rate and 125 m/min cutting speed while the smallest value has been calculated as 2042 N/mm² in 2.5 mm depth of cut, 0.4 mm/rev feed rate and 225 m/min cutting speed.

Analysis of variance (ANOVA) results applied in %95 confidence level in order to determine the level of cutting parameters' effect on specific cutting resistance have been demonstrated in Table3. Here, P values indicating importance level of each parameter and percentage contribution ratio (PCR) are demonstrated.

Table 3. ANOVA results for specific cutting resistance

Source	Degree of freedom (DF)	Sum of squares (SS)	Mean of squares (MS)	F ratio	P value	PCR (%)
V	2	0.777	0.3885	5.23	0.015	1.44
f	2	46.5156	23.2578	313.23	0.000	86.17
a	2	5.2054	2.6027	35.05	0.000	9.64
Error	20	1.4851	0.0743			2.75
Total	26	53.9831				100

It is demonstrated that most important factor on specific cutting resistance in machining of AISI P20 steel is the feed rate with %86.17 PCR. As far as can be seen from ANOVA results other parameters are depth of cut and cutting speed with %9.64 PCR and %1.44 PCR, respectively.

Artificial neural networks (ANN) has been developed for mathematical modeling of specific cutting resistance during machining of AISI P20 plastic mould steel with uncoated carbide cutting tool. Prediction performance of ANN model from experimental results has been determined by applying methods of root mean squared error (RMSE), coefficient of determination (R2), mean absolute percentage error (MAPE).

$$R^2 = 1 - \left(\frac{\sum_i (t_i - o_i)^2}{\sum_i (o_i)^2} \right) \quad (2)$$

$$RMS = \sqrt{MSE} = \sqrt{\frac{1}{p} \sum_i e_i^2} = \sqrt{\frac{1}{p} \sum_i (t_i - o_i)^2} \quad (3)$$

$$MSE = \frac{1}{p} \sum_i e_i^2 = \frac{1}{p} \sum_i (t_i - o_i)^2 \quad (4)$$

$$MAPE = \frac{1}{p} \sum_i \frac{|t_i - o_i|}{t_i} \times 100 \quad (5)$$

Pythia software has been used in ANN modelling of specific cutting resistance. Pythia software use Fermi function as a transfer function in training. Fermi function can be calculated as analytical with equation 6.

$$F(o) = \frac{1}{1 + e^{-4 \left(\sum_{i=1}^n I_i \cdot w_i - 0,5 \right)}} \quad (6)$$

Here, n shows neuron number used in hidden layer and wi shows weight values of neurons. Ni is the effect on ks of each neurons used in hidden layers. According to cutting parameters used in ANN model;

$$E_i = 4 \cdot (c_{1i} \cdot V + c_{2i} \cdot f + c_{3i} \cdot a - 0,5) \quad (7)$$

and then,

$$N_i = \frac{1}{1 + e^{-E_i}} \quad (8)$$

has been defined as shown in equation 7 and 8, respectively. Cij shows weights of each neuron used in hidden layer in the result of data set training in Pythia.

In order to investigate most suitable network topologies with different cycle and number of neurons by training experimental results with ANN after determining experiments for test and training, 21 experiments and remained 6 experiments were separated for training and test, respectively. Many trials were examined to determine suitable network topology by analyzing three inputs and one dependent output value in program data set.

Most suitable network topology was determined as 3-5-4-1 for modelling of specific cutting resistance in ANN. In addition, it was determined that two-level hidden layer having 5 neurons in first and 4 neurons in

second hidden layer must be performed for generated model. Hence, first level in hidden layer was generated of N1,...,N5 neurons while second level was generated of N6,...,N9. Output neuron of the network was N10. Most suitable topology used in specific cutting resistance prediction is given in Figure 3.1.

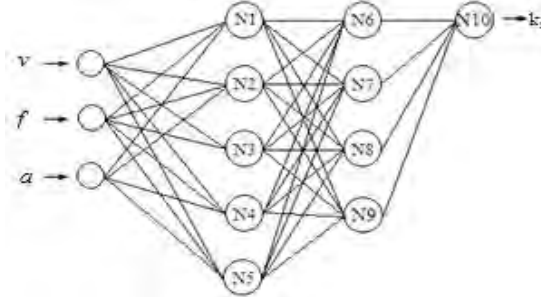


Figure 2- ANN topology generated for ks

After determining most suitable network topologies in prediction of ks, required parameters are entered and training of network is provided. The weights of neurons are found after training and mean deviation value is found from ANN output values and experimental results. The weight values (Cij) used in completing of effect on Ei value of each neuron has been given in Table 4.

Table 4. Weights of each neuron

i	C1i	C2i	C3i	C4i	C5i
The first level neurons					
1	-0,777399	0,428751	0,39563	----	----
2	-0,367236	-1,389032	-0,703825	----	----
3	-0,412545	-0,597023	-0,983634	----	----
4	-0,23794	-1,287044	-0,032885	----	----
5	-0,045476	0,538059	0,195262	----	----
The second level neurons					
6	-0,279342	0,2145	1,313014	1,233983	-0,25989
7	0,067828	-0,691304	-0,647513	-0,7691	0,811696
8	0,004732	2,233038	0,508012	1,92992	-0,2463
9	-0,787204	0,2191	0,104959	-0,32403	0,835195

Because network topology of ks has two level hidden layer, first level neurons (N1, ..., N5) have been stated with the help of Cij according to equation 8 in line with equation 7. Equations 9 and 10 have been respectively used for hidden layers. However, due to relation between second level neurons and first level neurons, equation 9 and 10 have been used for i= 6,7,8,9 instead of 7. The model of ks has been obtained with weight values in ANN network topology according to Fermi function (eqn 11). ks value in eqn 12 is predictive specific cutting resistance in modeling of ANN [13].

$$E_{i6-9} = w_{1i} \cdot f + w_{2i} \cdot V + w_{3i} \cdot a \quad (9)$$

$$E_{i6-9} = w_{i6} \cdot N_1 + w_{i7} \cdot N_2 + w_{i8} \cdot N_3 + w_{i9} \cdot N_4 \quad (10)$$

$$E_{i10} = \frac{1}{1 + e^{-4(-0,000772 \cdot N_6 + 1,204701 \cdot N_7 - 1,97249 \cdot N_8 + 1,2422722 \cdot N_9)}} \quad (11)$$

$$k_s = E_{i10} \cdot (k_{s_{max}} - k_{s_{min}}) + k_{s_{min}} \quad (12)$$

Comparison of experimental specific cutting resistance values and predicted values from ANN results in %95 confidence level has been given in Figure 2.

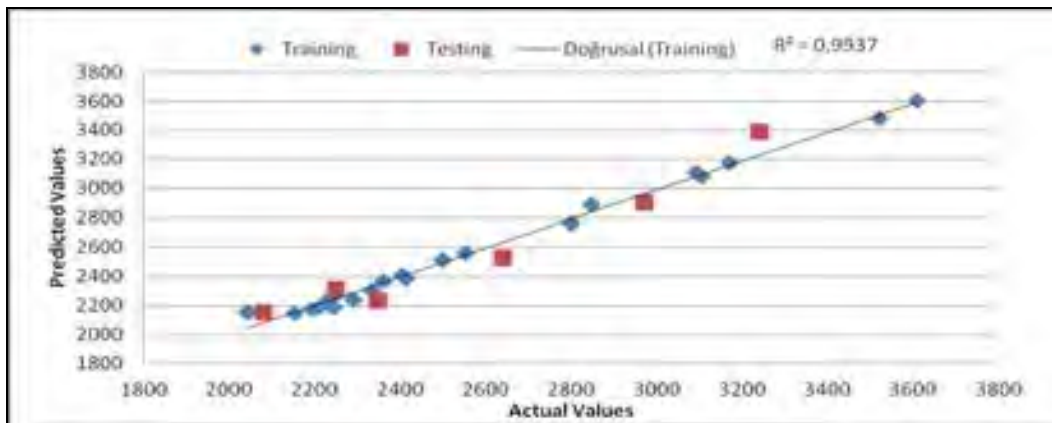


Figure 2. ANN performance of k_s values

Performances of mathematical models obtained from experimental results and ANN have been compared by different statistical error control methods. Mean absolute percentage error (MAPE) resulting on training and test was calculated as 4.388% and 17.720%, respectively by examining Table 5. Moreover, the coefficient of determination (R^2) is 99.9% for training data and 99.8% for the testing data in ANN model developed for specific cutting resistance. This shows that ANN model developed for k_s has high accuracy.

Table 5. Statistical Data For ANN Model

	RMS	R2	MAPE
ANN Training	3,613476363	0,999810133	1,103041779
ANN Test	10,27203622	0,998464727	3,768317177

4. CONCLUSION

- ✓ According to the formula Kinzle, smallest specific cutting resistance has been calculated as 2042 N/mm^2 in 27th experiment for depth of cut of 2.5 mm, feed rate of 0.4 mm/rev and cutting speed of 225 m/min while highest specific cutting resistance has been calculated as 3610 N/mm^2 in 1st experiment for depth of cut of 1mm, feed rate of 0.1 mm/rev and cutting speed of 125 m/min.
- ✓ According to ANOVA results, most important factor on specific cutting resistance in machining of AISI P20 steel is the feed rate with %86.17 PCR.
- ✓ Comparison of experimental and estimated specific cutting resistance values obtained from ANN analysis demonstrate that R^2 in the result of training and testing is about 99.8%. Therefore, the presented model can be used effectively to predict the specific cutting resistance in machining of AISI P20 plastic mould steel with uncoated carbide cutting tool.

REFERENCES

- [1]. Yaşar, N., "Plastik Kalıp Çeliklerinin Özgül Kesme Direncinin Deneysel Olarak Araştırılması", Gazi Üniversitesi Fen Bilimleri Enstitüsü Yüksek Lisans Tezi., Türkiye, Ankara., 2011.
- [2]. Süzginol, M., Kayır, Y. "DIN 1.2311 ve 1.2738 kalıp çeliklerinin işlenebilirliği", 3. Ulusal Talaşlı İmalat Sempozyumu, Ankara, 2012.
- [3]. Rech, J., Le Calvez, C., Dessoly, M. "A new approach for the characterization of machinability—application to steels for plastic injection molds", Journal of Materials Processing Technology, 152, 66–70., 2004.
- [4]. Zhang, J. H., "Theory and Technique of Precision Cutting", Pergamon Press, Oxford, 1-50., 1991.
- [5]. Kalpakjian, S., Schmid, S. R., "Manufacturing Processes for Engineering Materials", Prentice Hall, 404-460., 2003.
- [6]. Kadırgama, K., Abou-El-Hossein, K.A. "Predicting of cutting force model by using neural network", Journal of applied sciences, 6, 31-34., 2006.
- [7]. Yücel, E., Günay, M., "Modelling and optimization of the cutting conditions in hard turning of high-alloy white cast iron (Ni-Hard)". Proc IMechE Part C: J Mechanical Engineering Science, 227(10), 2280-2290., 2013.
- [8]. Gologlu, C., Sakarya, N. "The effects of cutter path strategies on surface roughness of pocket milling of 1.2738 steel based on Taguchi method", Journal of Materials Processing Technology, 206 (1-3), 7-15., 2008.
- [9]. Zain, M.A., Haron, H., Qasem, S.N., Sharif, S. "Regression and ANN models for estimating minimum value of machining performance", Applied Mathematical Modelling 36, 1477–1492., 2012.
- [10]. Asiltürk, İ., Çunkaş, M. "Modeling and prediction of surface roughness in turning operations using artificial neural network and multiple regression method", Expert Systems with Applications, 38: 5826–5832., 2011.

Modelling of Specific Cutting Resistance in Machining of Aisi P20 Plastic Mould Steel,
Nafiz Yaşar., M.Erdi Korkmaz., Mustafa Günay., Ulvi Şeker.

- [11]. Çaydaş, U., Haşçalık, A. “A study on surface roughness in abrasive waterjet machining process using artificial neural networks and regression analysis method”, Journal of Materials Processing Technology, 202: 574–582., 2007.
 - [12]. Karabulut, Ş., Güllü, A. “Farklı yavaşma açıları ile vermiküler grafitli dökme demirin frezelenmesinde kesme kuvvetlerinin araştırılması ve analitik modellenmesi”, Journal of the Faculty of Engineering and Architecture of Gazi University, 28 (1), 135-143., 2013.
 - [13]. Korkmaz, M., E., Günay, M.,” *Modelling Of Surface Roughness In Hard Turning Of Din 1.2210 Cold Work Tool Steel With Ceramic Tools*”, Proceedings of 19th International Conference. Mechanika, 135-140., 2014.
-

OPTIMISATION OF TOOL EDGE GEOMETRY AND CUTTING PARAMETERS IN HARD TURNING OF AISI 52100 USING TAGUCHI METHOD

Mehmet BOY

Karabük University, Vocational College, 78050, Karabük, Turkey,
mboy@karabuk.edu.tr

Halil DEMI

Karabük University, Department of Manufacturing Engineering, 78050, Karabük, Turkey,
hdemir@karabuk.edu.tr

Mustafa GÜNAY

Karabük University, Department of Mechanical Engineering, 78050, Karabük, Turkey,
mgunay@karabuk.edu.tr

İbrahim ÇİFTÇİ

Karabük University, Department of Manufacturing Engineering, 78050, Karabük, Turkey,
iciftci@karabuk.edu.tr

Abstract

An experimental investigation was conducted to determine the effects of cutting tool edge geometry, feed rate and cutting speed on surface roughness and resultant cutting forces in the hard turning of AISI 52100 steel with ceramic cutting tools. Ceramic inserts with two different edge preparations (chamfered and chamfered plus honed) were used. Three components of cutting forces and roughness of the machined surfaces were measured. Cutting speed, feed rate and cutting tool edge geometry were chosen as the cutting conditions (control factors). Taguchi's L16 orthogonal array was used for design of experiment. Optimum levels of the cutting conditions were determined using signal-to-noise (S/N) ratio, which was calculated for machining output variables (surface roughness and resultant cutting force) according to the 'the-lower-the-better' approach. Analysis of variance (ANOVA) was applied for observing the effect levels of cutting conditions on the quality characteristics (machining output) statistically. The analysis of variance results showed that the feed rate and tool edge geometry were the most significant factor on resultant cutting forces and surface roughness.

Keywords: *Hard turning, surface roughness, tool edge geometry, Taguchi, ANOVA*

1. INTRODUCTION

The hard turning process is defined as machining materials with hardness higher than 45 HRC. Hard turning is an alternative manufacturing process to conventional grinding in machining hardened components. Hard turning has many advantages in comparison to the grinding operations, such as higher material removal rates, more flexibility, lower energy consumption, elimination coolants, shorter set up time in complex parts and better surface integrity. Hard turning significantly reduces the production time, tooling costs and the machine tool investment, also presents a great contribution to sustainable manufacturing [1-5]. Cubic boron nitride (CBN) and ceramics are usually employed in hard turning operations, due to their high hardness, high abrasive wear resistance and chemical stability at high temperatures. The ceramic inserts have been very popular for its high productivity at milling and turning applications. Their application in metalworking has a lot of benefits as improved cutting performance, tool life and reduction in the costs. The mixed ceramic is recommended for continuous hard steel cutting, due to its high hardness and chemical stability but it is not recommended for the interrupted cutting as it does not have sufficient toughness for the operation [5-7].

The cutting process is greatly influenced by the machining parameters and the geometrical parameters of the cutting tool. Recently, works on cutting tools have focused on optimum micro geometry developments of the tool edge. Tool edge geometry plays a crucial role on the workpiece surface properties and the performance of the cutting tool, since the cut occurs mainly in the tool tip region as a result of the small depth of cut and feed rate used in hard turning. Cutting tool manufacturers provide various types of modifications to tool edge geometry. The modification of the tool edge geometry is referred to cutting edge preparation. Various types of cutting edge preparations, such as sharp, honed, chamfered, and chamfered plus honed cutting edges, are used in machining hardened materials. The aim of cutting edge preparation is to increase the strength of the cutting edge, increase the tool life, reduce the internal stress of the coating, reduce the risk of edge chipping, prepare the tool for coating and create the defined shape and size of the cutting edge [8-13]. The cutting edge geometry preparation influences thermomechanical aspects of cutting process, such as the shape of deformation zones, cutting forces, distribution of temperatures and stresses in cutting. These effects in machining affect the changes in chip formation and flow, tool wear resistance, tool life and machined surface integrity [13].

Effects of tool cutting edge in hard turning have been investigated using experimental and analytical approaches by many researchers. Effect of tool edge geometry and cutting conditions on the chip morphology in orthogonal hard turning of 100Cr6 steel is studied by Kountanya and et al.. They show that the edge radius does not influence the geometrical parameters of the chip, cutting forces decrease with increasing cutting speed and the chip formation frequency increases linearly with cutting speed, while a negative rake angle increases the chip pitch [14]. Thiele and Melkote used three-level factorial design to determine the effect of workpiece hardness and cutting edge geometry on surface roughness and cutting forces in finish hard turning of AISI 52100 steel using CBN tools. They found that increasing the edge hone radius tends to increase the average surface roughness and the effect of edge hone on the surface roughness decreased with an increase in workpiece hardness. It is also shown that the two-factor interaction of the workpiece hardness and cutting edge preparation on the surface roughness is very significant [15]. Lalwani et al. applied chamfered and honed edges to identify the effect of cutting parameters on cutting forces and surface roughness. They found that cutting speed has no significant effect on forces and surface roughness; however, the feed rate provides primary contribution and most significantly influences on the latter [16]. Almedia et al. investigated the effect of tool edge geometry, depth of cut and feed rate on surface roughness, tool wear and cutting force using silicon nitride ceramic. Silicon nitride ceramics have three different edge geometry (sharp, honed and chamfered edges) and CVD diamond coatings with ~15 μm thickness. They found that the honed tools are more prone to diamond film delamination from the cutting edge than the chamfered or sharp edged ones. While the flank wear is occurred the chamfered tools, the higher cutting forces are developed honed tools. Minimum surface roughness values ($R_a < 0,2 \mu\text{m}$) were obtained with the sharp edge tools [17]. Özel carried out cutting experiments and 3D finite element simulations to compare uniform and variable edge preparations. The most important finding was that variable micro-geometry insert edge design reduces heat generation and stress concentration along the tool cutting edge, whereas tool wear depth and predicted wear rate decreased with the use of a variable micro-geometry insert [18]. Kurt and Şeker investigate the effect of chamfer angle of polycrystalline cubic boron nitride cutting tool on the cutting forces and the tool stresses in finishing hard turning of AISI 52100 steel. The results obtained by them show that an angle of 20° has a major influence on the cutting forces and on Von Mises stresses [19].

Günay and Yücel investigated optimizing the cutting conditions for the average surface roughness (R_a) in machining of high-alloy white cast iron (Ni-Hard) at two different hardness levels (50 HRC and 62 HRC). ANNOVA results showed that feed rate is the most significant variable for Ni-Hard with 62 HRC while the cutting speed is the most significant for Ni-Hard with 50 HRC [20]. In a further work, they investigated the

effect of cutting conditions for cutting force and surface roughness. They found that depth of cut and feed rate is the most significant factor on surface roughness and cutting force for both the ceramic and CBN cutting tool. Also they obtained the smallest surface roughness with CBN insert during machining of Ni-Hard with 62 HRC [21]. Bouacha et al. investigated the R_a values created in hard turning of 64 HRC hardness AISI 52100 bearing steel with CBN cutting tool. They performed the machining tests according to the L_{27} orthogonal array of Taguchi experimental design method. They reported that the cutting parameters which are the most effective on R_a are the feed rate and cutting speed [22]. Özel et al. used Taguchi's L_{16} orthogonal array to determine the effects of the cutting tool edge geometry, workpiece hardness, feed rate and cutting speed on surface roughness and resultant forces in finish hard turning of AISI H13 steel using CBN tools [23]. Further, Özel and Karpat developed predictive model of surface roughness and tool wear in hard turning using regression and neural network for AISI H13 steel using CBN tools. They considered work material hardness, CBN content in tool material, edge radius of the CBN cutting tool, cutting speed, feed rate and cutting time as independent parameters [24]. This study aims at investigating the effects of cutting tool edge geometry, feed rate and cutting speed on surface roughness and resultant cutting force in hard turning of AISI 52100 steel with ceramic cutting tools of different edge preparations. Taguchi's design and analysis of experiment process has been used to achieve this purpose. L_{16} orthogonal array was used in the design of experiment. Furthermore, analysis of variance is used to determine the statistical significance of the cutting parameters. Finally, confirmation tests were carried out using the optimal cutting conditions which were determined by Taguchi optimization method.

2. EXPERIMENTAL

2.1. Workpiece Material

In this study, AISI 52100 bearing steel was used as a workpiece material. The cylindrical AISI 52100 specimens utilized in these experiments had a diameter of 60 mm and length of 200 mm. The specimens were through-hardened and tempered to obtain the hardness value of 60 ± 2 HRC. The hardness values were defined by the mean values of the measured workpiece hardness.

2.2. Cutting Tool and Geometry

Mixed ceramic (Al_2O_3+TiC) inserts with two different types of edge preparations were investigated in this study. These edge preparations include: a) "chamfered" (T-land) edges and b) "chamfered+honed" (S-land) edges as illustrated in Fig. 1. The cutting tools used were commercial grade ceramic inserts produced by Kyocera with the geometry of DNGA 150404 S/T02025 PT600M. PT600M is a special coating called "Megacoat". These inserts were clamped mechanically on a rigid tool holder with an ISO designation of DDJNR 2525M-1504.

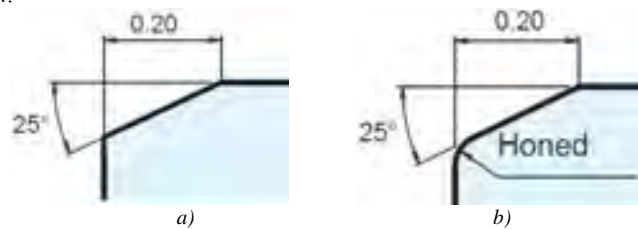


Figure 1. Type of edge preparations used in ceramic cutting tools: a) chamfered b) chamfered + honed

2.3 Experimental Design

A three-factor four-level factorial design was used to determine the effects of the tool edge geometry, feed rate and cutting speed on surface roughness and resultant forces in the hard turning of AISI 52100 steel. Four different levels of cutting speed (V_c) and feed rate (f) and two different levels of tool edge geometry (TEG) are chosen as cutting parameters (factors). The levels of factors were chosen within the intervals recommended by the cutting tool manufacturer. L_{16} orthogonal array of Taguchi method was used in the design of experiment. The factors and their levels are given in Table 1. The purpose of ANOVA is to determine which cutting parameters significantly affect the performance characteristics of independent variables. The ANOVA test was performed to evaluate the statistical significances of the fitted regression model and factors involved therein for the response factors namely F and R_a . From the experimental data the effects of three predictor factors (cutting speed, feed rate and cutting tool geometry) upon two response variables were analyzed by using MINITAB statistical software. Cutting forces were measured with a Kistler 9257 B type piezoelectric dynamometer and an associated 5019 B130 charge amplifier connected to PC employing Kistler Dynaware software. Longitudinal turning was conducted on CNC lathe (Johnford TC35)

at a constant depth of cut at 0.1 mm. The length of cut for each test was 20 mm in the axial direction. Average surface roughness (R_a) value which is one of the most important machinability criteria was measured according to ISO 4287 standard. R_a measurements were performed by using a Mahrsurf PS1 device with a cut-off length of 0.8 mm and sampling length of 5 m m. R_a values were calculated by averaging three roughness values obtained from three different positions of machined surface.

Table 1. Factors and their levels

Factors	Level 1	Level 2	Level 3	Level 4
A: Cutting speed, Vc (m/min)	60	80	100	120
B: Feed rate, f (mm/rev)	0.04	0.06	0.08	0.10
C: Tool Edge Geometry,(TEG)	S Type	T Type		

3. RESULTS and DISCUSSION

An analysis of variance (ANOVA) was applied to determine the statistically significance trends in the measured surface roughness and resultant cutting force. Separate ANOVA analyses were conducted for R_a surface roughness values and for resultant cutting forces i.e., feed, thrust, and main cutting forces. The lowest values of surface roughness and resultant cutting force will significantly improve the quality of machined surface and for lowering production costs. For this reason, “the lower-the-better” quality characteristic was used for the calculation of the S/N ratio. The experimental results and S/N ratios are given in Table 2.

Table 2. Experimental results and corresponding S/N ratios

Run	Control factors			Experimental results		Signal-to-noise ratio (S/N)	
	A	B	C	R_a (μ m)	F (N)	R_a	F
1	1	1	1	0.262	255.7	11.6340	-48.1546
2	1	2	1	0.346	244	9.2185	-47.7478
3	1	3	2	0.238	173.1	12.4867	-44.7659
4	1	4	2	0.352	167.6	9.0815	-44.4855
5	2	1	1	0.346	305.5	9.2185	-49.7002
6	2	2	1	0.341	299.6	9.3449	-49.532
7	2	3	2	0.424	227.8	7.4527	-47.1511
8	2	4	2	0.452	222.3	6.9068	-46.9401
9	3	1	2	0.625	311.4	4.0824	-49.8674
10	3	2	2	0.583	284.9	4.6817	-49.0944
11	3	3	1	0.423	344.3	7.4732	-50.7377
12	3	4	1	0.510	331.4	5.8486	-50.4083
13	4	1	2	0.912	344.1	0.8033	-50.7341
14	4	2	2	1.135	335.4	-1.0999	-50.5106
15	4	3	1	0.866	399.5	1.2496	-52.0297
16	4	4	1	0.844	385.7	1.4732	-51.7247

3.1. Effect of Feed Rate, Cutting Speed and Tool Edge Geometry on Surface Roughness

Curves of R_a surface roughness are shown in Fig. 2a and 2b. Fig. 2a shows the effect of cutting speed and feed rate on the R_a surface roughness parameter for the chamfered+honed edges. Fig. 2b shows the effect of cutting speed and feed rate on the R_a surface roughness parameter for the chamfered edges. These two figures showed that minimal value of surface roughness (R_a) was obtained at lowest feed rate (0.04 mm/rev). It can be seen from Fig. 2a and 2b that R_a value increases as the feed rate is increased from 0.04 mm/rev to 0.1 mm/rev. Specifically, the surface roughness increases as the feed rate increases as the surface roughness being proportional to the square of the feed rate. The surface roughness values are similar for two tool edge geometry. The lower surface roughness values were obtained with increasing cutting speeds by using chamfered+honed edge (Fig.3).

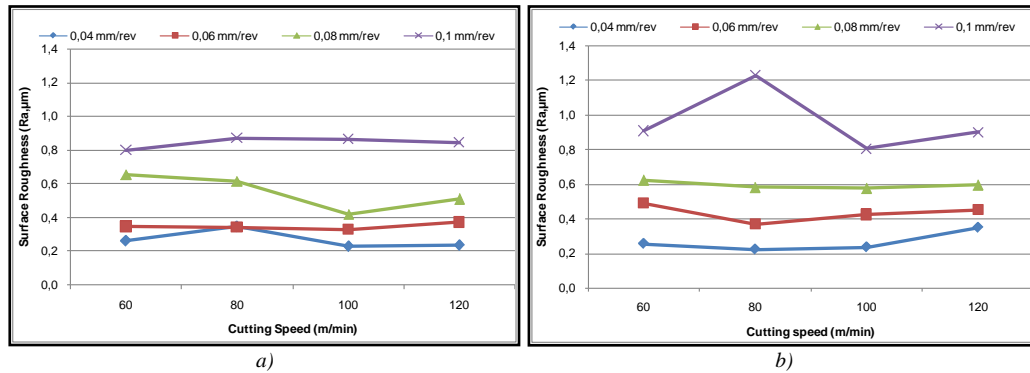


Figure 2. Effect of cutting speed and feed rate on surface roughness: a) chamfered+honed, b) chamfered.

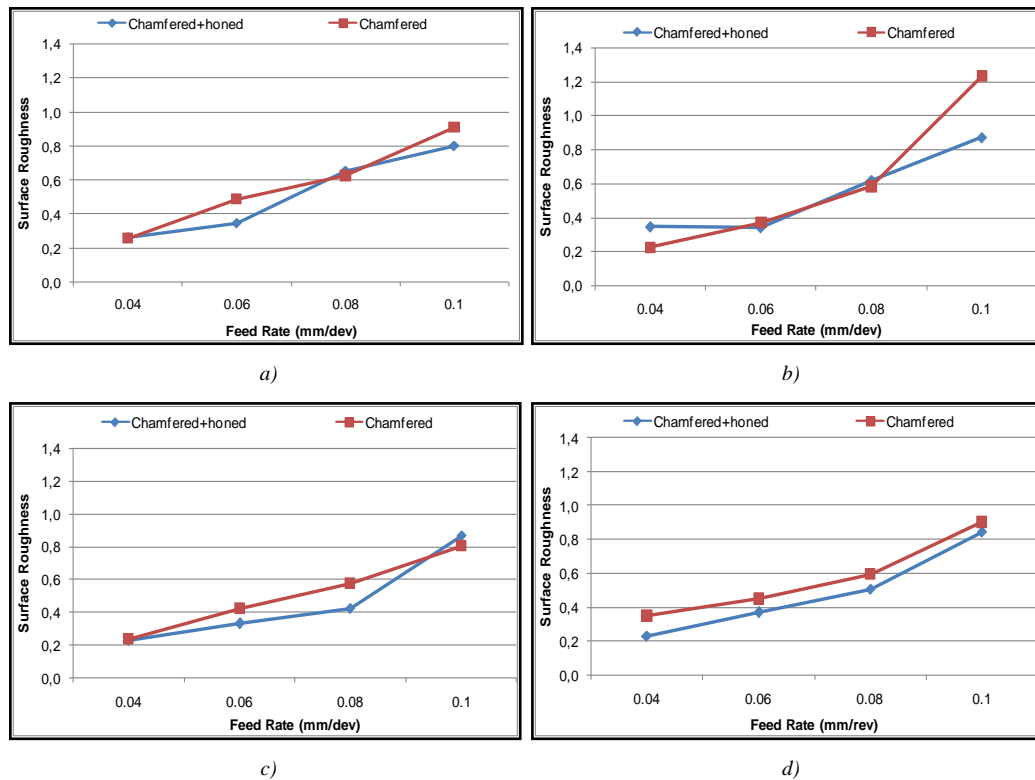


Figure 3. Effect of tool cutting edge and feed rate on surface roughness: a) 60, b) 80 c) 100 d) 120 m/min

3.2. Effect of Feed Rate, Cutting Speed and Tool Edge Geometry on Cutting Force

Figure 4a and 4b shows the effect of cutting speed and feed rate on the resultant cutting force for the chamfered+honed and chamfered edges, respectively. It is seen from Figure 4a and 4b that the feed and cutting force components increase with increasing the feed rate and generally decrease with increasing the cutting speed. Figure 4a and 4b shows that lower feed rate resulted in lower resultant cutting force. The increase in resultant cutting force with increasing the feed rate is due to an increase in chip load. However, drops in the cutting force with increasing the cutting speed are partly caused by a decrease in contact area and partly by a drop in shear strength in the flow zone as its temperature rises with increasing speed.

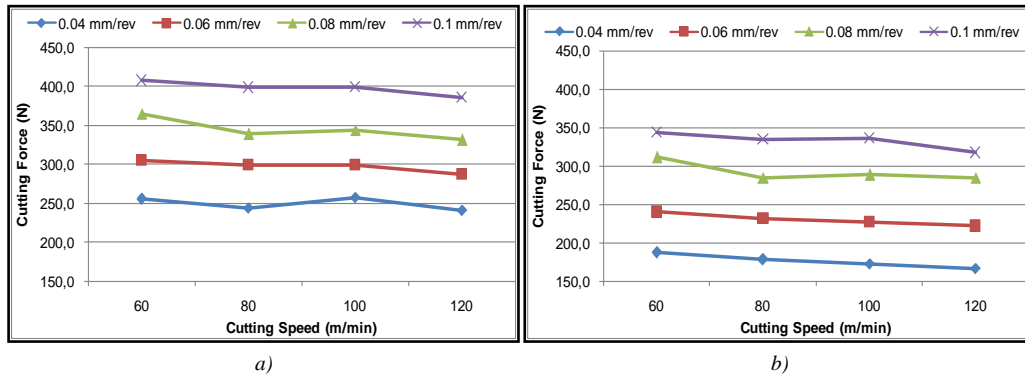


Figure 4. Effect of tool cutting speed and feed rate on resultant cutting force: a) chamfered+honed, b) chamfered.

It can be seen Figure 4a and 4b; lower cutting force was obtained with chamfered edge. This can be attributed to the sharper chamfered edge than honed edge. Chamfered edge provides excessive negative angle to the cutting action and results in high heat generation [23]. The cutting edge hone increases machining force and the contribution of the ploughing component of force. Increasing the ploughing force leads to more material side flow on the machined surface. Chamfer+honed edge affect chip formation and stress on machined surface. It is recommended that chamfer plus hone radius be used to obtain best residual stress profile [9,15].

3.3. ANOVA Results

An analysis of variance (ANOVA) was applied to determine the influence of cutting speed, feed rate and tool cutting edge on the machining output (R_a and F). ANOVA tables for surface roughness (R_a) and resultant cutting force (F) are given in Tables 3 and 5, respectively. The probability (P) values, which show the significance level of each factor and its degree of freedom (DF), sum of squares (SS), mean of squares (MS), F ratios and their percentage contribution ratio (PCR) can be seen here. This analysis was carried out for a significance level of $\alpha=0.05$, i.e. for a confidence level of 95%. Table 3 shows that the main effects of feed rate and tool edge geometry are significant to surface roughness. ANOVA results indicated that feed rate is the most effective parameter for R_a with percentage contribution ratio (PCR) values of 90.2%. The other factors that have effect on R_a are cutting speed with 2.5% of PCR and tool edge geometry with 3.1% of PCR (Table 3). Feed rate is the dominant parameter associated with the surface roughness. This is expected because it is well known that the theoretical surface roughness is primarily a function of the feed for a given nose radius and changes with the square of the feed rate value [23].

Table 3. ANOVA for S/N ratio of surface roughness

Source	DF	SS	MS	F-Ratio	P	PCR (%)
A	3	221.08	73.693	57.05	0.000	90.2
B	3	6.239	2.080	1.61	0.262	2.5
C	1	7.652	7.652	5.92	0.041	3.1
Error	8	10.334	1.292			4.2
Total	15	245.306				100

The most important criterion in the Taguchi method for analyzing experimental data is S/N ratio. The mean values of S/N ratios for surface roughness are given in Table 4. The different values (Δ) of S/N ratio between maximum and minimum are also shown in Table 4. Therefore, by considering the S/N ratios in Table 4, the optimum cutting conditions for the surface roughness were A1, B3 and C1. The smallest surface roughness and its S/N ratio that can be obtained according to these levels were calculated by using Eqs. (1) and (2). R_a value and its S/N ratio were determined as 0.245 μm and 12.221 dB, respectively.

$$\eta_G = \bar{\eta}_G + (\bar{A}_O - \bar{\eta}_G) + (\bar{B}_O - \bar{\eta}_G) + (\bar{C}_O - \bar{\eta}_G) \quad (1)$$

$$Ra_{cal} = 10^{-\eta_G/20} \quad (2)$$

In these equations, η_G is the S/N ratio calculated at the optimum levels (dB), $\bar{\eta}_G$ is the average S/N ratios of all variables (dB), $\bar{A}_O, \bar{B}_O, \bar{C}_O$ are the mean S/N ratios when the factors A, B and C are at optimum levels (dB), and Ra_{cal} is the calculated surface roughness (R_a) value.

Table 4. Response table for S/N ratios of surface roughness

Level	A	B	C
1	10.6052	6.4345	6.9326
2	8.2307	5.5363	5.5494
3	5.5215	7.1656	
4	0.6065	5.8275	
Δ	9.9986	1.6293	1.3832

Table 5 showed that the main effects of cutting speed and feed rate and edge geometry are all significant on the resultant cutting force. Table 5 shows that the most effective variable on the resultant cutting force is the feed rate with 72.6% of PCR. The other variables having effect on resultant cutting force are tool edge geometry with 22.2% and cutting speed with 4.7%. The error ratio was calculated as 0.5% and it is the smallest ratio. The mean values of S/N ratios for resultant cutting force are given in Table 6. The optimum cutting conditions for the resultant cutting force were A1, B4 and C2. According to Table 6, the smallest resultant cutting force was calculated by using Eqs. (2) and (3). Resultant cutting force value and its S/N ratio were determined as 171.28 N and -44.674 dB respectively.

Table 5. ANOVA for S/N ratio of cutting force

Source	DF	SS	MS	F-Ratio	P	PCR
A	3	55.6550	18.5517	358.38	0.000	72.6
B	3	3.6160	1.2053	23.28	0.000	4.7
C	1	16.9867	16.9867	328.15	0.000	22.2
Error	8	0.4141	0.0518			0.5
Total	15	76.6718				100

Table 6. Response table for S/N ratios of cutting force

Level	A	B	C
1	-46.29	-49.61	-50
2	-48.33	-49.22	-47.94
3	-50.03	-48.67	
4	-51.25	-48.39	
Δ	4.96	1.22	2.06

3.4. Confirmation Tests

Confirmation tests are a crucial step recommended by Taguchi to verify experimental conclusions. The purpose of the confirmation experiment is to validate the conclusions drawn during the analyzing. For this purpose, the following equations were used in the specification of the confidence interval (CI) for estimated surface roughness. Confirmation test was required in the present case study because the optimum combination of parameters and their levels i.e. A1B3C1 did not correspond to any experiment of the orthogonal array. Optimum combination of parameters and their levels i.e. A1B4C2 for resultant cutting force corresponded to experiment of the orthogonal array (OA). Therefore, it may be noted that if the optimal combination of parameters and their levels coincidentally match with one of the experiments in the OA, then no confirmation test is required.

$$CI = \sqrt{F_{0.05}(1, v_e) V_e \left(\frac{1}{n_{eff}} + \frac{1}{r} \right)} \quad (3)$$

$$n_{eff} = \frac{N}{1+v_T} \quad (4)$$

Table 7. Comparison between confirmatory test results and calculated values

Confirmatory Experiment results		Calculated values		Differences	
Ra _{mea} (μm)	η _{mea} (dB)	Ra _{cal} (μm)	η _{cal} (dB)	Ra _{mea} - Ra _{cal}	η _{mea} - η _{cal}
0.23	12.76	0.245	12.221	0.015	0.539

Here, v_e is the error degree of freedom, V_e is the error variance, n_{eff} is the repeating number of the experiments (Eq. 3). N is the total number of the experiments, v_T is the variable's degree of freedom and r is the number of confirmation tests (Eq. 4). Using Eqs. (3) and (4), confidence value of 2.39 dB was obtained

for surface roughness (Ra). Table 7 shows the differences between the values obtained by confirmatory tests and the values calculated by Eqs. (2) and (3) of the S/N ratios. It is seen that the difference of 0.539 dB is under 5% confidence interval of 2.39 dB for surface roughness. Therefore, the optimal control factor settings for all the cutting conditions were confirmed as confident.

4. CONCLUSIONS

In this study, effects of tool edge geometry, cutting speed and feed rate on the surface roughness and cutting forces in hard turning of AISI 52100 were optimized by Taguchi method. The results obtained from this study are given below:

1. According to the results of statistical analysis, it was found that the feed rate and tool edge geometry was the most significant factor on surface roughness with PCR of 90.2% and 3.1% PRC, respectively. The feed rate and tool edge geometry was the most significant parameters for resultant cutting force with PRC 72.6% and 22.2% PRC, respectively.
2. The optimum levels of the control factors for minimizing the surface roughness and resultant cutting force using S/N ratios were determined. The optimal conditions for surface roughness was observed at *A1-B3-C1* (i.e., feed rate = 0.04 mm/rev, cutting speed = 100 m/min and chamfer+honed edges). The optimal conditions for resultant cutting force was observed at the same levels *A1-B4-C2* (i.e., feed rate = 0.04 mm/rev, cutting speed = 120 m/min and chamfered edge).
3. Chamfer edge and chamfer+honed edges have similar trends on surface roughness. Cutting edge geometry, feed rate and cutting speed are all found to be effective on resultant cutting force. The lower resultant cutting forces were obtained by the chamfered edge.
4. Confirmation tests at optimal conditions were carried out. According to the confirmation test results, measured values are within the 95% confidence interval.

REFERENCES

1. Tönshoff, H.K., Arendt, C., Amor, R.B. "Cutting of hardened steel", *Annals of the CIRP*, vol. 49(2), pp.547-566, 2000.
 2. Byrne, G., Dornfeld, D., Denkena, B. "Advancing cutting technology", *Annals of the CIRP*, vol. 52(2), pp. 483-507, 2003.
 3. König, W., Berkold, A., Koch, K.F. "Turning versus grinding - a comparison of surface integrity aspects and attainable accuracies", *Annals of the CIRP*, vol. 42(1), pp. 39-43, 1993.
 4. Klocke, F., Brinksmeier, E., Weinert, K. "Capability profile of hard cutting and grinding processes", *Annals of the CIRP*, vol. 54(2), pp. 22-45, 2005.
 5. Qian, L., Hossain, M.R. "Effect on cutting force in turning hardened tool steels with cubic boron nitride inserts", *Journal of Materials Processing Technology*, vol. 191, pp. 274-278, 2007.
 6. Fñides, B., Yallese, M.A., Mabrouki, T., Rigal, J.F. "Surface roughness model in turning hardened hot work steel using mixed ceramic tool", *Mechanika*, vol. 3(77), pp. 68-73.
 7. Oliveira, A.J., Diniz, A.E., Ursolino, D.J. "Hard turning in continuous and interrupted cut with PCBN and whisker-reinforced cutting tools", *Journal of Materials Processing Technology*, vol. 209(12-13), pp. 5262-5270, 2009.
 8. Wan, L., Wang, D., Gao, Y. "Investigations on the effects of different tool edge geometries in the finite element simulation of machining", *Strojniški vestnik - Journal of Mechanical Engineering*, vol. 613, pp. 157-166, 2015.
 9. Dogra, M., Sharma, V.S., Dureja, J. "Effect of tool geometry variation on finish turning - A Review", *Journal of Engineering Science and Technology*, vol. 4(1), pp. 1-13, 2011.
 10. Fulemova, J., Janda, Z., "Influence of the cutting edge radius and the cutting edge preparation on tool life and cutting forces at inserts with wiper geometry", *Procedia Engineering*, vol. 69, pp. 565-573, 2014.
 11. Karpuschewskia, B., Schmidta, K., Prilukovab, J., Benoc, J., Mankovac, I., Hieud N.T. "Influence of tool edge preparation on performance of ceramic tool inserts when hard turning", *Journal of Materials Processing Technology*, vol. 213, pp. 1978-1988, 2013.
 12. Denkena, B., Biermann, D., "Cutting edge geometries", *CIRP Annals - Manufacturing Technology*, vol. 63, pp. 631-653, 2014.
 13. Rodriguez, C. J. C. "Cutting edge preparation of precision of cutting tools by applying micro-abrasive jet machining and brushing", Kassel University Press, Kassel, 2009.
 14. Kountanya, R., Al-Zkeri, I., Altan, T. "Effect of tool edge geometry and cutting conditions on experimental and simulated chip morphology in orthogonal hard turning of 100Cr6 steel", *Journal of Materials Processing Technology*, vol. 209, pp.5068-5076, 2008.
 15. Thiele, J.D., Melkote, S.N. "Effect of cutting edge geometry and work piece hardness on surface generation in the finish hard turning of AISI 52100 steel", *Journal of Materials Processing Technology*, vol. 94, pp. 216-226, 1999.
 16. Lalwani, D.I., Mehta, N.K., Jain, P.K. "Experimental investigations of cutting parameters influence on cutting forces and surface roughness in finish hard turning of MDN250 steel", *Journal of Materials Processing Technology*, vol.206, pp.167-179, 2008.
-

17. Almeidaa, F.A., Oliveiraa, F.J., Sousaa, M., Fernandesb, A.J.S., Sacramentoc, J., Silvaa, R.F. “Machining hardmetal with CVD diamond direct coated ceramic tools: effect of tool edge geometry”, “Diamond & Related Materials”, vol.14, pp. 651–656, 2005.
18. Özel, T. “Computational modelling of 3D turning: influence of edge microgeometry on forces, stresses, friction and tool wear in PCBN tooling”, *Journal of Materials Processing Technology*, vol. 209, pp. 5167–5177, 2009.
19. Kurt, A., Şeker, U. “The effect of chamfer angle of polycrystalline cubic boron nitride cutting tool on the cutting forces and the tool stresses in finishing hard turning of AISI 52100 steel”, *Materials and Design*, vol. 26, pp. 351-356, 2005.
20. Günay, M., Yücel, E., “Application of Taguchi method for determining optimum surface roughness in turning of high-alloy white cast iron”, *Measurement*, vol. 46, pp. 913–919, 2013.
21. Yücel, E., Günay, M., “Modelling and optimization of the cutting conditions in hard turning of high-alloy white cast iron (Ni-Hard)”, *Proc IMechE Part C: J Mechanical Engineering Science*, vol. 227(10), pp. 2280-2290, 2013.
22. Bouacha K., Yaltese M.A., Mabrouki T., Rigal J.F. “Statistical analysis of surface roughness and cutting forces using response surface methodology in hard turning of AISI 52100 bearing steel with CBN tool”, *Int. J. Refract. Met. Hard.*, vol. 28(3), pp. 349–361, 2010.
23. Özel, T., Hsu, T.K., Zeren, E. “Effects of cutting edge geometry, workpiece hardness, feed rate and cutting speed on surface roughness and forces in finish turning of hardened AISI H13 steel”, *Int. J. Adv. Manuf. Technol.*, vol. 25, pp. 262–269, 2005.
24. Özel, T., Karpat, Y., “Predictive modeling of surface roughness and tool wear in hard turning using regression and neural networks”, *Int. J. Mach. Tools Manuf.*, vol. 45, pp. 467–479, 2005.

Biography

Mehmet Boy, born in 1978, he received Ph.D. degree from Karabük University in 2015, Now, he is a lecturer in Vocational College in Karabük University. His main research interest is manufacturing technology. He is working on machining of hardened steels.

IMPROVEMENT OF LAUNDERING DURABILITY OF POLYPYRROLE COATED COTTON FABRICS

Zehra YILDIZ

Marmara University, Goztepe Campus, Faculty of Technology, Department of Textile Engineering, 34722, Istanbul, Turkey. zehra.yildiz@marmara.edu.tr

Onur ATAK

Marmara University, Goztepe Campus, Faculty of Technology, Department of Textile Engineering, 34722, Istanbul, Turkey.

İsmail USTA

Marmara University, Goztepe Campus, Faculty of Technology, Department of Textile Engineering, 34722, Istanbul, Turkey.

Abstract

In this study, chemical oxidative polymerization of pyrrole monomer has been performed onto the cotton fabric surfaces by using ferric chloride as oxidant and an aliphatic polyether with acidic groups as surfactant. Then the obtained PPy deposited cotton fabrics have been evaluated in terms of weight increment, surface electrical resistivity and electromagnetic shielding efficiency (EMSE). According to the results, weight increment, electrical resistance and EMSE values have been found as 73 %, $1.06 \times 10^3 \Omega$ and 23 dB respectively. In order to investigate the laundering durability of PPy deposition, fabric sample was coated by epoxyacrylate (EA) adhesive formulation and then cured by UV light. The characteristic peaks of PPy and EA have been proved by Fourier transform infrared (FTIR) spectroscopy. For the laundering durability testing, EA coated and un-coated, PPy deposited cotton fabrics have washed 3 times by ECE non-ionic detergent solution (4g/L) in order to observe the effect of EA layer. All tests were repeated after each washing process. Results proved that, EA layer helps to preserve PPy layer thus the shielding property. After 3 times washing, PPy deposited cotton fabric has showed just 1.23 dB EMSE value, whilst the sample with PPy+EA coating layers still showed 3.85 dB shielding efficiency.

Keywords: Polypyrrole, Cotton Fabric, Electromagnetic Shielding, Epoxyacrylate, UV-curing, Oxidative Polymerization

1. INTRODUCTION

In general, textile fabrics have dielectric character but can be converted into conductive surfaces by conductive polymer coating/deposition. In literature there are many researches exist investigating the conductive polymer usage onto the textile substrates such as polypyrrole (PPy), polyaniline, polythiophene etc. PPy is the promising one among these polymers considering its favorable properties such as high electrical conductivity and energy storage capacity, low cost, easy synthesis, environmentally friendly etc. PPy deposition or coating process has been extensively studied in literature including electrodes for electrochemical capacitors, cathode material for capacitive deionization technology, corrosion inhibition material, dye-sensitized solar cells, electromagnetic shielding materials etc. [1-5]. Chemical oxidative polymerization of pyrrole monomer has been performed on cotton, polyester, and polyamide fabric surfaces before in order to obtain electromagnetic shielding material and electrically conductive surfaces [6-8]. But there are just a few study exist considering the enhancement of conductive polymer durability onto the textile surfaces.

This study was aimed to improve the laundering durability of PPy coated cotton fabrics by using EA adhesive formulation. Firstly, chemical oxidative polymerization of pyrrole monomer has been performed onto the cotton fabric surfaces by using ferric chloride as oxidant and an aliphatic polyether with acidic groups as surfactant. PPy deposited cotton fabrics have been characterized by weight increment, surface electrical resistivity and EMSE measurements. Then to improve the laundering durability of PPy deposition, fabric sample was coated by EA adhesive formulation. After EA coating process samples were tested in terms of EMSE and electrical resistivity and the effect of EA layer has been observed.

2. EXPERIMENTAL

An easy way to comply with the symposium paper formatting requirements is to use this document as a template and simply type your text into it.

2.1. Materials

A plain weaved cotton fabric (113 g/m², 30 warp/cm, 22 weft/cm) was used as textile surface. Pyrrole (Py) monomer (Sigma-Aldrich, reagent grade), ferric chloride hexahydrate (FeCl₃·6H₂O, oxidant) (Merck), and aliphatic polyether with acidic groups (product number= 4242, acid value= 95-105 mgKOH/g) (DELTA-DC, surfactant) were used. Epoxy resin (EPIKOTE Resin 162) based upon diglycidyl ether of bisphenol-A with an epoxy equivalent weight (EEW) of 167-171 g e quiv.-1, acrylic acid (AA), triphenyl phosphine (TPP), hydroquinone (HQ), were all purchased from Sigma-Aldrich. Dipropylene glycol diacrylate (DPGDA) as reactive diluent was obtained from Allnex Corporation. 1-Hydroxycyclohexyl phenyl ketone (Irgacure 184) as photo initiator was obtained from Ciba Specialty Chemicals.

2.2. Methods

Chemical oxidative polymerization of pyrrole monomer has been performed according to a previous study [9]. Fabric samples in 10x10 cm dimensions were laid out in a glass vessel containing a magnetic stirrer, 30 mL pyrrole solution (1 M with distilled water) and surfactant (2.5%). Then the oxidant solution (30 mL 0.5 M FeCl₃ solution in distilled water) was added to the vessel drop wise in 30 minutes. Polymerization reaction was completed in 2h. The colour of the fabric was completely changed from white to black because of PPy deposition. Several washings (ethanol, 1 M HCl solution and distilled water) were applied on the fabric sample and then dried in room temperature. In order to preserve the PPy layer on cotton fabrics, EA was firstly synthesized according to the procedure that were previously told [10]. Then the obtained EA oligomer was applied on PPy coated samples via dip coating, and cured by UV-light. PPy and EA coated cotton fabric samples have been washed by a standard washing solvent (ECE non-ionic detergent 4g/L, in water) at 40 oC for ½ h [11].

2.3. Characterization

EMSE measurements in 0-3 GHz frequency range were carried out in Network Analyzer instrument (ROHDE&SCHWARZ) by using coaxial transmission line method [12]. Keithley 6517A Electrometer/High Resistance Meter instrument was used to measure the surface electrical resistivity [13]. All measurements were performed at 20 mA, 0.1 V. Weight increment after PPy deposition and weight loss values after several washing steps have been measured in an analytical balance (Acculab-ALC-80.4). Perkin Elmer Spectrum 100 FTIR spectrophotometer with an ATR sampling was used for characterization of PPy and EA layers.

3. RESULTS AND DISCUSSION

3.1. FTIR Spectroscopy

Figure 1 shows the FTIR spectra of pure cotton, PPy coated cotton fabric and PPy+EA coated cotton fabrics respectively. According to the figure, after PPy deposition process, the formation of PPy layer onto the fabric surface was proven by newly formed peaks namely; C=O stretching, C=C stretching, C-N stretching, C-H stretching, C-H wagging vibration and N-H stretching were located at 1720 cm⁻¹, 1550 cm⁻¹, 1309 cm⁻¹, 1040 cm⁻¹, 787 cm⁻¹, and 617 cm⁻¹ respectively. C-N stretching vibrations were seen in the bands of 1299 and 1166 cm⁻¹. The band at 672 cm⁻¹ belongs to the doped Cl⁻ ion on the PPy backbone. After EA coating process on to the PPy-deposited cotton fabric surface, the intensity of the characteristic ester carbonyl peak at 1720 cm⁻¹ increased. Additionally, the intensity of the broad peak at about 3460 cm⁻¹ which is assigned to secondary hydroxyl groups also increased stemming from the opening of epoxide rings.

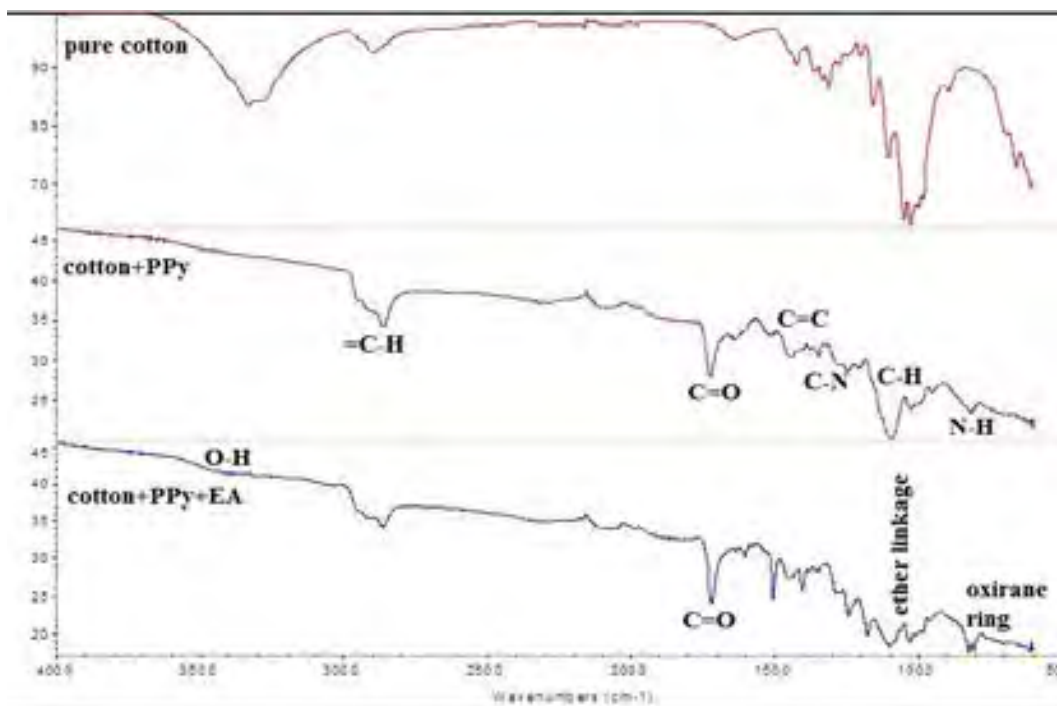


Figure 1. FTIR spectra of pure cotton, PPy coated cotton fabric and PPy+EA coated cotton fabric.

3.2. Weight Increment and Loss

Table 1 shows the weight increment after PPy deposition, EA coating processes and weight loss of PPy+EA coated samples after several washing steps. According to the table, after first washing step, a great weight loss of 16.68% was observed in the PPy coated cotton fabric. Whilst in PPy+EA coated fabric the weight loss value was only 5.78%. It is obvious that EA layer helped to keep the PPy deposition onto the fabric surface. These behavior also found after second and third washings. Weight loss of fabric with EA layer was always observed less than the samples with only PPy layer.

Table 1. Weight increment and weight loss (%) values of PPy and EA coated fabric samples before and after several washings.

PureCotton	Weight (g)		WeightLoss (%)		
	PPy+Cotton	PPy+EA+Cotton	Washing-1	Washing-2	Washing-3
1.14	1.98	---	16.68	2.91	2.49
1.14	1.98	2.11	5.78	1.03	1.01

3.3. Surface Electrical Resistivity

Surface electrical resistivity values of the PPy and EA coated cotton fabric samples before and after washing processes can be seen in Table 2. According to the table, after PPy deposition, cotton fabric became an electrically conductive surface. After washing steps, in PPy coated fabric, surface resistivity increases, in other words electrical conductivity decreases. In PPy and EA coated cotton fabric sample, after several

washings conductivity increases. After third washing, the conductivity value is higher than even its unwashed value. This result can be explained by the Maxwell-Wagner polarization effect [14]. Due to the increased polarity after EA coating on the molecular structure, conductivity increases with washing because of water hydroxyl ions.

Table 2. Surface electrical resistivity values of PPy and EA coated fabric samples before and after several washings.

Surface Electrical Resistivity (Ω/sq)					
Pure Cotton	PPy+Cotton	PPy+EA+Cotton	Washing-1	Washing-2	Washing-3
1.68×10^5	1.06×10^3	--	1.08×10^3	1.36×10^3	1.16×10^3
	1.06×10^3	1.02×10^3	1.03×10^3	0.91×10^3	0.84×10^3

3.4. EMSE Measurement

Figure 2 shows the EMSE results of PPy coated fabric sample before and after washing steps. Accordingly, after PPy deposition, a max shielding value of 24 dB was observed in the range of 2-2.5 GHz frequencies. The highest shielding loss was seen after first washing step. After third washing the EMSE value decreased till 1.23 dB.

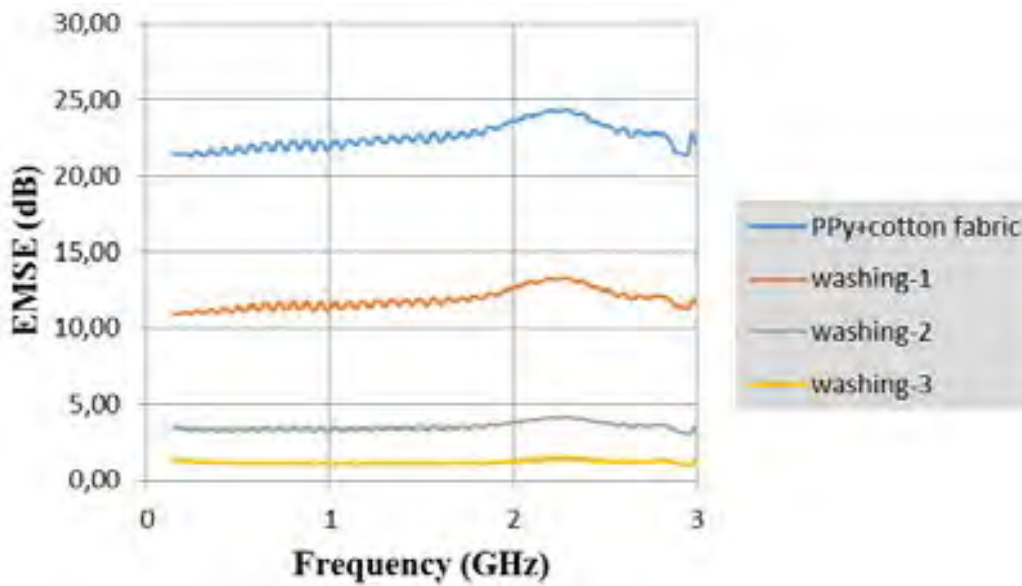


Figure 2. EMSE values of the PPy coated cotton fabric sample before and after several washings.

EMSE values of PPy and EA coated fabric sample before and after several washings can be seen in Figure 3. After first washing the EMSE value decreased to 16 dB and after third washing, the sample still shows about 5 dB EMSE result. The sample with PPy and EA layers shows better laundering durability comparing to the sample without EA layer. EA layer helps fabric to resist more washings.

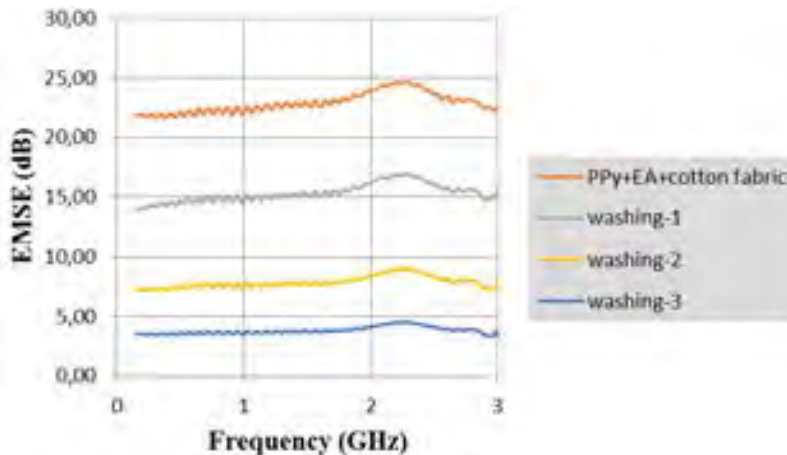


Figure 3. EMSE values of the PPy and EA coated cotton fabric sample before and after several washings.

4. CONCLUSIONS

In this study, the chemical oxidative polymerization of pyrrole monomer has been performed in the presence of oxidant and surfactant. After PPy formation on the fabric surface in order to keep the PPy layer on the fabric surface, EA coating process has been applied. The characteristic peaks of PPy and EA layers have been illustrated by FTIR spectroscopy. Weight loss, surface electrical resistivity and EMSE results were all in consistent with each other and showed that EA layer can be used to enhance the laundering durability of PPy coated cotton fabrics.

REFERENCES

- [1]. F. Liu, S. Wang, G. Han, R. Liu, Y. Chang, and Y. Xiao, "Multiwalled carbon nanotubes/polypyrrole/graphene/nonwoven fabric composites used as electrodes of electrochemical capacitor" *Journal of Applied Polymer Science*, vol. 131, 2014.
- [2]. K. Lota, G. Lota, A. Sierczynska, and I. Acznik, "Carbon/polypyrrole composites for electrochemical capacitors" *Synthetic Metals*, vol. 203, pp. 44-48, 2015.
- [3]. Y. Wang, L. Zhang, Y. Wu, S. Xu, and J. Wang, "Polypyrrole/carbon nanotube composites as cathode material for performance enhancing of capacitive deionization technology" *Desalination*, vol. 354, pp. 62-67, 2014.
- [4]. J. Xu, M. Li, L. Wu, Y. Sun, L. Zhu, et al. "A flexible polypyrrole-coated fabric counter electrode for dye-sensitized solar cells" *Journal of Power Sources*, vol. 257, pp. 230-236, 2014.
- [5]. H. Zhu, J. Hou, R. Qiu, J. Zhao, and J. Xu, "Perfluorinated lubricant/ polypyrrole composite material: Preparation and corrosion inhibition application" *Journal of Applied Polymer Science*, 131, 2014.
- [6]. S. Cetiner, "Dielectric and morphological studies of nanostructured polypyrrole-coated cotton fabrics" *Textile Research Journal*, 0040517514523180, 2014.
- [7]. S. Maiti, D. Das, and K. Sen, "Characterization of electro-conductive fabrics prepared by in situ chemical and electrochemical polymerization of pyrrole onto polyester fabric" *Materials Science and Engineering: B*, vol. 187, pp. 96-101, 2014.
- [8]. Z. Yildiz, U. İsmail, and A. Gungor, "Investigation of the electrical properties and electromagnetic shielding effectiveness of polypyrrole coated cotton yarns" *Fibres & Textiles in Eastern Europe*, 98, vol. 21, pp. 32-37, 2013.
- [9]. Z. Yildiz, I. Usta, A. Gungor, and H. A. Onen, "Investigation of Polypyrrole Coated Cotton Fabrics as Electromagnetic Shielding Material" in *Future Technical Textile 2014 Conference*, Istanbul, Turkey, 2014.
- [10]. Y. C. Su, L. P. Cheng, K. C. Cheng, and T. M. Don, "Synthesis and characterization of UV- and thermo-curable difunctional epoxyacrylates" *Materials Chemistry and Physics*, vol. 132, pp. 540-549, 2012.
- [11]. "TS EN ISO 105-C06: Textiles - Tests for colour fastness - Part C06: Colour fastness to domestic and commercial laundering," ed, 2012, p. p. 7.
- [12]. "ASTM D4935-10: Standard Test Method for Measuring the Electromagnetic Shielding Effectiveness of Planar Materials," ed, 2010, p. p. 10.
- [13]. "ASTM D257-07: Standard Test Methods for DC Resistance or Conductance of Insulating Materials," ed, 2007, p. p. 18.
- [14]. S. H. Mansour, N. Mostafa, and L. Abd-El-Messieh, "Electrical and positron annihilation study on epoxy and epoxy acrylate composites" *European Polymer Journal*, 43, pp. 4770-4782, 2007.

Biography

Zehra Yildiz is a research assistant in Marmara University, in Textile Engineering Department. She is a PhD student in Istanbul Technical University, in Polymer Science and Technology Department. Her main research areas are; conductive textiles, textile adhesives, functional polymeric textiles coatings.

A COMPARATIVE STUDY ON TARGET DENSITY FUNCTIONS

Ridvan Firat CINAR

Batman University, Technology Faculty, Dept.of Electronics and Comm. Eng., Batman/TURKEY
Sakarya University, Faculty of Engineering, Department of Electrical – Electronics, Sakarya/TURKEY

Askin DEMIRKOL

Sakarya University, Faculty of Engineering, Department of Electrical – Electronics, Sakarya/TURKEY

Motuma M. ABAFOGI

Sakarya University, Faculty of Engineering, Department of Electrical – Electronics, Sakarya/TURKEY

Zafer DEMIR

Anadolu University, Porsuk Vocational School, Department of Electricity and Energy, Eskisehir/TURKEY

Abstract

In this work a comparative approach on target density functions used in sensor imaging is presented. The target density functions that are widely used in medical and military engineering are considered in various theoretical methods. The target density function used in SAR – ISAR systems in the form of $\rho(x,y)$ considering the cartesian coordinates is employed with the Fourier approach. The image function $g(\rho, \theta)$ in one dimensional or $f(x,y)$ two dimensional form in the Radon Transform is considered with 1-D Fourier transform. With x (velocity) and y (range) variables, $D(x,y)$ target density function of Fowle - Naparst is considered for dense target environments. A new $G(R,\beta)$ shaped target density function which is different from the previously developed ones will be presented. The new target density function with the variables R as range and $\beta=\cos(\theta)$ as a function of scanning angle is reconstructed with phased array sensor approach.

Keywords: *phased array radar system, active sensor imaging, target density functions, ambiguity functions, Radon transform.*

1. INTRODUCTION

Active sensors devices that interpret the relation between sent and backscattered signals and receive various information about the target. The distribution of the target's reflectivity function on spatial plane is able to provide the target's image [1,2,14]. The range resolution of target area is related to bandwidth, while the cross range resolution varies with the aperture size. However, using large apertures in order to obtain high cross range resolutions is difficult to construct and also expensive. In 1950's a revolutionary invention called synthetic aperture radar was made by Wiley [11,12]. This invention provided new possibilities to coherently process the signals obtained from multiple radar elements from diverse angles related to target, or implement various geometrical approaches.

In this paper, system models that fit in with this approach are investigated and a new method is developed.

2. DENSITY APPROACHES

2.1. SAR – ISAR imaging

SAR (Synthetic Aperture Radar) – ISAR (Inverse Synthetic Aperture Radar) systems are powerful signal processing techniques with a wide range of applications that adapted various forms of problems. The basic goal of SAR-ISAR systems is to achieve a two dimensional planar image of the observed target. Synthetic aperture methods are used in order to obtain raw signals in SAR-ISAR systems.

The densities of Scattering centers can be shown on a two-dimensional planar image by applying Fourier based operations to the signals obtained under finite bandwidth and diverse aspect [1,4,9,11,14,15].

In this method, the basic steps of the ISAR approach that processes a three dimensional target's two dimensional image can be considered as:

$$s(t) = \int_{-\infty}^{\infty} \int_{-\infty}^{\infty} \rho(x, y) e^{-j2\pi f_0 \frac{2R_p(t)}{c}} dx dy \quad (1)$$

This equation assumes the condition that $2R_p(t)/c \leq T \leq TPRI + 2R_p(t)/c \leq T$. The term $\rho(x,y)$ is the density function of the target being imaged, $TPRI$ is pulse repetition interval, $R_p(t)$ is range, f_0 is carrier frequency and the c is the speed of propagation, (i.e., *light speed*). Range can be expressed as a function of time.

$$R_p(t) = R(t) + x \cos[\theta(t) - \alpha] - y \sin[\theta(t) - \alpha] \quad (2)$$

In this expression α is azimuth, $\theta(t)$ is the rotation angle as a function of time. After these operations, by taking inverse Fourier transform of $s(t)$, the $\rho(x,y)$ target density functions can be reconstructed as [4].

$$\rho(x, y) = \int_{-\infty}^{\infty} \int_{-\infty}^{\infty} X(f_x, f_y) e^{j2\pi(x f_x - y f_y) f_0 \frac{2R_p(t)}{c}} df_x df_y \quad (3)$$

$$f_x = \frac{2f_0}{c} \cos \theta(t) \quad \text{and} \quad f_y = \frac{2f_0}{c} \sin \theta(t) \quad (4)$$

2.2. Fowle-Naparst Approach

The Fowle-Naparst's work is one the first ideas that put target density function forward [7]. In accordance with this work, the density of the space which includes target is reconstructed via the Ambiguity function. The expression of the Ambiguity Function is given as;

$$A(x, y) = \int_{-\infty}^{\infty} u\left(t - \frac{x}{2}\right) \bar{v}\left(t + \frac{x}{2}\right) e^{-j2\pi y t} dt \quad (5)$$

In this function, x and y are the range and velocity of the target respectively. This approach was first introduced by Fowle [6] and then improved by Naparst [7] by employing the Ambiguity Function. In this work, an improved target density function $D(x,y)$ employing the ambiguity function which includes the variables velocity and range was developed.

The relation between the signal reflected from the target $e(t)$ and the signal sent $s(t)$ is expressed as

$$e(t) = \int_0^{\infty} \int_{-\infty}^{\infty} D(x, y) \sqrt{y} s(y(t-x)) dx dy \quad (6)$$

The target density function $D(x,y)$ that contains by the backscattered signal can be reconstructed by the following complex operations in vector space including the Ambiguity function given above.

$$D(x, y) = \sum_{n,m=0}^{\infty} \langle e_n, s_m \rangle A_{nm}(x, y) \quad (7)$$

In this expression s_m is the propagated signal and e_n is the backscattered signal (echoed). The Ambiguity function used has the following form.

$$A_{nm}(x, y) = \int_{-\infty}^{\infty} s_n(y(t-x)) \bar{s}_m(t) dt \quad (8)$$

Figure 1 represents an approximation of a Dirac function's target density function, for $x=0$ $y=1$, that is reconstructed by Ambiguity function based Fowle-Naparst approach [7].

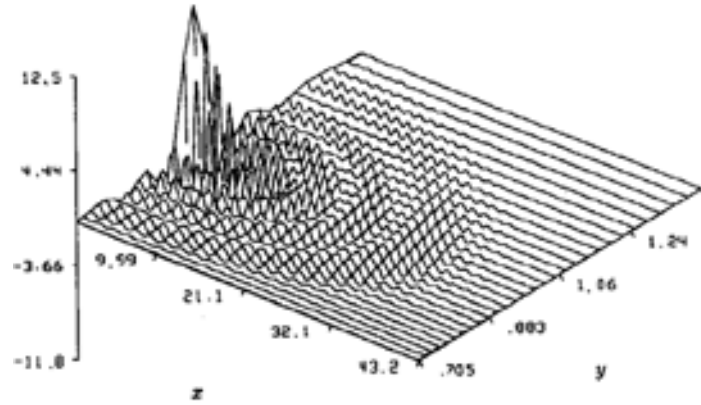


Figure 1. $D(x,y)$ approximation for $x=1, y=0$

2.3. Imaging by range-angle target density function

2.3.1. Background

In this paper, a new target density function that has different properties from the target density functions discussed above is presented. $G(R,\beta)$ formed new target density function contains the variables R as range and $\beta = \cos(\theta)$ as function of scanning angle. The newly defined target density function $G(R,\beta)$ represents the ratio of the amplitudes of the signal sent towards the point (R,β) to the backscattered signal.

The new approach introduced in this paper is imaging with phased array radar system. In this case our imaging scenario's schematic representation becomes:

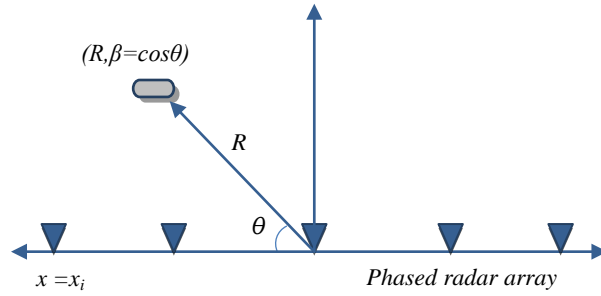


Figure 2. Imaging with phased array radar

As can be seen, this approach only takes the upper half plane of the coordinate system into account [3]. In this condition, the propagated pulse signal $p(t)$ is:

$$p(t) = \sum_{k=-\infty}^{\infty} A_k e^{j k \omega_0 t} \quad (9)$$

$$\omega_0 = 2\pi \times PRF \quad (10)$$

PRF term in this equation is the pulse repetition frequency. If this signal is modulated with $s_c(t)$ carrier signal which is expressed as:

$$s_c(t) = e^{j \omega_c t} \quad (11)$$

the modulated output signal becomes:

$$s_m(t) = p(t)s_c(t) \quad (12)$$

Echo from the point represented by $G(R, \beta)$ density function is:

$$s_r(x, t) = s_m(t - 2R/c - \beta x/c)g(R, \beta) \quad (13)$$

In this case, if the backscattered signal is the echo of the point scatterer located at R_1 , the signal that contains the image function can be showed as;

$$\left. \begin{aligned} s_r(x, t) &= \int_{-\infty}^{\infty} \int_{-\infty}^{\infty} s_m(t - 2R/c - \beta x/c)g(R, \beta)dRd\beta \\ &= \int_{-1}^1 \int_0^{R_1} s_m(t - 2R/c - \beta x/c)g(R, \beta)dRd\beta \\ &= \int_{-1}^1 \int_0^{R_1} p(t - 2R/c - \beta x/c) \\ &\quad \times e^{j \omega_c (t - 2R/c - \beta x/c)} g(R, \beta)dRd\beta \\ &= \int_{-1}^1 \int_0^{R_1} p(t - 2R/c - \beta x/c) \\ &\quad \times e^{-j \omega_c (2R/c + \beta x/c)} e^{j \omega_c t} g(R, \beta)dRd\beta \end{aligned} \right\} \quad (14)$$

The term $s_r(x, t)$ is the output of the radar system which consists phased array elements. For the solution to the algorithm, the next steps can be evaluated.

$$\begin{aligned}
 s_r(x, t) &= \int_{-1}^1 \int_0^{R_1} \sum_{k=-\infty}^{\infty} A_k e^{j k \omega_0 (t-2R/c-\beta x/c)} \\
 &\quad \times e^{-j \omega_c (2R/c+\beta x/c)} e^{j \omega_c t} g(R, \beta) dR d\beta \\
 &= \sum_{k=-\infty}^{\infty} A_k e^{j k \omega_0 t} \int_{-1}^1 \int_0^{R_1} e^{-j k \omega_0 (2R/c+\beta x/c)} \\
 &\quad \times e^{-j \omega_c (2R/c+\beta x/c)} e^{j \omega_c t} g(R, \beta) dR d\beta \\
 &= \sum_{k=-\infty}^{\infty} A_k e^{j (\omega_c+k \omega_0) t} \int_{-1}^1 \int_0^{R_1} e^{-j k \omega_0 (2R/c+\beta x/c)} \\
 &\quad \times e^{-j \omega_c (2R/c+\beta x/c)} g(R, \beta) dR d\beta \\
 &= \sum_{k=-\infty}^{\infty} A_k e^{j (\omega_c+k \omega_0) t} \int_{-1}^1 \int_0^{R_1} e^{-j (\omega_c+k \omega_0)(2R/c+\beta x/c)} \\
 &\quad \times g(R, \beta) dR d\beta
 \end{aligned} \tag{15}$$

The last equation that expresses the radar output is demodulated by $s_d(t)$

$$s_d(t) = e^{-j (\omega_c+k \omega_0) t} / A_k \tag{16}$$

$$\begin{aligned}
 s_r(x, t) &= (e^{-j (\omega_c+k \omega_0) t} / A_k) \left[\sum_{k=-\infty}^{\infty} A_k e^{j (\omega_c+k \omega_0) t} \right. \\
 &\quad \left. \times \int_{-1}^1 \int_0^{R_1} e^{-j (\omega_c+k \omega_0)(2R/c+\beta x/c)} g(R, \beta) dR d\beta \right] \\
 S(k, x) &= \int_{-1}^1 \int_0^{R_1} e^{-j (\omega_c+k \omega_0)(2R/c+\beta x/c)} g(R, \beta) dR d\beta \\
 &= \int_{-1}^1 \int_0^{R_1} e^{-j (\omega_c+k \omega_0)/c(2R/c+\beta x/c)} g(R, \beta) dR d\beta
 \end{aligned} \tag{17}$$

Last equation can be considered again as $G(k, \beta)$, for the k and β variables;

$$G(k, \beta) = \int_0^{R_1} g(R, \beta) e^{-j (\omega_c+k \omega_0) 2R/c} dR \tag{18}$$

$$S(k, x) = \int_{-1}^1 G(k, \beta) e^{-j (\omega_c+k \omega_0) \beta x/c} d\beta \tag{19}$$

$$S_k(x) = \int_{-1}^1 G_k(\beta) e^{-j (\omega_c+k \omega_0) \beta x/c} d\beta \tag{20}$$

The important matter in here is to extract the target density function $G(R, \beta)$. Therefore equation (20) can be considered as;

$$G_k(\beta) = \int_0^{R_1} g(R, \beta) e^{-j (\omega_c+k \omega_0) 2R/c} dR \tag{21}$$

To obtain the target density function from equation (21), the ambiguity function discussed in previous chapters (equation (54)) is employed. By considering the signal $s_m(t)$, we can make use of the correlation function – power spectral density relation.

The correlation between $s_m(t)$ and $s_n(t)$ signals can be expressed as:

$$R(\tau) = s_m(t) * s_n(-t) = \int_{-\infty}^{\infty} s_m(\tau) \overline{s_n(t + \tau)} dt \quad (22)$$

and in the symmetrical form;

$$R(\tau) = \int_{-\infty}^{\infty} s_m\left(\tau - \frac{t}{2}\right) \overline{s_n\left(\tau + \frac{t}{2}\right)} dt. \quad (23)$$

The power spectral density corresponding to the target is correlation function's Fourier transform, then the next steps can be formed:

$$\left. \begin{aligned} S(\omega) &= \int_{-\infty}^{\infty} R_x(\tau) e^{-j\omega\tau} d\tau \\ &= \int_{-\infty}^{\infty} \int_{-\infty}^{\infty} u(\tau) \overline{v(t + \tau)} dt e^{-j\omega\tau} d\tau \\ &= \int_{-\infty}^{\infty} \int_{-\infty}^{\infty} u(\tau) \overline{v(t + \tau)} e^{-j\omega\tau} d\tau dt \end{aligned} \right\} \quad (24)$$

for $\tau = \tau - \frac{t}{2}$;

$$\left. \begin{aligned} S(\omega) &= \int_{-\infty}^{\infty} \int_{-\infty}^{\infty} u\left(\tau - \frac{t}{2}\right) \overline{v\left(\tau - \frac{t}{2} + t\right)} e^{-j\omega\left(\tau - \frac{t}{2}\right)} d\tau dt \\ &= \int_{-\infty}^{\infty} \int_{-\infty}^{\infty} u\left(\tau - \frac{t}{2}\right) \overline{v\left(\tau + \frac{t}{2}\right)} e^{-j\omega\tau} d\tau e^{j\omega\frac{t}{2}} dt \\ &= \int_{-\infty}^{\infty} \left(\int_{-\infty}^{\infty} u\left(\tau - \frac{t}{2}\right) \overline{v\left(\tau + \frac{t}{2}\right)} e^{-j\omega\tau} d\tau \right) e^{j\omega\frac{t}{2}} dt \end{aligned} \right\} \quad (25)$$

$$A(t, \omega) = \int_{-\infty}^{\infty} u\left(\tau - \frac{t}{2}\right) \overline{v\left(\tau + \frac{t}{2}\right)} e^{-j\omega\tau} d\tau \quad (26)$$

$$S(\omega) = \int_{-\infty}^{\infty} A(t, \omega) e^{j\omega\frac{t}{2}} dt \quad (27)$$

Equation (21) that contains the $G(R, \beta)$ target density function is compared with the equation (27);

$$g(R, \beta) \equiv A(t, \omega) \quad (28)$$

Therefore the target density function can be expressed as:

$$G(R, \beta) = \int_{-\infty}^{\infty} s_m\left(t - \frac{\tau_R}{2}\right) \overline{s_n\left(t + \frac{\tau_R}{2}\right)} e^{j\beta t} dt \quad (29)$$

for $\tau = \frac{R}{2c}$

As a result, target density function is obtained by analyzing the relationship between Ambiguity Function and Correlation (Power Spectral Density) approaches.

2.3.2. Simulation

The simulated target is a fighter aircraft, digitally constructed by 120 point scatterers. The dataset of the simulated signal represents a complex matrix of the signal received by each unit of phased array system. And each received data has 64 samples [15].

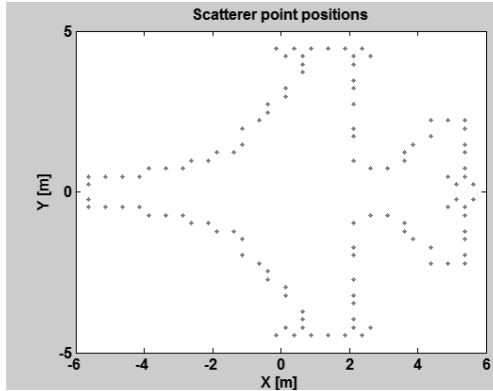


Figure3. Positions of the scatterer centers

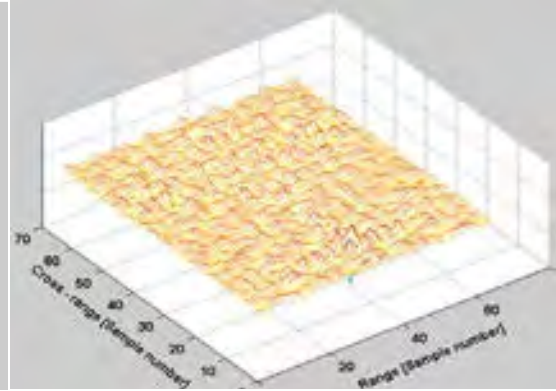


Figure4. Backscattered E-field from scattering centers

The radar operates at 8 GHz frequency with 525 MHz bandwidth. The total aspect angle diversity is 13.5°. In Figure5., schematic presentation of the process is given.

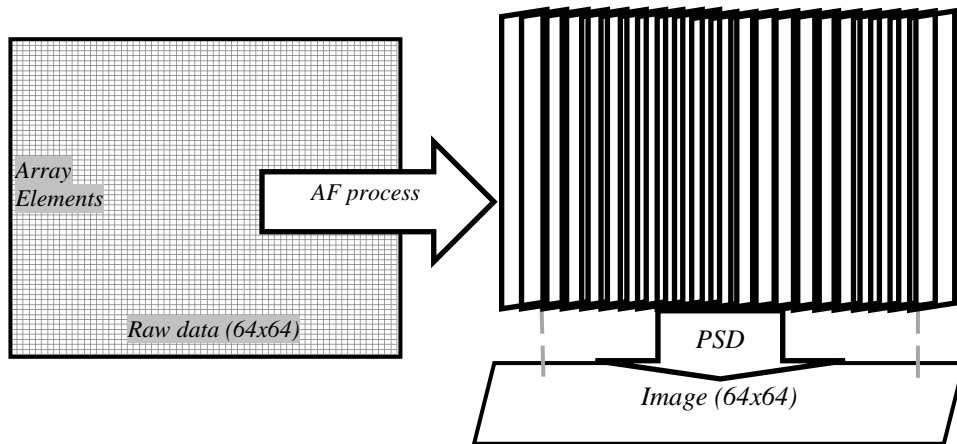


Figure5. Schematic representation of imaging process

During the ambiguity function process, only the right half plane of the ambiguity function is taken due to the symmetrical property of the ambiguity function.

Distribution and intensity of the side lobes around the peak points in the reconstructed image are directly related with signal choice [5,13].

In the imaging process of the Ambiguity Function, we expect a sharp peak to be on the scatterer point. However, this is impossible due to the natural imperfections of theoretical and computational processes such as finite bandwidth and noise [16].

2.3.3. Result

Figure6. shows the result image of reconstruction of the target density function by ambiguity function. In Figure7., ISAR image of the target is also given for comparison.

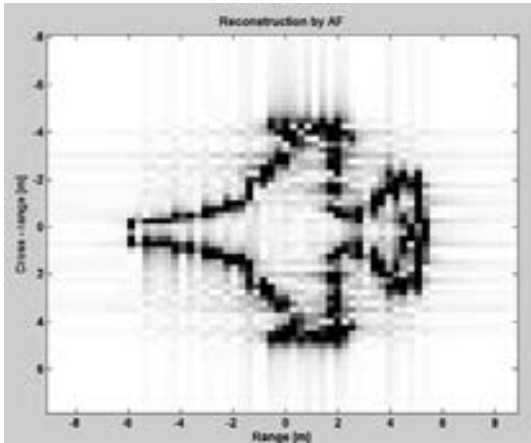


Figure 6. Image of target density function reconstructed by Ambiguity function

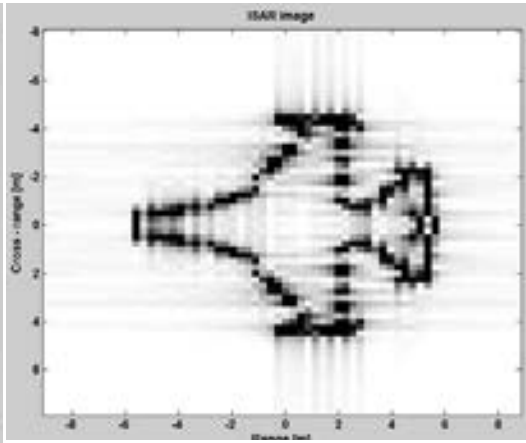


Figure 7. Conventional ISAR image

Alterations caused by the side lobes can be seen clearly in Figure 8. and Figure 9.

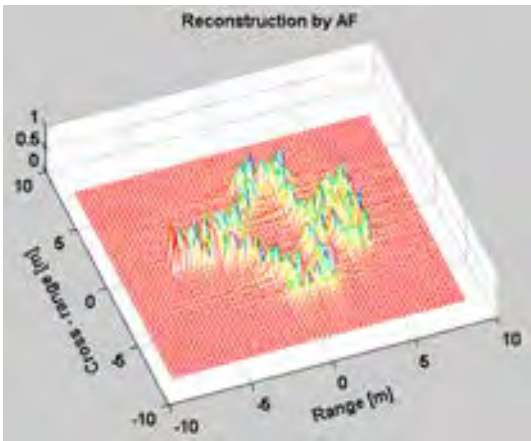


Figure 8. Normalized scatterer points intensities of target density function that reconstructed by ambiguity function

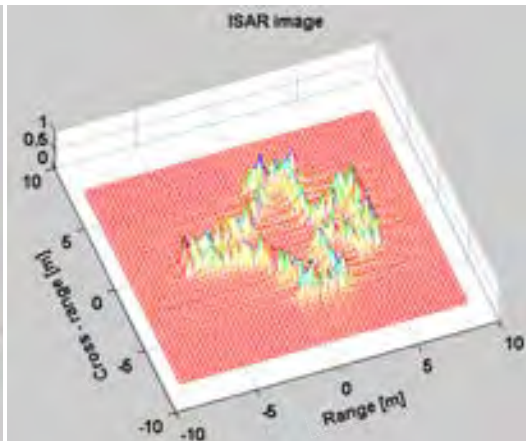


Figure 9. Normalized ISAR image of target

This technique certainly supports fundamental signal processing methods such as denoising, interpolation etc. Improvements on the reference signal enables us to get a finer result [13,16].

2.4. Radon Transform

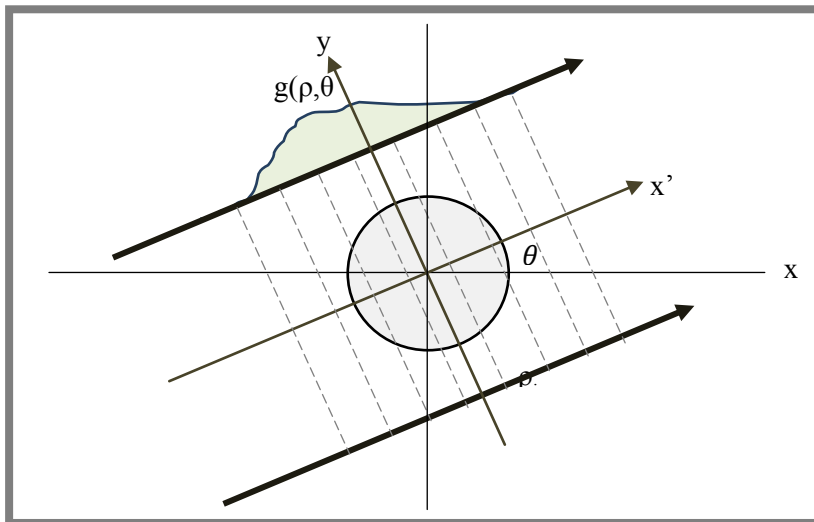


Figure 10. A CT scenario

For a given function g in a plane domain, Radon transform is defined for the variables (ρ, θ) on continuous space coordinates:

$$\left. \begin{aligned} G(\omega, \theta) &= \int_{-\infty}^{\infty} g(\rho, \theta) e^{-j2\pi\omega\rho} d\rho \\ &= \iint_{-\infty}^{\infty} f(x, y) e^{-j2\pi\omega(x\cos\theta + y\sin\theta)} dx dy \\ &= F(\omega \cos \theta, \omega \sin \theta) \\ &= \iint_{-\infty}^{\infty} f(x, y) e^{-j(\underline{u}x + \underline{v}y)} dx dy \end{aligned} \right\} \quad (30)$$

$$F(u, v) = \iint_{-\infty}^{\infty} f(x, y) e^{-j(\underline{u}x + \underline{v}y)} dx dy \quad (31)$$

$$f(x, y) = \frac{1}{4\pi^2} \iint_{-\infty}^{\infty} F(u, v) e^{j(\underline{u}x + \underline{v}y)} dx dy \quad (32)$$

By the explanations, in radon transform, whereas the projection of $g(\rho, \theta)$ is obtained by one dimensional slice projection, it corresponds to two dimensional Fourier transform as $f(x, y)$. In the light of this, the target density function in our paper as $G(R, \beta)$ can be taken as the following.

$$g(R, \beta) \equiv f(x, y) \equiv g(\rho, \theta) \quad (33)$$

3. CONCLUSIONS

This work represents existing and newly developed approaches on density functions. Relations between these approaches are investigated also. Angle dependent target density functions provide the advantages of imaging by diverse angles. This case is discussed both in theoretical background and application.

REFERENCES

- [1]. Skolnik, M.I., *Introduction to radar systems*, 1980.
- [2]. Woodward, P.M., *Probability and information theory with applications to radar*, 1957.
- [3]. Demirkol, A., "Range Density Function for Active Sensor Imaging", *Defence Science Journal* vol.57, no.3, pp.305-313, May 2007.
- [4]. Chen, V.C., Qian, S.: *Time frequency transform vs. fourier transform for radar imaging*. Time-Frequency and Time-Scale Analysis, 1996., *Proceedings of the IEEE-SP International Symposium on*, pp.389-392, 18-21 June 1996.
- [5]. Sowelam, S.M., Tewfik, A.H.: *Waveform selection in radar target classification*. *IEEE Transactions on information theory*, v.46, no.3, pp.1014-1029, May 2000.
- [6]. Fowle, E.N., Kelly, E.J., Sheehan, J.A.: *Radar system performance in a dense-target environment*. *IRE Int. Convention record*, no.4, pp.136-145, 1961.
- [7]. Naparst, H.: *Dense target signal processing*. *IEEE Transactions on information theory*, v.37, no.2, March, 1991.
- [8]. Birk, R., Camus, W., Valenti, E.: *Synthetic aperture radar imaging systems*", *Aerospace and Electronic Systems Magazine*, IEEE, v.10, Issue.11, pp.15-23, Nov.1995.
- [9]. Prickett, M.J.: *Principles of inverse synthetic aperture radar (ISAR) imaging*. *IEEE EASCON*, pp.340-344, 1980.
- [10]. Ausherman, D.A., Kozma, A., Walker, J., Jones, H.M., Poggio, E.C.: *Developments in radar imaging*. *IEEE Transactions on Aerospace and Electronic Systems*, v.20, no.4, pp.363-400, 1984.
- [11]. Chen, V.C., Ling, H.: *Time-Frequency transforms for radar imaging and signal analysis*, 2002.
- [12]. Soumekh, M., *Synthetic Aperture Radar Signal Processing with MATLAB Algorithms*, New York: Wiley, 1999.
- [13]. Levanon, Nadav, and Eli Mozeson. *Radar Signals*. New York: Wiley-IEEE, 2004.
- [14]. Chen V.C., Shie Qian, *Joint time-frequency transform for radar range-Doppler imaging [J]*. *IEEE Transactions on AES*, 1998. 34(2): pp.486-499.
- [15]. Özdemir C., *Inverse synthetic aperture radar imaging with MATLAB*, A John Wiley & Sons, Inc., Publication, 2012.
- [16]. P.M. Woodward, "Radar ambiguity analysis," *RRE Technical Note No. 731*, February 1967.
- [17]. Feeman, Timothy G., *The Mathematics of Medical Imaging, A Beginner's Guide*, Springer-Verlag New York, 2010.
- [18]. J. Breckling, Ed., *The Analysis of Directional Time Series: Applications to Wind Speed and Direction*, ser. Lecture Notes in Statistics. Berlin, Germany: Springer, 1989, vol. 61.

INVESTIGATION OF PHYSICAL PROPERTIES OF WOOLEN FABRICS ON THERMAL COMFORT

Zehra YILDIZ

Marmara University, Goztepe Campus, Faculty of Technology, Department of Textile Engineering, 34722,
Istanbul, TURKEY, zehra.yildiz@marmara.edu.tr

Nuray Oz CEVIZ

Marmara University, Apparel Science of Textiles, Istanbul, Turkey

Vedat DAL

Marmara University, Department of Textile Engineering, Istanbul, Turkey

Engin AKCAGUN

Mimar Sinan Fine Arts University, Apparel Science of Textiles, Istanbul, Turkey

Abdurrahim YILMAZ

Mimar Sinan Fine Arts University, Apparel Science of Textiles, Istanbul, Turkey

Mustafa ATMACA

Marmara University, Department of Mechanical Engineering, Istanbul, Turkey

Ahmet Berk KURTULUS

Marmara University, Department of Mechanical Engineering, Istanbul, Turkey

Abstract

In this study, three different woolen fabric samples having the same weight, composition and different thickness values have been investigated in terms of thermal comfort properties. Firstly, porosity of the fabrics has been calculated by using the warp/weft yarn counts and density values according to the theoretical model with cover factor. Then, thermal and water vapor resistance values have been measured by using PERMETEST Sensora instrument. Air permeability of fabrics has been measured by using a wind tunnel. The effects of porosity and thickness values on thermal comfort properties of fabrics have been discussed. Results proved that when the thickness increases the air permeability decreases. This situation can be explained with the structure effect of the fabric samples. In basket weave, because of the neat and dense character of the structure air permeability value is less than break twill structure. Considering the water vapor and thermal resistance values, because of the finest yarn count and the structure (twill) WB2 (wool blend) has the highest water vapor resistance result. This result is stemming from the fact that finer yarns have much more surface area to resist to the water vapor and thermal energy.

Keywords: *Thermal comfort, wind tunnel, cover factor, porosity, woolen, air permeability.*

1. INTRODUCTION

Comfort is a complex notion including physical, physiological, and psychological factors. It is the most important parameter determining the consumer preferences in garment technology. The thermal balance is the key factor to feel comfort and can be achieved by heat exchange between the human body and the surrounding. Heat exchange mechanism consists of conduction, convection, and radiation of heat, evaporation and heat production. The deterministic parameters of thermal comfort are heat and moisture transfer capability, air permeability, heat retention, static electrical tendency, water vapor resistance and water absorbency [1-3].

Recently, many researches have addressed the issue of thermal comfort parameters in textile industry such as footwear [4], technical textiles [5], surgical gowns [6], sportswear [7], ballistic applications [8] etc. In literature, thermal properties of various knitted fabrics produced by cotton, regenerated bamboo and cotton/bamboo yarns have been investigated. Results proved that thermal conduction of knitted fabrics decreases with increasing bamboo fiber ratio. Additionally, thermal conductivity decreases in fabrics made from fine yarns [2]. In a previous study, thermal resistance and water vapor permeability (WVP) values have been measured in various woven and knitted fabrics with different fiber types (polyester/wool, cotton, polyester). The highest thermal resistance and WVP values have been obtained in woolen fabric types [9]. In another study, thermal comfort properties of linen, cotton and viscose fabrics have been searched to see the effects of natural and regenerated cellulose blends. The highest thermal conductivity value was observed in linen/cotton fabric type comparing to other blends [10]. Thermal conductivity, WVP and thermal absorptivity in dry and wet state of cotton, cotton/PU and cotton/PES bed sheet fabrics have been investigated. Accordingly, cotton/PES knitted sheets with loops give the feeling of comfort in winter whilst in summer cotton woven bed sheet is much more comfortable [11].

Thermal resistance is a measure of the body's ability to prevent heat from flowing through it. Under a certain condition of climate, if the thermal resistance of clothing is small, the heat energy will gradually reduce with a sense of coolness [12]. In literature, just a few studies published related to thermal comfort of wool and woolen fabrics. For instance, the effects of atmospheric pressure plasma treatment on thermal conductivity, WVP, thermal resistance, air permeability and pilling propensity of 100 % wool fabrics have been investigated. Results proved that with plasma treatment, thermal resistance and WVP increased whilst thermal conductivity and air permeability decreased because of changing in fabric morphology [13, 14].

Fabric's porosity mainly affects the air flow of textiles. It can be said that stoma dimension and distribution is a function of fabric geometry. Porosity of textiles is mainly affected by the diameter of the yarn, surface formation techniques and the number of loop counts per unit area. Some important features such as air permeability, water permeability, dyeing properties are related to the porosity of the fabric [15, 16].

The aim of the study is to investigate the thermal comfort properties of woolen fabrics having different porosity and thickness values. Porosity values have been calculated by using the warp/weft densities and yarn counts according to the theoretical model. Thermal resistance, water vapor resistance and air permeability values of woolen fabrics have been measured and then compared in terms of their porosity and thickness values.

2. EXPERIMENTAL

2.1. Materials

Woolen fabric samples have been purchased from Bahariye Co. The physical properties and light microscopy images of the woolen fabric samples are presented in Table 1 and Figure 1 respectively.

Table 1. Physical properties of the tested samples.

Sample Number	Composition	Square Mass (g/m ²)	Thickness (mm)	Structure	Density (thread/cm)		Yarn Counts (Nm)	
					Warp	Weft	Warp	Weft
WB1	60% Wool / 40% PES	162	0.25	Basket Weave	28	31	37	38
WB2	60% Wool / 40% PES	162	0.26	Twill	38	36	46	58
WB3	60% Wool / 40% PES	162	0.28	Break Twill	36	36	40	47

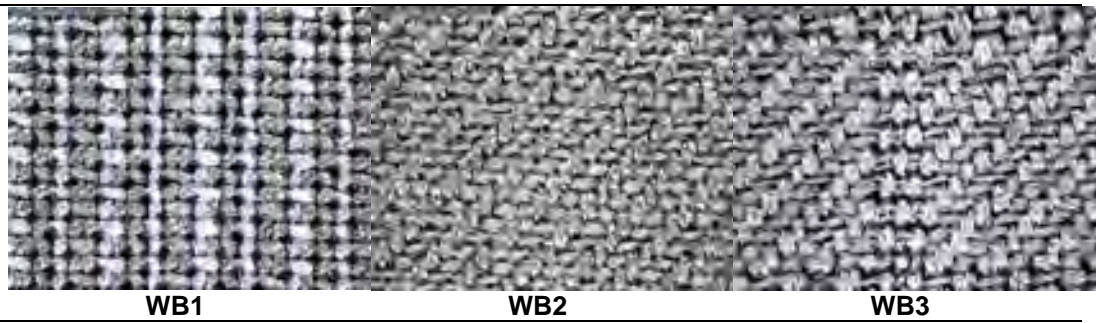


Figure 1. Light microscopy images of the tested samples.

2.2. Testing Methods

All samples have conditioned in a standard atmosphere at 65% RH, and 20 ± 2 °C for 24 h before measurements [17]. Fabric thicknesses have been measured in R&B cloth thickness tester (James H. Heal&Co. Ltd.) [18]. Warp/weft densities have been determined by using a loupe [19]. Fabric square mass and warp/weft yarn counts have been measured in an analytical balance (Acculab-ALC-80.4) [20, 21]. Water vapor permeability and thermal resistance measurements were performed by using PermetestSensora instrument and a wind tunnel has been employed to evaluate the air permeability of woolen fabrics (Fig.2). For thermal resistance and water vapor resistance measurement, fabrics samples were cut in 17x17 cm dimensions then located to PermetestSensora instrument equipped with a Skin Model measuring head. The measuring head was covered by a polyethylene membrane that protects the system from liquid water transform. During water vapor resistance testing, the pH of liquid water was set as 5.5 [11]. The air permeability has been measured using a hot-wire anemometer in the wind tunnel. Fabric samples have been cut in 13x13 cm dimensions then placed in the wind tunnel as can be seen in Figure 2. The probe was located when the flow direction was parallel with the axis of the probe. The velocity of air was set as 10m/s. The air permeability result illustrates the volume of air in milliliters which is passed through the 1 mm length fabric area per second [22]. Porosity value was determined by using warp/weft densities and yarn counts considering the cover factor of fabrics. Porosity measurement was carried out from the theoretical model as in previous studies [23-25].



WindTunnel



Sample in thewindtunnel



Permetest Sensora

Figure 2. Images of the wind tunnel and PermetestSensora instrument.

3. RESULTS AND DISCUSSION

3.1. The Effects of Thickness on Thermal Comfort

In this paper the thermal properties of woolen fabrics with different structures, thicknesses and porosities have been investigated. According to the Figure 3, the samples of WB1, WB2 and WB3 have the air permeability values of 1472, 1538 and 1616 mm/s respectively. It can be seen that when the thickness increases, air permeability increases. WB3 has the highest thickness value and has the highest air permeability. In general when the thickness increases the air permeability decreases but this situation can be explained with the structure effect of the fabric samples. In the sample of WB1 the structure is basket weave whilst WB3 has the break twill structure. In basket weave, because of the neat and dense character of the structure air permeability value is less than break twill structure.

The samples of WB1, WB2 and WB3 showed the water vapor resistance values of 2.5, 2.3 and 2.5 Pa.m².W⁻¹, and thermal resistance values of 1.06, 0.4 and 1.57 mK.m².W⁻¹ respectively. Considering the water vapor resistance and thermal resistance values it is obvious that in the sample of WB2, because of the finest yarn count and the loose structure (twill) WB2 has the highest water vapor permeability result. This result is stemming from the fact that finer yarns have much more surface area to convey the water vapor and thermal energy. In the sample of WB3, warp/weft yarn counts are much more than WB2 but less than WB1.

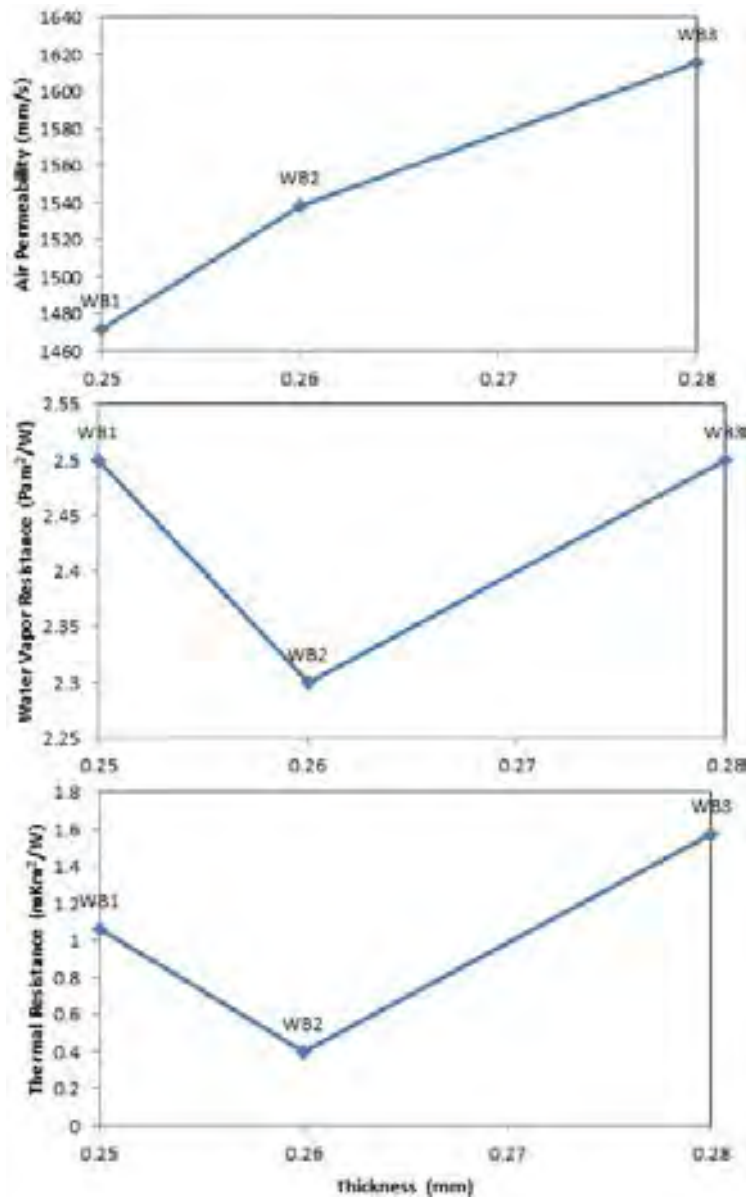


Figure 3. The effects of thickness on air permeability, water vapor resistance and thermal resistance.

3.2. The Effects of Porosity on Thermal Comfort

Fabric porosity values have been measured by using warp/weft yarn counts, densities and cover factor according to the theoretical model. Porosity values have found as 16.8, 13.3 and 10.9 % for the samples of WB1, WB2 and WB3 respectively. In Figure 4, the effects of porosity on air permeability, water vapor and thermal resistance values can be seen. Accordingly, whenever porosity increases air permeability decreases. The sample of WB3 has the highest air permeability even though has the least porosity value. This result can be explained with the difference of the structures of the fabric samples. WB1 and WB3 fabric samples have basket weave and break twill structure respectively. In basket weave, because of the neat and dense character of the structure air permeability value is less than break twill structure.

Woolen fabric samples showed similar results of water vapor resistance considering the thickness and porosity. It was observed that the sample (WB3) having the highest thickness value showed the highest thermal resistance. As mentioned before the result of low porosity value depends on the fabric structure such as break twill or basket weave.

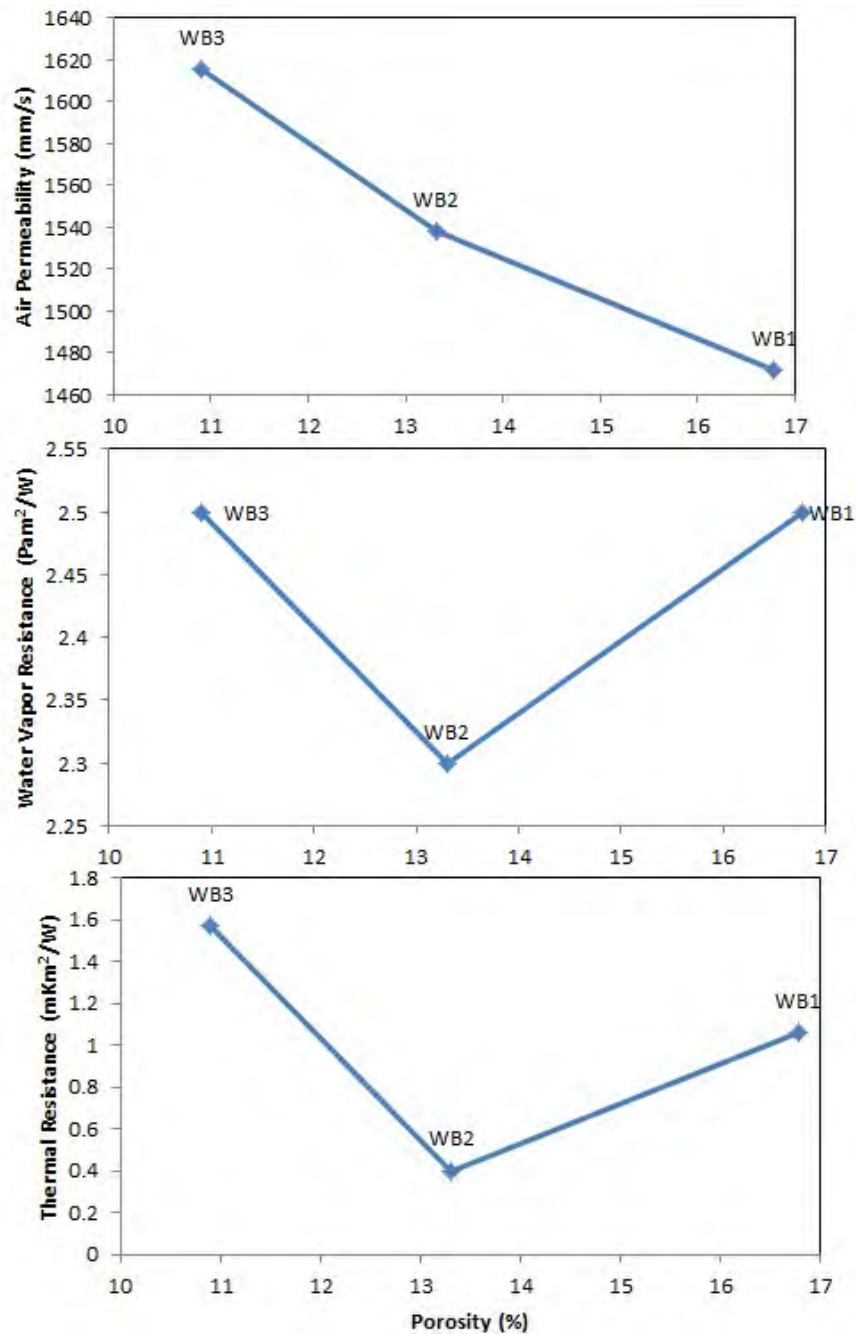


Figure 4. The effects of porosity on air permeability, water vapor resistance and thermal resistance.

4. CONCLUSIONS

This study was aimed to investigate the relation between porosity, thickness values and thermal comfort properties. For this purpose three different woolen fabrics were chosen having various porosity and thickness values. Results proved that fabric structure directly affects the air permeability of the fabric. The sample of WB1 in basket weave has less air permeability than WB2 (twill) and WB3 (break twill) despite having the least thickness and highest porosity values. Twill structure also has the least thermal and water vapor resistance values because of its loose structure.

REFERENCES

- [1]. K. Umbach, "Aspects of clothing physiology in the development of sportswear" *Knitting Technique*, 15, pp. 165-169, 1993.
- [2]. A. Majumdar, S. Mukhopadhyay, and R. Yadav, "Thermal properties of knitted fabrics made from cotton and regenerated bamboo cellulosic fibres" *International Journal of Thermal Sciences*, 49, pp. 2042-2048, 2010.
- [3]. J. Kwon, and J. Choi, "Clothing insulation and temperature, layer and mass of clothing under comfortable environmental conditions" *Journal of physiological anthropology*, 32, 11, 2013.
- [4]. A. M. Borreguero, B. Talavera, J. F. Rodriguez, J. L. Valverde, "Enhancing the thermal comfort of fabrics for the footwear industry" *Textile Research Journal*, vol. 83, pp. 1754-1763, 2013.
- [5]. X. Wang, M. Kainuma, L. Bao, and M. Nakazawa, "A novel approach for evaluating the air permeability of airbag fabrics" *Textile Research Journal*, vol. 76, pp. 66-70, 2006.
- [6]. O. Pamuk, M. J. Abreu, and Z. Ondogan, "An Investigation on The Comfort Properties for Different Disposable Surgical Gowns by Using Thermal Manikin" *Tekstil ve Konfeksiyon*, 2008.
- [7]. M. Hassan, K. Qashqary, H. A. Hassan, E. Shady, and M. Alansary, "Influence of sportswear fabric properties on the health and performance of athletes" *Fibres & Textiles in Eastern Europe*, pp. 82-88, 2012.
- [8]. R. F. Mahbub, L. Wang, L. Arnold, S. Kaneslingam, and R. Padhye, "Thermal comfort properties of Kevlar and Kevlar/wool fabrics" *Textile Research Journal*, 0040517514532157, 2014.
- [9]. Q. Guanxiong, Z. Yuan, W. Zhongwei, L. Jianli, and Z. Jie, "Comfort in Knitted Fabrics" in International Man-Made Fibers Congress, Dornbirn, Austria, pp. 112-124, 1991.
- [10]. S. B. Stanković, D. Popović, and G. B. Poparić, "Thermal properties of textile fabrics made of natural and regenerated cellulose fibers" *Polymer Testing*, vol. 27, pp. 41-48, 2008.
- [11]. L. Hes, M. Boguslawska-Baczek, and M. Geraldde, "Thermal Comfort of Bedsheets Under Real Conditions of Use," *Journal of Natural Fibers*, vol. 11, pp. 312-321, 2014.
- [12]. Q. Guanxiong, Z. Yuan, W. Zhongwei, L. Jianli, L. Min, and Z. Jie, "Comfort in Knitted Fabrics," in International Man-Made Fibers Congress Proceeding, p. 112, 1991.
- [13]. H. A. Karahan, E. Özdoğan, A. Demir, I. C. Koçum, T. Öktem, and H. Ayhan, "Effects of atmospheric pressure plasma treatments on some physical properties of wool fibers," *Textile Research Journal*, 2009.
- [14]. V. Goud and J. Udakhe, "Effect of low-temperature plasma treatment on tailorability and thermal properties of wool fabrics," *Pramana*, vol. 77, pp. 669-677, 2011.
- [15]. A. Çay, S. Vassiliadis, and M. Rangoussi, "On the use of image processing techniques for the estimation of the porosity of textile fabrics," 2004.
- [16]. I. Fatahi and A. A. Yazdi, "Assessment of the relationship between air permeability of woven fabrics and its mechanical properties" *surfaces*, 5, 6, 2010.
- [17]. "ISO 139: Textiles - Standard atmospheres for conditioning and testing," ed, 2006.
- [18]. "ISO 5084: Textiles - Determination of thickness of textiles and textile products," ed, 1998.
- [19]. "ISO 4602: Reinforcements - Woven fabrics - Determination of number of yarns Per unit length of warp and weft," ed, 2002.
- [20]. "ISO 12127: Textiles - Fabrics - Determination of mass per unit area using small samples," ed, 1999.
- [21]. "ISO 2060: Textiles - Yarn from packages - Determination of linear density (mass per unit length) by the skein method," ed, 1999.
- [22]. B. Saville, *Physical testing of textiles*: Woodhead Publishing Limited, 2003.
- [23]. E. Elnashar, "Volume porosity and permeability in double-layer woven fabrics" *AUTEX Research Journal*, 5, pp. 207-217, 2005.
- [24]. J. Militký, M. Vik, M. Viková, and D. Křemenáková, "Influence of fabric construction on their porosity and air permeability" in Proceedings of 2nd SIENTEX Conference "International Symposium of Textile Engineering, pp. 1-18, 2004.
- [25]. U. Syed, R. H. Wardman, and R. A. Jhatial, "Assessment of Inter-Yarn Zone Porosity of Plain Weave Fabrics," *Res J Eng Tech*, vol. 31, pp. 291-296, 2012.

Biography

Zehra Yildiz is a research assistant in Marmara University, in Textile Engineering Department. She is a PhD student in Istanbul Technical University, in Polymer Science and Technology Department. Her main research areas are; conductive textiles, textile adhesives, functional polymeric textiles coatings.

REMOVAL OF COLOR AND COD FROM WASTEWATER OF A LOCAL TEXTILE FACTORY BY COAGULATION

Müslün Sara TUNÇ

Firat University, Department of Environmental Engineering, 23100, Elazig, Turkey.
saratunc@firat.edu.tr

Özlem TEPE

Firat University, Department of Environmental Engineering, 23100, Elazig, Turkey.
otepe@firat.edu.tr

Abstract

Textile industries use large amount of water and complex chemicals during various processing stages such as desizing, scouring, bleaching, mercerising, dyeing, printing, and finishing. Textile industry wastewater containing intensive color, high pH and chemical oxygen demand (COD) and large amount of suspended solids impose environmental concern. Many methods such as physicochemical, chemical and biological processes and advanced oxidation processes have been reported for the decolorization of color wastewater. Among these, coagulation is one of widely used processes owing to relatively simple operation and low cost. The most commonly used coagulants in treatment of textile wastewater are Al(III) and Fe(III) salts. In this study, coagulation technique was applied to remove color and COD from wastewater supplied a local textile factory. The operating variables were type and dosage of coagulants. In present study, aluminum sulfate and ferric chloride that are readily soluble in water was used as coagulants. The evaluation of treatment efficiency was made using parameters of COD and color. Color was followed by absorbance at 436 nm, 525 nm and 620 nm wave lengths. At 500 mg/L ferric chloride determined as appropriate dosage, while removal efficiencies of color at 436 nm, 525 nm and 620 nm were found to be 84%, 92% and 86%, respectively, COD removal was achieved to be 31%. Removal efficiencies of color at 436 nm, 525 nm and 620 nm were found to be 82%, 85% and 79% using 700 mg/L aluminum sulfate, respectively. The maximum COD removal was achieved to be 26% at dosage of 700 mg/L aluminum sulfate. According to results obtained, coagulation technique may be a good pretreatment option to remove color from textile wastewater.

Keywords: *Textile wastewater, coagulation, removal of color and COD*

1. INTRODUCTION

Textile industry generally produces large volumes of wastewater. This wastewater with high pH, alkalinity and color also contains high concentration of organic matter, non-biodegradable matter, toxic substances, detergents and soaps, oil and grease, sulfide, and suspended/dissolved solids [1-4]. The release of the textile wastewater to the environment without proper treatment causes aesthetic problems for the receiving water bodies such as lakes and rivers. The accumulation of color prevents sunlight penetration and disturbs the ecosystem of receiving water. Also, the direct discharge of this wastewater characterized by very low biodegradable into sewage networks causes challenges in biological treatment processes [3].

Several methods involving physicochemical, chemical and biological processes, as well as some of new emerging techniques like sonochemical or advanced oxidation processes were used for treating of textile wastewater [3]. Even though the biological treatments are the cheapest and the simplest, they cannot be applied directly to most textile wastewaters because many dyes are also toxic to the microorganisms involved in these processes [5]. While these processes are generally efficient for biochemical oxygen demand (BOD₅) and suspended solids (SS) removal, they are largely ineffective for removing color. Because textile wastewater including various dyes and chemicals has very low biodegradability [1,6]. At the moment, alternative physical/chemical methods are used [5]. The coagulation process is a widely employed treatment process in order to remove suspended solids and organic matter as well as providing high color removal in textile wastewater [2,4]. Al(III) and Fe(III) salts are two principal inorganic coagulants used in wastewater treatment [1]. Coagulation for the textile wastewater has been used for many years as main treatment or pretreatment because of its low capital cost. However, the most essential disadvantages of this process are the generation of sludge, which has to be buried, and ineffective for removal of some soluble dyes [3,7]. Because of scarcity of landfill sites, the disposal of sludge is more problematic and expensive. Also, amount of sludge produced during coagulation process can be minimized by optimizing process parameters such as pH, dosage of coagulant/flocculant aids, mixing time, settling time, etc and suitable selection of coagulant. Addition, recycle of sludge is another alternative option [3].

In this study, coagulation technique was applied to remove color and COD from wastewater supplied a local textile factory. The effect of the operating variables such as type and dosage of coagulant was investigated. The effectiveness of the process is measured by color and COD removal.

2. MATERIALS AND METHODS

2.1. Chemicals

FeCl₃ 6H₂O and Al₂(SO₄)₃ 18H₂O used as coagulant were supplied from Merck. All chemical reagents used for the preparation of coagulants were analytical grade. FeCl₃ 6H₂O and Al₂(SO₄)₃18H₂O solutions were prepared daily. Distilled water was used throughout the study.

2.2. Characteristics of real textile wastewater

Wastewater sample used in this study was supplied from denim manufacturing factory located in Malatya, Turkey. The wastewater includes indigo dye. The wastewater samples were taken from rinsing after dyeing. Characteristics of wastewater are presented in Table 1. Wastewater to prevent change of characteristic of wastewater was kept in the refrigerator at +4°C before coagulation tests.

Table 1. Characterization of wastewaters of the textile factory used in the study

Parameters	Unit	Values
pH		10.35-10.39
COD	mg/L	640-650
Color		
436 nm	m ⁻¹	44-62.3
525 nm	m ⁻¹	40-53.3
620 nm	m ⁻¹	61-88.8

2.3. Coagulation experiments

Coagulation experiments was performed by running a series of jar tests using aluminum sulfate octodecahydrate (Al₂(SO₄)₃ 18H₂O) and ferric chloride hexahydrate (FeCl₃ 6H₂O) as coagulant agent. The experiments were carried out at room temperature (20±2 °C) using 500 mL wastewater samples by applying 11 different coagulant concentrations ranging from 50 mg/L to 1000 mg/L. A series of jar test experiments

was conducted by using 2 min rapid mixing at 120 rpm, 30 min slow mixing at 30 rpm, and 1 h settling. The experiments were carried out at the original pH of the wastewaters due to the chemical cost related issues by taking into consideration the high and continuous dyeing wastewater generation in the factory [8]. After settling, the supernatant samples were taken from a point of 3 cm below the surface for analysis of color and COD.

2.4. Analytical measurements

pH measurement was done by means of Thermo Scientific Orion 3 Star pH meter. COD was measured according to open reflux procedure described in Standard Methods for Water and Wastewater Examination [9]. The measurements of color were determined by measuring the absorbance values of the samples at three wavelengths (436 nm, 525 nm and 620 nm) by Shimadzu Model Spectrophotometer (1 cm cell width). In this way, color values were calculated according to equation as follows[10]:

$$\text{Color (m}^{-1}\text{)} = \frac{1000 \text{ Abs } (\lambda)}{d} \quad (1)$$

where Abs (λ) is the absorbance at given wavelength (λ) and d is cell width (mm).

Removal efficiency of COD and color were obtained according to the formula given below.

$$\text{Removal efficiency (\%)} = \frac{(C_0 - C)}{C_0} \cdot 100 \quad (2)$$

where C_0 is the initial absorbance or COD value of the wastewater before coagulation and C is the absorbance or COD value at the end of coagulation process.

3. RESULTS AND DISCUSSION

3.1. Coagulation with ferric chloride

Basic equation occurring during the coagulation process for ferric chloride salts is given with Eq. (3) as follows [11]:



Ferric chloride concentrations varying from 50 mg/L to 1000 mg/L by keeping original pH of the wastewater were applied for removing color and COD from the textile wastewater. Values of effluent color and color removal efficiency obtained after coagulation process performed using different coagulant dosages are shown in Figure 1 and 2, respectively. The effluent color values were obtained to be 7.2 m^{-1} , 3.2 m^{-1} and 8.7 m^{-1} at 436, 525 and 620 nm at $\text{FeCl}_3 \cdot 6\text{H}_2\text{O}$ coagulant dosage of 500 mg/L. As can be shown from Figure 2, color removal efficiencies obtained at coagulant dosage of 500 mg/L were determined as 84%, 92% and 86% at 436, 525 and 620 nm, respectively. On the other hand, when dosage of coagulant increased from 500 mg/L to 1000 mg/L, it was observed that color removal efficiencies increased about 6%. Because excess sludge occurs at high dosage of coagulant, optimum coagulant dosage for ferric chloride was accepted as 500 mg/L for removal of color from the textile wastewater used in this study. Unlu et al. [8] reported that ferric chloride provided 79% color removal at a much lower dose of 500 mg/L. All paragraphs must be justified, i.e. both left-justified and right-justified.

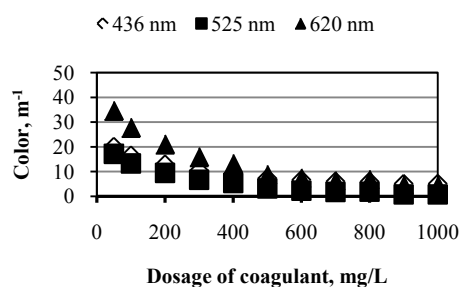


Figure 1. Change profile of effluent color with dosage of ferric chloride coagulant

Figure 3 shows effluent COD values and COD removal efficiencies obtained at coagulant dosages in the range of 50-1000 mg/L. At the dosage of 500 mg/L ferric chloride, it was obtained almost 31% COD removal efficiency. But as can be seen from Figure 3, it was not observed a considerable increase in the coagulant dosages above 500 mg/L for COD removal. Therefore, optimum ferric chloride dosage was determined as 500 mg/L for COD removal. COD removal efficiency was low. This may be related to the chemical composition of the wastewater, e.g. surface active materials of wastewater as expressed by Guida et al. [12].

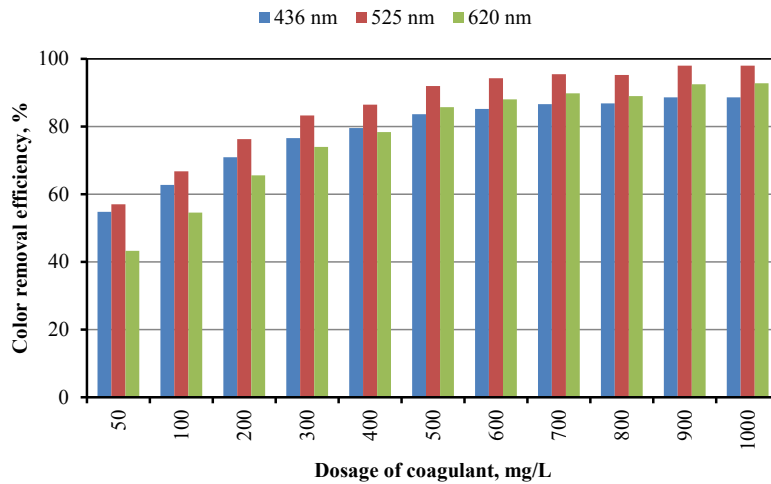


Figure 2. Effect of ferric chloride coagulant dosage on the color removal efficiency

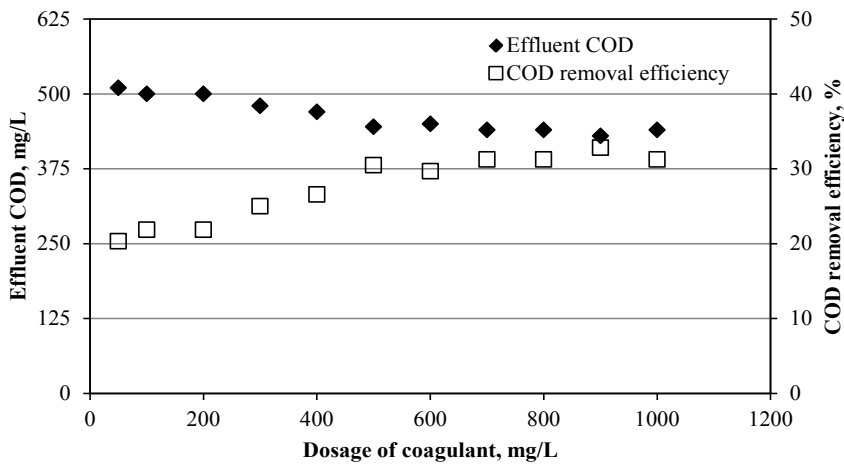


Figure 3. Effect of ferric chloride coagulant dosage on the COD removal efficiency and effluent COD

Table 2 shows change of effluent pH after the coagulation process performed by using ferric chloride and aluminum sulfate. pH of raw textile wastewater used on ferric chloride coagulation experiment was 10.48. It was observed the pH changing during coagulation process due to the formation of $Fe(OH)_3$, as already described in Eq. (3), which appears clearly in Table 2. Values of effluent pH decreased with increasing coagulant dosage.

3.2. Coagulation with aluminum sulfate

When aluminum sulfate is added to water or wastewater, $Al(OH)_3$ precipitation occurs according to the following equation (4) [11]:



Table 2. Change of effluent pH with type and dosage of coagulant

Dosage of coagulant (mg/L)	Values of effluent pH	
	FeCl ₃ 6H ₂ O	Al ₂ (SO ₄) ₃ 18H ₂ O
50	10.28	10.37
100	10.22	10.30
200	10.07	10.16
300	9.89	9.94
400	9.68	9.72
500	9.17	9.58
600	8.99	9.37
700	8.64	9.13
800	8.33	8.90
900	8.09	8.62
1000	7.91	8.36

Aluminum sulfate concentrations varying from 50 mg/L to 1000 mg/L like ferric chloride experiments were applied for the treatment of raw wastewater by keeping pH at the original wastewater. Color values of coagulated wastewater and color removals are shown in Figure 4 and 5. It was obtained an increase in color removal with an increase in coagulant concentration. Removal efficiencies of color at 436 nm, 525 nm and 620 nm were found to be 82%, 85% and 79% using 700 mg/L aluminum sulfate, respectively. Maximum color removal was obtained to be 88%, 92% and 87% at the dosage of 1000 mg/L at 436 nm, 525 nm and 620 nm, respectively. Furthermore, there was an increase almost 6-9% for color removal when coagulant dosage increased from 700 mg/L to 1000 mg/L. Unlu et al. [8] obtained 96% color removal efficiency at an alum dose of 1000 mg/L. Selcuk [11] stated that approximately 50-60% color was removed at 1500 mg/L aluminum sulfate. El-Gohary and Tawfik [6] investigated the color and COD removal from disperse and reactive dyes wastewater by means of coagulation/flocculation. They determined that the use of 200 mg/L alum reduced the color intensity by a value of 78.9%.

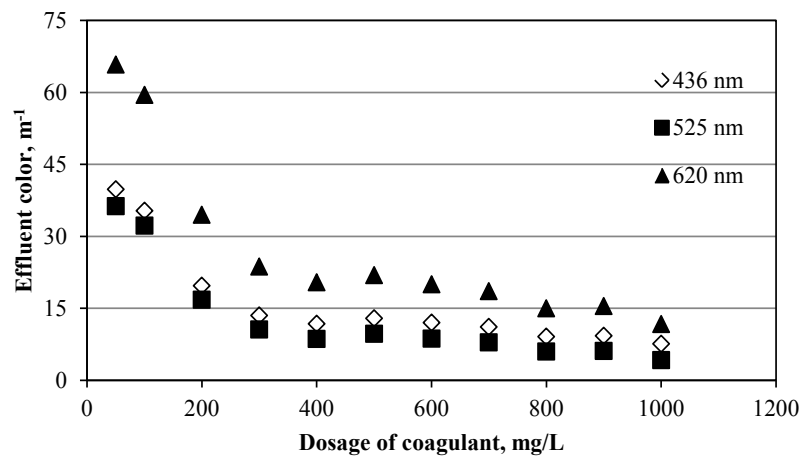


Figure 4. Change profile of effluent color with dosage of aluminum sulfate coagulant

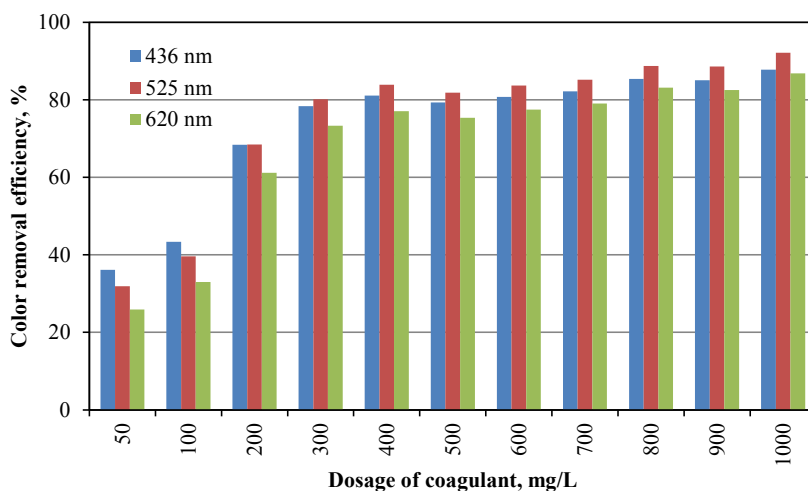


Figure 5. Effect of aluminum sulfate coagulant dosage on the color removal efficiency

Effect of aluminum sulfate coagulant dosage on the COD removal efficiency and effluent COD is shown in Figure 6. Maximum COD removal was obtained as 26 % in the dosage of 700 mg/L. Value of effluent COD obtained at this coagulant dosage was 480 mg/L.

As can be seen from Table 2, it was observed that values of effluent pH after coagulation process used aluminum sulfate as coagulant decreased because of the formation of $Al(OH)_3$, as already described in Eq. (4).

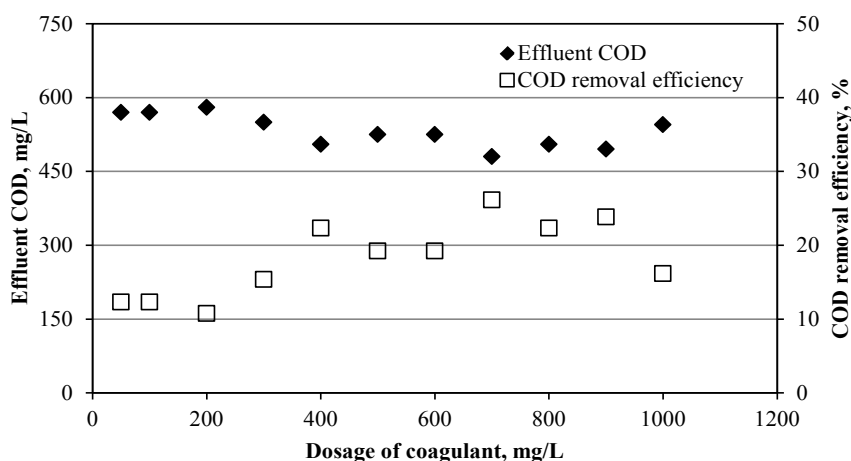


Figure 6. Effect of aluminum sulfate coagulant dosage on the COD removal efficiency and effluent COD

4. CONCLUSION

In this study, coagulation technique was applied to remove color and COD from wastewater supplied a local textile factory. Coagulation experiments were performed using aluminum sulfate and ferric chloride as coagulant agent. The experiments were carried out by applying 11 different coagulant concentrations ranging from 50 mg/L to 1000 mg/L. The effect of the operating variables such as type and dosage of coagulant was investigated. At 500 mg/L ferric chloride determined as appropriate dosage, while removal efficiencies of color at 436 nm, 525 nm and 620 nm were found to be 84%, 92% and 86%, respectively, COD removal was achieved to be 31%. Removal efficiencies of color at 436 nm, 525 nm and 620 nm were found to be 82%, 85% and 79% by using 700 mg/L aluminum sulfate, respectively. The maximum COD removal was achieved to be 26% at dosage of 700 mg/L aluminum sulfate. This process was effective for removing of color from raw textile wastewater used in the present study, but COD removal was quite low. This may be related to the chemical composition of the wastewater, e.g. surface active materials of wastewater. According to results obtained, coagulation technique may be a good pretreatment option to remove color from textile wastewater.

REFERENCES

- [1]. B.Y. Gao, Y. Wang, Q.Y. Yue, J.C. Wei, Q. Li, "Color removal from simulated dye water and actual textile wastewater using a composite coagulant prepared by polyferric chloride and polydimethyldiallylammonium chloride", *Separation and Purification Technology*, 54, 157-163, 2007.
 - [2]. S. Meriç, H. Selçuk, V. Belgiorno, "Acute toxicity removal in textile finishing wastewater by Fenton's oxidation, ozone and coagulation-flocculation processes", *Water Research*, 39, 1147-1153, 2005.
 - [3]. A. K. Verma, R. R. Dash, P. Bhunia, "A review on chemical coagulation/flocculation technologies for removal of colour from textile wastewaters", *Journal of Environmental Management*, 93, 154-168, 2012.
 - [4]. Y. Wei, A. Ding, L. Dong, Y. Tang, F. Yu, X. Dong, "Characterisation and coagulation performance of an inorganic coagulant-poly-magnesium-silicate-chloride in treatment of simulated dyeing wastewater", *Colloids and Surfaces A: Physicochem. Eng. Aspects*, 470, 137-141, 2015.
 - [5]. M. Chafi, B. Gourich, A.H. Essadki, C. Vial, A. Fabregat, "Comparison of electrocoagulation using iron and aluminium electrodes with chemical coagulation for the removal of a highly soluble acid dye", *Desalination*, 281, 285-292, 2011.
 - [6]. F. El-Gohary, A. Tawfik, "Decolorization and COD reduction of disperse and reactive dyes wastewater using chemical-coagulation followed by sequential batch reactor (SBR) process", *Desalination*, 249, 2009, 1159-1164, 2009.
 - [7]. M. Riera-Torres, C. Gutiérrez-Bouzán, M. Crespi, "Combination of coagulation-flocculation and nanofiltration techniques for dye removal and water reuse in textile effluents", *Desalination*, 252, 53-59, 2010.
 - [8]. M. Unlu, H. Yukseler, U. Yetis, "Indigo dyeing wastewater reclamation by membrane-based filtration and coagulation processes", *Desalination*, 240, 178-185, 2009.
 - [9]. APHA, AWWA and WPCF, *Standard methods for the examination of water and wastewater*, 17.th Edition, Washington D.C., 1989.
 - [10]. S. Barredo-Damas, M.I. Alcaina-Miranda, M.I. Iborra-Clar, J.A. Mendoza-Roca, "Application of tubular ceramic ultrafiltration membranes for the treatment of integrated textile wastewaters", *Chemical Engineering Journal* 192 211-218, 2012.
 - [11]. H. Selçuk, "Decolorization and detoxification of textile wastewater by ozonation and coagulation processes", *Dyes and Pigments*, 64, 217-222, 2005.
 - [12]. M. Guida, M. Mattei, C. Della Rocca, G. Melluso, S. Meriç, "Optimization of alum-coagulation/flocculation for COD and TSS removal from five municipal wastewater", *Desalination*, 211, 113-127, 2007.
-

ANALYSIS AND DESIGN OF PASSIVE AND ACTIVE INTERCONNECTED HYDRO-PNEUMATIC SUSPENSION SYSTEMS IN ROLL PLANE

Ferhat SAĞLAM

ASELSAN Inc., Ankara, Turkey,
fesaglam@gmail.com

Y. Samim ÜNLÜSOY

Middle East Technical University, Ankara, Turkey,
unlusoy@metu.edu.tr

Abstract

In this study, analysis and design of a half car model in roll plane with passive and active unconnected and interconnected Hydro-Pneumatic (HP) suspension systems are made. An interconnection configuration with a connection between the piston side oil volume and rod side oil volume of the right and left suspensions, respectively, is considered. The performance of the active unconnected HP and interconnected HP suspension systems are compared in terms of ride comfort and handling. Nonlinear mathematical models are developed for each suspension configuration. A state space model with state dependent coefficients is derived using extended linearization to be used in the controller design. A nonlinear control method, State Dependent Riccati Equation (SDRE) control is used for the active controllers. The active controllers are designed to improve the ride comfort and handling, and to control the attitude and leveling of the vehicle. The performances of the controllers are evaluated by time domain simulations. Comparisons of the active and passive, unconnected and interconnected HP suspension systems with respect to ride comfort and handling are performed to evaluate the relative advantage and disadvantage of each type. The results illustrate the advantages as well as disadvantages of the active interconnected HP suspension system as compared with the other suspension configurations.

Keywords: *Hydro-pneumatic suspension, active suspension, interconnected suspension, ride comfort, vehicle handling, attitude and leveling control, nonlinear control, State Dependent Riccati Equation Control*

1. INTRODUCTION

Vehicle handling and ride comfort are two conflicting performance requirements. There are various approaches to improve suspension performance such as the use of roll stabilizers or the use of more advanced suspension designs. With soft suspensions for better ride comfort, the roll stiffness of the vehicle is lowered. As a result high roll angles are developed with reduced handling performance. One of the solutions to this problem is the use of anti-roll bars, which add to roll stiffness without affecting the vertical stiffness of the vehicle. By this way, a soft suspension in bounce and a stiff suspension in roll can be obtained to some extent. Another method of improving the vehicle ride comfort and vehicle handling is the use of semi-active and the active suspensions. The use of Hydro-Pneumatic (HP) suspension systems facilitates the flexible and relatively straightforward implementation of such applications.

HP systems are used in military vehicles, off-road vehicles, and heavy commercial vehicles. They have some advantages with respect to conventional suspension systems [1]. One of the major advantages is that, active and the semi-active suspension applications can be easily applied to HP suspension systems. By introducing oil flow to or by extracting oil from oil volumes in the hydraulic cylinder an active HP suspension system can be obtained. Similarly, by controlling the valve openings, a semi-active suspension can be obtained. Another advantage of the HP suspension systems is that by connecting the oil volumes of different suspension units either hydraulically or pneumatically, interconnected HP suspension systems can be obtained. By interconnected HP suspension system, dynamics of the suspensions can be modified as required.

In the literature, one can find a relatively small number of publications focusing on the interconnected HP suspension systems, analyzing different connection configurations and their effects on handling and vehicle ride dynamics. Zhang et al. [2] modeled the interconnected HP suspension system using the half car model and they analyzed the dynamics of the suspension in frequency domain in the roll plane. Zhang et al. [3] investigated the ride comfort characteristics of the interconnected HP suspension system using the random road input. They further experimentally validated results of the model study. In the study of Zhang et al. [4], handling characteristic of the hydraulically interconnected HP suspension system was analyzed. Moreover, a detailed theoretical analysis of the interconnected HP suspension system for different connections in roll and pitch with a full vehicle model was studied in the PhD thesis of Cao [5].

In the literature, there are many studies about the active control of the mechanical suspensions. However, active controls of the HP suspension systems are covered in relatively few studies [6-10]. In these studies, active control of the single corner suspension model is studied. There are also few studies about the active control of the interconnected HP suspension systems [11-12]. In these studies, roll control of the active interconnected HP suspension system are studied. On the other hand, a literature search shows that active control of the interconnected HP suspension systems for combined ride comfort, handling, and attitude control has not been studied to any extent.

The aim of this study is the design and analysis of a vehicle with active interconnected HP suspension system using a roll plane vehicle model for ride comfort, handling, and attitude control. Moreover, comparisons of the active and passive interconnected and unconnected HP suspension system are performed. The active controller is designed with the aim of improving the ride comfort, handling and controlling the vehicle attitude and leveling. With the addition of the integral controller in the controller design, zero steady state suspension deflection values are obtained. The results are compared with the results of the active unconnected HP suspension system in the roll plane of the half car model. Moreover, vehicle ride, handling, attitude and the leveling characteristics of the passive interconnected and unconnected HP suspensions are compared. The evaluation and the comparison of the results are made with simulations in time domain using random road inputs. Moreover, handling characteristic of the vehicle models with different suspension units are examined by body disturbance inputs due to body inertial forces during steering maneuvers.

2. MODELING OF THE ACTIVE INTERCONNECTED HP SUSPENSION SYSTEM WITH A ROLL PLANE VEHICLE MODEL

In this part, the nonlinear mathematical model for the roll plane half car model with active interconnected HP suspension system will be performed. Passive interconnected and unconnected, and active unconnected HP suspension systems can be easily adapted from the active interconnected HP suspension system. State space model with state dependent matrices of the active half car models are obtained by the use of the State Dependent Riccati Equation Control. The definition of the parameters and the numerical values of these parameters used in the simulations are given in Table 1. In variable definitions the subscript "L" is used to define the left suspension and the subscript "R" is used to define the right suspension unit.

2.1. Half Car Model with Active Interconnected HP Suspension System

Schematic of the hydraulically interconnected HP suspension system in the roll plane is given in Figure 1. In deriving the equations of motion, oil is assumed as incompressible. Moreover, left and the right suspension dimensions are identical, and the connectors which connect the left and right suspensions together are assumed to be of the same dimensions. A detailed analysis of a passive single HP suspension system can be found in the M.Sc. thesis of Joo [13].

Left suspension force can be found as

$$P_{1L}A_p - P_{4L}A_{pr} - F_{fl} = F_L \quad (1)$$

From the polytropic gas equation, absolute gas pressure in the left suspension can be found as

$$P_{3L} = \frac{P_{30L} V_{30L}^\kappa}{\left[V_{30L} + A_p (z_{fpL} - z_{tL}) \right]^\kappa} \quad (2)$$

Oil flow rate through the orifice in the left suspension is

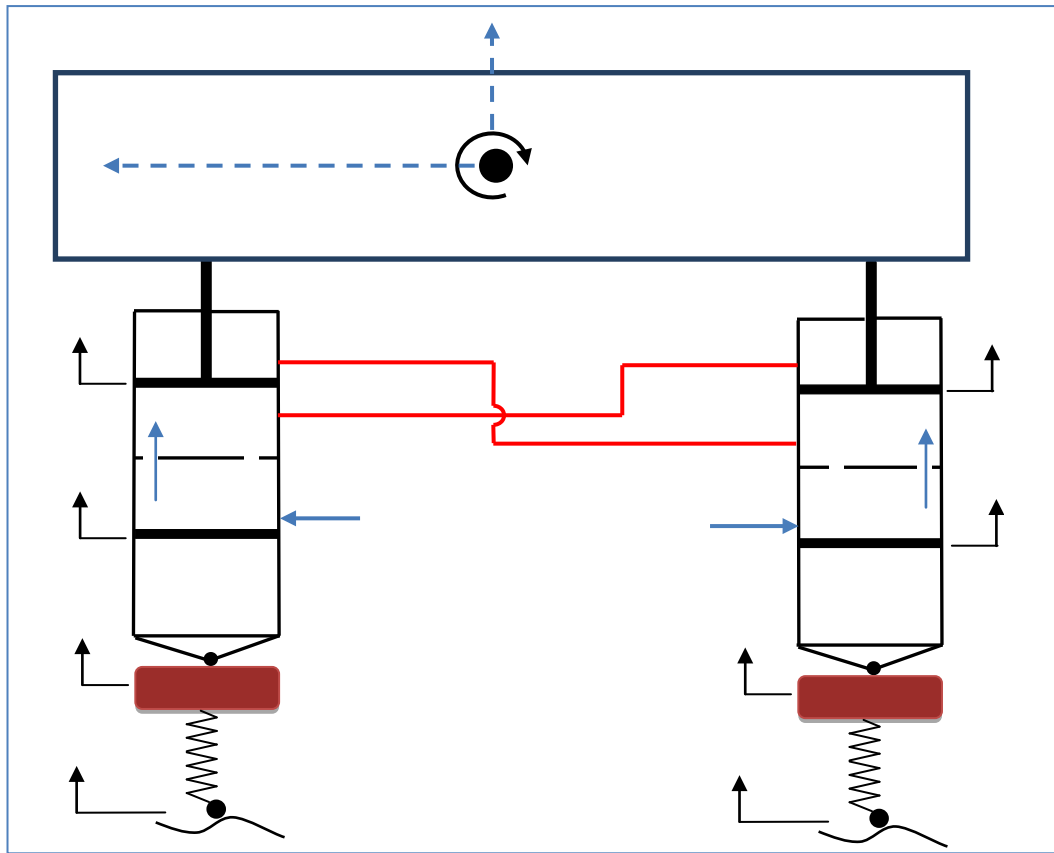


Figure 1. Active hydraulically interconnected HP suspension system in roll plane vehicle model

Table 1: Vehicle and suspension parameters

Parameter Definition	Symbol	Unit	Value	Parameter Definition	Symbol	Unit	Value
Sprung Mass	M	kg	3000	Orifice Opening	A_v	m^2	$1.6e-4$
Unsprung Mass	M_t	kg	150	Orifice Drag Coefficient	C_D	-	0.8
Floating Piston Mass	M_{fp}	kg	1	Track Width	t	m	2.4
Roll Moment of Inertia	I_{xx}	kgm^2	2539	Center of Gravity Height from Roll Center	h	m	1
Piston Area	A_p	m^2	0.007	Oil Density	ρ	kg/m^3	800
Rod Area	A_r	m^2	0.0042	Connector Length	L	m	2.4
Difference between Piston and Rod Area	A_{pr}	m^2	0.0028	Connector Diameter	D	m	0.025

Initial Gas Volume	V_{30}	m^3	0.0019	Oil Viscosity	μ	Pas	0.082
Atmospheric Pressure	P_{Atm}	bar	1				

$$Q_{2L1L} = C_d A_v \sqrt{\frac{2}{\rho} |P_{2L} - P_{1L}| \text{sign}(P_{2L} - P_{1L})} \quad (3)$$

From continuity equation, oil flow rate can also be written as

$$Q_{2L1L} = A_p (\dot{z}_{pL} - \dot{z}_{iL}) - A_{pr} (\dot{z}_{pR} - \dot{z}_{iR}) \quad (4)$$

Continuity equation for the second chamber of left suspension can be written as

$$Q_{aL} - Q_{2L1L} = A_p (-\dot{z}_{fpL} + \dot{z}_{iL}) \quad (5)$$

Flow rate Q_{4L1R} through the connector can be found as

$$Q_{4L1R} = R (P_{4L} - P_{1R}) \quad (6)$$

Assuming laminar flow, R can be written as

$$R = \frac{\pi D^4}{128 \mu L} \quad (7)$$

From the continuity equation, flow rate Q_{4L1R} can also be found as

$$Q_{4L1R} = A_{pr} (\dot{z}_{pL} - \dot{z}_{iL}) \quad (8)$$

From equations (6) and (8), pressure P_{4L} can be found as

$$P_{4L} = P_{1R} + \frac{A_{pr} (\dot{z}_{pL} - \dot{z}_{iL})}{R} \quad (9)$$

Equation of motion for the floating piston mass of left suspension is

$$(P_{3L} - P_{Atm} - P_{2L}) A_p - M_{fp} g - F_{fpL} = M_{fp} \ddot{z}_{fp} \quad (10)$$

The same procedure can be repeated to model the right suspension. The equations derived so far can be used for simulation studies. For controller design, however, some simplifications are to be made. Floating piston mass dynamics and friction forces are assumed as negligible as compared to pressure forces. Equations of motions for the half car model with active interconnected HP suspension system in bounce and roll directions are

$$F_L + F_R - F_z - Mg = M\ddot{z} \quad (11)$$

$$\frac{t}{2} (F_L - F_R) - M_\theta = I_{xx} \ddot{\theta} \quad (12)$$

where F_z and M_θ are the disturbance force and disturbance moment, respectively. Assuming small rotations, kinematical relationships can be written as

$$z_{pL} = z + \frac{t}{2} \theta, \quad z_{pR} = z - \frac{t}{2} \theta \quad (13)$$

Equations (1-13) define the mathematical model of the interconnected HP suspension system in the roll plane model of the vehicle.

2.2. Linear-Structured Model of the Active Hydraulically Interconnected HP Suspension System in Roll Plane Model

The equations derived in the previous part can be used for simulation studies. However, to be able to design a controller, a convenient form of the system equations is needed. In this study, a nonlinear State Dependent Riccati Equation Control (SDRE) is used to design the controller. For this reason, a linear structured model with state dependent coefficients should be obtained from the originally nonlinear system equations. The nonlinear system equations are converted into the linear-structured equation using the direct parameterization [14] or extended linearization [15].

In the active interconnected HP suspension system, there are two nonlinear elements; the orifice and the gas volume. The mathematical models for these elements are derived in the previous section. In the extended linearization of the gas model, the aim is to have a model equation as the well-known linear stiffness equation. For these reason, a polynomial is fitted to polytropic gas model as

$$(P_{3L} - P_{30L}) A_p = k_L (z_{fpL}) z_{fpL} = a_{1L} z_{fpL} + a_{2L} z_{fpL}^2 + a_{3L} z_{fpL}^3 + a_{4L} z_{fpL}^4 + a_{5L} z_{fpL}^5 + a_{6L} z_{fpL}^6 + a_{7L} z_{fpL}^7 + a_{8L} z_{fpL}^8 \quad (14)$$

$$(P_{3R} - P_{30R}) A_p = k_R (z_{fpR}) z_{fpR} = a_{1R} z_{fpR} + a_{2R} z_{fpR}^2 + a_{3R} z_{fpR}^3 + a_{4R} z_{fpR}^4 + a_{5R} z_{fpR}^5 + a_{6R} z_{fpR}^6 + a_{7R} z_{fpR}^7 + a_{8R} z_{fpR}^8 \quad (15)$$

where a_{iR} and a_{iL} are the polynomial coefficients, z_{fpTL} and z_{fpTR} are the relative displacement across the gas volumes for left and right suspension, and $k_L(z_{fpTL})$ and $k_R(z_{fpTR})$ are the state dependent gas stiffness coefficients in the left and right suspensions respectively.

Similarly, to get a convenient representation of the system equations, pressure drop through the orifice can be written as

$$F_{L,damp} = c_{L1} (\dot{z}_{pL} - \dot{z}_{iL}) + c_{L2} (\dot{z}_{pR} - \dot{z}_{iR}) \quad (16)$$

$$F_{R,damp} = c_{R1} (\dot{z}_{pL} - \dot{z}_{iL}) + c_{R2} (\dot{z}_{pR} - \dot{z}_{iR}) \quad (17)$$

where c_{Li} , c_{Ri} , are the state dependent damping coefficients for the left and right suspensions. Therefore, the left and the right suspension forces are expressed as

$$F_L = k_L z_{fpTL} - \frac{A_{pr} k_R z_{fpTR}}{A_p} - c_{L1} (\dot{z}_{pL} - \dot{z}_{iL}) - c_{L2} (\dot{z}_{pR} - \dot{z}_{iR}) \quad (18)$$

$$F_R = k_R z_{fpTR} - \frac{A_{pr} k_L z_{fpTL}}{A_p} - c_{R1} (\dot{z}_{pR} - \dot{z}_{iR}) - c_{R2} (\dot{z}_{pL} - \dot{z}_{iL}) \quad (19)$$

As Equations (18) and (19) illustrate, the nonlinear suspension forces are written in linear-structured form with state dependent coefficients. The equations derived in the previous section can be manipulated to obtain the state space equations with state dependent coefficients. States are defined as:

$$x_1 = \dot{z}, x_2 = \dot{z}, x_3 = \dot{\theta}, x_4 = z_{fpTL} = z_{fpL} - z_{iL}, x_5 = z_{fpTR} = z_{fpR} - z_{iR}, x_6 = z_{pL} = z_{pL} - z_{iL},$$

$$x_7 = z_{pR} = z_{pR} - z_{iR}, x_8 = z_{i0L} = z_{iL} - z_{0L}, x_9 = z_{i0R} = z_{iR} - z_{0R}, x_{10} = \dot{z}_{iL}, x_{11} = \int z_{pTL}, x_{12} = \int z_{pTR}$$

State space representation of the half car model with active interconnected HP suspension system is

$$\dot{x} = A(x)x + Bu + Dw \quad (20)$$

where x is the state vector, $A(x)$ is the state dependent system matrix B is the control input matrix, u is the control input, D is the disturbance input matrix, and w is the disturbance input vector. The obtained model is in linear state space form. However, since the system matrix depends on the states itself, the model is nonlinear. Therefore nonlinearities are preserved in the mathematical model. By this way, a nonlinear controller can be designed for the vehicle.

3. DESIGN OF CONTROLLER FOR ACTIVE SUSPENSION

HP suspensions comprise two nonlinear elements which are the gas volume and the orifice, and thus it has a nonlinear structure. While designing the active controller, these nonlinearities should be preserved in the design to represent the complete dynamics of the suspension. Therefore, a nonlinear controller should be used to design the active suspension. In this study, the State Dependent Riccati Equation (SDRE) control method is used to design the active controller for the half car model with the unconnected and the interconnected active HP suspension systems. Theory and application of the SDRE Control is studied in the references [14-16]. In the first step of this control method, the nonlinear equation of motion or the system equations are linearized using the method called as direct parameterization or extended linearization [14-15] as presented in detail in the previous section. In direct parameterization, the nonlinear differential equations are written as linear equations in which the nonlinearities are inserted into parameters. Therefore, nonlinear equations are converted into linear equations with state dependent coefficients. As the states are changed, the parameters are updated to preserve the nonlinearities of the system equations. Then the cost function to be minimized is formed. This cost function, J , is minimized by solving the Algebraic Riccati Equation at each state. Therefore the State Dependent Riccati Equation is solved in real time with changing state values and the control input is formed.

$$J = \frac{1}{2} \int \left(q_1 \dot{z}^2 + q_2 \dot{\theta}^2 + q_3 \dot{z}_{pTL}^2 + q_4 \dot{z}_{pTR}^2 + q_5 z_{pTL}^2 + q_6 z_{pTR}^2 + q_7 z_{i0L}^2 + q_8 z_{i0R}^2 + q_9 \left(\int z_{pTL} \right)^2 + q_{10} \left(\int z_{pTR} \right)^2 + R Q_{aL}^2 + R Q_{aR}^2 \right) dt \quad (21)$$

4. SIMULATIONS

After the controller is designed, performance of the active interconnected HP suspension systems in roll plane vehicle model is examined and will be compared with the active unconnected HP suspension system in the roll plane model. Performance evaluations will be carried out in time domain. Moreover, the designed controller will be examined in terms of the ride comfort, handling, and the vehicle attitude control. To be able to compare the interconnected and the unconnected suspensions, some design parameters of the suspensions

should be adjusted to similar values. One approach is to get similar vertical stiffness and vertical damping for both suspensions for the same vehicle. By this way, controlled comparisons can be made between the interconnected and the unconnected suspensions. Keeping the piston area and rod area constant, the vertical stiffness of the interconnected and the unconnected suspensions can be equalized by adjusting the initial gas volumes. Similarly, vertical damping of the interconnected and the unconnected suspensions can be equalized by adjusting the orifice opening area. By this way two similar suspensions having identical vertical stiffness and the damping can be obtained. To be able to analyze the ride comfort, the models will be simulated by random road displacement inputs. Further, to be able to analyze vehicle handling characteristics, body disturbance inputs due to steering disturbance inputs are used in the simulations.

4.1. Simulation with Random Road Inputs

To be able to examine and understand the behavior of the of the active interconnected HP suspension system, it should be evaluated under real road conditions. Thus random road displacement input data are used for the left and the right tires to simulate the roll and bounce dynamics of the vehicle. The random road displacement inputs adapted from the study of Kilic [17] represents the road displacement of asphalt concrete on bound base taken at 60 kph longitudinal velocity. Root mean square (rms) values of the results from the simulations are calculated and presented in Table 2. As Table 2 illustrates, in general, the vertical accelerations of the active unconnected and active interconnected HP suspension systems are similar. Both active suspensions have much lower vertical acceleration as compared to the passive suspensions. For roll acceleration performances, active unconnected HP suspension systems have slightly lower results as compared to the active interconnected HP suspension system. Similarly, passive unconnected HP suspension system has slightly lower roll acceleration with respect to passive interconnected HP suspension system. For suspension deflections of the left and right suspensions, active interconnected suspension has slightly lower results. To sum up, active performance of the interconnected and the unconnected HP suspension systems are similar. Active unconnected HP suspension system has slightly better roll acceleration performance with respect to active interconnected HP suspension system for the given road inputs.

Table 2: rms results of performance variables

	Active Unconnected	Passive Unconnected	Active Interconnected	Passive Interconnected
Vertical Acc. [m/s ²]	0.17	0.56	0.17	0.55
Roll Acc.[rad/s ²]	0.21	0.48	0.24	0.54
Left Flow Rate [L/min]	18.00	-	20.22	-
Right Flow Rate [L/min]	17.52	-	19.79	-
Left Suspension Deflection [mm]	7.18	12.38	6.69	10.40
Right Suspension Deflection [mm]	6.85	12.20	6.44	10.41

Simulation with Body Disturbance Forces

In this part, the handling performance of the half car model with active interconnected HP suspension system will be examined. When the car is cornering or when the wind forces are acting on the vehicle, the vehicle body rolls on the suspensions with negative effects on the handling performance of the vehicle. In order to reduce the roll angle of the body, higher roll stiffness is required. One way of increasing the roll stiffness of the vehicle is increasing the suspension stiffness. However, stiff suspension degrades the vehicle ride comfort. Another way of increasing the roll stiffness is the use of mechanical interconnection between left and right suspensions. Anti-roll bar is used to increase the roll stiffness without affecting the vertical stiffness. Similarly, hydraulically interconnected vehicle suspensions can also be used to increase the roll stiffness. In this part, the performance of the active hydraulic interconnection is to be examined in terms of the handling performance. Both steady state cornering and the double lane change maneuver inputs will be used to examine the handling performance of the active and passive unconnected and interconnected suspensions. The lateral acceleration input used in the simulations is given in Figure 2 and the simulation results are given in Figure 3 and 4.

Figure 3 illustrates the roll angle performance of the active and passive interconnected and the unconnected HP suspension systems. Passive unconnected HP suspension system has the highest roll angle and thus it has the worst result in terms of vehicle handling. Moreover, passive interconnected HP suspension system has the lowest roll angle and thus it has the best handling performance. Active interconnected HP suspension system has nearly 30-40% lower roll angle than the roll angle of the unconnected active HP suspension system. At steady state region due to integral control of the active controllers, both active suspensions have zero steady state suspension deflections. This shows the improved performance of the active interconnected and the unconnected suspensions with respect to passive suspensions. Since roll stiffness of the interconnected HP suspension system is higher than the roll stiffness of the unconnected HP suspension, interconnected HP

suspension has lower suspension deflections and thus roll angle. Therefore, the interconnected HP suspension system provides better handling performance. Next the handling performance of the active and passive unconnected and the interconnected HP suspension systems are compared in double lane change maneuver. The lateral acceleration obtained from the simulation of the double lane change maneuver is shown in Figure 5. Simulation results with the active and passive suspension systems are shown in Figures 6 and 7. As simulation results show, passive interconnected HP suspension system gives the best results and passive unconnected HP suspension system gives the worst results in terms of handling performance. This is due to the fact that, passive interconnected HP suspension system has higher roll stiffness and damping and thus it has better roll performance. Since the active interconnected HP suspension system is designed mainly for the compromised ride comfort and handling performances, it has some overshoot for the body disturbance input and so it has inferior results as compared with the passive interconnected HP suspension at transient region. However, as the weighting coefficients are adjusted to increase the roll performance, the handling performance of the active interconnected HP suspension system will be better. Moreover, performance of the active interconnected HP suspension system is better than the performance of the active unconnected HP suspension system nearly by 30 % in the maximum overshoot region.

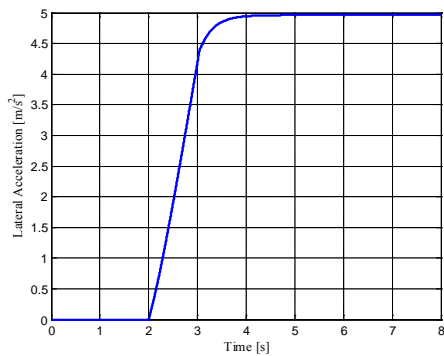


Figure 2. Lateral acceleration input

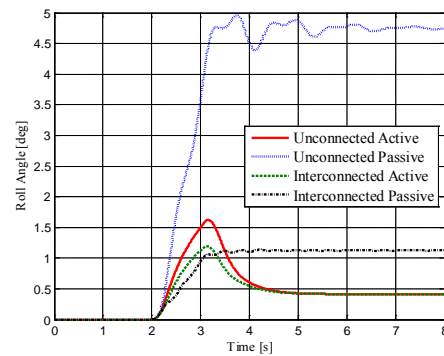


Figure 3. Sprung mass roll angle

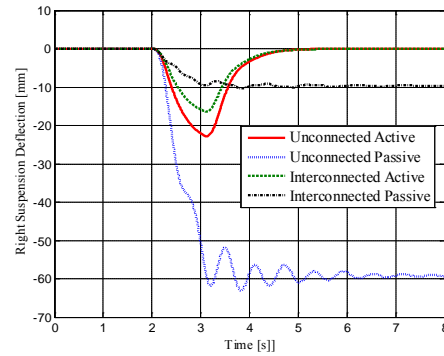
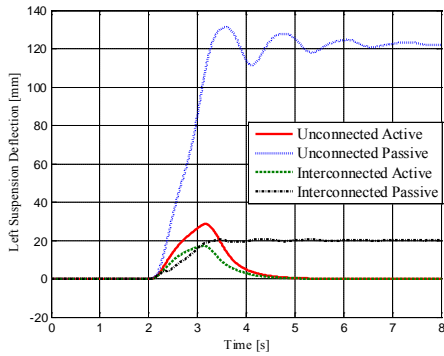


Figure 4. Left and right suspension deflections

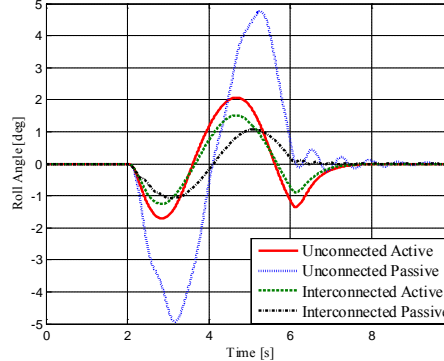
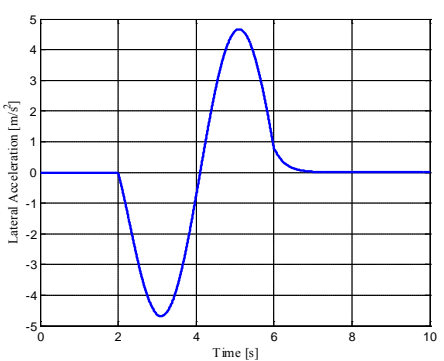


Figure 5. Lateral acceleration of double lane change maneuver

Figure 6. Sprung mass roll angle

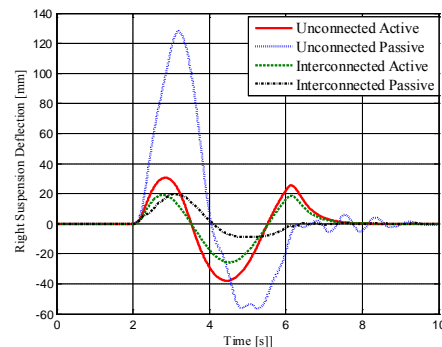
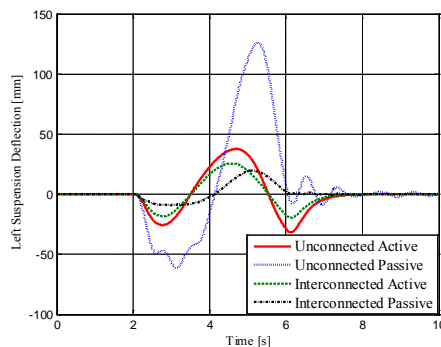


Figure 7. Left and right suspension deflections

5. CONCLUSION

The aims of this study were the examination of the performance characteristics of the active interconnected suspension system and the comparison of active interconnected HP suspension with the active unconnected HP suspension system. Using SDRE control method a nonlinear active controller for the interconnected and unconnected HP suspension systems was designed. For the sake of completeness, all simulations were also performed for the passive interconnected and unconnected HP suspension systems. It was shown that the active interconnected and unconnected HP suspension systems have similar performance bounce characteristics in terms of the ride comfort. The advantage of the active interconnected HP suspension system became apparent in its performance on handling characteristics. Active interconnected HP suspension system provided better handling performance than the active unconnected HP suspension system. These results were shown by the steady state cornering and double lane change maneuver simulations. Since the active suspensions have somewhat slow transient dynamics, passive interconnected HP suspension system produced better results in both maneuvers. This is due to high roll stiffness and damping of the passive interconnected HP suspension system. When the weighting parameters are adjusted to increase the handling performance of the controller, active suspensions may give better results. For passive suspensions there are some nonzero suspension deflection response values at steady state which are not desirable. Since active controllers are designed with integral control, zero steady state suspension deflections are guaranteed. It is observed that the active interconnected and unconnected HP suspension systems have similar ride comfort performances. However, active interconnected HP suspension system has better handling performance than the active unconnected HP suspension system. Therefore, if the main aim of the suspension design is to improve the handling performance alone, passive interconnected HP suspension system may be a simpler and cheaper alternative with a similar performance to that of an active unconnected HP suspension. On the other hand, if the aim is to get improved ride comfort and handling performances simultaneously, active interconnected HP suspension system is the better choice. Thus, according to the aim of the suspension design, both passive and active interconnected HP suspension systems may be implemented conveniently.

REFERENCES

- [1]. Bauer, W. (2011). *Hydropneumatic Suspension Systems*. Springer, Heidelberg.
- [2]. Zhang, N., Smith, W. A., Jeyakumaran, J. (2010). Hydraulically interconnected vehicle suspension: background and modeling. *Vehicle System Dynamics: International Journal of Vehicle Mechanics and Mobility*, 48:1, 17-40.
- [3]. Smith, W. A., Zhang, N., Jeyakumaran, J. (2010). Hydraulically interconnected vehicle suspension: theoretical and experimental ride analysis. *Vehicle System Dynamics: International Journal of Vehicle Mechanics and Mobility*, 48:1, 41-64. *Vehicle System Dynamics: International Journal of Vehicle Mechanics and Mobility*, 48:1, 41-64.
- [4]. Smith, W. A., Zhang, N., Hu, W. (2011). Hydraulically interconnected vehicle suspension: handling performance. *Vehicle System Dynamics: International Journal of Vehicle Mechanics and Mobility*, 49:1-2, 87-106, DOI: 10.1080/00423111003596743.
- [5]. Cao, D. (2008). *Theoretical Analyses of Roll-And Pitch-Coupled Hydropneumatic Strut Suspensions*. PhD. Thesis.
- [6]. El-Demerdash, S. M., Crolla, D. A. (1996). Hydro-pneumatic Slow-active Suspension with Preview Control. *Vehicle System Dynamics*, 25, pp. 369-386.
- [7]. Gao, B., Darling, J., Tilley, D. G., Williams, R. A., Bean, A., Donahue, J. (2005). Control of a Hydropneumatic Active Suspension Based on a Non-Linear Quarter-Car Model. *Proc. IMechE Vol. 220 Part I: J. Systems and Control Engineering*.
- [8]. Shi, J-W., Li, X-W., Zhang, J-W. (2009). Feedback Linearization and Sliding Mode Control for Active Hydropneumatic Suspension of a Special-Purpose Vehicle. *Proc. ImechE Vol. 224 Part D: J. Automobile Engineering*.

- [9]. Sağlam, F., Unlusoy, Y. S. (2014). State Dependent Riccati Equation Control of an Active Hydro-Pneumatic Suspension System. *Journal of Automation and Control Research*, Volume 1, Pages 1-10.
 - [10]. Sağlam, F., Ünlüsoy, Y. S. (2014). Hidro-Pnömatik Süspansiyonlu Araçlar İçin Tümüleşik Sürüş Konforu ve Yükseklik Kontrolü. OTEKON'14 7. Otomotiv Teknolojileri Kongresi 26 – 27 Mayıs, BURSA.
 - [11]. Rosam, N., Darling, J. (1997). Development and Simulation of a Novel Roll Control System for the Interconnected Hydragas® Suspension. *Vehicle System Dynamics: International Journal of Vehicle Mechanics and Mobility*, 27:1, 1-18, DOI: 10.1080/00423119708969320.
 - [12]. Schumann, A. R., Anderson, R. J. (2002). Optimal control of an active anti roll suspension for an off-road utility vehicle using interconnected hydragas suspension units. *Vehicle System Dynamics Supplement 37*, pp. 145-156.
 - [13]. Joo, F. R. (1991). Dynamic Analysis of a Hydropneumatic Suspension System. Concordia University, M.Sc. Thesis, Mechanical Engineering Department.
 - [14]. Mracek, C. P., Cloutier, J. R. (1998). Control Designs for the Nonlinear Benchmark Problem via the State-Dependent Riccati Equation Method *International Journal of Robust and Nonlinear Control*, 8, 401-433.
 - [15]. Çimen, T. (2008). State-Dependent Riccati Equation Control- A Survey. *Proceedings of the 17th World Congress, The International Federation of Automatic Control*, Seoul, Korea, July 6-11.
 - [16]. Bank, H. T., Lewis, B. M., Tran, H. T. (2007). Nonlinear Feedback Controllers and Compensators- A State Dependent Riccati Equation Approach. *Comput Optim Appl* 37, 177-218.
 - [17]. Kılıç, V. (2006). Determination of Road Surface Characteristics and Random Road Surface Generation. Unpublished Course Term Project, ME 513 Vehicle Dynamics, Mechanical Engineering Department, METU, Ankara, Turkey.
-

NUMERICAL INVESTIGATION OF THE EFFECT OF OBJECTS WITH DIFFERENT PROFILES ON FLOW CHARACTERISTICS

Mehmet AKÇAY

Pamukkale University, Department of Mechanical Education, 20070, Denizli, Turkey.
makcay@pau.edu.tr

Gürhan KÜLAHLI

Pamukkale University, Department of Automotive Engineering, 20070, Denizli, Turkey,
hyazici@pau.edu.tr

Hilmi YAZICI

Pamukkale University, Department of Automotive Engineering, 20070, Denizli, Turkey,
gkulahli@pau.edu.tr

Abstract

In this study, the effect of an object located between nozzle and plate on the flow characteristics occurred on the plate surface was examined. Objects with different profiles (triangle, square and circle) were placed between nozzle and impingement plate. The change of the air velocity on the impingement plate was examined depending on the radial distance (x/D). The nozzle diameter was taken as $D=8$ mm, the distance between nozzle and impingement plate as $H/D=1$ and nozzle entrance air velocity as $U_j=60$ m/s. In this numerical study, the air velocity on the impingement surface was resolved as 2D according to the standard $k-\epsilon$ turbulence model by using ANSYS/Fluent program.

Keywords: *Impinging air jet, numerical investigation, air velocity, standard $k-\epsilon$*

1. INTRODUCTION

In spite of their basic structures, impinging jets draw great attention since they have the feature of heat transfer in higher rates [1]. The working principle of impinging jet is based on increasing heat transfer by making the boundary layer thin. Therefore, it enables heat and mass transfer on the impingement surface by obtaining local heat transfer coefficient at a high value between fluid and surface [2]. Impinging air jets are used in many industrial areas such as glass tempering and shaping, cooling electronic devices and gas turbine wings, and drying paper and textile [3].

In general, it is possible to divide an impinging jet flow into three regions that are free jet region, stagnation region and wall jet region [4]. In Figure 1, an impinging jet and flow regions are presented. In free jet region, there are mass, momentum and energy transfer between the environment and the jet. The flow in this region is not affected from the impact surface [5]. The flow in the stagnation or impingement region does not have an exact direction and the flow in this region is affected by the target surface, slowing down in the vertical direction and speeding up in the parallel direction [6]. The stagnation point in which the velocities parallel and vertical to the surface are zero is also in this region. In the wall jet region, as r or x increases on the plate, the velocity components parallel to the surface reach the highest values from zero, and then drop to zero. The fluid that leaves the impingement region now flows parallel to the surface and this is called wall or side jet [5,7].

In impinging jet applications, heat transfer rates are affected from many parameters such as Reynolds number, jet-to-plate spacing, radial distance from stagnation point, Prandtl number, target plate inclination, confinement of the jet, nozzle geometry, curvature and roughness of the target plate and turbulence intensity at the nozzle exit [1]. Experimentally examining the effect of finned (rough) surface on local heat transfer coefficient between air jet and flat plate, Nakod et al. (2006) observed that heat transfer coefficient increased depending on the shape of roughness, the distance between nozzle and plate, and the Reynolds number [8].

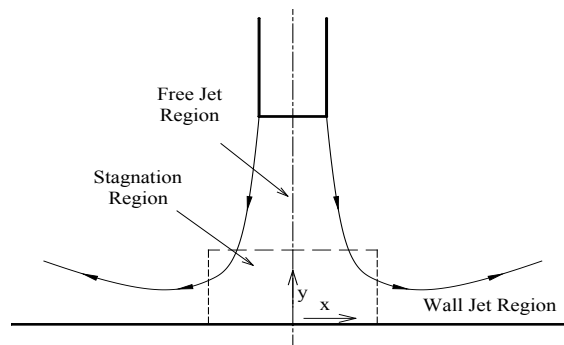


Figure 1. Impinging jet and flow regions

In the studies on numerically examining and analysing impinging jet applications, the $k-\epsilon$ turbulence model is widely used. For example, Atmaca (2007) analyzed jet flows having different ellipse sections by means of Standard $k-\epsilon$ turbulence method. According to the numeric results, the highest velocity for each type of jet was obtained at $x/D=0.3$, and the lowest at $x/D=50$ [9].

Using RNG $k-\epsilon$ and SST $k-\epsilon$ models, Chen et al. (2012) aimed to predict the flow structure of an isothermal impinging jet in a room [10]. Baydar and Ozmen (2005) experimentally and numerically examined the flow areas of confined jet. The numerical results obtained using the standard $k-\epsilon$ turbulence model is in agreement with the experimental results except for the nozzle-to-plate spacing less than one [11]. Seyedein et al. (1994) made a two-dimensional numeric simulation of the flow area of singly heated slot jet placed in a channel, and its heat transfer. To model the jet flow, they used the $k-\epsilon$ turbulence model in low and high Reynolds numbers [12].

In this study, the change of the air flow on impingement plate depending on the radial distance (x/D) and height from plate surface (y/D) is presented. The air velocity was measured by placing objects with different profiles between nozzle and impingement plate. The measurement of air velocity was done in certain distances over the impingement plate ($y/D=0.03-0.4$). In the study, objects with three different profiles (triangle, square and circle) and three different surface areas (5, 10 and 15mm²) were used. The nozzle diameter was taken as $D=8$ mm, the distance between nozzle and impingement plate as $H/D=1$ and nozzle entrance air velocity as $U_j=60$ m/s. The resolution process was performed numerically by using

ANSYS/Fluent. As for the turbulence model, standard k-epsilon ($k-\epsilon$) model and standard wall function features were used.

2. MATERIAL AND METHOD

In the study, by using an ANSYS/Fluent program, the effect of the objects placed between nozzle and impingement plate on the air velocity on impingement plate surface. 80 mm long and 8 mm in diameter circular nozzle was used. The thickness of impingement plate was taken as 4 mm, and the width as 100 mm.

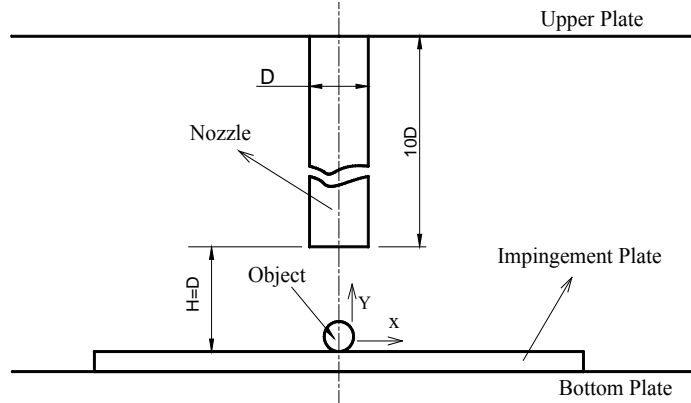


Figure 2. Schematic view of the impinging jet configuration

The measurement of air velocity was performed at $y/D=0.03-0.4$ starting from plate surface. The distance between nozzle and plate was taken as $H/D=1$ and nozzle entrance air velocity as $U_j=60$ m/s. Objects with triangle, square and circular profiles having 5, 10 and 15 mm² surface area were placed between nozzle and impingement plate. In Figure 2, the schematic view of the object (circle) placed between impingement plate and nozzle is presented.

In the study, the symmetry of air jet and impingement plate set was determined as the calculation area. In Figure 3, the schematic view of the calculation area evaluated in the study is given.

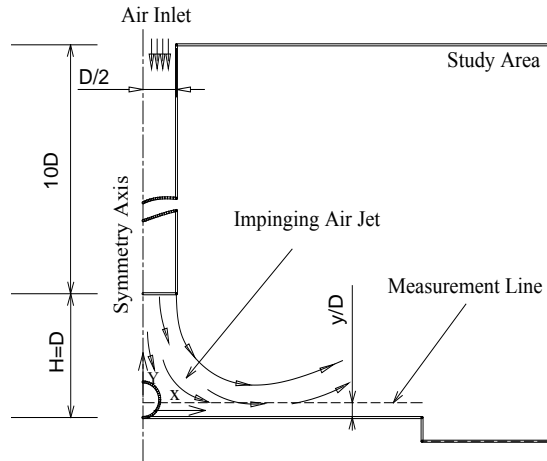


Figure 3. The calculation area

Using the SolidWorks program, 2D models of the calculation areas given in Figure 3 were formed for each object. The formed models were transferred to the ANSYS/Fluent software. A mesh was created in a suitable and sensitive way to analysis the air flow on the impingement plate. The mesh structure of the calculation area is shown in Figure 4.

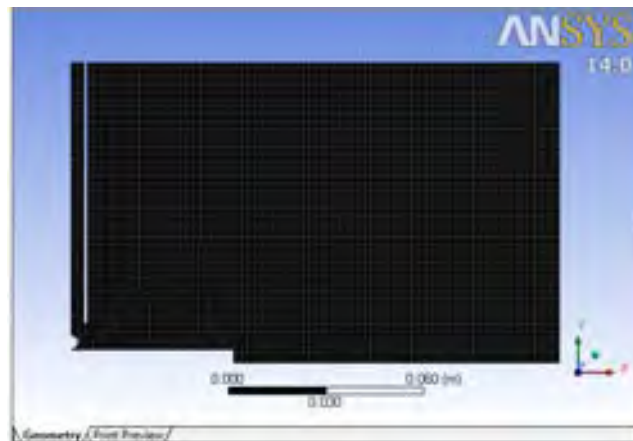



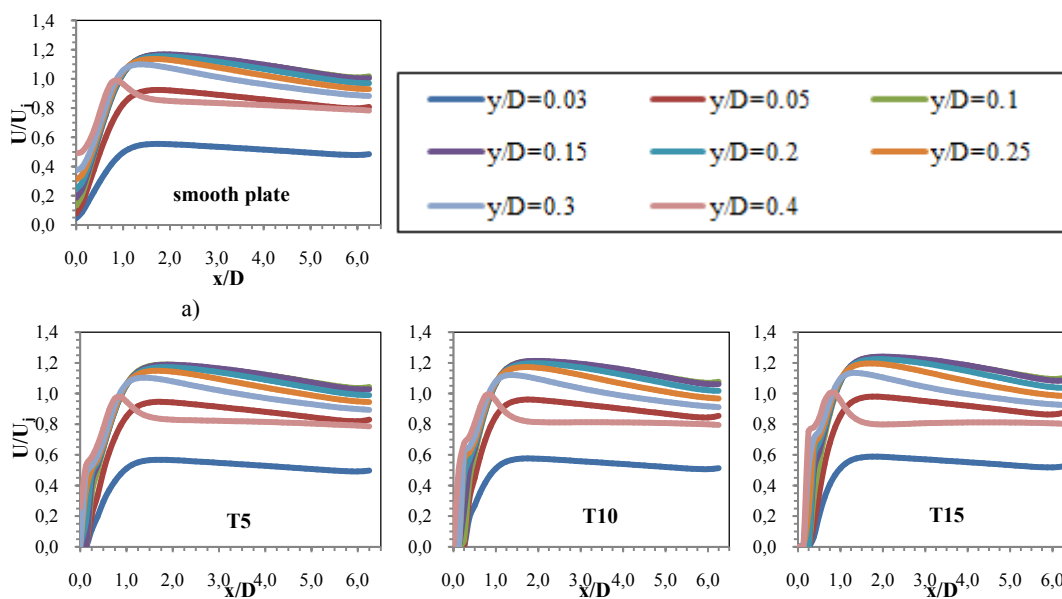


Figure 4. The mesh structure of the calculation area

After the meshing step, the confinement conditions of the calculation area were specified. In the study conducted using the ANSYS/Fluent package program, standard k-epsilon ($k-\epsilon$) model was used as the turbulence model and standard wall function was chosen. The information regarding the objects evaluated in the study and the mesh structure is presented in Table 1. As is seen in Table 1, the number of elements in the mesh structure that was created was found to vary at a low level depending on the geometric shape and size of the object.

Table 1. Evaluation parameters applied in the study

Object Profile	Model	Object Surface Area (mm ²)	Node	Elements	Figure
No object	smooth plate	-	54725	54080	
Triangle	T5	5	54719	54075	
	T10	10	54715	54072	
	T15	15	54704	54062	
Square	S5	5	54748	54103	
	S10	10	54722	54078	
	S15	15	54693	54048	
Circle	C5	5	54734	54086	
	C10	10	54717	54071	
	C15	15	54706	54060	



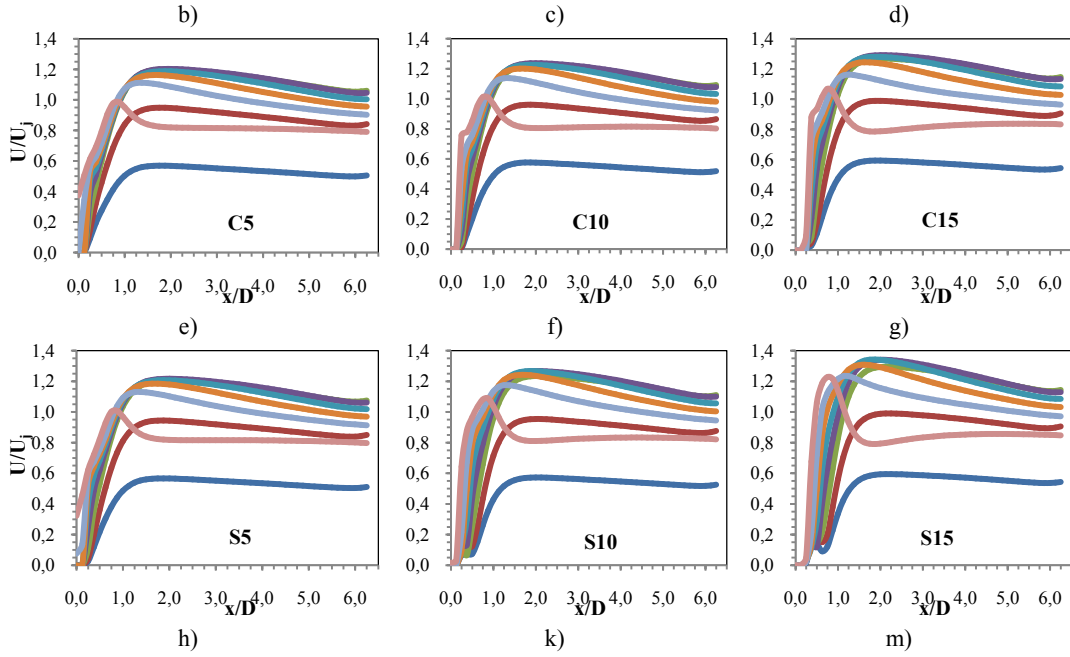


Figure 5. The change of air velocity with y/D depending on x/D

3. RESULTS AND DISCUSSION

In this study, the effect of objects with different profiles and surface areas placed on the impingement plate on the air velocity on the plate surface, and the related graphics were created. The velocity of the air and the radial distance on the plate surface was given as dimensionless. The velocity of the air was normalized by dividing the velocity of the air (U) on any radial distance from the stagnation point (x) to the jet entrance velocity of the air (U_j). Radial distance was normalized by the division of radial distance from the stagnation point (x) to the nozzle diameter (D). The change of the air velocity with the height from the plate ($y/D=0.03-0.4$) depending on the radial distance (x/D) is presented in Figure 5 for each object profile and surface area. As can be seen in Figure 5, it was found that the air velocity low at $x/D=0$, increased nearly to $x/D=2$, and constantly decreased from the point of $x/D=2$.

The measurement of the air velocity was done from certain distances (y/D) from the plate, and as the height increased, the air velocity also increased. The highest air velocities were obtained in an approximate range of $y/D=0.1-0.2$. It was observed that the air velocity dropped again after nearly $y/D=0.2$.

In Figure 6, the change of the air velocity based on the object profile (triangle, square and circle) depending on the radial distance (x/D) is presented. Since the highest velocities on the impingement plate for each object were obtained in an approximate range of $y/D=0.1-0.2$, the graphics were formed based on the rate $y/D=0.15$. As in seen in Figure 6, the maximum air velocity obtained in the case where there was no object on the impingement plate, was always lower than the maximum velocity obtained in the case where there was an object.

When the air velocities obtained were compared based on object profiles, it was found that for each surface area, while the lowest air velocities were obtained in triangle profile, the highest were in square profile. It was also observed that the difference of air velocity between the profiles went up with the increasing surface area.

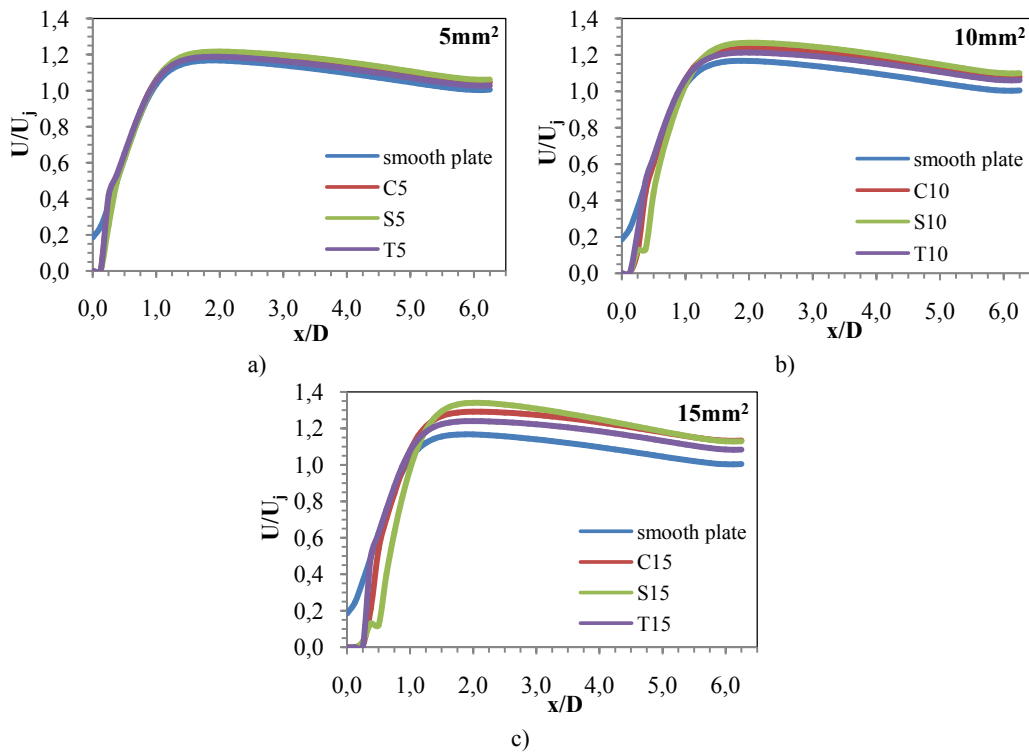
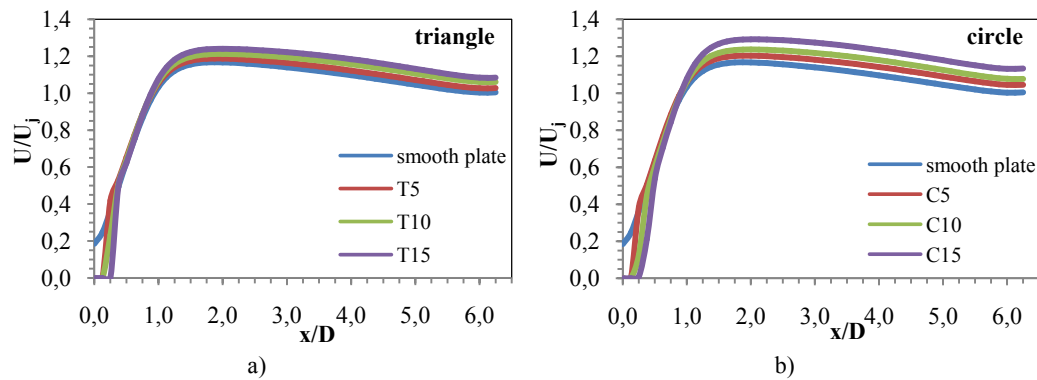


Figure 6. The change of air velocity with object profile depending on x/D

In Figure 7, the change of air velocity based on the object surface area depending on the radial distance (x/D) is presented. Similarly, the graphics were drawn based on the rate $y/D=0.15$. As can be seen in Figure 7, it was found that for each object, the air velocity on the plate surface went up with the increasing surface area. While the minimum air velocities were obtained with the objects having 5mm² surface area, the maximum air velocities were obtained with those having 15 mm² surface area. It was observed that the effect of the surface area of the objects with circle and square profiles on the air velocity was greater than that of those with triangle profile.



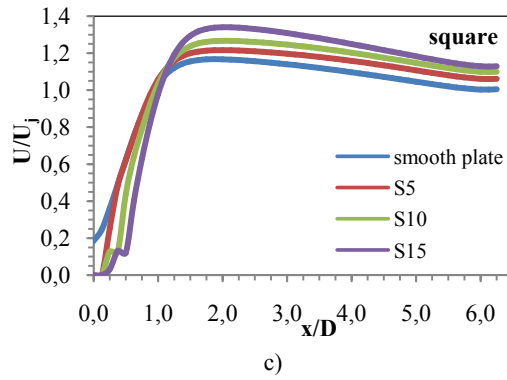


Figure 7. The change of air velocity with surface area depending on x/D

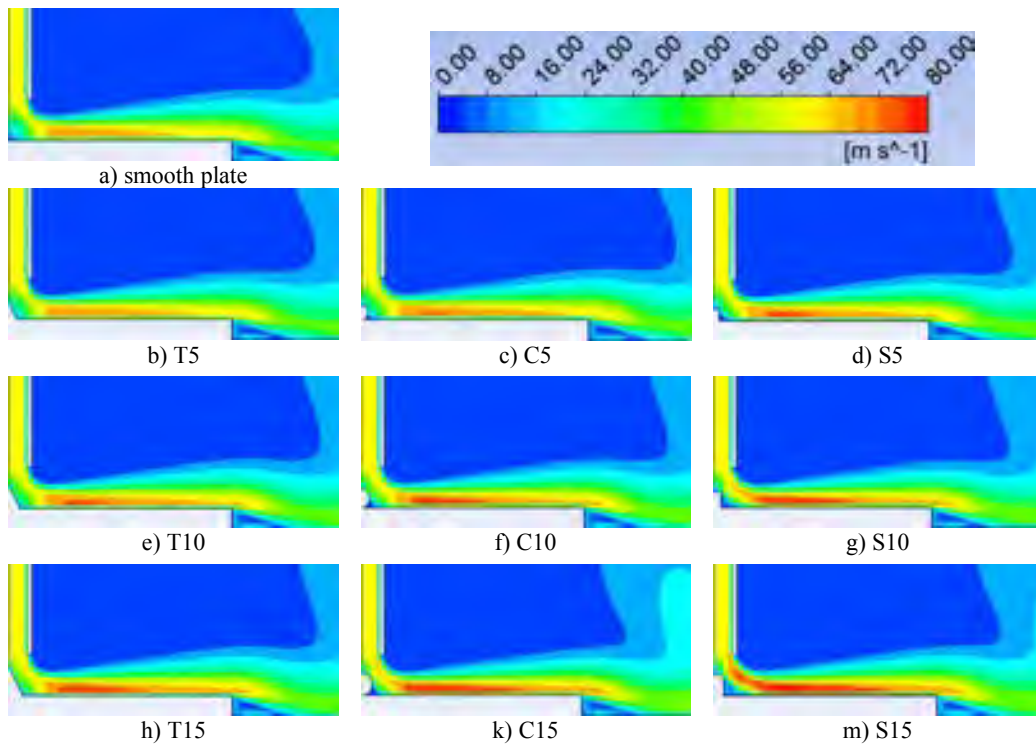


Figure 8. The velocity distributions on the impingement plate for each object profile

The velocity distributions on the impingement plate for each object profile (no object, triangle, square and circle) and surface areas (5, 10 and 15mm²) are presented in Figure 8. As is seen in Figure 8, it was observed that the air velocity on the plate increased with the object surface area, and the maximum velocity was obtained on the square profile (S15) having 15mm² surface area.

4. CONCLUSIONS

In this study, the change of the air flow on impingement plate depending on the radial distance (x/D) and height from plate surface (y/D) is presented. The air velocity on the plate was measured by placing objects with different profiles between nozzle and impingement plate. The resolution process was performed numerically by using ANSYS/Fluent program. As for the turbulence model, standard k-epsilon ($k-\epsilon$) model and standard wall function features were used.

It was observed that the air velocity on the region where the air jet impinges was low, increased while being moved away from the stagnation region, and started to decrease again after reaching the highest value at nearly $x/D=2$.

In the measurements done at certain heights (y/D) from the plate surface, the highest air velocities were obtained in an approximate range of $y/D=0.1-0.2$. It was observed that the air velocities dropped again after nearly $y/D=0.2$.

The maximum air velocity obtained in the case where there was no object on the impingement plate was always lower than the maximum air velocity obtained in the case where there was an object.

When the air velocities obtained were compared based on object profiles (triangle, square and circle), it was found that for each surface area, while the lowest air velocities were obtained in triangle profile, the highest were in square profile.

It was found that for each object profile, the air velocity on the plate surface went up with the increasing surface area. While the minimum air velocities were obtained with the objects having 5mm^2 surface areas, the maximum air velocities were obtained with those having 15mm^2 surface areas.

ACKNOWLEDGMENT

This work was financially supported by the BAP, Pamukkale University in Turkey.

REFERENCES

- [1]. M.D. Limaye, R.P. Vedula and S.V. Prabhu, "Local heat transfer distribution on a flat plate impinged by a compressible round air jet", *International Journal of Thermal Sciences*, 49: 2157-2168, 2010.
 - [2]. T. Demircan and H. Türkoğlu, "Numerical investigation of an oscillating two dimensional rectangular impinging air jet", *Journal of Thermal Science and Technology*, 27(1): 39-50, 2007.
 - [3]. F. Cirillo and G.M. Isopi, "Glass tempering heat transfer coefficient evaluation and air jets parameter optimization", *Applied Thermal Engineering*, 29(5-6): 1173-1179, 2009.
 - [4]. T.S. O'Donovan and D.B. Murray, "Jet impingement heat transfer-part I: mean and root-mean-square heat transfer and velocity distributions", *International Journal of Heat and Mass Transfer*, 50(17-18): 3291-3301, 2007.
 - [5]. M. F. Koseoglu, "Experimental and numerical investigation of electronics equipment cooling with impinging jets", PhD Thesis, Gazi University, Institute of Science and Technology, Ankara, 4-7, 339-351, 2007.
 - [6]. K. Bilen, "An experimental investigation of heat transfer characteristics of a normal and oblique air jet impinging on heated flat plate", PhD Thesis, KTU, Institute of Science and Technology, Trabzon, 1994.
 - [7]. F.P. Incropera and D.P. De Witt, *Fundamentals of Heat and Mass Transfer*, 4th ed., (trans. Derbentli et al.) Literatur Press, Istanbul, Turkey, 2001.
 - [8]. P. M. Nakod, S. V. Prabhu and R. P. Vedula, "Heat transfer augmentation between impinging circular air jet and flat plate using finned surfaces", *18. National & 7. ISHMT-ASME Heat and Mass Transfer Conference*, India, 4-6, 2006.
 - [9]. M. Atmaca, "Numerical analysis of the elliptical jet flow", *Electronic Journal of Machine Technologies*, 1:25-32, 2007.
 - [10]. H.J. Chen, B. Moshfegh and M. Cehlin, "Numerical investigation of the flow behavior of an isothermal impinging jet in a room", *Building and Environment*, 49: 154-166, 2012.
 - [11]. E. Baydar and Y. Ozmen, "An experimental and numerical investigation on a confined impinging air jet at high Reynolds numbers", *Applied Thermal Engineering*, 25: 409-421, 2005.
 - [12]. S.H. Seyedein, M. Hasan and A.S. Mujumdar, "Modeling of a single confined turbulent slot jet impingement using various k- ϵ turbulence models", *Appl. Math. Model*, 18: 526-537, 1994.
-

REMOVAL OF PHENOL FROM AQUEOUS SOLUTIONS BY PHOTO-FENTON PROCESS

Özlem TEPE

Firat University, Department of Environmental Engineering, 23100, Elazig, Turkey.
otepe@firat.edu.tr

Arzu Y. DURSUN

Firat University, Department of Environmental Engineering, 23100, Elazig, Turkey,
aydursun@firat.edu.tr

Abstract

Phenol and phenolic compounds are widely used as raw materials in the petrochemical industry and in oil refineries. They are toxic even in the presence of low concentration. Limited phenol concentration in drinking water was determined as $1\mu\text{g/L}$ by The World Health Organization. Many technologies have been used for treatment of phenolic wastewater. But there are few suitable processes for the complete removal. The fenton and photo-fenton processes are well-known examples. In this study, photo-fenton process were used for removal of phenol and the influence of operating parameters such as H_2O_2 , FeSO_4 and initial phenol concentrations was investigated. On the photo-fenton experiments, photo reactor was used. Phenol removal efficiency was obtained to be 56% using $\text{UV}+\text{H}_2\text{O}_2$ concentration of 0.4 mL/L (reaction time 15 minutes). The effect of FeSO_4 concentration (10-50 mg/L) was performed at pH 3, initial phenol concentration of 100 mg/L and H_2O_2 concentration of 0.4 mL/L. The maximum phenol removal efficiency was determined as 87% at FeSO_4 concentration of 50 mg/L (reaction time 30 minutes). Then, on the optimum conditions, effect of initial phenol concentrations was investigated and removal efficiencies of phenol and COD at the initial phenol concentration of 50 mg/L were determined to be 93% and %76, respectively. These results demonstrated that this process may be used for phenol removal.

Keywords: Phenol, phenol removal, photo-fenton, hydroxyl radical

1. INTRODUCTION

Phenol and phenolic compounds are widely used as raw materials in the petrochemical industry and oil refineries. They are toxic even in the presence of low concentration [1]. Limited phenol concentration in drinking water was determined as $1\mu\text{gL}^{-1}$ by The World Health Organization. Hence, elimination of phenol becomes necessity to preserve the environmental quality. Several treatment methods such as chlorination, ozonation, adsorption, solvent extraction, coagulation, flocculation and biological treatment have been used for treatment of wastewater containing phenol [2]. But there are few suitable processes for the complete removal. Advanced oxidation processes (AOP) are well-known examples.

These processes are known by the production of unselective and highly oxidant species (hydroxyl radicals) that cause major changes in the chemical structure of the contaminants until their complete mineralization. Since H_2O_2 has been proven to be highly efficient for mineralization of organic compounds, a lot of AOP use it as source of oxidant species. Besides, H_2O_2 is environmentally friendly since its self-decomposition converts to H_2O and O_2 . The oxidant action of H_2O_2 is significantly improved by adding Fe^{2+} as catalyst. This process known as fenton's reagent has widely been used because of its simplicity, and generates in an acidic medium. Fenton process has been expressed to improve when a source of radiation (usually a UV lamp) is added to the experimental set up. This is mainly due to the photolytic regeneration of Fe^{2+} from Fe^{3+} complexes, and the concurrent generation of $\cdot\text{OH}$ radicals in the system. This is known as photo-fenton process and its efficiency changes depending medium parameters such as pH, catalyst loading and hydrogen peroxide concentration [3].

Fenton and photo-fenton processes have been used in the treatment of contaminants like phenol, chlorophenols, nitrophenols, 2,4-dinitrophenol, caffeine, dyes [4-6].

In this study, photo-fenton process were used for removal of phenol and the influence of operating parameters such as H_2O_2 , FeSO_4 and initial phenol concentrations was investigated.

2. EXPERIMENTAL

2.1. Materials

The chemical structure of phenol is shown in Fig. 1. Hydrogen peroxide solution (30% w/w), ferrous sulfate heptahydrate ($\text{FeSO}_4 \cdot 7\text{H}_2\text{O}$), NaOH, and H_2SO_4 were obtained from Merck (Germany).

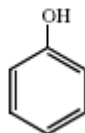


Figure 1. The chemical structure of phenol

2.2. Photo-Fenton Process

The photo-fenton reactions were carried out in a batch photoreactor. The radiation source was a low-pressure mercury ultraviolet (UV) lamp (30 W, $\lambda_{\text{max}}=254$ nm, manufactured by Philips), which was placed into a quartz sleeve and then into a cylindrical photoreactor. The volume of the reaction mixture was 2.5 L. The phenol solution was adjusted to pH=3.0, using 1 N NaOH or 1 N H_2SO_4 . The reaction was initiated by adding H_2O_2 and FeSO_4 .

2.3. Analytical Methods

The pH of solutions was measured using an Thermo Scientific Orion 3 Star pH meter. The residual phenol concentration in the medium was determined spectrophotometrically. The absorbance of the colored complex of phenol and p-nitroaniline was read at 470 nm [7]. The COD was determined according to standard methods [8].

3. RESULTS AND DISCUSSION

3.1. Effect of H_2O_2 concentration

In the photo-Fenton degradation process used UV light and Fenton reagents; H₂O₂ is converted to hydroxyl radical in a catalytic cycle with Fe ions acting as catalyst. Firstly, the hydroxyl radical is generated due to iron catalyzed decomposition of hydrogen peroxide as:



The formation of ·OH radical also occurs by the following reactions:



Reaction (3) in which Fe(III) catalyzes the generation of ·OH with the irradiation of UV light is followed by Reaction (1) and iron cycle between Fe(II) and Fe(III) occurs. Hydroxyl radicals generated in Reactions (1)–(3) can react with target organic contaminants and lead to the complete mineralization of them. The oxidative attack of OH radicals plays a vital role in degradation of organic contaminants in wastewater [9].

The effect of H₂O₂ concentration on phenol removal was studied at pH 3. The results obtained after the reaction time of 15 min are shown in Fig. 2. Removal percentage of phenol was determined to be 56% at 0.4 mL/L of H₂O₂ for 100 mg/L phenol concentration in photo-Fenton process. As can be seen from the figure, when H₂O₂ concentration exceeded 0.4 mL/L, phenol removal decreased. Sometimes removal efficiency of contaminants is negatively affected by increasing of the hydrogen peroxide. Because, at a higher H₂O₂ concentration, the scavenging of OH radicals will occur as expressed by Eqs. (4-6) [5]. This may be owing to auto decomposition of H₂O₂ to oxygen and water and recombination of OH radicals.



Excess of H₂O₂ will react with ·OH competing with organic pollutants and consequently reducing the efficiency of the treatment, the H₂O₂ itself contributes to the ·OH radical scavenging capacity. A higher dose of H₂O₂ means a higher production of hydroxyl radicals. Because the higher the H₂O₂ concentration the more favoured the occurrence of auto-scavenging reactions. H₂O₂ should be added at an optimal concentration to achieve the best removal [10]. Therefore, 0.4 mL/L of H₂O₂ concentration was considered as the optimum value for phenol removal. Phenol removal was observed in the absence of H₂O₂ and this may be due to the production of hydroxyl radicals by UV irradiation [11].

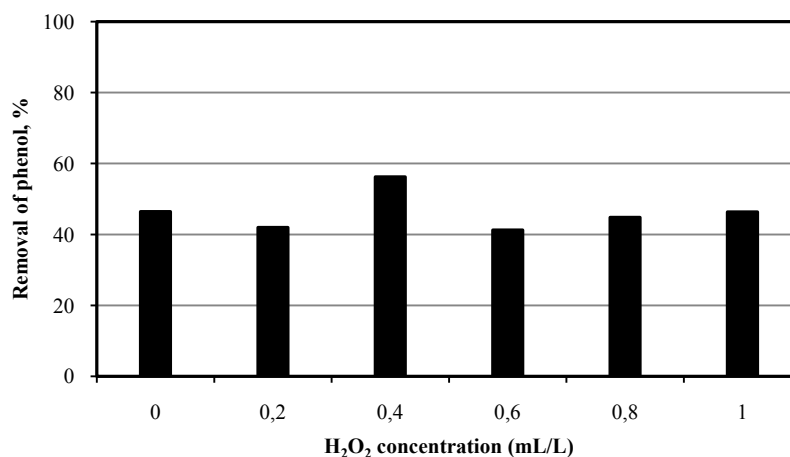


Figure 2. The effect of H₂O₂ concentration on the phenol removal by photo-fenton process

3.2. The effect of the amount of FeSO₄

The amount of ferrous ions is one of the main parameters influencing the fenton and photo-fenton processes. The effect of FeSO_4 on the phenol removal was studied at concentrations varying from 10 mg/L to 50 mg/L at pH 3, initial phenol concentration of 100 mg/L and H_2O_2 concentration of 0.4 mL/L. The results obtained are shown in Fig. 3-4. The maximum phenol removal efficiency was determined as 87% at FeSO_4 concentration of 50 mg/L after reaction time 30 minutes. But as can be seen from Figure 3, it was obtained approximately the same results at the other concentrations of FeSO_4 . Also, at all FeSO_4 concentrations, almost 70% of phenol concentration was removed in the first 5 minutes of reaction. Optimum FeSO_4 concentration was accepted as 50 mg/L for removal of phenol from aqueous solution used in this study.

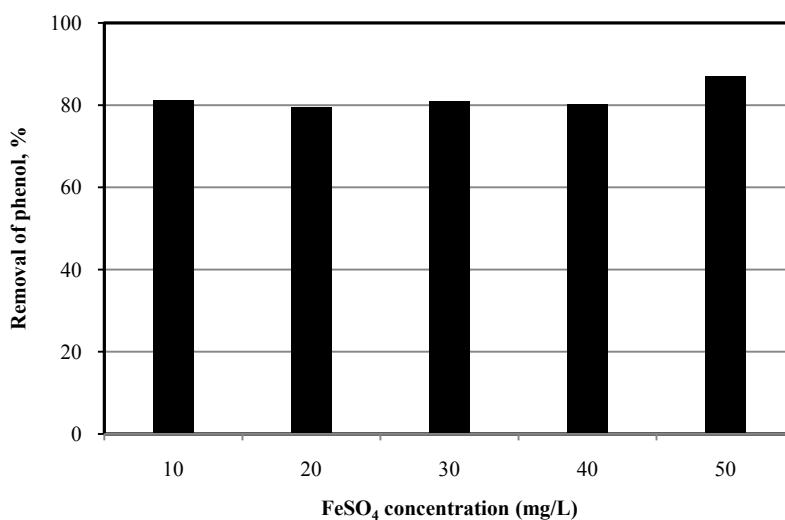


Figure 3. The effect of FeSO_4 concentration on the phenol removal by photo-fenton process

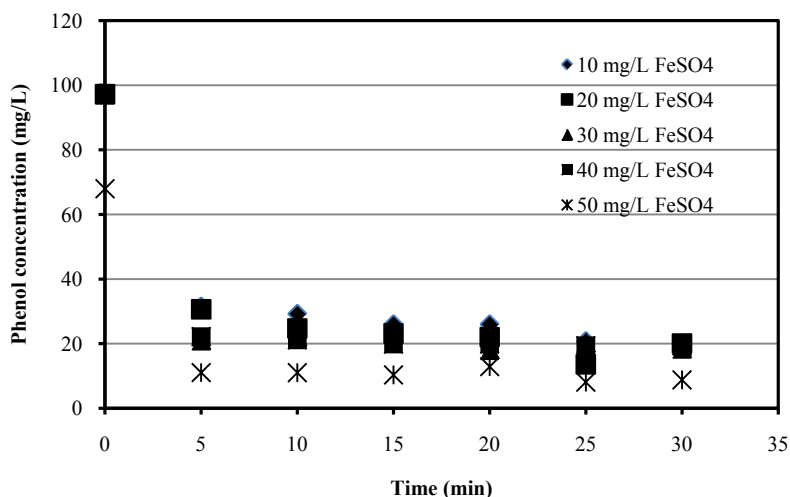


Figure 4. The change profile of phenol concentration with time on photo-fenton process

3.3. The effect of initial phenol concentration

Since the contaminant concentration has a significant effect in performance of treatment processes, the effect of phenol concentration on removal efficiency was investigated at different initial concentrations varying in the range of 50-1000 mg/L, as presented in Fig. 5-6. From these figures, it can be observed that the phenol removal efficiency decreased with the increase of the initial concentration. Increasing the phenol concentration from 50 to 1000 mg/L, phenol removal decreased from 93 to 6%. The increase in contaminant concentration increases the number of contaminant molecules [5] and at high contaminant concentrations, the removal of contaminant requires more time and thus greater quantities of H_2O_2 , and for this reason, the

removal rate decreases [12]. In addition to this, at high phenol concentrations, the photons entering the solution exhibit reduced penetration [5]. At initial phenol concentration of 50 mg/L, it was obtained COD removal of 76%.

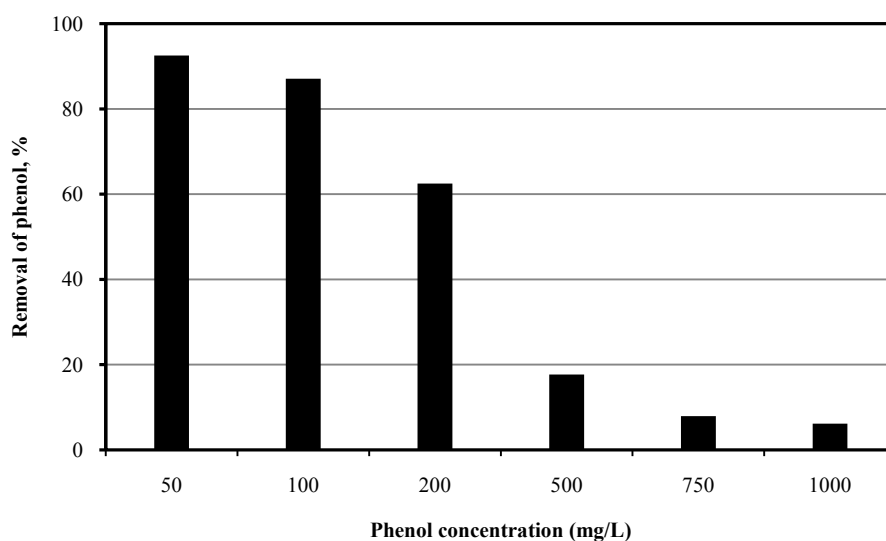


Figure 5. The effect of initial phenol concentration on the phenol removal by photo-fenton process

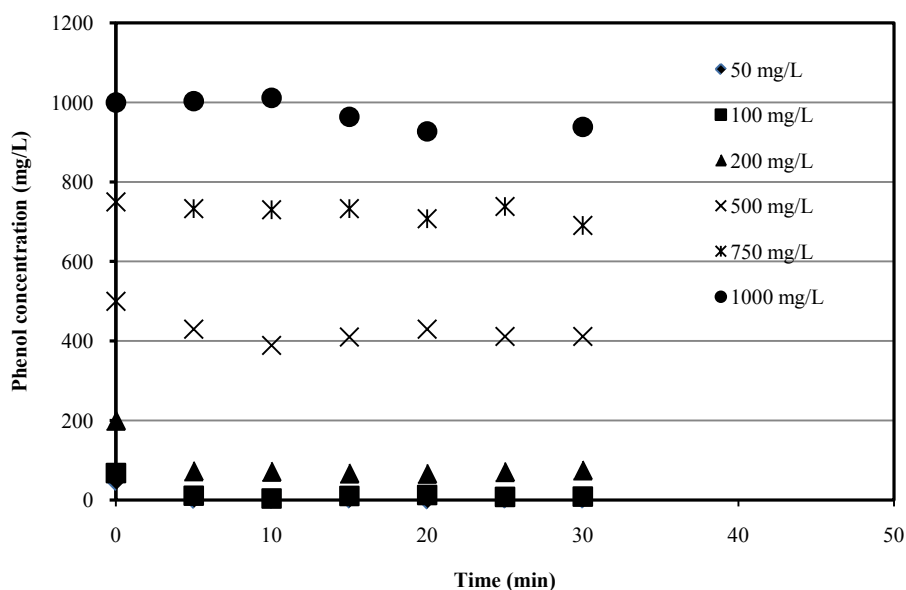


Figure 6. The change profile of initial phenol concentration with time on photo-fenton process

4. CONCLUSION

In this work, it was investigated the removal of phenol by photo-fenton process and effect of parameters such as H_2O_2 , $FeSO_4$ and initial phenol concentration on the removal efficiency. The photo-fenton experiments were performed by using photo reactor with the working volume of 2.5 L. At the end of reaction time of 15 minutes, phenol removal efficiency was obtained to be 56% when UV and H_2O_2 concentration of 0.4 mL/L were used. The effect of $FeSO_4$ concentration was investigated at pH 3, initial phenol concentration of 100 mg/L and H_2O_2 concentration of 0.4 mL/L by using $FeSO_4$ concentration varying in the range of 10-50 mg/L. At the end of reaction time of 30 minutes, the maximum phenol removal efficiency was determined as 87% at $FeSO_4$ concentration of 50 mg/L. Then, on the optimum conditions, experiments at different initial phenol concentrations was performed. Phenol removal decreased from 93 to 6% with increasing the phenol

concentration from 50 to 1000 mg/L. Removal efficiency of COD at the initial phenol concentration of 50 mg/L were determined to be 76%. These results demonstrated that this process may be used for phenol removal.

REFERENCES

- [1]. H. Yamasaki, Y. Makihata, K. Fukunaga, "Efficient phenol removal of wastewater from phenolic resin plants using cross linked cyclodextrin particles", *J Chem Technol Biotechnol* 81,1271–1276, 2006.
 - [2]. R. Aravindhan, J. Raghava Rao, B. Unni Nair, "Application of a chemically modified green macro alga as a biosorbent for phenol removal", *Journal of Environmental Management* 90, 1877–1883, 2009.
 - [3]. E. Martin del Campo, R. Romero, G. Roa, E. Peralta-Reyes, J. Espino-Valencia, R. Natividad, "Photo-Fenton oxidation of phenolic compounds catalyzed by iron-PILC", *Fuel* 138 149–155, 2014.
 - [4]. V. Kavitha, K. Palanivelu, "The role of ferrous ion in Fenton and photo-Fenton processes for the degradation of phenol", *Chemosphere* 55, 1235–1243, 2004.
 - [5]. Y. Saatci, "Decolorization and Mineralization of Remazol Red F3B by Fenton and Photo-Fenton Processes", *J. Environ. Eng.*, 136, 1000-1005, 2010.
 - [6]. A.G. Trovó, T.F.S. Silva, Jr.O. Gomes, A.E.H. Machado, W.B. Neto, Jr. P.S. Muller, D.Danie, "Degradation of caffeine by photo-Fenton process: Optimization of treatment conditions using experimental design", *Chemosphere* 90, 170–175, 2013.
 - [7]. D.F. Snell, C.L. Hilton, *Encyclopedia of Industrial Chemical Analysis*, Interscience Publishers, A Division of John Wiley and Sons Inc., New York, 1968.
 - [8]. APHA, AWWA and WPCF, *Standard methods for the examination of water and wastewater*, 17.th Edition, Washington, D.C., 1989.
 - [9]. T. Maezono, M. Tokumura, M. Sekine, Y. Kawase, "Hydroxyl radical concentration profile in photo-Fenton oxidation process: Generation and consumption of hydroxyl radicals during the discoloration of azo-dye Orange II", *Chemosphere* 82, 1422–1430, 2011.
 - [10]. E.E. Ebrahiem, M.N. Al-Maghrabi, A.R. Mobarki, "Removal of organic pollutants from industrial wastewater by applying photo-Fenton oxidation technology", *Arabian Journal of Chemistry*, article in press, 2013.
 - [11]. A. Babuponnusami, K. Muthukumar, "Advanced oxidation of phenol: A comparison between Fenton, electro-Fenton, sono-electro-Fenton and photo-electro-Fenton processes", *Chemical Engineering Journal* 183, 1–9, 2012.
 - [12]. Y. Samet, E. Hmani, R. Abdelhédi, "Fenton and solar photo-Fenton processes for the removal of chlorpyrifos insecticide in wastewater", *Water SA*, Vol. 38 No. 4, 537-542, 2012.
-

EVALUATION OF TANK CONTAINER LOGISTICS IN TURKEY

Olgay OKŞAŞ

Istanbul University, Department of Maritime Transportation Management Engineering, 34320, Avcilar, Istanbul, Turkey.
olgay.oksas@istanbul.edu.tr

Gökhan KARA

Istanbul University, Department of Maritime Transportation Management Engineering, 34320, Avcilar, Istanbul, Turkey.
karagok@istanbul.edu.tr

Abstract

Container transportation which allows a more efficient delivery of cargoes has an important share in the maritime transport. One of the special area of container transportation is tank container logistics which is used in the transport of liquid and gas cargoes. Tank containers are included for use to carry liquids and gases more economical, faster, safer and environmentally friendly and has found its place in the transportation of many liquid cargoes, primarily in chemical industry. In Turkey, it is obvious that tank container demand will increase and tank container logistics will become more important due to the growth of manufacturing sector in recent years. In this study, it is examined the advantages/disadvantages and important factors of tank container logistics, global status of tank container transportation and the share of Turkey in this market.

Keywords: *chemicals transportation, container logistics, tank container.*

1. INTRODUCTION

Chemical industry has an important role in global trade which world chemicals sales in 2013 are valued at €3,156 billion [1]. Container transportation has also an increasing trend year by year. Containerization makes transportation faster, easier, safer and allows door to door transfer. In this respect, container transportation meets the requirements of chemical industry especially for door to door service and relatively small cargoes which are not appropriate to load full tanker vessels. There are different ways to carry chemicals in containers such as drums, flexitanks, etc., but safety, reliability and economy are major advantages of tank containers [3]. In this study, the unique part of container transportation which is tank container is evaluated in different perspectives and the situation in Turkey is examined.

2. TANK CONTAINER LOGISTICS

Chemicals are almost in every manufactured product which is used in daily life. Transportation of either raw materials or final products of chemicals might be in big amounts by tanker vessels, or less by parcel tanker or in containers.

Containerization refers to the method of distributing materials in a unitized form. The most common “dry” containers are 20 x 8.5 x 8 ft [designated as 20 feet equivalent unit (TEU)] and 40 x 8.5 x 8 ft [40 feet equivalent units (FEU)] boxes. These containers can be seamlessly loaded onto ships, trucks, or rail using appropriate handling machinery [6]. The ability of easy handling of containers provides opportunity to arrange door to door shipments.

In order to load chemicals into dry containers, it's needed to use an additional loading equipment like drums or flexitanks. But a tank container is a special equipment which is simply a cylindrical tank set inside a frame of the standard dry container so that the machinery used for the dry containers can also handle the entire apparatus [6]. In the meantime, it allows to transport gas or liquid chemicals up to 35 m³ in one unit from the origin to the final destination without unloading chemical cargo on the way.



Figure 1. Tank container

Tank containers come in different sizes. Broadly, there are two major designs known as full-frame tank and beam-design tank. A standard tank container (TEU) can carry around 6300 gallons or 24 m³. Another type of design, known as through-frame swap body tank that meets the ISO length requirements, is wider or higher, which allows higher volumes (27–35 m³). The different types of tank containers are classified according to the type of chemical being transported. Tank containers move a range of chemicals from food products such as palm oil, beer, and tomato concentrate, to liquefied gases such as refrigerants [6].

Some of the advantages of tank containers for transport of liquid chemicals are [2]:

- They are environment-friendly, since they are less prone to spillage during filling and unloading, as well as leakage during transportation.
 - They permit a higher payload when compared to drums stowed in dry containers (43% more volume).
 - They can be handled mechanically, which results in cost savings, but also ensures safety when handling hazardous commodities.
-

- They provide secure door-to-door multi-modal transportation (by road, rail, sea or inland waterways), and do not require specialized port-side infrastructure.
- They are safe and durable, with a design life of 20–30 years.
- They can be cleaned and placed into alternate commodity service with minimum downtime.
- They can be used as temporary storage for customers with limited space or high-cost permanent storage.

In a typical tank container operation, to serve a standard customer order, a tank container operator would provide a tank (or multiple tanks) at the customer’s origin plant and arrange transportation for the tank across multiple modes to the destination plant. Transportation usually includes a truck leg at origin and destination and a steamship leg between a port near the origin to another port close to the destination. It may also include rail or barge legs at each end. Operators use depots for temporary storage, cleaning, and repair of empty containers [2].

A major challenge that the companies using tank containers face arises from the imbalance of product supply and demand, and thus an imbalance in the container flows across different regions. There are major flows of loaded containers from the production centers toward the various demand centers globally. However, equivalent flows of products from the demand centers, which can enable the return of the emptied containers to the production centers, often do not exist. As a result, empty containers accumulate at the demand centers, which must be “repositioned” to the production centers [6].

Another challenge in tank container logistics is to clean inside of the tank when a different type of commodity is needed to be transported in the same tank. This operation is usually given by depots where tank containers are stocked and must be arranged by experts as per regulations of chemicals.

3. TANK CONTAINER LOGISTICS IN THE WORLD AND IN TURKEY

As per International Tank Container Organization (ITCO)’s annual surveys, global tank fleet is shown in Table 1 for the years of 2013,2014 and 2015 with an increasing trend of total number.

Table 1. Global tank container per year [3]

	2013	2014	2015
Operators	116	176	192
Owned	140460	161300	194160
Leased	88000	103250	111540
Total	228460	265550	305700
Lessors	27	34	33
Idle	15000	17650	23400
Leasedtooperators	88000	103250	111540
Leasedtoshippers&others	47400	55600	60060
Total	150400	176500	195000
ShipperandOthers			
Owned	47400	55600	60060
Leased	47400	55600	60060
Total	94800	111200	120120
Estimatedmanufacture	39700	42620	48200
Disposals	0	-1000	-5000
EstimatedGrandTotal	338260	394400	444220

According to the table it’s needed to clarify some descriptions; Tank Operators are third party logistics companies that provide a door-to-door service to shippers and others that require transport of bulk liquids, powders or gases; Tank Lessors are companies that provide tank containers to operators, shippers and others, usually on a contractual term basis, where the lessee takes quiet possession and operates that tank as if it were owned; Shipper fleet (also referred to as producers or consignees), comprises tanks operated by chemical or food and drinks companies, whereas there is a major trend for shippers to outsource tank logistics to tank operators, there remains a significant fleet of tanks directly controlled by shippers [3].

The grow of grand total in 2014 is %16,5 compared with 2013 and it is %12,5 from 2014 to 2015. There is a considerable amount of new tank containers added to market each year.

Table 2 shows top 5 tank operators and their fleet as of April 2015. First three operators are mostly same in previous years as well. Another common point of top 5 operators is all of them are headquartered in Europe.

Table 2. Top 5 tank operators and fleet of tank containers as of April 2015 [3]

Operators \ Years	2015
Stolt Tank Containers	32000
HoyerGroup	29110
Bulkhaul Ltd.	20500
Newport	15000
BertschiGroup	13000

It's obvious to see the global growth of tank container industry in figure 2, which shows all parties (operators, lessors, shippers/others, manufacturers). Even there is a small decrease in shippers/others column in 2015, general trend is industry is growing steadily.

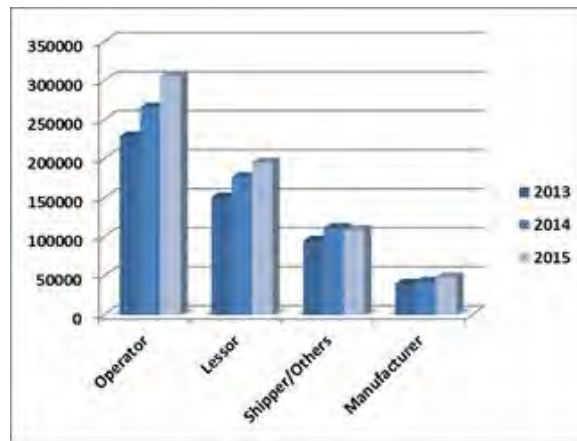


Figure 2. Global industry growth of tank container [3]

There are four tank operators which is headquarter in Turkey with the total of 880 tank containers. However, almost all big global operators has their local offices or agencies in Turkey especially in Istanbul and Kocaeli region. Also leasing companies are giving services to customers in Turkey. This means there is a competitive market in supply of tank container and this market is still growing with all parties.

Table 3. Top 5 tank operators and fleet of tank containers as of April 2015 [3]

Operators \ Years	2013	2014	2015
Bati Shipping&Trading	80	80	80
Ekol Logistics	100	100	100
GokbilTransportation	-	600	600
TLS Global Logistics	100	100	100

Tank container industry is a global industry. Positioning of tank containers has an important issue due to the importance of tank container supply when needed and most of operators stock their containers at transshipment ports or their hub centers where are easy to transfer to loading destinations.

4. CONCLUSIONS

Chemical industry and tank container fleet are growing day by day. According to statistical explanations in previous sections there are four tank operators which is headquarters in Turkey with the total of 880 tank containers but this doesn't mean that there are 880 tank containers in Turkey. As the positioning of tank containers is the most important point in tank container logistics, Turkey has a crucial location between Asia and Europe, and by using this geographical advantage Turkey might be an important hub point and can be more effective in this market. On the other hand manufacturing of tank containers is mostly materialized by China with almost %50 of the total manufacture. This market can also be an opportunity for Turkish investors. Numbers of tank containers might be very small when compared with dry containers but as they are very special equipments and needs necessary concern, this specialized area requires experts in either white or blue collar to improve logistics of tank containers locally and to be powerful globally.

REFERENCES

- [1]. *CeficChemdata International, Chemical Industry Profile, The European Chemical Industry Council*, 2014.
- [2]. Erera, A. L., Morales, J. C., & Savelsbergh, M., *Global intermodal tank container management for the chemical industry*, Transportation Research Part E: Logistics and Transportation Review, 41(6), 551-566, 2005.
- [3]. ITCO, *Tank Container Fleet Survey*, International Tank Container Organisation, 2015.
- [4]. ITCO, *Tank Container Fleet Survey*, International Tank Container Organisation, 2014.
- [5]. ITCO, *Tank Container Fleet Survey*, International Tank Container Organisation, 2013.
- [6]. Karimi, I. A., Sharafali, M., & Mahalingam, H., *Scheduling tank container movements for chemical logistics*, AIChE journal, 51(1), 178-197, 2005.
- [7]. UNECE, *Recommendations on the Transport of Dangerous Goods*, United Nations, New York and Geneva, 2009.

DETECTION OF THE WELD DAMAGES BY LAMB WAVE TECHNIQUE

Volkan Yusuf ŞENYÜREK

Istanbul University, Department of Maritime Transportation Management Engineering, 34320, Avcilar, Istanbul, Turkey.
olgay.oksas@istanbul.edu.tr

Mustafa DEMETGÜL

Istanbul University, Department of Maritime Transportation Management Engineering, 34320, Avcilar, Istanbul, Turkey.
karagok@istanbul.edu.tr

Hüseyin YÜCE

Istanbul University, Department of Maritime Transportation Management Engineering, 34320, Avcilar, Istanbul, Turkey.
karagok@istanbul.edu.tr

Abstract

Lamb waves are a type of ultrasonic waves has a wide range of applications in non-destructive testing. Most of the studies used simple and flat structures for breaking, cracking or corrosion damages. In this study, the detection of damage in the welding is examined. Two 4.5mm thickness AL2024 plates joined by overlay welding method. Damage was applied to the welded zone gradually. Three piezoelectric (PZT) discs were used to create surface waves and to monitor their propagation. For better examination, the envelopes of the monitored signals were calculated by using the Hilbert transform. Damages occurring in the welded zone, has led to reflections and attenuation in waves. The study indicated that degradation occurring in the weld can be identified with the Lamb wave technique.

Keywords: *Nondestructive testing, weld joining, Hilbert transform, Lamb wave.*

1. INTRODUCTION

Nondestructive testing is an important area for structural health monitoring. It increases damage safety and it decreases cost and time consumption of monitoring systems. Most common NDT techniques are; Penetration test, magnetic particle test, Eddy current test, X-rays and ultrasound test [1-3].

Ultrasonic waves can be used to inspect surface and subsurface defects for many materials like metal, wood and composite. Ultrasonic method has better penetration depth than other techniques. Also this technique gives damage location information. But this technique needs more training and skill.

Lamb wave is a type of plane sound wave and it is commonly used in NDT. In traditional ultrasonic technique, all surface must be scan for large area. This process cause to waste of time and workload. But the lamb waves can be propagated long distance in metals. So it can be used for large and long structures. Additionally, lamb waves can detect damages in thin plates unlike traditional ultrasonic wave [4, 5].

There are many different signal analysis methods for health monitoring, like as artificial neural network [6], genetic algorithm [7, 8], wavelet transform [9], frequency response [10] and Hilbert transform [11]. In this study Lamb wave technique was examined for aluminum plates that joined by weld. Both symmetric and antisymmetric Lamb waves were tested for comparison of modes.

1.1. Lamb wave

In solids, sound waves can propagate in four different modes that are based on the way the particles motion. Sound can propagate as longitudinal waves, shear waves, surface waves, and in thin materials as plate waves. Lamb waves (known as guided plane wave) are a kind of ultrasonic waves. These waves are guided between two free surfaces. There are two types of lamb waves. These are symmetric and antisymmetric modes. Symmetrical modes are shown with S0, S1, S3, ... and antisymmetrical modes shown with A0, A1, A2, ... symbols. Symmetric waves analogous to axial waves while antisymmetric waves similar to flexural waves (fig. 1). Lamb waves are very dispersive and wave speed depends to the frequency and plate thickness [12, 13].

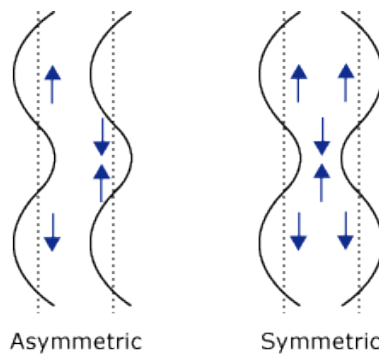


Figure 1. Representation of Lamb wave modes

1.2. Hilbert Transform

Hilbert Transform is used for to create analytic signal in signal processing. Analytic signal is the complex representation of a signal [14, 15]. Analytic signal $x_a(t)$ is obtained using real signal $x(t)$ as follows,

$$x_a(t) = x(t) + iH\{x(t)\} \quad (1)$$

Where, $H\{x(t)\}$ is Hilbert transform. An analytic signal is shown in polar form as,

$$x_a(t) = r e^{-i\theta} \quad (2)$$

Where r and θ are amplitude and phase of a analytical signal respectively. Signal amplitude corresponds to envelope of the signal. Hilbert transform of a $x(t)$ signal is defined as follow,

$$H\{x(t)\} = \frac{1}{\pi} \int_{-\infty}^{\infty} \frac{x(\tau)}{t-\tau} dt \quad (3)$$

This equation can be described in term of convolution theorem,

$$\frac{1}{\pi t} \quad H\{x(t)\} = x(t) * \quad (4)$$

2. EXPERIMENTAL WORKS

In this study two 250x500x4.5mm Al2024 plate are welded with overlay technique (fig. 2). Three piezoelectric sensors attached to the plate as shown figure 3. The diameter and thickness of the PZT disks were 12 mm and 0.2 mm, respectively. The experimental setup is presented in Figure 4. The arbitrary wave generator (AWG) (Agilent 33220A) was used to produce 6-cycles of sine wave. The sine wave was passed through the hamming window. The central frequencies of the generated signals were 60 kHz for A0 mode and 300 kHz for S0 mode in the experiments. The signal was applied to the S3 disc attached to the surface to generate Lamb waves. The generated Lamb waves propagated along the surface and generated electricity at the other PZT discs. The outputs of the PZTs were digitized by using a digital oscilloscope (Rigol 1104B) at 2.5 MHz sampling rate and transferred to PC. All the analysis was performed by using the MATLAB package.

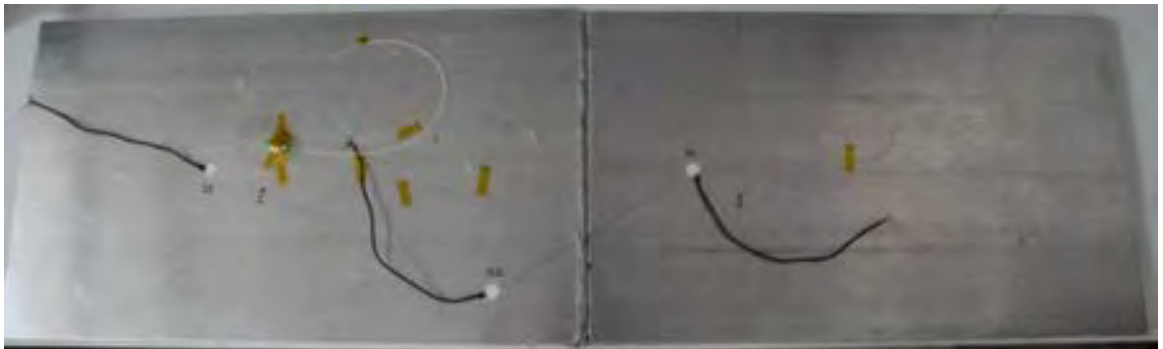


Figure 2. The welded Al2024 and sensors.

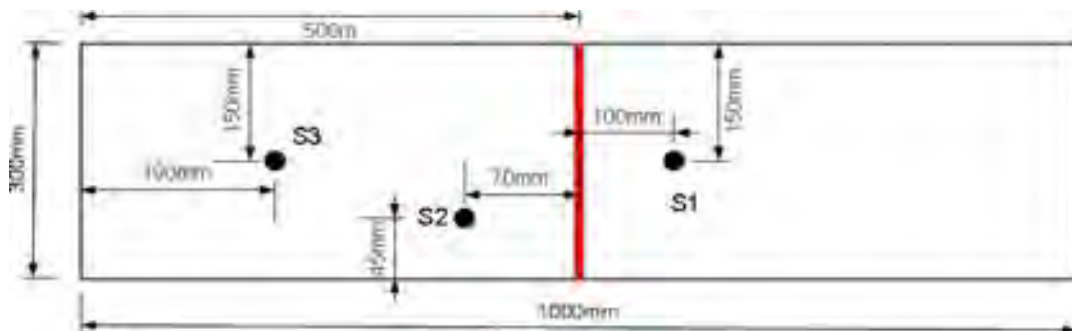


Figure 3. Layout of the sensors.

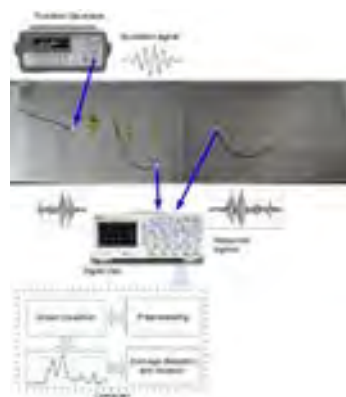


Figure 4. Experimental setup.

The damage was applied to the one side of welded zone as 2 mm width and 2.5 - 11 cm length (fig. 5). Damage scenario can be seen table 1.



Figure 5. Welded zone and damage that applied of it surface.

Table 1. Damages on welded zone.

Test Number	DamageLength (cm)	DamageWidth (mm)	SignalFrequency (KHz)
Test 1	---	---	60
Test 2	2.5	2	60
Test 3	5	2	60
Test 4	8	2	60
Test 5	11	2	60
Test 6	---	---	300
Test 7	2.5	2	300
Test 8	5	2	300
Test 9	8	2	300
Test 10	11	2	300

3. RESULTS AND DISCUSSION

If the excitation signal frequency is 60 KHz, Lamb wave propagate in A0 mode. Group velocity is 2000m/sec in this mode. The signal that send from S3, reaches to S1 in about 0.2msec. This duration called as time to flight (TOF). The first arriving signal amplitude has decreased with damage length. This is an expected result because of the sensor S1 is located after welded zone (fig. 6). Time - amplitude graphs are not convenient to distinguish damages. Hilbert transform has used to obtain of the envelope of signals (fig. 7).

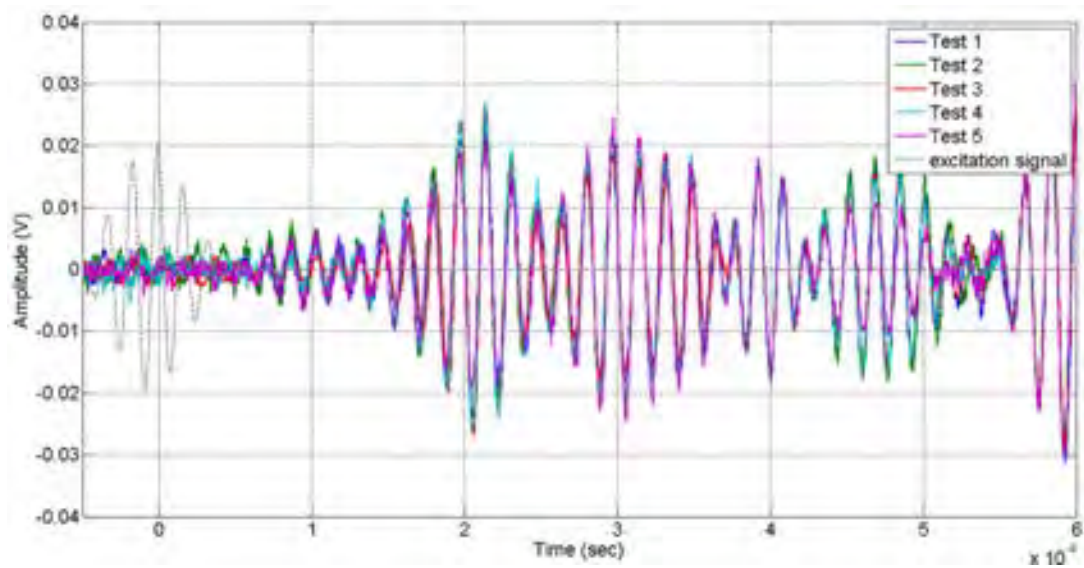


Figure 6. The signals from the sensor S1 when S3 sensor is excited in A0 mode.

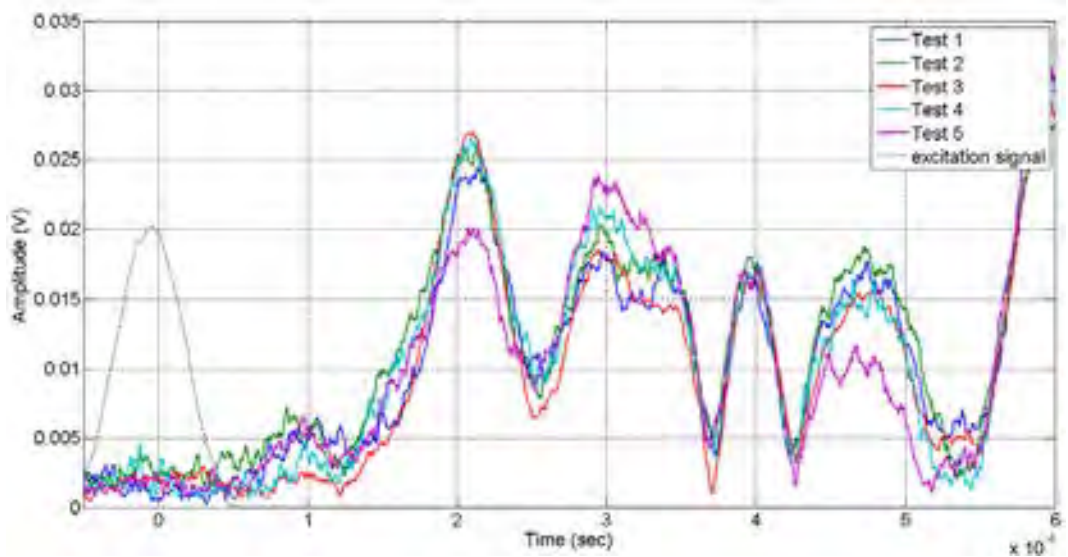


Figure 7. The envelope of the signal received from sensor S1 when sensor S3 is excited in A0 mode.

The envelopes of the signals that gathered from S2 are shown in figure 8. The graph shows that some signals reach to the sensor S2 after reflect from damage region.

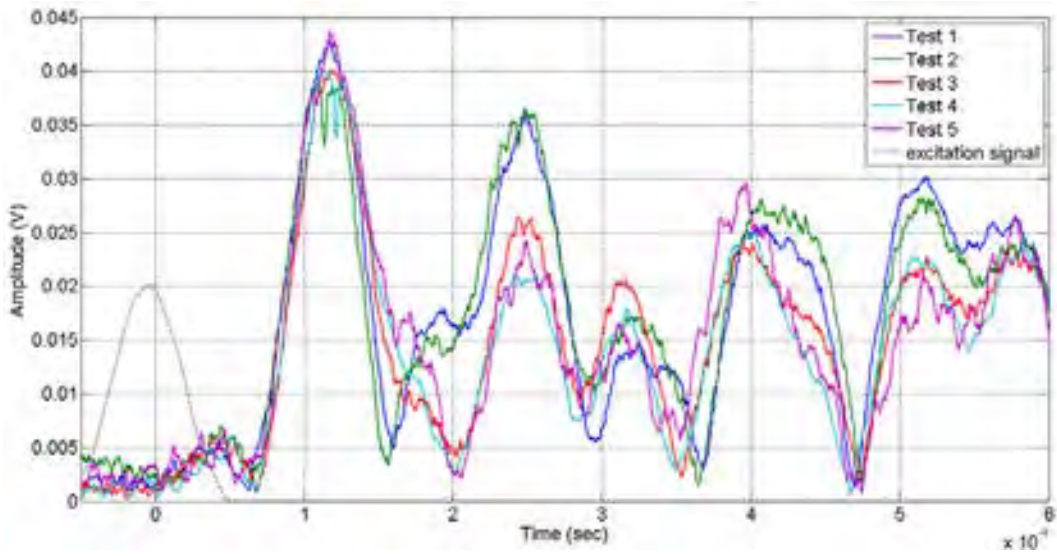


Figure 8. The envelope of the signal received from sensor S2 when sensor S3 excited in A0 mode.

When S3 is stimulated by 300 KHz frequency signal, A0 mode Lamb wave propagates in the plate. Group velocity is 2000m/sec in this mode. First signals arrives to the sensor S1 in 0.1msec. An important variation hasn't seen on first arrived signals with the damage length (fig. 9).

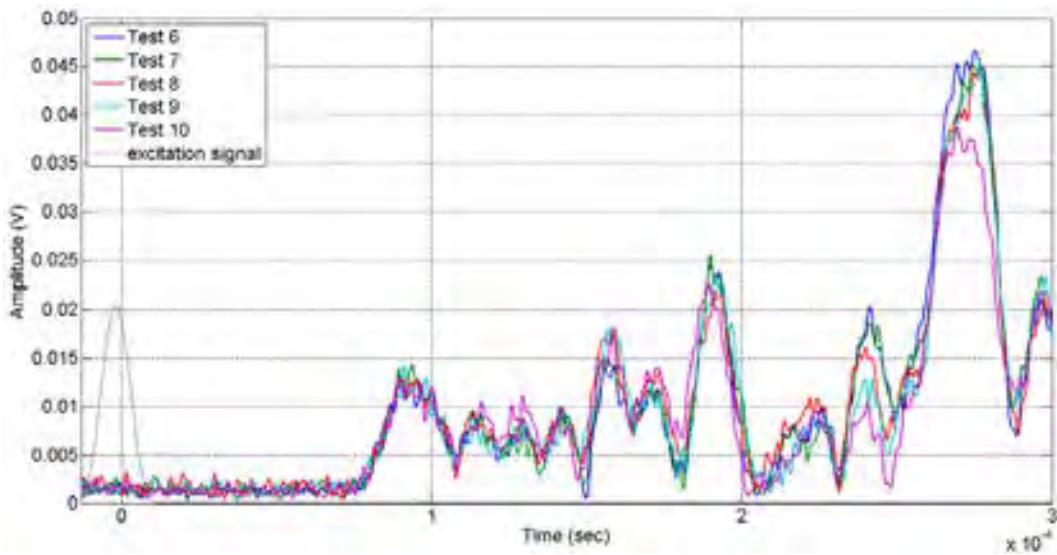


Figure 9. The envelope of the signal received from sensor S1 when sensor S3 excited in S0 mode.

Figure 10 shows the envelope of the signals that gathered from sensor S2. When the figure is examined, it can be seen that the signal amplitude increased with the damage length at 0.1 msec. This result shows that the Lamb waves reflect from damage zone.

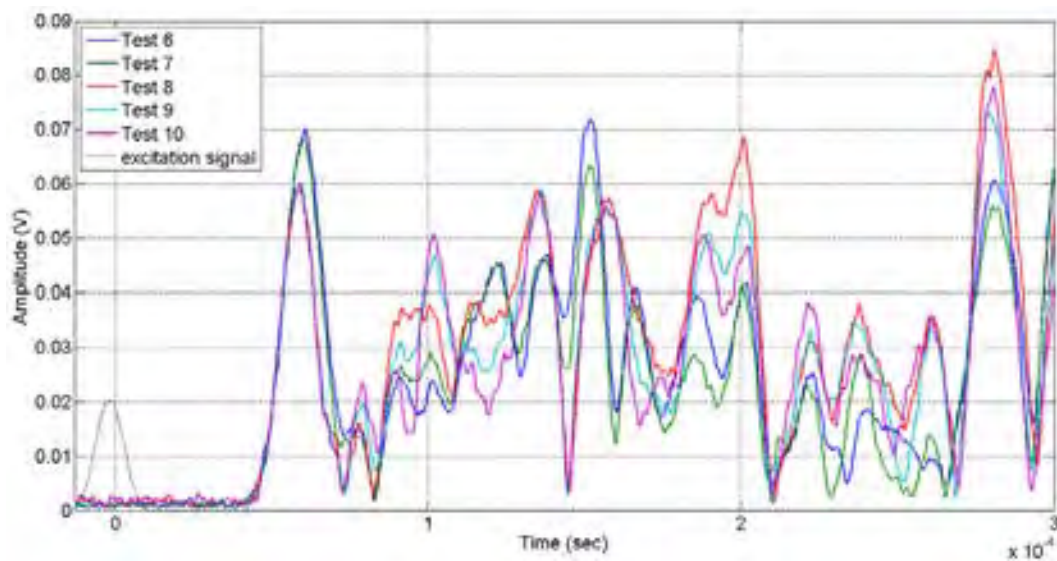


Figure 10. The envelope of the signal received from sensor S2 when sensor S3 excited in S0 mode.

4. CONCLUSIONS

In this study, weld damages were determined by using Lamb wave technique for aluminum plates. The two different Lamb wave modes S0 and A0 were compared. Welded zone decreased the amplitude of the signals in both modes. But the attenuation of S0 is higher than A0. This is because the wavelength of S0 mode is shorter. Wavelengths were calculated 17mm and 33mm for symmetrical and antisymmetrical waves respectively. This result shows that the antisymmetrical mode is more suitable for the detection of weld damage. However, if the sensor was located before the damaged zone, symmetrical waves were better than others.

ACKNOWLEDGMENT

This work was supported by the Turkish National Science Foundation under Grant 110M236.

REFERENCES

- [1]. Kobayashi, M., Wu, K. T., Song, L., Jen, C. K., Mrad, N. *Structural health monitoring of composites using integrated and flexible piezoelectric ultrasonic transducers*. Journal of Intelligent Material Systems and Structures, 2009, 20(2), 969-977
- [2]. Ness, S., Sherlock, C. N., Moore, P. O., McIntire, P. *Nondestructive testing overview*. (Vol. 10). American Society for Nondestructive Testing. Columbus (Ohio). 1996.
- [3]. Korla, S., Leon, R. A., Tansel, I. N., Yenilmez, A., Yapici, A., Demetgul, M. *Design and testing of an efficient and compact piezoelectric energy harvester*. Microelectronics Journal, 2011, 42(2), 265-270.
- [4]. Senyurek, V. Y. *Detection of cuts and impact damage at the aircraft wing slat by using Lamb wave method*. Measurement, 2015, 67, 10-23.
- [5]. Cawley, P., Alleyne, D. (1996). *The use of Lamb waves for the long range inspection of large structures*. Ultrasonics, 34(2), 287-290.
- [6]. Katsikeros, C. E., Labeas, G. N. *Development and validation of a strain-based structural health monitoring system*. Mechanical Systems and Signal Processing, 2009, 23(2), 372-383.
- [7]. Acciani, G., Brunetti, G., Fornarelli, G., Giaquinto, A. *Angular and axial evaluation of superficial defects on non-accessible pipes by wavelet transform and neural network-based classification*. Ultrasonics, 2010, 50(1), 13-25.
- [8]. Su, Z., Ye, L., Bu, X. *A damage identification technique for CF/EP composite laminates using distributed piezoelectric transducers*. Composite structures, 2002, 57(1), 465-471.
- [9]. Grabowska, J., Palacz, M., Krawczuk, M. *Damage identification by wavelet analysis*. Mechanical systems and signal processing, 2008, 22(7), 1623-1635.
- [10]. Kim, Y. H., Kim, D. H., Han, J. H., Kim, C. G. *Damage assessment in layered composites using spectral analysis and Lamb wave*. Composites Part B: Engineering, 2007, 38(7), 800-809.
- [11]. Lu, Y., Ye, L., Su, Z., & Yang, C. *Quantitative assessment of through-thickness crack size based on Lamb wave scattering in aluminum plates*. Ndt & E International, 2008, 41(1), 59-68.
- [12]. Giurgiutiu, V. *Structural health monitoring: with piezoelectric wafer active sensors*, Academic Press. 2007.

- [13]. Auld, B. A. Acoustic fields and waves in solids. Vol. 2, Wiley-Interscience, Chichester, Sussex, UK. 1993.
- [14]. Huang, N. E., Shen, S. S. (2005). *Hilbert-Huang transform and its applications*, Vol. 5, World Scientific.
- [15]. Quek, S. T., Tua, P. S., Wang, Q. *Detecting anomalies in beams and plate based on the Hilbert-Huang transform of real signals*. Smart materials and structures, 2003, 12(3), 447-460.

INVESTIGATION OF PRACTICAL DESIGN APPROACH FOR CIRCULAR STEEL BASE PLATES

Mutlu SEÇER

Dokuz Eylül University, Engineering Faculty, Department of Civil Engineering, 35160, Buca/Izmir, Turkey.
mutlu.secer@deu.edu.tr

Abstract

Circular steel base plates are commonly used for pipe and polygonal columns, such as wind turbine towers, lighting and advertisement poles. Although the explicit solutions based on various methods for rectangular base plates can be found in many design manuals and books, very limited studies exist for the design of circular base plates under different loading conditions. These types of connections are used in structures to resist gravity loads and function as part of lateral-load-resisting systems. Also, circular base plates and anchor bolts are the critical interface between the steel structures and the reinforced concrete foundations. Besides, these connections are often the final structural steel items to be designed but are the first items required on the work site. Consequently, structural design of circular base plates and assembly details are essential for the steel constructions. In this study, practical design approach for the design of circular steel base plates is presented accounting linear stress distribution assumption for compressive bearing area and a design example is given to show the implementation of this approach. Anchor bolt diameter, base plate dimensions and base plate thickness are determined for obtaining safe and cost-effective steel structure.

Keywords: *Base plate, anchor bolt, steel tower*

1. INTRODUCTION

Base plates are generally used to transfer steel column reactions to reinforced concrete foundations. Steel base plates are designed in rectangular or circular forms according to the column section geometry and structural load pattern. Rectangular base plates are frequently favored for I or box sections and circular base plates are typically preferred with pipe or round sections. Circular base plates are used in wind turbine towers, lighting and advertisement poles which are generally formed with one steel pipe or polygonal column. Since these types of structures are designed against severe wind and earthquake loads, they are also under high eccentricity.

In this study, circular base plates under high eccentricity are focused and a practical design approach is presented accounting linear stress distribution assumption for compressive bearing area. A design example is given to show the design phases. Anchor bolt diameter, base plate dimensions and base plate thickness are determined.

2. PRACTICAL DESIGN APPROACH FOR CIRCULAR BASE PLATES

Circular steel base plates under high eccentric loads are investigated with using a practical approach. Circular base plate is studied accounting elastic behavior and the maximum bearing stress is selected to be lower than the allowable value. Also, there are some other assumptions made for giving a practical approach. Compressive bearing stress is accounted as less than the half of the base plate and the resultant compressive bearing stress is located at center of gravity of the compressive bearing area. Anchor bolts in the half of the circular base plate are considered in tension from conservative perspective. The critical section used to determine the base plate thickness is calculated accounting the outside dimension of the round columns since stiffeners are used [1, 2].

Plan and section of a typical circular column and circular base plate under high eccentric loads is given in Figure 1.

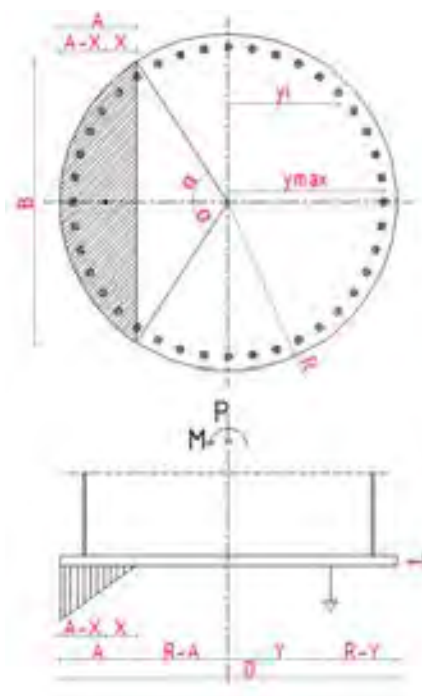


Figure 1. Circular base plate

In order to determine anchor bolt force and the geometry of the compression area, two equilibrium equations are written. In equation (1) compressive bearing stress and tension load relationship is given. In equation (2) sum of moments about the resultant bolt force is presented.

$$P + T = p_{max} \frac{X}{A} F_{comp} \quad (1)$$

$$P(e + Y) = p_{max} \frac{X}{A} F_{comp} [R - A + X + Y] \quad (2)$$

where; e is eccentricity which is ratio of moment divided by the axial force, R is radius of circular base plate, A is the length of the part of the base plate area under compression, Y is distance between center of gravity of the anchor bolt forces, F_{comp} is the part of the base plate area under compression. X is the distance from center of gravity of compressive stress bearing area to the zero stress section. p_{max} is allowable bearing stress and T is the sum of the anchor bolt forces in the half of the circle. P is the axial force acting on base plate center.

Since strain distribution is linear and sum of the anchor bolt forces in the half of the circle can be determined by using equilibrium equations, maximum anchor bolt force at outermost anchor bolt can be determined as equation (3).

$$T_{1,max} = \frac{T}{(1 + \frac{2}{y_1} \sum_{n=2}^n y_i)} \quad (3)$$

Equation (1) and equation (2) can't be solved explicitly; iteration process is used to investigate the unknowns. In the beginning, maximum allowable stress is determined using equations based on AISC approach as given in equation (4) [1].

$$p_{max} = 0.35 f_c \sqrt{\frac{A_2}{A_1}} \leq 0.7 f_c \quad (4)$$

where; p_{max} is maximum allowable bearing stress, f_c is concrete compression strength, A_1 and A_2 are plate and concrete areas.

On the first step a trial base plate size is selected and number of bolts accounting layout in the circular base plate is determined. Diameter of bolts is also decided on this step. In this manner, the center of bolts which is termed as Y is calculated accordingly. Afterwards compressive bearing area is calculated using equation (5) which is mainly based on AISC approach [1].

$$F_{comp} = 0.0174532 R^2 \alpha - R(R - A) \sin \alpha \quad (5)$$

where, α is the angle and also determined with equation (6).

$$\alpha = \arccos\left(\frac{R-A}{R}\right) \quad (6)$$

Center of gravity of the compression area can be calculated with using equation (7) and equation (8) with respect to the value of the angle α :

$$X = R \left[\frac{2 \sin^3 \alpha}{(3 \alpha - 1.5 \sin 2\alpha)} - \cos \alpha \right] \quad (\alpha \geq \frac{\pi}{4}) \quad (7)$$

$$X = 0.2 R \alpha^2 (1 - 0.0619 \alpha^2 + 0.0027 \alpha^4) \quad (\alpha < \frac{\pi}{4}) \quad (8)$$

After all unknowns of these equations are determined, equation (2) is controlled for the trial value. If the left and right sides of the equation (2) is not close enough, then a new trial value for Y should be selected. If two sides of the equation (2) are close enough, then the resultant bolt force can be determined from equation (1) and $T_{1,max}$ can be calculated using equation (3). The maximum force on outermost bolt T_{max} can be controlled using allowable anchor bolt load. If the value exceeds the allowable load limit, then bolt diameter or number of bolts can be increased. Likewise, base plate thickness can be determined using equation (9).

$$t_p = \sqrt{\frac{8M}{F_y}} \quad (9)$$

where; M is the moment for a 1 mm wide strip at the critical section and F_y is the yield stress of base plate steel material.

Main parameters of a circular base plate can be practically determined following the equations given above. This trial-and-error iteration approach gives opportunity to select the dimensions of the base plate, diameter and number of anchor bolts practically.

3. NUMERICAL EXAMPLE

Circular base plate for an advertisement pole is calculated according to the approach given in this study. Advertisement pole structure is presented with Figure 2. Column length is 20 m and façade area is 100 m². A circular base plate under high eccentric load is assumed and practical design approach is applied on control of the selected geometric properties of the base plate. Circular base plate used under advertisement pole column geometry is also given in Figure 3.



Figure 2. Advertisement pole

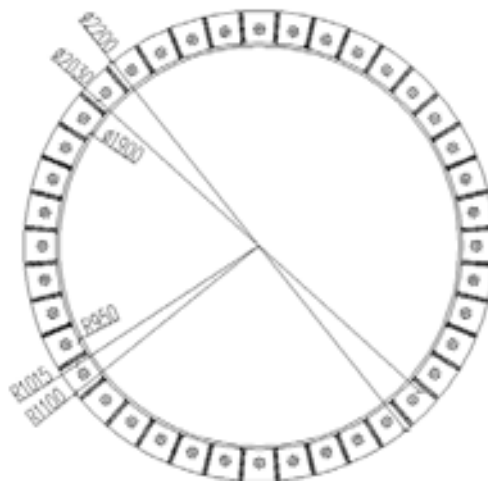


Figure 3. Circular base plate with anchor bolts

Circular base plate of the advertisement pole is designed under axial load of 326 kN and moment of 4 711 kN-m. The pole column is pipe section and the outside diameter of pipe is 1900 mm. Outside diameter of the circular base plate is 2200 mm and the thickness is 60 mm. The ratio of the concrete area on the top of the foundation to steel base plate area is 2/3. The allowable stress for the anchor bolts and the base plate are 112 MPa and 235 MPa, respectively. There are 40 bolts with the bolt diameter of 42 mm. The concrete compressive strength is assumed as 30 MPa. Allowable stress design approach for steel circular base plate is used and results are presented.

On the first step, the maximum design bearing stress is calculated as 12.86 MPa using equation (4). Since this value is below 21 MPa, bearing stress control is satisfied. As, there are 40 bolts and their diameter is 42 mm, center of gravity for anchor bolts is 668 mm.

Also, for a trial value length of the part of the base plate area under compression is selected as 499 mm. After following equations (5) and (6), compressive bearing area is calculated as 6481 cm² and α is determined as 56.9°. Since angle α is higher than $\pi/4$, equation (7) is used for calculating the center of gravity of the compression area. After all unknowns for the trial step are determined, equation (2) is controlled. Since, both sides of the equation (2) are almost the same, no further iteration is required. Accordingly, maximum anchor bolt force at outermost anchor bolt is calculated using equation (3) as 237.5 kN. The maximum anchor bolt

force is smaller than the allowable anchor force 281.2 kN. This shows that number and the diameter of the selected anchor bolts are enough in terms of anchor bolt force calculations. Likewise, base plate thickness is controlled using equation (9). The critical section is selected equal to the diameter of the column since stiffeners are provided and the base plate thickness is calculated as 52.4 mm. As base plate thickness is 60 mm, the thickness of the base plate is adequate.

4. CONCLUSIONS

In this study, a practical approach is presented for design of circular base plates that are commonly used for pipe or polygonal columns. Circular base plates are frequently used in wind turbine towers, lighting and advertisement poles. These types of circular base plates are designed to withstand loads that introduce high eccentricity such as wind and earthquake loads. Relationship between anchor bolt forces and base plate bearing stress is given and calculation steps are derived containing an iteration process. A numerical example is performed using practical procedure given with the calculation equations. Base plate dimension, base plate thickness, anchor bolt number and diameter are controlled.

REFERENCES

- [1]. American Institute of Steel Construction (AISC). Manual of steel construction, ASD, 9th Ed., Chicago, 1989.
- [2]. American Institute of Steel Construction (AISC). Column base plates, Chicago, 2003.

PRODUCTION OF ALUMIX 13 BASED METAL FOAMS USING POWDER METALLURGY

Halil KARAKOÇ

Hacettepe University, Ankara Chamber of Industry 1st Organized Industrial Zone Vocational School, 06935, Ankara, Turkey. halil.karakoc@hacettepe.edu.tr

Hanifi ÇINICI

Gazi University, Faculty of Technology, Department of Metallurgy and Materials Engineering, 06500, Ankara, Turkey
hcinici@gazi.edu.tr

Ramazan ÇITAK

Gazi University, Faculty of Technology, Department of Metallurgy and Materials Engineering, 06500, Ankara, Turkey
citak@gazi.edu.tr

Abstract

Metal foam using Alumix 13 was produced through powder metallurgy. Alumix 13 premix powder and 1% TiH₂ powder were mixed for 30 minutes using a three dimensional mixer. The mixture was then compacted using cold pressing with the application of 300 MPa of pressure, resulting in compacted block samples. The samples were sintered at a temperature of 500 °C for 45 minutes and then were extruded at the same temperature. Extruded product was rolled at 500 °C at thickness of 6 mm. The rolled product was cut into square bars. These were then foamed at varying temperatures (720 °C, 730 °C, 740 °C and 750 °C). The effects of foaming temperature on density, linear expansion and cell morphology were investigated.

Keywords: Alumix13, metallic foams, powder metallurgy

1. INTRODUCTION

Along with advances in technology, current engineering applications call for materials that bring together varying structural and functional properties. The use of metal foams have made inroads for use in such applications that require specific mechanical properties. Low density, high strength, and the ability to absorb vibration, sound and impact, are some of the distinguishing features of metal foams compared to other engineering materials [1-3]. Due to its functional properties, metal foam is used in the automotive industry, rail transport, aerospace, marine and military applications; it also has industrial uses including sandwich-structured composites, panels, impact energy absorbers, and heat exchangers [4]. Metal foam is manufactured using a number of different methods. One method that has been gaining increasing acceptance is the powder metallurgy (PM) method. The PM method incorporates a wide range of ways in which metal powders are processed to produce materials and components [5, 6]. In this study, metal foam was fabricated using Alumix 13 premix powder at four different temperatures (720 °C, 730 °C, 740 °C and 750 °C); the effects of foaming temperature on density, linear expansion and cell morphology were investigated.

2. EXPERIMENTAL

2.1. Materials and Methods

For the study, TiH₂ (foaming agent) was used as a precursor along with Alumix 13 powder (composition: 0.40%-0.60% Mg, 4.2%-4.8% Cu, 0.05%-0.25% Si, balance Al). To obtain a homogeneous mixture, these two powders were mixed for 30 minutes using a Turbula brand three dimensional mixer, in the ratio presented in Table 1. Using a 280 ton capacity hydraulic press, the mixed powders were cold pressed in a 60 mm diameter steel mold by applying a pressure of 300 MPa. The pressed block samples were sintered for 45 minutes at a temperature of 500 °C and then extruded at the same temperature. They were then rolled at 500 °C and shaped into preformed samples with thickness of 6 mm. These were cut into square bars (dimensions: 27mm by 27mm by 6mm) in preparation for use in foaming. The foaming process was accomplished in a steel vessel with a base of 27x27 mm² where, due to the exact fit with the preformed samples (extruded bars), the growth of the foam occurred in unidirectional expansion (upwards). The foaming process was carried out for 10 minutes, under four different temperatures (720 °C, 730 °C, 740 °C and 750 °C).

Table 1. Powder particle sizes and percentages by weight

Powder	Powder Particle Size	% by weight
Alumix 13	< 45 μm	99
TiH ₂	< 45 μm	1

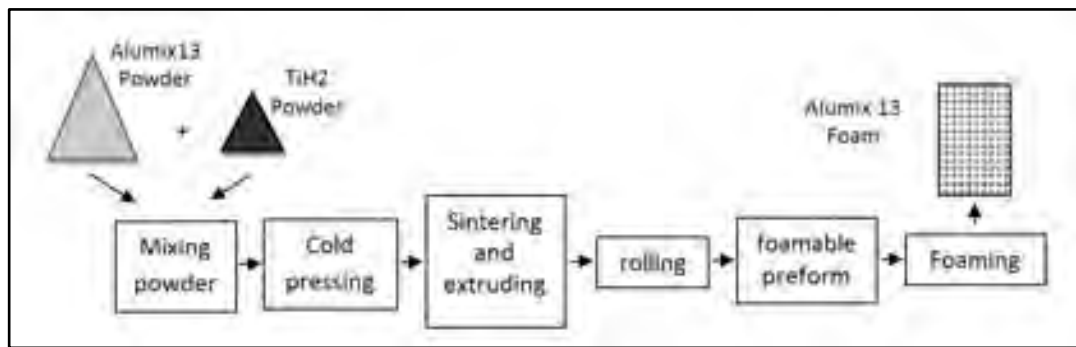


Figure 1. Process order for powder metallurgy used for obtaining preformed foamable samples

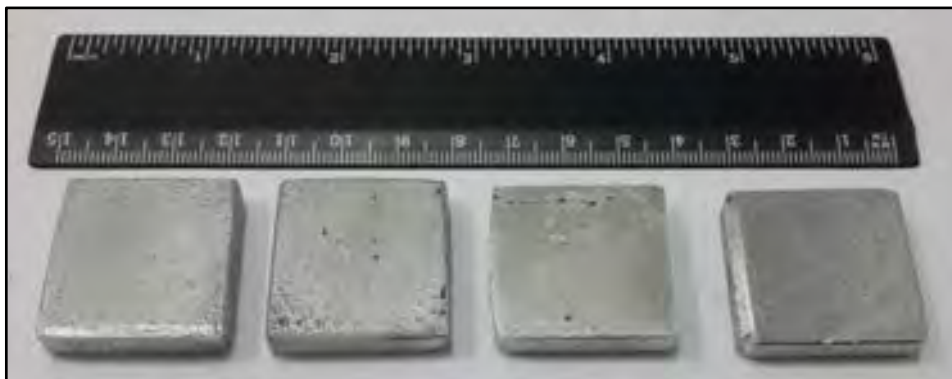


Figure 2. Preformed foamable samples (dimensions: 27mm x 27mm x 6mm) fabricated from Alumix 13

3. RESULTS AND DISCUSSION

A relative density of better than 99% was achieved for the preformed foamable samples fabricated using the Alumix 13 powder mix, which is interpreted as a significant accomplishment as it has direct affect on the density and foamability of the final foam product. Any residue left within the structure, as well as other process defects, may have negative effects on the process. As low-density foamable material has abundance of pores, it is possible to come across, following the foaming phase, non-homogeneous pore structures. Young and Kang (2004) have demonstrated that foams with uniform structures having less than 1% porosity may be obtained using the 6061 aluminum alloy [7]. Similarly, Paulin et al. have emphasized in their study that a relative density of 98% is the minimum required amount for obtaining successful results for foamability [8].

The linear expansion rates achieved for foamable preformed samples foamed for 10 minutes within a steel mold under varying temperatures are presented in Figure 3. Analysis of the graph indicates that as the foaming temperature increases, the percent linear expansion rate also increases. The highest linear expansion rate was achieved as 600% at temperature 750 oC while the lowest linear expansion rate was achieved as 183% at temperature 720 oC. In parallel to linear expansion rates, the densities of the samples were observed to change as well. Foam densities decreased as expansion rate increased (Figure 4).

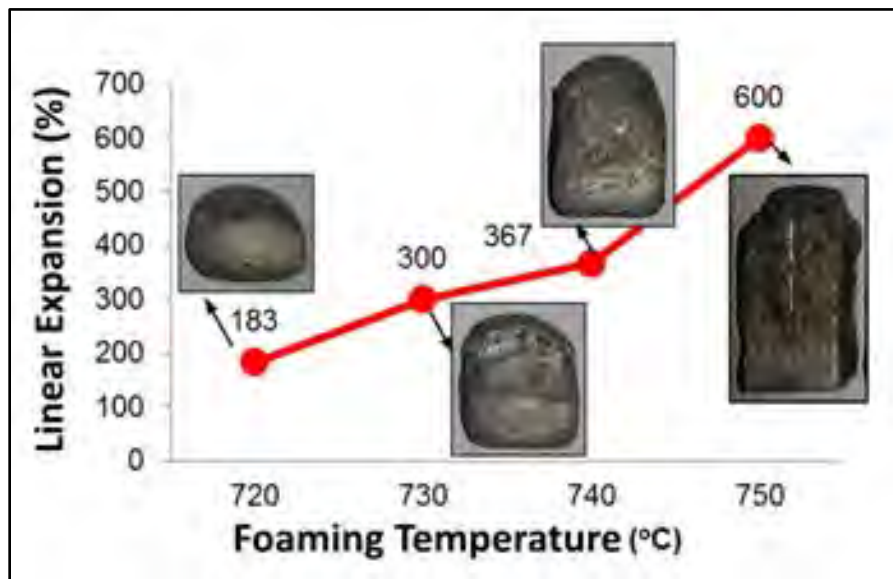


Figure 3. Effects of foaming temperature on linear expansion

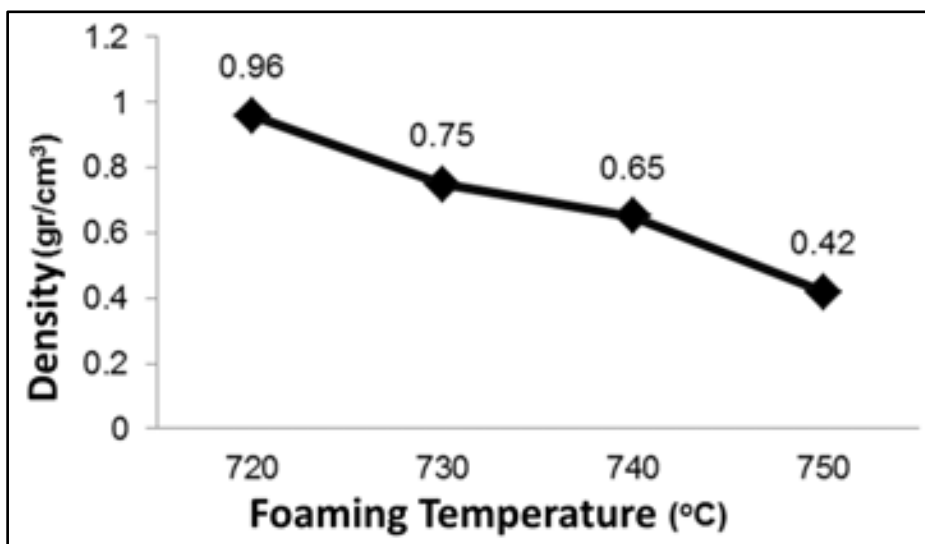


Figure 4. Effects of foaming temperature on density

The cross section photographs in Figure 5 show the cell morphology for the foam samples fabricated using Alumix 13. For lower temperature values, pore formation in the samples is observed to show homogeneous pores. However, outer wall thickness is observed to be thicker compared to other samples. This is observed to decrease as temperature is increased. In contrast, as temperature is increased, a thick layer is observed to form at the very bottom of the sample; this result is attributed to the effects of drainage. As temperature is increased, cell morphology is seen to be deforming in patches throughout the structure, with cells merging and combining to form larger cells.

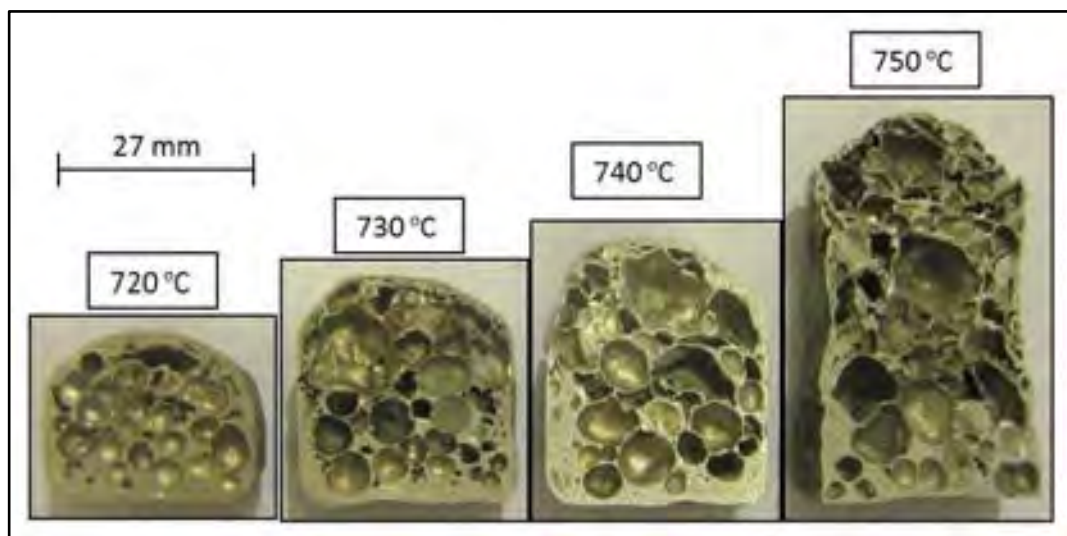


Figure 5. Metal foam produced from Alumix 13 at varying temperatures

4. CONCLUSIONS

Metal foam material was fabricated using Alumix 13 powder and powder metallurgy. Effects of foaming temperature on linear expansion, density and cell morphology were investigated for the process of metal foam production. An increase of up to 600% in linear expansion was observed in metal foam production as foaming temperature was increased. At the same time, density was observed to decrease as temperature increased. Along with increased temperature, an increase in cell mergings and outer wall deformation were also observed.

REFERENCES

- [1]. Sirong, Y., Jiaan, L., Yanru, L., Yaohui, L., "Compressive behavior and damping property of ZA22/SiCp composite foams", *Materials Science and Engineering A*, 325–328 (2007).
- [2]. Raj, R.E., Daniel, B.S.S., "Aluminum Melt Foam Processing for Light-Weight Structures", *Materials and Manufacturing Processes*, 525–530 (2007).
- [3]. Banhart, J., "Metallic foams: Challenges and Oportunities", *Eurofoam 2000*, MIT-Verlag Bremen, 13-20 (2000).
- [4]. Banhart, J., "Manufacture, characterisation and application of cellular metals and metal foams", *Progress in Materials Science*, 559-632 (2001).
- [5]. Gökmen, U. (2009). "Aluminum Particulate Reinforced Metal Foam Production Using Powder Metallurgy". Graduate Thesis, Gazi University, 1-81.
- [6]. Çinici H. and Türker M. (2006). "Investigation of Deformations on Aluminum Based Metal Foams Produced Using Powder Metallurgy". 13. 13th International Metallurgy and Materials Conference, Istanbul, Turkey, 854-860.
- [7]. Paulin, I., Sustarsic, B., Kevorkijan, V., Skapin, S. D., Jenko, M., "Synthesis of Aluminium Foams by the Powder-Metallurgy Process: Compacting of Pecursors", *Materials and Technology*, 45:13–19 (2011).
- [8]. Young, S.W., Kang, C.G., "Fabrication of foamable precursors by powder compression and induction heating process", *Metallurgical and Materials Transactions B*, 35B:769-776 (2004).

COMPUTATIONAL HYDRODYNAMIC ANALYSIS OF TURBULENT DUCT FLOW

Selcuk SELIMLI

Karabuk University, Department of Energy Systems Engineering, 78050, Karabuk, Turkey.
selcukselimli@karabuk.edu.tr

Ziyaddin RECEBLI

Karabuk University, Department of Energy Systems Engineering, 78050, Karabuk, Turkey.
zrecebli@karabuk.edu.tr

Erol ARCAKLIOGLU

Karabuk University, Department of Mechanical Engineering, 78050, Karabuk, Turkey.
arcakli@karabuk.edu.tr

Abstract

Hydrodynamic characteristic of liquid metal magnetohydrodynamics (MHD) turbulent internal flow under the magnetoviscous forces has been numerically studied. Computational liquid metal incompressible steady state turbulent flow simulation was occurred by ANSYS Fluent MHD module. Hydrodynamic parameters are flow velocity, dynamic and eddy viscosity, turbulent kinetic energy, turbulent intensity, density have been examined and concluded results have been verified with studies from literature. Due to the obtained results flow velocity, eddy viscosity, turbulence kinetic energy, turbulent intensity decreases by the increase of applied magnetic field and also positive directional electrical field. Parameters are dynamic viscosity and density increases by the increase of magnetic and positive directional electrical field. But also, increase in negative directional electrical field intensity increases flow velocity, eddy viscosity, turbulence kinetic energy, turbulent intensity, and decreases dynamic viscosity and density.

Keywords: *Electromagnetic field, hydrodynamic characteristics, MHD, turbulent flow.*

1. INTRODUCTION

Magnetohydrodynamic defines the hydrodynamic behavior of electrically conductive fluids under the imposed magnetic forces. Some of the studies that are related with the scope of this paper have been presented. Dritselis et al. (2011) investigated numerically the effect of Lorentz force on turbulent channel flow of electrically conducting fluids. The overall magnetic damping effect on turbulence is presented indirectly by the variation of the mean velocities [1]. Haq et al. (2015) determined the stagnation point flow of nano fluid with magneto-hydrodynamics effects. It is found that rising in Hartmann number gives the resistive type flow; subsequently velocity profile shows the decreasing behavior with an increase of magnetic parameter [2]. Huang and Fang (2007) clarified a new numerical method that could be applied to a 3D free surface flow in strong and non-uniform magnetic field. Results present that magnetic field suppresses the turbulent intensity and turbulent viscosity, and delay the fluid separation [3]. Jalil et al. investigated turbulent natural convection of molten sodium in a cubic cavity heated from one vertical wall and cooled from an opposing vertical wall with the other walls thermally insulated. It is assessed that turbulent kinetic energy, velocity fluctuation and so turbulence decreases by the increase in magnetic field strength [4]. Kirilov et al. (1995) argued review of experimental work on magnetohydrodynamic and heat transfer characteristics of liquid metal flows. It is evaluated that transverse magnetic field changes the velocity distribution and suppresses turbulent pulsations in channels [5]. Lee and Choi (2001) tried the direct numerical simulation technique to explain the Lorentz force on near wall turbulence structures. It is seen that the wall normal magnetic field is effective than the streamwise and spanwise magnetic fields in decreasing velocity and turbulent fluctuations [6]. Nakaharai et al. (2007) demonstrated the transverse magnetic field effect on the heat transfer of an electrically conducting turbulent fluid flow. It is studied that the magnetic field depresses the turbulent velocity fluctuation [7]. Reuter et al. (2008) assessed the parallel implementation of a nonlinear pseudo-spectral MHD code for the simulation of turbulent dynamos. It is presented that the magnetic field shows backward effect on the velocity and suppresses the turbulence pulsations [8]. Vire et al. (2011) pointed out that the performances of different subgrid scale models in large eddy simulations of turbulent channel flows. It is explained that in magnetohydrodynamics the Lorentz force breaks the flow and decrease the velocity fluctuation intensity, and also decreases the eddy-viscosity [9]. Zhao and Hu (2012) clarified an appropriate experimental system, to investigate the variation of density. It is evaluated the density of magnetic fluid increases by applied magnetic field increase [10]. Zikanov and Thess (1998) simulated numerically turbulent flow of electrically conducting incompressible viscous fluid under the influence of an imposed homogeneous magnetic field. It is concluded that strong magnetic field decays the MHD turbulence [11]. In this paper, steady state turbulent liquid metal flow hydrodynamic flow parameters are flow velocity, turbulent intensity; eddy viscosity, dynamic viscosity, turbulence kinetic energy and density have been investigated under the applied transverse magnetic and electrical field.

2. MATERIAL AND METHODS

Steady, turbulent, incompressible liquid metal flow in duct model that has constant wall temperature (T_w) has been studied computationally with ANSYS Fluent software MHD module. Studied duct model presented in Figure 1.

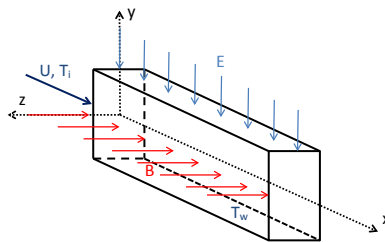


Figure 1. Duct model.

Created duct model by Gambit software meshed and parametric base mesh grid quality was assessed with different grid sized models in Table 1.

Table 1. Mesh grid quality parameters.

Meshing Size (m)	AspectRatio>1	Skewness<0.85	0<Orthogonal	Number of cell	Number of nodes
			Quality<1 (OQ≈1 excellent)		
0.0002	1.74	0.23	1	1,462,500	1,542,554

0.00025	1.71	0.24	1	756,000	807,744
0.0005	1.7	0.31	1	93,000	105,952
0.00075	1.68	0.47	1	29,400	35,376
0.001	1.65	0.53	1	12,000	15,402
0.0015	1.53	0.65	1	3,000	4,444

Determined software base parameters are given in Table. 1 showed that 0.0002 m and 0.00025 m grid sized models has satisfactorily good quality. CPU time and cost consideration directed to the study with 0.00025 m grid sized model.

3. RESULTS AND DISCUSSION

In this section steady state turbulent flow of liquid metal under the influence of magnetic and electrical field on hydrodynamic fluid flow parameters have been investigated. Turbulent intensity and average flow velocity values of the flow domain have been illustrated in Figure 2.

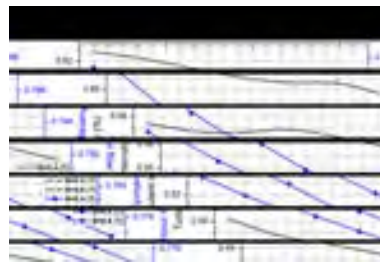


Figure 2. Average flow velocity and turbulent intensity.

Figure 2 presents that increase in each applied constant magnetic field induction turbulence fluctuations and motion of fluid depresses by the magnetic forces. Increase in constant magnetic field decreases the flow velocity and turbulent intensity. While imposing the magnetic field induction constantly, electrical field externally applied individually from positive and negative directions. Positive directionally applied electrical field upgrades the influence of magnetic field and so increase in electrical field reduces the flow velocity and turbulent intensity. Otherwise, increase in negative directionally applied electrical field retrenches the impact of magnetic field effect and so flow velocity and turbulent intensity rises up. In ref. [1, 2] mentioned that velocity profile shows the decreasing behavior with an increase of magnetic parameter. Additionally, in ref. [3] discussed that magnetic field suppresses the turbulent intensity and delay the fluid separation.

Figure 3 presents the combine effect of magnetic and electrical field on hydrodynamic flow parameters are dynamic and eddy viscosities.

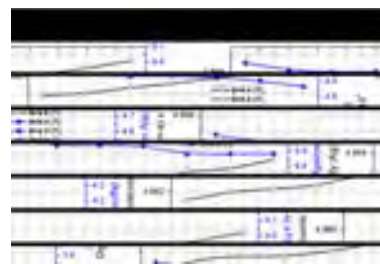


Figure 3. Dynamic and eddy viscosities.

Increase in applied magnetic field shows the reducing effect on the eddy viscosity because of suppression the turbulence. Swelling in applied magnetic field, gains the dynamic viscosity of the fluid. In case of application of positive directional electrical field on magnetic field applied flow domain, magnetic forces on the flow domain develops. Increase in positive directional electrical field decreases the eddy viscosity and increases the dynamic viscosity. Reverse directional application of electrical field decreases the dynamic fluid viscosity, but also increases the turbulent intensity. Similar case pointed in ref. [3, 9] that Lorentz force breaks the flow and decrease the velocity fluctuation intensity, and also decreases the eddy-viscosity.

Figure 4 clarifies the magnetic forces effect on the density and turbulence kinetic energy.

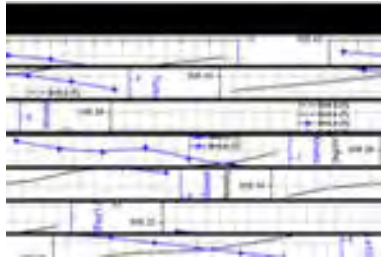


Figure 4. Density and turbulence kinetic energy

Domination of the liquid metal flow domain by the created magnetic forces could be interpreted because of the decrease in turbulence kinetic energy by the increase in magnetic field. Similarly increase in positive directional applied electrical field shows decreasing impact to the turbulent kinetic energy, too. Magnetic field effect is shortened by the increase in negative directional electrical field and so turbulent kinetic energy increases. Density of the fluid increases by the increase of magnetic field and positive directional electrical field. Increment in negative directional electrical field declines the fluid density in Figure 4. Increase in density by magnetic forces clarified in ref. [10] as density of magnetic fluid increases by applied magnetic field increase. Variation in turbulence kinetic energy by applied magnetic field evaluated in ref. [4] as turbulent kinetic energy decreases by the increase in magnetic field strength.

4. CONCLUSIONS

Liquid metal turbulent flow hydrodynamic parameters are flow velocity, turbulent intensity, dynamic viscosity, eddy viscosity, density and turbulence kinetic energy investigated to the case of applied magnetic field and together with electrical field.

1. Externally applied magnetic field increases the liquid metal dynamic viscosity and density.
2. Magnetic field suppresses the turbulence fluctuations and decreases the flow velocity, turbulent intensity, eddy viscosity, turbulence kinetic energy.
3. Increase in externally applied positive directional electrical field develops the dynamic viscosity and density of the liquid metal.
4. Positive directional electrical field declines the flow velocity, turbulent intensity, eddy viscosity, turbulence kinetic energy.
5. Negative directional electrical field reduces dynamic liquid viscosity and density.
6. Flow velocity, turbulent intensity, eddy viscosity and turbulence kinetic energy enhanced by negatively directed electrical field.

Domination of turbulent fluctuations and swirling in the flow domain by magnetic forces indirectly decreases the liquid metal temperature and so density and dynamic viscosity is raises up.

REFERENCES

- [1]. C. D. Dritselis, I. E. Sarris, D. K.Fidaros, and N.S. Vlachos, "Transport and deposition of neutral particles in magnetohydrodynamic turbulent channel flows at low magnetic Reynolds numbers,"*Int. J. Heat Fluid Fl.*, vol. 32, pp. 365-377, Apr. 2011.
- [2]. R. U. Haq, S. Nadeem, Z. H. Khan, and N. S. Akbar, "Thermal radiation and slip effects on MHD stagnation point flow of nano fluid over a stretching sheet,"*Physica E*, vol. 65, pp. 17-23, Jan. 2015.
- [3]. H. Huang, and Y. Fang, "MHD effect on heat transfer in liquid metal free surface flow around a cylinder,"*Eng. Appl. Comp. Fluid Mech.*, vol. 1, pp. 88-95, Feb. 2007.
- [4]. J. M. Jilal, T. K.Murtadha, and K. A. Al-tae'y, "Three-dimensional computation of turbulent natural convection in the presence of magnetic field,"*J. Indian Inst. Sci.*, vol. 86, pp. 705-721, Nov. 2006.
- [5]. I. R. Kirillov, C. B. Reed, L.Barleon, andK. Miyazaki, "Present understanding of MHD and heat transfer phenomena for liquid metal blankets,"*Fusion Eng. Des.*, vol. 27, pp. 553-569, Mar. 1995.
- [6]. D. Lee, and H. Choi, "Magnetohydrodynamic turbulent flow in a channel at low magnetic Reynolds number,"*J. Fluid Mech.*, vol. 439, pp. 367-394, July 2001.
- [7]. H. Nakaharai, J. Takeuchi, T.Yokomine, T.Kunugi, S.Satake, N. B. Morley, and M.Abdou, "The influence of a magnetic field on turbulent heat transfer of a high Prandtl number fluid,"*Exp. Therm. Fluid Sci.*, vol. 32, pp. 23-28, Oct. 2007.
- [8]. K. Reuter, F.Jenko, C. B. Forest, andR. A.Bayliss, "A parallel implementation of an MHD code for the simulation of mechanically driven, turbulent dynamos in spherical geometry,"*Comput. Phys. Commun.*, vol. 179, pp. 245-249, Aug 2008.
- [9]. A. Vire, D.Krasnov, T.Boeck, andB. Knaepen, "Modeling and discretization errors in large eddy simulations of hydrodynamic and magnetohydrodynamic channel flows,"*J. Comput. Phys.*, vol. 230, pp. 1903-1922, Mar. 2011.

- [10]. M. Zhao, and J. Hu, "Study on density of magnetic fluid in the strong magnetic field," *Second Int. Conf. Instru. Meas. Comp. Com. Contr.*, doi: 10.1109/IMCCC.2012.97, pp. 396-398.
- [11]. O. Zikanov, and A. Thess, "Direct numerical simulation of forced MHD turbulence at low magnetic Reynolds number," *J. Fluid Mech.*, vol. 358, pp. 299-333, Mar. 1998.
-

CFD THERMOPHYSICAL ANALYSIS OF MHD TURBULENT PIPE FLOW

Ziyaddin RECEBLI

Karabuk University, Department of Energy Systems Engineering, 78050, Karabuk, Turkey.
zrecebli@karabuk.edu.tr

Selcuk SELIMLI

Karabuk University, Department of Energy Systems Engineering, 78050, Karabuk, Turkey.
selcukselimli@karabuk.edu.tr

Erol ARCAKLIOGLU

Karabuk University, Department of Mechanical Engineering, 78050, Karabuk, Turkey.
arcakli@karabuk.edu.tr

Abstract

This study cares about the thermophysical investigation of magnetohydrodynamics (MHD) liquid metal incompressible steady state turbulent closed conduit flow under the imposed transversely magnetic and electrical field. Circular closed conduit model has been studied computationally by ANSYS Fluent MHD module. Thermophysical parameters are temperature and heat flux has been simulated and concluded results have been verified with literature studies. According to the results temperature and heat flux was decreasing by the applied magnetics and positive directional electrical field. Also applied negative directional electrical field increases two of them.

Keywords: *Magnetic and electrical field, MHD, thermophysical parameters, turbulent flow.*

1. INTRODUCTION

Electrically conductive fluids dynamic flow characteristics are the subject of magnetohydrodynamic science. Studies in literature is related with the subject of this study is evaluated and summarized. Branover et al. (1995) clarified the growth in fluctuation intensity with magnetic field. The temperature fluctuation intensity decreases with the increase in magnetic field [1]. Gajbhiye and Eswaran (2015) studied the effect of imposed magnetic field on fluid flow. Results presented that motion of the fluid is suppressed and so temperature decreases [2]. Huang and Li (2010) mentioned the fluid flow characteristic and heat transfer of MHD flow. It is concluded that the magnetic field have reverse influence on the thermal performance, and values reduces with magnetic parameter increase [3]. Huang and Li (2010) simulated numerically free surface MHD flow. Mentioned that Lorentz force created by magnetic field suppresses the motion of the flow and the velocity gradient is sharply decreases [4]. Kirillov et al. (1995) investigated a review of experimental work on magnetohydrodynamic and heat transfer characteristics of liquid metal flows. Magnetic field varies the velocity distribution in channels and suppresses turbulent fluctuations and so dominates the heat transfer [5]. Nakaharai et al. (2007) evaluated the mean temperature gradient is not influenced compared to the temperature fluctuation in the direction vertical to the magnetic field. Magnetic field suppresses the turbulent velocity fluctuation, then the turbulent heat flux and temperature is decreased [6]. Smolentsev et al. (2002) presented the turbulent flows and the free surface boundary conditions are adjusted with MHD effects. It is discussed that heat transfer degraded by the magnetic field increase [7]. Takeuchi et al. (2008) reported that experimental results on turbulent pipe flow under magnetic field. Results demonstrated that magnetic parameter modificate the mean flow velocity as well as turbulence reduction [8]. Yamamoto and Kunugi (2015) simulated numerically the turbulent channel flow imposed a wall normal magnetic field. Concluded that increase in magnetic parameter decreases the turbulent heat flux [9]. Zijovin et al. (2010) presented magnetohydrodynamic immiscible fluids flow in the presence of an applied electric and inclined magnetic field. It is determined that the increase in magnetic parameter decreases the temperature in the middle of the channel [10]. In this study, Lorentz force, which is created by magnetic field induction, effect on steady state liquid metal duct turbulent flow thermophysical parameters are temperature and heat flux under the normally oriented magnetic and also electrical field has been searched.

2. MATERIAL AND METHODS

Steady state incompressible turbulent flow of liquid metal has been searched in case of applied magnetic and electrical field. Heating of liquid metal with a high temperature constant wall temperature (T_w) closed conduit turbulent flow has been studied computationally by ANSYS software. Constructed pipe model is seen in Figure 1.

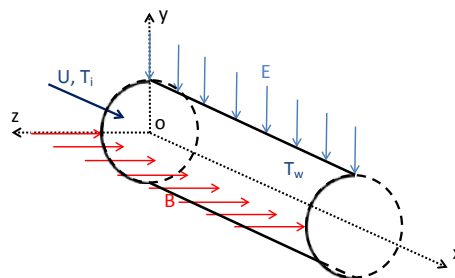


Figure 1. Pipe model.

Created pipe model with Gambit software meshed with different grid sizes and parameter base mesh study has been occurred. Evaluation of the mesh grid quality parameters are given in Table. 1.

Table 1. Mesh grid quality parameters.

Meshing Size (m)	AspectRatio>1	Skewness<0.85	0<Orthogonal Quality<1 (OQ≈1 excellent)	Number of cell	Number of nodes
0.0002	4.12	0.52	0.98	1,671,618	1,734,235
0.00025	4.1	0.54	0.97	836,178	876,159
0.0005	3.13	0.67	0.87	116,280	126,791
0.00075	3.02	0.75	0.83	33,567	38,178
0.001	2.63	0.83	0.81	13,617	16,324
0.0015	2.59	0.92	0.59	5,250	6,572

Mesh grid quality parameters are given in Table 1 determined that 0.0002 m and 0.00025 m grid sized models convincing to the analyses. CPU time consideration directed to occurrence of the analyses with 0.00025 m model.

3. RESULTS AND DISCUSSION

This paper cares the impact of magnetic and electrical field on thermophysical parameters of turbulent steady state liquid metal flow. In this respect central temperature values in case of application the magnetic and electrical field is visualized in Figure 2.

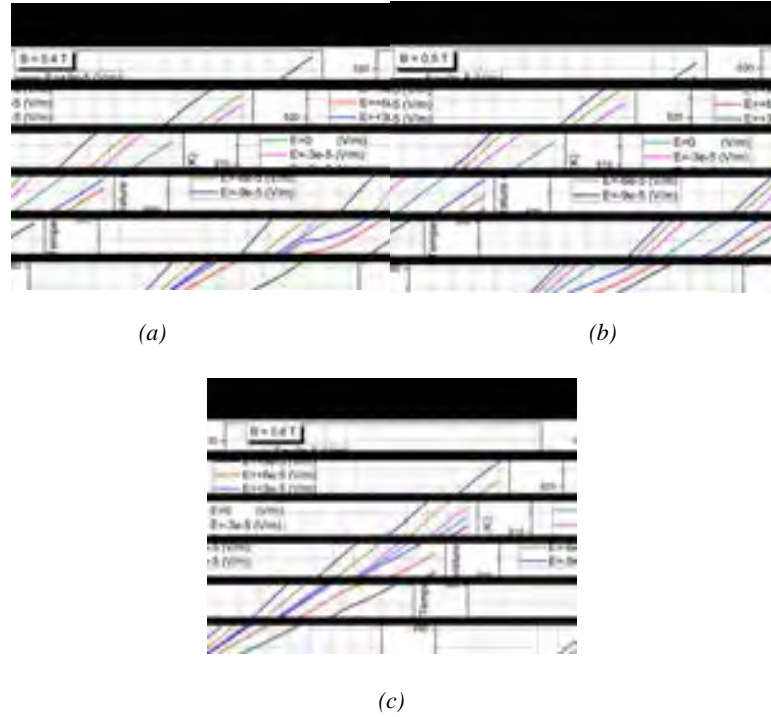
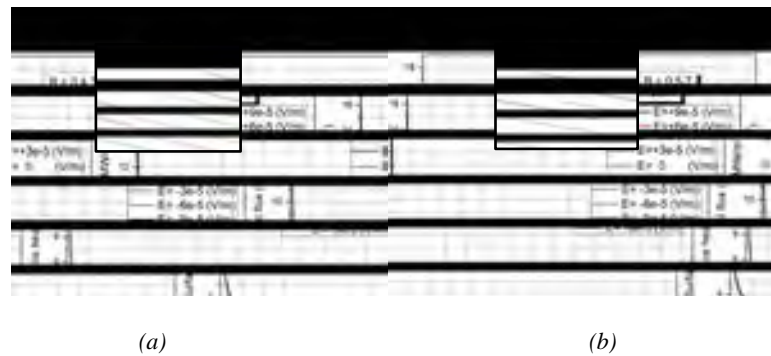


Figure 2. Central temperature through the model length.

Figure 2(a, b, c) could be assessed as increment of applied magnetic field on flow counter decreases the liquid metal temperature. While applying magnetic field constantly, electrical field applied with increasing values in positive and negative directions. Increasing the electrical field in positive direction decreases the liquid metal temperature. Reversing the electrical field direction to negative way temperature increases. Similar case concluded in ref. [2, 10] that the increase in magnetic parameter decreases the temperature in the middle of the channel.

Figure 3(a, b, c) shows the magnetic forces effect on the heat flux of the turbulent steady state flow of liquid metal.





(c)

Figure 3. Central temperature through the model length.

Surface heat flux values are seen in Figure 3(a, b, c) decreases by the application of magnetic field induction. By the application of electrical field in positive direction also decreases the heat flux. Reversing the direction of electrical field reduces the created magnetic forces and so enhances the surface heat flux. In ref. [6, 9] discussed that increase in magnetic parameter decreases the turbulent heat flux.

4. CONCLUSIONS

Thermophysical parameters are temperature and surface heat flux of steady state turbulent liquid metal flow has been investigated while magnetic and electrical field is imposing.

1. Turbulence fluctuations and flow velocity at close region of the model wall depressed by the magnetic forces and liquid metal temperature and surface heat flux is decreased by externally imposed magnetic field.
2. Positive directionally applied electrical field supports the effect of magnetic forces and so decreases the temperature and surface heat flux more and more by the absence of electrical field.
3. Electrical field applied through the negative direction weaken the magnetic forces and enforces the temperature and surface heat flux.

REFERENCES

- [1]. H. Branover, A. Eidelman, and M. Nagorny, "Use of turbulence modification for heat transfer enhancement in liquid metal blankets," *Fusion Eng. Des.*, vol. 27, pp. 719-724, Mar. 1995.
- [2]. N. L. Gajbhiye, and V. Eswaran, "Numerical simulation of MHD flow and heat transfer in a rectangular and smoothly constricted enclosure," *Int. J. Heat Mass Tran.*, vol. 83, pp. 441-449, Apr. 2010.
- [3]. H. Huang, and B. Li, "Heat transfer enhancement of free surface MHD-flow by a protrusion wall," *Fusion Eng. Des.*, vol. 85, pp. 1496-1502, Dec. 2010.
- [4]. H. L. Huang, and B. Li, "Heat transfer enhancement of free surface MHD-flow by the wall with non-uniform electrical conductivity," *Int. J. Energ. Env.*, vol. 1, pp. 1027-1038, Nov. 2010.
- [5]. I. R. Kirillov, C. B. Reed, L. Barleon, K. Miyazaki, "Present understanding of MHD and heat transfer phenomena for liquid metal blankets," *Fusion Eng. Des.*, vol. 27, pp. 553-569, Mar. 1995.
- [6]. H. Nakaharai, J. Takeuchi, T. Yokomine, T. Kunugi, S. Satake, N. B. Morley, and M. A. Abdou, "The influence of a magnetic field on turbulent heat transfer of a high Prandtl number fluid," *Exp. Therm. Fluid Sci.*, vol. 32, pp. 23-28, Oct. 2007.
- [7]. S. Smolentsev, M. Abdou, N. Morley, A. Ying, and T. Kunugi, "Application of the "K-e" model to open channel flows in a magnetic field," *Int. J. Eng. Sci.*, vol. 40, pp. 693-711, Mar. 2002.
- [8]. J. Takeuchi, S. Satake, N. B. Morley, T. Kunugi, T. Yokomine, and M. A. Abdou, "Experimental study of MHD effects on turbulent flow of Flibe simulant fluid in circular pipe," *Fusion Eng. Des.*, vol. 83, pp. 1082-1086, Dec. 2008.
- [9]. Y. Yomamoto, and T. Kunugi, "Direct numerical simulation of MHD heat transfer in high Reynolds number turbulent channel flows for Prandtl number of 25," *Fusion Eng. Des.*, vol. 90, pp. 17-22, Jan. 2015.
- [10]. S. M. Zijovin, D. D. Nikodijevic, B. D. Blagojevic, and S. R. Savic, "MHD flow and heat transfer of two immiscible fluids between moving plates," *T. Can. Soc. Mech. Eng.*, vol. 34, pp. 351-372, Sept. 2010.

WEB SERVER SECURITY SCANNER APPLICATION

Ali BULDU

Fuat MUNINOGLU

Resat MARZIOGLU

Kazim YILDIZ

Volkan Yusuf SENYUREK

Abstract

Internet world brings huge benefits to users and nearby it comes with so many security threats like; Stolen of credit card information, Grabbing of Web Site Domains, hacking e-mail accounts, gathering personal information and so on. Our aim in this application, understand web attack types, develop an algorithm according to the attack methods and writing a web security scanner to discover possible threats on web sites. Our resource belongs to the web security and attack based sites and documentation. We bring these different platforms together and develop our program in Python language that is also used by an important company called Google Object oriented programming Python; give us flexibility and fastest base 1 . Security Scanners do heavy process because of usage high Central Processing Unit(CPU) and Internet connection at the same time. Algorithm's in the program and libraries that is used has an important effect on the speed of workflow. We only import the necessary modules from libraries. So this highly affects the program performance 2 . Our program does these functions ; Discovers, Common Gateway Interface , Remote File Inclusion, SQL Injection exploits on Web Server gathering the Web Server information.

Keywords: *Web Server Security, Security System, Application of Security Scanner*

1. INTRODUCTION

There are two sides of danger in the internet security world, personal computer security and web server security, threatening users and web hosting companies. This program and documentation is surely not enough to defend a system, but gives some information about where to begin defending your network. Simply exposing backdoors of websites. On the other hand, OsmanWS is showing, how the firewalls can be passed through easily. We developed this program for educational purposes and teach security experts how to close backdoor. We share the roles between each other in two parts. First part is the security expert, described how to use hacking methods and discovering Exploits; Second part is the coding and developed searching algorithms. The Web Security can be divided into two main subjects. These are Personal Computer Security and Host Security. Our project basis on the Host Security side.

2. WEB SERVER SECURITY

2.1. Personal Computer Security

Most of the security threat of PC's is based on user. If the user is conscious about computer environments and knows the risk of Web Sites, he will get the highest personal computer security without getting any software & updates. Systems can be fixing for security threats and provide the highest security options for end users, but users can destroy the Security Wall so easy. User must have a secure personal firewall on the PC and have to configure it for best security and high performance. Usually, the personal firewalls needs huge memory and it cause to reduce performance. It is an annoying side of security but user must know the importance of Personal information.

The user, must upgrade the hardware if he needs more performance. Nowadays, Operating Systems come with a build in firewall for end user security. If the user wants to use other 3rd party Firewall & Antivirus Software, Operating Systems Firewall can be disabled for getting the highest performance. This is a way of increasing performance without changing hardware, but this is not recommended way. Most of virus & Trojan written for Windows Operating System because of its popularity. Flash disks, is the common house for hosting a virus & Trojan Horse. To avoid this, users must scan the disks usable & secure area with and updated antivirus tool without clicking on it.

2.2. Host Security

There are lots of attack types of Web Hosts and this cause high security risk for end users and Companies. Most of the vulnerabilities reason is coding mistakes. If the input of the forms could not filter, users can read the database, change the fields and grab all the information. Coding mistakes are cloning every day, because of the Web Sites Templates. Templates are websites for ready to publish and they are using from persons and companies. Most of Web Site owners uses that template and get the common risk of the template. Templates has got own database and own structure. If the user not modifies this structure, he will most probably get into trouble about the host. In addition this, Web Server Infrastructure must have the high bandwidth and Intrusion Detection System (IDS) has to be stand for security. In figure 1 web server security scanner process can be seen.

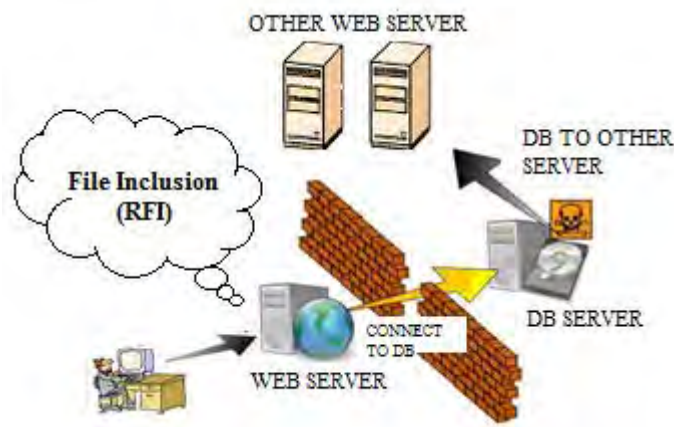


Figure 1. Web Server Security Scanner

3. WEB SERVER THREADS

There is some common methodology to get hold of whole web server or website itself. We describe 3 methods and describe of avoiding mistakes in coding. Basic coding and configuration mistakes can cause big damage your entire system.

- Remote File Inclusion
- SqlInjection
- Common Gateway InterfaceInjection

3.1. Remote File Inclusion

Remote File Inclusion (RFI) is technique which used to attack Internet websites from a remote computer. It uses a cross site scripting (XSS) to harm a web server.

It attacks to allow malicious users to run their own PHP code on a vulnerable website. The attacker is used his malicious code in the space provided for PHP programs on a web page. There is simple code like this:

```
<a
href=index.php?page=file1.php>Files</a><?
php
$page = $_GET[page];
include($page);
```

With these lines above, webmaster directed \$page input to the web users. If we try

```
http localhost index.php?page=http
www.osmanws.info
```

the page will directed to the www.osmanws.info. Hackers use <http://www.harmfulshell.com/C99.php> to get hold of entire system (The link placed at the end of the RFI).

Preventing RFI Injection

Code Based Prevention ;

RFI Occurs;

```
$field= $id[field];
```

Fix;

```
$field = "field".$id;
```

include, include_once, require, require_once, exec commands must use carefully.

Configuration Based Prevention;

With "disable_functions" you can secure your system easily. So injected Scripts like C99 shell will not affect your system.

4. DEVELOPING OF PROGRAM

4.1. Program Workflow

We coded the OSMAN Web Security program in Python language. Python is a dynamic object-oriented programming language that can be used for any software development. It can be learned in a few days and could offer support for other languages and tools. It has extensive standard libraries. Its users report substantial productivity for the development of higher quality, more maintainable code [6].

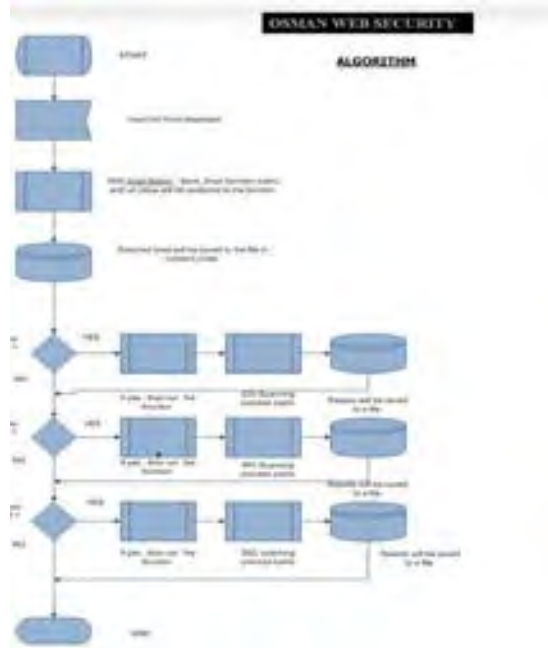


Figure 3. Flowchart of the program

4.2. Program Structure

Program can discover possible CGI, RFI , SQL exploits in the web site and also collects some important web server information. First user has to enter a valid URL without http:// in to the top box, like www.osmanws.com. After that user has to choose the exploit types need to be scanned. There are three options CGI, RFI and SQL. The more check box you select the longer you will wait Osmanws to finish process. As the last action we press to scan button and the process begins. After pressing scan button we have to wait until all boxes fill and we have to see scan complete caution in all threeboxes. This process may take several minutes. You can see which results are related to exploits and which one is hosting server information below [7]. After we scan a web site we can save results with clicking just one button (save all). This button will save all results with titles and will also save which backdoors you've scanned for this URL address. If you want to save only a specific part of the results you can select the partition and click save selected button. This button will also save the scanned doors into the word document. The word document mentioned is located in the folder that you have run Osmanws. The program must run at least one time to create register documents. The last button on the interface is clear all. This button clears all boxes for a new scan. In this work used python modules are:

- Tkinter – For User Interface
 - BeautifulSoup – Forgrabbinghreflinks
 - Urllib – Urloperations
 - urllib2- ExtendedUrloperations, Errorredetection
 - cgilinks – Includescommoncgiexploits
-



Figure 4: Program Interface

Our SQL Exploit detection algorithm looks for the key error of SQL with sending “ ‘ ” input at the end of the grabbed links.

Error: Microsoft OLE DB Provider for ODBC Drivers error '80040e14'

RFI algorithm is looking for the dangerous functions likely “include”, ”require”, “include_once”, ”require_once”. Some can easily find the weak points of system. In figure 5 when RFI algorithm is used we can see result screen.



Figure 5. GUI Explanation

CGI algorithm searches common CGI bugs that are collected from all over the world. CGI algorithm's result page can be seen in Figure 6.



Figure 6. Showing mistakes in coding

5. CONCLUSION

Digitalization of information needs high security precautions on coding and server infrastructure side. Prevention of hacking must grow parallel with the exploit and bugs. User input always has to be filtered and check twice. Server configuration has carefully done and unnecessary function must disable. Companies must do a penetration test in periodically.

This prototype program has some qualifications different than others. Usually, educational coding formats scan only one type of exploits. OsmanWS is concerned on three types of exploits and three different scan algorithms, checking database responses, scanning template links and searching particular words in source code. We tried to make this process as simple as possible and easy to learn. Also, you can find how to use an object oriented programming language with object oriented programming methods. OsmanWS is written by using template python libraries and user developed python libraries (like urllib2). We also added our own library for template cgi links. Research period of thesis had very wide angel to examining hacking methods and using python as a security language so result is very complex for a simple prototype program. Hopefully, reader can have an idea about web security after studied these methods.

REFERENCES

- [1]. Phyton. 2013. <http://www.python.org/>[Online][AccessesJanuary 2013].
 - [2]. Litvhfield, D.,Anley, C., Heasman,J. &Grindlay, B. 2005. The Database Hacker'sHandbook.
 - [3]. Anley, C. 2002. Advanced SQL injection in SQL serverapplications. White paper, NextGeneration Security Software Ltd.
 - [4]. Harris, S,iHarper, A.,Eagle, c. &Ness, j. 2008. Gray hat hacking: theethicalhacker'shandbook, McGraw-Hill.
 - [5]. PArduS. 2013. <http://www.pardus.org.tr>[Online][AccessedFebruary 2013]
 - [6]. Pardus-Linux. 2013. <http://wiki.pardus-linux.org/index/index.php/Phyton>[Online].[AccessedFebruary 2013]
 - [7]. Siddharth, S. 2008. MSSQL Server 2005 Login Information andsomeotherfunctions
-

APPLICATION OF DIGITAL IMAGE CORRELATION IN UNIAXIAL TENSILE TEST

Murat AYDIN

Karabuk University, Technology Faculty, Industrial Design Engineering Department, 78050, Merkez/Karabuk, Turkey.
murataydin@karabuk.edu.tr

in WU

Wayne State University, Mechanical Engineering Department, 48202, Detroit, Michigan, USA,
xin.wu@wayne.edu

Kerim ÇETINKAYA

Karabuk University, Technology Faculty, Industrial Design Engineering Department, 78050, Merkez/Karabuk, Turkey.

İbrahim KADI

Karabuk University, Technology Faculty, Industrial Design Engineering Department, 78050, Merkez/Karabuk, Turkey.

Mustafa YAŞAR

Karabuk University, Technology Faculty, Industrial Design Engineering Department, 78050, Merkez/Karabuk, Turkey.

Abstract

Application fields of non-contact measurement techniques have been recently increasing by means of optics and technological development in measurement applications. Digital image correlation (DIC) is the one and powerful non-contact measurement method that can be used to obtain elongation and strain as well. It is versatile and flexible measurement method can be adopted to many traditional test experiments such as tensile, compression, and bending in order to calculate mechanical properties of materials. In this study, DP600, DP800 and DP980 steel materials were performed to uniaxial tensile test and DIC technique was used to determine local strains in terms of comparison in different regions at the fracture area. While performing experiments, commercial DSLR camera was installed to capture videos under the white led lighting which is needed to decrease visual blurring and keep contrast as constant. Recorded videos were analyzed with VIC-2D software in an effort to calculate strain data. As a result, it was showed that the strains at the fracture area that were measured with DIC were higher than those measured which out of the fractured area and concluded that DIC method was appropriate and efficient technique to measure local strains in traditional uniaxial tensile test.

Keywords: *Digital Image Correlation, Tensile Test, Sheet Metal, Strain Measurement, Optical Measurement.*

1. INTRODUCTION

Rapid development of technology and improvements of optic instruments has caused widely usage of non-contact measurement techniques both in industry and private applications. Image based measurement methods has recently been popular not only traditional methods can not satisfy customer requirements but also specific instruments are very expensive and adapted hardly. To give an easy, low cost, and flexible solution for those problems, digital image correlation (DIC) method is developed and has been used in many fields such as automotive industry, material testing, and medical applications.

DIC technique is mainly based on the photogrammetry field which is a science of making measurements from photographs, especially for recovering the exact positions of surface points. Roots of image based measurements techniques dates back to Leonardo da Vinci writings about the perspective and imagery in 1480 and 1492 as pointed out by Doyle [1] and Gruner [2]. Photogrammetry and its mathematical improvements has been enhanced by means of development of optic tools and imaging technology, especially digital photogrammetry in 1985 up to present [3]. Hobrough [4] used digital image correlation so as to get position information. He purposed a tool that can be used to correlate high-resolution reconnaissance photography with high precision survey photography for calculating ground conditions. Yamaguchi [5] used laser speckles that are scanned by a linear image sensor in the diffraction field and made cross correlation function of the signal.

Ultrasonic approach was the prior studies in two dimensional measurement with digital image correlation. Peters [6] and Ranson [6] developed an approach. In their study, the ultrasonic waves were sent to the reference and deformed images and compared digital images of small areas as known subsets before and after process in order to calculate deformation measurements in material systems. They suggested to use continuum mechanics concept for measuring small areas in matching process to determine locating positions of all subsets. Sutton et al [7] improved some numerical algorithms based on earlier study and applied to experiments to record images with optical instruments and this is known today as 2D DIC. In the last decade, digital image correlation has been applied material testing experiments such as tensile, compression, bending and forming limit curves on the purpose of calculating mechanical properties of the sheet materials. One of the crack propagation study was accomplished by McCormick [8] and Lord [8]. They demonstrated the calculation of crack opening measurement using concrete specimens under compression and they suggested that output of DIC gives local deformation map which shows the cracks not visible to the human eye.

DIC measurement technique generally is adopted to material test experiments such as tensile, compression, and forming limit curves. Zhu et al [9] suggested the two cameras DIC system to measure true stress-strain curves of low carbon steel under uniaxial tension. They used dog bone specimen with 10mm circular cross section area. They calculated the true strain stress curves on the specimen using different local points along the length of the specimen and indicated that while region that enters the plastic zone provides axial plastic deformation because of decreasing cross sectional area, region that entered the plastic zone or not entered yet keeps constant deformed state. Dong et al [10] focused on an application of DIC under high temperature using micro scale pattern. They examined variety speckle patterns and sizes to get good correlation under the high temperature experiments and suggested that using a macro scale speckle patterns that is produced by ceramic based paint to micro scale caused the high number of errors of correlation when the subset size is too small. In addition, they found that fine-sprayed paint and abrasion of polished surface caused micro scale pattern stable under 1400 °C and errors were below 0.04 pixel.

2. EXPERIMENTAL

2.1. Materials

In this study, commercial automotive steels, DP600, DP800, and DP980 that consist of a ferrite matrix and a hard second phase, usually islands of martensite was used in order to calculate local strains using DIC method in uniaxial tensile test. The thicknesses of materials are 1.3mm and the tensile specimens were machined according to ASTM E8. Chemical compositions of these materials are given in Table 1.

Table 1. Chemical compositions of DP600, DP800, and DP980

DP800 [11]						
C % max	Si % max	Mn % max	P % max	S % max	Cr % max	Al _{tot} % max
0,160	0,250	1,90	0,020	0,004	0,500	0,015

DP980 [12]						
C % max	Si % max	Mn % max	Mo % max	B % max	Cr % max	Al _{tot} % max
0,135	0,05	2,1	0,35	0,007	0,15	0,45

DP600 [11]						
C % max	Si % max	Mn % max	P % max	S % max	Cr % max	Al _{tot} % max
0,120	0,300	1,660	0,020	0,004	0,500	0,020

2.2. Methods

All the mechanical tests were performed with 100 kN Instron 8801 uniaxial tensile machine. DIC is mainly used to calculate the displacement and strain over specified field in whole process. One of the crucial instruments in DIC measurement is the camera. The professional high resolution and high frame per second (fps) camera can increase the accuracy and precision of measure. In this study, Canon T3i DSLR with a 58mm diameter and 18-55mm (f/3.5-5.6) lens that has 1920x1080 resolution and 30fps was used, see Figure 1.

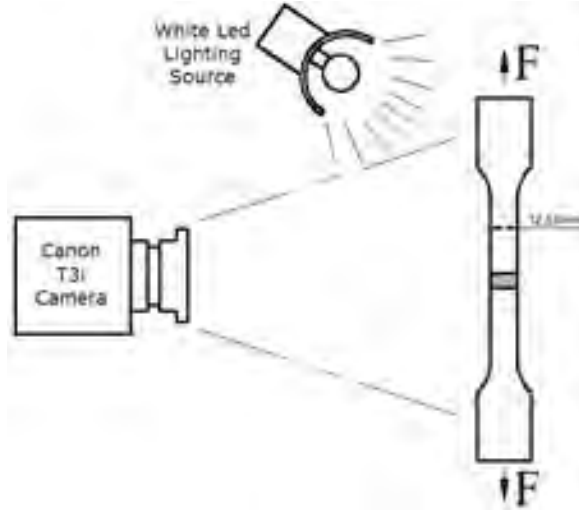


Figure 1. Schematic view of DIC setup

Creating random speckle pattern on the specimen surface is one of the important issues that can directly affect accuracy and precise of the correlation results. In order to obtain high and accurate correlation, the pattern size must be small. Experiments performed at room temperature, most of the water based paints can give proper correlation results to create speckle pattern. In this study, VHT FlameProof, a silicone ceramic based paint was used to create black speckles onto white background because of rapid drying time and high color contrast. As an example, DP600 painted specimen that consists of the calibration meter and dashed area of interest is shown in Figure 2. On the purpose of calculating local strains, five points were selected on horizontal alignment in the fracture area as seen in Figure 2(b). Point 1 is the nearest left edge of specimen and Point 3 is the middle of the fractured edge, and Point 5 is closed to the right edge of specimen out of fracture area. Lighting conditions is another important factor that is crucial for the correlation results. In this study, regular white led lighting source which was subjected to the specimen surface directly gives good correlation results.

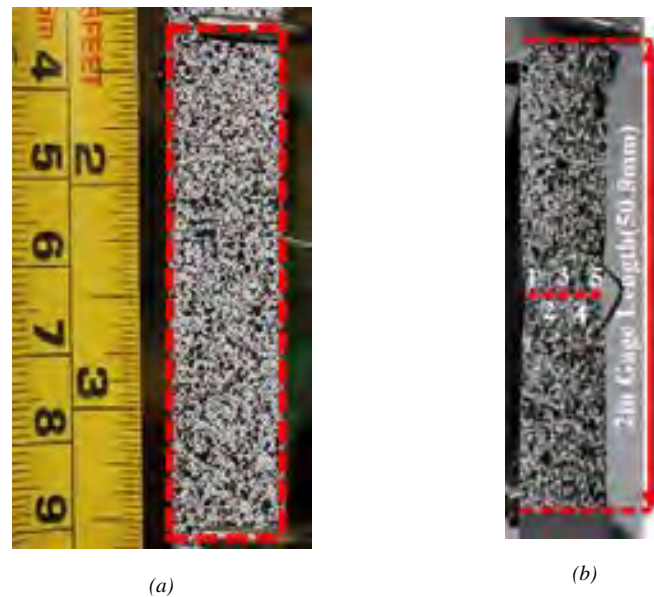


Figure 2. (a) Calibration meter and area of interest, (b) Virtual gage length and selected points

3. RESULTS AND DISCUSSION

In conventional tensile tests, regular extensometer which has 2in (50.8mm) gage length has been used in order to measure the elongation and calculate strain. On the other hand, regular extensometer is not able to install some special experiments as hot tensile tests or hot forming limit tests due to high temperature of test environment and require special equipment like ceramic grips. Therefore, these special tools increase the measurement setup's cost. As an alternative method, DIC, can easily adopt to room and high temperature material mechanic tests. Elongation can be calculated by DIC as well as physical extensometer measurement.

Uniaxial tensile tests were performed with 0.1mm/s cross head speed for three materials. The frames were created from test movies after the whole recorded processes. In the case of non-contact measurement, the extension was obtained from the images using VIC-2D software. Two boundaries were defined that overlay with the two gage length edges, which were created by two Scott types that shielded the paint. After the paint was dried, the types were peeled out. Figure 2 shows the clear boundary of the tensile gage length.

Converting pixels to millimeter was established with common tape measure onto specimen surface at the beginning of the uniaxial tensile test. The camera was setup as 1920x1080 pixels resolution and 16:9 aspect ratio and 16 bit depth of color. The total test times were 35.457 seconds for DP600, 23.779 seconds for DP800, and 18.706 seconds for DP980. The recorded videos were edited with video editing software to obtain series of image sequences. The images were got as 30 frames per second. The images were converted into greyscale format as a TIF file type that has better quality rather than other image types after getting image sequences. Performing correlation the image sequences were imported into VIC-2D software.

The DIC technique is based on tracking and matching process for each unique pattern regions among images or different times. The unique pattern of each location can be defined using subset size and step size to track and calculate displacements. The subset size for room temperature tensile tests is 24x24 pixels and step size 2x2 pixels. Figure 3 shows the Von Misses strains of the fractured areas for DP600, DP800, and DP980. On the scale bar, red color shows the maximum Von Misses strains in the fracture zone before the failure of specimens. Maximum Von Misses strains were found as 0.562, 0.296375, and 0.164625 for DP600, DP800, and DP980, respectively.

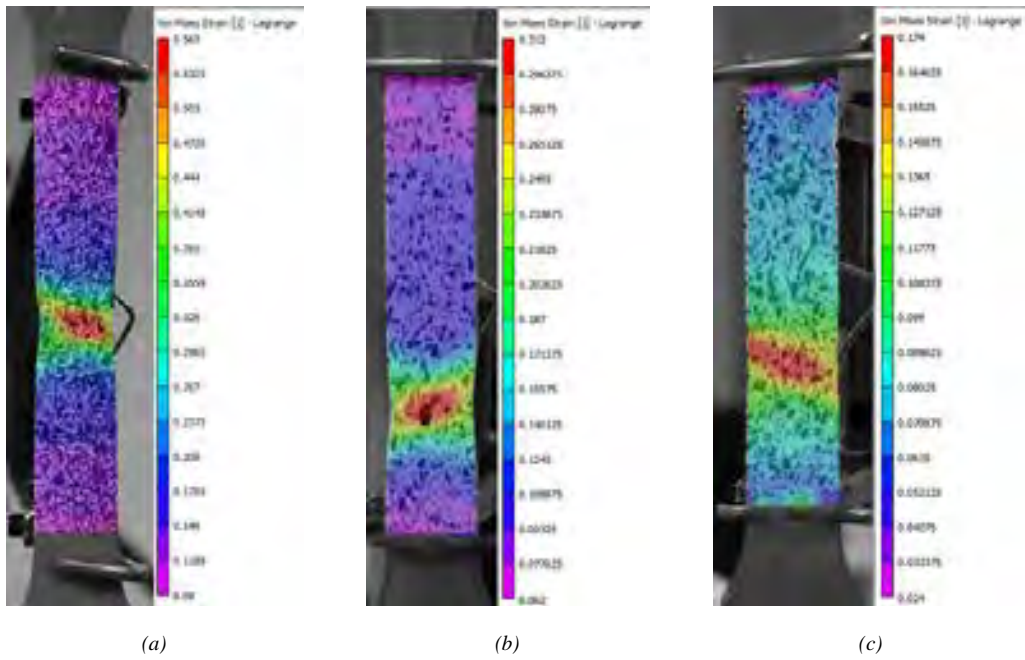


Figure 3. Von Mises strains before fracture. (a) DP600, (b) DP800, (c) DP980

Figure 4 shows the plot of the strains in y direction of five points that are shown in Figure 2(b). In Figure 4, Point 3 which is a middle point of the fracture area is always higher points that are slightly out of the fractured area.

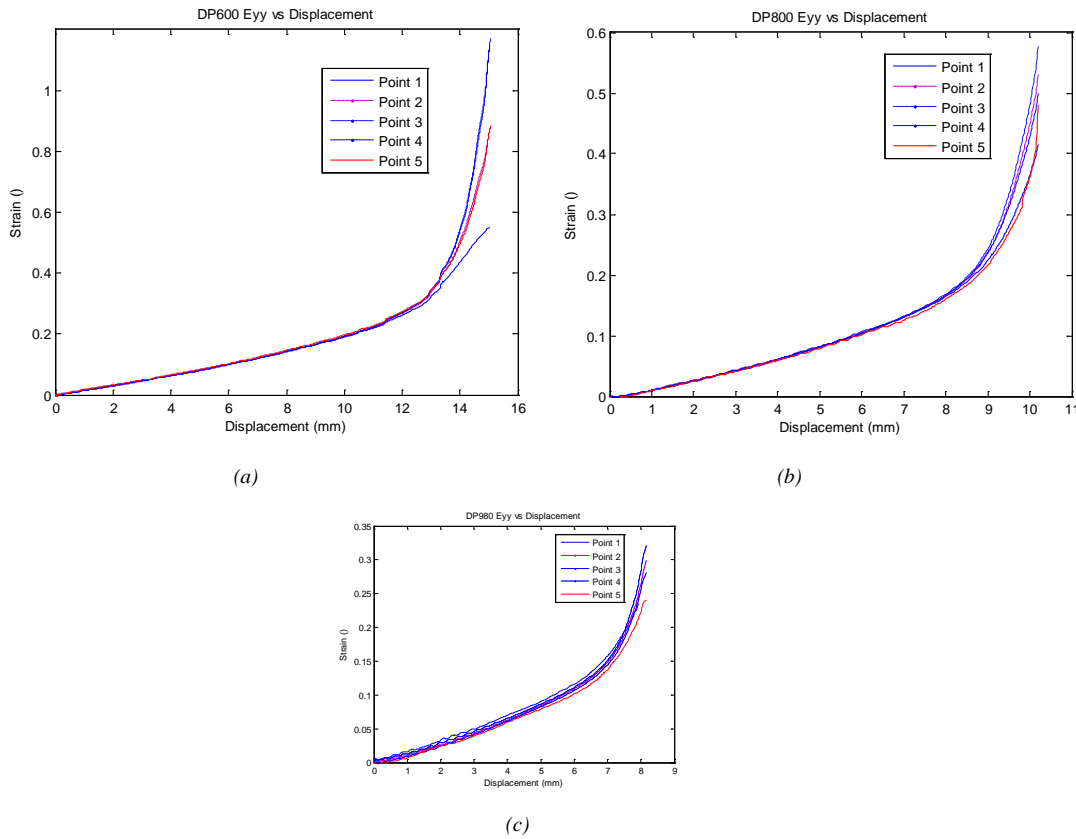


Figure 4. Strains in y direction of five points for (a) DP600, (b) DP800, and (c) DP980

4. CONCLUSIONS

In this study, DIC technique was performed to install uniaxial tensile test in order to get local strains. Three different material, DP600, DP800, and DP980, were used to calculate all points of strain curves versus displacement. Following conclusions can be made about the DIC method;

- 1) DIC can easily adapt to materials mechanical tests instead of traditional measurement methods.
- 2) A low cost, easy to setup and consumer camera system can be used for non-contact strain and displacement 2D measurements over flat specimens in uniaxial tensile test.
- 3) When the local strains take into account, the region (Point 3) which is the middle of the fracture area has always higher strains than the regions that are out of the fracture area for those materials.
- 4) The strains along the gage width are not homogenous. So, DIC method is an effective technique that can be used to determine local strain evolutions at the crack edge in notch specimens.

REFERENCES

- [1]. Doyle F. J., The historical development of analytical photogrammetry, *Photogrammetric Engineering*, 1964, 259–265.
 - [2]. Gruner H., Hugershoff R., *Photogrammetric Engineering*, Vol. 37, No. 9, 1971, 939–947.
 - [3]. Sutton M.A., Orteu J.J., Schreier H.W., *Image Correlation for Shape, Motion and Deformation Measurements*, Springer, 2009, 1-2.
 - [4]. Hobrough A.G.L., *The Photogrammetric Record*, Vol. 18, No. 104, 2003, 337–340.
 - [5]. Yoneyama S., Ogawa T., Kobayashi Y., Evaluating mixed-mode stress intensity factors from full-field displacement fields obtained by optical methods, *Engineering Fracture Mechanics*, Vol. 74, No. 9, 2007, 1399–1412.
 - [6]. Peters W.H., Ranson W.F., Digital imaging techniques in experimental stress analysis, *Optical Engineering*, Vol. 21, No. 3, 1982, 427–431.
 - [7]. Sutton M.A., Wolters W.J., Peters W.H., Ranson W.F., and McNeill S.R., Determination of displacements using an improved digital correlation method. *Image and Vision Computing*, Vol. 1, No. 3, 1983, 133–139.
 - [8]. McCormick N., Lord J., Digital Image Correlation, *Materials Today*, Vol. 13, No. 12, 2010, 52-54.
 - [9]. Zhu F., Bai P., Zhang J., Lei D., and He X., Measurement of true stress-strain curves and evolution of plastic zone of low carbon steel under uniaxial tension using digital image correlation, *Optics and Lasers in Engineering*, Vol. 65, 2015, 81-88.
 - [10]. Dong Y., Kakisawa H., and Kagawa Y., Development of micro scale pattern for digital image correlation up to 1400 °C, *Optics and Lasers in Engineering*, Vol. 68, 2015, 7-15.
 - [11]. SSAB Swedish Steel, 07-10-11,
 - [12]. Sreenivasan S., Xia M., Lawson S., and Zhou Y., Effect of laser welding on formability of DP980 steel, *Journal of Engineering Materials and Technology*, Vol. 130, 2008, 1-9.
-

THE MICROSTRUCTURE AND HARDNESS ANALYSIS OF DECARBURIZATION FOLLOWED BY BORONIZING AISI D3 TOOL STEEL

Arzum ULUKÖY

Pamukkale University, Department of Manufacturing Engineering, 20100, Denizli, Turkey.
aulukoy@pau.edu.tr

Yavuz KAPLAN

Pamukkale University, Department of Manufacturing Engineering, 20100, Denizli, Turkey.

Volkan ONAR

Pamukkale University, Department of Manufacturing Engineering, 20100, Denizli, Turkey.

Merve YILDIZ

Pamukkale University, Department of Manufacturing Engineering, 20100, Denizli, Turkey.

Emre ARMAĞAN

Pamukkale University, Department of Manufacturing Engineering, 20100, Denizli, Turkey.

Okan ÇARIK

Pamukkale University, Department of Manufacturing Engineering, 20100, Denizli, Turkey.

Ahmet Çetin CAN

Pamukkale University, Department of Mechanical Engineering, 20100, Denizli, Turkey.
acan@pau.edu.tr

Abstract

In this study, X210Cr12 (AISI D3, 1.2080) steel was subject to heat treatments including decarburizing, boronizing and hardening. Decarburizing and boronizing were carried out in a salt bath consisting of 60% NaCl and 40% NaCO₃ for 1 and 3 hours at 850 °C, and a liquid medium containing 70% borax and 30% silicon carbide for 5 hours at 980 °C, respectively. The microstructures of the diffusion layers were examined by means of optical microscopy. The microhardness profiles of these layers were studied by a Vickers indenter. The hardness value obtained by the decarburizing followed by boronizing process is 10% higher than a boronized specimen's hardness. The transition zone was enlarged approximately 4,5 mm via 3 hours decarburizing followed by boronizing process.

Keywords: Tool steel, boronizing, decarburizing, microstructure, hardness, transition zone

1. INTRODUCTION

Boriding can be described in the simplest way that a boride layer forms via diffusion of boron atoms to a material surface via thermochemical or electrochemical reactions [1]. As a result of boronizing a very thin, but very hard (1600-2000 HV), boride layer is obtained on the material surface depending on the chemical composition of the base material. If the process is applied to the iron-based material, the boride zone will consist of iron borides mainly.

The process can be applied to a wide range of metals and cermets [1],[2]. Solid, paste, gaseous, and plasma medium can be used as boron-yielding media. The other single or combined boriding methods can be listed as follows: physical vapor deposition (PVD), chemical vapor deposition (CVD), ion implantation, plasma spraying, multicomponent boriding, plasma sintering, ultra-fast boriding [2]-[12].

FeB and/or Fe₂B phases occur on the boronized steel surface. Despite having less hardness and less thermal expansion coefficient than the FeB phase, only the Fe₂B phase formation is preferred. If the two-phase layer is formed on the surface, incompatibility between the FeB/Fe₂B phases can increase the tendency of crack formation both the layer and between the layer and surface [1],[2],[5]-[8],[13]-[15]. Obtaining a one-phase Fe₂B layer or multicomponent boride layer is very useful especially to reduce brittleness [5], [6]. For this purpose, laser heat treatment (LHT) or multicomponent boronizing can be used [5-8], [13]-[16]. The length of multi-component transition zone is higher than the boronizing process. Thus, a small hardness gradient is provided between the boride layer and the core [5], [6],[16].

The directivity of elements in the base material affects boronized layer's properties such as hardness, and boride layer thickness. In addition, forming borides with N, Cu, or Ni can reduce the brittleness of the boride layer [8]. While Ni and C are diffused onto the material core and accumulate below the boride layer, Cr and Mn move opposite direction [2], [17]. The directivity of alloying elements affects the boride layer properties, also.

AISI D3 (1.2080) steel is an air/oil hardening cold-work alloy tool steel which has high carbon high chromium. The steel has approximately 2,1% C content and this situation can make diffusion of boron atoms difficult from surface to the matrix.

In this study, AISI D3 (1.2080) steel was subject to decarburizing before boronizing in order to facilitate boron atoms diffuse easier. The hardness of the boride layer and transition zone was determined. Thus, the effect of carbon content reduced on the surface by decarburizing process was investigated.

2. EXPERIMENTAL

2.1. Materials

High carbon and high chromium AISI D3 (X210Cr12, 1.2080) cold work tool steel (10 mm diameter) was used in the experiments. The chemical composition of the test material can be seen in Table 1.

Table 1. Chemical composition of the experimental material (wt%)

C	Cr	Si	Mn	P	S
2,2	11-13	0,252	0,247	0,025	0,0065

2.2. Methods

Boronizing, decarburizing, and boronizing followed by decarburizing process were applied to the test material. Boronizing experiments were performed in a salt bath consisting of 70% Na₂B₄O₇+ 30% SiC. Process temperature was selected 980 °C for 5 hours. The boronizing process was carried out in a salt bath consisting of borax and SiC. A borax and SiC salt bath mixture was applied to the same steel by Yuksel et al. and obtained 1900 HV hardness at the surface [18].

Decarburization process was applied in a salt bath consisting of 60% NaCl and 40% NaCO₃ at 850 °C for 1 and 3 hours. Karakullukcu [19], [20] decarburized AISI D3 steel in a furnace at 900 °C for 4 hours and then used a solid boronizing media for 3 or 5 hours. The work showed that the thickness and hardness of the boride layer was increased with increasing decarburization time. Ulukoy et al. [16], [21] found a one-phase iron boride layer (Fe₂B at the surface of 21NiCrMo₂ (AISI 8620) steel) after boronizing, borocarburing, and borodecarburizing. It was found that as a result of increasing decarburizing time the hardness of boride layer and length of transition zone was increased proportionally borocarburing specimens.

The abovementioned processes, the specimens' heat treatment parameters, and carried out specimens' numbers are seen Table 2. All of the specimens were cooled in oil. Afterwards, salt and oil wastes on

specimens' surfaces were cleaned with water. After surfaces were polished via using grinding papers (200,400,600,800,1000, and 1200 grids) and solutions (3 μm , 6 μm), specimens were etched by 4% nital for metallographic examinations. The microhardness from surface to the matrix was measured by a standard Vickers microhardness tester under 50 g load. The coating's surface morphology was examined through an optical microscope.

Table 2. The parameters of specimens' heat treatments

Number of Specimen	Process		
	Decarburizing		Boronizing
	Duration time (h)		Duration time (h)
	1	3	5
1	-	-	-
2	x	-	-
3	-	x	-
4	-	-	x
5	x	-	x
6	-	x	x

3. RESULTS and DISCUSSION

3.1. Microstructure

The optical microstructure images of the steel without any heat treatment (1), 1 h decarburized (2) and 3 h decarburized (3) are shown in Figure 1, Figure 2, and Figure 3. Decarburized regions are clearly seen in the images. The decarburized zone reached approximately 200 and 300 μm , 1 h decarburized and 3 h decarburized specimens respectively. Decarburized layer thickness increased in parallel with increasing decarburization time.

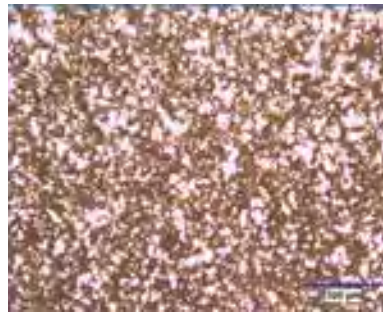


Figure 1. The microstructure of AISI D3 steel



Figure 2. The microstructure of 1 h decarburized AISI D3 steel (2)



Figure 3. The microstructure of 3 h decarburized AISI D3 steel (3)

Boride layer morphology was determined using optical examinations of borided (4), 1 h decarburized followed by boronizing (5), and 3 h decarburized followed by boronizing (6) specimens. The boride zone reached approximately 50-65 μm . The morphologies are shown in Figure 4, Figure 5, and Figure 6, and the morphologies were similar to earlier obtained morphologies on borided same steel [18]. The obtained layer thickness' are 50 μm , 65 μm , and 50 μm for borided (4), 1 h decarburized and borided (5), and 3 h decarburized and borided (6) specimens, respectively. Although 3 h decarburizing did not affect the boride layer thickness, the obtained layer thickness was increased by 1 h decarburizing process.



Figure 4. The microstructure of boronized AISI D3 steel (4)



Figure 5. The microstructure of 1 h decarburized followed by boronizing AISI D3 steel (5)



Figure 6. The microstructure of 3 h decarburized followed by boronizing AISI D3 steel (6)

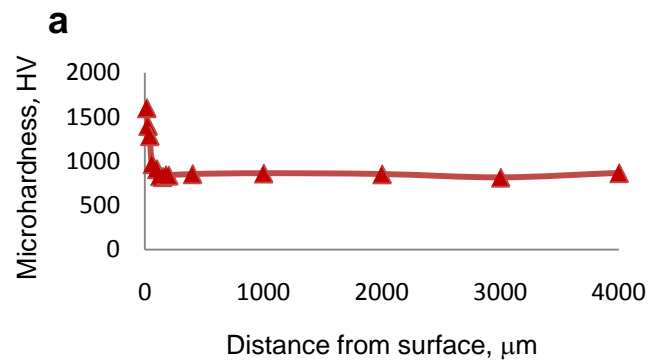
3.2. Hardness

The hardness of untreated AISI D3 steel is approximately 400 HV (1). The hardness value raised 820 HV with quenching in oil. Decarburizing lowers the hardness value 820 HV to 500HV. While the carbon ratio is decreased on the surface with increasing decarburizing time, the hardness value decreases proportionally. Obtained hardness values are compatible with previous works [22].

Figure 7a shows that boronized specimen's hardness distribution (4). 1600 HV hardness value was obtained at the surface and the hardness gradient was suddenly decreased after 150 μm from surface to the matrix. The substrate hardness appears around 200 μm from the surface.

Figure 7b shows that 1 h d ecarburized and then boronized specimen's hardness distribution (5). 1577 HV hardness value was obtained at the surface and the hardness gradient was suddenly decreased after 200 μm from surface to the matrix and hardness of this region was obtained 833 HV. But, the hardness gradient showed an increase from this region through the matrix, as seen in Figure 7b. Carbon atoms accumulate below the boride layer and this situation can form hard carbides under the boride zone. Thus, the transition zone length and hardness increase. It can be said that decarburizing process contributes increasing of transition zone length and hardness gradient before applying boronizing process.

Figure 7c shows that 3 h de carburized and then boronized specimen's hardness distribution (6). 1620 HV hardness value was obtained at the surface and the hardness gradient was suddenly decreased after 125 μm from surface to the matrix and hardness of this region was obtained 903 HV. But, the hardness gradient showed an increase from this region through the matrix just like other decarburized and boronized specimen (5), as seen in Figure 7c. All hardness values through the cross section (from surface to the matrix) were increased compared to all specimens. Hardness values were increased even in the core of material.



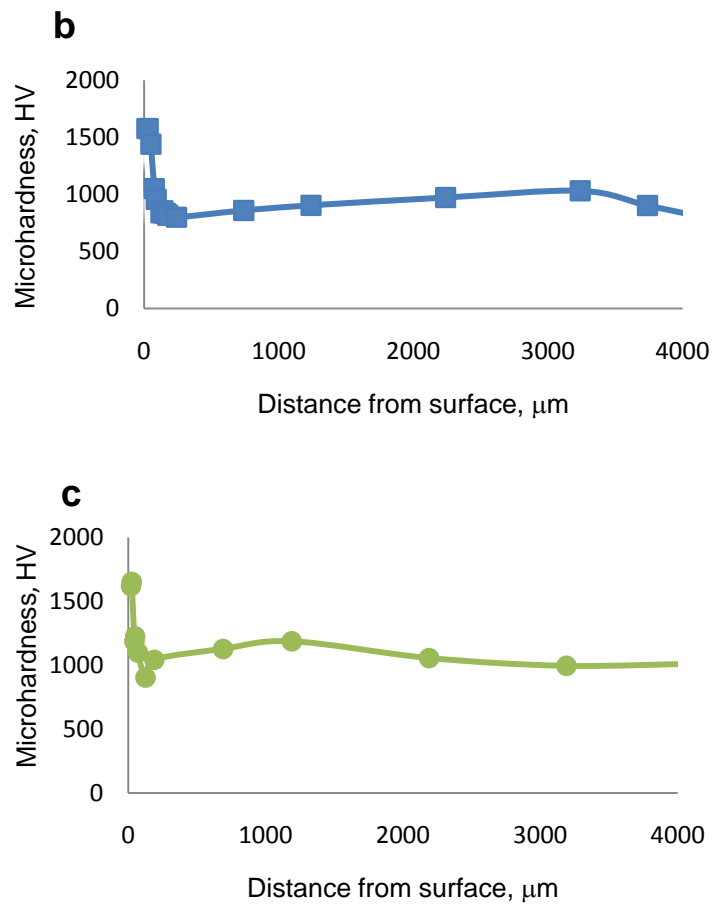
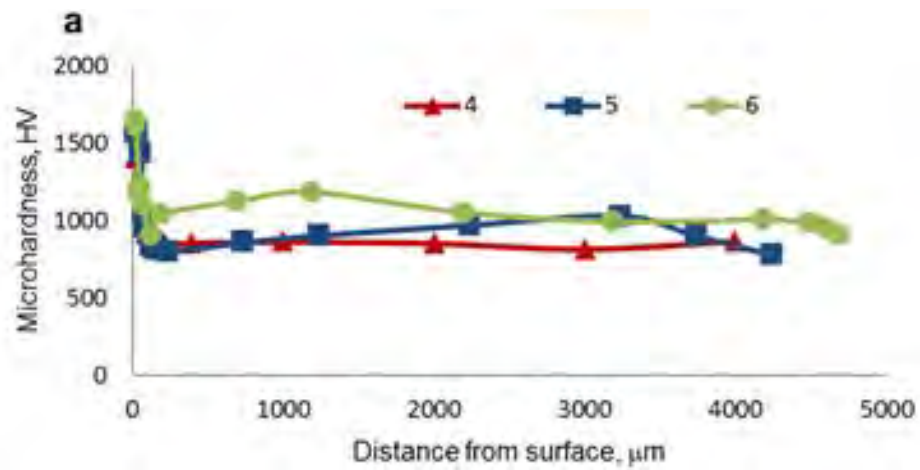


Figure 7. The microhardness distribution of boronized (a), 1 h decarburized and boronized (b) and 3 h decarburized and boronized (c) AISI D3 steel



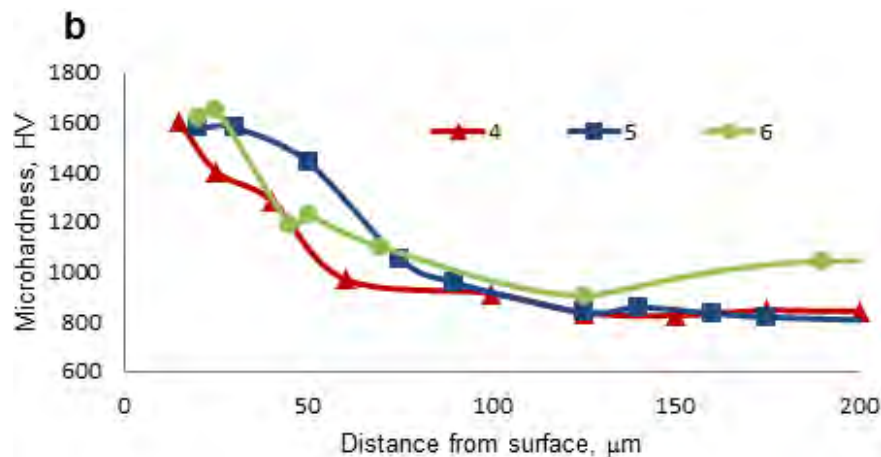


Figure 8. The microhardness distribution of boronized (4), 1 h decarburized and boronized (5) and 3 h decarburized and boronized (6) AISI D3 steel: a) at 5000 μm ; b) at 200 μm

4. CONCLUSIONS

In this study, AISI D3 (1.2080) steel was subject to decarburizing, boronizing and hardening. It was determined that the hardness values decreased at the surface after decarburizing. The transition zone enlarged and hardness values were increased even in the core of material via decarburizing followed by boronizing process.

The steel used as test material has high carbon and chromium content. The carbon content at the surface decreased after decarburizing process and decreasing carbon content facilitates boron atoms diffusion. It is known that carbon moves into the material core during boronizing and carbon atoms accumulate below the boride layer. This situation can form hard carbides under the boride zone. Thus, the transition zone length and its hardness increase. It can be said that decarburizing process contributes increasing of transition zone length and hardness gradient before applying boronizing process.

REFERENCES

- [1]. A. G. Von Matuschka, *Boronizing*, The Alden Press Ltd, 1980.
- [2]. A. K. Sinha, *ASM Metals Handbook-Vol 04: Heat Treating*, ASM Int., 1991.
- [3]. Jr. W. L. Aves, and G. A. Aves, "Borocarburing ferrous substrates," U.S. Patent Documents 4495006, 1985.
- [4]. Jr. W. L. Aves, "Pack composition for carburosiliconizing ferrous substrates," U.S. Patent Documents 4539053, 1985.
- [5]. A. Pertek, and M. Kulka, "Characterization of complex (B + C) diffusion layers formed on chromium and nickel-based low carbon steel," *Appl. Surf. Sci.*, vol. 202 (3-4), pp. 252-260, 2002.
- [6]. M. Kulka, A. Pertek, "Characterization of complex (B + C + N) diffusion layers formed on chromium and nickel-based low-carbon steel," *Appl. Surf. Sci.*, vol. 218, pp. 113-122, 2003.
- [7]. S. Sen, "The characterization of vanadium boride coatings on AISI 8620 steel," *Surf. and Coatings Techn.*, 190(1), pp. 1-6, 2004.
- [8]. Y. A. Balandin, "Boronitriding of die steels in fluidized bed," *Metal Science and Heat Treatment*, vol. 46(9-10), pp. 385-387, 2001.
- [9]. L. G. Yu, K. A. Khor, and G. Sundararajan, "Boriding of mild steel using the spark plasma sintering (SPS) technique," *Surf. Coat. Tech.*, vol. 157(2-3), pp. 226-230, 2002.
- [10]. C. H. Xu, J. K. Xi, and W. Gao, "Improving the mechanical properties of boronized layers by superplastic boronizing," *J. Mater. Process. Tech.*, vol. 65(1-3), pp. 94-98, 1997.
- [11]. C. L. Ge, and R. C. Ye, "Research on self-propagating eutectic boriding," *J. Mater. Process. Tech.*, vol. 124(1-2), pp. 14-18, 2002.
- [12]. S. Timur, G. Kartal, O. L. Eryilmaz, A. Erdemir, "Ultra-fast boriding of metal surfaces for improved properties," US Patent 20100018611, 2010.
- [13]. P. Gopalakrishnan, P. Shankar, R. V. Subba Rao, M. Sundarand S. S. Ramakrishnan, "Laser surface modification of low carbon borided steels," *Scripta Mater.*, vol. 44(5), pp. 707-712, 2001.
- [14]. M. Kulka and A. Pertek "Microstructure and properties of borocarbured 15CrNi6 steel after laser surface modification," *Appl. Surf. Sci.*, vol. 236(1-4), pp. 98-105, 2004.
- [15]. A. Pertek and M. Kulka, "Two-step treatment carburizing followed by boriding on medium-carbon steel," *Surf. Coat. Tech.*, vol. 173(2), pp. 309-314, 2003.
- [16]. A. Ulukoy, A. C. Can, Y. Ozmen, S. Tasgetiren, "Borocarburing of decarburized gears made from 21NiCrMo2 (AISI 8620) steel," *Proceedings of the Institution of Mechanical Engineers, Part L: Journal of Materials Design and Applications*, vol. 229, pp. 226-235, June 2015.

- [17]. K. Matiasovsky, M.Chrenkova-Paucirova, P.Fellner, M.Makya, "Electrochemical and thermochemical boriding in molten salts," *Surface and Coatings Technology*, vol. 35, pp. 133-149, 1988.
- [18]. M. Yuksel, A. C. Can and Y. Ozmen, "X210Cr12 (1.2080) takımçeliğinin tuz banyosunda borlanması," *Turkish J. Eng. Env. Sci.*, vol. 19, pp. 97-101, 1995.
- [19]. F. Karakullukçu, "Dekarbürize işleminin AISI H13 çeliğinin borlanma davranışına etkisi," M. Sci. Thesis, Sakarya University, Graduate School of Science, Sakarya, Turkey, 2002.
- [20]. F. Karakullukçu, K.Genel, M. İpek, "Dekarbürizasyonun AISI H13 çeliğinin borlanma davranışına etkisi," *Sakarya University Journal of Science*, vol. 6 (3), pp. 59-62, 2002.
- [21]. A. Ulukoy, "Boriding process application to gears made of 21NiCrMo2 (AISI 8620) together with carburizing," M. Sci. Thesis, Pamukkale University, Graduate School of Science, Denizli, Turkey, 2005.
- [22]. G. Parrish, *Carburizing: Microstructure and Properties*, ASM Int., 1999

Biography

Arzum ULUKÖY has a B.S. degree in Mechanical Engineering from Yildiz Technical University, a M.S. degree and a PhD degree in Mechanical Engineering from Pamukkale University. She has worked in Pamukkale University since 2002.

Specialties: Boronizing, borocarburing, fatigue, fretting, functionally graded material, mechanical design.

DETERMINATION OF THE EFFECTS OF OPERATING PARAMETERS ON THE RESIDUAL TURBIDITY OF QUARTZ SUSPENSIONS BY DESIGN OF EXPERIMENTS

Adem TAŞDEMİR

Eskişehir Osmangazi University, Department of Mining Engineering, 26480,
Batı Meşelik/İstanbul, Turkey. atadem@ogu.edu.tr

Tuba TAŞDEMİR

Eskişehir Osmangazi University, Department of Mining Engineering, 26480,
Batı Meşelik/İstanbul, Turkey. tubat@ogu.edu.tr

Abstract

This research represents the results of flocculation of quartz particles in suspensions with an anionic flocculant by applying response surface method (RSM). The experiments were designed and carried out according to the Bohn-Behnken Design (BBD) which is a type of RSM. A BBD with five independent parameters at three levels was applied to jar test studies to investigate the effect of variables examined on quartz flocculation process. Flocculant dosage, rapid mixing time, rapid mixing rate, solid ratio and settling time were tested to evaluate the main and interaction effects of these factors on residual turbidity. An empirical quadratic model with a high correlation coefficient was obtained for the estimation of residual turbidity within the investigated ranges of parameters.

Keywords: *Quartz suspension, Flocculation, Response surface method, Box-Behnken Design.*

1. INTRODUCTION

Dewatering is a process identified as a part of solid/liquid separation and is an important process in most mineral processing operations. Generally, dewatering is accomplished by sedimentation or filtration ([1], [2]). Aggregation of fine particles in mineral suspensions can be carried out by applying methods such as coagulation, flocculation or agglomeration methods [3]. Knowledge of detailed information while applying an aggregation method on a special material are necessary to understand the mechanisms and to use less possible amount of reagents during the processes.

Flocculation is usually a necessary pretreatment step in many dewatering streams containing significant quantity of very fine particles. The purpose of flocculation is to form aggregates or flocs from finely dispersed particles with the help of long chain polymers which are referred to as flocculants. Flocculation of suspended particles by polymeric flocculants is a multistep process. A classical coagulation/flocculation process consists of three separate steps: i) Rapid or flash mixing: the suitable chemicals (coagulants/flocculants and if required pH adjusters) are added to the wastewater stream, which is intensively mixed at high speed. ii) Slow mixing (coagulation and flocculation): the wastewater is only moderately stirred in order to form large flocs, which are easily settled out. iii) Sedimentation: the floc formed during flocculation is allowed to settle out and is separated from the effluent stream ([4], [5]).

In a flocculation process applied, finding the optimum flocculation conditions is a very important entity. The flocculation of fine particle suspensions is a complex process and the effectiveness of the process depends not only on the usage of appropriate chemical reagents (coagulants, flocculants, etc.) but also on how they are applied. Flocculation is affected by the complex interactions between a numbers of factors. These factors may include slurry properties such as particle size and surface charge of particles, solution chemistry, pH and physical variables such as mixing intensity (rate), mixing time and settling time. Each of them determines the flocculation rate and efficiency in term of settling rate, supernatant turbidity and sediment volume ([6], [7]). Therefore, determination of the flocculation behavior of the suspensions is important for an efficient solid/liquid separation. Jar test is one of the most efficient and commonly used methods to determine optimum flocculation conditions.

Classical jar test experiments are usually carried out by systematically changing the level of one factor at a time (OFAT). In OFAT jar test experiments, optimum flocculation conditions are determined by varying a single factor while holding the level of the other factors constant [8]. The level of the factor that results in the best response (e.g. lowest residual turbidity) is then selected and used in subsequent tests which continue in the same manner for other factors [9]. But it is time consuming and does not fully explore the whole experimental space to find the best factors' conditions. Also, it is incapable of identifying the interaction effects resulting from the factors being considered. The classical jar test experiments of OFAT and studying the effect of the variable on the response is a complicated technique, particularly in a multivariate system as in the case of flocculation or if more than one response are of importance. Design of experiments (DOE) is statistical techniques which can be used for optimizing such multivariable systems. For these reasons, DOE has been proposed for the jar tests to overcome the shortcomings and to determine the influences of individual factors and their interactive influences.

The response surface methodology (RSM) which is a combination of experimental, regression analysis and statistical inferences is one of the DOE approach. It is useful for modeling and analyzing problems in which responses of interest are influenced by several factors or variables and in which objective is to optimize the responses. The RSM not only reduces the cost and time, but also provides required information about the interaction effects with minimum number of experiments [10].

There are many scientific works investigating effect of slurry properties such as flocculant dosage, pH on flocculation in the literature ([11]-[21]). However, fewer researches exist about the mixing conditions on flocculation ([4], [21]-[26]). The effect of mixing conditions under constant slurry properties on residual turbidity for the flocculation of quartz sample with anionic flocculant used in this work have been investigated recently by us [25]. Results of this study showed that the effect of rapid mixing rate and time are more important factors compared to slow mixing rate, slow mixing time and settling time. We have also previously examined the effect of slurry properties (flocculant dosage, pH and solid ratio) at constant mixing and settling conditions on residual turbidity for the same material [13]. According to this research, the efficiency of quartz flocculation was dependent to a large extent pH of the suspensions and the excellent results were obtained at alkaline media. However, the results at natural pH were not good compared to acidic or alkaline suspensions. Interaction between solid ratio and flocculant dosages on residual turbidity of suspensions were found to be significant in all pH values tested.

In this study, the effects of five independent variables which include the slurry and mixing conditions of flocculation process namely, flocculant dosage, rapid mixing rate, rapid mixing time, solid ratio and settling

time on the flocculation behavior of quartz suspensions were investigated at natural pH of the suspensions. Since numerous numbers of experiments are needed to research the effects of five variables tested, the efficiency of flocculation under tested conditions was determined to examine the main and interaction effects between these variables by the application of five parameter Box-Benhken design (BBD).

2. EXPERIMENTAL

2.1 Materials and Method

A pure quartz sample from Çine region of Turkey was obtained and used in the experiments. The particle size of the sample was less than 20 µm sieve aperture. According to the particle size distribution determined by Malvern Mastersizer 2000, d_{90} , d_{50} and d_{10} diameters were obtained as 15.7 µm, 2.2 µm and 0.6 µm respectively. According to the XRD results all the peaks belonged to quartz and the sample contains more than 95.6 % SiO₂ content indicating that the sample is pure enough. The quartz sample which may causes pollution was chosen as a pollutant material since it is considered as one of the common components present in soils and clays [27].

SPP 508 (supplied from Superkim, Turkey) polymer was used for the flocculation of synthetically prepared fine quartz suspensions. Medium anionic SPP 508 is a high molecular weight ($15-22 \times 10^6$ g/mol) polyacrylamide with 28% degree of ionization. A solution of polymer (0.01%) was prepared using distilled water. The pH of the solutions was not changed during the experiments and held constant at its natural pH. The neutral pH of samples was determined as 7.95 for all solid ratios by a pH-meter (Orion 5 Star).

A jar test apparatus (Velp Scientifica FC6S) was used in order to determine the effectiveness of flocculant in the experimental conditions tested. It consists of a set of six beakers, which can be stirred simultaneously at specified speed. The flocculation tests consisted of three stages. First, the flocculant was added to the suspension and a rapid mixing was initiated. The objective is to obtain complete mixing of the flocculant with the suspension to maximize the effectiveness of destabilization of colloidal particles and initiate flocculation. Critical parameters for this stage are the rapid mixing time (duration) and the rapid mixing rate (intensity). Second, the suspension was slowly stirred to increase contact between flocculating particles and to facilitate the development of large flocs. In each experiment, a 10 minute slow mixing at 30 rpm was applied. Finally, mixing was terminated. The flocs are allowed to settle at predetermined settling times and then the turbidity of the supernatants was measured.

The turbidimeter (HF Scientific) was used to measure the residual turbidity. The turbidity is expressed in NTU (Nephelometric turbidity units). The initial turbidity of the samples were determined as 306 NTU for 0.1% solid ratio sample, 2496 NTU for 0.55% solid ratio sample and 4400 NTU for 1.0% solid ratio sample.

2.1 Design of Experiments

The surface response method RSM, using the Box-Behnken experimental design, yielded correlations between the residual turbidity of quartz suspensions and the five independent factors. The RSM involves an empirical model to evaluate the relationship between a set of controllable experimental factors and observed results. Factors considered included the flocculant dosage (mg/l), rapid mixing time (min), rapid mixing rate (rpm), solid ratio (%) and settling time (min). They are represented by *A* to *E*, respectively. The low, middle and high levels of each variable were designated as -1, 0 and +1 respectively, as listed in Table 1. The experiments were carried out according to the BBD which is given in Table 2.

Table 1. Factors and levels for experimental design using BBD

Variables	Ranges and coded levels		
	-1	0	+1
A: Flocculant dosage (mg/l)	0.02	0.41	0.80
B: Rapid mixing time (min)	1	3	5
C: Rapid mixing rate (rpm)	100	200	300
D: Solid ratio (%)	0.1	0.55	1.0
E: Settling time (min)	5	15	25

Table 2. Box-Behnken design of five experimental variables in coded units

Run	Factors					Run	Factors				
	A	B	C	D	E		A	B	C	D	E
1	-1	-1	0	0	0	24	0	-1	-1	0	0
2	1	-1	0	0	0	25	0	1	-1	0	0
3	-1	1	0	0	0	26	0	-1	1	0	0

4	1	1	0	0	0	27	0	1	1	0	0
5	0	0	-1	-1	0	28	-1	0	0	-1	0
6	0	0	1	-1	0	29	1	0	0	-1	0
7	0	0	-1	1	0	30	-1	0	0	1	0
8	0	0	1	1	0	31	1	0	0	1	0
9	0	-1	0	0	-1	32	0	0	-1	0	-1
10	0	1	0	0	-1	33	0	0	1	0	-1
11	0	-1	0	0	1	34	0	0	-1	0	1
12	0	1	0	0	1	35	0	0	1	0	1
13	-1	0	-1	0	0	36	-1	0	0	0	-1
14	1	0	-1	0	0	37	1	0	0	0	-1
15	-1	0	1	0	0	38	-1	0	0	0	1
16	1	0	1	0	0	39	1	0	0	0	1
17	0	0	0	-1	-1	40	0	-1	0	-1	0
18	0	0	0	1	-1	41	0	1	0	-1	0
19	0	0	0	-1	1	42	0	-1	0	1	0
20	0	0	0	1	1	43	0	1	0	1	0
21	0	0	0	0	0	44	0	0	0	0	0
22	0	0	0	0	0	45	0	0	0	0	0
23	0	0	0	0	0	46	0	0	0	0	0

The independent variables and the mathematical relationship between the response Y and these variables can be approximated by a quadratic polynomial equation (1):

$$Y = b_0 + b_1A + b_2A + b_3A + b_4A + b_5A + b_{12}AB + b_{13}AC + b_{14}AD + b_{15}AE + b_{23}BC + b_{24}BD + b_{25}BE + b_{34}CD + b_{35}CE + b_{45}DE + b_{11}A^2 + b_{11}B^2 + b_{33}C^2 + b_{44}D^2 + b_{55}E^2 \quad (1)$$

Where; Y is the predicted response variable (turbidity), b_0 is the model constant, $b_1 - b_5$ linear coefficients, $b_{12}, b_{13}, b_{14}, b_{15}, b_{23}, b_{24}, b_{25}, b_{34}, b_{35},$ and b_{45} are the cross product coefficients and $b_{11}, b_{22}, b_{33}, b_{44}$ and b_{55} are the quadratic coefficients [28]. Factors and levels and Box-Behnken design of five experimental variables in coded units are given in Table 1 and Table 2 respectively.

3. RESULTS AND DISCUSSIONS

3.1 Model Fitting

The residual turbidity values obtained and predicted by the BBD model in each experiment are presented in Table 3. Analysis of the Box-Cox plots showed that residuals could be reduced significantly by a log transformation since the residual turbidity values has broad range of response from 3.3 to 62 NTU.

Table 3. Response results and predicted turbidities in supernatants

Run	Turbidity		Ln of Turbidity		Run	Turbidity		Ln of Turbidity	
	Obs.	Pre.	Obs.	Pre.		Obs.	Pre.	Obs.	Pre.
1	57	48.13	4.04	3.84	24	19.2	25.79	2.95	3.12
2	38	26.15	3.64	3.34	25	7.5	6.31	2.01	1.86
3	27	32.90	3.3	3.27	26	3.5	10.42	1.25	1.83
4	11	13.93	2.4	2.28	27	3.3	2.44	1.19	1.45
5	14	16.76	2.64	2.86	28	9.3	22.97	2.23	3.06
6	19.8	13.79	2.99	2.54	29	21.7	36.04	3.08	3.81
7	15	20.71	2.71	2.93	30	62	53.82	4.13	4.10
8	7.5	4.44	2.01	1.56	31	7.3	-0.21	1.99	1.86
9	16	19.63	2.77	2.71	32	18.5	13.86	2.92	2.56
10	5	5.66	1.61	1.91	33	3.8	3.30	1.34	1.62
11	15	19.38	2.71	2.75	34	17	12.92	2.83	2.49
12	4.5	5.91	1.5	1.91	35	4.2	4.23	1.44	1.73
13	53	47.39	3.97	3.98	36	34	35.95	3.53	3.41
14	19	19.46	2.94	3.18	37	16.3	14.47	2.79	2.63
15	31.6	30.31	3.45	3.08	38	32.5	34.94	3.48	3.39
16	12.5	17.29	2.53	2.39	39	16.8	15.47	2.82	2.69
17	17.2	15.18	2.84	2.84	40	32	24.55	3.47	3.00
18	7.9	10.68	2.07	2.20	41	16	4.52	2.77	2.07
19	17.2	13.38	2.84	2.68	42	8.9	15.55	2.18	2.44
20	11.5	12.48	2.44	2.42	43	5.5	8.13	1.7	1.73
21	4.6	6.69	1.52	1.78	44	7	4.29	1.95	1.59
22	4.6	6.69	1.53	1.78	45	7.2	4.29	1.97	1.59
23	4.8	6.69	1.57	1.78	46	4.8	4.29	1.57	1.59

The Box-Cox plot provides a guideline for selecting the correct power law transformation ($y' = y^\lambda$). For this reason, the dependent variable produced after transformation transformation was named as Ln (Turbidity).

After evaluation of experimental results, a quadratic function for the residual turbidity in terms of coded factors was obtained with a determination coefficient of 0.84 (R^2) and hence correlation coefficient of 0.9165 (R) as:

$$\begin{aligned} \ln(\text{Turbidity}) = & 1.68 - 0.37A - 0.41B - 0.42C - 0.23D + 0.012E - 0.12AB + 0.03AC - 0.75AD + \\ & 0.02AE + 0.22BC + 0.05BD - 0.01BE - 0.26CD + 0.04CE + 0.09DE + 1.15A^2 + 0.25B^2 + 0.23C^2 + \\ & 0.47D^2 + 0.29E^2 \end{aligned} \quad (2)$$

According to this result, the 84 % of the variance can be explained by Eq. 2 and 16% of the variance could not be defined by the model.

3.2 Main Effects of Parameters

The main effect of individual variables of A , B , C , D and E and the perturbation plot which shows the comparison of all factors are plotted in Fig. 2 (a-e) and Fig. 2(f) respectively. In Fig. 2 (a-f), the log transformed residual turbidity is plotted by changing only one factor over its range while the others held constant at their center points. Therefore, both individual and perturbation plots show the main effects of these parameters on residual turbidity at center points of parameters. All individual variables were found to have their own important effect of residual turbidity. It is seen that variables have a curvature effect indicating that the turbidity removal by quartz flocculation within the investigated ranges of variables could be adequately explained by a second order model used in this study. Since the flocculation is considered as a second order rate process, the quadratic model by BBD can adequately describe the flocculation of quartz suspensions within the ranges of variables tested. According to the main effects plots in Fig. 2, the flocculant dosage, A , was the most effective parameter (Fig. 2.a). Initially, the residual turbidity decreases as the increasing of A and thereafter again increases. Altered rapid mixing time (B) and rapid mixing rate (C) affect the residual turbidity. An increase in these operating variables results in an improvement supernatant turbidity as seen in Fig 2 (b-c). While keeping the all parameters at their middle values, solid ratio had a quadratic effect on residual turbidity as shown in Fig. 2(d). Settling time (E) had less a little curvature effect on the response (Fig. 2.e). However, it is not very significant statistically in the investigated range.

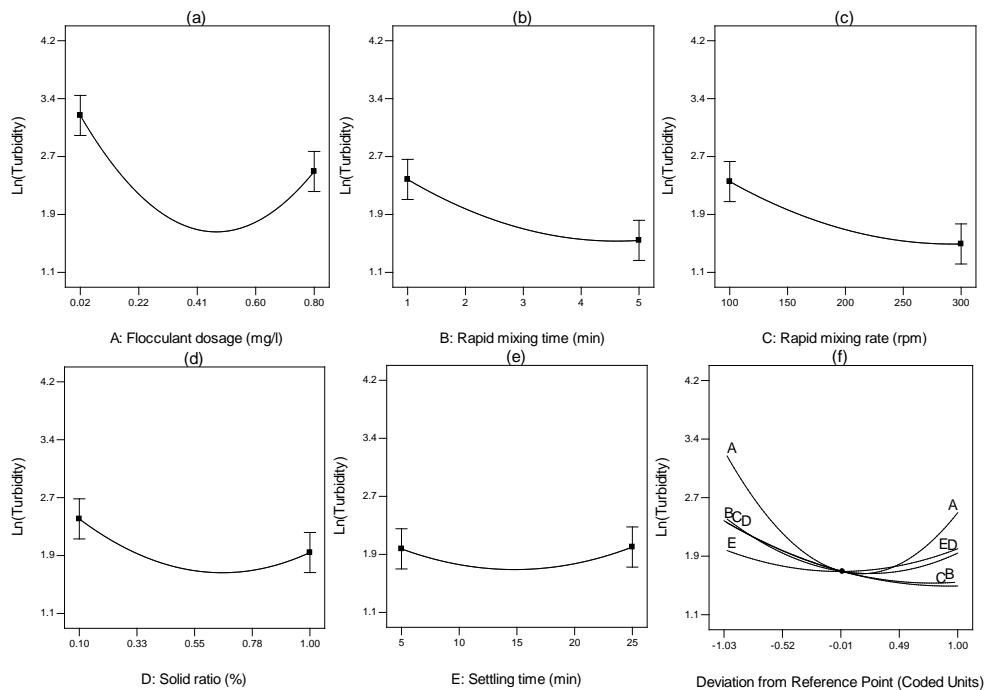


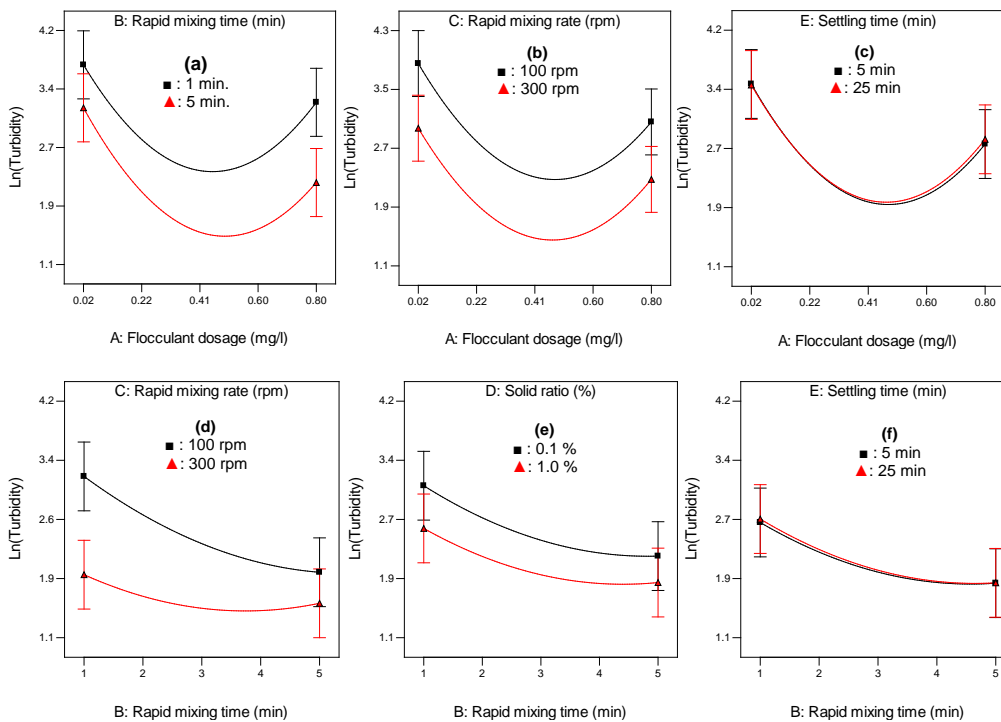
Figure 2. Main effects of flocculation variables (a-e) and perturbation plot for the response (f). For each factor, the remaining factors have held at their middle levels.

3.3 Interactions Between Factors

Figure 3 (a-i) shows the second order interactions among the factors and curvature effects as predicted by the second order model. The log transformed residual turbidity is plotted by changing only one factor over its range while the others held constant at their center points in Fig. 3 (a-i). It should be noted that the response variable values plotted as a function of one operating parameter over a range of values and the other parameter at two levels indicate the parameter interaction effects. In other words, lines in parallel indicate no parameter interaction effects between the two variables considered. Fig. 3 shows that there are no significant interactions between the variables represented on these plots. The most efficient interaction was found

between flocculant dosage (*A*) and solid ratio (*D*) and it is given in Fig. 4. However, we can see that altered the process variables from their low values to high values affect the responses significantly (Figs. 3.a, 3.b, 3.d, 3.e and 3.g). On the other hand, changing settling time from 5 min. to 25 min. did not affect the responses considerably since the flocs quickly settle out within the first 5 minute (Figs. 3.c, 3.f, 3.h and 3.i).

In the interaction plots presented in Fig. 3, we can see the effect of rapid mixing rate and time on the residual turbidity of quartz suspensions achieved. In Fig. 3(a, b, d, e, f, g and h) it can be seen clearly that increasing rapid mixing rate from 100 to 300 rpm and increasing the rapid mixing time from 1 to 5 minutes reduces the supernatant turbidities of quartz suspensions. These plots indicate that higher turbidity removal can be achieved by keeping the rapid mixing time and rate at their maximum values when the other variables held constant at their middle values. The first stage of flocculation process is to add the flocculant to the suspension and then a rapid and high intensity mixing is initiated. Reference [7] states that the initial mixing intensity and the mixing time are the most important parameters in the determining the size of the flocs formed and rapid mixing conditions can have major effects on the flocculation process [7]. The flocculants are usually added as fairly concentrated and viscous solutions during the flocculation process. Therefore, intense mixing is needed to achieve rapid and uniform distribution of the polymer molecules throughout the suspension [29]. The objective is to obtain complete mixing of the flocculant with the suspension to maximize the effectiveness of destabilization of suspended particles. The effects of fast stirring rate on flocculation process are well known and some detailed studies have been carried out ([22]-[26]). Reference [7] showed that the poor performance of a flocculation process in the many applications could be attributed to inadequate mixing [6]. If the fast mixing rate is not enough, the flocs are hardly grow and longer flocculation time is required. Insufficient mixing can also lead to local overdosing and restabilization of some particles, which is responsible for the residual haze in suspensions ([22]-[24]). On the contrary, too high intensity of mixing rate and long mixing time may cause breakup of flocculated flocs and this may cause detrimental effects on flocculation [30]. According to Fig. 3d, at constant solid ratio, flocculant dosage and settling time, more stirring time is required at low stirring rate of 100 rpm to achieve the same turbidity in the supernatant solution. However, at highest stirring rate of 300 rpm, residual turbidity remains almost constant after 3 min fast mixing time.



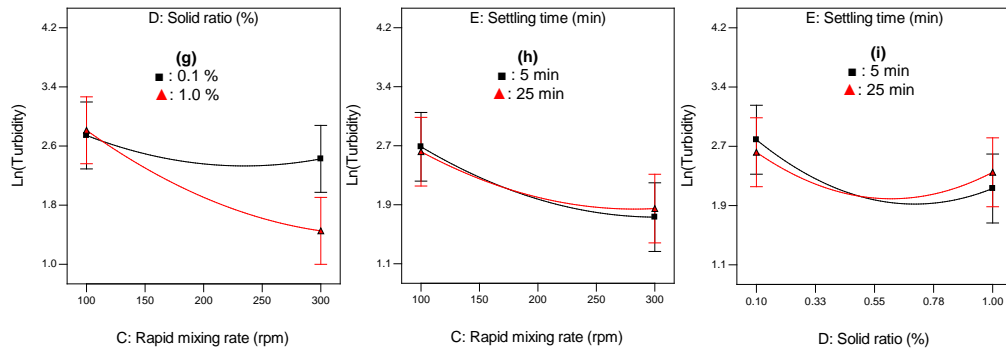


Figure 3. Interaction plots showing effects of flocculation parameters on residual turbidity. For each pair of factors, the remaining factors have held at their midpoint values.

The effects of fast mixing rate/time and solid ratio on residual turbidity are shown in Fig. 3e and 3g when the other variables held constant at their midpoints. As seen in these plots, there are no clear interactions between rapid mixing rate-solid ratio and rapid mixing time-solid ratio parameters. Increasing rapid mixing time decreases the residual turbidity for all solid ratios but it has a more pronounced effect for the higher solid ratio at constant mixing rate of 200 rpm, flocculant dosage of 0.41 mg/l and settling time of 15 minutes (Fig. 3e). In addition, higher turbidity removal was achieved with increasing rapid mixing time from 1 min. to 5 min. Confirming these findings, it was shown that the effects of mixing conditions are much more apparent for suspensions with higher solid concentrations ([22], [23],[26]). Also, these findings confirmed that flocculation is a second order rate process and flocculation rate depends on the square of particle concentration [29]. These may due to the higher collision probability which causes adsorption of flocculant molecules onto particle surfaces and flocculation of particles for the higher particle concentrations. It is possible to achieve the same turbidity values at rapid mixing rate of 100 rpm for all solid concentrations but less turbidity are accomplished by increasing the mixing rate for the solid ratio of 1.0% while the residual turbidity values remain almost constant for the solid ratio of 0.1% (Fig. 3g). These results may be attributed to the increase in collision probability between the quartz particles and flocculant at higher solid concentrations [30].

The effects of flocculant dosage and solid ratio on residual turbidity while keeping the other variables at their midpoint levels are shown on the interaction and contour plots in Fig. 4.

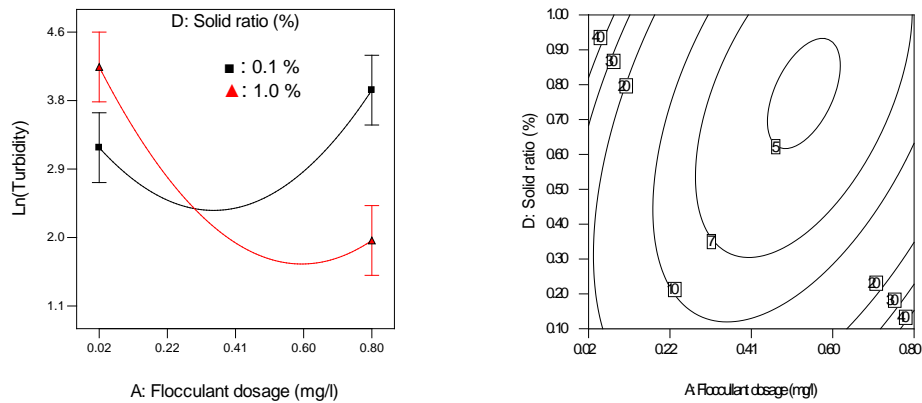


Figure 4. Interaction graph (left) and contour plot (right) of residual turbidity showing effect of solid ratio and flocculant dosage. The other variables are held constant at their midpoint levels.

As seen from these plots, there is an important interaction between the solid ratio and flocculant dosages. The residual turbidity is decreased with increasing flocculant dosages then increases again after a critical flocculant dosage for the both low and high solid ratio. As seen, less amount of flocculant is sufficient for the solid content of 0.1%. It is well known from the literature that, the optimum polymer dosage generally increases proportionally when particle concentration increases [29]. These critical flocculant dosages indicate the half surface coverage point described by References [2] and [31]. Excess amount of flocculant higher than optimum dosages starts to reverse effect on the residual turbidity for all solid concentrations. In Fig. 3a and 3b, we can see similar effect of flocculant dosage with rapid mixing speed and time and on the supernatant turbidity at constant solid ratio of 0.55% and settling time of 15 minutes. In these figures, residual turbidity decreases with increasing of flocculant dosage up to an optimum dosage and then increase again with over dosage of flocculant.

3.4 Simplified Model for Residual Turbidity

Since some terms of the model in Eq. (2) do not statistically significant at 95% significance level, removal of them did not change the R^2 significantly and a simpler model containing less parameter was obtained for estimating the residual turbidity. The other model terms in Eq. 3 were obtained after removing the insignificant terms (Prob >F more than 0.1) in Eq. 2 for the model improvement by applying backward elimination procedure. Final second order equation in terms of coded factors for the supernatant turbidity estimation was obtained as:

$$Ln(\text{Turbidity}) = 1.68 - 0.37A - 0.41B - 0.42C - 0.23D + 0.012E - 0.75AD + 1.15A^2 + 0.25B^2 + 0.23C^2 + 0.47D^2 + 0.29E^2 \quad (3)$$

According to the interaction effect analysis, flocculant dosage and solid ratio (AD) on supernatant turbidity were found statistically significant compared to other interactions between variables. The determination coefficient, R^2 , hence correlation coefficient, R , were calculated to be 0.82 and 0.9055 respectively.

4. CONCLUSIONS

Flocculation is defined as a second order rate process. This study confirmed the quadratic effects of investigated parameters on the residual turbidity of quartz suspensions resulted from jar test of flocculation process and showed that the mixing conditions (rapid mixing rate and time) and flocculant dosage had a great influence on the flocculation process. The second order equation obtained from the BBD method can be used to determine the optimum flocculation conditions of quartz suspensions within the investigated ranges of variables.

The second order effect of flocculant dosage (A^2) was found to be the most significant factor to have the largest effect on supernatant turbidity and this was followed by the linear effect of rapid mixing rate (C), linear effect of rapid mixing time (B), the two level interactions between flocculant dosage and solid ratio (AD), the linear effect of flocculant dosage (A), the second order effect of solid ratio (D^2). Moreover the main effect of solid ratio (D), the second order effect of settling time (E^2), the second order of rapid mixing time (B^2) and the second order of rapid mixing time (C^2) were determined to affect the residual turbidity of suspensions. It should be realized that this order of significance is valid strictly within the range of parameter values tested in this study.

ACKNOWLEDGEMENT

This study presents preliminary results of a project supported by Scientific Research Projects Committee of Eskişehir Osmangazi University (Project No: 200815020).

REFERENCES

- [1]. R. Hogg, "Flocculation and dewatering," *International Journal Mineral Processing*, vol. 58, pp. 223-236, 2000.
- [2]. T. Tripathy and De, B. Ranjan, "Flocculation : A New Way to Treat the Waste Water," *Journal of Physical Sciences*, vol. 10, pp. 93-127, 2006.
- [3]. A. Özkan, H. Uçbeyiay, and S. Düzyol, "Comparison of stages in oil agglomeration process of quartz with sodium oleate in the presence of Ca (II) and Mg(II) ions," *Journal of Colloid and Interface Science*, vol. 329, pp. 81-89, 2009.
- [4]. J. M. Ebeling, P. L. Sibrell, S. R. Ogden and S. T. Summerfelt, "Evaluation of chemical coagulation- flocculation aids for the removal of suspended solids and phosphorus from intensive recirculating aquaculture effluent discharge," *Aquacultural Engineering*, vol. 29, pp. 23-42, 2003.
- [5]. M. Rossini, J. Garrido and M. Garcia Galluzzo, "Optimization of the coagulation-flocculation treatment influence of rapid mix parameters," *Water Research*, vol. 33(8), pp. 1817-1826, 1999.
- [6]. Ü. İpekoğlu, *Dewatering and Methods*, İzmir, Turkey: Dokuz Eylül University, Mining Faculty Impress, No: 179, 1997.
- [7]. J. Gregory, *Particles in Water: Properties and Process*, London, United Kingdom: University College, 2005.
- [8]. T. K. Trinh, and L. S. Kang, "Application of response surface method as an experimental design to optimize coagulation tests," *Environmental Engineering Research*, vol. 15(2), pp. 63-70, 2010.
- [9]. M. Zainal-Abideen, A. Aris, F. Yusof, Z. Abdul-Majid, A. Selamat, and S. I. Omar, "Optimizing the Coagulation Process in A Drinking Water Treatment Plant-Comparison Between Traditional and Statistical Experimental Design Jar Tests," *Water Science & Technology*, pp. 496-503, 2012.
- [10]. J. P. Wang, Y. Z. Chen, X. W. Ge, H. Q. Yu, "Optimization of coagulation-flocculation process for a paper-recycling wastewater treatment using response surface methodology," *Colloids and Surfaces A: Physicochem. Eng. Aspects*, vol. 302, pp. 204-210, 2007.
- [11]. T. Taşdemir, and H. Kurama, "Fine Particle Removal from Natural Stone Processing Effluent by Flocculation," *Environmental Progress & Sustainable Energy*, vol. 32(2), pp. 317-324, 2013.
- [12]. E. Sabah, and C. Açiksöz, "Flocculation Performance of Fine Particles in Travertine Slime Suspension," *Physicochemical Problems of Mineral Processing*, vol. 48(2), pp. 555-566, 2012.
- [13]. A. Taşdemir, T. Taşdemir, and H. Kılıç, "Usage of Box-Behnken Experimental Design for The Flocculation of Quartz Suspensions," in *Proc. The 14th Balkan Mineral Processing Congress*, 2011, pp. 250-256.
- [14]. E. Sabah, and Z. E. Erkan, "Interaction mechanism of flocculants with coal waste slurry," *Fuel*, vol. 85, pp. 350-359, 2006.

- [15]. A. Sworska, J. S. Laskowski, G. Cymerman, "Flocculation of the Syncrude fine tailings Part I. Effect of pH, polymer dosage and Mg^{2+} and Ca^{2+} cations," *International Journal of Mineral Processing*, vol. 60, pp. 143–152, 2000.
- [16]. P. Somasundaran, and S. Krishnakumar, "Adsorption of surfactants and polymers at the solid-liquid interface," *Colloids Surfaces A: Physicochemical and Engineering Aspects*, pp. 491-513, 1997.
- [17]. M.L. Taylor, G.E. Morris, P.G. Self, and R.St.C. Smart, "Kinetics of Adsorption of High Molecular Weight Anionic Polyacrylamide onto Kaolinite: The Flocculation Process," *Journal of Colloid and Interface Science*, vol. 250, pp. 28–36, 2002.
- [18]. J.M. Henderson, and A.D. Wheatley, "Factors Affecting the efficient flocculation of tailings by polyacrylamides," *Coal Preparation*, vol. 1987(4), pp. 1-49, 2007.
- [19]. X. Yu, and P. Somasundaran, "Role of Polymer Conformation in Interparticle-Bridging Dominated Flocculation," *Journal of Colloid and Interface Science*, vol. 177, pp. 283-287, 1996.
- [20]. L. Besra, D. K. Sengupta, S. K. Roy, and P. Ay, "Influence of polymer adsorption and conformation on flocculation and dewatering of kaolin suspension," *Separation and Purification Technology*, vol. 37, pp. 231-246, 2004.
- [21]. B. Ersoy, "Effect of pH and polymer charge density on settling rate and turbidity of natural stone suspensions," *International Journal of Mineral Processing*, vol. 75, pp. 207 – 216, 2005.
- [22]. J. Gregory, and L. Guibai, "Effects of dosing and mixing conditions on polymer flocculation of concentrated suspensions," *Chemical Engineering Communications*, vol. 108, pp. 3-21, 1991.
- [23]. M.M. Nourouzi, T.G. Chuah, and T.S.Y. Choong, "Optimization of flocculation process for cut-stone wastewater Effect of rapid mix parameters," *Desalination and Water Treatment*, vol. 22, pp. 127-132, 2010.
- [24]. M. A. Yukselen, and J. Gregory, "The effect of rapid mixing on the break-up and re-formation of flocs," *Journal of Chemical Technology and Biotechnology*, vol. 79, pp. 782–788, 2004.
- [25]. T. Taşdemir, and A. Taşdemir, "Effect of Mixing Conditions on Flocculation" in *Proceedings of XIIIth International Mineral Processing Symposium*, 2012, pp. 831-837.
- [26]. A. Sworska, J. S. Laskowski, and G. Cymerman, "Flocculation of the Syncrude fine tailings Part II. Effect of hydrodynamic conditions," *Int. J. Miner. Process.*, vol. 60, pp. 153–161, 2000.
- [27]. M.G. Kılıç, Ç. Hoşten, and Ş. Demirci, "A Parametric Comparative Study of Electrocoagulation and Coagulation Using Ultrafine Quartz Suspensions," *Journal of Hazardous Materials*, vol. 171, pp. 247-252, 2009.
- [28]. D. C. Montgomery, *Design and Analysis of Experiments*. 5th Edition, Hoboken, New Jersey: John Wiley & Sons, Inc., 2001.
- [29]. B. Boltoa, and J. Gregory, "Organic polyelectrolytes in water treatment," *Water Research*, vol. 41, pp. 2301-2324, 2007.
- [30]. K. Miyamoto, K. Tojo, M. Yokota, Y. Fujiwara, and T. Aratani, "Effect of Mixing on Flocculation," *Ind. Eng. Chem. Fundam.*, vol. 21, pp. 132-135, 1982.
- [31]. S. Biggs, M. Habgood, G. J. Jameson, and Y. Yan Y, "Aggregate structures formed via a bridging flocculation mechanism," *Chemical Engineering Journal*, vol. 80, pp. 13–22, 2000.
-

THE PARAMETRIC STUDY ON INTERCOOLER IN TURBOCHARGER DIESEL ENGINE

Yasar SEN

Sapanca Vocational School, Dept. of Electrical and Energy, Sakarya University, Sakarya, Turkey,
ysen@sakarya.edu.tr

Kemal ERMIS

Faculty of Technology, Dept. of Mechanical Engineering, Sakarya University, Sakarya, Turkey,
ermis@sakarya.edu.tr

Abstract

An intercooler, placed between the intake manifold and turbocharger, is a utility used to cool the heated air as a result of compression of the turbo in turbo-charged engine. Using an intercooler allows more air to be heated as a result of compression of the Turbocharger and enters into the cylinder in the engine block. This way, with the pressure provided by the turbocharger the intercooler contributes to a power increase. The maximum engine power can be achieved with the help of coldest air entering the engine. Therefore, a larger size intercooler means more air molecules can take to send more cold air into the engine. Thus, increase of the air quantity obtained by cooling results in increased fuel economy and engine power and so, allows the improvement of durability and reduction of emissions. In order to receive the output expected from the intercooler, the intercooler sizing, geometric shape and type of the fins must be well designed. In this study the intercooler size, type of surface and its thermodynamic parameters were studied for diesel engine. According to the obtained results, louvered surface type on airside and flat surface type on the gas-side were found to be the best choice for design. When it was designed, it was observed that fuel consumption is reduced about 4%, the effective power is increased by about 18 kW and the heat discharged from the exhaust has fallen 1%.

Keywords: *Inter-cooler, Parametric study, Engine*

1. INTRODUCTION

The intercooler; a device disposed between the turbocharger and the engine intake manifold heat exchanger is meant to do the cooling. Intercooler is a cooling device used to cool the heated air that is result of the compression of the turbo-charged turbo engines. Turbo compression as a result of heated air, so the hot air through the intercooler cooling by increasing air density, which helps to cool more air molecules enter into the cylinders in the engine block. Cooling and increasing gas intake manifold air molecules heats the air is taken in from here again and subjected to compression. The heated air expands. So it is the result of previous warming of the air going into the engine from the turbo pressure increases. To ensure the power rollers need to increase more air molecules is not enough just to increase the power of the engine pressure [1]. Motor revenues will be at the highest power that we can get the cold weather. This causes the intercooler to their large size always means that more air molecules can parse and send to colder air motor. Thus, by providing an increased amount of air and cooling;

- 1) improving fuel economy,
- 2) Increasing the engine power,
- 3) increasing the motor resistance,
- 4) Reduction of good combustion engine gas emissions, in particular, is improved [1].

All turbocharged air before entering the engine cylinders in the engine after the explosion in the air passes through an intake air filter element means turbocharger intercoolers and sent from there. Suffered compression heats the air, the heated air expands and causes the warming of the air from the turbo is not being hot is due to undergo compression. Intercooler compressor as high-pressure and density increase, but also increases the air temperature. This increase in temperature increases the volume of air. Nevertheless, the main problem of higher air temperature is producing the engine combinations. This solution is used as an intercooler. Temperature rise in the compressor calculated by the following equation.

$$T_2/T_1 = (P_2/P_1)^{k-1/k} \quad T_2 = T_1 * (P_2/P_1)^{0.286}$$

T_1 = absolute temperature of the air entering the compressor

T_2 = the absolute temperature of the air exiting the compressor

P_1 = absolute pressure inside the compressor

P_2 = absolute pressure at the outside of the compressor

However; temperature, the compressor must be replaced by adiabatic efficiency. Therefore, the actual temperature rise;

$\Delta T = \eta_{ab}$ = compressor efficiency is defined as the adiabatic

2. FOR INTERCOOLER FINS USED, THERE ARE VARIOUS GEOMETRIC SHAPES TUBES TESTED

- 1) Rectangular longitudinal wings,
- 2) Triangular cross-section longitudinal wings,
- 3) Parabolic profiled longitudinal wings,
- 4) Rectangular circular wings,
- 5) Hyperbolic profiled circular wings,
- 6) Dimensional parabolic longitudinal wings,
- 7) in the heat source with a bar,
- 8) Both sides heat given width, length and thickness. [2];

To assess their performance compared to bodies and surfaces, two factors must be considered. They are [3];

a) Activity; the amount of heat transferred from the fin surface is the ratio of the amount of heat transferred to the bottom surface side.

b) Efficiency; the heat transferred from the fin surface is transferred into a substrate temperature equal to any temperature heat is the ratio of the fin.

An intercooler temperature will reduce the charge entering the engine in the following situations [4].

1-Motor will receive between 15-20% more power.

2-Engine will be less prone to detonation.

3-Lower inlet temperatures will also give about the same amount of exhaust temperature as the exhaust temperature that comes with longer exhaust valve and turbocharger life.

3. SUPERCHARGING PRINCIPLE

Supercharging pressure also results in increases temperature and density. However, if the density of cooled air before entering the cylinder filling can be increased. This is accomplished by a so-called intercooler. Thus, the same filling pressure would be provided more air into the cylinder[5].

In supercharged engines, three parts take place which are cooling the air cooler in filling out the intercooler, the working principle of the heat exchanger, and water-to-air or air-to-air interaction [6].

4. INTERCOOLER STRUCTURE

Intercooler consists of 3 parts [7,8]:

- 1) Air boilers,
- 2) Tubes (air channels),
- 3) Fins

Air boilers are divided into the boiler input and output. They are usually placed on the right and left sides of the honeycomb. The boiler inlet and outlet port to ensure uniform distribution of the air to the tube are made in a shape widening toward.

The tubes (ducts); the temperature on the air passing through the channels that are to be given to the flap. It is designed in such a way that a fin between two tubes. To provide better heat transfer by air turbulence vanes disposed on the inner tube.

Fins; Heat on the tube are cooled by air by allowing the transmission element. Surface areas of the fins increases, the air-contacting surface increases. This point is a factor limiting the flap surface area. Intercooler is generally used as the material aluminum alloy. It is preferred for the reason of the aluminum alloy; too much aluminum heat transfer coefficient, inexpensive and considered to be mild. Intercooler boiler tubes and fins made of the same material and are combined with Noclock Breyzing methods under heat. Intercooler usually arranged so that the front of the radiator and the radiator 2 to 3 cm range [9]. Intercooler valuations are taken into consideration while designing, limitations determined by the characteristics of the vehicle by the engine manufacturer companies.

These are:

- 1) intercooler inlet and outlet temperatures
- 2) intercooler size
- 3) intercooler airflow passing
- 4) intercooler cooling power
- 5) Compressor efficiency
- 6) Turbine efficiency

5. INTERCOOLER SIZING AND PARAMETRIC CALCULATIONS

The technical specifications of the motor used

Cylinder bore (D)	100 mm
Stroke (S)	100 mm
Number of cylinders (\dot{I})	4
Compression ratio (ϵ)	16,1
The number of rotations - revolution (n)	2500 d/d
The turbocharger pressure rise rate (ρ)= P_k/P_o	1.8
Volumetric efficiency (η_v)	0.90
Volumetric efficiency (λ)	1.7
Fuel Diesel Engine	50

If possible, aluminum wing material within acceptable heat transfer coefficient between plates;
k = 237 W/mK

6.1. Heat transfer and the free flow areas

$$\alpha_h = \frac{A_h}{V_{total}} = \frac{b_h \cdot \beta_h}{b_h + b_g + 2 \cdot a} \text{ Air Side; } \alpha_h = 397.45 \text{ m}^2/\text{m}^3; \text{ Gas Side; } \alpha_g = 753.271 \text{ m}^2/\text{m}^3$$

The total heat transfer area of both sides;

$$A_{top} = \alpha_a \cdot V \quad A_{a,top} = 4.689 \text{ m}^2 \quad A_{g,top} = 10.15 \text{ m}^2$$

The front contact surface area ratio of the flow field;

$$\sigma = \frac{A_c}{A_{fr}} = \alpha_r \cdot \sigma_{a,g} = a_h \cdot \frac{r_{hh}}{4} \text{ that; } \sigma_a = 0.387 \text{ m}^2 \quad \sigma_g = 0.488 \text{ m}^2$$

Fluid flows through the area;

$$A_{c,a} = \sigma_h \cdot A_{frh} = 0.075 \text{ m}^2 \quad A_{c,g} = \sigma_g \cdot A_{frg} = 0.019 \text{ m}^2 \text{ located in the}$$

6.2. Fluid properties

Then, firstly, to verify efficacy of approximately 0.75 can be considered [42]. Using this approach, the definition of effectiveness

$$\varepsilon = 0.75 \quad \varepsilon = \frac{C_h \cdot (T_{hc} - T_{hg})}{C_{min} \cdot (T_{gg} - T_{hg})}, \text{ for } C_{air} \leq C_{gas}; \quad T_{airout} = 350.75 \text{ K} \quad T_{gasout} = 312.25 \text{ K}$$

The average air temperature;

$$T_{a,av} = \frac{T_{hg} + T_{hc}}{2} = 321.875 \text{ K}$$

Average Gas Temperature:

$$T_{g,av} = \frac{T_{gg} + T_{gv}}{2} = 341.125 \text{ K}$$

Table 2. The fluid (air-Gas) Specifications for Average Temperature

	Air side	Gas side
μ , Pa.s	19.5×10^{-6} Pa.s	20.4×10^{-6} Pa.s
Pr	0.708	0.706
Pr 3/2	0.794	0.792
Cp	1006 J/kgK	1008 J/kgK

The specific heat values in the above table can be adjusted for dry air and moist air;

Humidity = 0.015 kg H₂O /kg dry air admission is made, X_{c,w} = 1.013

According to this; C_{phcorrection} = X_{c,w} C_{ph} = 1019 J/kgK C_{pgcorrection} = X_{c,w} C_{pg} = 1021.1 J/kgK

For verification then accepting a pressure drop of 2% would be carried out if both parties accordingly;

Air (cool) side output pressure; P_{ad} = P_h - (P_h x 0.02) P_{hd} = 9.93 x 10⁴

Gas (hot) side output pressure; P_{gd} = P_g - (P_g .x0.02) P_{gd} = 1.764 x 10⁵

Specific volumes of input and output for both sides; calculated from the ideal gas equation.

The intensity of the necessary adjustment for humidity Figure 'Read correction factor is multiplied by ten.

X_{c,wd} = 0.992 [9]

Specific volume is calculated as follows;

R = 8.314 J / molK M = 28,996.10-3 kg / mol, including

$$\text{Air Side; } v_{a,in,out} = \frac{1}{\rho_{hg}} = \frac{(R/M) \cdot T_{hg}}{X_{c,wd} \cdot P_h} \quad v_{a,in} = 0.837 \text{ m}^3/\text{kg} \quad v_{a,out} = 1.022 \text{ m}^3/\text{kg}$$

$$v_{a,m} = \frac{V_{hg} + V_{hk}}{2} = 0,929 \text{ m}^3/\text{kg}$$

Gas Side, $v_{g,in,out} = \frac{1}{\rho_{gg}} = \frac{(R/M) \cdot T_{gg}}{X_{cwd} \cdot P_g}$; $v_{g,in}=0.595 \text{ m}^3/\text{kg}$ $v_{g,out} = 0.512 \text{ m}^3/\text{kg}$

$$V_{g,m} = \frac{V_{gg} + V_{gc}}{2} = 0,553 \text{ m}^3/\text{kg}$$

6.3. The presence of the Reynolds number

If the input and output temperature of a radiator in the normal difference in size $\Delta t = 20^\circ \text{C}$ is considered the amount of heat transferred from the coolant $Q_c = 51583 \text{ J/s}$ and $C_{psu} = 4179$

Air flow = $Re_h = \frac{4r_h \cdot G_h}{m_h}$; $Re_h = 1.899 \times 10^3$ Gas flow rate $Re_g = \frac{4r_g \cdot G_g}{m_g}$; $Re_g = 680.5456.4$

Stanton, Prandtl number and surface of the main characteristics

Air side; $St \cdot Pr^{\frac{2}{3}}_{air} = 9.155 \times 10^{-3}$ $f_a = 0.043$ $Sta = 0.012$

Gas side; $St \cdot Pr^{\frac{2}{3}}_{gas} = 7.395 \times 10^{-3}$ $f_g = 0.032$ $Stg = 9.337 \times 10^{-3}$

6.5. Heat transfer coefficients

Air Side; $h_h = St_h \cdot Gh \cdot C_{ph}$ $h_h = 96.012 \text{ W/m}^2 \cdot \text{K}$

Gas Side; $h_g = St_g \cdot G_g \cdot C_{pg}$ $h_g = 50.447 \text{ W/m}^2$

6.6. Wing effectiveness of

Air Side Cold End; $m_h = \sqrt{\frac{2h_h}{-k \cdot \delta_h}}$; $m_h = 73.01 \text{ m}^{-1}$; $h_{fh} = \frac{\tan m_h l_h}{m_h l_h} h_{fh} = 0.982$

Gas Side (Hot Party); $m_g = \sqrt{\frac{2h_g}{-k \cdot \delta_g}}$; $m_g = 52.922 \text{ m}^{-1}$ $\eta_{fg} = \frac{\tanh m_g l_g}{m_g l_g} \eta_{fg} = 0.984$

6.7. Surface effectiveness of

Surface effectiveness can be found using the following formula.

$$h_{oh} = 1 - \frac{A_{ah}}{A} (1 - h_{fh}) \text{ air side; } h_{oh} = 0.989 \text{ gas side; } h_{og} = 0.986$$

6.8. The overall heat transfer coefficient

All these parameters are no longer found after calculating a total heat transfer coefficient

$$\frac{1}{U} = \frac{1}{\eta_{oh} \cdot h_h} + \frac{1}{(A_g/A_h) \cdot \eta_{og} \cdot h_g} \quad U = 50.463 \text{ W/m}^2 \cdot \text{K}$$

6.9. NT and the heat exchanger effects

Air Side Heat Capacity; $C_{air} = W_{air} \cdot C_p \text{ correction} = 628.944 \text{ kW/K}$

Gas Heat Capacity of Parties; $C_{gas} = W_{gas} \cdot C_p \text{ correction} = 102.78 \text{ kW/K}$

Rates of capacity;

$$\frac{C_{min}}{C_{max}} = \frac{C_{gaz}}{C_{hava}} \frac{C_{min}}{C_{max}} = 0,163 \quad N_{tu,maks} = \frac{A_{htop} \cdot U_h}{C_{min}} \quad N_{tu,maks} = 2.302$$

In addition, using this case N_{ti} and heat capacity ratio B from the effectiveness of the graph in Figure B.1. $\epsilon = 0.88$ when read

Reformulated (6.6.) Output temperatures for each side using the calculated similarly

$$T_{air} = 360.76 \text{ K} \quad T_{gasout} = 302.24 \text{ K}$$

(Cold) (hot)

Wherein the hot side outlet temperature of the air to the intake manifold will be important for us because at this temperature. Inlet temperature of the intake manifold according to calculations made previously was required to be 303 K. According to this result, the selected type and size of heat exchanger is provided this requirement are suitable.

6.10. Pressure drop

Before the calculation

$$\frac{A_{atop}}{A_{ca}} \text{ air} = \frac{l}{r_{ha}} = 62.64 \quad \frac{A_{gtop}}{A_{cg}} \text{ gas} = \left(\frac{l}{r_{hg}}\right) = 534.21$$

Air-side	Gas side
$K_{ch} = 0.52$	$K_{cg} = 0.55$
$K_{eh} = 0.30$	$K_{eg} = 0.20$

Acceleration due to gravity is assumed to be 9.81 m/s^2 ;

Air-side;

$$\Delta P_h = \epsilon h^2 \cdot \frac{V_{hg}}{2 \cdot g \cdot Ph} \cdot \left[(K_{ch} + 1 - \sigma h^2) + 2 \cdot \left(\frac{V_{hg}}{V_{h\zeta}} - 1 \right) + \left(f_{hite} \cdot \frac{A_{htop}}{A_{ch}} \cdot \frac{V_{hort}}{V_{hg}} \right) - (1 - \sigma h^2 - K_{eh}) \left(\frac{V_{hg}}{V_{h\zeta}} \right) \right]$$

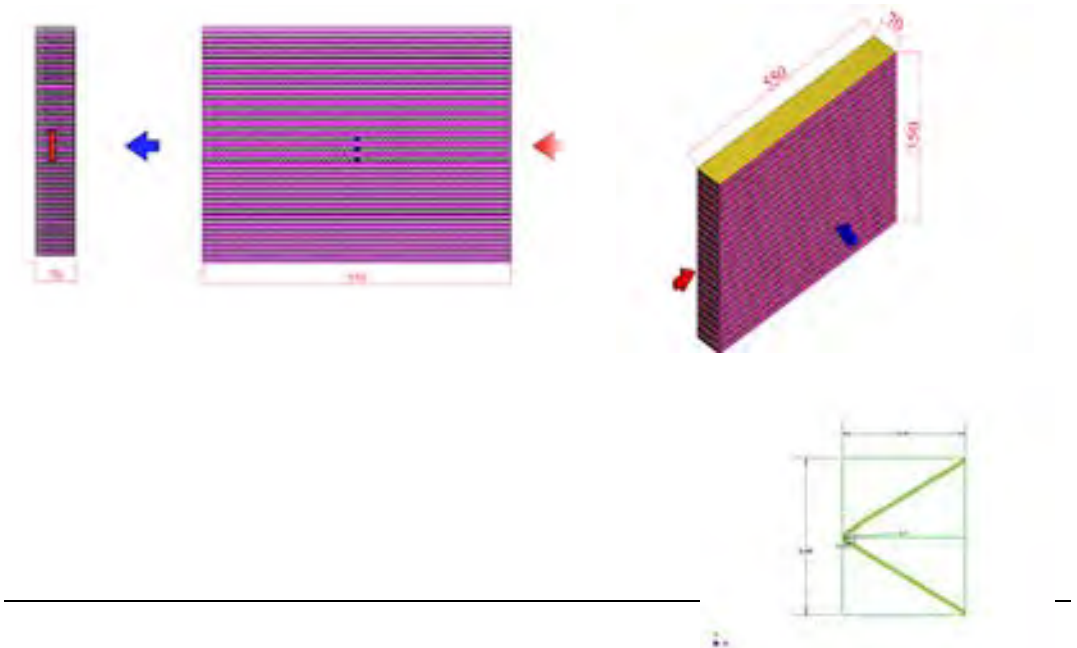
$$\left(\frac{\Delta P_h}{P_i} \right) = 1.033 \times 10^{-4} = 0.103$$

Gas side;

$$\Delta P_g = \epsilon g^2 \cdot \frac{V_{gg}}{2 \cdot g \cdot Pg} \cdot \left[(K_{cg} + 1 - \sigma g^2) + 2 \cdot \left(\frac{V_{gg}}{V_{g\zeta}} - 1 \right) + \left(f_{gite} \cdot \frac{A_{gtop}}{A_{cg}} \cdot \frac{V_{gort}}{V_{gg}} \right) - (1 - \sigma g^2 - K_{eg}) \left(\frac{V_{gg}}{V_{g\zeta}} \right) \right]$$

$$\left(\frac{\Delta P_g}{P_i} \right) = 8.19 \times 10^{-5} = 0.0819 \quad \text{results obtained.}$$

In this study, the intended intake manifold filling gas temperature (303 K) to obtain the intended intercooler sizes, the size of the flaps used and sectional images is shown in the Figures.



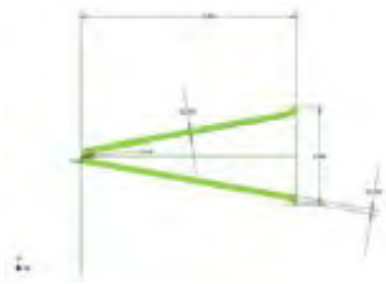


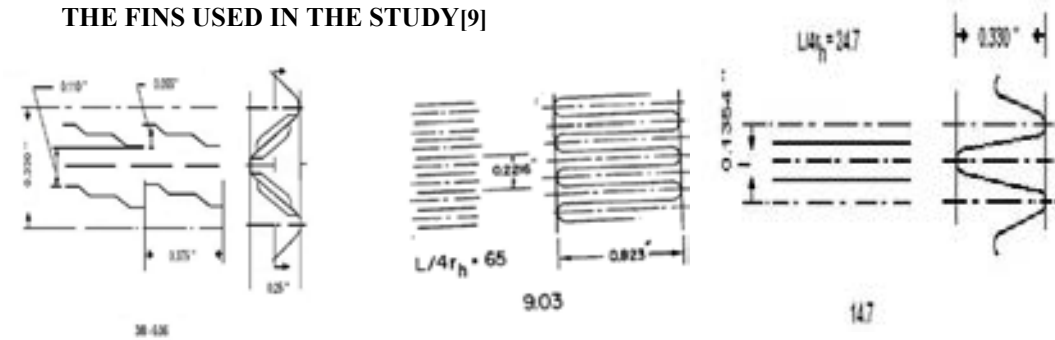
Figure 1; is designed intercooler
The fins on the air Party Appearance

Figure 2; is designed intercooler
The fins on the gas Party Appearance

Table 3; parameter values used in the fin study

Air Side		Gas Side				
Surface	3/8-60.6	9.03	11.1	14.77	15.08	19.86
Plate spacing (b), m	6.35×10^{-3}	20.90×10^{-3}	6.35×10^{-3}	8.38×10^{-3}	10.62×10^{-3}	6.35×10^{-3}
Hydraulic Radius $4r_h$, m	4.453×10^{-3}	4.64×10^{-3}	3.08×10^{-3}	2.59×10^{-3}	2.67×10^{-3}	1.875×10^{-3}
Fin thickness (δ), m	0.152×10^{-3}	0.203×10^{-3}	0.152×10^{-3}	0.152×10^{-3}	0.152×10^{-3}	0.152×10^{-3}
Transferarea/Volume between plates (β)	$840 \text{m}^2/\text{m}^3$	$800.5 \text{m}^2/\text{m}^3$	$1204 \text{m}^2/\text{m}^3$	$1378.0 \text{m}^2/\text{m}^3$	$1358.3 \text{m}^2/\text{m}^3$	$1840.6 \text{m}^2/\text{m}^3$
Fin or extended area/Total area	0.640	0.888	0.756	0.844	0.870	0.849

7. GEOMETRICAL CROSS-SECTIONAL SHAPE OF THE FINS USED IN THE STUDY[9]



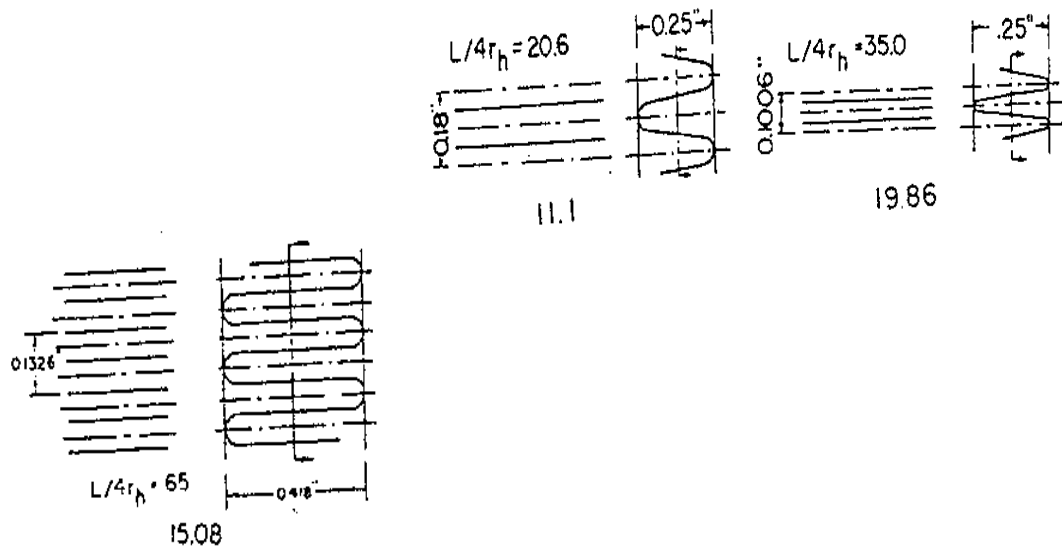


Table 4. The comparison of the calculated results table

Surfaces Code		Air Side Plate-fin surfaces, louvered fins	Gas side Plate-fin surfaces, Plain fins				
		3/8-6.06	14.77	9.03	11.1	15.08	19.86
Calculated Fluid specification	c_p , J/kgK	1019	1021.1	1021.1	1021.1	1021.1	1021.1
	Pe , Pa	9.93×10^4	1.764×10^5	1.764×10^5	1.764×10^5	1.764×10^5	1.764×10^5
Reynolds number Re		1899	680.545				
		3428.1		839.3			
		1638.3			877.6		
		2194.5				613.8	
		1638.2					574.44
$St.Pr^{2/3}$		9.155×10^{-3}	7.395×10^{-3}				
		3.10×10^{-3}		6.69×10^{-3}			
		9.506×10^{-3}			5.664×10^{-3}		
		2.253×10^{-3}				8.04×10^{-3}	
		9.50×10^{-3}					8.66×10^{-3}
Heat transfer coefficient, W/m^2K		101.2	51.10				
		59.69		31.83			
		87.7			37.81		
		22.06				38.5	
		87.7					69.75
Fin factor		0.982	0.984	0.995	0.996	0.991	0.992
Surface factor		0.989	0.986	0.993	0.989	0.992	0.991
Total heat transfer coefficient, W/m^2K			50.463	37.03	30.95	18.1	31.56
Exit temperature		360.76 K	302.24 K				
		337.6 K		325.3 K			
		349.2 K			313.7K		
		337.6 K				325.4 K	
		345 K					317K

8. CONCLUSIONS AND RECOMMENDATIONS

Theoretical calculations are done for modifying the intercooler for improving the performance value of the existing tractor engine in this study. This study is presented below in the form of conclusions and recommendations obtained from the results of computer calculations.

The performance of the engine used for the calculations at high speed while (2500' d / d) and Intercooler in charge air outlet temperature of 370 K from 303 K by comparison to reduced specific fuel consumption and consequently characteristic calculation was determined the effectiveness of inter-cooling method. Since turbocharger outlet gas temperature is high, the engine will be absorbed into the cylinder with turbocharger to affect the volume of the filler aircraft engines to reduce the temperature of the turbocharger, exhaust gas between the block, so to increase the volume of charge air intercooler is needed in the design.

Because it is important at the same time in the fins of the geometric structure of the area where the intercooler cover over the motor if the key is that thought and air intake design, intercooler size needs to be done in the best possible way to achieve the desired engine block inlet temperature.

The above characteristics were compared to data presented diesel engine intercooler taken on the basis of the parametric values of the most commonly used size available on the market as a result of geometric design of the fins kept constant effective survey data.

0.07 x 0.55 x 0.35 m is the size of the intercooler designed to achieve the intended temperatures have been identified. Fin design, derived from literature for research to airside louvered fin intercooler 3/8 to 6.06 as the selected surface design, has been preferred for the gas side. These results were compared with 9.03; 11.1; 14.77; 15.08; 19.86. Fin surface design structure was presented in the tables on comparisons of the results obtained by the calculations. When the 14.77 type of side surface design is used, the cylinder air temperature in the intake manifold of the engine is dropped from 370 K from to a value of 302.24 K.

The study design dimensions and geometric finned intercooler in the cylinder air filling the temperature in the engine's intake manifold, 370 K from 302.24 K-value of lowering the engine speed up to 2500 rev / d, while the decrease in the specific fuel consumption, the effective power is increased, the increase in torque, the heat from the effective work equivalent rises, the heat expended for cooling is reduced when discharged from the exhaust heat is low, the combustion is reduced in the last temperature, an increase of combustion pressure and expansion end pressure and the indicated pressure to very low TA though some value change results such as an increase was determined.

According to the study results, the modified engine with turbocharger, for increasing the inlet temperature of the reduction of the intake manifold and engine performance of engines for improving parametric values are recommended Intercooler.

REFERENCES

1. *Mack Technical Bulletin, Econdyne Fuel Efficiency – Mack's New Chassis Mounted Charge – Air Cooling, Page 3 – 7 March 1996.*
 2. *DA SÖZ, A.K., Isı Geçisi, ITÜ, Cilt 1, 1974.*
 3. *KAKAÇ, S., Örneklerle Isı Transferi, ODTÜ, 7. Baskı, 1987.*
 4. *LILLY, L.R.C., Diesel Engine Reference Book, Butterworthsand Company, London, England, 1984.*
 5. *BORAT, O., BALCI, M., SÜRME, A., ÇıtenYanmalıMotorlar, Cilt 1, G.Ü.T.E.F, Ankara, 1994.*
 6. *ERGENEMAN, M., İçtenYanmalıPistonluMotorlardaAsırDoldurma, ITÜ, İstanbul, 1990.*
 7. *ANDERSSON, J., BENGTSON, A., ERICKSON, S., The Turbocharged and Intercooled 2. 3 Liter Engine for the Volvo 760, SAE Paper 850253, 1985.*
 8. *AKICI, S., AraSoğutucununDizelMotorlarınaEtkileri, Marmara Üniversitesi Fen BilimleriEnstitüsü, İstanbul, 1999*
 9. *KALE INTERCOOLER – RADYATÖR, Tamir – BakımKitabı, 1996*
 10. *KAYS, W., M., LONDON, A., L., Compact Heat Exchangers, Krieger Publishing Company, Malabar, Florida.*
-

A NEW MODIFIED SHAH CORRELATION ON CONDENSATION HEAT TRANSFER IN PLAIN TUBES

Kemal ERMIS

Faculty of Technology, Dept. of Mechanical Engineering, Sakarya University, Sakarya, Turkey,
ermis@sakarya.edu.tr

Yasar SEN

Sapanca Vocational School, Dept. of Electrical and Energy, Sakarya University, Sakarya, Turkey,
ysen@sakarya.edu.tr

Abstract

Condensation is an important phenomenon in many industrial applications. Condensation occurs when the temperature of a vapor is reduced below its saturation temperature. Small hydraulic diameter, multi-port extruded aluminum tubes are widely used in automotive refrigerant condensers. Applications of condenser have been developed for heat transfer in small diameter tubes having rectangular shapes. This study provides condensation heat transfer data for R-134a in small hydraulic diameter plain extruded three aluminum tubes, having different rectangular ports for 1.26 mm, 1.82 and 2.64 mm of hydraulic diameters. Condensation heat transfer are obtained 8 kW/m² heat flux for 300-1000 kg/m²s mass velocity and 20-80% vapor qualities at 40 oC and 65 oC saturation temperature. The experimental data are compared with the Shah correlation. Condensation coefficient is over-predicted with a mean absolute deviation of 27% and 55% at 40 oC and 65 oC respectively by the Shah correlation. A new modified the Shah correlation is presented for small hydraulic tubes by changing constant to 2.8.

Keywords: *Condensation, Heat transfer, Modified Shah Correlation, Small hydraulic diameter*

1. INTRODUCTION

Condensation is an important phenomenon in many industrial applications. Condensation occurs when the temperature of a vapor is reduced below its saturation temperature. In equipment such as air-conditioning condensers, this process takes place when the vapor flows in a tube that is cooled by an exterior fluid such as air. As the vapor condenses inside the tube, its latent energy of the vapor is released, heat is transferred to the tube wall, and the condensate formed. Substantial advances have been made in enhancement of film condensation. The surface geometries of interest include horizontal and vertical tube orientations. A number of enhancement geometries have been identified and tested that many of which are described by Webb [1]

There have been many correlations or models to predict condensation heat transfer coefficient inside tubes, such as those obtained by, Boyko et al. [2], Soliman et al. [3], Cavallini et al. [4, 5], Bandhauer et al. [6], Garimella [7], Shah [8, 9] etc. Some of the investigators obtained heat transfer correlations based entirely one empirical method while others used a semi-analytical approach. Many of the empirical correlations do not include sufficient variables to describe the condensate flow, and the functional dependencies. Conversely, the semi-analytical and analytical approaches have usually given more accurate results and also more involved results than the empirical methods. None of the mentioned models or correlations has found to be good for all tube diameters (1-40 mm) and wide range of saturation temperatures. These correlations were developed for large tubes that it's have inside diameter greater than 7 mm hydraulic diameter.

This study shows condensation heat transfer gradient for R-134a in a multi-port extruded three aluminum tubes, having different rectangular ports for 1.26 mm, 1.82 and 2.64 mm of hydraulic diameters. Condensation heat transfer are obtained 8 kW/m² heat flux for 300-1000 kg/m²s mass velocity and 20-80% vapor qualities at 40 °C and 65 °C saturation temperature. The experimental data are compared with the Shah correlation. The condensation coefficient increases with decreasing hydraulic diameter for all tubes.

Shah [8] and Cavallini et al. [4] correlations are popular correlations for use tubes. The Shah correlated 474 data points for ten fluids covering a very wide range of parameters with a mean deviation of 15.4%. Shah [8] recommended this correlation for general use provided all the following conditions are fulfilled $u_v > 3$ m/s, $Re_l > 350$, $Re_v > 35000$. The Shah correlation has been accepted for prediction of condensation in a plain tube. Dobson [10] correlation has been found to predict refrigerant condensation data very well with the Shah correlation and he showed is very accurate for condensation heat transfer in a 3.14 mm inside diameter copper tube. But Yang and Webb [11] tested condensation heat transfer in a multi-port extruded aluminum tube with hydraulic diameter 1.33 mm and 2.64 mm at 65 °C saturation temperature. They found that the Shah correlation over-predicted the condensation coefficient by 50 - 80% respectively. Experimental data showed that condensation coefficient is over-predicted with a mean absolute deviation of 27% and 55% at 40 °C and 65 °C respectively by the Shah correlation [12]. In this study, a new modified the Shah correlation is presented for small hydraulic tubes by changing constant to 2.8 in the correlation.

2. EXPERIMENTAL STUDY

2.1. Tubes Tested

Figure 1 shows photos of the tubes and Table 1 lists their geometrical dimensions. The descriptive code used to describe the code is as in the format X-YY-ZZ, where first digit (X) is the minor tube diameter, the second digits (YY) are the major tube diameter, and the third digits (ZZ) are the numbers of ports in the tube.



a) Tube A, 3-16-12, ($D_h = 1.26$ mm)



b) Tube B, 3-16-8, ($D_h = 1.82$ mm)



c) Tube C, 3-16-4, ($D_h = 2.64$ mm)

Figure 1. Photographs of tested

Table 1. Dimensions of the tubes tested

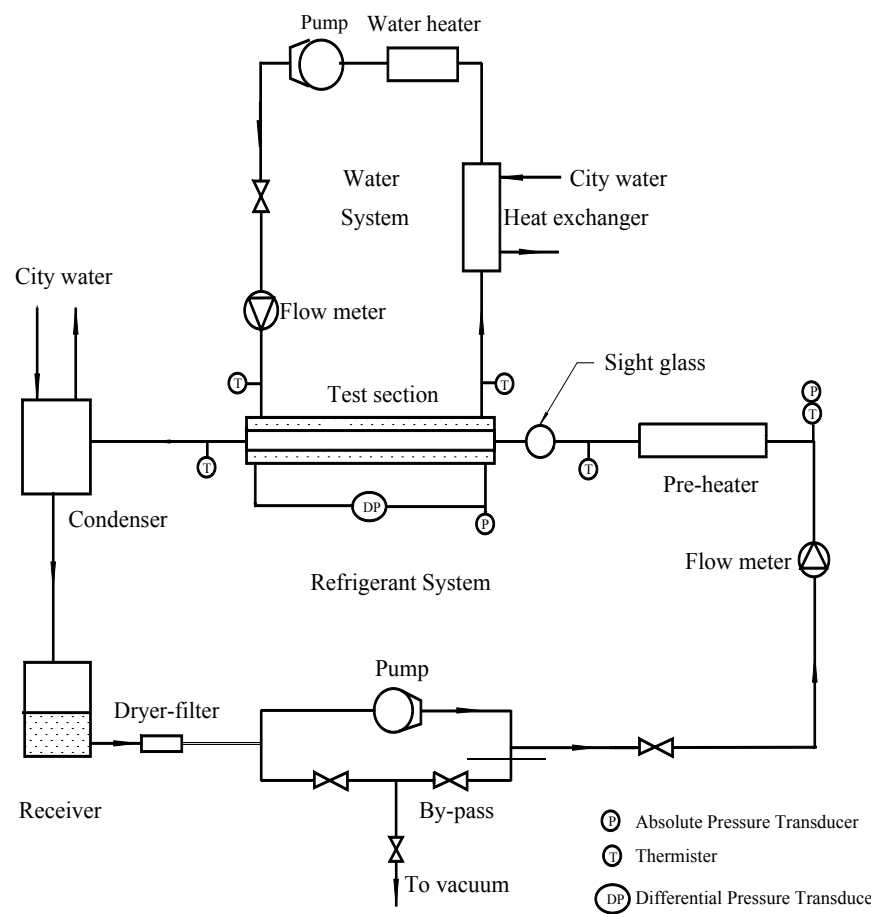
	Tube A	Tube B	Tube C
Description and Item	3-16-12	3-16-8	3-16-4
Number ports, Np (-)	12 rectangular	8 rectangular	4 rectangular
Major diameter, w (mm)	18	16	16

Minor diameter, b (mm)	3	3	3
Wall thickness, t (mm)	0.4	0.40	0.5
Flow area, A_c (mm ²)	23.46	26.79	27.27
Hydraulic Diameter, D_h (mm)	1.26	1.82	2.64
Wetted Perimeter, P (mm)	74.32	58.92	41.36

*Refer to Figure 1

2.2. Test Facilities

Figure 2 shows a schematic diagram of the test facility. It includes the test section, refrigerant system and water system. A cross-section view of the test section is shown in Figure 3. Refrigerant flows inside tube, with high velocity cooling water in the annulus. The test tube is 508 mm long and is centered within the water



channel. The test section is designed such that the waterside heat transfer coefficient is larger than that of the refrigerant side. The water is flowed inside 1 mm wide annulus around the test section outer surface. An electric pre-heater controls the vapor quality entering the test section. The refrigerant is condensed against cooling water flowing in the annulus. The two-phase mixture leaving the test section enters a post-condenser and then the condensate is drained to the receiver. The sub-cooled refrigerant liquid is then passed through a dryer and a gear pump. The gear pump transports the liquid to the electric pre-heater. A flow meter installed between the gear pump and the pre-heater and measures refrigerant flow rate. The refrigerant flow rate is independently controlled by the gear pump. The inlet vapor quality is determined by the heat input to the pre-heater, which is independently controlled. The test section saturation temperature is controlled by adjusting the cooling water flow rate to the post-condenser. The heat transfer rate is controlled by adjusting the temperature and flow rate of the cooling water. Thus, inlet the vapor quality, mass velocity and heat flux are independently controlled.

Figure 2. Schematic diagram of test facility

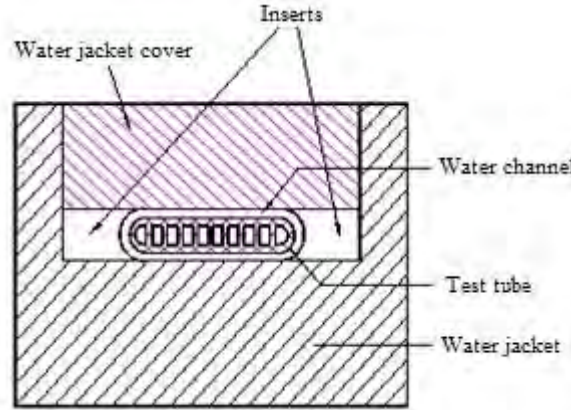


Figure 3. Cross-section view of the test section

Water is moved by a variable speed centrifugal pump and enters the annulus side of the test section at a known temperature and flow rate. The water condenses the refrigerant flowing in the test section. The heated water leaves the test section and goes to a water-to-water heat exchanger. The cooled water goes to a storage tank, in which an electric cartridge heater is installed. The water is heated to the desired temperature. A turbine flow meter is placed between the pump and the test section to measure water flow rate.

2.3. Data Acquisition and Equations

The data measuring instruments consist of five thermistors, two pressure transducers for measuring absolute pressures, one differential transducer for measuring pressure drop and two turbine flow meters to measure refrigerant and water flow respectively.

The modified Wilson plot method as described by Farrell et al. [13] was used to calibrate the annulus waterside heat transfer coefficient. The total heat transferred in the test section was determined from an energy balance on the water flow in the annulus:

$$q_t = m_w c_{pw} (T_{w,out} - T_{w,in}) \quad (1)$$

The vapor quality entering the test section (x_{in}) is calculated from an energy balance on the pre-heater. The heat input to the refrigerant from the pre-heater (q_r), is the sum of the sensible and latent heat.

$$q_r = q_{sensible} + q_{latent} \quad (2)$$

Where:

$$q_{sensible} = m_r c_{pr} (T_{sat} - T_{pre,in}) \quad (3)$$

$$q_{latent} = m_r h_{fg} x_{pre,out} \quad (4)$$

The test section inlet quality (x_{in}), which is also the pre-heater exit quality ($x_{pre,out}$), is calculated from Equation (2), (3) and (4).

$$x_{in} = \frac{1}{h_{fg}} \left[\frac{q_r}{m_r} - c_{pr} (T_{sat} - T_{pre,in}) \right] \quad (5)$$

The vapor quality change in the test section was given by:

$$\Delta x = \frac{q_t}{m_r h_{fg}} \quad (6)$$

Finally, the average quality in the test section was:

$$x_{avg} = x_{in} - \Delta x / 2 \tag{7}$$

The refrigerant side heat transfer coefficient was determined from the overall heat transfer coefficient and the calibrated annulus heat transfer coefficient (h_a). The overall heat transfer coefficient (U_o) based on the outside area was provided by:

$$U_o = \frac{q_t}{A_a \Delta T_{ln}} \tag{8}$$

Where, ΔT_{ln} is the log-mean temperature. Assuming no fouling resistance in the annulus, the refrigerant heat transfer coefficient was determined by the equation:

$$h_i = \frac{I}{\left(\frac{I}{U_o} - \frac{I}{h_a} \right) \frac{A_i}{A_a} - \frac{tA_i}{kA_{avg}}} \tag{9}$$

Where, A_{avg} is the average of the inside and outside areas of the tube, t is the tube wall thickness and k is the tube wall conductivity. Table 2 shows summary of test conditions.

Table2. Summary of test conditions

TUBE	A 3-16-12	B 3-16-8	C 3-16-4
Fluid	R-134a	R-134a	R-134a
T_{sat} (°C)	40-65	40-65	40
Mass Velocity (kg/m ² -s)	300,600,1000	300,600,1000	300,600,1000
Heat Flux (kW/m ²)	8	8	8

3. EXPERIMENTAL RESULTS

The condensation heat transfer coefficient of R-134a refrigerant inside plain tube A, tube B and tube C, plotted as a function of the vapor quality are shown in Figures 4 for mass velocities of $G = 300, 600, 1000$ kg/m²s at 40 °C saturation temperature and constant heat flux ($q'' = 8$ kW/m²).

The condensation coefficients increase with decreasing hydraulic diameter at 40 °C saturation temperature in the plain tubes. Figure 4 shows that the condensation heat transfer coefficient increases with increasing vapor quality and mass velocity for 40 °C saturation temperature.

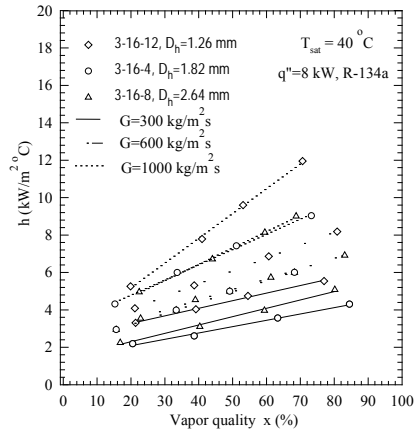


Figure 4. Condensation heat transfer coefficient in plain tubes at 40 °C.

Like figure 4, the condensation heat transfer coefficient of R-134a refrigerant inside plain tube A and tube B plotted as a function of the vapor quality are shown in Figures 5 for mass velocities of $G = 300, 600, 1000 \text{ kg/m}^2\text{s}$ at 65 °C saturation temperature and constant heat flux ($q'' = 8 \text{ kW/m}^2$).

The condensation coefficients increase with decreasing hydraulic diameter in the plain tubes. Also figure 5 shows that the condensation heat transfer coefficient increases with increasing vapor quality and mass velocity for 65 °C saturation temperature.

4. NEW MODIFIED SHAH CORRELATION

Shah [2] recommended this correlation for general use provided all the following conditions are fulfilled $uv > 3 \text{ m/s}$, $Re_l > 350$, $Re_v > 35000$. The Shah correlation has been accepted for prediction of condensation in a plain tube. The experimental data are compared with the Shah correlation for condensation inside small diameter tubes in Figure 6. Condensation coefficient is over-predicted with a mean absolute deviation of 27% and 55% by the Shah correlation at 40 °C and 65 °C respectively as shown in Figure 6.

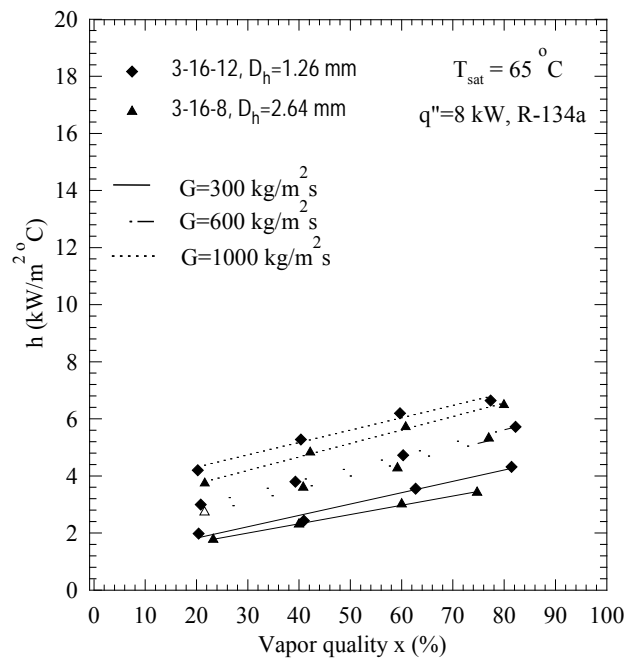


Figure 5. Condensation heat transfer coefficient in plain tubes at 65 °C.

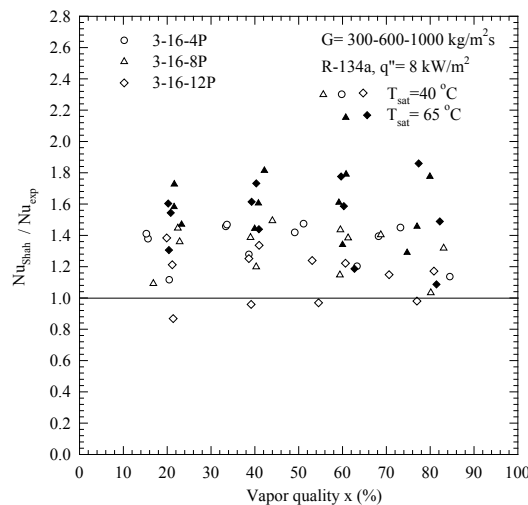


Figure 6. Prediction of the condensation heat transfer for plain tubes using the Shah correlation at 40 °C and 65 °C.

The over-prediction is more serious as the saturation temperature gets higher. Therefore, it is necessary to develop a new correlation for predicting condensation coefficient inside small diameter tubes. For review, the Shah correlation is repeated as follows:

$$Nu = Nu_l \left[1 + \frac{a}{P_{re}^b} \left(\frac{x}{1-x} \right)^{0.76} \right] \quad (10)$$

Where; the constant a and the exponent to the reduced pressure b are 3.8 and 0.38 respectively, Nu ; Nusselt number (hD/k), Nu_l : liquid Nusselt number and P_{re} reduced pressure ratio ($P/P_{critical}$).

The reduced pressure range of Shah's database used to develop the above equation was between 0.011 and 0.44. Shah [8] recommended the general use of his correlation only in this range. The reduced pressure P_{re} is about 0.47 at $T_{sat} = 65\text{ }^\circ\text{C}$ for R-134a. It is marginally out of the range of the correlation. Shah [9] improved and extended his general correlation for heat transfer during condensation in plain tubes. But, this improved correlation stated that it has range of hydraulic diameter over 2 mm as same before his study. An easy way to comply with the symposium paper formatting requirements is to use this document as a template and simply type your text into it.

In this study, the results of experimental data's analysis show that the constant a is 2.8 in Shah correlation. When the modified Shah correlation constant a changed by 2.8 instead of 3.8, result showed predictions of the condensation coefficient were found to be better than given by the original Shah correlation in the present study, The condensation coefficient is predicted very well with a mean absolute deviation of 8% by the Modified Shah correlation at both the 40 °C and 65 °C predictions in shown Figure 7.

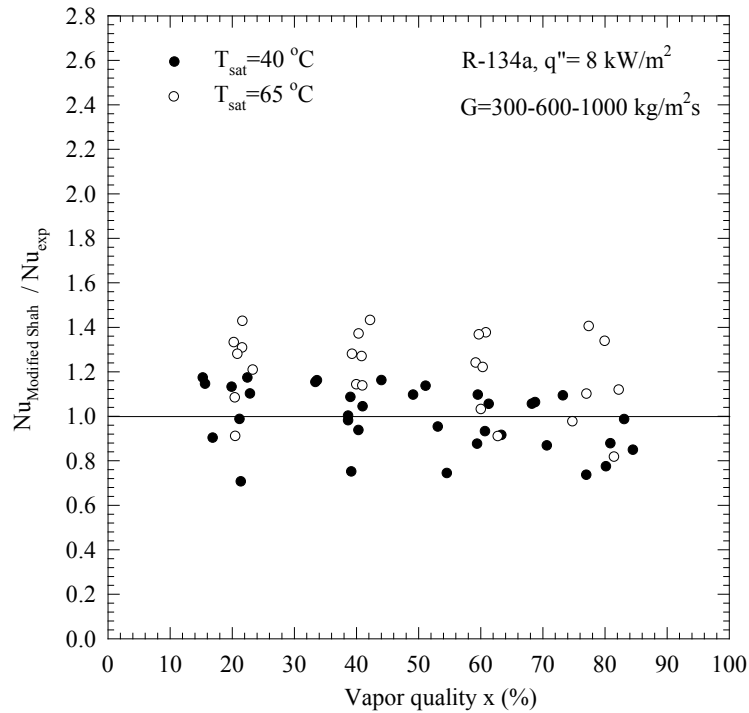


Figure 7. Prediction of the condensation heat transfer data for plain tubes using the Modified Shah correlation

5. CONCLUSIONS

- Heat transfer coefficients for R-134a condensation are reported for hydraulic diameters having 1.26, 1.82 and 2.64 mm plain tubes.
- The heat transfer coefficient for condensation increases with decreasing hydraulic diameter for tubes.
- The data show that the condensation coefficients increase with increasing mass velocity and vapor quality.

- The Shah correlation can be used for small diameter tubes with the tube diameter down to 3 mm, but when the saturation temperature is getting higher, reduced pressure (Pred) increases over 0.44, it tends to fail and over-predict condensation heat transfer.
- Condensation coefficient is over-predicted with a mean absolute deviation of 27% and 55% by the Shah correlation at 40 °C and 65 °C respectively.
- Condensation coefficient is predicted very well with a mean absolute deviation of 8% by using The Modified Shah correlation.
- Modified Shah correlation is recommended to predict condensation heat transfer for smaller tubes than 3 mm based on the hydraulic diameter.

REFERENCES

- [1]. R.L. Webb and N.H.Kim, *Principles of enhanced heat transfer*, 2nd ed., Taylor & Francis Group (New York), 2005.
- [2]. L.D.Boyko and G.N.Kruzhilin, "Heat transfer and hydraulic resistance during condensation of steam in a horizontal tube and a bundle of tubes", *International Journal of Heat and Mass Transfer*, 10, 361-373,1967.
- [3]. M.Soliman, J.R.Schuster and P.J. Berenson, "A General heat transfer correlation for annular flow condensation" *ASME Journal of Heat Transfer*, 90, 267-27,1968.
- [4]. A. Cavallini and R.Zecchin, "A high velocity condensation of organic refrigerants inside tubes", *Proceedings of the eighth international congress of refrigeration*, 2, 193-200,1971.
- [5]. A.Cavallini, D.D.Col, L.Doretto, M.Matkovic, L.Rossetto, et al.. "Condensation heat transfer and pressure gradient inside multipoint minichannels" *Heat Transfer Eng.*, 26(3,) 45-55,2005.
- [6]. T.M. Bandhauer and A.Agawal, S.Garimella "Measurement and modeling of condensation heat transfer coefficients in circular microchannels", *Journal of Heat Transfer*, 128, 1050-1059,2006.
- [7]. S.Garimella, "Condensation flow mechanisms in microchannels: basis for pressure drop and heat transfer models." *Heat Transfer Engineering*, 25(3):104-116,2004.
- [8]. M.M. Shah, "General correlation for heat transfer during film condensation inside pipes." *International Journal of Heat Mass Transfer*, 36(7), 547-556, 1979.
- [9]. M.M. Shah, "An improved and extended general correlation for heat transfer during condensation in plain tubes. *HVAC&R Res.*", 15(5), 889-913,2009.
- [10]. M.K.Dobson, "An experimental evaluation of internal condensation of refrigerants R-12 and R-134a" *ASHRAE Transactions*, 100(1), 744-754,1994.
- [11]. C.YYang and R.L.Webb, "Condensation of r-12 in small hydraulic diameter extruded aluminum tubes with and without micro-fins." *International Journal of Heat and Mass Transfer*, 39 (4), 791-800.1996.
- [12]. K. Ermis, "Experimental study of condensation inside plain and micro-fin tubes". *PhD thesis*, Sakarya University, Turkey,1998.
- [13]. Farrell P., Wert K. and Webb R.L. "Heat transfer and friction characteristics of turbulent radiator tubes." *SAE Transactions*, 100, 218-230,1991.

CONTROLLED RECIRCULATION IN VENTILATION OF UNDERGROUND MINES- APPLICATIONS IN TURKEY AND IN THE WORLD

Cem ŞENSÖĞÜT

Dumlupinar University, Department of Mining Engineering, 43100, Kutahya, Turkey.
sensogut@dpu.edu.tr

İbrahim ÇINAR

Selcuk University, Department of Mining Engineering, 42075, Konya, Turkey

Abstract

As many underground mines have started to exploit reserves at deeper horizons and at locations remote from surface connections, it has become rather difficult to deliver adequate levels of airflow at these remote working areas. In the present work, the effect of controlled recirculation of ventilating air emphasized as an alternative for improving the environmental conditions in deep underground mines on the possible heat, humidity, dust and gaseous contaminant formations are given in details. Additionally, the applications of this method carried out in Turkey and in some other countries in the world are also presented together with their interpretations.

Keywords: *Underground mining, mine air, ventilation, controlled recirculation*

1. INTRODUCTION

The primary purpose of a mine ventilation system is to provide a safe and suitable working environment. As workings become more extensive and mechanized, this objective becomes increasingly difficult and costly to achieve. When a mine ventilation network encounters difficulties in providing adequate airflow to the faces, alternative ventilation methods must be introduced if the production cycle is to be continued. The following methods are commonly used to improve or maintain the ventilation requirements.

- An increase in the capacity or number of the fans,
- Reducing the airway resistance,
- Constructing a satellite shaft or borehole and
- Controlled recirculation of ventilating air.

Only the method of recirculating air amongst the above mentioned techniques is the cheapest and the most easily applicable one if the conditions are suitable enough.

1.1. The Theory of Controlled Recirculation

Recirculation may be explained by the re-use of air within a part of a mine. It is generally achieved by diverting a controlled proportion of the return air into the intake airway by means of a booster fan located either in a recirculation cross-cut or inline with the main airflow (Figure 1) [1-3].

The very first known recorded study into the recirculation of air was conducted by Lawton at Birmingham University [4]. The objective of his investigations were to increase the cooling power of air in coal faces in deep mines experiencing problems caused by heat and humidity, by locally increasing the air velocity. He concluded that the increased air velocities were not sufficient enough for the general use of recirculation and that there was no significant increase in the general body contaminant level in the recirculated air.

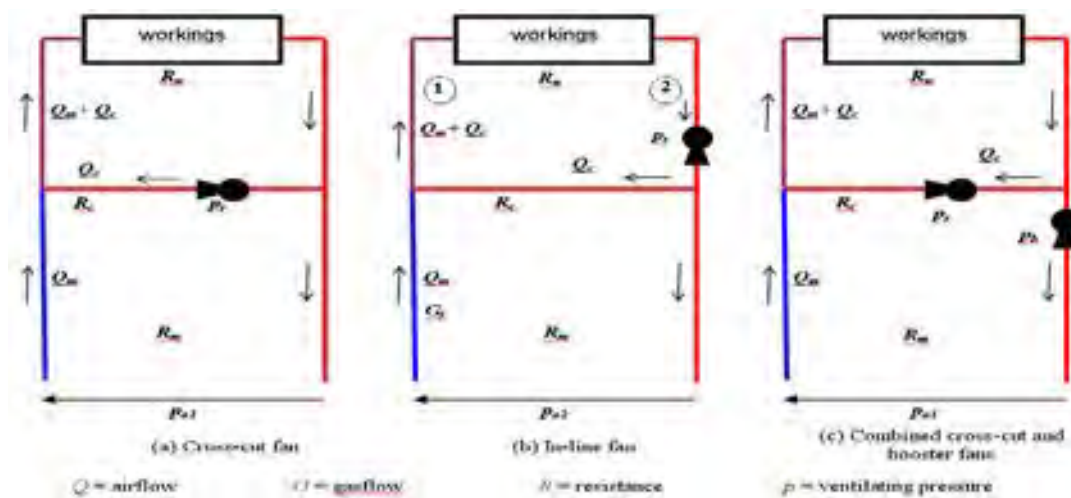


Figure 1. Simple layout of controlled recirculation

2. CONTROLLED RECIRCULATION APPLICATIONS IN THE WORLD

Some of the applications realized in the world are given below.

2.1. In The United Kingdom

The first underground investigation of wide scale recirculation in Britain was achieved at Wearmouth Colliery, British Coal in 1983 [5]. The workings of this mine are remotely located under the North Sea at the distances over 10 km from the fresh air supplying shafts. In order to tackle the problem of delivering fresh air to these workings, two solutions were investigated. The first one was to sink shafts out to sea and the second was to employ controlled recirculation. It was accepted that the second method had its advantages, being

cheaper, safer and achieved by the present technology. A recirculation fraction of 30% was realized and no considerable change in the gaseous contamination was detected (Figure 2).

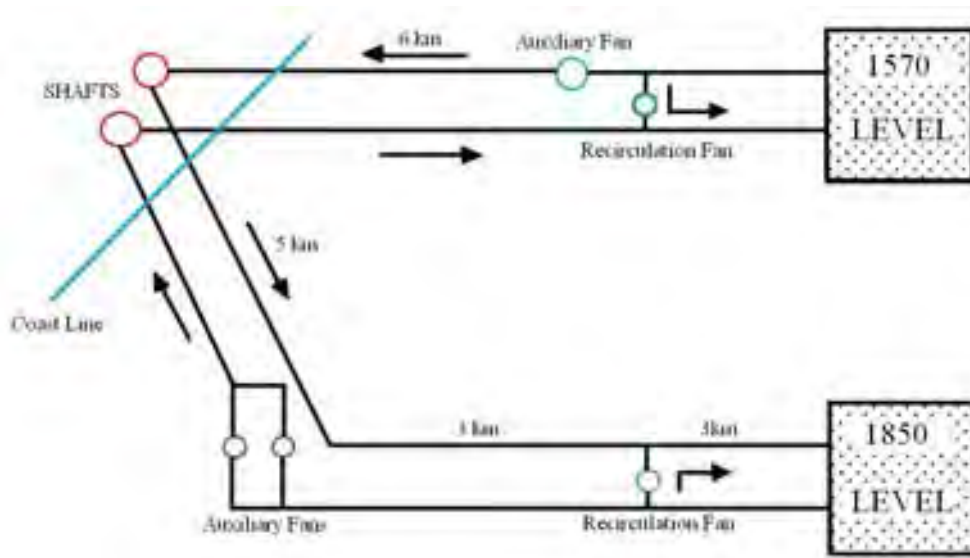


Figure 2. Schematic of workings at Wearmouth Colliery

2.2. In South Africa

Heat is one of the major environmental problems encountered in deep South African gold mines. The methods which used to be employed to maintain the refrigeration have gradually become insufficient due to the practical difficulties in operating and maintaining the necessary equipment. As an alternative to supply of air from surface, the controlled recirculation was employed in a gold mine (Lorraine) in South Africa by Burton et al [6]. By taking the recirculation fraction of 70%, the fresh airflow to the district was reduced from 35 to 15 m³/s in these trials. In addition, the wet bulb temperature in the recirculation intake fell from 27.9 to 22 °C (Figure 3).

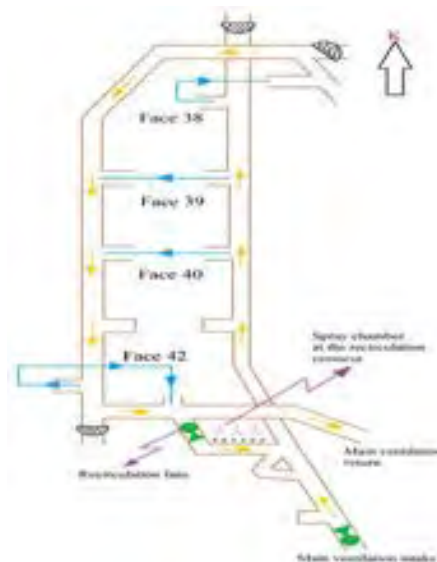


Figure 3. A schematic diagram of Lorraine Gold Mine recirculation zone

2.3. In Canada

Controlled recirculation investigation was conducted at Ruttan Mine, where copper and zinc are extracted in 1986 [7]. During this trial, gas and dust concentrations were measured in the return air of the major working areas to evaluate the potential for recirculating air into the intake air in winter to reduce heating costs. The findings of the investigations showed that there was excellent possibility to reduce winter heating costs by means of controlled recirculation and that recirculation should take place as close to surface as possible due to the decrease of up to 50% in the contaminant concentration levels in the return airway. Another application was practised in a Canadian potassium mine in Rocanville and it was shown that the contents of gaseous contaminants and dust concentrations were not increased causing any problem [8].

2.4. In Australia

The economic viability of controlled district cross-cut recirculation was examined in 1987 using an experimental mine which silver and lead were originally mined before it was closed down in 1928 [9] (Figure 4).

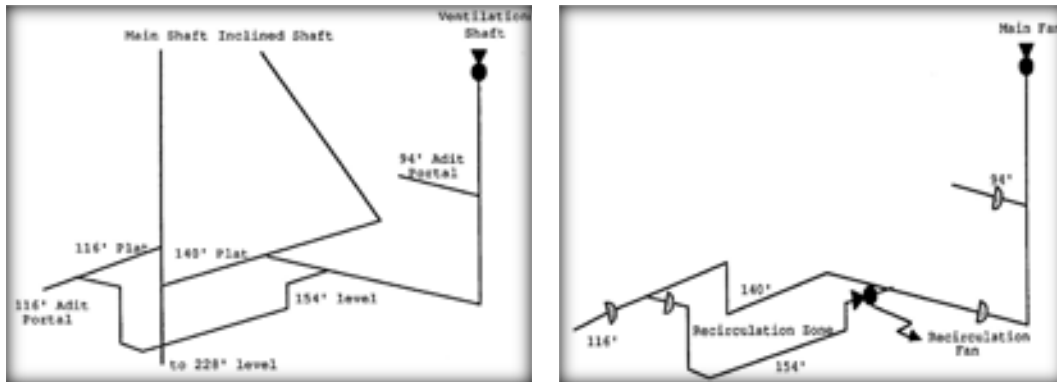


Figure 4. An experimental layout of mine workings and recirculation zone

It was concluded that controlled cross-cut recirculation is highly economic for deep or extensively mechanized metalliferous mines where the problems regarding heat encountered in their lower levels due to the minimum fresh air requirements being completely lower than those desired and feasible air quantities needed to control the climate.

3. CONTROLLED RECIRCULATION APPLICATIONS IN TURKEY

The first implementation of controlled recirculation in a roadway was achieved in the Central Anatolian Lignites in Cayirhan [10, 11] in order to determine the effect of recirculation on dust concentration. The schematic layout of the system is shown in Figure 5. It was revealed that the controlled recirculation of air in a heading would not cause an increase in dust concentrations.

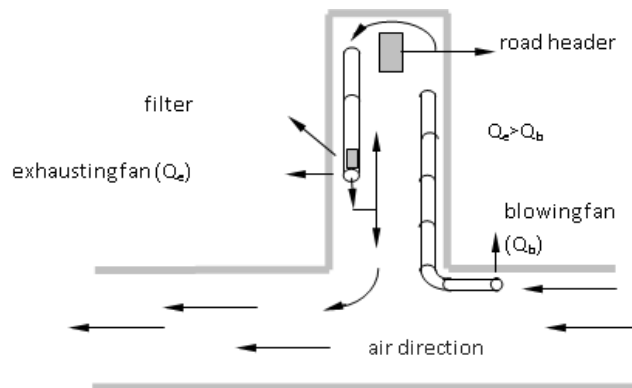


Figure 5. Recirculation of ventilating air system in a roadway

3.1. Darkale Colliery (Uyar Mining)

Darkale Colliery is 93 km to the city of Manisa, 90 km to the city of Balikesir, and 1 km to the county of Soma. The coal was first discovered in 1916 in the region. The production of coal has been performed in the site since then according to conditions of the current period.

All works at Darkale Colliery are performed at a level of 105 m to 240 m. The deepest point is vertically 120 m. There are three production faces. The chain conveyors and belt conveyors are used for coal transportation. The thickness of the coal varies between 3 m and 5 m with the intermediate cuts. The coal seams in this thickness allow longwall production method with block caving in which coal seams are horizontally distributed in different levels and there is 10 m or 12 m distance between the faces.

The dust concentration, airspeed, air pressure, roadway section, and gases were measured at 73 different locations on the predetermined route in the underground mine of Uyar Mining Darkale Colliery. The measurements were started from the mine entrance (+241,50 m.) then continued along the route and raise, and taken at the predetermined 73 points and ended at the outlet of airway (+240,20 m). Figure 7 provides the sketch of the routes where measurements were performed.

There are 2 large blower fans of 1200 m³/min and 800 m³/min in Darkale Colliery in order to meet the requirement for underground ventilation. The first fan with the larger capacity located at the mine entrance operates constantly. The second fan is activated when necessary. It also functions as a substitute fan. Simultaneous continual operation of two fans poses a risk to ventilation requirements because they provide an intense airstream; thus only one fan is operated. Measurement was taken from the first fan when it was in operation (Figure 6).

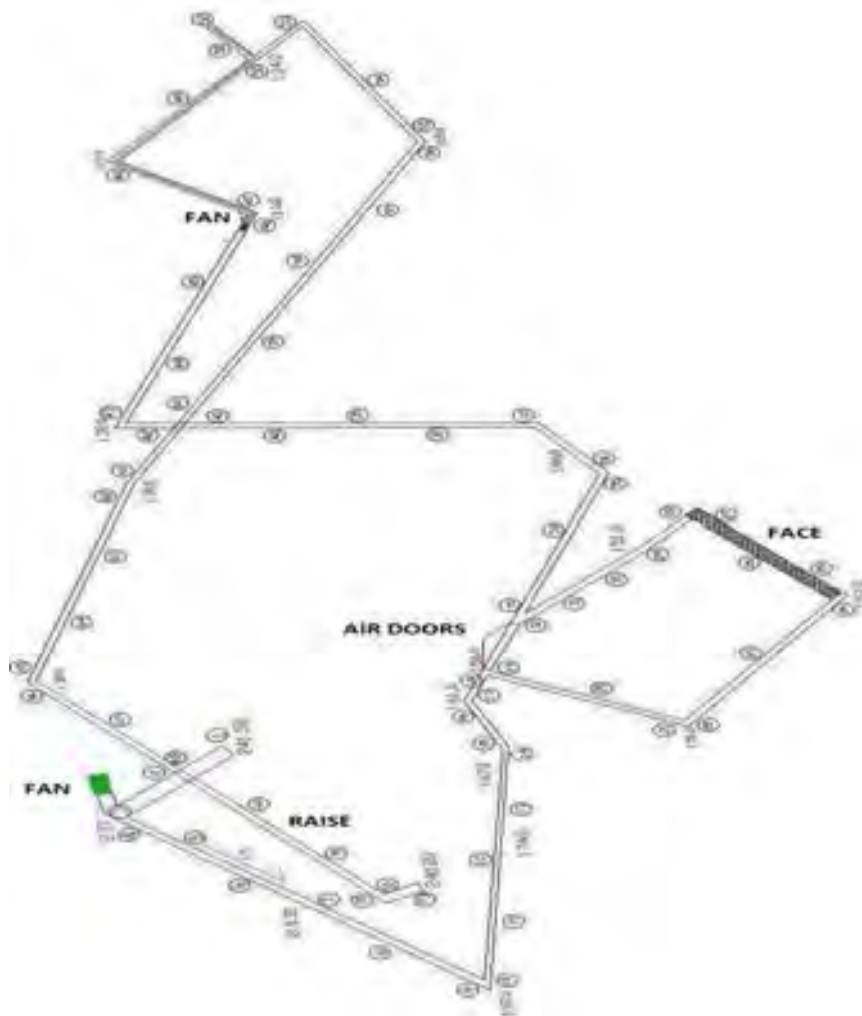


Figure 6. The sketch of the routes where measurements were performed

Auxiliary fans of 40 m³/min are also used in the pit to ventilate the areas in which the auxiliary drive, blind spots, and main ventilation fall short. There is one auxiliary fan on the measurement route used for ventilation. There are a total of 6 auxiliary fans of 40 m³/min used at different locations of the pit.

The measurements showed that the CO₂ concentration ranged between 0,03% and 0,32%. This rate is under the national permitted limit of 0.5% maximum in the mines. The CO₂ concentration was gradually increased from the mine entrance along the route. This indicates that the fresh air to the mine is gradually polluted along the route. The concentration of CO₂ was severely increased from the measurement point number 24 between two faces on the route. This increase in the concentration was further grew as moved along the route and approached to the raise. The cause of increased CO₂ was that the circulating air in the mine, i.e. the fresh air blown by the fan, decreasingly lost its effect as it reached to each measurement point in the forward direction. The concentration of CO₂ started to decrease again with the increased fresh air at outlet of raise.

The concentration of CO was not present except for the 3rd face and raise on the route according to CO measurements in the pit. The measured values in the face ranged from 12 to 16 ppm. This was between 9 and 15 ppm at the raise. These values are under the maximum allowable operation limits of 50 ppm for CO concentration.

The cause of CO concentration in the face was that the coal gets heated in the faults behind the faces. The cause of CO concentration at the raise was the near face number 1. Besides, it is normal to have some CO concentration here as the entire air of the mine is discharged at the raise after circulating. Spontaneous combustion of coal and formation of CO was one of the serious problems of the pit in the past as well as now.

In the measurement of O₂ performed from the mine entrance, a periodic decrease was present from the measurement point in the face cross-cut number 21. The main cause of this decrease was that the volume of air to the face was controlled. The decreasing airspeed from the face cross-cut resulted in decreased concentration of O₂ in these areas. Furthermore, the CO concentration found in the face indicates that the coal consumes oxygen as it gets heated. This is another factor affecting the combustion-related decreased O₂. The concentration of O₂ was significantly increased with the effect of circulation of fresh air from the measurement point number 32 at the air outlet of the face. This increase was within normal limits along the route to the raise. The decrease at the raise appeared to be normal because the entire polluted air of the mine was accumulated and discharged at the raise.

The air pressure at the mine entrance was measured with airspeed being (+241,50 m) 2,27 m/s, temperature being 19,8°C, and the atmospheric pressure being 744,9 mmHg, and periodically increased from the mine entrance. This periodic increase remained along the route in the mine and was gradually decreased as approached to raise, and measured at the outlet of raise and measurement point number 72 with airspeed being (+240,20 m) 1,62 m/s, temperature being 20,9 °C, and the atmospheric pressure being 745,8 mmHg. This shows that there was a pressure difference of 0,9 mmHg in the level difference of 1,3 m between the mine entrance and raise outlet. According to the principle that the air moves from the high pressure to the low pressure which is the basic requirement of natural ventilation, the level difference of 1,3 m there will not be sufficient to provide natural ventilation. The main factor here was the airstream and pressure produced by the fan. The airspeed higher than 2 m/s from the point number 4 where fan joins the air of the mine was effective in increased pressure.

There was a reverse current to the point number 4 (between the mine entrance and the fan) in the direction of mine entrance, i.e. towards to point number 1. The cause of this was that some volume of the air blown by the fan that joined the mine air at point number 4 escaped towards the mine entrance. The mine air was regulated from the point number 4 and lost its acceleration and decreased along the mine. This decrease was further increased as approached to face cross-cut and reduced well after the point number 24 in the face, being under 1,03 m/s. The air velocity which reduced down to 0,39 m/s from the air outlet of the face was again increased from the point number 33 being higher than 1,76 m/s.

The temperature being 19,8 °C at the mine entrance was slightly decreased with the effect of the fan from the point number 4. Loss of acceleration in the air velocity and the temperature were increased as going down deeper. From the point number 24 where the velocity of air was fully decreased, the temperature raised up to 23,8 °C at the face cross-cut and as entered the face, and up to 25,6 °C at the air outlet of the face. The temperature reduced with the increased air velocity and remained at same values to the raise. The cause of the high temperature raised up to 24,9 °C in the midway of raise was that the entire air of the mine was accumulated and discharged there. The temperature reduced again towards the outlet of raise.

The dust measurements in the mine varied from the mine entrance to the interior sections. The main cause of this variation and increase was that operations in the working sites and the transportation equipment in almost all roadways. The dust concentration in the mine varied from 0,109 to 3,230 mg/m³. The measured values for dust concentration were generally under the threshold limit values as permitted by the regulations.

3.1.1. Assessment of auxiliary ventilation measurements

The fan installed on the route to provide fresh air to auxiliary drive is located at the measurement point number 46 and blows air to the face of the auxiliary drive which is the measurement point number 52. Figure 7 provides the sketch of area of this auxiliary ventilation.

The fan located at the measurement point number 46 to provide fresh air to the auxiliary drive blows air to the point number 52 at the face of auxiliary drive. This is also to transfer the air at the point number 46 to the point number 52. Thus, the circulation of air is ensured without being affected by the decreased air velocity from the point number 46 and the pollution of CO₂. The concentration of CO₂ measured as 0.9% at the point number 46 continued to increase from this measurement point and reduced down to 0.10% at the face of the auxiliary drive which was the measurement point 52. This indicates that a volume of air almost equal to the concentration of CO₂ at the measurement point number 46 was transferred to the measurement point number 52. In this way, operations at the face of the auxiliary drive are possible to continue.



Figure 7. The sketch of the routes where measurements were performed

No CO concentration was present in the area with auxiliary fan (between the measurement point number 46 and the measurement point number 53).

The dust concentration which was measured to be 0,862 mg/m³ at the measurement point number 45 which was the nearest measurement point to auxiliary ventilation area with respect to forward direction of the route was measured to be 0,322 mg/m³ at the measurement point number 46 at which the fan was installed. The dust concentration remained at the same level as a result of that decrease and increased as approached to auxiliary drive. It was measured to be 0,294 mg/m³ at the measurement point number 52, i.e. face of the auxiliary drive. This measured value was within normal limits at the time of measurement because no works were being performed to produce dust at the auxiliary drive such as mining and exploding [12].

3.2. Turab Colliery

Turab Mining underground mine is a subcontractor operating under Cenne Colliery and in the site with License Number I.R. 617. It commenced production in 1988 and currently continues operation. Ermenek lignite basin located in the Western Toros Mountains covers around an area of 620 km².

The mine is located in the village of Cenne, the county of Ermenek, the province of Karaman. The mine is 25 km to Ermenek, and approximately 170 km to Karaman.

The coal seam is fissured and tortuous in the TurabMining underground mine. Under these circumstances, the roadways are established in the hanging wall (marn) before the coal seam is entered; the coal seam is cut in cross-cuts; the short walls of 25 to 30 m are established to apply short-wall production method with block caving.

3.2.1. Measurements in Turab Colliery

The dust concentration, air velocity, air pressure, roadway section, and gases were measured at 8 different points on the predetermined route in the TurabMining underground mine. The measurements were started from the mine entrance (+892,59 m) then continued along the route and raise, and taken at the predetermined 8 points and ended at the outlet of raise (+894,99 m). The mean of gas measurements performed in the mine is presented in the Table 1, and the mean of pressure, temperature and dust measurements performed in the mine is presented in the Table 2. Figure 8 provides the sketch of the route where measurements were performed.

Table 1. The results of measurement of gases

measuring points	CO ₂ %	CO ppm	O ₂ %	measuring points	CO ₂ %	CO ppm	O ₂ %
1	0,03	0	20,4	5	0,60	0	19,5
2	0,05	0	20,1	6	0,40	0	20,0
3	0,77	31	19,0	7	0,42	0	20,1
4	0,42	8	19,2	8	0,03	0	20,5

Table 2. The results of measurement of pressure, temperature and dust concentration

measuring points	pressure mmHg	Temp. °C	dust content mg/m ³	measuring points	pressure mmHg	Temp. °C	dust content mg/m ³
1	687,6	22,7	0,054	5	692,5	21,0	0,118
2	692,6	20,6	0,058	6	692,4	19,6	0,068
3	691,6	21,3	0,123	7	689,4	18,5	0,083
4	691,6	22,0	0,084	8	687,0	21,5	0,071

The mean of air flows of 8 measurement points along the route of the pit is presented in the Table 3.

Table 3. Air flow analysis in the measurement point

measuring points	area m	air velocity m/s	air flow m ³ /s	measuring points	area m	air velocity m/s	air flow m ³ /s
1	7,1	0,93	6,60	5	4,8	0,31	1,49
2	7,2	0,40	2,88	6	3,3	0,94	3,10
3	5,3	0,12	0,64	7	3,3	0,67	2,21
4	3,8	0,22	0,84	8	3,3	0,75	2,48

The air flow reduced down to 0,64 m³/h, which was the lowest level, at the measurement point number 3 referred to as drive 1 where production was performed. Depending on the air flow, the concentration of CO₂, which was 0,03% at the mine entrance, raised to 0,77%; the CO concentration, which was 0 ppm at the mine entrance, raised to 31 ppm; and the concentration of O₂, which was 20,4% at the mine entrance, reduced to 19,0%. The dust concentration was at the highest being 0,123 mg/m³ in this area.



Figure 8. The schematic layout of routes

3.2.2. Assessment of Recirculated Air Measurements

The measurement stations were set up at the points shown in Figure 9 in the development roadways with auxiliary ventilation as part of works for re circulation of mine air. The gas (O_2 , CO, CO_2 , CH_4) and dust concentrations, volume of air, temperature and pressure values were measured at these stations.

To detect any changes in 7 predetermined measurement points, which were likely to occur due to the method applied, inlet of blower ventilator (1), between the outlet of blower fan and the face (2), inlet and outlet of suction fans (3 and 5), the route where the air is re-sucked (4), outlet of development roadway (6), and main ventilation way (7) were selected.

The rate of recirculation of main air was increased in a controlled way during the operations, and gas (O_2 , CO, CO_2 , CH_4) and dust concentrations, the volume of air, temperature and pressure values were measured and recorded. The operations were started with initial rate of recirculation of mine air being around 10% and later a variation of 20% and 30% occurred in recirculation of mine air. The Tables 4, 5 and 6 show these variations.

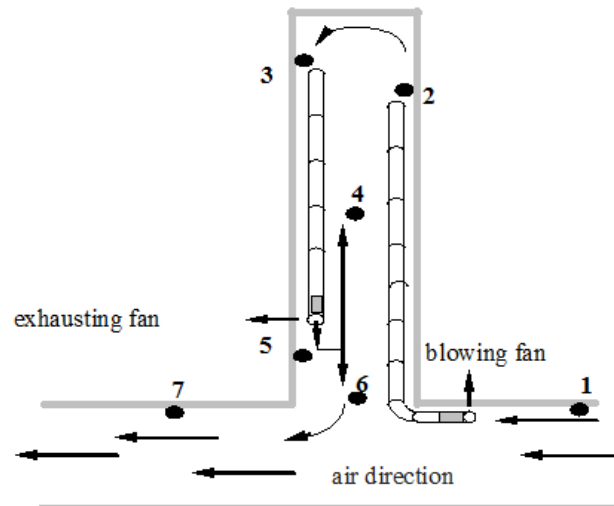


Figure 9. The measurement points

Table 4. Results of 10 % recirculation fraction

measuring points	airspeed m/s	pressure mmHg	dust content mg/m ³	Temp. °C	O ₂ %	CO ppm	CO ₂ %	CH ₄ %
1	1,21	751,8	0,325	21,8	20,8	0	0,09	0
2	1,34	752,1	0,538	22,1	20,2	30	0,22	0
3	1,51	752,1	0,269	21,6	20,7	12	0,15	0
4	1,17	751,9	0,391	21,9	20,4	19	0,19	0
5	1,53	752,1	0,382	21,8	20,5	18	0,19	0
6	1,40	752,0	0,489	21,9	20,5	16	0,17	0
7	1,23	751,7	0,561	21,9	20,5	16	0,18	0
RR, %	gallerylength, m		area, m ²					
12,7	162		6,82					

Table 5. Results of 20 % recirculation fraction

measuring points	airspeed m/s	pressure mmHg	dust content mg/m ³	Temp. °C	O ₂ %	CO ppm	CO ₂ %	CH ₄ %
1	1,25	751,6	0,412	21,7	20,6	0	0,08	0
2	1,41	752,0	0,645	23,1	19,8	42	0,32	0
3	1,72	752,1	0,372	21,3	20,3	21	0,21	0
4	1,31	751,9	0,394	21,9	20,5	15	0,15	0
5	1,53	752,0	0,386	21,4	20,4	14	0,15	0
6	1,45	752,1	0,495	21,6	20,4	10	0,16	0
7	1,26	751,8	0,480	22,0	20,4	5	0,16	0
RR, %	gallerylength, m		area, m ²					

22,0	170	6,82
------	-----	------

Table 6.Results of 30 % recirculation fraction

measuring points	airspeed m/s	pressure mmHg	dust content mg/m ³	Temp. °C	O ₂ %	CO ppm	CO ₂ %	CH ₄ %
1	1,18	751,9	0,260	21,9	20,7	0	0,10	0
2	1,38	752,5	0,581	23,5	19,6	35	0,41	0
3	1,80	752,5	0,109	21,1	20,6	11	0,19	0
4	1,45	751,9	0,352	21,8	20,4	18	0,17	0
5	1,54	752,2	0,298	21,0	20,5	17	0,17	0
6	1,28	752,3	0,381	21,5	20,7	9	0,15	0
7	1,20	751,8	0,295	22,0	20,5	10	0,14	0
RR, %	gallerylength, m			area, m ²				
30,4	181			6,82				

For three different conditions under which the works were performed, different air flows were obtained in the volumes of air with respect to recirculation of mine air, and significant improvement was achieved in the dust concentration, temperature and gas (O₂, CO, CO₂, CH₄) concentrations [12].

4. RESULTS AND DISCUSSIONS

Results obtained from the theoretical and in-situ works carried out both in Turkey and in the world proved that environmental conditions in underground mines regarding gaseous contaminants, dust, heat and humidity would be improved especially due to increasing velocity and quantity of air.

By the implementation of controlled recirculation of mine air, the air quantity increased will cause to dilute the concentrations of contaminants which are over the safety limits. Underground mines moved away from surface connections due to mining operations will encounter deficiencies for delivering adequate amount of air where necessary. Therefore, the method of recirculation of ventilating air has become more important considering the fact that it would be difficult to open a new surface connection or enlarge the existing roadways.

ACKNOWLEDGMENT

CemSensogut and Ibrahim Cinar gratefully wish to record their thanks to the Scientific Research Funds of Dumlupinar and Selcuk Universities in conducting this research.

The views expressed in this paper are those of the authors and not necessarily those of the sponsors.

REFERENCES

- [1]. C. Sensogut, "Computer Simulation of Gaseous Contaminant Distribution in Ventilation Networks with Special Reference to Controlled District Recirculation". *PhD Thesis, Nottingham Univ.*, 246p.1989
- [2]. C. Sensogut and S.Sarac, "Recirculation of Mine Air – A New Alternative". *7th Coal Congress of Turkey*, Zonguldak, pp. 177-188,1990 (in Turkish).
- [3]. I. Lowndes and C. Sensogut, "Computer Simulation of Radon Contamination Levels Around Controlled District Recirculation Circuits". *Mining Science and Technology*, vol. 10, pp. 177-189, 1990.
- [4]. B. R. Lawton, "Local Cooling Underground by Recirculation". *Trans. Ins. Min. Eng.*, vol. 85, pp. 63-76,1933.
- [5]. A. J. Pickering and R. Robinson, "Application of Controlled Air Recirculation to Auxiliary Ventilation System and Mine District Ventilation Circuits". *3rd Int. Mine Vent. Cong.* pp. 315-322, 1984.
- [6]. R. C. Burton, W.Plenderleith and J. M. Stuart, "Recirculation of Air in the Ventilation and Cooling of Deep Gold Mines". *3rd Int. Mine Vent. Cong.*, pp. 291-299, 1984.
- [7]. A. I. Hall, J. P.Saindon, L. D. Nel and S. G.Hardcastle, "Controlled Recirculation Investigation at Ruttan Mine". *Proc. of 3rd Mine Vent. Symp.*, edited by J.M. Mutmanky, 1987.
- [8]. A. E. Hall, D. M. Mchaina and S.Hardcastle, "Controlled Recirculation in Canadian Underground Potash Mines". *Min. Sci. and Tech.*, vol. 10, pp. 305-314, 1990.
- [9]. J. M. Anderson and W.Gostylla, "The Economic Feasibility of Recirculation in Underground Mines". *4th Int. Mine Vent. Cong.*, Brisbane, Queensland, pp. 309-316, 1988.

- [10]. O. Cetin, "Dust Control in Mechanized Roadways of OAL Colliery", *MSc Thesis, Osmangazi Univ.*, 86p (in Turkish), 1995.
 - [11]. S. Sarac and O. Cetin, "Recirculation of Ventilating Air Trial in OAL Colliery", *11th Coal Congress of Turkey*, Bartin, pp. 25-42 (in Turkish), 1998.
 - [12]. I. Cinar and C. Sensogut, "Controlled Recirculation of Ventilating Air in Underground Coal Mining, *19th Coal Congress of Turkey*, pp. 1-12, 2014 (in Turkish).
-

DRY SLIDING WEAR BEHAVIORS OF CAST Fe_3Al AND $Fe_{32.5}Al_{15}Ti$

Osman TORUN

AKÜ Bolvadin Vocational School, 03300 Afyonkarahisar, Turkey,
otorun@aku.edu.tr

Abstract

The base alloy Fe_3Al and $Fe_{32.5}Al_{15}Ti$ alloy were prepared by vacuum arc melting under argon atmosphere. The microstructure of the alloys were examined by optical microscopy. The results showed that microstructure of $Fe_{32.5}Al_{15}Ti$ alloy was different from that of Fe_3Al alloy. Hardness values of both alloys measured and hardness measurement demonstrated that the cast $Fe_{32.5}Al_{15}Ti$ alloy is harder than the cast Fe_3Al . The dry sliding wear test of these alloys were performed by ball on disc geometry using tungsten carbide ball. It was observed that the wear resistance of the cast $Fe_{32.5}Al_{15}Ti$ alloy was higher than that of Fe_3Al alloy. Worn surface of both alloys were analyzed by scanning electron microscopy equipped with energy dispersive spectroscopy.

Keywords: *Intermetallics compound, Fe_3Al , Dry sliding, Wear.*

1. INTRODUCTION

Ordered intermetallic compounds are of interest for high temperature application because of their potential for high temperature stability, high creep resistance, high melting point and low density. Among the intermetallics, compounds based on the aluminides are of particular interest because many possess oxidation resistance due to their ability to form protective oxide films on surfaces [1]. Recently, considerable efforts have been devoted to improving the ductility of nickel aluminides at ambient temperatures by controlling microstructure and alloy additions [2–4]. Strengthening concepts include solid solution hardening, precipitation of incoherent phases such as carbides, borides and other intermetallic phases, increasing the order, and generation of two-phase coherent microstructures. Compared to other iron aluminide-base alloys, the present Fe–Al–Ti alloys show a higher yield stress and creep resistance at high temperatures. The Fe–Al–Ti alloys on the base of the L21-ordered $\text{Fe}_2(\text{Fe}, \text{Ti})\text{Al}$ are promising for further development for high-temperature applications due to their improved strength at high temperatures in combination with a high oxidation resistance [5,6]. Considerable amount of economical loss occurs because of corrosion and wear in mechanical parts of machinery and equipment. In order to reduce this loss, properties of wear-resistant features and surface of materials should be improved [7]. There have been various works on wear properties of iron aluminides. FeAl alloys showed good wear properties and the wear resistance in room temperature. The wear rate of the aluminides increased with the increase of applied load and sliding speed and the wear resistance of the aluminides decreased with the increase in aluminum contents [8, 9]. Xingsheng Guan et al. investigated wear behaviors of Fe-28Al (PM) and Fe-28Al-10Ti (PM) alloys. In this study, the wear behaviors of the cast Fe_3Al and Fe32.5Al15Ti were examined.

2. EXPERIMENTS

Fe_3Al and Fe32.5Al15Ti alloys were melted in a copper crucible cooled by water and then cast in a steel mold (8 mm in diameter) in a vacuum arc melting furnace (designed specially) under pure argon atmosphere. To prevent oxidation, furnace was evacuated to 5.0×10^{-2} mbar then filled with Argon. Cylindrical samples were machined to 5 mm length for wear tests. The microstructures of the both alloys was observed with a light microscope and XRD analyses were taken. Hardness values were measured from surface of samples by means of Vickers indenter with a load of 100 g. The dry sliding wear tests were performed with ball-on-disk geometry (CSM Tribometer) at 15 cm/s sliding speed under 15N normal load and ambient atmosphere. The schematic illustration of wear test equipment is shown in Fig 1.

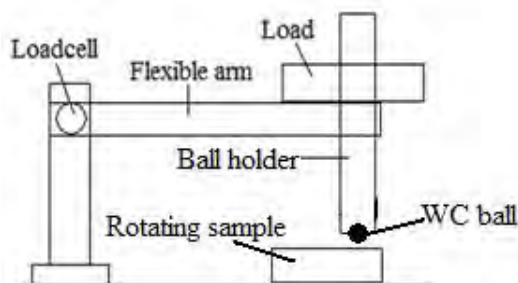


Figure 1. Schematic illustration of pin-on-disk wear test equipment.

The sample was inserted a rotating deck and a WC ball of 3 mm in diameter was pushed against it as a counter material. The wear of WC ball was negligible in comparison with the specimen. The wear rates were determined as volume loss. The tests were performed at 100 m sliding distance, and the total distance was 300 m. The wear area of the worn surfaces measured with a profilometer and the volume losses were calculated. The coefficients of friction were measured by the machine during wear tests.

3. RESULTS AND DISCUSSION

Microstructures of as-cast Fe_3Al and Fe32.5Al15Ti are illustrated in Fig. 2. These figures demonstrated that the microstructure of Fe32.5Al15Ti was different from that of the cast Fe_3Al . While Fe_3Al has single phase, Fe32.5Al15Ti alloy has L21 $\text{Fe}_2(\text{Fe}, \text{Ti})\text{Al}$ + C14 Laves phases [5, 6]. No porosities were observed in both alloy.

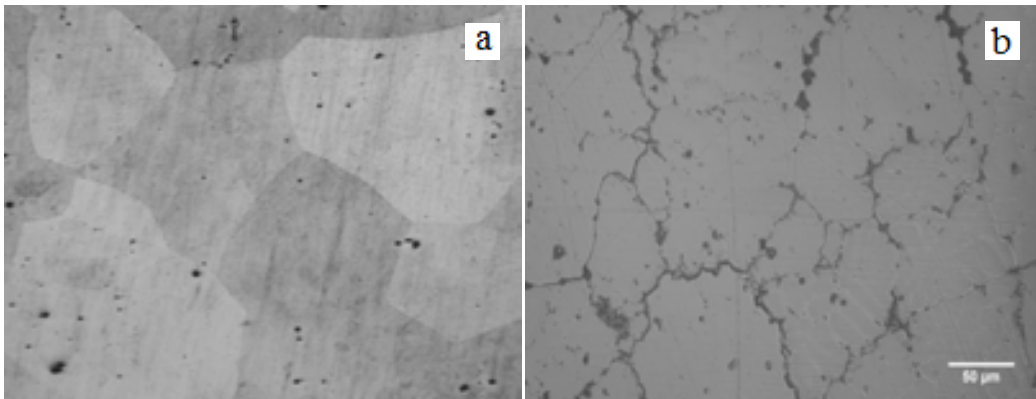


Figure 2. The microstructures of as-cast alloys. (a) Fe_3Al (b) $Fe_{32.5}Al_{15}Ti$

Microhardness values were measured from the surface of both alloys by means of Vickers indenter with a load of 100 g. Hardness of the cast $Fe_{32.5}Al_{15}Ti$ alloy (560 ± 15 HV) is higher than that of as-cast Fe_3Al alloys (310 ± 15 HV).

Volume loss of the cast Fe_3Al and $Fe_{32.5}Al_{15}Ti$ alloys are showed in Fig. 3 The cast $Fe_{32.5}Al_{15}Ti$ alloy shows lower wear rate than the cast Fe_3Al alloy for 15 cm/s 15 N load and sliding speeds. It can be thought that the cast $Fe_{32.5}Al_{15}Ti$ alloy has more wear resistance than the cast Fe_3Al alloy, because $Fe_{32.5}Al_{15}Ti$ alloy is much harder than the cast Fe_3Al alloy. As seen from Fig. 3, the volume loss increased with increase in sliding distance for both alloys. The cast Fe_3Al and $Fe_{32.5}Al_{15}Ti$ alloys can easily form a thin oxide film on the their surface due to high aluminum content. The formation of oxides at the interface of the cast Fe_3Al alloy is more than that of the cast $Fe_{32.5}Al_{15}Ti$ alloy. As a result, the volume loss for the cast Fe_3Al is higher than for $Fe_{32.5}Al_{15}Ti$ alloy.

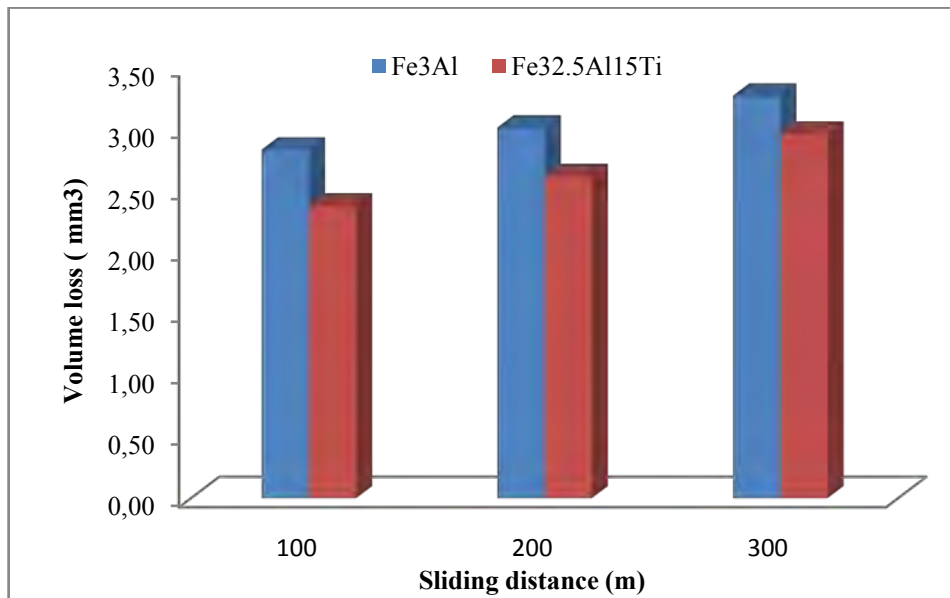


Fig 3. The volume losses of the cast Fe_3Al and $Fe_{32.5}Al_{15}Ti$ alloys for 15 N normal load and 15 cm/s sliding speed.

4. CONCLUSION

The base alloy Fe₃Al and Fe_{32.5}Al₁₅Ti alloy were prepared by vacuum arc melting under argon atmosphere. Hardness of the cast Fe₃Al and Fe_{32.5}Al₁₅Ti alloys were found 310±15 and 560±15 HV respectively. The wear resistance of the cast Fe₃Al and Fe_{32.5}Al₁₅Ti alloys were determined using WC ball. The cast Fe_{32.5}Al₁₅Ti alloy shows much higher wear resistance than the cast Fe₃Al alloy for 15 N normal load and 15 cm/s sliding speed. The coefficients of friction of Fe_{32.5}Al₁₅Ti alloy are lower than that of Fe₃Al alloy for all sliding conditions.

ACKNOWLEDGE

The research was supported by Afyonkocatepe University Research Foundation, Afyonkarahisar, Turkey.

REFERENCES

- [1]. Kim, Y. S., Kim, Y. H., Sliding wear behavior of Fe₃Al based alloys. *Material Science and Engineering A*, 258 (1998), 319-324.
 - [2]. Chan, R.W., *Proceedings of Materials Week '96 on Nickel and Iron Aluminides: Processing, Properties, and Applications*, Ohio, 7-9 October 1996, edited by S.C. Deevi, V.K. Sikka, P.J. Maziasz and R. W. Chan, USA, ASM international, 1997, p.3
 - [3]. Liu, C.T., Kumar K.S., *Ordered Intermetallic Alloys, Part I: Nickel and Iron Aluminides*, *Journal of Materials Science*, May (1993) 38-44.
 - [4]. Guan X., Iwasaki, K., Kishi, K., Yamamoto, M., Tanaka, R., Dry Sliding wear of Fe-28Al and Fe-28Al-10Ti alloys. *Materials Science and Engineering A*, 366 (2004) 127-134.
 - [5]. Basu, A., Dutta Majumdar, J., Alphonsa, J., Mukherjee, S., Manna, I., Corrosion resistance improvement of high carbon low alloy steel by plasma nitriding. *Materials Letters*, 62 (2008) 3117-3120.
 - [6]. Yun-tao, X., Dao-xin, L., Dong, H., Improvement of erosion and erosion-corrosion resistance of AISI420 stainless steel by low temperature plasma nitriding. *Applied Surface Science*, 254 (2008) 5953-5958.
 - [7]. Skolek-Stefaniszyn, E., Kaminski, J., Sobczak, J., Wierzchon, T., Modifying the properties of AISI 316L steel by glow discharge assisted low-temperature nitriding and oxynitriding. *Vacuum*, 85 (2010) 164-169.
 - [8]. YildizSirin, S., Sirin, K., Kulac, E., Effect of the ion nitriding surface hardening process on fatigue behavior of AISI 4340 steel. *Materials Characterization*, 59 (2008) 351-358.
 - [9]. Munoz Riofano, R.M., Casteletti, L.C., Canale, C.F., Totten, G.E., Improved wear resistance of P/M tool steel alloy with different vanadium contents after ion nitriding. *Wear*, 265 (2008) 57-64
 - [10]. Wang, J., Xiong, J., Peng, Q., Fan, H., Wang, Y., Li, G., Shen, B., Effects of DC plasma nitriding parameters on microstructure and properties of 304L stainless steel. *Materials Characterization*, 60 (2009) 197-203.
 - [11]. Castro, G., Fernandez-Vicente, A., Cid, J., Influence of the nitriding time in the wear behaviour of an AISI H13 steel during a crankshaft forging process. *Wear*, 263 (2007) 1375-1385.
 - [12]. Terres, M.A., Ben Mohamed, S., Sidhom, H., Influence of ion nitriding on fatigue strength of low-alloy (42CrMo4) steel: Experimental characterization and predictive approach. *International journal of Fatigue*, 32 (2010) 1795-1804.
 - [13]. Wen, D. C., Microstructure and corrosion resistance of the layers formed on the surface of precipitation hardenable plastic mold steel by plasma-nitriding. *Applied Surface Science*, 256 (2009) 797-804.
 - [14]. Celikyurek, I., Baksan, B., Torun, O., Gurler, R., Boronizing of iron aluminide Fe₇₂Al₂₈. *Intermetallics*, 14 (2006) 136-141.
 - [15]. Ekmekçiler, E., Polat, A., Usta, M., Hard boride coating on iron aluminide (FeAl). *Surface and Coatings Technology*, 202 (2008) 6011-6015.
-

ENERGY EFFICIENCY ENHANCEMENT OF A HOUSEHOLD REFRIGERATOR USING WITH OIL COOLING CONDENSER

Erdoğan KILIÇASLAN

Karabuk University, Department of Energy Systems Engineering, 78200, 100. Yil/Karabuk, Turkey.
alperergun@karabuk.edu.tr

Alper ERGÜN

Karabuk University, Department of Energy Systems Engineering, 78200, 100. Yil/Karabuk, Turkey.

Engin GEDIK

Karabuk University, Department of Energy Systems Engineering, 78200, 100. Yil/Karabuk, Turkey.

Bahadır ACAR

Karabuk University, Department of Energy Systems Engineering, 78200, 100. Yil/Karabuk, Turkey.

Engin ÖZBAŞ

Ondokuz Mayıs University, Yesilyurt Demir-Celik Vocational School, 55330, Tekkekoy/Samsun, Turkey.

Abstract

An oil tank condenser is proposed for increasing overall performance of household refrigerator. A wire-tube condenser on the household refrigerator chosen as an experimental set was tested and energy consumption was measured. The greatest specialty of this work is using oil tank on the condenser. A novel refrigerator with oil tank condensers and an ordinary refrigerator with conventional hot-wall condensers are compared by means of COP and energy consumption. As a result of this study, according to the energy consumption, condenser with an oil tank (tank is full of oil) was found as % 65 and % 63 more effective than natural convection with unloaded and loaded situation respectively. Using a condenser placed inside the oil tank has caused to increase energy efficiency of the household refrigerator and to decrease energy consumption

Keywords: Household refrigerator, energy consumption, performance of coefficient (COP), condenser.

1. INTRODUCTION

Demand for energy determining to economic, political and social events is increasing day by day in the world. Countries should have to take precautions for use their existing energy sources efficiently by searching the new methods. Due to a large amount of energy consumed by the household refrigerator-freezers which accounts for approximately 6% of the electrical energy produced worldwide and they are widely used in the world now and consume a large amount of energy [1]. It must be improved with using the new novelties of the refrigerators to improve the performance or saving energy. So, this topic is particularly important for devices produced in large numbers, such as domestic refrigerators and freezers [2]. For example household refrigerators, on the whole, consume a large amount of energy since hundreds of millions are currently in use, and dozens of millions are coming onto the market every year [3]. The condenser is an important component of a household refrigerator and its heat transfer performance has a significant effect on the efficiency because all thermal load produced by the refrigerator must be released to ambient by the condenser through nature convection and radiation [4].

Energy saving and performances of refrigerators can be improved by: i) using high efficiency compressor, which has a direct impact on the coefficient of performance (COP) of cooling system; ii) optimizing the match and control of the system by adopting advanced circulation; iii) improving the thermal insulation of refrigerators by thickening the insulation or using other advanced thermal insulation techniques; and iv) optimizing the heat-transfer of the evaporator and the condenser [5]. Last century, a kind of regenerator for energy storage by PCM (Phase Change Material) latent heat was introduced. The regenerator placed into the refrigerator could improve the refrigerator efficiency by reducing the start frequency of the compressor [6]. In recent years, Azzouz et al. [7,8] presented an energy storage method by adding a thick slab PCM on the backside of the evaporator, which improved the COP of household refrigerator by 10%-30% approximately. Neto et al. [9] presented the application of a hot-water storage tank which was heated by the waste heat of the condenser. Diseconomy and inconvenience were two main disadvantages of this technique. Researchers also tried to use the phase change material (PCM) as heat storage unit to achieved continuous heat dissipation. It was evaluated that this method could increase the refrigerator efficiency by 20% approximately [10]. Yang et al. [11] investigated the performance of household refrigerator numerically and experimentally. Obtained results indicate the temperature distributions from the numerical simulation were qualitatively in line with the experimental measurements at the end of the study. Patil [12] has used two different type condensers to improve refrigeration efficiency. When used micro-wire condenser the refrigeration capacity and COP increase was found as 10% and 17% respectively according to used U type condenser. However it is seen that to use evaporative type condenser is increasing refrigeration efficiency about 30% [13, 14]. In the paper studied by Tissot [15] it was aimed to improve energy efficiency while water sprays application to the condenser unit of a household refrigerator. It has been found that at the end of the study about 28.9% COP increasing. Kılıcaslan [16] investigated performance of a commercial refrigerator with using different sized chimney instead of condenser fan.

In the present work it is aimed to improve overall refrigerator performance and reduce to energy consumption of a household refrigerator. For this purpose a household refrigerator which condenser unit was submerged to the oil tank was used as an experimental test. In the next sections, the methodology is presented, as well as the main results.

2. METHODOLOGY

The experimental test rig was a 180 L household refrigerator which was originally designed for R134a refrigerant with 139 g charge. The most important specifications of the refrigerator are summarized in Table 1.

Table 1. Technical specifications of household refrigerator test unit.

Fresh food volume	180
Voltage	190-220 V
Current rating	0.8 A
Frequency	50 Hz
Number of doors	1
Refrigerant type	R134-a
Refrigerant charged	139 gr
Compressor capacity	160 W

Condenser dimension	0.55 x 0.87 m
Condenser pipe outer and inner diameter	0.0048 and 0.0038 m
Condenser pipe length	10.8 m
Relief type evaporator dimension	0.22 x 0.5 m
Capillary tube length	2.8 m
Capillary tube outer and inner diameter	0.0018 and 0.0004 m
Oil tank dimension	0.9 x 0.6 x 0.02 m

A schematic diagram of a vapor compression refrigeration cycle used in household refrigerators and its pressure-enthalpy diagram are shown in the Figs. 1 and 2. The P-h diagram is well known which frequently used analysis of vapor-compression refrigeration cycles. Processes, 1-2, 2-4, 4-5 and 5-1 represent the various processes such as compression, condensation, expansion and evaporation respectively.

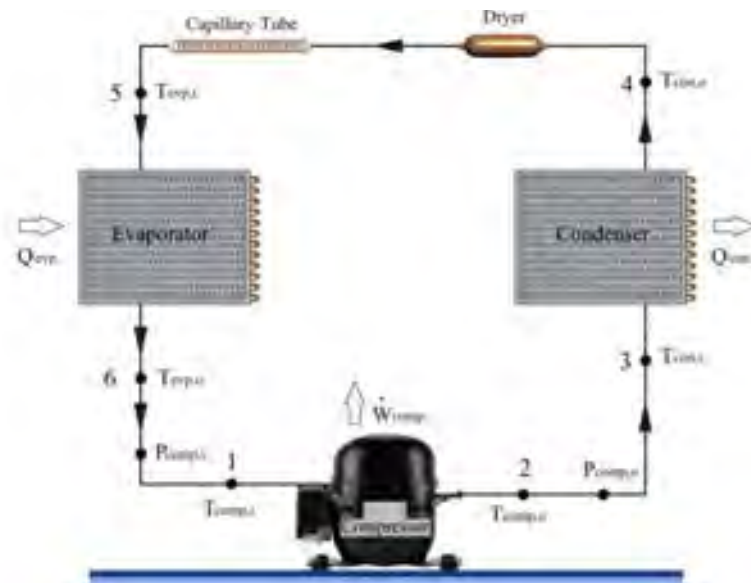


Figure 1. Schematic diagram of the refrigeration cycle.

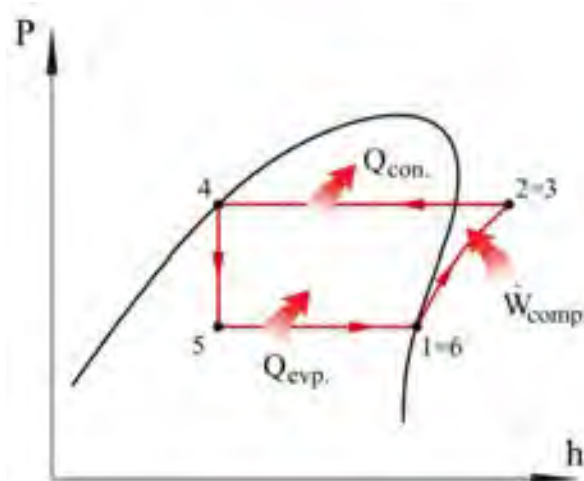


Figure 2. P-h diagram of the ideal vapor compression refrigeration cycle.

An oil cooled condenser located at the back side of the refrigerator is used as shown schematically in Figure 3 (a). The condenser area of the refrigerator was designed and produced to take place in the oil tank. The test unit used for experimental set as shown in the Figure 3 (b).

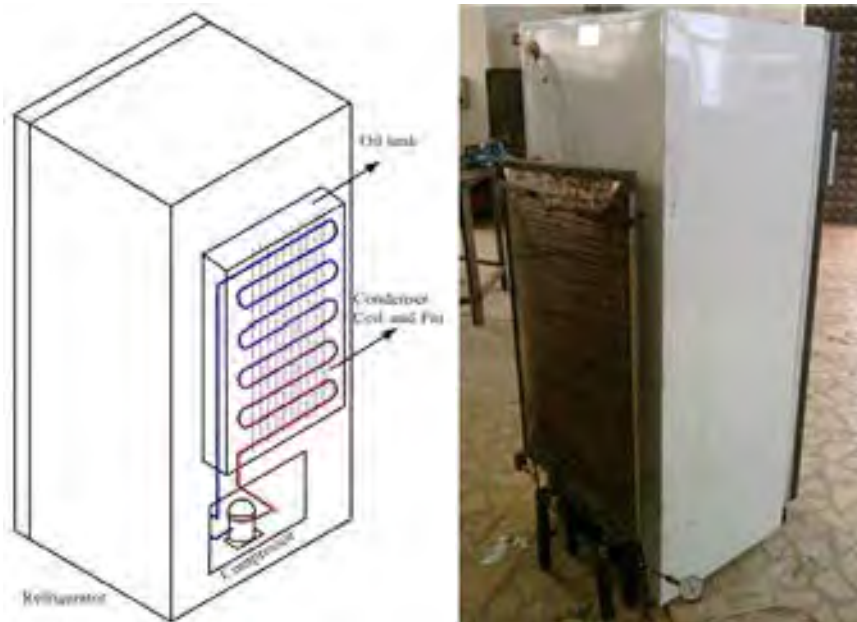


Figure 3. (a) Condenser and the oil tank section of the test unit. (b) Model refrigerator used in the experiments.

Experimental test unit is consisting of compressor, condenser, capillary tube, filter-dryer and the oil tank which produced in the laboratory of the Energy of Karabük University, Turkey. The oil tank was produced with metal sheet 0.5 mm in thick and 1x1.20x0.025 m dimensions using welding technique as shown in the Figure 4. Produced oil tank was placed outside of the refrigerator with using special holding equipment which produced metal materials and then, they all prepared for the tests.

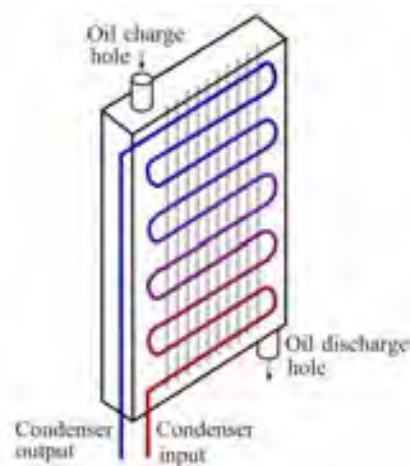


Figure 4. Schematic view of oil tank and condenser.

Tests were realized for the natural convection (NC) while condenser inside the oil tank with no oil and then, the same tests were repeated by the putting the condenser in the oil tank with oil. Temperatures at various points showing in Figure 1 (compressor, condenser, evaporator, etc.) were measured with K type Ni-Cr thermocouples. The uncertainty of temperature measurement is estimated to be ± 0.3 °C. Same procedure was realized for the pressure measurements using manometers with uncertainty ± 1 kPa for the all points. In addition, the consumed voltage and current were recorded. Analyzing these data, the energy consumption and efficiency were calculated. There was no significant change in ambient temperature during the tests. Temperature change is almost constant as 22 °C. To determine the efficiency values of the system in the

loaded situation a lump has 60 Watt power was placed at the evaporation section. In here digital thermometer was used to measure the temperatures. Experiments were realized in the situation which loaded and unloaded of the system without oil (oil tank empty) and with oil.

Enthalpy values of the points were obtained according to measured temperatures for the R134a refrigerant. Thermodynamics properties of the natural convection (NC) and natural convection with oil tank (NCOT) were given Table 2 for the loaded and unloaded situation.

Table 2. Thermodynamics properties of the NC and NCOT for loaded and unloaded situation.

Exp	Case	$T_2=T_3$	T_5	$T_1=T_6$	$P_2=P_3$	$P_1=P_5=P_6$	$h_2=h_3$	h_5	$h_1=h_6$
		$^{\circ}\text{C}$	$^{\circ}\text{C}$	$^{\circ}\text{C}$	kPa	kPa	kJ/kg	kJ/kg	kJ/kg
NCOT	Loaded	66	38	-15.2	1100	20	445.96	253.48	393.75
NC		92.4	60.6	-5.4	1970	80	461.68	288.31	399.75
NCOT	Unloaded	69	38.4	-11.76	1290	24	445.92	254.06	396.24
NC		82.8	57.4	-13.4	1700	40	454.64	283.13	394.53

2.1. Performance of refrigerator

For the coefficient of performance (COP) calculations following relations were used. Energy balance for a steady-flow condition can be expressed as:

$$q_{net} - w_{net} = \Delta h + \Delta ke + \Delta pe \quad (1)$$

where q_{net} and w_{net} describes the net heat and work input, Δh is the enthalpy change, Δke is the kinetic energy change and Δpe is the potential energy change in the system. It can be defined as, a transferred energy to any system via heat and work is equal to energy changing inside the system.

All four components associated with the vapor-compression refrigeration cycle are steady-flow devices, and thus all four processes that make up the cycle can be analyzed as steady-flow processes. The kinetic and potential energy changes of the refrigerant are usually small relative to the work and heat transfer terms, and therefore they can be neglected [17]. Then the steady flow energy equation on a unit-mass basis reduces to:

$$(q_i - q_o) + (w_i - w_o) = h_o - h_i \quad (2)$$

where q , w and h are the heat, work and enthalpy respectively while i and o describe the subtitle of input and output. The condenser and the evaporator do not involve any work, and the compressor can be approximated as adiabatic. In this instance amount of heat removed from condenser unit and absorbed from evaporator section of the refrigerator working as vapor-compressed refrigeration cycle can be expressed with following Equations 2.3 and 2.4 while the work expressed with Equation 2.5 for our system.

$$\dot{Q}_{evap} = \dot{m}(h_6 - h_5) \quad (3)$$

$$\dot{Q}_{cond} = \dot{m}(h_3 - h_4) \quad (4)$$

$$\dot{W}_{comp.} = \dot{m}(h_2 - h_1) \quad (5)$$

In the expressions 2.3 and 2.5 $\dot{Q}_{evap.}$, $\dot{Q}_{con.}$ and $\dot{W}_{comp.}$ defined as capacity of the evaporator, condenser and compressor which are the main components of the refrigeration system. The efficiency of a refrigerator is expressed in terms of the coefficient of performance, COP. The objective of a refrigerator is to remove heat from the refrigerated space. To accomplish this objective, it requires a work input of $\dot{W}_{comp.}$. Consequently, the overall performance of the refrigerator is estimated from COP calculated as the ratio between the heat extracted by the evaporator and the electrical energy supplied to the compressor which can be expressed as:

$$COP = \frac{\dot{Q}_{evap.}}{\dot{Q}_{comp.}} = \frac{h_6 - h_5}{h_2 - h_1} \quad (6)$$

In the relation 2.6 the COP values were calculated via measured enthalpy values for R134 ba sed on temperatures and pressures.

3. RESULTS AND DISCUSSIONS

Experiments were performed for NC and then same experiments were repeated for the NCOT. Oil tank was filled with 10 lt 20/50 synthetic oil. Before the measure of the parameters the experimental set was run about 2 hours to get steady conditions. Measured temperatures values of t he inlet and outlet points of t he compressor, condenser and evaporator of the experimental system were registered for the NC and NCOT. The obtained results from these tests were plotted as shown in Figures 5 and 6 for loaded and unloaded situations.

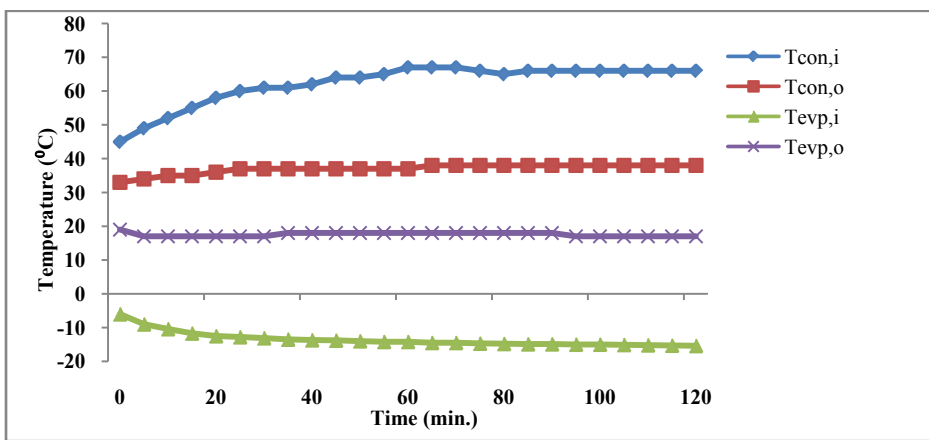


Figure 5. Temperature changes of the basic components of the system for NCOT unloaded situation.

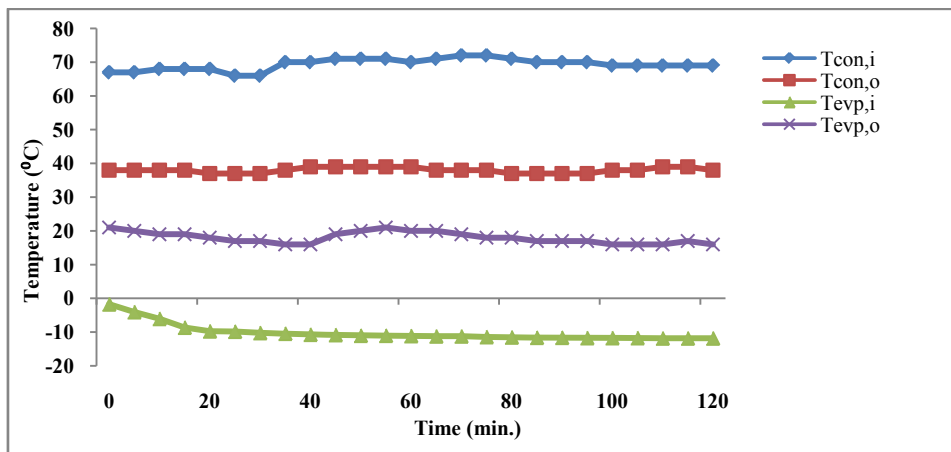


Figure 6. Temperature changes of the basic components of the system for NCOT loaded situation.

In Figure 5 temperatures change has been shown versus experimental time for the unloaded situation of NCOT. The maximum temperature differences of the evaporator outlet and inlet points was found as 32.4 °C which would be used COP calculations for the unloaded situation while this value was found as 27.8 °C for the loaded situation of the system. Using 60 W loads in the evaporator section has led to decrease about 15% of temperature differences between inlet and outlet of the evaporator. Likewise, same tendency were observed

other temperatures of the system components. Calculated COP values were plotted graphically as shown in Figure 7 for the NC and NCOT.

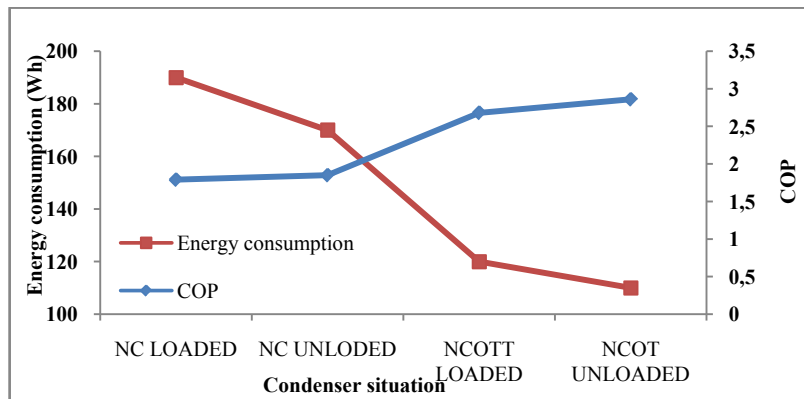


Figure 7. Energy consumption and COP values of the NC and NCOT.

As can be seen from the Figure 8 the higher COP value was found where the oil tank is full of oil in each case. In NC the COP values was found as 1.85 and 1.79 for the loaded and unloaded situations respectively. In the natural convection with oil tank (NCOT) the COP values were found as 2.68, and 2.86 for the loaded and unloaded situation respectively. According to condenser design (NC or NCOT) the highest values have been taken at the condenser with oil tank as 2.68 and 2.86 for the loaded and unloaded situation. In the experiments an electric meter was used for measure of the energy consumption of compressor and obtained data recorded to personal computer. Energy consumption was measured on the basis of 60 minutes' duration. Changing of energy consumption values depend on the condenser design of the refrigeration system was shown also in the Figure 7. It can be clearly seen from the figure the highest energy consumption was occurred in the loaded situation of the system as 190 Wh for NC. It is seen that lower energy consumption has occurred all times for the NCOT according to NC. When we used the condenser with oil tank (NCOT) has caused to decrease energy consumption not only loaded but also unloaded situation of the refrigeration system. Energy consumption values were found as 120 and 110 Wh for the loaded system and unloaded system. As can be seen from these results the system which has lower energy consumption is the NCOT and the greatest energy consumption is the NC. Figure 8 shows the variety of COP values regarding three cases as i) oil tank empty, ii) original case (without oil tank) and iii) oil tank charged with full of oil.

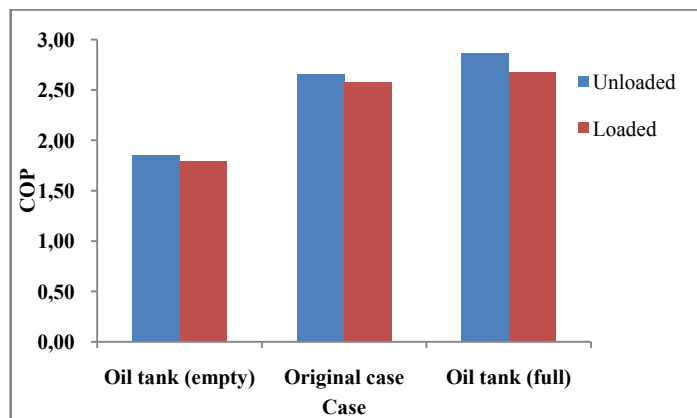


Figure 8. Comparison of the COP values for the three case study.

As can be clearly seen from the figure when oil tank charged with oil it has caused to increase COP value. In the situation where oil tank is empty COP was decrease according to original case due to difficulty of heat transfer of the condenser. On the other hand when original case was compared with third case (oil tank full of

oil) the COP values became higher in the case where oil tank is full. When the tank filled with oil has led to increase COP values as about %7 and %4 for the unloaded and loaded situation respectively.

4. CONCLUSION

In this study the cooling performance of a household refrigerator has been investigated experimentally. In the experiments natural convection (NC) and natural convection with oil tank (NCOT) type condenser were tested. Based on the results obtained, the following conclusions are drawn:

- Natural convection oil tank (NCOT) system has consumed lower energy according to natural convection (NC).
- Using of the submerged condenser coil to the oil tank has caused to increase COP values and to decrease energy consumption.
- When it is compared NCOT with NC regarding its energy consumption, it was found that 63% and 65% more advantage in the situation loaded and unloaded respectively.
- The applicability of the NCOT to the existing household or commercial refrigerator device has led to a great amount of energy saving.
- Different oil tank design and circulation of oil in the tank is an option to increase the efficiency of the system which should be investigated for the future studies.

REFERENCES

- [1]. X.D. Yuan and W.L. Cheng, "Multi-objective optimization of household refrigerator with novel heat-storage condensers by Genetic algorithm," *Energy Conversion and Management*, vol. 84, pp. 550-561, 2014.
 - [2]. E. Björk and B. Palm, "Performance of a domestic refrigerator under influence of varied expansion device capacity, refrigerant charge and ambient temperature," *International Journal of Refrigeration*, vol. 29, pp. 789-798, 2006.
 - [3]. C.J.L. Hermes, C. Melo, F.T., Knabben, J.M., and Gonçalves JM. "Prediction of the energy consumption of household refrigerators and freezers via steady-state simulation," *Applied Energy*, vol. 86, pp. 1311-1319, 2009.
 - [4]. W.L. Cheng and X.D. Yuan, "Numerical analysis of a novel household refrigerator with shape-stabilized PCM (phase change material) heat storage condensers," *Energy*, vol. 59, pp. 265-276, 2013.
 - [5]. A.K. Gholap and J.A. Khan, "Design and multi-objective optimization of heat exchangers for refrigerators," *Applied Energy*, vol. 84, pp. 1226-1239, 2007.
 - [6]. Z.S. Chen and M.Y. Chen, "Characteristic of temperature of a refrigerator with an accumulator of cold," *J Univ of Sci and Tech of China*, vol. 24, pp. 104-108, 1994.
 - [7]. Azzouz, K., Leducq, D., Gokin, D., (2008). Performance enhancement of a household refrigerators by addition of latent heat storage. *International Journal of Refrigeration*, 31, 892-901.
 - [8]. K. Azzouz, D. Leducq, and D., Gokin "Enhancing the performance of household refrigerators with latent heat storage: an experimental investigation," *International Journal of Refrigeration*, vol. 32, pp. 1634-1644, 2009.
 - [9]. I.M. Neto, A. Padilha, and V.L. Scalón, "Refrigerator COP with thermal storage," *Applied Thermal Engineering*, vol. 29, pp. 2358-2364, 2009.
 - [10]. J. Ye and D. Ying, "An interrupted condenser with heat storage". Patent Number: CN98100512.8. 2002.
 - [11]. K.S. Yang, W.R. Chang, I.Y. Chen, and C.C. Wang, "An investigation of a to p-mounted domestic refrigerator," *Energy Conversion and Management*, vol. 51, pp. 1422-1427, 2010.
 - [12]. P.A. Patil, "Performance analysis of HFC-404a vapor compression refrigeration system using shell and u-tube smooth and micro-fin tube condensers," *Exp Heat Trans*, vol. 25, pp. 77-91, 2012.
 - [13]. Z. Wang, L. Wang, and W. Fu, "Performance assessment for three kind of condenser in refrigerating system", *Int Conf on Adv Mechatronic Sys (ICAMEchS)*, Luoyang CHINA, Sep. 25-27 2013.
 - [14]. T.M.T. Huynh and H. Sato, "Proposal of an eco-friendly high-performance air conditioning system. Part I: Possibility of improving existing air-conditioning system evaporator condenser," *Int J Ref-Revue Int Du Froid*, vol. 36, pp. 1589-1595, 2013.
 - [15]. J. Tissot, P. Boulet, and F. Trinquet, "Improved energy performance of a refrigerating machine using water spray upstream of the condenser," *Int J Ref-Revue Int Du Froid*, vol. 38, pp. 93-105, 2014.
 - [16]. E. Kılıçaslan, "Performance analysis of refrigeration systems," PhD Thesis, Marmara University Institute of Pure and Applied Sciences, Turkey June. 2002.
 - [17]. Y.A. Cengel and M.A. Boles, *Thermodynamics: An engineering approach*. 5th ed. Boston, USA: McGraw-Hill, 2001.
-

EVALUATING WATER QUALITY CLASSES AND TROPHIC LEVEL FOR LAKE SAPANCA BASIN

Seda TÜNAY

Sakarya University, Environmental Engineering Department, Esentepe Campus, 54187, Sakarya, Turkey

Temel TEMİZ

Kocaeli University, Civil Engineering Department, Umuttepe Campus, Kocaeli, Turkey

Osman SÖNMEZ

Sakarya University, Civil Engineering Department, Esentepe Campus, 54187, Sakarya, Turkey

Beytullah EREN

Sakarya University, Environmental Engineering Department, Esentepe Campus, 54187, Sakarya, Turkey

Mahnaz GÜMRÜKÇÜOĞLU

Sakarya University, Environmental Engineering Department, Esentepe Campus, 54187, Sakarya, Turkey

Rabia KÖKLÜ

Sakarya University, Environmental Engineering Department, Esentepe Campus, 54187, Sakarya, Turkey

Emrah DOĞAN

Sakarya University, Civil Engineering Department, Esentepe Campus, 54187, Sakarya, Turkey

Bülent ŞENGÖRÜR

Sakarya University, Environmental Engineering Department, Esentepe Campus, 54187, Sakarya, Turkey

Abstract

In this study, important water quality parameters were analyzed on measurement stations selected on tributaries and Lake Sapanca between 2012 and 2014. According to obtained results, water quality classes for tributaries and lake; and trophic level for lake have been assessed based on conventional procedures such as Surface Water Quality Management Directive (SWQM) (Turkey) and Carlson Trophic Index (TSI). Water quality classes were identified as 2nd class for Lake Sapanca and 4th class for tributaries according to conventional procedure (SWQM). Trophic level for Lake Sapanca was determined as eutrophic for TP (Total Phosphorus), oligotrophic for secchi disc and mesotrophic for Chlorophyll-a based on both of indexes; and as mesotrophic for TN (Total Nitrogen) based on SWQM. Lake Sapanca Basin and sub-basin areas were determined by using Geographic Information System (GIS). In this way, the measurement points were associated with the measurement results, and water quality pollution maps were created based on the water quality classes of tributaries and Lake Sapanca Basin.

Keywords: *Lake Sapanca, water pollution, water quality class, trophic level*

1. INTRODUCTION

Lake Sapanca is one of the internal water catchments of Marmara Region and it is located on a tectonic hole, which is situated between Izmit Bay and Adapazari Meadow and runs parallel to Iznik Lake (Fig. 1). It's the major water resource supplying drinking water as well as water for industrial and agricultural uses. The lake is fed by the tributaries with seasonally changing flow rates, and by the sources in the lake bottom. The most important and largest streams that drain into the lake are the Harmanli, Maden, Kurudere, Degirmendere, Balikhane, Kasabasin, Yanik, Karacay, Mahmudiye, Istanbul, Keci and Sarp Streams. There is no direct discharge of waste into the lake chemical pollutants of both domestic and agricultural origin find their way into the lake through surface-runoff [4].

¹ Sakarya University, Environmental Engineering Department, Esentepe Campus, 54187, Sakarya, Turkey

² Sakarya University, Civil Engineering Department, Esentepe Campus, 54187, Sakarya, Turkey

³ Kocaeli University, Civil Engineering Department, Umuttepe Campus, Kocaeli, Turkey

Akkoyunlu et al. (2011) observed that there is a historical threat of eutrophication in Sapanca Lake although there is no high risk for the recent years. Morkoc et al. (1998) studied on the trophic characteristics of Sapanca Lake and stated that it is a typical warm-monomictic and an oligotrophic lake. Consequently, contaminant source and beneficial uses, water quality classification and trophic levels should be determined for reduction of pollution at Sapanca Lake.

In this study, water quality characteristics should be investigated current and future by considering land use in the basin. The important water quality parameters were measured at selected 12 stations on tributaries and 6 stations on Lake Sapanca and the water quality classes and trophic level for lake have been assessed based on conventional procedures such as Surface Water Quality Management Directive (SWQM) (Turkey) and Carlson Trophic Index (TSI). Trophic levels of the lake and specified water quality classes have been identified. Basin pollution maps has been created and shown on Geographic Information System (GIS) by using measurement results and measurement

2. MATERIALS AND METHODS

2.1. Materials

The latitude and longitude of Lake Sapanca is 40° 41" N / 30° 15" E. The lake has a length 16 km east-west / 5 km north-south, surface area of about 46 km² and a catchment area of about 252 km². The elevation varies between about 31 and 33 m and for elevation 31,5, lake has a the volume of about 1120 × 10⁶ m³. The maximum and average depths of the lake are approximately 61m and 25 m respectively (Table 1)

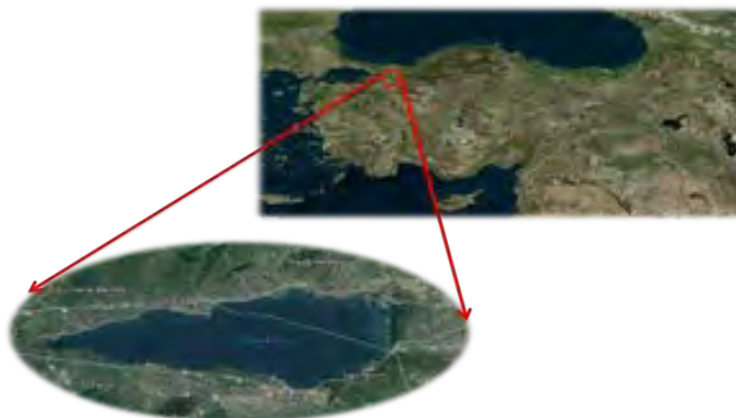


Figure 1. Lake Sapanca location map (Google Earth, 2014)

Table 1. Sapanca catchment and lake characteristics [3]

Catchment Area	252 km ²
Lake Surface Area	46 km ²
Lake Volume	1120 × 10 ⁶ m ³ (for elevation 31,5)
Average Depth	25 m
Maximum Depth	61 m
Hydraulic Retention Time	8,41 yr (2013)

In order to assess Lake Sapanca water pollution, 6 monitoring stations have been selected in the lake and 12 monitoring stations have been on streams feeding the lake (Harmanlı, Maden, Kurudere, Degirmendere, Balikhane, Kasabasin, Yanik, Karacay, Mahmudiye, Istanbul, Keci and Sarp Streams) (Fig.2). Water samples were collected from September 2012 to November 2013 once or twice a month on streams and once a season in lake. Samples in the lake are collected at depths of surface, 5, 10, 15, 20 and 25 meters in horizontal-type byRuttner water sampler and on streams were collected from the surface. The depths of the stations in the lake are shown in Table 2.



Figure 2. (a) Sampling stations in lake

(b) Sampling stations on streams

Table 2. Lake Sapanca sampling station depths

Sampling stations	Depth(m)
A – Water intake area	26
B – Seka Park	2
C - Eşme	22
D - Richmond	19
E – Lake center	56
F – Çark river	2

2.2. Methods

The water quality parameters of temperature, pH, dissolved oxygen, conductivity, specific conductance, salinity, total dissolved solids (TDS) and ORP were measured by YSI Professional Plus multiparameter on

land. For the measurement of TN, NO₃ N, NO₂ N, NH₃ N, TN and PO₄ P parameters, sampling bottles were brought to the laboratory and values were measured by spectrophotometer (MERCK NOVA 60). And likewise, a spectrophotometer was used to determine chlorophyll a [7] and visibility was determined by a limnological Secchi disc with a diameter of 20 cm.

Trophic levels for Lake Sapanca have been assessed based on conventional procedures such as Surface Water Quality Management Directive (SWQM) (Turkey) and Carlson Trophic State Index (TSI). To determine the trophic state, based on SWQM, secchi depth, chl-a, total phosphorus and total nitrogen values are used; based on the Carlson Trophic State Index, secchi depth, chl-a and total phosphorus values are used. The formulations used by Carlson are given below [2]:

$$TDI(SD) = 60 - 14,41x \ln(SD) \tag{1}$$

$$TDI(Chl - a) = 9,81x \ln(Chl - a) + 30,6 \tag{2}$$

$$TDI(TP) = 14,42 x \ln(TP) + 4,15 \tag{3}$$

Table 3. Carlson's trophic state index values and classification of lakes[5]

TSI Values	Trophic Status
< 30	Oligotrophic
30-40	Oligotrophic
40-50	Mesotrophic
50-60	Eutrophic
60-70	Eutrophic
70-80	Eutrophic
>80	Eutrophic

Table 4. Limiting values of trophic classification system in lakes [6]

Trophic State	TP(µg/L)	TN(µg/L)	Chl-a (µg/L)	Secchi Disc Depth (m)
Oligotrophic	≤10	≤350	<3.5	>4
Mesotrophic	10>TP≥30	350>TN≥650	3.5-9.0	4-2
Eutrophic	30>TP≥100	650>TN≥1200	9.1-25.0	1.9-1
Hypereutrophic	>100	>1200	>25.0	<1

3. RESULTS AND DISCUSSIONS

This study presented the trophic states for selected 6 sampling stations in the lake. The trophic states based on Carlson and SWQM are given in Table 5 and Table 6. Trophic level for Lake Sapanca was determined as eutrophic for TP (Total Phosphorus), oligotrophic for secchi disc depth and mesotrophic for Chlorophyll-a based on both of indexes; and as mesotrophic for TN (Total Nitrogen) based on SWQM. The trophic states for TP, TN, secchi disk depth and chl-a are given by Geographic Information System (GIS) maps in Figure 3.

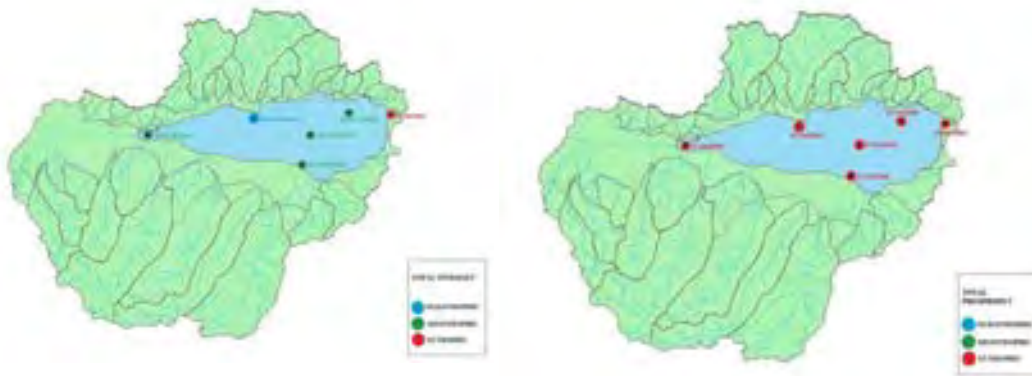
Table 5. Trophic states of Lake Sapanca

CARLSON TSI		02.10.2012	14.11.2012	11.04.2013	30.07.2013	19.08.2013	24.03.2014
WATER INTAKE AREA	TSI(TP)	EUTROPHIC	EUTROPHIC	EUTROPHIC	EUTROPHIC	EUTROPHIC	EUTROPHIC
	TSI(SD)	OLIGOTROPHIC	OLIGOTROPHIC	OLIGOTROPHIC	MEZOTROPHIC	OLIGOTROPHIC	OLIGOTROPHIC
	TSI(CHL)				OLIGOTROPHIC	MEZOTROPHIC	MEZOTROPHIC
SEKA PARK	TSI(TP)	EUTROPHIC	EUTROPHIC	EUTROPHIC	EUTROPHIC	EUTROPHIC	EUTROPHIC
	TSI(SD)						
	TSI(CHL)				MEZOTROPHIC	OLIGOTROPHIC	MEZOTROPHIC
EŞME	TSI(TP)	EUTROPHIC	EUTROPHIC	EUTROPHIC	EUTROPHIC	MEZOTROPHIC	EUTROPHIC
	TSI(SD)	OLIGOTROPHIC	OLIGOTROPHIC	OLIGOTROPHIC	OLIGOTROPHIC	OLIGOTROPHIC	OLIGOTROPHIC
	TSI(CHL)				MEZOTROPHIC	OLIGOTROPHIC	EUTROPHIC
RICHMOND	TSI(TP)	EUTROPHIC	EUTROPHIC	EUTROPHIC	EUTROPHIC	EUTROPHIC	EUTROPHIC
	TSI(SD)	OLIGOTROPHIC	OLIGOTROPHIC	OLIGOTROPHIC	MEZOTROPHIC	OLIGOTROPHIC	OLIGOTROPHIC
	TSI(CHL)				MEZOTROPHIC	MEZOTROPHIC	MEZOTROPHIC
LAKE CENTER	TSI(TP)	EUTROPHIC	EUTROPHIC	MEZOTROPHIC	MEZOTROPHIC	EUTROPHIC	EUTROPHIC
	TSI(SD)	OLIGOTROPHIC	OLIGOTROPHIC	OLIGOTROPHIC	MEZOTROPHIC	OLIGOTROPHIC	OLIGOTROPHIC
	TSI(CHL)				OLIGOTROPHIC	OLIGOTROPHIC	MEZOTROPHIC
ÇARK SHUTTER	TSI(TP)	EUTROPHIC	EUTROPHIC	EUTROPHIC	OLIGOTROPHIC	EUTROPHIC	EUTROPHIC
	TSI(SD)						
	TSI(CHL)				MEZOTROPHIC	MEZOTROPHIC	MEZOTROPHIC

Table 6. Trophic states of Lake Sapanca

SWQM TSI		02.10.2012	14.11.2012	11.04.2013	30.07.2013	19.08.2013	24.03.2014
WATER INTAKE AREA	TSI(TP)	EUTROPHIC	EUTROPHIC	EUTROPHIC	MEZOTROPHIC	EUTROPHIC	EUTROPHIC
	TSI(SD)	OLIGOTROPHIC	OLIGOTROPHIC	OLIGOTROPHIC	MEZOTROPHIC	OLIGOTROPHIC	OLIGOTROPHIC
	TSI(TN)	MEZOTROPHIC	OLIGOTROPHIC	MEZOTROPHIC	MEZOTROPHIC	MEZOTROPHIC	MEZOTROPHIC
SEKA PARK	TSI(CHL)				OLIGOTROPHIC	MEZOTROPHIC	MEZOTROPHIC
	TSI(TP)	EUTROPHIC	EUTROPHIC	EUTROPHIC	EUTROPHIC	MEZOTROPHIC	MEZOTROPHIC
	TSI(SD)						
EŞME	TSI(TN)	OLIGOTROPHIC	OLIGOTROPHIC	OLIGOTROPHIC	MEZOTROPHIC	OLIGOTROPHIC	EUTROPHIC
	TSI(CHL)				MEZOTROPHIC	OLIGOTROPHIC	MEZOTROPHIC
	TSI(TP)	EUTROPHIC	EUTROPHIC	EUTROPHIC	HYPEREUTROPHIC	MEZOTROPHIC	EUTROPHIC
RICHMOND	TSI(SD)	OLIGOTROPHIC	OLIGOTROPHIC	OLIGOTROPHIC	OLIGOTROPHIC	OLIGOTROPHIC	OLIGOTROPHIC
	TSI(TN)	EUTROPHIC	OLIGOTROPHIC	OLIGOTROPHIC	OLIGOTROPHIC	OLIGOTROPHIC	EUTROPHIC
	TSI(CHL)				MEZOTROPHIC	MEZOTROPHIC	MEZOTROPHIC
LAKE CENTER	TSI(TP)	HYPEREUTROPHIC	MEZOTROPHIC	MEZOTROPHIC	MEZOTROPHIC	MEZOTROPHIC	HYPEREUTROPHIC
	TSI(SD)	OLIGOTROPHIC	OLIGOTROPHIC	OLIGOTROPHIC	MEZOTROPHIC	OLIGOTROPHIC	OLIGOTROPHIC
	TSI(TN)	MEZOTROPHIC	OLIGOTROPHIC	OLIGOTROPHIC	MEZOTROPHIC	OLIGOTROPHIC	EUTROPHIC
ÇARK SHUTTER	TSI(CHL)				OLIGOTROPHIC	OLIGOTROPHIC	MEZOTROPHIC
	TSI(TP)	MEZOTROPHIC	MEZOTROPHIC	EUTROPHIC	OLIGOTROPHIC	EUTROPHIC	EUTROPHIC
	TSI(SD)						
	TSI(TN)	HYPEREUTROPHIC	OLIGOTROPHIC	OLIGOTROPHIC	EUTROPHIC	MEZOTROPHIC	MEZOTROPHIC
	TSI(CHL)				MEZOTROPHIC	MEZOTROPHIC	MEZOTROPHIC

Water quality classes for general conditions, nutrient parameters and oxygen parameters in the lake are given by the GIS maps in Figure 4. As shown in the figure, the lake is 1st class for general parameters, 2nd class for nutrient parameters and 2nd class for oxygenating parameters.



(a) Lake trophic states for TN

(b) Lake trophic states for TP

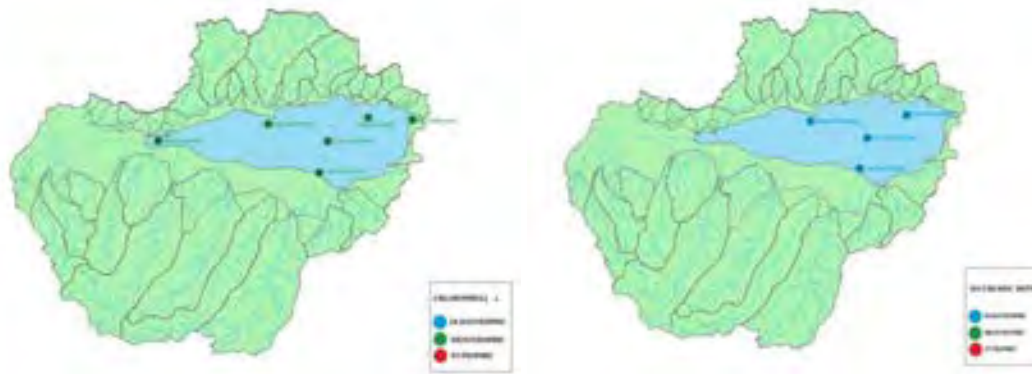
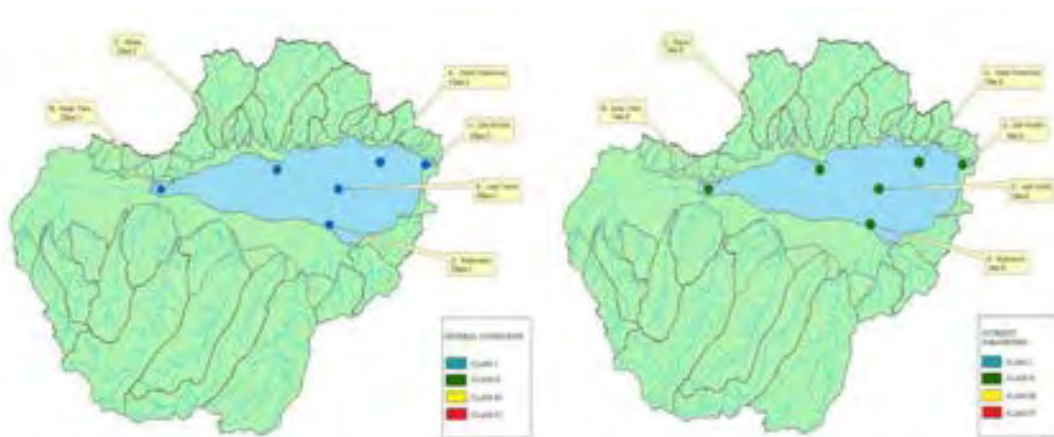


Figure 3. (c) Lake trophic states for Chl-a

(d) Lake trophic states for Secchi Disc Depth

Water quality classes for general conditions, nutrient parameters and oxygenating parameters on streams are given by the GIS maps in Figure 5. As shown in the figure, Keci, Istanbuldere, Maden and Kurtkoy Streams are 1st class and the other streams are 2nd class for general parameters; Harmanli, Kurudere and Degirmendere streams are 3rd class and the other streams are 4th class for nutrient parameters and only Keçi Stream is 2nd class and the other streams are 1st class for oxygenating parameters.



(a) Water quality classes in Lake Sapanca for general conditions

(b) Water quality classes in Lake Sapanca for nutrient parameters



Figure 4. (c) Water quality classes in Lake Sapanca for oxygenating parameters



(a) Water quality classes in streams for general conditions



(b) Water quality classes in streams for oxygenating parameters



Figure 5. (c) Water quality classes in streams for nutrient parameters

4. CONCLUSIONS

According to obtained results, water quality classes were identified as 2nd class for Lake Sapanca and 4th class for tributaries according to conventional procedure (SWQM). Trophic level for Lake Sapanca was determined as eutrophic for TP (Total Phosphorus), oligotrophic for secchi disc and mesotrophic for Chlorophyll-a based on both of indexes; and as mesotrophic for TN (Total Nitrogen) based on SWQM. By considering that Sapanca Lake is an important source for drinking water, observation stations for continuous and instantaneous monitoring should be established on Balikhane, İstanbul, Mahmudiye, Karaçay, Yanık, Maden and Kasabasin Streams discharged to Sapanca Lake will be an important step for water quality control. It is required that to take precautions for point and non-point sources and to arrange an integrated management plan. Destruction of forests and increased urbanization should be prevented as soon as possible. both the lake and streams fed by underground water must be protected and detected.

5. ACKNOWLEDGEMENTS

This paper was prepared with multidisciplinary research project (2012-01-04-016) supported by Scientific Research Project Unit Sakarya University.

6. REFERENCES

- [1] Akkoyunlu, A., Akiner, M.E. (2012). Pollution Evaluation in Streams Using Water Quality Indices: A Case Study from Turkey's Sapanca Lake Basin. *Ecological Indicators*, 18, 501-511.
- [2] Carlson, R.E. (1977). A trophic state index for lakes. *Limnology and Oceanography*. 22(2): 361-369.
- [3] DSI, The Sapanca Lake pollution study, Technical Report, State Water Works Publ., 135, Ankara, 1984 (in Turkish)
- [4] Morkoc E, Tugrul S, Ozturk M, Tufekci H, Egesel L, Tufekci V, Oya S, Legovic T. (1998). Trophic characteristics of the Sapanca Lake (Turkey). *CCACAA* 71: 303-322.
- [5] Prasad. A. G., Siddaraju (2012). Carlson's Trophic State Index for the assessment of trophic status of two Lakes in Mandya district, *Advances in Applied Science Research*, 3 (5): 2992-2996.
- [6] Republic of Turkey Ministry of Forestry and Water Affairs, Surface Water Quality Management Directive SWQM. 30 November 2012. <http://www.resmigazete.gov.tr/eskiler/2012/11/20121130-5.htm>
- [7] Youngman, R. E. (1978). The measurement of chlorophyll. *Wat. Res. Centre tech. Rep. TR 82*, Medmenham, U.K., 23 pp.

APPLICATION OF THE ENVIRONMENTAL AND SAFETY INTEGRATED MANAGEMENT SYSTEMS IN THE ENERGY SECTOR

Asude ATEŞ

Sakarya University, Environmental Engineering Department, 54187, Sakarya, TURKEY.
aates@sakarya.edu.tr

Bülent ŞENGÖRÜR

Sakarya University, Environmental Engineering Department, 54187, Sakarya, TURKEY
sengorur@sakarya.edu.tr

Rabia KÖKLÜ

Sakarya University, Environmental Engineering Department, 54187, Sakarya, TURKEY,
rkoklu@sakarya.edu.tr

Abstract

Taking the necessary measures to evaluate the environmental impacts; and preventing, overcoming and controlling the adverse effects that may occur in business management are the indications of the importance attached to the environment. This can be achieved through the establishment of the environmental management system. The standard representing the environmental management system is the ISO 14001:2004 standard. However, as well as the establishment of the system, it is essential to evaluate the factors that may cause risks independently in terms of occupational health and safety; and to take measures before the accidents and incidents occur. In such a case, the guiding standard is the ISO 18001: 2007 standard. These two standards are similar as they are based on operation, system cycle, proactive approach and risk management. Its preparation and application in an integrated way lead to a reduction in the workload and documentation; and to an increased productivity and motivation. In this study, the integrated establishment and application of the environmental and occupational health and safety systems at a Natural Gas Combined Cycle Power Plant has been evaluated. This integrated model's positive contributions on both systems were evaluated in terms of its environmental and occupational health and safety performances; and the measurable efficiency capacities that the model will provide for the organizations serving in this type of energy industry were calculated.

Keywords: *Environment, Risk management, system, reduction, efficiency*

1. INTRODUCTION

In this study, an evaluation has been carried out regarding the establishment and implementation of an integrated management system including the Natural Gas Combined Cycle Power Station ISO 14001: 2004, Environmental management system and OHSAS 18001: 2007 and Occupational Health and Safety management system, in addition, an integrated management system model is proposed covering these two management systems.

Necessary measures is an indication of the importance given to the environment with regard the evaluation of the effect of the environment in the management of enterprises, the prevention and elimination of the negative effects that may occur and can be kept in check. ISO 14001 Environmental Management Systems, first published in 1996 and revised in November 2004, is a standard used to establish an environmental management system for the use of enterprises [3]. Although, Environmental Management System is a part of the management system for managing the size of the environment and the development of environmental policies and the enactment of them, it does not replace the legislation or require the best technology or occupational health and safety.

Regardless of Environmental Management, enterprises shall provide the safety and health at work by evaluating risk factors and take precautions before accidents and incidents happen. OHSAS 18001 Occupational health and safety management system standard, which was published in 1999 and developed on the basis of the BS 8800 standard, a guide standard for the enterprises in terms of establishing an occupational health and safety management system [2]. This standard covers the terms of OHS management system so that enterprises can control occupational health and safety risks and optimization of the performance. Similarly, occupational health and Safety Management System does not replace the legislation or require the best technology or does not include control of the environment outside the scope of job security. Enterprises can establish the ISO 14001 and OHSAS 18001 management system standards in an integrated way rather than creating separately. In this study, firstly, the reasons of establishment of an integrated system will be analyzed by putting these two standards in mind. Then power plant-specific system requirements and applications will be discussed.

2. MATERIALS AND METHODS

Information about combined cycle is given following because Natural Gas Combined Cycle Plants of environmental and occupational health and safety management systems are examined in this study. When electricity is produced in two stages at combined cycle gas turbine, yields are increasing. Gas turbines and steam turbines used together in combined cycle power plants. As well as electric energy obtained from the gas turbine used gas as fuel, turbine exhaust steam with high-temperature by sending to the waste heat boiler is also provided additional electricity generation. Thus, combined cycle efficiency can yield approximately 55-60% in this type of power plants.

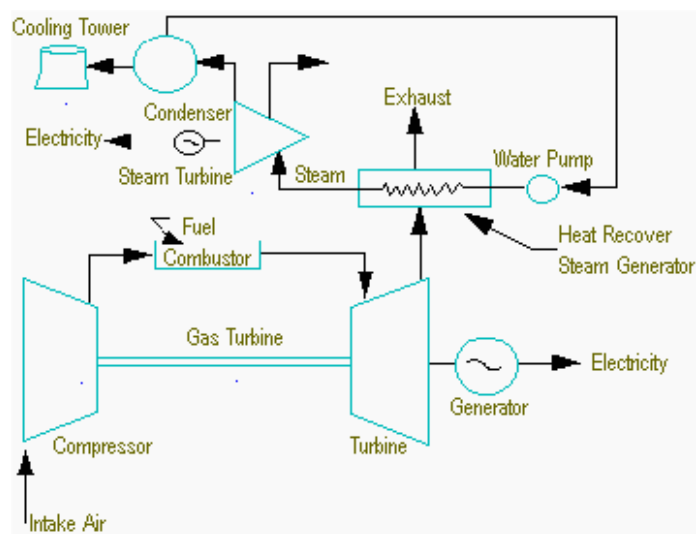


Figure 1. Combined cycle power plant scheme

2.1. The Typical Environmental Specifications of Energy Power Stations

Environmental application is related to Natural Gas Combined Cycle power plant follows as: Power plants are subject to permission about emission and wastewater issues. The environment permission must to obtain for establishment and operation of the enterprises that have air emission, waste water , are within Environmental Permits and License Regulations. It's transcended and worked for provision of relevant regulations and limit values in evaluating air emissions originating from these enterprises [4].

Emissions: The most important emission is nitrogen oxides in power plants. Due to use of special incineration technologies, the values are 20-30 mg/Nm³ for nitrogen oxides. Also, the limit value is 300 mg/Nm³ in the relevant regulation. In this respect, it can be said that this value is far below the limit values.

Waste water: The wastewaters originate from the plant are demineralized water preparation unit regeneration wastewaters; domestic wastewaters; plant waters and bluffing won (open field external) drainage water.

Waste management: Due to the raw material is natural gas, the product is electric that are in Natural Gas Combined Cycle power plant, it is not possible formation of waste. Only, wastes consist of general daily activities and maintenance works.

2.2. Compare of 14001 and 18001 standards

The most important problems in system setup are cost, time, requirement expert staff and work load issue. These problems are removed by integrated system [1]. Table 1 shows the common items of standards and they are compatible to integration has been introduced there.

Table 1 Compare of the integrated standard parameters of 14001 and 18001

ISO 14001	OHSAS 18001
4.3.1 Environmental Dimensions	Hazard Identification, Risk Assessment and Determining Controls
4.3.2 Legal and Other Requirements	Legal and Other Requirements
4.3.3 Objectives and Programs	Objectives and Programs
4.4.1 Resources, Roles, Responsibility and Authority	Resources, Roles, Responsibility, Accountability and Authority
4.4.2 Speciality, Training and Awareness	Competence, Training, and Awareness
4.4.3 Communication	Communication, Participation and consultation
4.4.4 Documentation	Documentation
4.4.5 Control of Documents	Control of Documents
4.4.6 Activity control	Operational Control
4.4.7	Emergency Preparedness and Response
4.5.1 Monitoring and measurement	Performance Measurement and Monitoring
4.5.2 Evaluation of Compliance	Evaluation of Compliance
4.5.3 Non-conformity, Corrective and Preventive Action	Incident Investigation, Non-conformity, Corrective and Preventive Action
4.5.4 Control of Records	Control of Records
4.5.5 Internal Audit	Internal Audit
4.6 Management Review	Management Review



Figure 2. Plan, Do, Check and Act system of 14001

3. RESULTS AND DISCUSSION

This section, by examining the efficiency in terms of environmental and occupational health and safety, the natural gas cycle power plant implemented the integrated management system has been analyzed and interpreted statistical data on an annual basis.

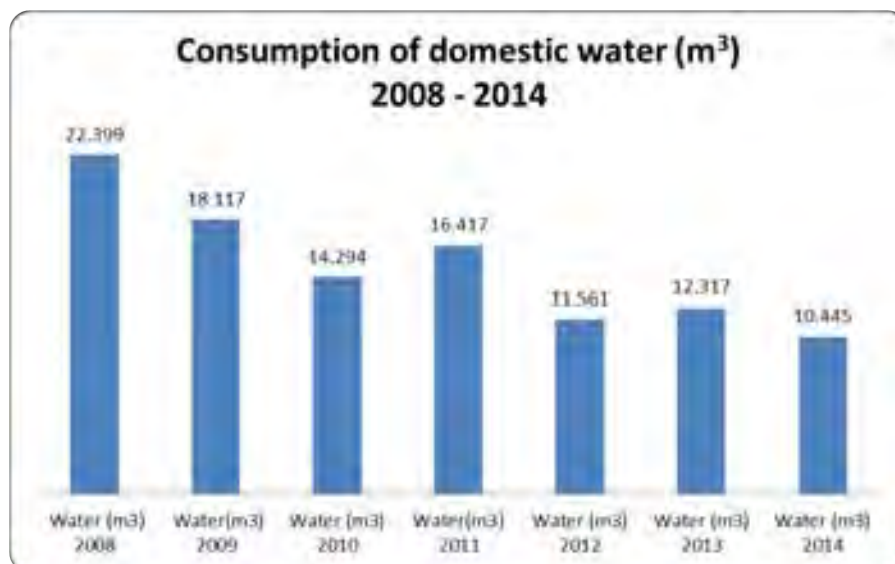


Figure 3. Consumption of raw water between 2008-2014

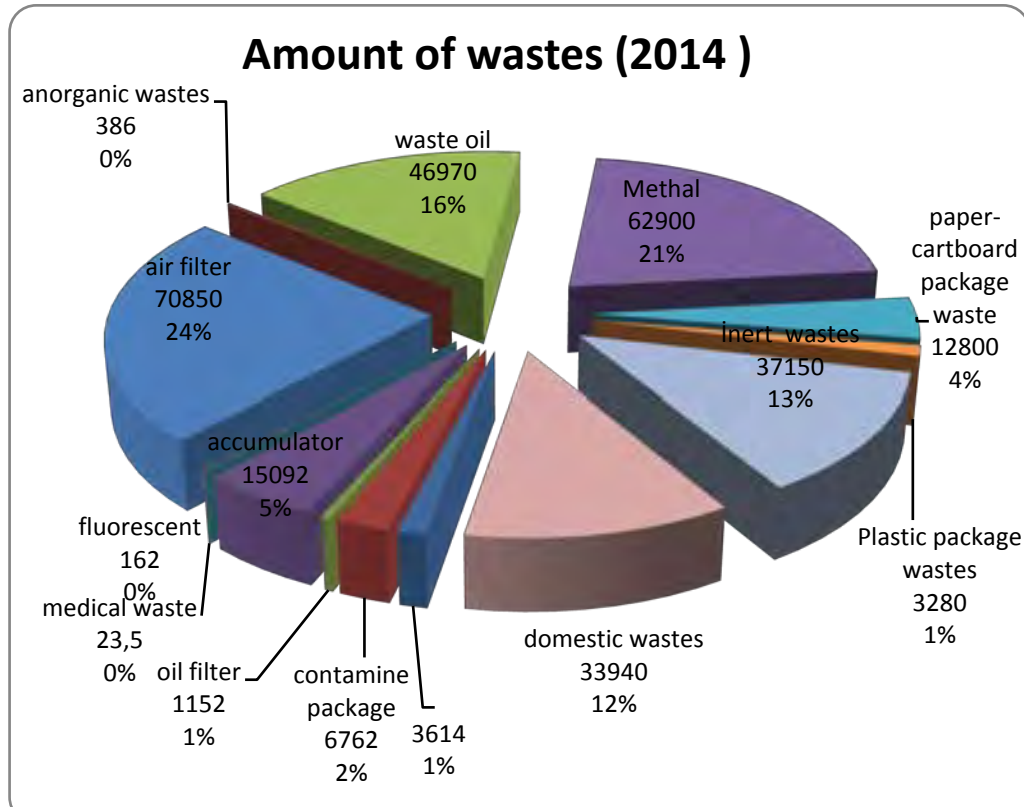


Figure 4. Waste distribution of 2014

Figure 3 is shown the change of water consumption amount between 2008 and 2014. As a result of implementing a regular integrated management based on legal terms and regulations for waste management, by providing recycling of waste given Figure 4, it was obtained income approximately \$ 55,858. It was calculated the expenses of waste as \$ 11205 for transfer and \$13700 for disposal. As can be seen, gain of \$ 30,953 per year was obtained with an applicable integrated management system. Figure 5 is shown the reduction of electricity that sources from office part of the system between years 2008-2014.

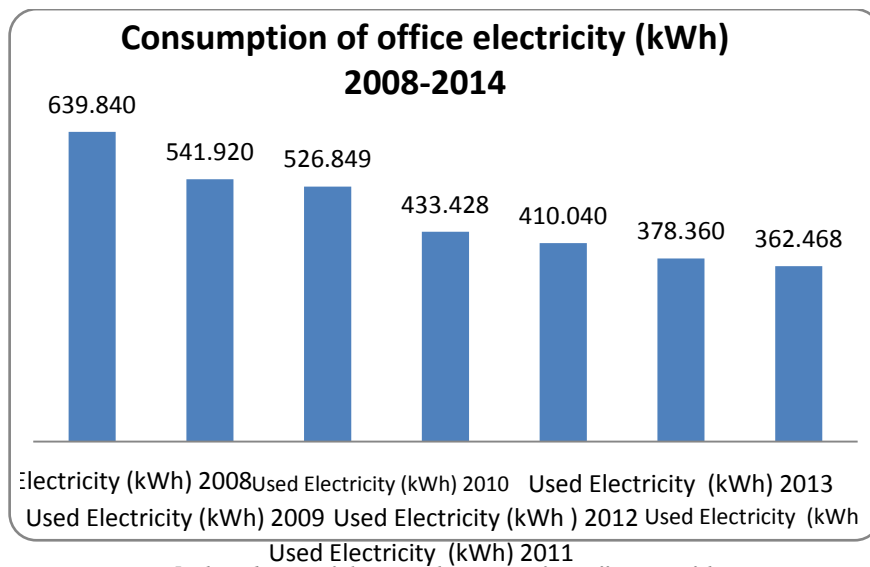


Figure 5. The reduction of electricity that sources from office part of the system

It is the made great care period of between June and August when accidents are dense. There has been about 200 people in the business of operating conditions but this number has reached 700 people in the maintenance period. Avoidable level of work accidents which can be cured with first aid and medical attention occurred in 2014. It is a significantly lower number for such a sector. This situation can be considered as an advantage implementing an integrated management system.

4. CONCLUSION

After all, when integrated management system implemented in energy sector, as examples are given above, are practiced separately, will make negativity in terms of time, cost and labor. Even though, preference of Energy industry with this type of integrated management systems has great benefits of the environment with ease-of-use natural gas, on the other hand, carrying large risk in terms of environmental and occupational health and safety is the general structure of the sector.

However, aforementioned management systems' set up and operation are favorable in this type of power plant considering the easy use.

Moreover, although there are many obstacles to set up and operate this type of systems in many companies, mostly no problem has been encountered regarding the funds transfer and staff employment in these types of power plants, as the level of education is higher in general minimal problems have been experienced in terms of the adoption and operation of the system.

Energy stations generally has been evaluated negatively in terms of environment, however, benefit is that according to the thermal power plant natural gas is a relatively clean fuel and certification is an instrument that can prove that enterprises' effect on the environment was not as expected.

At the same time, these types of power plants are large industrial plants and big business accidents may happen in these atmospheres.

Establish and implement of Occupational Health and Safety as management system brings convenience systematically and helps studies to be carried out systematically from emergency situations to risk assessments.

Personnel, working in this type of plant, have high level of education in general which is an advantage in terms of understanding and implementation of the risk.

In terms of environmental and occupational health and safety, Management systems standards which are built at the same logic, are valid not only for all enterprises but also Natural Gas Combined Cycle Power Plant which provides great convenience.

REFERENCES

- [1] Mırdıkoğlu, Bengü, 2007, ISO 14001 EMS Standard: The study: The problems and hardship in the enterprises, Post graduated thesis, Ankara University, Social Science Institute, Socail Environment Science Institute, 140-147.[2] OHSAS 18001:2007 Occupational Health and Safety Management Systems – Requirements, OHSAS Project Group 2007[3] TS EN ISO 14001 Environmental Management Systems – Requirements, 2005, TSE, Ankara.
- [4] Keskinel, Fikret, 2006, The production in Turkey and Natural Gas Combined Cycle power plant, İstanbul Civil Engineering Chamber , İstanbul Bulletin, 86, s.19-26
- [5] İSGİP (The projet of Occupational Health and Safety) Project Edition, The European Union's Good Practices Occupational Health and Safety Management Systems, T.C. Ministry of Labor and Social Security, Occupational Health and Safety General Directorate, 8-13.
- [6]www. [ustainablecitiescollective.com/david-thorpe/286801/iso-14001-revision-reaches-milestone-updating-standard-environmental-management](http://sustainablecitiescollective.com/david-thorpe/286801/iso-14001-revision-reaches-milestone-updating-standard-environmental-management)

THE CONCEPT OF URBAN FOREST IN TURKEY, SITUATION TODAY AND TARGETS

Atilla ATIK

İnönü University Faculty of Fine Arts and Design Department of Landscape Architecture, 44280, Malatya, Turkey.
atikatilla@hotmail.com

Fürüzan ASLAN

İnönü University Faculty of Fine Arts and Design Department of Landscape Architecture, 44280, Malatya, Turkey.

Abstract

Urban people remain away from nature depending on the rapid increase of population, industrialisation and construction density and so the recreation need of people also increases. The concept of urban forest, which was used first in 1960, can be defined as the forest areas around cities used for ecological and recreational functions beyond obtaining wood raw material. Urban forests were first seen at the beginning of 2000s in Turkey with the first one constituted by General Directorate of Forestry in 2003. In the scope of the study, the development stage of the concept of urban forest in Turkey and the urban forests completed and being completed were evaluated. In this respect, distribution, surface areas, geographical characteristics, social equipment elements, infrastructure features, flora and fauna of urban forest all over the country were determined. With the help of data obtained, urban forest were categorised under different categories. While there was only one urban forest constituted on an 140-ha area in Turkey in 2003, in 2011, this number was totally 475 constituted on a 62701 – ha area. Related institution to this issue targets in short term to constitute an urban forest in every city while in middle and long term expanding these forest to provincial areas by getting the views of urban people about the planning, renovating and improving ones constituted and being and to be constituted.

Keywords: *Urban forest, Population growth, Open green area, Recreation, Turkey.*

$$P + T = p_{max} \frac{X}{A} F_{comp} \quad (1)$$

$$P(e + Y) = p_{max} \frac{X}{A} F_{comp} [R - A + X + Y] \quad (2)$$

where; e is eccentricity which is ratio of moment divided by the axial force, R is radius of circular base plate, A is the length of the part of the base plate area under compression, Y is distance between center of gravity of the anchor bolt forces, F_{comp} is the part of the base plate area under compression. X is the distance from center of gravity of compressive stress bearing area to the zero stress section. p_{max} is allowable bearing stress and T is the sum of the anchor bolt forces in the half of the circle. P is the axial force acting on base plate center.

Since strain distribution is linear and sum of the anchor bolt forces in the half of the circle can be determined by using equilibrium equations, maximum anchor bolt force at outermost anchor bolt can be determined as equation (3).

$$T_{1,max} = \frac{T}{\left(1 + \frac{2}{y_1} \sum_{n=2}^n y_i\right)} \quad (3)$$

Equation (1) and equation (2) can't be solved explicitly; iteration process is used to investigate the unknowns. In the beginning, maximum allowable stress is determined using equations based on AISC approach as given in equation (4) [1].

$$p_{max} = 0.35 f_c \sqrt{\frac{A_2}{A_1}} \leq 0.7 f_c \quad (4)$$

where; p_{max} is maximum allowable bearing stress, f_c is concrete compression strength, A_1 and A_2 are plate and concrete areas.

On the first step a trial base plate size is selected and number of bolts accounting layout in the circular base plate is determined. Diameter of bolts is also decided on this step. In this manner, the center of bolts which is termed as Y is calculated accordingly. Afterwards compressive bearing area is calculated using equation (5) which is mainly based on AISC approach [1].

$$F_{comp} = 0.0174532 R^2 \alpha - R(R - A) \sin \alpha \quad (5)$$

where, α is the angle and also determined with equation (6).

$$\alpha = \arccos\left(\frac{R-A}{R}\right) \quad (6)$$

Center of gravity of the compression area can be calculated with using equation (7) and equation (8) with respect to the value of the angle α :

$$X = R \left[\frac{2 \sin^3 \alpha}{(3 \alpha - 1.5 \sin 2\alpha)} - \cos \alpha \right] \quad \left(\alpha \geq \frac{\pi}{4}\right) \quad (7)$$

$$X = 0.2 R \alpha^2 (1 - 0.0619 \alpha^2 + 0.0027 \alpha^4) \quad \left(\alpha < \frac{\pi}{4}\right) \quad (8)$$

After all unknowns of these equations are determined, equation (2) is controlled for the trial value. If the left and right sides of the equation (2) is not close enough, then a new trial value for Y should be selected. If two sides of the equation (2) are close enough, then the resultant bolt force can be determined from equation (1) and $T_{1,max}$ can be calculated using equation (3). The maximum force on outermost bolt T_{max} can be controlled using allowable anchor bolt load. If the value exceeds the allowable load limit, then bolt diameter or number of bolts can be increased. Likewise, base plate thickness can be determined using equation (9).

$$t_p = \sqrt{\frac{8M}{F_y}} \quad (9)$$

where; M is the moment for a 1 mm wide strip at the critical section and F_y is the yield stress of base plate steel material.

Main parameters of a circular base plate can be practically determined following the equations given above. This trial-and-error iteration approach gives opportunity to select the dimensions of the base plate, diameter and number of anchor bolts practically.

3. NUMERICAL EXAMPLE

Circular base plate for an advertisement pole is calculated according to the approach given in this study. Advertisement pole structure is presented with Figure 2. Column length is 20 m and façade area is 100 m². A circular base plate under high eccentric load is assumed and practical design approach is applied on control of the selected geometric properties of the base plate. Circular base plate used under advertisement pole column geometry is also given in Figure 3.



Figure 2. Advertisement pole

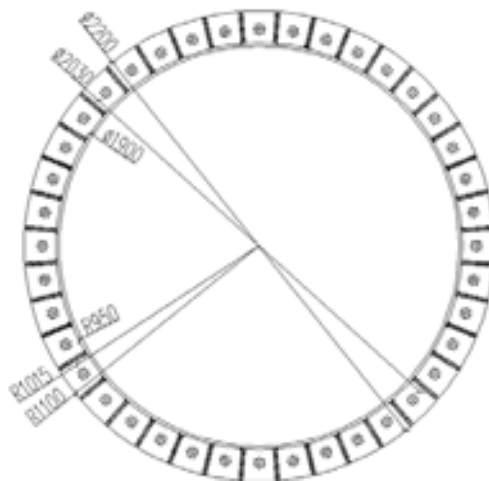


Figure 3. Circular base plate with anchor bolts

Circular base plate of the advertisement pole is designed under axial load of 326 kN and moment of 4 711 kN-m. The pole column is pipe section and the outside diameter of pipe is 1900 mm. Outside diameter of the circular base plate is 2200 mm and the thickness is 60 mm. The ratio of the concrete area on the top of the foundation to steel base plate area is 2/3. The allowable stress for the anchor bolts and the base plate are 112 MPa and 235 MPa, respectively. There are 40 bolts with the bolt diameter of 42 mm. The concrete compressive strength is assumed as 30 MPa. Allowable stress design approach for steel circular base plate is used and results are presented.

On the first step, the maximum design bearing stress is calculated as 12.86 MPa using equation (4). Since this value is below 21 MPa, bearing stress control is satisfied. As, there are 40 bolts and their diameter is 42 mm, center of gravity for anchor bolts is 668 mm.

Also, for a trial value length of the part of the base plate area under compression is selected as 499 mm. After following equations (5) and (6), compressive bearing area is calculated as 6481 cm² and α is determined as 56.9°. Since angle α is higher than $\pi/4$, equation (7) is used for calculating the center of gravity of the compression area. After all unknowns for the trial step are determined, equation (2) is controlled. Since, both sides of the equation (2) are almost the same, no further iteration is required. Accordingly, maximum anchor bolt force at outermost anchor bolt is calculated using equation (3) as 237.5 kN. The maximum anchor bolt

force is smaller than the allowable anchor force 281.2 kN. This shows that number and the diameter of the selected anchor bolts are enough in terms of anchor bolt force calculations. Likewise, base plate thickness is controlled using equation (9). The critical section is selected equal to the diameter of the column since stiffeners are provided and the base plate thickness is calculated as 52.4 mm. As base plate thickness is 60 mm, the thickness of the base plate is adequate.

4. CONCLUSIONS

In this study, a practical approach is presented for design of circular base plates that are commonly used for pipe or polygonal columns. Circular base plates are frequently used in wind turbine towers, lighting and advertisement poles. These types of circular base plates are designed to withstand loads that introduce high eccentricity such as wind and earthquake loads. Relationship between anchor bolt forces and base plate bearing stress is given and calculation steps are derived containing an iteration process. A numerical example is performed using practical procedure given with the calculation equations. Base plate dimension, base plate thickness, anchor bolt number and diameter are controlled.

REFERENCES

- [1]. American Institute of Steel Construction (AISC). Manual of steel construction, ASD, 9th Ed., Chicago, 1989.
- [2]. American Institute of Steel Construction (AISC). Column base plates, Chicago, 2003.

DETERMINATION OF PUBLIC EXPECTANCY AND APPROACH OF URBAN PEOPLE TOWARDS URBAN FOREST: SAMPLE OF MALATYA-TURKEY

Fürüzan ASLAN

İnönü University Faculty of Fine Arts and Design Department of Landscape Architecture, 44280, Malatya, Turkey.
furuzan.aslan@inonu.edu.tr

Atilla ATIK

İnönü University Faculty of Fine Arts and Design Department of Landscape Architecture, 44280, Malatya, Turkey.
atikatilla@hotmail.com

Abstract

Objective of the study is to determine the suggestions and views of urban people for Malatya Urban Forest continuing to be constituted using a participatory planning and design approach. For this aim a questionnaire study was conducted among urban people using rational approach. In addition to demographic and socio-economic data, views of participants for the importance, utilisation possibilities and ecological and recreative benefits of urban forest were investigated.

As the result of the study, 84.3% of participants thought that urban forest project is an important project for Malatya and they support it. As the education and socioeconomic levels increase the rate of participants thinking that urban forest project is a required project for the city also increases. Among the participant 90.7% of those university graduate thought that the most important value urban forest adds to the city is "having a utilisation area away from stress but close to the city in nature". When the education level decreases participant views change to utilisation ways as "an ideal picnic area for the city". According to questionnaire results, public utilisation of urban forest was clearly determined first by its accessibility infrastructure and location, followed by security and maintenance. For the design of the area, participants thought that the least possible amount of artificial structures should be constituted in the area. It was determined as the result of the data evaluated that urban people in Malatya city are willing for the urban forest to be constituted in their city, think that such a project may increase the recreative and liveability value of the city, however; they worry about maintenance and security issues and at planning stages these issues should be taken under consideration.

Keywords: *Urban forest, Questionnaire, Urban people, Demographic variable, Malatya.*

1. Introduction

Benefits and contributions of urban open green spaces to urban people have been determined in several studies carried out by various authors from various disciplines. It was stated in such studies that urban open green space systems can reduce psychological stress and mental disorders among urban people, have decreasing effect on obesity, allow for physical activity, contribute to protective health care [1-9].

Urban forestry can be defined as to ensure the sustainability of tree planted or forest areas in or close proximity of urban areas; to constitute new tree planted areas; and to plan maintenance, repairing and management processes of such areas in order to contribute to public health and social, psychological and economic prosperity and wellbeing of urban people.

Urban people feel dominantly the need of going away from cities in order to escape from noise and stress of cities, breathe easily and recreate themselves. Such a condition causes an increase in the demand and need for urban forests.

Definition of urban forest in Turkish forestry can be clarified as "the man-made or natural forest areas with predetermined borders and private entrance which are located or constituted in or close proximity of cities; planned to have primary function of meeting recreation needs of urban people and basic infrastructures and simple facilities to serve for their visitors or dwellers from each age group to satisfy their excursive needs as well as offering possibilities for these people to perform various activities such as sports, relaxing and sightseeing without destroying natural structure of forests [10].

2. Materials and Methods

Objective of the study is to determine the suggestions and views of urban people for Malatya Urban Forest continuing to be constituted using a participatory planning and design approach.

For this aim a questionnaire study was conducted among urban people using rational approach. In addition to demographic and socio-economic data, views of participants for the importance, utilisation possibilities and ecological and recreative benefits of urban forest were investigated. Questionnaire forms were completed using face to face method in all neighbourhoods of the city in order to include almost all the views from all parts of the city. According to Addresses Based Population Recording System of Turkish Statistics Institution (TSI), population of the city is 769 544 in 2014 [11]. When considered this value, sample size was calculated in 5% error and 90% confidential interval to be 272 people minimum.

3. Results and Discussion

Socio-demographic characteristics of the participants in the questionnaire survey are given in Table 1 and Figs. 1-6. It can be seen that 70.2%, 37.5%, 59.2%, 64.3% and 90.8% of the participant are married, 21 to 40 years old and in active working life, respectively. Rate of male participants is 9.6% more than males. When education level of the participants is taken into consideration, it can be stated that high school graduates have the largest rate followed by university graduate and primary school graduates, respectively. About 64% of participants reported that they have a mean monthly income of 2001 to 3000 TL (Turkish Liras).

Table 1. Socio-demographic characteristics of the participants.

Socio-demographic characteristics	Name of characteristics	Label	Number	%	Sdt. Dev.	Scale
Gender	Female (1)	FEML	123	45.2		
	Male (2)	MALE	149	54.8		
	TOTAL		272	100	0.499	1-2
Marital Status	Single (1)	SING	81	29.8		
	Married (2)	MAR	191	70.2		
	TOTAL		272	100	0.627	1-2

Age	≤20 (1)	YONG	8	2.9
	21-40 (2)	MYNG	102	37.5
	41-60 (3)	MDDL	93	34.2
	≥61 (4)	ELDRL	69	25.4
	TOTAL		272	100 0.6091-4
Education Level	Primary School (1)	PRIM	41	15.1
	Secondary school (2)	SCND	19	6.9
	High school (3)	HIGH	103	37.9
	Vocational school (4)	VOCS	29	10.7
	University graduate (5)	UNIG	65	23.9
	Master education (6)	MAST	15	5.5
TOTAL		272	100 1.2771-6	
Occupational Status	Working (1)	WRKN	161	59.2
	Retired (2)	RTRD	53	19.5
	Unemployed (3)	UNEM	13	4.8
	Housewife (4)	HOWF	29	10.7
	Student (5)	STDT	16	5.8
TOTAL		272	100 1.3711-5	
Income Level	≤1000 TL (1)	IL1	36	13.2
	1001-2000 TL (2)	IL2	28	10.3
	2001-3000 TL (3)	IL3	175	64.3
	3001-4500 TL (4)	IL4	26	9.6
	≥4501 TL (5)	IL5	7	2.6
TOTAL		272	100 1.1031-5	

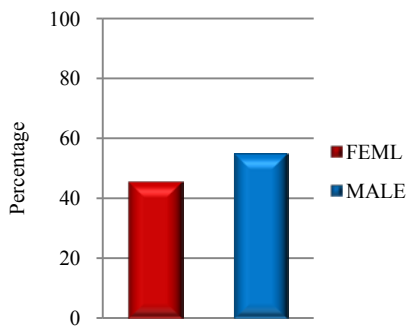


Figure 1. Gender

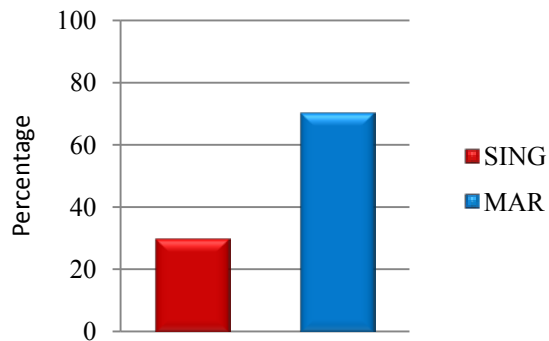


Figure 2. Marital Status

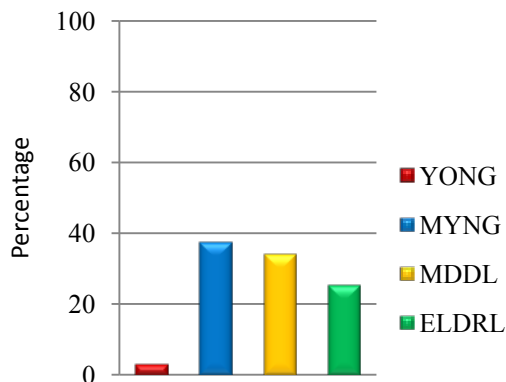


Figure 3. Age

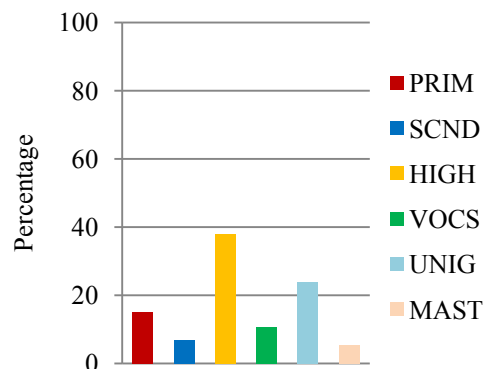


Figure 4. Education Level

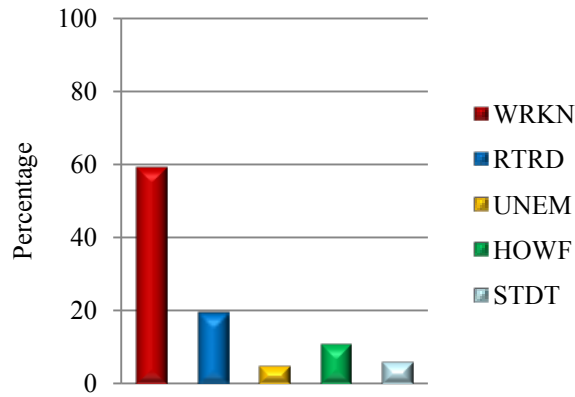


Figure 5. Occupational Status

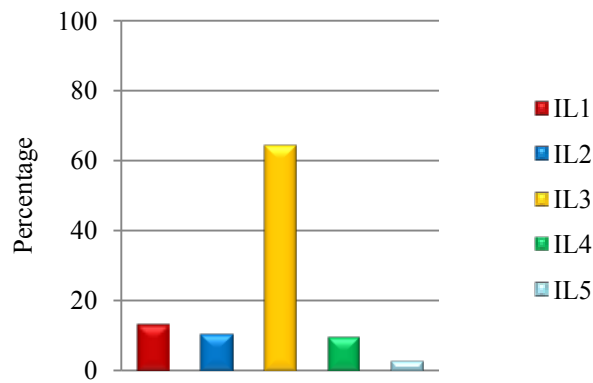


Figure 6. Income Level

Table 2. Participant' views about the urban forest.

Type of variable	<i>I think urban forest project is an important project for Malatya and I support it.</i>	
	Yes (%)	No (%)
Gender		
FEML	81.5	18.5
MALE	89.4	10.6
Marital Status		
SING	83.2	16.8
MAR	93.5	6.5
Age		
YONG	89.1	10.9
MYNG	80.9	19.1
MDDL	87.7	12.3
ELDRL	93.0	7.0
Education Level		
PRIM	62.3	37.7
SCND	69.0	31.0
HIGH	73.5	26.5
VOCS	80.5	19.5
UNIG	89.9	10.1
MAST	98.3	1.7
Occupation		

WRKN	82.2	17.8
RTRD	85.3	14.7
UNEM	76.1	23.9
HOWF	83.8	16.2
STDT	90.0	10.0
Income Level		
IL1	71.5	28.5
IL2	82.0	18.0
IL3	90.8	9.2
IL4	91.3	8.7
IL5	97.6	2.4
TOTAL	84.3	15.7

As the result of the study, 84.3% of participants thought that urban forest project is an important project for Malatya and they support it. As the education and socioeconomic levels increase the rate of participants thinking that urban forest project is a required project for the city also increases (Table 2). Among the participant 90.7% of those university graduate thought that the most important value urban forest adds to the city is "having a utilisation area away from stress but close to the city in nature". When the education level decreases participant views change to utilisation ways as "an ideal picnic area for the city". According to questionnaire results, public utilisation of urban forest was clearly determined first by its accessibility infrastructure and location, followed by security and maintenance. For the design of the area, participants thought that the least possible amount of artificial structures should be constituted in the area.

It was determined as the result of the data evaluated that urban people in Malatya city are willing for the urban forest to be constituted in their city, think that such a project may increase the recreative and liveability value of the city, however, they worry about maintenance and security issues and at planning stages these issues should be taken under consideration.

References

1. Annerstedt, M., Ostergren, P., Bjork, J., Grahn, P., Skarback, E., Wahrborg, P. (2012), "Green qualities in the neighbourhood and mental health - results from a longitudinal cohort study in Southern Sweden", *BMC Public Health*, 12, 337.
2. Ward Thompson, C., Roe, J., Aspinall, P., Mitchell, R., Clow, A., Miller, D. (2012), "More green space is linked to less stress in deprived communities: evidence from salivary cortisol patterns", *Landscape and Urban Planning*, 105(3), 221-229.
3. Grahn, P., Stigsdotter, U. (2003), "Landscape planning and stress", *Urban Forestry and Urban Greening*, 2, 1-18.
4. Hung, C., Chang, C. (2004), "A study of the restorative effects of urban and natural recreational settings". In: Relf, D. (Ed.), *Expanding Roles for Horticulture in Improving Human Well-Being and Life Quality*, *ActaHorticulturae*, 639, ISHS 2004, pp. 235-239.
5. Nielsen, T. S., Hansen, K. B. (2007), "Do green areas affect health? Results from a Danish survey on the use of green areas and health indicators", *Health and Place*, 13, 839-850.
6. Hansmann, R., Eigenheer-Hug, S.M., Berset, ., Seeland, K. (2010), "Restorative effects of sports activities in suburban forests, parks, and fitness centres", *SchweizerischeZeitschriftfür das Forstwesen*, 161, 81-89.
7. Toftager, M., Ekholm, O., Schipperijn, J., Stigsdotter, U., Bentsen, P., Gronbaek, M., Randrup, T., Kamper-Jorgensen, F. (2011), "Distance to Green Space and Physical Activity: A Danish National Representative Survey", *Journal of Physical Activity & Health*, 8, 741-749.
8. Mitchell, R. (2012), "Is physical activity in natural environments better for mental health than physical activity in other environments?", *Social Science & Medicine*, 2012, 1-5.
9. Mitchell, R., Popham, F. (2008), "Effect of exposure to natural environment on health inequalities: an observational population study", *The Lancet*, 372, 1655-1660.

10. Atik, A., Yilmaz, B., Taçoral, E.i, Bayazit, Ş. İ.,Kılıç, M., (2014) "Urban Forests and Their Contributions to Urban Sustainability," *Urban And Urbanization*, St. KlimentOhridski University Press Sofia, 134-148, ISBN: 978-954-07-3772-0.
11. TSI (2014), www.tuik.gov.tr.

NUMERICAL ANALYSIS ON OXY-FUEL COMBUSTION FOR DIFFERENT MIXTURE RATE

Osman İPEK

Barış GÜREL

Mehmet KAN

Abstract

CO₂, CO and NO_x emissions are one of the major problems for pulverized coal combustion. In oxy-fuel combustion method, CO₂-H₂O-O₂-N₂ mixture was used for the combustion of coal. Thus, oxy-fuel combustion process produced low CO and NO_x emissions on the other hand, air isn't suitable for combustion in oxy-fuel process. In this study, oxy-fuel combustion method has been investigated for different mixture rates burned pulverized coal. The numerical analysis for air combustion and three different recirculating flue gas mixture rate, was made by ANSYS-FLUENT 14 commercial software. Analysis of the oxy-fuel combustion process were performed by using realizable k-ε turbulence model, multiple surface reactions char combustion method, single rate devolatilization method, DO radiation method and second-order upwind discretization method. In this analysis, were used to three stage combustion burner. Primary stage, include coal+recirculating flue gas, secondary and tertiary stage include %95 O₂ + % 5 O₂. In these analysis, were investigated affect on flame temperature, mass fraction of the CO₂ and NO_x emissions using different recirculating flue gas mixture rate %CO₂, %H₂O, %O₂ (0/0/21, 59.5/37.5/3, 77.6/19.4/3).

Keywords: *Oxy-fuel combustion, pulverized coal combustion burner, CO₂ and NO_x emissions*

1. INTRODUCTION

According to European Union Environmental Legislation, CO and NO_x emission limits are 200 mg/Nm³ and 800 mg/Nm³ respectively. Lignites with calorific value lower than 3000 kcal/kg is classified as low quality lignites. Therefore, 88% of the Turkey lignites are low quality. In this study, differences between combustion with air and, oxy-fuel that is known as clean coal burning technology have been investigated in the mixture burner for four different mixture rates. Literature studies on the oxy-fuel pulverized coal combustion are given below.

Davidson and Santos [4], 2010, in their studies, investigated oxy-fuel pulverized coal combustion system. They burned low quality coal mixing with recirculating flue gas and combustion air which is separated N₂. As a result of studies, they determined that occur CO₂ and H₂O in the furnace. Other hand, they determined that oxy-fuel combustion process can be made as technical and, it is necessary that manufacturing of large capacity and commercial scale systems more economical than other alternatives. Spero [9], 2009, in his study, he stated function of O₂ injection and distribution in the combustion zone that flame stability, heat transfer of radiation and gas composition. Davidson [3], 2007, he stated more advantages for oxy-fuel combustion that capture emissions that isn't include chemical reactions after combustion. Li, et., all.[8], 2013, in this study, they investigated NO_x And SO_x emission effect of recirculating flue gas in the co-combustion furnace. In this study, they created Aspen-Plus model of volumetric combustion. They investigated decreasing of NO_x and SO_x emissions for combusting % 100 biomass, %45 biomass and %100 lignite. According to this study results, they stated lower NO_x and SO_x emissions for increasing biomass in the fuel mixture. They stated that increasing of recirculating flue gas rate in the mixture reduce the high rate NO_x emissions and increase the slightly rate SO_x emissions. In the all work conditions, they stated NO_x emissions is nearly zero for recirculating of flue gas rate is more than or equal % 10 and biomass combustion less than consume energy from coal combustion. Buhre, et., all.[2], 2005, reported, reported that oxy-fuel combustion reduce high rate NO_x emissions in their work and that there is need new researches to development oxy-fuel coal combustion technology.

In the study NO_x, CO₂ distribution and temperature in the test furnace for different mixture rates in mixer burner combustion that designed by researchers were investigated by using ANSYS-FLUENT 14 commercial software.

2. NUMERICAL ANALYSIS

As could be seen in Figure 2, mesh structure of geometry that test boiler and mixer geometry in Figure 1 was formed 96088 tetrahedral mesh in 21013 nodes by using Ansys-Meshing software. The solution accuracy was increased by creating more frequent intervals boundary layer mesh for burner and wing geometry.

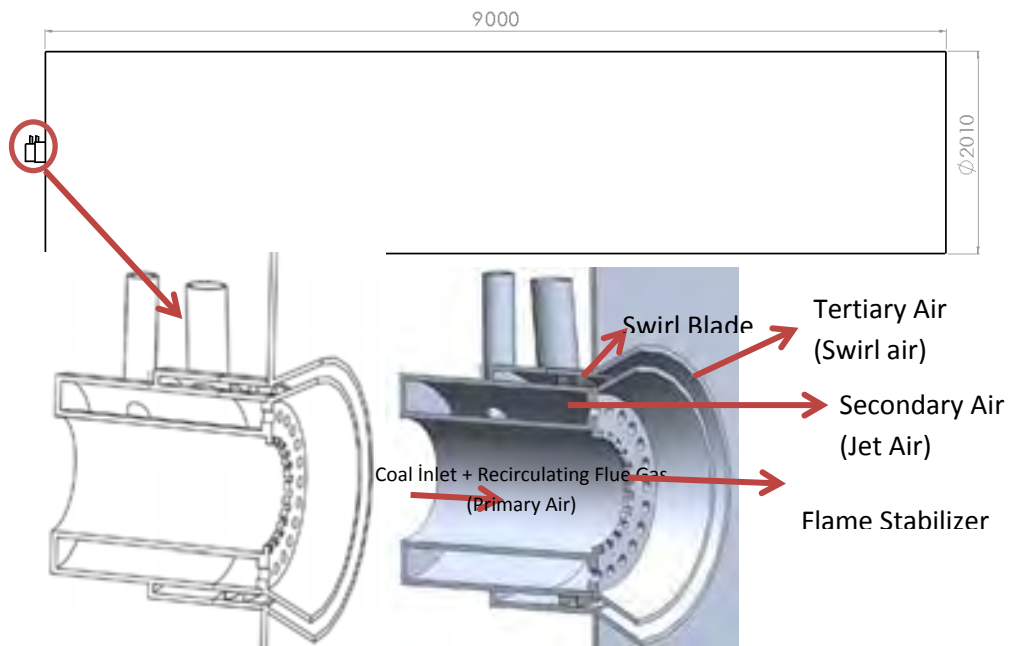


Figure 1. Test Furnace and Mixer Burner

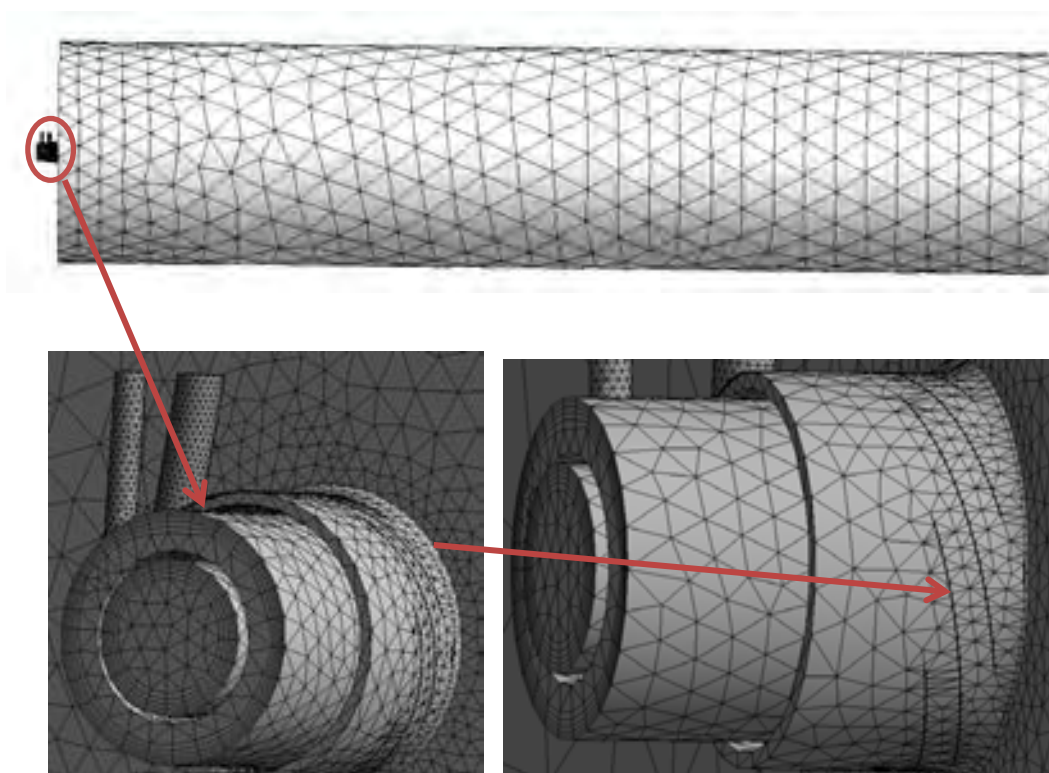


Figure 2. Grid Structure of Test Furnace and Burner

2.1. Boundary Conditions

Combustion analysis were performed for pulverized coal combustion with air and combustion air that mixing recirculating flue gas and air and mixture contents are given in Table 1.

Table 1. Boundary Conditions of Analysis

	Analysis 1		
	Primary	Secondary	Tertiary
Mass Flow Rate (kg/s)	0,082	0,218	0,032
% O₂	21	21	21
% CO₂	0	0	0
% H₂O	0	0	0
	Analysis 2		
	Primary	Secondary	Tertiary
Mass Flow Rate (kg/s)	0,082	0,09	0,021
% O₂	3	95	95
% CO₂	59,5	0	0
% H₂O	37,5	0	0
	Analysis 3		
	Primary	Secondary	Tertiary
Mass Flow Rate (kg/s)	0,082	0,09	0,021
% O₂	3	95	95
% CO₂	77,6	0	0
% H₂O	19,4	0	0

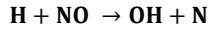
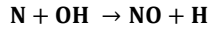
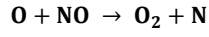
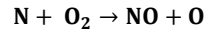
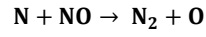
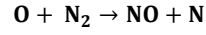
2.2. Materials and Methods

In the combustion analysis, Realizable k-e turbulence method [7], FR-ED (Finite Rate-Eddy Dissipation) volatile matters combustion model[7] were used and multiple surface reactions char combustion model[7] were used for modeling the combustion of the carbon in the particle surface. In the discrete phase modeling, Eulerian-Lagrange [7] approach were used and DO (Discrete Ordinates) radiation model [7] were used for radiation modelling in the analysis. NO_x consist of three forms that temperature, prompt and fuel. NO_x caused by temperature is expressed by

Zeldovich NO_x formation mechanism. In the Zeldovich NO_x formation mechanism was used Quasi-Steady State Assumption that reaction rate with reference taken on [1], NO_x caused by Prompt and fuel for calculating were used by De-Soete modeling [5;6]. Equations are given that used for combustion and NO_x emissions analysis in Table 1. In the analysis, the inlet temperature of the coal was 25 °C, primary, secondary and third stage air temperatures 325 °C. In this analysis; GLİ Tunçbilek coal, which elemental and proximity analysis were given in Table 3 were used. Equations, reactions and constants that using methods in this analysis were given in Table 2.

Table 2. Equations, Reactions and Constants That Using Methods in Combustion and NO_x Emission Analysis

Turbulence method	
Continuity	
$\frac{\partial}{\partial t} (\rho k) + \frac{\partial}{\partial x_i} (\rho k u_i) = \frac{\partial}{\partial x_j} \left[\left(\mu + \frac{\mu_t}{\sigma_k} \right) \frac{\partial k}{\partial x_j} \right] + G_k + G_b - \rho \varepsilon - Y_M + S_k$	(1)
$\frac{\partial}{\partial t} (\rho \varepsilon) + \frac{\partial}{\partial x_i} (\rho \varepsilon u_i) = \frac{\partial}{\partial x_j} \left[\left(\mu + \frac{\mu_t}{\sigma_k} \right) \frac{\partial \varepsilon}{\partial x_j} \right] + C_{1\varepsilon} \frac{\varepsilon}{k} (G_k + C_{3\varepsilon} G_b) - C_{2\varepsilon} \rho \frac{\varepsilon^2}{k} + S_\varepsilon$	(2)
Discrete Phase Modelling	
$\frac{d\mathbf{u}_p}{dt} = \mathbf{F}_D(\mathbf{u} - \mathbf{u}_p) + \frac{\mathbf{g}_x(\rho_p - \rho)}{\rho_p} + \mathbf{F}_x$	(3)
Devolatilization Combustion Model	
$R' = T^\beta A e^{-E/RT} \left(P_n - \frac{R'}{D} \right)^N$	(4)
Combustion Reactions	
Vol + 2,979O₂ → 1CO + 4,17H₂O	
CO + 1/2 O₂ → CO₂	
H₂ + 1/2 O₂ → H₂O	
C_s + 1/2 O₂ → CO	
C_S + CO₂ → 2CO	
C_s + H₂O → H₂ + CO	
Discrete Ordinates Radiation Modelling	
Particle Emissivity: 0.9 [2]	
Particle Scattering Factor: 0.9 [2]	
NO_x Modelling	
Thermal NO_x Zeldovich Mechanism Reactions [16]	



Quasi-Steady-State Assumption [1]

$$\frac{dNO}{dt} = 2 k_{f,1}[\text{O}][\text{N}_2] \frac{\left(1 - \frac{k_{r,1}k_{r,2}[\text{NO}]^2}{k_{f,1}[\text{N}_2]k_{f,2}[\text{O}_2]}\right)}{\left(1 + \frac{k_{r,1}[\text{NO}]}{k_{f,2}[\text{O}_2] + k_{f,3}[\text{OH}]}\right)} \quad (\text{mol}/\text{m}^3 - \text{s}) \quad (5)$$

Table 3. GLİ-Tunçbilek Coal Elemental and Proximity Analysis

Elemental (ultimate) analysis	C	72,9
	H	5
	O	14,7
	N	2,5
	S	4,9
Proximate analysis	Ash	32,6
	Moisture	13
	Volatile Matter	14,8
	Fixed Carbon	39,53

3. RESULTS

In the study results, temperature, total NO_x emissions and mass fraction of CO₂ distributions in the furnace for four analysis were given in Figure 3-5.

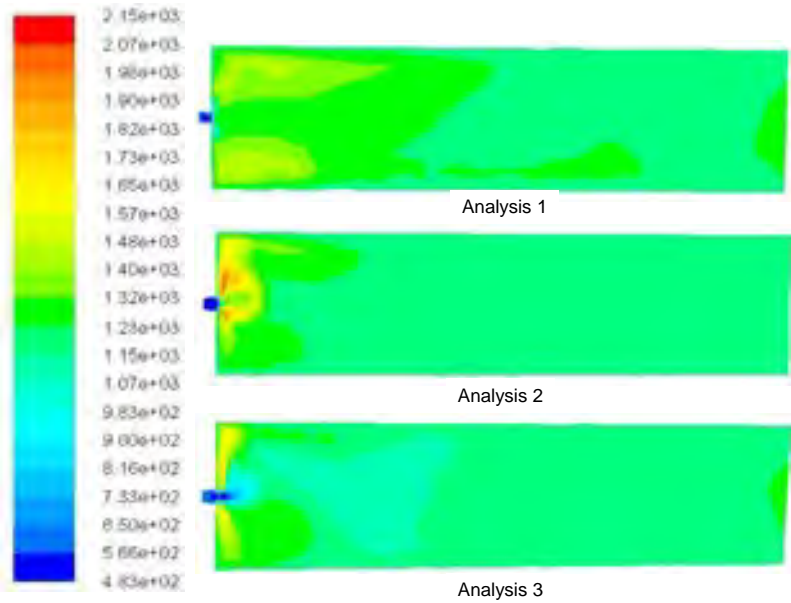


Figure 3. Temperature Distribution in The Furnace

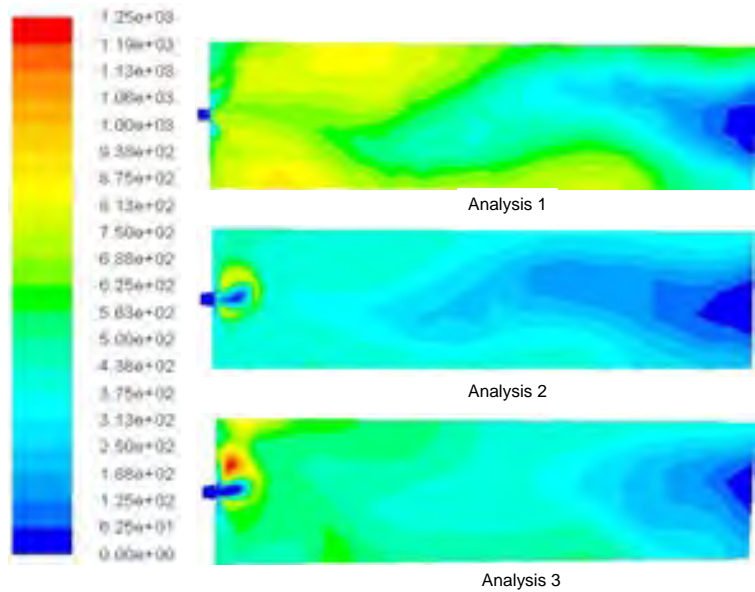


Figure 4. Total NO_x Distribution in The Furnace

Results that obtained above analysis were given in Table 4.

Table 4. Analysis Results

	Flame Temperature (K)	Total NO_x Emissions of Furnace	Mean CO₂ Mass Fraction of Furnace	Furnace Outlet Mean Temperature	Combustion Efficiency (%)

		Outlet(mg/s)	Outlet (%)	(K)	
Analysis 1	1450	376	25,1	1217	98
Analysis 2	2100	207	57,4	1220	98
Analysis 3	2110	262	73,7	1256	98,1

Results which were given in Table 4 were graphed Figure 6-11.

4. CONCLUSIONS

Oxy-fuel combustion is subject which is used recently years and open to improvement with new researches. Oxy-fuel combustion provides same heat release and low emissions with less fuel consumption. Also, increasing CO₂ concentration with recirculating flue gas and utilize CO₂ that using CO₂ capture and storage system in post combustion. Committed analysis results, as shown less flue gas with using less combustion air and although, increasing NO_x concentrations but total NO_x emissions decrease were shown due to decreasing recirculating mass flow rate. In this study results, as shown more than % 50 high flame temperature can be reached for oxy-fuel combustion to air combustion and less than % 45 total NO_x emissions of furnace outlet. Also, CO₂ mass fraction of furnace outlet can be reached %80 were shown due to increasing CO₂ mass fraction of recirculating flue gas.

ACKNOWLEDGEMENTS

REFERENCES

- [1] Baulch D.L., D. D. Drysdall, D. G. Horne, and A. C. Lloyd. Evaluated Kinetic Data for High Temperature Reactions. 1,2,3. Butterworth1973.
- [2] B. J. P. Buhre, L.K. Elliott, C.D. Sheng, R.P. Gupta, T.F. Wall, Oxy-fuel combustion technology for coal fired power generation, Progress in Energy and Combustion Science, 31 (2005) 283–307..
- [3] R M. Davidson, 2007, Post-combustion carbon capture from coal fired plants-solvent scrubbing. CCC/125. London, UK, IEA Clean Coal Centre, 58 pp (Jul 2007).
- [4] R.M. Davidson,S.O. Santos, 2010, Oxyfuel combustion of pulverised coal, CCC/168, IEA Clean Coal Centre, 2010/07 Report.
- [5] G.G. De Seote, 1975, Overall reaction rates of no and N2 formation from fuel nitrogen, Proc. Comb. Inst., 15 1093-1102.
- [6] G.G. De Seote, 23th Symp. (Int.) on Comb., The Combustion Institute, 1990,
- [7] B.Gurel , O.Ipek ,M. Kan, 2014. “Numerical Analysis In Pulverised Coal Fired Furnace For Different Burner Geometries”, International Conference On Computational And Experimental Science And Engineering, Antalya, Turkey.
- [8] J. Li, X.Zhang , W. Yang, W. Blasiak, 2013, Effects of Flue Gas Internal Recirculation on NOx and SOx Emissions in a Co-
- [9] C. Spero, 2009, 1 st International Oxyfuel Combustion Conference. Wrap up #5. Paper presented to: 1st oxyfuel combustion conference, Cotbus, Germany, 8-11 Sep 2009.

CONVERTING A UNIVERSAL MACHINE TO COMPUTER NUMERICAL CONTROLLED MACHINE WITH MICROCONTROLLER AND CONCURRENT CONTROL

Kürşat Mustafa KARAOĞLAN

Karabuk University, Faculty of Technology, Department of Mechatronic Engineering, 78050, Merkez/Karabuk, Turkey.
mzeyveli@karabuk.edu.tr

Metin ZEYVELI

Karabuk University, Eskipazar Vocational School, 78400, Eskipazar/Karabuk, Turkey.
kkaraoglan@karabuk.edu.tr

Abstract

All universal machine tools have their own specific work skills. These are identified depending on the machine design hardware. Universal machine tools with CNC machines, which is the same as the physical design and construction of a number of operational can work with more sensitive and economically. It is possible to simulate a graphic piece can begin for manufacturing. Also with the computer system, progress, speed values such as instantaneous as can be achieved. In this study, universal turning machine has been converted to computer-aided turning machine with microcontroller based embedded software and electronic systems. Universal turning machine system has been controlled with operator software that can work concurrent, suitable motor drive, advanced microprocessor. Electronic system design provides the operator with the possibility of manual and automatic operation.

Keywords: *Converting machine, cnc design, concurrent control, microcontroller.*

1. INTRODUCTION

Computer Numerical Control (CNC) machine tools which are used in a wide variety of industries today are the basic production machines of manufacturing industry. With the advancement of information technologies the software and hardware components of CNC machines are also improving rapidly [1]. The solution proposals presented by these computer-aided machines to the needs of production processes are directly related to software and hardware design. Rapidly meeting the demand for products in the industry, minimizing time consumption with advanced designs and production methods and, most importantly, increasing manufacturing quality are essential elements [2]. The fact that the machines used in the industry are computer-aided ensure that production is improved and production costs are lowered. Due to the fact that production at CNC machines is a highly-paid activity, businesses can obtain CNC machines by purchasing or making special designs thereof [3]. Celik et al. included the design of a fabric cutting machine which was controlled by a software prepared in Pascal Language and moved on x-y plane [4]. In their study Demir et al. dealt with the design and manufacturing of a three-axis mini CNC milling machine. In this study they ensured axis movements with step motors and performed the control of these motors through a control card [5]. Mendi et al. suggested that the classical machines at hand would be converted to programmable versions with Programmable Logic Control (PLC) due to their high cost. For this purpose they examined the control and automation elements used in press machines which would be produced in their study [6]. Polat turned a classical NC milling machine, which performed axis movements with step motors, into a computer-aided machine with a control software which communicated with hardware units through parallel port and was prepared with basic programming language. As a result, the controllability of the machine was improved [7]. In his study, Pekozcan dealt with the conversion of a conventional turning machine into a computer aided one. DC was used as spindle motor and step motors were used for axis movements. Rotation control of the spindle motor was calculated with the help of an encoder and transmitted to the control unit. In addition, dynamic accuracy of the machine was also examined [8].

In our study a universal turning machine is transformed into a computer-aided one. Axis motors were added to the universal machine and instant control of axis movements (X and Z) was ensured. Step motors chosen for axis was included in the system according to thrust power calculations. The entire control of machine system was ensured concurrently and real-time in a computer-aided manner through the control panel which included the prepared microcontroller, driver, power unit, sensor collector systems. Communication with control computers was realized through serial communication paths. Conversion of the universal turning machine into a computer-aided one ensured that design and execution of manufacturing procedures in a fast, accurate and optimum manner.

2. MATERIAL AND METHOD

Universal machines realize manufacturing procedures under operator control. This has several disadvantages in terms of manufacturing. Production losses can occur at machines due to personal errors. In addition, time losses occur due to calibration, measurement control, manual movement etc. On computer-aided machines, serial and accurate production is possible as human factor is negligible in production processes [9]. Instalment of axis motors to the universal machine, placement of on-machine manual operations circuit and instant communication was ensured between the machine and prepared control unit and the produced axis movements and spindle motor control was converted into computer-aided version. On the universal machine (Optimum D 180 x 300 Vario Model) the chosen step motors as appropriate for axis movements (X, Z) was installed to the worm gear axis. These motors perform their movement (G, M) according to the manufacturing codes generated as a result of the design through the axis driver card located inside the control unit. Spindle motor, on the other hand, was controlled by the developed microcontroller placed inside the control unit (Arduino DUE). All signal data received from the machine system is sent from signal collector unit to the microcontroller systems. Instant communication was ensured with the computer using serial communication paths from microcontroller systems communication between microcontrollers and the machine was ensured through signal organizer electronic circuits and measures were taken with electrical protection circuits against interferences, system failures and other errors. The operator is able to instantly monitor all kinds of situations on the machine, initiate and maintain production (Figure 1).

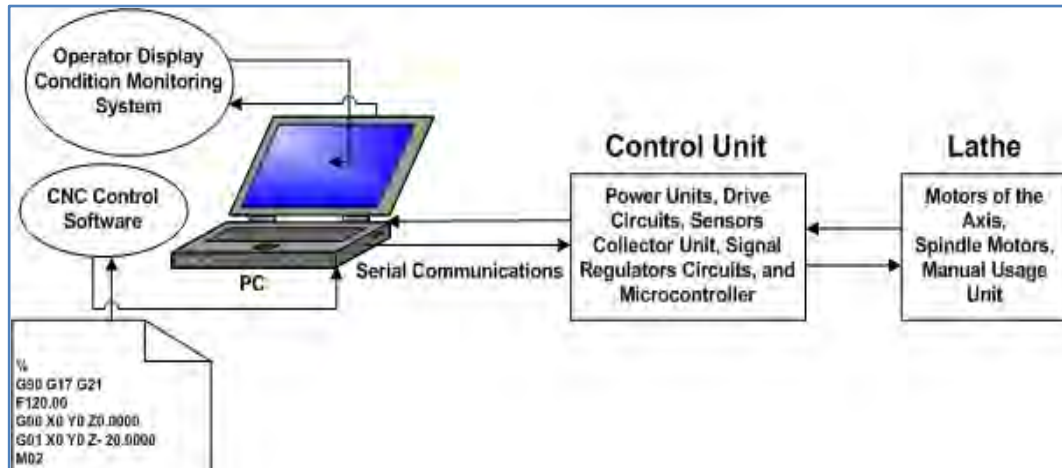


Figure 1. Block diagram of the system

2.1. Mechanical System

The universal turning machine system (Optimum D180 x 300 Vario Model Lathe) that we used in our study has a 600 Watt Permanent Magnet (P.M.) DC Motor as spindle motor. It can work at 150/2500 rpm intervals variable-speed through potentiometer. Start-up/ stop functions of the system in computer-aided manner and starting and maintaining manufacturing depending on the number of rotations that occur as a result of the design can be performed concurrently. In addition, spindle motor can be used manually with the electronic system which was integrated on the machine. The control of the spindle motor on the turning machine was performed by Arduino DUO microcontroller located inside the control panel. Step motor which ensures the movements of Z axis is installed onto the worm shaft with the designed transmission element (coupler) (Figure 2).



Figure 2. General view from computer-aided turning machine system

2.2. Axis Movements

Linear and circular turning can be performed with the turning machine which is a kind of CNC supported machines. In addition these machines have two fundamental axis namely X and Z axis. The movement of the flange and the car on the machine was ensured with step motors (2.2 Nm). Step motors were installed on the machine axis with fixing and transmission elements (coupler and motor fixing material) (Figure 3). Step motors installed on their thrust power. It was ensured that the system works in a rigid manner without vibrations, and instant control of the axis was provided. Step motors were controlled with drivers which were checked by the MK1 microcontroller inside the control unit. MK1

microcontroller works in a computer-controlled manner depending on the G and M programming codes which occur as a result of the design belonging to production.

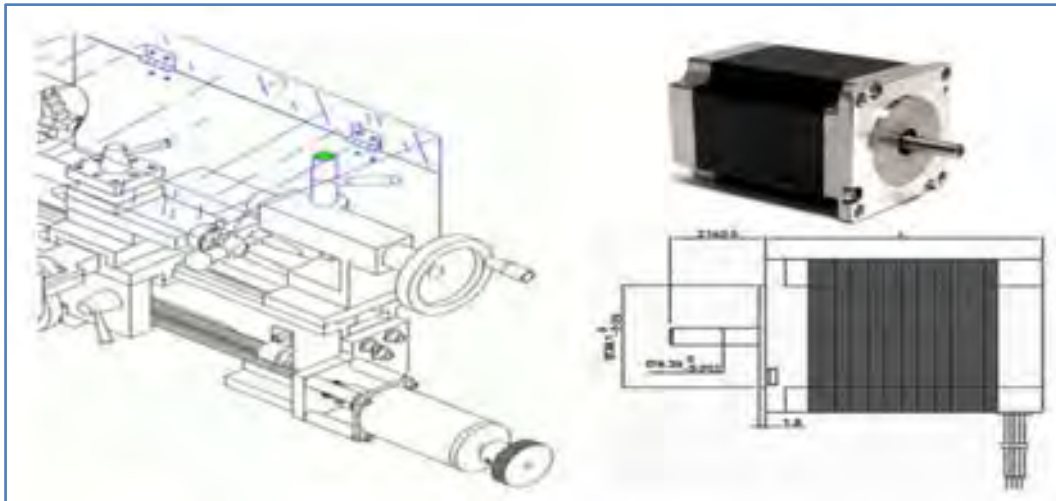


Figure 3. Step motor and control of axis movements

2.3. Application Software and CAM (Computer Aided Manufacturing)

The control of step motors which provide the axis movements (X and Z) on the machine with Computer Aided Manufacturing was ensured with manufacturing process programming codes (G and M). With the MK1 microcontroller which is serial-interface connected to the computer which is connected to the machine, instant control of step motors was performed with manufacturing programming codes. Axis motors were controlled concurrently. During production the situation of machine axis motors can be instantly monitored through CAM software interface (Figure 4).

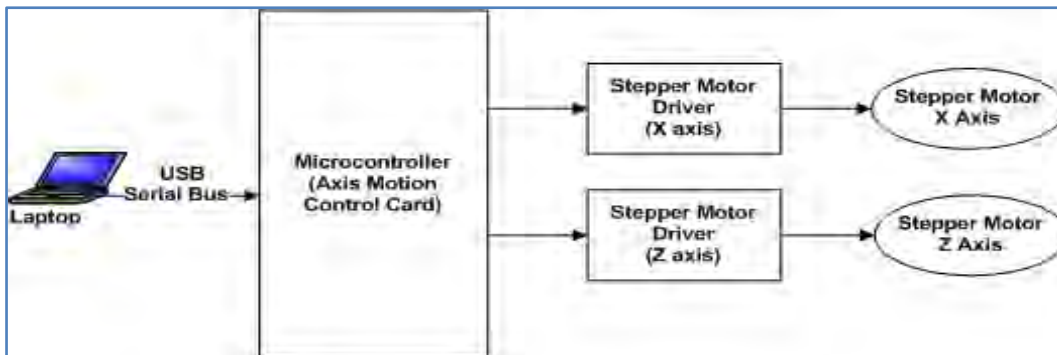


Figure 4. Application software and control card

2.4. Control Unit

In our study step motors and drivers with 2 X and Y axis pitch angles of 2.2 Nm and 1.8° were used. These drivers are being operated at 24-50 Volt supply and 1.5 - 4.5 Ampere intervals. These motors which provide axis movements are controlled in a computer-aided manner with MK1 microcontroller which operates with 5 Volt supply. Machine spindle motor (600 W att P.M. DC) is controlled by a developed Arduino DUE microcontroller with 32 bit AT91SAM3X8E processor, 12 bit ADC resolution which can work at 7-12 Volt supply interval. Power sources (5-36 Volt, 12 Volt) and protection circuits were installed on the unit so that the electrical system of the control unit could be operated without interruption. The communication between Arduino DUE microcontroller which controls the spindle motor and control computer is performed in a bidirectional and instant fashion. Analog signal exchange between Arduino DUE microcontroller and spindle motor is realized through organizer circuits and signal collector unit. In addition, the control of the manual control unit of the system located on the machine is performed by the operator through Arduino DUE microcontroller. In this sense it has been ensured that all operations on the machine can be monitored instantly through computer. In addition, the panel prepared for manual usage by the operator on the machine

Development Sensor Based System Software For The Control Of Motor And Axis Motion On The CNC Turning Machine. Metin Zeyveli, Kürşat Mustafa Karaođlan

is controlled by an electronic circuit prepared with 4-channel relay card (Figure 5) so that the operator is equipped with manual opportunities such as start-up/stop of the machine, determining the direction (left/right) of the spindle motor, automatic/manual usage and calibration of motor rotation speed. In our study spindle motor and axis movement motors for optimum and accurate control of the machine were performed through different microcontrollers without any trade-offs from concurrent working principle. As a result, it was aimed that in further studies the control of spindle and axis movements could be performed with artificial intelligence techniques.



Figure 5. Control unit, 4-channel relay card, and manual usage unit

3. CONCLUSION AND RECOMMENDATIONS

In this paper a universal turning machine was re-equipped and converted into a computer-aided machine. A less costly method was proposed for companies. In addition, with this method time losses caused by operator errors (measurement, control, manual action etc.) were minimized. Step motors were installed on X and Z planes for turning machine movements. It was ensured that drivers belonging to the step motors which ensure axis movements could be executed by a microcontroller which operated CNC programming codes (G and M). Rotation control of machine spindle motor was instantly controlled by an improved 32-bit Arduino DUE microcontroller with 12 bit resolution. Thus, more accurate and optimum control of the axis and spindle motors was ensured without compromising the integrity of manufacturing so that turning machine could also be used manually through the machine with the designed electronic circuits. As a result, the operator was equipped with flexibility of usage.

This study has been supported by the Department of Karabuk University Scientific Research Project. Project Number: KBI-BAP-13/2-YL-027

REFERENCES

- [1]. Xia, W., Zheng, L., Huan, J., Lei, P. (2005). A complete CAD/ CAM/ CNC solution for STEP – compliant. Manufacturing, Robotics and Computer-Integrated Manufacturing, 31, 1–10.
- [2]. Kabas, K., Cetinkaya, K. (2011). Masaüstü CNC Dik İşleme Tezgađı Tasarımı ve Soğutma Sıvısı Uygulaması. International Advanced Technologies Symposium (IATS'11), Elazığ, Turkey.
- [3]. Uyanık, S., Simsek, I., Aytan, N., Onat, M., Erdal, H. (2009). 3 Eksenli Yüzey İşleme Tezgađının Bilgisayar İle Kontrolü. 5. Uluslararası İleri Teknolojiler Sempozyumu (IATS'09), Karabük, Türkiye.
- [4]. Celik, A., Kayacan M., Aydođan, T., Cakir, A. (2002). Bilgisayar Kontrollü Kumaş Kesme Makinası Tasarımı ve İmalatı. Politeknik Dergisi Journal of Polytechnic Cilt: 5 Sayı: 2 s. 173-177.
- [5]. Demir, M., Kuncan, M., Ertunç, M. (2013). 3 Eksenli Mini Cnc Freze Tezgađı Tasarımı ve İmalatı. Otomatik Kontrol Ulusal Toplantısı, TOK2013, Malatya.
- [6]. Mendi, F., Külekci, M. (1999). Geleneksel Tezgađların Plc Yardımıyla Programlanabilir Hale Dönüştürülmesi. Niğde Üniversitesi Mühendislik Bilimleri Dergisi, Cilt 3 Sayı 1, 48-60.
- [7]. Polat, H. (1998). Klasik NC Tezgađlarının CNC Tezgađlarına Dönüştürülmesi. Gazi Üniversitesi, Fen Bilimleri Enstitüsü, Elektrik Eğitimi A.B.D.
- [8]. Peközcan, A. (1999). Konvansiyonel Bir Torna Tezgađının Bilgisayar Nümerik Kontrollü Hale Dönüştürülmesi ve Dinamik Duyarlılığın Araştırılması. Osmangazi Üniversitesi, Fen Bilimleri Enstitüsü., Makine Mühendisliği A.B.D.
- [9]. Kuşçu, H. Bilgisayar Destekli Üretim (CNC Tezgađlar) [PDF document]. Retrieved from Lecture Notes Online Web site: http://hilmi.trakya.edu.tr/ders_notlari/Cam/CNCler.pdf

EFFECT OF MICROWAVE PRETREATMENT ON NICKEL EXTRACTION FROM LATERITIC NICKEL ORE IN HYDROCHLORIC ACID

Tevfik AĞAÇAYAK

Selcuk University, Department of Mining Engineering, 42075, Selcuklu/Konya, Turkey.
tevfik@selcuk.edu.tr

Merve KÖSELER

Aldridge Minerals, Mining LLC. ,06690 Ankara, Turkey

Selma DÜZYOL

Selcuk University, Department of Mining Engineering, 42075, Selcuklu/Konya, Turkey.

Abstract

In this paper, the leaching conditions of Sivrihisar (Adatepe) limonite type lateritic ore in hydrochloric acid solution were investigated. Leaching experiments were carried out using conventional and microwave-assisted method. Stirring speed, acid concentration, temperature, solid/liquid ratio and particle size of the ore were selected as conventional experimental parameters. All of the microwave-assisted leaching experiments were carried out using pre-heated samples at determined optimum conventional leaching conditions. The samples were treated with different microwave powers (0, 90, 180, 360 and 600 W) and pretreatment time (0, 1, 3, 5, 7, 10, 15 and 20 min). Experimental results demonstrated that microwave-assisted leaching can be applied effectively and efficiently to the nickel extraction from lateritic ore. Consequently, the higher dissolution and the higher Ni recoveries in the microwave-assisted leaching process were obtained in less leach time.

Keywords: *Lateritic ore, nickel, leaching, microwave-assisted, hydrochloric acid.*

1. INTRODUCTION

Nickel is an important metal and mainly used in production of stainless steel and alloys because of its resistance to corrosion and high temperature [1, 2]. Laterites are formed by weathering of ultramafic rocks. Lateritic ore essentially may be classified as either limonite or serpentinite ore types [3]. Nickeliferous laterites, derived mainly from olivine-bearing ultramafic rocks such as dunite, olivine-pyroxene peridotite, their serpentinitized equivalents outcrop over a wide domain, are economically exploitable reserves of nickel and cobalt [4]. Approximately 70% of the world's nickel reserves are contained within laterite ores, with the remaining nickel associated with sulphide deposits [3,5-6]. However, 60% of world's nickel production is provided by sulfidic nickel ores [3,7-9]. The production of nickel from lateritic ores includes pyrometallurgical and hydrometallurgical processes [10]. Several leaching studies about lateritic nickel extraction have been performed using different solutions, such as sulphuric acid [11-21], hydrochloric acid [2,15, 22-26] nitric acid [15,27], ammonia [28-30], citric acid, oxalic acid and acetic acid [31-33].

In microwave heating systems, electromagnetic energy transforms to heat in materials directly. Therefore, contrary to the conventional systems, in microwave heating the heat moves inside of the material to outside. The inner parts of the material are hotter than its surface, so evaporation of the water from inside to outside and the diffusion is more simpler. During drying of the material the shell formation is not observed and the water evaporates easily. Microwave energy is usually used in preheating, baking, blanching, cooking, pasteurization, sterilization, drying and dehydration [34,35]. Electrical and magnetic fields occur in microwaves in the form of electromagnetic energy [36]. The microwave energy is a non-ionized electromagnetic radiation with a frequency of 300 MHz to 300 GHz. Microwave causes the moving of molecules or ions by providing reflection and absorbance. For this reason, when they are absorbed by any material, they produce some heat [37]. In recent years, the microwave treatment of minerals has become a major focus of interest and carried out some extensive studies on the microwave processes. These studies include: microwave assisted ore milling, microwave assisted carbothermic reduction of metal oxides, microwave assisted mineral leaching, microwave assisted drying and microwave assisted waste management issues [38].

One of the most important of these studies is microwave-assisted acid leaching. According to some researchers, compared to conventional leaching process, microwave-assisted leaching increases the metal extraction and reduces the leaching time. Microwave-assisted leaching experiments were carried out using lateritic nickel ore in different acid medium and it was concluded that nickel extraction increased efficiently by some authors [39-41].

In this study, conventional and microwave-assisted leaching conditions of Sivrihisar (Adatepe) laterite ore, in hydrochloric acid medium were investigated.

2. EXPERIMENTAL

2.1. Materials

In this study, lateritic nickel ore obtained from the different places of the Adatepe (Sivrihisar) deposit in Eskişehir province of Turkey was used. The samples were crushed by using jaw crusher and then ground by using rod mill. The samples were sieved into four particle size fractions (-212+150, -150+106, -106+75 and -75+53 µm) for experiments. Elemental analysis of each size fraction is given in Table 1.

Table 1. Elemental analysis of the different size fractions of the sample.

Particle size fractions [µm]	Elements [W%]			
	Ni	Fe	Co	Mn
-212 +150	1.43	39.93	0.043	0.064
-150 +106	1.37	22.70	0.039	0.045
-106 +75	1.29	25.83	0.033	0.036
-75 +53	1.30	18.67	0.027	0.024

2.2. Methods

In the experimental studies, the effects of stirring speed, hydrochloric acid concentration, temperature, solid/liquid ratio and particle size on the nickel extraction from lateritic ore were investigated. A pyrex glass of 1L was used as a leaching reactor and put in temperature controlled water bath. It was closed by a rubber cover. The temperature ranged from 40 to 96°C ($\pm 0.2^\circ\text{C}$) of the leach solution in the reactor was provided by

a thermostatically controlled water bath. The leach solution was stirred by Heidolph RZR 2021 model mechanical stirrer with teflon lined impeller. Microwave-assisted leaching were carried out by using the optimum results of the conventional leaching. The pre-heating process was applied on different microwave powers (0, 90, 180, 360 and 600 W) and pretreatment time (1, 3, 5, 7, 10, 15 and 20 min). For the microwave processing of the ore sample, kitchen-type microwave oven (at 2.45 GHz frequency) adjusted to different powers were used.

3. RESULTS AND DISCUSSION

3.1. Conventional Leaching Studies

In this stage, the conventional leaching studies were presented. Stirring speed, acid concentration, temperature, solid/liquid ratio and particle size of the ore were selected as conventional experimental parameters. The results of effects of those parameters were given below, separately.

The effect of stirring speed on the dissolution of Ni was performed at different stirring speeds. The results from these experiments are shown in Figure 1. The results of experiments showed that the dissolution percentage of nickel was independent of the stirring speed. For that reason, all subsequent experiments were carried without stirring. In order to determine the effect of hydrochloric acid concentration, the experiments were performed by varying HCl concentration in the range of 0.5–2.0 mol/L at 50°C. The results from these experiments are shown in Figure 2. As seen from Figure 2, the dissolution recovery of Ni increased with increasing hydrochloric acid concentration.

The effect of temperature on nickel extraction was examined in 50–80 °C temperature and 2.0 M HCl concentration at 120 minute leaching time. The results from these experiments are shown in Figure 3. As seen from Figure 3, the nickel dissolution recovery increased with increasing temperature.

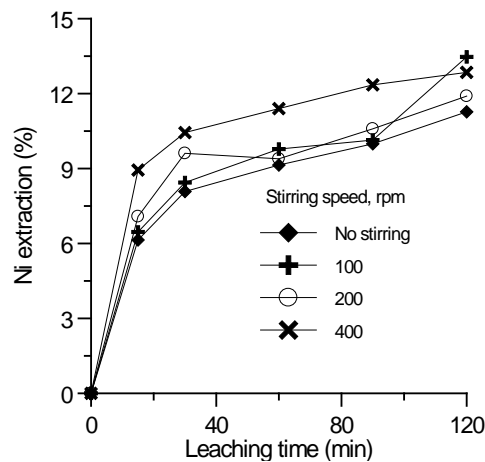


Figure 1. The effect of stirring speed on the nickel extraction (HCl: 0.5 M; temperature: 50 °C; solid/liquid ratio: 5/500 g/mL; particle size: -106+75 µm, leaching time: 120 min).

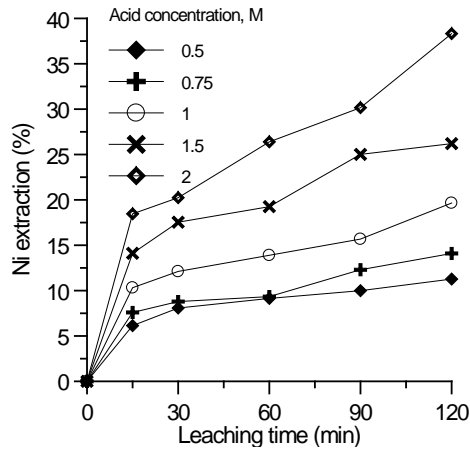


Figure 2. The effect of acid concentration on the nickel extraction (Temperature: 50 °C; stirring speed: no stirring; solid/liquid ratio: 5/500 g/mL; particle size: -106+75 μm, leaching time: 120 min).

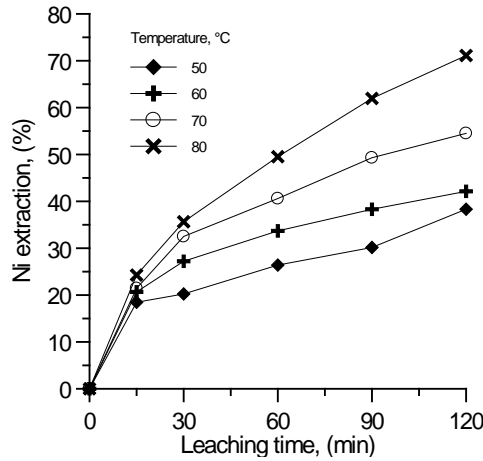


Figure 3. The effect of temperature on the nickel extraction (HCl: 2 M; stirring speed: no stirring; solid/liquid ratio: 5/500 g/mL; particle size: -106+75 μm, leaching time: 120 min).

The effect of solid/liquid ratio were investigated at solid/liquid ratio values of 5/500, 10/500, 15/500 and 20/500 g/mL. The obtained results are shown in Figure 4. It was found that high dissolution occurred at low solid/liquid ratios. The best solid/liquid ratio to dissolve nickel from lateritic ore was at 5/500 g/mL.

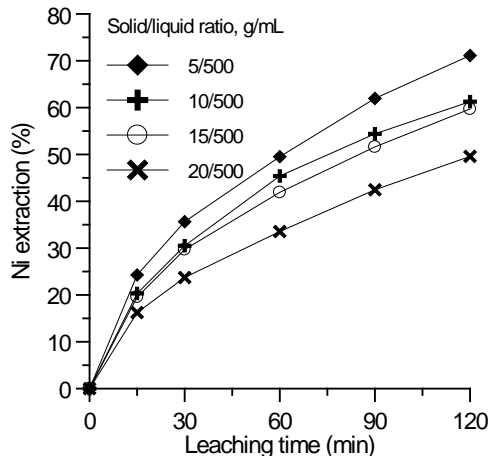


Figure 4. The effect of solid/liquid ratio on the nickel extraction (HCl: 2 M; temperature: 80  C; stirring speed: no stirring; particle size: -106+75  m, leaching time: 120 min).

The experiments for determination of the effect of particle size on the dissolution of nickel were performed at various particle size fractions in hydrochloric acid solution. As seen in Figure 5, the nickel dissolution recovery increases with decreasing particle size.

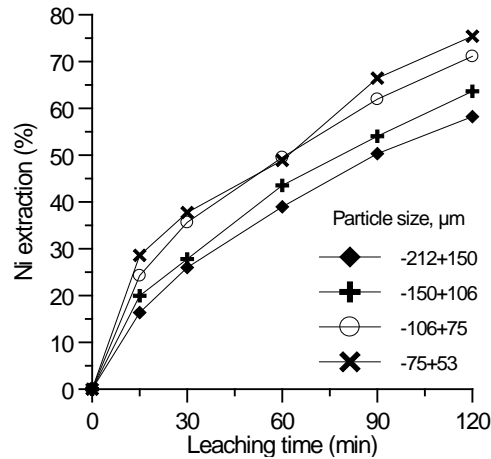


Figure 5. The effect of particle size on the nickel extraction (HCl: 2 M; temperature: 80  C; stirring speed: no stirring; solid/liquid ratio: 5/500 g/mL, leaching time: 120 min).

3.2. Microwave pretreatment leaching studies

In this stage, the microwave pretreatment leaching studies were presented. Microwave power and pre-heating time were selected as microwave-assisted leach experimental parameters. The results of effects of those parameters were given below, separately. All of the microwave-assisted leaching experiments were carried out using pre-heated samples at determined optimum conventional leaching conditions (HCl: 2 M ; temperature: 80  C; stirring speed: no stirring; solid/liquid ratio: 5/500 g/mL, leaching time: 120 min). The pretreatment process consists of different microwave powers (0, 90, 180, 360 and 600 W) and pretreatment time (0, 1, 3, 5, 7, 10, 15 and 20 min). In the first stage of the study, the sample in the fraction of -75+53  m was pre-heated during 15 minutes at different microwave powers (0, 90, 180, 360 and 600 W). The experimental results were shown in Figure 6.

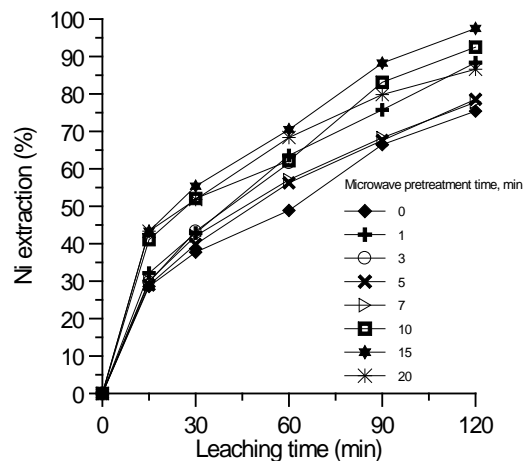


Figure 6. The effect of microwave power on nickel extraction.

As a result of the microwave-assisted leaching experiment, Ni extraction was increased with increasing microwave power until 360 W. The optimum Ni extraction was obtained using 360 W microwave power in 120 min leaching time. In the second stage of the study, the sample in the fraction of $-75+53 \mu\text{m}$ was pre-heated at different times (0, 1, 3, 5, 7, 10, 15 and 20 min) using 360 W microwave power. The experimental results were shown in Figure 7.

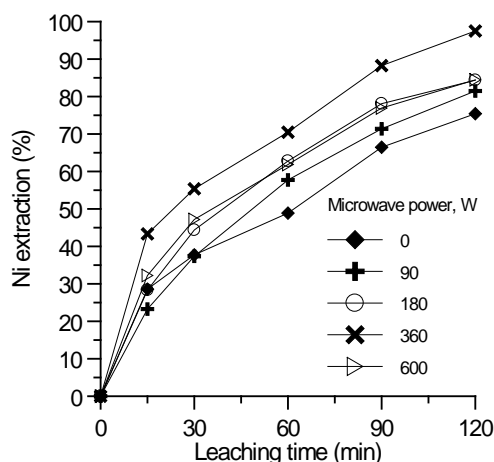


Figure 7. The effect of microwave pretreatment time on nickel extraction.

As a result of the microwave-assisted leaching experiment, Ni extraction was increased with increasing pretreatment time. The maximum extraction (97,5 % Ni) was obtained at 15 min pretreatment time in 120 min leaching.

4. CONCLUSIONS

In the present study, the leaching conditions of Sivrihisar (Adatepe) lateritic ore in hydrochloric acid solution were investigated. Leaching experiments were carried out using conventional and microwave-assisted method. Stirring speed, acid concentration, temperature, solid/liquid ratio and particle size of the ore were selected as conventional experimental parameters. As a result of the conventional leaching studies, it was determined that stirring speed had no effect on Ni extraction. While Ni extraction increased with increasing HCl concentration and temperature, decreased with increasing solid/liquid ratio and particle size. The optimum conventional leaching conditions were determined as: (HCl: 2 M; temperature: 80 °C; stirring speed: no stirring; solid/liquid ratio: 5/500 g/mL, leaching time: 120 min).

Microwave power and pretreatment time were selected as microwave-assisted leach experimental parameters. All of the microwave-assisted leaching experiments were carried out using pre-heated samples at determined optimum conventional leaching conditions. According to microwave-assisted leaching it was observed that Ni extraction increased with increasing microwave power and pre-heating time. Consequently, the maximum extraction (97,5% Ni) was obtained using 360 W microwave power at 15 min pretreatment time in 120 min leaching.

ACKNOWLEDGMENT

This study was supported by The Research Foundation of the Selcuk University under the Project Numbers: 11201045 and 1570119.

REFERENCES

- [1] J. Li, D. Xiong, H. Chen, R. Wang and Y. Liang, "Physicochemical factors affecting leaching of laterite ore in hydrochloric acid," *Hydrometallurgy*, vol.129(130), pp.14–18, 2012.
- [2] K. H. Park and C.W. Nam, "Status and prospect of nickel resources and processing," *Trending Metals Mater. Eng*, vol. 21, pp.1–9, 2008.
- [3] M. Elias, "In Giant Ore Deposits: Characteristics, genesis and exploration, Nickel laterite deposits – geological overview, resources and exploitation," CODES special publication 4, Tasmania, pp. 205–220, 2001.
- [4] E. A. Tufan, "Formation and Properties of Ni-Laterites, Balikesir University," *Journal of Natural and Applied Science*, vol. 16(2), pp. 68-78, 2014.
- [5] J. M. Soler, J. Cama, S. Galí, W. Meléndez, A. Ramírez and J. Estanga, "Composition and dissolution kinetics of garnierite from the Loma de Hierro Ni-laterite deposit, Venezuela," *Chemical Geology*, vol. 249, pp. 191–202, 2008.

- [6] M. Landers, R.J. Gilkes and M. Wells, "Dissolution kinetics of dehydroxylated nickeliferous goethite from limonitic lateritic nickel ore," *Applied Clay Science*, vol. 42, pp. 615–624, 2009.
 - [7] S. A. Gleeson, C. R. Butt and M. Wlias, "Nickel laterites: a review," *SEG Newsletter, Society of Economic Geologists*, vol. 54, pp. 12–18, 2003.
 - [8] N. W. Brand, C. R. M. Butt and M. Elias, "Nickel laterites: classification and features" *Journal of Australian Geology and Geophysics*, vol. 17, pp. 81–88, 1998.
 - [9] A. D. Dalvi, W. Bacon and R.C. Osborne, "*The past and the future of nickel laterites*," PDAC 2004 International Convention, Toronto, 2004.
 - [10] A. Deepatana, J. A. Tang and M. Valix, "Comparative study of chelating ion exchange resins for metal recovery from bioleaching of nickel laterite ores," *Minerals Engineering*, vol. 19, pp. 1280–1289, 2006.
 - [11] D. Georgiou and G. V. Papangelakis, "Sulphuric acid pressure leaching of a limonitic laterite: chemistry and kinetics," *Hydrometallurgy*, vol. 49, pp. 23–46, 1998.
 - [12] T. Agacayak and V. Zedef, "Dissolution kinetics of a lateritic nickel ore in sulphuric acid medium," *Acta Montanistica Slovaca*, vol. 17(1), pp. 33–41, 2012.
 - [13] W. Luo, Q. Feng, L. Ou, G. Zhang and Y. Chen, "Kinetics of saprolitic laterite leaching by sulphuric acid at atmospheric pressure," *Minerals Engineering*, vol. 23(6), pp. 458–462, 2010.
 - [14] S. Stopic, B. Friedrich and R. Fuch, "Kinetics of sulphuric acid leaching of the Serbian nickel laterite ore under atmospheric pressure," *Metallurgica Journal of Metallurgy*, pp. 235-244, 2003.
 - [15] O.S Ayanda, F.A. Adekola, A.A. Baba, O.S. Fatoki and B. J. Ximba, "Comparative Study of the Kinetics of Dissolution of Laterite in some Acidic Media," *Journal of Minerals & Materials Characterization & Engineering*, vol. 10(15), pp. 1457-1472, 2011.
 - [16] D.H. Rubisov, J. M. Krowinkel and V. G. Papangelakis, "Sulphuric acid pressure leaching of laterites universal kinetics of nickel dissolution for limonites and limonitic/saprolitic blends," *Hydrometallurgy*, vol. 58(1), pp. 1–11, 2000.
 - [17] S. Agatzini-Leonardou and I. G. Zafiratos, "Beneficiation of a Greek serpentinitic nickeliferous ore Part II. Sulfuric acid heap and agitation leaching," *Hydrometallurgy*, vol. 74, pp. 267–275, 2004.
 - [18] R. G. McDonald and B. I. Whittington, "Atmospheric acid leaching of nickel laterites review (Part I). Sulphuric acid technologies," *Hydrometallurgy*, vol. 91(4), pp. 35–55, 2008.
 - [19] C. K. Thubakgale, R. K. K. Mbaya and K. Kabongo, "A study of atmospheric acid leaching of a South African nickel laterite," *Minerals Engineering*, vol. 54, pp. 79–81, 2013.
 - [20] M. Landers, R. J. Gilkes and M. Wells, "Dissolution kinetics of dehydroxylated nickeliferous goethite from limonitic lateritic nickel ore," *Applied Clay Science*, vol. 42, pp. 615–624, 2009.
 - [21] F. Mohammadreza, N. Mohammad, S. S. Ziaeddin, "Nickel extraction from low grade laterite by agitation leaching at atmospheric pressure," *International Journal of Mining Science and Technology*, vol. 24, pp. 543–548, 2014.
 - [22] T. Agacayak, V. Zedef and S. Aydogan, "Leaching of lateritic nickel ores of Karacam (Eskisehir-Turkey) with hydrochloric acid," *11th International Multidisciplinary Scientific Geo-Conference&EXPO SGEM, Modern Management of Mine Producing, Geology and Environmental Protection, Albena-Varna/Bulgaria*, vol. 1, pp. 1155–1162, 2011.
 - [23] E. O. Olanipekun, "Kinetics of leaching laterite," *International Journal of Mineral Processing*, vol. 60, pp. 9–14, 2000.
 - [24] B. Wang, Q. Guo, G. Wei, P. Zhang, J. Qu and T. Qi, "Characterization and atmospheric hydrochloric acid leaching of a limonitic laterite from Indonesia," *Hydrometallurgy*, vol. 129-130, pp. 7–13, 2012.
 - [25] Q. Guo, J. Qu, B. Han, P. Zhang, Y. Song and T. Qi, "Innovative technology for processing saprolitic laterite ores by hydrochloric acid atmospheric pressure leaching," *Minerals Engineering*, vol. 71, pp. 1–6, 2015.
 - [26] R. G. McDonald and B. I. Whittington, "Atmospheric acid leaching of nickel laterites review. Part II. Chloride and bio-technologies," *Hydrometallurgy*, vol. 91, pp. 56–69, 2008.
 - [27] B. Ma, C. Wang, W. Yang, B. Yang and Y. Zhang, "Selective pressure leaching of Fe (II)-rich limonitic laterite ores from Indonesia using nitric acid," *Minerals Engineering*, vol. 45, pp. 151–158, 2013.
 - [28] Y. Zhai, W. Mu, Y. Liu and Q. Xu, "A green process for recovering nickel from nickeliferous laterite ores," *Trans. Nonferrous Met. Soc. China*, vol. 20, pp. 65–70, 2010.
 - [29] S. Chen, X. Guo, W. Shi and D. Li, "Extraction of valuable metals from low-grade nickeliferous laterite ore by reduction roasting-ammonia leaching method," *J. Cent. South Univ. Technol.*, vol. 17, pp. 765–769, 2010.
 - [30] M. Zuniga, F. Parada and E. Asselin, "Leaching of a limonitic laterite in ammoniacal solutions with metallic iron," *Hydrometallurgy*, vol. 104, pp. 260–267, 2010.
 - [31] S. Sahu, N. C. Kavuri and M. Kundu, "Dissolution kinetics of nickel laterite ore using different secondary metabolic acids," *Brazilian Journal of Chemical Engineering*, vol. 28(2), pp. 251–258, 2011.
 - [32] S. K. Behera, L. B. Sukla and B. K. Mishra, "Leaching of nickel laterite using fungus mediated organic acid and synthetic organic acid: a comparative study," *Proceedings of the XI International Seminar on Mineral Processing Technology*, pp. 946–954, 2010.
 - [33] L. B. Sukla and V. Panchanadikar, "Bioleaching of lateritic nickel ore using a heterotrophic micro-organism," *Hydrometallurgy*, vol. 32, pp. 373-379, 1993.
 - [34] E.T. Thostenson and T.W. Chou, "Microwave processing: fundamentals and applications," *Composites: Part A*, vol. 30, p.1055, 1999.
 - [35] D. D. Dincov, K. A. Parrott and K. A. Pericleous, "Heat and mass transfer in two-phase porous materials under intensive microwave heating," *Journal of Food Engineering*, vol. 65, p. 403, 2004.
 - [36] K. Barani, S.M. Javad Koleini and B. Rezaei, "Magnetic properties of an iron ore sample after microwave heating," *Separation and Purification Technology*, vol. 76, pp. 331–336, 2011.
 - [37] K.E. Haque, "Microwave energy for mineral treatment processes—a brief review," *International Journal of Mineral Processing*, vol. 57, pp. 1–24, 1999.
-

- [38] S.W. Kingman, Ph.D. Thesis, *The effect of microwave radiation on the comminution and beneficiation of minerals and ores*, University of Birmingham, 1998.
 - [39] X. Che, X. Su, R. Chi and J. Yu, "Microwave assisted atmospheric acid leaching of nickel from laterite ore," *Rare Metals*, vol. 29 (3), pp. 327–332, 2010.
 - [40] X. Zhai, Q. Wu, Y. Fu, L. Ma, C. Fan and N. Li, "Leaching of nickel laterite ore assisted by microwave technique," *Transactions of Nonferrous Metals Society of China*, vol. 20, pp. 77–81, 2010.
 - [41] Koseler M., MSc Thesis, *Determining leaching conditions of Adatepe (Karaçam) lateritic ore under microwave effect*, Selcuk University, Turkey, 2012.
-

NUMERICAL INVESTIGATION OF AL₂O₃-WATER NANOFUID FLOW AND HEAT TRANSFER IN SUDDEN EXPANSION CHANNELS

Engin GEDİK

Corresponding author: Karabük University, EnergySystemsEngineeringDepartment, Karabük, Turkey.
egedik@karabuk.edu.tr

Muhammed Atif TOPAL

Karabük University, Undergraduate student of EnergySystemsEngineeringDepartment, Karabük Turkey.
atif.topal@hotmail.com

Alper ERGÜN

Karabük University, EnergySystemsEngineeringDepartment, Karabük, Turkey.
alperergun@karabuk.edu.tr

Bahadır ACAR

Karabük University, EnergySystemsEngineeringDepartment, Karabük, Turkey.
bacar@karabuk.edu.tr

Abstract

In the present work forced convection heat transfer were investigated numerically for the fully developed fluid flow of incompressible viscous laminar flow under the constant wall heat flux in sudden expansion channels. Two fluids were selected as water and Al₂O₃-water nanofluid for considered problem. The flow assumed to be uniform in the channel inlet and numerical computations were performed for the fully developed laminar flow conditions. Ansys Fluent code, commercially available software based on finite volume approach was used to calculate the governing continuity, momentum and energy equations. Obtained results from numerical study was plotted graphically and discussed in detail taking into consideration non dimensional parameters such as Reynolds number, h (convective heat transfer coefficient) and ϕ nano particle volume fraction. The highest increase in h was calculated about 24.2% for 2% Al₂O₃ and 51% for 4% Al₂O₃ respectively according to base fluid (water) at highest value of $Re=500$.

Keywords: *Forced convection, Al₂O₃-water nanofluid; sudden expansion; CFD*

1. INTRODUCTION

Energy is the indispensable part of today society which indicator of development. Restricted energy sources and hazardous effect to the environment has led to people to investigate new energy source or use energy technologies efficiently. Therefore, studies being performed in the area of energy efficiency are of vital importance. Enhancement of heat transfer is the way for saving energy. Since higher heat transfer rates are desirable in modern industrial applications, conventional fluids are not favored any longer and enhancement in heat transfer characteristics of working fluids has become an important concern for scientists [1]. Due to their superior heat transfer characteristics nanofluids are the attractive for the researchers in the area of universities and industries. These fluids are the suspensions of the solid particles with the sizes under 100 nm in base fluids such as water, oil and ethylene glycol. In the past 20 years many researchers have been studying the properties of nanofluids, and it's expected to be the next generation of heat transfer technology due to the better thermal performances compared to that of traditional heat transfer fluid [2]. Various studies have been done using nanofluids to investigate convective heat transfer characteristics in different geometries and flow natures experimentally and numerically [3]. Sudarmatji et al. [2] has investigated the convective heat transfer and pressure drop of nanofluid, using alumina-water nanofluid under laminar flow regime.

The volume concentration of the nanoparticles was varied with 0.15%, 0.25% and 0.5%. The separation in the fluid flow can be generated from a sudden change in flow geometry. Due to this fact sudden expansion are used in a wide range of engineering applications such as mechanical, chemical, civil, and nuclear industries it is an important issue that must be addressed by terms of nanofluid flow heat transfer characteristic. So, the expansion plays an important role in the design of many engineering applications like refrigeration, extrusion, free jets and where heat transfer is required. [7,8]. Some studies focused on the sudden expansion which exhibit an influence on the fluid flow and heat transfer behaviors. Togun et al. [9] examined a numerical study of heat transfer to turbulent and laminar Cu/water flow over a backward-facing step. In this simulation, three volume fractions of nanofluid (0%, 2% and 4%), a varying Reynolds number from 50 to 200 for the laminar range and 5000 to 20,000 for the turbulent range, an expansion ratio of 2 and constant heat flux of 4000 W/m²K were considered. Bae and Kim [10] studied numerically the turbulent flow in axisymmetric sudden expansions channel with a chamfered edge. In the numerical study CFD software, Fluent code have been used. Simulations were performed in their study for the dimensionless chamfer lengths varying from 0.02 to 0.5, expansion ratios between 2 and 6, and chamfer angles of up to 45° at a Reynolds number of 3×10⁵. Al-aswadi et al. [11]. Laminar forced convection flow of nanofluids over a 2D horizontal backward facing step placed in a duct is numerically investigated using a finite volume method. A 5% volume fraction of nanoparticles is dispersed in a base fluid besides using various types of nanoparticles such as Au, Ag, Al₂O₃, Cu, CuO, diamond, SiO₂, and TiO₂. The Reynolds number was in the range of 50 ≤ Re ≤ 175. Christopher et al. [12] studied numerically laminar forced convection heat transfer from two-dimensional sudden expansion flow of different nanofluids. They have reported that the Nusselt number reaches peak values near the reattachment point and reaches asymptotic value in the downstream of the flow regime.

Motivated by the above studies in the present work flow and convective heat transfer in aluminum oxide–water (Al₂O₃-water) nanofluid in a sudden expansion channel for laminar flow regime which Re number vary between 50 to 500 were examined numerically. Based on the recommended concentrations for Al₂O₃-water [13, 14] nanofluid as effective volume concentrations of nanoparticles in the range of 0% to 4% were used in the numerical study. The effects of pertinent parameters such as Re number, convective heat transfer coefficient h, and volume concentration φ on the heat transfer characteristic of nanofluid were discussed with the help of graphs.

2. MATERIAL AND METHOD

Let us consider the problem of a steady, incompressible, laminar flow of pure water and Al₂O₃-water nanofluid in sudden expansion pipe in the axisymmetric two dimensional xy-planes along the x-direction as can be seen from the Figure 1. Flow separates at the corner and reattach along the top wall. The expansion ratio R₂/R₁ equals to 2, L₁/R₁=200 and L₂/R₂=250. The flow is subjected to uniform velocity from pipe inlet and reaches fully developed regime in the entrance of orifice then reaches again to fully developed flow regime at outlet of the pipe giving sufficient distance from the orifice. In the Figure 1 a, b and c denotes the

wall of the geometry which was not applied constant heat flux for a and b and applied for c as $q_w=100$ W/m²K. Inlet temperature is assumed at ambient temperature as 300 K. No-slip boundary conditions apply at the pipe wall for the velocity.

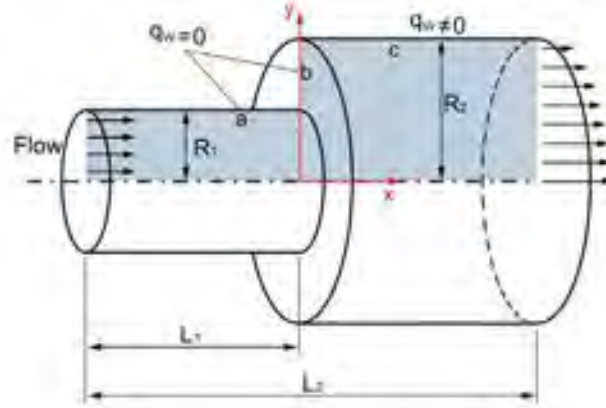


Figure 1 Schematic view of the considered problem

The governing equations were solved numerically with the aid of commercially available Ansys Fluent 15.0 code based on the finite volume method according to associated initial and boundary conditions. Due to symmetry, the computational domain covers only half of the pipe. A finite volume technique was implemented for discretizing governing equations inside the computational domain (gray area of the Figure 1). In the CFD analysis the SIMPLE algorithm was used to link the pressure and velocity fields and a second-order upwind scheme was used to obtain higher numerical accuracy with the residual convergence criterion was less than 10^{-6} for the continuity, momentum and energy equations.

A mesh converged study were performed using various mesh densities to ensure that the h convective heat transfer coefficient is converged for $Re=50$. The working fluid for the mesh testing is water where mesh sizes 200×20 and 300×40 for upstream and downstream respectively confirms a mesh converged solution. Several mesh size of the geometry is performed. The h responses for various mesh size are shown in Figure 2. It shows that the h is increasing for smaller cell number and became almost constant after cell number 16000. According to the test, a mesh was determined which has 16000 cells due to it shows less than 1% differences in h compared to the others.

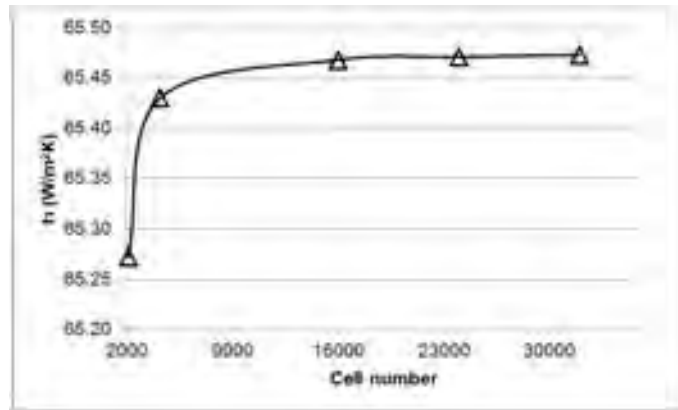


Figure 2. Mesh converged study

The physical properties of the nanofluid are calculated using specific correlations [1, 8, 9, and 15]. The effective density of nanofluid ρ_{nf} is described as;

$$\rho = \varphi \rho_p + (1 - \varphi) \rho_{bf} \quad (2.1)$$

The viscosity of the nanofluids is described as;

$$\mu = \mu_{bf}(1 + a_{\mu}\varphi + b_{\mu}\varphi^2)a_{\mu} = 39.11, b_{\mu} = 533.9(2.2)$$

Thermal conductivity of the nanofluids is described as;

$$k = k_{bf}(1 + a_k\varphi + b_k\varphi^2)a_k = 7.47, b_k = 0(2.3)$$

The heat capacity is given as;

$$c = \frac{\varphi\rho_p c_p + (1-\varphi)\rho_{bf} c_{bf}}{\rho} \quad (2.4)$$

In above relations ρ , μ , k and φ are the density, dynamic viscosity, thermal conductivity and the volume concentration of nanofluid and subscripts, p and bf imply nanoparticle and base fluid respectively. The computations of the thermophysical properties of the nanofluids used in this CFD simulation were given Table.1

Table.1 Thermophysical properties of water-Al₂O₃ nanofluids at 20 °C

φ (%)	ρ (kgm ⁻³)	k (Wm ⁻¹ K ⁻¹)	μ (kgm ⁻¹ s ⁻¹)	C_p (Jkg ⁻¹ K ⁻¹)
0	998.20	0.6000	0.001003	4182.00
2	1055.83	0.6896	0.002001	3931.45
4	1113.47	0.7792	0.003428	3706.84
100	3880	36	-	773

According to the first law of thermodynamics the energy transferred from heated wall surface of the computational domain is equal to fluid gained energy described as;

$$\dot{m}c\Delta T = hA_s\Delta T \quad (2.5)$$

To determine the convective heat transfer coefficient, h equations 2.6 was used in the present study.

$$\dot{m}c(T_o - T_i) = hA_s(T_w - T_b)(2.6)$$

where \dot{m} denotes mass flow rate, A_s is the surface area, c is the heat capacity and T_o , T_i , T_w and T_b describe outlet, inlet, wall and bulk temperature respectively.

3. RESULT AND DISCUSSION

In the present study fluid flow and heat transfer characteristic of Al₂O₃-water nanofluids examined numerically. Simulations are performed for different Reynolds numbers of 50, 100, 150, 200, 250, 300, 350, 400, 450 and 500 for various types of nanoparticles with 0%, 2% and 4% volume concentration of nanofluid. The mixture of the nanoparticles and the base fluid can be assumed as a homogeneous single phase fluid.

It is known from the open literature and described in detail by the Al-Aswadi et al. [14] the flow passing to the sudden expansion geometrical channels expands and induced inlet flow separates at the sudden expansion, forming a counter-clockwise rotating vortex. After that, the velocity profile reattached and redeveloped approaching a fully developed flow as fluid flows towards the channel exit. Figure 3 shows the streamlines at the beginning of expansion for the laminar flow regimes at 0% (pure water), 2% (Al₂O₃-water) volume fraction and Reynolds number in 100 and 500. It is clear from the figure, the recirculation region expanded with the increase of Reynolds number for the laminar regime where the largest recirculation region was obtained at Re = 500, which corresponds to the greatest heat transfer enhancement.

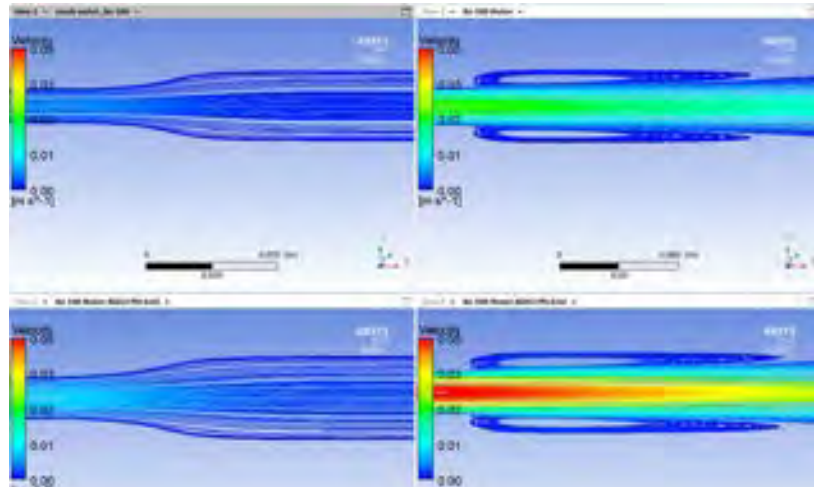


Figure 3 Streamline of velocity at expansion ratio 2 with volume fraction 0% and 2% at $Re = 50$ and 500

Figure 4 shows the velocity change at the pipe outlet for varying Reynolds number 50 to 500 for pure water, 2% and 4% Al_2O_3 . The flow developed after recirculation region and become fully developed conditions at the pipe outlet. It is obviously seen from the figure increasing of Reynolds numbers has caused to increase velocity as expected. In addition that increases in volume fraction increase velocities. The highest value of the velocity was found for the nanofluid has 4% volume fraction about two times greater than pure water.

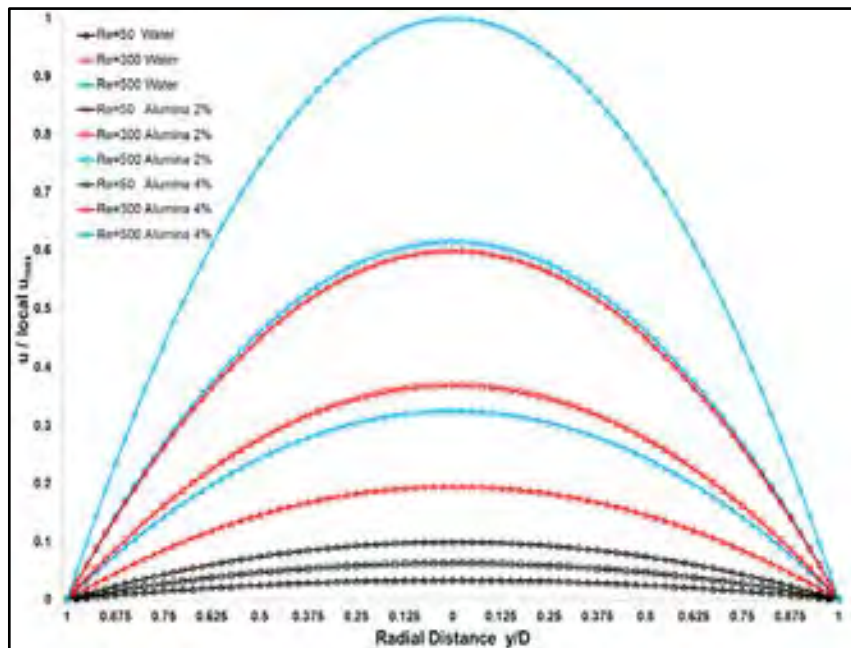


Figure 4 Variation of normalized axial velocity the outlet, $Re = 50, 300$ and 500 for pure water, 2% and 4% Al_2O_3

The pressure drop variation with axial distance for different nanofluid volume fractions at $Re=300$ is presented in Figure 5. As it can be seen from the figure, the pressure drop changes depend on the increase nanofluid volume fraction. According to the results, the largest decrease in pressure occurred for 4% Al_2O_3 -water nanofluid. The pressure drop is changed from 14 Pa to 0.94 Pa on the expansion region ($x=0$) and the pressure curve of the flow which is away from the expansion region it decreases linearly until it reaches zero Pascal at the exit.

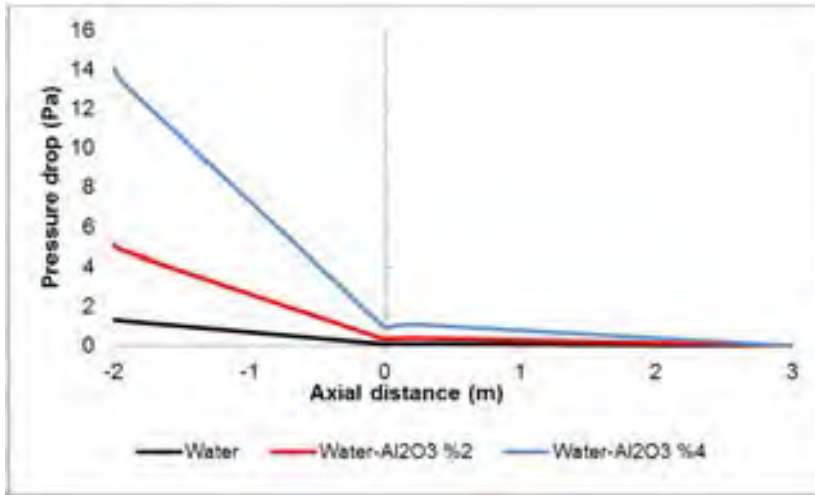


Figure 5 Variation of static pressure drop throughout the axial flow direction with different volume fraction of nanofluids

Temperature from the radial distance is shown in Figure 6 for all fluids and Reynolds number 300. Temperatures profile is plotted at the reattachment point after sudden expansion to see variations for the all three fluids. As can be clearly seen from the figure higher temperatures changes occur near the wall and reattachment region of the flow. The changes in temperatures become closer and linearly nearer to centerline. Maximum temperature changes were observed for the water and it reduced with increasing volume fraction for both nanofluids.

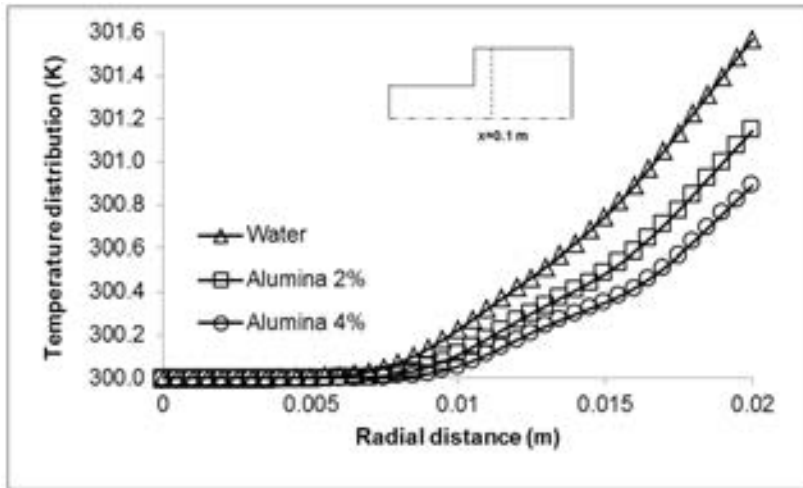


Figure 6 Temperature distributions throughout the radial distance $X=0.1$ $Re=300$

Figure 7 shows the variation in surface Nusselt number for the Reynolds numbers 50, 100, 300 and 500 and the volume fractions of Al_2O_3 2%. The surface Nusselt number profile increased suddenly at the expansion region and then decreased gradually up to the exit. It is also clear that the Nusselt number increased with increase in Re number.

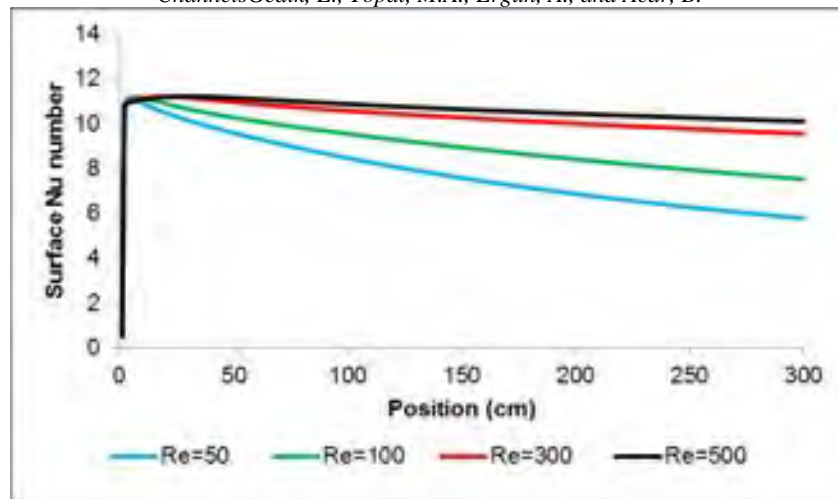


Figure 7 Effect of Reynolds number on surface Nusselt number for 2% Al_2O_3

The effects of Reynolds number on convective heat transfer coefficient, h value for flow in sudden expansion are presented in Figure 8. It can be seen that the h increases with increase of Reynolds number for all cases where the maximum h observed with higher Reynolds number. Furthermore increase in convective heat transfer coefficient has been seen with increasing of volume fraction of nanofluid. When pure water was used heat transfer coefficient was change between 65.4 and 69.2 W/m^2K . In the situation where Al_2O_3 -water was used with the 2% volume fraction the heat transfer coefficient was found between 76 - 86 W/m^2K and whereas it varies 86.7 to 104.6 W/m^2K for nanofluid which volume fraction 4%. The highest increase is calculated about 24.2% for 2% Al_2O_3 and 51% for 4% Al_2O_3 according to base fluid (water) at highest value of Reynolds number.

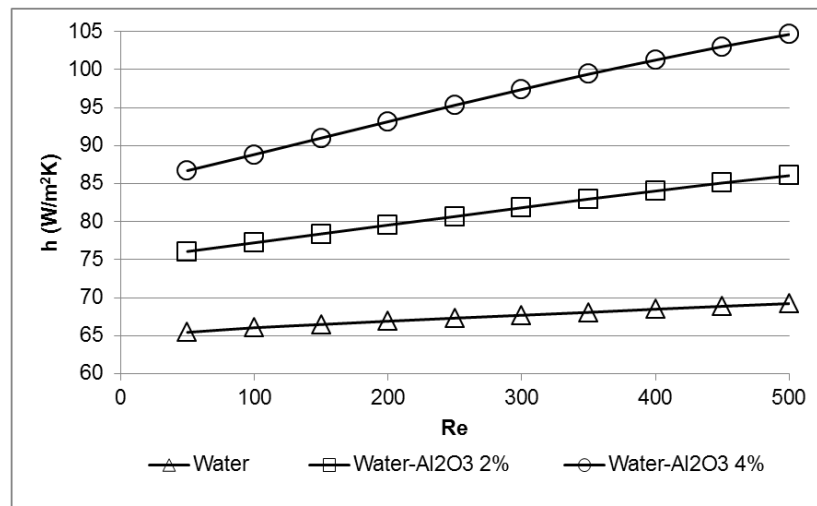


Figure 8 Variations of convective heat transfer coefficient with Reynolds number

4. CONCLUSION

In the present study it is aimed to investigate the fluid flow and convective heat transfer characteristic in the sudden expansion pipe geometry. For this purpose a series of numerical computations were performed using Ansys Fluent code which solving process based on Finite Volume Method. Numerical simulations were reported for 2D laminar forced convection over expansion geometry in a pipe using pure water and water- Al_2O_3 nanofluids has different volume fraction. The effect of some parameters such as Reynolds number, volume fractions of nanofluids and heat transfer coefficient was reported and based on the results obtained, the following conclusions are drawn:

- In sudden expansion the recirculation size and the reattachment length increase as Reynolds number increases.
- It is concluded that the convective heat transfer coefficient increases with flow Reynolds number and nanofluid solid volume fraction.
- The surface Nusselt number increased with increase in Re number.
- The highest increase in h was calculated about 24.2% for 2% water- Al_2O_3 and 51% for 4% water- Al_2O_3 respectively according to base fluid (water) at highest value of $\text{Re}=500$.

REFERENCES

- [1] A. Malvandi, S.A.Moshizi, and D.D. Ganji, "Effect of magnetic fields on heat convection inside a concentric annulus filled with Al_2O_3 -water nanofluid," *Advanced Powder Technology* 25: 1817-1824, 2014.
 - [2] S. Sudarmadji, S. Soeparman, S.Wahyudi, and N.Hamidy, "Effects of Cooling Process of Al_2O_3 - water Nanofluid on Convective Heat Transfer," *FME Transactions* 42: 155-161, 2014.
 - [3] B.C. Pak, and Y. I. Cho, "Hydrodynamic and heat transfer study of dispersed fluids with submicron metallic oxide particles," *Experimental Heat Transfer* 11: 151-170, 1998.
 - [4] D. Wen, and Y. Ding, "Experimental investigation into convective heat transfer of nanofluids at the entrance region under laminar flow conditions," *International Journal of Heat and Mass Transfer*, 47: 5181-5188, 2004.
 - [5] J.Y. Jung, H.S. Oh, and H.Y.Kwak, "Forced convective heat transfer of nanofluids in microchannels," *Proceedings of the ASME International Mechanical Engineering Congress and Exposition*, Chicago. 2006.
 - [6] H. Xie, Y. Li, and W. Yu "Intriguingly high convective heat transfer enhancement of nanofluid coolants in laminar flows," *Physics Letters A*, 374: 2566-2568, 2010.
 - [7] R. Manica, A.L. De Bortoli, "Simulation of sudden expansion flows for power-law fluids," *J. Non-Newtonian Fluid Mech.* 121: 35-40, 2004.
 - [8] A. Sh. Kherbeet, H.A. Mohammed, K.M.Munisamy, R.Saidur, B.H. Salman, I.M.Mahbubul, "Experimental and numerical study of nanofluid flow and heat transfer over microscale forward-facing step," *International Communications in Heat and Mass Transfer* 57: 319-329, 2014.
 - [9] H. Togun, M.R.Safaei, R. Sadri, S.N. Kazi, A.Badarudin, K.Hooman, E.Sadeghinezhad, "Numerical simulation of laminar to turbulent nanofluid flow and heat transfer over a backward-facing step," *Applied Mathematics and Computation* 239: 153-170, 2014.
 - [10] Y. Bae, Y. I. Kim, "Prediction of local pressure drop for turbulent flow in axisymmetric sudden expansions with chamfered edge," *Chemical Engineering Research and Design* 92: 229-239, 2014.
 - [11] A.A. Al-aswadi, H.A. Mohammed, N.H.Shuaib, A. Campo, "Laminar forced convection flow over a backward facing step using nanofluids," *International Communications in Heat and Mass Transfer* 37: 950-957, 2010.
 - [12] D.S. Christopher, P. Rajesh Kanna, G.R.Madhusudhana, P.Venkumar, H.A. Mohammed, "Numerical Investigation of heat transfer from a Two-Dimensional Sudden Expansion flow using nanofluids," *Numerical Heat Transfer, Part A*, 61: 527-546, 2012.
 - [13] M. Beck, Y. Yuan, P. Warrier, A.Teja, "The thermal conductivity of alumina nanofluids in water, ethylene glycol, and ethylene glycol + water mixtures," *J Nanopart Res* 12:1469-77.
 - [14] H. Togun, G.Ahmedi, T.Abdulrazzaq, A.J.Shkariah, S.N.Kazi, A.Badarudin, M.R.Safaei, "Thermal performance of nanofluid in ducts with double forward-facing steps," *Journal of the Taiwan Institute of Chemical Engineers* 47: 28-42, 2015.
 - [15] M. Corcione, "Heat transfer features of buoyancy-driven nanofluids inside rectangular enclosures differentially heated at the sidewalls," *International Journal of Thermal Science* 49: 1536-1546, 2010.
-

OPTIMAZATION OF CONTROL PARAMETERS OF 2-DOF TWIN-ROTOR MIMO SYSTEM

Gonca Ozmen KOCA

Sengul DOGAN

Abstract

Twin-Rotor MIMO System modelling a real helicopter offers a highly nonlinear and a complicated control problem. In this paper, classical proportional-integral-derivative control with optimized controller parameters is applied to handle challenges of the system control. The Pattern Search (PS) and Genetic Algorithm (GA) are employed for the optimization of coupled controller's parameters to obtain fast step response and good control performance. Performance of the controllers are illustrated with step response by simulation studies. Simulations are performed with linearized model of Twin-Rotor MIMO system by using MATLAB program.

Keywords: *Twin rotor, helicopter, optimization, genetic algorithm, pattern search*

1. INTRODUCTION

2-DoF Twin-Rotor MIMO System (TRMS) developed by Feedback Instruments (1998) is a tool that aids researching of modelling, control and identification of helicopters. Some studies handled the control of TRMS having nonlinear and complicated dynamics as a real helicopter. The nonlinear H_∞ control method is implemented for a laboratory helicopter [1, 2]. The inverse model control of TRMS is applied. The adaptive neuro-fuzzy inference system is used to improve the control performance [3]. The comparison of some classical control methods e.g. PID, Ziegler–Nichols and pole placement with intelligent methods fuzzy logic and genetic algorithm (GA) are investigated [4]. A straightforward method is used to control a TRMS [5]. In the study, least squares parametric identification is implemented.

Other studies by optimizing the control parameters of the classical PID controller aim to better control performance [6]. A proportional–integral–derivative (PID) compensator is applied for the TRMS. The control parameters of compensator are tuned by GA [7]. The Stochastic Multi-Parameters Divergence Optimization method is used for tuning PID parameters of closed loop twin rotor system control [8].

In this study, The Pattern Search (PS) and Genetic Algorithm (GA) are used for the optimization of coupled PID controller's parameters to reach fast step response and good control performance. There are three parameters of each controller for tuning.

The system definition is given in Section II. The control structure and implementation of the system is given in Section III. The simulation results of the entire system is demonstrated in Section IV. Lastly, conclusion is presented in Section V.

2. DEFINITION OF THE SYSTEM

2-DoF TRMS is a lab-scale helicopter used for researches. This system consists of a beam pivoted on a tower that can be move freely in both plane: horizontal and vertical. There are main and tail rotors at both ends of the beam. Rotors are driven by DC motors. A counterbalance weight arm is fixed to the beam. The schematic diagram of the TRMS is given in Fig.1.

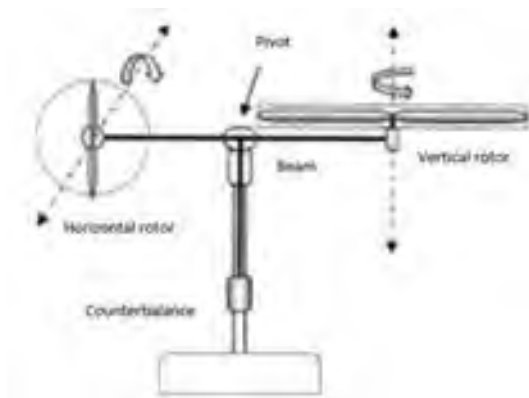


Figure 1. Schematic diagram of the TRMS

The linear model of the TRMS can be described by four transfer functions between motors inputs and angle outputs [9]. The model description is illustrated in Fig.2.

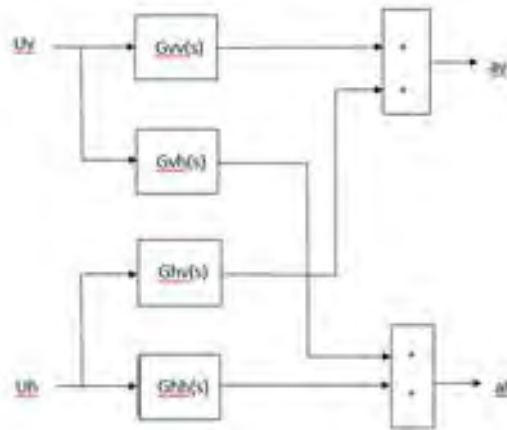


Figure 2. Linear model of the TRMS

$G_{vv}(s)$, $G_{vh}(s)$, $G_{hv}(s)$ and $G_{hh}(s)$ describe the transfer functions is given below;

$$G_{vv}(s) = \frac{0.01657s^2 + 0.4194s + 2.454}{s^3 + 1.487s^2 + 4.403s + 5.449} \quad (1)$$

$$G_{vh}(s) = \frac{0.02248s + 0.4527}{s^2 + 0.4099s + 0.2181} \quad (2)$$

$$G_{hv}(s) = \frac{0.04986s + 0.0962}{s^2 + 0.2377s + 4.902} \quad (3)$$

$$G_{hh}(s) = \frac{0.0009888s^2 + 0.03361s + 0.4065}{s^3 + 1.345s^2 + 0.4568s + 0.3826} \quad (4)$$

for main vertical, vertical-horizontal, horizontal-vertical and main horizontal [9]. U_v and U_h are motor inputs that the control outputs. a_v and a_h are angles. v and h indicates vertical and horizontal respectively.

3. CONTROL STRUCTURE

The TRMS is a highly nonlinear and complicated control problem needs an effective control action. The basic approach to control the system is PID with optimized parameters. The control structure of the system is given by Fig.3.

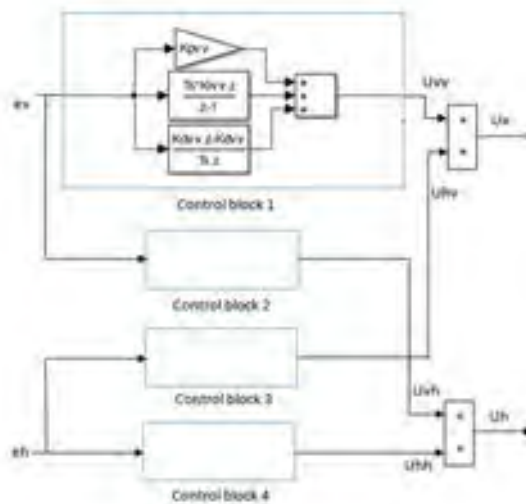


Figure 3. Schematic block diagram of the control structure

As it appears on the diagram that three variables (K_p , K_i , K_d) are tuned to find the best control performance for each control block. The error e_v and e_h are described as,

$$e_v = R_v - a_v \quad (5.a)$$

$$e_h = R_h - a_h(5.b)$$

where R_v and R_h are desired outputs and a_v and a_h are real system outputs for vertical and horizontal plain. The control outputs are defined as,

$$U_v = \left(K_{p_{vv}} + T_s K_{i_{vv}} \frac{z}{(z-1)} + \frac{K_{d_{vv}}(z-1)}{T_s z} \right) e_v(z) + \left(K_{p_{hv}} + T_s K_{i_{hv}} \frac{z}{(z-1)} + \frac{K_{d_{hv}}(z-1)}{T_s z} \right) e_h(z) (6.a)$$

$$U_h = \left(K_{p_{vh}} + T_s K_{i_{vh}} \frac{z}{(z-1)} + \frac{K_{d_{vh}}(z-1)}{T_s z} \right) e_v(z) + \left(K_{p_{hh}} + T_s K_{i_{hh}} \frac{z}{(z-1)} + \frac{K_{d_{hh}}(z-1)}{T_s z} \right) e_h(z) (6.b)$$

Tuning of control parameters is needed to reach good control performance and effective result. In this study, PS and GA optimization algorithms are used to optimize control parameters.

3.1. PS Optimization

The entire document should be in Times New Roman. Type 3 fonts must not be used. Other font types may be used if needed for special purposes.

Pattern Search (PS) which does not need any derivative data is a direct search method for solving optimization problems [10]. Different from conventional optimization methods, it searches trial points around the current point for finding the point has less objective function value than the current point. Thus, it does not require differentiable or continuous objective function. The method can be summarized as follows:

Step1. Initialize with X_0 which is the initial value of the optimization parameter chosen from the available value between lower and upper band of the parameters and updated in each time.

Step 2. The first step value is determined as;

$$\Delta = U_b - L_b \quad (7)$$

where U_b is upper and L_b is lower bounds of the X . The new value of the parameter is expressed by F and :

$$F_k = X_k + \Delta_k \{k \in (1, \dots, n)\} \quad (8)$$

where Δ_k is the step value for k .

Step 3. If fitness value of F_k is better than X_k , then

$$X_k \leftarrow F_k \quad (9)$$

Else receive half of the Δ_k

$$\Delta_k \leftarrow \frac{\Delta_k}{2} (10)$$

Step 4. The above steps are reiterate until stopping criterion is achieved. Depending on the problem, the stopping criteria can be chosen as minimum tolerance, maximum number of iterations, and maximum number of evaluations of the objective function or maximum time.

3.2. GA Optimization

Genetic algorithm (GA) is one of the optimization methods and inspires from natural genetics structure. In this study, GA is also used to adjust control variables in order to provide a good control performance. The basic scheme of the GA is shown in Fig. 4.

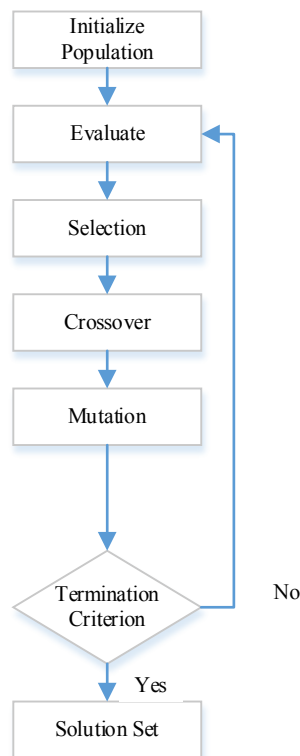


Figure 4. The scheme of genetic algorithm

The most common steps in GA methods are given in below:

Step1. Create initial population according to the solution of the problem. The initial population of GA is shown in Fig.5.



Figure 5. The initial population of GA

Step2. Evaluate the fitness function for each individual. Fitness function is an evaluation criteria for GA.

Step3. Select the individuals according to fitness function. The higher the fitness value, the higher the chance of being selected.

Step4. Create new population after crossover and mutation process which is given in Fig.6.

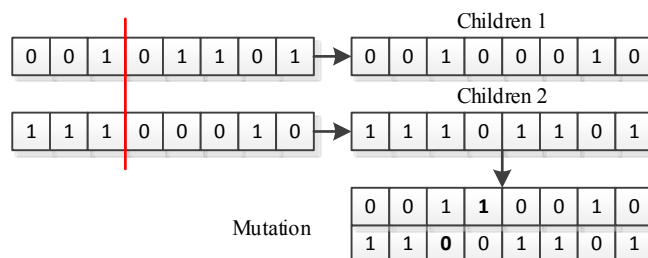


Figure 6. Crossover and Mutation process of GA

Step5. Evaluate the fitness function for each individual and this process proceeds up to the most convenient solution which is given iteration number.

4. SIMULATION RESULTS

Optimizing the PID control parameters is an area still widely studied for different applications. In this study, PS and GA are used to optimize control parameters for nonlinear TRMS and the effectiveness of these algorithms are investigated for the same conditions. Table1 shows the parameters of the algorithms. The simulation studies are carried out in MATLAB environment. The sample time is chosen as $1e-3sec$. The objective function is taken as [6],

$$F = \int_0^{\infty} (t|e_v(t)| + t|e_h(t)| + U_v^2(t) + U_h^2(t))(11)$$

in order to minimize the errors in two planes. The controller parameters are restricted between 0 and 2.

Table1. Parameters of optimization algorithms

PS	Iterations	12000
GA	Iterations	12000
	Elite count	2
	Crossover fraction	0.80

The best optimized PID controller parameters of each algorithm are given in Table 2. Algorithms are tried for 20 times to find the best parameters. The step time responses and errors for two planes are illustrated in Fig.7, Fig.8, Fig.9 and Fig.10 respectively.

Table2. The best optimized PID controller parameters of each algorithm

Optimization Methods	PS	GA		
Controller Parameters	K_{pvv}	2.0000	K_{pvv}	1.3562
	K_{ivv}	0.8711	K_{ivv}	0.9708
	K_{dvv}	0.0049	K_{dvv}	0.0271
	K_{pvh}	0	K_{pvh}	0.9942
	K_{ivh}	1.8828	K_{ivh}	0.3609
	K_{dvh}	0	K_{dvh}	0.0038
	K_{phv}	2.0000	K_{phv}	0.4783
	K_{ihv}	0.3760	K_{ihv}	0.4750
	K_{dhv}	0.8682	K_{dhv}	0.6604
	K_{phh}	1.6035	K_{phh}	0.6192
	K_{ihh}	2.0000	K_{ihh}	0.5259
	K_{dhh}	0.7363	K_{dhh}	1.0576

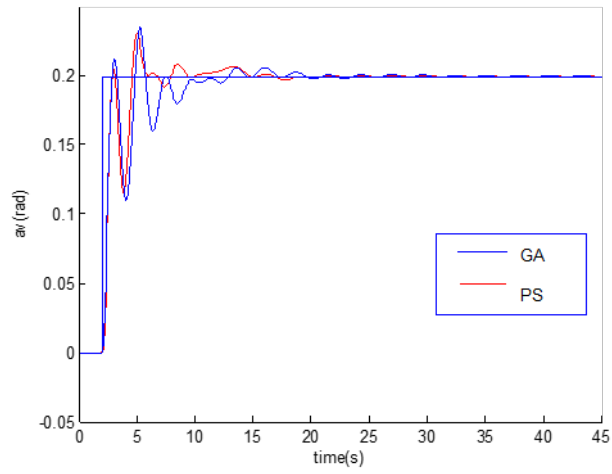


Figure 7. Step response for the vertical plane

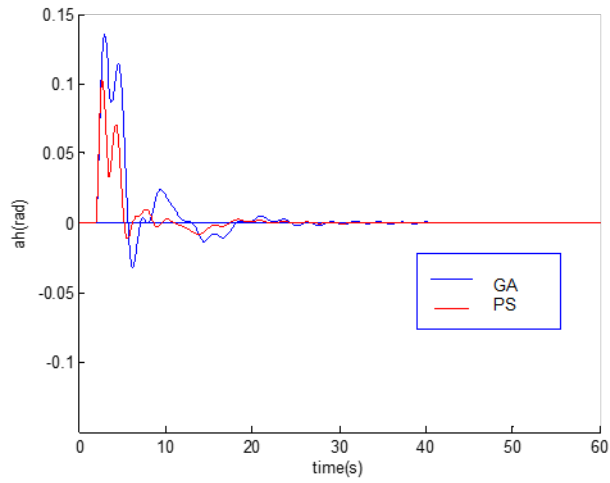


Figure 8. Step response for the horizontal plane

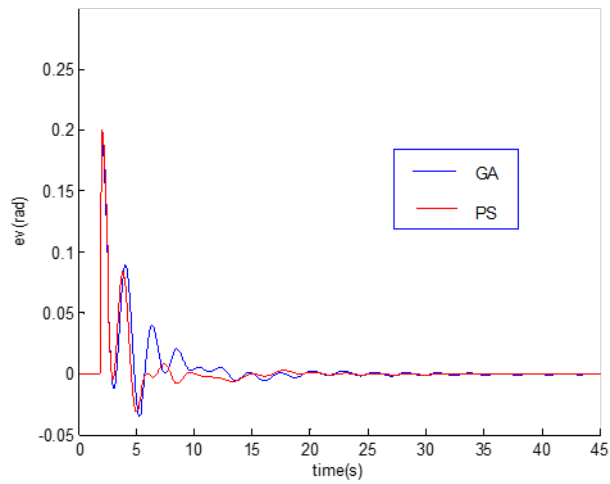


Figure 9. Error for the vertical plane

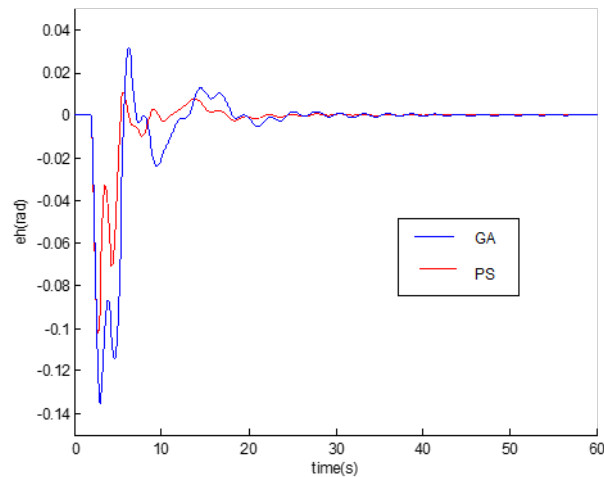


Fig.10. Error for the horizontal plane

It can be seen from figures that PS and GA have acceptable step response for nonlinear TRMS problem. The performance of the PS is better than GA especially in horizontal plane. In addition the computation time of the PS is shorter than GA.

5. CONCLUSION

The objective of this study is to determine PID control parameters for coupled TRMS system by using optimization techniques. The PS algorithm provide better control performance in vertical and horizontal planes with the tuned control parameters than the GA. PS is a direct optimization method finds the best optimized parameter with certain manner whereas GA uses so many populations. The computation time of PS is also shorter than GA.

REFERENCES

- [1] Lopez-Martinez, M. Vivas, C. & Ortega, M. G., *A Multivariable Nonlinear H_∞ Controller for a Laboratory Helicopter* Decision and Control, 2005 and 2005 European Control Conference. CDC-ECC '05. 44th IEEE Conference on, 12-15 Dec. 2005, pp. 4065-4070.
- [2] V. S., Rao, Mukerji, M., George, V. I., Kamath, S. and Shreesha, C., *System Identification and H_∞ Observer Design for TRMS*, International Journal of Computer and Electrical Engineering, vol. 5, December 2013, pp. 563-567.
- [3] Toha, S. F., Tokhi, M. O., *Dynamic nonlinear inverse-model based control of a twin rotor system using adaptive neuro-fuzzy inference system*, Computer Modeling and Simulation, Third UKSim European Symposium on, 25-27 Nov. 2009, pp.107-111.
- [4] Juang, J.-G., Lin, R.-W. and Liu, W.-K., *Comparison of classical control and intelligent control for a MIMO system*, Applied Mathematics and Computation, vol. 205, 2008, pp.778-791.
- [5] Belkheiri, M., Rabhi, A., Boudjema, F., Bosche, A. and Elhajjaji, J., *Model Parameter Identification and Nonlinear Control of a Twin Rotor MIMO System – TRMS*, 15th IFAC Symposium on System Identification, 2009, pp. 1487-1492.
- [6] Moness, M., Moustafa, A. M., *Tuning a Digital Multivariable Controller For a Labscale Helicopter System via Simulated Annealing and Evolutionary Algorithms*, Transactions of the Institute of Measurement and Control, 2015, pp.1-20.
- [7] Juang, J.-G., Liu, W.-K. and Lin, R.-W., *A hybrid intelligent controller for a twin rotor MIMO system and its hardware implementation*, ISA Transactions, vol. 50, 2011, pp. 609-619.
- [8] Alagoz, B. B., Ates, A. and Yeroglu, C., *Auto-tuning of PID controller according to fractional-order reference model approximation for DC rotor control*, Mechatronics, vol. 23, 2013, pp. 789-797.
- [9] Al-Debes, R., *Twin Rotor MIMO System*, Measurements and Control Lab Technical Notes (EE 448), University of Jordan, fetweb.ju.edu.jo/staff/ee/nazeeh/.../exp3.pdf.
- [10] Sahu, B. K. and Mohanty, P. K., *Robust Analysis and Design of Pid Controlled AVR System Using Pattern Search Algorithm*, 2012 IEEE international Conference on Power Electronics, Drives and Energy Systems, 2012, Bengaluru, India.

RESEARCH DATA MANAGEMENT SYSTEM PROPOSAL HAVING CONFIDENTIALITY AND PRIVACY

Feriřtah DALKILIÇ

Dokuz Eylöl University, Department of Computer Engineering, İzmir,
feristah@cs.deu.edu.tr

Enis KARAARSLAN

Muğla Sıtkı Koçman University, Department of Computer Engineering, Muğla,
enis.karaarslan@mu.edu.tr

Abstract

Research datasets are collected during research projects all around the world. The value of research datasets continues to exist also after the projects. It is important to keep them available to be used for further researches. However, there are practical, legal and ethical issues in archiving and sharing this research data. There should be mechanisms by which researchers can share scientific data while preserving data privacy and confidentiality. In this paper, a web based research data management system is proposed where researchers can upload and share their research data. A web interface with the user authentication is generated as a prototype. The user will be able to upload the research data, and can specify which fields to be anonymized. CryptDB is used to keep the specified database fields encrypted to provide privacy and confidentiality. The user password for logging in the system is used to create the encryption/decryption key. The platform will also provide services that researchers can share their research data while preserving the privacy of the data. The modules will include privacy tests like k -anonymity. Research data can be shared fully or partially between researchers. It is aimed to provide data summarization and statistical methods as services to the users. These services can also be used to create subsets of the research data. Surveillance, Epidemiology, and End Results Program (SEER) research data will be used as the test data source in this work. Implementation details, performance issues and recommendations will be given in the paper.

Keywords: Confidentiality, information privacy, encryption, privacy test, research data management

1. INTRODUCTION

Research datasets are collected during research projects all around the world. The value of research datasets continues to exist also after the projects. It is important to keep them available to be used for further researches. Research data sharing is discussed in [1-3]. As stated in [3], we need ways to make these research data discoverable, available and reusable by others.

There are practical, legal and ethical issues in archiving and sharing the research data. There should be mechanisms by which researchers can share scientific data while preserving data privacy and confidentiality. Confidentiality covers two related concepts, which are data confidentiality and privacy. Data confidentiality satisfies that there can be only authorized access to private/confidential data. Privacy satisfies that the owners of the data control the data collected about them and who stores and access that data [4]. Some researchers do not even store their data in the servers which they don't administer. They want to be sure who got access to that data and if this work/data is cited in their studies. We need cryptology methods to achieve the confidentiality so that only authorized access will be possible. Research data also contains some personal data which will require special handling[5]. In order to satisfy privacy, some fields could be anonymized. Anonymization is hiding the identity and/or the sensitive data of record owners, assuming that sensitive data must be retained for data analysis [6, 7]. Anonymization may be implemented with some methods like data summarization and/or statistical methods. Privacy tests like k-anonymity should be used to understand the privacy level of the data. Providing such services will make the amount of shared datasets increased.

In this paper, a solution which is a step to solve the confidentiality and privacy issues of the research data management process is proposed. In the first section, the proposed model RDMS-CP will be explained. Then the implementation and methods will be given. Data sharing using session keys and privacy preserving data sharing methods will be explained and possible future work will be given.

1. DEVELOPING MODELS FOR RESEARCH DATA MANAGEMENT

We propose RDMS-CP (Research Data Management System with Confidentiality and Privacy) model, which is based on CryptDB[8] and privacy algorithms. We constrain our model to handle small datasets. The system will provide services for data summarization and applying statistical methods. Researchers will be able to share research data fully or partially for a given time period.

1.1. Related Work

Data in its original form typically contains sensitive information about individuals, and publishing such data will violate individual privacy. Privacy-preserving data publishing (PPDP) provides methods and tools for publishing useful information while preserving data privacy. Many approaches have been proposed for different data publishing scenarios. Different approaches to PPDP have been summarized and evaluated systematically as a survey in [9].

Online Data Journals are becoming widely used to share data between researchers. In a recent work [3], more than 100 currently existing data journals are analyzed. There are environments like D4Science.org, which provide social network environments and means to share data [10]. To our knowledge, a system which also provides confidentiality and privacy was not done before.

1.2. RDMS-CP Model System Architecture

CryptDB [11] is a system developed in MIT which provides practical and provable confidentiality for database systems [8, 11]. CryptDB acts like proxy between the application and the database [8]. Data will be written encrypted to the database. CryptDB a system is used to secure the connection between database server and applications. The system handles and obstructs the following two threats[8]:

- Admin Access: The database administrator (DBA) may try to learn private data. The DBA has root access on the device and may implement attacks like snooping on the DBMS server.
-

- **Attacker Access:** The attacker can attack and take the control of application and the DBMS servers. The system can make sure the confidentiality of logged-out users' data.

CryptDB allows the DBMS server to execute SQL queries on the data, except some of queries such as selections, projections, joins, aggregates and orderings are performed on ciphertexts. CryptDB gets queries from the applications with a secure way and sends them to database servers. After that database server sends encrypted data then CryptDB decrypts it and sends it to applications. For the encryption system CryptDB uses Random (RND), Deterministic (DET), Order-preserving encryption (OPE), Join (JOIN and OPE-JOIN), and Word search (SEARCH). Symmetric encryption is used and user/password is used for the keys. CryptDB uses user-defined functions (UDFs) to perform cryptographic operation in the DBMS [8]. The system architecture is given in Figure 1.



Figure 1. System architecture

In scope of this study, a database schema has been designed to handle such a system. When creating the data tables, a data table name convention has been followed. Project description is located at the beginning of the table names (Example: RDMS_ for Research Data Management System). The second descriptions are 3-character extension indicating the content-type of the table. ER-Diagram containing the administrative tables and the user tables are given in Figure 2.



Figure 2. ER-diagram – administrative tables and user tables

The system can be used by both registered and unregistered users. However, unregistered users have limited rights. An unregistered user can only search and access to the datasets which are shared publicly. The use-case diagram of the RDMS can be seen in Figure 3.

When a user login to the system, the user can monitor, download and delete his/her own existing datasets or can upload a new dataset. If the user wants to share a dataset with other users, he/she able to define a sharing profile. Some necessary tasks have to be completed before completion of profile definition. The user should specify the sharing type for each data table and data column as private, anonymized or public. After that, user can share dataset with other users for a specified time period by specifying their user names or e-mail addresses. When the database owner decides to share a database publicly, anyone using the system can search and access this database. A sample user interface for sharing datasets is given in Figure 4.

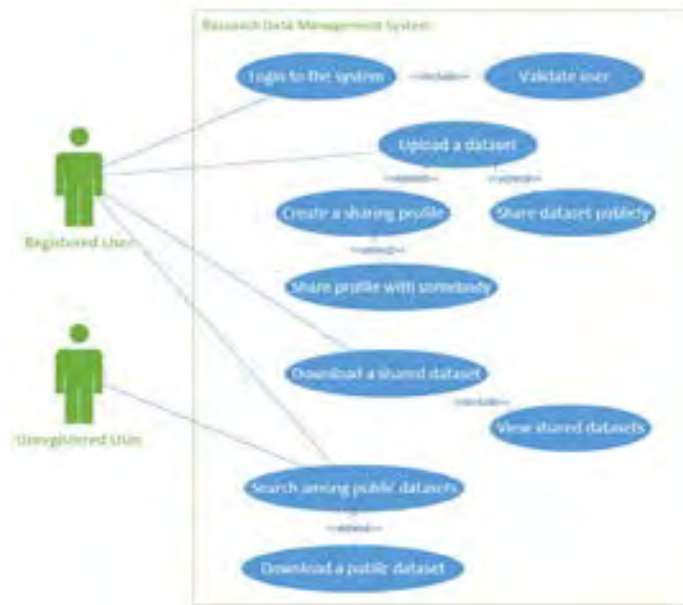


Figure 3. Use-Case Diagram

A registered user can display and download the datasets which have been shared with him/her by other users from the “Shared with me” option located at the left frame of the page. User cannot access to the private tables and columns, and the tables that are shared with him are anonymized.

The design of pages is simple and common UI elements are used to feel users more comfortable. The flow of the usage is similar with document sharing systems, ensuring user a familiar environment and enabling the user to get things done quicker. Pre-chosen fields reduce the burden on the user. Unnecessary elements are avoided and plain language is used on labels and in messaging.



Figure 4. Sample user interface for sharing datasets

2. EXPERIMENTAL

An ordinary PC with 8 GB Ram, i5 3.20 Ghz processor is used as a server. CryptDB is installed on a Linux platform. Ubuntu 12.04 is preferred as the setup processes were clearly defined and tested for this version. Mysql 5.5.14 is used as database, Apache 2.2.22 used as a web server. Setup procedures and installation files of CryptDB can be found the official website of the CryptDB [11]. Web interface is coded in JAVA. Eclipse platform is used when developing the interface.

SEER Research Data [12] is used as a test dataset. This dataset is anonymized so no privacy methods will be applied to it. We used this dataset to test the system in uploading data to the database and implementing privacy tests. We also generated a hospital (patient/doctor) dataset by using dummy values. Anonymization and privacy tests are implemented on this dataset.

Uploading the datasets encrypted to the database, executing queries on these datasets, reading data from the encrypted database and sharing dataset to another researcher on the system are the implementations that are made in the prototype.

In this study, two functions will be discussed: “Data sharing using session keys” and “Privacy preserving data sharing”. During the data sharing phase, user A wants to share a dataset with user B. Session-keys are used and the process is shown in Figure 5. The process is as follows:

- User A reads the dataset from the database decrypting with his/her own key (Key A)
- User A shares this dataset with User B by using the session key.
- User B writes the dataset to the database encrypting with his/her own key (Key B)

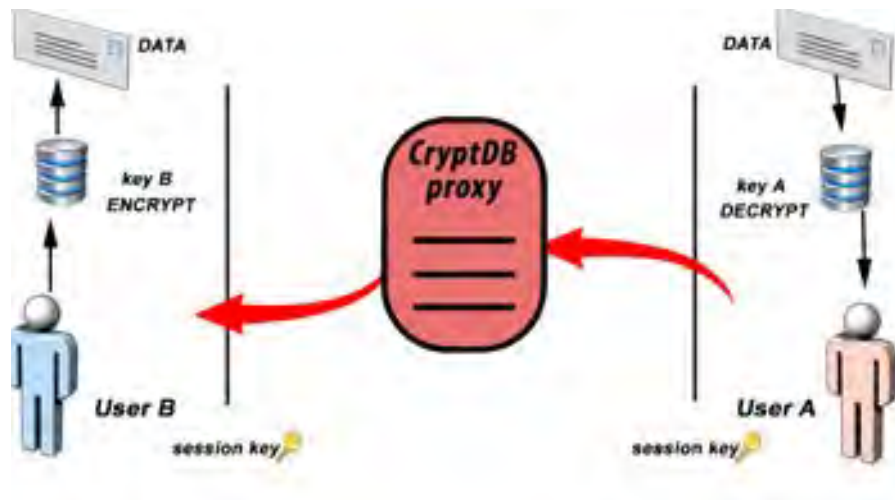


Figure 5. Dataset Sharing between two users

Before mentioning about the privacy preserving data sharing, it should be useful to explain the privacy threats. We can list privacy attack models as Record Linkage, Attribute Linkage, Table Linkage and Probabilistic Attack [9]. In all types of linkages attacks, we assume that the attacker knows the attributes that could potentially identify the record owner. In record and attribute linkages, we also assume that the attacker knows that the victim's record is in the released table, and tries to identify the victim's record and/or sensitive information from the table. In table linkage, the attack seeks to determine the presence or absence of the victim's record in the released table. A data table is considered to be privacy-preserving if it can effectively prevent the attacker from successfully performing these linkages.

To prevent record linkage, the k-anonymity privacy model has been proposed [7, 13]. If one record in the table has some value on the attributes that could potentially identify record owner, at least $k-1$ other records also have the same value. In other words, the minimum group size on these attributes is at least k . A table satisfying this requirement is called k-anonymous.

The proposed model will provide some tools for implementing privacy tests like k-anonymity to understand the privacy level of the resulting dataset. Bigger k-anonymity values mean better privacy level [14]. Data owner (researcher) will be able to implement the following methods to increase the privacy before sharing the data:

- Not sharing a column contains sensitive information about individuals
- Data summarization
- Statistical methods

3. RESULTS AND DISCUSSION

CryptDB environment is installed and tested without any problems. CryptDB can support operations over encrypted data for 99.5% of columns seen in the trace. CryptDB has low overhead, reducing throughput by 14.5% for phpBB, 26% for queries from TPC-C compared to unmodified MySQL [8].

The proposed system is not optimized for big data and current model will only be sufficient to share small datasets. However, we believe that this will also be sufficient for most the surveys and we will also work on enhancing this model in the following studies.

However, we encountered some challenges when we wanted to implement data sharing between users by using session keys. We found some solutions about the issue and working on it.

4. CONCLUSIONS

Data sharing by preserving privacy and confidentiality is a promising approach to information sharing while data sharing increasing between researchers, companies, and organizations. In this study, we proposed a model where researchers can share their data with confidentiality and privacy. The proposed solution writes the datasets encrypted to the database and the performance impact is between %14 to %25 depending on the system. The web interface is easy to use and built in functions will ensure privacy of the shared data. We think that providing such services will increase data sharing among researchers and several academic studies will benefit from it. Possible future works may include adding social networking services, artificial intelligence and big dataset handling. We are also working on using this model on different implementation areas.

ACKNOWLEDGEMENTS

This research is a joint work between MSKU NetSecLab (<http://netseclab.mu.edu.tr/>) and DEU SRG | Security Research Group (<http://srg.cs.deu.edu.tr/wp/>).

We'd like to thank Mehmet Beşir Eren for his involvement (installing and testing the test environment) in this project.

REFERENCES

- [1]. C. L. Borgman, "Research Data: Who will share what, with whom, when, and why?," China-North America Library Conference, Beijing, 2010
 - [2]. J. Furner, "The Conundrum of Sharing Research Data," *Journal of the American Society for Information Science and Technology*, vol. 62, 6, 2011.
 - [3]. L. Candela, D. Castelli, P. Manghi, A. Tani, "Data journals: A survey," *Journal of the Association for Information Science and Technology*, 2015.
 - [4]. S. William, *Cryptography and Network Security: Principles and Practice*, 5th ed., Pearson/Prentice Hall, 2011.
 - [5]. (2013) OECD Guidelines on the Protection of Privacy and Transborder Flows of Personal Data. [Online]. Available: <http://www.oecd.org/sti/ieconomy/oecdguidelinesontheProtectionofPrivacyandTransborderFlowsOfPersonalData.htm>
 - [6]. T. Dalenius, "Towards a methodology for statistical disclosure control," *Statistik Tidskrift*, vol. 15, pp. 429–444, 1977
 - [7]. P. Samarati, and L. Sweeney, "Generalizing data to provide anonymity when disclosing information," in *Proc. of the 17th ACM SIGACT-SIGMOD-SIGART (PODS)*, New York, 188, 1998.
 - [8]. R. A. Popa, C. M. S. Redfield, N. Zeldovich, H. Balakrishnan, "CryptDB: protecting confidentiality with encrypted query processing," in *Proc. of the 23rd ACM Symposium on Operating Systems Principles. ACM*, 2011.
 - [9]. B. C. M. Fung, K. Wang, R. Chen, and P. S. Yu, "Privacy-preserving data publishing: A survey of recent developments," *ACM Computing Surveys (CSUR)*, vol. 42, 4(14), 2010.
 - [10]. M. Assante, L. Candela, D. Castelli, F. Mangiacrapa, P. Pagano, I. Italian, "A Social Networking Research Environment for Scientific Data Sharing: The D4Science Offering," *An Int. J. Grey Lit.* 10, pp. 151–158, 2014.
 - [11]. CryptDB. [Online]. Available: <http://css.csail.mit.edu/cryptdb>
 - [12]. Surveillance, Epidemiology, and End Results (SEER) Program Research Data, National Cancer Institute, DCCPS, Surveillance Research Program, Surveillance Systems Branch, released April 2014, based on the November 2013 submission. [Online]. Available: www.seer.cancer.gov
 - [13]. P. Samarati, and L. Sweeney, "Protecting privacy when disclosing information: its enforcement through generalization and suppression," SRI International, Tech. Rep., 1998.
 - [14]. J. Sedayao, R. Bhardwaj, N. Gorade, "Making Big Data, Privacy, and Anonymization work together in the Enterprise: Experiences and Issues," in *Proc. of the 3rd International Congress on Big Data*, Anchorage, Alaska, pp. 601 – 607, 2014.
-

HYBRIDIZATION OF ELECTRIC VEHICLE WITH FUEL CELL BASED ON TWO CONTROL STRATEGIES

Mustafa Umut KARAOĞLAN

Dokuz Eylül University, Department of Computer Engineering, İzmir,
mustafa.karaoglan@deu.edu.tr

Nusret Sefa KURALAY

Muğla Sıtkı Koçman University, Department of Computer Engineering, Muğla,
kuralay@deu.edu.tr

Abstract

Nowadays, alternative power sources like fuel cells and their applications on vehicles have increased permanently. Fuel cells generate electric energy without storing ability of it instead of a chemical battery. Electric energy produces as long as a fuel supply is maintained. Compared with hybrid vehicle that uses ICE (Internal Combustion Engine) and battery as power sources, it has the advantages of high energy efficiency and much lower emissions. In the future, fuel cell vehicles will be used widely in the world because of deficiency of petroleum fuels and environmental limitations. These concerns push researches to study about fuel cell vehicles and existence of such studies will lead to create our own fuel cell vehicle designs and technology. This study investigates fuel cell hybrid electric vehicles (FCHEV) and its design parameters such as electric motor, fuel cell stack and battery capacity including two control strategies. Propulsion system and control strategy will be created according to theoretical models. Analyzing propulsion system of FCHEV in a driving cycle, battery state of charge positions and vehicle range are main purpose of this study.

Keywords: *Fuel Cell, hybrid electric vehicle, control strategy, drive cycle simulation*

1. INTRODUCTION

Electric vehicle drive train system has a long history in automotive industry. After the development of environmental awareness and economic concerns, electric and hybrid power trains have gained interests again. Battery is the only energy source in electric vehicles [6]. Vehicle mass and price are high because of batteries mass and costs related with their type and technology. Main disadvantages of electric vehicles such as their costs and low range limitation cause by improving hybrid technology [3,8]. Hybrid power train with internal combustion engine is the most common systems in automotive industry. Some of main weak points of the hybrid system with internal combustion engine are their air pollution causing and lower efficiency. Hybridization of the fuel cell system with a power source is an effective technology to overcome the disadvantages of electric alone powered and hybrid powered with internal combustion engine. So fuel cell hybrid electric vehicles have many advantages, such as higher energy efficiency and lower emissions compared to internal combustion engine vehicles [5,8].

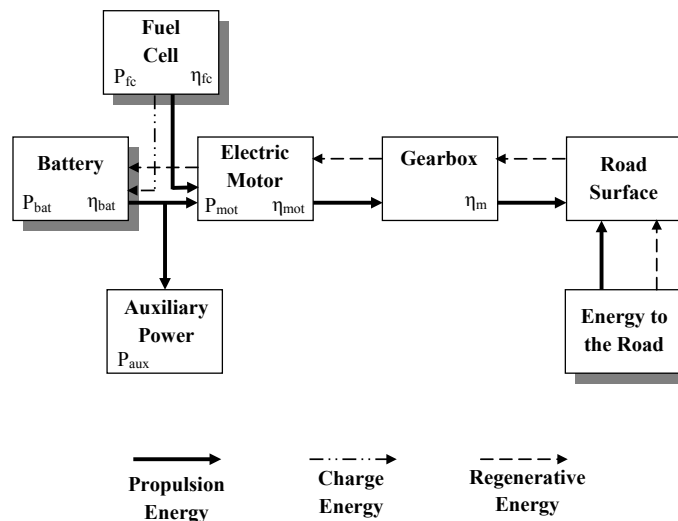


Figure 1. Structure of fuel cell hybrid power train.

The fuel cell hybrid electric vehicle has different features from ICE based hybrid power trains as control strategy. It generally consists of fuel cell system as primary power source and battery is the second. Fuel cell can use as range extender in some applications [7]. According to the power or torque command, controller controls the motor current output and energy flows between the fuel cell system and battery [8]. Electric motor converts the power to mechanical energy and transmits to tires through the gearbox that construction of power train shown in figure 1. Both fuel cell and battery could supply propulsion power to electric motor individual and together. Additionally fuel cell could charge battery according to control strategy and state of charge. Average auxiliary power is determined 100 W and it supplied by battery at any operating conditions. Main energy source is considered 4 lead acid batteries are 12 V and 60 Ah each. It has 2.88 kWh capacity and 0.85 average efficiency (η_{bat}).

Direct methanol fuel cell (DMFC) is used as range extender with 20 liter fuel tank capacity, 1 molar methanol inside includes 640 gr methanol mass. Methanol which lower heating value (LHV_m) is 19940.6 kJ/kg can be directly used as the fuel for a fuel cell. Methanol is a liquid fuel that can be easily stored, marketed for vehicle application and economic organic fuel so it could be independent from fossil fuels called advantages of DMFC systems. Maximum power of fuel cell is 1.5 kW (P_{fc}) with constant 0.2 A/cm² current density in 400 cm² electrode surface area assuming constant working efficiency 0.2 (η) and 3 mm thickness each cell. Totally 63 fuel cells are needed for 1.5 kW fuel cell stack power.

Electric motor is a DC motor that has 11 kW power (P_{mot}) and 73 Nm rated power in 1440 D/d. Propulsion power from the electric motor arrives gearbox that occurs 2 stage constant ratio ($i=6$) and differential gears. During the braking, battery which has relatively high power rate can recuperate the braking energy via opposite line of power train.

2. CONTROL STRATEGIES OF HYBRID POWERTRAIN

Control strategy of power train is a control rule that is preset in the vehicle controller and commands the operation of each component such as battery and fuel cell system. Vehicle controller receives operation

commands from driver that mostly related with the vehicle speed according to the drive cycle 'INRETS urbainfluide 1' (figure 2). Length of single cycle of it is 1890.17 m in 680 seconds total drive cycle:

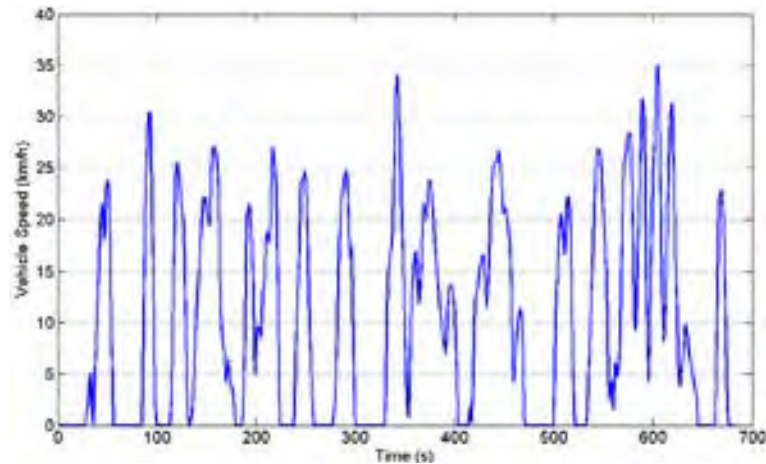


Figure 2. Vehicle speed in drive cycle

Power outputs of fuel cell stack and battery are controlled according to the operation commands. Main parameters of determination power output are current battery state of charge (SOC) which is a measure of the present charge capacity of the battery, methanol storage and power demand from the road.

Two control strategies are designed called strategy 1 and strategy 2 in this study to power train simulation. In these algorithms there are various operating modes, such as the battery alone mode or fuel cell and battery hybrid mode. Control strategy 1 is similar with max SOC of power source control strategy. The target of this control strategy is to maintain the SOC of battery at its pre-determined level. Control strategy 2 is based on fuel cell on-off working situation. Driving long time with low load in high speed for instance on a highway causes battery can be easily charged to its full level or desired level. In this case fuel cell is working just between two SOC levels. Constant voltage can be taken from fuel cell at constant current density. Thus fuel cell operates in optimum efficiency area which is the main advantage of strategy 2.

Algorithm of strategy 1 has detailed as shown in figure 3. If methanol does not exist in fuel tank, fuel cell is not operated and all of power requirement is supplied by battery. Otherwise state of charge (SOC) is checked by the controller. If the SOC is more than %80, fuel cell system is not operated and the power requirement as $P_{mot} + P_{aux}$ is supplied by battery. While SOC level decrease under %75, the fuel cell operates full of its capacity and the power requirement is supplied by battery and fuel cell together. If SOC level is between %75 and %80, the power requirement for motor (P_{mot}) and the maximum power (1,5 kW) which is produced by fuel cell is compared and if the power requirement for motor (P_{mot}) is more than the maximum power which is produced by fuel cell than the fuel cell is worked full of its capacity (P_{fcmax}). If the power requirement for motor is less than the maximum power which is produced by fuel cell and it has positive sign, the fuel cell will produce power which is necessary for system else, the fuel cell does not operated while braking in negative sign power requirement.

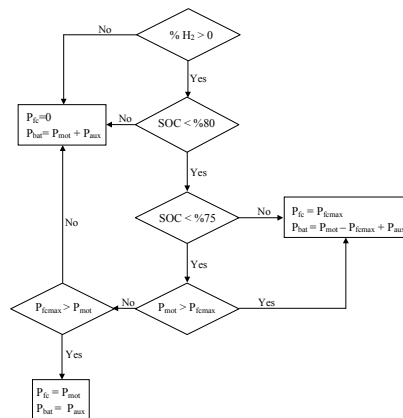


Figure 3. Flowchart of control strategy 1

Main difference with strategy 1 and strategy 2 is about SOC level as shown in figure 4. In strategy 2, fuel cell operating SOC level is %85 and if the state of charge is less than %85, it will be checked that SOC is more or less than %70. In addition, if SOC is less than %70, the fuel cell will work full of its capacity and the power requirement will be supplied by battery and fuel cell. Also if it is between 70 and 80 percent and $SOC_n < SOC_{n+1}$ which means that the battery is charging, the fuel cell will work full of its capacity (P_{fcmax}) until SOC equals %85. If $SOC_n > SOC_{n+1}$ which means that the battery is discharging, the fuel cell will not work.

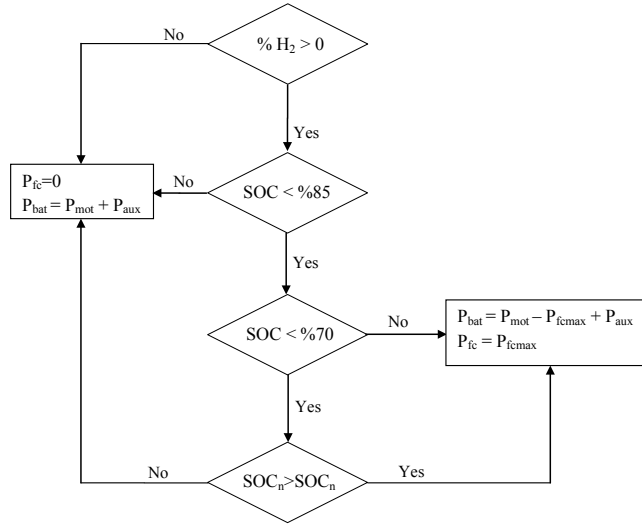


Figure 4. Flowchart of control strategy 2

3. ANALYSIS METHOD AND SIMULATION RESULTS

Electric motor has to produce required power in order to overcome resistance forces and losses of propulsion system for the continuity of motion of the vehicle. Resistance forces consist of rolling resistance force (F_R) and air resistance forces (F_L) in no grade road conditions. Additionally, with vehicle move up grade, grading resistance (F_{ST}) and under acceleration conditions, acceleration force (F_B) occurs. Those resistance forces can be expressed as:

$$F_R = f_R \cdot G \quad (1)$$

$$F_L = \frac{1}{2} \cdot \rho_L \cdot A \cdot C_W \cdot V^2 \quad (2)$$

$$F_{ST} = G \cdot \sin \alpha \quad (3)$$

$$F_B = \lambda \cdot m \cdot a^+ \quad (4)$$

Coefficient of formulations and parameters of vehicle design is shown in table 1. Resistive forces on vehicle tires determine the power requirement of vehicle. Vehicle speed change with driving cycle thus required power on electric motor is calculated by the function of mechanical and electric motor efficiency.

Table 1. Vehicle design parameters

Parameters	Value	Unit
Rolling Resistance Coefficient (f_R)	0,009	-
Vehicle Frontal Area (A)	2	m ²
Acceleration of Gravity (g)	9,81	m/s ²
Vehicle Mass (m)	500	kg
Aerodynamic Drag Coefficient (C_W)	0,33	-
Tire Dynamic Radius (r_{dyn})	0,3	m
Air Density (ρ_L)	1,2	kg/m ³
Inertial Factor (λ)	1,05	-
Mechanical Efficiency (η_M)	0,85	-
Auxiliary Power (P_{aux})	100	W
Gear Ratio	6	-
Battery Efficiency (η_B)	0.85	-

Efficiency of a traction motor varies with its operating points the speed and torque. Changing of efficiency with driving cycle speed as regarding constant gear ratio is shown in figure 5.

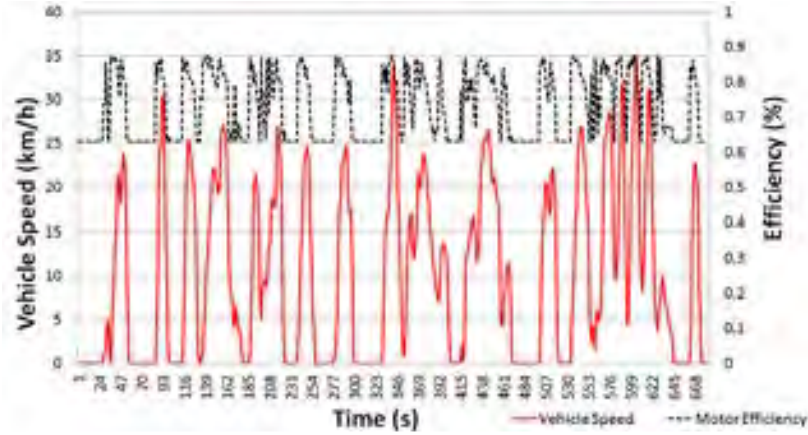


Figure 5. Efficiency of electric motor during drive cycle time operation

During the drive cycle, power requirement on electric motor is function of rolling, air and accelerating resistance forces. Road slope is neglected in calculation and grading resistance is not considered. During braking, regenerative energy is stored by the function of negative acceleration (a^-), mechanical and electric motor efficiency and gear ratio (i_F) between electric motor and tire. Constant gear & differential system has 6 ratio that is for speed and torque converting. Power requirement with recuperation (P_{mot}) and battery power (P_{bat}) on battery alone mode, during the cycle time is:

$$P_{mot} = \frac{(F_R + F_{ST} + F_B + \lambda \cdot m \cdot a^- \cdot \eta_M^2 \cdot \eta_{EM}^2 \cdot i_F) \cdot V}{1000 \cdot \eta_M \cdot \eta_{EM}} \quad (5)$$

$$P_{bat} = \frac{P_{mot}}{\eta_{bat}} + \frac{P_{aux}}{1000 \cdot \eta_{bat}} \quad (6)$$

According to formulation of required motor power and control strategies, battery and fuel cell power output are shown in figure 6. Drive cycle is created by repeatedly 11 INRETS urbainfluide 1 cycle that has 7480 seconds, because of observing methanol fuel depletion. As mentioned before, in strategy 1, fuel cell does not operating until SOC level is arriving %80 after 1233 seconds from starting simulation and total operating time of fuel cell in strategy 1 is 5503 seconds. In strategy 2, fuel cell operates just 1701 seconds on its full power capacity. Fuel cell operates constantly in strategy 2 that independent from electric motor power requirement. On the other hand, strategy 1 controls the SOC level and it depends on power requirements which is purpose to maintain %75 SOC until there is no methanol in fuel tank. Battery could charge when braking or amount of fuel cell power is maximum that is under motor power requirement.

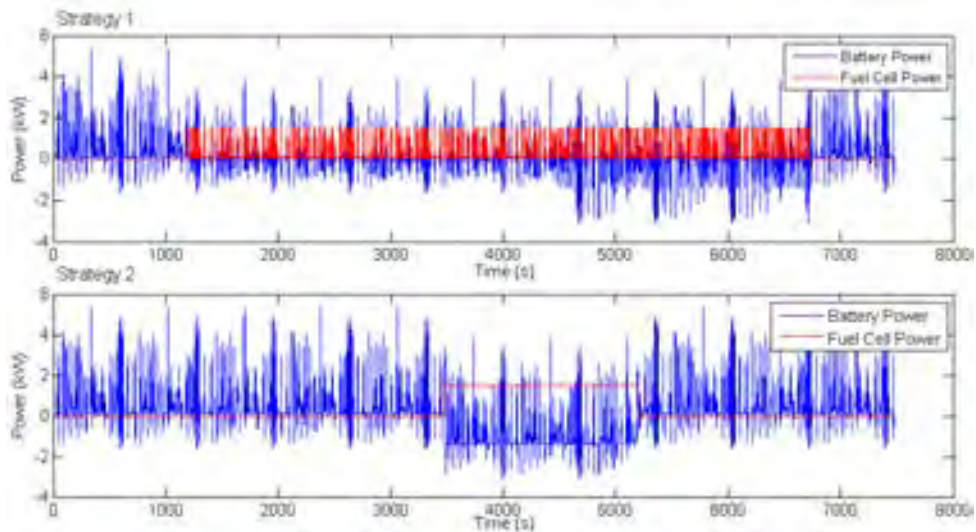


Figure 6. Battery and fuel cell power output in each control strategies

Fuel cell power (P_{FC}) demand shown in figure 6 and methanol consumption (B_{met}) is determined by control strategies. Strategy 1 includes longer time for fuel cell operating than strategy 2 that gives peak power in runtime and hence methanol consumption decreases rapidly. Methanol consumption that can be obtained for both strategies by function of fuel cell power is defined:

$$B_{met} = \frac{1000}{LHV_m \cdot \eta} \cdot \int_0^t P_{FC} \cdot dt \quad (7)$$

Methanol consumption is shown in figure 7 according to equation (7) for 11 drive cycle such as figure 6. Consumption of methanol in strategy 1 is depended for power demand of road surface unlike strategy 2. Fuel cell operates its maximum capacity in strategy 1 which is clearly shown rapidly reducing consumption line in strategy 2. In the case that vehicle has much methanol fuel capacity, consumption will be started when SOC level reach %70 according to control strategy 2 on continuation of test cycle. Consumption in strategy 1 decreases with same characteristic at same condition.

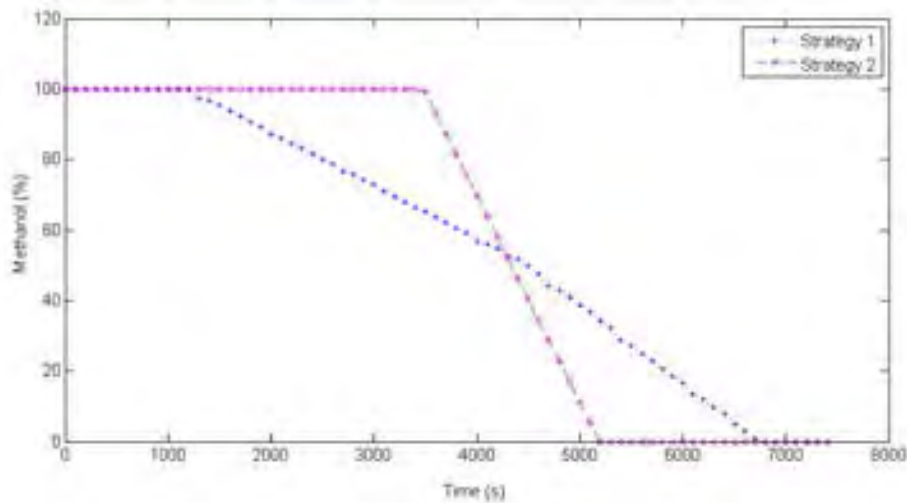


Figure 7. Methanol consumptions fuel cell in each control strategies

For a single driving cycle, energy taken from battery in electric mode (Q_{elc}) can be defined as several methods such as area under the power requirement of battery (P_{bat}) or SOC decreasing (ΔSOC) per cent of battery capacity (Q_{Bat}) in unit kW/h (8).

$$Q_{Elc} = Q_{Bat} \cdot \Delta SOC = \frac{1}{3600} \int_0^t P_{bat}(t) \cdot (dt) \quad (8)$$

Battery power requirement in electric mode at one driving cycle and SOC variation until cycle end are shown in figure 8. Initial SOC is % 85 at beginning of cycle simulation and it falls % 82.15 at cycle's end. Energy requirement at one driving cycle in electric mode which is between SOC differences (ΔSOC) 0.082 kWh.

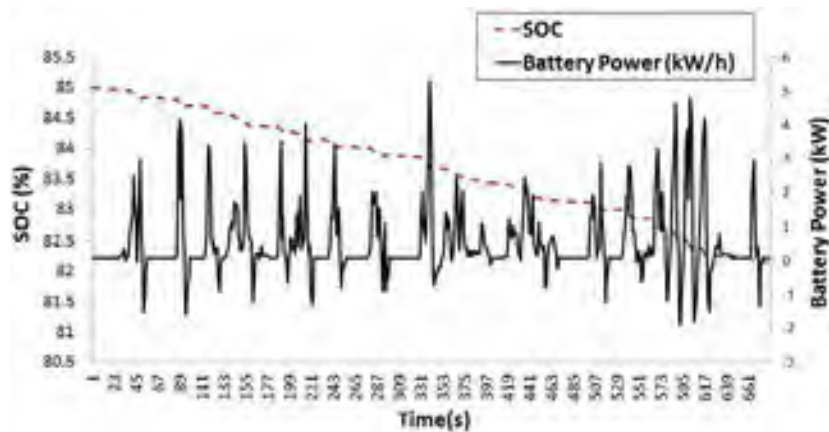


Figure 8. Battery power and SOC in driving cycle at electric only mode

Energy requirement is calculated and shown in figure 8 for electric mode. Fuel cell and battery power for strategy 1 and 2 consist of 11 driving cycle. Except related driving cycles, vehicle operates only electric mode which calculated in above (8).

The state of charge (SOC) is the amount of capacity that is left after starting to discharge from a fully charged condition. With an accurate measure of SOC, cell damage can be avoided by controlling the current. There is not any sensor available to measure SOC directly and thus it must be estimated. In mathematical form, the instantaneous SOC which Q_{Bat} is the capacity of battery and P_{bat} is the instantaneous power on battery can be expressed as:

$$SOC = \int_0^t \frac{Q_{Bat} \cdot \frac{SOC(t) - P_{bat}(t)}{SOC_{int}} - P_{bat}(t)}{Q_{Bat} \cdot \frac{SOC(t)}{SOC_{int}}} \cdot SOC(t) \cdot 100 \cdot dt \quad (9)$$

The other important parameter, battery SOC can be estimated after the output power of the battery has been determined for all strategies and battery alone mode for comparison in figure 7. Electric mode is for just comparison that is not including any fuel cell operation region. SOC level is permanently decreasing till cycle end although increasing by recuperation. Two main control strategies are changing with fuel cell operation. SOC of strategy 2 is swiftly increasing and decreasing between its upper and lower level until fuel is depleted.

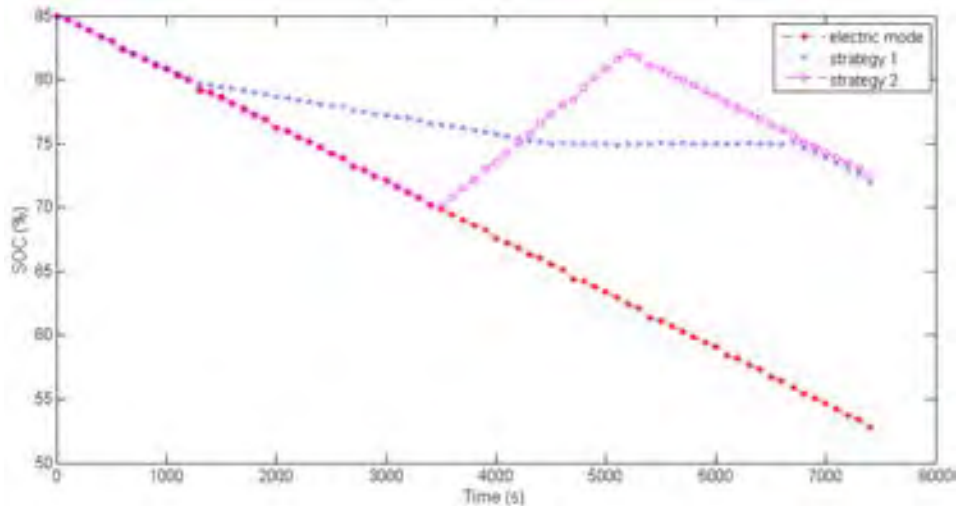


Figure 9. Estimated SOC variations for each strategies and electric only mode

SOC value operates its working range that is limited between upper and lower limits. Battery damages may occur while deep discharging and regenerative braking energy reduces during over charging in upper limits of SOC. Lower limit of SOC is %10 to prevent shorten battery life and upper limit of SOC is %90 to store regenerative energy while battery charge level is high. Battery SOC level decreasing starts its initial level (SOC_{int}) % 85 in both strategies during test cycle. It arrives %71.65 for first strategy and % 72.12 for second strategy is representing $\Delta SOC_{1,2}$. Vehicle range (S_v) is sum of hybrid mode in 11 drive cycle and electric only mode ranges. As considering one cycle length (S_{cycle}) is 1890.17, vehicle range can be described by:

$$S_v = \frac{Q_{Bat} \cdot (80 - \Delta SOC_{1,2})}{100 \cdot Q_{Elc}} \cdot S_{cycle} + 11 \cdot S_{cycle} \quad (10)$$

4. CONCLUSIONS

Vehicle range is calculated both two strategies according to (9). Strategy 1 provides 65.35 km vehicle range is more efficient than strategy 2 which has 65.03 km range. Vehicle range in only electric mode is lower than hybrid modes which ignoring fuel cell system. Electric vehicle provides just 54.43 km. Fuel cell system increase range with additional costs and mass. For energy consumption, 20 liter methanol fuel at 1 molar or approximately 2 liter pure methanol provides about 10 km.

Fuel cell using as range extender with different principle control strategies causes extra costs eventually. Beyond these control strategies effect directly energy consumption and vehicle range. Fuel cell operates in wide area between minimum and maximum power outputs in strategy 1. It increases fuel cell and battery

efficiency which is proper for urban traffic. Second strategy is proper for long range usage which fuel cell operates in its maximum. This choice allows constant operation of fuel cell with constant fuel flow rate. It makes easier of the flow control. Advantage of higher efficiency at first strategy achieve about 300 m extra ranges. But it has to be tested on vehicle before final decision about advantages and disadvantages.

Application of fuel cell as a range extender in electric vehicle enhances driving for daily usage. Hybridization contributes to becoming prevalent of electric vehicle with range extender because of eliminating range concern that is the main disadvantage of battery electric vehicle. Researches and applications about hybrid vehicle technology lead to increase preferability in the public eye whereby economic and environmental progress.

ACKNOWLEDGEMENTS

We are grateful for the support of **International Conference on Engineering and Natural Science** for helping make this conference possible.

REFERENCES

- [1]. Guzzella, L., Sciarretta, A. 2005. *Vehicle Propulsion Systems* (3. edition). Springer, New York.
 - [2]. Karaođlan, M.U. 2014. *Elektrik tahrikli bir binek otomobilin tahrik sisteminin matematiksel modellenmesi ve simülasyonu*. Master of Science. Dokuz Eylul Üniversitesi, İzmir.
 - [3]. Kuralay, N.S. 2008. *Motorlu taşıtlar temel ve tasarım esasları, yapı elemanları*, Cilt:1, (1). İzmir: Makina Mühendisleri Odası.
 - [4]. Kuralay, N.S. 2013. *Motorlu taşıtlarda hibrit tahrik temeli ve tasarım esasları, yapı elemanları, çözümlü tasarım problemleri* (1). İzmir: Makine Mühendisleri Odası.
 - [5]. Larminie, J., Dicks, A. 2003. *Fuel Cell Systems Explained (Second Edition)*. Wiley Press, UK.
 - [6]. Larminie, J., Lowry, J. 2003. *Electric Vehicle Technology Explained* (2. edition). Wiley Press, UK.
 - [7]. Tolj, I., Lototsky, M. V., Davids, M. W., Pasupathi, S., Swart, G., Pollet, B. G. 2013. "Fuel cell-battery hybrid powered light electric vehicle (golf cart): Influence of fuel cell on the driving performance", *International Journal of Hydrogen Energy*, 38, 10630-10639.
 - [8]. Ehsani E., Gao, Y., Emadi, A. 2010. *Modern Electric, Hybrid Electric, and Fuel Cell Vehicles Fundamentals, Theory, and Design*. CRC Press, USA.
 - [9]. Odeim, F., Roes, J., Wülbeck, L., Heinzl, A. 2014. "Power management optimization of fuel cell/battery hybrid vehicles with experimental validation", *Journal of Power Sources*, 252, 333-343.
 - [10]. Zheng, C. H., Kim, N. W., Cha, S. W. 2012. "Optimal control in the power management of fuel cell hybrid vehicles", *International Journal of Hydrogen Energy*, 37, 655-663.
 - [11]. Sohn, Y. J., Kim, M., Lee, W. Y. 2012. "The computer-aided analysis for the driving stability of a plug-in fuel cell vehicle using a proton exchange membrane fuel cell", *International Journal of Hydrogen Energy*, 37, 1893-1904.
 - [12]. Feroldi, D., Serra, M., Riera, J. 2009. "Energy management strategies based on efficiency map for fuel cell hybrid vehicles", *Journal of Power Sources*, 190, 387-401.
 - [13]. Thounthong, P., Rael, S., Davat, B., Sadli, I. 2006. "A control strategy of fuel cell/battery hybrid power source for electric vehicle applications", *Power Electronics Specialists Conference*.
 - [14]. Mi, C., Masrur, M. A., Gao, D. W. 2011. *Hybrid Electric Vehicles Principles and Applications with Practical Perspectives*. Wiley Press, UK.
 - [15]. Mashadi, B., Crolla, D. 2012. *Vehicle Powertrain Systems*. Wiley Press, UK.
 - [16]. Jiang, Z., Gao, L., Blackwelder, M. J., Dougal, R. A. 2004. "Design and experimental tests of control strategies for active hybrid fuel cell/battery power sources", *Journal of Power Sources*.
 - [17]. Hwang, J. J., Chang, W. R. 2012. "Characteristic study on fuel cell/battery hybrid power system on a light electric vehicle", *Journal of Power Sources*, 207, 11-119.
 - [18]. Hodkinson, R., Fenton, J. 2001. *Lightweight Electric/Hybrid Vehicle Design*. Butterworth-Heinemann, Oxford.
-

THEORETICAL APPROACH FOR MODELING AND SIMULATION OF ELECTRICAL PASSENGER CAR POWER TRAIN SYSTEM

Mustafa Umut KARAOĞLAN

Dokuz Eylül University, Department of Computer Engineering, İzmir,
feristah@cs.deu.edu.tr

Nusret Sefa KURALAY

Muğla Sıtkı Koçman University, Department of Computer Engineering, Muğla,
enis.karaarslan@mu.edu.tr

Abstract

Growing number of vehicles causes increase in fuel consumption and exhaust gases discharge into atmosphere. Alternative vehicle options such as electric vehicle or powertrain systems like hybrid propulsion can overcome these disadvantages. Therefore, hybrid electric and battery electric vehicles which include electric propulsion systems are located in the focus of researches. In this study, mathematical model of electric vehicle powertrain system was created. Power and torque requirement of electric motor and gearbox are calculated based on optimum performance characteristics. Systems simulation results such as electric driveline system power outputs and battery state of charge changes are investigated for drive cycles considering with electric motor efficiency and battery resistance. Vehicle range is calculated and parameters that effect range were investigated. Theoretically calculated state of charge and battery current results compared with the results of ADVISOR program, which commonly used for hybrid and electric vehicle analysis in literature.

Keywords: *Electric vehicle, drive cycle simulation, automotive, advisor*

1. INTRODUCTION

Electric vehicles have a very long history but, until the oil crisis they cannot gain any market share. After the 1970's with financial issue and increasing worries about air pollution, the electric vehicles gained interest again. Electric motors are used as driving machine for vehicle propulsion in electric vehicles and all energy to propel the vehicle is carried in batteries. So electric motor is powered by energy storage system that existing on the vehicle. These systems consist of batteries or super capacitors. With those components, storage of regenerative energy is the main characteristic behavior of electric vehicle. Also no pollutant emissions do not occur because of there is no fuel combustion in electric vehicle systems. In the case of environmental awareness and various environmental protocols gradually getting serious, the importance of these advantages can easily seen in electric vehicles. However, electric vehicles still have critical disadvantages which need to be solved. Main challenges are short driving range, long charging time and high cost of vehicle [21].

Permanent magnet synchronous motor with constant ratio reduction - differential at the end of motor are used main propulsion component in examined concept front wheel drive electric vehicle. Torque and speed of the motor are controlled by the inverter which inverts the battery DC voltage to a three phase AC voltage for electric motor. After electric motor, torque in the differential reaches front wheels via homokinetic joints.

2. MATHEMATIC MODELS AND DESIGN PARAMETERS

In order to be able to estimate the energy consumption and driving range according to driving cycle of electric vehicles, it is necessary to have a proper model of vehicle [21]. Creating a longitudinal vehicle model is suitable to calculate drive train behaviors and capacity of components. Longitudinal vehicle model is about specifying the vehicle velocity profile with driving cycle and calculating vehicle loads from wheels to energy storage system corresponding to velocity profile with reflux method.

During the movement of a vehicle, driving resistance forces occurs that requires overcoming by motor traction power. Sum of resistance forces determines the required force that transmitted from electric motor to driven wheels for the forward movement of vehicle. Maximum velocity, maximum grading and acceleration ability can determine with calculated total traction forces according to resistance forces.

Electric motor has to produce required power in order to overcome resistance forces and losses of propulsion system for the continuity of motion of the vehicle. Resistance forces consist of rolling resistance force (F_R) and air resistance forces (F_L) in no grade road conditions. Additionally, with vehicle move up grade, grading resistance (F_{ST}) and under acceleration conditions, acceleration force (F_B) occurs. Those resistance forces are:

$$F_R = f_R \cdot G \quad (1)$$

$$F_L = \frac{1}{2} \cdot \rho_L \cdot A \cdot C_W \cdot V^2 \quad (2)$$

$$F_{ST} = G \cdot \sin \alpha \quad (3)$$

$$F_B = \lambda \cdot m \cdot a^+ \quad (4)$$

Choosing electric motor's capacity in designed vehicle is determined by maximum velocity and maximum grade of vehicle. Because of this, total resistance forces that transmitted vehicle's wheel with no acceleration motion must be calculate.

As a vehicle's characteristic, %25 grade ability and maximum 160 km/h velocity are determined for this concept electric car that suitable for urban drive. In order to achieve maximum velocity value, required power (P) is shown (eqn.5) with constant mechanical and electric motor efficiency:

$$P = \frac{(m \cdot g \cdot f_R + \frac{1}{2} \cdot \rho_L \cdot A \cdot C_W \cdot V^2) \cdot V}{1000 \cdot \eta_M \cdot \eta_{EM}} \quad (5)$$

With this equation, maximum electric motor power for maximum vehicle velocity is calculated as 55 kW and chose electric motor with 55 kW power (P_M) and 160 Nm torque (M_M). Maximum electric motor torque and total drive ratio (i) from motor to wheels are important factor to calculate grading ratio of vehicle. For %25 grading ratio, reduction gear-differential ratio has to find. As grading slope angle α , electric motor maximum torque M_M , reduction gear-differential ratio i:

$$i = (f_R \cdot m \cdot g \cdot \cos \alpha + m \cdot g \cdot \sin \alpha) \cdot \frac{r_{dyn}}{M_M \cdot \eta_M \cdot \eta_{EM}} \quad (6)$$

According to coefficients and parameters of vehicle (table 1), reduction gear-differential ratio from motor to wheels are 6 (eqn.6).

Table 1. Vehicle Design Parameters

Parameters	Value	Unit
Rolling Resistance Coefficient (f_R)	0,009	-
Vehicle Frontal Area (A)	2	m ²
Acceleration of Gravity (g)	9,81	m/s ²
Vehicle Mass (m)	1000	kg
Aerodynamic Drag Coefficient (C_W)	0,33	-
Tire Dynamic Radius (r_{dyn})	0,282	m
Air Density (ρ_L)	1,2	kg/m ³
Inertial Factor (λ)	1,3	-
Mechanical Efficiency (η_M)	0,85	-
Electric Motor Efficiency (η_{EM})	0,9	-

There is no need to use manual transmissions with many different gear ratios in electric vehicles because of the electric motor torque-speed characteristic. Constant gear ratio reduction gears with differential designed to increase motor torque and decrease motor speed (Fig. 1.) Two stages helical gears are used in reduction gears for their basic advantages such as silent and more efficient works. Number of teeth in first gear is 20, second gear is 41, third gear is 20 and forth gear is 59 with 20° pressure angle and 20° helix angle at reduction gears. Differential side and spider gears have 18 teeth in differential unit after constant gear ratio reduction gears. Gearbox is installed to electric motor output shaft at front axle.

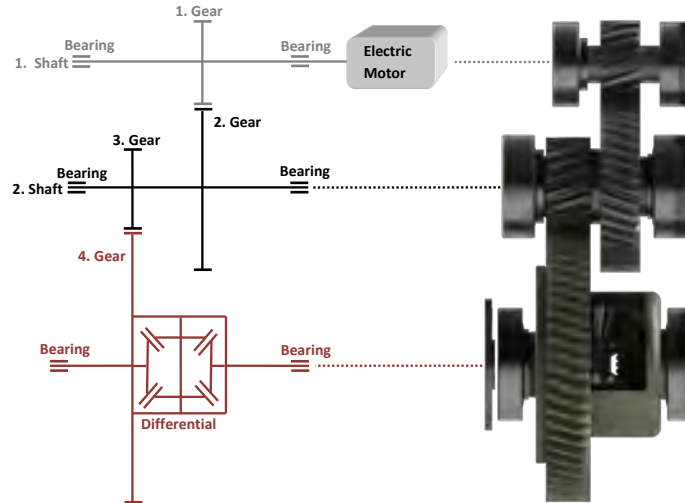


Figure 1. Reduction Gears & Differential Design Scheme

As gear materials hardened cementation steel 20MnCr5 used in reduction gear-differential assembly (Fig. 1). Outer protective cover part is designed in two parts that coupled with bolts. O-rings take places between cover and shaft bearing, one 50x40x8 and two 50x35x8 radial sealing ring also used electric motor input bearing and differential output shaft's bearing.

Maximum vehicle velocity and grading ability can calculate by transporting total resistance moments corresponding total resistance forces as rolling, air and grading forces to maximum electric motor torque curve. These curves' intersection point is the maximum velocity of the vehicle for no grading resistance and the point for maximum motor torque is the grading ability of the vehicle. For these three forces, moment of motor shaft (M_R):

$$M_R = \frac{(F_R + F_L + F_{ST}) \cdot r_{dyn}}{\eta_M \cdot \eta_{EM} \cdot i} \quad (7)$$

One of the most critical design parameters is maximum range of electric vehicle. As considered that urban usage is more proper for electric vehicle, 120 km range is desired and chose 18 kWh capacity lithium ion battery. Two parallel connected 1.2 kWh lead acid battery takes place in storage system additional to lithium ion battery. Because of that, total lithium ion battery capacity takes 17 kWh.

As lithium ion battery, most suitable battery of hybrid and electric vehicle applications is lithium ion phosphate (LiFePO₄) that uses phosphate as cathode material for rechargeable lithium batteries. This type of batteries offers good electrochemical performance with low resistance. The key benefits are enhanced safety, good thermal stability, tolerant to abuse, high current rating and long cycle life. With 20 A h cell capacity LiFePO₄ (LFP) battery cell has 140 Wh/kg specific energy and 840 W/kg specific power. A single cell weight is 455 gram and cell voltage is 3,2 V. For 17 kWh total lithium battery capacity, 24 battery module with 11 cell in each module is used so total battery weight is almost 120 kg for the electric vehicle. Modules connected in serial with each other to create operating voltage for electric motor. This application includes 2 battery package each has 12 serially connected modules that produces 422 V each packages.

Battery location is very important issue in electric vehicle. Common application at battery location is using vehicle floor for battery packages. As increasing of battery capacity, its volume has to increase and more space requirements for battery will occur. This reason fact on the luggage space and it becomes disadvantages in urban driving for customers. Vehicle floor is most proper area in hybrid and electric vehicle for not only luggage volume but also improves vehicle roll dynamics which causes center of gravity of vehicle becomes lower.

The height of battery module is 207 mm but there is 170 mm height in vehicle floor (Fig 2). Battery module must locate horizontal position thus its height just is 166 mm while there is no problem locating floor and operating. 24 modules horizontally located which 4 modules as transverse (4x265=1060 mm) and 6 modules as longitudinal (6x207=1242 mm). Totally, battery packages fit on floor with rectangle placement.

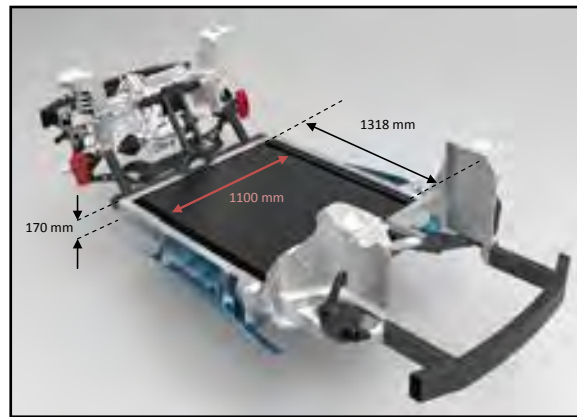


Figure 2. Battery Location at vehicle floor

Since the battery is a nonlinear system, the models usually used in electric vehicles can simplify electrochemical model was proposed based on electrochemical theory and could fully describe the characteristics of power battery by using mathematics to describe the inner action of the battery [9]. Power management and estimating state of charge (SOC) in battery systems which is established by mathematics model are as vital as production of battery. Battery management systems fulfill SOC estimation during operating which include operation changes such as current, SOC and battery resistance according the battery model. SOC is function of battery current that occurs for vehicle resistance forces. State of charge measurement is not possible directly so, it must determine while establishing model to calculate battery characteristics and SOC. Several battery models are developed for that nowadays.

This study uses Rint battery model to estimate SOC which v is open circuit voltage as ideal voltage source and R is internal resistance of battery. Both parameters are function of temperature and SOC. For instance battery internal resistance is higher in low temperatures. Loading current “ i ” is positive in discharge and negative in charge conditions.

Charging and discharging current depends on operating time such as braking and accelerating conditions on drive cycle. For both condition charge and discharge currents are expressed as:

$$i_{charge} = \frac{-v + \sqrt{v^2 + 4 \cdot R \cdot P(t)_{charge}}}{2 \cdot R} \quad (8)$$

$$i_{discharge} = \frac{v - \sqrt{v^2 - 4 \cdot R \cdot P(t)_{discharge}}}{2 \cdot R} \quad (9)$$

3. ANALYSIS OF MODEL FOR DRIVE CYCLES

The driving pattern in a given specific region can be represented as a driving cycle, which is basically a vehicle speed-time profile. Vehicles move irregular and unpredictable drive conditions in their operating times. Legislative and non-legislative drive cycles created for conventional vehicles and electric vehicles to measure their fuel and exhaust emission or energy consumption and power requirement of electric vehicles along the variable drive routes in cycle times.

Typical examples of legislative driving cycles are; FTP-72 (Federal Test Procedure) cycle used in the USA, NEDC (New European Driving Cycle) used in Europe (Fig 3). These driving cycles are used for emission certification and are imposed by the governments. On the other hand, non-legislative driving cycles such as Istanbul Drive Cycle (IDC) are used for energy conservation and pollution evaluation research. Legislative cycles is referred as modal or polygonal cycles, which are developed theoretically combining different driving modes such as constant acceleration, constant deceleration and constant speed. Non-legislative cycles are called real-world driving cycles which are developed by using "real-world" actual driving data [4].

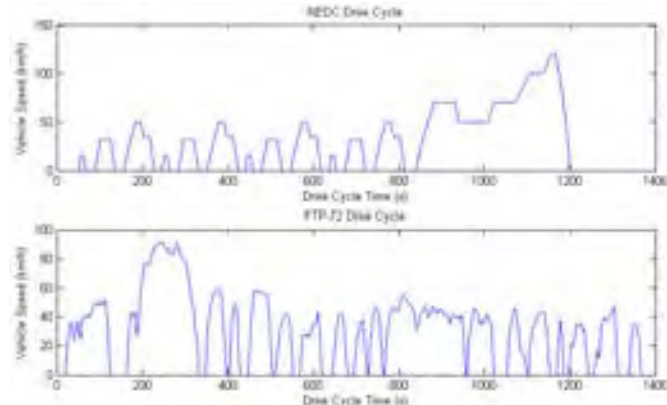


Figure 3. Vehicle Speed at NEDC and FTP-72 Drive Cycles

Various operating conditions of vehicle demand different operating points in maximum motor torque area for different vehicle speeds. According to motor torque and speed, permanent magnet synchronous motor efficiency considered in drive cycle analysis.

Wheelbase of concept electric vehicle (L) 2.511m and height of center of gravity (h) 0.57 m. Longitudinal location of center of gravity assumed in the middle of wheelbase ($L_F/L=\Psi=G_R/G=0.5$) as L_O is the distance between front axle and center of gravity and G is the total vehicle weight. Because of the vehicle is front wheel drive, regenerative energy from braking (recuperation) can store via front axle to battery. Calculation of front axle braking ratio ($i_F=B_R/B_T$) is necessary to consider for true results of SOC and battery current. While braking starts, static axle loads change and dynamic axle loads (G_F^* , G_R^*) have to be considered. As braking forces in front and rear axle are B_F and B_R with tire road friction coefficient of axles in braking are f_F and f_R , braking acceleration ratio z means a^-/g . In ideal braking z is equal to μ that is tire road friction coefficient. Abbreviation of X is the ratio of vehicle center of gravity height and wheelbase distance. If in ideal braking $\mu=f_F=f_R=z$:

$$\frac{B_T}{G} = \sqrt{\left(\frac{1-\Psi}{2 \cdot X}\right)^2 + \frac{1}{X} \cdot \frac{B_F}{G}} - \left(\frac{1-\Psi}{2 \cdot X}\right) \quad (10)$$

Total braking force (B_T) depends on negative acceleration (a^-) value in driving cycle that analyzed. During the cycle time total brake force is:

$$B_T = m \cdot a^- \quad (11)$$

Braking ratio ($i_F=B_F/B_T$) can be found by equations 13. Braking ratio changes permanent in braking time according to drive cycle.

During the NEDC drive cycle that recognized road slope, power requirement on electric motor is function of rolling, air and accelerating resistance forces. Power requirement without recuperation (P_M) during the cycle time with vehicle parameters in Table 1 is:

$$P_M = \frac{(m \cdot g \cdot f_R + \frac{1}{2} \cdot \rho_L \cdot A \cdot C_W \cdot V^2 + \lambda \cdot m \cdot a^+) \cdot V}{1000 \cdot \eta_M \cdot \eta_{EM}} \quad (12)$$

In case of including recuperation, power requirement can express as:

$$P_M = \frac{(F_R + F_{ST} + \lambda \cdot m \cdot a^+ + \lambda \cdot m \cdot a^- \cdot \eta_M \cdot \eta_{EM} \cdot i_F) \cdot V}{1000 \cdot \eta_M \cdot \eta_{EM}} \quad (13)$$

The main purpose of the battery is to provide power for the wheels. However, a modern car has also other loads which the battery should supply. These loads are either due to safety such as light, wipers, horn, etc. and/or comfort like radio, heating, air conditioning, etc. These loads are not constant. Total average power consumption of accessories (P_{acc}) could take 800 W that provided from battery. Battery power requirement (P_B) at drive cycle is as [kW]:

$$P_B = \frac{P_M}{\eta_B} + \frac{P_{i_c}}{1000 \cdot \eta_B} \quad (14)$$

Initial value of state of charge (SOC_{int}) is assumed %80 in the beginning of analysis for total battery capacity (Q_{Bat}) that is 17 kWh. SOC is the function of battery power and it depends on drive cycle characteristics. Battery energy is the sum of power requirements of battery for cycle time from beginning of cycle to end of cycle (t). Percentage of SOC for driving cycle is:

$$SOC = \int_0^t \frac{Q_{Bat} \cdot \frac{SOC(t) - P_B(t)}{SOC_{int} \cdot 3600}}{Q_{Bat} \cdot \frac{SOC(t)}{SOC_{int}}} \cdot SOC(t) \cdot 100 \cdot dt \quad (15)$$

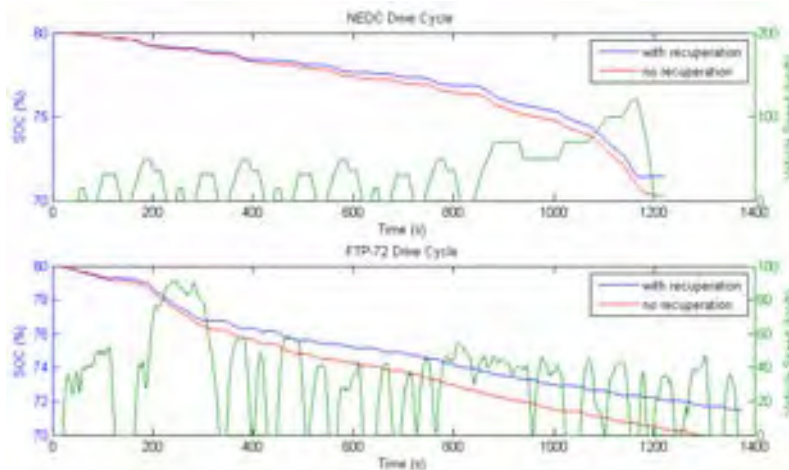


Figure 4. SOC Changes in Drive Cycles with Recuperation Situation

Battery power can calculate for both recuperation and non recuperation operation. Equation 12 and 13 includes motor power that can be expressed as recuperated or not recuperated. For both conditions, SOC can be calculated. As the main advantages of electric vehicles, vehicle range and total efficiency increase thanks to energy storage with recuperation. Change of SOC with drive cycle is shown in figure 4 for both recuperation conditions.

Battery produces current for power requirements during the drive cycle. Discharge current is positive and charge current is negative in braking. Battery cell voltage (v), battery temperature and internal resistance (R) of battery cell effect battery current. Assuming that battery operates in 25 °C constant temperature, open circuit voltage of battery increase with SOC. Internal resistance of battery cell is constant after %40 SOC in both charge and discharge. Low SOC values cause increase of internal resistances. Minimum SOC value is determined for resistance characteristic of battery at low SOC in automotive applications. Maximum value of SOC is determined to life cycle of battery. Electric vehicles use %10-20 for minimum SOC and %80-90 for maximum SOC. Operating range of SOC is taken %10-90 in this study.

Battery currents are calculated according to equation 10 with considered internal resistance and cell voltage changes of battery for both cycles (Fig. 5).

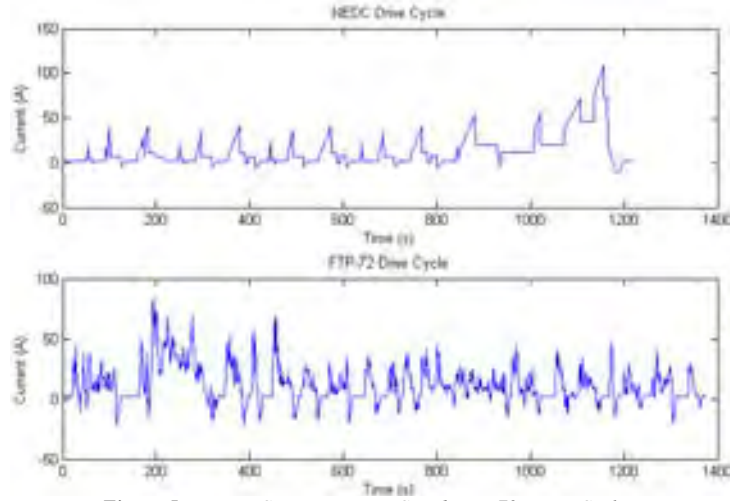


Figure 5. Battery Current in NEDC and FTP-72 Drive Cycles

Electric vehicle describes its energy consumption (kWh/100km) just as conventional vehicle's fuel consumption criteria. The area beneath battery power for traction in drive cycle is energy of battery. At the end of test cycle, total battery energy consumption (Q_{cycle}) is:

$$Q_{cycle} = \frac{\int_0^n P_B \cdot dt}{3600} \text{ [kWh]} \quad (16)$$

Range of electric vehicle depends on battery capacity and number of cycle is repeated by vehicle. Previously mentioned maximum limits (SOC_{max}) and minimum limits (SOC_{min}) of SOC is used for calculating number of cycle that electric vehicle is driven. Range of electric vehicles according to different drive cycles (S_{range}) is:

$$S_{range} = n_{cycle} \cdot \frac{S_{cycle}}{1000} \text{ [km]} \quad (17)$$

Driving range is related with energy storage system capacity and vehicle mass. Increasing of battery capacity causes more battery mass that is needed and extra cost arising from greater capacity.

4. VERIFICATION OF ANALYTIC MODEL WITH ADVISOR

To verify results that obtained from theoretical model, Advanced Vehicle Simulator (ADVISOR) had been used. ADVISOR was created in the MATLAB/Simulink environment.

MATLAB provides an easy-to-use matrix-based programming environment for performing calculations while Simulink can be used to represent complex systems graphically using block diagrams.

Theoretically obtained state of charge history and battery current results for NEDC and FTP-72 drive cycles compared with ADVISOR results shown in Figure 6. Realistic approach could be possible with true examination of SOC and battery current history in electric vehicles. Verification of results with ADVISOR shows that accurate SOC estimation can be done.

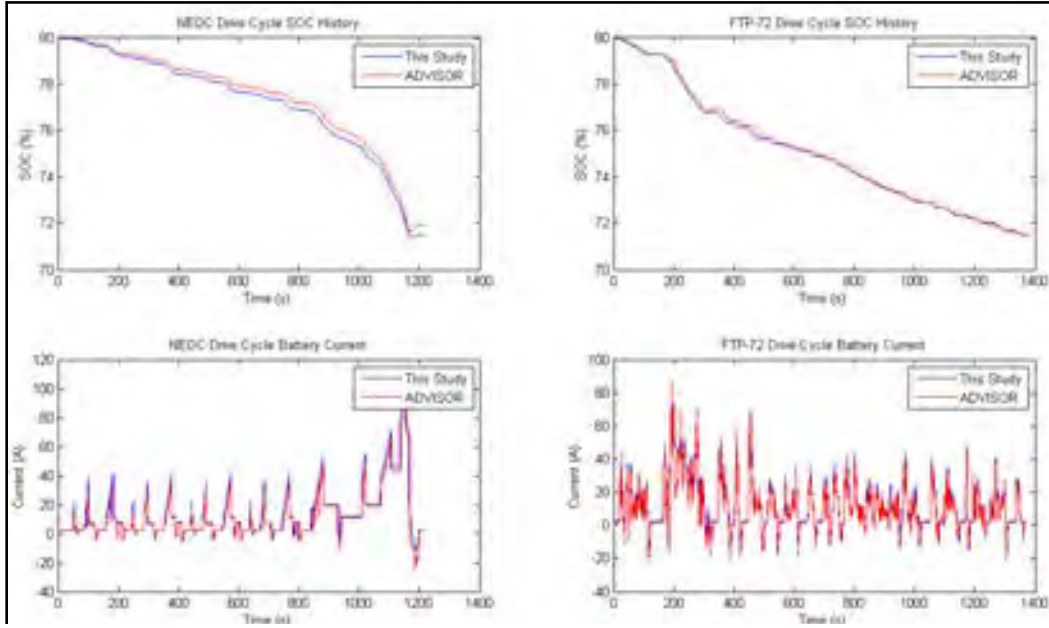


Figure 6. Comparison of SOC and Battery Current at NEDC vs FTP-72 Drive Cycles

5. CONCLUSION

Energy consumption and vehicle range can calculate for each drive cycles. According to equations (20) and (22), maximum energy consumption 15.77 kWh/100km occurs in NEDC. Naturally high energy consumption causes lower driving range as 107.8 km. Energy consumption of FTP-72 cycle is calculated 14.62 kWh/100km that enable for 116.3 km driving range at same cycles. Power output of component and energy consumption simulation is crucial for determining battery capacity and cost analysis. Beyond the legislative drive cycles, Istanbul Drive Cycle (IDC) gives more reliable results to urban usage in Turkey conditions.

The entire analysis model for the powertrain of EVs has been developed, based on mathematical approaches, to describe vehicle and battery parameters like SOC and battery current in consideration of both mechanical and electrical sub-systems. The theoretical analysis models have been validated, by comparison with the simulation model developed with the Matlab/Simulink platform, by testing with the NEDC and FTP-72 drive cycles. Based on theoretical analysis of the EV powertrain, various influences on the vehicle have been investigated and analyzed with respect to the mechanical and electrical quantities.

ACKNOWLEDGEMENTS

We are grateful for the support of **International Conference on Engineering and Natural Science** for helping make this conference possible.

REFERENCES

- [1]. Akyazi, Ö., Küçükali, M. ve Akpınar A. S. (2011). *Sürekli miktatsız senkron motorun hız denetiminin farklı bulanık üyelik fonksiyonları kullanılarak gerçekleştirilmesi*. Elektrik-Elektronik ve Bilgisayar Sempozyumu. 311-315.
- [2]. Amaç, A., Şahin, Y. ve Aras, F. (2008). *ADVISOR ile otomotiv elektrik sistemlerinin benzetimi ve analizi*. Elektrik-Elektronik-Bilgisayar Mühendisliği Sempozyumu ve Fuarı.
- [3]. Boyalı, A. (2008). *Hibrit elektrikli yol taşıtlarının modellenmesi ve kontrolü*. RhD Thesis: Istanbul Technical University, İstanbul.
- [4]. Dinç, C., Soruşbay, C., Ergeneman, M. ve Göktaş, A.G. (2012). *Development of a driving cycle for the estimation of vehicle emissions*. 6. Otomotiv Teknolojileri Kongresi.
- [5]. Dorrell, D., Popescu M., Staton D.A., Knight A.M. ve Evans L. (2010). *Comparison of different motor design drives for hybrid electric vehicles*. Energy Conversion Congress and Exposition.
- [6]. Ehsani, M., Gao, Y. ve Emadi, A. (2010). *Modern electric, hybrid electric and fuel cell vehicles fundamentals, theory, and design (2)*. USA: CRC Press
- [7]. Ergeneman, M. (2013). Enerji ekonomisi ve çevre için seyir çevrimlerinin önemi. Otam Aylık Bülten, 45, 2-5.
- [8]. Erhan, K., Ayaz, M. ve Özdemir, E. (2013). *Elektrikli araç şarj istasyonlarının güç kalitesi üzerine etkileri*. Akıllı Şebekeler ve Türkiye Elektrik Şebekesinin Geleceği Sempozyumu.
- [9]. He, H., Xiong, R. ve Fan, J. (2011). *Evaluation of lithium-ion battery equivalent circuit models for state of charge estimation by an experimental approach*. Energies, 4, 582-598.
- [10]. Jiang, B. (2013). *From electrode materials to dynamic models of li-ion cells*. Lisans Tezi: The Ohio State University, USA.
- [11]. Johnson, V.H. (2002). *Battery performance models in ADVISOR*. Journal of Power Sources, 110, (321-329).

- [12]. Karaođlan, M.U. (2014). *Elektrik tahrikli bir binek otomobilin tahrik sisteminin matematiksel modellenmesi ve simülasyonu*. Master of Science Thesis: Dokuz Eylul University, İzmir.
 - [13]. Keskin, A. (2009). *Hibrit taşıt teknolojileri ve uygulamaları*. Mühendis ve Makina, 50, 12-20.
 - [14]. Kuralay, N.S. (2008). *Motorlu taşıtlar temel ve tasarım esasları, yapı elemanları*, Cilt:1, (1). İzmir: Makina Mühendisleri Odası.
 - [15]. Kuralay, N.S. (2013). *Motorlu taşıtlarda hibrit tahrik temeli ve tasarım esasları, yapı elemanları, çözümlü tasarım problemleri* (1). İzmir: Makina Mühendisleri Odası.
 - [16]. Maddala, R. (2003). *Modeling of hybrid electric vehicle batteries*. Yüksek Lisans Tezi: Texas Tech University, Texas.
 - [17]. Mi, C., Masrur, M.A. ve Gao, D.W. (2011). *Hybrid electric vehicles principles and applications with practical perspectives (1)*. UK: Wiley.
 - [18]. Odvarka, E., Mebarki, A., Gerada, D., Brown, N. ve Ondrusek, C. (2009). *Electric motor-generator for a hybrid electric vehicle*. Engineering Mechanics, 16, 131-139.
 - [19]. Polat, B.D. ve Keleş, Ö. (2012). Lityum iyon pil teknolojisi. Metalurji Mühendisleri Odası, 42-48.
 - [20]. Sauer, U.D. (2009). *Elektrische energiespeicher in hybrid und elektrofahrzeugen. Seminar für Kraftfahrzeug un Motorentechnik*, Berlin.
 - [21]. Sayın, A.A. ve Yüksel, İ. (2011). *Elektrikli renault fluence aracı, lityum-iyon bataryasının modellenmesi ve batarya yönetimi*. Mühendis ve Makina, 52, 75-82.
-

DEVELOPMENT SENSOR BASED SYSTEM SOFTWARE FOR THE CONTROL OF MOTOR AND AXIS MOTION ON THE CNC TURNING MACHINE

Metin ZEYVELI

Karabuk University, Faculty of Technology, Department of Mechatronic Engineering, 78050, Merkez/Karabuk, Turkey.
mzeyveli@karabuk.edu.tr

Kürşat Mustafa KARAOĞLAN

Karabuk University, Eskipazar Vocational School, 78400, Eskipazar/Karabuk, Turkey.
kkaraoglan@karabuk.edu.tr

Abstract

Computer Numerical Control (CNC) machines that forms the basis of modern production is a manufacturing technology open to development today. In this study, real-time control of the axis and spindle motor was done on a CNC turning machine, and software based sensor condition monitoring system was developed. Providing the progress of the piece and spindle rotational speed for a certain work piece according to the information in the database improves the performance and precision of the production. Also, it can minimize the operator-based errors. Concurrently monitoring the sensor values like real-time current, power, speed and temperature taken from the CNC on graphical user interface display such as temperature sensor data taken from CNC as well as operator-interacted control ability and recording all data related to the piece in a database improves the work quality.

Keywords: *cnc, condition monitoring, sensor control, user interface design, database.*

1. INTRODUCTION

Condition Monitoring Systems (CMS) have become essential components due to increased demand for low cost and improved production in manufacturing industry as well as its effective role in detecting potential failures. Using a developed instant monitoring system in production processes allows optimum usage of machinery elements and prevention of unwanted situations. It prevents damages with excessive costs and aids reliable and uninterrupted continuation of manufacturing. For this reason, CMS are important for maximizing the quality of material produced. CMS can also be used in Computer Numerical Control (CNC) turning machines which constitute the foundations of production can be defined as a technique which aims at real-time monitoring of the working characteristics of the machine and the prediction of possible errors, failures, maintenance needs and production [1]. Real-time monitoring systems designed with this technique are used in such processes as failure detection, signal processing and maintenance management etc. in a number of fields as real-time condition monitoring systems, energy, transportation, aviation etc. [2-6].

Condition monitoring systems support instant control of the system and ensure its traceability. Depending on the determined reaction periods, it obtains data and guarantees these processes without interruption. These systems can be used through specific and general software operated on the hardware depending on the requirements of control, automatic control and condition monitoring [7]. In high-speed machining (HSM) systems monitoring of the components which constitute the system plays a critical role. Design of this monitoring system is important for continuity of the system and its higher performance. Several studies have been conducted on defining in the shortest possible time the situations which can have a negative impact on manufacturing processes and increasing the efficiency of CNC supported turning machines. These studies can be found in the literature with the title "Tool Condition Monitoring (TCM)". In one of these studies the 4 main approaches for determining system tool abrasions were discussed. These approaches are cutting strengths, acoustic emission (AE), vibration and motor current. Camacho et al. worked on the traceability through spindle motor of current signals during Tool Condition Monitoring process [8]. In addition to the condition monitoring systems which actively use sensor systems in manufacturing industry, control applications can also be integrated according to platforms (web, portable). Thanks to the rapidly growing software technologies today, instant remote control and CMS have been designed using web-based technologies. Only a short time after the start of web technologies, since 1993, several methods have been proposed in order to create shared systems working through web. When it is evaluated from the point of existing systems, HTML, Java Applets, ActiveX, VRML technologies can be used in developing client interface. Lihui Wang et al. developed a web-based condition monitoring system coded with real-time java programming language for remote production.

In this study a signal collecting unit which made use of position data belonging to the axis as well as spindle motor and progress speed data and communication was established with clients through server [9]. In addition to this study, in our study all start and stop processes belonging to manufacturing can be operated on web and client computers so that the instant sensor data of the turning machine can be monitored. A multi-layered condition monitoring software with Object-Oriented Programming (OOP) architecture coded with C# language was developed. In addition, engine current and temperature signals have been added to the sensor collective system which operates instantly. Pan et al. studied on remote condition monitoring system which communicates through sensor data collection system using socket programming with C++ language [10]. Romero et al. examined current signals on milling machine and presented a system without sensors, and worked on detecting toolset abrasions using instant current signals [11]. Yahya Işık presented some approaches on on-line toolset condition methods on TCM methods [12].

In our study, control and execution of production processes is performed through software and micro-controller instruments. Data transfers between system condition monitoring, control software and micro-controller and application of synchronize and concurrent working principle during internal processes directly affects the reliability and performance of the system. Thanks to multi-threading property, concurrent operating procedures and double-sided instant working monitoring and control software was developed. With OOP and n-Tier features simplicity, reliability, performance and improvability was targeted. With material machinability software and manufacturing parameter values related to the material are presented to the user. In addition, with the condition monitoring system and control software included in our study operator errors are minimized.

2. METHOD

In this paper with condition monitoring system designed using the serial communication protocol on an NC machine transformed into CNC-supported turning machine and control software instant two-way data exchange was performed. In this turning machine a direct current engine was used which was frequently used in industrial machines as spindle motor that could reach up to high-rotation 2500 RPM speed, with 600 Watt

power. Control of the axis (programming of progress and interruption functions) was ensured with G codes. For axis motors (X and Y axis) delicate-driven step motors were used. Communication between spindle motor on CNC turning machine and sensor data connected to the motor and user condition monitoring software was performed real-time with the software embedded in the microcontroller with 32 bit AT91SAM3X8E processor and 12 bit (analogue reading) resolution. Analog signals belonging to the spindle motor such as rotation, current, motor working condition, motor rotation direction and automatic-manual user module signals designed electronically were organized by data collection and organization unit so that concurrent data exchange was ensured. All sensor data were sent real-time to the condition monitoring software which used serial communication protocol. Advanced graphic components and instant list displays made condition monitoring system interface more practical. In addition, the feature of switching to machinability catalogue software through condition monitoring and software system (Figure 1).

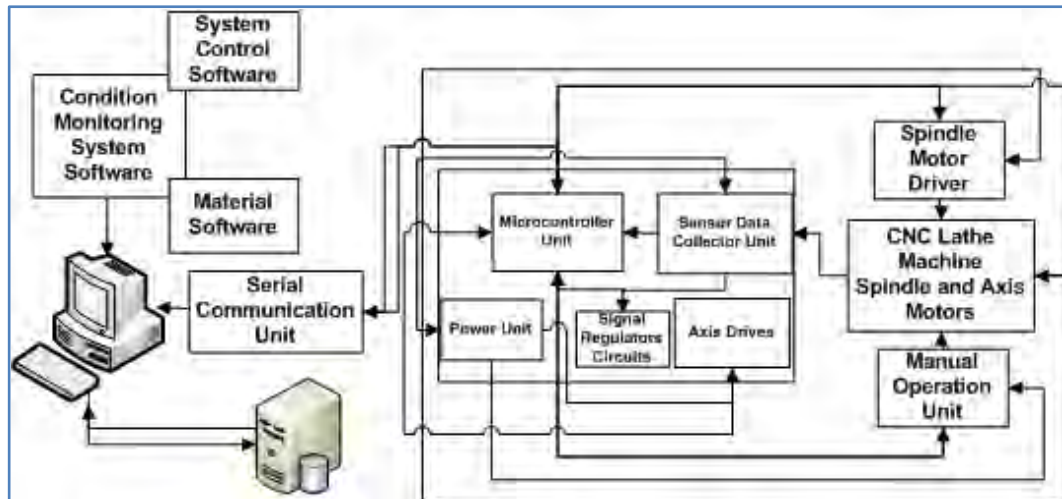


Figure 1. General design of the system

2.1. Software belonging to the system

Condition monitoring and control software designed for operator use on CNC supported turning machine was prepared by using C# programming language with the purpose of presenting and reporting sensor data connected to system hardware (current, rotation, temperature, spindle motor condition, spindle motor direction, spindle motor working style, situations of the motors which ensure axis movements, manual user panel signals) to the user on a real-time basis. In addition, with its object-oriented programming technique, a condition monitoring system and control software prepared with multi-layer architecture operates on a richly structured machinability material database. All manufacturing sensor data received through the system are recorded instantly on the database. It is now possible to examine and analyses past productions when desired. All communication between turning machine sensor systems and the user were performed through the software on the microcontroller which had decision-making ability. The embedded software in use was prepared on a platform which functionally acted as Arduino IDE code editor and compiler with a syntax similar to C language. In terms of software we can divide our study into two parts, namely condition monitoring, control system and embedded system. These software were prepared according to two-way, synchronize and concurrent working principle. The software and axis movements which process the G-codes provide these systems with progress and interruption functions were controlled (Figure 2).

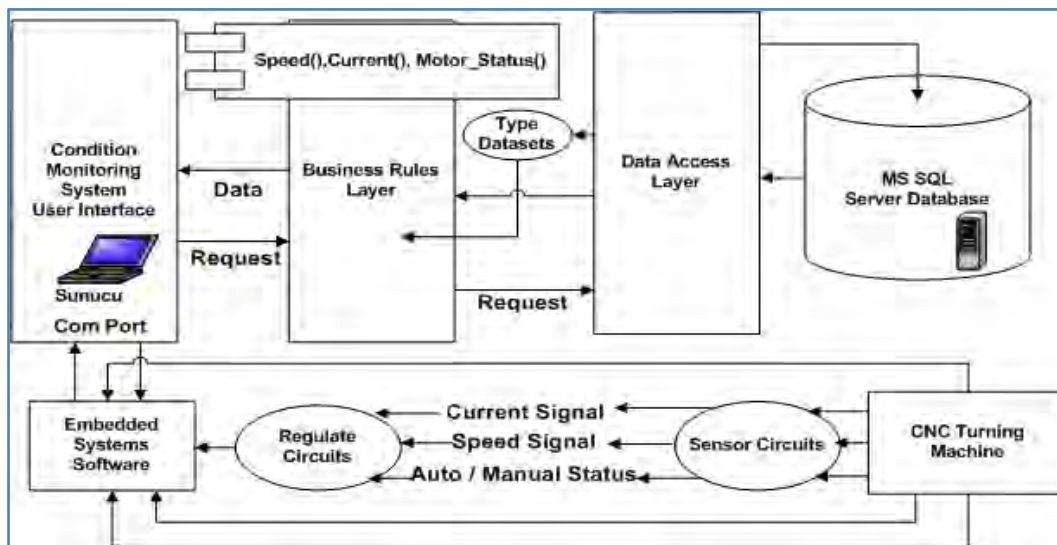


Figure 2. General design of software systems

2.2. Condition Monitoring System and Control Software

The condition monitoring and control software included in our study conducts its communication through advanced micro-controller using serial communication. This communication was designed as two-way and concurrent. Instant data received from sensor collector unit through microprocessor were continuously read in a cycle by condition monitoring and control software. As a result of the interpretation and separation of received data, monitoring of the condition of the system from software interface was ensured. Depending on the instant condition of the software it was ensured that the system could be initiated or executed (Figure 3).

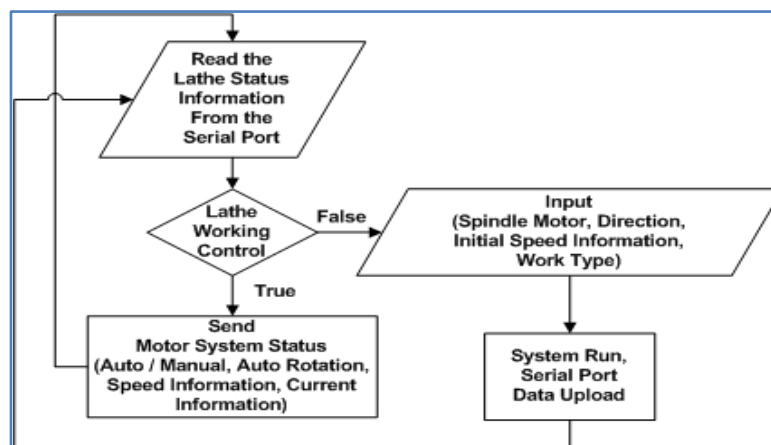


Figure 3. Basic algorithm of condition monitoring system and control software

In the .Net Framework platform which had rich software components, condition monitoring system and turning machine control software was developed with object-oriented programming technique with multi-layer architecture on Visual Studio Integrated Development Environment (IDE). The software developed with C# language used a multi-channelled structure and concurrent working techniques with pipelining principle. While sensor data were being read from serial port concurrently using multi-thread, renewal of condition monitoring system, data recording and operation of sending to serial port were ensured synchronously. All production processes on the turning machine are now instantly traceable and manageable through buttons electronically designed on software interface. The created CMS presents sensor data (current, rotation, temperature, rotation direction, motor status and operation mode) in the form of a graphical and dynamic list to the user. In addition, with determination of the start-up rotation information of the spindle motor presented to the user, start-up, stop and other usage options (motor direction, auto/manual usage) a more flexible and high-performance system has been prepared. Start-up rotation data specific to materials can either be determined by the user or chosen through the database, as a result of which operator error are minimized (Figure 4).



Figure 4. Condition monitoring system and control software interface

2.2.1. Embedded System Software

The open source coded electronic development card, Arduino, which is included in our study, is also remarkable in terms of automation due to its flexible and easy-to-use nature. The simplicity of programming development interface is similar to C/C++ language family in terms of syntax, hence, software development, compilation and loading stages are not complicated.

Continuous reading of spindle motor on CNC turning machine and sensor data connected to the motor such as rotation, current, temperature, system status, motor direction and operation mode as well as their communication with condition monitoring system real-time with serial communication was performed by the most developed Arduino DUE microcontroller with 32 bit AT91SAM3X8E processor and 12 bit ADC resolution (Figure 5).

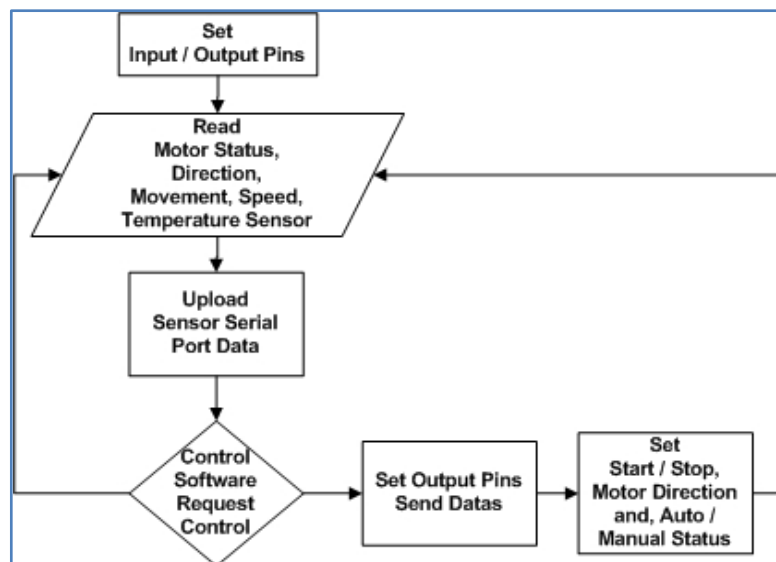


Figure 5. Basic algorithm of embedded system software

2.3. CAM Design and Axis Movements

In addition to condition monitoring system and control software, driving of step motors which ensure axis movements on the turning machine with G and M codes generated depending on the design and the application of the planned production was performed by an MK1 control card and software which is connected to the system with Universal Serial Port. G and M codes required for the operation of CNC turning

machines were sent to the control card which performs the control of axis movements through CAM (Computer Aided Manufacturing) computer. Step motors (X, Z axis) connected to the CNC machine turning machine were controlled concurrently through MK1 control card (Figure 6).

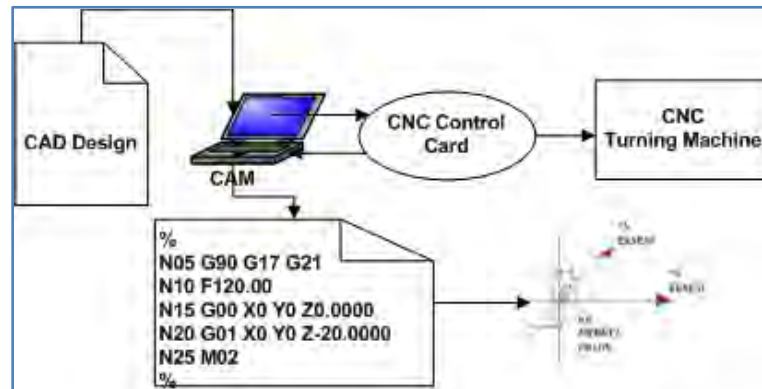


Figure 6. Application of the design

2.4. Conclusion and Recommendations

Execution of production processes in modern production and its performance through software and microcontroller instruments affect production accuracy and quality. It helps optimum utilization of machine equipment and prevention of unwanted situations (abrasion and breakage of toolsets) and reliable and uninterrupted continuation of production. With the condition monitoring and control software prepared in this study, operator was equipped with current, rotation, temperature and spindle motor data instantly and he was allowed to instantly control the turning machine and monitor sensor data (current, rotation, temperature, spindle motor status, spindle motor type of usage, axis movements). Application of concurrent and real-time working principles between software and hardware units increased the reliability and performance of the system. In addition, recording on the database of all sensor data belonging to manufacturing allowed for analysis of all past studies. With the help of material database and active system control unit presented to the CNC operator, higher performance and more active manufacturing management was ensured and user errors were minimized.

This study has been supported by the Department of Karabuk University Scientific Research Project. Project Number: KBI-BAP-13/2-YL-027

REFERENCES

- [1]. Han, Y., & Song, Y. H. (2003). Condition Monitoring Techniques for Electrical Equipment. IEEE Transactions on Power Delivery, Vol. 18, No. 1.
- [2]. Phillips, P., & Diston, D. (2011). A Knowledge Driven Approach to Aerospace Condition Monitoring. Knowledge-Based Systems 24, 915–927.
- [3]. Kusiak, A., Zhang, Z., Verma, A. (2013). Prediction, Operations, and Condition Monitoring In Wind Energy. Energy 60, 1-12.
- [4]. Asada, T., Roberts, C., Koseki, T. (2013). An algorithm for improved performance of railway condition monitoring equipment: Alternating-current point machine case study. Transportation Research Part C, 30, 81, 92.
- [5]. Uysal, A., & Bayir, R. (2013). Real-time condition monitoring and fault diagnosis in switched reluctance motors with Kohonen neural network. J Zhejiang Univ-Sci C (Comput & Electron), 14, (12):941-952.
- [6]. Irfan, M., Saad, N., Ibrahim, R., Asirvadam, V.J. (2013). Development of an Intelligent Condition Monitoring System for AC Induction Motors using PLC. (2013). IEEE Business Engineering and Industrial Applications Colloquium (BEIAC).
- [7]. Arpaia, P., Matteis, E., Inglese, V. (2015). Software for measurement automation: A review of the state of the art. Measurement, 66, 10–25.
- [8]. Camacho, S, Ruiz, H., Ocampo, J., Correa, J. (2011). Tool breakage detection in CNC high-speed milling based in feed-motor current signals. Int J Adv Manuf Technology, 53:1141–1148.
- [9]. Wang, L., Orban, P., Cunningham, A., Lang, S. (2004). Remote real-time CNC machining for web-based manufacturing. Robotics and Computer-Integrated Manufacturing, 20, 563–57.
- [10]. Pan, M., Li, P., Cheng, Y. (2008). Remote online machine condition monitoring system. Measurement, 41, 912–921.
- [11]. Jesus, R., Gilberto, H., Villalobos, T., Carlos, J. (2003). Driver current analysis for sensorless tool breakage monitoring of CNC milling machines. International Journal of Machine Tools & Manufacture, 43,1529–1534
- [12]. Isik, Y. (2004). Talaşlı İmalatta On-Line Toolset Durumu İzleme Yöntemleri. (2004). Uludağ Üniversitesi Mühendislik-Mimarlık Fakültesi Dergisi, Cilt 9, Sayı 1.

CONTROL OF THE ENERGY FLOW WITH PLC FOR BATTERY SUPPORTED HYBRID GENERATION SYSTEM IN CASE OF A SUPPLYING TO LOCAL AREA

Yavuz KOCA

Afyon Kocatepe University, Faculty of Engineering, Department of Electrical Engineering, Afyon, TURKEY

Ahmet YÖNETKEN

Afyon Kocatepe University, Faculty of Engineering, Department of Electrical Engineering, Afyon, TURKEY

Yüksel OĞUZ

Afyon Kocatepe University, Faculty of Technology, Department of Electrical and Electronic Engineering, Afyon, TURKEY,
yukseloguz@aku.edu.tr

Tolga ÖZER

Afyon Kocatepe University, Faculty of Technology, Department of Electrical and Electronic Engineering, Afyon, TURKEY,
yukseloguz@aku.edu.tr

Abstract

This paper proposes to provide the energy continuity of a standalone distributed (off-grid) hybrid power system applied which consists of solar power, wind power, battery storage and the load. A battery group was integrated to the system for obtaining continuous energy. Furthermore, a PLC (Programmable Logic Controller) supported control system was designed and integrated in order to provide efficiency during the power generation. The system was applied by lighting the laboratories of the Electrical and Electronic Engineering Department of Technology Faculty in the AfyonKocatepe University.

Keywords: *Energy saving, Hybrid Power System, Off-Grid, Energy Flow Control*

1. INTRODUCTION

Energy is an indispensable component of our daily lives. Taking the rapidly increasing energy demand and diminishing fossil fuel sources into consideration, generation of clean energy from renewable energy sources come into prominence with each passing days.

Presently, fossil fuels, coal, natural gas and fuel oil are respected as the basic energy sources which meet the most of the energy needs of the present system. However, the obvious vulnerability and the potential risks of these energy sources gathered the attention on renewable energy sources.

The widespread usage of renewable energy systems came together with the cooperation of different kinds of energy sources. Such energy systems are called as hybrid power generation systems. Hybrid power generation systems can be formed with a combination of many different energy sources and storage devices. Specifically, solar and wind powers are two of the most widely used renewable energy sources in a hybrid power generation system. Usually, off grid wind and solar power generation systems are operated with gas turbine, diesel generators, fuel cells and battery groups. Furthermore, the continuity of the energy and system performance are enhanced at the same time [5].

Efficiency control mode is necessary for hybrid power systems. In order to control the process, a data acquisition system which is widely used in renewable energy source (RES) applications in order to collect data regarding the installed system performance, for evaluation purposes, has to be created[3].

There are several inspiring studies conducted relevant to the hybrid power generation systems. For instance, Nelson et al tried to meet the electricity need of an off-grid house in the Northwest Pacific region while comparing the system including the wind-solar-fuel cell with the one including wind-solar-battery group from the economical perspective. As a result, wind-solar-battery system was observed as more economical than wind-solar-fuel cell and electrolysis system. However, it was estimated that the fuel cell and electrolysis systems would be more economical in the future parallel with the development in these technologies [6].

Furthermore, [4] tried to apply a hybrid power system which includes photovoltaic panels, wind turbine and fuel cells on a mobile home in their study. Solar and wind energy was used as the primary source and while fuel cell was the secondary one. Again, [2] studied the control of an off-grid hybrid power generation system which was composed of photovoltaic panels, wind turbine and Proton Exchange Membrane Fuel Cells (PEMFC). Also, [8] showed the operation of a small network comprised of the wind, photovoltaic and fuel cell power sources. Additionally, [7] developed a prediction algorithm for energy storage. Moreover, [1] controlled the simulated standalone distributed hybrid power system which consists of solar power, wind power, battery storage and the load by using Matlab-Simulink. The control system controlled the converter system with using maximum-power-point tracking (MPPT) algorithm. Also, [9] designed a novel micro turbine for the solar-wind hybrid power system. Two types of wind-solar hybrid system with the same capacity were set up in Tianjin, and the power output of the two systems were measured and simulated by the TRNSYS software. It was observed that the designed wind turbine hybrid system had more wind power output, especially at lower wind speed. Furthermore, [10] presented standalone hybrid solar-wind system with battery energy storage for a remote island. He observed that the combination of solar energy, wind energy and battery storage could supply continuous power to the island.

In line with the abovementioned studies, this study is based on a research project on power supply for laboratory lightning. In this context, the hybrid power generation system including wind-solar energies supported by a battery group in order to provide energy continuity was developed. The energy flow was controlled with a PLC controller in the system. Additionally, the load control was carried out by PIC controller.

2. HYBRID POWER GENERATION SYSTEM AND COMPONENTS

Basically, applied hybrid power generation system included solar panels, wind turbine and battery groups. There were three mono crystalline solar panels in the system, which were at 190W power and 24V output. Also there was a 600W 3-phase permanent magnet synchronous generator wind turbine which was 360° rotatable by wind direction. Additionally, there were six 100 Ah gel batteries. Battery group was used to store the energy surplus when possible and to provide the energy continuity when needed. Electrical energy production was controlled by PLC. The generated current and voltage data were recorded at certain periods by a computer system. Also, load was controlled by PIC16F877 microcontroller and fed by means of DC-DC converters because of unbalanced output voltage of the electricity generated from wind and solar power sources. Although the DC-DC converter input voltage was in the range of 18-72V, output voltage was at 24V constant value. Moreover, electrical energy generated by the hybrid energy system was converted to 220V

AC energy with using 3kW power of inverter. As a result, consumer electricity demand was provided. Hybrid power generation system diagram can be seen in Figure 1.

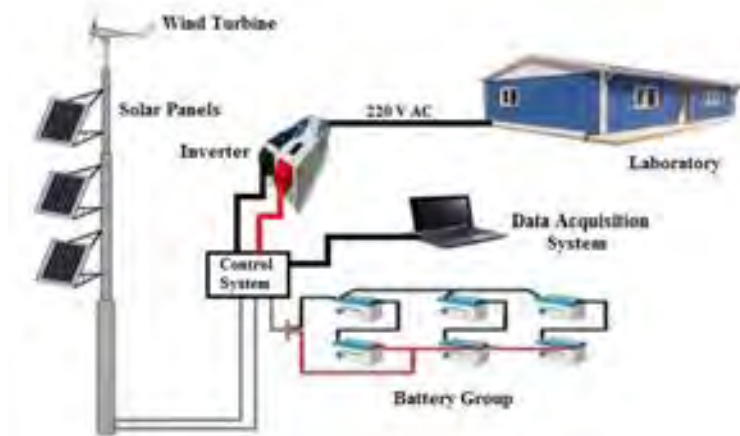


Figure 1. Hybrid power generation system diagram

2.1. Data Acquisition and Control System

Every controlled system need to data acquisition system for evaluating sensors outputs according to control strategy. If there is a control process in a study data acquisition system has to be in this system.

In our study, data acquisition system was created based on Delphi program and PLC S01 type of controller. PLC has 8 digital inputs and 8 digital outputs. PLC was used for as an evaluating center and determining algorithms were applied in PLC for hybrid system controlling. Delphi program was used for created a system interface and data processing. Created hybrid system interface is monitorized the taken data from voltage and current sensors as a graphical and numerical mode. Data acquisition logic steps were shown basically in Figure 2.

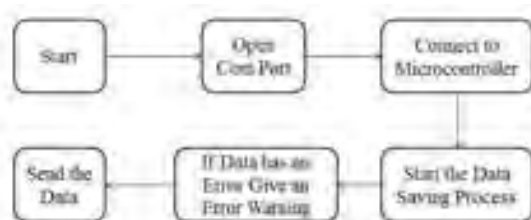


Figure 2. Data acquisition logic steps

In data acquisition system solar voltage, wind turbine voltage and battery voltage values were taken as analog input our power generation system. And these analog variables was transferred to the analog inputs of PLC controller. And digital outputs which are related to solar, wind, battery and load control were controlled according to these analog inputs value. The energy generated from solar and wind energy sources were saved separately as a wathours (Wh).

2.2. Control System Strategy

The energy generated in wind turbine and solar panels of hybrid power generating system was collected in 24 V stable DC bars by means of DC-DC converters. Battery group was collected to DC Busbar at the same time. Besides, stable DC was be converted to AC by means of inverter on the control unit and made ready for the operating voltage of the consumers.

The data flow of energy generated from solar panels and wind turbine was organized via the designed a PLC based microcontroller. The power to lighting the laboratory with LED fluorescent lamps was the load to be supplied by the hybrid power generating system. Wind turbine and solar panels were assessed as the main

power sources in the hybrid power generation system. The energy required for the load was met with the energy produced by wind turbine and solar panels. If the wind turbine and the solar panels did not meet the required power of the load, the battery group provided the required energy in line with the energy flow control system. On the other hand, if there was energy surplus while lighting the laboratory, it was stored in battery groups if their charge rate is below 95%.

The algorithm illustrating the running order of the system according the amount of power demanded and generated can be seen in the Figure 3.

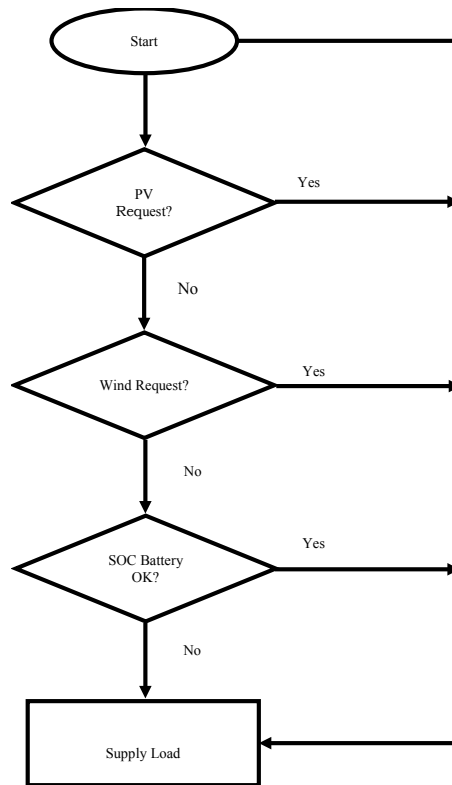


Figure 3. Algorithm for energy management in the proposed hybrid power generation system.

3. EXPERIMENTAL RESULTS AND DISCUSSION

Solar and wind energies are used as the primary sources of the energy for the system, it is obvious that the meteorological conditions were very determinant for the amount of generated power. For this reason, it was very critical to develop a power management strategy in order to control the operation of the system's components and to use the generated power effectively. The main goal of the energy control system was to meet the power requirement of the load without cut off. It was assumed that the less battery group was used, the more its operating life would be. Main factors effecting the power flow management strategy were amount of power generated and battery group charging rate.

The data regarding the power generated by the hybrid power generation system was imported between the months of August – December. Data belonging to the production and consumption units was recorded in every 10 seconds from 08:00 am to 06:00 pm. The system was designed to charge the batteries after 06:00 pm. Electrical energy produced by solar panels and wind turbine fed the system instantly and they met the energy requirement of armatures connected to load control system. In case of energy surplus, battery group was engaged to store it. Electricity meter was connected to the entrance of the lighting line in order to determine the total electricity consumption. In this context, the total energy generated, loss energy, stored energy and consumed energy was illustrated in the Figure 4 as a kWh. As shown Figure 4 graphic in August month maximum energy was obtained from the solar energy. And in this time period charging rate of the batteries is maximum point when we compared to other months of the data were taken. Maximum consumed energy data were obtained in November month. According to this graphic can be said solar panel is more efficiency than wind sources. Because large part of the energy are met with solar panels. In Figure 5 the hybrid system efficiency rates can be seen according to months. System efficiency has decreased slightly

from August to November. System efficiency was seen minimum value in December month. This condition was stemmed from the data being received was from the half of December month.

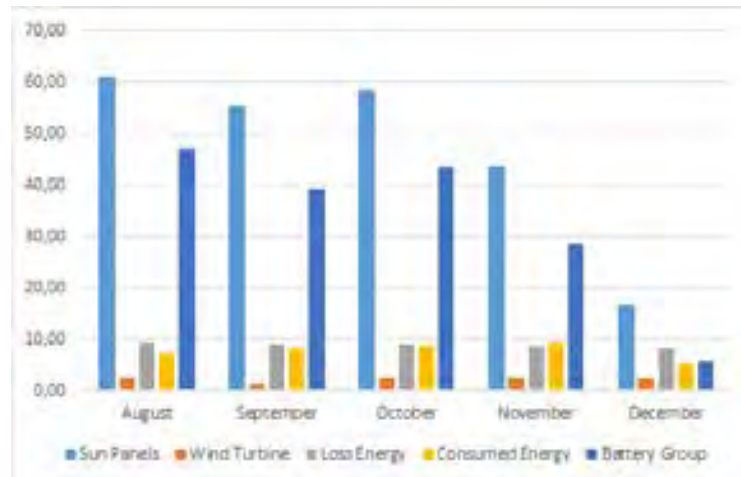


Figure 4. Produced values according to sources at the hybrid generation system with loss and stored energy(kWh).

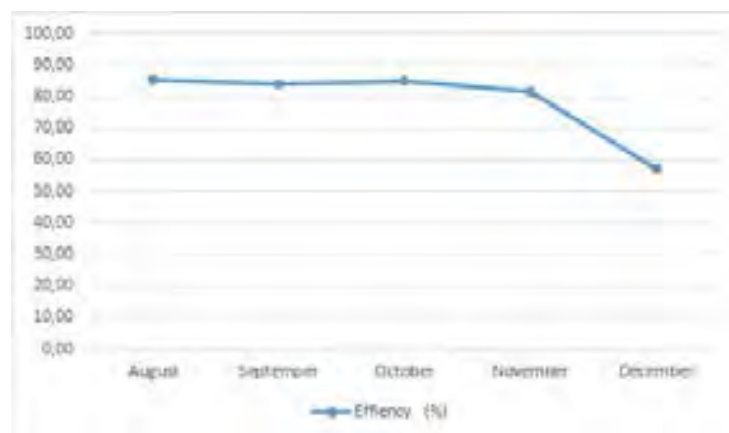


Figure 5. Efficiency rates in the hybrid power generation system by month.

4. CONCLUSIONS

In this study, it was focused on different power management strategies including off-grid hybrid power generation systems and hybrid power generation system integratable to grid. Hereby, continuous power flow was provided in power demand system. Furthermore, an effective management mechanism was built by controlling the frequency of energy sources' engagements by means of the algorithm developed. Moreover, the power surplus was stored in battery group due to the microcontroller and the different algorithms in power management strategies. The frequency of operation and the operation order of power sources were optional.

ACKNOWLEDGMENT

This research has been supported by grant number 113E310 from The Scientific and Technological Research Council of Turkey (TUBİTAK).

REFERENCES

- [1]. Dan Shen, A. I. (2014). A Hybrid Wind-Solar-Storage Energy Generation. IEEE.
 - [2]. Dursun, E. &. (2012). Comparative evaluation of different power management strategies of a stand-alone PV/Wind/PEMFC hybrid power system. *International Journal of Electrical Power & Energy Systems*, 34(1), 81-89.
 - [3]. EftichiosKoutroulis, K. K. (2003). Development of an integrated data-acquisition. *Renewable Energy*.
 - [4]. Eroglu, M. D. (2011). A mobile renewable house using PV/wind/fuel cell hybrid power system. *International Journal of Hydrogen Energy*, 36(13), 7985-7992.
 - [5]. Nasiraghdam, H. &. (2012). Optimal hybrid PV/WT/FC sizing and distribution system reconfiguration using multi-objective artificial bee colony (MOABC) algorithm. *Solar Energy*, 86(10), 3057-3071.
 - [6]. Nelson, D. B. (2006). Unit sizing and cost analysis of stand-alone hybrid wind/PV/fuel cell power generation systems. *Renewable energy*, 31(10), 1641-1656.
 - [7]. Niknam, T. G. (2012). Probabilistic energy and operation management of a microgrid containing wind/photovoltaic/fuel cell generation and energy storage devices based on point estimate method and self-adaptive gravitational search algorithm. *Energy*.
 - [8]. Niknam, T. K. (2011). Optimal operation management of fuel cell/wind/photovoltaic power sources connected to distribution networks. *Journal of Power Sources*, 196(20), 8881-8896.
 - [9]. Qunwu Huang, Y. S. (2015). Multi-turbine wind-solar hybrid system. *Renewable Energy*.
 - [10]. Tao Ma, H. Y. (2014). A feasibility study of a stand-alone hybrid solar-wind-battery system. *Applied Energy*.
 - [11]. Karnik, "Performance of TCP congestion control with rate feedback: TCP/ABR and rate adaptive TCP/IP," M. Eng. thesis, Indian Institute of Science, Bangalore, India, Jan. 1999.
 - [12]. J. Padhye, V. Firoiu, and D. Towsley, "A stochastic model of TCP Reno congestion avoidance and control," Univ. of Massachusetts, Amherst, MA, CMPSCI Tech. Rep. 99-02, 1999.
 - [13]. *Wireless LAN Medium Access Control (MAC) and Physical Layer (PHY) Specification*, IEEE Std. 802.11, 1997.
-

TOXIC AND HAZARDOUS WASTE MANAGEMENT

Sakine UGURLU KARAAĞAÇI

Karabuk University, Engineering Faculty, Environmental Engineering Department, 78050-Karabuk-TURKEY.
sakineugurlu@karabuk.edu.tr

Abstract

Every year, billions of tons of solid wastes are discarded into our environment. These wastes range in nature from common household trash to complex materials in industrial wastes, range in nature from common household trash to complex materials in industrial wastes, such as hospitals and laboratories. Waste is defined as 'any material that are no longer desired and has no current or substance that has been discarded or otherwise designated as a waste material, or one that may become hazardous by interaction with other substances. Hazardous waste is a waste which could potentially threaten human health or the environment. This includes waste which exhibit one of seven hazardous characteristics: ignitability (flammability), corrosively, reactivity (oxidizer), toxicity (poison), infective, radioactivity and bioaccumulation effect. Hazardous waste may either be in the form of solid, liquid, semi-solid or contained gaseous material. Waste Management Strategies play an important role in defining a hazardous waste. These steps may include; the source of the waste, generators, waste transport, waste storage, appropriate treatment technologies, final disposal. Hazardous wastes should be identified and disposed of in a manner that will most effectively protect the environment. All the producers and the recipients of waste need to follow certain standard operative procedures (SOP) to manage the waste in accordance with the existing law and waste regulations. The legislators of each country should create regulations enforcing the safe management of the hazardous waste.

Keywords: waste, toxic waste, hazardous waste, classification, management.

1. INTRODUCTION

Every year, billions of tons of solid wastes are discarded into our environment. These wastes range in nature from common household trash to complex materials in industrial wastes, such as hospitals and laboratories. Waste is defined as any material that is no longer desired and has no current or substance that has been discarded or otherwise designated as a waste material, or one that may become hazardous by interaction with other substances. Sources of hazardous waste include hospitals, timber treatment, petrol storage, metal finishing, paint manufacture, vehicle servicing, tanneries, agriculture/horticulture, electricity distribution and dry cleaning.

Toxic waste definition: A general term used to refer to chemical compounds produced by industry which, if they are ingested or breathed in by humans, can cause physiological damage. The disposal of toxic wastes is a major environmental problem in all countries. The waste may be liquid, solid, or sludge and contain chemicals, heavy metals, radiation, dangerous pathogens, or other toxins. Even households generate hazardous waste from items such as batteries, used computer equipment, and leftover paints or pesticides. Hazardous waste is generated by everybody. Households commonly generate unwanted gasoline, brake and windshield wiper fluid, cleaning supplies, paints and paint thinners, lead acid batteries, used computer equipment and construction materials (i.e. asbestos), pesticides and others. Hospitals and nursing stations generate unwanted needles and waste human tissue, body fluids and biotic cultures. Business and industry generate many different types of hazardous waste including used motor and lubricating oil, cleaning solvent, drilling fluid and cuttings and mine tailings.

2. CLASSIFICATION OF HAZARDOUS WASTE

Hazardous waste includes waste which exhibit one of seven hazardous characteristics: ignitability (flammability), corrosively, reactivity (oxidizer), toxicity (poison), infectivity, radioactivity and bioaccumulation effect. Hazardous waste may either be in the form of solid, liquid, semi-solid or contained gaseous material. Any discarded material, liquid or solid that contains substances known to be; fatal to humans or lab animals in low doses, toxic, carcinogenic, mutagenic, or teratogenic to humans or other life-forms, ignitable with a flash point less than 60°C, corrosive, explosive or highly reactive.

A useful listing of hazardous characteristics is that provided by the United Nations (1989) as part of recommendations relating to the transport of dangerous goods. Examples from this listing are given in Table 1.

Table 1 - Examples of Hazardous Characteristics: Extracted From U.N. Listing (1989)

U.N. Class Number	Hazardous Characteristic
1	Explosive
3-4	Flammable
5	Oxidizing
6	Poisonous/Infectious
7	Radioactive
8	Corrosive
9	Toxic (Delayed or Chronic)/Eco-toxic

Substances that are not on the list but are toxic are also considered hazardous waste and subject to EPA's rules.

3. MANAGEMENT OF HAZARDOUS WASTE

Hazardous wastes are poisonous by products of manufacturing, farming, city septic systems, construction, automotive garages, laboratories, hospitals, and other industries. The waste can harm humans, animals, and plants if they encounter these toxins buried in the ground, in stream runoff, in groundwater that supplies drinking water, or in floodwaters. Some toxins, such as mercury, persist in the environment and accumulate. Humans or animals often absorb them when they eat fish.

Proper waste management simply makes good sense. Minimizing or eliminating the generation of hazardous and other waste helps to reduce the hazards and costs associated with its handling, storage, transport, recycling, treatment and disposal. It also reduces the impacts waste could have on the environment, human and worker health and safety and reduces the global emission of greenhouse gases by minimizing the use of raw materials. Another term commonly used to describe activities that reduce the amount of material entering a waste stream or being released to the environment is 'pollution prevention'. For hazardous waste the hierarchy is as follows:

- Eliminate the production of hazardous waste.
- Where elimination is not possible apply methods to reduce the quantity or hazard involved.
- Minimize amount of waste for disposal by recycling, reuse and/or recovery. This includes the recovery of energy which may be available from the waste.
- Treat waste to stabilize, immobilize, contain or destroy hazardous properties.
- Dispose of residues with a minimum of environmental impact.

Appropriately contain, isolate and store hazardous waste for which no acceptable treatment or disposal option is currently available. Waste minimization benefits you:

- Significantly lowering costs,
- Reducing potential health hazards,
- Reducing potential long-term liabilities for disposal,
- Promoting environmental ethics,
- Preventing pollution.

It is the responsibility of every investigator who generates waste to incorporate the principles of waste minimization into experimental design.

4. TREATMENT OF HAZARDOUS WASTES

The purpose of treating hazardous waste is to convert it into nonhazardous substances or to stabilize or encapsulate the waste so that it will not migrate and present a hazard when released into the environment. Stabilization or encapsulating techniques are particularly necessary for inorganic wastes such as those containing toxic heavy metals. According to the CAE Report (1992), treatment methods can be generally classified as chemical, physical and/or biological.

4.1. Chemical Methods: neutralization, oxidation, reduction, hydrolysis and precipitation.

2. Physical Methods: a) Encapsulation: Immobilizing hazardous materials by stabilization and incorporation within a solid matrix such as cement concrete or proprietary organic polymers prior to and filling. b) Filtration/Centrifuging/Separation: Physically separating phases containing hazardous substances from other nonhazardous constituents.

3. Biological Methods: These involve the use of microorganisms under optimised conditions to mineralise hazardous organic substances e.g. the use of pseudomonas under aerobic conditions break down phenols.

4. Thermal Methods: These are the treatment processes which involve the application of heat to convert the waste into less hazardous forms. It also reduces the volume and allows opportunities for the recovery of energy from the waste.

4. CONCLUSIONS

Some of the waste currently produced by industrial chemical processes possess hazardous properties and require special attention in respect to disposal. Concern relating to these wastes has resulted in the development of international conventions aimed at controlling their movement. These conventions also assist in the management of these wastes by providing listings that can be used as the basis for a identification and classification scheme.

A hierarchy to assist decision making is available to promote sustainability from waste management and this places emphasis on the elimination or minimization of the production of hazardous waste.

Established chemical, physical, and or biological methods are available to stabilize or break down most hazardous waste to a form which will have minimal adverse effect on health, safety and or the environment.

REFERENCES

- [1]. Anonymous, (1989). Recommendations of the UN Committee of Experts on the Transport of Dangerous Goods; United Nations, New York; 1989.
- [2]. Anonymous, (2010). Environmental Guideline for the General Management of Hazardous Waste, Department of Environment, Government of Nunavut.
Web site: <http://env.gov.nu.ca/programareas/environmentprotection>.
- [3]. Anonymous, 2014. Hazardous Waste Disposal Guide.
Website <http://www.research.northwestern.edu/ors/>

[4]. CAE Report, (1992).Centre for Advanced Engineering (CAE), University of Canterbury, Christchurch; Our Waste: Our Responsibility.

[5]. N. Thon, The Management of Hazardous Waste. XIV-Environment-B-Hazardous Waste.

Biography: She is working at Karabuk University, Engineering Faculty, Environmental Engineering Department.

STRUCTURAL ANALYSIS OF THE WHEEL VEHICLE'S SUSPENSION CONVEYOR

Mesut DURAT

Mesut Durat,, University Department Of Machining Engineering 54055 Sakarya/Turkey
durat@sakarya.edu.tr

Ferit FİCİCİ

Ferir Fııcı, University Department Of Machining Engineering 54055 Sakarya/Turkey,
fficici@sakarya.edu.tr

Selçuk KARAKULAK

Selçuk Karakulak,, University Department Of Machining Engineering 54055 Sakarya/Turkey,

Zekeriya AYPARÇASI

Zekeiya Ayparçası, Sakarya University Department Of Machining Engineering 54055 Sakarya/Turkey
zekeriyaayparcasi@gmail.com

Abstract

Control technologies progressively developing in technological vehicles increase the number of studies examining the behaviors of vehicles in different road conditions. Additionally, optimization studies are performed for different road profiles of suspension systems. In this study, helical spring suspension system used in an off-road vehicle was modeled. In this study, vehicle with maximum compression and swing arm suspension system in the publication of the maximum movement scenarios stemming from the roof barrier formation by analyzing dynamic forces on axle conveyor have been detected. Suspension conveyor, is one of the load-bearing parts of the system based on the dynamic effects of the vehicle on road conditions, was examined by the finite elements method. All these analyzes were conducted in the CREO program.

Keywords: *Suspension systems, Dynamic analysis, Finite elements analysis*

1. INTRODUCTION

Vehicle suspension system, is composed of suspension arms, springs and dampers, in order to filter and transmit all the forces between the body and the road. Springs carry the body mass and insulate the body against road distortion, and this brings driving comfort. Damper supports driving safety and driving comfort. Its mission is to absorb the body and Wheel oscillations where the avoidance of wheel oscillation does mean driving safety.

Suspension systems must ensure the wheels to hold on to the road, as well as they carry the vehicle weight. Road handling of the vehicle is of vital importance; because the active safety, balance and comfort of the vehicle depends on the healthy function of this system. In an intervened structure, the vertical energy of all the wheels, is transmitted to the chassis which moves in the same direction. In this case, wheels might lose their contact with the road entirely. Also, the wheels might crash into the road under the influence of gravity.[1]

Control technologies, gradually developing in technological vehicles, increase the study for the analysis of vehicles' behaviors under different road conditions, and these technologies are also used for the optimization studies of suspension systems for different road profiles.[2]

Many studies have been carried out recently, in order to model the behaviors of the suspension systems of rubber-tired vehicles under different road conditions. Different suspension systems are used in different vehicles. Today, especially in land vehicle applications; double-wishbone, fully independent, hydro-pneumatic or helical spring suspension systems are used in order to make the minimal transmission of the vibration coming from the road to the body section, and in order to enable the use of vehicle with maximum performance.[3]

The primary duty of suspension systems, is to be mobile connectors between the wheel group and the chassis. The guides with respect to the vehicle body in longitudinal and transverse direction of the wheel depending on the brake, drive and semi-forces that the vehicle applies, enable the support of spring and stabilizers by receiving the vertical forces transmitted to the vehicle body through the wheel[4,5].

In this study, a helical spring suspension system of a rubber-tired vehicle, was modeled. Then, this system was modeled by a computer-aided design program, and its dynamical analysis was carried out in a Creo-MECHANISM environment, a finite element analysis program. With respect to the loads acquired in dynamic analyses, a structural analysis study was carried out by means of Creo-SIMULATE, in order to verify the materials selection and the suspension conveyor, which is a critical part of the helical spring suspension system. A double-wishbone, fully independent helical spring suspension system used in a land vehicle, was modeled and, the spindle conveyor exposed to dynamic stress in the system, was analyzed by finite elements method.

2. MATERIALS AND METHODS

An easy way to comply with the symposium paper formatting requirements is to use this document as a template and simply type your text into it.

2.1. The Modeling of Helical Spring Suspension System

Four main bottom assembly complexes composing the helical spring suspension system, can be classified as wheel, spring-damper, lower arm and upper arm. Wheel wishbones connection is composed of global, suspension arm conveyor pin joints, and spring-damper complex lower arm body connection is composed of pin joints. Forces coming from the road, are transmitted to wishbones via wheel complex, and to the body connection via spring-damper. Helical spring suspension system was modeled by the Creo program. Here, each part composing the helical spring suspension system, was modeled separately, their bottom assembly was carried out separately and then, the assembly of the entire system, was carried out (Figure 1).

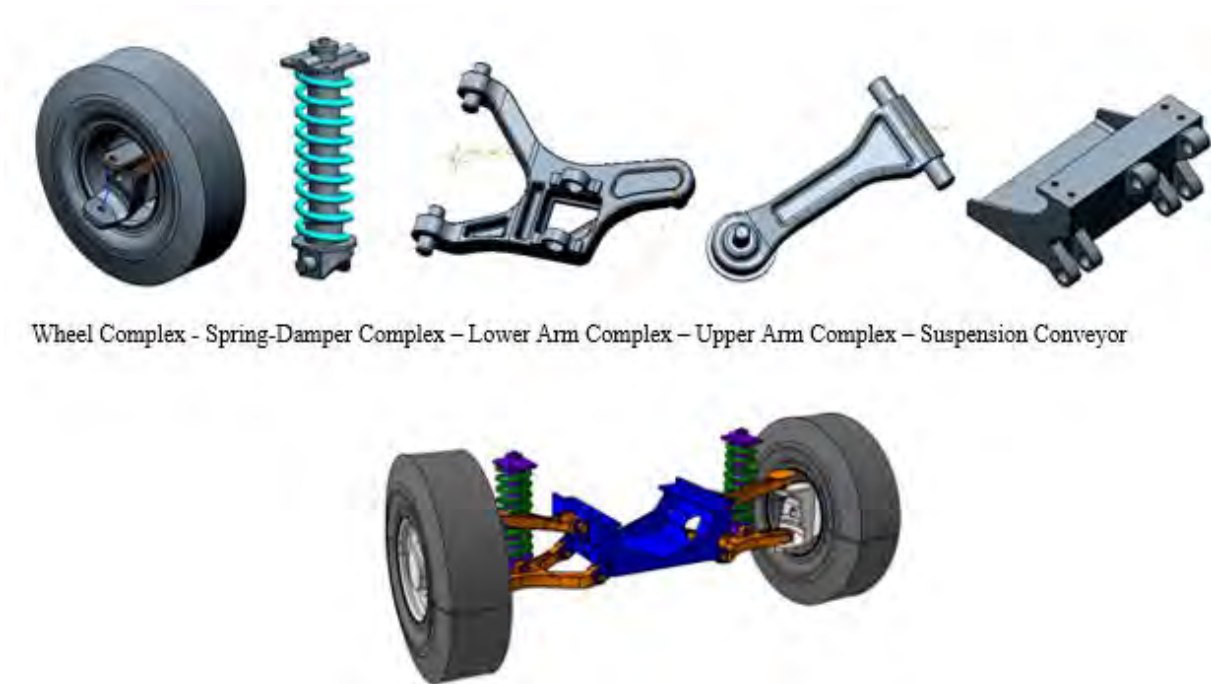


Figure 1. The Assembly of Helical Spring Suspension System

After the model was transferred to Creo-MECHANISM program, the essential parts were placed, and other parts were not analyzed because they had no effect in the function of the mechanism. While the vehicle moves in various road profiles, the wishbones move up and down in accordance with the road profile. The movement of wishbones, transmit the motion to the suspension conveyor. Helical spring-damper complex is attached to lower arm and to vehicle body. The force transmitted via the spring-damper, is transferred to lower arm and to body, and thus, it makes the vehicle move. The spring-damper absorbs the force coming from the road profile, and it enables the comfortable drive. The connection and joints established, are shown in Table 6.1.

Table 1.Connection and Joints

	Name	Joint Type	Content	Displacement			Rotation		
				x	y	z	x	y	z
1	Conveyor-Ground	Planar	Object-Ground	Fixed	Fixed	Free	Fixed	Fixed	Fixed
2	Lower arm-Conveyor	General	Object-Object	Fixed	Fixed	Free	Free	Fixed	Fixed
3	Upper arm-Conveyor	General	Object-Object	Fixed	Fixed	Free	Free	Fixed	Fixed
4	Body-Conveyor	Planar	Object-Object	Fixed	Fixed	Free	Fixed	Fixed	Fixed
5	Wheel-Upper arm	General	Object-Object	Fixed	Fixed	Free	Free	Fixed	Fixed
6	Wheel-Lower arm	General	Object-Object	Fixed	Fixed	Free	Free	Fixed	Fixed
7	Lower arm-Spring	Rotary	Object-Object	Fixed	Fixed	Fixed	Free	Fixed	Fixed
8	Spring-Body	Rotary	Object-Object	Fixed	Fixed	Fixed	Free	Fixed	Fixed

2.2. Modeling of Road Profile

Track tests mean that, a vehicle at a particular speed would be passed on bumps with different dimensions, which were placed in a particular pattern. All the parameters were determined by standards. This study conducted, had been designed in the manner that, the road profile wheel would rotate in 200mm vertical direction, and the acceleration in the vertical direction, was taken as 2.5g.

In Figure 2, the road profile that would transmit the vertical acceleration motion to the helical spring suspension system, is modeled. In Figure 6.3, the road and helical spring suspension system joint cam road, are described.

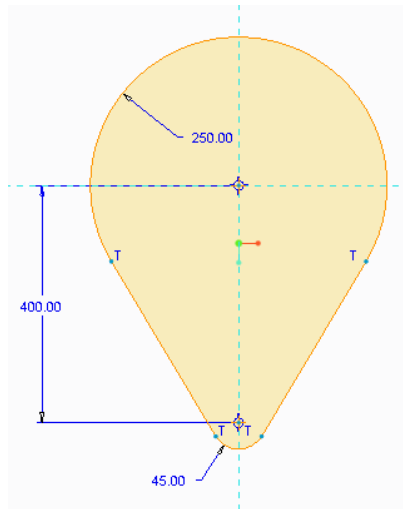


Figure 2. Road Profile

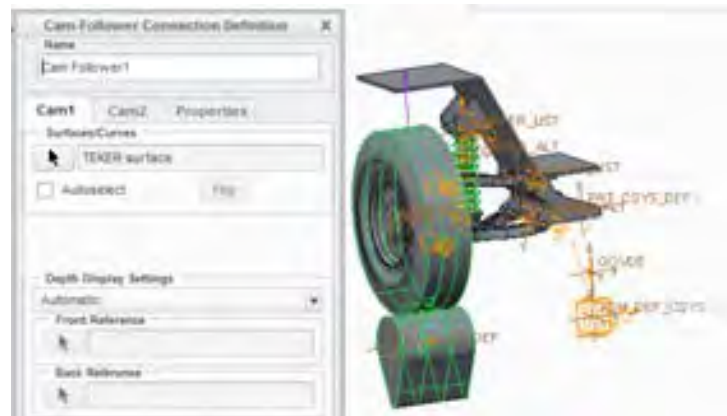


Figure 3. Road-Helical Spring Suspension System Cam Road

In Table 2, the weights related to the parts used in the system, are given. In Table 3, the properties of GGG 50 Materials, are indicated.

Table 2. Part Weights

Conveyor	100	Kg.
Lower arm	50	Kg.
Upper arm	25	Kg.
Wheel Complex	185	Kg.
Spring Complex	40	Kg.
Body	2680	Kg.

Table 3. GGG 50 Material Properties

Elastic Module	165 GPa
Poisson Fixed	0,3
Yield Point	390 MPa
Ultimate Tensile Stress	580 MPa
Intensity	7,83e-9 t/mm ³

In Figure 4, the gravitational acceleration is entered to the system as 9806.65mm/sec² in Z axis.



Figure 4. Recognition of gravitational acceleration

3. MATERIALS AND METHODS

3.1. Detection of Dynamic Analysis and Forces

In Figure 5, the graphic related to the displacement in Z axis; between the wheel axis and the ground; when the road profile made 2 full rotations, was measured in mm/sec.

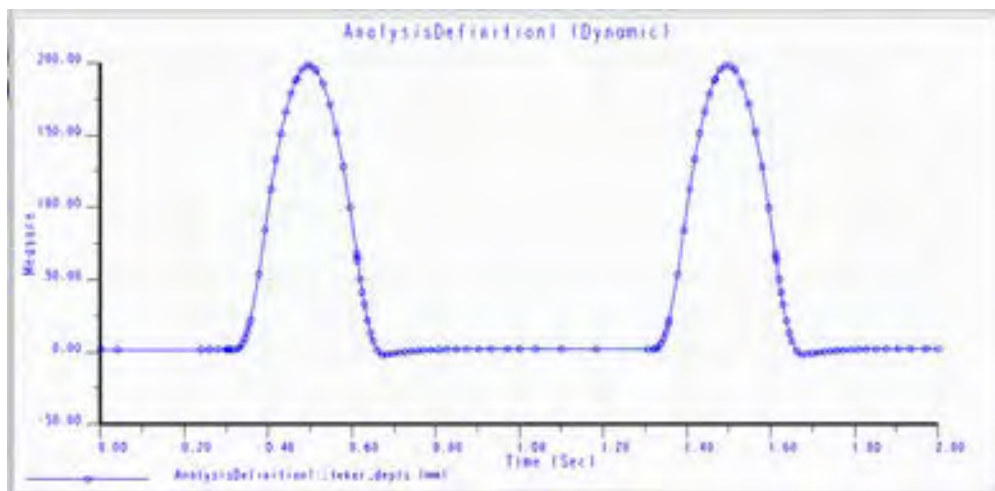


Figure 5. Distance between the Wheel Center and The Road (Z)

In Figure 6, the vertical acceleration of any point on the body, was measured in Z axis, and the value was adjusted at 2,5g level; by increasing the cycle that the servo motor, whose body acceleration is defined, would do in a minute, the acceleration value can be enhanced optionally.

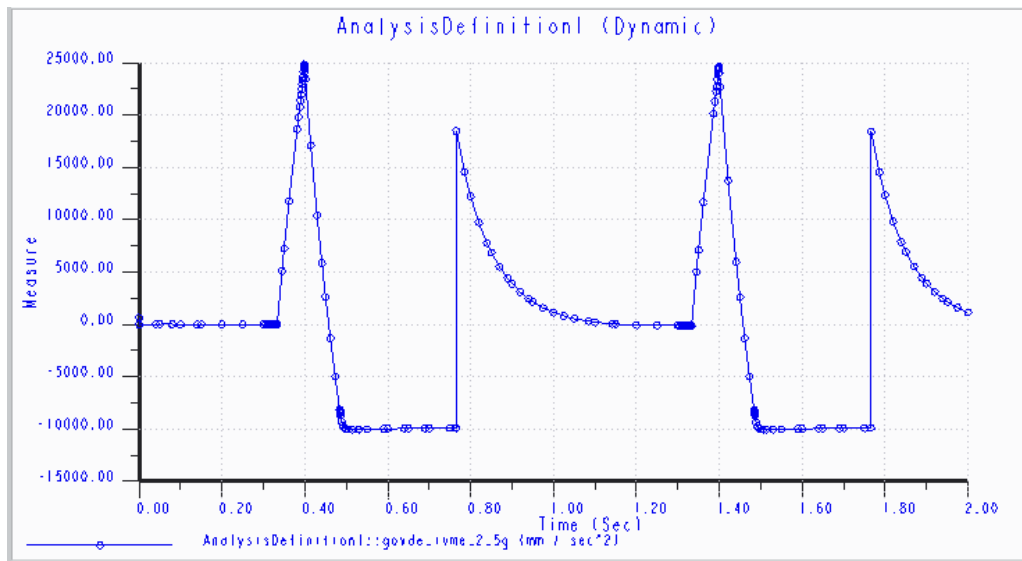


Figure 6. Body (Z) Acceleration (mm/sec)

In Figure 7, the spring characteristic is shown in N/mm.

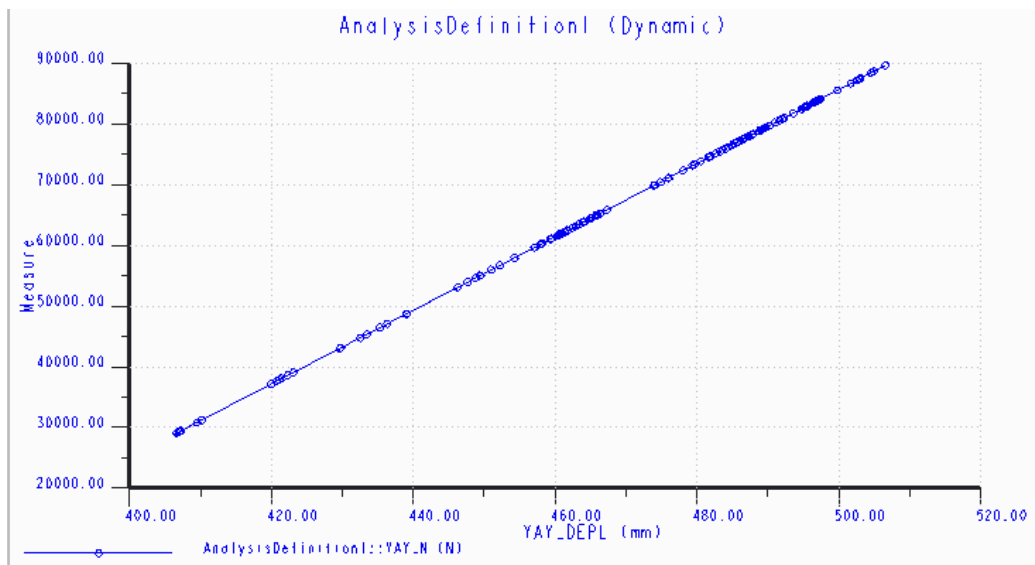


Figure 7.Spring Characteristic (N/mm)

In Figure 8, the force dynamic wheel motion affecting the damper spring, is measured in N/sec.

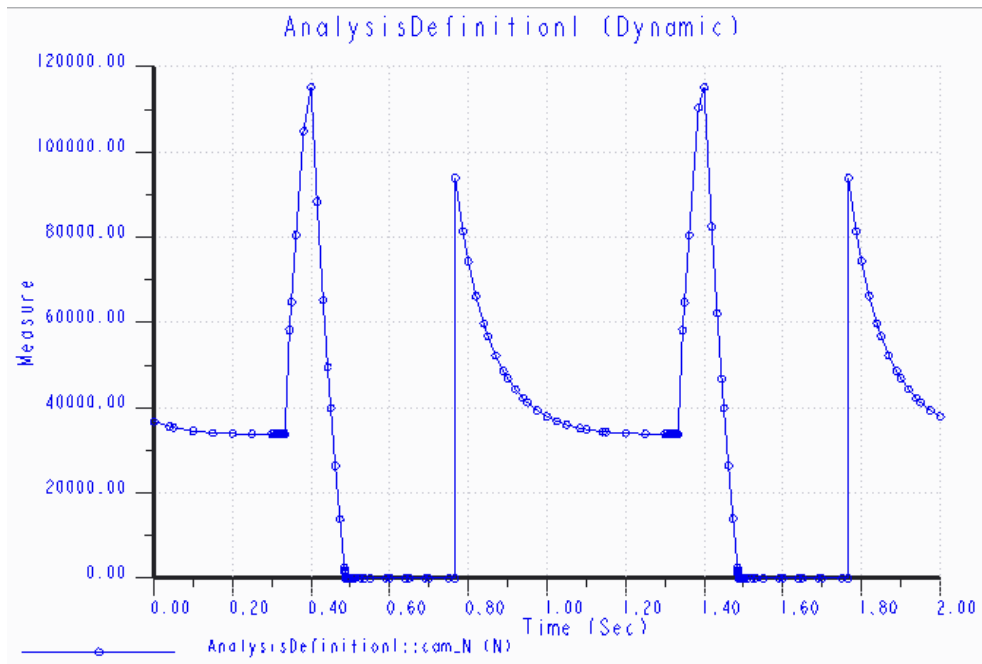


Figure 8. Dynamic Wheel Load (N/sec)

3.2. 1. Verification of the Crea Model by Mathematical Methods

Technical features of the vehicle, belongs to six-wheel land vehicle. In case of a total loading of 21 tons, the static load affecting our axle, would be 34146 N. As different loading conditions occur around middle axle and the centre of gravity, middle axle values were used in the operations. In Figure 9, static axle load for a single wheel, is shown.



Figure 9. Static axle load (for a single wheel)

Motor	: 1600Nm (max. torque)
Transmission	: 1:3.49 (1st Gear)
Wheel	: Ø1180, Rs=555mm, Rd=575mm, Nr=4250kg, Pr=95N/cm ² , P1=95N/cm ²

Axles : 3480kg, Unspringed mass 250kg.

During the vehicle movement, dynamic forces affect the wheels through contact points. For the analysis of axle conveyor, the use of these dynamic forces, is essential. Dynamic loads are calculated by the multiplication of the static loads affecting the axle, with the coefficients acquired in accordance with the static force and wheel features for per wheel regarding to the curves obtained experimentally. While time resistance is analyzed, the situations in which sudden overloading conditions occur, are taken into consideration. When the vehicle clears the bump, an excessive load coming from the road, affects the contact point of the wheel.

The condition of wheel being on a straight road, the compression of spring when the vehicle clears the bump of 20cm, and the force transferred to the ground, were calculated; and when the graphic results in the Crea was analyzed, it was observed that the values were compatible. In Figure 10, the acceleration in the vehicle, is shown.

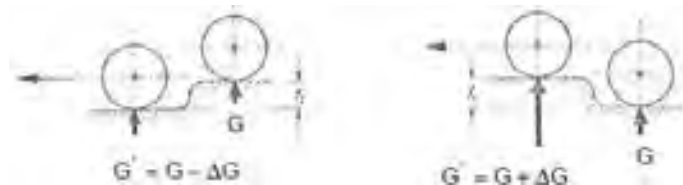


Figure 10. Acceleration in the vehicle

K: Spring Coefficient (N/cm)

F: Bump Height (cm)

G: Wheel Load (N)

$$G' = G \pm \Delta G$$

$$G' = G + K x f$$

$$G' = 34146 + 6050 x 20$$

$$G' = 155146 N$$

(1)

(2)

In Figure 11, the graphic related to the force transmitted by the wheel to the ground during the static equilibrium state of the vehicle, and the graphic related to the force that the vehicle applies on the ground when there is maximum spring compression, is shown.

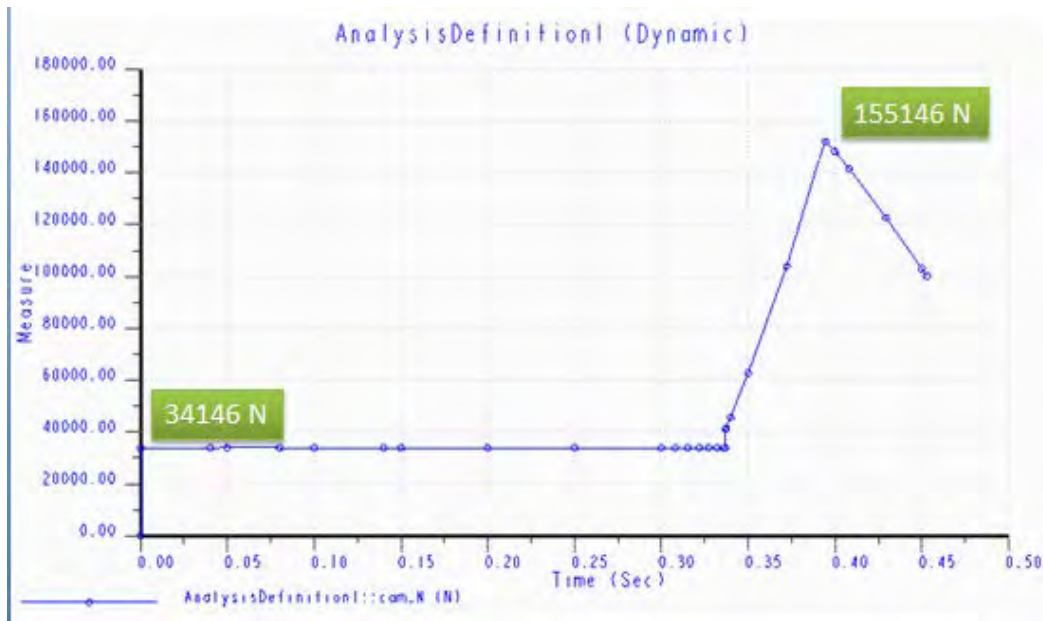


Figure 11. Creo static wheel load graphic (N/sec)

3.2.2 Transfer of Forces on the Parts

The transfer of forces that we acquired in dynamic analysis, on the parts, is shown in Figure 12. The loading was carried out by means of arm connections. Force values are shown in Table 4.

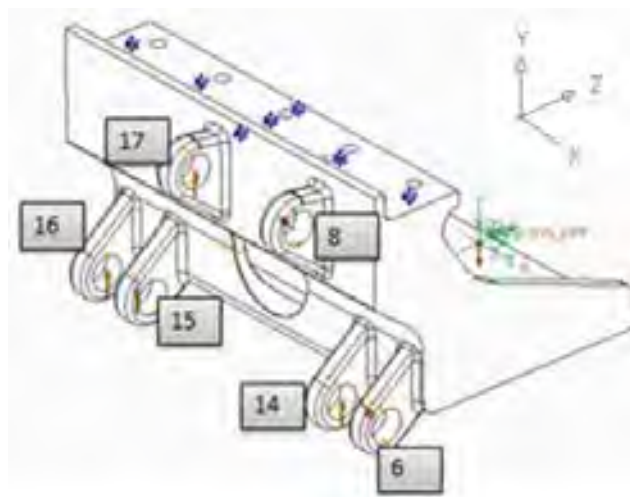


Figure 12. Visual positions of forces

Table 4. Force Values (N)

FORCE	X	Y	Z
6	-65694,7 N	-147245 N	262365 N
14	0 N	17129,3 N	0 N
15	0 N	17129,3 N	0 N

16	0 N	17129,3 N	0 N
8	67292 N	-26083,5 N	-206057 N
17	570,81 N	168801,3 N	0 N

Stress and displacement values are given in Figure 13. And in Figure 14, stress values related to maximum and critical points on the part, are marked. Because the values are over the resistance of materials, an optimization will be carried out on the part, thus, stress values can be reduced 390 MPa.

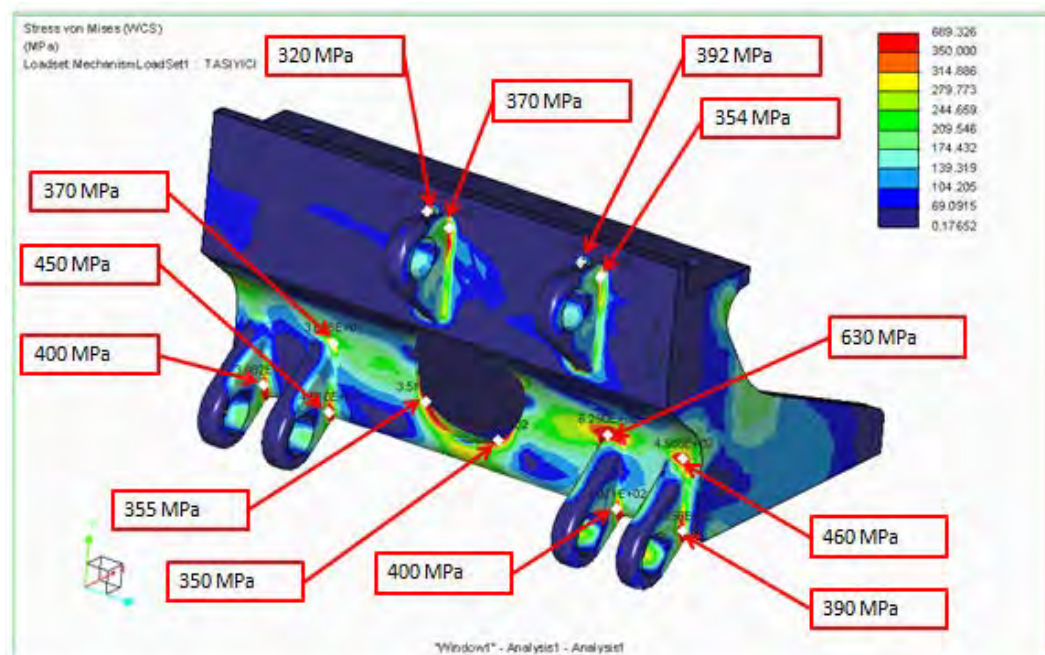


Figure 13. Stress values composed as a result of the analysis

Displacement Mag (WCS)
(mm)
Deformed
Max Disp 9.2316E-01
Scale 6.3694E+01
Loadset:MechanismLoadSet1 : TASIYICI

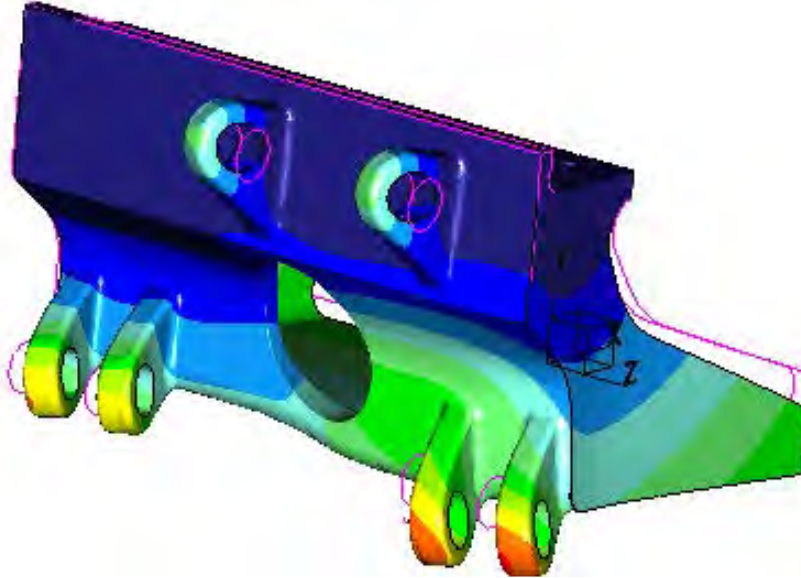


Figure 14. Displacement values composed as a result of the analysis

4. CONCLUSION

As a result of this study, the following outcomes have been reached;

- After all the necessary recognitions had been completed, dynamic analyses were carried out by the Creo program and forces were obtained
- The accuracy of the forces obtained by the Creo program, was proven by mathematical methods.
- A static analysis was carried out using these forces, and it was determined that the stress values acquired, were under the yield point, 390Mpa, of the part.

REFERENCES

- [1]. J.E.,Hartka, "Advanced Suspension System for Tracked Combat Vehicles", Institute for Defense Analysis, IDA Paper P-3448, August 1998, USA.
- [2]. E., Yaz, "Tam Araç Modeline Uygulanan Değişken Sönümlü Yarı-Aktif Askı Sisteminin Optimizasyonu", Yüksek Lisans Tezi, Gazi Üniversitesi, Fen Bilimleri Enstitüsü, Ankara, Haziran 2006
- [3]. H., Wang, Q., Rui, X., He, "The prediction technology study of fatigue life for key parts of tracked vehicle systems", Journal of Academy of Armored Force Engineering, 20(1), sf: 44-47, 2006.
- [4]. MA., Zheng-Dong, N.C., Perkins, "A track-wheel-terrain interaction model for dynamic simulation of tracked vehicles", Vehicle System Dynamics, Vol:37, No:6, sf:401-421, 2002.
- [5]. N. S., Kuralay, "Motorlu Taşıtlar Temel ve Tasarım Esasları, Yapı Elemanları, Cilt 1, Maimne Mühendisleri Odası, İzmir.

EFFECT OF HEAT TREATMENT ON THE MECHANICAL PROPERTIES, COLOR CHANGE AND DIMENSIONAL STABILITY OF FIR WOOD

Hamiyet ŞAHİN KOL

Karabuk University Faculty of Forestry Forest Industrial Engineering Department, Karabuk/TURKEY,
hsahinkol@karabuk.edu.tr

Yusuf SEFİL

İzzet Baysal Vocational and Technical High School, Bolu/TURKEY,
yusuf_gardas@hotmail.com

Sema AYSAL

Corresponding author: Karabuk University Faculty of Forestry Forest Industrial Engineering Department,
Karabük/TURKEY, semaaysal@karabuk.edu.tr

Abstract

*Heat treatment alters chemical, physical, and mechanical properties of wood. In this study, some mechanical and physical properties of heat treated fir (*Abies nordmanniana* subsp.) wood at temperatures 170, 180, 190, and 212 °C for 2 h with ThermoWood method were determined. The results were compared with kiln-dried reference samples. As a result, due to the increasing of heat treatment temperature, as the bending strength (MOR) was decreasing, the compression strength parallel to the grain and modulus of elasticity increased. Also when the treatment temperature increased, equilibrium moisture content decreased. It was seen that a significant increase of dimensional stability.*

Keywords: Heat treatment, Thermowood, Physical properties, Mechanical Properties, Fir Wood

1. Introduction

Wood as a raw material has been used for centuries for indoor and outdoor applications. Recently, with an increasing environmental awareness, use of heat treated wood material, that produced in order to increase the lifetime of the scarce resource of wood products with an environmentally friendly method, has been increased. Heat treatment of wood is an effective method to improve dimensional stability and durability of wood without any toxic chemicals.

There are four different heat treatment methods of wood that are common: The Finnish process (ThermoWood) uses steam, German method (OHT-Oil Heat Treatment) heated oil, the Dutch method (Plato Wood) uses a combination of steam and warm air and the French processes (Rectification and Bois Perdure) an inert gas (Esteves et al., 2008; Rapp, 2001). The thermowood process is known as the most successful method in Europe (Boonstra, 2008).

Heat treated wood has several application fields such as exterior cladding, window and door joinery, paneling, garden furniture, sauna furniture, flooring and decking etc. (Yıldız et al., 2006; Özçifçi et al., 2009; Viitaniemi, 2000). The mechanical properties of heat treated wood are essential for the performance of wood products in these kind of applications. The mechanical properties of wood such as modulus of rupture (MOR) and modulus of elasticity (MOE), compression resistance parallel to the grain are important where the load-bearing capacity is needed. Besides all these in the humid conditions like saunas, bathrooms and garden furniture dimensional stability of wood is significant. Therefore these properties of wood have been mostly studied by the researchers.

Several studies showed that heat treatment of wood improves physical properties of wood by reducing hygroscopicity and improving dimensional stability (Yıldız et al., 2006; Viitaniemi, 1997; Santos, 2000). But in addition to these desired properties, heat treatment also causes negative effects like reduced mechanical properties (Cao et al., 2012; Yıldız et al., 2006; Esteves et al., 2007a,b; Shi et al., 2007).

The amount of the change in the mechanical properties of wood during heat treatment depends on some factors such as process type, the maximum temperature reached in the process, and the holding time at that temperature (Shi et al., 2007). In addition to, in all cases of thermal treatment, the changes on the mechanical properties of wood depends on the chemical composition of the material used (Windeisen et al., 2007).

Fir (*Abies bornmülleriana*) is the main wood species naturally grown and commonly used in the forest products industry in Turkey. Therefore it is the potential wood species for industrial-scale heat treatment. The main objective of this study is to provide some information about the mechanical and physical properties of heat-treated *Abies bornmülleriana* using the ThermoWood process in various temperatures.

2. Material and Method

Wood species

The data used in this study have been collected within a larger project to assess the physical and mechanical properties of heat-treated Fir (*Abies bornmulleriana* Mattf.). The sample trees used for the present study were obtained from the Bolu Forestry Departments. With the aim of avoiding from errors during sampling, extreme cases were taken into account such as excessively knotty trees and containing reaction wood or slope grain. Sections with 2 m length were cut between 1.30 and 3.30 m height of trees to obtain samples for tests. The planks chosen for experiments were cut from the sapwood region of the sections with 2 m length and planed on four sides to form a cross section of 25-140 mm². Prior to heat treatment process, the material was dried using a conventional warm air kiln drying approximately at a temperature of 70 °C to a moisture content of 11–15%. The second selection of the raw material was performed at this stage. The density and moisture content of the planks, conditioned at room temperature and 65% relative humidity (RH), were measured and 20 planks with a small variation in density from each species were selected for further experiments. Then these 2 m long planks were split from the middle and cut into five 40 cm long pieces and the other halves of these 20 test planks were left as a reference material (later also called untreated control which was dried at conventional warm air kiln drying temperature of 70 °C) and the other halves were heat-treated under steam at five different temperatures according to Figure 1. Thus, the kiln-dried materials were divided into six subgroups, five of which were to be heat-treated under steam at five different temperatures (later also called treated samples) and one of which was left untreated (later also called untreated control).

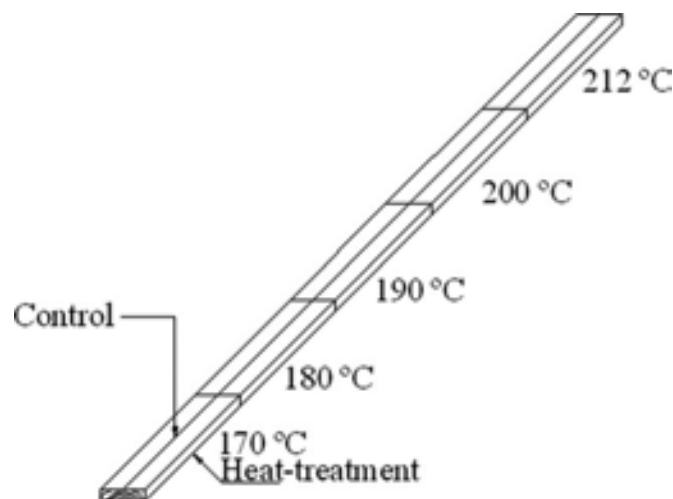


Figure 1. Descriptions of the wood materials used in tests.

Heat treatment

Kiln-dried planks (2,5 cm thickness, 7 cm width, and 40 cm long) were subject to heat treatment using various schedules. Heat treatment was carried out under accurate conditions under steam with a laboratory kiln from Nova ThermoWood in Gereede, Turkey. Steam is used during the drying and heat treatment as a protective vapor. Protective gas prevents the wood from burning and also affects the chemical changes taking place in wood. According to desired end-use of the material, the heating temperature can vary between 170 °C and 215 °C with treatment time 2-3 h. The heat treatment was applied according to the method described

in the Finnish ThermoWood Handbook. At first, the temperature of the kiln was raised near to 100 °C. When the temperature inside the wood had risen to near the same temperature, the raising of the kiln temperature was carefully continued to the actual treating temperature. The target temperatures were 170, 180, 190, 200, and 212 °C. The time of thermal modification at the target temperature was 2 h in every test run. After the heat-treatment phase, the temperature was lowered to 80 to 90 °C using water spray system. Conditioning was carried out to moisten the heat treated wood and bring its moisture content to 4–7%. After heat treatment, only the planks that were free of defects were selected for further testing.

Determination of the degree of thermal modification:

The weight loss that occurred by heat treatment was determined. Firstly the planks were conditioned to a constant weight then weighed before and after the heat treatment.

Weight loss (%), WL was calculated according to equation below;

$$WL = \frac{W_{ut} - W_t}{W_{ut}} * 100 \quad (1)$$

where, W_u is the weight of the sample before the heat treatment (g); W_t is the dry weight of the sample after the heat treatment (g).

Dry weight (g), W_{dry} , was calculated according to the equation below;

$$W_{dry} = 100 * \frac{W_u}{u + 100} \quad (2)$$

where, W_u is the weight of the sample at moisture content u (g); u is the moisture content of the sample (%).

The tests were carried out according to Turkish Standards (TSE) and 20 replicates were used in each test for treated and untreated fir. The properties were determined based on the specimens with dimension of 2x2x3 cm for equilibrium moisture content (TS 2471), 3x3x1,5 cm for anti-shrink efficiency (ASE1) and anti-swelling efficiency (ASE2) (radial, tangential and volumetric according to TS 4086), 2x2x3 cm for compression strength parallel to grain (TS 2595), 2x2x30 cm for bending strength (TS 2474), 2x2x30 cm for modulus of elasticity in bending (TS 2478). The differences in properties of heat treated fir wood was provided by calculating the property difference between heat treated and untreated wood samples of the same species as a percentage of the untreated wood property according to the equation below:

$$D(\%) = \frac{M_{ut} - M_t}{M_{ut}} * 100 \quad (3)$$

Where, D (%) is difference of property (MOE, MOR, CS, Anti-Swelling and Anti-Shrinkage); M_{ut} is the mean value of untreated samples; and M_t is the mean value of the heat treated samples.

3. Result and Discussion

Generally, heat treatment improved some physical properties such as dimensional stability, equilibrium moisture content of wood (shown at Table 1) but reduces some mechanical properties such as bending strength (shown at Table 2).

Table 1. Changes on the some physical properties of fir wood with increasing temperature

Heat Treatment Temperature (°C)	Weight Loss after heat-treatment (%)	Equilibrium moisture content (%)	Volumetric swelling (%)	Volumetric shrinkage (%)	Tangential Swelling (%)	Radial Swelling (%)	Tangential Shrinkage (%)	Radial Shrinkage (%)
Cont	0	11,18 ± 0,40	14,30 ± 0,72	12,85 ± 0,47	9,95 ± 0,98	4,34 ± 0,62	9,04 ± 0,54	3,80 ± 0,47
170	1,7 ± 0,20	9,3 ± 0,41	13,13 ± 0,69	12,33 ± 0,60	9,13 ± 0,60	4,00 ± 0,36	8,86 ± 0,54	3,47 ± 0,60
180	1,8 ± 0,20	8,2 ± 0,65	11,26 ± 0,60	12,07 ± 0,38	7,98 ± 0,50	3,27 ± 0,23	8,83 ± 0,32	3,24 ± 0,38
190	2,5 ± 0,19	7,2 ± 0,66	10,57 ± 0,42	11,16 ± 0,48	7,48 ± 0,33	3,09 ± 0,25	8,16 ± 0,37	3,00 ± 0,48
200	2,8 ± 0,20	6,5 ± 0,49	9,87 ± 0,65	9,78 ± 0,29	6,94 ± 0,46	2,93 ± 0,31	6,96 ± 0,28	2,82 ± 0,29
212	5,4 ± 0,19	6 ± 0,55	9,56 ± 0,57	8,90 ± 0,26	6,73 ± 0,37	2,82 ± 0,30	6,21 ± 0,26	2,69 ± 0,26

Weight loss

The weight losses and some physical properties of the samples used in the tests are presented in Table I. The results showed that after the heat treatment the weight losses on the wood materials increased and the higher heat treatment temperature caused greater weight losses in the samples. It is clear that when the treatment temperature increased, the weight losses also increased correspondingly. It is stated that the minimum weight losses (1,7%) in Fir wood were in treated samples at 170 °C, maximum weight losses (5,4%) were in treated samples at 212 °C treatment temperature (Table I).

Similar results have been indicated by several authors (Seborg et al., 1953; Stamm, 1956; Rusche, 1973; Fung et al., 1974). Feist and Sell (1987) indicated that weight loss of beech wood was between 10-15% at temperature 180-200 °C. Then again in another study, spruce wood has 0,8% weight loss at 170 °C and at temperature 200 °C this rate became 15,5% (Fengel, 1966). Özçifçi et al. (2009) determined that heat treated yellow pine wood at various temperatures (150, 170, 190 °C) for 4 hours has a weight loss of about 1.22%, 2,14%, 3,43%. In the same study they found that the weight loss is increased with increased treatment time.

Equilibrium Moisture Content (EMC)

In the treated samples equilibrium moisture content decreased comparing with the control samples. With increasing temperature, the equilibrium moisture content was reduced. When the minimum decrease of the equilibrium moisture content was 19,5 % at 170 °C, the maximum decrease of the equilibrium moisture

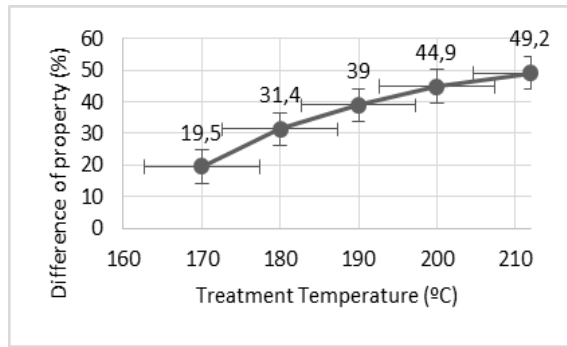


Figure 2. Increase rate of EMC of heat treated fir wood.

content was 49,2% at 212 °C (Table I). The reasons of the decreasing equilibrium moisture content could be degradation of hemicelluloses and amorphous zone of cellulose (Bhuiyan and Hirai, 2005; Tjeerdsma et al., 1998; Tjeerdsma and Militz, 2005; Esteves et al., 2007).

Anti-swelling efficiency (ASE₁)

ASE₁ of treated samples were increased compared with the control samples and with the increasing temperature, the ASE₁ of wood was also increased. When the minimum increase of the ASE₁ rate was 8,1% at 170 °C, the maximum increase of the ASE₁ was 33,1% at 212 °C (Figure 2).

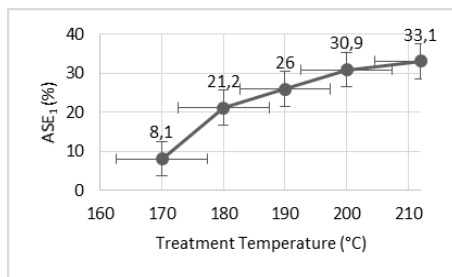


Figure 3. Increase rate of ASE₁ of heat treated fir wood.

Anti-shrink efficiency (ASE₂)

ASE₂ of treated samples were increased compared with the control samples and with the increasing temperature, the ASE₂ of wood also increased. The minimum increase of ASE₂ was 4,1 % at 170 °C, while the maximum increase of the ASE₂ was 30,7% at 212 °C .

Many studies show that the dimensional stability generally develops with the increasing treatment temperature and the treatment time. In addition that the treatment technique also effects the dimensional stability (Yıldız, 2002; Stamm et al., 1946; Kaygın et al., 2009; Akyıldız et al., 2009; Esteves et al., 2007b).

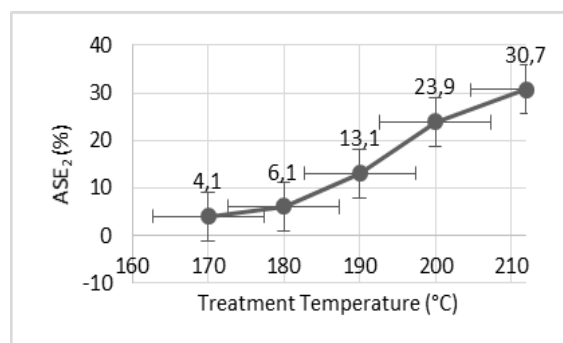


Figure 4. Increase rate of ASE₂ of heat treated fir wood.

Usually, degradation of wood starts apparently at a temperature of about 165°C (Stamm and Hansen, 1937) and hemicelluloses are more sensitive than the other components against to high temperature (Fengel and Wegener, 1984; Stamm, 1964). When wood is heated, the hemicelluloses begin to degrade, and this degradation process ends with the production of methanol, acetic acid and various volatile heterocyclic compounds, such as furans, γ -valerolactone, etc. (Hill, 2006). Chang and Keith (1978) reported that there is a relationship between volumetric shrinkage and weight loss of wood. The presence of free hydroxyl groups of wood polysaccharides has a significant effect on the absorption and desorption (Boonstra and Tjeerdsma, 2006). Heat treatment helps the reducing free hydroxyl groups (Pizzi et al., 1994). The reasons of the improvement of the dimensional stability may be carbohydrates and especially depolymerization of hemicelluloses that cause reducing of total amount of hydroxyl groups (Burmester, 1975; Kollman and Schneider, 1963). After heat treatment a large number of hydrophilic hydroxyl groups are reduced due to the replacement of hydrophilic oxygen-acetyl groups hence the dimensional stability is increased considerably (Cao et al., 2012).

Compression strength parallel to grain (CS)

The CS increased in heat treated Fir wood samples comparing to the control samples. When the minimum CS value of samples was 51,95 N/mm² at 170°C, the maximum value was 56,46 N/mm² at 212 °C (Table 2).

According to test results CS was enhanced 4,4% at 170°C and this increase continued to the temperature of 212°C. The similar test results are indicated in ThermoWood Handbook 2003 and also Şahin Kol (2010) indicated that CS increased by 4,2% for treated at 212°C pine wood and 17% for treated at 190°C fir wood. Boonstra et al. 2007 exposed the Scots pine samples 2 stages (first step hydrolysis at 165 °C for 30 min and second step curing at 180°C for 6 h) heat treatment. The CS was increased by 28% after treatment.

The reasons of increase of the compressive strength in longitudinal direction might be:

1. Decrease of amount of bound water in the heat treated wood - Reducing hydrogen bonding between organic polymers (cell wall constitutes) depends on the increased amount of bound water and it is concluded with decreasing of the strength properties of wood because the strength is not only connected with covalent bounds but also hydrogen intramolecular bounds (Fengel and Wegener, 1984).

2. Increase of the crystalline cellulose due to degradation and/or crystallization of amorphous cellulose (Boonstra, 2007),

3. Increase of cross linking of the lignin polymer network - improves the strength of the middle lamella which effects the strength properties of the cell wall (Boonstra, 2007),

4. Degradation of the hemicelluloses matrix (Boonstra, 2007).

There are also opposite results comparing to these results in the literature and according to the other studies the compression resistance reduced rate of 2%-32% (Schneider, 1973; Korkut, 2002; Unsal and Ayrılmış, 2005; Korkut et al., 2008; Yıldız et al., 2002). It might be also related to heat treatment method.

Table 2. Changes on the some mechanical properties of fir wood with increasing temperature

Heat Treatment Temperature (°C)	Compression resistance parallel to fibre (N/mm ²)	Bending Strength (N/mm ²)	Modulus of Elasticity (N/mm ²)
Control	49,78 ± 4,75	88,55 ± 6,71	9254,42 ± 1044,47
170	51,95 ± 1,37	86,19 ± 8,31	9964,7 ± 855,88
180	53,08 ± 1,40	84,66 ± 9,11	9668,61 ± 1258,78
190	55,10 ± 1,31	82,81 ± 9,35	9587,8 ± 947,41
200	56,04 ± 1,66	78,99 ± 9,50	9386,6 ± 987,54
212	56,46 ± 5,96	75,23 ± 16,19	9294,19 ± 2091,67

Bending strength (MOR)

Comparing with control samples, bending strength of treated samples was reduced. When the treatment temperature increased, the bending strength decreased, contrarily. When the minimum bending strength value of samples was 75,23 N/mm² at 212 °C, the maximum bending strength of samples was 86,19 N/mm² at 170 °C (Table 2).

According to test results MOR was reduced 2,7% at 170°C and this decrease continued to the temperature of 212°C. The maximum reduction was 15% at temperature of 212°C (Figure 5).

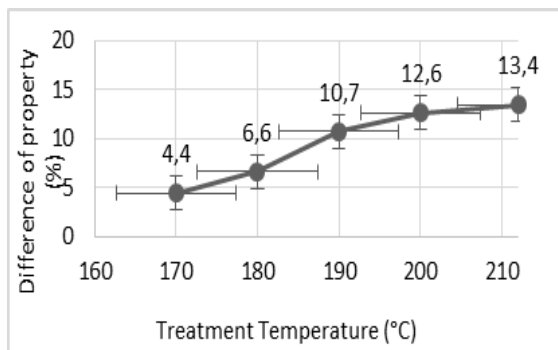


Figure 5. Increase rate of CS of heat treated fir wood.

In many studies it is clear that the heat treatment reduces the bending strength with the rates of 1-72% (Yıldız, 2002; Johansson and Moren, 2006; Esteves et al., 2007a; Esteves et al., 2007b; Shi et al., 2007; Korkut, 2008; Korkut et al., 2008).

It is attributed that decrease in the bending strength is related to degradation of hemicelluloses. Because at lower treatment temperature, in cellulose and lignin neither depolymerization nor degradation are observed. Besides there is a positive relation between hemicelluloses content and bending strength (Sweet and Winandy, 1999; Winandy and Lebow, 2001; Winandy and Morell, 1993).

Modulus of elasticity (MOE)

Comparing with control samples, MOE of treated samples increased. When the treatment temperature increased, the MOE increased, simultaneously. The minimum MOE value of samples was 9294,19 at 212 °C while the maximum MOE of samples was 9964,7 at

170 °C (Table 2). There was a significant increase between control samples and the heat treated samples. But this increase has continued to decrease from temperature 170°C (6,2%) to 212°C (%0,4).

It is also similar in literature. Shi et al. (2007) found that there was an increase 17% in fir wood. Bekhta and Niemz (2003) indicated that the change of modulus of elasticity value was insignificant. According to Hillis and Rozsa (1978), the effects of higher temperature and longer treatment time on the MOE were explained and they indicated that because of wood consists of partially crystal micro fibrils and on a large scale hemicelluloses and lignin, when it is modified above a significant temperature, most of the amorphous polymeric components may convert their glassy structures to elastic. At the conversion temperature from glassy structure to elastic, particular polymers have enough energy that reduces the mutual gravitational forces. Thus the wood polymers can be converted to elastic or mostly plastic construction.

Recognizable increase in the modulus of elasticity might be based on increasing of the relative cellulose content after heat treatment although the hemicelluloses degraded. Lower moisture content of treated wood than control also effects the modulus of elasticity (Boonstra, 2007).

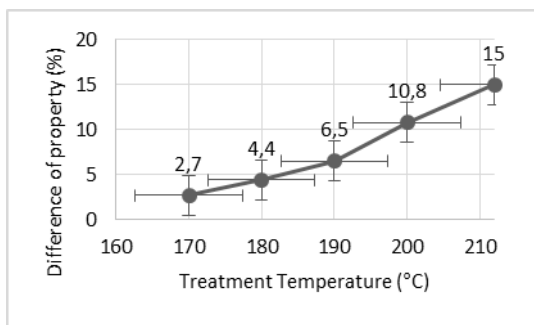


Figure 6. Decrease rate of MOR of heat treated fir wood.

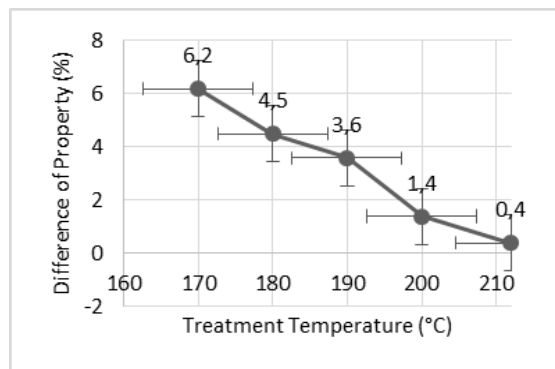


Figure 7. Increase rates of the MOE compared with the control samples

4. Conclusions

The results of this study indicated that the compression resistance values of fir wood were increased with increasing temperatures which is the similar with literature. Bending strength values were reduced after heat treatment comparing with control. By this thermal modification, some mechanical properties of wood are reduced, but the most important property of heat treated wood compared to untreated wood is reducing the equilibrium moisture content of the treated wood and as a consequence of this shrinkage and swelling of the wood is also reduced without using any water repellents.

References

- Akyildiz, M. H., Ates, S., & Özdemir, H. (2009): Technological and chemical properties of heat-treated Anatolian black pine wood. *African Journal of Biotechnology*, 8(11).
- Bekhta, P., & Niemz, P. (2003): Effect of high temperature on the change in color, dimensional stability and mechanical properties of spruce wood. *Holzforschung*, 57(5), 539-546.
- Bhuiyan, T. R., & Hirai, N. (2005): Study of crystalline behavior of heat-treated wood cellulose during treatments in water. *Journal of Wood Science*, 51(1), 42-47.
- Boonstra, M. (2008): A two-stage thermal modification of wood. Ph.D. Thesis in Applied Biological Sciences: Soil and Forest management. Henry Poincare university- Nancy, France.
- Boonstra, M. J., & Tjeerdsma, B. (2006): Chemical analysis of heat treated softwoods. *Holz als Roh- und Werkstoff*, 64(3), 204-211.
- Boonstra, M. J., Van Acker, J., Tjeerdsma, B. F., & Kegel, E. V. (2007): Strength properties of thermally modified softwoods and its relation to polymeric structural wood constituents. *Annals of forest science*, 64(7), 679-690.
- Burmester, A. (1975): The dimensional stabilization of wood. *Holz als Roh- und Werkstoff*. 33 (9), 333-335.
- Cao, Y., Lu, J., Huang, R., & Jiang, J. (2012): Increased dimensional stability of Chinese fir through steam-heat treatment. *European Journal of Wood and Wood Products*, 70(4), 441-444.
- Chang, C. I., & Keith, C. T. (1978): Properties of heat-darkened wood: II. Mechanical properties and gluability.
- Chow, S. Z. and Mukai, H. N. (1972): Effect of thermal degradation of cellulose on wood polymer bonding. *Wood Science*. 4(4), 202-208.
- Esteves, B., Domingos, I., & Pereira, H. (2008): Pine wood modification by heat treatment in air. *BioResources*, 3(1), 142-154.
- Esteves, B., Marques, A. V., Domingos, I., & Pereira, H. (2007): Influence of steam heating on the properties of pine (*Pinus pinaster*) and eucalypt (*Eucalyptus globulus*) wood. *Wood Science and Technology*, 41(3), 193-207.
- Feist, W. C., & Sell, J. (1987): Weathering behaviour of dimensionally stabilized wood treated by heating under pressure of nitrogen gas. *Wood Fiber Sci*, 19(2), 183-195.
- Fengel, D. (1966): On the changes of the wood and its components within the temperature range up to 200 °C-Part III: Thermally and mechanically caused structural changes in spruce wood. *Holz als Roh- und Werkstoff*, 24(11). 529-536.
- Fengel, D., & Wegener, G. (Eds.). (1983): *Wood: chemistry, ultrastructure, reactions*. Walter de Gruyter.
- Finnish Thermo Wood Association. (2003): *Thermo Wood Handbook*. Helsinki, Finland.

- Fung, D. P. C., Stevenson, J. A. and Shields, J.K. (1974). The effect of heat and on the dimensional and anatomical properties of Douglas fir. *Wood Science*, 7(1): 13-20.
- Hill CAS (2006): *Wood modification: chemical, thermal and other processes*. Wiley, New York.
- Hillis, W. E., & Rozsa, A. N. (1978): The softening temperatures of wood. *Holzforschung-International Journal of the Biology, Chemistry, Physics and Technology of Wood*, 32(2), 68-73.
- Johansson, D., & Morén, T. (2006): The potential of color measurement for strength prediction of thermally treated wood. *Holz als Roh-und Werkstoff*, 64(2), 104-110.
- Kaygin, B., Gunduz, G., & Aydemir, D. (2009): Some physical properties of heat-treated Paulownia (*Paulownia elongata*) wood. *Drying Technology*, 27(1), 89-93.
- Kol, H. S. (2010): Characteristics of heat-treated Turkish pine and fir wood after ThermoWood processing. *Journal of Environmental Biology*, 31, 1007-1011.
- Kollmann F., Schneider A., (1963): Über das Sorptionsverhalten wärmebehandelter Hölzer, *Holz Roh- Werkst.* 41 87–94.
- Kollmann, F., & Schneider, A. (1963): Über das sorptionsverhalten wärmebehandelter Hölzer. *Holz als Roh-und Werkstoff*, 21(3), 77-85.
- Korkut, S. (2008): The effects of heat treatment on some technological properties in Uludağ fir (*Abies bornmuelleriana* Mattf.) wood. *Building and environment*, 43(4), 422-428.
- Korkut, S., Kök, M. S., Korkut, D. S., & Gürleyen, T. (2008): The effects of heat treatment on technological properties in Red-bud maple (*Acer trautvetteri* Medw.) wood. *Bioresource Technology*, 99(6), 1538-1543.
- Mitsui, K. (2006): Changes in color of spruce by repetitive treatment of light-irradiation and heat treatment. *Holz als Roh-und Werkstoff*, 64(3), 243-244.
- Özçifçi, A., Altun, S., & Yapıcı, F. (2009): Effects of heat treatment on technological properties of wood. In *5th International Advanced Technologies Symposium (IATS'09)*, May (pp. 13-15).
- Pizzi, A., A. Stephanou, M.J. Boonstra and A.J. Pendlebury. (1994): A new concept on the chemical modification of wood by organic anhydrides. *Holzforschung*, 48, 91-94.
- Rapp, A.O. (2001): Review of heat treatment of wood. In: *Proceedings of COST E22 Environmental optimisation of wood protection*. Antibes, France. p. 6.
- Rusche, H.(1973): Thermal degradation of wood at temperatures up to 200 C. part II. reaction kinetics of loss of mass during heat treatment of wood. *Holz als Roh-und werkstoff*, 31 (8).
- Santos, J.A. (2000): Mechanical behavior of Eucalyptus wood modified by heat. *Wood Sci. Technol.*, 34, 39-43.
- Schneider, V. A. (1973): Investigations on the convection drying of lumber at extremely high-temperatures. *Holz Roh-U. Werkstoff*, 31,198–206

- Seborg, R. M., Tarkow, H., & Stamm, A. J. (1953): Effect of heat upon the dimensional stabilisation of wood. *Journal Forest Products Research Society*,3(9).
- Shi, J. L., Kocaefe, D., & Zhang, J. (2007): Mechanical behaviour of Quebec wood species heat-treated using ThermoWood process. *Holz als Roh-und Werkstoff*, 65(4), 255-259.
- Stamm, A. J. (1964): *Wood and cellulose science*. Wood and cellulose science. USA.
- Stamm, A. J., & Hansen, L. A. (1937): Minimizing wood shrinkage and swelling Effect of heating in various gases. *Industrial & Engineering Chemistry*, 29(7), 831-833.
- Stamm, A. J., Burr, H. K., & Kline, A. L. (1946): Heat stabilized wood (staybwood). Forest Products Laboratory, Madison, USA. 1-7.
- Sweet, M. S., & Winandy, J. E. (1999): Influence of degree of polymerization of cellulose and hemicellulose on strength loss in fire-retardant-treated southern pine. *Holzforschung*, 53(3), 311-317.
- Tjeerdsma, B. F., & Militz, H. (2005): Chemical changes in hydrothermal treated wood: FTIR analysis of combined hydrothermal and dry heat-treated wood. *Holz als Roh-und Werkstoff*, 63(2), 102-111.
- Tjeerdsma, B. F., Boonstra, M., Pizzi, A., Tekely, P., & Militz, H. (1998): Characterisation of thermally modified wood: molecular reasons for wood performance improvement. *Holz als Roh-und Werkstoff*, 56(3), 149-153.
- TS 2471 (1976): Wood, Determination of Moisture Content for Physical and Mechanical Tests, TSE. Ankara.
- TS 2474(1976): Wood-determination of ultimate strength in static bending. TSE. Ankara.
- TS 2478 (1976): Wood-determination of modulus of elasticity in static bending TSE, Ankara.
- TS 2595(1976): Wood-determination of ultimate stress in compression parallel to grain. TSE, Ankara.
- Unsal, O., & Ayrimis, N. (2005): Variations in compression strength and surface roughness of heat-treated Turkish river red gum (*Eucalyptus camaldulensis*) wood. *Journal of Wood Science*, 51(4), 405-409.
- Viitaniemi, P. (1997): ThermoWood – Modified wood for improved performance. In: Proceedings of wood the ecological material the 4th Euro-wood symposium. Stockholm, Sweden. Sep 22-23 1997 Tratek Rapport. 9709084. pp. 67-69.
- Viitaniemi, P. (2000): New properties for thermally-treated wood. *Indust Horizons*. March, 9.
- Winandy, J. E., & Lebow, P. K. (2001): Modeling strength loss in wood by chemical composition. Part I. An individual component model for southern pine. *Wood and Fiber Science*, 33(2), 239-254.
- Winandy, J. E., & Morrell, J. J. (1993): Relationship between incipient decay, strength, and chemical composition of Douglas-fir heartwood. *Wood and Fiber Science*, 25(3), 278-288.
- Windeisen, E., Strobel, C., & Wegener, G. (2007): Chemical changes during the production of thermo-treated beech wood. *Wood Science and Technology*,41(6), 523-536.
- Yildiz, S. (2002): Effect of heat treatment on water repellence and anti-swelling efficiency of beech. The International Research Group On Wood Preservation, Document No: IRG/WP 02-40222.

Yildiz, S., Gezer, E. D., & Yildiz, U. C. (2006): Mechanical and chemical behavior of spruce wood modified by heat. *Building and Environment*, 41(12), 1762-1766.

COMPARISON OF ENERGY AND EXERGY EFFICIENCY OF THE REFRIGERANTS INSTEAD OF R22 IN AIR-TO-AIR HEAT PUMPS

Fadime ŞİMŞEK

Kastamonu University, Department of Environmental Engineering, 31200, Kastamonu/Turkey.
fsimsek@kastamonu.edu.tr

Kemal ÇOMAKLI

Atatürk University, Department of Mechanical Engineering, 25100, Erzurum, , Turkey
kcomakli@atauni.edu.tr

Ömer ÇOMAKLI

Atatürk University, Department of Mechanical Engineering, 25100, Erzurum, Turkey
ocomakli@atauni.edu.tr

Abstract

The refrigerants instead of R22 limited usage due to the harmful effects of greenhouse and ozone layer has important area in the literature. The objective of this study is to investigate the usage of alternative refrigerants (R134a, R407C, R404A) instead of limited usage R22 and their performance in heat pump systems. It is investigated experimentally the effects of evaporator air inlet temperature (from 24 0C to 32 0C), evaporator air mass flow rate (from 0,58 kg/s to 0,74 kg/s), condenser air inlet temperature (from 24 0C to 32 0C), condenser air mass flow rate (from 0,57 to 0,73 kg/sn) on the coefficient of performance and exergetic efficiency values of vapor compression heat-pump system. As results, it was found that R134a has the highest COP values and R404A the lowest COP values at similar operating conditions at the heat pump system designed for R22. The COP values for R407C are found to be nearly equal to the COP values for R22 but a little less. Considering the experimental studies conducted; as it is the case for COP values, R134a had the highest exergy efficiency and R404A had the lowest exergy efficiency. So that exergy efficiency also changed as similar to COP values. The results show that these refrigerants can be used at the heat pump systems designed for R22.

Keywords: Alternative refrigerant, R22, Heat pump, COP

1. INTRODUCTION

The refrigerants used refrigerating systems, which have been needed in a number of fields in life from food preservation to the essentials of high life standards, are rapidly becoming more and more harmful to the upper stratosphere layer of the atmosphere and causing more global warming. There has been gradually increasing efforts aiming both to invent alternative refrigerants, which are applicable with slight modifications in existing cooling systems, and to obtain new refrigerants, which can work compatibly with new cycle models to be developed with new designs in classic systems in order to solve the rapidly-growing global warming problem.

It was determined in Molina and Rowland (1974) that halogenated hydrocarbons containing chlorine and bromine caused holes in ozone in the upper parts of the atmosphere (ODP) and displayed greenhouse effect (GWP); therefore, gradual elimination of halogenated hydrocarbons has been brought to agenda since that day. Within the framework of Montreal Protocol 1987 and London Conference 1992; production of CFC (chlorofluorocarbon) and HCFC (hydro-chlorofluorocarbon) refrigerants was restricted. In the signatory countries, production of CFC type refrigerants such as R11 and R12 was ended in 1996 and production of HCFC type refrigerants such as R22 is going to be ended in 2030 [1]. Due to the fact that the aforementioned refrigerants are going to be banned; studies aiming to obtain alternative refrigerants that can replace with those refrigerants in existing systems have gained more importance.

R22 is generally used as the refrigerant employed in heat pump applications and air conditioning. With the increasing concerns related to ozone layer, Montreal Protocol set a program to eliminate refrigerants containing R-22 and chlorine; which encouraged making vigorous efforts to find appropriate refrigerant for replacement. [2]. In recent years, a number of studies in literature related to performance and selection of new refrigerants, which are ozone-friendly and do not cause global warming in heat pump applications at low temperature, have been conducted in order to analyze heat pump performance with new refrigerants that could be an alternative for R22 in existing and new systems.

In a system, where HFC227, CFC114, and HFC134a were used as refrigerants, different condenser and evaporator temperatures were used. When it was operated with different refrigerants; the heat pump's COP and heating capacity were compared. Consequently, it was observed that HFC227 is a good refrigerant that is capable of operating at an evaporator temperature over 30°C. It was observed in the system where HFC 227 was used that the heating COP value ranged between 3.5 and 4.5 at a condensing temperature of 75°C. [3]. R22, R12, R134a, R410A, and R407C refrigerants were examined in a solar-aided heat pump. It was observed at the end of the examination that the COP of R12 was the highest COP after R22 and R134a; that the decrease in system performance is 2-4% at a collector temperature of 0-20°C when R12 is replaced with R134a; and that, among the mixture refrigerants, R410a – although not more efficient than R134a – is more efficient than both R404A and R407C. It was also observed that R410A refrigerant has 15-20% less COP compared to R134a [4]. In a vapour compression heat pump system where R22, R407C, and R134a are used; effect of primary variables on significant characteristics was investigated. Cabello et al., observed that compression rate increased with R22 compared to other refrigerants and that power consumption reduced. [5].

In a theoretical study examining the effects of refrigerants on ozone layer; it was stated that R134a and R401A were the appropriate ones among the refrigerants of R134a, R401A, R401B, R409A which were shown as alternatives for R12; that R404A was the appropriate one among the refrigerants of R402A, R402B, R408A, R404A and R507 which were shown as alternatives for R502; that R407C and R410A were the appropriate ones among the refrigerants of R407C, R410A, R404A and R507 which were shown as alternatives for R22; and that it would be more appropriate to use R123 refrigerant instead of R11 and R508B instead of R13. [6]. In the study examining HFC (R404A and R410A) and HC (R290) refrigerants for cooling at ambient temperature; it was observed that R410A is an environment-friendly alternative to replace with R22 in applications at ambient temperature. [7]. In an air-to-air heat pump; R22, R134a, R404A and R407C refrigerants were tested. COP of the heat pump, in which R134a was used, increased up to 4.5% compared to R22 and its capacity decreased by 37.8%. Once R407C was used in the heat pump; the capacity increased at the rate of 7.86% but COP decreased by 5.92% compared to R22. When the heat pump in which R404A refrigerant was used was compared to R22; a decrease was observed in COP and capacity. [8]. In a solar-aided heat pump system; R22, R717, and R744 were tested. It was determined that R711 was a more appropriate alternative for R22 in terms of overall performance and operation parameters and it required substantial modifications in heat pumps. Due to low critical temperature and high operational pressures; it was found that R744 was not suitable for solar-aided heat pumps. Furthermore, R290 and R1270 were presented as alternative for R22 [9]. In a water to water heat pump, R407C and R134a were used. Three stream methods were determined on the system. It was observed in all of the three methods that the performance of the system with R407c was higher than performance of the system with R134a in large

volume rates [10]. In a cooling system, R22 and R407C were used. When R407C's thermodynamic properties and general performance were compared with those of R22; it was observed that R407C's COP was lower at the rate of 5-17%. It was consequently concluded that the system required more electrical power when operated with R407C in comparison with R22 in order to meet the same cooling load. It was also observed that R407C's performance improved along with the increases in condenser and evaporator temperatures. [11]. In another system where R22 and R407C were used; R407C's performance got closer to performance of R22 as the evaporator temperature increased. However; the decrease in COP_c and evaporator capacity was caused by the decrease in evaporator temperature. [12]. R22 is generally used as the refrigerant employed in heat pump applications and air conditioning. With the increasing concerns related to ozone layer, Montreal Protocol set a program to eliminate refrigerants containing R-22 and chlorine; which encouraged making vigorous efforts to find appropriate refrigerant for replacement. [2].

In this study, the set up comprised of an air-to-air vapor compression heat pump, a scroll compressor, plate-fin air-cooled condenser, thermostatic expansion valve, a plate-fin air-cooled evaporator, electrical air heater in order to keep the air temperature passing into the evaporator and condenser at the desired level. As results, it was found that R134a has the highest COP values and R404A the lowest COP values at similar operating conditions at the heat pump system designed for R22. The COP values for R407C are found to be nearly equal to the COP values for R22 but a little less. The results show that these refrigerants can be used at the heat pump systems designed for R22. Considering the experimental studies conducted; as it is the case for COP values, R134a had the highest exergy efficiency and R404A had the lowest exergy efficiency. So that exergy efficiency also changed as similar to COP values.

2. EXPERIMENTAL

2.1. Materials

Table 1 illustrates characteristics of alternative refrigerants that could replace with R22 such as R134a, R404A, R407C. R407C is a zeotropic mixture containing HFC32 and HFC-125. R407C could replace with R22 as an interim solution in existing systems and current production sites until new methods are developed. R134a was classified as A1 by ASHRAE as (low poison, burn diffusionless). R134a has very good performance and heat transfer properties and a good alternative for screw and centrifugal compressors. The fact that it is accepted in automotive industry is related to its abundance. [13].

Table 1. Characteristics of R22 and alternatives of R22. [14,15,16].

Refrigerant	R22	R-134a	R404A	R407C
Composition (wt %)	-	-	R125/143a/134a (44/52/4)	R32/125/134a (23/25/52)
Molar mass (kg/kmol)	86.48	102.03	97.6	86.2
Boiling point at 1 atm (°C)	-40.80	-26.1	-46.5	-43.7
Freezing point (°C)	-160.00	-101	-118	
Critical temperature (°C)	96	101.06	72.1	86.05
Critical pressure (bar)	49.9	40.64	37.32	46.34
Critical density (kg/m ³)	513	508	488.5	512.7
Latent heat of vaporization (kJ/kg)	234.7	215.5	208.9	243.8
Ozone depletion potential(ODP)	0.055	0	0	0
Global warming potential(GWP)	1700	1300	3700	1600

2.2. Methods

The testing apparatus was designed as a heat pump that could operate in air-to-air, water-to-water, air-to-water, and water-to-air modes depending on the heat transfer refrigerants used in the evaporator and condenser. Data that were obtained from the heat pump's operation in air-to-air mode were assessed in this study.

Temperature and pressure of the working fluid were measured at several locations of interest, as shown in Figure 1.[17]. K-type chrome-nickel thermocouples were used to measure the temperatures of the working fluid and thermocouples were calibrated with a digital temperature controller. The working fluid temperatures were measured at the inlets and outlets of the evaporator, condenser and compressor. Six bourdon type

manometers were installed at the inlets and outlets of the condenser, compressor and evaporator to measure the pressures. Compressor input current was measured using an ampermeter.

Figure 2[18] shows a schematic diagram of the experimental set up. The main elements of a scroll compressor powered by a 1,5 HP, a plate-fin air-cooled condenser, thermostatic expansion valve, a plate-fin air-cooled evaporator and electrical air heater in order to keep the air temperature passing into the evaporator and condenser at the desired level. Sight glass is installed at the outlets from the evaporator to provide visual confirmation of the refrigerant state and other auxiliary equipments.

Before the commencement of the experiments; a leak check was applied on the system by using 15 bars of R22; and since it was observed that there was no change in manometer indicators after an adequate period of time, it was understood that there was no leaking. Then, the system was vacuumed and made free of foreign substance and moisture.

Flow rate of the refrigerant used in the system was measured by using a gas flowmeter. Water flow rates of the condenser and evaporator were measured by using flowmeters placed at the condenser and evaporator inlets. When experimental conditions were ensured; the system was operated for 1 hour until it reached to the stable regime. In the system that reached the stable regime; temperature and pressure values in the main points shown in Figure 2 were measured and followed up by a monitor. While flow rate of the refrigerant used in the system was measured by a gas flowmeter, water flow rates of the condenser and evaporator were measured by flowmeters placed at the condenser and evaporator inlets. After each experiment was completed; temperature values were recorded from the thermocouples; pressure values from the manometers; flow rates from the flowmeters; current and volt values into the compressor from the ampermeter. Air inlet temperatures of the condenser and evaporator were ensured by 5 heaters, each of which had a capacity of 1 kW, placed at the air channel inlet.

The compressor and the system were discharged in order to obtain basic performance results after the measurements were completed. Then, the system was charged with the refrigerant in order to test. This procedure was continued also for R404A, R407C, and R134a.



Figure 1. Schematic view of the production process

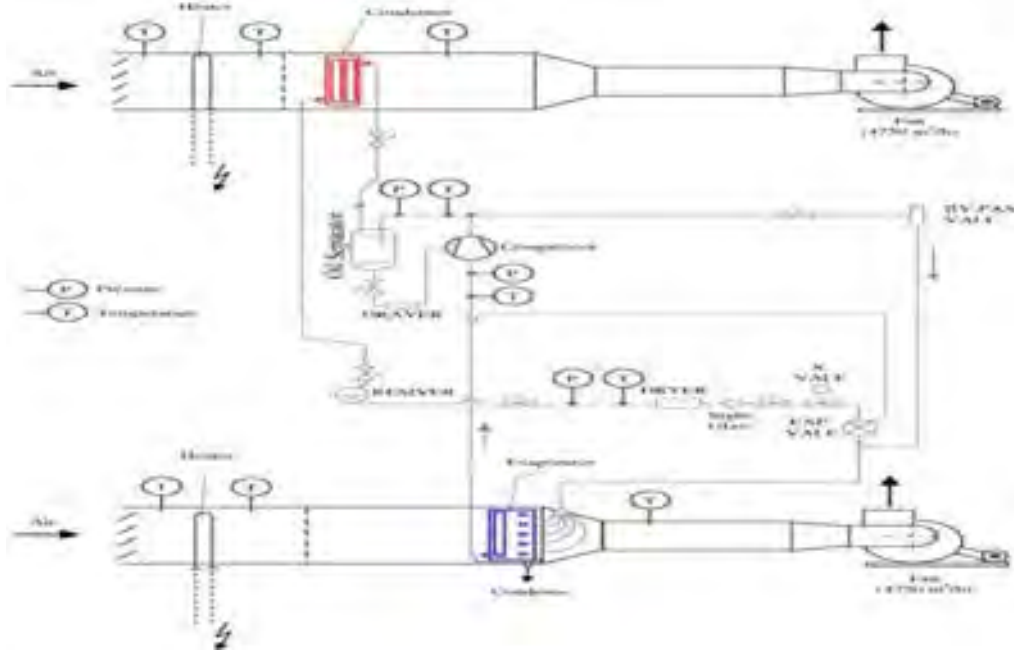


Figure 2. Schematic drawing of heat pump experiment system

2.3. Characterizations

Mass of the refrigerant measured on a precision balance; compressor inlet power measured by the wattmeter; air flow rate measured by the flowmeter; pressure values measured by the manometer and sensitive data containing temperatures measured by thermocouples were recorded following every experimental study. Energies that enter in and exit from the ideal heat pump cycle, primarily \dot{m}_r , which is the massive flow rate of the refrigerant circulating in air-to-air cycle, are explained as follows [18].

Compressor power;

$$\dot{W}_C = I.W.U.Cos\varphi.\sqrt{3} \quad (3.1)$$

Where U, I and Cos φ are voltage (V), current (A) and power factor, respectively. The power factor is measured from ammeter. The coefficient of performance (COP) for a heat pump cycle indicates the overall power consumption for a desired output and was evaluated using the following equation: Condenser capacity; in the event that heat transfer environment is air;

$$\dot{Q}_C = \dot{m}_r (T_{c.out} - T_{c.in}) \quad (3.2)$$

Evaporator capacity; in the event that heat transfer environment is air;

$$\dot{Q}_E = \dot{m}_r (T_{e.in} - T_{e.out}) \quad (3.3)$$

From the aforementioned values; COP of heat pump is found as;

$$COP_{IP} = \frac{\dot{Q}_C}{\dot{W}_C} \quad (3.4)$$

Exergetic efficiency is generally defined as:

$$\eta_{ek} = \text{Exergy outlet} / \text{Exergy inlet}$$

or;

$$\eta_{ek} = \frac{\dot{m}_r [h_{c.out} - h_{c.in} - T_o (s_{c.out} - s_{c.in})]}{\dot{W}_C + \dot{m}_r (h_{E.in} - h_{E.out} - T_o (s_{E.in} - s_{E.out}))} \quad (3.5)$$

2. .. SULTS AND DISCUSSION

COP values of pure refrigerants which were obtained as a result of the experiments conducted on the heat pump while condenser and evaporator refrigerants were in air-to-air mode and tested within the same operation range without making any modifications on system components were obtained as specified below. It is seen from Figure 3 that as evaporator air inlet temperature increased, COP values of all pure gases used increased even slightly; which indicates that COP value of the heat pump was considerably affected by the condenser air inlet temperature.

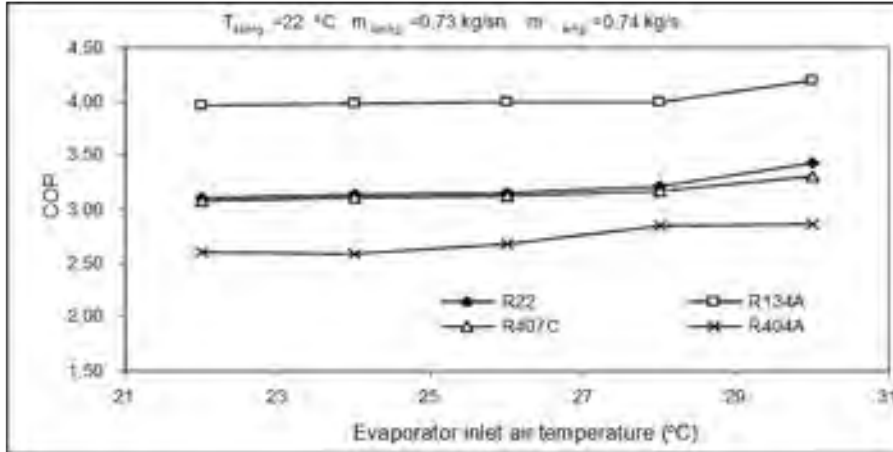


Figure 3. Alteration of performance coefficient for refrigerants depending on evaporator inlet temperature

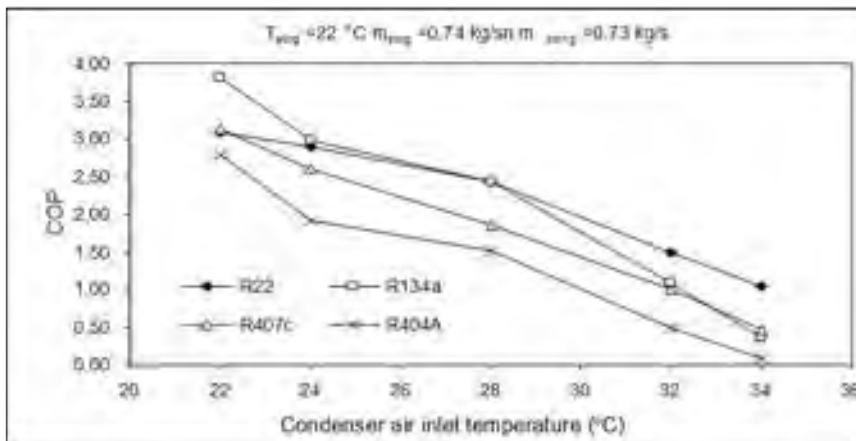


Figure 4. Alteration of performance coefficient for refrigerants depending on condenser air temperature

As it is seen in Figure 4; as condenser air inlet temperature increased, COP values of all pure gases used substantially decreased significantly. It was seen in all the refrigerants used in Figure 5 and Figure 6 that COP increased even slightly as evaporator and condenser air flow rate increased.

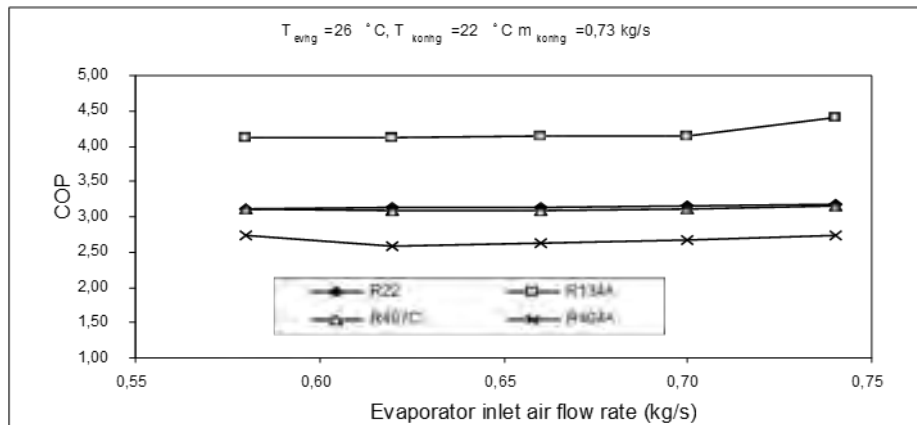


Figure 5. Alteration of performance coefficient for refrigerants depending on evaporator air flow rate

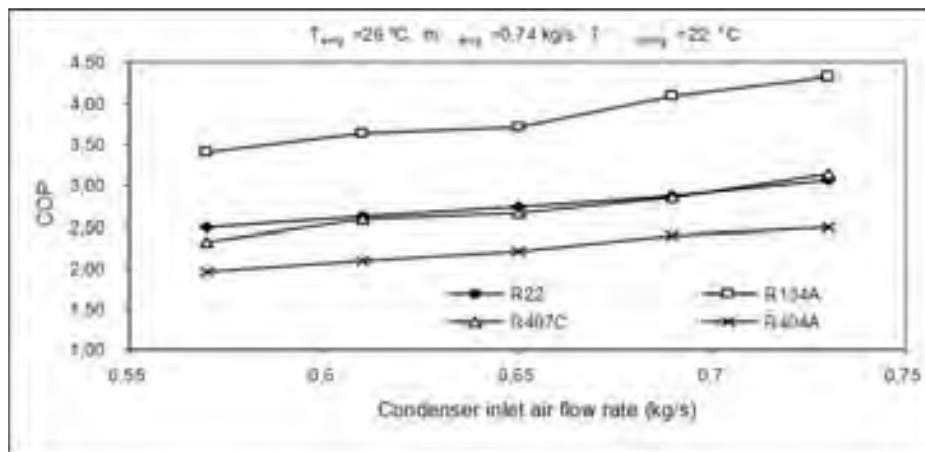


Figure 6. Alteration of performance coefficient for refrigerants depending on condenser air flow rate

Figure 7, Figure 8, Figure 9, and Figure 10 show alteration in exergy efficiencies of the refrigerants used in accordance with examined parameters. Considering experimental studies; it was observed that exergy efficiency changed in parallel with COP values.

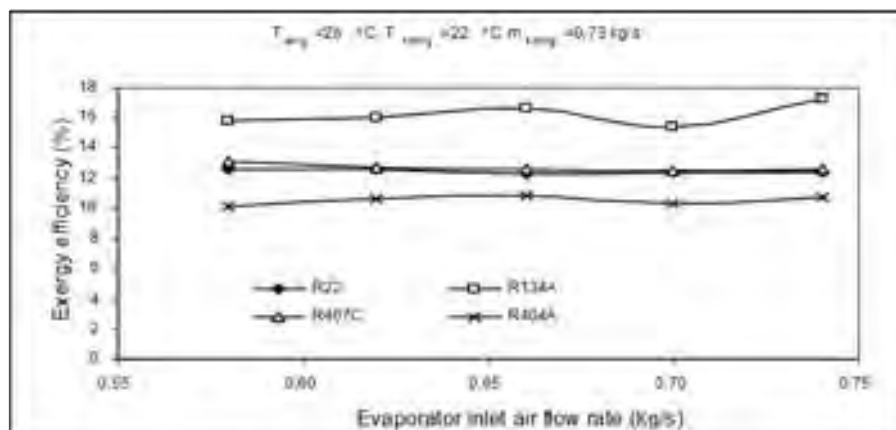


Figure 7. Alteration of exergy efficiency for refrigerants depending on evaporator air flow rate

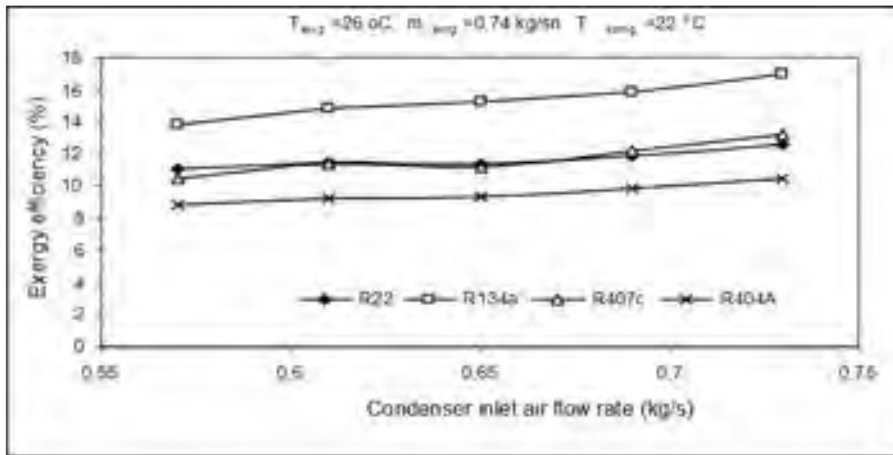


Figure 8. Alteration of exergy efficiency for refrigerants depending on condenser air flow rate

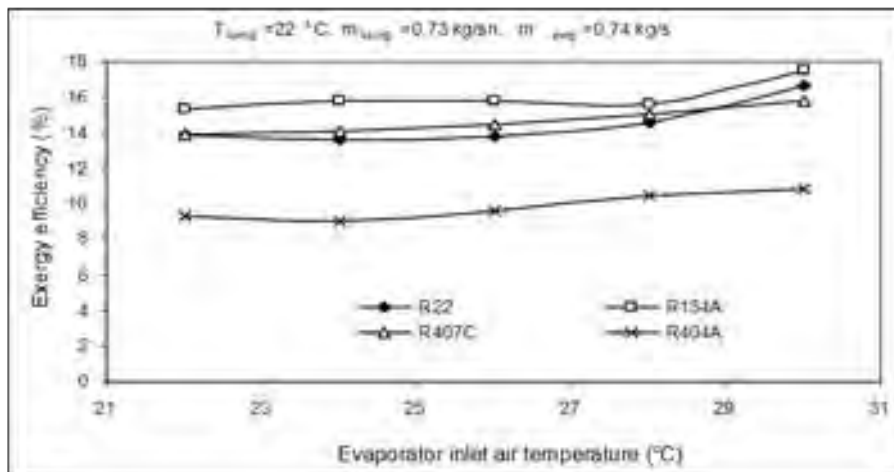


Figure 9. Alteration of exergy efficiency for refrigerants depending on evaporator air flow temperature

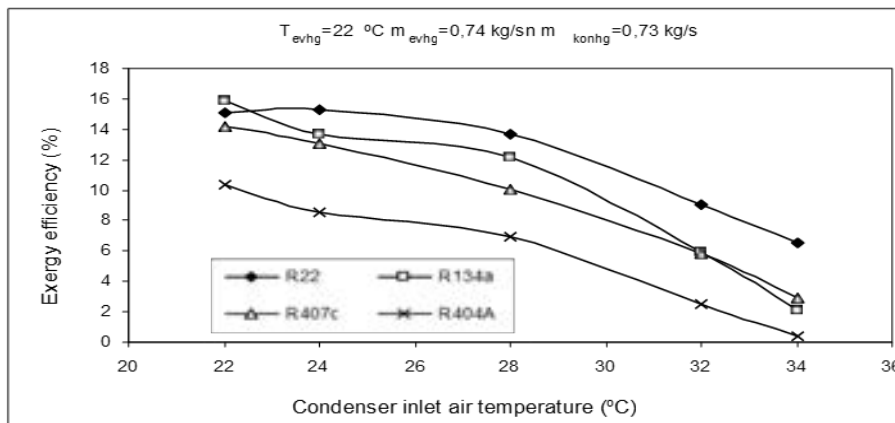


Figure 10. Alteration of exergy efficiency for refrigerants depending on condenser air flow temperature

4. CONCLUSIONS

1. Considering all of the experimental studies conducted when the heat pump was on air-to-air operation mode; while the highest COP value belonged to R134, the lowest COP value belonged to R404A. It was observed that the COP value of R407C was very close to R22 but slightly lower. Therefore, it was

determined that R134a, R407C and R404A could be administrated successfully without making any modification in a heat pump system which was installed for R22 and operated on air-to-air mode.

- Figure 11 illustrates comparison of the COP values of the pure refrigerants that were alternatives for R22 used in air-to-air heat pump with those of R22 refrigerant.

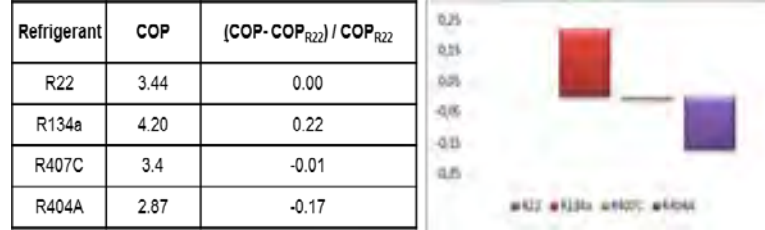


Figure 11. Comparison of the COP values of the pure refrigerants that are alternatives for R22 used in air-to-air heat pump with those of R22 refrigerant

- It was generally observed in all of the refrigerants used in the air-to-air heat pump system that COP increased even slightly with the increase in weld temperature; that COP decreased as condenser heat transfer refrigerant inlet temperature increased; and that COP increased even slightly as the air flow rate in condenser and evaporator increased.
- Considering the experimental studies conducted; as it is the case for COP values, R134a had the highest exergy efficiency and R404A had the lowest exergy efficiency. As it is seen from the figures; exergy efficiency also changed as similar to COP values.

ACKNOWLEDGMENTS

The authors wish to thank The Scientific Research Project Unit of the Atatürk University (Project number - 2005/16) and TÜBİTAK (Project number -105M030) for support.

REFERENCES

- D. Jung, H.J. Kim, O. Kim, "A study on performance of multi-stage heat pumps using mixtures," Int. J. Refrig., vol 22 (5), pp 402-413, 1999.
- M. Kim, "Performance evaluation of R22 alternative mixtures in a breadboard heat pump with pure cross-flow condenser and counter-flow evaporator," Energy, vol 27, pp 167-181, 2002.
- B. Rakhesh, G. Venkatarathnam, S.S.Murthy, "Performance comparison of HFC227 and CFC114 in compression heat pumps," Applied Thermal Engineering, vol 23, pp 1559-1566, 2003.
- F.B. Gorozabel, Chata, S.K. Chaturvedi, A. Almogbel, "Analysis of a direct expansion solar assisted heat pump using different refrigerants," Energy Conversion and Management, vol 46(15-16), pp 2614-2624, 2005.
- R. Cabello, E. Tornello, J.Navarro-Esbri, "Experimental evaluation of a vapour compression plant performance using R134a, R407c and R22 as working fluids," Applied Thermal Engineering, vol 24, pp 1905- 1917, 2004.
- A. Onat, M. İmal ve A.T. İnan, "Soğutucu akışkanların ozon tabakası üzerine etkilerinin araştırılması ve alternatif soğutucu akışkanlar," KSÜ Fen ve Mühendislik Dergisi, 7 (1), vol 32-38, pp 2004.
- M.W. Spatz, S. Motta, "An evaluation of options for replacing HCFC-22 in medium temperature refrigeration systems," International Journal of Refrigeration, vol 27 (5), pp 475-483, 2004.
- H. Wu, P. Shu, Y. Zhao, Z. Xing, "Experimental study on performance enhancement of heat pump with screw compressor. American Society of Mechanical Engineers," Advanced Energy Systems Division, vol 44, pp 453-459, 2004.
- C. Chaichana, L. Aye, W.W.S. Charters, "Natural working fluids for solar-boosted heat pumps," International Journal of Refrigeration, vol 26 (6), pp 637-643, 2003.
- L. Rajapaksha, K.O. Suen, "Influence of reversing methods on the performance of a reversible water-to-water heat pump", Applied Thermal Engineering, vol 23 (1), pp 49-64, 2003.

- [11]. A. Greco, "R407c as an alternative to R22 in vapour compression plant: An experimental study," *Int. Journal of Energy Research*, 21, 1087-1098, 1997.
 - [12]. B. Mongey, N.J. Hewitt, J.T. McMullan, "R407c as an alternative to R22 in refrigeration systems," *Int. Journal of Energy Research*, vol 20, pp 245-254, 1996.
 - [13]. Anonim, *Application Guide*, (2002). "Refrigerants", AG 31-007, McQuay International
 - [14]. A. Cavallini, "Working fluids for mechanical refrigeration, review paper," *Int. J. Refrig* 19(8), 485-96, 1996.
 - [15]. L. Mattarolo, "Refrigerants end environment protection. In :1," *Ulusal Soğutma ve İklimlendirme Sempozyumu*, İstanbul Turkey, 16-18 May, 51-70, 1990.
 - [16]. S. Karagöz, M. Yılmaz, O. Comaklı, O. Ozyurt, "R134a and various mixtures of R22/R134a as an alternative to R22 in vapour compression heat pumps," *Energy Conversion and Management*, vol 45, pp181-196, 2004.
 - [17]. F. Simsek, "Investigation of energy and exergy efficiency of heat pumps with zeotropic refrigerant mixtures," Ph. D. Thesis, Atatürk University Institute of Applied Sciences Department of Mechanical Engineering, Erzurum, 2009.
 - [18]. K. Comaklı, F. Simsek, O. Comaklı, B. Sahin, "Determination of optimum working conditions R22 and R404A refrigerant mixtures in heat pumps using Taguchi method," *Applied Energy*, vol 86, pp.2451-2458. 2009.
-

PRACTICING TRANSHUMANCE IN TURKEY: EXAMPLES OF PAST AND PRESENT

Binali ÇOMAKLI

Ataturk University, Faculty of Agriculture, Department of Agronomy, ERZURUM.
bcomakli@atauni.edu.tr

Mahmut DAŞCI

Ataturk University, Faculty of Agriculture, Department of Agronomy, ERZURUM.

Abstract

Yaylacilik is an agricultural activity, villagers move from permanent settlements to uplands with herd in certain periods of year, especially during warmer summer months. Traditional animal raising system, called yaylacilik in Turkish, is one of the best using of upland rangelands, particularly in rough terrain regions. This system is similarly practiced in other regions of the world, such as China, India, Canada, and Greece. In this system, domestic animals, such as sheep, goats, cattle, and horse are grazed on a rangeland around permanent settlements approximately until summer, and thereafter the herds are moved to upland pastoral areas until autumn. Animal owners move together with herds and live with their families in yayla (upland). The objective is to keep the animals in suitable conditions during hot summer periods and provide better quality forage for animals. But in recent years, livestock basis yaylacilik activities have decreased; only a few families in some regions continue to yaylacilik activity in Turkey. As a result of the reduction use of upland rangelands for yaylacilik activities, touristic activities have been started in this area.

Keywords: *Yayla, upland rangeland, yaylacilik activity, herd*

1. INTRODUCTION

Yaylacilik is an agricultural activity, villagers move from permanent settlements to uplands with herd in certain periods of year, especially during warmer summer months. Traditional animal raising system, called yaylacilik in Turkish, is one of the best using of upland rangelands, particularly in rough terrain regions. This system is similarly practiced in other regions of the world, such as China, India, Canada, and Greece ([1]; [2]; [3]; [4]). In this system, domestic animals, such as sheep, goats, cattle, and horse are grazed on a rangeland around permanent settlements approximately until summer, and thereafter the herds are moved to upland pastoral areas until autumn [5].

2. VEGETATIONS OF YAYLA RANGELANDS

Heavy grazing and grazing during wrong seasons are the most important rangeland degradation factors ([6]; [7]). The rangelands around the permanent settlements are heavily overgrazed and damaged by the impacts of grazing practices ([8]; [9]; [10]) but the condition of many nomadic or seminomadic pastoral areas is generally not so bad, and many rangelands can even be considered to be in good condition ([3]; [11]; [12]).



Figure 1. An example for upland rangeland vegetations

3. YAYLACILIK ACTIVITY

Seminomadic animal raising system was commonly employed in the highlands of Turkish lands since the beginning of its early history. Animal breeders graze their animals freely around permanent lower altitude settlements for approximately 1 month, from mid-April to mid-May. Thereafter, the settlement's animals are combined into herds and grazing is conducted regularly on the rangelands close to permanent settlements for 1 month from approximately May to June. In June, when the forage dries out on these rangelands due to dry summer conditions, animals are driven to a temporary settlement located on uplands (yayla) and animal owners move and live with their families there until September [5].

Each family let their animals graze freely around temporary individual settlements until all the animals arrive at the upland, which takes about 2-3 weeks [5] (Figure 2).



Figure 2. Freely grazed animals around the temporary settlements in yayla

Then, the settlement's animals are combined in herds and systematic grazing starts and continue until autumn (by the end of September). In this system, the rangelands around temporary settlements and water resources are exposed to more grazing pressure than the other sites. The duration of the grazing season in uplands is about 105 days, of which about 15 days is free at the beginning of the season and regular grazing under herds is 90 days.



Figure 3. Animals and owners moved to yayla with together and live in there until the end of yayla period

Animal owners move together with herds and live with their families in yayla (upland). The objective is to keep the animals in suitable conditions during hot summer periods and provide better quality forage for animals. But thousands of years of the traditional activity have not made in recently, only a few families in some regions continue to yaylacilik activity in Turkey. As a result of the withdrew of the using of upland rangelands for yaylacilik activity, touristic activities have been started in this area.

Due to the withdrawal from yaylacilik activity, most yayla areas are only used for animal grazing at last years.



Figure 4. An example for abandoned yayla in Turkey



Figure 5. Using of yayla area for recreational or touristic activity

REFERENCES

1. Chang, C. and A. Tourtellotte, *Ethnoarchaeological Survey of Pastoral Transhumance Sites in the Grevena Region, Greece*. J. Field Archae. Vol. 20, 249-264. 1993.
2. Smith, P.E.L., *Transhumance Among European Settlers in Atlantic Canada*. The Geograp. J. 161:79-86. 1995.
3. Miller, D.J., *Nomads of the Tibetan Plateau Rangelands in Western China-Part Three: Pastoral Development and Future Challenges*. Rangel., vol. 21, 17-20. 1999.
4. Nautiyal, S., K.S. Rao, R.K. Maikhuri and K.G. Saxena., *Transhumant Pastoralism in the Nanda Devi Biosphere Reserve, India*, Mount. Res. and Devel., 23: 255-262. 2003.

5. Comakli, B., M. Dasci, A. Koc, *The Effects of Traditional Grazing Practices on Upland (Yayla) Rangeland Vegetation and Forage Quality*. Turk J Agric For. Vol. 32. 259-265. 2008.
6. Comaklı, B. and O. Mentese, Mera ıslahını gerektiren nedenler. *T. C. Orman Bakanlığı Araşt. ve Erozyon Kont. Gen. Müdürlüğü Anadolu Su Havzaları Rehabilitasyon Projesi, Mera Islahı Eğitim-Uygulama Semineri*. 28-30 Haziran, Erzurum, Turkey, pp. 1-9. 1999.
7. Holechek, J.L., R.D. Pieper and C.H. Herbel, *Range Management: Principles and Practices*. Prentice Hall, New Jersey. p. 607. 2004.
8. Willms, W.D., S.M. Meginn and J.F. Dormaar. 1993. Influence of litter on herbage production in the mixed prairie. *J. Range Manage.* 46: 320-324.
9. Tosun, F. 1996. T urkiye’de kaba yem üretiminde çayır-mera ve yembitkileri yetiştiriciliğinin dünü, bugünü ve yarını. *Turkiye III. Çayır- Mera ve Yembit. Kong.*, 17-19 Haziran, Erzurum, pp. 1-4.
10. Taylor, C.A.J.R., M.H. Ralphs and M.M. Kothmann. 1997. T echnical note: Vegetation response to increasing stocking rate under rotational stocking. *J. Range Manage.* 50: 439-442.
11. Erkovan, H.I., A. Koc and Y. Serin, Some vegetation properties of Bayburt (Turkey) Province Rangeland. *Grassland Science in Europe*, Vol. 8: 26-28 May, Pleven, Bulgaria, pp. 617-619. 2003,
12. Kadioğlu, S., Cihanlı köyü (Tortum, Erzurum) Yayla Mera Vejetasyonunun Mevcut Durumu. Ataturk Univ., Fen Bil. Enst., Tarla Bitkileri Anabilim Dalı. (yayınlanmamış yüksek lisans tezi). Erzurum. p. 45. 2003.

ANALYSIS AND BACK-CALCULATION MODELLING OF THE 10 JANUARY 2015 UZUNTARLA (TRABZON-TURKEY) SNOW AVALANCHE EVENT

Abdurrahim AYDIN

Düzce University, Faculty of Forestry, Konuralp Campus, 81620 Düzce, Turkey,
aaydin@duzce.edu.tr

Remzi EKER

Corresponding author: Düzce University, Faculty of Forestry, Konuralp Campus, 81620 Düzce, Turkey,
remzieker@duzce.edu.tr

Yunus BARIŞ ODABAŞI

General Directorate of Combating Desertification and Erosion, Republic of Turkey Ministry of Forestry and Water Affairs,
Ankara, Turkey, ybodabasi@ormansu.gov.tr

Abstract

A deadly snow avalanche, which fatally buried five workers, occurred on 10 January 2015 in the Uzuntarla region of Trabzon Province, Turkey. The victims were employed at the construction site of a hydroelectric power plant (HP). The avalanche was released at 12:00 noon and half an hour after the event, rescue units were able to reach the area. Two workers in a truck were luckily saved from death when the snow mass flowed over the rear of their trailer. Rescue work continued for five days due to the harsh topographical and climatic conditions of the region. In this study, the Uzuntarla snow avalanche was analyzed according to field observations made one week after the event. In addition, by taking the field observations into account, ELBA+ simulation software was used for back calculation of the avalanche in order to calibrate friction parameters. With regard to the fit between the observed extent and the calculated extent of the avalanche as well as to observed flow heights, the Coulomb friction was found to be 0.275 for the starting zone, 0.25 for the track, and 0.295 for the run-out zone.

Keywords: *YBack Calculation, ELBA+, Numerical Simulation, Snow Avalanche, Trabzon-Uzuntarla (Turkey)*

1. INTRODUCTION

Due to its geographical location, geology and topography, Turkey commonly experiences snow avalanches [1]. On average, 24 people die in snow avalanches every year in Turkey, mainly in the eastern part of Anatolia and in the eastern Black Sea region [2]. According to GDDA (2009), between 1951 and 2006, 676 avalanches were recorded in the Turkish avalanche archives, with a total of 1325 fatalities and 365 injured. Out of the 1325 deaths, 120 (9%) were soldiers, 27 (2%) were hunters, 18 (1.4%) were skiers and climbers, 12 (0.9%) were buried in cars on highways, one (0.08%) was a worker and the remaining 1147 (86.6%) were local inhabitants trapped in their houses. Avalanche statistics demonstrate that avalanches in Turkey mainly affect settlements. Moreover, in recent years, winter tourism has gained importance in Turkey, and the casualties have been increasing accordingly. As an example, on 25 January 2009, an avalanche in Zigana pass in Trabzon Province in Turkey's eastern Black Sea region buried 17 mountaineers, 10 of whom lost their lives [2].

A deadly snow avalanche, which fatally buried five workers, occurred on 10 January 2015 in the Uzuntarla region of Trabzon Province. The workers were employed at a hydroelectric power plant (HP) construction site. The avalanche was released at 12:00 noon and half an hour after the event, rescue units were able to reach the area. Two workers in a truck were luckily saved from death when the snow mass flowed onto the rear of their trailer. Rescue work continued for five days due to the harsh topographical and climatic conditions of the region. In this study, the Uzuntarla snow avalanche was analyzed according to field observations made one week after the event. In addition, by taking the field observations into account, ELBA+ simulation software was used for back calculation of the avalanche in order to calibrate friction parameters.

2. MATERIAL AND METHODS

2.1. Uzuntarla Snow Avalanche of 10 January 2015

The snow avalanche event occurred in the Kavlatan region of Uzuntarla Village in the Çaykara sub-district of Trabzon Province, Turkey. A location map is given in Figure 1. The exact location is between the coordinates of 600002.6 – 4492998.9E and 602009.7 – 4490996.2N in the UTM European Datum 1950.



Figure 1. Location map of Uzuntarla snow avalanche site

Information relating to the avalanche disaster, which resulted in the death of five workers, was obtained on the spot from villagers and workers who had witnessed the accident and helped with the rescue efforts. According to the witnesses, the avalanche event was released at 12 noon and half an hour later, rescue units were able to reach the area to help the victims. The avalanche occurred in a HP construction area, and an electric pole and a canvas shelter located next to the entrance of the HP tunnel were destroyed as a result of the accident. In addition, a power unit and a dozer were rendered inoperative (Figure 2). The locations of objects affected by the avalanche are given in Figure 3.



Figure 1. Objects affected by the avalanche



Figure 2. The locations of objects affected by the avalanche

According to the form of the starting zone, the event was a slab avalanche which flowed over an older snow layer. Two workers who survived the accident described how a powdery cloud suddenly covered everything around them at the moment the avalanche struck. From this information, it could be deduced that a powder avalanche had most likely occurred. As shown in Figure 4, there are two potential release areas over the avalanche path. The avalanche initiated from release area number 2. The width of the release zone is 130 m and it is located at an elevation of between 2070 and 2010 m. The extent of the avalanche obtained from the fieldwork is given in Figure 5.

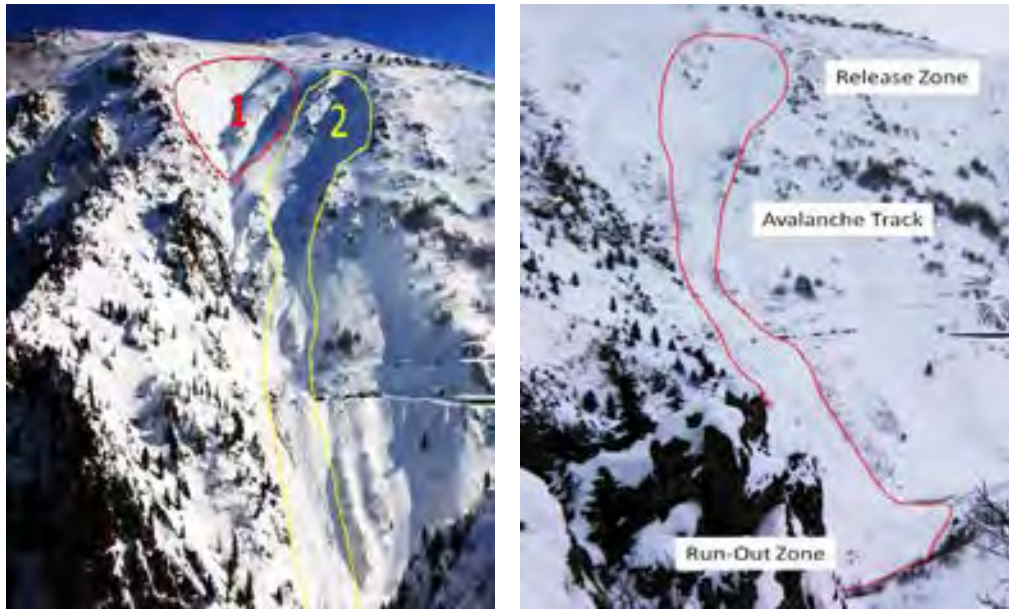


Figure 3. General view of the avalanche path and release zones

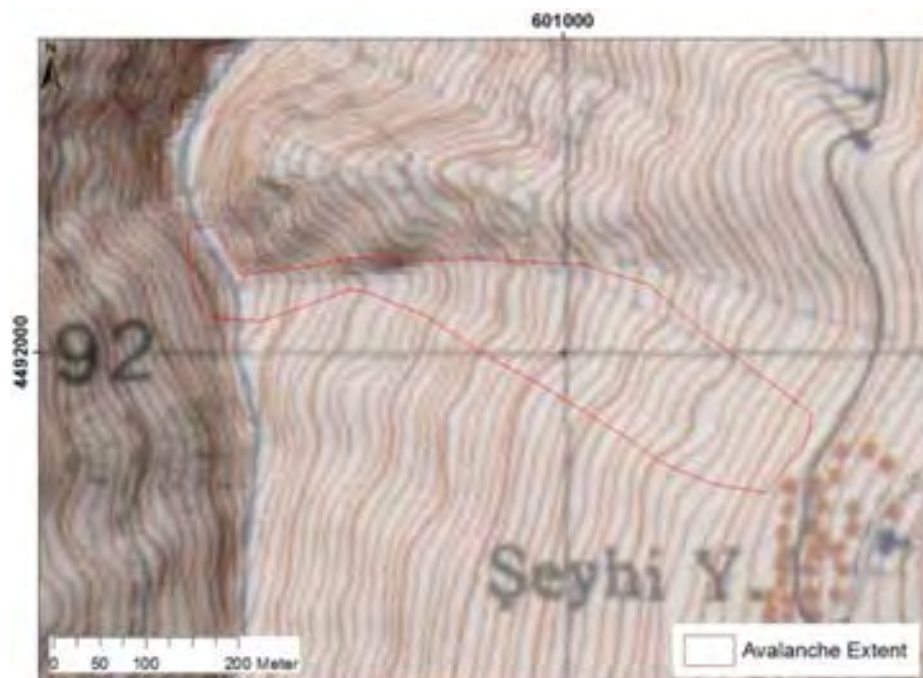


Figure 4. The extent of the Uzuntarla avalanche site

As seen from the slope map in Figure 6a, the region generally has very steep slopes of greater than 28° , which is the lower limit for avalanche occurrence. The altitude of the region where the avalanche event happened is

1500 m (a.s.l). A longitudinal profile of the avalanche path is given in Figure 6b. There is no forest cover in the avalanche area or its surroundings.

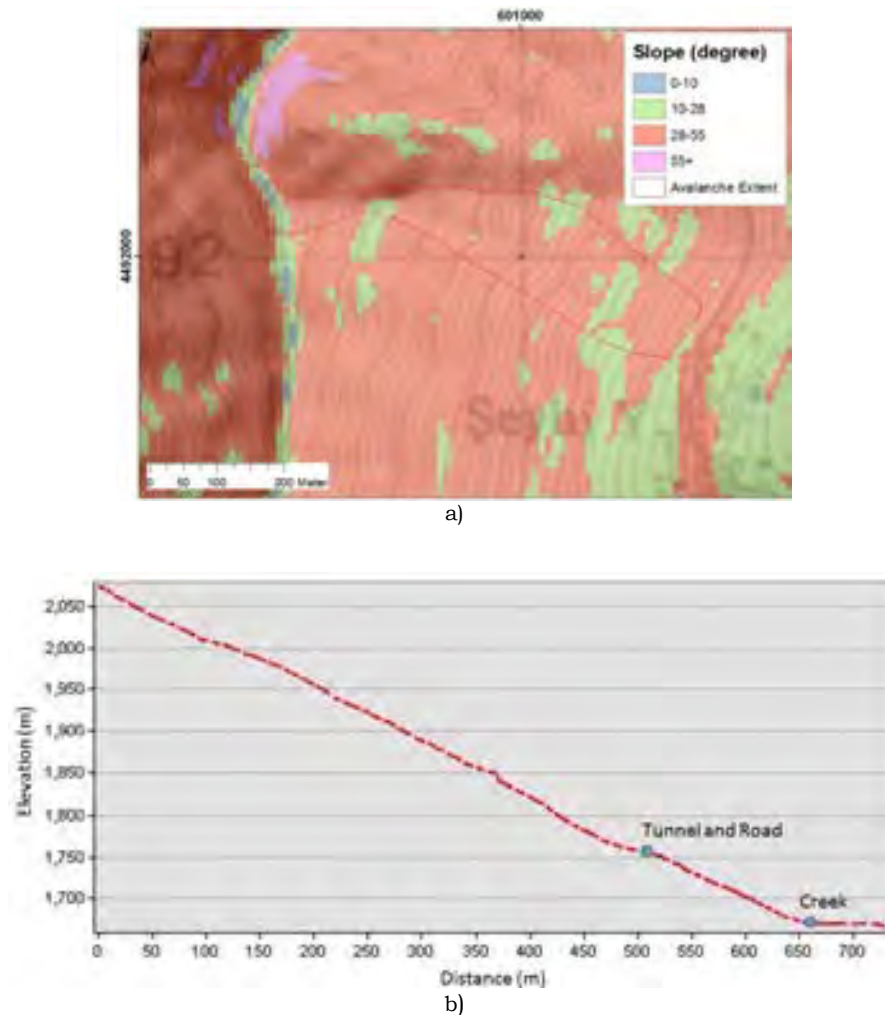


Figure 5. a) Slope map of the area, b) Longitudinal profile of the avalanche path

According to information obtained from witnesses, a snowfall of slightly more than one meter (110 – 115 cm) had occurred in the 72 hours preceding the event. As stated by the villagers, the snowfall was less than that of previous snowfalls in the region over the last three years. It was observed that the snow depth, which varied depending on the topographical characteristics of the slopes, could be greater than 3 m in valleys and gullies in the region. Moreover, the winds have an important role in the deposition of snow over the leeward slopes. The predominant wind direction is generally from the south to the north, or vice versa; however, 70% of the winds blow from the south. The air temperature at the moment of the avalanche release was -8°C .

2.2. Numerical Avalanche Simulation with ELBA+ Software

ELBA+ (Energy Line Based Avalanche) software was developed at the University of BodenKultur according to the parametric calibrations of 147 well-recorded avalanche events throughout Austria [3]. ELBA+ has been commonly used for hazard mapping, avalanche protection measures and design purposes [4]. ELBA+ simulations are based on the Voellmy model containing two parameters: the Coulomb friction μ and the velocity squared dependent turbulent friction ξ . In addition to these two parameters, release areas (m^2), release height (m), snow density in the release zone (kg/m^3) and Digital Elevation Model (DEM) data are necessary inputs for simulations, with entrainment and resistance areas being optional. All spatial and table information for these inputs were prepared by ELBA+ Add-ins for ArcMap (Figure 7a). After completing preparation for all the data inputs, the simulation process was carried out by the ELBA+ Simulation Module (Figure 7b). In this study, the DEM data was created from a 1/25000-scale topographical map. Based on field observations, the release zone was digitized over the topographical map of the area. The entrainment, release

height, and snow density (based on measurements one week later in the field) were selected as 0.3 m, 1.6 m, and 230 kg/m³, respectively. Turbulent friction was calculated as a function of flow height and roughness, while the simulation was run by the software. Hence, in order to calibrate the Coulomb friction for the starting zone, track, and run-out zone separately, various scenarios were created according to the extent of the Uzuntarla avalanche.

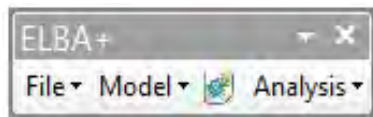


Figure 6a. ELBA+ Add-ins for ArcMap

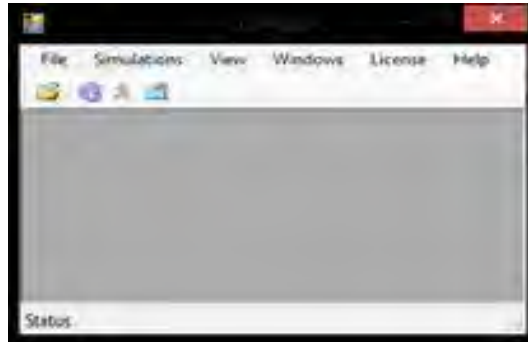


Figure 7b. ELBA+ Simulation Module

3. RESULTS AND DISCUSSION

In this study, a back calculation was made for the calibration of the friction parameter. To this aim, different scenarios were prepared using ELBA+ numerical snow avalanche simulation software. With regard to the fit between the observed extent and the calculated extent of the avalanche as well as to the observed flow heights, the Coulomb friction was found to be 0.275 for the starting zone, 0.25 for the track, and 0.295 for the run-out zone. The calculated extent of the avalanche is shown in Figure 8.

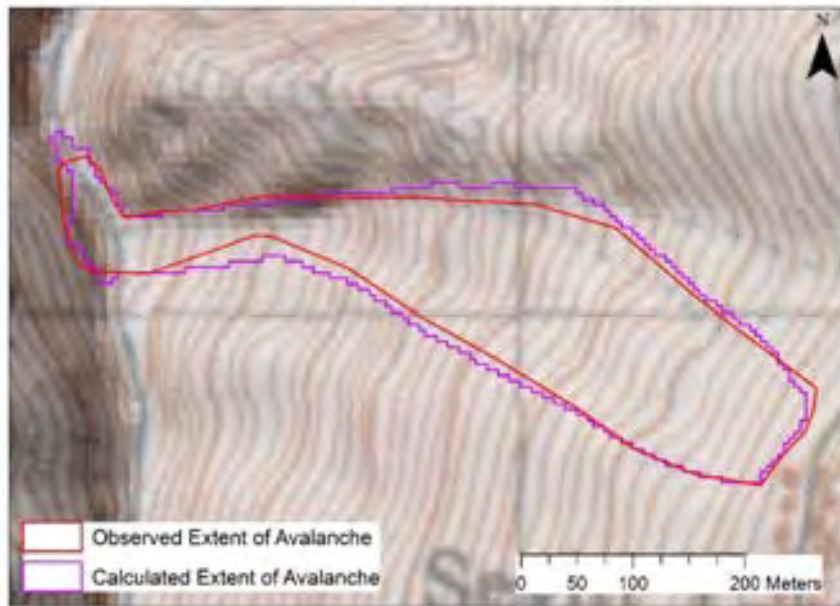


Figure 7. Calculated extent of the Uzuntarla snow avalanche

The simulation maximum velocity map of the event results is given in Figure 9a. According to the simulation results, the maximum velocity of the snow avalanche was 27 m/s. The velocity of the flowing avalanche had reached more than 20 m/s at the locations of victims and other objects. The impact pressure map is shown in Figure 9b. The maximum impact pressure value was 220 kPa. The flow height map of the event is depicted in Figure 9c. According to the simulation results, the maximum flow height of the event was 10 m.

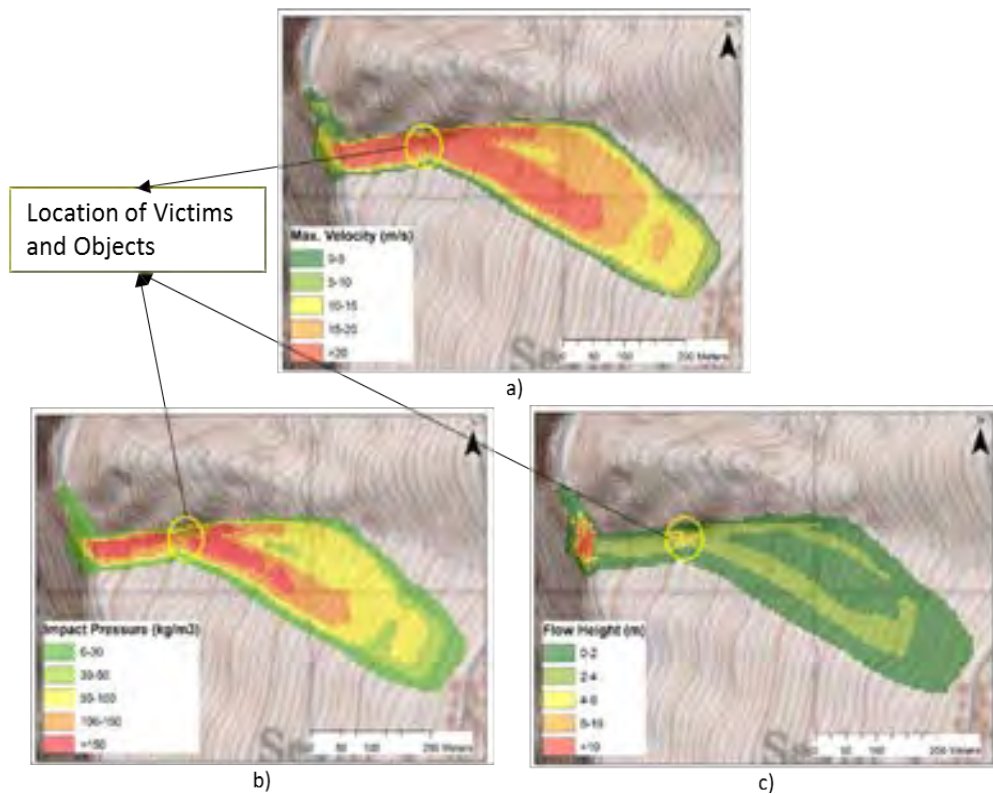


Figure 8. Avalanche dynamics maps of the event derived from simulation results (yellow circle shows the place of victims)

No field observations were made concerning the velocity and impact pressure of the event, although it was found that the flow height results of the simulation were compatible with the fieldwork measurements. According to the measurements and information obtained from witnesses, the flow heights over the location of the victims varied between 3 m and 6 m. An example of flow heights measured in the field is shown in Figure 10.



Figure 9. Observed flow heights of the event

4. CONCLUSIONS

A deadly snow avalanche event, which fatally buried five workers, occurred on 10 January 2015 in Uzuntarla-Trabzon, Turkey. In this study, the Uzuntarla avalanche event was analyzed according to field measurements and observations made one week after the event. According to witnesses, the avalanche event was released at 12 noon and half an hour later, rescue units were able to reach the area to help the victims. The avalanche occurred on a HP construction site. In the accident, an electric pole and a canvas shelter located next to the entrance of the HP tunnel were destroyed. In addition, a power unit and a dozer were damaged. The ELBA+ simulation software was used to perform back calculations for the avalanche friction parameters by taking the field observations into account. To this aim, different scenarios were proposed using ELBA+ numerical snow avalanche simulation software. With regard to the fit between the observed extent and the calculated extent of the avalanche as well as to the observed flow heights, the Coulomb friction was found to be 0.275 for the starting zone, 0.25 for the track, and 0.295 for the run-out zone. No field observations were made concerning the velocity and impact pressure of the event, although it was found that the flow height results of the simulation were compatible with the fieldwork

REFERENCES

- [1]. I. Güler, "International cooperation for solving the avalanche problem in Turkey". *Natural Hazards*, vol. 18, pp. 77–85, 1998.
- [2]. A. Aydın, Y. Bühler, M. Christen, and I. Güler, "Avalanche situation in Turkey and back-calculation of selected events", *Nat. Hazards Earth Syst. Sci. Discuss.*, 2, 581–611, 2014.
- [3]. G. Volk and K. Kleemayr, "Lawinensimulationmodell ELBA". *Wildbach und Lawinenverbau*, 63. Jg. Heft 138, 1999.
- [4]. S. Sauermoser and D. Illmer, "The use of different avalanche calculation models practical experiences". In: *International congress INTERPRAEVENT in the Pacific Rim (Matsumoto, Japan)*, 2:741–750, 2002.

THE FACTORS EFFECT THE EXTERNAL BONDED PATCH REPAIRED IN LAMINATED COMPOSITE MATERIALS

Şükrü ÇETİNKAYA

Dicle University, Mechanical Engineering Department, Diyarbakır, Turkey,
scetinkaya@dicle.edu.tr

Haşim PIHTILI

Fırat University, Mechanical Engineering Department, Elazığ, Turkey
hpihtili@firat.edu.tr

Hayri YILDIRIM

Dicle University, Diyarbakır Technical Vocational School, Diyarbakır, Turkey,
hayriyildirim0021@hotmail.com

Abstract

In this study, woven glass and carbon fibres reinforced composite materials have been produced with eight laminates. For experimental study, specimens with 10 mm internal hole were prepared. Then, these specimens have been repaired by using adhesive and composite patches with different parameters in necessary curing temperatures and laboratory conditions. By performing the unidirectional tensile test, the ultimate failure loads of these repaired specimens were indicated. By comparing these ultimate failure loads of repaired specimens that prepared with different parameter, the effects of several repair parameters on the ultimate failure strength are investigated. These repair parameters are patch bonded area (D/W ratio), adhesive thickness, patch thickness and fibres orientation angles (0, 15, 30, 45).

Keywords: *Laminate Composite Materials, bonded repair, patch, adhesive, failure strength*

1. Introduction

By performing technological improvements, applications of composite materials have been increased both commercial and military aircraft structures applications in recent years, because of their excellent properties. Due to high cost of these materials, maintenance of them, have been important. In industry, spare parts repair of these composite materials, have been preferred than replacement of spare parts. Sometimes, replacements of the damaged spare parts are costly and unnecessary. More structures with defects or local damages can be repaired successfully.

In industry, various repair techniques have been successfully applied. Among them, adhesively bonded structural repair has gained more favour than mechanically fastened structural repair for the reason that fiber reinforced composites are essentially bonded in nature. Therefore, in recent years, considerable experimental and numerical studies have been conducted to investigate the influence of different repair parameters on the stress distributions, ultimate strength and stress intensity factor of the bonded repaired structures [1]. A number of authors [1-9,11] have studied the analysis of failure mechanism of the bonded patch repair in laminated composite materials. Wisnom M.R. [10] has reviewed the size effects in the testing of fibre-composite materials. Predictive fracture model for composite bonded joints has been proposed by Goyal V.K. and et al. [12]. Principles and practices of adhesive bonded structural joints and repairs have studied by Davis M. [13]. Little research has been carried out to analyse the ultimate failure load of repaired structures with various repair parameters.

In aircraft applications, less weight is the important criteria for the maintenance of the parts. For such repair applications in laminated composite materials, external bonded patch repair technique has been more preferable than using mechanical fastened repair. Because, using mechanical fasteners increase the weight and the stress concentration factor of the repaired structures. Also, in external patch bonding repair, the optimum quantity of repair materials must be used in order to protect weight increment of the repaired structure. These main repair materials are adhesives and composite patches. The adhesives and patches should have been used in minimum quantity in repairs without decrease the load carrying capacity of the structures. Also, in adhesively bonded repairs, the stresses that occur in bonded joints are more uniform than that of pinned joints. These stress representations for various connections are illustrated in Fig. 1.

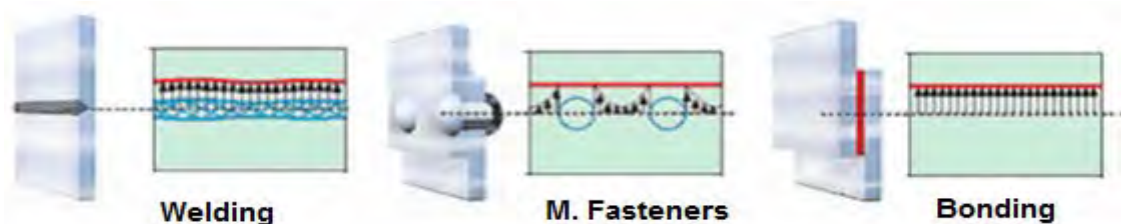


Figure 1. Presentation of stress concentration effects for various joint techniques

In this study, various experimental specimens have produced with different repair parameters. Then, by performing unidirectional tensile testing to these prepared specimens, the ultimate failure loads of them were indicated. By analysing these failure loads of the specimens, the effects of repair parameters have been specified.

2. Experimental

The current work investigated the performance of the external bonded patch repairs under tensile loading by indicating the ultimate failure loads of repaired laminated composite structures. For this

study, eight plies laminated woven glass and carbon fibres reinforced parent plates were used. By using these parent plates, experimental specimens were prepared. 10 mm holes were drilled in the center of the parent plates to simulate the damages in the structures. Then, these damaged specimens were repaired by using adhesive and composite patches with different parameters in necessary curing temperatures and laboratory conditions. The repaired experimental specimens were shown in Fig. 2. The materials that used for parent plate specimens, adhesives and patches in repair were listed in Table1. During the tests, specimens were subjected to longitudinal tensile loads on tensile testing machine in order to indicate the failure loads of repaired structures.

Table 1. Materials that were used in repair of laminated composite materials

Bonding type	Parent Materials	Adhesive	Patch Material
W.L.	Woven carbon fibres	Hysol EA9396	0020989
	Woven glass fibres	Hysol EA9396	0021438-09
Prepreg	Woven carbon fibres	C992275 ADH FILM	C992268-14
	Woven glass fibres	C991957-37 ADH FILM	C992270



Figure 2. Presentation of repaired experimental specimens

3. Results and discussion

3.1. Effect of fibres orientation angle of laminates:

In order to discuss the effect of fibres orientation angle to the failure load of repaired structure; four different repaired specimens were prepared with both W.L. patch and prepreg patch bonding techniques. After performing the unidirectional testing to these specimens, the ultimate failure loads were indicated in Fig. 3. Fig. 3 shows that; for all repaired specimens, the ultimate failure loads were decrease by increasing the fibres orientation angles of parent plates. The maximum failure load was obtained at 0° fibres orientation angle of parent plate that repaired with W.L. patch bonding technique. The minimum failure load was obtained at 45° fibres orientation angle of parent plate that repaired with W.L. patch bonding technique. In failure load values, at 0° fibres orientation angle, there is % 7.1 difference presented between W.L. patch and prepreg patch. This difference in failure loads were presented as % 22.6 value for the fibres orientation angle of 45° in laminate. The minimum differences in these values were occurred in 15°. This value was indicated as %2. This difference is caused by the peeling effect of the bonded patch. In W.L. bonded patch, peeling is occurred more easily then prepreg patch bonded technique with increasing the fibres orientation angle of the parent laminates.

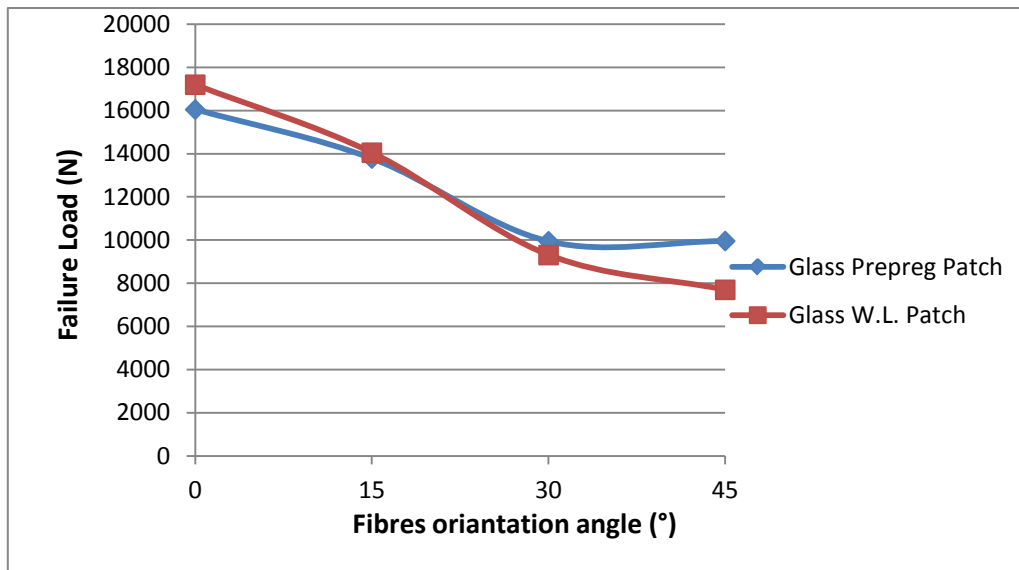


Figure 3. Presentation of the effect of fibres orientation angle of parent plates to the failure load of repaired structures by glass prepreg and wet layout patches.

3.2.Effect of patch thickness

The effect of the patch thickness to the ultimate failure loads of repaired structure was indicated in Fig. 4. The ultimate failure loads of the structures repaired with prepreg bonding technique were increased by increasing the patch thickness (increase the ply number). But, for the structure that repaired with W.L. bonding technique, the failure loads have increased gradually to the patch thickness of the 3 plies values and after that, the peeling effect has occurred in repaired structure than, the failure load decrease dramatically. Increase the bonded patch thickness after a certain value (3 plies) in repair of the laminate composite materials does not improve the ultimate failure load. Increase the patch thickness further in repair of air craft structures may cause the weight stability effect. This is the main drawback in repairs of such applications.

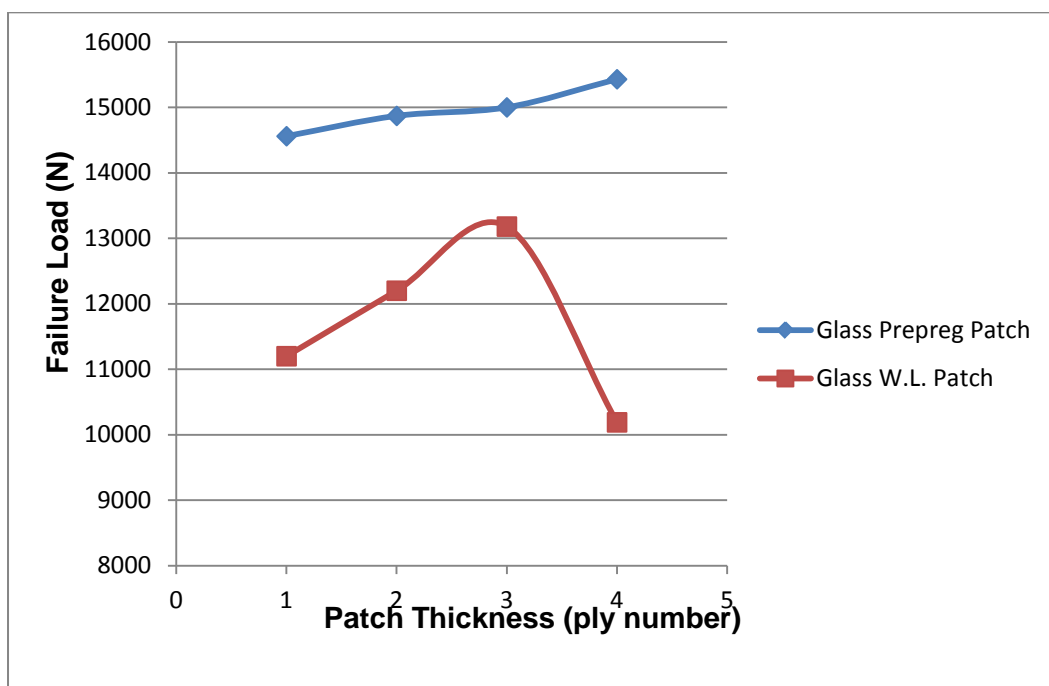


Figure 4. Effect of patch thickness to the failure load of repaired structures with glass prepreg and wet layout patches.

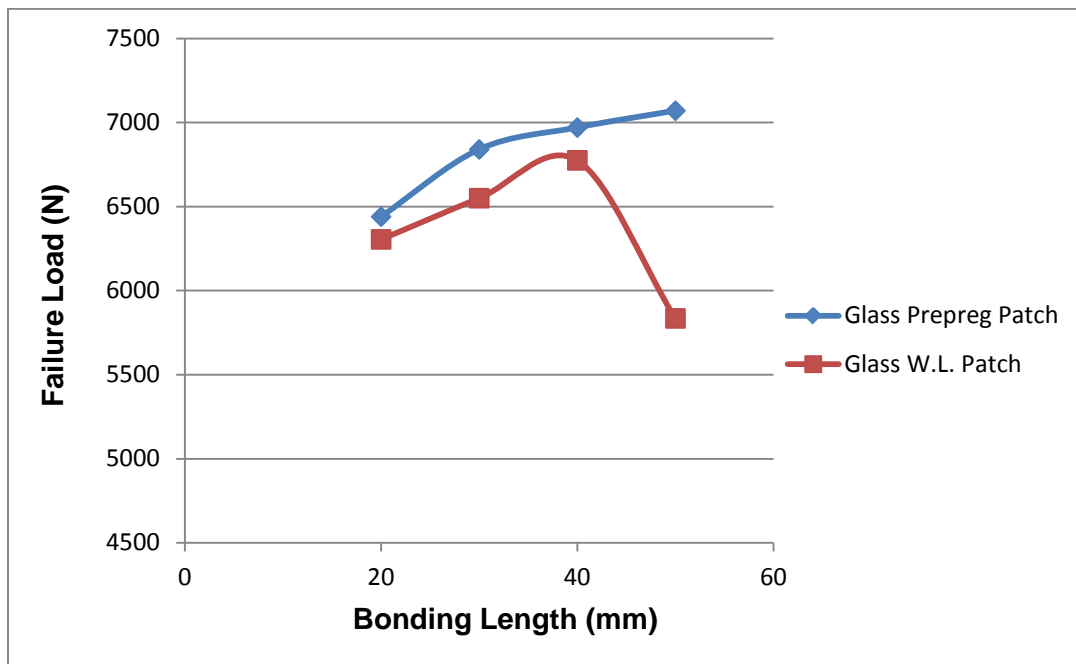


Figure 5. Presentation of the effect of bonding length to the failure load of W/D=2 glass repaired structures with glass prepreg and wet layout patches.

3.3.Effect of bonding length

In external bonded patch repairs, if the patch overlap length or bond length too short, the entire adhesive layer is under high shear stress. In the case of longer bond length, most of the load is carried at the ends of the bonded overlap which is the reason for why too large patches fails to enhance the expected ultimate strength [14]. Effect of bonding length of the patch to failure loads in repaired structures has presented in Fig. 5. The failure loads of structures repaired with glass prepreg patch bonding were increased gradually by increasing the bonding length in repair. In that repair with glass W.L. patch bonding; the failure loads were increased to the bonding length of 40 mm gradually, than decrease dramatically to the 5850 N value due to peeling effect that presented in W.L. applications. In bonded patch repair, for both W.L. and prepreg techniques, 40 mm value of bonding length, was seen as the optimum value.

3.4.Effect of bonding area (W/D ratio)

Effect of bonding area (W/D ratio) to the ultimate failure loads was presented in Fig. 6. By changing the W/D ratio from 2 to 4 in repair with carbon fibres prepreg, the failure loads of the repaired laminated plates have been changed from 20000 N to 50000 N value. In repair of woven laminated composite materials, the change of W/D ratio has major effect in ultimate failure loads of repaired parent plate materials. Increase the W/D ratio further in repair of structures may cause the weight stability effect. For this reason, in repair of laminated composite materials the W/D ratio should be in optimum value.

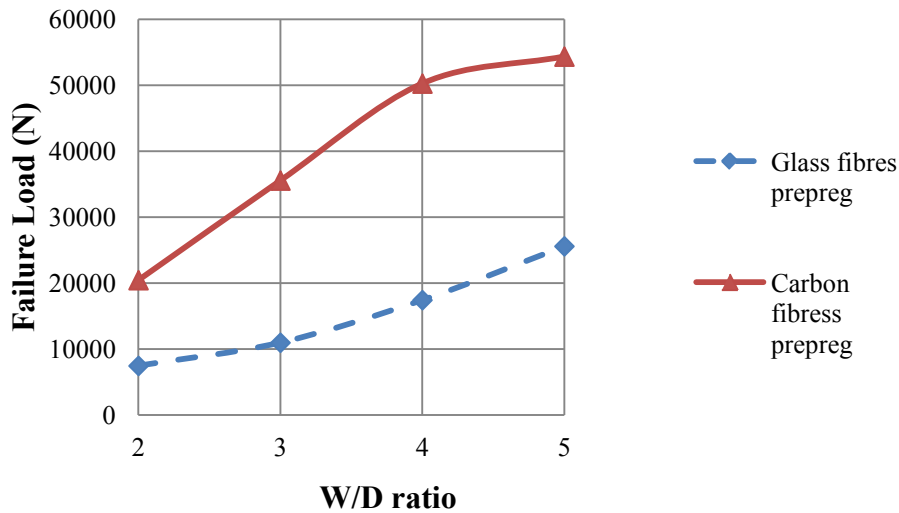


Figure 6. Presentation of the effect of W/D ratio to the failure load glass and carbon fibres reinforced plates repaired structures with glass and carbon prepreg patches.

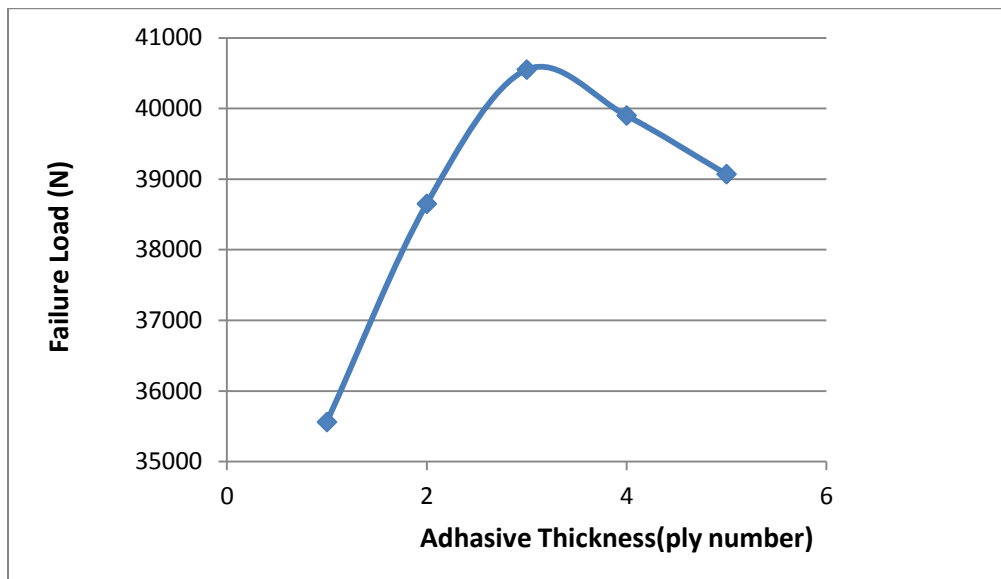


Figure 7. Presentation of the effect of adhesive thickness to the failure load of W/D=3 carbon parent laminated composite that repaired with carbon prepreg patches.

3.5. Effect of adhesive thickness

The adhesives, which bond the patches and parent plates together, are always regarded as the weakest chain in the bonded repair, and play an essential role. Therefore, careful selection of its parameters is very important [1]. In this study, effects of adhesive thickness were studied with the W/D=3 carbon parents laminated composite specimens that repaired with carbon prepreg patches by using various adhesive film thicknesses. The effect of adhesive thickness in repair of laminated composite materials with external bonded patch to the ultimate failure loads was illustrated in Fig. 7. For each adhesive film ply thickness was taken as 0.2 mm. The maximum ultimate failure load (40750N) was obtained with 3 plies adhesive thickness (0.6 mm) in repair of woven carbon fibres laminated parent plates with external carbon prepreg bonded patches.

The adhesive material which bonds the patch to the parent laminate is considered as the most important factor in the repair design. If the adhesive layer is too thin, it will be stiff and brittle which can result to a shear failure initiation in high stress regions near the patch and hole edges, causing the

damage propagates across the entire overlap region. However, if the adhesive layer is too thick it will be too plastic and under loading it is expected to deform quickly which weakens the effectiveness of load transfer between the parent laminate and patches [14].

4. CONCLUSIONS

In the present study, experimental study is carried out to investigate different repair parameters effects on the ultimate failure load of adhesively bonded repaired structures, and the following conclusions can be drawn from this study.

1. The ultimate failure loads of structures that repaired with external bonded patch were decrease by increasing the fibres orientation angles of parent plates. The maximum failure load was obtained at 0° fibres orientation angle of parent plate.
2. The ultimate failure loads of the structures repaired with prepreg bonding technique were increased by increasing the patch thickness. But, for the structure that repaired with W.L. bonding technique, the failure loads have increased gradually to the patch thickness of the 3 plies values and after that, the peeling effect has occurred easily and this decrease the failure loads of repaired structures.
3. Ultimate failure loads of repaired structures can be increased by choosing the optimum repair parameters, such as patch dimensions, adhesive thickness, bonded area and bonding length.
4. In repair of air craft structures, due to weight stability, optimum quantity of repair materials should be used.

References

1. Liu X., Wang G. (2007). *Progressive failure analysis of bonded composite repairs. Composite Structures*, 81, 331-340.
2. Papanikos P., Tserpes K.I., Pantelakis Sp.(2007). *Initiation and progression of composite patch debonding in adhesively repaired cracked metallic sheets. Composite Structures*, 81, 303-311.
3. Xiaoquan C., Baig Y., Renwei H., Yujian G., Jikui Z., (2013). *Study of tensile failure mechanisms in scarf repaired CFRP laminates. International Journal of Adhesion & Adhesives*, 41, 177-185.
4. Breitzman T.D., Larve E.V., Cook B.M., Schoeppner G.A., Lipton R.P. (2009), *Optimization of a composite scarf repair patch under tensile loading. Composites: Part A*, 40, 1921-1930.
5. Tse P.C., Lau K.J., Wong W.H. (2002), *Stress and failure analysis of woven composite plates with adhesive patch-reinforced circular hole. Composites: Part B*, 33, 57-65.
6. Jones R., Chiu W.K. and Smith R., (1995), *Airworthiness of Composite Repairs: Failure Mechanisms. Engineering Failure Analysis*, 2, 117-128.
7. Cheng P., Gong X. J. , Hearn D., Aivazzadeh S., (2011), *Tensile behaviour of patch-repaired CFRP laminates. Composite Structures*, 93, 582-589.
8. Her S. C. (1999), *Stress analysis of adhesively-bonded lap joints. Composite Structures*, 47, 673-678.
9. Campilho R.D.S.G., Moura M.F.S.F., Domingues J.J.M.S., (2009), *Numerical prediction on the tensile residual strength of repaired CFRP under different geometric changes. International Journal of Adhesion & Adhesives*, 29, 195-205.
10. Wisnom M. R., (1999), *Size effects in the testing of fibre-composite materials. Composites Science and Technology*, 59, 1937-1957.
11. Madani K., Touzain S., Feaugas X., Cohendouz S., Ratwani M., (2010), *Experimental and numerical study of repair techniques for panels with geometrical discontinuities. Computational Materials Science*, 48, 83-93.
12. Goyal V.K., Johnson E.R., Goyal V.K., (2008), *Predictive strength-fracture model for composite bonded joints. Composite Structures*, 82, 434-446.

13. Davis M., Bond D., (1999), *Principles and practices of adhesive bonded structural joints and repairs. International Journal of Adhesion & Adhesives*, 19, 91-105.
14. Caminero M.A., Pavlopoulou S., Lopez-Pedrosa M., Nicolaisson B.G., Pinna C., Soutis C., (2013), *Analysis of adhesively bonded repairs in composites: Damage detection and prognosis. Composite Structures*, 95, 500-517.

SOME EXAMPLE OF MISMANAGEMENT PRACTICES IN NATURAL VEGETATION IN TURKEY

Mahmut DAŞCI

Ataturk University, Faculty of Agriculture, Department of Agronomy, ERZURUM.
mtasci@atauni.edu.tr

Binali ÇOMAKLI

Ataturk University, Faculty of Agriculture, Department of Agronomy, ERZURUM.

Abstract

Animal husbandry is a major segment of the economy and rangelands and meadows are the most important feed resources for animal husbandry in Turkey. Turkey has 14.6 million ha rangeland and meadow areas and the distribution of these areas show great variation among the regions of the country. The North East Anatolia region has the largest pasture and meadow area, the lowest area is in Marmara region. In grazing season, all small livestock and vast majority of large livestock depend on rangelands. On the other hand, the high quality roughage need of livestock in long winter periods is mainly obtained from natural meadows. The produced feed in pasture and meadow areas is not adequate for animal's need due to mismanagement practices and some other factors as social and cultural factors. The main problem of the rangelands is overgrazing. In addition to overgrazing, early and late season grazing practices is another problem with the rangelands. In all regions the rangelands is grazed as long as climatic conditions are favorable for grazing. Especially early spring and late fall grazing causes degradation of rangelands because these periods are critical for rangeland plants. In Turkey, however, meadows are managed for the production of the winter feed for livestock by individual owners. They may also be used for grazing in early spring or late summer after harvesting. Traditionally grazing of meadows in early spring leads to decrease in yield and forage quality. Meadows are irrigated by a surface irrigation system from the beginning of early summer to harvest time. In this irrigation system too much irrigation water is applied, the surface of the meadows becomes excessive wet. The soil structure is then damaged by the poor irrigation management which also affects the forage quality. In rangelands and meadows, suitable management practices are necessary for sustainability.

Keywords: *Rangeland, meadow, mismanagement, suitable management*

1. INTRODUCTION

Rangelands occupy a considerable part of the total land areas in Turkey. Animal production is one of the major segments of the Country and the rangelands are the main food source for livestock in summer periods. On the other hand, the high quality roughage need of livestock in long winter periods is mainly obtained from natural meadows. The produced feed in pasture and meadow areas is not adequate for animal's need [1] due to mismanagement practices and some other factors as social and cultural factors.

Natural rangelands have many benefits for human beings and wild and domestic animals. Forage production for animals, conservation of biodiversity and limiting of soil erosion are some benefits of the rangelands [1]. Most rangelands are affected by the mismanagement practices negatively. Many problems of the pastures can be attributed to various factors [2]. Heavy and untimely grazing is one of the most important rangeland degradation factors [3] and some extreme environmental factors, such as prolonged drought lasted some years, can accelerate to this process. In many rangelands, soil erosion is an important process of land degradation related to low vegetation cover [4] and overgrazing is one of the most important reasons of the low vegetation cover. Standard, continuous stocking may decrease to produce all the forage of rangeland vegetation and often results in selective and incomplete grazing [5].

2. EXAMPLES OF MISMANAGEMENT PRACTICES

2.1. Early Spring-Late Fall Grazing

Early spring grazing is one of the most important mismanagement practices in Turkey rangelands. Rangelands should not be grazed until the 4-leaf stage or when the plants are at least 6 to 15-20 cm tall. Grazing native rangelands before the third leaf stage can result in the loss of over 60% of the potential forage yield. Grazing a pasture too early will result in the vegetation being removed before the plants have had a chance to replenish root reserves. Grazing one week too early in the spring will sacrifice three weeks of grazing in the fall. Grazing is continued until late fall. There is snow in this period.

As seen in figure 1, the snow doesn't melt, but grazing has been started



Figure 1. An example for early grazing of rangelands in Turkey

In Turkey, however, meadows are managed for the production of the winter feed for livestock by individual owners. They may also be used for grazing in early spring or late summer after harvesting. Traditionally grazing of meadows in early spring leads to

decrease in yield and forage quality. Similar to pastures, meadows are grazed until late fall after harvest.



Figure 2. Early spring grazing of meadows in Turkey



Figure 3. Late fall grazing of Rangelands in Turkey

2.2. Heavy Grazing

Another problem is heavy grazing and uneven spatial distribution of grazing during the grazing season. Especially the rangelands around the permanent settlements are heavily grazed and damaged by the impacts of grazing practices.



Figure 4. Heavy grazing on rangelands in Turkey



Figure 5. Heavily grazed rangelands in Turkey

2.3. Grazing of Marginal Rangeland Areas

The marginal rangeland areas have various problems such as high slope, too much rocky, high level groundwater and severe erosion.



Figure 6. Animals are grazing on rangelands have too much rock.



Figure 7. Grazing on rangelands has erosion problem.

2.4. Irregular Spatial Distribution of Animals

One of the important problems with present grazing practices is uneven spatial distribution of grazing. Current grazing management causes overgrazing some sites of rangelands such as around the watering points. Therefore, the plant cover is worse in these areas than that in the other sites. To solve these problems suitable grazing management plans and developing new watering points are necessary to ensure more even distribution of grazing pressure.



Figure 8. Irregular distribution of grazing animals

2.5. Using of the Rangelands for Different Purposes

Main usage of the rangelands is animal grazing but in Turkey rangeland areas sometimes can be used for different purposes, such as sand and mineral production.



Figure 9. Sand production on rangelands in Turkey.

2.6. Late Harvesting in Meadows

In Turkey, especially in Eastern Anatoli Region, meadows are harvested at too late period when the plants are at the full flowering. Whereas the harvest is must be made proper time when the dominant species are at the beginning of flowering.



Figure 10. Plant species are at full flowering periods but harvest was not made yet in meadow.

2.7. Improper Irrigation Practices in Meadows

Meadows are irrigated by a surface irrigation system from the beginning of early summer to harvest time. This is the most common method of irrigating meadows in Turkey, especially in the Eastern Anatolia Region which has wide meadow areas [6]. If too much irrigation water is applied, the surface of the meadows becomes excessive wet, especially in the early spring period. The soil structure is then damaged by the poor irrigation management [7] which also affects the forage quality [8]. Irrigation systems must be managed properly and not use more water than is necessary [9].



Figure 11. Using too much water in meadow.

CONCLUSSION

Appropriate grazing management will increase forage productivity and quality on rangelands. Standard, continuous stocking may decrease to produce the yield of rangeland vegetation and often results in selective and incomplete grazing. This can also leads to lower live-weight gains per acre of rangelands.

In suitable rangeland sites controlled, rotational grazing system must be practiced. Because in this grazing system lets regular grazing of rangelands by animals while allows ungrazed sites time to regrow. Controlled grazing allows for animals to graze the forage that is the most nutritious and palatable. Controlled grazing reduces soil erosion, improves air and water quality, and increases a variety of plant species. Regardless of the grazing technique, the goal should be to provide the amount and quality of forage animals need while maintaining the vigor of the plants.

REFERENCES

1. Altin, M., A. Gokkus, A. Koc, *Çayır ve Mera Yönetimi*. T.C. Tarım ve Köyişleri Bakanlığı Tarımsal Üretim ve Geliştirme Genel Müdürlüğü Yay., Ankara, Turkey. 2005.
2. Soni, B.K., Animal carrying capacity, including concepts and definition, methods for assessment and use of standard stock units, Evaluation and mapping of tropical African rangelands. *Proceedings of the Seminar International Livestock Centre for Africa*, March 3-8, Bamako-Mali. Available: <http://www.fao.org/wairdocs/ilri/x5543b/x5543b00.HTM>, 1975.
3. Comakli, B., M. Dasci, A. Koc, *The Effects of Traditional Grazing Practices on Upland (Yayla) Rangeland Vegetation and Forage Quality*. Turk J Agric For. Vol. 32, pp.259-265. 2008.
4. Schlesinger, W., J. Reynolds, G. Cunningham, L. Huenneke, W. Jarrell, R. Virginia and W. Whitford, *Biological Feedbacks in Global Desertification*. Science, Vol. 247,1043-1048. 1990.
5. Anonymous., *Pasture, Rangeland and Grazing Operations Highlights*. U.S. Environmental Protection Agency. 2015.

6. Comakli, B., and Ö. Mentese, An investigation on meadow problems of Erzurum. *Eastern Anatolia Agriculture Congress*, Erzurum, Turkey. Vol. 1, pp. 429–440. 1998.
7. Brereton, A. J., *Analysis of Effects of Water-table on a Grassland Farming System*. In: 'Land and Water Use'. (Eds V. A. Dodd and P. M. Grace.) pp. 2685–2695. (Balkema: Rotterdam.) 1989.
8. Siemer, E. G. Management options for improving meadows. In: '*Proceeding of the Third Intermountain Meadow Symposium*'. (Ed. E. G. Siemer.) pp. 233 –241. (Colorado State University: Fort Collins, CO.) 1991.
9. Esham, B. A., *Sustainable agriculture*. *Journal of Irrigation and Drainage Engineering*. Available: www.en.wikipedia.org/w/index.php, 2007.

PERFORMANCE ANALYSIS OF TURBOCHARGED 2-STROKE DIESEL ENGINE

Ümit GÜNEŞ

Yildiz Technical University, Naval Architecture and Marine Engineering, 34349, Beşiktaş, İstanbul, Turkey.
unues@yildiz.edu.tr

Yasin ÜST

Corresponding author: Yildiz Technical University, Naval Architecture and Marine Engineering, 34349, Beşiktaş, İstanbul, Turkey. yust@yildiz.edu.tr

A. Sinan KARAKURT

Yildiz Technical University, Naval Architecture and Marine Engineering, 34349, Beşiktaş, İstanbul, Turkey.
asinan@yildiz.edu.tr

Abstract

Turbocharger systems are very important for vessels in terms of increasing energy efficiency and reducing green gas emissions. Ambient conditions (winter, ISO and summer) effect intake air temperature so do turbocharger efficiency. Engine load and fuel types that effect exhaust gas energy level are the other parameters for the turbocharger efficiency. In this study, a new numerical method is improved for enthalpy and entropy calculation based on exhaust gas components. Also two-stroke Diesel engine performance which operates various ambient conditions is analyzed in terms of thermal efficiency, engine load, specific fuel oil consumption (SFOC), exergy efficiency and exegeric performance coefficient (EPC). The results show that the highest thermal efficiency is obtained in winter ambient condition and turbocharger efficiency increases when fuel-oil quality is better.

Keywords: *Ambient Condition, Two-Stroke Diesel Engine, Energetic Efficiency, Exegetic Performance Coefficient*

1. INTRODUCTION

Waste heat recovery systems become important in recent years. While total efficiency is increasing, global warming effect is decreasing result of decreasing emissions by using waste heat recovery systems [1]. Combine systems, steam and gas cycle used together, are the most significant way to get more heat recover. In this system the efficiency can reach up to 60%. The result of this system, large scale of waste heat is recovered, EEDI gets better and the emissions decrease [2].

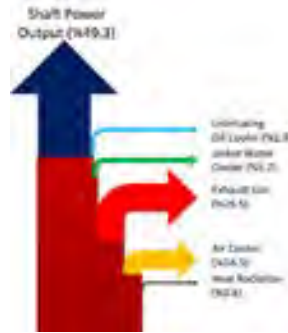


Figure 1. Net power and heat losses in a ship [3]

Waste heat which is not used and 2T Diesel shown in figure 1. It is shown that not used exhaust gases and sent to environment has a significant ratio (25%). So it is the best way to increase the energy efficiency.

Exhaust gas temperature after engine depends on many parameters. The most important ones are engine load and ambient condition.

Air temperature changes with ambient conditions. The compression demanding power also changes with ambient condition to make air target pressure. Compressor gets the power from the turbocharger turbine. Exhaust gas temperature is effected the changing power demand.

Vessels work in three ambient condition: [4].

- ISO ambient condition
- Tropical ambient condition
- Winter ambient condition

Properties	ISO	Tropical	Winter
Barometric Pressure (Bar)	1	1	1
Turbocharger Air Intake Temperature (°C)	25	45	10
Charge Air Coolant Temperature (°C)	25	32	10
Relative Air Humidity (%)	30	60	60

Ambient conditions and some properties belongs to them are shown in table 1. The most important factor for exhaust gases temperature is ambient condition.

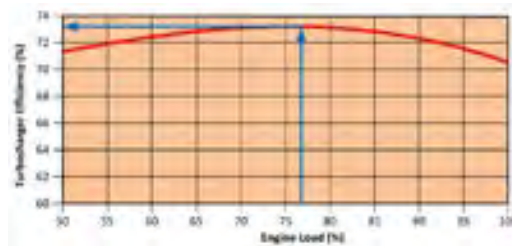


Figure 2. Turbocharger efficiency depending on engine load [5]

Energy is transferred effectively from exhaust gas to the turbocharger turbine when the turbocharger efficiency is higher. High turbocharger efficiency makes the exhaust gas temperature lower because of more energy transfer from exhaust gas to the turbocharger.

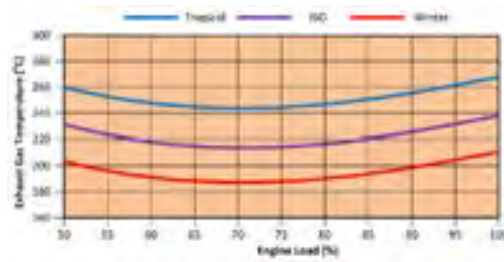


Figure 3. Exhaust gas temperature after turbocharger outlet depending on engine load [6]

The high efficiency leads to low exhaust gas temperature in figure 3. Also the lowest exhaust gas temperature occurs in 70-80% engine load. The highest exhaust gas temperature occurs in tropical ambient condition and the lowest exhaust gas temperature occurs in winter ambient condition.

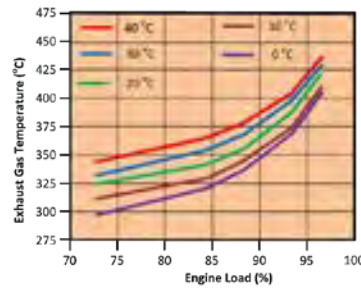


Figure 4. Exhaust gas temperature before turbocharger outlet depending on ambient condition [7]

Hountalal et al [7] indicates that the effect of different ambient temperature on the exhaust gas temperature in figure 4. This figure is used for the equation of the temperature versus engine load. When turbine outlet temperature is known, turbine inlet temperature can be found by using these equations approximately. In this study turbine inlet temperature is calculated by using this approach.

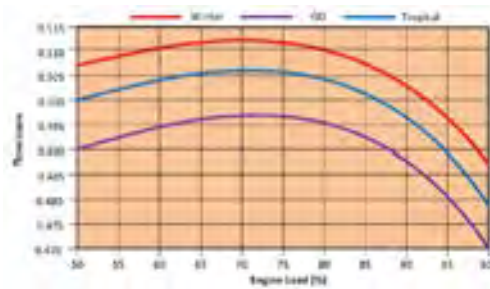


Figure 5. Engine efficiency depending on ambient condition

The effect of air temperature takes from ambient on engine efficiency in figure 5. As this result when the air temperature decreases, the engine efficiency increase. Engine efficiency reaches highest value in winter ambient condition and lowest value in tropical ambient condition.

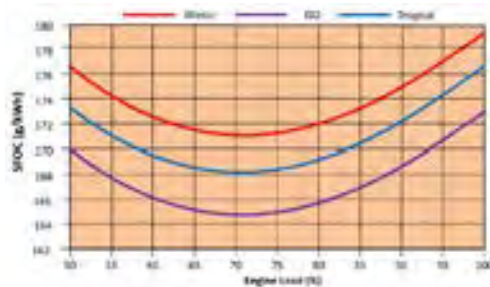


Figure 6. SFOC depending on ambient condition

The effect of air temperature takes from ambient on SFOC in figure 6 for MAN 7K98ME-C7-TII. As this result when the air temperature decreases, SFOC also decreases and the fuel oil consumption for producing same power also decreases so the engine efficiency increases. SFOC reaches highest value in tropical ambient

condition and lowest value in winter ambient condition.

2. MATHEMATICAL METHOD

2.1. Component of Exhaust Gas

Exhaust gas components changes depend on various factor. The most important ones are combustion efficiency and fuel specifications. 2T Diesel Engine generally use heavy fuel oil (HFO). General HFO fuel specifications and exhaust gas components is shown in figure 7.



Figure 7. Some component which are occurs after HFO combustion [8]

Three main components, air, fuel oil and lubrication oil, goes into the engine in combustion process. Air includes 21% Oxygen (O₂) and 79% Nitrogen (N₂). Fuel oil includes 97% hydrocarbon (HC) groups and 3% sulfur (S). In combustion process some lubrication oil also is included but the rate of it is low. Lubrication oil includes %97 HC groups, %2.5 CA groups and %0.5 sulfur.

Exhaust gases of HFO includes 76.2% N₂, % 14 O₂, 5.1 % H₂O and %4.5 CO₂. In this study it is assumed that exhaust gas has 4 main component (N₂, O₂, H₂O and CO₂) and all analyses are done for this assumption.

2.2. Exhaust Gas temperature after Funnel

SO_x which is included in fuel react with water in low temperature. After this reaction sulphuric acid is occurs and it causes corrosion. So it is not possible for decreasing the exhaust gas temperature bellow the dew point of sulphuric acid. The rage of sulphuric acid is 3 % for HFO [9].

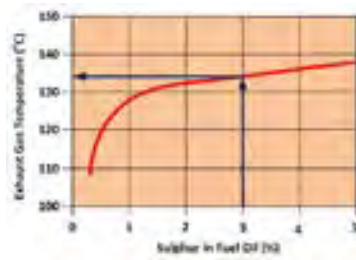


Figure 8. Dew point depending on sulfur ratio in fuel [8]

Dew point of HFO which has 3% sulfur is 135 °C in figure 8. Because of this result, the exhaust gas temperature for waste heat recovery cannot be lower than 145 °C (135°C + pinch point for heat exchanger). When analyzed the real system, the exhaust gas temperature cannot decrease lower than 160°C [8].

2.3. Enthalpy Calculation of Exhaust Gas

An Eq 1 was developed by Domingues et al [10] to calculate exhaust gas enthalpy value using experimental results. Specific heating value of exhaust gas is calculated in the Eq. 1 when the temperature range is 400 K to 1200 K.

$$C_{p,E} = (956 + 0.3386 \cdot (T_E + 273) - 2.476 \cdot 10^{-5}) \cdot (T_E + 273)^2 \quad (1)$$

Enthalpy of exhaust gas is calculated by using temperature and specific heat in Eq. 2.

$$h_E = C_{p,E} \cdot T_E \quad (2)$$

Figure 9 is drawn for enthalpy value versus various exhaust gas temperature by using Eq. 2.

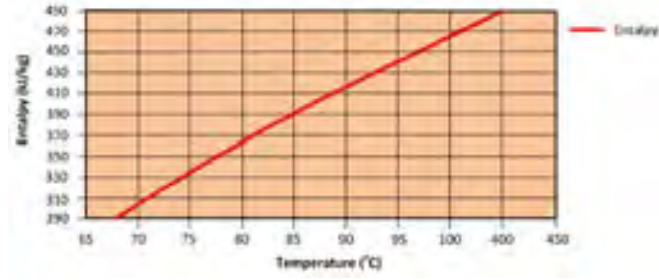


Figure 9. Enthalpy change of exhaust gas depending on temperature and pressure

2.4. Entropy Calculation of Exhaust Gas

Entropy calculations of exhaust gases are more difficult than enthalpy calculations which calculate by formulas that given by Bejan [11]. Entropy values of all elements in the exhaust gas must be separately calculated and then total entropy value will be found. Every state points entropies can be calculated with Eq. 3

where S^+ , a , b , c and d values can be read from Table 2 and also $\gamma = 10^{-3}T$.

Calculated entropy values from Eq. 3 are subjected to pressure correction in Eq.4.

$$\bar{s}_k = \bar{s}_k^o - R \ln \frac{X_k \cdot P}{P_0} \quad (3)$$

where (\bar{s}_k^o) is equal to Eq. 3, R is ideal gas constant, X_k is mass ratio of respective component in the exhaust gases, P is exhaust pressure, P_0 is standard ambient pressure and (\bar{s}_k) refers to respective element entropy value. Entropy value of the exhaust gases can be calculated with Eq. 5 while summing every elements entropies.

$$\sum_k X_k \bar{s}_k \quad (4)$$

The constants required for entropy calculation depending on the elements of the exhaust gas are given in Table 2 and (\bar{s}^o) is calculated in accordance with terms of reference value of 25 °C temperature and 1 bar pressure.

Table 2. Exhaust gases element entropy calculation constants [27]

Element	Formula	% (x)	S^+	a	b	c	d	\bar{s}_k^o
Nitrogen	$N_2(g)$	14	16.203	30.418	2.544	-0.238	0	191.610
Oxygen	$O_2(g)$	76.2	36.116	29.154	6.477	-0.184	-1.017	205.146
Carbon dioxide	$CO_2(g)$	4.5	-87.078	51.128	4.268	-1.469	0	213.794
Water	$H_2O(g)$	5.1	-11.750	34.376	7.841	-0.423	0	188.824

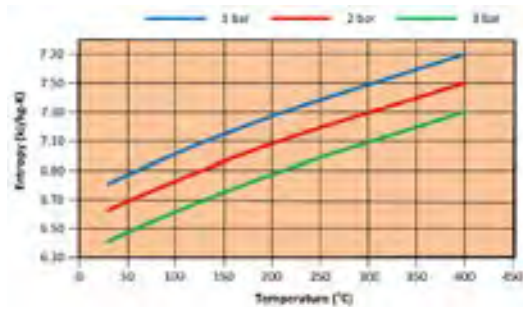


Figure 10. Exhaust gases entropy changing depends on temperature and pressure [11]

Exhaust gases entropy changing with temperature for three different pressures is given in figure 10 which shows that when pressure increases the exhaust gas entropy values decrease.

2.5. Turbocharger Pressure

The aim of turbocharger system is to obtain more power from smaller size engine. According to this, higher engine inlet air pressure means more power can be derived from the engine. Moreover, increasing inlet air pressure at compressor increases the compressor power consumption.

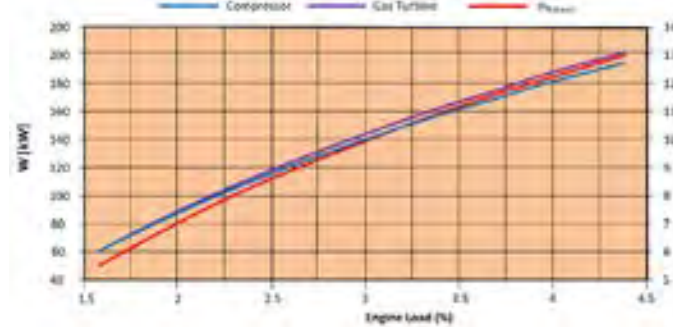


Figure 11. The compression power in turbocharger depending on compression ratio

Power consumption of 7L60ME-C8-TII engine turbocharger system which depends on turbocharger air pressure is shown in figure 11. It is showed that increasing inlet air pressure increases the power linearly.

$$\dot{m}_K = 0.982 * \dot{m}_{GT} \quad (5)$$

The relationship between air flow rate in compressor and exhaust flow rate in gas turbine is given by Eq. 5 [12]. Accordingly, air flow rate is almost equal to the exhaust air flow. Required compressor power for compressing the air to a certain pressure will be provided from the gas turbine. The produced power in gas turbine that required for compressor can be found from figure 11 when certain air compression pressure is defined. If flow rates of compressor and gas turbine are same the temperature difference in gas turbine will be found in figure 10.

2.6. Energy and Exergy Analyses

2.6.1. Energy Analysis

Energy and exergy definitions of thermodynamic model have to be studied before waste heat recovery systems. General energy equation is defined below for steady state open system

$$\dot{Q}_i + \dot{W}_i + \sum_i \dot{m} \left(h + \frac{V^2}{2} + gz \right) = \dot{Q}_o + \dot{W}_o + \sum_o \dot{m} \left(h + \frac{V^2}{2} + gz \right) \quad (6)$$

where (\dot{Q}_i) and (\dot{Q}_o) are inlet and outlet heat transfer rates, (\dot{W}_i) and (\dot{W}_o) are inlet and outlet powers $(\dot{m}_i h)$ and $(\dot{m}_o h)$ are inlet and outlet enthalpies, $\left(\dot{m}_i \frac{V^2}{2} \right)$ and $\left(\dot{m}_o \frac{V^2}{2} \right)$ are inlet and outlet kinetical energy of system, $(\dot{m}_i gz)$ and $(\dot{m}_o gz)$ are inlet and outlet potential energies.

2.6.2. Exergy Analysis

Exergy values of every state points in steady state open system are calculated by Eq.7.

$$\dot{E}_i^F = \dot{m}_i [(h_i - h_o) - T_o (s_i - s_o)] \quad (7)$$

where (\dot{E}_i^F) is physical exergy, (\dot{m}) is flow rate, (h_i) is entalpy, (s_i) is entropy and subscripts "0" is refer to ambient conditions.

$$\dot{E}_{j,i} = \dot{E}_{i,j} + \dot{E}_{v,j} \quad (8)$$

where $(\dot{E}_{i,j})$ is exergy inlet, $(\dot{E}_{o,i})$ is exergy outlet and $(\dot{E}_{v,i})$ is exergy destruction in the processes.

Exergy destruction of control volume in a steady state is defined as Eq. 9.

$$\dot{E}_{y,i} = \left\{ \sum \left[\dot{Q} \left(1 - \frac{T_0}{T} \right) \right]_{i,j} - \sum \left[\dot{Q} \left(1 - \frac{T_0}{T} \right) \right]_{o,j} \right\} + \sum (\dot{W}_i - \dot{W}_o) + \sum (\dot{E}_i - \dot{E}_o) \quad (9)$$

where (\dot{Q}_i) and (\dot{Q}_o) are refer to inlet and outlet heat rates.

2.7. Turbocharger System

2.7.1. Principles of turbocharger system

Turbocharger system supports higher pressure and lower volume air than atmospheric conditions to engine by using exhaust gases energy which allows to design more power from lower size cylinder

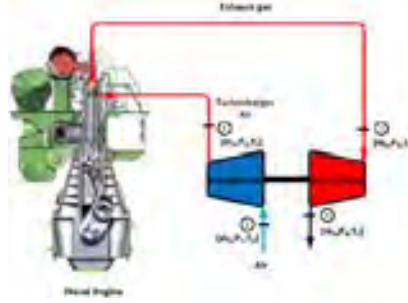


Figure 12. Turbocharger System

General layout of a turbocharger system is shown in figure 12 which consists of turbine and compressors section. Turbine is on the exhaust section and compressor is on the suction section and a shaft connects turbine to compressor. Exhaust gases waste heat energy converts to mechanical energy in turbine transfers via shaft to compressor to compress and support more air flow.

2.7.2. Thermodynamic model of turbocharger system

Air compressor supports air at higher pressure and rate and also lower volume in turbocharger system Compressor power consumption is approximately equal to turbine power and real compressor power is found with the ratio of ideal compressor power to compressor efficiency ($\eta_{K,M}$).

$$\dot{W}_K = \frac{\dot{m}_1 \cdot k \cdot R \cdot T_1}{k - 1} \left[\left(\frac{P_2}{P_1} \right)^{\frac{k-1}{k}} - 1 \right] \cdot \frac{1}{\eta_{K,M}} \quad (10)$$

Kinetic energy of exhaust gases is converted to mechanical energy in the gas turbine whose power is obtained by Eq. 11.

$$\dot{W}_{GT} = \dot{m}_3 \cdot C_{p,E} \cdot (T_3 - T_4) \quad (11)$$

Chemical exergy of fuel is calculated with Eq. 12 [13].

$$e_y^k = \left[1.0401 + 0.1728 \cdot \frac{H}{C} + 0.0432 \cdot \frac{O}{C} + 0.2169 \cdot \frac{S}{C} \cdot \left(1 - 2.0628 \cdot \frac{H}{C} \right) \right] \cdot \text{LHV} \quad (12)$$

where H, C, O and S are refer to hydrogen, carbon, oxygen and sulphur. It is suppose that fuel consist of 87.4% carbon, 9.5% hydrogen and 3% sulphur [14] and LHV is 42700 kj/kg for heavy fuel oil [15].

Chemical exergy is very important however physical exergy is negligible for combustion processes. Flow rate and chemical exergy rate of fuel are calculated with Eq. 13-14.

$$\dot{m}_y = \dot{m}_E - \dot{m}_H \quad (13)$$

$$\dot{E}_y = e_y^k \cdot \dot{m}_y \quad (14)$$

Table.3. General Formulations of Turbocharger System

Ex Des.	EPC	E	y
General	$EPC_1 = \frac{\dot{E}_c}{\dot{E}_{y,i}} = \frac{\dot{E}_g}{\dot{E}_{y,i}} - 1$	$\epsilon_i = \frac{\dot{E}_c}{\dot{E}_g} = 1 - \frac{\dot{E}_y}{\dot{E}_g}$	$y_i = \frac{\dot{E}_{y,i}}{\dot{E}_{y,T}}$
Compressor	$\dot{E}_{Y,K} = \dot{E}_1 + \dot{W}_K - \dot{E}_2$ $EPC_K = \frac{\dot{E}_2}{\dot{E}_{Y,K}}$	$\epsilon_K = \frac{\dot{E}_2}{(\dot{E}_1 + \dot{W}_K)}$	$y_K = \frac{\dot{E}_{Y,K}}{\dot{E}_{Y,T}}$
Gas Turbine	$\dot{E}_{Y,GT} = \dot{E}_3 - \dot{E}_4 - \dot{W}_{GT}$ $EPC_{GT} = \frac{(\dot{E}_4 + \dot{W}_{GT})}{\dot{E}_{Y,GT}}$	$\epsilon_{GT} = \frac{(\dot{E}_4 + \dot{W}_{GT})}{\dot{E}_3}$	$y_{GT} = \frac{\dot{E}_{Y,GT}}{\dot{E}_{Y,T}}$
Diesel Engine	$\dot{E}_{Y,DM} = \dot{E}_Y - \dot{W}_{DM}$ $EPC_{DM} = \frac{\dot{W}_{DM}}{\dot{E}_{Y,DM}} = \frac{\dot{E}_Y}{\dot{E}_{Y,DM}} - 1$	$\epsilon_{DM} = \frac{\dot{W}_{DM}}{\dot{E}_Y} = 1 - \frac{\dot{E}_{Y,DM}}{\dot{E}_Y}$	
GT+DE system	$\dot{E}_{Y,DM} + \dot{E}_{Y,GT} + \dot{E}_{Y,K}$ $EPC_{sistem} = \frac{(\dot{E}_4 + \dot{W}_{DM})}{(\dot{E}_{y,GT} + \dot{E}_{y,DM})}$	$\epsilon_{Sistem} = \frac{(\dot{E}_4 + \dot{W}_{DM})}{(\dot{E}_1 + \dot{E}_Y)}$	

3. RESULTS AND DISCUSSION

Table 5-6 are calculated from component efficiencies (Table 4) and thermodynamic model for turbocharger system. Calculations have done at ISO ambient condition and 80% engine load for MAN 7L60ME-C8-TII engine.

Table.4. Efficiency of Turbocharger Components

Mechanical Efficiency (η_m)	(%)	98
Isentropic Efficiency of Compressor ($\eta_{K,i}$)	(%)	65
Isentropic Efficiency of Turbine ($\eta_{c,i}$)	(%)	90

State properties are given at ISO ambient condition and 80% engine load in Table 5

Table.5. The Property of the states

State	T (°C)	P (bar)	h (kJ/kg)	s (kJ/kg.K)	\dot{E} (kW)	\dot{E}
1	25	1	299.5	6.867	30.26	$\dot{m}_1[(h_1 - h_0) - T_0(s_1 - s_0)]$
2	180	3.43	455.2	6.933	5087	$\dot{m}_2[(h_2 - h_0) - T_0(s_2 - s_0)]$
3	322.8	3.99	684.5	7.194	12004	$\dot{m}_3[(h_3 - h_0) - T_0(s_3 - s_0)]$
4	216	1.50	521	7.132	6597	$\dot{m}_4[(h_4 - h_0) - T_0(s_4 - s_0)]$

Exergetic performance parameters of the system components for ISO conditions and 80% engine load are shown in Table 6. The highest exergy destruction and also exergy destruction rate occurs in compressor beyond the diesel engine is seen from the result.

Table.6. Exergetic Performance Coefficient of the System Component

System Components	E_y (kW)	EPC_i	ϵ_i	y_i
Diesel Engine	13286	0.986	0.496	0.9606
Compressor	323	15.75	0.94	0.0233
Gas Turbine	221.5	53.19	0.959	0.0160
Total	13830	0.9487	0.7257	1

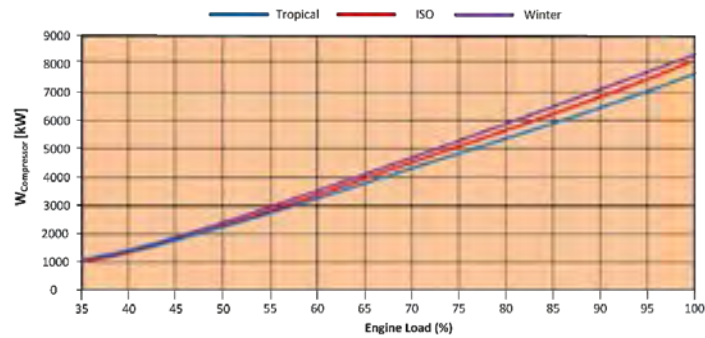


Figure 13. Compressor Power of MAN 7L60ME-C8-TII Engine for ambient conditions and engine load

Compressor inlet power in the turbocharger system for different ambient conditions and different engine loads are shown in figure 13. Compressor needs more power because of increasing compressed air flow rate at higher engine load and the lowest power consumption is seen at tropical conditions.

4. CONCLUSIONS

Performance of two-stroke Diesel engine operating various ambient conditions have been analyzed with respect to thermal efficiency, engine load, specific fuel oil consumption (SFOC), exergy efficiency and exergetic performance coefficient (EPC). The results show that the highest thermal efficiency is obtained in winter ambient condition and turbocharger efficiency increases when fuel-oil quality is better. A new numerical method is also improved for enthalpy and entropy calculation according to exhaust gas components. The compressor of turbocharger system needs more power at higher engine load and the lowest power consumption is obtained at tropical conditions.

Acknowledgments

The authors are thankful to Yildiz Technical University Institute of Science and Technology for providing opportunity to study on this subject.

References

- [1] E. H. Wang, H. G. Zhang, B. Y. Fan, M. G. Ouyang, Y. Zhao, and Q. H. Mu, "Study of working fluid selection of organic Rankine cycle (ORC) for engine waste heat recovery," *Energy*, vol. 36, no. 5, pp. 3406–3418, May 2011.
- [2] D. Marek, "On the possible increasing of efficiency of ship power plant with the system combined of marine diesel engine, gas turbine and steam turbine, at the main engine - steam turbine mode of cooperation," *Pol. Marit. Res.*, vol. 16, no. 59, pp. 47–52, 2009.
- [3] Bent Ørdrup Nielsen, "Waste Heat Recovery System," 07-Jan-2011.
- [4] MAN Diesel & Turbo, "Influence of Ambient Temperature Conditions Main engine operation of MAN B&W two-stroke engines."
- [5] Volkmar Galke, "Turbo Compound System with Power Turbine and Generator," 28-Jul-2011.
- [6] MAN Diesel & Turbo, "Engine room and performance data for 7S80MC-C8.2-TII with 2 x MAN TCA77-21 and high load tuning." MAN Diesel & Turbo, 25-Jun-2013.
- [7] Dimitrios T. Hountalal, Antonis K. Antonopoulos, Nikolaos F. Sakellaris, Georgios N. Zovanos, Efthimios G. Pariotis, and Roussos G. Papagiannakis, "Computational Investigation of the Effect of Ambient Conditions on the Performance of Turbocharged Large Scale Marine Diesel Engines," presented at the The 25th international conference on efficiency, cost, optimization, simulation and environmental impact of energy systems, Perugia, Italy, 2012.
- [8] MAN Diesel & Turbo, "Soot Deposits and Fires in Exhaust gas Boilers."
- [9] MAN Diesel & Turbo, MAN B&W S70ME-C8-TII Project Guide Electronically Controlled Two-stroke Engines, 1st Edition. MAN Diesel & Turbo, 2010.
- [10] A. Domingues, H. Santos, and M. Costa, "Analysis of vehicle exhaust waste heat recovery potential using a Rankine cycle," *Energy*, vol. 49, pp. 71–85, Jan. 2013.
- [11] A. Bejan, G. Tsatsaronis, and M. Moran, *Thermal Design and Optimization*, 1st ed. Wiley-Interscience, 1995.
- [12] MAN Diesel & Turbo, MAN B&W L60ME-C8-TII Project Guide Electronically Controlled Two-stroke Engines, 1st Edition. MAN Diesel & Turbo, 2010.
- [13] Perihan Sekmen and Zeki Yılbaş, "Application of Energy and Exergy Analyses To A CI Engine Using Biodiesel Fuel," *Math. Comput. Appl.*, vol. 16, no. 4, pp. 797–808, 2011.
- [14] K. D. Bartle, J. M. Jones, A. R. Lea-Langton, M. Pourkashanian, A. B. Ross, J. S. Thillaimuthu, P. R. Waller, and A. Williams, "The combustion of droplets of high-asphaltene heavy oils," *Fuel*, vol. 103, pp. 835–842, Jan. 2013.
- [15] MAN Diesel & Turbo, MAN B&W S35ME-B9-TII Project Guide Electronically Controlled Two-stroke Engines, 1st Edition. MAN Diesel & Turbo, 2010.

ANALYSIS OF THE TURKMEN TENTS THAT PROVIDE ENERGY EFFICIENCY BY USE OF NATURAL MATERIAL FROM THE SOCIO-ECONOMIC AND ENVIRONMENTAL POINT OF VIEW

Gülşen CENGİZ

Dokuz Eylül University, Department of Architecture, 35000, Buca/İzmir, Turkey.

glschn@hotmail.com

Abstract

The Turkmen tent has been used for more than two thousand years and represents a significant part of Turk culture and lifestyle. Turkmen tents were preferred for years due to its many properties such as use of natural and local material, being economic, light weight and ease of mantling and dismantling. In addition, Turkmen tents are energy efficient and sustainable structures since they have the abilities to increase interior air quality, have natural insulation, climatization, as well as natural and local material usage. For these reasons, Turkmen tents do not degrade the environment.

Keywords: *Turkmen tents, Socio-economic, Environment*

Analysis of the Turkmen Tents that Provide Energy Efficiency by Use of Natural Material from the Socio-Economic and Environmental Point of View, Gülşen Cengiz

1. ORIGINS OF TURKMENS, LANGUAGE AND CULTURAL STRUCTURE

Turkmen is a term. Not only people live in Turkmenistan, which is a Turkic republic**, but also members of whole Oghuz tribes (Oghuz Turks) are called Turkmen. They speak Turkmen, a member of Turkic language, takes part of Altai Language family. In older times, they had belief of “Göktengri” and “Shaman”. Now, majority of them are muslims. They live in Turkmenistan, Turkey, Azerbaijan in the first place, and also in Balkans, Afghanistan, Pakistan, Russia, Ukraine, Iraq, Syria and Iran. They live in lands, ranging from middle Asia to Europe with Turk migrations. And these Turk migrations caused migration of tribes.

*Turkic languages: Oghuz group: Istanbul Turkish (or Turkish), Azerbaijani, Turkmen; Kipchak group: Kazakh, Kyrgyz, Karakalpak, Nogay, Karachay, Bashkir, Kumuk; Uyghur group (Chagatay group): Uzbek, Uigur, Salar; Yakutia group: Yakutia; Chuvash group: Chuvash.

**Turkic Republics: Republics, originated from Turk.



Analysis of the Turkmen Tents that Provide Energy Efficiency by Use of Natural Material from the Socio-Economic and Environmental Point of View, Gülşen Cengiz

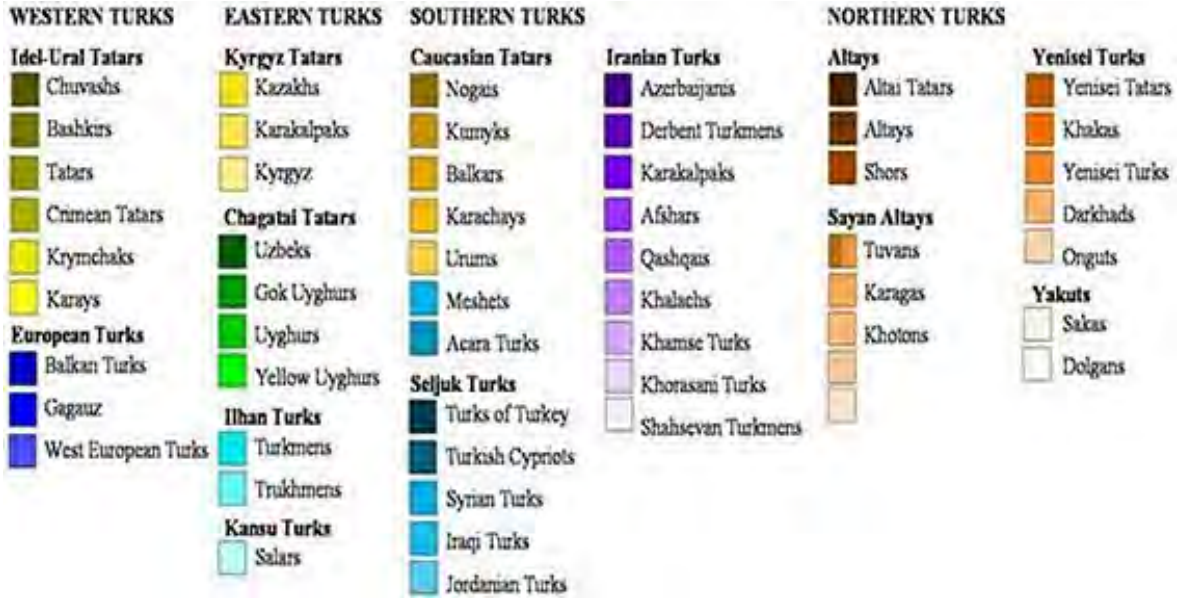


Figure 1. A map shows the areas in which Turkic people live [12]

2. YORUK TURKMEN CULTURE

Yoruk Turkmenis are nomadic Turkmenis. In middle Asia, they lived in urban land and low altitudes in winters, plateau and uplands in summers. Their archery skills are very good. Therefore although they lived via animal husbandry, they also hunted and gathered. Their lives were spent in Turkmen tents which is also called “Yurt”. These tents wholly represent the Turkmen culture. Since they carry their tents with them on camels, they packed light. At the present time this tradition continues with the use of summer (beach house or mountain house) or winter houses (urban house).



Figure 2. Turkmen tent with black hair felt [9]

Analysis of the Turkmen Tents that Provide Energy Efficiency by Use of Natural Material from the Socio-Economic and Environmental Point of View, Gülşen Cengiz



Figure 3. Inside of a Turkmen tent with traditionally Turkmen , during migration by camels [11]



Figure 4. Turkmen tent [9]

3. MATERIALS AND CONSTRUCTION OF TURKMEN TENTS

Natural materials are used in Turkmen tents. These are stones, straws, shrubs, wood, carpet, and hair tent cover. Usually they sheared sheep and goats, and spinned their hair for covering roof top and walls. These hair tents have water repellent properties and they dry quickly. Commonly walls are made from stones, straws and shrubs. Yet sometimes there is wood in modern examples. There are Turk patterns on plaited walls, carpets and hair tent covers. Principal posts, supported with sticks around them, are used as structural elements. The size of tents depends according to size of family. Tents with 3-5-7 principal posts are common. To send water away from the tent, channels are dugged around it. In the front of the tent, there is a half open area with only its top covered.

Analysis of the Turkmen Tents that Provide Energy Efficiency by Use of Natural Material from the Socio-Economic and Environmental Point of View, Gülşen Cengiz



Figure 5. Interior of a Turkmen tent [11]



Figure 6. Turk patterns on Turkmen carpets [1] [11]

4. PROCESS OF CONSTRUCTING TURKMEN TENT AND DESIGN CRITERIAS

Principal posts (3-5-7 piece) are put in place and supported with sticks. Top of the tent is covered with hair tent cover. Walls are put up with different materials. Differing materials can be used in the same tent roof due to its orientation. In modern examples, wooden structures are used as a wall. After this, walls are covered with hair tent cover. In addition the walls are stabilized with wrapping straw around it. The North side is enclosed with sacks or large closet for bedding. To prevent moisture from the base, a line of slate stone is paved on the ground. Carpets with Turk pattern are laid on the slate paved ground. Tents for winter are covered with shrub walls. These shrubs are also used for cooking, heating and lighting in daily life. For winter tents, entrance is designed facing South. In this way, day light enters inside. In summer, entrance of the tent is positioned to face North. Thereby, Northern winters enter inside. In entrance, there is a place for taking off shoes, and nearby is an empty place that serves as a kitchen service area. Apart from compulsory kitchen supplies, they make leathers and weavings by themselves. In summer, white hair tent cover is used for reflect daylight to prevent over heating. In winter black hair tent is used for absorbing day light. In entrance, the tents consist semi open space with top cover.

Analysis of the Turkmen Tents that Provide Energy Efficiency by Use of Natural Material from the Socio-Economic and Environmental Point of View, Gülşen Cengiz

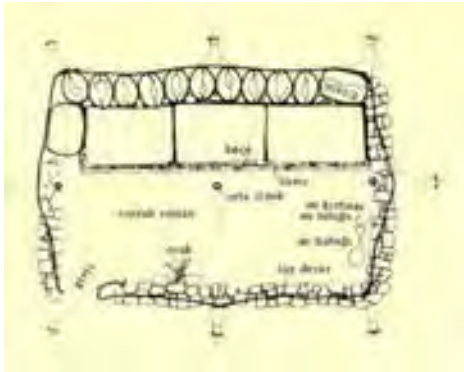


Figure 7. Plan [7]

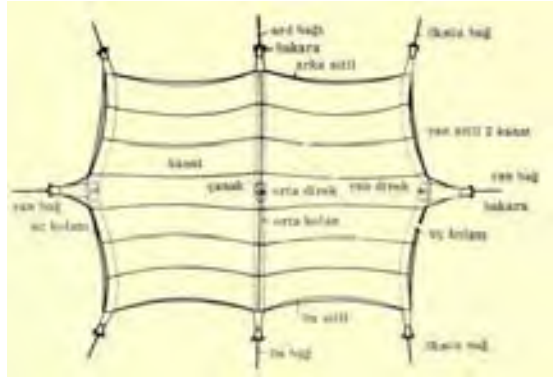


Figure 8. Roof plan [7]

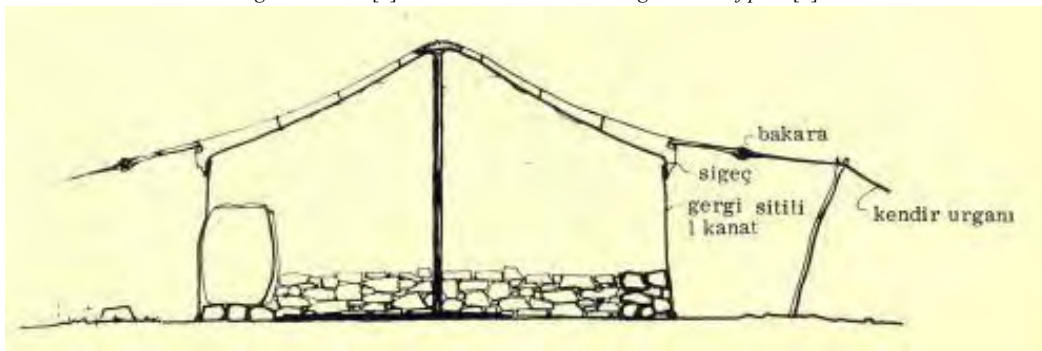


Figure 9. Turkmen tent's section [7]



Figure 10. Making top cover of tent with swing tent flap side by side [8]

Analysis of the Turkmen Tents that Provide Energy Efficiency by Use of Natural Material from the Socio-Economic and Environmental Point of View, Gülşen Cengiz



Figure 11. Pitch a tent[8]



Figure 12. Digging channels around tent[8]

Analysis of the Turkmen Tents that Provide Energy Efficiency by Use of Natural Material from the Socio-Economic and Environmental Point of View, Gülşen Cengiz



Figure 13. Creating half open place covered from top in the entrance of tent [8]



Figure 14. A pitched up Turkmen tent with it's half open entrance [8]

5. ANALYSIS OF THE TURKMEN TENT FROM ENVIRONMENTAL POINT OF VIEW

Materials used in Turkmen tents are completely natural. Hair tent covers have water repellent and quick drying properties. Nowadays, water resistant hair tent covers are available. With it's semi porous properties they help with natural ventilation and improve interior air quality. The entrance faces South in the summer and faces North in the winter, thus cause natural lighting and cliamtisation effects are evident. Shrub walls and large closet for bedding block North winds in winter and create a natural buffer zone. Felt has natural insulation properties and is cold proof in

Analysis of the Turkmen Tents that Provide Energy Efficiency by Use of Natural Material from the Socio-Economic and Environmental Point of View, Gülşen Cengiz

winter and hot proof in summer. In winter, black felt absorb day light. In summer, white ones reflect day light and cools the interior. Therefore, interior comfort and natural climatization is possible.

6. CONCLUSION

The Turkmen tent has been used for more than two thousand years and represents a significant part of Turk culture and lifestyle. Turkmen tents were preferred for years due to its many properties such as usage of natural and local material, being economic, light weight and ease of mantling and dismantling. In addition, Turkmen tents are energy efficient and sustainable structures since they have the abilities to increase interior air quality, have natural insulation, climatization, as well as natural and local material usage. For these reasons, Turkmen tents do not degrade the environment.

REFERENCES:

- [1]. AHARON, A., 6 August 2005, http://www.turkotek.com/misc_00030/two-sided_asmalyk.htm (Download date: 27 October 2014)
- [2]. *Ancyclopaedia of Britannica*, 27 October 2014, *Altaic Languages*, <http://global.britannica.com/EBchecked/topic/17472/Altaic-languages> (Download date: 27 October 2014)
- [3]. *Ancyclopaedia of Britannica*, 27 October 2014, *Turkic People*, <http://global.britannica.com/EBchecked/topic/609972/Turkic-peoples> (Download date: 27 October 2014)
- [4]. *Ancyclopaedia of Britannica*, 27 October 2014, *Turkmen* <http://global.britannica.com/EBchecked/topic/610111/Turkmen> (Download date: 27 October 2014)
- [5]. *Central Intelligence Agency*, 27 October 2014, <https://www.cia.gov/library/publications/the-world-factbook/geos/tx.html#People> (Download date: 27 October 2014)
- [6]. DOĞAN, M., DOĞAN, C., 27 October 2014, *Yörüklerin Hayat Tarzı*, <http://www.journals.istanbul.edu.tr/iusskd/article/viewFile/1023000482/1023000438> (Download date: 27 October 2014)
- [7]. KADEMOĞLU, O., *Mayıs 1974, Yörüklerde Üç Direkli Karaçadır*, <http://dergi.mo.org.tr/dergiler/4/469/6874.pdf> (Download date: 27 October 2014)
- [8]. KAVAS, K., 2013, *Mimariyi "Dokumak": Anadolu – Batı Toros Göçerlerinde Çevre - Kültür İlişkisi*, <http://yavinlar.yesevi.edu.tr/files/article/644.pdf> (Download date: 27 October 2014)
- [9]. SBB, 27 October 2014, http://www.sektorbilgibankasi.com/firma/7158/madran-kil-cadir-ve-kil-tarama-imalati/urun.goster_2509_kil-cadiri-ve-yoruk-cadiri.html (Download date: 27 October 2014)
- [10]. SUMER, F., *Oğuzlar (Türkmenler) Tarihleri- Boy Teşkilatı Destanları*, 1999, İstanbul
- [11]. *The Metropolitan Museum of Art*, 27 October 2014, http://www.metmuseum.org/learn/for-educators/publications-for-educators/~/_media/Files/Learn/For%20Educators/Publications%20for%20Educators/Islamic%20Teacher%20Resource/Unit6.pdf (Download date: 27 October 2014)
- [12]. *University of Michigan*, 27 October 2014, <http://www.umich.edu/~turkish/turkic.html> (Download date: 27 October 2014)

PARTICLE SWARM OPTIMIZATION APPROACH TO SOLVE SINGLE MACHINE TOTAL WEIGHTED TARDINESS PROBLEM WITH UNEQUAL RELEASE DATE

Serdar ÖZER

Corresponding author: Trakya University, Technology Transfer Office, Edirne / Turkey, Turkey.
serdarozer@trakya.edu.tr

Tarik ÇAKAR

Sakarya University, Engineering Faculty, Industrial Engineering Department, 54187 Esentepe Campus,
Sakarya / TURKEY, tcakar@sakarya.edu.tr

Abstract

Real-world manufacturing systems are affected by various, which must be taken into consideration to obtain an effective schedule. Single machine total weighted tardiness problem (SMTWT) is a well-known strongly NP hard problem. This paper is concerned with solving the single machine total weighted tardiness problem with unequal release date using Particle Swarm Optimization (PSO). PSO is one of the population based optimization method, which never filters the solution alternatives. Population members of PSO are called particles, each particle flies in the search space with a velocity. PSO has been applied to SMTWT with unequal release date problem. To escape local minima Simulated Annealing (SA) method has been used, to help PSO algorithm. In this study groups of jobs have been generated using some parameters. FCFS, SPT, LPT, EDD, CR have been applied to generated problems. PSO has been applied to obtained solutions from FCFS, LPT, SPT, EDD, CR heuristics. Through the analyses of experimental results, its highly effective performance with substantial margins in solution quality. PSO provides sufficient conditions for optimality in SMTWT problem with unequal release date. Also it is understandable form the results that EDD is the best heuristics for SMTWT problems.

Keywords: *Particle Swarm Optimization, Total Weighted Tardiness Problem, Single Machine Scheduling*

Particle Swarm Optimization Approach to Solve Single Machine Total Weighted Tardiness Problem With Unequal Release Date, Serdar OZER and Tarik CAKAR

1. INTRODUCTION

We study the single machine total weighted tardiness problem subject to unequal release dates. Particle swarm optimization method which provides better solutions for a single machine total weighted tardiness problem with unequal release dates, $1 \mid r_i \mid \sum w_i T_i$ is presented. Despite the fact that customer orders cannot reach simultaneously in daily life problems, according to the literature and the best of our knowledge we know that there is only one exact approach on the $1 \mid r_i \mid \sum w_i T_i$ problem. Chu and Portmann [1] proposed in their paper that this problem could be simplified using corrected due dates, i.e. if $r_j + p_j > d_j$ then d_j takes the value $r_j + p_j$. Jobs will be processed without interrupting on a single machine which can process only one job at a time. If job j is completed after due date d_j , a tardiness penalty is exceeds for each time unit, thus $T_j = \max\{0, (C_j - d_j)\}$, where C_j and T_j are the completion time and the tardiness of the job j , respectively. The aim is to find a schedule minimizing the total weighted tardiness of all jobs given that any jobs cannot start processing before its release date. It is stated that the total tardiness problem with unequal release dates, $1 \mid r_i \mid \sum w_i T_i$ is NP-hard by Rinnooy Kan [2]. In a paper of Lawler, the total weighted tardiness problem, $1 \mid \sum w_i T_i$, has been shown strongly NP-hard, therefore the researchers know that unequal release date problems are already strongly NP-hard. Solution methods based on enumeration have been proposed for both weighted and unweighted situations when all jobs are initially present. Branch and bound (B&B) algorithms has been presented by Chu [3] and Dessouky and Deogun [4] to minimize total flow time, $1 \mid r_i \mid \sum F_i$, whereas Bianco and Ricciardelli [5] and Hariri and Potts [6] take into consideration the total weighted completion time problem, $1 \mid r_i \mid \sum w_i C_i$. Potts and Van Wassenhove [7] has proposed a B&B algorithm for the minimization of the weighted number of late jobs.

2. PARTICLE SWARM OPTIMIZATION (PSO)

PSO is one of the latest evolutionary optimization techniques and it is based on the metaphor of social interaction an communication such as bird flocking and fish schooling. Since it is population – based and evolutionary in nature, the members in a PSO algorithm tend to follow the leader of the group, i.e., the one with the best performance. The details of PSO algorithm will be described in the following section. Although PSO is still new in evolutionary computation field, it has been applied to a wide range of applications such as power and voltage control, optimal power flow design and task assignment problem [8][9][10].

The following formula is used to construct the initial continuous position values of the particle:

$$x_{ij}^0 = x_{\min} + (x_{\max} - x_{\min}) * U(0,1)$$

where $x_{\min} = 0.0$, $x_{\max} = 4.0$, and $U(0,1)$ is a uniform random number between 0 and 1. Initial continuous velocities are generated by similar formula as follows:

$$v_{ij}^0 = v_{\min} + (v_{\max} - v_{\min}) * U(0,1)$$

where $v_{\min} = -4.0$, $v_{\max} = 4.0$ and $U(0,1)$ is a uniform random number between 0 and 1.

As the formulation of the SMTWT problem suggests that the objective is to minimize the total weighted tardiness, the fitness function value is the total weighted tardiness for the particle of the population or swarm. That is,

$$f_i^k(S_i^k) = \sum_{j=1}^n w_{ij} T_{ij}$$

Where S_i^k is the corresponding sequence of particle X_i^k . For simplicity, $f_i^k(S_i^k)$ will be denoted as f_i^k . The complete computational flow of the PSO algorithm for the SMTWT problem can be summarized as follows:

Step 1: Initialization

- Set $k = 0$, $m =$ twice the number of dimensions
- Generate m particles randomly as explained before, $\{X_i^0, i = 1, \dots, m\}$ where $X_i^0 = [x_{i1}^0, \dots, x_{in}^0]$.
- Generate initial velocities of particles randomly $\{V_i^0, i = 1, \dots, m\}$ where $V_i^0 = [v_{i1}^0, \dots, v_{in}^0]$.
- Apply the SPV rule to find the sequence $S_i^0 = [s_{i1}^0, \dots, s_{in}^0]$. of particle X_i^0 for $i = 1, \dots, m$
- Evaluate each particle i in the swarm using the objective function f_i^0 for $i = 1, \dots, m$.
- For each particle i in the swarm, set $PB_i^0 = X_i^0$, where $PB_i^0 = [pb_{i1}^0 = x_{i1}^0, \dots, pb_{in}^0 = x_{in}^0]$ along with its best fitness value, $f_i^{pb} = f_i^0$ for $i = 1, \dots, m$.

Particle Swarm Optimization Approach to Solve Single Machine Total Weighted Tardiness Problem With Unequal Release Date, Serdar OZER and Tarik CAKAR

- Find the best fitness value $f_i^0 = \min \{f_i^0\}$ for $i = 1, \dots, m$ with its corresponding position X_i^0 .
- Set global best to $GB^0 = X_i^0$ where $GB^0 = [gb_1 = x_{1,1}, \dots, gb_n = x_{1,n}]$ with its fitness value $f_{gb} = f_i^0$

Step 2: Update iteration counter

$k = k + 1$

Step 3: Update inertia weight

$w^k = w^{k-1} * a$ where a is decrement factor.

Step 4: Update velocity

$v_{ij}^k = w^{k-1}v_{ij}^{k-1} + c_1r_1(pb_{ij}^{k-1} - x_{ij}^{k-1}) + c_2r_2(gb_j^{k-1} - x_{ij}^{k-1})$

Step 5: Update position

$X_{ij}^k = x_{ij}^{k-1} + v_{ij}^k$

Step 6: Find Sequence

Apply the SPV rule to find the sequence $S_i^k = [s_{i1}^k, \dots, s_{in}^k]$ for $i = 1, \dots, m$

Step 7: Update personal best

Each particle is evaluated by using its sequence to see if personal best will improve. That is, if $f_i^k < f_i^{pb}$ for $i = 1, \dots, m$, then personal best is updated as $PB_i^k = X_i^k$ and $f_i^{pb} = f_i^k$ for $i = 1, \dots, m$

Step 8: Update global best

Find the minimum value of personal best.

$f_1^k = \min \{f_i^{pb}\}$ for $i = 1, \dots, m$

if $f_1^k < f^{gb}$, then the global best is updated as $GB^k = X_i^k$ and $f^{gb} = f_1^k$

Step 9: Stopping criterion

If the number of iteration exceeds the maximum number of iteration, or maximum CPU time, then stop, otherwise go to step 2.

The basic elements of PSO algorithm is summarized as follows:

Particle: X_i^k denotes the i^{th} particle in the swarm at iteration k and is represented by n number of dimensions as $X_i^k = [X_{i1}^k, \dots, X_{in}^k]$, where x_i is the position value of the i^{th} particle with respect to the j^{th} dimension ($j = 1 \dots n$).

Population: pop^k is the set of m particles in the swarm at iteration k , i.e., $pop^k = [X_1^k, \dots, X_m^k]$

Sequence: We introduce a new variable S_i^k , which is a sequence of jobs implied by the particle X_i^k . It can be described as $S_i^k = [S_{i1}^k, \dots, S_{in}^k]$, where S_{ij}^k is the assignment of job j of the particle i in the processing order at iteration k with respect to the j^{th} dimension.

Particle velocity: V_i^k is the velocity of particle i at iteration k . It can be defined as $V_i^k = [V_{i1}^k, \dots, V_{in}^k]$, where V_{ij}^k is the velocity of particle i at iteration k with respect to the j^{th} dimension.

Inertia weight: w^k is a parameter to control the impact of the previous velocities on the current velocity.

Personal best: PB_i^k represents the best position of the particle i with the best fitness until iteration k . So, the best position associated with the best fitness value of the particle i obtained so far is called the personal best. For each particle in the swarm, PB_i^k can be determined and updated at each iteration k . In a minimization problem with the objective function $f(S_i^k)$ where S_i^k is the corresponding sequence of particle X_i^k , the personal best PB_i^k of the i^{th} particle is obtained such that $f(S_i^k) \leq f(S_i^{k-1})$ where S_i^{k-1} is the corresponding sequence of personal best PB_i^{k-1} and S_i^{k-1} is the corresponding sequence of personal best PB_i^{k-1} . To simplify, we denote the fitness function of the personal best as $f_i^{pb} = f(S_i^k)$. For each particle, the personal best is defined as $PB_i^k = [pb_{i1}^k, \dots, pb_{in}^k]$ where pb_{ij}^k is the position value of the i^{th} personal best with respect to the j^{th} dimension.

Global best: GB^k denotes the best position of the globally best particle achieved so far in the whole swarm. For this reason, the global best can be obtained such that $f(S^k) \leq f(S_i^k)$ for $i = 1, 2, \dots, m$ where S^k is the corresponding sequence of global best GB^k and S_i^k is the corresponding sequence of particle best PB_i^k . To simplify, we denote the fitness function of the global best as $f^{gb} = f(S^k)$. The global best is then defined as $GB^k = [gb_1^k, \dots, gb_n^k]$ where gb_i^k is the position value of the global best with respect to the j^{th} dimension.

Termination criterion: It is a condition that the search process will be terminated. It might be a maximum number of iteration or maximum CPU time to terminate the search.

Pseudo code of the PSO algorithm;

Initialize parameters

Initialize population

Find sequence

Evaluate

Do; *Find the personal best*

Find the global best

Update velocity

Particle Swarm Optimization Approach to Solve Single Machine Total Weighted Tardiness Problem With Unequal Release Date, Serdar OZER and Tarik CAKAR

Update position
Find sequence
Evaluate
Apply local search (optional)
While (Termination)

Initial Population

The first step to solve SMTWT using PSO algorithm is to define the initial coordinate and speed of PSO particle randomly $x_{ij}^0 = x_{min} + (x_{max} - x_{min}) * U(0,1)$ where $x_{min} = 0.0$, $x_{max} = 4.0$ and $U(0,1)$ is between 0 and 1 uniform random number. Similarly for the initial speed: $v_{ij}^0 = v_{min} + (v_{max} - v_{min}) * U(0,1)$ where is $v_{min} = -4.0$, $v_{max} = 4.0$ and $U(0,1)$ uniform random number. In this paper, PSO algorithm is prepared for 10 particle, while finding the initial value of 5 of these particles, the sequences that are set up by the results of FCFS, SPT, EDD, LPT, CR algorithms is used, and 5 particles of PSO algorithms is provided to start to work on this solution.

3. EXPERIMENTAL DESIGN

In this study, each SMTWT problem scheme was tested on a set of randomly generated data. We have tested problems with 50, 70 and 100 jobs, which were generated as: for each job i , p_i and w_i were generated from two uniform distributions, [1, 10] and [1, 100] to create low or high variation, respectively. Here as stated early, p_i and w_i refers to an integer processing time and an integer weight, respectively. The proportional range of due dates (RDD) and average tardiness factor (TF) were selected from the set {0.1, 0.3, 0.5, 0.7, 0.9}. d_i , an integer due date from the distribution $[P(1-TF-RDD/2), P(1-TF+RDD/2)]$ was produced for each job i , here, P refers to total processing time. Release dates are generated from a uniform distribution between 0 and $\mu \sum p_j$. As summarized in Table 1, we considered and evaluated 1200 example sets and took 100 replications for each combination resulting among 120.000 randomly generated runs.

Table-1 Experimental design

FACTORS	RANGE
NUMBER OF JOBS	50-70-100
PROCESSING TIME RANGE	[1-10], [1-100]
WEIGHT RANGE	[1-10], [1-100]
RDD	0.1 0.3 0.5 0.7 0.9
TF	0.1 0.3 0.5 0.7 0.9
μ	0.0 0.5 1.0 1.5

Table 2. TWT Results of PSO algorithms

PRIORITY RULES	TOTAL WEIGHTED TARDINESS	AFTER PSO	Improvement (%)
SPT-50	850712	801597	0.068
EDD-50	1211347	968020	0.081
LPT-50	1829357	1103658	0.096
FCFS-50	1765308	989632	0.102
CR-50	1056978	856975	0.098
SPT-70	965874	903658	0.072
EDD-70	1569874	1125689	0.085
LPT-70	1996352	1263254	0.099
FCFS-70	1963247	1256987	0.115
CR-70	1205846	986321	0.121
SPT-100	1102547	965742	0.089
EDD-100	1695325	1012548	0.092
LPT-100	2013657	1459862	0.136
FCFS-100	2102356	1506941	0.133
CR-100	1358901	998754	0.119

Particle Swarm Optimization Approach to Solve Single Machine Total Weighted Tardiness Problem With Unequal Release Date, Serdar OZER and Tarik CAKAR

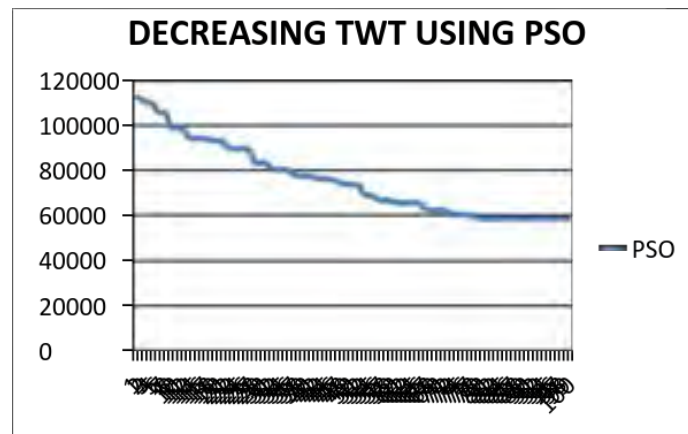


Figure 1. Decreasing total weighted tardiness for an example problem using PSO

Results show that PSO algorithm can improve the TWT for single machine. It can be seen in table 2. Also a particular problem how PSO works in a particular problem can be seen.

4. CONCLUSION

In this paper we presented a solution approach to Machine Total Weighted Tardiness Problem with unequal release dates (SMTWT). Results of the PSO algorithm show that SMTWT can be solved by using PSO algorithm. PSO can improve the results of some priority rules (EDD, SPT, LPT, FCFS, CR), which can be seen on the results. For further research, to solve SMTWT with unequal release date problem can be used a hybrid PSO system.

REFERENCES

- [1] Chu, C. and Portman, M.C., 1992, Some new efficient methods to solve the $n | 1 | r_i | \sum w_i T_i$ scheduling problem, *European Journal of Operation Research*, 1992, 58, 404-413.
- [2] Rinnooy Kan, A.H.G., 1976, *Machine scheduling problems: Classification complexity and computations*, Nijhoff, The Hague.
- [3] Chu, C., 1992, A Branch-and-bound algorithm to minimize total tardiness with unequal release dates, *Naval research logistics*, 39, 265-283.
- [4] Dessouky, M.I. and Deogun, J.S., 1981, Sequencing jobs with unequal ready times to minimize mean flow time, *SIAM Journal of Computing*, 10, 192-202.
- [5] Bianco, L. and Ricciardelli, S., 1982, Scheduling of a single machine to minimize total weighted completion time subject to release dates, *Naval Research Logistics*, 29(1), 151-167.
- [6] Hariri, A.M.A., and Potts, C.N., 1983, An algorithm for single machine sequencing with release dates to minimize total weighted completion time, *Discrete Applied Mathematics*, 5, 99-109.
- [7] Potts, C.N. and Van Wassenhove, L.N., 1985, A Branch and bound algorithm for total weighted tardiness problem, *Operation Research*, 33, 363-377.
- [8] Tasgetiren, F. M., Liang, Y., Sevcli, M., Gencyilmaz, G., 2004, Particle Swarm Optimization Algorithm for Single Machine Total Weighted Tardiness Problem, *Evolutionary Computation IEEE*, 1413.
- [9] Kennedy, J., Eberhart, R. C., 1995, "Particle Swarm Optimization", *Proc. Of the IEEE Int. Conference on Neural networks*, 4, 1942-1948.
- [10] Wilke D. N., 2005, Analysis of the Particle Swarm Optimization Algorithm, Master Thesis, Mechanical and Aeronautical Engineering, University of Pretoria.

SAPANCA LAKE AIR POLLUTION ORIGINATING FROM TRANSPORTATION-INVESTIGATION OF HEAVY METAL EMISSIONS

Hülya DEMIREL

Corresponding author: Sakarya University, Environmental Protection and Control Program, 54000, Sakarya, Turkey.
hsemercioglu@sakarya.edu.tr

Asude ATEŞ

Sakarya University, Environmental Engineering Department, 54187, Sakarya, TURKEY,
aates@sakarya.edu.tr

Şeref SOYLU

Bilecik Seyh Edebali University, Mechanical Manufacturing Engineering Department, 11230, Bilecik, Turkey,
seref.soylu@bilecik.edu.tr

Abstract

Due to the population growth and the quality improvement of people's lives due to industrialization; the number of vehicles in traffic is increasing rapidly in the developing cities. This situation causes air pollution originating from transportation. Transportation-originated emissions of heavy metals are serious threats for the ecology and human health. Particles of heavy metals are released to the atmosphere from the vehicles because of the brake and tire wears, vehicle and road corrosion, oil leaks and exhaust systems. These pools of emissions on the roads are usually moved to different places by the effects of wind and rain. Especially, they seriously affect the water resources that are close to the highways. Sapanca Lake which is an important source of drinking water has two highways on both northern and southern parts. The aim of this study is the annual investigation of emissions affecting the Sapanca Lake. D-100 highway and E-80 TEM Anatolian motorways are surround Sapanca Lake; therefore their best sections to determine the effects of the roads were selected; and the traffic characteristics between 08:00 and 08:00 to next day were examined. Total monitoring period is 24 hours. The vehicles that used these highways were classified as cars, buses, light duty vehicles, trucks and motorcycles. The emission amounts were calculated for each vehicle class by using CORINAIR (COPPERT III) emission factors (EF) and fuel consumption per km (FC).

Keywords: Air pollution, transportation, traffic density, heavy metal effect

1. INTRODUCTION

Today, factors such as rapid population growth, unguided urbanization, technological developments, unconscious use of natural resources and industrialization have ruined the ecological balance and cause environmental pollution. Environmental pollution-causing pollutant sources are classified as industry, warming and traffic. Increase of environmental pollution, adversely affect the quality of water resources. Domestic, industrial and agricultural wastewater discharged to surface water sources without purifying primarily cause the deterioration in water quality. However, the number of vehicles used for the transportation needs of people and fossil fuels used for heating in residential areas also adversely affect the quality of water.

Particulate matter (PM), nitrogen oxides (NO_x), carbon monoxide (CO) and hydrocarbons (HC) are the primary pollutants caused by motor vehicles.

Traffic, according to the inventory of the EU15, is responsible for the 42% of total NO_x emissions, 47% of total CO emissions and 18.4% of total PM emissions [1]. Apart from these pollutants, heavy metals are released to the atmosphere by vehicles such as lead (Pb), cadmium (Cd), nickel (Ni), copper (Cu), chromium (Cr), zinc (Zn).

Traffic-borne heavy metals emissions both threaten human health and cause serious ecological problems. Motor vehicles-borne pollutants exist as gas and particle in the atmosphere [2]. Heavy metals result from the brakes and tyre wear, transportation and road corrosion, oil spills and exhaust systems. Traffic-borne heavy metals emissions are examined as exhaust and non-exhaust emissions in the studies. Many emission inventories, modeling studies have been carried out to determine the deterioration of air and water quality caused by traffic, however, these studies has been in region scale.

Traffic-borne emissions inventory is prepared in a study carried out in Italy and COPERT III model was used. CO, NMVOC SPECIES, PM and NO_x emissions for the year 2001 is examined as 79, 520 tone, 11, 547 tone, 1867 tone and 19, 380 tone [3].

Traffic-borne PM and heavy metals emissions (Pb, Cu, Cr, Se, Zn, Ni and Cd) between the years 1996-2001 are examined in a study carried out in India by using COPERT III model. The amount of heavy metals Cu and Zn has been largely high [4].

Kummer and his friends examined the heavy metals which are released through European road transport services. They calculated the country-based exhaust and non-exhaust emission quantities by identifying the vehicles' activities and fuel consumption amounts [5].

Traffic-borne NO_x concentration and in parallel, the heavy metal emissions are examined in a study carried out in Sweden by using COPERT III model. It is understood that Cu emissions results in 90% from brake wear and 90% of Ni emissions and 40% of Zn emissions result from exhaust [6].

Gunawardena and his friends examined the traffic-borne MN, Pb, Cu, Zn and Cr emissions sources and transportation routes [7]. Vehicles are counted on the selected routes for these types of studies and emission quantities are calculated by determining the emission factor from the literature. In our country, similar studies are carried out in order to determine the air pollution originated from regional-based traffic [8].

Traffic-borne air quality is identified in a university campus. Vehicles are classified in the study and identified according to the emission factors of 1 week, CO, NO_x, VOC, SO₂ and PM₁₀ emissions respectively defined as 54,1kg, 21,3kg, 7,6kg, 2,8kg and 1kg [2].

Air pollution resulted from the highway traffic in the city center is examined in a study carried out in Izmir. Vehicles are classified in the study and it is found out that CO. 108 tone, NO_x 48 tone, and PM₁₀ 2 tone by using CORINAIR emission factors [9].

In a study carried out in Kocaeli, vehicle counts were made throughout the main roads between the years 2003-2004-2006. With the help of the COPERT III model, PM emission was analyzed as 199 tons-155 tons-150 tons and NO_x emission was analyzed as 3860 tons-4036 tons-4029 tons. The highest emission was analyzed in the highway [10].

During the studies carried out in Sakarya, roads were chosen according to the intensity of inner city traffic and vehicle counts were made between 08:00-22:00 and traffic characteristics were examined. CO, HC, NO_x and PM emissions were determined by using COPERT III emission factors [11, 12,13].

E-80 TEM Anatolian motorway and the D-100 highway which surround the Sapanca Lake, an important source of drinking water for Marmara region, should be examined in terms of road traffic intensity and emissions.

Especially E-80 TEM Anatolian motorway is the most important highway of Turkey. For this reason, traffic-induced air pollution which is affecting the Sapanca Lake should be examined.

Our aim in this study is determination the traffic density of roads that are surrounding the Sapanca Lake and examination the traffic-borne heavy metals that effect on the quality of water resources. The resulting data will provide an inventory of traffic-borne exhaust emissions of heavy metals which can affect the lake.

2. MATERIALS AND METHODS

Since transport activities are not steady and involve variety of vehicles at different sizes and after-treatment technologies, quantification of their emissions is a seriously difficult in Turkey.

To quantify heavy metal emissions from E-80 motorway that has high traffic density and D-100 highway are surrounding Sapanca Lake, vehicle classification, making of vehicle counts on roads to determine real time traffic density and calculation of traffic-borne emissions, respectively. Also, as can be seen from Figure 1, these roads too close to Sapanca Lake. So, these roads have a great importance for water quality of Sapanca Lake. As heavy metal emissions were determine, E-24 road is parallel to E-80 motorway is considered.

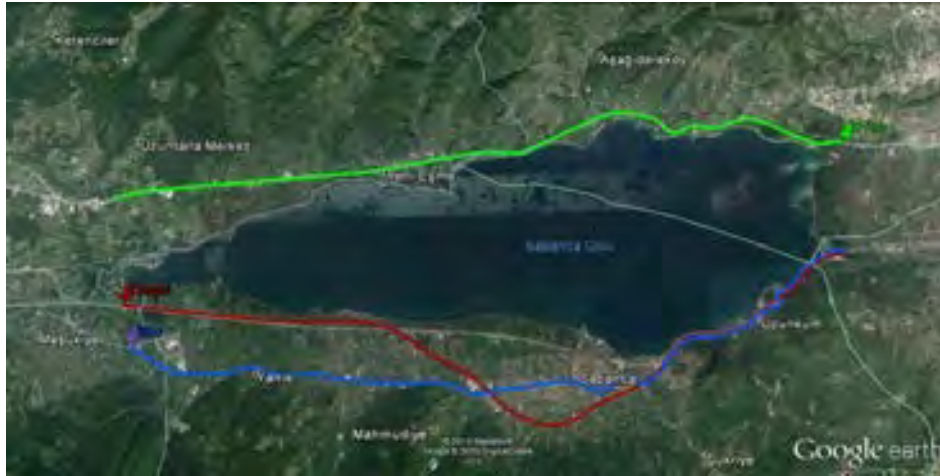


Figure 1. Sapanca Lake and it's surrounding roads

2.1. Vehicle Classification

Classification was based on vehicle class (busses, trucks, light duty vehicles, passenger cars, motorcycles), fuel, and engine volume. These are the main specifications to determine Euro classification and emission factors of a vehicle.

2.2. Making of Vehicle Counts on Roads to Determine Real Time Traffic Density

The vehicles were monitored in the three roads are surrounding Sapanca Lake. The monitoring started at 08:00 and continued until 08:00 to next day. E-80 motorway and D-100 highway have a great importance in the road transport. Trucks are allowed to pass to road at certain times during the day. Therefore, 24-hours nonstop count was made manually to determine the number of reliable vehicles on all roads.

2.3. Quantification of Traffic-Borne Heavy Metal Emission

Traffic-borne heavy metals consist of fuel consumption and tyre-brake wear. So, heavy metal emissions are divided into exhaust emission (fuel consumption) and non-exhaust emissions (fuel evaporation, tyre and brake wear) [4, 5, and 14]. In this work, heavy metal exhaust emissions were examined.

The traffic-borne emissions are calculated by using the well-known Equation 1. The emission amounts are calculated separately by using Equation 1 according to vehicle kilometers for each vehicle class.

$$E = EF \times A \quad (1)$$

E: Emission (gr)

EF: Emission Factor (gr/km)

A: Activity of Vehicle (km)

Heavy metal exhaust emissions occur depending on fuel consumption. Therefore, it needs to be known amount of fuel consumption. After determining fuel consumption and the activity of a vehicle class in E-80 motorway, E-24 road and D-100 highway. Emission amounts were calculated separately by using Equation 1.2 for each vehicle class. To determine vehicle activities, road lengths were calculated by using Google Earth and length of Sapanca Lake was considered. Vehicles were counted both one day in weekday and one day in weekend, it was calculated average daily number of vehicle for each vehicle class.

$$E = EF \times A \times F \tag{2}$$

E: Heavy Metal Emission (μg)

EF: Heavy Metal Emission Factor ($\mu\text{g}/\text{kg-fuel}$)

FC: Fuel Consumption ($\text{g-fuel}/\text{km}$)

Heavy metal emission factors and fuel consumption per kilometer for each vehicle class were obtained from CORINAIR (COPPERT III) [14].

Engine volumes that are used to determine the fuel consumption were determined according to the statistics of General Directorate of Highways and Turkish Statistical Institute [15]. Emission inventory was constituted by using emission factors shows in Table 1. In the emission calculations, passenger cars and light duty vehicle were considered as 73% gasoline of passenger cars, 27% diesel of passenger cars and 50% gasoline and 50% diesel of light duty vehicles.

3. RESULTS AND DISCUSSION

3.1. Traffic Characteristics

In order to satisfy a transport need of the people, there are various vehicles at different sizes with different technologies. Most of vehicles are their energy sources that are fossil fuels. Emissions such as NO_x, PM, CO, HC and heavy metals occur from the combustion of fossil fuels. Also, these emissions emit to the ambient air depending on their engine technology. The amount of the emissions is dependent on both engine technology, fuel consumption and activity of the vehicles. Transport activities of the people are dependent on their economic and social situations and there is no any easy way to determine these activities for every transport vehicle.

Table 1. Heavy metal emission factors for all vehicle categories in $\mu\text{g}/\text{kg fuel}$

Vehicle category		As	Cd	Cr	Cu	Hg	Ni	Pb	Se	Zn
Passenger Car	Gasoline	0,3	10,8	16	42	8,7	13	33,2	0,2	216 3
	Diesel	0,1	8,7	30	21,2	5,3	8,8	52,1	0,1	173 8
Light Duty Vehicle	Gasoline	0,3	10,8	16	42	8,7	13	33,2	0,2	216 3
	Diesel	0,1	8,7	30	21,2	5,3	8,8	52,1	0,1	173 8
Bus	Diesel	0,1	8,7	30	21,2	5,3	8,8	52,1	0,1	173 8
Truck	Diesel	0,1	8,7	30	21,2	5,3	8,8	52,1	0,1	173 8
Motorcycle	Gasoline	0,3	10,8	16	42	8,7	13	33,2	0,2	216 3

According to the results of 24-hours nonstop count; total number of vehicles for E-80 motorway, E-24 road and D-100 highway is 39159, 12330 and 18205, respectively. Figure 2 and 3 shows vehicle statistics in all roads. 49% of total vehicles are passenger car in E-80 motorway, 67% of total vehicles are passenger car in E-24 road and 51% of

total vehicles are passenger car in D-100 highway. Numbers of passenger car are 19326 in E-80 motorway, 8287 in E-24 road and 9331 in D-100 highway during all day.

31% of total vehicles are truck in E-80 motorway, 7% of total vehicles are truck in E-24 road and 25% of total vehicles are truck in D-100 highway. Also, it's seen that the number of motorcycles is too few in all roads. Percentages of the motorcycles are 0,00048%, 0,0052% and 1% in E-80 motorway , E-24 road and D-100 highway, respectively. Numbers of motorcycle are 19 in E-80 motorway, 65 in E-24 road and 91 in D-100 highway during all day.

3.2. Emission Inventory

Heavy metal exhaust emissions depend on fuel consumption. If vehicle activities increase, fuel consumption increases, too. Consequently, a larger amount of emission emits to the ambient air. Heavy metals are trace elements, so these amounts are too few. Nevertheless, heavy metals have serious importance in terms of health. In this work, traffic-borne heavy metal emissions were calculated for roads are surroundings Sapanca Lake.

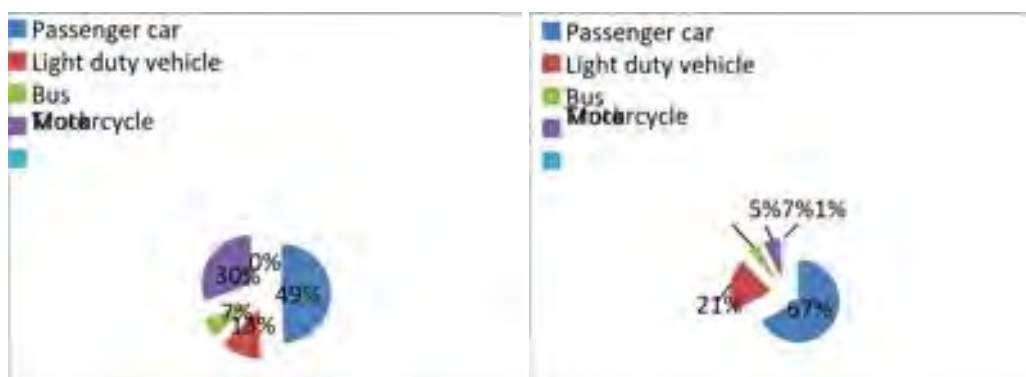


Figure 2. E-80 Motorway and E-24 Road vehicle statistics

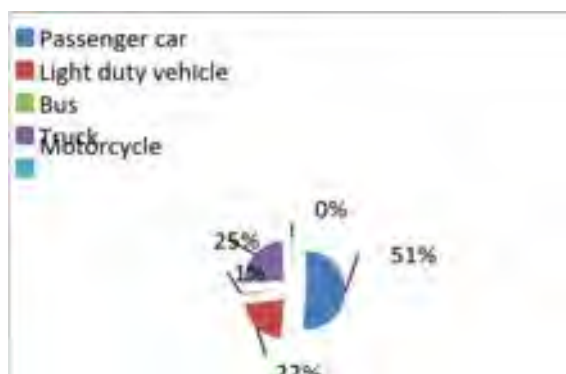


Figure 3. D-100 Highway vehicle statistics

Table 2 shows the annual heavy metal emission for E-80 motorway, E-24 road and D-100 highway. As heavy metal emissions are examined, Zn 95270,3 g/year and As 8,2 g/year and Se 6,7 g/year are least among heavy metals emit to the ambient air. Especially, Zn is extreme level for heavy metal pollution among the others. Their order of magnitude ranked as follows Zn > Pb > Cu > Cr > Ni > Cd > Hg > As > Se. Due to Zn and Pb are in fuel composition, among these emissions, Zn and Pb contribute significantly to the ambient air.

Table 2. The amount of heavy metal emission for all roads in g/year

Roads	As	Cd	Cr	Cu	Hg	Ni	Pb	Se	Zn
E-80 Motorway	4,8	296,1	848,1	848,9	197,6	316,3	1516,9	4,0	59186,6
E-24 Road	1,5	72,1	173,4	231,1	51,4	80,2	320,3	1,1	14415,7
D-100 Highway	2,0	108,4	287,8	327,4	74,6	118,0	521,7	1,6	21667,9
Total amount	8,2	476,5	1309,3	1407,4	323,6	514,6	2358,9	6,7	95270,3

As can be seen clearly in Figure 4, E-80 motorway has higher traffic density than the others, has highest heavy metal emission amounts. The amounts of Cd, Ni, Cr and Cu emissions are 476,5 g/year, 514,6 g/year, 1309,3 g/year and 1407,4 g/year, respectively.

The percentages of heavy metal except Zn, As and Se shows in Figure 5. The highest emission percentages are Pb, Cu and Cr, respectively.

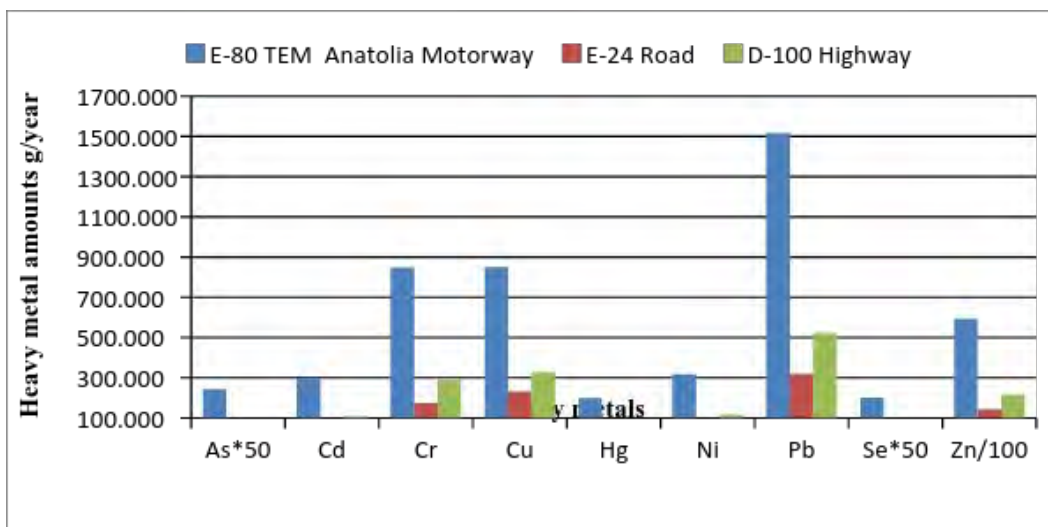


Figure 4. Heavy metal amounts for all roads (g/year)

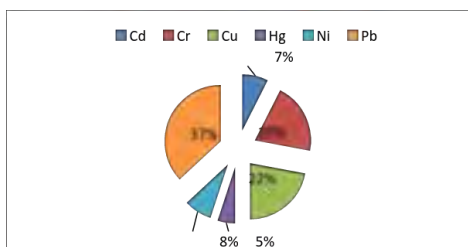


Figure 5. Percentages of total heavy metal amounts except Zn, As and Se (g/year)

4. CONCLUSION

Determination of pollutant loads of emissions by using emission factors, gives general information only. In our country, there is no any work about emission factors that are used in examination of traffic-borne air pollution. Therefore, CORINAIR (COPPET III) emission factors were used in this work. Solely, it's necessary constitution of emission factors that accord with the conditions in Turkey. Moreover, emission factors that depend on traffic activities and road properties have to constitute in regional-based.

Traffic activities are carried out with many different classes of vehicles and each vehicle class has its unique activity characteristics. So, traffic-borne emission quantifications must be based on real time activities of the vehicles. Passenger cars and trucks are dominating in E-80 motorway with proportions of 49% and 31%, respectively. Passenger cars are dominating in D-100 highway with proportions of 51%, trucks and light duty vehicles are 25% and 22% of total vehicles in this road, respectively.

While predicting traffic-borne emissions, vehicle activities have a profound effect on the emission predictions and, in turn, it will have the same effect on air quality predictions. Therefore using real time vehicle activities have great importance for reliable emission quantification.

ACKNOWLEDGMENT

Sefanur Tok, Gizem Özcan, Serdar Belirmiş, Mücahit Arıcan, Ahmet İşcan, Fatih Samed Keskin and Emir Arık are acknowledged for their contribution to the vehicle activity monitoring..

REFERENCES

- [1] Elbir T., Koca H.,2013, The Determination of Air Quality Originates From Road Traffic in University Campus, Air Pollution Researches Joournal 2, 45 – 54.
- [2] ETC/ACC 2005, 2004, Air Emissions Spreadsheet for Indicators, Copenhagen, Denmark.
- [3] Bellasio R., Bianconi R., Corda G., Cucca P., 2007, Emission Inventory for the Road Transport Sector in Sardinia (Italy), Atmospheric Environment 41, 677–691.
- [4] Kumari G., Attri A. K., Panis L. I.,Gurjar B. R., 2013, Emission Estimates of Particulate Matter and Heavy Metals from Mobile Sources in Delhi (India), J Environ. Science & Engg. Vol. 55, No. 2, p. 127-142.
- [5] Kummer U., Pacyna J., Pacyna E., Friedrich R.,2009, Assessment of Heavy Metal Releases From the Use Phase of Road Transport in Europe, Atmospheric Environment 43, 640–647.
- [6] Johansson C., Norman M., Burman L., 2009, Road Traffic Emission Factors for Heavy Metals, Atmospheric Environment 43, 4681–4688.
- [7] Gunawardena J., Egodawatta P., Ayoko A. G., Goonetilleke A., 2013, Atmospheric Deposition as a Source of Heavy Metals in Urban Stormwater, Atmospheric Environment 68,235-242.
- [8] Elbir T., Müezzinoğlu A., Bayram A., Seyfioglu R., Demircioglu H., 2001, Air Pollutant Emission Inventory of Aegean Region, DEÜ Engineering Faculty, Engineering Sciences Journal,3,2,21-27.
- [9] Elbir T., Bayram A., Altıok H., Seyfioglu R., Ergün P., Simsir S., 2010, Determination Of The Air Pollution from Road Transport In the City Center of Izmir, DEÜ Engineering Faculty, Engineering Sciences Journal,12,1,1-17.
- [10] Çetin S., Karademir A., Pekey B., Ayberk S., 2006, Emission inventory of Traffic-borne Air Pollutants in Kocaeli, Symposium on Urbanization and transportation Problems of Kocaeli.
- [11] Soylu, S., 2007, Estimation of Turkish Road Transport Emissions, Energy Policy, Volume 35, Issue 8, Pages 4088-4094, 2007.
- [12] Soylu, S., Gümrükçüoğlu, M., Bal, A., Şentürk, G., Aydınlar, B., 2009, Examination of Urban Transport Characteristics and its Emissions - Adapazarı Case Study, (Poster no: 064) ETTAP-09 17th Transport and Air Pollution Symposium - 3rd Environment and Transport Symposium.
- [13] Semercioglu H., Bal A., Ay E. F., Soylu Ş., 2010, Examination of Hourly Emissions from Transport and Adapazarı Urban Traffic Characteristics, IV. National Air Pollution and Control Symposium, 507-518.
- [14] Ntziachristos, L., Samaras, Z., 2012, EMEP EPA emission inventory guidebook, https://www.google.com.tr/?gws_rd=ssl#q=Exhaust+emissions+from+road+transport , 04.09.2015.
- [15] General Directorate of Highways, 2014, Traffic and Transportation Data, <http://www.kgm.gov.tr/Sayfalar/KGM/SiteTr/Istatistikler/TrafikveUlasim.aspx> ,04.09.2015.

AN ADSORPTION STUDY OF METHYLENE BLUE FROM AQUEOUS SOLUTION WITH A LOW COST MATERIAL

Nur AYAZ

Rabia KOKLU

Cigdem OZER

Sakarya University, Environmental Engineering Department, Esentepe Campus, 54187, Sakarya, TURKEY
E-mail: cozer@sakarya.edu.tr

Abstract

In this study, the use of nail particles as a new low-cost adsorbent for adsorption of methylene blue (MB) from solution has been researched. Methylene blue (MB) which may be originated from different industries such as textile, printing, paper etc. is widely used as a reference material of dye removal processes. The adsorption of dyes from the aqueous solutions has been investigated by several researchers on numerous adsorbents but the main issue is the cost along with the capacity of adsorbents for adsorption process. The purpose of this paper is to bring out a new alternative for low cost adsorbents. For this purpose MB adsorption on nail particles at different contact times, pH, adsorbent doses and initial MB concentration has been investigated. Obtained data from the adsorption studies MB using nail particles were applied to Langmuir and Freundlich isotherm models and correlation coefficients were indicated. The MB adsorption process was found in harmonious with Freundlich isotherm model according to high correlation coefficient. Consequently, it can be expressed that nail particles can be used as adsorbent for MB adsorption.

Keywords: MB, adsorption, low cost, coiffeur waste

water resources. Dye contaminated wastewater originated from various industries such as textile, paper, plastics, leather, cosmetic and paint is a major concern because of their hazardous effects on the water bodies and also people health. Among dyes MB is the most frequently used material in textile industry despite the harmful effects. Removing dyes from waste water is an important issue, thus many methods such as biological treatment [1], coagulation-flocculation [2], flotation/ electrocoagulation [3], oxidation [4] and adsorption [5] have been used.

The adsorption is the most preferred method because of efficiency, easy applicability and affordability. The other factor that makes adsorption effective is selection of adsorbent. For this purpose, miscellaneous adsorbents such as fly ash [6], hair [7], tea leaves [8], eggshell [9], wheat straw [10], neem leaf powder [11], raw beech sawdust [12] and orange peel [13] have been used for adsorption of MB.

In this paper, MB adsorption on nail particles at different contact times, pH, adsorbent doses and initial MB concentration has been investigated. Obtained data from the adsorption studies MB using nail particles were applied to Langmuir and Freundlich isotherm models and correlation coefficients were indicated. The MB adsorption process was found in harmonious with Freundlich isotherm model according to high correlation coefficient.

2. MATERIALS AND METHODS

2.1. Preparation of adsorbent

Nail samples, obtained from a local barber's shop, were washed with distilled water and was dried in oven at 400C for 24 hours. The dry samples were cut manually to the minimum possible size and the length varied from 1 to 3 mm.

2.2. Experimental Studies

The stock dye solution was prepared by dissolving required amount of MB in 1 litre of distilled water. The adsorption tests were carried out in a batch system by varying the pH, dose of adsorbent, contact time and initial concentration of dye. The study of the effect of pH was carried out by adding the dose of adsorbent to 75 mg and varying the pH from 3 to 11. The dose of adsorbent (75 mg) is placed into contact with an aqueous solution of MB and with an initial concentration ranging from 1 mg/L to 20 mg/L. Dye aqueous solutions at different concentrations with pH 7 were brought into contact with 75 mg of adsorbent for 2 hours at room temperature. After stirring time, the residual concentrations of MB were determined with an UV spectrophotometer, spectrophotometer (Hitachi, U-1800, Tokyo, Japan) at a wavelength of 663 nm. The amount of adsorbed MB by adsorbent was calculated using the following formula [14]:

$$q = (C_0 - C_t) \frac{V}{m} \quad (1)$$

Where q is the amount of adsorption of MB per unit weight within adsorbent (mg/g), C_0 is the initial concentration of MB solution (mg/L), C_e is the equilibrium concentration of the solutions (mg/L), V is the volume of solution (mL).

3. RESULTS AND DISCUSSION

3.1. Effect of pH

To examine the effect of pH on MB adsorption onto nail particles, experiments were carried out at initial dye concentration of 10 mg/L, adsorbent dosage of 75 mg and equilibrium time of 120 min, and the results are shown in Fig. 1. The maximum uptake obtained at pH value of 11 which may be due to the electrostatic attraction between dye and adsorbent surface at high pH values. It is decided to continue at original pH value (pH =7) because of non-significant difference of adsorbed amount of MB between pH 7 and 11.

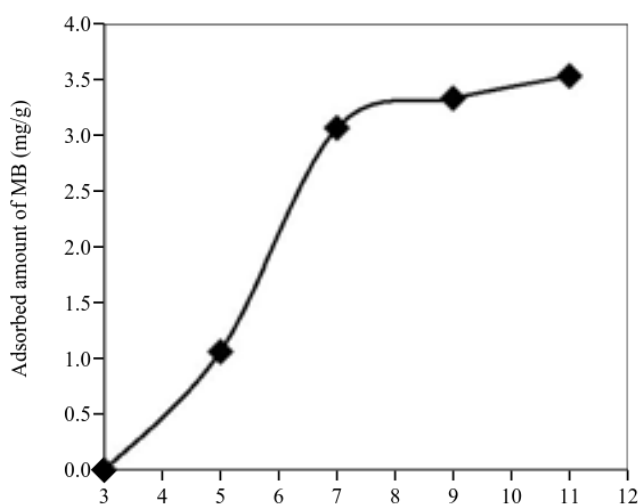


Figure 1. Effect of initial pH on the removal of methylene blue

3.2. Effect of Initial MB Concentration

The effect of different initial MB concentrations on adsorption process was analysed with the range of concentrations from 1 to 20 mg/L, adsorbent dosage of 75 mg and equilibrium time of 120 min and shown in Fig. 2.

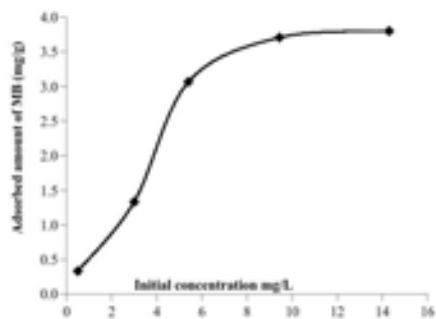


Figure 2. Effect of initial dye concentration on the removal of MB

3.3. Effect of Contact Time

Effect of contact time for the adsorption of MB on the nail particles at initial concentration of 10 mg/L with the adsorbent dose of 75 mg was investigated up to 8 hours. As seen from Fig. 3 the slight changes were observed for the uptake of MB from 2 to 8 hours. Therefore the equilibrium time of MB adsorption on nail particles found to be 2 hours.

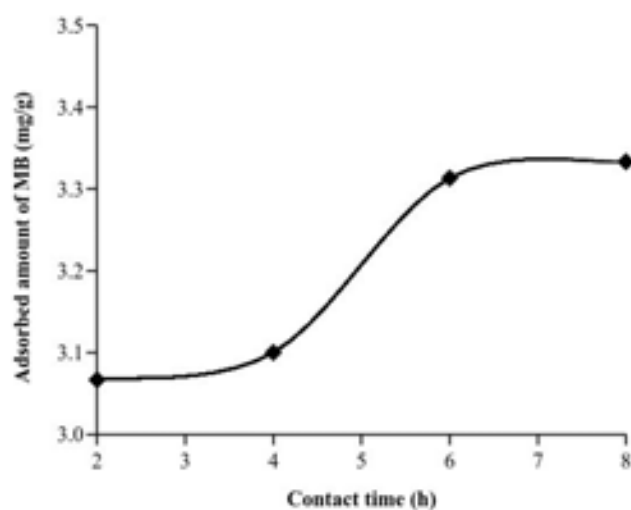


Figure 3. Effect of contact time on the removal of MB

3.4. Effect of Adsorbent Dosage

The adsorbent dosage has an important role in the adsorption and in the percentage of removal. The adsorption of MB onto nail particles was practiced by varying adsorbent dosage (50–150 mg) while keeping the initial MB concentration at 10 mg/L for 120 min (Fig.4.). The MB adsorption capacity of nail particles decreased with increasing adsorbent amount. Maximum adsorption percentage was obtained at 75 mg adsorbent dosage (Fig.5.).

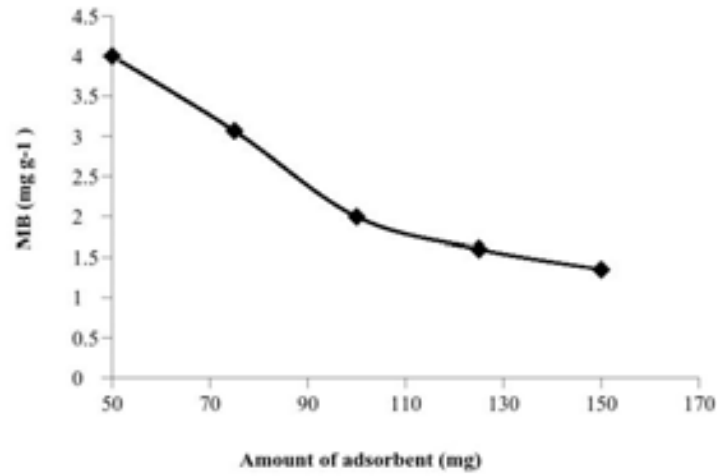


Figure 4. Effect of adsorbent dosage on the removal of MB

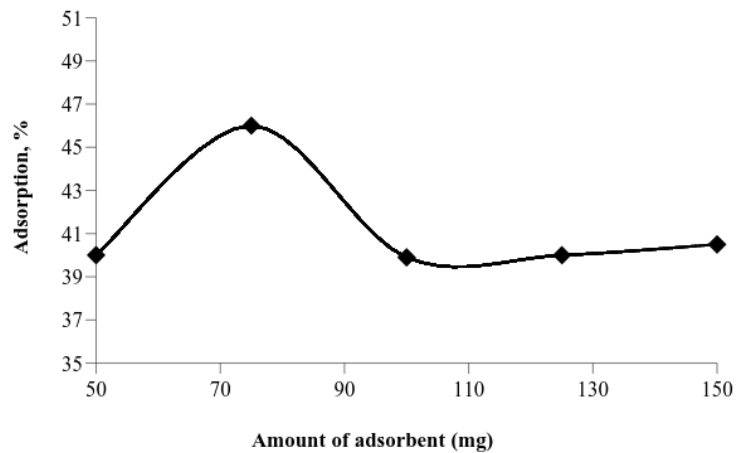


Figure 5. MB adsorption percentage versus adsorbent dosage

3.5. Adsorption Isotherm

The Langmuir and Freundlich equations are in common use for describing adsorption isotherms for water and wastewater treatment applications. In this study, adsorption isotherms were analysed according to the linear form of the Langmuir and Freundlich isotherms. The experimental data were well described by the Freundlich isotherm model with high correlation coefficient ($R^2=0,96$). The Freundlich adsorption isotherm represents the relationship between the amount of dye adsorbed per unit mass of the adsorbent q_e and the concentration of the dye in solution at equilibrium. The Freundlich adsorption isotherm and its linearized form are described with following equations [14]:

$$q_e = K_F C_e^{1/n} \quad (2)$$

$$\log q_e = \log K_f + (1/n) \log C_e \quad (3)$$

Where, q_e is adsorbed MB by per unit mass of the adsorbent and C_e is the concentration of MB at equilibrium.

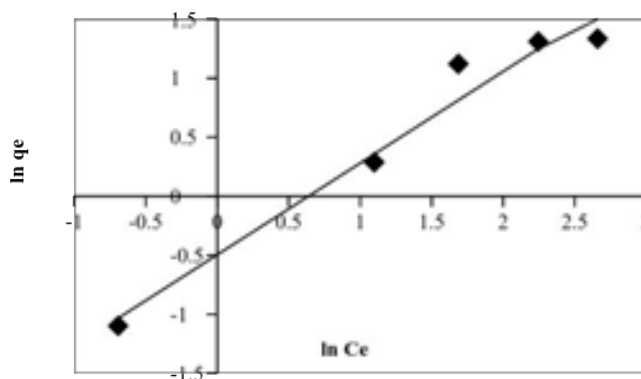


Figure 6. Freundlich isotherm plots of MB adsorption on nail particles

4. CONCLUSIONS

In this study, the ability of coiffeur waste to adsorb MB has been investigated and has been shown that nail particles can be used as an affordable adsorbent for Methylene Blue adsorption. Nail particles has been used without any activation procedure being applied. Nevertheless, adsorption percentage has been obtained to be 46%. The obtained results show that when the activation process applied to the nail particles higher yields can be obtained. Therefore, this situation will be considered in planning future studies.

REFERENCES

- [1]. Garc'ia-Monta'no, J., Dom'enech, X., Garc'ia-Hortal, J.A., Torrades, F., Peral, J. (2008). The testing of several biological and chemical coupled treatments for Cibacron Red FN-R azo dye removal. *Journal of Hazardous Materials*, 154, 484–490.
- [2]. Riera-Torres, M., Guti'erez-Bouz'an, C., Crespi, M. (2010). Combination of coagulation–flocculation and nanofiltration techniques for dye removal and water reuse in textile effluents. *Desalination*, 252, 53–59.
- [3]. Emamjomeh, M.M., Sivakumar, M. (2009). Review of pollutants removed by electrocoagulation and electrocoagulation/flotation processes. *Journal of Environmental Management*, 90, 1663-1679.
- [4]. Akrou, H., Jellali, S., Bousselmi, L. (2015). Enhancement of methylene blue removal by anodic oxidation using BDD electrode combined with adsorption onto sawdust. *C. R. Chimie*, 18 110–120.
- [5]. Aboua, K.N., Yobouet, Y.A., Yao, K.B., Gone, D.L., Trokourey, A. (2015). Investigation of dye adsorption onto activated carbon from the shells of Macore fruit. *Journal of Environmental Management*, 156, 10-14
- [6]. Kumar, K.V., Ramamurthi, V., Sivanesan, S. (2005). Modeling the mechanism involved during the sorption of methylene blue onto fly ash. *J. Colloid Interface Sci.* 284,14–21.

An Adsorption Study of Methylene Blue from Aqueous Solution with a Low Cost Material
Nur Ayaz, Rabia Koklu and Cigdem Ozer

- [7]. McKay, G., Ramprasad, G., Pratapamowli, P. (1986). Equilibrium studies for the adsorption of dyestuffs from aqueous solution by low-cost materials. *Water Air Soil Pollut.*, 29, 273–283.
- [8]. Hameed, B.H. (2009). Spent tea leaves: a new non-conventional and low-cost adsorbent for removal of basic dye from aqueous solutions, *J. Hazard. Mater.* 161, 753–759.
- [9]. Mak, S.Y., Chen, D.H. (2004). Fast adsorption of methylene blue on polyacrylic acid bound iron oxide magnetic nanoparticles. *Dyes Pigments*, 61, 93–98.
- [10]. Batzias, F.A., Sidiras, D.K., Schroeder, E., Weber, C. (2009). Simulation of dye adsorption on hydrolyzed wheat straw in batch and fixed-bed systems. *Chem. Eng. J.*, 148, 459–472.
- [11]. Bhattacharyya, K.G., Sharma, A. (2005). Kinetics and thermodynamics of methylene blue adsorption on neem (*Azadirachta indica*) leaf powder. *Dyes Pigments*, 65, 51–59.
- [12]. Batzias, F.A., Sidiras, D.K. (2004). Dye adsorption by calcium chloride treated beech sawdust in batch and fixed-bed systems. *J. Hazard. Mater.*, B114, 167–174.
- [13]. Annadurai, G., Juang, R., Lee, D. (2002). Use of cellulose-based wastes for adsorption of dyes from aqueous solutions. *J. Hazard. Mater.*, B92, 263–274.
- [14]. Wang, P., Du, M., Zhu, H., Bao, S., Yang, T., Zou, M. (2015). Structure regulation of silica nanotubes and their adsorption behaviors for heavy metal ions: pH effect, kinetics, isotherms and mechanism. *Journal of Hazardous Materials*, 286, 533–544.

A NUMERICAL METHOD TO FIND THE TRANSIENT TEMPERATURE DISTRIBUTION OF HOLLOW CYLINDERS

Hakan PEKEL

Corresponding author: Nigde University, Department of Mechanical Engineering, 51240, Nigde, Turkey
hpekel@nigde.edu.tr

Vebil YILDIRIM

Cukurova University, Department of Mechanical Engineering,
vebil@cu.edu.tr

Abstract

In scope of this study, we investigated one-dimensional transient hyperbolic heat conduction problem of thick walled hollow cylinders made of isotropic and homogeneous materials. As is well known, it is important to know temperature distribution more accurately to determine the effects on the system due to thermal loading. In order to correctly predict the transient temperature distribution for hollow cylinders we employ a numerical method called Durbin's Inverse Laplace Transform technique. By using this method, the analytical solution of the differential equations in the Laplace domain are converted in an accurate manner to their corresponding numerical values in the time domain. The temperature distribution through the radial coordinate for different thermal relaxation time values are demonstrated in non-dimensional form.

Keywords: Durbin's method, Inverse Laplace transform, Non-Fourier heat conduction, One-Dimensional heat problem, Transient hyperbolic heat conduction

1. INTRODUCTION

Heat conduction analysis of some kind of structures is of great importance, as they are used as thermal shields. Temperature gradients cause thermal stresses that may result in crack growth and eventually fracture of the structure. Hence, to design a reliable material structure working under severe thermal loadings, it is crucial to know the temperature distribution within it. For instance a material composition called Functionally Graded Material (FGM) is applied for cases in which high thermal properties are required.

As is well known, Fourier heat conduction theory cannot accurately fully explain the conduction of heat caused by highly varying thermal loading such as thermal shock [1]. To better explain heat conduction in solids, non-Fourier heat conduction theories have been developed. One of the tough non-Fourier theories is hyperbolic heat conduction theory which accounts for the finite speed of thermal energy propagation by introducing a new material property is called thermal relaxation time. Thermal relaxation time is the time that the temperature field needs to adjust itself to thermal disturbances. This theory is called hyperbolic heat conduction because it results in a hyperbolic differential equation for temperature rather than the parabolic one obtained using Fourier's law.

Although there are a mass of studies on the Fourier heat conduction in FGMs and Fourier heat conduction in homogenous materials, the number of the studies on the hyperbolic heat conduction is limited.

Jabbari et al. [2] developed a general analysis of one-dimensional steady-state thermal stresses in a hollow thick cylinder made of FGM. The temperature distribution is assumed to be a function of radius, and the direct method is used to solve the heat conduction equations derived from Navier equations. Ootao and Tanigawa [3] studied a theoretical treatment of transient thermoelastic problem involving a functionally graded hollow cylinder due to uniform heat supply. The transient one-dimensional temperature is analyzed by the method of Laplace transformation.

Babaei and Chen [4] first worked out the transient hyperbolic heat conduction in a functionally graded hollow sphere, and then they investigated the hyperbolic heat conduction in a functionally graded hollow cylinder [5].

Guo and Noda [6] studied the thermal stresses of a thin cylindrical shell subjected to a thermal shock and made of a functionally graded material (FGM) are studied. The problem studied for a FGM cylindrical shell is reduced to a plane problem. A perturbation method is used to solve the thermal diffusion equation for FGMs with general thermal properties. Then, the transient thermal stresses are obtained. The results show that the thermal shock is much easier to result in failure than the steady thermal loading.

Another study in one-dimensional form is presented by Akbarzadeh and Chen [7]. They investigated both transient and steady-state heat conduction of FGM cylinders in dual-phase lag using semi-analytical solutions for parabolic-type, hyperbolic and also classical Fourier model. Their demonstrations indicate the relations among the phase lag of heat flux, the thermal wave speed and the transient temperature.

The purpose of the present study is to determine numerically in an accurate manner the temperature distribution of a thick-walled hollow cylinder due to varying thermal relaxation time values. Durbin's Inverse Method is employed to transform the problem in Laplace domain to the time domain. The method is also satisfied with a test function.

2. THE GOVERNING EQUATIONS

When the cylinder is infinitely long, end effects can be ignored. Pekel [8] studied the hyperbolic heat conduction problem of infinitely long and thick-walled cylinder made of FGM materials with the assumption that all material properties are a function of radial coordinate except Poisson's ratio. From this study, for a special case, the hyperbolic heat conduction equation of hollow thick-walled cylinders made of homogeneous and isotropic materials is rewritten as follows.

$$\frac{\partial^2 T}{\partial r^2} + \frac{1}{r} \frac{\partial T}{\partial r} = \frac{1}{\kappa} \left(\frac{\partial T}{\partial t} + \tau \frac{\partial^2 T}{\partial t^2} \right) \quad (2.1)$$

where T is the temperature, r is the radial coordinate measured from the center of the hollow cylinder, $\kappa = \frac{k}{\rho C_p}$ is the thermal diffusivity, k is the thermal conductivity, ρ is the density, C_p is the specific heat, t is the time, and τ is the thermal relaxation time. In equation (2.1) it is assumed that there is no heat generation in the cylinder. Introducing the following dimensionless variables

$$\begin{aligned}
R &= \frac{r}{r_o} \Rightarrow r = r_o R \\
\theta &= \frac{T - T_\infty}{T_{w_o} - T_\infty} \Rightarrow T = \theta(T_{w_o} - T_\infty) + T_\infty \\
\xi &= \frac{\kappa t}{r_o^2} \Rightarrow t = \frac{\xi r_o^2}{\kappa} \\
\varepsilon_o &= \frac{\kappa \tau}{r_o^2} \Rightarrow \tau = \frac{\varepsilon_o r_o^2}{\kappa}
\end{aligned} \tag{2.2}$$

where r_o is the radius at the outer surface, T_{w_o} the temperature at the outer wall and T_∞ is the ambient temperature.

Hence, the equation (2.1) takes the following dimensionless form:

$$\frac{\partial^2 \theta}{\partial R^2} + \frac{1}{R} \frac{\partial \theta}{\partial R} = \left(\frac{\partial \theta}{\partial \xi} + \varepsilon_o \frac{\partial^2 \theta}{\partial \xi^2} \right) \tag{2.3}$$

Laplace transform of equation (2.3) is

$$\frac{d^2 \tilde{\theta}}{dR^2} + \frac{1}{R} \frac{d \tilde{\theta}}{dR} = s(1 + \varepsilon_o s) \tilde{\theta} \tag{2.4}$$

where “ $\tilde{\cdot}$ ” refers to the quantity in Laplace domain, and s is the Laplace parameter.

Equation (2.4) the second degree non-homogeneous differential equation in Laplace domain, govern the temperature behavior of the cylinder made of the isotropic and homogeneous material in the hyperbolic heat conduction. In this study this equation is solved in a closed form by using Mathematica’s build-in functions to investigate the temperature history along the radial coordinate, r , by using the following boundary conditions.

$$\begin{aligned}
\tilde{\theta} &= 1/s \Rightarrow R = 1 \\
\tilde{\theta} &= 0 \Rightarrow R = 0.6
\end{aligned} \tag{2.5}$$

The solution of the temperature distribution in the Laplace domain is obtained in terms of Bessel’s functions [9] and hypergeometric function as follows.

$$\frac{(BesselJ(0,0.6A)BesselY(0,2B)) - (BesselY(0,0.6A)C(1,D))}{R[(BesselJ(0,0.6A)BesselY(0,A)) - (BesselJ(0,A)BesselY(0,0.6A))]} \tag{2.6}$$

where

$$\begin{aligned}
A &= -i\sqrt{s(1 + s\varepsilon_o)} \\
B &= -iR\sqrt{s(1 + s\varepsilon_o)} \\
C &= \text{Hypergeometric0F1Regularized} \\
D &= \frac{1}{4}sR^2(1 + s\varepsilon_o)
\end{aligned} \tag{2.7}$$

In this study, the analytical solution given in equation (2.7) in the Laplace domain is transformed into the numerical solution in the real domain by using Durbin’s inverse method.

3. THE DURBIN'S INVERSE METHOD

The Laplace transform of a real function $f(t)$ with $f(t) = 0$ for $t < 0$ is

$$F(s) = L[f(t)] = \int_0^{\infty} e^{-st} f(t) dt \quad (3.1)$$

Its inversion formula is defined by

$$f(t) = L^{-1}[F(s)] = \frac{1}{2\pi i} \int_{a-i\infty}^{a+i\infty} e^{st} F(s) ds \quad (3.2)$$

where s is the Laplace parameter and a is an arbitrary real number greater than the real parts of all the singularities of $F(s)$.

$$s = a + iw \quad (3.3)$$

Since it is difficult to get analytically the inverse Laplace transformation for a complicated function, some numerical methods is used to obtain an approximate solution. Therefore numbers of numerical inversion methods have been developed and tested to demonstrate the simplicity and the accuracy for typical functions. Some of them are treated Fourier series approximations. Fourier series were first employed by Dubner and Abate [10] for the numerical inversion of Laplace transforms. Durbin improved the method in 1974 [11] and derived the approximation formula over the interval $[0, 2T]$.

$$f(t) = \frac{e^{at}}{T} \left[\begin{array}{l} -\frac{1}{2} \operatorname{Re}\{F(a)\} + \sum_{k=0}^{\infty} \operatorname{Re}\left\{F\left(a + i\frac{k\pi}{T}\right)\right\} \cos \frac{k\pi t}{T} \\ - \sum_{k=0}^{\infty} \operatorname{Im}\left\{F\left(a + i\frac{k\pi}{T}\right)\right\} \sin \frac{k\pi t}{T} \end{array} \right] - E_1 \quad (3.4)$$

where E_1 represents the discretization errors in the Durbin's Fourier's expansion formula. Hence, by taking N finite number of terms in the infinite series in equation (3.4), the estimated value of $f(t)$ comes to the following formula.

$$f_N(t) \cong \frac{e^{at}}{T} \left[\begin{array}{l} -\frac{1}{2} \operatorname{Re}\{F(a)\} + \sum_{k=0}^N \operatorname{Re}\left\{F\left(a + i\frac{k\pi}{T}\right)\right\} \cos \frac{k\pi t}{T} \\ - \sum_{k=0}^N \operatorname{Im}\left\{F\left(a + i\frac{k\pi}{T}\right)\right\} \sin \frac{k\pi t}{T} \end{array} \right] \quad (3.5)$$

That is

$$f(t) = f_N(t) - E_1 + E_2 \quad (3.6)$$

where E_2 represents the truncation errors in the approximation. It is proved that the discretization error is much smaller than the truncation errors.

In equation (3.5.) the choice of the parameters a, T , and N is somewhat arbitrary. It is generally recommended that $5 \leq aT \leq 10$ and $5 \leq N \leq 5000$. The choice of those free constrains is very important for minimizing both discretization and truncation errors in the computation of $f(t)$ in the real-time domain. The dependence of the discretization and truncation errors on the free parameters is the biggest disadvantage of Durbin's method. By a suitable choice of these parameters the discretization error becomes arbitrarily small, but at the same time the truncation error grows to infinity and vice versa.

Durbin's approximation formula for the interval $[0, T]$ with the Lanczos factor L_k may also be used in the following form [12].

$$f(t_n) \cong \frac{2e^{an\Delta t}}{T} \left[-\frac{1}{2} \operatorname{Re}\{F(a)\} + \operatorname{Re} \left\{ \sum_{k=0}^{N-1} \left[F\left(a + i\frac{2k\pi}{T}\right) L_k \right] e^{i\frac{2\pi kn}{N}} \right\} \right] \quad (3.7)$$

$$L_k = \frac{\sin \frac{k\pi}{N}}{\frac{k\pi}{N}} \quad (n = 0, 1, 2, \dots, N-1)$$

where p_k gives the k^{th} Laplace parameter, Δt is the time increment, and $T = N\Delta t$ is the solution interval.

$$p_k = a + i\frac{2k\pi}{T} \quad (3.8)$$

$$N = \frac{T}{\Delta t}$$

4. SOLUTIONS

4.1. Test Function

To verify the numerical results of the algorithm devised in this study based on the Durbin's approach, the following function in the Laplace domain is considered.

$$F(s) = \frac{1}{1 + s^2 + s^4} \quad (4.1.)$$

Its corresponding solution in the time domain is given analytically as follows

$$F(t) = \frac{1}{6} e^{-t/2} \left(-3(-1 + e^t) \cos \left[\frac{\sqrt{3}t}{2} \right] + \sqrt{3}(1 + e^t) \sin \left[\frac{\sqrt{3}t}{2} \right] \right) \quad (4.2.)$$

Figure 1 shows the comparison of both the analytical and present numerical solutions. Here t is from 0 to 10 with 0.5 increments ($N=100$). Table 1 presents the relative percentage errors between the analytical and numerical results.

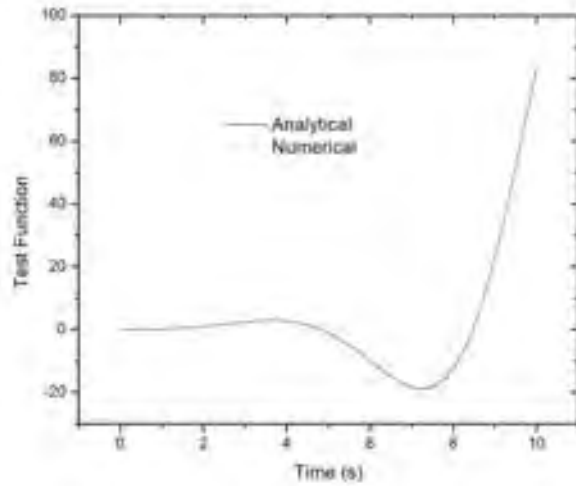


Figure 1. Comparison of analytical and numerical results

Table 1. Relative errors for some points

Time	Analytical Result	Numerical Result	Percentage Error
1.3	0.335254	0.33985	1.370793
2.8	2.251547	2.24194	-0.42668
5.2	-2.43359	-2.45294	0.795143
6.7	-16.4301	-16.3439	-0.52485
9.8	70.97771	70.7509	-0.31955

4.2. Homogeneous and Isotropic Cylinder

Now, it's time to get the real-time the temperature distribution of the hollow cylinder made of homogeneous and isotropic material by considering equation (2.6). The dimensionless temperature distribution through the wall thickness is presented in Figure 1. using three different dimensionless times as $\xi = 0.126$, 0.336 , and 3.486 . The dimensionless time $\xi = 3.486$ almost corresponds to the steady state case. These results are agreed well with the results in the study in reference [5].

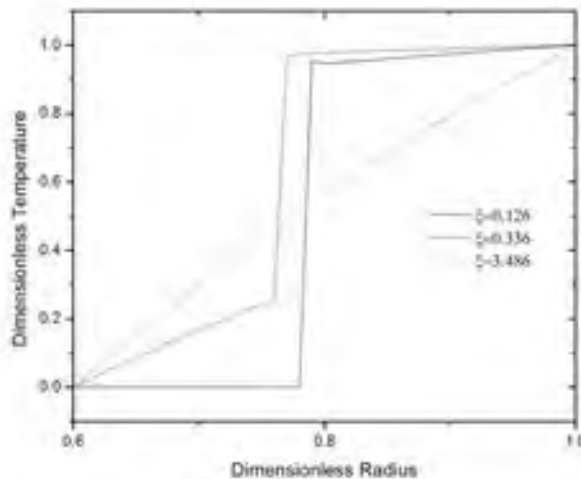


Figure 1. Temperature distribution along the wall thickness

The Figure 2 illustrates the temperature history in the middle of the thickness of the wall. Effect of thermal relaxation time on the non-dimensional temperature for a homogeneous cylinder is also shown in the same figure.

These curves have almost similar character of Jiang's curves [1]. As seen from this figure, the temperature in the hollow cylinder gradually approaches the final thermal equilibrium value. For larger thermal relaxation time, the temperature waves have similar appearance, whereas the amplitudes of temperature variation are clearly different.

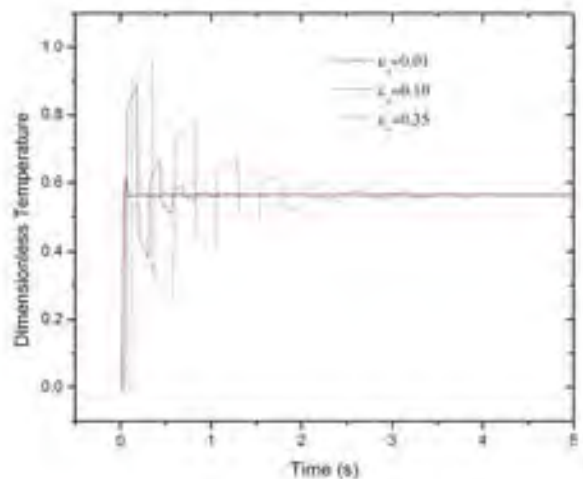


Figure 2. Temperature distribution in the middle of the cylinder

5. CONCLUSION

The present study handled the transient temperature behavior of the thick-walled hollow homogeneous cylinders under the constant temperatures on the boundary surfaces by both analytical and numerical manner. At first, one-dimensional heat conduction problem in a hollow cylinder is solved analytically in the Laplace domain response with the Bessel's functions and hypergeometric function. After that Durbin's Inverse Method is employed to obtain the real time response of the cylinder.

The findings show that the temperature amplitudes increases with the higher thermal relaxation time values. It's understood that when hyperbolic heat conduction theory is employed, the temperature field demands a finite amount of time to adjust to thermal disturbances.

REFERENCES

- [1]. F. Jiang, "Solution and analysis of hyperbolic heat propagation in hollow spherical objects," *Heat Mass Transfer*, vol. 42, pp. 1083-1091, 2006.
- [2]. M. Jabbari, S. Sohrabpour and M.R. Eslami, "Mechanical and thermal stresses in a functionally graded hollow cylinder due to radially symmetric loads," *International Journal of Pressure Vessels and Piping*, vol. 79, pp. 493-497, 2002.
- [3]. Y. Ootao and Y. Tanigawa, "Transient thermoelastic analysis for a functionally graded hollow cylinder," *Journal of Thermal Stresses*, vol. 29, pp. 1031-1046, 2006.
- [4]. M.H. Babaei and Z. Chen, "Transient hyperbolic heat conduction in a functionally graded hollow sphere," *Int. J. Thermophys.*, vol. 29, pp. 1457-1469, 2008.
- [5]. M.H. Babaei and Z. Chen, "Transient hyperbolic heat conduction in a functionally graded hollow cylinder," *Journal of Thermophysics and Heat Transfer*, vol. 24, pp. 325-330, 2010.
- [6]. L.C. Guo and N. Noda, "An analytical method for thermal stresses of a functionally graded material cylindrical shell under a thermal shock," *Acta Mech.*, vol. 214, pp. 71-78, 2010.
- [7]. A.H. Akbarzadeh and Z.T. Chen, "Heat conduction in one-dimensional functionally graded media based on the dual-phase-lag theory," *Proc IMechE Part C: J Mechanical Engineering Science*, vol. 227(4), pp. 744-759, 2012.
- [8]. H. Pekel, "Dynamic thermal stress analysis of FGM cylinders," PhD thesis, Cukurova University, Adana, Turkey, Sep. 2014.
- [9]. A.L. Rabenstein, *Introduction to Ordinary Differential Equations Second Enlarged Edition with Applications*. Academic Press, New York, 1972.
- [10]. H. Dubner and J. Abate, "Numerical inversion of Laplace transforms by relating them to the finite Fourier cosine transform," *J. ACM*, vol. 15 (1), pp. 115-123, 1968.

- [11]. F. Durbin, "Numerical inversion of Laplace transforms: an efficient improvement to Dubner and Abate's method," *Comput. J.*, vol. 17, pp. 371-376, 1974.
- [12]. G.V. Narayan, Numerical operational methods in structural dynamics. PhD thesis, University of Minnesota, Minneapolis, USA, 1979.

BIOGRAPHY

Hakan Pekel was born in 1982 in Adana, Turkey. He graduated from the Mechanical Engineering Department at Selcuk University in 2004. After his experience with a couple of years in industry he worked for a Research Assistant at Nigde University. His doctorate degree is from Cukurova University in 2014. He spent almost one year at Virginia Polytechnic and State University in the US as a Visiting Scholar. Right now, he has an Assist Prof. position at the Mechanics division of the Nigde University. He studies theoretically on mechanic and thermal stresses of FGMs.

REMOVAL RATE OF HERBICIDE TRIFLURALIN IN AGRUCULTURAL SUNFLOWER FIELD IN NATURAL PERIOD

Gokhan ONDER ERGUVEN

Corresponding author: Yildiz Technical Univercity, Department of Environmental Engineering, 34220, Esenler/Istanbul, Turkey. gokhanondererguven@gmail.com

Hurrem BAYHAN

Bahar IKIZOGLU

Levent KUZU

Gurdal KANAT

Abstract

In this study, The Trifluralin herbicide active ingredient, sold under the trade name "Tefralin 480" was, supplied by an agricultural products shop and applied to the sunflower agricultural field in Kirklareli City at Thrace region, with concentration of 200ml/1000m². This herbicide contains 480 grL⁻¹ of Trifluralin. Experiments were conducted on soil samples obtained from farming areas around the city of Kirklareli and the majority of farms selected from the area have been cultivating sunflower and wheat for several years. All samples were collected randomly from the top 0–20 cm of soil following the standard procedure about 6 months and stored in glass vessels at an ambient temperature. According to the field study results, Trifluralin could be decreased to %43 and this shows that Trifluralin can be stay in the soil for long time. Trifluralin's stability in spring and summer months is faster than autumn months because of the low irrigation effect and sunflowers phytoremediation capacity and other effects such climate conditions and soil properties. In September and October, removal rate is more slow than summer.

Keywords: Trifluralin, sunflower, herbicide, active ingredient

1. INTRODUCTION

Herbicides are used intensively in Turkish sunflower agriculture, with Trifluralin (α,α,α -trifluoro-2,6-dinitro-N,N-dipropyl-p-toluidine) being used on almost all sunflower fields in Turkey since the 1970s [1]. Trifluralin keeps the crops free from weeds in the early stages by controlling annual grass weeds and certain small-seeded broad-leaved weeds. The average half-life of Trifluralin in the field is 45 days in most soils, and less than 10 percent of applied Trifluralin remains one year after application [2]. In a soil used for the disposal of various pesticides (Diuron, Trifluralin, Carbofuran), only Trifluralin could still be detected after many years [3,4].

2. MATERIAL and METHOD

2.1. Chemicals and Reagents

The Trifluralin herbicide active ingredient, sold under the trade name “Tefralin”, was supplied by an agricultural products shop. This herbicide contains 480 gr L⁻¹ of Trifluralin. Trifluralin standard was supplied by Sigma Aldrich as a yellow powder with 99.9 percent purity from Dr. Ehrenstorfer GmbH Co. Acetone and hexane were obtained from Merck. All used chemicals were of GC grade. Analytical standards for GC calibration in the range of 0.1-100 mg/L were prepared from methanol of the working standard solution.

2.2. Soil Sample Collection

Experiments conducted on soil samples obtained from farming areas around the city of Kırklareli and the majority of farms selected from the area have been cultivating sunflower and wheat for several years. All samples were collected randomly from the top 0–20 cm of soil following the standard procedure and stored in glass vessels at an ambient temperature [5] The soil samples were analyzed at the Trakya Agricultural Research Institute, and their properties are listed in Table 1.

Table 1. Characteristics of soil samples used in study

PARAMETER	VALU E
Depth, cm	0-20
pH in water	6.5
Organic carbon, %	2.1
Clay, %	62
Sand, %	32
Silt, %	5
Moisture Content, %	21

10-gram soil samples taken over 6 months from agricultural field were taken and mixed with anhydrous sodium sulphate to form a free-flowing powder. The samples was extracted with solvent once using ultrasonic extraction [6], and a portion of the extract was collected for cleanup and was analyzed. In order to determine the percent dry weight, a separate portion of the sample was weighed out at the same time as the portion used for analytical determination. Immediately after weighing the sample aliquot to be extracted, 10 g aliquot of the sample was measured out into a tared crucible. This aliquot was dried overnight at 105°C and allowed to cool in a desiccator before weighing, although this oven-dried aliquot was not used for the extraction. The percent dry weight was calculated as follows: approximately 10 g of the sample was weighed into a 200 ml beaker, and 1.0 ml of matrix spiking and surrogate spiking solutions were added to each sample. The sample was scanned ultrasonically twice for 30 min with 50 ml of the extraction solvent mixture (50% acetone and 50% Hexane for GC analyses). The extract decant was filtered through Whatman No.41 filter paper using a Buchner funnel. The aliquot of the sample was placed into a concentrator

Removal Rate of Herbicide Trifluralin in Agrucultural Sunflower Field in Natural Period, Gokhan Onder Erguven[@], Hurrem Bayhan, Bahar Ikizoglu, S. Levent Kuzu, Gurdal Kanat,

tube in a warm bath and evaporated to 1 ml volume using a gentle stream of clean, dry nitrogen, after which it was analyzed.

The internal wall of the concentrator tube was rinsed several times with solvent during concentration. The extract then was analyzed for the target analyses using the EPA 8081B method over six months [7].

2.3. Instruments

Perkin Elmer Clarus 500 gas chromatograph used for carrying out the quantification of Trifluralin, and the oven temperature program used during the analysis was 70°C (2 min), 25°C/min to 145°C, 3°C/min to 190°C, and finally 5 min hold at 190°C. Trifluralin was detected using an electron capture detector (ECD), The total oven program was 25 minutes. The inlet temperature was kept at 250°C and the detector temperature at 320°C. and a capillary column of HP-5MS, 30 m x 0.25 mm x 0.25 µm, was used in the equipment.. The make-up gas was ultra pure nitrogen at 30 ml/min flow and the carrier gas was ultra pure helium (He) at 1.2 ml/min flow. Five standards were prepared with concentrations of between 1 and 50 ng/µl for the calibration process. Stability was checked with the medium standard after each 10 sample injection. The average determination coefficient value of the calibration curve (R^2) was 0.999.

In order to determine the recovery efficiency, all samples were spiked with surrogate and internal standards with tetrachloro-m-xylene (TMCX) used as the surrogate standard. The surrogate standard was spiked to the sample prior to extraction.. Average recovery efficiency was 86 percent. Quintozene was used as the internal standard, and was spiked just before capping the chromatography vials. Any sample concentrations falling below the LOD value were ignored. The limit of detection (LOD) values were calculated for each congener as average blank concentrations plus three times the standard deviations Blank samples were corrected for each set of analysis, and all results were blank corrected.

3. RESULTS and DISCUSSION

Removal rate of Trifluralin according to taken the results from GC-ECD over 6 months is given in figure 1.

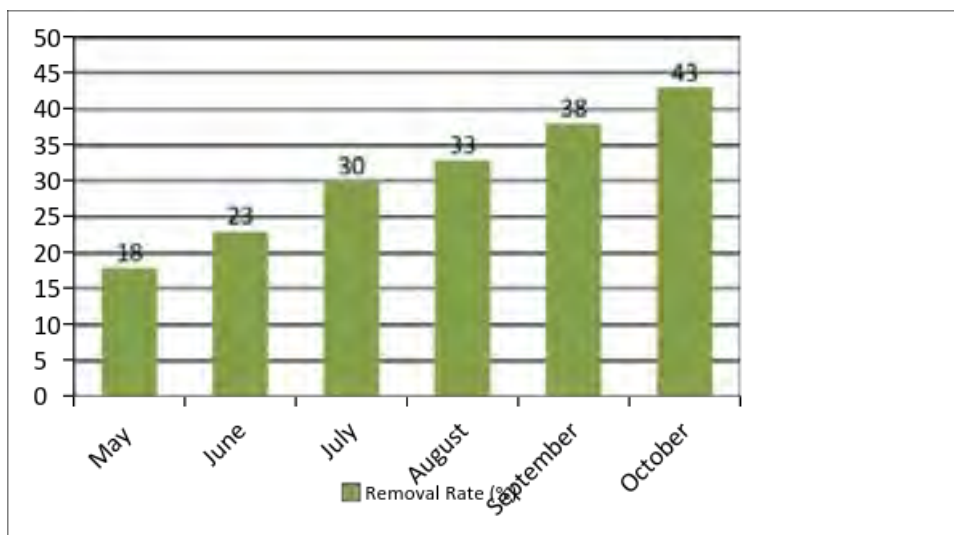


Figure 1. Removal rate of Trifluralin in natural period

4. CONCLUSION

According to the field study results, Trifluralin amount in 6 months from application date (April 2012), to October 2012, could be decreased to %43 and this shows that Trifluralin can be stay in the soil still 6 months period. In the summer season, removal rate is faster than autumn season. This rate is about %20. This means, Trifluralin can effected from sunlight, microorganism activity in soil and climate conditions. At the irrigation season of September and October months, Trifluralins removal rate is a bit slower. According to the Scientists studied with Trifluralin, amount of Trifluralin in soils is related to soil characteristics, adsorbtion-desorbption properties of soil, crop types and pest types in the field, climateeffects such sunlight, bioremediation, irrigation, humidity or other effects as application concantration and methods, slope of field etc.

Biography: Gokhan Onder Erguven was born in Kirklareli, Turkey on November 2, 1982. He received the engineering degree in environmental engineering from the “Trakya” University, Tekirdag, Turkey, in 2007. He received the M.Sc degree in the department of Agricultural structures and irrigation of natural sciences institute, “Namik Kemal” University, in 2010. Since 2011, He is academic at environmental engineering department of, Yildiz Technical University, Istanbul, Turkey. His research interests pesticides, natural treatment, environmental pollution, bioremediation.

ACKNOWLEDGMENT

This research has been supported by Yildiz Technical University Scientific Research Projects Coordination Department. Number: 2012-05-02-KAP07

REFERENCES

- [1]. Sagliker, 2009. Effects of Trifluralin on soil carbon mineralization at different temperature Conditions. *European Journal of Soil Biology* 45, 473–477.
- [2]. Vencill, W.K. (Ed.). 2002. *Herbicide Handbook*, 8th edition. Weed Science Society of America, Champaign, IL. pp. 440–443.
- [3]. Fernandes, C.C., Pizano, A.M., Morales, A.M., 2013. Characterization, modes of action and effects of Trifluralin. A Review, dx.doi.org/10.5772/55169.
- [4]. Johnston, W.H., Camper, N.D., 1991. Microbial degradative activity in pesticide pretreated soil, *Journal of Environmental Science and Health B* 26, 1–14.
- [5]. Carter, M.R, Gregorich, E.G., 2006. *Soil Sampling and Methods of Analysis*, Second Edition by Taylor & Francis Group, LLC. International Standard Book Number -13, 978-0-8493-3586-0 (Hardcover)
- [6]. EPA, 2007a. Ultrasonic Extraction. EPA Method 3550C Revision 3, U.S. Environmental Protection Agency, Washington, DC.
- [7]. EPA, 2007b. Organochlorine Pesticides by Gas Chromatography. EPA Method 8081B -1 Revision 2, U.S. Environmental Protection Agency, Washington, DC

EVALUATION OF PRESPLITTING BLASTING OPERATION IN APA-HOTAMIS IRRIGATION (AHI) CHANNEL CONSTRUCTION

Bilgehan KEKEC

Selcuk University, Department of Mining Engineering, 42070, Konya, Turkey.
kecec@selcuk.edu.tr

Niyazi BILIM

Selcuk University, Department of Mining Engineering, 42070, Konya, Turkey.
bilim@selcuk.edu.tr

Mumin YUCE

lci Holding, Konya, Turkey, muminyuce@hotmail.com

Abstract

Drilling and blasting techniques are commonly used in mining operation, dam, highway and tunnel construction. Some application need to controlled blasting techniques due to hazard of blasting. Also, controlled blasting techniques may positively contribute to economy in some project. In this study, presplitting blasting operations which is a controlled blasting technique and applied to Apa-Hotamış Irrigation Channel (AHI) project were evaluated. Technical parameters such as explosive types, blasting method and drilling design were investigated and presented. Also, case study of cost account for 100 meter length and 45 meter width of their irrigation channel construction were calculated and presented.

Keywords: *Controlled blasting, Irrigation channel, Presplitting blasting*

1. INTRODUCTION

Explosive are commonly used in mining operation, dam, highway and tunnel construction. Excavation with blasting operation is the most economic and effective methods for production of raw materials and loosen of rock units. In the result of the mining activities, dam, highway and tunnel construction done by using blasting activity, some problems may be occur which negatively effect to construction project and rock loosen process. In this type projects, controlled blasting techniques are used to avoid from excessive excavation and protection of main rock strenght except excavation section.

Controlled blasting is defined as general name of special blasting methods improved to avoid from the risk of mining, dam, channel and highway blasting [1]. Contour balasting teqhniques have classified as line drilling, cushion blasting, smooth blasting and presplitting [2]. Researchers [3], [4], [5] indicated that controlled blasting effect to excavation quality and economy. Also; blasting induced some problems such as rock slope, overbreak may be prevented with controlled blasting techniques. Excessive excavation lead to financial loss and time loss. In this states, expensive concrete materials replaced to overbreak. Incremental cost is an undesirable status in excavation operations. Geological factors directly effect to blasting achievement [6]. Thus, controlled blasting techniques must be used in special design such as channel, tunnel etc. In this study, Apa-Hotamış region in Konya-Turkey was selected for investigation and evaluation. This Project is called as AHI.

In this project, excavation operation have been continued with drilling and blasting method. Drilling and blasting have been carried out with presplitting that is a controlled blasting technique. Technical parameters of blasting such as explosive types, blasting method and drilling design were investigated and presented. Also, a case cost account were calculated for a specific [circumstance](#).

2. GEOLOGICAL SETTING OF AHI PROJECT

Project area is located Konya city in Turkey. Konya is located at the center of Anatolian peninsula and due to its economic activities; it has been expanded in last 20 years to reach around a million populations. Apa-Hotamış transmission (AHI) channel construction is located east of the Çumra town and continue among the Kuşça-Apasaraycık-Dineksaray-Yenisu-Yörükcamili-Kosoba-Ortaoba-Süleymanhacılı-Adakale villages (Fig.1).

The total lenght of the AHI channel is about 135 km and cahannel widht is about 45 m. AHI channel will be used both irrigation and derivation. Numerous geological units are seen along the AHI project route. These units may be classified as Ardıçlı formation, Geyikdağı formation, Belkuyu formation, Bozkır formation, Kozludere formation. Main rocks where excavation operation with blasting was carried out are generally limestone, dolomitic limestone, sandstone and some volcanics such as andesite, dasite, gabbro [7].

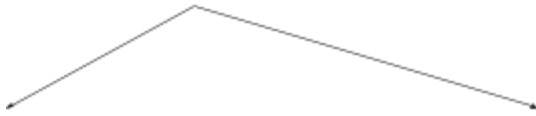


Figure 1. Apa-Hotamış transmission (AHI) channel construction route

3. PRESPLITTING BLASTING

Presplitting blasting is the most successful and widely adopted controlled blasting method. Main aim of presplitting method is creating an artificial line (Figure 2). Thus, over breaking of main rock is avoided. In this method, presplitting hole is exactly drilled at the end of production holes and hole diameters should generally be 30-120 mm and should not be used stemming [2]. The spacing between holes varies between 10 to 20 times the hole diameter.



Figure 2. Hole paths left by presplitting

Additionally; Presplitting blasting method has some advantages with regard to reduction of blast induced environmental effects. One of the most important of these advantages is blast induced vibration waves. Presplitting plane forming after the blasting prevent to propagation of vibration waves [1], [8]. Equations can be used in order to prepare a presplitting blasting plan for calculation of charge and distance of presplitting hole [9].

$$D=8.25 * 10^{-5} * d^2 \quad (1)$$

D : Explosive amount for per meter, (kg/m)
d : Hole diameter, (mm)

$$S=10 \text{ or } 12 * d \quad (2)$$

S : Spacing between presplitting holes, (mm)

4. DRILLING AND BLASTING PROCESS

Drilling process have been carried out with drilling machine (Figure 3). Blastholes diameter drilled 89 mm diameter and blastholes depth arranged according to channel section in the project. Also, blastholes drilled 80 degree angle.



Figure 3. Drilling machine

The main concern of this project is building an irrigation channel with correct section under controlled blasting action. Blastings were also used to obtain homogeneous fragmentation for easy excavation and loading. Therefore their blasting design had been performed to obtain suitable excavation section and minimum environmental effect such as vibration and airblast. The main explosive material used for production blasting in project is ANFO (Figure 4a). For detonation purposes, gelatine dynamite (Figure 4b) and its capsule (Figure 4c). Explosives used for presplitting blasting are only gelatin dynamite. Connection between presplitting holes were provided with detonating cord. The waste materials obtained from drilling process were used in production holes as stemming. However, in presplitting holes, stemming were not used.



(a)

(b)

(c)

Figure 4. The main blasting materials

Rock blasting parameters in the project has the following common characteristics;

Distance between presplitting holes	: 0.9-1 m
Distance between production holes	: 3 m
Blasthole diameter	: 89 mm
Blasthole length, depth	: 6-6.5 m
Production holes	: 150
Presplitting holes	: 356
Delay time	: Non-Delay

5. PRESPLITTING APPLICATION AND COST CALCULATION

Presplitting is a controlled blasting technique with applications in mining and various construction projects. The main objectives of pre-splitting applications are preventing excessive break in main rock and controlling excessive ground vibrations induced production blasting. This technique is especially effective in excessive break control through providing a separating surface between the main rock and production blasting. Thus, excessive excavation may be avoided with this technique. An illustrate presplitting and production blasting pattern adopted in some parts of this project and its results was presented in Figure 5.

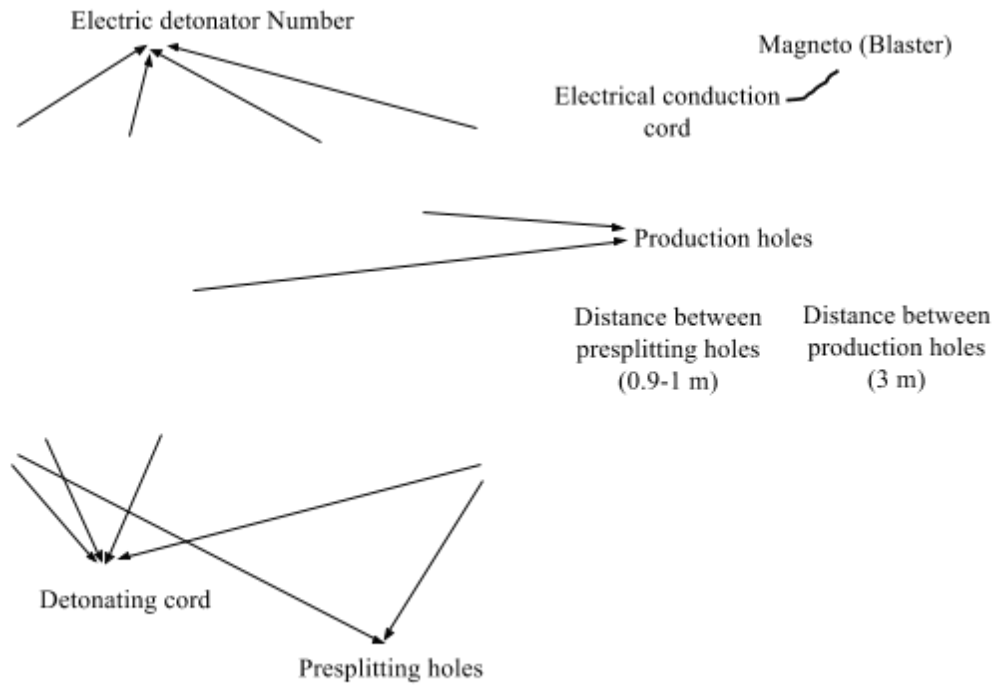


Figure 5. Presplitting and production blasting pattern

As seen in Figure 5, both presplitting and production blastholes were separately detonated from each other. In other words each blasting holes group were detonated with different electric detonator (Number:0-2-4-6-8-10-12). Thus presplitting holes detonated first and then production holes detonated from inside to outside. In the result of the blasting, loosen rocks split off along a line and it became easily excavability (Figure 6).

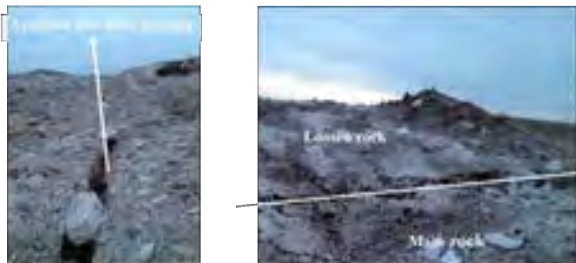


Figure 6. Artificial line formed after blasting and loosen rocks

Excavability is very important parameter for rock units. In mining and construction projects, excavation cost determines to total costs most of times. Blasting technique is one of the most important and economic method applied for reduction of excavation cost. Excavation working which is outside of the plan lead to time loss and hidden cost. As seen Figure 6, artificial line formed after blasting determines to irrigation channel section (Figure 7). Also, it avoids to excessive excavation.



Figure 7. Irrigation channel section

A case cost study was given for this study. Under conditions given in Figure 5, the cost account for 100 meter length (B-BI) and 45 meter width (A-AI) of the irrigation channel construction were calculated. According to this circumstance,

Total production holes	: 462
Gelatin dynamite amount per production holes	: 0.5 kg
Total gelatin dynamite amount for production holes	: $627 \cdot 0.5 = 231$ kg
ANFO amount per production holes	: 17.5 kg
Total ANFO amount for production holes	: $17.5 \cdot 462 = 8085$ kg
Total presplitting holes	: 200
Gelatin dynamite amount per presplitting holes	: 5
Total gelatin dynamite amount for presplitting holes	: $5 \cdot 0.5 \cdot 200 = 500$ kg
Total explosive amount	: 8085 kg ANFO 731 kg Gelatin dynamite
Detonating cord for a line of production holes connections	: 100m
Total detonating cord for all production holes connections	: $100 \cdot 14 = 1400$ m
Detonating cord per presplitting holes	: 7 m
Detonating cord for presplitting holes	: $7 \cdot 200 = 1400$ m
Detonating cord for surface connection	: 200 m
Total detonating cord	: $1400 + 1400 + 200 = 3500$ m
Total electric detonator	: 16
Non-delay detonator	: 462
Electrical conduction cord	: 500 m

When the total materials used in case study were multiplied by the unit price, total cost calculated asabuto 8520 ABD dollars.

6. CONCLUSION

Controlled blasting techniques are commonly used in mining, tunnel, dam and special construction projects. Presplitting blasting is one of the very important controlled technique. This method has great success if blasting pattern is selected suitable. The formation is an important parameter for success of blasting. Also, this technique is cost effective method specially in hard rocks.

Presplitting blasting applied at AHI Project is very important in terms of contractor company. The main objectives of presplitting applications in this project are preventing excessive excavation cost and appropriate channel construction section.

Some conclusions based on the present case calculation and evaluations can be summarized as below.

- Excavation section forming after presplitting blasting provide convenience to concreting operations.
- Time loss and financial loss can largely be avoided.
- Excavation costs arised from excessive excavation were reduced as depending on presplitting blasting. Also, excavation rate was positively affected.
- Blast induced environmental effect are very important problem specially near to residential area. Artificial line forming after presplitting blasting largely prevent to these effects.

REFERENCES

- [1]. Ö. Akkoyun, Bir manyezit açık ocak işletmesinde uygulanan kontrollü patlatma çalışması, *Kayamek 2004- VII. Bölgesel Kaya Mekaniği Sempozyumu.*, Sivas, Türkiye, 2004.
- [2]. S.O. Olofsson, *Applied Explosives Technology for Construction and Mining*, 2nd Edition, Applex, Arla, Sweden, p. 304, 1988.
- [3]. H. Yingguo, L. Wenbo, C. Ming, Y. Peng and Y. Jianhua, "Comparison of Blast-Induced Damage Between Presplit and Smooth Blasting of High Rock Slope," *Rock Mech. Rock Eng.*, vol.47 pp. 1307–1320, 2014.
- [4]. W. B. Lu, M. Chen, X. Geng, D.Q. Shu and C. B. Zhou, "A study of excavation sequence and contour blasting method for underground powerhouses of hydropower stations," *Tunn. Undergr. Space Technol.* Vol. 29, pp. 31–39, 2011.
- [5]. S. K. Mandal, M. M. Singh and S. Dasgupta, "Theoretical concept to understand plan and design smooth blasting pattern," *Geotech Geol Eng.* Vol. 26(4) pp.399–416, 2008.
- [6]. S. Kahraman and A. Kılıç, "Kontrollü Patlatma Yöntemleri ve Tarsus Ayrımı- Gaziantep Otoyolu T2 Tüneli uygulaması," *Madencilik*, vol. 39 (2), pp. 23–28, 2000.
- [7]. AHI Project engineering geology report, 2011.
- [8]. B. Kekeç, "Blasting induced ground vibration determination according to the some rock materials and rock mass properties," *PhD Thesis, Selcuk University*, p.213, 2010.
- [9]. C. J. Konya and E. J. Walter, *Controlled Blasting and Surface Blast Design*, Prentice-Hall, USA, 1990.

REMOVAL RATE OF HERBICIDE ACLONIFEN IN AGRUCULTURAL SUNFLOWER FIELD IN NATURAL PERIOD

Gokhan ONDER ERGUVEN

Corresponding author: Yildiz Technical University, Department of Environmental Engineering, 34220, Esenler/Istanbul, Turkey. gokhanondererguven@gmail.com

Hurrem BAYHAN

Yildiz Technical University, Department of Environmental Engineering, 34220, Esenler/Istanbul, Turkey.

Bahar IKIZOGLU

Yildiz Technical University, Department of Environmental Engineering, 34220, Esenler/Istanbul, Turkey.

Levent KUZU

Yildiz Technical University, Department of Environmental Engineering, 34220, Esenler/Istanbul, Turkey.

Gurdal KANAT

Yildiz Technical University, Department of Environmental Engineering, 34220, Esenler/Istanbul, Turkey.

Abstract

Aclonifen has been used almost in all sunflower fields in Thrace region since 2000s. Microbial degradation, photodegradation, irrigation effect, adsorption-desorption mechanism, soil character, humidity, soil temperature are an important mechanism controlling the fate of pesticides in soils and is generally considered to be desirable both from an environmental as well agricultural perspective. In this study, The Aclonifen herbicide, sold under the trade name "Chekic 600" was, supplied by an agricultural products shop and applied to the sunflower agricultural field in Kırklareli City at Thrace region, with concentration of 200ml/1000m². This herbicide contains 600 grL⁻¹ of Aclonifen. Experiments were done on soil samples obtained from farming areas around the Kırklareli City. The majority of the farms selected in the area have been cultivating sunflower and wheat for several years. All samples were collected randomly from the top 0–20 cm of soil following the standard procedure about 12 months and stored in glass vessels at a low temperature. According to the field study results, Aclonifen residual is about %11 and this shows that Aclonifen can be stay in the soil for long time. The fast removal rate can be seen in the irrigation season of September to October as % 18 and the slowest rate is on December to March as %7 because of the low soil and air temperature. From March to April, removal rate is about %14 with effect of increasing temperature in soil and low irrigation.

Keywords: Aclonifen, sunflower, herbicide, active ingredient

1. INTRODUCTION

Aclonifen, usually used as the sodium salt, is a herbicide that is currently not approved for EU use. It is highly soluble in water and in many organic solvents. It is non-volatile. It may leach to groundwater under certain conditions. It is moderately persistence in soil systems and can be very persistent in aquatic systems. It has a moderate mammalian toxicity and a high potential for bioaccumulation. It is a recognised irritant. It is relatively non-toxic to birds and earthworms but more so to honeybees and most aquatic organisms [1].

Aclonifen shows several characteristics which differ from the other members of its chemical family, especially its two complementary modes of action and a very high conjugation potential in sunflower. These features explain its high selectivity for sunflower and also explain that, after pre-emergence treatment, the a.i. was readily transformed into polar derivatives which remain segregated inside the roots. Thus, the chemical derivatives issued from the use of this a.i. are absent from the sunflower leaves and, consequently, from the flowers and the seeds. The modes of action, uptake, transfer and conjugation of this a.i. in sunflower, as compared to the weeds associated to this culture; show that not only pre-emergence treatments are possible for this a.i. but also post-emergence application [2].

Aclonifen can metabolise in both sediment and water systems at a moderate rate with DT50 values of 11.2 days and 17.3 days. Aclonifen steadily partitioned to the sediment and degraded [3].

Selectively killed weed close to cultivated plants which do have to remain unaffected, is the necessary condition for using herbicides in agronomy [4]. This challenge is generally not a simple one and farmers do have to pay much attention to the effectiveness and selectivity of such a chemical operation which depends on several factors, especially climatic (temperature, rain, hygrometry) and agronomic factors (soil nature, development stage of the culture, weed species and nature of the planted cultivars). That is why the careful observation of the symptoms of the herbicidal action on the culture and on the weeds is a precious source of information [5].

Aclonifen is a diphenylether herbicide that contains Nitrogen. Nitrodiphenyl ether herbicides are potent herbicides. Some metabolites and parent compounds are considered as possible mutagens and endocrine disruptors. Both properties pose serious hygienic and environmental risks (Keum et al. 2008). Environmental dissipation of nitrodiphenyl ether herbicide occurred through physical removal or photochemical and biological degradation [6,7].

2. MATERIAL and METHOD

2.1. Chemicals and Reagents

Aclonifen herbicide, under the trade name “Chekic 600”, was supplied by an agricultural products shop. This herbicide contains 600 gr L⁻¹ of Aclonifen active ingredient. Aclonifen standard was supplied as a yellow powder with 99.9% purity from Dr. Ehrenstorfer GmbH Co. Acetone and hexane were obtained from Merck. Analytical standards for LC-MS-MS calibration were in the range of 0.1-100 mg/L. Methanol was chosen as diluting solvent.

2.2. Soil Sample Collection

Experiments were done on soil samples obtained from farming areas around the Kirklareli City. The majority of the farms selected in the area have been cultivating sunflower and wheat for several years. Soil with no background of Aclonifen concentration was collected from an organic farm. All samples were collected randomly from the top 0–20 cm of soil following the standard procedure and stored in glass vessels at an ambient temperature [8]. Properties of the soil samples were analysed at the Trakya Agricultural Research Institute. The properties of the soil are listed in Table 1. The climatic conditions of studied agricultural field over 12 Months taken from Kirklareli Meteorological Service are listed in Table 2.

Table 1. Characteristics of soil samples used in study

PARAMETER	VALU E
Depth, cm	0-20

Removal Rate of Herbicide Aclonifen in Agrucultural Sunflower Field in Natural Period, Gokhan Onder Erguven[@], Hurrem Bayhan, Bahar Ikizoglu, S. Levent Kuzu, Gurdal Kanat,

pH in water	6.5
Organic carbon, %	2.1
Clay, %	62
Sand, %	32
Silt, %	5
Moisture Content, %	21

Table 2. Climate contitions of studied agricultural field

Date	Average Relative Humidity (%)	Average Local Pressure (hPa)	Average Temperature(C ⁰)	Soil Temperature at 20 ⁰ C	Average Solar Radiation kWh/m2 [9]	Average Irrigation (mm)
2012 April	76	1005	13,7	13,3	4,61	70
2012 May	78	1007	17,4	20,4	5,72	114,4
2012 June	65	1009	23,2	23,8	6,44	9,4
2012 July	60	1006	26,3	26,5	6,53	3,2
2012 August	57	1009	25,7	21,9	5,79	4,4
2012 September	63	1010	20,9	15,6	4,49	4
2012 October	78	1010	17,0	9,9	2,88	118,4
2012 November	91	1011	12,5	5,9	1,80	30,4
2012 December	93	1011	4,5	14,8	1,30	138,8
2013 January	92	1010	4,5	3,9	1,56	108,8
2013 February	91	1010	6,8	4,6	2,29	82,4
2013 March	86	1007	8,8	7,5	3,44	54,8
2013 April	80	1009	12,1	13,1	4,61	22,8

Over 12 months (from application date of May 2012 to April 2013), 10-gram samples were taken and mixed with anhydrous sodium sulphate to form a free-flowing powder. The samples was extracted with solvent once using ultrasonic extraction [10], and a portion of the extract was collected for cleanup and was analyzed. In order to determine the percent dry weight, a separate portion of the sample was weighed out at the same time as the portion used for analytical determination. Immediately after weighing the sample aliquot to be extracted, 10 g aliquot of the sample was measured out into a tared crucible. This aliquot was dried overnight at 105oC and allowed to cool in a desiccator before weighing, although this oven-dried aliquot was not used for the extraction. The percent dry weight was calculated as follows: approximately 10 g of the sample was weighed into a 200 ml beaker, and 1.0 ml of matrix spiking and surrogate spiking solutions were added to each sample. The sample was scanned ultrasonically twice for 30 min with 50 ml of the extraction solvent mixture (50% acetone and 50% Hexane for LC-MS-MS analyses). The extract decant was filtered through Whatman No.41 filter paper using a Buchner funnel. The aliquot of the sample was placed into a concentrator tube in a warm bath and evaporated to 1 ml volume using a gentle stream of clean, dry nitrogen, after which it was analyzed. The internal wall of the concentrator tube was rinsed several times with solvent during concentration. Then, the extract was analyzed for the target analytes using the EPA 1614 method [11]

2.3. Instruments

The quantification of Aclonifen was performed by LC-MS-MS (Dionex Ultimate 3000) equipped with a C18 Thermo Accucore column 100mm x 2.1mm 2.6 mic. Owen temperature of the column was 400⁰C and Auto Sampler temperature was 50⁰C. Retention time was 9.0 min. Mass (Thermo Access Max) HESI ion source was 3500 volt and

Removal Rate of Herbicide Aclonifen in Agrucultural Sunflower Field in Natural Period, Gokhan Onder Erguven[@], Hurrem Bayhan, Bahar Ikizoglu, S. Levent Kuzu, Gurdal Kanat,

Ion Transfer Tube temperature was 2700C. Sheath and Aux gas were 50 Arb and 15 Arb, quantification limit was 15 ppb. Collisure gas pressure was 1.5 mTorr. LOD and LOQ values were 4 ppt and 15 ppt. Ion transmissions were; for primary ion 265.1, second ions 182.1 and 247.9. The quantification (method detection) limit was 0,1-1 mg kg⁻¹. The average value of determination coefficient (R²) of the calibration curve was 0.999.

All samples were spiked with surrogate and internal standards in order to determine the recovery efficiency, with tetrachloro-m-xylene (TMCX) used as the surrogate standard. The surrogate standard was spiked to the sample prior to extraction. Quintozene was used as the internal standard, and was spiked just before capping the chromatography vials. Average recovery efficiency was 86 percent. The limit of detection (LOD) values were calculated for each congener as average blank concentrations plus three times the standard deviations. Any sample concentrations falling below the LOD value were ignored. Blank samples were corrected for each set of analysis, and all results were blank corrected.

3. RESULTS and DISCUSSION

Removal rate of Aclonifen according to taken the results from LC-MS-MS over 12 months is given in fig. 1.

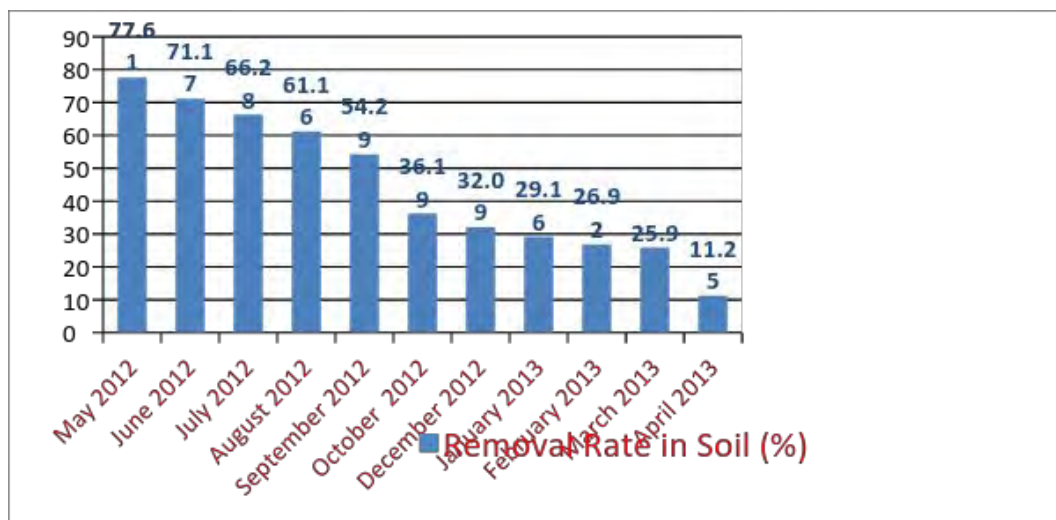


Figure 1. Removal rate of Aclonifen in natural period

4. CONCLUSION

According to the study results, Aclonifen amount in a year period, from application date (May 2012) to April 2013, decreased about % 89 and this shows that Aclonifen can be stay in the soil for a long time. Aclonifen residuals in soil decreases from % 78 to % 54 in spring and autumn periods and from %54 to %36 in Sempember-October months with effects of rainfall. Residual amount of Aclonifen from December to April is nearly %21 because of the low sunlight effect, low rainfall and soil temperature.

Biography:

Gokhan Onder Erguven was born in Kırklareli, Turkey on November 2, 1982. He received the engineering degree in environmental engineering from the “Trakya” University, Tekirdag, Turkey, in 2007. He received the M.Sc degree in the department of Agricultural structures and irrigation of natural sciences institute, “Namık Kemal” University, in 2010. Since 2011, He is academic at environmental engineering department of, Yildiz Technical University, Istanbul, Turkey. His research interests pesticides, natural treatment, environmental pollution, bioremediation.

Removal Rate of Herbicide Aclonifen in Agrucultural Sunflower Field in Natural Period, Gokhan Onder Erguven[@], Hurrem Bayhan, Bahar Ikizoglu, S. Levent Kuzu, Gurdal Kanat,

ACKNOWLEDGMENT

This research has been supported by Yildiz Technical University Scientific Research Projects Coordination Department. Number: 2012-05-02-KAP07

REFERENCES

- [1]. PPDB 2015 : Pesticide Properties DataBase. <http://sitem.herts.ac.uk/aeru/ppdb/en/Reports/15.htm>
- [2]. Kilinc 2011 "Aclonifen: The identikit of a widely used herbicide" African journal of agricultural research). 6:2411-2419.
- [3]. ECHA, 2011. ANNEX 1 – BACKGROUND DOCUMENT TO RAC OPINION ON ACLONIFEN. Committee for Risk Assessment RAC Annex 1 Background document to the Opinion proposing harmonised classification and labelling at Community level of Benzenamine, 2-chloro-6-nitro-3-phenoxy- (Aclonifen) ECHA/RAC/ CLH-O-0000001543-79-03/A1 14 September 2011
- [4]. Tissut M, Delval JM, Ravanel P. 2006. Plantes, herbicides et désherbage ACTA, Paris, France, pp, 635.
- [5]. Scalla R. 1991. Les herbicides: Mode d'action et principes d'utilisation. INRA, Paris, France, pp, 450.
- [6]. Andreoni, V.; Colombo, M.; Gennari, M.; Nègre, M.; Ambrosoli, R. Cometabolic degradation of acifluorfen by a mixed microbial culture. J. EnViron. Sci. Health B. 1994, 29, 963–987.
- [7]. Scrano, L.; Bufo, S. A.; D'Auriab, M.; Meallier, P.; Behecti, A.; Shramm, K. W. Photochemistry and photoinduced toxicity of acifluorfen, a diphenyl-ether herbicide. J. EnViron. Qual. 2002, 31, 268–274.
- [8]. Carter, M.R, Gregorich, E.G., 2006. Soil Sampling and Methods of Analysis, Second Edition by Taylor & Francis Group, LLC. International Standard Book Number -13, 978-0-8493-3586-0 (Hardcover)
- [9]. solarelectricityhandbook.com/solar-irradiance.html
- [10]. EPA, 2007.Ultrasonic Extraction. U.S. Environmental Protection Agency, Washington, DC.
- [11]. EPA 1614 method, Brominated Diphenyl Ethers in Water Soil, Sediment and Tissue by HRGC/HRMS (EPA, 2007).

LOAD FREQUENCY CONTROL OF THREE AREA POWER SYSTEM BY USING PID, FUZZY AND FUZZY-PID CONTROLLER

Kadir GÜLER

Afyon Kocatepe University, Faculty of Technology, Department of Electrical and Electronic Engineering Afyon, TURKEY
kdrgrl26@gmail.com

Yüksek OĞUZ

Afyon Kocatepe University, Faculty of Technology, Department of Electrical and Electronic Engineering Afyon, TURKEY
yukseloguz@aku.edu.tr

Ahmet YÖNETKEN

Afyon Kocatepe University, Faculty of Engineering, Department of Electrical Engineering Afyon, TURKEY

Abstract

In this study, a solution is tried to be created as response to the load–frequency problems in power systems by using PID and Fuzzy Logic controllers. The load-frequency control of a three area power system was performed by using PID, Fuzzy Logic and Fuzzy Logic-PID controllers. The load and frequency control was efficiently achieved by assigning different values to controller gains. A linearized model of a three area power system was applied respectively to PID, Fuzzy Logic and Fuzzy Logic- PID controllers. Experimental data was attained by using PID, Fuzzy Logic and Fuzzy Logic- PID logic controller.

Keywords: Power system, PID Control, Fuzzy Control, Load-Frequency Control.

1. INTRODUCTION

Electric energy is one of the most used energy resources because it is fast, easy and economical to convey and easy to use from the generation point to the consumer. Electric energy is transported to the consumer through large power systems today. The mission of electric power systems is to generate electric energy that has terminal voltage and system frequency economically and is to transport and distribute it.

Power systems generally consist of production units, transmission lines and distribution networks. While, transmission network provides the installation and running of medium and high tension lines related to the transportation of electric energy from generation point to consumption area; distribution network provides the installation and running of low tension lines from transmission network to the last user. The task of the generation unit is to generate the electric energy which has terminal voltage and standardized constant and stable rate frequency economically and without harming the environment [1].

To keep the frequency constant and steady in nominal value is one of the main problems of electric power systems. The value of the frequency essentially depends on the balance of the active powers that are generated and consumed in the network. Increase or decrease in consumed power in comparison with the generated power causes alterations in rotational speed of generators that is to say it causes alterations in system frequency.

Power systems are generally designed to meet their consumption by their own production units. When consumption increases, production units also enhance their production by using the reserves. Keeping the frequency under control depends on the stabilization of generated and consumed active powers in the system [2].

Automatic Generation Control (AGC) or Load Frequency Control (LFC) is a very important issue to command and control of the power system to provide quality, sufficient and safe electric energy. AGC is feedback control system that adjusts generator output power to stabilize defined frequency. Interconnected power control system is divided into three areas [10].

Load Frequency Control (LFC) has been used as a part of Automatic Generation Control electric power system program for years. One of the objectives of AGC is to stabilize system frequency at nominal value (50Hz). When power system is run stably, demands of load increases or kinetic energy decreases at generator power source unit and as a result speed and frequency alter. Therefore, load frequency control provides power system to work safely [11 – 14].

2. THE DESIGN AND APPLICATION OF PID, FUZZY AND FUZZY-PID CONTROLLERS FOR THREE AREA POWER GENERATOR SYSTEM

2.1. PID Control

PID Control algorithm forms control output by processing the system failure through three mathematical operations and then adding it. Its impact on the system is classified as defined below.

- Proportional Response: It affects the controller output as a multiplication of failure by a definite "Gain" value.
- Integral Response: It indicates its impact proportionally to the total amount failure in all areas from the time when the control process starts in controller output, to the time when the impact is calculated. The integral response represents the total amount of failure of system in the past.
- Derivative Response: It affects controller output directly proportionate to the failure alteration.
-

There is not a standard specification for PID applications. According to Karl Astrom PID algorithm is like the equations (1) and (2) below:

$$u(t) = k_p e(t) + k_i \int_0^t e(\tau) d\tau + k_d \frac{de}{dt} \quad (1)$$

$$e(t) = r(t) - y(t) \quad (2)$$

u(t): Control Impact

$e(t)$: Error Function
 $r(t)$: Reference input
 $y(t)$: System output

Proportional controllers (K_p) have an impact on decreasing the rise time and they decrease it, however, they never remove it completely (steady state failure). Integral controller (K_i) has an impact on removing the steady state failure, however, it may cause transient response to get worse.

Derivative controllers (K_D) has an impact on increasing the steadiness of the system, it reduces exceeding and adjusts the transient response. The responses of each controller K_p , K_i , K_D in a closed loop are summarized in Table 1.

Table 1. The effect of the controller in close loop system

Closed Loop Response	Rise Time	Exceeding	Setting Time	Steady State Error
K_p	Decreases	Increases	Alters a little	Decreases
K_i	Decreases	Increases	Increases	Vanishes
K_d	Alters a little	Decreases	Decreases	Alters a little

Simulation block diagram of a three area power generation system by PID in Matlab/Simulink program is shown in Figure 1 below. Proportional, integral and derivative gains are seen in Figure 1 PID block diagram.

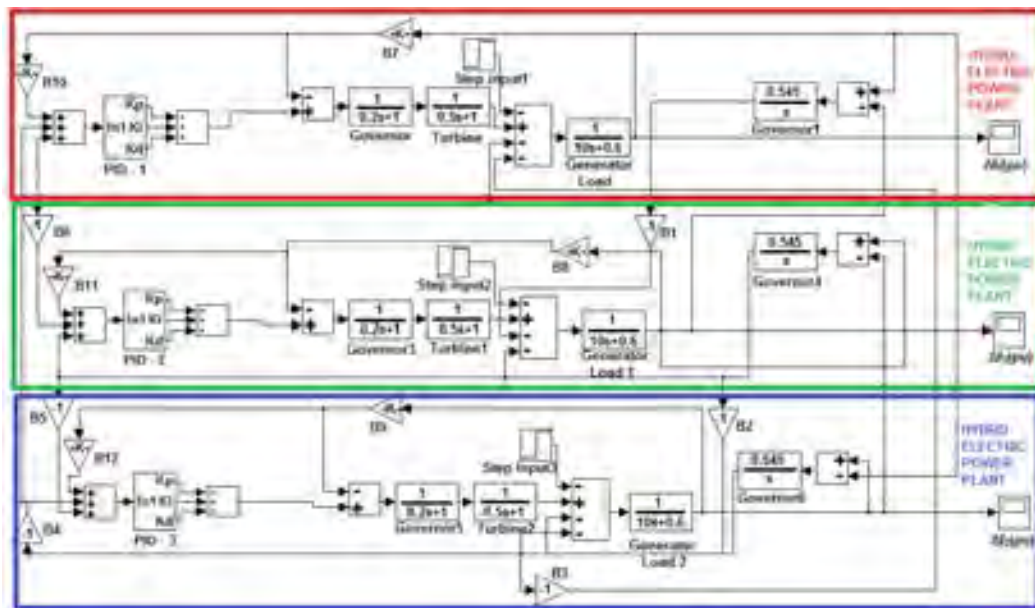


Figure 1. Simulation block diagram of load-frequency control of a three area power generation system by using PID Controller

2.2. Fuzzy Logic Control

Fuzzy Logic Control is known as a process of thought or a methodology of problem solving in control systems engineering and it is used in control systems when there is no concrete input and mathematical models. Fuzzyfication is the process to obtain a clear amount in fuzzy logic experiment method [15]. Regardless of the conditions or extents of the decision makers, they have to function in an environment of uncertainty. The accuracy of the decisions will be provided to the degree that the aforesaid uncertainty is transformed into a risk. However, if the decision makers use the classical scientific approach and the methods included in this approach during the decision making process, the results gained in the end will be directional decisions such as good – bad, ugly – beautiful, right – wrong, yes – no, black – white or 0-1. In fact, real life is not based on absolute distinctions. In other words, the existence of thousands shades of grey along with the absolute black and absolute white should not be forgotten in a decision environment.

Fuzzy logic controller consists of three main units as it is shown in Figure 2. The first one is fuzzyfication interface, the second is interference rule engine and the third one is defuzzyfication interface. Process operators for load frequency control are variable failures (e) and failure alterations (de).

The main units of Fuzzy Logic are shown in Figure 2 below.

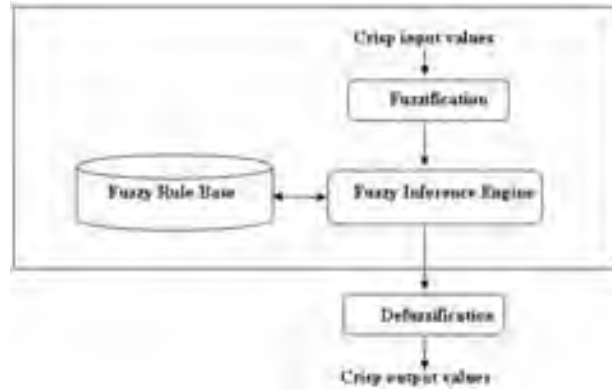


Figure 2. Fuzzy Logic Controller Scheme

In the scheme in Figure 2 fuzzyfication unit becomes the first part of fuzzy process system. The information which gets into the unit as accurate or feedback results undergo some changes in scale here and become fuzzy. In other words, a membership value is assigned to each information and turned into a linguistic structure and then sent to the rule process unit. The information that reaches the rule process unit are combined with the rule processing information such as if ... and ... then ... else that are based on a database which is stored in rule process unit. Aforesaid logical propositions can be set by numeric values with respect to the structure of the problem. In the last step, gained results are sent to the defuzzyfication unit by using logical decision propositions with respect to the structure of the problem [16, 17].

Simulation block diagram of load – frequency control of a three area power generation system by using fuzzy logic controller is shown in Figure 3 below.

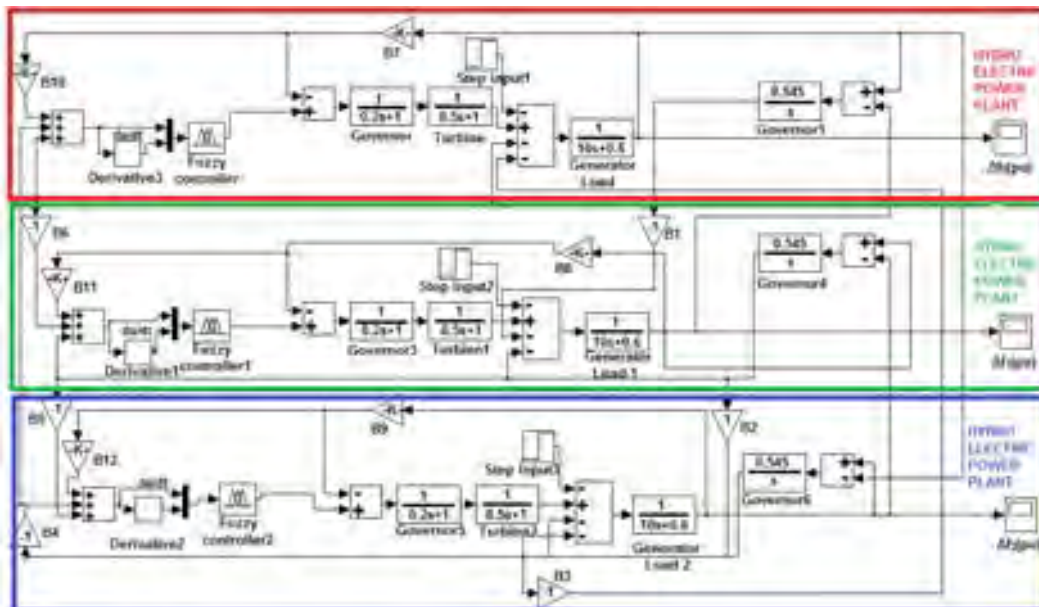


Figure 3. Simulation block diagram of load – frequency control of a three area power generation system by using fuzzy logic controller

2.3. FUZZY – PID Controller

Fuzzy systems are knowledge and rule based systems. “If-then” rules form the basis of fuzzy logic. There are two ways of descriptions of fuzzy logic in the literature:

- Real world is way too complicated to describe very clearly and certainly. Therefore, there is an obligation to create an approximation.
- Important knowledge for real systems are gained from two sources. The first source is people's experiences and the other is sensor measurement and mathematical models gained by physical laws. The aim is to design the system by using these two knowledge sources [3].

After this stage, the design of the system can be applied using human information, experience, mathematical model and sensor knowledge. Fuzzy control is defined by Zadeh and Mamdani as to combine specialist knowledge and experience during the control process where there is an uncertainty. Being not to require suitable mathematical model for controlling is the advantage of fuzzy control systems.

In the course of time, fuzzy logic which is the basic foundation of fuzzy logic based control is accepted as being closer to human mentality and linguistic variables than classical logic [3].

Fuzzy logic has an easy compatible structure with most of the applications in the industry. Adding to this, it does not necessitate control parameters to be definite. Moreover, it enables applications to be performed faster.

The rules of fuzzy logic are prepared by the specialists in the subject. To form the rules, step response, failure signal and its derivative of the system are used [4]. Traditional control techniques do not yield beneficent results in complicated and nonlinear systems such as power systems and this brings the use of fuzzy logic controller into the foreground [5]. Thanks to these controllers, complex cases such as varied load alteration and load – frequency control can be resolved quite easily. Fuzzy logic controller is more convenient for the solution of wide ranged control problems in systems whose reliability is important, because traditional controllers are slower and less efficient in nonlinear applications [6-8].

Although a lot of advanced control theories and techniques have been designed in recent years, PID controllers have been continuing to be frequently used in industrial applications [9]. To improve the performances of power systems (rise time, time-out, etc.), the use of fuzzy logic controllers to set the PID gains is approved within the experiences of specialists. Fuzzy – PID controller have been analyzed and developed in recent years and satisfactory performances at various control phases have been presented. Fuzzy membership functions which are used for load – frequency control of three area power generation system are shown in Figure 4. K_p and K_i rule table of fuzzy logic controller is shown in Table 2.

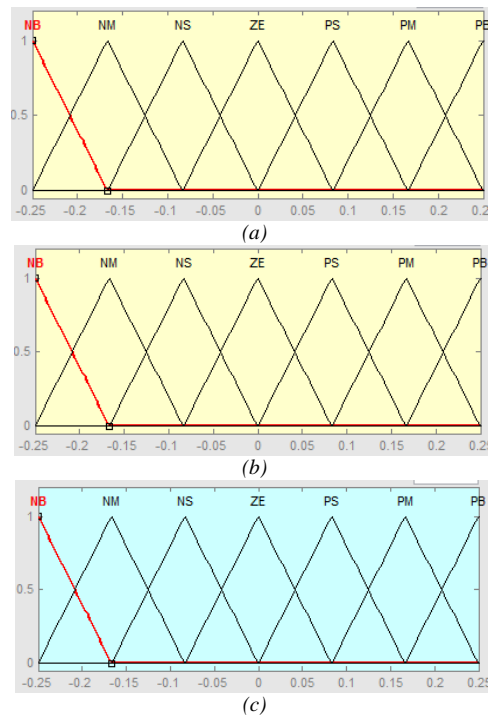


Figure 4. Membership functions of (a) failure, (b) failure derivative and (c) output for a three area power generation system.

The table consisted of 7 x 7, total 49 rules, of Fuzzy – PID controller which is designed for three area power generation system is shown in Table 2.

Table 2. Fuzzy rule table for load- frequency control

		e						
		NB	NM	NS	ZE	PS	PM	PB
de	NB	NB	NB	NM	NB	NM	NS	ZE
	NM	NB	NB	NB	NM	NS	ZE	PM
	NS	NB	NB	NM	NS	ZE	PS	PM
	ZE	NB	NM	NS	ZE	PS	PM	PB
	PS	NM	NS	ZE	PS	PM	PB	PB
	PM	NS	ZE	PS	PM	PB	PB	PB
	PB	ZE	PM	PM	PB	PB	PB	PB

Simulation block diagram of load – frequency control of a three area power generation system by using fuzzy – PID controller is shown in Figure 5.

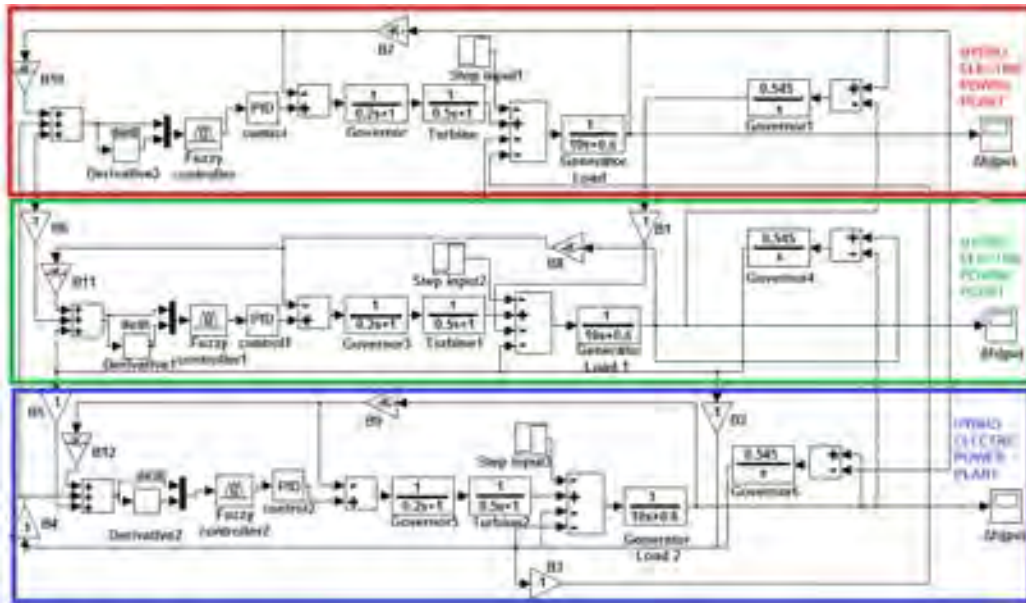


Figure 5. Simulation block diagram of load – frequency control of a three area power generation system by using Fuzzy – PID controller

As a result of all the components generated from the formed fuzzy membership functions, rule tables and control surfaces, a Fuzzy- PID simulation is created as in Figure 5.

3. RESULTS OF SIMULATION AND DISCUSSION

In this study, PID, fuzzy logic and fuzzy – PID controllers are used for load – frequency control of three area power generation system. As it is deduced from the simulation results shown in Figures 6, 7, and 8 below, when compared to traditional control methods used in power systems, it is clearly understood that dynamic impact responses of PID, fuzzy logic and fuzzy – PID controllers are more efficient.

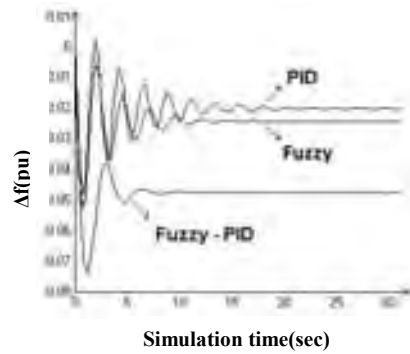


Figure 6. Load frequency control at 0.01 p.u. loading status

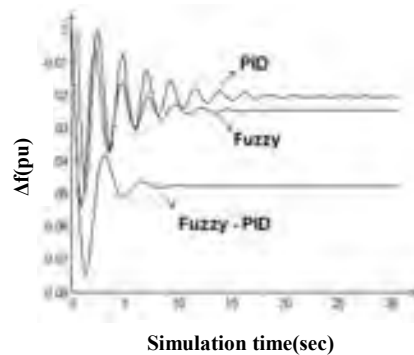


Figure 7. Load frequency control at 0.05 p.u. loading status

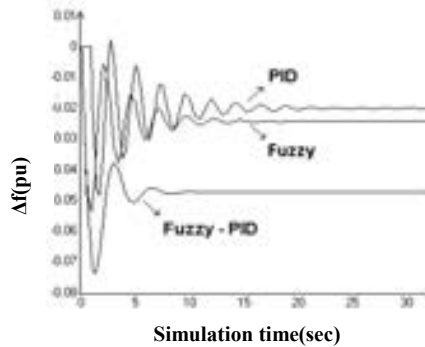


Figure 8. load frequency control at 0.09 p.u. loading status

In this study, all hydroelectric power plants are accepted as identical. All the parameters are applicable for all areas. PID controller gain factors are K_P : 5, K_I : 1.5, K_D : 2.7 and R: 2.43, B: 9.059, M: 10.0, D: 0.60.

As it is understood from the simulation results above, it is deduced that the application of Fuzzy – PID controllers in power systems is more effective. As it is seen in Figures 6, 7, 8, the results of Fuzzy – PID controller is apparently effective.

4. CONCLUSION

These controllers which have been preferred in industrial applications recently provide apparently easy, fast and efficient control process compared to traditional control systems. In addition to provide a better dynamic

performance, the use of Fuzzy logic – PID controller also reduces frequency oscillations in a considerable extent. In this study, all the drawbacks of PID and Fuzzy Logic controllers are removed by using Fuzzy logic – PID controllers which provides a better dynamic response. We can conclude that carrying out the load – frequency control of a power generation system by using fuzzy logic – PID controller with a better dynamic response is a more efficient and operative control method.

REFERENCES

- [1]. Bergen, R., Vittal, V., "Power System Analysis 2th ed.", Prantice Hall, USA, 375-400 (2000).
 - [2]. Elgerd, O.I., Fosha, C.E., "Optimum megawatt frequency control of multi – area electric energy systems", IEEE Transactions on Power Apparatus and Systems, 89(4):556-563 (1970).
 - [3]. Wang, Li-Xin, A Course in Fuzzy Systems and Control, Prentice Hall, 1997
 - [4]. S. Tesnjak, S. Mikus, O. Kuljaca, Load-frequency fuzzy control in power systems, Proceedings of the 5th SONT, Simpozij o Novim Tehnologijima, pp. 136-139, Poree, 1995.
 - [5]. T., Tilli, Automatisierung mit Fuzzy-Logic, Franzis-Verlag, München, 1992.
 - [6]. E. Cam ve I. Kocaarslan, " Load frequency control in two area power system using fuzzy logic controller ", Energy Conversion and Management, Vol. 46, No. 2, pp. 233-243, 2005.
 - [7]. C. C. Lee, " Fuzzy Logic in Control Systems: Fuzzy Logic Controller – Part I ", IEEE Transactions on Systems, Man. And Cybernetics, Vol. 20, No. 2, pp. 404-418, 1990.
 - [8]. C. C. Lee, " Fuzzy Logic in Control Systems: Fuzzy Logic Controller – Part II ", IEEE Transactions on Systems, Man. And Cybernetics, Vol. 20, No. 2, pp. 419-435, 1990.
 - [9]. G. Chen, Conventional and fuzzy PID controllers: an overview, Intelligent Control & System 1 (1996) 235–246.
 - [10]. George-Gross, Lee J.W. 2001. Analysis of Load Frequency Control Performance Assessment Criteria, IEEE transaction on Power System, Vol. 16, No. 16, pp. 520-525.
 - [11]. Kothari D. P., Nagrath I.J., 2003. Modern Power System Analysis, Tata Mc Gro Hill, Third Edition.
 - [12]. Kundur P, 1994. Power System Stability and Control, Mc Graw hill New York.
 - [13]. Wadhawa C.L., 2007. Electric Power System. New Age International Pub.
 - [14]. Elgerd O. I. 1971. Electric Energy System Theory; An Introduction, Mc Gro Hill.
 - [15]. Ross T.J. 1995. Fuzzy logic with engineering application. Mc Gro Hill, International Edition.
 - [16]. Yen J., Langari R., Zadeh L., "Industrial Applications Of Fuzzy Logic And Intelligent Systems", IEEE Press, New York, 1995
 - [17]. Chen G., Pham T.T., "Introduction To Fuzzy Sets, Fuzzy Logic, and Fuzzy Control Systems", CRC Press, Florida, 2000
-

SALT BATH NITRIDING OF FE72AL28 INTERMETALLIC ALLOY

İbrahim ÇELIKYÜREK

Eskişehir Osmangazi University, Department of Metallurgical and Materials Engineering, 26480, Eskişehir, Turkey.
cibrahim@ogu.edu.tr

Abstract

The iron aluminide Fe₇₂Al₂₈ was produced in a vacuum arc melting furnace. The alloys were nitrided by salt bath nitriding process at 580°C for durations of 3 and 6 hours. The nitride layers were characterized with light optical microscopy, scanning electron microscopy equipped with energy dispersive X-ray spectroscopy, X-ray diffraction, and micro hardness measurements. The results showed that the nitride layer thickness increased with an increase in nitriding duration, while the layer hardness did not vary. The nitride layers were composed chiefly of iron nitride and aluminum nitride phases, and also include some carbide phase.

Keywords: *Intermetallics compound based on Fe₃Al, Nitriding, Scanning electron microscopy, X-ray diffraction, hardness.*

1. INTRODUCTION

Iron aluminides based on the Fe_3Al compounds have a potential to use in applications where high temperature oxidation and sulfidation occur. Research efforts have been focused on process, development and enhancement of room temperature ductility together with the characterization of physical properties such as mechanical properties, oxidation and corrosion [1-4].

One of the most important material properties is friction and wear. Considerable amount of economic losses occur due to the wear in the mechanical parts. In order to reduce these losses, the properties of materials and/or the surface properties of materials should be improved. There are several surface modification methods to improve the surface friction properties and wear resistance. One of them is nitriding which can be performed to a variety of steels [5-13]. Iron and some other alloying elements like chromium, aluminum, and so on can form a hard nitride layer which increase the surface hardness and friction properties and wear resistance. Iron aluminides can be thought as a class of high alloy steels. Either iron or aluminum can form some nitride phases with merging nitrogen. Both iron and aluminum nitrides have high hardness, and therefore can modify the surface. This will be resulted in better friction properties and higher wear resistance.

There are only a limited works has been published about surface modification of iron aluminides. Recently, the boronizing was performed to the iron aluminides based on Fe_3Al [14] and FeAl [15]. But, there is no work has been published on the carburizing and nitriding which are the most common surface hardening methods. In this study, the salt bath nitriding process was performed to iron aluminide $\text{Fe}_{72}\text{Al}_{28}$, and the nitride layer was characterized.

2. EXPERIMENTAL

The iron aluminide $\text{Fe}_{72}\text{Al}_{28}$ alloy was fabricated in a vacuum arc melting furnace under pure Ar atmosphere. To prevent oxidation furnace was evacuated to $5 \cdot 10^{-2}$ millibar then filled with pure Ar. The alloy was melted in a copper crucible cooled with water and casted in a steel mould. The castings were machined to cylindrical form in diameter of 8mm and 10mm in length. The flat surfaces of the samples were grinded and polished with $1\mu\text{m}$ diamond paste. The samples were nitrided in a salt bath at 580°C for 3 and 6 hours.

The cross sections of samples were grinded up to 1000 mesh paper and polished with $1\mu\text{m}$ diamond paste. The nitride layer formed on the surface was identified using LOM and SEM equipped with EDXS. The nitride layer thicknesses were measured. The nitride layers were characterized using line-scan analysis. The hardness deviations were determined with measuring the micro hardness from surface up to the matrix. The phase distributions of the samples were determined by XRD analysis directly on the flat surface of the specimens using copper X-ray radiation.

3. RESULT AND DISCUSSION

The light optical micrographs of the nitrided samples are shown in fig. 1. The cross-sectional micrographs showed that the nitride layer formed on the surface had a smooth morphology, but not a tooth-like morphology as in the boronizing of iron aluminides [14,15]. The layer thickness was increased with increasing nitriding duration. The layers had thicknesses of 13 and $17\mu\text{m}$ for 3 and 6h nitriding treatment respectively.

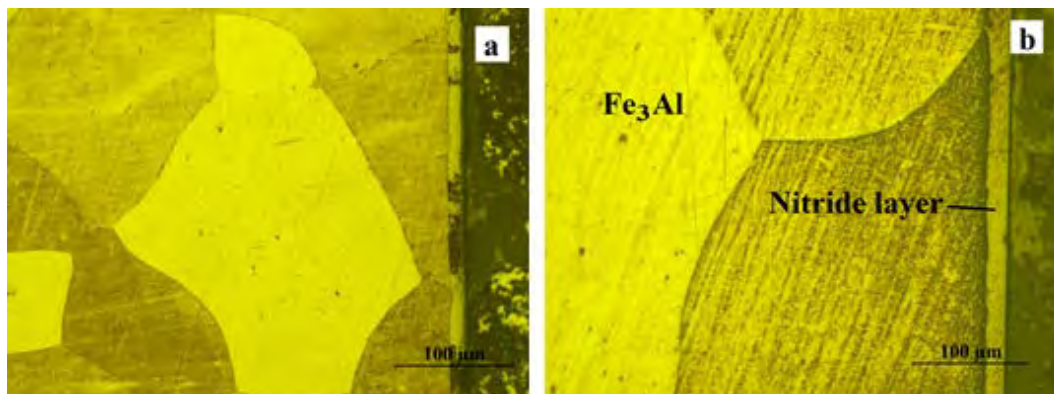


Figure 1. The cross-section optical micrographs of nitride layer, a) 3h and b) 6h treated samples.

The SEM micrographs, composition, and line-scan analysis of the nitride layers are given in Fig. 2. SEM-EDXS studies showed that the nitride layers contain aluminum, iron, nitrogen, and carbon atoms for all treated samples. While amounts of aluminum atom in the nitride layer are close to the matrix, amounts of iron

atom are lower than the matrix. In addition, according to line-scan analysis (fig. 2) the distribution of nitrogen in the layer is stable. While the amounts of Al and Fe in the nitride layer were increasing with increase in nitriding duration, C and N were decreased. It was seen that the compositional gradients of aluminum, iron and nitrogen atoms are almost same for all treated samples.

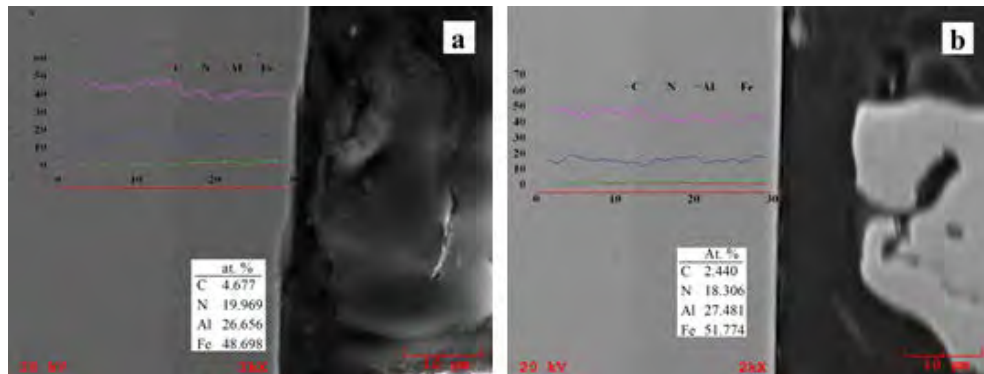


Figure 2. The SEM micrographs and line-scan analysis of the nitride layers, a) 3h and b)6h treated samples.

Neither in optical microscopy nor SEM investigations was it not observed if there is a diffusion zone between the nitride layer and the matrix Fe_3Al . These findings were confirmed by micro hardness measurements (Fig 3) of nitride layers.

The micro hardness gradients from surface to matrix are given in Fig. 3. The hardness of the nitride layers for all treated samples were almost same and had a value of about 1200 $HV_{0.05}$. The hardness of Fe_3Al was approximately 300 $HV_{0.05}$. It is obvious from the figure that the hardness's do not vary throughout the nitride layer and decrease sharply at the end of the nitride layer for all treated samples. The hardness of nitride layer did not vary with increasing nitriding duration.

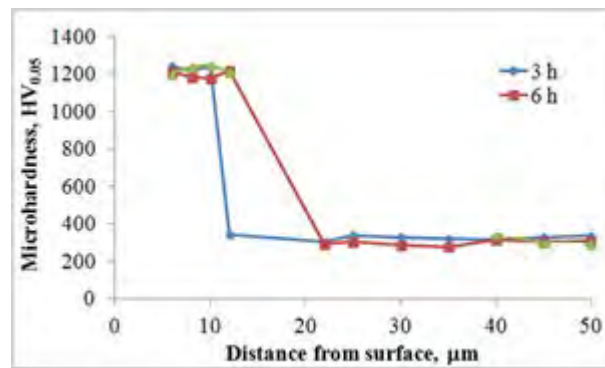


Figure 3. The micro hardness deviations of nitrided samples.

Fig. 4 shows the XRD patterns taken directly from flat surface of the nitrided samples. It can be seen from the XRD results that the layers mainly composed of AlN and Fe_3N , and also contain some $Fe_3AlC_{0.5}$ and $FeN_{0.33}$ or Fe_2N phases.

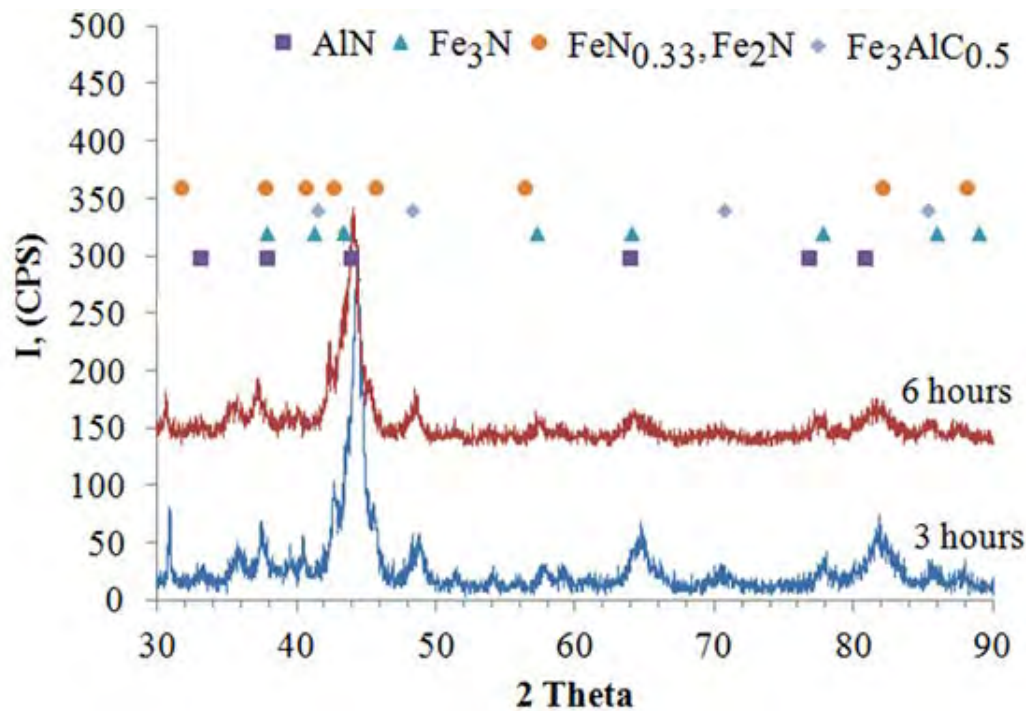


Figure 4. X-ray diffraction patterns of the samples nitrided for 3h, 6h, and 9h.

4. CONCLUSION

The iron aluminide $Fe_{72}Al_{28}$ was nitrided by salt bath nitriding process at $580^{\circ}C$ for 3, 6, and 9 hours. The nitride layer thickness increased with increasing nitriding duration. The layers were mainly composed of Fe_3N and AlN nitrides, and also included some $Fe_3AlC_{0.5}$ carbide. The nitride layers had hardness of about $1200\text{ HV}_{0.05}$ and did not vary throughout the layer while the matrix Fe_3Al had only $300\text{HV}_{0.05}$. The nitriding duration did not affect the layer hardness clearly.

REFERENCES

- [1]. Kim, Y. S., Kim, Y. H., Sliding wear behavior of Fe_3Al based alloys. *Material Science and Engineering A*, 258 (1998), 319-324.
- [2]. Chan, R. W., Proceedings of Materials Week '96 on Nickel and Iron Aluminides: Processing, Properties, and Applications, Ohio, 7-9 October 1996, edited by S.C. Deevi, V.K. Sikka, P.J. Maziasz and R. W. Chan, USA, ASM international, 1997, p.3
- [3]. Liu, C.T., Kumar K.S., Ordered Intermetallic Alloys, Part I: Nickel and Iron Aluminides, *Journal of Materials Science*, May (1993) 38-44.
- [4]. Guan X., Iwasaki, K., Kishi, K., Yamamoto, M., Tanaka, R., Dry Sliding wear of $Fe-28Al$ and $Fe-28Al-10Ti$ alloys. *Material Science and Engineering A*, 366 (2004) 127-134.
- [5]. Basu, A., Dutta Majumdar, J., Alphonsa, J., Mukherjee, S., Manna, I., Corrosion resistance improvement of high carbon low alloy steel by plasma nitriding. *Materials Letters*, 62 (2008) 3117-3120.
- [6]. Yun-tao, X., Dao-xin, L., Dong, H., Improvement of erosion and erosion-corrosion resistance of AISI420 stainless steel by low temperature plasma nitriding. *Applied Surface Science*, 254 (2008) 5953-5958.
- [7]. Skolek-Stefaniszyn, E., Kaminski, J., Sobczak, J., Wierzchon, T., Modifying the properties of AISI 316L steel by glow discharge assisted low-temperature nitriding and oxynitriding. *Vacuum*, 85 (2010) 164-169.
- [8]. Yildiz Sirin, S., Sirin, K., Kulac, E., Effect of the ion nitriding surface hardening process on fatigue behavior of AISI 4340 steel. *Materials Characterization*, 59 (2008) 351-358.
- [9]. Munoz Riofano, R.M., Casteletti, L.C., Canale, C.F., Totten, G.E., Improved wear resistance of P/M tool steel alloy with different vanadium contents after ion nitriding. *Wear*, 265 (2008) 57-64
- [10]. Wang, J., Xiong, J., Peng, Q., Fan, H., Wang, Y., Li, G., Shen, B., Effects of DC plasma nitriding parameters on microstructure and properties of 304L stainless steel. *Materials Characterization*, 60 (2009) 197-203.
- [11]. Castro, G., Fernandez-Vicente, A., Cid, J., Influence of the nitriding time in the wear behaviour of an AISI H13 steel during a crankshaft forging process. *Wear*, 263 (2007) 1375-1385.
- [12]. Terres, M.A., Ben Mohamed, S., Sidhom, H., Influence of ion nitriding on fatigue strength of low-alloy (42CrMo4) steel: Experimental characterization and predictive approach. *International journal of Fatigue*, 32 (2010) 1795-1804.

- [13]. Wen, D. C., Microstructure and corrosion resistance of the layers formed on the surface of precipitation hardenable plastic mold steel by plasma-nitriding. *Applied Surface Science*, 256 (2009) 797–804.
 - [14]. Celikyurek, I., Baksan, B., Torun, O., Gurler, R., Boronizing of iron aluminide Fe72Al28. *Intermetallics*, 14 (2006) 136-141.
 - [15]. Ekmek iler, E., Polat, A., Usta, M., Hard boride coating on iron aluminide (FeAl). *Surface and Coatings Technology*, 202 (2008) 6011-6015.
-

THE RESEARCH OF THE ECONOMIC IMPACT OF GRANITE DUST REMAINS USAGE IN AUTO BRAKE PADS

Halil KILIÇ

Kırklareli Uni. Technical Sciences MYO, Machine Program, Kırklareli, halil.kilic@klu.edu.tr

Mustafa TİMUR

Afyon Kocatepe Uni. Technology Fac. Automotive Engineering, Afyon, ibrahimmutlu@aku.edu.tr

İbrahim MUTLU

Kırklareli Uni. Technology Fac. Mechatronics Engineering, Kırklareli, mustafatimur@klu.edu.tr

Sinan SAVAŞ

University of Leicester Mechanical Engineering, Leicester, ss592@le.ac.uk

Abstract

The pads used in auto brakes are made of the composition of a large number of materials. What is expected from a pad is that it provides the minimum friction and corrosion values, does not give damage to environment, and does contribute to country economy. In the study carried out for this purpose, from the materials composing brake pad component was produced brake pad involving granite dust instead of barite. The granite dust, which is the smallest size granite waste, is the waste which occurs during the cutting of blocks and plates in marble workshops and whose size is below 250 μm . The 30% of the processes granite are thrown away as dust and particles. In the cutting process, it is carried to sediment tanks accompanied by water and the granite dust subsiding in the pools is then taken into dumpsites. The majority of this amount is left as waste and cause environmental problems.

Following a series of milling-screening process for this purpose, auto brake pad added by granite dust with new formulation was manufactured using some additive agents. In order to determine the usability of the produced pads, braking performance was examined in brake test device. In the light of the results, considerable results were obtained both in the utilization of waste materials and in decreasing the cost of production.

Keywords: Barite, Brake Pad, Granite Dust and Friction.

1. Introduction

Most substance used as a waste consists of recyclable materials. In recent years, Existence of alternative use areas has started to gain important in Turkey. To use industrial waste in different areas helps to solve some environmental problems caused by this waste in some extent.

Reprocessing and reproduction of marble industry waste is exposed to % 60 feedstock [1]. Once granite and marble blocks are machined %30-dust waste is been comprised. Production results in Marble Factory comprise two type waste including part and dust. During production, dust wastes comprise mud together with water. Water and dust parts are been separated from each other by sending this mud to plants. Later, dust particles are been transported by pressing to waste storage areas [2].

Although marble and granite dust waste used in many sectors, the added the low proportion amount have caused large masses in waste areas. It is been understood that vast majority of dust and particle waste is not been recycled. Research and development activities plays important role in recycling of marble waste [3].

Main aim of this study is to evaluate the usage of marble and granite dust produced from marble machining. Fort his purpose, marble waste is been grinded to produce marble dust and it is used as additive in brake pads. Various additives are made new formula of additive.

2. Experimental

2.1. Production stages of Brake pads

Mass rate is been used to identify material rates while different experimental samples that contain different contents. Contents of brake pads including friction materials, binding and other additive materials is been weighted 0,001gr precision. After that, the mixture is been mixed to obtain homogeneity. Finally, the samples are been pressed in suitable dimensions to get ready for production. The stages of the production of brake pads are shown in Figure 1.



Figure 1. Production stages of brake pads

After production, friction coefficient and time plots of experimental samples are been produced.

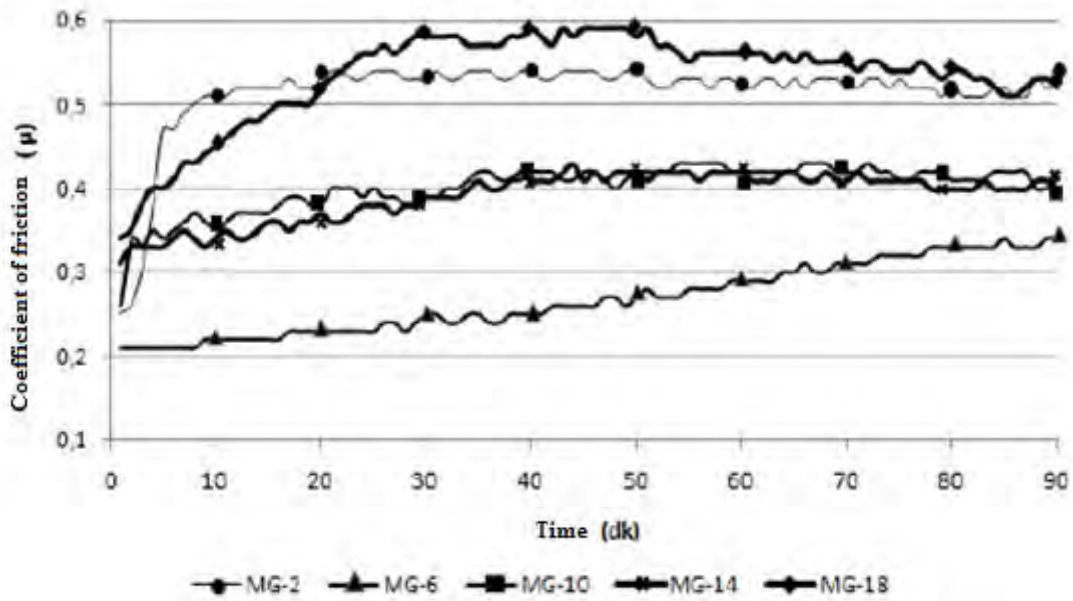


Figure 2. Friction coefficient and time plots of experimental samples that has marble and granite additive under 1,05 Mpa

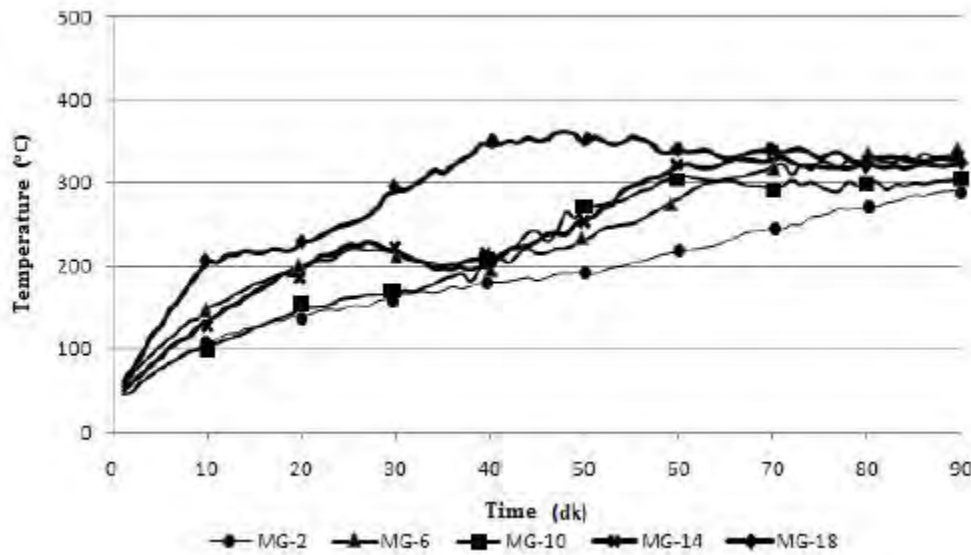


Figure 3. Temperature and time plots of experimental samples that has marble and granite additive under 1,05 Mpa

Citation: Kılıç, H., Investigation of usability of marble waste In automotive brake pads manufacturing, M.Sc.Thesis, Afyon Kocatepe University, Graduate School of Natural and Applied Sciences (2010).

While there is a rise in friction coefficient of sample coded MG-2, after 1200 second there is a decline in friction coefficient together with the increase in temperature (Figure 2 and Figure 3). The sample

coded MG-2 has optimum and stable friction coefficient together with temperature rise. At the beginning of the experiment, there is a wavy decline in the friction coefficient of the sample coded MG-18. There might be incompatibility in the components of the sample coded MG-18 since it contains 18% granite dust and 39% marble dust.

One important desired feature of brake pads is to have minimum friction coefficient change together with temperature rise while breaking. As it can be seen in Figure 3, the sample coded MG-6 has lowest friction coefficient. The sample coded MG-18 has highest friction coefficient and has similarities with the sample coded MG-14. After 1800 second, all samples have stable friction tendency [4].

2.2. The Contribution of Granite Dust Usage to Economy

Granite is the light colored magmatic rocks that include quartz, feldspar, mica and minerals in its composition. Granite is in the group of tough rocks, and its toughness is accepted as 6,5 mohs. Granite is a material that is durable against corrosion, press, strike, and resistant to atmosphere effects and dissolution. Granite dust is the tiniest granite waste. They are the granite particles that come into existence in the marble processing factories during the cutting of blocks and plates and most of which is under 250 μm . Although the particle size distributions of the dust wastes do not fit properly to the ideal calcite particle size to be used in the manufacture of pad filling material, it seems possible to obtain proper size material following the screening-grinding process [5, 6, 7].

One of the most important problems for marble cutters is the emergence of tiny marble dust wastes occurring out of the mouth of the saws that do the cutting process of the machines during the cutting of granite [8]. The knife thickness of the saws is about 5mm; blocks are normally cut as 20 mm plates. Thus, 5mm of it turns into dust in every 25 mm thickness according to the cut surface area of the marble or granite block. Therefore, approximately 20% of the processed granite weight comes out as waste [9].

In the manufacture of each pad, barite is used at the rates of 10-40% as a filling material. Considering that 20% barite is used on average in the production of each pad, 1500 ton/year is used for pad production. The price of barite changes between 60-90 ton/\$ depending on the thinness of the barite. Again, if 75 ton/\$ is taken as the average figure, and 2,7 TL/\$ currency value is taken, the cost of barite is 202,5 ton/TL. As 1400 ton/year barite is used in the brake pad production with a roughly made accounting, $1400 \text{ (ton barite)} \times 202,5 \text{ (ton/TL)} = 283500 \text{ TL}$ is used in total for brake pad production. As an alternative to barite, if granite dust is used, it is assumed that it will be made considerable contribution to the country's economy.

3. CONCLUSION

In this study, a research is conducted about investigation of applicability of granite dust in the brake pads as additive instead of using barite and new brake pad produced by granite dust as additive. In the experiment results for the samples that are made granite dust additive, average friction coefficient is in the acceptable range based on Turkish Standard TS 555.

The production of granite is 300,000 tone/year and waste range of granite 325%. If these factors are taken into consideration, it is noted that there is a great amount of raw material for reuse. In this field, there are many research and development opportunities for granite waste and recycling of them. A detailed comparison between the cost of barite and the cost of drying, cleaning and grinding of granite dust needs to be conducted. It can be possible to use granite as an additive material instead of barite. If the economic analysis of granite more advantageous than barite.

References

1. Gurer C., Akbulut H., Kurklu G. (2004). *Construction Industry Recycling and Reassessment of a different structure as a Source of Raw Materials.. 5. Symposium on Industrial Raw Materials. 28-36, İzmir.*
2. Onur S. (2012). *Evaluation of waste derived from marble and natural stone Business. Standard, 606, 70-74 (Ankara).*
3. Demir İ, Başpınar M. S., Abadan S., Kahraman E., Ünal O. (2014). *Investigation of the availability of marble dust as recycling material in the production of aerated concrete.*
4. Kato, K. (1990), *Tribology of Ceramics, Wear. 136:117-133.*
5. Önenç, D. İ., (1998). *Sedimenter The geological formations in rock marble block to prevent the reception Products. MTA Natural Resources and Economic Bulletin. No:1-2, 61- 63 (Ankara).*
6. Kun, N.,(2000). *Marble Geology and Technology. Marble union. 149 (İzmir)*
7. Ceylan H., Saraç, S., Özkahraman T., (2001). *To investigate the usefulness of the filler the production of marble dust waste. Turkey 3 marble symposium. Congress book, 297- 307.*
8. Kılıç, H. (2010). *Investigation of usability of marble waste In automotive brake pads manufacturing, M.Sc.Thesis, Afyon Kocatepe University, Graduate School of Natural and Applied Sciences (Afyonkarahisar).*
9. Vijayalakshmi, V., Singh, S., Bhatnagar, D. (2001). *Marble Slurry: A New Resource Material For Entrepreneurs. Science Tech Entrepreneur Project, 9, (India).*
10. Gemalmayan, N. (1984). *Experimental investigation of the properties of friction materials. PhD Thesis, Gazi Üniversty Faculty of Engineering and Architecture (Ankara)*
11. Mutlu, İ. (2002). *Production of ceramic additive automotive brake lining and investigation of its braking characterization. PhD Thesis, Sakarya University Graduate School of Natural and Applied Sciences (Sakarya).*
12. Yıldız, Ö., Eskikaya, Ş. (1995). *Evaluation of Afyon marble dust Waste. I. Turkey Marble Symposium Proceedings, 45-52.*

OPTIMIZATION OF SURFACE ROUGHNESS IN WIRE-CUT EDM OF AA6061/B4CP USING RESPONSE SURFACE METHOD

Şener KARABULUT

Department of mechanical program, Hacettepe University, 06935, Ankara/
TURKEY, senerkarabulut@hacettepe.edu.tr

Halil KARAKOÇ

Department of mechanical program, Hacettepe University, 06935, Ankara/
TURKEY

Ömür Kaya KALKAN

Department of mechanical program, Hacettepe University, 06935, Ankara/
TURKEY

Ramazan ÇITAK

Department of mechanical program, Hacettepe University, 06935, Ankara/
TURKEY

Abstract

In the present paper, the influences of cutting parameters on surface roughness in wire electric discharge machining of (WEDM) process of particle- reinforced aluminium AA6061 alloy composite were investigated. The composites were produced using 15% weight fraction of 15 wt.% B4C using powder metallurgy. Experimental trials were performed based on Taguchi L18 (21 x 32) with a mixed orthogonal array and WEDM cutting parameters were optimized for the best surface quality. The investigation results were evaluated by response surface plots and main effect graphs. The machined surface of the metal matrix composite was investigated using scanning electron microscopy (SEM) micrographs. The effect of WEDM machining variables were determined by using analysis of variance (ANOVA). The analysis result showed that the most significant cutting parameter was peak current (IP) for surface roughness. The SEM and optical micrographs were indicated that the reinforced B4C particles were homogeneously distributed in the matrix structure. Mathematical models have also been generated for the surface roughness using regression analysis. Confirmation tests were carried out to determine the prediction performance of the mathematical models and the surface roughness was predicted with an acceptable mean squared error.

Key words: Wire electric discharge machining, Surface roughness, Taguchi method, Response surface methodology

1. INTRODUCTION

Metal matrix composites (MMCs) have been widely investigated in recent years and are now utilized in many engineering fields including aerospace, military, automotive industries, electronic packaging and sporting goods because of their low density in combination with their excellent wear resistance, high specific strength, hardness, and fracture toughness [1–6]. However, machinability of MMCs is considered difficult in connection with hard reinforcement elements in matrix structure [1–7]. Boron carbide (B4C) is extremely hard reinforcement materials with the superior properties such as good wear resistance, high hardness, low specific weight, corrosion resistance, high melting point, adequate resistance to chemical agents and good mechanical properties. These outstanding performances of B4C is made it a preferable reinforced material and widely used in numerous industrial applications requiring high resistance such as in the nuclear industry, for tank armour, and ballistic protections. Hence, several researchers have studied the production and machinability properties of MMCs reinforced with B4C in recent years [8,9]. However, there are two main problem hindering the superior properties of B4C, one is required the very high temperature for its sintering and the other is the low fracture toughness [10]. Wire electrical discharge machining (WEDM) is a high precision machining method widely used for hard materials, metallic alloys and graphite that would be very difficult to cut with traditional machine tools using the best economic cutting tools. In wire-cutting technique, a thin single-strand metal wire is machined the workpiece with submerged in a tank of deionized water by the use of heat from electrical sparks. WEDM uses a nonstop cutting wire electrode to machine the desired shape alongside the cutting path using 0.05–0.30 mm in diameter thin copper, brass or tungsten wire and can machine very small corner radius with high precision [11]. Motorcu et al. studied the influences of cutting parameters on the surface roughness and material removal rate (MRR) in cutting of Al/B4C/Gr hybrid composites using WEDM depend on the wire speed, pulse-on time and pulse-off time. They observed that the most significant parameter on surface roughness and MRR was the wire speed with a 85.94% contribution rate [12]. Yan et al. investigated the effects of machining process on surface roughness (Ra), cutting width, material removal rate and wire breakage behavior in the WEDM of Al6061 with different reinforcement ratios Al₂O₃p composites. The test result showed that the Al₂O₃ reinforcement volume fraction has effective parameters on the Ra, kerf and MMR. They also reported that a high wire speed, very low wire tension and high flushing rate must be chosen to prevent wire breakage [13]. Shandilya et al. studied the effect of the input parameters on average cutting speed during WEDM of Al6061/SiC metal matrix composite. Servo voltage was the more significant input parameter on average cutting speed than pulse-off time and wire feed rate [14]. The surface roughness and material removal rate were increased with increase in pulse-on time and decreased with increase in pulse-off time. MRR was influenced interactions between pulse-on time (Ton) and pulse-off time (Toff), pulse-on time (Ton) and peak current (IP), pulse-off time (Toff) and peak current (IP). Pulse-on time (Ton) and peak current (IP) were affected the machined surface roughness [15]. Satish kumar et al. investigated the effects of different machining parameters on MRR and Ra in the WEDM of Al6063/SiC MMC at different reinforcement ratios. The researchers reported that surface quality and MRR were decreased with the increasing percentage volume fractions of SiC particles [16]. Surface roughness and gap width were mainly affected the pulse-on time in the WEDM of Al 6061 reinforced with Al₂O₃ particle MMC [17]. Pulse-on time and current were the most effective parameters for machining speed and surface quality in the WEDM of Al-SiC metal matrix composite [18].

2. EXPERIMENTAL MATERIALS AND METHOD

The experimental workpieces were produced from high-purity aluminum 6061 mixed with 15% commercial-grade B4C powders using powder metallurgy method. The median size of Aluminum 6061 powder used in metal matrix composite (MMC) was 100µm and B4C powders had average size of 10µm. Aluminum alloy and B4C powders were mixed to achieve homogeneity for 45 min in a three-dimensional Turbula mixer. The mixed powders were compacted by cold pressing under 300 MPa. The specimens were sintered in a vacuum furnace at 550 oC temperature for 60 minutes and they were extruded using a pre-heated extrusion mold of temperature 500 oC for 1 hour. The thickness of produced composite sheets was 12.7 mm. Workpiece materials were analyzed using scanning electron microscopy (SEM) and energy dispersive spectroscopy (EDS). The optical micrographs of the surface texture of the machined composite and B4C reinforcement elements can be seen in Figure 1. As shown in Figure 1, B4C particles are homogeneously distributed into the matrix structure. The chemical compositions of Al6061 alloy are presented in Table 1.

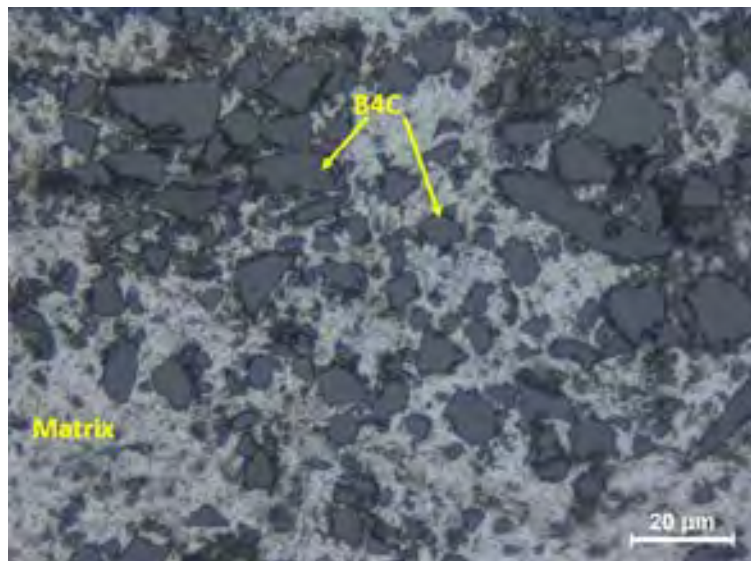


Figure 1. Microstructure of Al6061/B₄C

Table 1. Chemical composition of Al 6061 alloy Elements

Element	Fe	Si	Cr	Mn	Mg	Zn	Cu	Ti	Al
AA6061	0,5	0,6-1,0	0,1	0,2-0,8	0,8-1,2	0,25	0,6-1,1	0,1	Balance



Figure 2. Experimental set-up for WEDM machining

The experiments were performed on the Mitsubishi MV1200 series CNC WEDM. Rectangular parts of size $31.7 \times 6.35 \times 12.7$ were cut from the workpiece material as shown in Figure 2. A brass wire electrode of diameter 0.30 mm was used as the cutting tool for conducting the experiments and deionized water was used as the dielectric fluid. The machined surface of the workpiece were measured using Mitutoyosurfest SJ210 device. Surface quality was measured at four different machined surface and calculated the average surface roughness value. Machining parameters and their levels used in the WEDM of MMCs are listed in Table 2.

Table 2. Machining parameters with their levels

Factor	Process parameters	Level 1	Level 2	Level 3
A	Wire tension (Wt)	10 g	13 g	
B	Spark gap voltage (SV)	30 V	60 V	80 V
C	Peak current (IP)	8 A	10 A	13 A

An easy way to comply with the symposium paper formatting requirements is to use this document as a template and simply type your text into it.

3. EXPERIMENTAL RESULTS AND DISCUSSION

The purpose of this study is to investigate the effect of wire-EDM machining parameters on the surface roughness during cutting of B4C reinforced metal matrix composite. The effects of spark gap voltage, peak current and wire tension on surface roughness using a brass electrode were investigated. The experiments were carried out based on the Taguchi L18 (21 x 32) with a mixed orthogonal array and ANOVA has been employed using statistical software Minitab 16 to determine the significant contribution of machining parameters. The experimental time and cost can be decreased by using orthogonal arrays by reducing the number of tests and minimizes the effects of parameters that cannot be controlled. Furthermore, it ensures a simple, powerful, and systematic approach to specifying the optimal machining factors during the experiments. A number of external factors not considered in the experimental design can affect the experimental results. These external factors and their effect on the results in terms of quality characteristics is named “the noise.” The signal-to-noise ratio (S/N ratio) computes the accuracy of the quality characteristic. The S/N ratio is calculated in two process. First, mean squared deviation (MSD) between the experimental results and optimal values are calculated by equation (1). Second, computed MSD results are converted by using equation (2) [19]. Then, the cutting parameters are analyzed based on the S/N. There are three different signal-to-noise ratios and individual desirability functions: larger is better, nominal is best, and smaller is better. S/N ratio indications can be selected depending on the aim of the experiments. The objective of this investigation is to minimize the surface roughness value. Therefore the-smaller-the-better has been chosen to calculate the S/N ratios by using following formulas (eq.1–eq.2).

$$MSD = (y_1^2 + y_2^2 + y_3^2 + \dots + y_n^2)/n \quad (1)$$

$$S/N = -10 \times \text{Log}_{10}(MSD) \quad (2)$$

Where y is the measured value of surface roughness and n is the number of experiments in the experiments. A higher value of S/N means the signal is much higher than the random effects of noise factors. Higher values of S/N ratios are described as control factor settings that minimized the effects of the noise factor, therefore a high signal to noise ratio is always preferred.

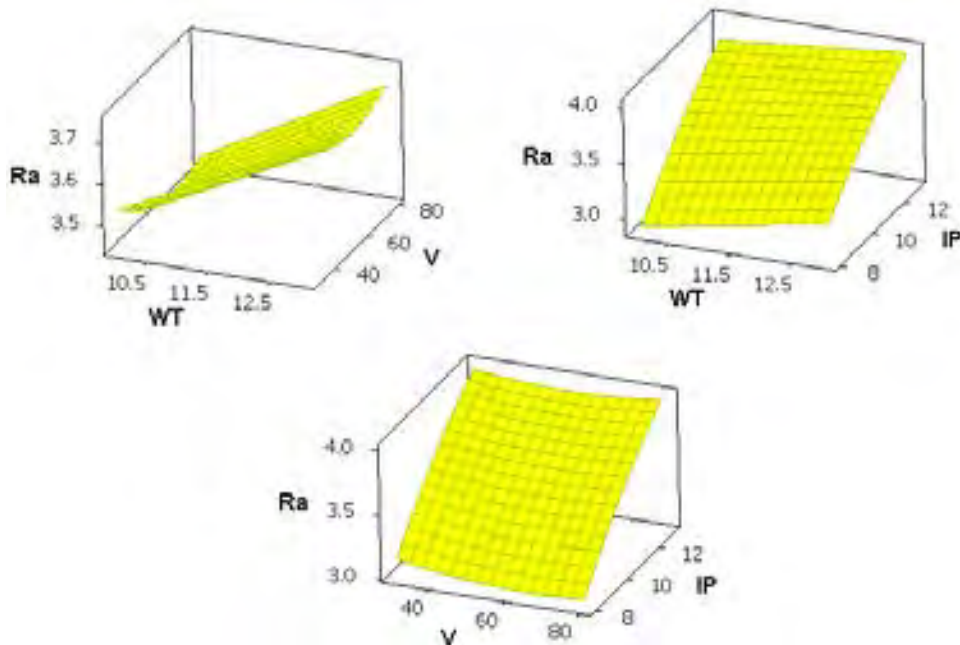


Figure 3. 3D response surface plots relationship between the WEDM parameters

The 3D response surface plots that obtained response surface method by RSM model in Minitab 16 software were utilized to specify the relationship between the WEDM parameters and surface roughness as shown in

Figure 3. Response surface method is a statistical method and used to determine the relation between various independent parameters and dependent parameters. Figure 3 indicates the influence of spark gap voltage, peak current and wire tension on the mean quality of machined surface roughness during wire-EDM of MMC. The machined surface quality was decreased with an increase in the peak current and the best surface roughness was observed at lowest peak current and wire tension. This was attributed to low cutting speed at lowest peak current. This is because of increase peak current that lead to a higher cutting speed and resulted the decreasing surface quality. Normally, increasing wire tension produces an improved surface quality of machined part due to reducing wire vibration and deflection [20]. On the contrary, surface quality was decreased with increase in wire tension in this study. This may be attributed increasing forces acting on the wire electrode and wire breakage with increase in wire tension. It was also observed that the brass wire electrode broken at higher wire tension. This can be ascribed that the harder B4C particles caused to fast wear of brass wire at higher peak current and wire tension depend on increasing cutting temperature.

One of the most significant aim of this experimental study is to determine an acceptable surface roughness using optimal machining parameters. The signal-to-noise ratios and response surface optimization methods were performed in order to specify the best cutting parameters in the WEDM of MMCs. The WEDM parameters, calculated average test results, desirability values, and the S/N ratios for surface roughness are listed in Table 3. The optimal wire-EDM parameters and their levels were determined based on the S/N ratios (Table 4). The higher S/N ratios and composite desirability values indicate the optimum machining parameters and better quality of surface roughness. The best WEDM factors based on the response table for S/N in the machining of Al6061/B4C, the optimal surface roughness values were defined as factor A (Level 1, S/N = 10.579), factor B (Level 2, S/N = 3.485), and factor C (Level 3, S/N = 3.077). In the WEDM of Al6061/B4C, the best machining parameters are determined as a peak current of 8 A, spark gap voltage of 68.89 V and wire tension of 10; the optimized surface roughness value is Ra=2.8849 μm and the desirability value is 0.97336 as shown in Figure 4.

Table 3. Experimental parameters and measured surface roughness values

Trials Number	Wire tension (Wt)	Spark gap voltage (SV)	Peak current (IP)	Surface roughness (Ra)	S/N ratio
1	10	30	8	3.06	-9.714
2	10	30	10	3.3	-10.370
3	10	30	13	4.01	-12.063
4	10	60	8	2.89	-9.218
5	10	60	10	3.43	-10.706
6	10	60	13	3.78	-11.550
7	10	80	8	2.85	-9.097
8	10	80	10	3.4	-10.630
9	10	80	13	3.92	-11.866
10	13	30	8	3.3	-10.370
11	13	30	10	3.68	-11.317
12	13	30	13	4.02	-12.085
13	13	60	8	3.21	-10.130
14	13	60	10	3.44	-10.731
15	13	60	13	4.16	-12.382
16	13	80	8	3.15	-9.966
17	13	80	10	3.78	-11.550
18	13	80	13	3.96	-11.954

Table 4. Response table for Signal to Noise Ratios (Smaller is better)

Level	Wire tension (Wt)	Spark gap voltage (SV)	Peak current (IP)
1	-10.579	-10.987	-9.749
2	-11.165	-10.786	-10.884
3		-10.844	-11.983
Delta	0.586	0.200	2.234

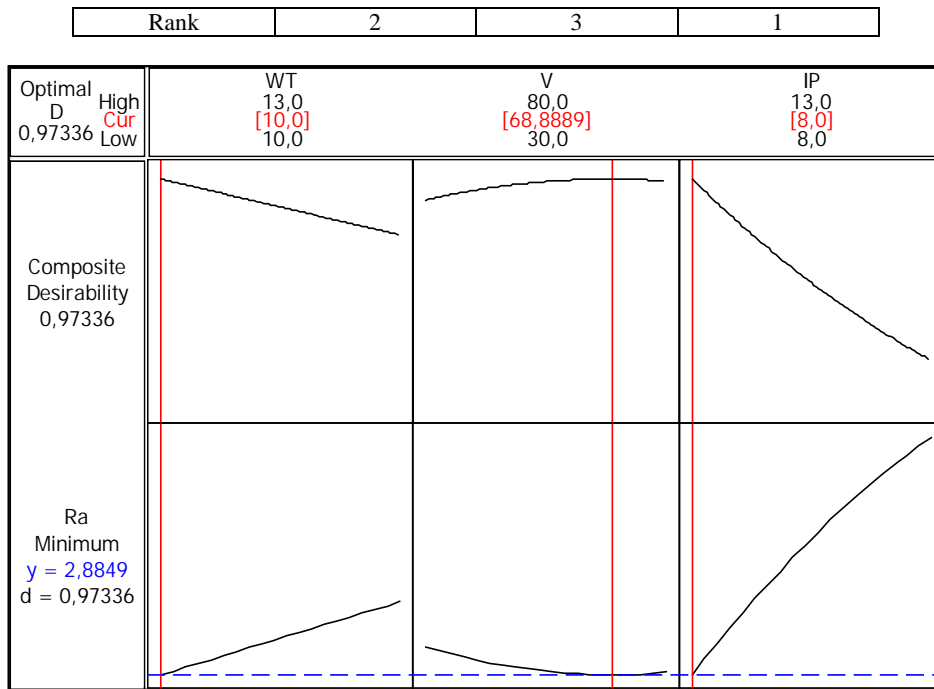


Figure 4. Optimal Wire-EDM parameters in WEDM of Al6061/B4C

The analysis of variance (ANOVA) and main effect plots were performed to investigate the influences parameters on surface roughness and contribution rate of Wire-EDM parameters on the quality of machined surface. The statistical significance levels were analyzed by the machining parameter's P and F values at the 95% confidence level. If the P values are smaller than 0.05, the experimental models are considered at a significant level of 95%. The WEDM parameters, P values, and their contribution level for surface roughness are presented in Table 5. From the result of ANOVA, the peak current is the most effective machining parameters with an 84.9% contribution of total variation on surface roughness in the WEDM of Al6061/B4C. The next effective WEDM parameter is wire tension with a percentage contribution of 8.33% for Al6061/B4C. It was observed that the spark gap voltage was not showed a meaningful effect on surface roughness in the WEDM of MMCs.

Table 5. Analysis of Variance

Source	DF	Seq SS	Adj SS	Adj MS	F	P	Significance level %
Regression	3	2.64982	2.64982	0.88327	68.562	0.000000	
WT	1	0.23576	0.23576	0.23576	18.300	0.000766	8.33%
V	1	0.01011	0.01011	0.01011	0.785	0.390594	0.35%
IP	1	2.40395	2.40395	2.40395	186.602	0.000000	84.9%
Error	14	0.18036	0.18036	0.01288			6.37%
Total	17	2.83018					

As shown in mean effect plots in Figure 5, the effect of spark gap voltage on surface roughness was almost constant. It can be seen from the mean effect plots that surface quality was decreased with increasing peak current from 8 A to 13 A and wire tension from 10 g to 13 g. At the base of the RSM and Taguchi methods, a regression analysis equation for surface roughness was also developed. The following regression equations were obtained for Al6061/B4C metal matrix composite using the least-square method in the regression analysis. R² values of the equations obtained from the regression for surface roughness were computed as 93.63%.

$$R_a = 0.869055 + 0.0762963 \times WT + 0.00115351 \times V + 0.177851 \times IP \quad (3)$$

$$R - S_q = 93.63\%$$

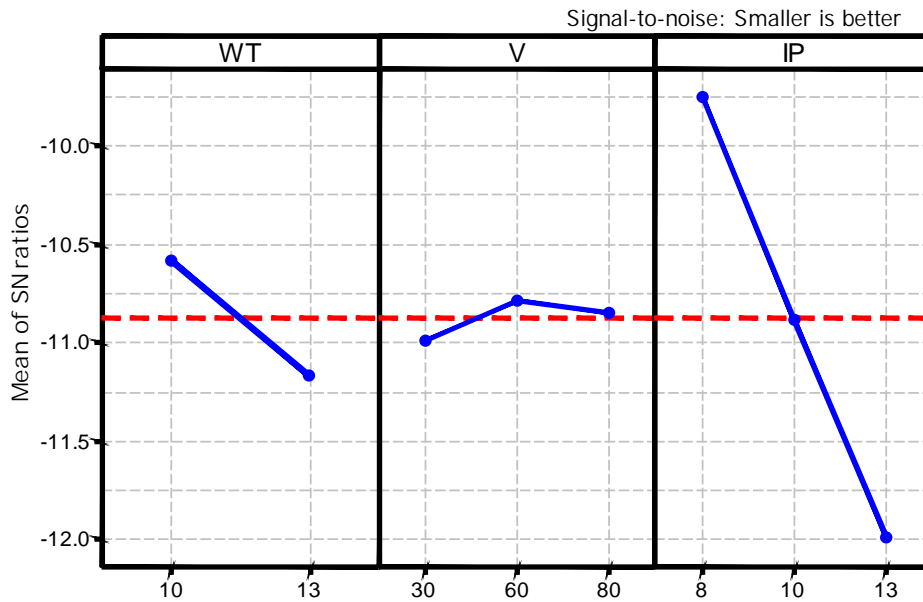


Figure 5. Effect of machining parameters on surface roughness

In order to verify the experimental process six confirmation experiments were carried out within the limits of predetermined WEDM conditions. The measured surface roughness were controlled for the precision of the predicted values calculated from models. Experimental values and predicted values with the percentage of prediction error rates are presented in Table 6. As seen in Table 6, the estimated values based on the regression model with the least residual errors are very close to the experimental results and prediction errors are in the acceptable range.

Table 6. Confirmation experiments and results

Wire tension (Wt)	Spark gap voltage (SV)	Peak current (IP)	Surface Roughness (Ra)	Predicted Surface Roughness	Prediction Error
10	8	42	3.22	3.006	6.63%
13	8	42	3.24	3.235	0.15%
13	10	42	3.51	3.591	2.31%
10	10	42	3.72	3.362	9.62%
10	13	42	4.17	3.896	6.58%
13	13	42	4.24	4.125	2.72%

4. CONCLUSIONS

In this experimental study, aluminium 6061/B4C metal matrix composite was successfully produced by a powder metallurgy method and investigated for the effect of wire-EDM parameters on surface roughness using brass wire electrode. The WEDM experiments were performed based on the Taguchi L18 orthogonal array. The investigation results were examined using 3D surface plots, S/N ratio results, ANOVA, and main effect graphs. The signal-to-noise ratios, central composite desirability of response surface method, and regression model were used to specify the ideal WEDM parameters for surface roughness. The following conclusions can be drawn from the experimental study:

- The machined surface quality was worsening with an increase in the peak current and the best surface roughness was observed at lowest peak current and wire tension. Surface quality was decreased with increase in wire tension.
- Brass wire electrode was broken at higher wire tension. It can be suggested a very low wire tension to avoid wire breakage during WEDM of MMCs with reinforced B4C.
- The optimal WEDM parameters are determined as a peak current of 8 A, spark gap voltage of 68.89 V and wire tension of 10; the optimized surface roughness value is Ra=2.8849 μm and the desirability value is 0.97336

- From the result of ANOVA, the peak current is the most significant wire-EDM parameters with an 84.9% contribution of total variation on surface roughness in the WEDM of Al6061/B4C.
- The spark gap voltage was not showed a meaningful effect on surface roughness in the WEDM of MMCs.
- The estimated values based on the regression model with the least residual errors are very close to the experimental results and prediction errors are in the acceptable range.

ACKNOWLEDGEMENTS

The authors wish to thank Hacettepe University Scientific Research Projects Coordination Unit for the financial support of this experimental research, supported by the Scientific Research Projects Grant funding number #1743 and POYRAZ CNC Company for WEDM machine tool

REFERENCES

- [1] Mindivan, H., Baydogan, M., Kayali, E. S., Cimenoglu, H. T. Wear behaviour of 7039 aluminum alloy. *Materials Characterization*, 54, 263–269. (2005).
 - [2] Sadat, A. B. Surface Integrity When Machining Metal Matrix Composites. *Machining of Metal Matrix Composites*. Chapter 4, 51-61. (2012).
 - [3] Wang, J., Lin, W., Jiang, Z., Duan, L., Yang, G. (2014). The preparation and properties of SiCw/B4C composites infiltrated with molten silicon. *Ceramics International*, 40, 6793–6798.
 - [4] Manna, A., Bhattacharayya, B. A study on machinability of Al/SiC-MMC. *Journal of Materials Processing Technology*, 140, 711–716. (2003).
 - [5] Soy, U., Ficici, F., Demir, A. Evaluation of the Taguchi method for wear behavior of Al/SiC/B4C composites. *Journal of Composite Materials*, 46, 851–859. (2011).
 - [6] El-Gallab, M. Sklad M., Machining of Al/SiC particulate metal-matrix composites Part I: Tool performance. *Journal of Materials Processing Technology*. 83, 151–158.(1998).
 - [7] Karabulut, Ş., Optimization of surface roughness and cutting force during AA7039/Al2O3 metal matrix composites milling using neural networks and Taguchi method. *Measurement*, 66, 139-149(2015).
 - [8] Thuault, A., Marinel, S., Savary, E., Heuguet, R., Goeuriot, D., Agrawal, D. Processing of reaction-bonded B4C–SiC composites in a single-mode microwave cavity. *Ceramics International*, 39, 1215–1219, (2013).
 - [9] Sahoo, A.K., Pradhan, S., Modeling and optimization of Al/SiCp MMC machining using Taguchi approach. *Measurement*, 46, 306–307, (2013).
 - [10] Wang, J., Lin, W., Jiang, Z., Duan, L., Yang, G. (2013). The preparation and properties of SiC w / B 4 C composites in fi ltrated with molten silicon, 40, 6793–6798.
 - [11] Amitesh, G., Jatinder, K. An Investigation into the Machining Characteristics of Nimonic 80a Using CNC Wire-EDM. *International Journal of Advanced Engineering Technology*, 3, 170-174. (2012).
 - [12] Motorcu, A. R., Ekici, E., Kuş, A. Investigation of the WEDM of Al/B4C/Gr reinforced hybrid composites using the Taguchi method and response surface methodology. *Science and Engineering of Composite Materials*. doi:10.1515/secm, (2015).
 - [13] Yan, B. H., Tsai, H. C., Huang, F. Y., Lee, L. C. Examination of wire electrical discharge machining of Al2O3p/6061Al composites. *International Journal of Machine Tools and Manufacture*, 45(3), 251-259.(2005).
 - [14] Shandilya, P., Jain, P. K., Jain, N. K. RSM and ANN Modeling Approaches For Predicting Average Cutting Speed During WEDM of SiCp/6061 Al MMC. *Procedia Engineering*, 64, 767–774,(2013).
 - [15] Goswami, A., Kumar, J. Optimization in wire-cut EDM of Nimonic-80A using Taguchi’s approach and utility concept. *Engineering Science and Technology, an International Journal*, 17(4), 236–246,(2014).
 - [16] Satishkumar D., Kanthababu M., Vajjiravelu V., Anburaj R., Sunda- rrajan N.T., Arul H. *Int. J. Adv. Manuf. Tech*, 56, 975 – 986,(2011).
 - [17] Chiang, K., Chang, F. Optimization of the WEDM process of particle-reinforced material with multiple performance characteristics using grey relation analysis, *J. Mater. Process. Technol.* 180 96-110.(2006).
 - [18] Fard, R.K., Afza, R. A., Teimouri, R. Experimental investigation, intelligent modeling and multi-characteristics optimization of dry WEDM process of Al- SiC metal matrix composite, *J. Mater. Process*, 15; 483–494, (2013).
 - [19] Roy, R. K. *A Primer on the Taguchi Method*. Society of Manufacturing Engineers.
 - [20] Nourbakhsh, F., Rajurkar, K. P., Malshe, a. P.,Cao, J. (2013). Wire Electro-Discharge Machining of Titanium Alloy. *Procedia CIRP*, 5, 13–18(1990).
-

THE FRICTION WELDING OF FEAL INTERMETALLIC ALLOY AND AISI 316 STAINLESS STEEL

İbrahim CELIKYUREK

Eskişehir Osmangazi University, Department of Metallurgical and Materials
Engineering, 26480, Eskişehir, Turkey

Osman TORUN

Afyon Kocatepe University Bolvadin Vocational School,
Bolvadin / Afyonkarahisar

Bedri BAKSAN

Eskişehir Osmangazi University, Department of Metallurgical and Materials
Engineering, 26480, Eskişehir, Turkey. baksan@ogu.edu.tr

Akın OZCAN

Eskişehir Osmangazi University, Department of Metallurgical and Materials
Engineering, 26480, Eskişehir, Turkey

Abstract

In this study the friction welding of FeAl intermetallic alloy with AISI 316 stainless steel was successfully realized. The FeAl intermetallic alloy was melted in vacuum arc melting furnace, stock bar AISI 316 stainless steel was used as opposite welding material. The welding was done at constant 1000 rpm friction speed, 50, 100 and 150 MPa friction pressures and 6, 9 and 12 seconds friction durations. The welding qualities were measured by shear strength tests. The best joining strength of 281 MPa was obtained in 150 MPa friction pressure and 12 seconds duration. The hardness variations from FeAl to 316 stainless steel were measured by microhardness test. The welding interface was examined by scanning electron microscopy (SEM), and line scan analysis revealed that at the welding interface the alloying elements' quantities were decreasing, which means that at both sides of the matrices alloying elements seemed to be diffused in each other.

Key words: Intermetallic compounds based on FeAl, friction welding, scanning electron microscopy, hardness

1. INTRODUCTION

The ordered intermetallic compounds are a unique class of metallic materials, under a certain critical temperature [1,2]. Intermetallic compounds are the materials to fill the gap between metallic and ceramic materials both for service temperature and for mechanical properties. Due to high interatomic bonding strength and still having metallic bonds the intermetallic compounds are less susceptible to crack formation [3,4].

In these materials group nickel, iron and titanium aluminides are more attractive for high temperature applications. In last three decades the studies are involved in understanding the properties of these materials. The main disadvantages of the Al based and other ordered intermetallic compounds are the low ductility and brittle cracking at ambient temperature. Weldability is a specific issue related to fabrication technologies that is a major concern for Fe₃Al alloy [5]. Earlier studies on welding of Fe₃Al have mainly focused on fusion welding using gas tungsten arc (GTAW) and electron beam welding (EBW). These studies showed that cracking susceptibility depended upon alloy composition. Fe₃Al modified with chromium, niobium and carbon exhibited good weldability. B and Zr additions promoted hot cracking in these alloys [6]. Recently, Chiang et al. investigated the effects of the different alloying additions and microstructures on the mechanical properties and weldability, with a special focus on the influence of moisture-induced environmental embrittlement [7]. Ma et al. reported that the performance and weldability of the Fe₃Al were greatly influenced by the B₂ / DO₃ transformation [8]. In a recent study, Kratochvil et al. investigated weldability of Fe₃Al type alloy with hardened structure [9].

Friction welding is a solid state or non-fusion bonding technique to weld different materials as well as polymeric materials [8-13]. In friction welding process parameters friction speed, time and pressure, and the forging time and pressure. There has been few works on friction welding of Fe₃Al-type alloys. Skatchley et al. investigated the friction welding of a Fe₃Al based oxide dispersion strengthened (ODS) alloy [13]. In the present study, cast Fe₆₀Al₄₀ alloys were welded by friction welding and microstructure and mechanical properties of the welded samples were examined.

2. EXPERIMENTAL

The alloy Fe₆₀Al₄₀ was prepared by arc melting under argon atmosphere from iron and aluminum of 99.99 wt. % and 99.7 wt. % purity, respectively. The samples were homogenized at 1100 °C for 96 hours and cooled in furnace. The cylindrical cast alloy samples which have 8 mm diameter were machined to 50 mm length. The friction welding experiments were carried out by continuously driven friction welding machine [14] at constant friction pressure of 150 MPa, and 6, 9, and 9 seconds of duration times. The friction welding process is given schematically in Fig.1. After welding, the welded samples were cut normal to the welding interface. The surfaces of the welded samples were ground with 1200 grinding paper and polished 1 mm diamond paste then the samples were etched with a mixture of H₂O (30 ml), HNO₃ (30 ml), HCl (20 ml) and HF (20 ml). The microstructure was observed with an optical microscope and scanning electron microscopy (SEM). The chemical compositions of the weld zone and the base alloy were determined by using energy dispersive spectroscopy (EDS). Microhardness values were measured on both sides of the welded samples by means of Vickers indenter with a load of 100 g. The shear test were performed to determine strength of the welded zone using an electromechanical universal test machine (Shimadzu AG-IS-250) at room temperature. Fracture surfaces of the welds were observed by scanning electron microscopy.

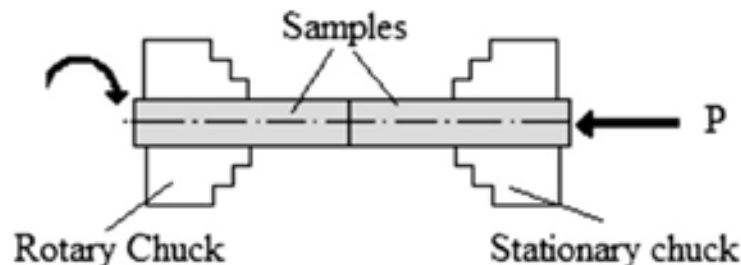


Figure 1. Schematic view of friction welding process

3. RESULTS AND DISCUSSION

3.1. Microstructure

Macrograph of the welded sample for 12 s is shown in Fig. 2. The flash was observed in all welded samples because of plastic deformation during welding. Flash formation increased with increase in burn off. Optical micrographs of the welded samples for 6, 9 and 12 s are given in Fig. 3. As seen from the micrographs, all welds exhibited a sound welding without any pore and crack along the weld interface. There are two main regions apparent in all welded samples: The fully plastic deformed dynamically recrystallized zone and deformed zone. Plastic deformation increased with increasing the friction welding time. The micrographs demonstrate that there is not an important change in the width of the deformed zone with increase in the friction welding time. Scanning electron microscopy (SEM) Energy Dispersive Spectra (EDS) area analysis revealed the composition of alloy elements in the welds (Fig. 4). Analysis results indicate that composition of welded zone and the base alloy is similar.



Figure 2. Macrograph of cross section of sample welded at 1000 rpm friction speed, 150 MPa friction pressure, and 12 seconds of friction time light colored area is 316 SS, dark colored area is Fe₆₀Al₄₀.





Figure 3. Optical micrographs of the welded samples. a) 6 s b) 9 s and c) 12 s.

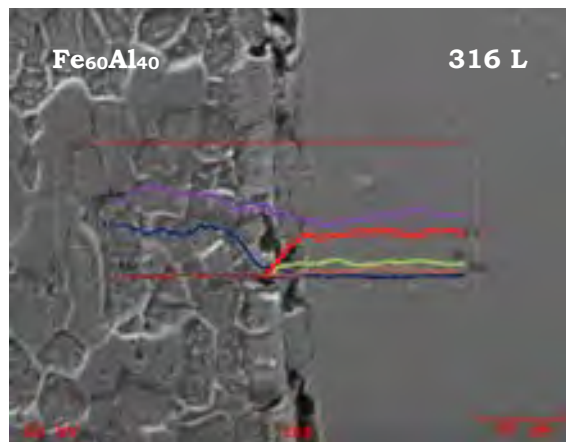


Figure 4. SEM and line scan analysis of sample welded at 1000 rpm friction speed, 150 MPa friction pressure and 12 s duration time

3.2. Mechanical properties

Microhardness values of all welds from the weld center to the both sides are given in Fig. 5. According to the results of test, microhardness profiles for all welding times are found to be similar. Hardness of the recrystallized zone is higher than that of the base alloy due to formation of very fine grains.

To determine the strength of the weld interface accurately the shear test was used. The shear strengths of welded samples were determined by using a specially designed testing apparatus [15]. The shear and bending strengths of the welds and the base alloy are shown in Fig.6. Test results demonstrate that the shear strength values of the welds are greater than the base metal. This situation shows that the structure with very fine grains formed due to dynamic recrystallization during the friction welding has more strength than the matrix.

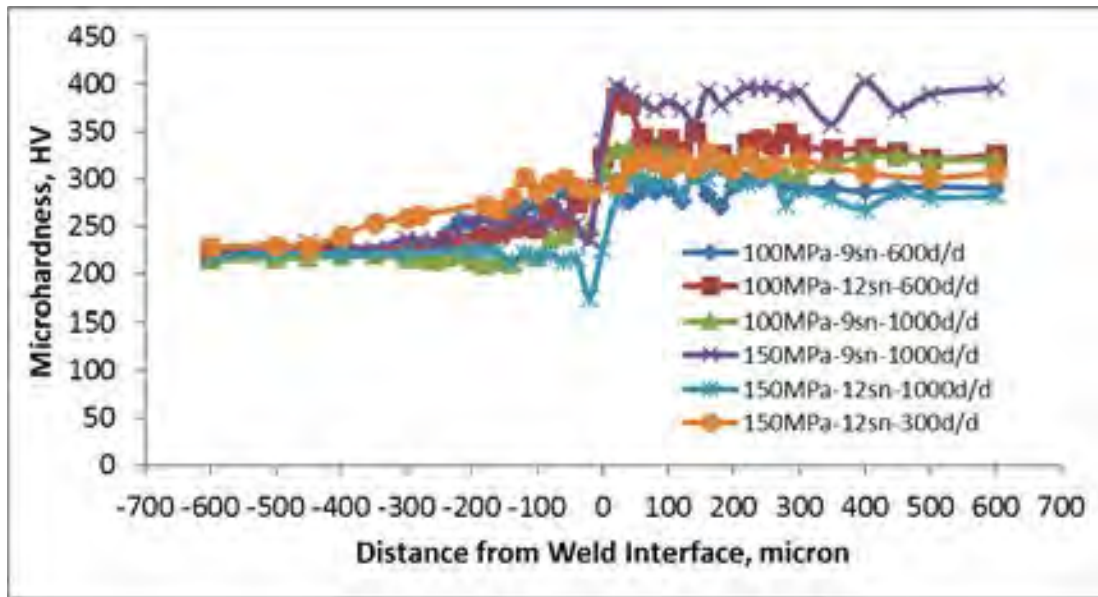


Figure 5. Microhardness profiles of the welded samples from the weld center to both sides.

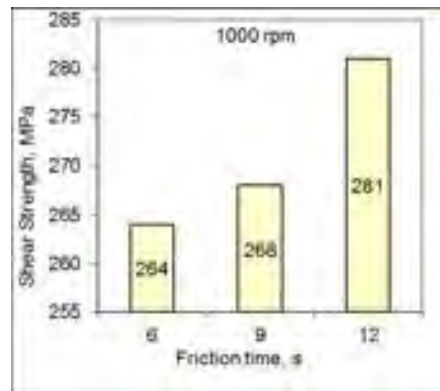


Figure 6. Shear strengths samples of 1000 rpm friction speed versus friction time

The shear strength values for all friction-welding times are very close to each other. Although the width of the recrystallized zone increased with increase in the friction welding time, the shear strength of the welds did not show an important change. The shear strengths of the welds are independent of change in the friction welding time.

4. CONCLUSIONS

In this study, the friction welding of the cast Fe₆₀Al₄₀ alloy were carried out successively by friction welding. Microstructure studies revealed two different zones at the weld interface; recrystallized fully deformed zone and deformed zone. The micrographs clearly indicate a sound welding at the weld region which is free from pore and crack. The shear strengths of the welds are

very close to each other. The shear strengths of the welds are slightly increasing due to the process time. The structure with very fine grains formed during the friction welding exhibited more strength than the matrix.

REFERENCES

- [1]. Liu C.T., Stiegler J.O., Metals Handbook, 10. ed., Vol. 2, pp. 913-942, Ohio, USA.
- [2]. Çelikyürek İ, Demir Aluminatların Borlanması ve Aşınma Özelliklerinin Belirlenmesi, Eskişehir Osmangazi Üniversitesi, Fen Bilimleri Ens. Dissertation 2007 (in Turkish).
- [3]. Liu C.T., Kumar K.S., Ordered Intermetallic Alloys I. Nickel and Iron Aluminides, J. O. M., 38, 1993.
- [4]. Froes F.H., Suryanarayana C., Eliezer D., Synthesizing process and modeling advanced materials, J. Mat. Sci. Vol. 27, 1992, p. 5113.
- [5]. Santella ML. In: Deeevi SC, Sikka VS, Maziasz PJ, Cahn RW, editors. Proceedings of materials Week'96 on nickel and iron aluminides: processing, properties, and applications, Ohio, 7-9 October 1996. USA: ASM International; 1997. p. 321-3.
- [6]. David SA, Zacharia David SA, Zacharia T. Weldability of Fe3Al-type aluminide, T. Weld J 1993;72(5):201-7.
- [7]. Chiang CC, Wang SH, Chen JS, Chu JP, Hsu YF. Bending embrittlement of as-welded FeAl alloys, Intermetallics 2007;15:564-70.
- [8]. Ma H, Li Y, Gerasimov SA, Wang J, Sun W. Investigation of transformation models of B2 → DO3 ordered structures for Fe3Al intermetallic under welding condition, Mater Lett 2008;62:1953-6.
- [9]. Kratochvil P, Neumann H. Welds of Fe3Al-type alloy with hardened structure, Intermetallics 2009;17:378-80.
- [10]. Özdemir N. Investigation of the mechanical properties of friction-welded joints between AISI 304L and AISI 4340 steel as a function rotational speed, Mater Lett 2005;59:2504.
- [11]. Ates, H, Turker M, Kurt A. Effect of friction pressure on the properties of friction welded MA956 iron-based superalloy, Mater Des 2007;28:948-53.
- [12]. Lee WB, Kim YJ, Jung SB. Effects of copper insert layer on the properties of friction welded joints between TiAl and AISI 4140 structural steel, Intermetallics 2004;12:671-8.
 - [13]. Sketchley PD, Threadgill PL, Wright IG. Rotary friction welding of an Fe3Al based ODS alloy, Mater Sci Eng 2002;A329-331:756-62.
 - [14]. Karabulut A, Tasgetiren S. Continuously Driven Friction Welding Machine, Makine Teknolojileri Elektronik Dergisi 2004;3:38-46 (in Turkish).
 - [15]. Torun O, Gurler R, Baksan B, Celikyurek I. Diffusion bonding of iron aluminide Fe72Al28 using a pure iron interlayer, Intermetallics 2005;13:801-4.

INVESTIGATION OF THE TEST DEVICE DETERMINING CHARACTERISTICS OF AUTOMOTIVE BRAKE PADS

Mustafa TIMUR

Kırklareli University, Faculty of Technology, Mechatronik Eng., Kırklareli/TURKEY
mustafatimur@klu.edu.tr, tel:+90 288 2142083, fax:+90 288 2142084

Hilmi KUŞÇU

Trakya University, Faculty of Engineering and Architecture, Machine Eng., Edirne/TURKEY
hilmi@trakya.edu.tr, tel:+90 284 2261217, fax:+90 284 2261225

Sinan SAVAŞ

University of leicester, Faculty of Mechanical Engineering, Leicester/England
Sinan38_1982@hotmail.com, tel: +90 232 7506000, fax:+90 232 7506015

Abstract

To learn about the coefficient of friction of the brake disk and the tribological properties of the materials to learn the various test devices have been developed. Friction and wear resistance test method used to measure the number of models to be the cause of much friction and wear mechanisms and tribological system is because of the over. For this reason, large part of the studies of friction and wear at present are done by using determined by the international standard test specifications and parameters. In the design used in friction materials, the most important factor of friction event is coefficient of friction and wear. Basic properties requested of a brake pad are suitable to the standards of corrosion resistance, friction coefficient and economical. These features in determining the precise hardware with automatic control unit and the importance of testing equipment is quite significant. Earlier studies that are conducted to learn about and considering the coefficient of friction of the brake discs to find the tribological properties of the materials, various testing devices have been developed. In our country and in developed countries it is possible to show examples of this work. In this study , a number of research studies have been conducted to examine automobile brake pads used in determining the characteristics of the test equipment used for the purpose for what and contribution to Turkey industry.

Key words: Test device, Tribology, Design, Coefficient of friction

1. Introduction

Nowadays, several industrial companies are interested in R&D activities to improve the efficiency performance of the friction material [1,3]. When the roughness decreased hard and shiny surfaces can be obtain which means the sliding surface is caused slide more easily over one another. Therefore, new pads are being passed through some tests such as crushing, shear, abrasion, and heat and water resistance at the stage of their construction. The negative reasons described above are intended to reduce to a minimum the pads of the potential adverse effects occur while driving [3]. The brake pads wear out as a result of friction of the brake disc and the pad and there have been substantial research efforts to prevent this matter. The performance of the brake pads has been increased as a result of tribology experiments. A number of test equipments have been designed and built to investigate different wear types. One of the most important mechanisms in the automobiles is the brake system since the life safety of the people is relying on these systems. A car should stop in the shortest distance when the driver press down the brake and thus this is related with the coefficient of friction. A number of test equipments have been developed to explore the coefficient of friction and tribological features of the materials of the brake pads.

2. Materials and Method

There are principles in product design. Good designers develop techniques that help them to implement these principles. There is a process for design: it starts from a place and there are steps to follow. This process of getting design right is applicable in most design contexts. Although some steps may be skipped, the basic process is sound.

Ertas and Jones [4] define “design process” as “...begins with an identified need and concludes with satisfactory qualification and acceptance testing of the prototype”.

Voland [5] uses the term “the engineering design process” and composes this process into five stages; 1) need assessment, 2) problem formulation, 3) abstraction and synthesis, 4) analysis, and 5) implementation.

In the development of the test devise Volland’s design method has been followed. The outcome has been found a successful product design.

3. Testing Device Used for Testing Brake Pads Used in Automobiles

Hilmi Kuşçu and Mustafa Timur designed and built the ‘Testing device used for testing friction coefficient of brake pads used in automobiles’.



Figure 1 The testing device used for testing brake pads used in automobiles

The test device is shown in;

Figure 1 is designed as it gives reliable results according to the experimental standards. It has been paid particular attention on the detail of design and manufacture of the test device in order to run experiments in a convenient way. Coefficient of friction of the brake pads can be examined under different factors including different speed, temperature, pressure etc. The device can produce graphs for Coefficient of friction- Temperature, Coefficient of friction- Time, Temperature- Time. In order to spin the brake disc in the experiment set-up an electric motor with the power 7,5 KW and 1400 RPM/min is been used. The speed of disk is 6 m/s is obtained by 1400 RPM/min.

The first step considered in the manufacture of the test device is to design of the mechanic part of the brake system in a vehicle. The parts that are used in the device including a disc, an electric motor in order to spin the disc, a caliper and pad for sheet metal in order to place brake pad on the caliper. The mechanic system of the test device is placed on the table. The second step considered in order to braking in the mechanic part, the pressure generating the pedal load is controlled by the hydraulic unit. The hydraulic unit is placed under the table. A number of experiments were performed to validate the results of the test device and its reproducibility. The results obtained from the test device is given in [1].

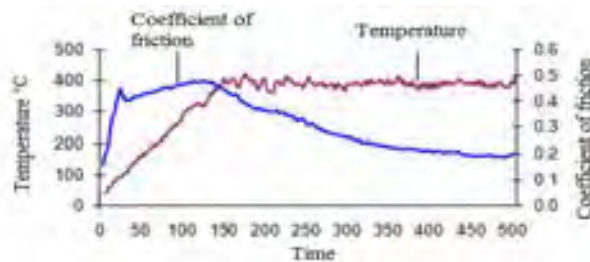


Figure 2 A Graph of Friction material's Temperature - Friction Coefficient - Time



Figure 3 A graph of Friction Material's Friction Coefficient –Time

İbrahim Mutlu and Recep Koç designed and built a 'Test device used for testing friction coefficient of brake pads used in automobiles'. The values in the device can be perceived as desired interval and saved them on computer. The device can produce graphs for Coefficient of friction- Temperature, Coefficient of friction- Time and Temperature- Time. Speed change and pressure can be adjusted by manually. Figure 4 shows the test device in a schematic way [2].

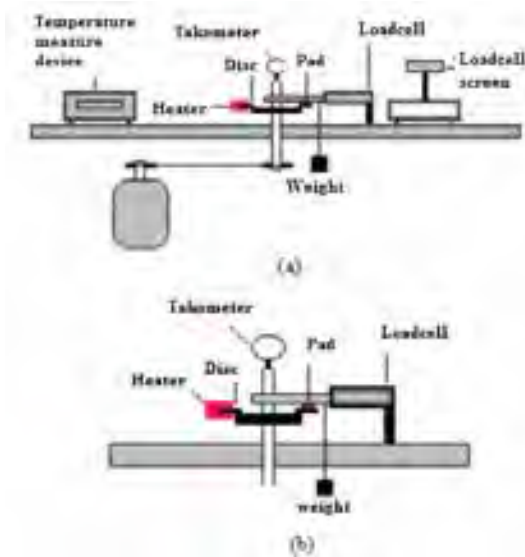


Figure 4 Experimental set-up

The methodology developed at the surface engineering Laboratory in NJIT by R. Dubrovsky and A. Titov consists of a variety of research techniques in terms of quality and quantity of analysis experiments results. These methods are included in the assessment of friction coefficient and wear rate [6].

Wear test device built by Y. Karaoğlu and O. Eldoğan is another example work which investigates the tribological features of brake pads. The purpose of this project is the same as the first example work. Figure 5 shows the general view of the wear test device. In this device, a brake disc is used in the current cars. Hydraulic pressure is applied from both surfaces of the disc. Experimental work is managed from a computer [8].

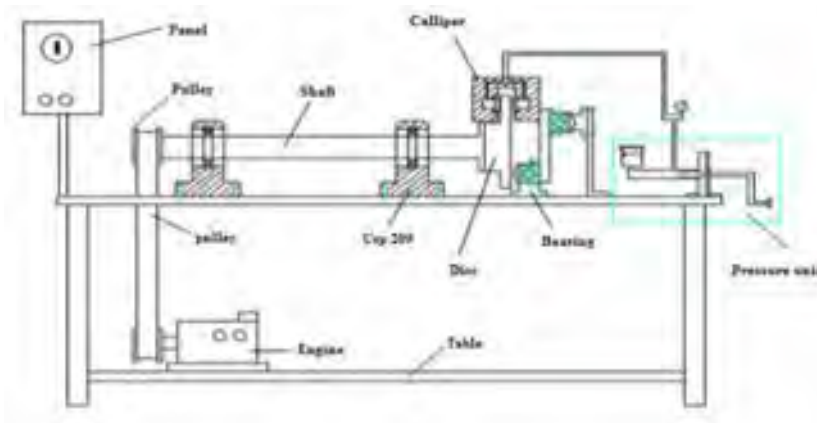


Figure 5 General view of the wear test device

M. Demiral and M. Yaşar designed and built a tribotest test device with a pin-disc system which examines wear and friction of Aluminum bronze. An AC electric motor with a power of 1.5 kW and 1500 RPM/min is used. A speed adjuster device has been used to adjust the slip rate. Figure 6 shows the top view of the tribotest device [9].

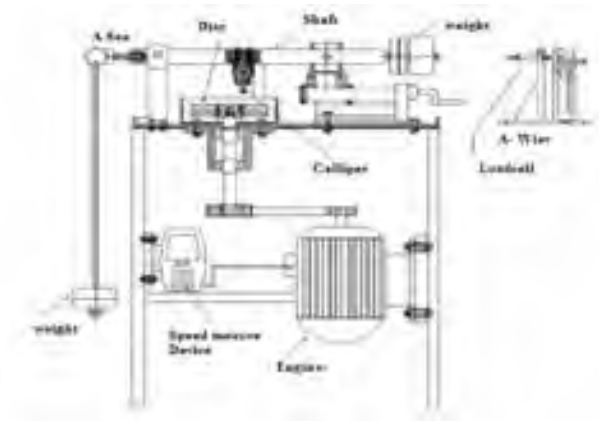


Figure 6 Tribotest device

Figure 7 shows the test device is made by Michael Ericsson and his friends that the purpose of the device is to test the friction coefficient of friction materials. The device is made in 2002 at the University of Cambridge. The main difference of this device from others is a torque meter is been used. In this way, the obtained data under which torque is been able to examined and relevant graphics can be produced.



Figure 7 A test device is made by Michael Ericsson and his friends [10]

Figure 8 shows different type of friction coefficient test device. The quality control test procedure is been made according to SAE J661 standards. The equipment on the friction materials of friction coefficient provides accurate data. The device is controlled by a computer and the results are given in graphics.



Figure 8 The test device is made by Chase Machine [1]

Figure 9 shows the test device works based on Reciprocator (shuttling) that moves linearly. An inverter is controlling the electric motor in the device and the computer is controlling slip rate. Normal load and Friction force is being measure by a loadcell the computer programme evaluates these forces and produces graphics as Coefficient of friction-Time or Way. The distance-measuring sensor that amounted the device measures 10-micron accuracy. This sensor is able to measure and save the changes of the height even the experiments is running.

The systems such as roller bearing or slippers that touches each other and moves according to each other, frictions occurs so that this makes parts moves away each other. Therefore, in real systems, both faces are abraded out and pieces stay between the parts. The distance measured system used in the designed and built tribotest device is able to do suitable measurement

- Coefficient of friction- Time
- Coefficient of friction- Way
- Wear amount – Time
- Wear amount – Way
- Wear rate- Time
- Wear rate- Way
- Wear resistance –Time
- Wear resistance –Way

Graphics can be drawn automatically and saved as data.



Figure 9 The test device works based on Reciprocator (shuttling) [7]

4. Results

The more improved sensitivity and impact capability in the cars' parts mean safe drive in the automotive sector. Especially brake systems play very important role in human safety. Friction coefficient and wear resistance that have appropriate standards are very important characteristics of the brake pads. It is very important to know these characteristics and to choose suitable brake pads according to them. Therefore there is need to have accurate test devices in order to make brake pads that have desired properties.

Nowadays, it can be seen that there is a number of tests are performed on the brake pads. Tribological event between the parts have been examined with the test devices and desired information (Friction Coefficient, wear amount and friction force) is obtained.

One of the purposes of this work is to promote original designs of test devices to identify Friction Coefficient, wear amount and friction force of car pads.

References

1. Kuşçu, H., Timur, M., (July 2014.), "Detection of thermal interaction and wearing resistance of automotive break pads formed as a result of friction with automatic test system", PhD Thesis, Trakya Univ. Institute of Science, Edirne.
2. Mutlu İ., Koç R., (2005), 'Design of Friction Tester for Automotive Brake Pads' Kahramanmaraş Sütçü İmam U. Technoloji Science, P. 1, 79-84.
3. Gemalmayan, N., (1984), "Experimental Investigation of the Properties of Friction Materials" Gazi Üniv. Institute of Science, Phd Tesis, Ankara.
4. Atila, E. and Jesse, C.J., (1996), "The Engineering Design Process", 2nd Edition,, John Wiley & Sons, Inc., New York.
5. Gerard, V., (2004), *Engineering by Design, 2nd Edition, Pearson Prentice Hall, New York.*
6. Demirci A. H., (July 1987), 'Technical Dry Friction Abrasion Test Setup A Design and Manufacturing', U.U Machine Eng. Machine science Volume 29, Issue 330.
7. Soydaş S., Yılmaz M., (2006), 'Abrasion Tester Universal Design and Manufacturing' Kocaeli Univ. Institute of Science, Master's Tesis, Kocaeli.
8. Karaoğlu Y., Eldoğan O., (2006), 'Wear tester device of design and manufactur' Sakarya Univ. Institute of Science, Master's Tesis, Sakarya.
9. Demiral M., Yaşar M., (2006), 'Cu-Al-Fe Alloy investigation of wearing behavior', Zonguldak Karaelmas Univ. Karabük.
10. Eriksson, M., Lord, J., Jacobson, S., (2001), "Wear and contact conditions of brake pads: dynamical in situ studies of pad on glass", *Wear*, 249, pp. 272–278, Londra.

EFFECTS OF PISTON MOTION ON SPECIFIC SURFACES OF THE CYLINDER LINER IN A COMPRESSION IGNITION ENGINE

Mehmet ÇAKIR

Marine Engineering Operations Department, Yildiz Technical University, Besiktas, 34349, Istanbul Turkey,
Tel: 0 212 383 28 54, Corresponding author: mecakir@yildiz.edu.tr

Ismail Hakkı AKÇAY

Department of Machine Engineering, Suleyman Demirel University, 32100, Isparta, Turkey

Abstract

A large part of the engine friction in internal combustion engine is between the piston-ring cylinder-wall contacts. The cylinder liner and piston-ring wear are very important for performance, fuel economy and engine life in internal combustion engine. In this study, surface morphologies on the Central Region (CR) and Bottom Dead Center (BDC) region of cylinder liner was investigated after the diesel engine worked 200 hours. The microstructural analyses of worn surfaces were examined by SEM. Surface deformations were compared between the two regions. As a result of, the abrasive wear was observed deeply formed axial scratches. It was observed surface deformations of the CR are less than surface deformations of the BDC for the formation of hydrodynamic lubrication regimes on the CR.

Keywords: *Engine wear, Cylinder liner-piston ring contact.*

1. Introduction

The mechanical frictions in piston assembly are extremely important for performance, fuel economy and engine life in internal combustion engine. The distribution of frictional losses between piston rings and cylinder liner vary on cylinder liner contact areas with position of each piston ring. And, different lubrication regimes consist on cylinder liner in case of engine operation.

The oil film between piston rings and cylinder liners in internal combustion engines is the first factor for the tribological performance of the system (Tamminen et al., 2006). Also, another factor on engine performance is cylinder liner wear. Cylinder liner wear in automotive engines have gained importance because of the mandatory emission standards. Because, the cylinder wear can cause to the engine blow-by. A lot of researchers have been studied because of the importance of lubrication regime and wear in internal combustion engine (Radil 1997; Wang et al. 1998; Ma et al. 2004; Ma et al. 2006; Cakir and Akcay 2014).

Shuster and Mahler (1999), studied to effects of metallurgical and metrological examinations of cylinder liner and piston ring surfaces before and after 150, 1000 and 4000 hours of heavy duty diesel engine testing. They investigated to different composition coatings and methods of application. In conclusion, they reported that adhesive wear particles of iron on the working surfaces of molybdenum based and chrome plated piston rings may indicate the early stages of a scuffing wear mechanism. Truhan et al. (2005) developed a method for evaluate the friction and wear behavior of piston ring and cylinder liner materials. The result of their work, they reported that the soot and particulate contents have a major effect on wear of the flat cast iron and less of an effect on the ring for the studied materials.

In this study, surface morphologies on the Central Region (CR) and Bottom Dead Center (BDC) region of cylinder liner was investigated after the diesel engine worked 200 hours. The microstructural analyses of worn surfaces were examined by SEM. Surface deformations were compared between the two regions. As a result of, the abrasive wear was observed deeply formed axial scratches. It was observed surface deformations of the CR are less than surface deformations of the BDC for the formation of hydrodynamic lubrication regimes on the CR.

2. Experimental Setup

The experimental work was conducted on a production four stroke, single cylinder, air-cooled diesel engine. The engine specifications are given in Table 1. The engine was operated for 200 hours. Metallurgical examinations were performed by SEM on the cylinder liner surfaces before and after 200 hours worked engine testing.

Table 1. Engine Specifications

Type	Diesel, air cooled, four stroke
Cylinder number	1
Bore X Stroke	102,5 mm x 100 mm
Displacement	825 cc
Compression ratio	17:1
Engine speed max.	3000 rpm
Engine power max.	17 hp

3. Experimental Results

The cylinder liner surfaces were visualized by SEM (100X) before engine test. Figure 1 shows the honing marks on the cylinder liner surfaces.

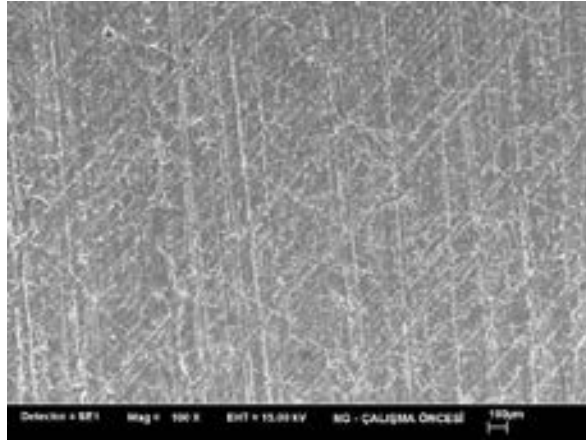


Figure 1. Honing marks on cylinder liner (100X)

On inspection of Figure 1, it can be seen that the surface have the axial scratches which named as honing marks. The surface SEM analyses of cylinder liner middle and bottom region are illustrated after the diesel engine worked 200 hours in Figure 2 and 3.

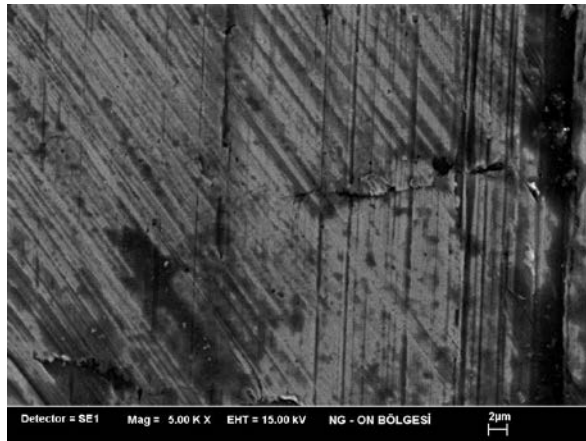


Figure 2. The SEM analysis of cylinder liner middle region (5.000X)

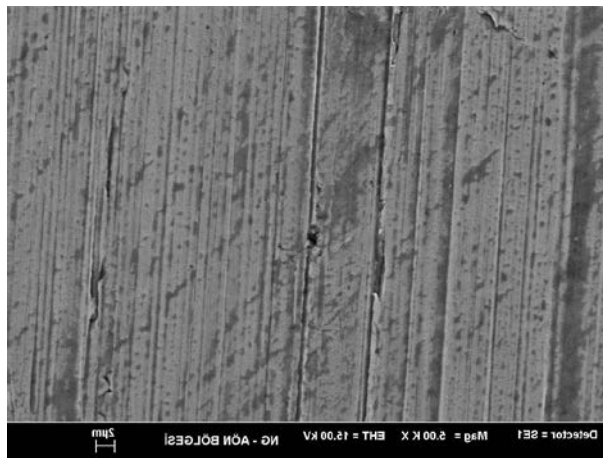


Figure 3. The SEM analysis of cylinder liner bottom region (5.000X)

The vertical lines in the Figure 2 and Figure 3 are wear scratches which destroyed with plastic deformation on the surface. While honing lines more clearly seen on the middle region in Figure 2, they almost lost in the bottom region in Figure 3. This case illustrates that the decrease of surface roughness due to wear on the bottom region of cylinder liner. Whereas, the piston apply to the cylinder surface the largest vertical force in reciprocating engines. Figure 4 typically shows to the force changes on the cylinder liner surface between the two dead centers.

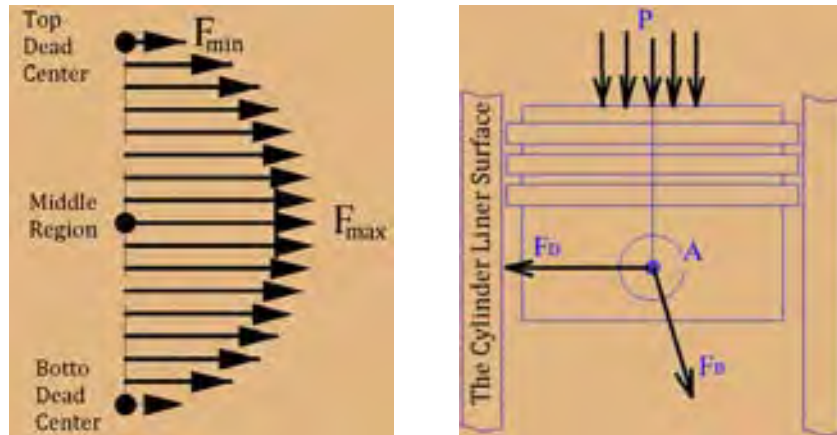


Figure 4. Exchange force applied to the cylinder liner surface.

The force distributions on thrust surface of piston are as shown in Figure 4. While force exerted on the surface has a maximum in the middle region, the force exerted on the bottom dead center region is the lowest. The piston speed shows similar to the force distributions.

The cylinder liner-piston contact lubrication regime varies from boundary and mixed at the top and bottom of the stroke to fully hydrodynamic during the middle region (Spencer, 2010). Friction force will be lower in the occurrence of hydrodynamic lubrication. Because it is no metal to metal contact.

4. Conclusions

In this study, surface morphologies on the Central Region (CR) and Bottom Dead Center (BDC) region of cylinder liner was investigated after the diesel engine worked 200 hours. As a result, may conclude the following:

Engine testing results indicated that the bottom region is more worn than the middle region. The mixed lubrication regime is dominated by bottom region due to metal-metal contact. So bottom region wear is more than middle region wear. The low wear in the middle region is a result of hydrodynamic lubrication.

The cylinder liner wear in internal combustion engine can be reduced with the increase of hydrodynamic lubrication regime region. So, reducing the metal to metal contact between piston ring and cylinder liner, wear can be reduced.

Acknowledgement

This work was sponsored by Unit of Scientific Research Projects of Suleyman Demirel University (Project Number: 2667-D-11). Experimental data are taken from reference (Cakir, 2013).

References

1. Cakir M, 2013. *The Experimental Investigation of the Effects on Engine Performance Values of Borided Cast Iron Cylinder Liner in a Single-Cylinder Air-Cooled Engine*, University of Suleyman Demirel, Graduate School of Natural and Applied Sciences, Ph. D. Thesis, p.121 Isparta.
2. Cakir M., Akçay İ. H., 2014. "Frictional Behavior between Piston Ring and Cylinder Liner in Engine Condition with Application of Reciprocating Test" *IJMET*, 11 (1), 57-71.
3. Ma Y., Li S., Jin Y., 2004. *Impacts of friction-modified fully formulated engine oils on tribological performance of nitrided piston rings sliding against cast iron cylinder bores*, *Tribol. Trans.* 47, 421-429.
4. Ma Z., Henein N. A., Bryzik W., 2006. *A model for wear and friction in cylinder liners and piston rings*, *Tribol. Trans.* 49, 315-327.
5. Radil K. C., 1997. *Test method to evaluate cylinder liner-piston ring coating for advanced heat engines*, NASA Center for Aerospace Information, NASA TM-107526 ARL-MR-362.
6. Shuster M., Mahler F., 1999. *Metallurgical and Metrological Examinations of the Cylinder Liner-Piston Ring Surfaces after Heavy Duty Diesel Engine Testing*, *Tribology Transactions*, 42:1, 116-125.
7. Spencer A., 2010. *Optimizing Surface Texture for Combustion Engine Cylinder Liners*, Lulea University of Technology, Licentiate Thesis, 104p.
8. Tamminen J., Sandstroma C. E., Andersson P., 2006. *Influence of Load on the Tribological Conditions in Piston Ring and Cylinder Liner Contacts in a Medium-Speed Diesel Engine*, *Tribology International* 39, 1643–1652.
9. Truhan J. J., Qub J., Blau P. J., 2005. *The Effect of Lubricating Oil Condition on The Friction and Wear of Piston Ring and Cylinder Liner Materials in a Reciprocating Bench Test*, *Wear* 259, 1048–1055.
10. Wang H. S., Chao G. Y., Xiang X. H., Dao W. J., Mzhong Z., 1998. *Distributed law of hydrodynamic lubrication of a cylinder liner of an internal combustion engine*, *Tribol. Trans.* 41-4, 610-614.

ANALYSIS OF LAMINATED COMPOSITE PLATES USING ELEMENT-FREE GALERKIN METHOD

Özkan ÖZBEK

Gaziantep University, Mechanical Engineering Department, 27310, Şehitkamil/Gaziantep, Turkey.
ozkanozbek@gantep.edu.tr

Ömer Yavuz BOZKURT

2Gaziantep University, Mechanical Engineering Department, 27310, Şehitkamil/Gaziantep, Turkey.
oybozkurt@gantep.edu.tr

Abstract

The desire to use materials with high strength/weight or stiffness/weight ratio is increased the importance of composite materials nowadays. Due to this, much attention has been devoted to the numerical analysis of composite plates. The performance of well-known numerical methods, Finite Element Method (FEM) and Boundary Element Method (BEM), are based on the quality mesh structures. Meshfree methods are free from the meshes and the drawbacks of mesh-based interpolation techniques. Because of its high convergence rate, Element-Free Galerkin Method (EFGM) is one of the most widely used meshfree method in solid body mechanics and it is a promising candidate for the analysis of composite materials. In this study; deflection analysis of laminated composite plates are studied using EFGM. Several laminated composite plate problems are solved using EFGM and the displacement results of EFGM solutions are compared with the results of exact and FEM solutions at the critical points.

Keywords: Laminate, composite plate, element-free Galerkin method, meshfree methods

1. INTRODUCTION

Nowadays, composite materials have played an important role in the engineering applications that require high strength/weight or stiffness/weight ratios. Because of that, analysis of composite materials have gained great significance. Several plate theories are present for the bending analysis of composite plates in the literature such as are Classical Plate Theory (CLPT) [1], First Order Shear Deformation Theory (FSDT) [1], Higher Order Shear Deformation Theory (HSDT) [1] etc. The FSDT, also known as Mindlin-Reissner plate theory, is widely used since it includes transverse shear effects and its simplicity.

Due to the complex structure of composite materials, several numerical methods, such as FEM, BEM and meshfree methods, have been used for the analyses of composite laminates in the literature. Sheikh et al. [2] used FEM on the solution of composite plates having different shapes. Moments and stresses using BEM were examined by Albuquerque and his friends [3]. Haddad et al. [4] applied to Finite Difference Method (FDM) for free vibration analysis of composite plates.

The performances of FEM and BEM depend on mesh quality of the problem model. Meshfree methods have been developed to overcome this limitation. Element-Free Galerkin Method (EFGM), which was originally developed by Belytschko [5], is one of the most widely used meshfree method in solid mechanics due to its simplicity and high convergence rate. Also, many scientists propose that EFGM has good solution accuracy in solid mechanics [6]. The EFGM is seen as a promising candidate for the analysis of composite materials. It was used by Belinha and Dinis for the analysis of anisotropic plates and laminates [7]. Also, EFGM has been preferred for the various analysis of composite plates such as buckling problems [8], vibration problems [9], bending problems [7], crack analysis [10], fracture analysis [11], etc.

In this study, EFGM and FEM programs, based on FSDT, have been written on MATLAB programming environment for the deflection analysis of laminated composite plates. Several numerical examples are solved using particular number of nodes in the problem domain. The displacement results of EFGM are presented and compared with the results of FEM and exact solution in terms of accuracy.

2. FIRST SHEAR DEFORMATION THEORY (FSDT) FOR THE LAMINATED COMPOSITE PLATES

A typical Mindlin-Reissner plate with mid-plane lying in the x-y plane of Cartesian coordinate system is depicted in Fig 1. The displacement field of a point at a distance z to the mid-plane can be written as

$$\mathbf{u} = \begin{Bmatrix} u \\ v \\ w \end{Bmatrix} = \begin{Bmatrix} -z\theta_x(x,y) \\ -z\theta_y(x,y) \\ w(x,y) \end{Bmatrix} \quad (1)$$

where (u, v, w) are the displacements of the plate in the x, y, z directions. θ_x and θ_y are the rotations of cross-section of the plate about y and x axes, respectively. The linear strains in the Mindlin-Reissner plate are the strains resulting from bending are obtained in terms of the rotations, θ_x , θ_y and of the mid-surface displacement, w, as

$$\boldsymbol{\varepsilon} = \begin{Bmatrix} \varepsilon_{xx} \\ \varepsilon_{yy} \\ \gamma_{xy} \\ \gamma_{yz} \\ \gamma_{xz} \end{Bmatrix} = \begin{Bmatrix} -z \frac{\partial \theta_x(x,y)}{\partial x} \\ -z \frac{\partial \theta_y(x,y)}{\partial y} \\ -z \frac{\partial \theta_x(x,y)}{\partial y} - z \frac{\partial \theta_y(x,y)}{\partial x} \\ -\theta_y(x,y) + \frac{\partial w(x,y)}{\partial y} \\ -\theta_x(x,y) + \frac{\partial w(x,y)}{\partial x} \end{Bmatrix} \quad (2)$$

Using the generalized Hooke's law for orthotropic linear elastic materials, the stresses for the i^{th} layer is given as,

$$\boldsymbol{\sigma}^i = \bar{\mathbf{c}}^i \boldsymbol{\varepsilon} \quad (3)$$

where

$$\boldsymbol{\sigma}^i = \{\sigma_{xx} \quad \sigma_{yy} \quad \tau_{xy} \quad \tau_{yz} \quad \tau_{xz}\}^T \quad (4)$$

$$\bar{\mathbf{c}}^i = \mathbf{T}^T \mathbf{c}^i \mathbf{T} \quad (5)$$

where \mathbf{c}^i is the material matrix of the i^{th} layer. It includes six independent material properties that are $E_1, E_2, \nu_{12}, G_{12}, G_{13}$ and G_{23} . The material matrix of the orthotropic materials can be written as

$$\mathbf{c}^i = \begin{bmatrix} \frac{E_1}{1-\nu_{12}\nu_{21}} & \frac{E_1\nu_{21}}{1-\nu_{12}\nu_{21}} & 0 & 0 & 0 \\ \frac{E_1\nu_{12}}{1-\nu_{12}\nu_{21}} & \frac{E_2}{1-\nu_{12}\nu_{21}} & 0 & 0 & 0 \\ 0 & 0 & G_{12} & 0 & 0 \\ 0 & 0 & 0 & G_{23} & 0 \\ 0 & 0 & 0 & 0 & G_{31} \end{bmatrix} \quad (6)$$

and \mathbf{T} is the transformation matrix, which has lay-up of the laminae, can be given as

$$\mathbf{T} = \begin{bmatrix} \cos^2\theta & \sin^2\theta & -\sin 2\theta & 0 & 0 \\ \sin^2\theta & \cos^2\theta & \sin 2\theta & 0 & 0 \\ \sin\theta \cos\theta & -\sin\theta \cos\theta & \cos^2\theta - \sin^2\theta & 0 & 0 \\ 0 & 0 & 0 & \cos\theta & -\sin\theta \\ 0 & 0 & 0 & \sin\theta & \cos\theta \end{bmatrix} \quad (7)$$

where the θ is the lay-up or orientation of fiber on the i^{th} lamina.

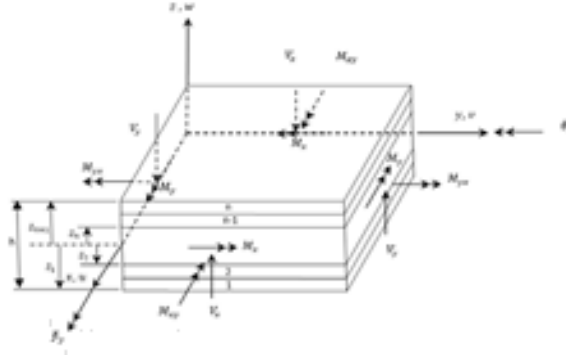


Figure 1. A typical laminate plate

Considering the $\{\varepsilon_{xx} \varepsilon_{yy} \gamma_{xy}\} = z \{\bar{\varepsilon}_{xx} \bar{\varepsilon}_{yy} \bar{\gamma}_{xy}\}$ the stresses on the top face of layer (i) are

$$\begin{aligned} \sigma_{xx}^{z_i+1} &= z_{i+1} [\bar{c}_{11}^i \bar{\varepsilon}_{xx} + \bar{c}_{12}^i \bar{\varepsilon}_{yy} + \bar{c}_{13}^i \bar{\gamma}_{xy}] \\ \sigma_{yy}^{z_i+1} &= z_{i+1} [\bar{c}_{12}^i \bar{\varepsilon}_{xx} + \bar{c}_{22}^i \bar{\varepsilon}_{yy} + \bar{c}_{23}^i \bar{\gamma}_{xy}] \\ \tau_{xy}^{z_i+1} &= z_{i+1} [\bar{c}_{13}^i \bar{\varepsilon}_{xx} + \bar{c}_{23}^i \bar{\varepsilon}_{yy} + \bar{c}_{33}^i \bar{\gamma}_{xy}] \\ \tau_{xz}^{z_i+1} &= [\bar{c}_{44}^i \gamma_{xz} + \bar{c}_{45}^i \gamma_{yz}] \\ \tau_{yz}^{z_i+1} &= [\bar{c}_{45}^i \gamma_{xz} + \bar{c}_{55}^i \gamma_{yz}] \end{aligned} \quad (8)$$

The bending moments (M_{ij}) and the shear forces (V_{ij}) are

$$\begin{aligned} M_{xx} &= \sum_i^n \int_{z_i}^{z_{i+1}} z \sigma_{xx}^i dz \\ M_{yy} &= \sum_i^n \int_{z_i}^{z_{i+1}} z \sigma_{yy}^i dz \\ M_{xy} &= \sum_i^n \int_{z_i}^{z_{i+1}} z \tau_{xy}^i dz \end{aligned} \quad (9)$$

and

$$V_{xx} = k_{sh} \sum_i^n \int_{z_i}^{z_{i+1}} \tau_{xz}^i dz \quad (10)$$

$$V_{yy} = k_{sh} \sum_i^n \int_{z_i}^{z_{i+1}} \tau_{yz}^i dz$$

where k_{sh} is the shear correction factor. Substituting the stress values in Eqs. (8) into moment in Eqs. (9) and shear forces in Eqs. (10):

$$\begin{aligned}
 M_{xx} &= \sum_i^n \left[\frac{z_{i+1}^3}{3} - \frac{z_i^3}{3} \right] [\bar{c}_{11}^i \bar{\epsilon}_{xx} + \bar{c}_{12}^i \bar{\epsilon}_{yy} + \bar{c}_{13}^i \bar{\gamma}_{xy}] \\
 M_{yy} &= \sum_i^n \left[\frac{z_{i+1}^3}{3} - \frac{z_i^3}{3} \right] [\bar{c}_{12}^i \bar{\epsilon}_{xx} + \bar{c}_{22}^i \bar{\epsilon}_{yy} + \bar{c}_{23}^i \bar{\gamma}_{xy}] \\
 M_{xy} &= \sum_i^n \left[\frac{z_{i+1}^3}{3} - \frac{z_i^3}{3} \right] [\bar{c}_{13}^i \bar{\epsilon}_{xx} + \bar{c}_{12}^i \bar{\epsilon}_{yy} + \bar{c}_{13}^i \bar{\gamma}_{xy}] \\
 V_{xx} &= k_{sh} \sum_i^n [z_{i+1} - z_i] [\bar{c}_{44}^i \gamma_{xz} + \bar{c}_{45}^i \gamma_{yz}] \\
 V_{yy} &= k_{sh} \sum_i^n [z_{i+1} - z_i] [\bar{c}_{45}^i \gamma_{xz} + \bar{c}_{55}^i \gamma_{yz}]
 \end{aligned} \tag{11}$$

The Eqs. (11) can be arranged as in the following form:

$$\mathbf{M} = \begin{bmatrix} M_{xx} \\ M_{yy} \\ M_{xy} \end{bmatrix} = \sum_i^n \mathbf{D}^i \mathbf{L} \Phi \left(\frac{z_{i+1}^3}{3} - \frac{z_i^3}{3} \right) = \left[\sum_i^n \mathbf{D}^i \left(\frac{z_{i+1}^3}{3} - \frac{z_i^3}{3} \right) \right] \mathbf{L} \Phi$$

$$\mathbf{V} = \begin{bmatrix} V_{xx} \\ V_{yy} \end{bmatrix} = k_{sh} \sum_i^n [\mathbf{A}_{sh}^i (\nabla \mathbf{w} - \Phi)(z_{i+1} - z_i)] = k_{sh} \left[\sum_i^n \mathbf{A}_{sh}^i (z_{i+1} - z_i) \right] (\nabla \mathbf{w} - \Phi) \tag{12}$$

where,

$$\mathbf{L} = \begin{bmatrix} -\frac{\partial}{\partial x} & 0 & -\frac{\partial}{\partial y} \\ 0 & -\frac{\partial}{\partial y} & -\frac{\partial}{\partial x} \end{bmatrix} \tag{13}$$

$$\Phi = \{\theta_x \quad \theta_y\}^T \tag{14}$$

$$\nabla = \left\{ \frac{\partial}{\partial x} \quad \frac{\partial}{\partial y} \right\}^T \tag{15}$$

and \mathbf{D}^i and \mathbf{A}_{sh}^i are the material properties related with bending and shear effects. They can be written in the matrix forms, as follows:

$$\mathbf{D}^i = \begin{bmatrix} \bar{c}_{11}^i & \bar{c}_{12}^i & \bar{c}_{13}^i \\ \bar{c}_{12}^i & \bar{c}_{22}^i & \bar{c}_{23}^i \\ \bar{c}_{13}^i & \bar{c}_{23}^i & \bar{c}_{33}^i \end{bmatrix} \tag{16}$$

$$\mathbf{A}_{sh}^i = \begin{bmatrix} \bar{c}_{44}^i & \bar{c}_{45}^i \\ \bar{c}_{45}^i & \bar{c}_{55}^i \end{bmatrix} \tag{17}$$

In the absence of mass forces, the equilibrium equations obtained using the virtual work principle are given as,

$$\mathbf{L}^T \mathbf{M} - \mathbf{V} = 0 \tag{18}$$

$$\nabla^T \mathbf{V} + \mathbf{b} = 0$$

where \mathbf{b} is the vector of applied external forces. EFGM is used for the solution of this system equations.

3. ELEMENT-FREE GALERKIN METHOD

3.1. Moving-Least Square (MLS) Approximation

The MLS approximation for the function of a field variable $u(\mathbf{x})$ in a local domain Ω is defined at a point \mathbf{x} as

$$u^h(\mathbf{x}) = \sum_{i=1}^m p_i(\mathbf{x}) a_i(\mathbf{x}) = \mathbf{p}^T(\mathbf{x}) \mathbf{a}(\mathbf{x}) \tag{19}$$

where m is the number of basis terms, $\mathbf{p}^T(\mathbf{x}) = \{p_1(\mathbf{x}), p_2(\mathbf{x}), p_3(\mathbf{x}), \dots, p_m(\mathbf{x})\}$ is the vector of monomial basis functions, $\mathbf{a}^T(\mathbf{x}) = \{a_1(\mathbf{x}), a_2(\mathbf{x}), a_3(\mathbf{x}), \dots, a_m(\mathbf{x})\}$ is the vector of coefficients, and $\mathbf{x}^T = [x, y]$ is the position vector for 2D problems. The monomials are selected from the Pascal triangle with providing minimum completeness to build the basis function $\mathbf{p}^T(\mathbf{x})$. For example, the linear and quadratic basis functions in 2D problems can be given by

$$\mathbf{p}^T(\mathbf{x}) = [1, x, y], \quad m = 3 \tag{20}$$

$$\mathbf{p}^T(\mathbf{x}) = [1, x, y, x^2, xy, y^2], \quad m = 6 \tag{21}$$

The difference between the function $u(\mathbf{x})$ and its local approximation $u^h(\mathbf{x})$ must be minimized by weighted discrete L_2 norm to obtain the vector of coefficients $\mathbf{a}(\mathbf{x})$.

$$J = \sum_{i=1}^n w(\mathbf{x} - \mathbf{x}_i) [\mathbf{p}^T(\mathbf{x}_i) \mathbf{a}(\mathbf{x}) - u_i]^2 \quad (22)$$

where n is the number of nodes in the support domain of point \mathbf{x} , u_i is the nodal value of u at $\mathbf{x} = \mathbf{x}_i$, $w(\mathbf{x} - \mathbf{x}_i)$ is the weight function associated with the influence domain of node i . From weight function properties, it must be greater than zero for all nodes in the support domain of point \mathbf{x} .

The minimization of weighted residual with respect to $\mathbf{a}(\mathbf{x})$ at any arbitrary point \mathbf{x} gives

$$\frac{\partial J}{\partial \mathbf{a}} = 0 \quad (23)$$

which can be written as a set of linear equations.

$$\mathbf{A}(\mathbf{x}) \mathbf{a}(\mathbf{x}) = \mathbf{B}(\mathbf{x}) \mathbf{U}_s \quad (24)$$

where $\mathbf{U}_s = \{u_1, u_2, u_3, \dots, u_n\}^T$ is the vector of nodal values of field function for the nodes of support domain. The matrices \mathbf{A} and \mathbf{B} have the following forms

$$\mathbf{A}(\mathbf{x}) = \sum_{i=1}^n w_i(\mathbf{x}) \mathbf{p}(\mathbf{x}_i) \mathbf{p}^T(\mathbf{x}_i), \quad w_i(\mathbf{x}) = w(\mathbf{x} - \mathbf{x}_i) \quad (25)$$

$$\mathbf{B}(\mathbf{x}) = [w_1(\mathbf{x}) \mathbf{p}(\mathbf{x}_1) \quad w_2(\mathbf{x}) \mathbf{p}(\mathbf{x}_2) \quad \dots \quad w_n(\mathbf{x}) \mathbf{p}(\mathbf{x}_n)] \quad (26)$$

The matrix \mathbf{A} is called as weighted moment matrix of MLS and if it is non-singular $\mathbf{a}(\mathbf{x})$ can be written as

$$\mathbf{a}(\mathbf{x}) = \mathbf{A}^{-1}(\mathbf{x}) \mathbf{B}(\mathbf{x}) \mathbf{U}_s \quad (27)$$

The local approximation $u^h(\mathbf{x})$ can be rewritten by substituting Eq. (19)

$$u^h(\mathbf{x}) = \sum_{i=1}^n \phi_i(\mathbf{x}) u_i = \Phi^T(\mathbf{x}) \mathbf{U}_s \quad (28)$$

where Φ^T is the vector of MLS shape functions and it can be expressed as

$$\Phi^T(\mathbf{x}) = \{\phi_1(\mathbf{x}) \quad \phi_2(\mathbf{x}) \quad \dots \quad \phi_n(\mathbf{x})\} = \mathbf{p}^T(\mathbf{x}) \mathbf{A}^{-1}(\mathbf{x}) \mathbf{B}(\mathbf{x}) \quad (29)$$

The partial derivatives of shape function can be achieved by the following equation.

$$\Phi_{,i} = (\mathbf{p}^T \mathbf{A}^{-1} \mathbf{B})_{,i} = \mathbf{p}_{,i}^T \mathbf{A}^{-1} \mathbf{B} + \mathbf{p}^T \mathbf{A}_{,i}^{-1} \mathbf{B} + \mathbf{p}^T \mathbf{A}^{-1} \mathbf{B}_{,i} \quad (30)$$

where

$$\mathbf{A}_{,i}^{-1} = -\mathbf{A}^{-1} \mathbf{A}_{,i} \mathbf{A}^{-1} \quad (31)$$

The spatial derivative are designated with index i following a comma. The weight functions are one of the most important points for derivation of MLS shape functions. The continuity and locality features of the MLS approximation are mainly based on weight functions. The weight function must be positive inside the support domain by taking its maximum value at the centre of support domain and must be zero outside the support domain using a monotonically decrease. There are various weight functions in literature [6]. The cubic spline weight function is used in this work and is given by

$$w_i(\mathbf{x} - \mathbf{x}_i) = w(\bar{r}_i) = \begin{cases} 2/3 - 4\bar{r}_i^2 + 4\bar{r}_i^3 & \bar{r}_i \leq 0.5 \\ 4/3 - 4\bar{r}_i + 4\bar{r}_i^2 - 4/3\bar{r}_i^3 & 0.5 < \bar{r}_i \leq 1 \\ 0 & \bar{r}_i > 1 \end{cases} \quad (32)$$

For rectangular influence domain in 2-D problems, weight functions can be obtained by

$$w(\bar{r}_i) = w(r_x) w(r_y) = w_x w_y \quad (33)$$

$$r_x = \frac{|x-x_i|}{r_{wx}} \text{ and } r_y = \frac{|y-y_i|}{r_{wy}} \quad (34)$$

where r_{wx} and r_{wy} are the size of support domain in the x and y direction.

3.2. Galerkin Weak Form and Enforcement Boundary Conditions

The Galerkin weak form for Mindlin-Reissner plates can written as

$$\int_{\Omega} \delta(\mathbf{L}_d \mathbf{u})^T \mathbf{D} \mathbf{L}_d \mathbf{u} d\Omega - \int_{\Omega} \delta(\mathbf{L}_u \mathbf{u})^T \mathbf{b} d\Omega - \int_{\Gamma_t} \delta(\mathbf{L}_u \mathbf{u})^T \mathbf{t}_\Gamma dS + \delta \int_{\Gamma_u} \frac{1}{2} (\mathbf{u}_b - \mathbf{u}_\Gamma)^T \alpha (\mathbf{u}_b - \mathbf{u}_\Gamma) d\Gamma = 0 \quad (35)$$

The discrete system equation can be written as

$$(\mathbf{K} + \mathbf{K}^\alpha) \mathbf{U} = (\mathbf{F} + \mathbf{F}^\alpha) \quad (36)$$

where \mathbf{K} is the global stiffness matrix and is obtained by assembling the point stiffness matrices

$$\mathbf{K}_{ij} = \int_{\Omega} \mathbf{B}_i^T \mathbf{D} \mathbf{B}_j d\Omega \quad (37)$$

in which

$$\mathbf{B}_i = \begin{bmatrix} 0 & 0 & 0 & \frac{\partial \phi_i}{\partial x} & \frac{\partial \phi_i}{\partial y} \\ \frac{\partial \phi_i}{\partial x} & 0 & \frac{\partial \phi_i}{\partial y} & \phi_i & 0 \\ 0 & \frac{\partial \phi_i}{\partial y} & \frac{\partial \phi_i}{\partial x} & 0 & \phi_i \end{bmatrix}^T \quad (38)$$

and the \mathbf{K}^α is the matrix of penalty factors defined by

$$(\mathbf{K}^\alpha)_{ij} = \int_{\Gamma_u} \varphi_i^T \boldsymbol{\alpha} \varphi_j d\Gamma \quad (39)$$

where φ_i is a diagonal matrix. If the relevant DOF is free, the diagonal elements of φ_i are equal to 0, otherwise equal to 1.

The force vector \mathbf{F} in Eq. (35) is the global force vector assembled using the nodal force vector of

$$\mathbf{F}_i = \int_{\Omega} (\mathbf{L}_u \Phi_i)^T b d\Omega + \int_{\Omega} (\mathbf{L}_u \Phi_i)^T t_r dS \quad (40)$$

where Φ_i is a diagonal matrix of shape functions.

The \mathbf{F}^α vector shows the forces obtained by the implementation of essential boundary conditions and can be obtained as follows

$$\mathbf{F}_i^\alpha = \int_{\Gamma_u} \varphi_i^T \boldsymbol{\alpha} u_r d\Gamma \quad (41)$$

4. NUMERICAL RESULTS AND DISCUSSIONS

In this section, a few numerical examples have been performed to demonstrate the applicability and the accuracy of the EFGM. Plates with boundary conditions, thickness ratios, number of layers, fiber orientations and materials are studied. The results are provided in terms of normalized displacements for the convenience of comparison and validated by comparing them with analytical results taken from the literature and FEM results. The behaviour of all composite materials used is considered as linear elastic. The value of shear correction factor is constant and taken as 5 / 6 for all examples. The properties of materials used in the examples are given in Table 1. The linear polynomial basis, cubic spline weight function, 2.5 for the dimensionless support domain size and 7 × 7 Gauss quadrature integration points are used in all EFGM solutions.

Table 1. Properties of laminated composite plates

	M1	M2	M3
$E1, Pa$	250×10^9	40×10^6	300×10^9
$E2, Pa$	10×10^9	1.0×10^6	12×10^9
G_{12}, Pa	5×10^9	0.6×10^6	6×10^9
G_{13}, Pa	5×10^9	0.6×10^6	6×10^9
G_{23}, Pa	2×10^9	0.5×10^6	2.4×10^9
ν_{12}	0.25	0.25	0.25

4.1. Simply supported laminated composite plates under uniformly distributed load

The deformation of a simply supported square laminated plate subjected to a uniformly distributed transverse load $q = 100 \text{ kN/m}^2$ is analysed using different lamination schemes with thickness/span ratios of $h / L = 0.1, h / L = 0.05$ and $h / L = 0.01$. The laminates used are orthotropic laminate with one layer of $[0^\circ]$ orientation, symmetric cross-pplies with three, four, five and seven layers of $[0^\circ/90^\circ/0^\circ], [0^\circ/90^\circ/90^\circ/0^\circ], [0^\circ/90^\circ/0^\circ/90^\circ/0^\circ]$ and $[0^\circ/90^\circ/90^\circ/0^\circ/90^\circ/90^\circ/0^\circ]$ orientations, respectively. The material M1, presented in Table 1, is used in this example.

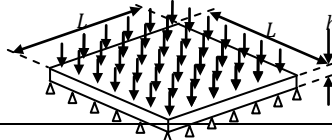


Figure 2. Simply supported laminated composite square plate

Due to the symmetry, only a quarter of plate is modelled using 441 nodes in the EFGM and FEM solutions. The dimensionless center deflection of plate is presented in Table 2. It can be seen that the accuracy of EFGM solution is near to the exact solution and is better than the FEM.

Table 2. Central deflections $100wE_2h^3/(qL^4)$ under uniform transverse load

h/L	Lay-up	FEM	EFGM	Exact [12]
0.01	0	0.662553	0.659729	0.6528
	0/90/0	0.680383	0.677547	0.6697
	0/90/90/0	0.694267	0.691600	0.68333
	0/90/0/90/0	0.698297	0.695732	0.6874
	0/90/90/0/90/90/0	0.701414	0.698928	0.6896
0.05	0	0.737233	0.734517	0.7262
	0/90/0	0.769471	0.766675	0.7572
	0/90/90/0	0.781553	0.778914	0.7694
	0/90/0/90/0	0.769781	0.767292	0.7581
	0/90/90/0/90/90/0	0.767333	0.764929	0.7575
0.1	0	0.966699	0.963153	0.9519
	0/90/0	1.038240	1.034393	1.0219
	0/90/90/0	1.040156	1.036504	1.025
	0/90/0/90/0	0.986117	0.982779	0.9727
	0/90/90/0/90/90/0	0.969344	0.966131	0.9643

4.2. Simply supported angle-ply square plate under uniformly distributed load

The deformation of an angle-ply simply supported square plate subjected to a uniformly distributed transverse load $q = 1$ is examined using four layers $[\theta^\circ/-\theta^\circ/\theta^\circ/-\theta^\circ]$. The solutions are presented with a constant thickness-to-span ratio, h / L , of 0.1. The material M2 is used in this example.

Because of the asymmetry, the whole plate is modelled using 441 nodes in the EFGM and FEM solutions. Table 3 presents the dimensionless center deflection of plate. It is visible that the accuracy of EFGM solution is more accurate than the FEM. Also, it can be achieved to exact results by particular number of nodes used in the solution.

Table 3. Central deflections $100wE_2h^3/(qL^4)$ under uniform transverse load

Arrangement of layers $[\theta^\circ/-\theta^\circ/\theta^\circ/-\theta^\circ]$	FEM	EFGM	Exact [12]
-5/+5/-5/+5	6.922555	6.892311	6.741
-15/+15/-15/+15	6.205659	6.180749	6.086
-30/+30/-30/+30	4.841598	4.820746	4.825
-45/+45/-45/+45	4.430046	4.410081	4.426

4.3. Clamped laminated composite plates under uniformly distributed load

Clamped laminated square plate with four different aspect ratios of $h / L = 0.1$, $h / L = 0.05$, $h / L = 0.02$ and $h / L = 0.01$ are analyzed to determine deformations under the uniformly distributed transverse load $q = 1$. The unidirectional laminate of material M3 is used with four layer of $[0^\circ/90^\circ/90^\circ/0^\circ]$ orientation. Due to the symmetry, only a quarter of plate is modelled using 441 nodes in the EFGM and FEM solutions. The dimensionless center deflection of plate is presented in Table 4. A close agreement between the results of EFGM and exact solution is shown for all thickness ratios examined. Again the results of EFGM is better than the FEM ones.

Table 4. Central deflections $100wE_2h^3/(qL^4)$ under uniform transverse load

h/L	FEM	EFGM	Exact [13]
0.1	0.465766	0.46542	0.4651
0.05	0.234185	0.234522	0.2342
0.02	0.158636	0.159152	0.159
0.01	0.147079	0.147363	0.1475

5. CONCLUSIONS

In this study, the EFGM based on First Order Shear Deformation Theory is successfully implemented in the bending analyses of laminated composite plates. The results for the analyzed plates are in good agreement with the results of exact solutions. It is also shown that the accuracy of EFGM solutions are better than the FEM ones for the analyzed plates.

REFERENCES

- [1]. J. N. Reddy, A. A. Khdeir, "Buckling of vibration of laminated composite plates using various plate theories," *AIAA Journal*, 27(12), 1808-1817, 1989.
 - [2]. A. H. Sheikh, S. Haldar, D. Sengupta, "A high precision shear deformable element for the analysis of laminated composite plates of different shapes," *Composite Structures*, 55(3), 329-336, 2002.
 - [3]. A. Reis, E. L. Albuquerque, F. L. Torsani, L. P. Junior, P. Sollero, "Computation of moments and stresses in laminated composite plates by the boundary element method," *Engineering Analysis with Boundary Elements*, 35, 105-113, 2010.
 - [4]. S. K. Numayr, R. H. Haddad, M. A. Haddad, "Free vibration of composite plates using the finite difference method," *Thin-Walled Structures*, 42, 399-414, 2004.
 - [5]. T. Belytschko, "Meshless methods an overview and recent developments," *International Journal for Numerical Methods in Engineering*, 38, 1655-1679, 1996.
 - [6]. G.R. Liu, *Mesh Free Methods Moving Beyond The Finite Element Method*, Taylor and Francis Group, (2003).
 - [7]. J. Belinha, L. M. J. S. Dinis, "Analysis of plates and laminates using the element-free Galerkin method," *Computers and Structures*, 84, 1547-1559, 2006.
 - [8]. A. G. Arani, Sh. Maghamikia, M. Mohammadimehr, A. Arefmanesh, "Buckling analysis of laminated composite rectangular plates reinforced by SWCNTs using analytical and finite element methods," *Journal of Mechanical Science and Technology*, 25(3), 809-820, 2011.
 - [9]. M. R. Aagaah, M. Mahinfalah, G. N. Jazar, "Natural frequencies of laminated composite plates using third order shear deformation theory," *Composite Structures*, 72, 273-279, 2006.
 - [10]. S. S. Ghorashi, S. R. Sabbagh-Yazdi, S. Mohammadi, "Element free Galerkin method for crack analysis of orthotropic plates," *Computational Methods in Civil Engineering*, 1, 1-13, 2010.
 - [11]. S. S. Ghorashi, S. Mohammadi, S. R. Sabbagh-Yazdi, "Orthotropic enriched element free Galerkin method for fracture analysis of composites," *Engineering Fracture Mechanics*, 78, 1906-1927, 2011.
 - [12]. J. N. Reddy, *Mechanics of laminated composite plates*, CRC Press, 1996.
 - [13]. P. Umasree, K. Bhaskar, "Accurate flexural analysis of clamped moderately thick cross-ply rectangular plates by superposition of exact untruncated infinite series solutions," *Journal of Reinforced Plastics Composite*, 24(16), 1723-1736, 2002.
-

OPTIMUM AUTOFRETTAGE PRESSURE FOR A HIGH PRESSURE CYLINDER OF A WATERJET INTENSIFIER PUMP

Hakan ÇANDAR

University of Gaziantep, Mechanical Engineering Department, 27310 Şehitkamil/Gaziantep, TURKEY
candar@gantep.edu.tr

Hüseyin FİLİZ

University of Gaziantep, Mechanical Engineering Department, 27310 Şehitkamil/Gaziantep, TURKEY
hfiliz@gantep.edu.tr

Abstract

Walled cylinder which is commercially used as a high pressure cylinder of a waterjet intensifier pump. Bilinear kinematic hardening model is used in the derivation of analytical model based on plane strain, Von-Mises yield criteria and incompressible volume assumptions. Elasto-plastic radius is dependent on autofrettage pressure and optimum value of autofrettage pressure is found as a value that will give minimum value of maximum Von-Mises stress on the wall of the cylinder under operating pressure. Hence, considering elasto-plastic radius as the design variable, its optimum value is determined for the specified operating pressure. Reverse yielding owing to Bauschinger effect is used as the only non-linear constraint, matlab© optimtool finds optimum value of the elasto-plastic radius and the corresponding autofrettage pressure is then calculated. By using ANSYS 14©, stress analysis of the autofrettaged cylinder has been performed and the results obtained from both methods are found to be almost the same.

Keywords: *Autofrettage, Kinematic hardening, Bauschinger effect, Optimization, FE analysis*

1. INTRODUCTION

High pressure cylinders of a waterjet intensifier pump are subjected to an alternating internal pressure at a certain frequency. Failure of these cylinders is due to higher values of alternating stress components at the inner surface. In order to improve fatigue behaviour of these cylinders a compressive residual stress at the inner surface must be created. Autofrettage process is one of the efficient methods using for this purpose. In the autofrettage process, a certain amount of internal pressure is applied to the cylinder so that the inner part of its wall becomes partially plastic. The pressure is then released and the outer elastic part of the wall tries to compress the inner plastic part. Thus, residual compressive stress at the inner surface is achieved.

Analytical model for autofrettage process first proposed by Hill [1] is elastic-perfectly plastic model. Many researchers have been used this model in their studies. Topçu and Filiz [2] compared the performance characteristics of shrink fit and autofrettage process by going through analytical and numerical analysis. Majzoobi et al. [3] studied on the determination of the best autofrettage pressure by going through analytical and numerical analysis. Hojjati and Hassani [4] stated the optimum autofrettage pressure and radius by theoretically and by finite-element modeling based on von mises yielding criteria. Rayhan et al. [5] pointed out that working pressure and the ratio of outer to inner radius effects the optimum autofrettage pressure.

Elastic-perfectly plastic assumption cannot be used for most of the materials due to Bauschinger effect and strain hardening. Huang [6] proposed an autofrettage model considering the material strain hardening relationship and Bauschinger effect, based on actual tensile-compressive curve of material. He found that the smaller Bauschinger effect coefficient causes the reverse yielding to take place more easily and affects the residual stress distribution. White et al. [7] developed an improved isotropic-kinematic hardening model and they defined the Bauschinger effect as one of the most important physical properties to be modelled. Eun Yeup Lee et al. [8] investigated elastic- perfectly plastic and strain hardening models for autofrettaged compound cylinder. They found that the compressive residual stress of the strain hardening model is smaller than that of the elastic- perfectly plastic model because of the Bauschinger effect. Ragab et al. [9] used a generalized material behaviour model includes reverse yielding, non-linear hardening and Bauschinger effect.

In this study, going through the studies mentioned above, an analytical model is generated in order to evaluate the value of the optimum value of elasto-plastic radius so that maximum Von-Mises stress developed on the wall of the cylinder will be minimized under operating pressure. Autofrettage pressure, elasto-plastic radius and operating pressure are all interrelated to each other. Loading the cylinder with autofrettage pressure and then unloading the cylinder will create compressive residual stress at the inner surface of the cylinder which will help in reducing the stresses developed under operating pressure. The problem here is to determine the optimum value of autofrettage pressure which gives minimum Von-Mises stress under operating pressure. Due to kinematic hardening behaviour, autofrettage pressure is limited to a value at which reverse yielding begins. This is considered as a nonlinear constraint in optimization process. By using Matlab optimtool, optimum value of elasto-plastic radius is determined. Optimum autofrettage pressure and corresponding Von-Mises stresses through the wall of the cylinder are then calculated. In order to verify the results, finite element model of the cylinder is created in ANSYS environment and the results obtained from both analytical and FEM analyses are compared.

2. THEORETICAL ANALYSIS

2.1. Basic equations

When a hollow cylinder with closed ends is pressurized as shown in Figure 1, radial stress (σ_r), tangential stress (hoop stress, σ_t) and longitudinal stress (σ_z) are developed. These stresses are the principal stresses. From the force equilibrium on the infinitesimally small element, equation (1) is obtained.

$$\sigma_r + r \frac{d\sigma_r}{dr} - \sigma_t = 0 \quad (1)$$

and corresponding strains ϵ_r and ϵ_θ are given in terms of the radial displacement, u , as:

$$\begin{aligned} \epsilon_r &= \frac{du}{dr} \\ \epsilon_\theta &= \frac{u}{r} \end{aligned} \quad (2)$$

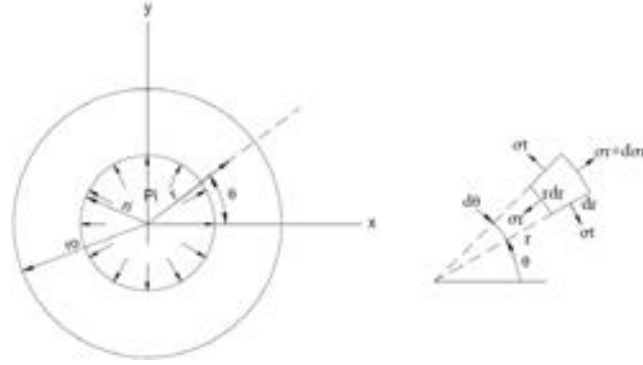


Figure 1 Cross section of a thick walled cylinder under internal pressure

and the elastic constitutive relations are;

$$E\varepsilon_r = \sigma_r - \nu(\sigma_\theta + \sigma_z)$$

$$E\varepsilon_\theta = \sigma_\theta - \nu(\sigma_r + \sigma_z)$$

$$E\varepsilon_z = \sigma_z - \nu(\sigma_r + \sigma_\theta) \quad (3)$$

During autofrettage process, the cylinder is located between two holders that restrict the elongation in longitudinal direction which results plain strain case. Another consideration is about material stress-strain relationship. It is assumed that equivalent stress-strain relationship is the same as stress-strain relationship of simple tension-compression test. In addition to these, incompressible volume assumption ($\varepsilon_r + \varepsilon_\theta + \varepsilon_z = 0$) and Von Mises yielding criteria are used. Von-Mises criterion suggests that, equivalent stress (Von Mises stress) σ_i , and equivalent strain ε_i are:

$$\sigma_i = \sqrt{\frac{1}{2}[(\sigma_\theta - \sigma_r)^2 + (\sigma_r - \sigma_z)^2 + (\sigma_z - \sigma_\theta)^2]} \quad (4)$$

$$\varepsilon_i = \frac{\sqrt{2}}{3} \sqrt{[(\varepsilon_\theta - \varepsilon_r)^2 + (\varepsilon_r - \varepsilon_z)^2 + (\varepsilon_z - \varepsilon_\theta)^2]} \quad (5)$$

For plain strain assumption, $\varepsilon_z = 0$, equation (3) gives;

$$\sigma_z = \frac{1}{2}(\sigma_\theta + \sigma_r) \quad (6)$$

Substituting equation (6) into equation (4) gives;

$$\sigma_\theta = \frac{2}{\sqrt{3}}\sigma_i + \sigma_r \quad (7)$$

$$\sigma_z = \frac{1}{\sqrt{3}}\sigma_i + \sigma_r \quad (8)$$

The radial stress σ_r can be obtained from equations (1), (7) and (8)

$$\sigma_r = \int \frac{2}{\sqrt{3}} \frac{\sigma_i}{r} dr \quad (9)$$

And equivalent strain is obtained from equations (2) and (5) and by using plane strain and incompressible volume assumptions;

$$\varepsilon_i = \frac{2}{\sqrt{3}} \frac{c}{r^2} \quad (10)$$

where c is an integration constant.

2.2. Stress-Strain Relationship

In general, materials exhibit different characteristics in elastic and plastic region. In this work, material stress-strain relationship is assumed to be bilinear kinematic hardening model which is shown in Figure 2. The model is considered to consists of elastic region (O-A) and plastic region (A-B) and can be described by two equations.

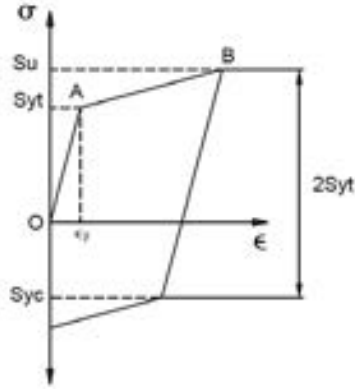


Figure 2 Material stress strain curve based on bilinear kinematic hardening model

Elastic region (O-A)

$$\sigma = E \cdot \epsilon \tag{11}$$

Plastic region (A-B)

$$\sigma = S_y + T \cdot (\epsilon_p - \epsilon_y) \tag{12}$$

where S_y , ϵ_y , ϵ_p and T are yield stress, yield strain, plastic strain and tangent modulus respectively. Arranging equation (12) yields,

$$\sigma = A + T \cdot \epsilon_p \tag{13}$$

where A is a constant and depends on S_y , ϵ_y and T .

$$A = S_y - T \cdot \epsilon_y \tag{14}$$

2.3. Stress Analysis

Stresses developed in the loading and unloading stages of autofrettage process are analyzed by using proper boundary conditions. Stresses in the operating stage are considered to be superposition of residual stresses and the elastic stresses due to the operating pressure.

2.3.1. Loading Stage

(a) Elastic region (O-A)

Substituting equations (10) and (11) into equation (9) gives

$$\sigma_{re} = -\frac{2}{3} \frac{E}{r^2} c_{e1} + c_{e2} \tag{15}$$

Substituting equations (10), (11) and (15) into equation (7) gives

$$\sigma_{\theta e} = \frac{2}{3} \frac{E}{r^2} c_{\theta 1} + c_{\theta 2} \tag{16}$$

Substituting equations (10), (11) and (15) into equation (8) gives

$$\sigma_{ze} = c_{e2} \tag{17}$$

(b) Plastic region (A-B)

Substituting equations (10) and (13) into equation (9) gives

$$\sigma_{rp} = \frac{2}{\sqrt{3}} A \ln r - \frac{2}{3} \frac{T}{r^2} c_{p1} + c_{p2} \tag{18}$$

Substituting equations (10) and (13) into equation (7) gives

$$\sigma_{\theta p} = \frac{2}{\sqrt{3}} A (1 + \ln r) + \frac{2}{3} \frac{T}{r^2} c_{p1} + c_{p2} \tag{19}$$

Substituting equations (10) and (13) into equation (8) gives

$$\sigma_{zp} = \frac{1}{\sqrt{3}} A (1 + 2 \ln r) + c_{p2} \tag{20}$$

Boundary conditions

The following boundary conditions exist when the cylinder is subjected to internal pressure P_a as shown in Figure 3.

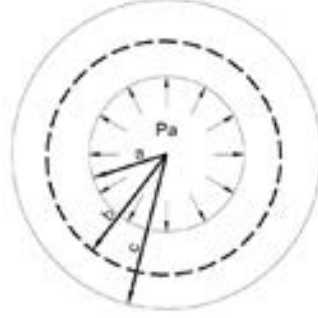


Figure 3 Radii of elastic-plastic zones

1. Both of the equivalent stresses in the elastic zone and plastic zone ($r=b$) are equal the yield stress of the material.

(a) at $r=b$, $\sigma_{ie}=S_y$, c_{e1} is found as;

$$c_{e1} = \frac{\sqrt{3} S_y}{2 E} b^2 \quad (21)$$

(b) at $r=b$, $\sigma_{ip}=S_y$, c_{p1} is found as;

$$c_{p1} = \frac{\sqrt{3} (S_y - A)}{2 T} b^2 \quad (22)$$

2. The radial stress σ_r at the outer surface ($r=c$) and the inner surface ($r=a$) are equal to zero and $-P_a$ (autofrettage pressure) respectively.

(a) at $r=c$, $\sigma_{re}=0$, c_{e2} is found as;

$$c_{e2} = \frac{1}{\sqrt{3}} S_y \frac{b^2}{c^2} \quad (23)$$

(b) at $r=a$, $\sigma_{rp}=-P_a$, c_{p2} is found as;

$$c_{p2} = -\frac{2}{\sqrt{3}} A \ln a + \frac{1}{\sqrt{3}} (S_y - A) \frac{b^2}{a^2} - P_a \quad (24)$$

Loading stress distribution

(a) Elastic region (O-A)

Substituting equations (21) and (23) into equations (15) to (17) gives;

$$\sigma_{re} = \frac{1}{\sqrt{3}} S_y b^2 \left(\frac{1}{c^2} - \frac{1}{r^2} \right) \quad (25)$$

$$\sigma_{\theta e} = \frac{1}{\sqrt{3}} S_y b^2 \left(\frac{1}{c^2} + \frac{1}{r^2} \right) \quad (26)$$

$$\sigma_{ze} = \frac{1}{\sqrt{3}} S_y \frac{b^2}{c^2} \quad (27)$$

(b) Plastic region (A-B)

Substituting equations (22) and (24) into equations (18) to (20) gives;

$$\sigma_{rp} = \frac{2}{\sqrt{3}} A \ln \frac{r}{a} + (S_y - A) \left(\frac{1}{a^2} - \frac{1}{r^2} \right) - P_a \quad (28)$$

$$\sigma_{\theta p} = \frac{2}{\sqrt{3}} A \left(1 + \ln \frac{r}{a} \right) + \frac{b^2}{\sqrt{3}} (S_y - A) \left(\frac{1}{a^2} + \frac{1}{r^2} \right) - P_a \quad (29)$$

$$\sigma_{zp} = \frac{1}{\sqrt{3}} A + \frac{2}{\sqrt{3}} A \ln \frac{r}{a} + \frac{1}{\sqrt{3}} (S_y - A) \frac{b^2}{a^2} - P_a \quad (30)$$

2.3.2. Unloading Stage

When the autofrettage pressure is totally removed, the unloading will be elastic if there is no reverse yielding. In this case, unloading stresses follow the Lamé equations. As a result, residual stresses developed elastic and plastic parts of the cylinder are calculated as;

(a) Residual stresses developed in elastic part of the cylinder ($b \leq r \leq c$)

$$\sigma_{re} = \frac{1}{\sqrt{3}} S_y b^2 \left(\frac{1}{c^2} - \frac{1}{r^2} \right) - P_a \frac{a^2}{c^2 - a^2} \left(1 - \frac{c^2}{r^2} \right) \quad (31)$$

$$\sigma_{\theta e} = \frac{1}{\sqrt{3}} S_y b^2 \left(\frac{1}{c^2} + \frac{1}{r^2} \right) - P_a \frac{a^2}{c^2 - a^2} \left(1 + \frac{c^2}{r^2} \right) \quad (32)$$

$$\sigma_{ze} = \frac{1}{\sqrt{3}} S_y \frac{b^2}{c^2} - P_a \frac{a^2}{c^2 - a^2} \quad (33)$$

(b) Residual stresses developed in plastic part of the cylinder ($a \leq r \leq b$)

$$\sigma_{rp} = \frac{2}{\sqrt{3}} A \ln \frac{r}{a} + \frac{b^2}{\sqrt{3}} (S_y - A) \left(\frac{1}{a^2} - \frac{1}{r^2} \right) - P_a - P_a \frac{a^2}{c^2 - a^2} \left(1 - \frac{c^2}{r^2} \right) \quad (34)$$

$$\sigma_{\theta p} = \frac{2}{\sqrt{3}} A \left(1 + \ln \frac{r}{a} \right) + \frac{b^2}{\sqrt{3}} (S_y - A) \left(\frac{1}{a^2} + \frac{1}{r^2} \right) - P_a - P_a \frac{a^2}{c^2 - a^2} \left(1 + \frac{c^2}{r^2} \right) \quad (35)$$

$$\sigma_{zp} = \frac{1}{\sqrt{3}} A + \frac{2}{\sqrt{3}} A \ln \frac{r}{a} + \frac{1}{\sqrt{3}} (S_y - A) \frac{b^2}{a^2} - P_a - P_a \frac{a^2}{c^2 - a^2} \quad (36)$$

2.3.3. Operating Stage

When the operating pressure is acting, the stresses developed in the cylinder will be reduced due to compressive residual stresses developed at the inner surface of the cylinder.

(a) Stresses developed in elastic part of the cylinder under operating pressure ($b \leq r \leq c$)

$$\sigma_{re} = \frac{1}{\sqrt{3}} S_y b^2 \left(\frac{1}{c^2} - \frac{1}{r^2} \right) - P_a \frac{a^2}{c^2 - a^2} \left(1 - \frac{c^2}{r^2} \right) + P_w \frac{a^2}{c^2 - a^2} \left(1 - \frac{c^2}{r^2} \right) \quad (37)$$

$$\sigma_{\theta e} = \frac{1}{\sqrt{3}} S_y b^2 \left(\frac{1}{c^2} + \frac{1}{r^2} \right) - P_a \frac{a^2}{c^2 - a^2} \left(1 + \frac{c^2}{r^2} \right) + P_w \frac{a^2}{c^2 - a^2} \left(1 + \frac{c^2}{r^2} \right) \quad (38)$$

$$\sigma_{ze} = \frac{1}{\sqrt{3}} S_y \frac{b^2}{c^2} - P_a \frac{a^2}{c^2 - a^2} + P_w \frac{a^2}{c^2 - a^2} \quad (39)$$

(b) Stresses developed in plastic part of the cylinder under operating pressure ($a \leq r \leq b$)

$$\sigma_{rp} = \frac{2}{\sqrt{3}} A \ln \frac{r}{a} + \frac{b^2}{\sqrt{3}} (S_y - A) \left(\frac{1}{a^2} - \frac{1}{r^2} \right) - P_a - P_a \frac{a^2}{c^2 - a^2} \left(1 - \frac{c^2}{r^2} \right) + P_w \frac{a^2}{c^2 - a^2} \left(1 - \frac{c^2}{r^2} \right) \quad (40)$$

$$\sigma_{\theta p} = \frac{2}{\sqrt{3}} A \left(1 + \ln \frac{r}{a} \right) + \frac{b^2}{\sqrt{3}} (S_y - A) \left(\frac{1}{a^2} + \frac{1}{r^2} \right) - P_a - P_a \frac{a^2}{c^2 - a^2} \left(1 + \frac{c^2}{r^2} \right) + P_w \frac{a^2}{c^2 - a^2} \left(1 + \frac{c^2}{r^2} \right) \quad (41)$$

$$\sigma_{zp} = \frac{1}{\sqrt{3}} A + \frac{2}{\sqrt{3}} A \ln \frac{r}{a} + \frac{1}{\sqrt{3}} (S_y - A) \frac{b^2}{a^2} - P_a - P_a \frac{a^2}{c^2 - a^2} + P_w \frac{a^2}{c^2 - a^2} \quad (42)$$

2.4. Autofrettage Pressure

The autofrettage pressure can be obtained by equating radial stress components at elastic plastic interface ($r=b$). That is:

$$\sigma_{re} = \sigma_{rp} \quad (\text{at } r=b)$$

$$P_a = \frac{1}{\sqrt{3}} \left[2A \ln \frac{b}{a} + (S_y - A) b^2 \left(\frac{1}{a^2} - \frac{1}{b^2} \right) - S_y b^2 \left(\frac{1}{c^2} - \frac{1}{b^2} \right) \right] \quad (43)$$

3. DETERMINATION OF OPTIMUM AUTOFRETTAGE PRESSURE

3.1. High Pressure Cylinder of a Waterjet Intensifier Pump

Intensifier pump is the heart of a waterjet cutting machine and mainly consists of piston assembly, check valve assemblies, low pressure cylinder and high pressure cylinders as shown in Figure 4.

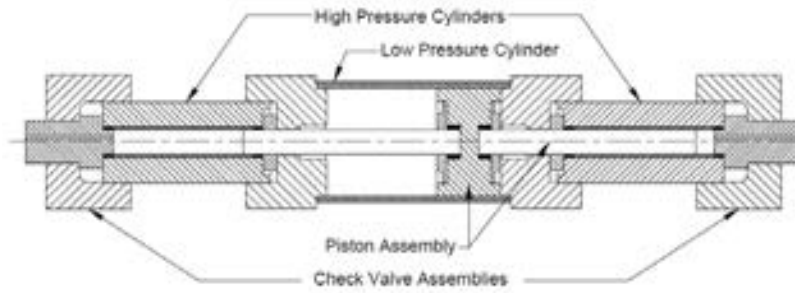


Figure 4 Sectional view of an intensifier pump [10]

High pressure cylinders are essential part of the intensifier pump where ultra-high pressure (410 MPa) develops. In the design of these cylinders, alloy steels are widely used due to some mechanical properties such as high strength to weight ratio, toughness, resistance to fatigue and corrosion. In this intensifier unit AISI 4340 alloy steel is used as the cylinder material. The cylinder has 14 mm inner, 38 mm outer radius and 160 mm length. Chemical composition, mechanical properties and tensile stress-strain relationship are given in Table 1,2 and Figure 5 respectively.

Table 1 Chemical composition of AISI 4340 alloy steel [11]

%Fe	%Ni	%Cr	%C	%Mo	%Others
96.6	1.8	0.8	0.4	0.25	0.1

Table 2 Mechanical properties of AISI 4340 [11]

Treatment	Yield Strength in Tension (MPa)	Yield Strength in Compression (MPa)	Ultimate Tensile Strength (MPa)	Modulus of Elasticity (GPa)	Tangent Modulus (MPa)	Brinell Hardness	Poisson's Ratio
Q&T (510°C) oil	1200	1130	1270	200	1489	400	0.3

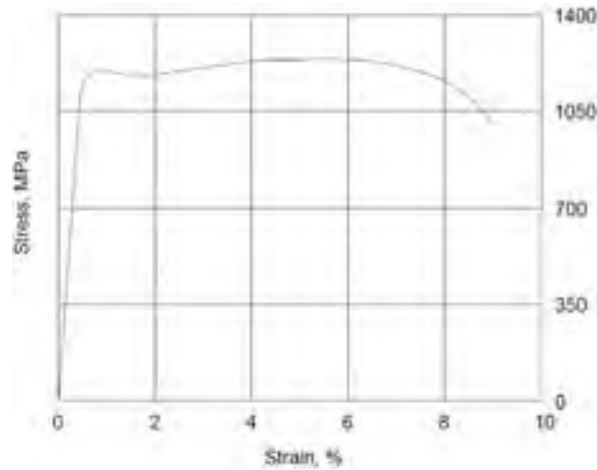


Figure 5 Tensile stress-strain curve of AISI 4340 [11]

Without autofrettage process the stresses developed through the wall of the cylinder is easily calculated by using Lamé equations. Figure 6 represents all stress components of the cylinder under 410 MPa operating pressure. It is seen in the figure that maximum von mises stress (821,7 MPa) occurs at the inner surface of the cylinder. It is actually this stress magnitude which will result fatigue failure for cyclic loading. This level is reduced by the compressive residual stress due to autofrettage process which will result an increase in fatigue life.

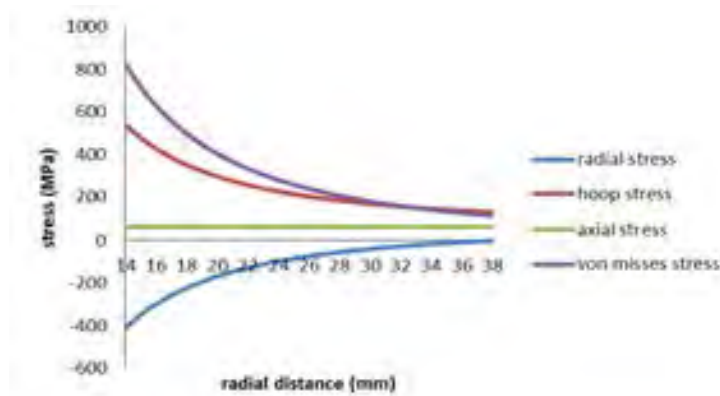


Figure 6 Stress distribution for non-autofretted high pressure cylinder under operating pressure of 410 MPa

3.2. Optimization

The amount of autofrettage pressure is to be applied in the wall of the cylinder is an important issue in the autofrettage process. With an increase in the autofrettage pressure, maximum von mises stress at critical section (elasto-plastic radius) in operating stage decreases to a minimum value, but after a specific value of autofrettage pressure it begins to increase as shown in Figure 7.

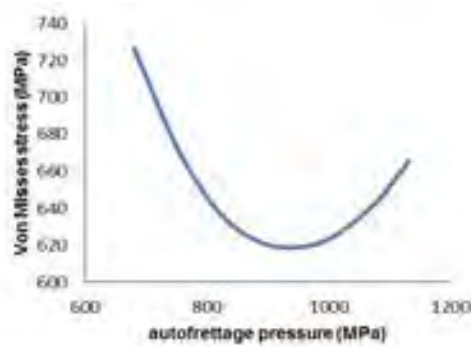


Figure 7 Von mises stress developed at elasto-plastic radius due to operating pressure for different autofrettage pressures

As seen in equation (43), for a specific cylinder, Autofrettage pressure becomes the function of elasto-plastic radius and the problem is a one variable optimization problem with a non linear constraint. By using constrained nonlinear minimization solver with interior point algorithm in Matlab Optimtool the optimum amount of elasto-plastic radius is determined.

After autofrettage process, von mises stress distribution under operating pressure decreases through the wall of the cylinder and the maximum von mises stress occurs at the elasto-plastic radius. Thus, objective function is the minimization of von mises stress at this point and written as;

$$\text{Minimize, } f = \sigma_{ie} = \sigma_{ip}, \text{ at } r = b$$

When the autofrettage pressure is removed (unloading stage) residual von mises stress must not exceed yield stress in compression of the material which depends on the amount of strain hardening. Otherwise, reverse yielding starts due to Bauschinger effect. This is a nonlinear inequality constraint and expressed as;

$$\sigma'_{\text{unloading}} \leq S'_{yc} \text{ where } S'_{yc} = 2S_y - \sigma'_{\text{loading}}, \text{ at } r = a$$

$$\sigma'_{\text{unloading}} \leq 2S_y - \sigma'_{\text{loading}}$$

$$\sigma'_{\text{loading}} + \sigma'_{\text{unloading}} - 2S_y \leq 0$$

Another consideration is the lower and upper limits of elasto-plastic radius (b), which must be between inner radius (a) and outer radius (c);

$$a < b < c$$

Results

From all this considerations, optimum elasto-plastic radius is found as;

$$b_{\text{optimum}} = 18.862 \text{ mm}$$

and by substituting it in equation (45), optimum autofrettage pressure is calculated as;

$$P_{\text{aoptimum}} = 936.260 \text{ MPa}$$

Stress distributions through the wall of the cylinder; loading, unloading and operating stages are given in Figures 8, 9, 10 respectively. Maximum von mises stress after autofrettage process is decreased to 618.93 MPa from 821.7 MPa comparing to non-autofrettaged cylinder.

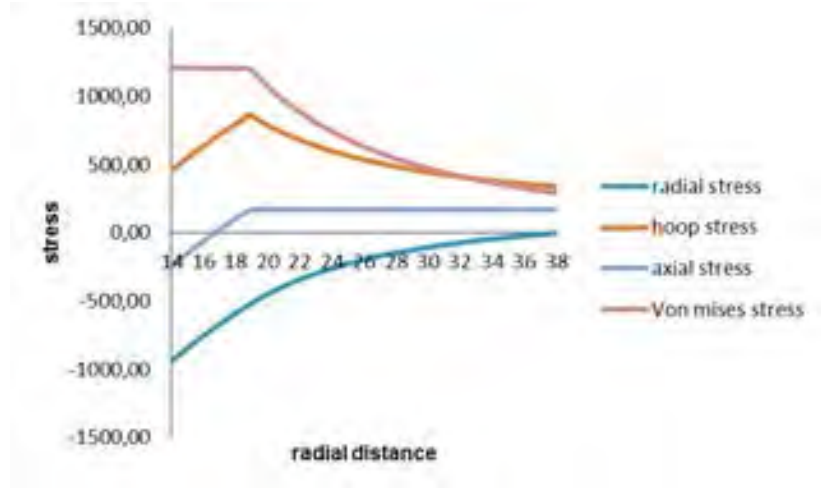


Figure 8 Stress distributions through the wall of the cylinder-loading stage

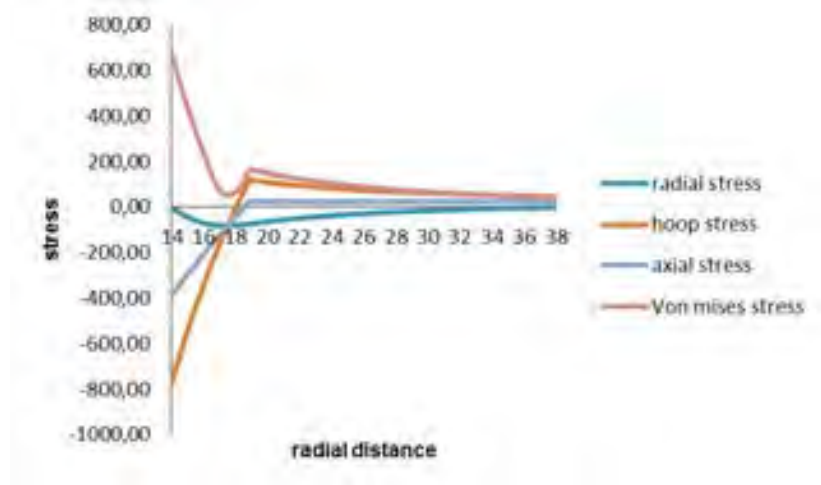


Figure 9 Stress distributions through the wall of the cylinder-unloading stage

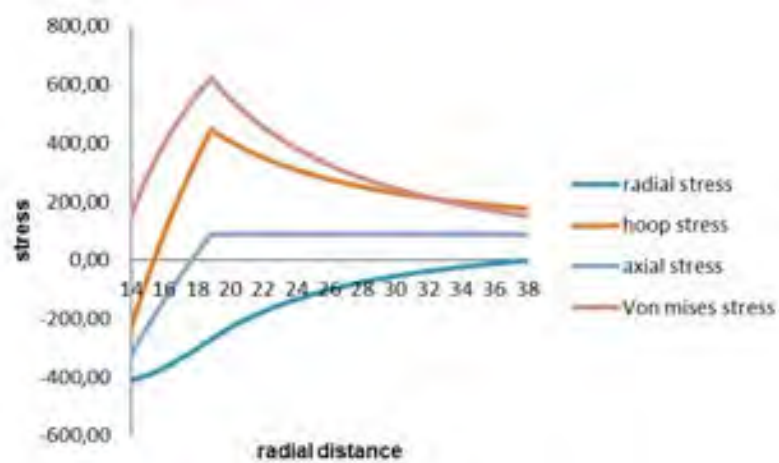


Figure 10 Stress distributions through the wall of the cylinder-operating stage

4. FEM ANALYSIS

In this section validation of analytic model has been shown by comparing to the 2D finite element model created in ANSYS 14. Quarter of the cylinder is modelled by using PLANE183 element. Plane strain assumption and symmetric boundary conditions are chosen. Uniform and regular meshes are used with 0.15 element sizes. Loading, unloading and operating stages are solved step by step. Default parameters of ANSYS 14 are used for the rest.

Figures 11 to 13 represents von mises stress distribution through the wall of the cylinder for loading, unloading and operating stages respectively and all stress components for each stage is given in Figures 14 to 16. Comparison of analytical results with respect to FE results is also tabulated in Table 4.

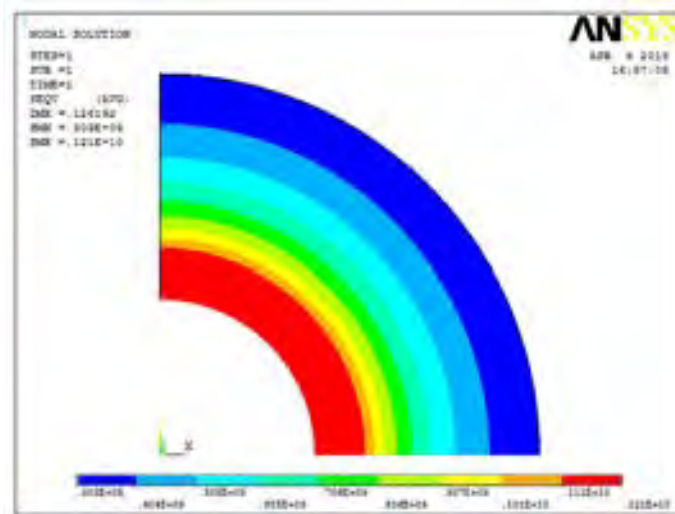


Figure 11 Stress distribution-loading stage

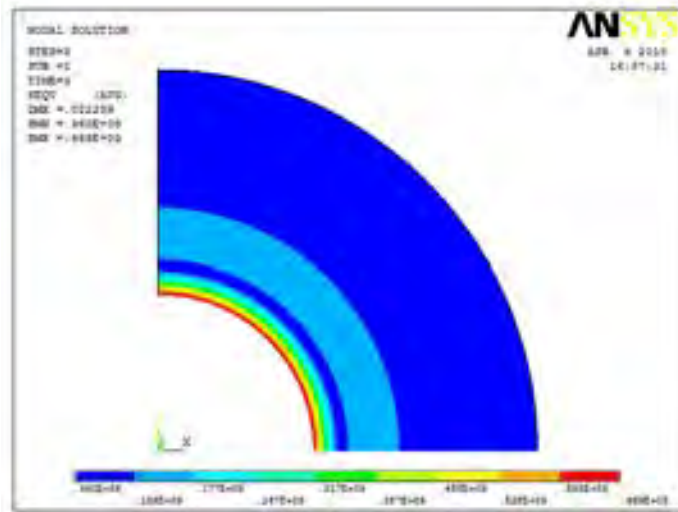


Figure 12 Stress distribution-unloading stage

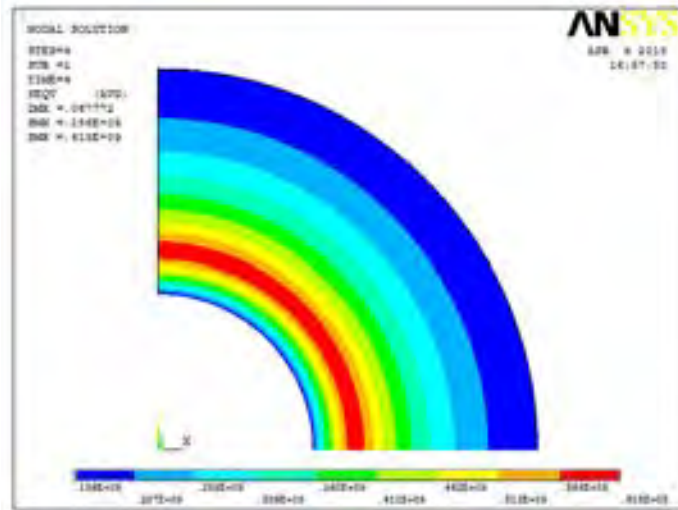


Figure 13 Stress distribution-operating stage

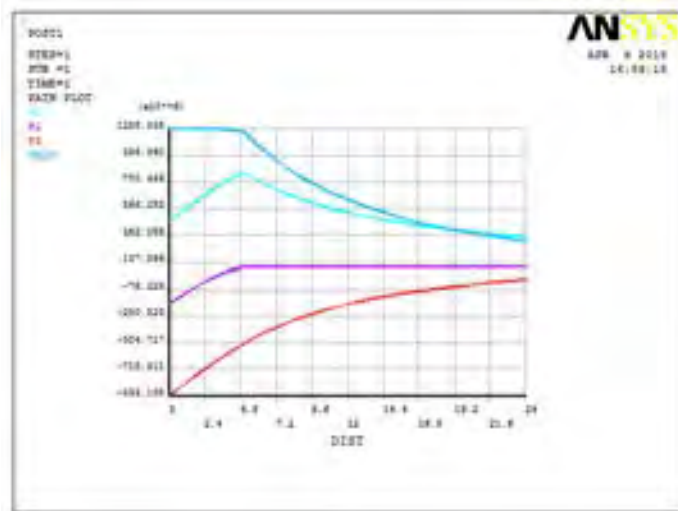


Figure 14 All stress components-loading stage

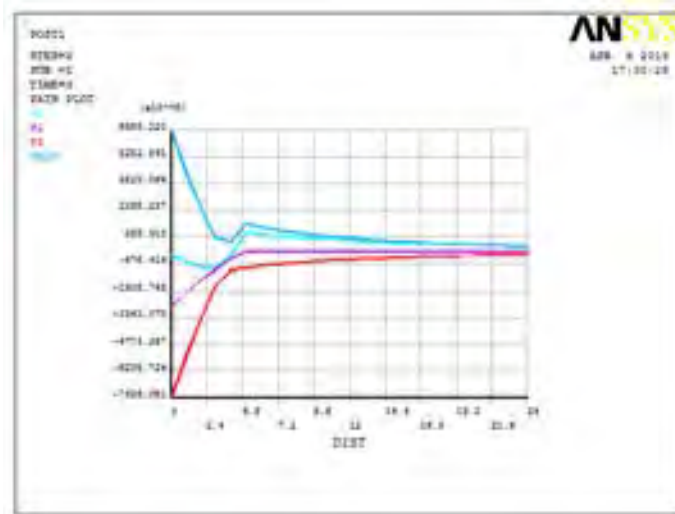


Figure 15 All stress components-unloading stage

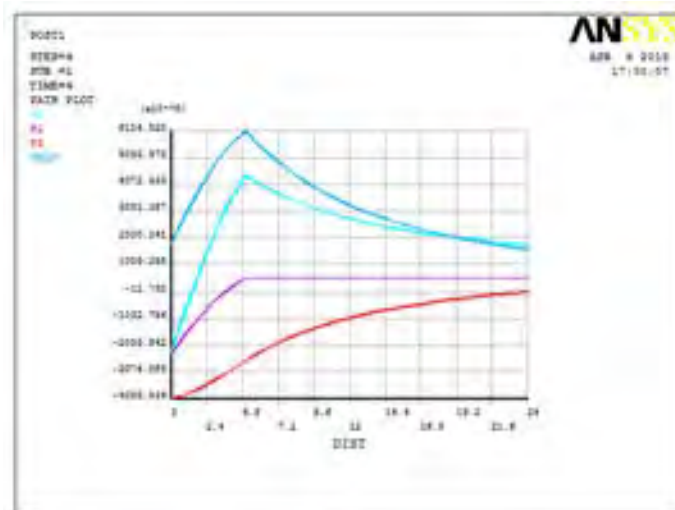


Figure 16 All stress components-operating stage

Table 4 Comparison of analytical results with respect to FE results

Von Mises Stress	Analytical Results (MPa)	ANSYS results (MPa)
Inner surface	152.54	177.46
Elasto-plastic radius	618.93	615.00
Outer surface	152.49	156.45

5. CONCLUSION

In this study analytical approach for the determination of optimum autofrettage pressure of a thick walled cylinder is presented. Bilinear kinematic hardening model is used in the analysis. Optimum value of autofrettage pressure is found as a value that will give minimum value of maximum Von-Mises stress on the wall of the cylinder under operating pressure. Considering elasto-plastic radius as the design variable, optimum value of the elasto-plastic radius is found by using matlab© optimtool. By using ANSYS 14©, stress analysis of the autofrettaged cylinder has been performed. The use of analytical approach and finite element method is illustrated with a specific high pressure cylinder. Optimum value of autofrettage pressure and maximum von misses stress in operating stage are found as 936.26 MPa and 618.93 MPa respectively. As illustrated in Table 4, results for both analytical and finite element method are almost the same. In non-autofrettage cylinder, Von-Mises stress was 821.7 MPa which shows the advantage obtained from autofrettage process. The effect of reduction in Von-mises stress will be seen as an improvement in fatigue behaviour of the cylinder.

REFERENCES

- [1] Hill R. (1950). The mathematical theory of plasticity, Oxford University Press, New York.
 - [2] Topçu F. and Filiz İ.H. (2009). Yüksek basınç silindirleri tasarımında farklı yöntemler, Makine Tasarım ve İmalat Teknolojileri Kongresi, Konya.
 - [3] Majzoobi G., Farrahi G. and Mahmoudi A. (2003). A finite element simulation and an experimental study of autofrettage for strain hardened thick-walled cylinders. Materials Science&Engineering, vol.A359, 326-331
 - [4] Hojjati H., and Hassani A. (2007). Theoretical and finite element modelling of autofrettage process in strain-hardening thick-walled cylinders. International Journal of Pressure Vessels and Piping. vol.84, 310-319.
 - [5] Rayhan A.M., Ghosh N.C. and Alam T.E. (2010). Optimum design of pressure vessel subjected to autofrettage process. World Academy of Science, Engineering Technology. vol. 4, 10-26.
 - [6] Huang X. (2005). A general autofrettage model of a thick-walled cylinder based on tensile-compressive stress-strain curve of a material. J. Strain Analysis, vol. 40, 599-607.
 - [7] White C., Bronkhorst C. and Anand L. (1990). An improved isotropic-kinematic hardening model for moderate deformation metal plasticity. Mechanics of Materials, vol.10.
 - [8] Lee E.Y., Lee Y.S., Yang Q.M., Kim J.H., Cha K.U. and Hong S.K. (2009). Autofrettage process analysis of a compound cylinder based on the elastic-perfectly plastic and strain hardening stress-strain curve. Journal of Mechanical Science and Technology, vol. 23, no. 12, 3153-3160.
 - [9] Ragab A., Abbas A. and Khorshied S. () "Experimental verification of the autofrettage process for thick-walled tubes," Proc Instn Mech Engrs, vol. 215 Part C, pp. 727-736
 - [10] "Waterjet Component Service INC.", Component Report, Majet Su Jeti ile Kesme Sanayi, Bixsan Sanayi Sitesi, Istanbul, TURKEY
 - [11] ASM International, "Atlas of stress-strain curves", Materials Park OH 44073-0002, pp. 108, 2002
-

THE EFFECTS OF FEATHER COLOR ON HATCHABILITY TRAITS, GROWTH PERFORMANCE, AND SURVIVAL RATE IN JAPANESE QUAILS (COTURNIX COTURNIX JAPONICA)

Kadir ÖNK

Department of Crop and Animal Production, Kars Vocational College, Kafkas University, TR-36100,
Kars - TURKEY.

Mehmet SARI

Department of Animal Science, Faculty of Veterinary Medicine, Mehmet Akif Ersoy University, TR-15030,
Burdur - TURKEY

Muammer TILKI

Department of Animal Science, Faculty of Veterinary Medicine, Kafkas University, TR-36100,
Kars - TURKEY

Serpil ADIGÜZEL İŞIK

Department of Animal Science, Faculty of Veterinary Medicine, Kafkas University, TR-36100,
Kars - TURKEY

Tuncay TUFAN

Department of Animal Nutrition and Nutritional Diseases, Faculty of Veterinary Medicine,
Kafkas University, TR-36100, Kars - TURKEY

Abstract

This study was conducted to determine the effects of feather color on hatchability traits, growth performance, and survival rate in Japanese quails. Quails having piebald, yellow, white and brown feather color were used in this study. For this purpose, a total of 1975 quails (Piebald: 561, Yellow: 428, White: 484 and Brown: 502) hatched from a total of 2796 eggs obtained from a total of 2796 quails (Piebald: 826, Yellow: 580, White: 708 and Brown: 682) whose ages were between 10 and 12 weeks were studied. The effect of feather color on hatchability, hatching and late embryonic death rate was found to be statistically significant. It has been determined that hatchability for yellow, brown, white and piebald were 73.79%, 73.60%, 68.36% and %67.91% respectively and hatching weight for the same feather colors were 80.00%, 78.07%, 72.67% and 73.91%. The effect of different feather color on values of survival rates in different growth periods were statistically significant ($P < 0.001$). From the first to sixth week, survival rate was the highest in piebald and white quails and the lowest in brown and yellow quails. In this study, the effect of different feather color on growth performance was also statistically important ($P < 0.001$). Live weights of piebald colored quails were higher than the quails having other colors from the hatching to the sixth week. In conclusion, there is a need to evaluate yellow and brown quails in respect to the hatching traits and the advantages of piebald and yellow quails in respect to growth performance and to conduct further studies to determine genetic parameters for growth and hatching traits of quails having different feather color.

Keywords: Quails, feather color, hatching traits, survival rate, growth performance.

1. Introduction

The Japanese quail is the smallest avian species in poultry farming, which is used for their yields, and is recommended as a practical and applicable option for meeting animal protein (meat and eggs) deficit in developing countries (Ernts 1978, Koçak 1985, Panda ve Singh 1990). Factors affecting hatching efficiency and accordingly business profitability in quail production are fertilization rate, hatching performance, hatchability, and embryonic mortality. The leading factors that affect growing in quails include race, feeding, age, sex, feed consumption and feed efficiency, coop conditions, and diseases (Koçak 1985).

Numerous studies have been conducted in order to determine the characteristics of live weight of Japanese quail. Average live weights from hatching to various age periods have been calculated in different levels by many researchers. The number of studies conducted on the growing, survival, slaughtering, and carcass characteristics of chicks hatching from the eggs of Japanese quails with different feather colours is very limited.

The purpose of this study was to determine the effect of the feather colour on the hatching and growing characteristics and survival of Japanese quails.

2. Materials and Methods

This study was conducted at the Quails Unity Application and Research Farm of the Faculty of Veterinary Medicine, Kafkas University in Kars, Turkey. In this study, Japanese quail with different colored feathers (piebald, yellow, white and brown) were used. Quails were divided into groups of 2 males and 8 females and 4 males and 16 females from every colour group. Breeding quails were fed with a feed containing 20% crude protein and 2900 kcal/kg energy (NRC, 1994). Eggs obtained from breeding quails were placed in incubator. Wing numbers were attached to hatching chicks, they were weighed by using a 0.01 grams precision scale to record their hatching weights and their growing was followed for 6 weeks through weighing every week.

Hatching chicks were fed *ad libitum* with a feed containing 24% crude protein and 2900 kcal/kg energy for a period of 6 weeks (NRC, 1994). Table 1 illustrates the ration compound used to feed the mother and juvenile population in the study and its nutritional values. Quail chicks used in the study were grown in apartment-shaped cages having dimensions of 110 x 45 x 100 cm, with 5 floors and containing sections with the dimensions of 20 x 45 x 100 cm on each floor. In the first week after hatching, they were kept in the temperature of 35-37 °C, this temperature was reduced a few degrees gradually every week and reached to 20-21 °C in the 5th week. Lighting was given for 24 hours.

Fertility (%) = (number of fertilized eggs / total numbers eggs placed into incubator) x 100.

Hatchability of incubated eggs (%) = (number of released chicks / total number of egg placed into incubator) x 100.

Hatchability of fertile eggs (%) = (number of released chicks / number of fertilized eggs placed into incubator) x 100.

Statistical Analyses

Least Squares Method was used in SPSS statistical computer program in examining the growth of the quails. According to this model;

For the growth characteristics of quails within the weeks 0-6,

The following equation was formed: $Y_{ijk} = \mu + a_i + b_j + e_{ijk}$.

Where; Yijklm is the examined yield characteristics value of any quail, μ is the expected mean value, ai is the feather colour (i: 4-; white, yellow, brown, and piebald), bj is sex (male, female), and eijk is the error term.

Chi-Square Test was used to conduct the statistical evaluation of hatching characteristics and survival.

Table 1. Ingredient and nutrient content of the basal diets, (%)

Ingredient	Layer Diet	Grower Diet
Corn	53.00	57.20
Soybean	36.00	33.00
Vegetable oil	3.25	-
Fish flour	-	7.60
Lime stone	6.00	1.00
Dicalciumphosphate	1.00	0.50
DL-Methionine	0.10	0.10
Salt	0.30	0.25
Vit.-Min. Premix ¹	0.35	0.35
Analysed nutrient composition, DM basis		
Crude protein %	20.08	24.04
Metabolic energy, kcal/kg	2908	2900

¹Provided per kg concentrate: Vitamin A, 21000 IU; Vitamin D₃, 4200 IU; Vitamin E, 52.5 mg; Vitamin K₃, 4.38 mg; Vitamin B₁, 5.25mg; Vita-min B₂, 12.25 mg; Vitamin B₆, 7 mg; Vitamin B₁₂, 0.03 mg; Folic acid, 1.75 mg; D-Biotin 0.08 mg; Vitamin C, 87.5 mg; Niacin, 70 mg; Cal-D-Pantothenat, 14 mg; Choline chloride 218.75 mg; Fe, 140 mg; Zn, 105 mg; Cu, 14 mg; Co, 0.35 mg; I, 1.75 mg; Se, 0.26 mg; Mn, 140 mg.

²Provided by calculation (NRC, 1994)

3. Results

Table 2 illustrates hatching results of eggs of quails with different feather colours. According to Table 2; while fertilization, early embryonic mortality, and dead-in-shell rates of quails with different feather colours were statistically insignificant ($p > 0.05$); hatching performance, late embryonic mortality rates and hatchability were found statistically significant ($p < 0.05$, $p < 0.01$). While hatching performance rate was higher in quails with the feather colours of yellow, brown, white, and piebald respectively, hatchability was higher in quails with feather colours of yellow, brown, piebald, and white. While late period embryonic mortality rate was highest in the white feathered quails, it was lowest in yellow feathered quails.

Table 2. Hatching results of eggs of quails with different feather colours

Feather colour	Total eggs (number)	Fertility rate (%)	Hatching performance (%)	Hatchability of fertile eggs (%)	Early embryonic mortality (%)	Late embryonic mortality (%)	Dead-in-shell (%)
		NS	*	**	NS	*	NS
Piebald	826	91.88	67.91b	73.91b	13.04	5.01b	8.04
Yellow	580	92.24	73.79a	80.00a	10.28	4.11b	5.61
White	708	94.07	68.36b	72.67b	10.96	7.66a	8.71
Brown	682	94.28	73.60a	78.07a	11.35	4.36b	6.22
Total	2796	93.10	70.63	75.87	11.53	5.34	7.26

NS: Non significant ($P > 0.05$), *: $P < 0.05$, **: $P < 0.01$, a, b: The differences among the values bearing different superscript on the same row line are significant ($P < 0.05$).

Table 3. Survival rate of quails with different feather colours

Feather colour	Hatching (adet)	1. week (%)	2. week (%)	3. week (%)	4. week (%)	5. week (%)	6. week (%)
		***	***	***	***	***	***
Piebald	561	87.70a	82.71a	80.21a	79.86a	79.68a	78.97a
Yellow	428	78.27b	71.50b	69.15b	68.46b	66.12b	65.65b
White	484	83.68a	79.34a	77.89a	77.07a	76.86a	74.03a
Brown	502	78.88b	70.12b	68.33b	68.13b	66.93b	66.73b

Total	1975	82.43	76.26	74.26	73.72	72.81	71.76
--------------	-------------	--------------	--------------	--------------	--------------	--------------	--------------

***: $P < 0.01$, a, b: The differences among the values bearing different superscript on the same row line are significant ($P < 0.05$).

Table 3 illustrates survival values of quails with different feather colours in various growing phases. When Table 3 was examined, it was observed that survival values were statistically significant ($p < 0.001$). Within the period from the first week until the 6th week, survival was highest in piebald and white feathered quails; whereas, it was lowest in brown and yellow feathered quails.

Table 4 shows live weight levels of quails with different feather colours in various ages (hatching-42nd day). Hatching weights and live weights in the following weeks among quails with different feather colours were found to be statistically significant ($p < 0.001$).

Table 4. Live weight levels of quails with different feather colours in various ages (hatching-42nd day)

	Hatching weights (g)		7th day live weights (g)		14th day live weights (g)		21st day live weights (g)		28th day live weights (g)		35th day live weights (g)		42nd day live weights (g)	
	n	$\bar{X} \pm S\bar{x}$	n	$\bar{X} \pm S\bar{x}$	n	$\bar{X} \pm S\bar{x}$	n	$\bar{X} \pm S\bar{x}$	n	$\bar{X} \pm S\bar{x}$	n	$\bar{X} \pm S\bar{x}$	n	$\bar{X} \pm S\bar{x}$
Colour		***		***		***		***		***		***		***
Piebald	561	8.44±0.03a	492	20.57±0.25a	464	44.02±0.55a	450	78.92±0.87a	448	116.36±1.12a	447	157.05±1.19a	443	189.23±1.27a
Yellow	428	7.66±0.04d	335	15.54±0.30d	306	33.80±0.67c	296	61.34±1.07bc	293	91.83±1.38bc	283	126.01±1.50b	281	152.11±1.59b
White	484	8.10±0.04b	405	17.43±0.27b	384	35.90±0.60b	377	62.63±0.95b	373	93.19±1.23b	372	124.81±1.31bc	368	151.20±1.39bc
Brown	502	7.94±0.03c	396	16.45±0.27c	352	33.12±0.63c	343	59.32±0.99c	342	88.87±1.28c	336	121.64±1.38c	335	147.31±1.45c
Sex								***		***		***		***
Male							753	62.93±0.67	749	93.37±0.87	740	126.55±0.94	732	150.84±0.99
Female							713	68.18±0.70	707	101.76±0.90	698	138.20±0.97	695	169.09±1.03
Colour * Sex								NS		NS		NS		NS
Piebald	Male						208	76.29±1.27	208	112.31±1.63	208	151.99±1.75	206	179.21±1.85
	Female						242	81.56±1.18	240	120.42±1.52	239	162.12±1.63	237	200.25±1.73
Yellow	Male						154	58.96±1.48	152	88.13±1.91	148	120.73±2.07	146	144.52±2.20
	Female						142	63.72±1.54	141	95.52±1.98	135	131.29±2.17	135	159.09±2.07
White	Male						208	60.48±1.27	207	89.48±1.64	207	118.73±1.75	204	143.31±1.86
	Female						169	64.78±1.41	166	96.90±1.83	165	130.89±1.96	164	159.09±2.07
Brown	Male						183	55.93±1.36	182	83.55±1.75	177	114.77±1.89	176	137.30±2.00
	Female						160	62.65±1.45	160	94.19±1.86	159	128.50±2.00	159	157.32±2.11
Total	1975	8.03±0.02	1628	17.50±0.14	1506	36.70±0.31	1466	65.55±0.49	1456	97.56±0.63	1438	132.38±0.68	1427	159.96±0.71

NS: Non significant (P > 0.05), ***: P < 0.01, a, b, c, d: The differences among the values bearing different superscript on the same row line are significant (P < 0.05).

While hatching weight was highest in the quails with piebald feathered colour, it was lowest in the quails with yellow feather. Hatching weights and 7th day live weights were in the quails with piebald, white, brown and yellow feather colours respectively from the highest to the lowest. Live weight gains were found in piebald, white, yellow and brown feathered quails on the 21st day, 28th day, 35th day and 42nd day.

As sex can be decisively determined in the 3rd week in quails, sex-related values were given after the 3rd week. The correlation among quails according to sex was statistically significant ($p < 0.001$) and female quails had higher live weights than male quails on all days.

The effect of interaction of the colour x sex systems on the 21st, 28th, 35th, and 42nd day growth characteristics was found to be statistically insignificant ($p > 0.05$).

4. Discussion

Fertilization rate, early period embryonic mortality rates, and dead-in-shell mortality rates among the hatching characteristics of quails with piebald, yellow, white, and brown feather colours in the study were determined to be statistically insignificant ($p > 0.05$).

Average fertilization rate of the quails was found to be 93.10% in the study. This rate was higher than the general rate of 92.40% reported by Çağlayan and Yılmaz (2006) in quails with white, brown and piebald feather colours. Fertilization rate was higher than the rate of 70.81-86.31% reported by Dere et al., (2009) in the study, where they analyzed the effect of mother's age, egg weight, storage period, and temperature on fertilization and hatching performance, the general rate of 88.15% reported by Kırmızıbayrak and Altınel (2001) based on eggs obtained from quails in different age groups, the general rate of 89.03% reported by Şeker et al., (2004) based on mother's age and egg weight groups and the rate of 60.70-70.90% reported by Şeker et al., (2006) in another study; whereas, this rate was similar to the rate of 93.10% reported by Shafey and Al-mohsen (2002) in the study where they determined the embryonic growing, hatching time, and hatching performance of meat-type breeding quails hatched under continuous green light, and the rate of 93.33% reported by Silici et al., (2011) regarding groups fed with a feed containing 1.5% of grinded grape seed; and was lower than the rates of 94.00% and 96.67% reported by Silici et al., (2011) based on the control group and the group fed with a feed containing 1.0% of grinded grape seed.

Hatching performance was statistically significant in the study ($p < 0.05$). Hatching performance was higher in yellow (73.79%), brown (73.60%), white (68.36%), and piebald (67.91%) coloured quails respectively and the mean value was 70.63%. This obtained value was lower than the general rate of 78.86% reported by Çağlayan and Yılmaz (2006); was similar to rate of 67.71% reported by Kırmızıbayrak and Altınel (2001), and the rate of 67.88-72.52% reported by Ertürk and Çelik (2004) based on trial groups 1, 2, 3, 4 and the control group; and was higher than the rate of 57.44% reported by Saylam SK (1999) and the rates of 29.00-49.00% reported by Alkan et al., (2008).

In this study, hatchability was statistically significant ($p < 0.01$). It was higher than the rates of 68.93%, 69.38%, 60.78%, and 55.76% reported by Sarıca and Soley (1995), and the rates of 69.29%, 70.94%, 73.30%, 72.26%, and 65.89% reported by Küçükylmaz et al., (2001); was lower than the rates of 86.13-87.12% reported by Silici et al., (2011) and the rate of 92.21% reported by Çağlayan and İnal (2006); and was similar to the rate of 78.96% reported by Sarı et al. (2010).

Early period embryonic mortality rate was 11.53% and the late period embryonic mortality rate was 5.34% in the study. Early period embryonic mortality rate was lower than the rate of 14.65% reported by Çağlayan and Yılmaz (2006), and the rate of 27.30% reported by Laçın et al., (2008); was higher than the rates of 4.02-6.30% reported by İpek et al., (2003), 8.84% reported by Şeker et al., (2004), and 8.64% reported by Sarı et al., (2010). Late period embryonic mortality rate was lower than the rate of 6.09% reported by Sarı et al., (2010), and 26.50% reported by Laçın et al., (2008); was similar to the rates of 5.11% and 5.45% reported by İpek et al., (2003) based on the mother age groups of 10-14 and 15-18.

Dead-in-shell rate was higher than the rate of 6.25% reported by Kırmızıbayrak and Altinel (2001) according to group with egg weights of 9-10 g, and the rate of 6.31% reported by Sarı et al., (2010); was similar to the rate reported by Kırmızıbayrak and Altinel (2001) according to group with egg weights of 12-13 g; and was lower than the rates of 10.10-26.87% in other egg weight groups and age groups.

The survival rate in the study was 82.43% in the 1st week; however, it reduced in the following weeks and was 71.76% in the 6th week. It was lower than the survival rates of 98.76-100.00% reported by Sarıca and Soley (1995) between 2nd-6th weeks, 80.38-89.15% reported by İnal et al., (1996), 95.10-100.00% reported by Nazlıgül et al., (2005) according to different egg weight groups, and 96.8-74.88% reported by Garip and Dere (2006); on the other hand, it was similar to the rates of 74.04-79.17% reported by İnal et al., (1996) in the 5th generation.

Hatching weights of white and piebald feathered quails were respectively 8.10 and 8.44 grams and this value was similar to 8.11-8.57 grams reported by Çağlayan and Yılmaz (2006). Hatching weight in brown feathered quails was 7.94 grams and this value was lower than 8.86 grams reported by Yılmaz and Çağlayan (2008) and Çağlayan and Yılmaz (2006).

The general average hatching weight of quails with different feather colours was 8.03 g. This value was similar to 8.23 g reported by Kırmızıbayrak and Altinel (2001) and 8.20 g reported by Sezer (2007), and was higher than the weights of 6.00 g reported by Almedia et al., (2002), 7.28-7.26 g reported by Alkan et al., (2008), 7.61 g reported by Saatçı et al., (2003) and 7.39-7.40 g reported by Nariç and Aksoy (2012).

No colour comparisons were made since there have been no studies conducted on the live weight levels of quails with different feather colours in different ages.

The 7th day live weight which was determined as 15.50 g in the study was lower than the weights of 28.25 g reported by Kalpak and Söğüt (2009), 24.83 g reported by Alkan et al., (2012) and 22.94-23.93 g reported by Nariç and Aksoy (2012); was similar to the weight of 17.12 g reported by Şahin et al.,(2011); and was higher than the weight of 10.36-13.75 g reported by Aytaç and Karabayır (2012).

The 14th day live weight was 36.70 g in this study. This value was lower than the weights varying between 41.86-74.00 grams reported by Saatçı et al., (2003), Shookhmand et al., (2007), Seker et al., (2009), Sarı et al., (2010), and Nariç and Aksoy (2012); was higher than the weights varying between 17.31-32.42 grams reported by Özbey and Erkmén (2000) and Şahin et al., (2011).

The 21st day live weight which was 65.55 g in this study was lower than the weights varying between 75.02-115.23 grams reported by Saatçı et al., (2003), Metin Sezer (2007), Seker et al., (2009) and Sarı et al., (2010); was similar to the weights of 66.74 and 58.82 grams reported by Arslan et al., (2001) in natural and wetted lathyrus sativus groups, 63.90 grams reported by Bonos et al., (2010) according to the control group, and

66.41 grams reported by Alkan et al., (2012); and was higher than the weights of 37.13 grams reported by Sahin et al., (2011), and 52.96 grams reported by Sahin et al., (2012).

The 28th day live weight was 97.56 g in this study. This value was lower than the weights varying between 108.13-158.81 grams reported by Denek et al., (2007), Sezer (2007), Sari et al., (2010), Şahin et al., (2011) and Alkan et al., (2012); and was similar to the weight of 99.67 grams reported by Sahin et al., (2012).

The 35th day live weight was 132.38 g in this study. This result was lower than the weights varying between 141.05-186.77 grams reported by Saatçı et al., (2003), Denek et al., (2007), Sezer (2007), Sari et al., (2010) and Sahin et al., (2012); and was similar to the weights of 132.84 g reported by Sarıca (1998) in the continuous and blinking lightning groups exposed to red light, 127.00-135.80 g reported by Vali et al., (2005), 132.60 g reported by Yalçın et al., (2007) in the group consuming low energy level ration, and 134.65 g reported by Kalpak and Söğüt (2009).

The 42nd day live weight was 159.96 g in this study. This rate was lower than the weights of 192.30 g reported by Sezer (2007), 174.56 g reported by Kalpak and Söğüt (2009), 190.98 g reported by Alkan et al., (2012), 173.86 g reported by Yıldırım and Öztürk (2012), and 234.00 g reported by Alkan et al. (2013); was similar to the weights of 162.48 g reported by Vali et al., (2005) and 162.20 g reported by Yalçın et al. (2007); and was higher than the weight of 150.68 g reported by Arslan et al., (2001).

The fact that the average live weight levels of quails with different feather colours in different ages in this study were lower than other conducted studies was associated with the lower values of yellow, white, and brown feathered quails. Live weight levels of quails with piebald feather colour in the study on various days were similar to other studies.

Consequently, it is required to conduct further studies evaluating the advantages of the yellow and brown feathered quails in terms of hatching characteristics and piebald and yellow coloured quails in terms of growing performance and determining the genetic parameters related to growing and hatching characteristics of quails with different feather colours. In terms of growing performance, piebald feathered quails had the highest value, which was followed by yellow feathered group. Therefore, further studies on determining the genetic parameters related to growing and hatching characteristics of quails with different feather colours are required.

References

1. Alkan S, Karabağ K, Galic A ve ark. Effects of genotype and egg weight on hatchability traits and hatching weight in japanese quail. *S Afr J Anim Sci.*, 38 (3): 231-237. 2008.
2. Alkan S, Karşlı, T., Galiç, A., Karabağ, K., Balcıoğlu, M.S.: Japon bıldırcınlarında (*coturnix coturnix japonica*) canlı ağırlığa ait genetik parametrelerin şansa bağlı regresyon modeli kullanılarak tahmin edilmesi. *Kafkas Univ. Vet. Fak. Derg.*, 18 (6): 935-939, 2012.
3. Alkan, S., Karşlı, T., Karabağ, K., Galiç, A.: Farklı hatlardaki Japon bıldırcınlarında (*coturnix coturnix japonica*) farklı kesim yaşı ve cinsiyetin karkas özelliklerine etkisi. *Süleyman Demirel Üniv. Zir. Fak.si Derg.*, 8 (1):12-18, 2013.
4. Almeida, M.I.M.; Oliveira, E.G.; Ramos, P.R.; Veiga, N.; Dias, K.: Growth performance of meat male quails (*coturnix coturnix japonica*) of two lines under two nutritional environments. *Archives of Veterinary Sci.*, 7 (2): 103-108, 2002.

5. Arslan, C., Şeker, E., İnal, F.: Bildircinlerin rasyonlarına katılan adi mürdümügün (*Lathyrus sativus* L.) ıslatılmasının büyüme performansı üzerine etkisi. *Kafkas Univ Vet Fak Derg.*, 7 (1): 27-32, 2001.
6. Aytaç, S., Karabayır, A.: The effect of floor differences in cages on the incubation results and live weight of Japanese Quails. *J. Anim. Vet. Adv.*, 11 (8): 1204-1207, 2012.
7. Bonos, E.M., Christaki, E.V., Florou-Paneri, P.C.: Performance and carcass characteristics of Japanese quail as affected by sex or mannan oligosaccharides and calcium propionate. *South African Journal of Animal Sci.*, 40 (3):173-184, 2010.
8. Çağlayan, T., İnal, Ş.: Bildircinlerde kuluçkalık yumurta ağırlığının kuluçka sonuçları ile büyüme ve yasama gücüne etkisi. *Vet. Bil. Derg.*, 22 (1-2): 11-19, 2006.
9. Çağlayan, T., Yılmaz, A.: Farklı tüy rengine sahip bildircinlerde kuluçka özellikleri ile büyüme ve yaşam gücü. *Veterinarium*, 17, 18-25, 2006.
10. Denek, N., Kaplan, O., Avcı, M., Can, A.: Effects of microbial Phytase on growth performance, carcass yield, biochemical parameters, oxidative stress and faecal Phosphorus content of Japanese quails. *J. Anim. Vet. Adv.*, 6 (8): 1031-1035, 2007.
11. Dere, S., İnal, Şeref, İ., Çağlayan, T., Garip, M., Tilki, M.: the effects of parent age, egg weight, stronge length and temperature on fertility and hatchability of japanese quail eggs. (*Coturnix Coturnix Japonica*). *J Anim Vet Adv.*, 8 (7): 1289-1291, 2009.
12. Ernts, R.A.: Raising and propagating Japanese quail. *Agr. Sci. Univ. of California. Leaflet* 2738. 1978.
13. Ertürk, M.M., Çelik, S.: Damızlık japon bildircini (*coturnix coturnix japonica*) rasyonlarında tavuk kesimhane artıkları ununun soya küspesi yerine kullanım olanakları: 2- kuluçka ve yumurta kalite özelliklerine etkileri. *Akdeniz Üniv. Zir. Fak. Derg.*, 2004, 17 (1): 67-74, 2004
14. Garip, M., Dere, S.: Bildircin yumurtalarında depolama süresi ve sıcaklığının civcivlerin büyüme ve yaşama gücüne etkisi. *Vet. Bil. Derg.*, 22 (1-2): 69-74, 2006.
15. İnal, Ş., Dere, S., Kırıkçı, K., Tepeli, C.: Japon bildircinlerinde (*coturnix coturnix japonica*) canlı ağırlığa göre yapılan seleksiyonun yumurta verimi, yumurta ağırlığı, fertilite, kuluçka randımanı ve yaşama gücüne etkileri. *Vet. Derg.* 12 (2) 5-14, 1996.
16. İpek, A., Şahan, Ü., Yılmaz, B.: Japon bildircinlerinde (*Coturnix coturnix japonica*) çıkış ağırlığının gelişme ve yumurta verim özelliklerine etkisi. *Uludağ. Üniv. Zir. Fak. Derg.*, 7(1): 23-32, 2003.
17. Kalpak, O., Soğut, B.: Effect of feed restriction on growth performance of japanese quail (*Coturnix coturnix japonica*). *J Anim Vet Adv.*, 8 (6): 1079-1082, 2009.
18. Kırmızıbayrak, T., Altınel, A.: Japon bildircinlerinin (*Coturnix coturnix japonica*) önemli verim özellikleriyle ilgili bazı parametreler. *İstanbul Üniv. Vet. Fak. Derg.*, 27 (1): 309-328, 2001.
19. Koçak, Ç. Bildircin Üretimi. *Ege Zootekni Derneği Yayınları. No: 1.* 1985.
20. Küçükylmaz, K., Başer, E., Erensayın, C., Orhan, H., Arat, E.: Japon bildircinlerinde damızlık yumurta ağırlığının kuluçka sonuçları, besi performansı ve yumurta verim özellikleri üzerine etkisi. *Hayvancılık Araştırma Derg.*, 11 (1): 6-12, 2001.
21. Laçın, E., Çoban, O., Sabuncuoğlu, N.: Effects of egg storage material and storage period on hatchability in japanese quail. *Asian-Aust. J. Anim. Sci.*, 21 (8):1183-1188, 2008.

22. Narinç, D., Aksoy, T.: Effects of mass selection based on phenotype and early feed restriction on the performance and carcass characteristics in Japanese Quails. *Kafkas Univ. Vet. Fak. Derg.*, 18 (3): 425-430, 2012.
23. Nazlıgöl, A., Türkyılmaz, MK., Bardakcıoğlu, H.E.: Japon Bildircimlerinde (*Coturnix coturnix japonica*) kuluçkalık yumurta ağırlığının çıkış ağırlığı büyüme performansı ve yaşama gücüne etkisi. *İ.Ü. Vet.Fak. Derg.*, 31 (2): 33-40, 2005.
24. NRC: Nutrition requirements of poultry. Ninth Revised Edition, National Academy Press, Washington, DC. 1994.
25. Özbey, O., Ekmen, F.: Japon bildircimlerinde mevsim ve yerleşim sıklıklarının büyüme, yaşama gücü ve karkas üzerine etkileri. *Y.Y.Ü. Vet. Fak. Derg.*, 11 (1): 28-33, 2000.
26. Panda, B., Singh, R.P.: Development in processing quail. *J. World Poultry Sci.* 46, 219-234, 1990.
27. Saatçı, M., Ap Dewi, I., Aksoy, A.R.: Application of REML procedure to estimate the genetic parameters of weekly live weights in one-to-one sire and dam pedigree recorded Japanese quail. *J. Anim. Breed. Genet.*, 120, 23-28, 2003.
28. Sarı, M., Saatçı, M., Tilki, M.: Japon bildircimlerinde (*coturnix coturnix japonica*) canlı ağırlığa ait özelliklerin genetik parametrelerinin REML metodu ile hesaplanması. *Kafkas Univ Vet Fak Derg.*, 16 (5): 729-733, 2010.
29. Sarı, M., Tilki, M., Saatçı, M., ışık, S. Önk, K.: Japon bildircimlerinde (*coturnix coturnix japonica*) ebeveyn yaşı, yumurta ağırlığı ve şekil indeksinin kuluçka özellikleri ve yaşama gücü üzerine etkisi. *F.Ü. Sağ. Bil. Vet. Derg.*, 24 (2): 93 – 97, 2010.
30. Sarıca, M. ve Soley, F.: Bildircimlerde (*Coturnix coturnix japonica*) Kuluçkalık yumurta ağırlığının kuluçka sonuçları ile büyüme ve yumurta verim özelliklerine etkileri, YUTAV Uluslararası Tavukçuluk Fuarı ve Konferansı, 24-27 Mayıs, İstanbul, 475-484, 1995.
31. Sarıca, M.: Işık rengi ve aydınlatma şeklinin bildircimlerin büyüme ve karkas özellikleri. *Turk. J. Vet. Anim. Sci.*, 23, 367-372, 1998.
32. Sezer, M.: Genetic parameters estimated for sexual maturity and weekly live weights of japanese quail (*coturnix coturnix japonica*). *Asian-Aust. J. Anim. Sci.*, 20 (1): 19-24, 2007.
33. Shafey, T. M. ve Al-Mohsen, H.: Embryonic growth, hatching time and hatchability performance of meat breeder eggs incubated under continuous green light. *Asian-Aust. J. Anim. Sci.*, 15, 1702-1707, 2002.
34. Silici, S., Güçlü Kocaoğlu, B., Kara, K.: Effect of supplementation of crushed grape seed on breeding quail (*coturnix coturnix japonica*) diet on production, hatching performance, and egg quality. *Sağlık Bilimleri Dergisi (Journal of Health Sciences)* 20 (1): 68-76. 2011.
35. Şahin, T., Aksu Emalı, D., Kaya, İ., Sarı, M., Kaya, Ö.: The effect of single and combined use of probiotic and humatein quail (*coturnix coturnix japonica*) diet on fattening performance and carcass parameters. *Kafkas Univ. Vet. Fak. Derg.*, 17 (1): 1-5, 2011.
36. Şeker, İ., Kul, S., Bayraktar, M.: Effects of parental age and hatching egg weight of japanese quails on hatchability and chick weight. *International Journal of Poultry Sci.*, 3 (4): 259-265, 2004.
37. Şeker, İ., Bayraktar, M., Kul, S.: Effect of preincubation long-term storage and warming on hatchability of japanese quail eggs (*Coturnix coturnix japonica*) *Archiv für Geflügelkunde.* 70 (1): 35-40, 2006.
38. Vali, N., Edriss, M.A., Rahmani, H.R.: Genetic parameters of body and some carcass traits in two quail strains. *International Journal of Poultry Sci.*, 4, 296-300, 2005.

39. Yalçın, S., Buğdaycı, K.K., Özsoy, B., Erol, H.: Farklı enerji düzeylerindeki rasyonlara L-karnitin ilavesinin bıldırcınlarda performans ve bazı kan parametreleri üzerine etkisi. Ankara Üniv Vet Fak Derg., 54, 127-132, 2007

40. Yıldırım, A ve Öztürk, E.: Japon bıldırcını rasyonlarında soya küspesi yerine pamuk tohumu küspesi ikamesinin büyüme performansı ve karkas özellikleri üzerine etkisi. GOÜ. Zir. Fak. Derg., 29 (2): 55-62, 2012.

41. Yılmaz, A., Çağlayan, T.: Farklı Tüy Rengine Sahip Japon Bıldırcınlarında (*Coturnix coturnix japonica*) Yumurta Ağırlığı, Şekil İndeksi ve Çıkım Ağırlığı ile Bu Özellikler Arası İlişkiler. F.Ü. Sađ. Bil. Vet. Derg., 22 (1): 5-8, 2008.

DETERMINATION OF OXYGEN GAIN IN HYDRAULIC STRUCTURES

Asli SARI

Department of Survey and Projects, Istanbul Metropolitan Municipality, Turkey,
asli.sari@ibb.gov.tr

Tuba BOSTAN

Department of Civil Engineering, YTU, Istanbul, Turkey,
bostan@yildiz.edu.tr

Ali COŞAR

Department of Civil Engineering, YTU, Istanbul, Turkey,
cosar@yildiz.edu.tr

Abstract

Dissolved oxygen concentration in rivers is one of the most vital parameters for water quality and aquatic life. Hydraulic structures built in river systems increase oxygen saturation by supplying natural aeration. Smooth and stepped spillways are of those systems that provides natural aeration. In this article, the contribution of oxygen saturation from smooth and stepped spillways with various flowrates is studied. In the experiments, a smooth spillway and a five stepped spillway structure are used respectively. The studies showed that stepped spillways provide a better aeration efficiency than smooth spillways for all flowrate cases considered. In addition, it's observed that aeration efficiency of stepped spillways varies according to flowrate and stream flow regime. The stepped spillways demonstrated "nap flow regime" in low flowrates and "skimming flow regime" in high flowrates.

Key words: *Aeration efficiency, smooth spillways, stepped spillways, nap flow regime, skimming flow regime*

1 Introduction

Although hydraulic structures are used these days for a variety of purposes, including drinking water supplies, electricity generation, and irrigation, the fact that these structures help increase the aeration efficiency of water and therefore provide natural water treatment is normally ruled out. On the other hand, cascades, especially on stepped spillways, and the subsequent hydraulic jump, decrease the amount of required dissolved oxygen, and thus contribute to the permanence of natural life. The stepped structures that are widely used, especially in drinking water treatment facilities, can also be used for aeration purposes in the vicinity of rivers or on the coastline. Natural aeration is defined as the process of oxygen passing into the water, without the use of special equipment. There are three mechanisms that enable natural aeration; these include jet streams, hydraulic jumps, and cascades. To ensure natural aeration, hydraulic jumps and jet streams are used together with hydraulic structures, such as stepped channels (cascades) or spillways, depending on the location and purpose of aeration.

The process of oxygen transfer from air to water is composed of the following steps: air ingresses into the water, air is transported from the aeration area, and oxygen is dissolved inside air bubbles in the water (Küçükali, 2006).

The experimental studies show that there is a linear correlation between the energy lost in natural aeration applications and the amount of oxygen ingress into the water. This implies that the aeration efficiency increases with increasing amounts of lost energy of water.

The particles floating on the water surface and suspended particles have an impact on the hydrodynamic properties and aeration efficiency of the stream by decreasing the surface tension and impeding air-water surface area. The salt and chlorine content of the water increases the solubility rate. The change in the concentration of oxygen dissolved in the water with temperature is shown in Figure 1.

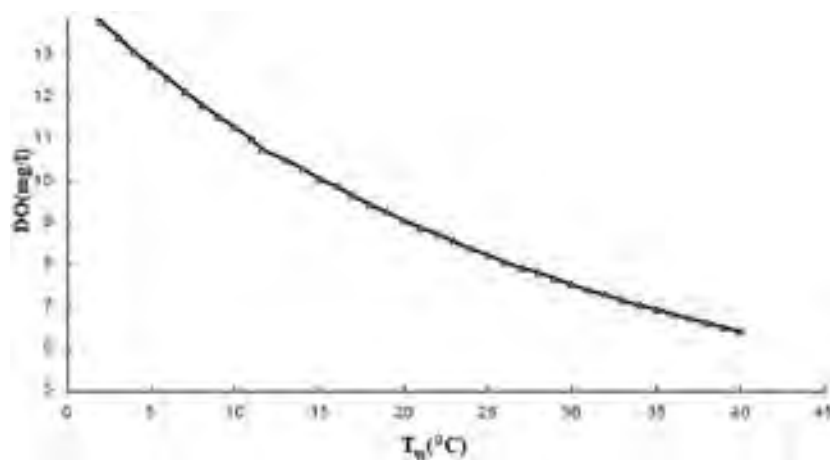


Figure 1. The change in the concentration of oxygen dissolved in the water with temperature (Colt, 1984)

2 Studies about the Aeration

Scholars have begun to study on air water streams quite recently. The first successful study in this field was carried out by R. Ehrenberger in Austria. Later on, another study was conducted by L.G. Straub in the North America (Chanson, 2002).

Natural aeration studies concentrate mostly on hydraulic structures, where the inclination is especially high ($J_o > 0,002m/m$), such as water gates, hatchways, and stepped channels. The physical and chemical characteristics of water change with temperature, and this affect the air, water, and gas dynamics. The aeration equations are given for standard temperature values. The equation developed by Gulliver et al. (1993) is used to calculate the aeration efficiency in standard temperature values.

Gameson (1957), Chanson (1995), Ervine (1998) and Gulliver et al. (1998) are a few of successful scholars, whose work focuses on aeration performance of hydraulic structures.

Gameson is the first researcher, who worked on the oxygen transfer in hydraulic structures such as water gates, hatchways, and spillways in 1957. Gameson, who took upstream and downstream measurements of dissolved oxygen concentrations, showed that the aeration performance of stepped spillways and water gates was better than the other hydraulic structures.

In Rajaratnam study in 1961, he observed the point distribution of air content in the water, for a variety of Fr_1 values inside the hydraulic jump. In this study, the greatest air ingress was shown to take place at the beginning of the jump (Küçükali, 2006).

Leutheusser et al. (1973), and Babb and Aus (1981) discovered that the largest air concentration and the most air bubbles were in the beginning of the hydraulic jump. In addition, Leutheusser et al. (1973) showed that stream conditions played an important role in the determination of aeration efficiency in the hydraulic jump (Küçükali, 2006). Hoyt and Sellin, in their experimental study in 1989, calculated the amount of air ingress. Chanson (1995) summarized the previous studies on hydraulic jumps. Avery and Novak (1978) worked on the oxygen transfer in the hydraulic jump and water gates, and showed that the oxygen transfer rate was a function of the Reynolds and Froude numbers of the stream. Avery and Novak (1978) and Wilhelms et al. (1981) showed that the aeration efficiency in the hydraulic jump increases with increasing Re numbers.

Stepped spillways are among the most widely used hydraulic structures recently in open channels and dams, due to their advantages in relation to energy loss and aeration. On the other hand, these structures have been used for centuries. The oldest stepped spillway is found in Greece (Akarnanian).

In recent years, spilled channels are used not only for civil engineering applications, but also within the realm of environmental engineering, in treatment systems, and for aesthetic purposes.

Stepped spillways are basically constructed by stepping the spillway (Ağırlioğlu, 2007). In stepped spillways, the total cascade is divided into a number of smaller cascades. In the design of a stepped spillway, a number of factors, including economic, hydraulic, geologic, hydrologic, social, and environmental factors, should be taken into consideration.

In the design of a stepped spillway, firstly, the flow regime is determined. There are three possible flow regimes in stepped spillways. These are nappe flow regime, transition flow regime, and skimming flow regime. The flow regimes in a stepped spillway can be seen in Figure 2.

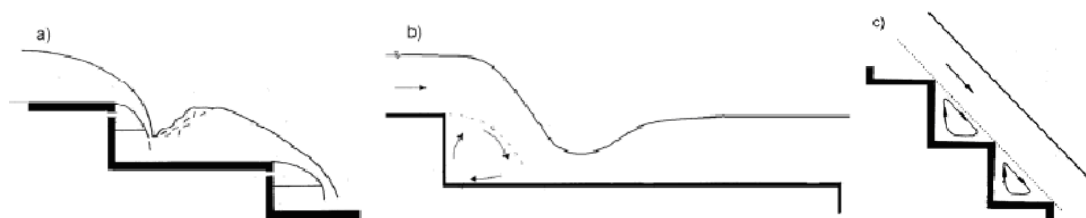


Figure 2. The flow regimes in stepped spillways (Murillo, 2006)
a) Nappe flow regime b) Transition flow regime c) Skimming flow regime

3 Testing System

The tests that were carried out in order to identify the effect of hydraulic structures in open channels on oxygen transfer took place in the Yıldız Technical University, Faculty of Civil

Engineering, Hydraulic, Coastal, and Harbor Engineering Laboratories. In these tests, different hydraulic structures were placed inside the open channel, and the effect of these on aeration efficiency was examined through oxygen measurements before and after the structures.

The tests were carried out inside the linear open channel with a rectangular section, which was 12 m long, 40 cm wide and 65 cm high. The channel floor is horizontal and the sides of the channel are made of glass (Figure 3).



Figure 3. Channel used for tests

The flow inside the channel was provided by means of two tanks placed on the bottom and top segments of the channel. The water stored in the bottom tank was pumped to the top tank, and transferred to the channel from here. In this way, the water was circulated throughout the system. The amount of the flow through the channel can be adjusted using the valve at the egress of the top tank. The rate of the flow inside the channel was determined by means of the triangular weir placed at the entrance to the channel and the rating curve. The flow depths in the channel, on the other hand, were measured by a limnimeter. A water gate was placed at the end of the channel so that the flow depths can be adjusted.

In the experimental part of this study, two different hydraulic structures, both made of sheet steel, were used. The first of these was a 30 cm high and 60 cm long spillway. The spillway crest was 20 cm. The second hydraulic structure that was used for testing purposes, on the other hand, was a 30 cm high and 60 cm long five-step spillway. In this spillway, the step widths were 12 cm, while step heights were 6 cm. In order to ensure that all three flow regimes can be observed during the tests, different flow rates were used.

A hydraulic structure constructed in an open channel helps the water gain oxygen through the formation of turbulence and air bubbles in the channel. These two hydraulic structures were placed at a distance of 3 m from the beginning of the channel and oxygen measurements were taken before and after placing the structure. In order to prevent oxygen intake during water flow from the tank to the channel and to calm the flow, a brick was placed at the entrance to the channel.

The dissolved oxygen and temperature measurements before and after the structure in the flow were made by means of two YSI EcoSense DO200 manual oxygenmeters. Before the tests began, the oxygenmeters were calibrated at the Yıldız Technical University's Environmental Engineering Department.

The measurement range of the oxygenmeter for dissolved oxygen was 0-20 mg/L with $\pm 2\%$ sensitivity. These values were $(-6) - (46) ^\circ\text{C}$ and $\pm 0.3 ^\circ\text{C}$, respectively, for temperature measurements.

To be able to determine the aeration efficiency of the hydraulic structures used in the tests, the dissolved oxygen concentration in the inflow should be below the saturation level. In order to reduce the dissolved oxygen concentration, sodium sulfite (Na_2SO_3), and cobalt chlorite (CoCl_2) as a catalyzer were added to the bottom tank. As oxygen is consumed during this reaction, the dissolved oxygen amount inside the water is reduced. On the other hand, dissolved oxygen values were not able to be reduced to zero, due to oxygen gain in the tank entrance and exit, as well as inside the channel.

In order to calculate the oxygen efficiency of hydraulic structures used in these tests, the dissolved oxygen values in the water, before and after the structures were placed in the channel, were measured every 30 seconds. The dissolved oxygen amounts were measured for each structure for different flow rate values, and E_{20} values were calculated.

4 Investigation of Aeration Efficiency in Spillways

The aeration efficiency was investigated in two different structures for different flow rate values. In the stepped structures, nappe, transition, and skimming flow regimes were generated, and the effect of these flow regimes on oxygen gain was examined.

The hydraulic structures used for testing purposes and the changes that occurred on flow regimes are shown in Figure 4.



Figure 4. Five-step system (nappe, transition, and skimming flow)

In the case of the nappe flow regime, the flow behaves like a different cascade system in each step. The nappe flow is observed in small flow rate values. With increasing flow rate values, the nappe flow regime changes first into the transition flow regime, and then into the skimming flow regime.

The flow in the transition flow regime looks like a skimming flow in the first step of the hydraulic structure, while it looks more like a nappe flow in the following steps. Vortices are observed on the steps.

In the skimming flow regime, on the other hand, a straight flow is observed on the steps, almost as if there were no steps at all. With increasing flow rates, the flow regime changes from transition flow to skimming flow, and the flow becomes steadier.

The oxygen measurements were taken for each structure for each flow rate value, before and after the placement of the structure inside the channel. For each data series, a aeration efficiency value was calculated. Because different temperatures are generated during the tests, E_{20} values were calculated using the Equation (1) for 20°C, so as to allow a comparative analysis (Gulliver, 1990).

$$1 - E_{20} = (1 - E_T)^{1/f_T} \quad (1)$$

where, f_T is the temperature correction factor and is calculated using Equation (2)

$$f_T = 1 + 0.02103(T_w - 20) + 8.261 \times 10^{-5} (T_w - 20)^2 \quad (2)$$

Table 1 shows the flow conditions and results obtained from different testing systems.

Table 1. Flow regimes in spillway and five-step spillway systems

Spillway System				Five-Step Spillway System			
Nappe (cm)	Q (l/s)	E20	Flow Regime	Nappe (cm)	Q (l/s)	E20	Flow Regime
2.8	130	0.167134	Nappe	3.6	130	0.26299	Nappe

4.4	135	0.15256	Nappe	4.6	135	0.280632	Nappe
5.2	140	0.131422	Nappe -Transition	5.5	140	0.221217	Nappe - Transition
6.7	145	0.102654	Nappe - Transition	6.7	145	0.186518	Nappe - Transition
7.7	150	0.087468	Transition -Skimming	7.5	150	0.169734	Transition -Skimming
8.8	155	0.075546	Transition -Skimming	8.5	155	0.12267	Transition -Skimming
9.8	160	0.048753	Skimming	9.5	160	0.08291	Skimming
10.5	165	0.035056	Skimming	10.2	165	0.060565	Skimming

The flow rate and E_{20} values obtained for each structure are graphically shown below. As can be seen from Figure 5, the highest aeration efficiency value was obtained for lowest flow rate level, where the contact duration was the maximum. With increasing flow rate values, the aeration efficiency was observed to decrease.

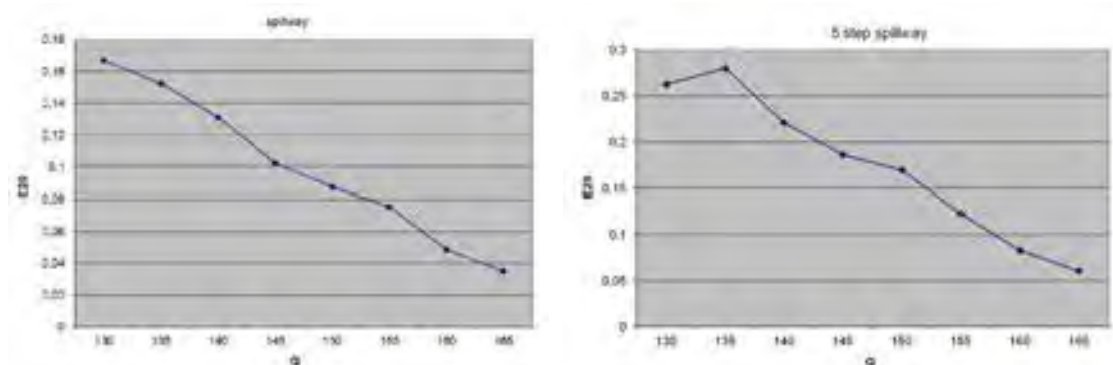
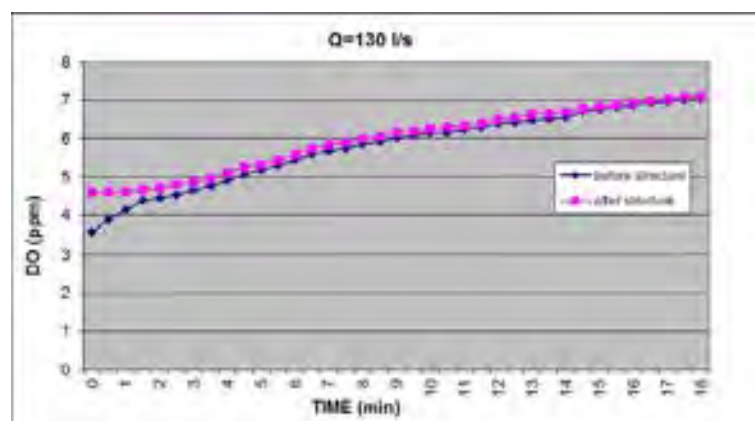


Figure 5. Change in E_{20} with flow rate values in spillway and five-step spillway systems

In the nappe flow regime, a certain amount of increase was observed in the aeration efficiency with increasing flow rates. As the flow changed into the transition flow regime, the aeration efficiency began to decrease. During the skimming regime, on the other hand, the aeration efficiency decreased with increasing flow rate values.

In addition, the tests showed that the saturation level is generally achieved to a large extent in the first 20 minutes. The oxygen gain is quite rapid in the beginning, while the gain becomes gradually slower as the saturation level is approached, because the need for oxygen decreases. This shows that the oxygen transfer rate between water and air is a function of dissolved oxygen content in the water (Figure 6-7).



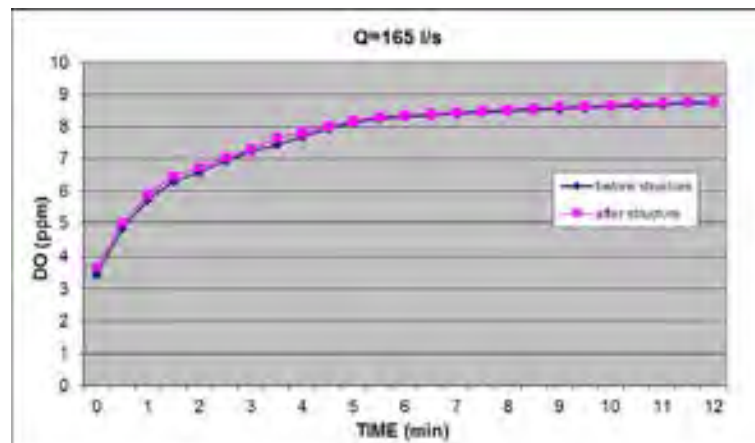
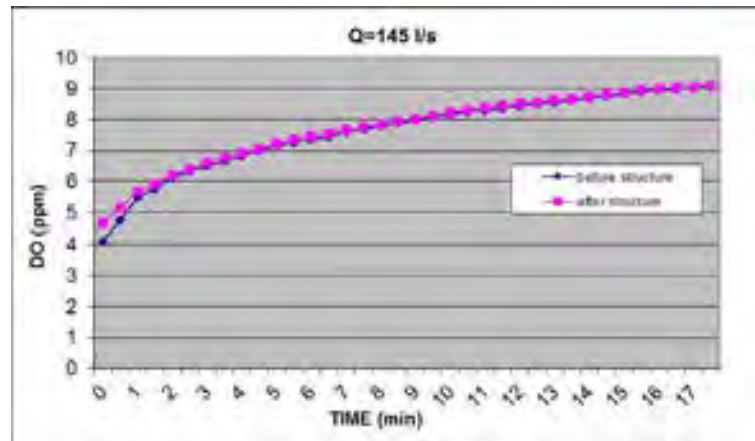
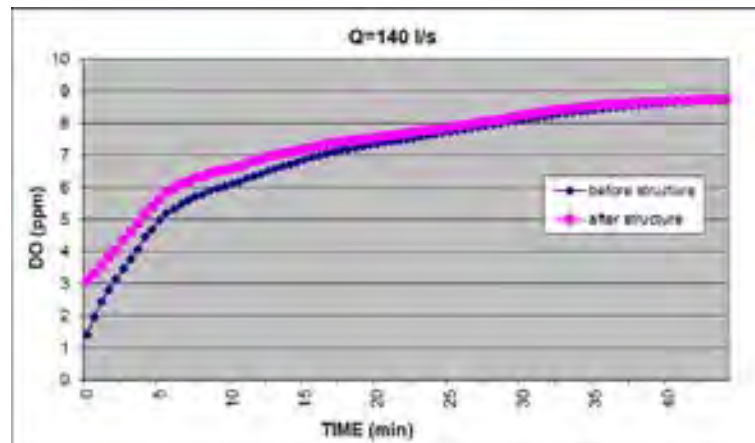


Figure 6. Time-dependent change in dissolved oxygen concentration in the spillway (for different flow rate values)



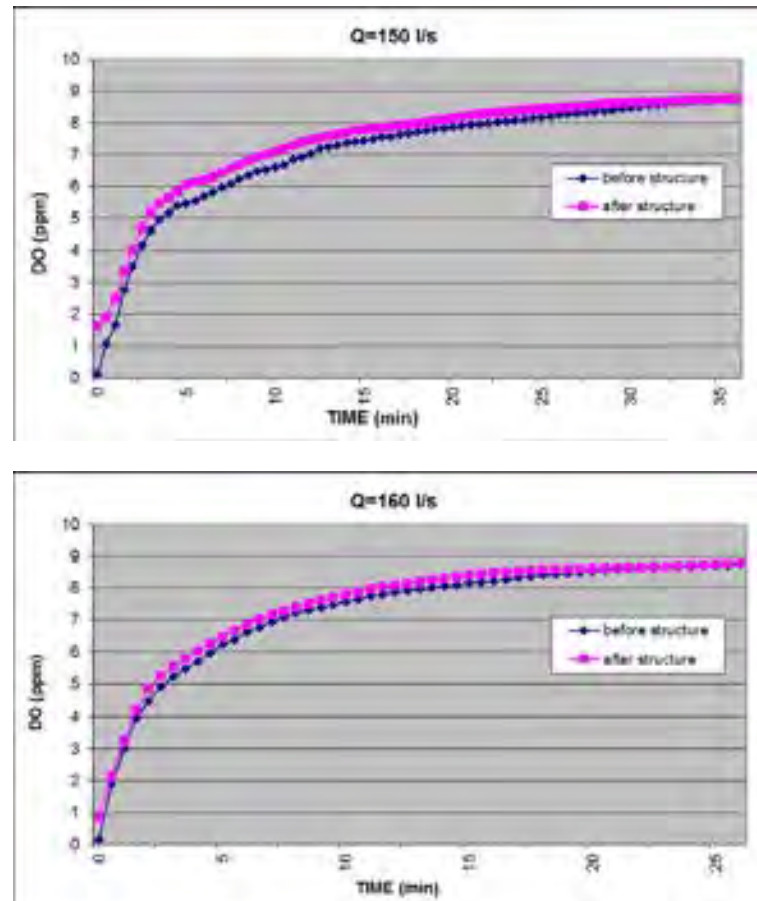


Figure 7. Time-dependent change in dissolved oxygen concentration in the stepped spillway (for different flow rate values)

In the spillway systems, the change in dissolved oxygen values before and after the hydraulic structure was rather small and oxygen gain was low (Figure 6). In the stepped spillway system, on the other hand, the difference in dissolved oxygen values before and after the hydraulic structure was placed in the channel was quite high in comparison to spillways systems (Figure 7). In addition, the amount of this difference varied based on flow conditions (nappe flow, transition flow, and skimming flow), changing depending on increasing flow rate values. The highest gain value was observed in the nappe flow regime. The gain level was smaller in the transition flow, and the lowest gain values were obtained in the skimming flow regime.

5 Results

In this study, the aeration efficiency of different hydraulic structures was experimentally investigated, and the following results were obtained:

1. During the study, the nappe flow regime was observed to have the lowest flow rates. As the flow rate increased, the flow regime first changed into the transition flow, and then into the skimming flow regime.
2. The aeration efficiencies of stepped spillways and spillways were examined, and it was shown that the aeration efficiencies of stepped spillways are higher than that of spillways.
3. The aeration efficiency values were different in all three flow regimes. The results showed that the highest amount of aeration takes place in the nappe flow regime. This is because in the nappe flow regime, aeration takes place at every step via plunge jet and hydraulic jump, and therefore turbulence and contact duration is higher.

4. Within the same system, aeration efficiency decreases with increasing flow rates and with changing flow regimes (transition flow, skimming flow).

References

- 1-Ağırlioğlu N., (2007). *Baraj Planlama ve Tasarımı* (Cilt 1), Su Vakfı Yayınları, İstanbul.
- 2-Avery, S. T. and Novak, P. (1978). Oxygen transfer at hydraulic structures. *J. Hydr. Engrg.*, ASCE, 104, 1521-1540.
- 3-Babb, A.F. and Aus, H.C. (1981). Measurements of air in flowing water. *J. Hydr. Div.*, ASCE, 107, 1615-1630.
- 4-Chanson, H. and Toombes, L. (2002). Air-water Flows Down Stepped Chutes: Turbulance and Flow Structure Observations. *International Journal of Multiphase Flow*, 28:1737-1761.
- 5-Chanson H. (1995). *Hydraulic Design of Stepped Cascades, Channels, Weirs and Spillways*, Pergamon, Oxford, UK, Jan., 292 pages (ISBN 978-0-08-041918-3).
- 6-Colt, J., (1984). Computation of dissolved gas concentration in water as functions of temperature salinity and pressure. Fisheries Society Special Publication, 14, Bethesda, MD.
- 7-Ervine, D. A. (1998). Air entrainment in hydraulic structures: a review. *Proc. Instn Civ. Engrs Wat., Marit. & Energy.*, 130, 142-153.
- 8-Gameson, A.L.H. (1957). Weirs and aeration of rivers., *J.Inst. Water Engrg*, 11 : 477-490
- 9-Gulliver, J.S., and Rindels, A.J. (1990). Indexing gas transfer in self aerated flows, *J.Envir. Engrg.*, ASCE, 116, 503-523.
- 10-Gulliver, J.S., and Rindels, A. J. (1993). Measurement of air-water oxygen transfer at hydraulic structures. *J.Hydr. Engrg.*, ASCE, 119, 327-349.
- 11-Gulliver, J.S., Wilhelms S. C., and Parkhill K.L. (1998). Predictive capabilities in oxygen transfer at hydraulic structures. *J. Hydr. Engrg.*, ASCE, 124, pp. 664-671.
- 12-Hoyt, J.W., and Sellin, R.H.J. (1989). Hydraulic jump as mixing layer. *J. Hydr. Engrg.*, ASCE, 115, 1607-1613.
- 13-Küçükali, S., (2006). *Hidrolik Sıçramanın Havalandırma Verimliliğinin İncelenmesi*, Doktora Tezi, İTÜ, Fen Bilimleri Enstitüsü, İstanbul.
- 14-Leutheusser, H.J., Resch, F.J., and Alemu, S. (1973). Water quality enchancement through hydraulic aeration. XV IAHR Congress, Istanbul, Turkey, 2-7 September, 167-175.
- 15-Murillo, R. E. (2006). *Experimental Study of The Development Flow Region on Stepped Chutes*. Doctoral Thesis, Department of Civil Engineering University of Manitoba Winnipeg, Manitoba, Canada.
- 16-Rajaratnam, N., (1961). An Experimental Study of Air Entrainment Characteristics of Hydraulic Jump. *J. Institution of Engineers (India)*, 42, 247-273.
- 17-Wilhelms, S.C., Clark, L., Wallace, J.R., and Smith, D.R. (1981). *Gas transfer in hydraulic jumps*. Techn. Report E-81-10, US Army Engineer Waterways Experiment Station, CE, Vicksburg Miss., USA.

USE OF RAINWATER IN RECREATIONAL IRRIGATION OF A UNIVERSITY CAMPUS IN TURKEY

Assoc. Prof. Dr. Ahmet Doğan

1Assoc.Prof.Dr. atYıldız Technical University, Civil Engineering Department, İstanbul, Turkey e-mail:
ahmet@yildiz.edu.tr Tel:(90)212 383 5173

Abstract

Hot and dry summers require extensive recreational irrigation in urban areas and university campuses that have large green areas. Populated metropolitan areas have already vast amount of water demand for drinking and domestic use. Water requirement for recreational irrigation generally have secondary priority, none the less public attention enforces the city managers and university campus administrators to keep the green environment as green even during hot and dry summers. Therefore during the rainy season, rainwater should be collected and stored to use for recreational irrigation in dry seasons of the year. This task requires to construct large storage facilities with piping and pumping equipment. In this study feasibilityof rainwater harvesting project for a university campus is investigated and cost of the collection and storage facilities are compared with the alternate cost of water use from public supply network. It is found out that use of rainwater solely for recreational irrigation is not economically feasible because the cost of rainwater collection system will be paid back in 55-75 years.

Keywords: Rainwater collection, rain harvesting, recreational irrigation

1. Introduction

Recreational irrigation in urban areas, public parks and university campuses with large green areas require extensive amount of recreational irrigation water in summer seasons. Populated metropolitan areas have already vast amount of water demand for drinking and domestic use. Water demand for recreational irrigation generally has secondary priority compared to domestic use, none the less public attention enforces the city managers and university campus administrators to keep the green environment as green even during hot and dry summers. Water usage from city water distribution network is costly in large metropolitan cities like İstanbul with the population of about 15 Million people. Since water supply is limited, high water pricing policy is applied in these type of cities. Therefore, recreational irrigation should be carried out using alternative sources such as rainfall harvesting. During the rainy season, rainwater should be collected and stored to use for irrigation in dry seasons of the year.

In this study, possibility of rainwater harvesting for using recreational irrigation at the Davutpaşa Campus of Yıldız Technical University of İstanbul is investigated. The public pressure enforces the university campuses should be as green as possible to provide a pleasant and relaxing educational environment to the students as well as for faculty members. The recreational irrigation of the campus area was responsible for the major cost of total utility bill of the campus. To cut this major cost to a reasonable amount, rainwater usage in irrigation should be considered. Annual distribution of irrigation water requirement of recreational plants, i.e., grass, shows that most of the irrigation take place from April to September whereas most of the precipitation falls between September and April in İstanbul. Therefore, the rainwater should be collected and stored during the wet season to be able to use it during the irrigation season. This inversely correlated rainfall and irrigation distributions requires to build storage facilities in the campus for rainwater harvesting project.

Land use and land cover characteristics of the university campus area was analyzed to classify the pervious and impervious surfaces to be able to calculate what percentage of the rainfall can be collected. For this analysis GIS maps and Google Earth satellite images were used (Figure 1). Roof areas, parking lots, pervious or semi-pervious walking paths and roads were classified and their total area was determined. Rainfall-runoff coefficients for roofs and parking lots were assumed to be 0.90 as 10% of the rainfall to be used for initial abstraction and evaporation losses. The rest of the campus area was considered that 35% of the precipitation goes to runoff while 65% of the rainfall satisfies the initial abstraction, infiltration, and evapotranspiration losses.

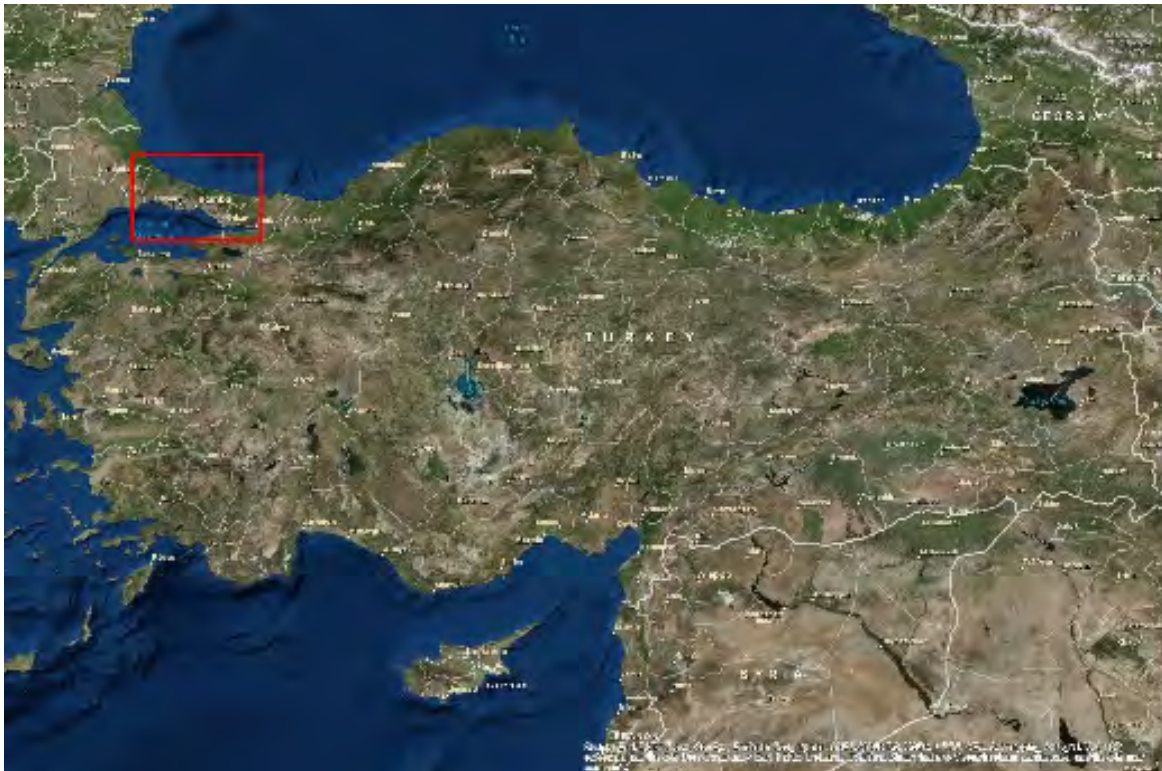
2. Study Area

Davutpaşa Campus of Yıldız Technical University had been served as a military base during the Ottoman Empire Era and Republic of Turkey from 1831 to 1999. Then it was turned over to Yıldız Technical University to serve as its second campus area. It is located European side of İstanbul at the district of Esenler (Figure 1). From climate perspective, the campus area is considered to have the properties of the Marmara region which is located in a transition zone between the Mediterranean climate (humid and subtropical) on the Aegean Sea region and the oceanic climate on the Black Sea region. Humid continental climate prevails in the interior parts of the region more abundantly. Summers are characterized warm and humid, whereas winters are cold and wet with occasional snow

storms. January is the coldest month of the year with 4.9°C mean monthly temperature. In July, monthly mean temperatures in the region can reach as high as 23.7 °C. The region receives an average of 595-mm rainfall annually with high spatial variability. The annual rainfall reaches exceeds 800 mm in İstanbul and the eastern part of the region while the central and western parts reach values of less than 600 mm. Although the region is characterized with wet winters, summer rainfalls are not negligible, comprising nearly 12 % of the annual rainfall (Kömüşcü and Çelik, 2013).

2.1 Analysis of Meteorological Data

The precipitation data for the campus area was collected from a meteorological station that was established in 2011 for a research project, therefore it has partial rainfall data and yet it has some missing data either. Therefore 2011 and 2012 rainfall records of this station were compared with historical records of other meteorological stations in close proximity region to estimate the missing rainfall data. The rainfall records of AKOM Meteorological Station that was 15 km away, north east of the campus and Florya Meteorological Station was also 13 km south west of the campus were analyzed. It was found out that monthly records of AKOM station is generally 5-10 mm higher while the records of Florya Station is also slightly higher than the records campus rainfall measurements, therefore it was decided to use records of average conditions of İstanbul meteorological data for this study. Long time average rainfall records of İstanbul are obtained from Sarıyer Meteorological Station that was accepted as representative meteorological station for İstanbul by Turkish State Meteorological Service (DMI). Long time average rainfall between 1954 and 2014 for İstanbul is obtained for this station as 808.3 mm/year with 129 rainy days and 236 days without rain (Table 1 and Figure 2).



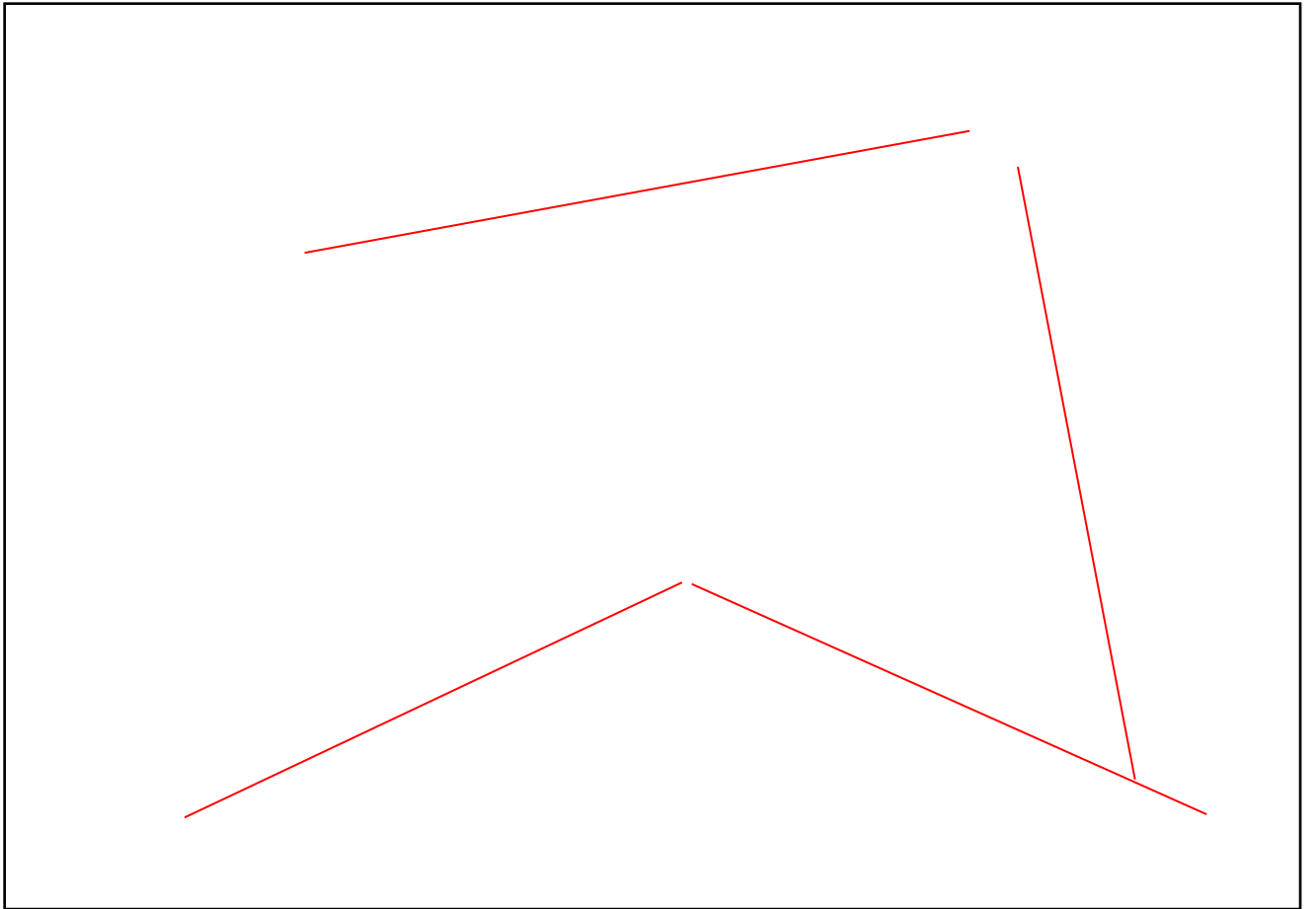


Figure 1. General Google Earth View of Davutpaşa Campus of Yıldız Technical University as of 2015.

Potential Evapotranspiration (PET) data representing İstanbul climate is obtained from Elmalı Dam Reservoir (Figure 3). This PET data is used to calculate crop water demand of grass.

Table 1. Long time average rainfall between 1954 and 2014 for İstanbul

Average Monthly Rainfall of 1954-2014 in İstanbul				
Months	Rainy Days	Non-Rainy Days	Rainfall (mm/month)	Daily Average Rainfall (mm/day)
Jan	17.5	13.5	105.3	6.02
Feb	15.2	12.8	77.3	5.09
Mar	13.8	17.2	71.8	5.20
Apr	10.4	19.6	44.9	4.32
May	8.1	22.9	34.1	4.21
Jun	6	24	34	5.67
Jul	4.2	26.8	31.6	7.52
Aug	4.9	26.1	39.8	8.12
Sep	7.3	22.7	57.9	7.93
Oct	11.2	19.8	87.7	7.83
Nov	13.3	16.7	101.3	7.62
Dec	17.3	13.7	122.6	7.09
Total	129	236	808.3	
Rainy Season (October-March) Total Precip. (mm)=				566 (70%)
Irrig. season (April-September) Total Precip.(mm)=				242.3 (30%)
Rainy Season (October-March) # of Rainy Days=				88.3 (68%)
Irrig. season (April-September) # of rainy days=				40.9 (32%)

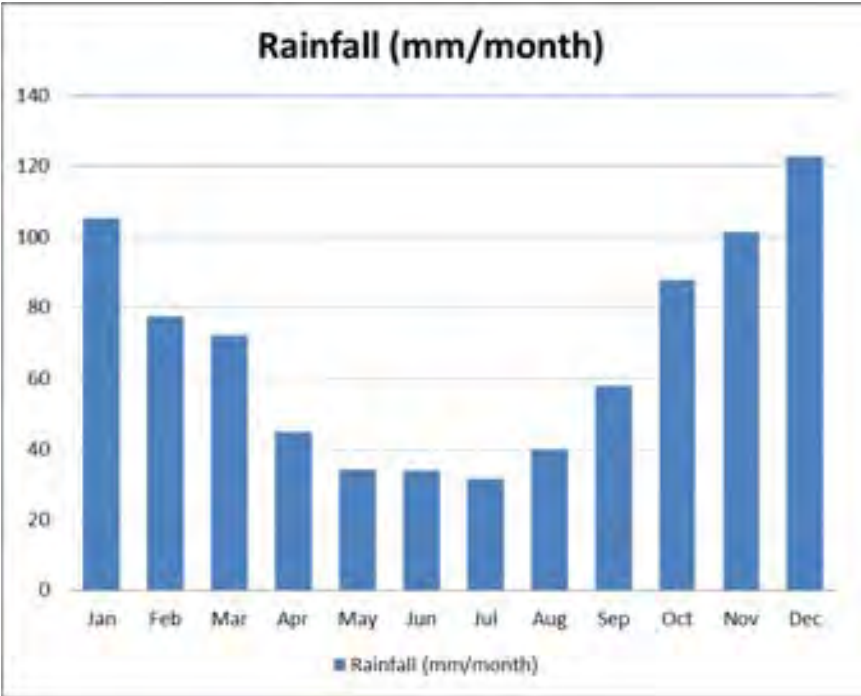


Figure 2. Longtime Average (1954-2014) Precipitation in İstanbul.

2.2 Analysis of land use/ land cover of the campus

Davutpaşa Campus of Yıldız Technical University has a total area of 1,263,280 m². The soil type in the campus area composes mostly clay, scattered limestone, and greywacke. Therefore soil type can be classified as less pervious or impervious. The campus area consists of educational and administrative building, sports fields, student and faculty housings, roads, parking lots, irrigated land and some non-irrigated wood and barren land. The total area of campus is classified as pervious and impervious to determine their rainfall runoff coefficients. According to the land use classification shown in Table 2, majority of the campus area (62.5%) covered with grass, wood, and natural vegetation without any building on it. The rainfall runoff coefficient for this area was assumed as 0.35. Buildings and surrounding parking lots and walkways comprises about 10.1% of the campus area that has a rainfall runoff coefficient of 0,90. Roads made of asphalt and concrete occupies 17.2% of the campus area with rainfall runoff coefficient of 0.85. There are some barren distant areas of campus that constitutes %10.1 percent of the campus field.

Table2. Land Use Classification of the Campus Area and Their Rainfall-Runoff Coefficients.

Main Categories of Campus Area					
	Area	Percent Area	Runoff Coefficient	Annual Precipitation	Harvestable Rainfall
	m ²	%		mm/year	m ³ /year
Natural and Grass or Lawn Covered Fields	789,561	62.5	0.35	808.3	223371
Rooftops and Parking Lots of school Buildings	128,210	10.1	0.90	808.3	93269
Concrete or Asphalt Roads	217,426	17.2	0.85	808.3	149384
Distinct Disused Field	128,083	10.1	0.35	808.3	36235
Total Campus Area	1,263,280	100.0	0.49	808.3	502259

3. Rainfall Harvesting

Rainwater harvesting is a technology used for collecting and storing rainwater from rooftops and land surface using different techniques. Commonly used systems are constructed of three principal components; namely, the catchment area, the collection device, and the conveyance system. The system needs annual maintenance by simply cleaning of the storage tanks before the start of the major rainfall season. The augmentation of municipal water supplies with harvested rainwater is essential for the reliability of the system. The capital cost of rainwater harvesting systems is highly dependent on the type of catchment, conveyance and storage tank materials used.

The feasibility of rainwater harvesting in a given location is highly dependent upon the amount and distribution of rainfall. As rainfall is usually unevenly distributed throughout the year, rainwater harvesting can serve as only supplementary sources of water. The viability of rainwater harvesting systems is also a function of cost and quantity of water available from other sources. The decision maker has to make an economic analysis to balance the total cost of the harvesting system against the cost of available water supplied from other sources.

Provided that rainwater harvesting has been determined to be feasible, there are different methods available to determine the required size of the storage tanks. These methods are mostly applicable

for rooftop catchment systems only, and detail guidelines for design of these storage tanks can be found in Gould (1992) and Pacey and Cullis (1989).

Rainwater harvesting appears to be one of the most promising alternatives for supplying freshwater while the sharp increase of water demand due to population growth and water scarcity due to climate change and urbanization. In this study rational method is used in rainfall harvesting methodology. Rational method is most widely used method in urban hydrology (Chin, 2000) and stormwater collection design of small watersheds. Rational method relates the peak runoff rate, Q_p , to the rainfall intensity, i , by the relation

$$Q_p = C.i.A \quad (1)$$

where C is the runoff coefficient and A is the area of the catchment.

In rational method, the main purpose is to find the peak flow rates for designing the pipe capacity to carry the amount of rainwater collected during the specified duration of rainfall event. Therefore, the rainfall intensity in Equation 1 needs to be chosen as the maximum rainfall intensity for a given duration, for a given return period. However, in this study, rainwater harvesting is solely aimed to determine the total amount of rainfall to be collected at the end of each consecutive day. So that the rational method for this study is modified to calculate only collectable daily rainfall poured on to rooftops and parking lots. As a result, daily rainfall, area of rooftops and parking lots, and the runoff coefficient are considered in Equation 1 to calculate the amount of rainwater to be able to collected and stored.

Map of the campus area is analyzed using GIS to determine the areas of rooftops, parking lots, and irrigated fields. Surface area of rooftops and parking lots are substituted in Equation 1 to find harvestable rainfall. Total area to be used in rainfall harvesting is 128,210 m² and from this 93,269 m³ of rainwater can be collected. The amount of harvestable rainfall volumes from rooftops are calculated in Table 3.

As a summary, İstanbul, on average, receives 808 mm rainfall, that pours 1,021,109 m³ rainwater on the campus area of which 502,258 m³ can be harvested theoretically but only 18.5 % of the total rainwater (93,269 m³) can be collected feasibly from readily available rooftops and parking lots. The remaining water runoff. Precipitations between October and March provide 70% of total rainwater while the rest of the rainwater comes during irrigation season. This non-uniform distribution of the precipitation requires to store excess water during wet season to use for irrigation when needed.

Table3. Amount of Rainfall to be collected on rooftops and parking lots in the campus area.

Rooftops Distribution	Area	Harvestable Rainfall	Annual Harvestable Rainfall
	m ²	m ³ /day	m ³ /year
Administrative Buildings	18,801	37	13,677
Student Facilities and Gymnasium	9,329	19	6,787
Faculty of Electrical Engineering	10,686	21	7,774
Faculty of Science and Literature	8,496	17	6,181
Faculty of Material and Chemical Eng.	10,735	21	7,809
Faculty of Civil Engineering	16,691	33	12,142
Faculty of Foreign Lang.	5,449	11	3,964
Teknopark	19,395	39	14,109
Library and Conference Center	7,038	14	5,120
Dormitories	4,596	9	3,344
Faculty Housing	7,769	15	5,652
Historical Buildings	1,797	4	1,308
New Planned School Building	7,427	15	5,403
Total	128,210	256	93,269

4. Determination of Storage Volume

Provided that the harvestable water has been calculated, the irrigation demand for the campus area needs to be determined. Plant cover type and corresponding areas are determined from GIS analysis. Plant types and their daily water requirement is obtained from the Campus Irrigation Facility as seen in Table 4.

Table 4. Currently applied irrigation water schedule in the campus

Irrigation water requirement for various plants on the campus				
Plant Type	Water Requirement (mm/week)	Water Requirement (mm/day)	Average Daily Requirement (mm/day)	Percent Area (%)
Grass	38-50	5,4-7,1	6.4	60
Lawn	13-25	1,9-3,6	2.6	33
Bush	25-38	3,6-5,4	4.6	2
Tree	25-38	3,6-5,4	4.6	1
Rose	50	7,1	7.1	2
Flowers	38-50	5,4-7,1	6.4	2
Net Irrigation Water Requirement			5.11	100
Gross Irrigation Requirement (Efficiency of 0.9)			5.67	

Water requirement of grass and other plants should actually be equivalent to the potential evapotranspiration (PET). Therefore long term average PET values for İstanbul is obtained from Elmalı Dam ET Station which is at the Asian Side of the İstanbul (Figure 3).

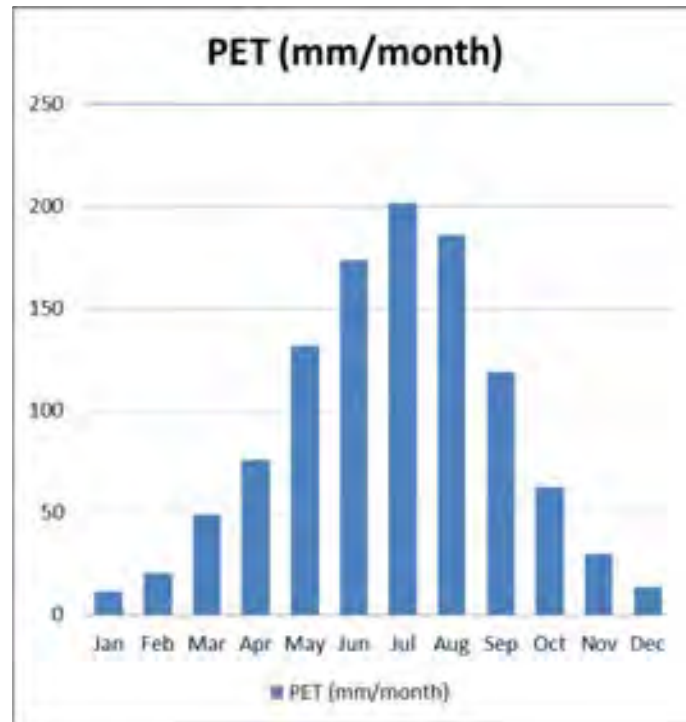


Figure 3. Long term Average Potential Evapotranspiration Measurements (1968-2014) at Elmalı Dam in İstanbul

PET values of April to October are assumed to be the irrigation requirements of the recreational cover plants of the campus. PET values of non-rainy days only should be provided as irrigation water to the plants. In rainy days there is assumed to be no irrigation if rain water is enough for the plant in that day. Using this logic the monthly irrigation requirements are calculated (Table 5 and Figure 4). As seen from Table 5, currently applied irrigation schedule comply well with the irrigation requirement calculated from PET and rainfall measurements.

Table 5. Irrigation Demand Calculated from PET and Rainfall Measurements

Irrigation Water Requirement						
Months	PET (mm/month)	Rainy Days	Non-Rainy Days	Daily Average Rainfall (mm/day)	Daily PET (mm/day)	Irrigation Requirement (mm/month)
Jan	11	17.5	13.5	6.02	0.84	
Feb	21	15.2	12.8	5.09	1.60	
Mar	49	13.8	17.2	5.20	2.84	
Apr	76	10.4	19.6	4.32	3.87	75.87
May	132	8.1	22.9	4.21	5.75	144.15
Jun	173	6	24	5.67	7.23	173.40
Jul	202	4.2	26.8	7.52	7.52	201.54
Aug	186	4.9	26.1	8.12	7.13	186.17
Sep	119	7.3	22.7	7.93	5.23	118.75
Oct	62	11.2	19.8	7.83	3.15	62.41
Nov	29	13.3	16.7	7.62	1.76	
Dec	14	17.3	13.7	7.09	1.00	
Total	1074	129	236			962.30



Figure 4. Monthly Irrigation Demand

After determining the amount of water required for irrigation and the amount of harvestable rainfall volume, the required storage volume for the rain harvesting project is calculated using mass balance method. In that method, the larger of deficit or excess volume of water is chosen as storage volume (Table 6). It was found out that the harvestable rainfall water in campus area is enough to meet all the irrigation requirement with construction of 55,000 m³ of storage tanks. The tanks need to be started to get filled in October. In March, all the storage tanks get full and 4562 m³ of water is spilled away as surcharge water. It is structurally convenient to build 11 storage tanks with volumes of 5000 m³ each. The distribution of this 11 storage tanks with close proximate locations of irrigation fields is given in Table 7.

Table 6. Calculation of Water Storage Volume

Calculation Storage Volume Requirement (m ³)						
Months	Harvestable Rainfall (m ³ /month)	Irrigation Requirement (m ³ /month)	Difference= (Supply- Demand)	Excess of Deficit Water (m ³)	Volume of Water in Storage (m ³)	Surcharge of Water
Jan	12150		12150		42358	
Feb	8920		8920		51277	
Mar	8285		8285	29355	59562	4562
Apr	5181	6288	-1806		-1806	
May	3935	11948	-9341		-11146	
Jun	3923	14372	-12046		-23192	
Jul	3646	16704	-14914		-38106	
Aug	4592	15430	-12552		-50658	
Sep	6681	9842	-4255	-54913	-54913	
Oct	10120	5173	4372		4372	
Nov	11689		11689		16061	
Dec	14147		14147	30207	30207	
Total	93269	79757	Excess Water =	59562	Total Storage Capacity=	
			* Gross Irrigation=Net Irrigation/Efficiency (Effi)	Water Deficit=	55000 m³	
The storages should be started to get filled in October						

Table7.Number of storage tanks required for Irrigation with rain harvesting project

Name	Irrigated Area (m ²)	Percent Area	Storage Volume	Number Storages of 5000 m ³
Administrative Building and Interior Garden	36469	44	20000	4
Exterior Garden of Administrative Building	10435	13	5000	1
Surrounding Area of Faculty of Civil Engine	6000	7	5000	1
Surrounding Area of Faculty of Electrical E	15250	18	10000	2
Surrounding Area of Librariry	5713	7	5000	1
Football Field	7920	10	10000	2
Flowers	600	1		
Main Entrance and Surrounding Area	495	1		
Total	82882	100	55000	11

5. Discussion of the Results

Davutpaşa Campus area of Yıldız Technical University has readily available 128210 m²rooftops and parking lots suitable to implement rainharvesting project for recreational irrigation. Annual rainfall 808 mm over this surface area results in collecting 93,269 m³ of rainwater. Over the campus area, currently, 82,882 m²recreational area is irrigated. Total irrigation demand under average climate conditions of İstanbul should be equivalent to PET values of the irrigation months from April to October. PET measurements of Elmalı Dam site in İstanbul in those month is 962 mm. Some portion of this PET is satisfied with available precipitation occurred during the irrigation season while the rest of PET is supplied by irrigation. Using this logic, irrigation water requirement is calculated as 79,757 m³ of water annually. Due to the fact that 70 % of the rainfall occurs during winter season and only 30 % occurs during the irrigation season, 55,000 m³ of rainwater has to be stored starting from October until March to use it from April to September.

Irrigated areas over the campus are scattered therefore 11 storage tanks with volume of 5000 m³ of each have to be constructed at proper locations around the campus. Dimensions of each storage tank will be 27,5 by 36.5 by 5 m. The construction and installation cost of unit price of the storage tanks is estimated as \$188.7/m³ (500 TL/m³) which makes the total cost of 11 storage tanks is about 10.3 Million USD (Table 8.). Unit cost of the water from city network for public organizations like universities is \$2.43/m³ (6.44 TL/m³). Total annual cost of recreational irrigation for 79,757 m³ of water is about 0,194 Million USD. According to financial analysis, the initial investment of 10,3 million USD can be compensated in 53 years with annual instalment of 0,194 million USD, equivalent of water bill for recreational irrigation, and with zero interest rate. If the interest rate is 0.5% and 1% then this depreciation duration will be about 62 and 75 years, respectively.

Table 8. Financial analysis of the costs of rain harvesting project and recreational irrigation from public water supply network.

Cost Analysis	Unit Cost (\$/m ³)	Volume (m ³)	Cost (\$)
Cost of Storage Facilities	188.68	55000	\$10,377,358
Cost of Water per Year	2.43	79757	\$193,825
<i>Interest Rate</i>	<i>Number of Years to Compensate Rain Harvesting Project Cost for Different Interest Rates</i>		
0	53.5		
0.5	62.5		
1.0	75.5		

6. Conclusion

In this study, the possibility of rain harvesting to use for recreational irrigation of Davutpaşa Campus of Yıldız Technical University is investigated. Although the amount of annual rainfall water is more than the recreational irrigation requirement, 70% of the rainwater has to be stored to use it during irrigation season which requires construction of storage tanks. When the initial investment cost of rainwater collection system is compared with the alternate cost of public supply water compared under various interest rates of 0, 0.5, and 1%, the project cost will be paid off in 53, 63, and 75 years, respectively.

Although rainwater harvesting is considered as one of the most promising alternatives for supplying freshwater while the sharp increase of water demand and water scarcity due to population growth, global warming, and urbanization, the rainwater collection system for recreational irrigation of the university campus does not seem to be economically feasible with these price of alternative source of public water supply. The viability of rainwater harvesting systems is also a function of cost and quantity of water available from other sources. The decision maker has to make an economic analysis to balance the total cost of the harvesting system against the cost of available water supplied from other sources. If the water price of public supply increases due to water scarcity and high demand then it may be feasible. From the current financial perspective this project is not applicable but it is highly recommended to implement such a project for environmental perspective as well as for future economical perspective. This type of projects should be implemented with the augmentation of municipal water supplies for the reliability of the system.

7. References

- Chin, D.A., 2000. Water Resources Engineering. Prentice hall, Upper saddle River, NJ.
- Gould, J.E. 1992. Rainwater Catchment Systems for Household Water Supply, Environmental Sanitation Reviews, No. 32, ENSIC, Asian Institute of Technology, Bangkok.
- Kömüştü, A.E. and Çelik S., 2013. Analysis of the Marmara flood in Turkey, 7–10 September 2009: an assessment from hydrometeorological perspective. *Nat Hazards*, 66:781–808.
- Pacey, A. and A. Cullis 1989. Rainwater Harvesting: The Collection of Rainfall and Runoff in Rural Areas, WBC Print Ltd., London.

INVESTIGATION OF THE TRIBOLOGICAL PERFORMANCE OF A DOPED SEMI-SYNTHETIC ENGINE OIL

Murat KAPSIZ

Sakarya University, Faculty of Technology, Department of Mechanical Engineering, 54187,
Sakarya-Turkey.

Ferit FIÇICI

Sakarya University, Faculty of Technology, Department of Mechanical Engineering, 54187,
Sakarya-Turkey.

Ramazan ŞENER

Sakarya University, Faculty of Technology, Department of Mechanical Engineering, 54187,
Sakarya-Turkey.

Abstract

The semi-synthetic oils are used in internal combustion engines owing to their good performances and low costs. However, these oils do not show satisfying tribological performance in engines. It is also known that their performances could be improved by adding various synthetic additives. Semi-synthetic oils look attractive with their high usage rate due to high cost of synthetic oils and recommendations of engine manufacturers. Improving the tribology performance of semi-synthetic oils with oil additives is an affordable and easy way. In this research, the effects of different additives on the tribological performance of the semi-synthetic engine oils were investigated.

Keywords: Engine Tribology, Semi-synthetic Oil, Friction Modifier

1. INTRODUCTION

Global OEMs (Original Equipment Manufacturer), fuel and lubricant additive manufacturers are attempting to meet the challenges of changing consumer needs and new legislation for a cleaner environment and energy conservation [1]. More effective or enhanced lubrication is needed to meet the increasingly more stringent operational conditions of new engine systems. The fuel economy, durability, and environmental legislation of all engines are closely related to the effectiveness of the lubricants being used. Poor or inefficient lubrication may result in high friction and wear losses, which can in turn adversely affect the fuel economy and durability of these engines [2-5]. The engine oils performance and oil additives one of the most harmful environments in the internal combustion (IC) engine [6]. Due to the negative effect of the friction and wear over the engine efficiency, durability and noise, the interest of engine industry and oil manufacturers in engine friction research has been continuously growing. Thus there is an urgent need for new engine systems with higher fuel economy and lower emissions than before, and this can be achieved by the development and broad uses of low friction materials, coatings, and lubricants [7-9]. In a modern IC engine, the engine friction could consume up to 10-20% of the fuel used [10-13] by the engine.

As with engine oil, the key operating tribological parameter in an engine is the lubricant film thickness separating the interacting engine part surfaces. The relationship between film thickness and friction coefficient is a curved line from which it is possible to define the different lubrication regimes. Different engine parts rely on different regime of lubrication during a single cycle. Some of these like journal and thrust bearings are designed to operate in the hydrodynamic lubrication regime, whereas others like piston rings that slide inside liners are developed to perform in mixed or boundary lubrication regime. Metal-to-metal contact is expected to take place only at low speed and high loads for the first ones, while surface contact occurs for the second ones: in the last condition, the surfaces should be protected to avoid failure of the engine [14].

Optimal engine oil can be obtained considering the influence of several factors [6]. The most important ones are the energy lost (due to friction), oil consumption and wear. Thin lubricating films cause a high friction force which decreases efficiency and cause surface interaction leading to wear. On the other hand, thick films may lead to greater oil consumption, which is a direct contributor to hydrocarbon emissions.

Improving new oil additive will have positive effects not only on friction reduction but also on the function of the whole engine performance. Reducing friction loss also means that the nature's reserves are saved and that the running costs of the vehicle are reduced [15].

A major contributor to overall engine friction is the relative motion between the cylinder liner and piston ring. More recent studies suggest that due to improved design, in-cylinder friction has been reduced to approximately 40-55% of total engine friction. Despite this reduction in engine friction, further reductions are desired to improve engine performance and fuel efficiency [16-18].

This study investigates how the two aspects of oil formulation, semi-synthetic oil and oil with additives (friction modifier) effect the tribological performance in a piston ring-cylinder liner. Experiments are carried out at different loads, temperatures and speeds. The objective is to obtain results closer to the engine conditions.

2. ENGINE TRIBOLOGY

Lubrication between the piston assembly and cylinder is a key area of potential improvement by reduction of the frictional loss and the source of pollutant formation. It is understood that the piston assembly accounts for the greatest portion of mechanical loss in engines [19].

The power cylinder is a major contributor to the overall mechanical friction of the engine. Mechanical power spend approximately 10–15% of the total fuel energy. Approximately half of this mechanical loss is because of friction at the cylinder liner–piston ring interface [20-22].

The piston ring/cylinder liner contact is a major contributor to engine frictional losses. It is estimated that nearly 40% of losses in an engine occur at this contact interface [23].

Therefore, a proper understanding and prediction of this frictional loss is essential in an effort to improve efficiency of reciprocating internal combustion engines. It is well known that piston rings operate in the full range of lubrication regimes (i.e., boundary, mixed, hydrodynamic) [24].

To meet competitive durability goals in the automobile industry, it is necessary to have improved understanding of the effect of wear in the cylinder liner piston assembly. Cylinder liners require some of the most critical surface properties in terms of functionality. Piston ring and cylinder liner wear is a very important factor in determining effective engine life [20].

3. LUBRICATION REGIMES AND OIL ADDITIVES

Tribology of internal combustion engine must involve an understanding of the concept of regime of lubrication. Stribeck diagram is a good explanation for the regime of lubrication. Stribeck diagram, in the form of a plot of two non-dimensional groupings: the coefficient of friction (μ) on the ordinate and a variation of the Sommerfeld grouping ($\eta N/P$) as abscissa; where η is the dynamic viscosity, N is rotational speed and P is specific load. With the development of the understanding of regimes of lubrication, this plot has increasingly incorporated the film thickness ratio, or parameter, (λ) on the abscissa as shown in Figure 1, the modified Stribeck diagram. This diagram is briefly explained in Table 1 [25].

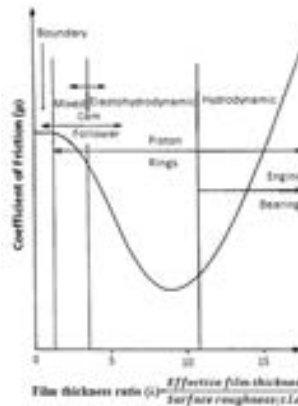


Figure 1. The modified Stribeck diagram [25]

Friction modifiers are additives designed to reduce friction in boundary lubrication regime. Molybdenum dithiocarbamate (MoDTC) is a commonly used organometallic modifier that works by bonding flakes of molybdenum disulfate (MoS₂) onto surface asperities, thereby it reduces friction in boundary lubrication regime. Stearic acid (C₁₈H₃₆O₂) is an example of an organic modifier. Organic modifiers are believed to work by weakly bonding themselves to metal surfaces, thereby forming a lubricating surface film.

Table 1. Description of lubrication regimes [25]

Regime of Lubrication	Features
Hydrodynamic	Full fluid film lubrication in which the surfaces are completely separated. The dynamic viscosity of the lubricant is its most important property
Elastohydrodynamic	Nominally also full fluid film lubrication with surface separation, but a more concentrated mechanism where elastic deformation of the surfaces and the effect of pressure on viscosity are important
Mixed	There is surface asperity interaction to some degree and the characteristics of both Elastohydrodynamic and Boundary Lubrication are influential
Boundary	The surfaces are in normal contact with behavior characterized by the chemical (and physical) actions of thin films of molecular proportions

Black et al. [26] illustrate the benefits molybdenum friction modifier on cam-follower wear, Grene and Risdon [27] report that molybdenum friction modifier improves gasoline engine fuel economy by 3–5%. Noorman et al. [28] evaluated a friction modifier of unspecified composition on gasoline engine friction at different speeds and loads and measured an FMEP reduction of 6–11%. Benvenuti et al. [29] ran a gasoline engine through different test cycles using 20W-50 oil without molybdenum friction modifier and 10W-30 oil with molybdenum friction modifier.

Since friction modifiers reduce boundary friction and the ratio of boundary friction to hydrodynamic friction varies with engine condition and engine design, the advantages of modifier depend on engine operating condition and engine design. High temperature, high load, low speed conditions tend to increase boundary friction. High-tension piston rings and substandard lubrication systems are design features that also increase boundary friction [30].

4. MATERIAL AND METHODS

4.1. Semi-synthetic Oil and Oil Additives

The American Petroleum Institute (API) uses composition and properties to categorize base oils into five groups. This study uses the same convention. Semi-synthetic engine oils with friction modifier and without friction modifier were tested under the same sliding conditions. Oil properties are shown in Table 1. Friction modifier has nano-scale boron particles. Boron particles have been measured to be in sizes of 200 nm.

Table 2. Semi-synthetic oil properties [31]

SAE Viscosity Grade		10W-40
Density, 15°C kg/m	ASTM 4052	0.873
Flash Point, COC, °C	ASTM D 92	226
Viscosity Index	ASTM D 2270	154
Pour Point, °C	ASTM D 97	-33
Kinematic Viscosity		
40°C mm ² /s	ASTM D 445	91,18
100°C mm ² /s		13.76

Two different performance categories of with friction modifier and without semi-synthetic gasoline engine oils, were selected as test lubricants. Tribo-systems consisting of the tribomates and lubricants were operated in a reciprocating tribotester. The frictional forces were recorded and examined for frictional behaviours. Weight loss of the all samples, were determined as a function of sliding distance and test loads. Weighting was performed with an analytic balance with a sensitive of 0.1 mg [31].

4.2. Piston Ring and Cylinder Liner Specimens

Wear tests were performed with the top and bottom samples. The top specimens are ring samples cut directly from the production-chrome coated piston rings. The bottom specimens with a shape of flat cylindrical made of a production cast iron cylinder bore samples material composed of pearlite, ferrite, and graphite structures. Piston rings manufactured by chrome coating procedures, were used with the same cast iron cylinder bore to form the tribo-contact system. Piston ring and cylinder liner specifications are shown in Table 2. Also chemical composition of piston ring and cylinder liner are presented in Table 3.

Table 3. Piston ring and cylinder liner specifications

Sample	Material	Surface treatment	Hardness (HV _{0.1})	Roughness(R _a ,µm)
Ring	Cast iron	Chrome coated	920	0.121
Liner	Cast iron	Honing	20.3	1.052

Table 4. Chemical compositions of piston ring and cylinder liner

Sample	C	Cu	S	Mn	Si	P	Fe
Ring	3.62	0.117	0.043	0.416	2.4	<1	Balance
Liner	3.45	0.1	0.05	0.4	2.1	0.4	Balance

4.3. Reciprocating Test Rig

The wear tests were conducted under lubricated sliding conditions in accordance with ASTM G133-05 standard. The schematic diagram of reciprocating wear testing rig, contact geometry and test sample are shown in Figure1. Load on the pin was applied using dead weights by way of lever arm loading system.

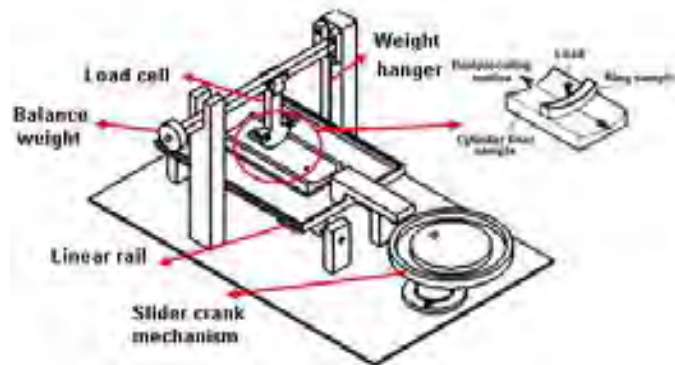


Figure 2. Reciprocating test rig, contact geometry and test sample [31].

The reciprocating test was designed to measure friction force, wear and surface temperature. Test conditions are presented Table 4.

Table 5. Tribotest conditions

Test specifications	Values
Load, N	60-80
Temperature, °C	70
Stroke, mm	100
Oil supply, ml/h	0.5
Distance, m	1000
Semi-synthetic oil, SAE	10W40
Friction Modifier (FM) Ratio	20%

5. MATERIAL AND METHODS

Variations of friction coefficient (μ) of cylinder liner and piston ring with the different test conditions are shown in Figure. 2 and 3. Friction coefficient has been changed on different loads and speeds. The coefficient of friction at a low load is small. Load increases friction coefficient. The reason for this is that it shows the boundary friction behavior of friction with the increase of the load. Semi-synthetic oil film deteriorates with increasing load. This increases the friction coefficient. The most significant factor affecting the oil film showed deterioration of the friction coefficient is high load. With the increasing speed tends to decrease the friction coefficient. This is because of rising rates, oil hydrodynamic effect is to show healing properties. Figure 1 is given by the speed of change of the friction coefficient. The coefficient of friction decreases with increasing speed. Friction modifier, the effect of reducing the coefficient of friction is observed markedly.

Semi-synthetic oil friction coefficient values ranged from 0.21 to 0.3 at 60N load in Figure 2. FM additives of 20% with stirring semi-synthetic oil experiments were repeated in the same conditions. An additive to improve the friction as FM coefficient of friction decreased rate of 10-29% at 60N load. Thus, friction coefficient ranged between 0.15 and 0.27.

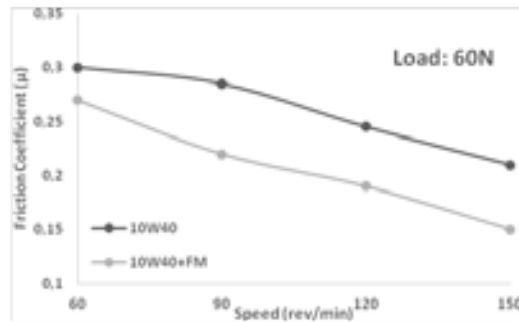


Figure 3. Friction coefficient of piston ring with cylinder liner in 60 N

Semi-synthetic oil friction coefficient values ranged from 0.38 to 0.27 at 80N load in Figure 3. FM additives of 20% with stirring semi-synthetic oil experiments were repeated in the same conditions. An additive to improve the friction as FM coefficient of friction decreased by 16-23% at 80N load. Thus, friction coefficient ranged between 0.21 and 0.32.

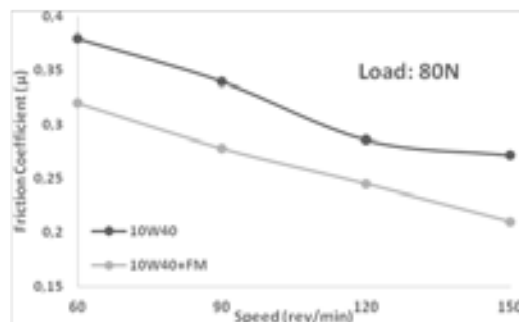


Figure 4. Friction coefficient of piston ring with cylinder liner in 80 N.

Variations of wear of cylinder liner and piston ring with the different test conditions are shown in Figure 4 and 5. Wear has been changed on different loads and speeds. Value of wear is lower at 60N than 80N loads. Load increases value of wear indicates increase tendency. The reason for this is that it shows the boundary friction behavior of friction with the increase of the load. Terms of boundary friction wear is also directly affected. Terms of increasing metal to metal contact in the boundary friction and wear mechanisms are triggered. The resulting adverse conditions increase wear. Figure 3 is given by the speed of change of the piston ring wear. The value of wear decreases with increasing speed. This situation is similar to the coefficient of friction. It is also seen in the modifier effects of friction wear values.

Semi-synthetic oil value of piston ring wear ranged from 0.0025g to 0.0017g at 60N load in Figure 4. An additive to improve the wear as FM value of wear decreased rate of 26-41% at 60N load. Thus, value of piston ring wear ranged between 0.0018 and 0.001.

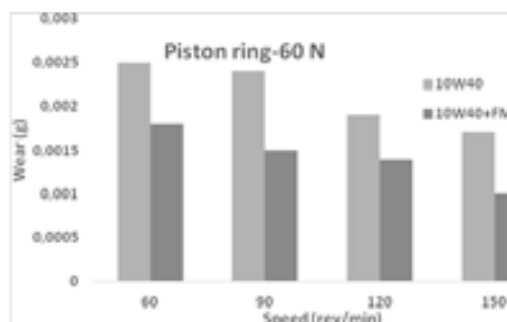


Figure 5. Wear of piston ring at 60N

Semi-synthetic oil value of piston ring wear ranged from 0.0029g to 0.0021g at 80N load in Figure 5. An additive to improve the wear as FM value of wear decreased rate of 23-24% at 80N load. Thus, value of piston ring wear ranged between 0.0022 and 0.0016.

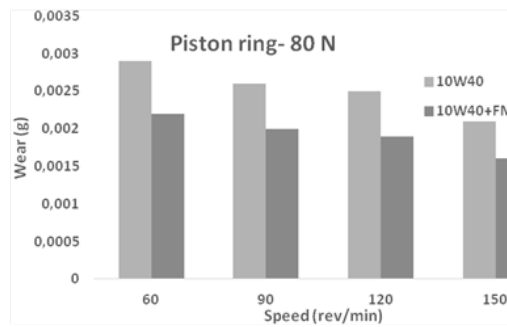


Figure 6. Wear of piston ring at 80N

Semi-synthetic oil value of cylinder liner wear ranged from 0.07g to 0.057g at 60N load in Figure 6. An additive to improve the wear as FM value of wear decreased by 12-15% at 60N load. Thus, value of piston ring wear ranged between 0.061 and 0.049.

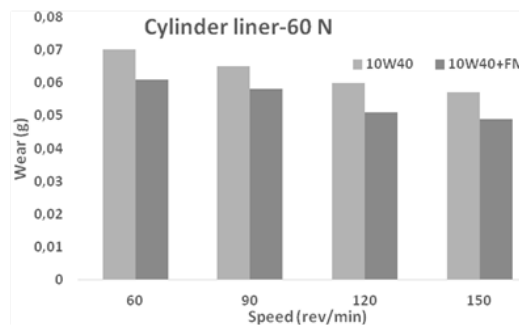


Figure 7. Wear of cylinder liner at 60N

Semi-synthetic oil value of cylinder liner wear ranged from 0.09g to 0.08g at 80N load in Figure 7. An additive to improve the wear as FM value of wear decreased by 7-11% at 60N load. Thus, value of piston ring wear ranged between 0.081 and 0.071.

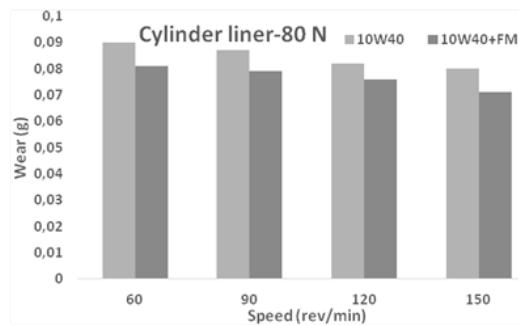


Figure 8. Wear of cylinder liner at 80N

6. CONCLUSION

The experiments carried out on a reciprocating wear test rig allow to subtraction the following observations:

- Test conditions are selected in a manner similar to the lubrication conditions in internal combustion engines. Experiments are conducted in the boundary and hydrodynamic conditions.
- The friction coefficient is reduced due to the increase of the speed. This is because of the contribution of speed to the hydrodynamic friction.
- The value of wear is reduced due to the increase of the speed. This is due to the contribution of speed to the hydrodynamic friction and due to the reduction in the adhesive effect.
- Friction Modifier affected both friction coefficient and value of wear. Changing the mixing ratio (%20) could be a possible subject for future studies.
- The tribological performance of semi-synthetic oil is increased with the oil additives. Thus, an economical alternative solution has been developed to fully synthetic oils.

REFERENCES

- [1]. Simon C. Tung, Hong Gao Tribological characteristics and surface interaction between piston ring coatings and a blend of energy-conserving oils and ethanol fuels, *Wear* 255 (2003) 1276–1285
- [2]. A. Erdemir, “Review of engineered tribological interfaces for improved boundary lubrication”, *Tribology International* 38 (2005) 249–256
- [3]. Richardson DE. Review of power cylinder friction for diesel engines. *Trans ASME J Eng Gas Tur Power* 2000;122:506–19.
- [4]. Priest M, Taylor CM. Automobile engine tribology—approaching the surface. *Wear* 2000;241:193–203.
- [5]. Taylor CM. Automobile engine tribology—design considerations for efficiency and durability. *Wear* 1998;221:1–8.
- [6]. Dhunput, M Teodorescu and C Arcoumanis “Investigation of cavitation development in the lubricant film of piston-ring assemblies”, *Journal of Physics: Conference Series* 85 (2007) 012005
- [7]. Beardsley MB, Happoldt PG, Kelley KC, Rejda EF, Socie DF. Thermal barrier coatings for low emission, high efficiency diesel engine applications. SAE Paper No. 1999-01-2255.
- [8]. Johnson DR, Diamond S. Heavy vehicle propulsion materials: recent progress and future plans. SAE Paper No. 2001-01-2061.
- [9]. Singh G, Graves RL, Storey JM, Partridge WP, Thomas JF, Penetrante BM, Brusasco RM, Merritt BT, Vogtlin GE, Aardahl CL, Habeger CF, Balmer ML. Emission control research to enable fuel efficiency. SAE Paper No. 2000-01-2198.
- [10]. Straton, J. T. and P. A. Willermet (1983). “An Analysis of Valve Train Friction in Terms of Lubrication Principles”, SAE TECHNICAL PAPER SERIES, 830165
- [11]. Uras, H. and D. Patterson (1987). “Measurement of Piston Ring Assembly Friction in Reciprocating Machines”, ASME, 87-ICE-55
- [12]. Rezeko and Henein (1984) “A New Approach to Evaluate Instantaneous Friction and Its Components in Internal Combustion Engines”, SAE 840719
- [13]. Taraza, D., N. Henein and W. Bryzik (2000). “Friction Losses in Multi-Cylinder Diesel Engines”, SAE TECHNICAL PAPER SERIES, 2000-01-0921.
- [14]. A. Borghia, E. Gualtieri, D. Marchetto, L. Moretti, S. Valeri, “Tribological effects of surface texturing on nitriding steel for high-performance engine applications” *Wear* xxx (2008) xxx–xxx

- [15]. Staffan Johansson, Per H. Nilsson, Robert Ohlsson, Cecilia Anderberg, Bengt-Goran Rosen, "New cylinder liner surfaces for low oil consumption" Tribology International
- [16]. Leustek, M.E., Sethu, C., Bohac, S., Filipi, Z., Assanis D. "CRANK-ANGLE RESOLVED IN-CYLINDER FRICTION MEASUREMENTS WITH THE INSTANTANOUES IMEP METHOD" Proceedings of WTC III September 12-16, 2005, Washington, D.C. USA
- [17]. Mcgeehan, J.A., "A Literature Review of the Effects of Piston and Ring Friction and Lubrication Oil Viscosity on Fuel Economy," SAE Paper 780673, 1978.
- [18]. Sandoval, D. and Heywood, J., "An Improved Friction Model for Spark-Ignition Engines," SAE Paper 2003-01-0725, 2003.
- [19]. Nakada M. Trends in engine technology and tribology. TribolInt 1994;27(1):3-8. - Sung-Woo Cho, Sang-Min Choi *, Choong-Sik Bae, Frictional modes of barrel shaped piston rings under flooded lubrication, Tribology International 33 (2000) 545-551
- [20]. Dhananjay Kumar Srivastava a, Avinash Kumar Agarwal, Jitendra Kumar, Effect of liner surface properties on wear and friction in a non-firing engine simulator, Materials & Design, Volume 28, Issue 5, 2007, Pages 1632-1640
- [21]. Kovach JT, Tsakiris EA, Wong LT. Engine friction reduction for improved fuel economy. SAE Paper 820085.
- [22]. Koch F. PIFFO-Piston friction force measurements during engine operation. SAE Paper 960306.
- [23]. Jeng, Y. (1992), "Theoretical Analysis of Piston-Ring Lubrication Part 1-Fully Flooded Lubrication," Trib. Trans., 35, pp 696-706.
- [24]. NATHAN W. BOLANDER, FARSHID SADEGHI Deterministic Modeling of Honed Cylinder Liner Friction, Tribology Transactions, 50: 248-256, 2007
- [25]. M. Priest C.M. Taylor, "Automobile engine tribology — approaching the surface" Wear 241 _2000. 193-203
- [26]. Black AL, Dunster RW, Sanders JV, McTaggart FK. Molybdenum disulphide deposits—their formation and characteristics on automotive engine parts. Wear 1967;10:17-32.
- [27]. Green AB, Risdon TJ. The effect of molybdenum-containing, oilsoluble friction modifiers on engine fuel economy and gear oil efficiency. SAE Pap 1981;811187.
- [28]. Noorman MT, Assanis DN, Patterson DJ, Tung SC, Tserogounis SI. Overview of techniques for measuring friction using bench tests and fired engines, SAE Paper 2000-01-1780. SAE Trans—J Fuels Lubr 2000;109.
- [29]. Benvenuti LH, Coelho EPD, Filho AS, Ribeiro E, Campos JFL, Possuelo RB, et al. Fuel economy performance evaluation of 5W-30 low friction oil, SAE Paper 2002-01-3530, 2002.
- [30]. Martin Skjoedt, Ryan Butts, Dennis N. Assanis, Stanislav V. Bohac "Effects of oil properties on spark-ignition gasoline engine friction" Tribology International 41 (2008) 556-563
- [31]. Murat Kapsiz, Mesut Durat, FeritFicici, "Friction and wear studies between cylinder liner and piston ring pair using Taguchi design method", Advances in Engineering Software 42 (2011) 595-603.

INVESTIGATION OF MECHANICAL PROPERTIES OF CHASSIS PROFILE DESIGNED FOR LIGHT VEHICLES

Deniz SOYEL DOGAN

Sakarya Üniversitesi Fen Bilimleri Ens. Makina Eğitimi Böl, Sakarya, Türkiye,
E-posta: deniz_soyel@hotmail.com

Ahmet DEMİRER

Sakarya Üniversitesi Teknik Eğitim Fakültesi Makina Eğitimi Böl., Sakarya, Türkiye,
E-posta: ademirer54@yahoo.com

Abstract

Development of high strength new materials which are light and therefore enable fuel saving without giving up safety and comfort is among the important targets of automobile manufacturers. Preference of aluminum, which stands up among light weight metals with its cost, good workability, corrosion resistance and recycling characteristics and properties such as both vehicle weight reduction and absorption of energy that occurs during crash, etc., increases each year in light metal selection required for fuel saving in the developing automotive industry. When a material is subject to cold forming, the hardness and strength of that material improve due to distortion occurring in its cage structure. Sheet metals which go through plastic shaping become more in this way compared to ready extrusion profiles. In the present study, open profiles, which are designed as light weight AA5754 chassis profile of 2mm thickness and shaped by bending machine and casting in eccentric press and named as P1 and P1r, were compared with their solid flat forms in terms of resistance characteristics such as tensile strength, hardness and charpy impact resistance. As a result of the performed tests, P1 and P1r profiles were compared with flat sheet and the best values were obtained from P1r profile. It was determined that there was 12.54% increase in tensile strength, 36.42% charpy impact resistance and 3.1% in hardness in P1r profile in comparison to flat sheet.

Key Words: Chassis profile, AA5754, Cold forming.

1. Introduction

Chassis is the main structure carrying various systems of the vehicle and bodywork. For the chassis to be resistant, light, rigid and few parts and its mechanical parts to be mounted and dismounted easily, it is required that it has also low cost despite of this [1].

Aluminum is one of the mostly found elements in nature and mostly used metals in engineering structures after steel. Aluminum and its alloys are used in the manufacturing of many pieces in vehicle construction as casting, sheet and profile state.

Two types of alloys are suggested for aluminum extrusion trunk profiles; 6xxx (Al-Mg-Si) series have the highest shaping ability and 7xxx (Al-Zn-Mg) series have the highest resistance among aluminum alloys and used in the construction of aircraft parts and in places requiring high resistance. Many aluminum alloys other than these can be used in extrusion however these two alloys generate the best results in terms of reproducibility and performance characteristics [2].

Researchers studied soft steel and magnesium alloys (AA 6XXX) in terms of resistance and tested tensile, bending and energy absorbance characteristics of both material groups. As a result, it was determined that energy absorbance capacity of magnesium alloys was 10 fold higher than that of soft steel. They indicated that because of this performance, magnesium alloys can be used in many places as well as in bumper rod profiles of automobiles or door inner surfaces [3].

In another study, steel as a chassis profile material and AA 6063 material were compared and aluminum alloy of 73.1 HBW hardness was used. According to the obtained results from materials that were obtained from materials that were subjected to three point bending and various resource experiments; AA 6063 is a material that is adaptable to extrusion, resource and heat treatment and has sufficient mechanical characteristics. Furthermore, it was observed that energy absorption of AA6063 was 2 folds higher in comparison to that of steel [4].

Cold forming is plastic deformation event occurring at temperatures (room temperature) under recrystallization temperature. Distortion occurs in the cage structure of a crystalline structure material that goes through plastic deformation. The greatest distortion takes place in the borders of slide planes and particles and as the deformation rate increases distortion rate also increases. In this case, deformation hardening takes place in the material. In case distortion occurs in the cage structure of a material, hardness and strength of that material increase [5, 2].

In a study scrutinizing the contributions of cold forming to a material, it was indicated that material hardness increased 40-100% in corner regions of the sections in comparison to the plane parts. The reason for the reach of this increase to a maximum value in the middle points of corner folds is maximum cold forming process in these points. Increase of material hardness is directly proportional

to resistance but is inversely proportional to ductility. In other words, as the hardness increases resistance increases but ductility decreases and the material becomes more brittle. Because of the cold forming process, there was increase in the corner regions of the sections and approximately 50% increase was obtained in yield strength and 15% increase in tensile strength in comparison to the plane parts. As a result, plastic shaped sheet materials become more resistant in comparison to the extrusion profiles [6].

In the present study, P1 and P1r open profiles which are designed as light chassis profile were shaped from AA5754 sheet material of 2mm thickness by the aid of bending machine and eccentric press. The designed profiles' mechanical resistance was compared with their flat sheet forms (tensile, charpy impact resistance and hardness).

In the first stage of the study, tensile, charpy impact and hardness samples were obtained by laser cutting of AA5754 unshaped sheets according to the standards. In the second stage of the study, ear parts of the open profiles were bent by bending machine and their final shape was formed in eccentric press molds. In the third stage, standard samples were cut over bent profiles by the wire erosion method and tested. The obtained results were compared with one another.

2. Experimental Studies

2.1. Material and Method

Chemical content of AA5754/H111 alloy material that was used in the study is shown in Table 1.

The most preferred alloy is 6063 for standard profile manufacturing in the market among 6000 series alloys that are apt to shaping by extrusion. In the present study, the reason that we used 5754 aluminum alloy material is that it has high cold forming ability and has characteristics closest to A6063. Moreover, the welding ability of the material is rather high.

Table 1. Chemical content of material that was used in the experiments [7]

Numerical and Chemical Symbols	Si	Fe	Cu	Mn	Mg	Cr	Zn	Ti	Others (Total)
AA5754 EN AW-Al Mg3 (%)	0,40	0,40	0,10	0,50	2,6-3,6	0,30	0,20	0,15	0,15

In order to see the mechanical properties of AA5754 sheet, tensile, hardness and charpy samples of four units each were obtained by laser cutting method.



Figure 1. a) Tensile samples, b) Tensile equipment and c) Pulled samples

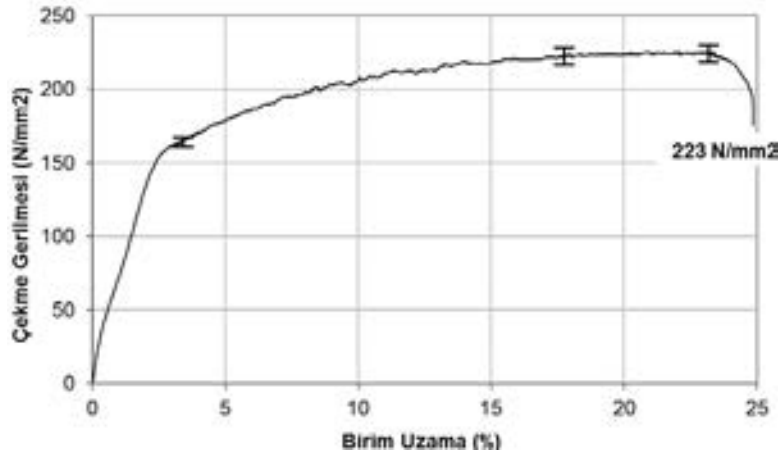


Figure 2. Distension - % unit elongation graphic of AA5754 sheet

Pulled samples obtained by laser cutting method according to the standards were put through a pulling test at 10mm/min velocity at room temperature in Shimadzu equipment of 50kN capacity (Figure 1). Distension - % elongation graphics obtained as a result of pulling experiment are shown in Figure 2. HBW hardness measurement of AA5754 sheet and with $V=5\text{m/s}$ velocity, and Charpy resistance measurement was made by Instron brand test equipment (Figure 3).

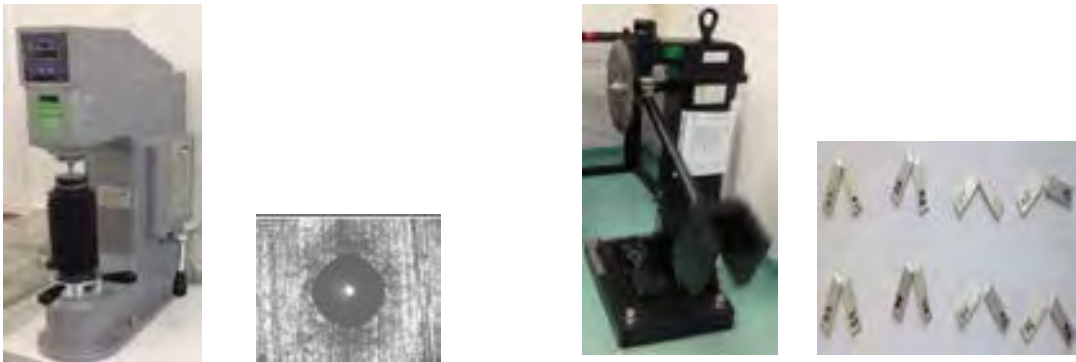


Figure 3. a) Hardness measurement equipment and measurement trace, b) Charpy equipment and tested Charpy samples

Sheet metals were cut at 2 x 112 x 300mm dimensions by laser cutting method and 5mm ear parts of the profiles (P1 and P1r) were bent first by bending machine. Then, final shapes of flat (P1) and radius (P1r) profiles were formed in molds (Figure 5).

The reason for shaping the flat sheets in bending machine and eccentric press is to benefit from superiorities of cold forming. These are greater dimension sensitivity, narrower tolerances and better surface quality and superior mechanical properties (because of strain hardening, hardness and resistance increase), no need for heating and hardening of parts, and desired directed characteristics of the product [8,9].

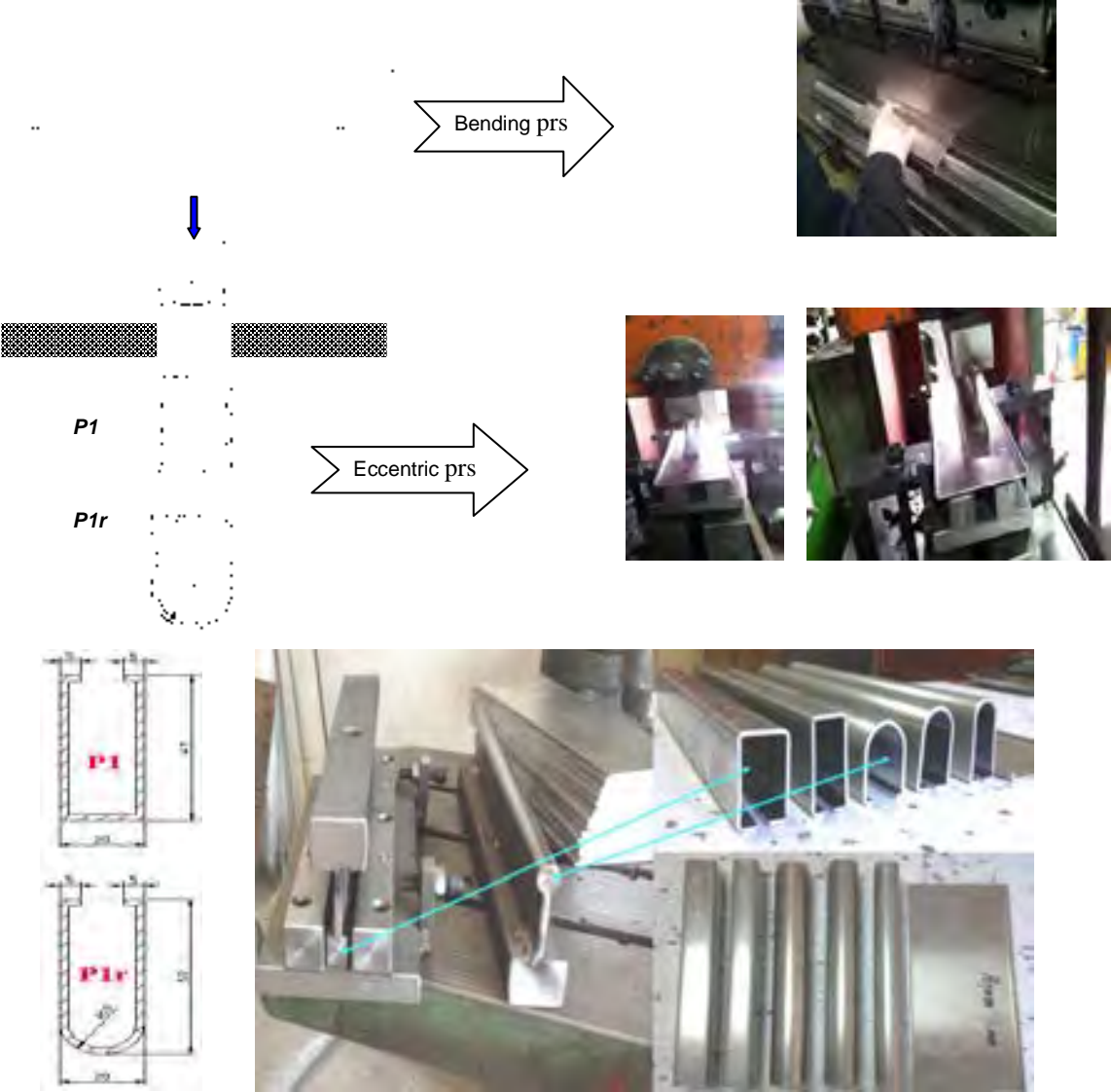


Figure 5. Technical pictures, molds and samples of plane and radius profiles (P1 and P1r)

Standard charpy and pulling samples were cut (Figure 6) by wire EDM process at the upper and side of shaped profiles and mechanical tests were performed.

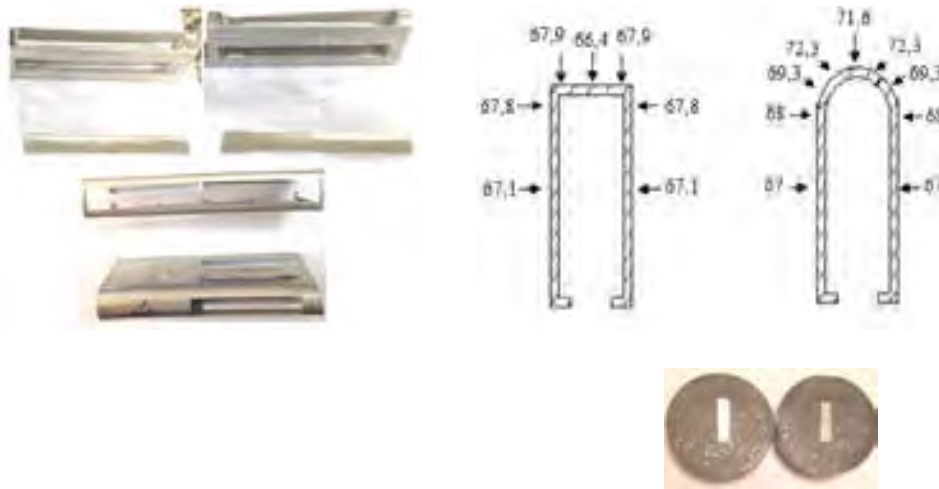


Figure 6. Samples of profiles obtained by wire EDM process and hardness (HBW) measurements

Hardness measurements were made at various places of both side and upper regions of the shaped profiles. Radius part of P1r profile was divided into two parts and after bakelite pouring, hardness values of the upper part were measured (Figure 6). Results of pulling test of P1 and P1r profiles, and obtained tension-% strain (unit elongation) graphics are shown in Figure 7.

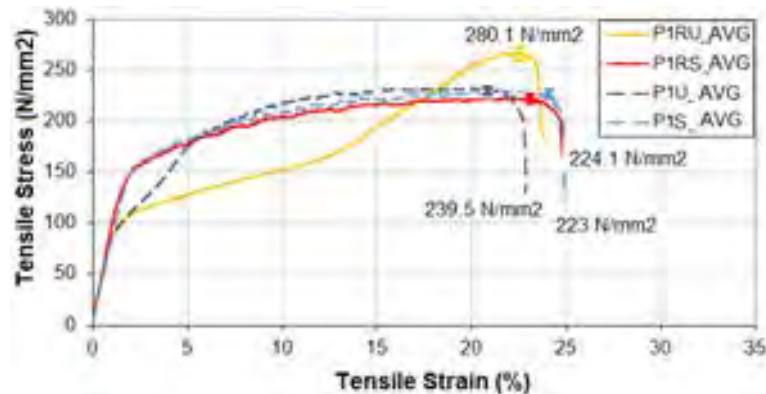


Figure 7. Tensile stress- % strain (unit elongation) graph of P1 and P1r profiles

Test results of shaped and unshaped samples were compared with one another in Table 2.

Table 2. The average mechanical characteristics of unshaped sheet, plane and radius profiles (P1 and P1r) and rectangular profile

	Sheet	P1		P1r		Rectangular Box Prf. (40x20x2)
		P1 -upper	P1 -side	P1r -upper	P1r -side	
Avg. Tensile Stress (N/mm ²)	223±1,9	239,5	223,5	280,1	224,1	223
Avg. Charphy (joule)	7	9,6	9,4	9,9	9,3	7

Avg. Hardness (HBW)	67	67,15 ±0,75	68	70,15±2,15	68	64
----------------------------	----	-------------	----	------------	----	----

Note: P₁ upper, P1r upper= Sample taken from the upper part of profile, P1 side, P1r side= Sample taken from the side of profile

3. Results and discussion

Pulled, charpy and hardness test samples were obtained from flat sheets and profiles (P1 and P1r) that are bent and shaped according to standards by laser cutting and wire EDM process. Test results of the samples were compared with each other.

When test results of P1 and P1r profiles were compared with the flat sheet, it was observed that there was 3.24% **increase** in average tensile resistance of P1 profile, 35.71% increase in charpy, and 1% increase in hardness, and 12.54% increase in P1r profile's pulling strength, 36.42% increase in impact resistance and 3.1% increase in hardness.

Increase in mechanical values of P1 and P1r profiles occurred due to cold forming event. As a result of cold forming, tensile strength, yield strength and hardness increased, and breakage elongation value decreased approximately 8%. It is known that these changes originate from distortion in the cage and particle structures of the material [10].

It is seen clearly in Table 4 that "P1 side and P1r side" tensile, charpy and hardness values of the samples taken from the sides of P1 and P1r profiles are almost close to those of the flat sheet. The reason for this is that side regions of the profiles were subject to cold forming excessively. Despite all, there was an increase reaching 36% in mechanical values of "P1 upper and P1r upper" samples taken from the upper part of the same profiles. Especially high values of the parts close to the corners illustrate that these regions were subject to cold forming in a high rate.

The results obtained from the conducted study are parallel to the studies of Tama and Kaplan [6]. It is thought that P1r could be a more appropriate design example among the studied samples in terms of mechanical values of chassis profiles designed for small vehicles, high impact resistance, good energy absorbance, and being light and easily cold forming with low cost.

References

1. http://www.obitet.gazi.edu.tr/obitet/chassis_and_powertrain/chassis_and_body.htm, October 2010
2. Eker, A. A., (2008) "Aluminum and Alloys Lecture Notes", Technical University of Yıldız.
3. Easton, M., Song, W.Q., and Abbott, T., (2006) "A comparison of the deformation of magnesium alloys with aluminium and steel in tension, bending and buckling, *Materials and Design*", 27-935–946.

4. Demirel, O.,(2012) "Development of automobile chassis parts via aluminum extrusion and sand casting technology", ODTÜ Institute of Science and Technology, Master Thesis, Ankara.
5. Çapan, L.,(2010) "Plastic Deformation of Metals", Çağlayan Bookstore (İSTANBUL) 5th edition.
6. Tama, Y. S., Kaplan, H.,(2007) "Cold Forming Cold Forming Methods and Impact on Job Mechanical Properties of Steel Materials", 2th Steel Structures National Symposium, TMMOB Civil Engineers, Eskişehir Department.
7. TS EN 573_3 Aluminium and aluminium alloys - Chemical composition and form of wrought products - Part 3: Chemical composition and form of products. ICS 77.150.10; 2014.
8. Gülmez, T.,(2011) "Manufacturing Processes Lecture Notes", İTÜ Faculty of Machine (İstanbul).
9. www.newagepublishers.com(Plastic Deformation of Metals and Related Properties), 2015.
10. Savaşkan, T.,(1999) "Materials Science and Testing of Materials", First Edition, Derya Bookstore (Trabzon).

EFFECTS OF TEREBINTH (PISTACIA TEREBINTHUS L) OIL ADDITION TO QUAILION GROWTH PERFORMANCE, CARCASS TRAITS, SOME BLOOD PARAMETERS AND COMPOSITION OF BREAST MEAT FATTY ACID

Cavit ARSLAN

Kafkas University, Faculty of Veterinary Medicine, Department of Animal Nutrition and Nutritional Disease,
36100 Kars, TURKEY. Mobile: +90 536 388 23 54. E-mail: carslan42@hotmail.com.

Tuncay TUFAN

Kafkas University, Faculty of Veterinary Medicine, Department of Animal Nutrition and Nutritional Disease,
36100 Kars, TURKEY. Mobile: +90 536 388 23 54.

Aydin DAŞ

Bingöl University, Agricultural Faculty, Department of Animal Science, 12100 Bingöl,
TURKEY

Abstract

Development of high strength new materials which are light and therefore enable fuel saving without giving up safety and comfort is among the important targets of automobile manufacturers. Preference of aluminum, which stands up among light weight metals with its cost, good workability, corrosion resistance and recycling characteristics and properties such as both vehicle weight reduction and absorption of energy that occurs during crash, etc., increases each year in light metal selection required for fuel saving in the developing automotive industry. When a material is subject to cold forming, the hardness and strength of that material improve due to distortion occurring in its cage structure. Sheet metals which go through plastic shaping become more in this way compared to ready extrusion profiles. In the present study, open profiles, which are designed as light weight AA5754 chassis profile of 2mm thickness and shaped by bending machine and casting in eccentric press and named as P1 and P1r, were compared with their solid flat forms in terms of resistance characteristics such as tensile strength, hardness and Charpy impact resistance. As a result of the performed tests, P1 and P1r profiles were compared with flat sheet and the best values were obtained from P1r profile. It was determined that there was 12.54% increase in tensile strength, 36.42% Charpy impact resistance and 3.1% in hardness in P1r profile in comparison to flat sheet.

Key Words: Chassis profile, AA5754, Cold forming.

1. Introduction

Various subtherapeutic antibiotics have been used as feed additives since 1940's to enhance growth performance and to prevent disease in livestock, particularly poultry. Usage of antibiotics as feed additives was banned in European Union in 2006 (EU, 2003) due to the antibiotic residue risk in animal products and the potential evolving of antibiotic resistant bacteria. This action has led to acceleration in the number of research on alternative natural feed additives, such as probiotics, prebiotics, organic acids, herbs, spices and various plant extracts, in animal production (Alcicek et al., 2004). Certain aromatic plants themselves and essential oils (EO) derived from them have increasingly been used for such purpose. The EO, extracted mainly from herbs and spices is a complex mixture of various compounds, which consist of aromatic and volatile substances (Jang et al., 2007). Essential oils may exhibit a range of potentially beneficial properties, including antimicrobial effects in gut (Jang et al., 2007), antioxidant (Vichi et al., 2001), antiparasitic (Hafez and Hauck, 2006), and a digestive stimulant (Hernandez et al., 2004; Jang et al., 2007).

The genus *Pistacia* comprises 16 or 20 recognised species (Couladis et al., 2002; Ozcan 2004, Topcu et al., 2007; Kavak et al., 2010). *Pistacia terebinthus* L. (terebinth or the turpentine tree), is a small tree, widely distributed in the Mediterranean region and west Asia, (Couladis et al., 2002; Ozcan 2004, Topcu et al., 2007; Kavak et al., 2010), especially southeast of Turkey (Ozcan, 2004). The main nutrients in the fruit of terebinth are ether extracts (35.26-47.52 %) (Matthaus and Ozcan, 2006; Kızıl and Turk, 2010). It thus contains at low rates crude protein (6.4 %) and crude ash (1.5 %) (Kızıl and Turk, 2010). The fruits include 0.1 % essential oils (Kızıl and Turk, 2010), and 0.06-0.16 % (Ozcan et al., 2009) or 0.73 % (Couladis et al., 2002) volatile fatty acids. It also contains macro- (Ca, P, K, Na, Mg, S) and micro-elements (Fe, Al, Zn, Cu, Mn, Se, Co, Cr) (Ozcan 2004; Kızıl and Turk, 2010) as well as tocopherols, tocotrienols, sterols and other phenolic constituents (Matthaus and Ozcan, 2006; Topcu et al., 2007).

Different part of the terebinth tree has got a lot of pharmacologically active substance. For example, there have been α -pinene, terpinolene and limonene in the shell of terebinth fruit (Kusmenoglu et al., 1995), α -pinene, β -pinene, sabinene and terpinene in the resin branches of terebinth (Papageorgiou et al., 1999) and α -pinene, limonene, α -felandrene, terpinolene, p-cymen-8-ol and caryophyllene oxide in the mature fruit of terebinth (Couladis et

al., 2002; Ozcan et al., 2009). Furthermore, there have been flavonoid compounds, such as luteolin, luteolin-7-glucoside and apigenine-7-glucoside in the leaf extract of terebinth (Kavak et al., 2010).

Kavak et al., (2010) have indicated that terebinth leaf extract shows higher antioxidant capacity. Some of the active compounds, such as luteolin and luteolin-7-glucoside, in the terebinth (Kavak et al., 2010) and α -pinene in the salvia, (Tzakou et al., 2001)- α -pinene also exist in terebinth - have antimicrobial effect. Topcu et al., (2007) have found that fruits of terebinth contain phenolic and flavonoids, such as quercetin and α -tocopherol, both are used as standard antioxidant compounds. Essential oils obtained from the leaves of terebinth have antifungal activities (Duru et al., 2003). De Whalley et al., (1990) and Yee, (1996) have reported that terebinth fruit has hypocholesterolemic and arteriosclerosis preventive effect because of its unsaturated fatty acid and tannin content. Bakirel et al., (2003) have established that dried terebinth fruits have a hypolipidemic effect on the hyperlipidaemic rabbits without toxic effect.

There have been a lot of researches on the usage of certain aromatic plants/herbs/spices such as black cumin seed, thyme, cinnamon, forelock of mercury, peppermint, rosemary, garlic and essential oils (EO) derived from these plants or commercial EO as feed additives in the poultry feeding. On the other hand, there has been, as to date, no research on the usage of terebinth fruit oil (TFO) in poultry feeding. Therefore, the study aimed to assess supplementation of TFO to diet on growth performance, carcass traits, some blood parameters and fatty acid composition of breast meat in quail.

2. Materials and Methods

2.1 Birds, experimental design, housing environment and diets

Two hundred and forty unsexed day old Japanese quail chicks (*Coturnix coturnix japonica*) were allocated randomly to three dietary treatment groups. Each treatment had 4 replicate pens with 20 birds per pen. The experimental diets consist of an unsupplemented basal diet, based on corn and soybean meal (Table 1). Basal diets were supplemented with 0 (Control), 130 mg/kg (Trial I), or 260 mg/kg TFO (Trial II). The TFO was first mixed into the vegetable oil component of the ration, and then the oil mixture was added to the basal diets. All essential nutrients contained in the basal diet met the requirements suggested by the NRC (1994) for quails. The

experimental diets were in mash form. The experimental diets were given ad libitum d 1-21 starter diet; d 22-42 grower diet.

Table 1. Ingredient and nutrient content of the basal diets, (g/kg)¹.

Item	Starter (d 1-21)	Grower (d 22-42)
Ingredient		
Corn	400.0	370.0
Wheat	61.5	202.5
Vegetable oil	50.0	43.0
Soybean meal	380.0	250.0
Sunflower meal	80.0	100.0
Dicalcium phosphate	83.0	15.0
Limestone	13.5	12.8
Vit. / min. premix ²	3.5	3.5
Salt	3.0	3.0
DL-Methionine	0.2	0.2
Calculated analysis, DM basis ³		
Metabolizable energy, MJ/kg	12.55	12.55
Calcium	0.80	0.90
Total phosphor	0.65	0.70
Lysine	1.42	1.11
Methionine+Cysteine	0.77	0.67
Linoleic acid	1.55	1.49
Analysed nutrient composition, DM basis		
Dry matter	889.9	890.3
Crude protein	239.2	204.9
Ether extract	70.9	64.8
Crude fibre	43.5	41.0

¹The basal diets were the same in the all groups. Treatment diets were supplemented with 130 or 260 mg/kg of terebinth fruit oil.²Supplied per kg diet: Vit A, 8400 IU; vit D₃, 44800 IU; vit E, 56 mg; vit K₃, 2.24 mg; vit B₁, 1.68 mg; vit B₂, 4.48 mg; niacin, 33.6 mg; cal.D-pantothenate, 10 mg; vit B₆, 2.8 mg; vit B₁₂, 9 µg; D-biotin, 0.112 mg; folic acid, 1.12 mg; vit C, 56 mg; manganese, 59 mg; iron, 47 mg; zinc, 47 mg; copper, 47 mg; cobalt, 0.112 mg; iodine, 0.56 mg; selenium, 0.100 mg; molybdenum, 0.582 mg.³: Calculated based on NRC (1994) data of feedstuffs nutrient tables.

Body weights of the birds and feed intake of each replicate pen was recorded at the beginning of the study and at the end of each period. Feed conversions per pen were calculated at the 21- and 42 d of study. At 42 d of the study, 20 birds (5 birds from each replicate) of similar body weight were selected from each group, weighed and slaughtered for determination of the carcass traits and the internal organ weights. In the slaughtering process blood samples were also taken. Blood samples were centrifuged at 3000 g for 10 minutes. Serum samples were

stored -20 °C for analyses. From the middle of 1 to 3 both sides of the breast meat, meat samples were taken for fatty acid analyses and were stored at -20 C until analysis.

2.2. Analytical procedures

Dry matter, crude protein (N x 6.25, micro-Kjeldahl), crude fat, crude fibre and crude ash in the diets were determined in accordance with AOAC (2000) methods. Blood biochemistry analyses included the measurement of total cholesterol, high density lipoprotein (HDL), aspartate amino transferase (AST), alkaline phosphatase (ALP), total protein, albumin and globulin. Concentrations of blood parameters were analysed by an auto analyser (Beckman Coulter AU5800), using the commercial kits. Concentrations of individual fatty acids were determined using gas chromatography (HP Agilent 7890) according to methods described by Paquot (1979).

2.3. Statistical analyses

The statistical processing of data was performed using the SPSS program, based on a one-way ANOVA, with $P \leq 0.05$ considered to be significant. After ANOVA, significantly different means for each variable were separated using Duncan's multiple-range tests.

3. Results

Crude nutrient contents of the fruit of terebinth used for making TFO were analysed as follows; 94.36 % dry matter, 38.91 % crude fat, 10.07 % crude protein and 3.26 % crude ash, in dry matter basis. Fatty acid composition of the TFO is shown in Table 2. The dominating fatty acid in the TFO was oleic acid (46.82 %). The other fatty acids are linoleic-(23.07 %), palmitic-(22.00 %), stearic-(4.61 %), palmitoleic-(2.14 %), and linolenic acid(1.36 %).

Growth performance parameters of the birds are shown in Table 3, carcass traits and relative organ ratio are shown in Table 4, serum composition is given in Table 5 and fatty acid profiles of breast meat of the birds are given in Table 6.

Table 2. Fatty acid composition of terebinth fruit oil used in this study.

Fatty acid	C16:0	C16:1	C18:0	C18:1	C18:2	C18:3
Amount, g/kg	220.0	21.4	46.1	468.2	230.7	13.6

C16:0= Palmitic acid, C16:1= Palmitoleic acid, C18:0 = Stearic acid, C18:1 = Oleic acid, C18:2 = Linoleic acid, C18:3 = Linolenic acid

Table 3. Effects of dietary terebinth fruit oil supplementation on the performance of quails.

Item	Control	Trial I	Trial II	SEM	Sig.
Body weight, g					
1 d	8.6	8.6	8.5	0.05	NS
21 d	92.8 ^b	90.1 ^b	98.6 ^a	0.78	***
42 d	194.1 ^b	194.7 ^b	204.5 ^a	1.64	*
Daily weight gain, g/d					
1 to 21 d	3.98	3.89	4.13	0.06	NS
22 to 42 d	4.88	5.10	5.09	0.06	NS
1 to 42 d	4.43 ^b	4.49 ^b	4.61 ^a	0.04	***
Daily feed intake, g/d					
1 to 21 d	7.69	7.43	8.03	0.14	NS
22 to 42 d	19.25	18.27	18.99	0.24	NS
1 to 42 d	13.47 ^a	12.70 ^b	13.55 ^a	0.17	*
Feed conversion, g/g					
1 to 21 d	1.93	1.91	1.95	0.02	NS
22 to 42 d	3.95	3.59	3.74	0.07	NS
1 to 42 d	2.94 ^a	2.74 ^b	2.82 ^{ab}	0.04	*

NS: Non significant ($P > 0.05$). ^{ab}Mean values in the same row with a common letter are significantly different (*: $P < 0.05$, *** $P < 0.001$).

Table 4. Effects of dietary terebinth fruit oil supplementation on the carcass yield traits of quails.

Item	Control	Trial I	Trial II	SEM	Sig.
Body weight, g	194.2 ^b	194.8 ^b	204.1 ^a	1.66	*
Carcass weight, g	134.5 ^{ab}	131.3 ^b	137.7 ^a	1.08	*
Carcass ratio, %	69.33	67.51	67.56	0.46	NS
The relative organ ratio to the carcass weight, %					
Breast	32.11	32.37	32.61	0.42	NS
Leg	23.12	22.74	22.43	0.15	NS
Wing	10.62	10.18	10.91	0.15	NS

Heart	1.54	1.57	1.58	0.02	NS
Liver	3.35	3.93	4.13	0.15	NS
Gizzard	3.59	3.69	3.44	0.07	NS

^{ab}Mean values in the same row with a common letter are significantly different (*: P <0.05).

NS: Non significant (P > 0.05).

Table 5. Effects of dietary terebinth fruit oil supplementation on the serum parameters of quails.

Item	Control	Trial I	Trial II	SEM	Sig.
Total cholesterol, mg/dL	230.3	201.4	212.0	8.16	NS
HDL, mg/dL	135.7	115.0	83.0	10.04	NS
AST, IU/L	280.1	310.6	299.3	14.47	NS
ALP, IU/L	786.8	936.0	813.3	30.07	NS
Total protein, g/dL	2.81	2.77	3.22	0.10	NS
Albumin, g/dL	0.98	1.00	1.10	0.04	NS
Globulin, g/dL	1.83	1.77	2.13	0.07	NS

NS: Non significant (P > 0.05).

Table 6. Effects of dietary terebinth fruit oil supplementation on the fatty acid composition of breast meat of quails, g/kg.

Item	Control	Trial I	Trial II	SEM	Sig.
C14:0	4.9	5.3	4.4	0.03	NS
C16:0	260.9	241.6	254.2	0.37	NS
C17:0	2.1	1.6	1.7	0.06	NS
C18:0	180.6	164.1	173.0	0.54	NS
Σ SFA	448.0	412.6	432.8	0.83	NS
C16:1	24.8	30.2	28.9	0.23	NS
C18:1	158.1	181.1	146.4	0.89	NS
Σ MUFA	177.8	211.3	175.3	1.09	NS
C18:2	277.6	274.7	284.1	0.32	NS
C18:3	22.0	21.8	18.2	0.35	NS
C20:4	64.9	69.3	80.0	0.35	NS
Σ PUFA	364.5	365.8	382.3	0.81	NS

Σ PUFA/ Σ SFA	0.82	0.90	0.88	0.02	NS
-----------------------------	------	------	------	------	----

C14:0= Myristic acid, C16:0= Palmitic acid, C16:1= Palmitoleic acid, C17:0= Heptadecanoic acid, C18:0 = Stearic acid, C18:1 = Oleic acid, C18:2 = Linoleic acid, C18:3 = Linolenic acid, C20:4= Arachidonic acid, SFA= Saturated fatty acids, MUFA= Monounsaturated fatty acids, PUFA= Polyunsaturated fatty acids. NS: Non significant (P > 0.05).

4. Discussion

In this study, supplementation of 260 mg/kg TFO to diet induced an increase on the live weight of the birds both at the starter and grower periods when compared to the birds in the Control and 130 mg/kg TFO supplemented groups (Table 3). Weight gain of the birds in the 260 mg/kg TFO supplemented group was higher than those of the other groups in overall the study. The results on the live weight and weight gain of the birds indicated that supplementation of high level TFO (260 mg/kg) to diet improved live weight and weight gain. This was not achieved in the low level TFO supplemented group (130 mg/kg). The improvement on the live weight of bird in the 260 mg/kg TFO supplemented group may be related to the antibacterial agents, such as luteolin and luteolin-7-glucoside (Kavak et al., 2010), α -pinene (Tzakou et al., 2001), antioxidant compounds, such as quercetin and α -tocopherol (Topcu et al., 2007), and high linoleic acid content of the TFO used in this study (Ayfer, 1973; Ozcan 2004; Kizil and Turk, 2010). In addition, Jang et al., (2004) reported that a commercial blend of EO showed a marked increase in digestive enzyme activities of the pancreas and intestinal mucosa from broiler chickens, leading in a significant growth performance. Further, Hernandez et al., (2004) indicated that two different plant extracts improved the digestibility of the feeds for broilers. Similar result was also reported by Lee et al., (2003), which indicates that EO in diets encourages secretions of endogenous digestive enzymes, which then enhance nutrient digestion and gut passage rates in chickens. Live weights of the birds were similar in the Control and 130 mg/kg TFO supplemented groups. This situation may be related to the basal diets used in the present study, which had adequate and balanced nutrient content, high digestibility, and optimum environmental conditions during the research. It has been proposed that dietary EO supplementation as growth stimulators could not give positive effect when chickens are raised at optimal condition such as highly digestible diets and clean condition (Botsoglou et al., 2002). As known, well-nourished, healthy chicks do not respond to antibiotic supplements if they are

housed under clean and disinfected conditions. In addition, antimicrobial agents may have more impact when the diet used is less digestible (Lee et al., 2003).

In this study, supplementation of 130 mg/kg TFO induced lower feed intake than those of the other groups in overall the study ($P < 0.05$). In contrast to this study, Kamel (2001) suggested that herbs, spices and various plant extracts have appetiser and digestion-stimulating properties and antimicrobial effects. In addition, supplementation of 130 mg/kg TFO improved feed conversion when compared to Control group. Kucukyilmaz et al., (2012) have conducted two experiments to determine the effects of supplementation EO, which contains certain active substances found also in the TFO (such as terpinene, α -pinene, limonene, caryophyllene), on the growth performance in broilers. In experiment I (within October – November period); they have not found differences on the live weight, feed intake, and feed conversion among the groups. However, in experiment II (including April to May); they have documented higher live weight and improved feed conversion in the EO supplemented group than those of the Control group. Likewise, Khosravini (2013) has designed a study in broilers on the usage of *Satureja khuzistanica* oils, which contains some essential oils located in the TFO. He found that 0.5, 1.0, 1.5, 2.0 and 2.5 g/L oil supplementation via by drinking water negatively affected weight gain, feed intake and feed conversion of the birds when compared to Control. Alcicek et al., (2003) have also supplemented 24, 48, and 72 mg/kg commercial blend of EO to broiler diets, respectively. They have found that supplementation of 24 mg/kg EO do not affect growth performance of birds, but 48 and 72 mg/kg EO supplementation has improved live weight and feed intake. In another study, Alcicek et al., (2004) have determined that, supplementation of 36 or 48 mg/kg blend of EO, obtained from different plants, do not affect live weight, decreased feed intake and unchanged weight gain and feed conversion of broilers.

In the present study, supplementation of 260 mg/kg TFO to diet significantly increased ($P < 0.05$) the slaughter body weight of birds when compared to other groups (Table 4). The carcass weight was also higher in 260 mg/kg TFO supplemented group than that of the 130 mg/kg TFO supplemented group. Higher slaughter body weight and carcass weight in the 260 mg/kg TFO supplemented diet group than those of the other groups originated from the higher final live weight of the birds at the end of the study in this group. Both 130 and 260 mg/kg TFO supplementation induced no difference on the carcass ratio and, carcass parts and visceral

organ ratio to carcass weight when compared to the Control group. Similar results were found by Kucukyilmaz et al., (2012) in broilers. Khattak et al., (2014) reported that 300, 400 and 500 g/ton EO supplementation to diet increased carcass weight but not 100 and 200 mg/kg in broilers. They also determined that 300 and 400 mg/kg EO supplementation induced higher breast ratio when compared to other groups. Alcicek et al., (2004) found that 36 mg/kg EO supplementation did not affect carcass ratio, but 48 mg/kg supplementation increased it. Similarly, it was found that 24 mg/kg EO supplementation to diet did not affect carcass ratio but 48 and 72 mg/kg increased (Alcicek et al., 2003). Results on the carcass traits in this study and other studies indicated that oil type and their doses could be alter carcass traits of birds.

In this study, it was determined that 130 or 260 mg/kg TFO supplementation to diet did not affect serum compositions of the broilers used (Table 5). The present results indicated that active compounds in the TFO did not affect serum lipid- and protein metabolism parameters and liver enzymes activities. The results showed that 130 or 260 mg/kg TFO supplementation to diet had no effect on the total cholesterol concentration in quail. Similar to present study, Lee et al., (2003) found no differences on total cholesterol and HDL cholesterol concentrations in broilers fed with supplemented EO diets. Khattak et al., 2014 reported that no significant effect on the total cholesterol concentration depending on the supplementation of EO could be associated either ineffective in inhibiting hepatic 3-hydroxy-3-methylglutaryl coenzyme A reductase or due to their fast degradation rate in the liver of broilers. However, De Whalley et al., 1990 and Yee (1996) reported that terebinth fruits contain tannin and it has a hypocholesterolemic effect. In other hand, the absence or presence of hypo-cholesterolaemic effects of components in an animal depend on breed, gender, age and also on the composition of the diet.

In the present study, 130 or 260 mg/kg TFO supplementation to diet did not affect fatty acid composition of the breast meat in quails (Table 6). But, the total SFA amounts in the breast meat of birds fed with 130 or 260 mg/kg TFO supplemented birds, respectively, were 7.90 and 3.39 % lower than those of the birds in the Control group. The decrease in the total SFA amount in the both TFO supplemented group were originated from the decrease in the palmitic-, heptadecanoic- and stearic acid amount in these groups when compared to Control group. The numerical decrease in the total SFA of the breast meat of quail fed with 130 or 260 mg/kg TFO, may be related to the numerical decrease in the serum total cholesterol concentrations of these

birds (Table 5). In contrast the total SFA, 130 or 260 mg/kg TFO supplementation to diets induced a 0.36 and 4.88 % increase in the total PUFA amount respectively, when compared to Control group. The numerical increase in the total PUFA in the both TFO supplemented group were primarily related to increase in the arachidonic acid. The numerical decrease in total SFA but numerical increase in the total PUFA in both TFO supplemented groupshave indicated that consumption of carcass from these birds may be poses a lower risk of coronary heart disease. The PUFA accepted is also a more vulnerable indicator to lipid peroxidation. Although there were no statistical differences ($P < 0.062$), it is worth to state that the PUFA:SFA ratio was numerically higher in the both TFO supplemented group than that of the Control group. The increase in the PUFA:SFA ratio might be explained by the antioxidant capacity of terebinth oil (Topcu et al., 2007; Kavak et al., 2010).

5. CONCLUSIONS

In conclusion, supplementation of 260 mg/kg TFO to diet increased body weight and weight gain, when compared to the Control and 130 mg/kg TFO supplemented groups in quail. Yet, supplementation of 130 mg/kg TFO decreased feed intake of the birds when compared to the Control and 260 mg/kg TFO supplemented groups. Supplementation of 130 mg/kg TFO improved feed conversion, as compared to the Control group. Supplementation of TFO at both doses had no effect on the carcass ratio, carcass parts and visceral organ ratio to the carcass weight, serum parameters and fatty acid composition in the breast meat of birds. These affirmative resultshave indicated that TFO may be used as an alternative supplement at these doses in quail diets. Additionally, first findings on usage of TFO as feed additives in quails were demonstrated with this study. However, further and more complete evaluations are required to establish the effect of TFO supplementation in diets on the performance of poultry.

References

ALCICEK, A., BOZKURT, M. & CABUK, M.(2003) The effect of an essential oil combination derived from selected herbs growing wild in Turkey on broiler performance. South African Journal of Animal Science, **33**: 89-94.

ALCICEK, A., BOZKURT, M. & CABUK, M. (2004) The effect of a mixture of herbal essential oils, an organic acid or a probiotic on broiler performance. South African Journal of Animal Science, **34**: 217-222.

A.O.A.C.: Official Methods of Analysis of AOAC International. 1th Ed., AOAC International, Maryland, USA, 2000.

AYFER, M.(1973)

Bazı önemli pistaci türlerinin meyvelerinde yağ miktarları ile yağ asitlerinin çeşit ve oranları ve bunlarda bazı kimyasal sistematiğe yarayan özellikleri üzerine araştırmalar. Ankara Üniversitesi Ziraat Fakültesi Dergisi, **1**: 128-133.

BAKIREL, T., SENER, S., BAKIREL, U., KELES, O., SENNAZLI, G. & GUREL, A. (2003) The investigation of the effects of Pistacia terebinthus L. upon experimentally induced hypercholesterolemia and atherosclerosis in rabbits. Turkish Journal of Veterinary and Animal Science, **27**: 1283-1292.

BOTSOGLOU, N.A., FLOROU-PANER, P., CHRISTAKI, E., FLETOURIS, D.J. & SPAIS, A.B. (2002) Effect of dietary oregano essential oil on performance of chickens and on iron-induced lipid oxidation of breast, thigh and abdominal fat tissues. British Poultry Science, **43**: 223-230.

COULADIS, M., OZCAN, M., TZAKOU, O. & AKGUL A. (2002) Menengiç (Pistacia terebinthus L.) ağacının değişik organlarında uçucu yağ bileşimi. 14. Bitkisel İlaç Hammaddeleri Toplantısı, Bildiriler, 29-31 Mayıs 2002, Eskisehir, Türkiye.

De WHALLEY, C.V., RANKIN, S.M., HOULTH, J.R.S., JESSUP, W. & LEAKE, D.S. (1990) Flavonoids inhibit the oxidative modification of low density lipoproteins by macrophages. Biochemical Pharmacology, **39**: 1743-1748.

DURU, M.E., ÇAKIR, A., KORDALI, S., ZENGİN, H., HARMANDAR, M., İZUMİ, S. & HIRATA, T. (2003) Chemical composition and antifungal properties of essential oils of three Pistacia species. Fitoterapia, **74**: 170-176.

EUROPEAN UNION (2003) Regulation (EC) No 1831/2003 of the European Parliament and of the Council of 22 September 2003 on additives for use in animal nutrition. Official Journal of European Union Legislation, **268**: 29-43.

HAFEZ, H.M. & HAUCK, R. (2006) Efficacy of a herbal product against Histomonas meleagridis after experimental infections of turkey poults. Archive of Animal Nutrition, **60**: 436-442.

HERNANDEZ, F., MADRID, J., GARCIA, V., ORENGO, J. & MEGIAS, M.D. (2004) Influence of two plant extracts on broiler performance, digestibility, and digestive organ size. *Poultry Science*, **83**: 169-174.

JANG KO, Y.H., YANG, H.Y., HA, J.S., KIM, J.Y., KIM, J.Y., KANG, S.Y., YOO, D.H., NAM, D.S., KIM, D.H. & LEE, C.Y. (2004) Influence of essential oil components on growth performance and the functional activity of the pancreas and small intestine in broiler chickens. *Asian-Australian Journal of Animal Science*, **17**: 394-400.

JANG, I.S., KO, Y.H., KANG, S.Y., LEE, C.Y. (2007) Effect of a commercial essential oil on growth performance, digestive enzyme activity and intestinal microflora population in broiler chickens. *Animal Feed Science and Technology*, **134**: 304-315.

KAMEL, C. (2001) Tracing Modes of Action and Roles of Plant Extracts in Non-ruminants. Pages 135-150 in *Recent Advances in Animal Nutrition*. P.C. Garnsworthy and J. Wiseman, ed. Nottingham University Press, Nottingham, UK.

KAVAK, D.D., ALTIOK, E., BAYRAKTAR, O., ULKU S. (2010) Pistacia terebinthus extract: As a potential antioxidant, antimicrobial and possible β -glucuronidaseinhibitör. *Journal of Molecular Catalysis B: Enzymatic*, **64**: 167–171.

KHATTAK, F., RONCHI, A., CASTELLI, P. & SPARKS, N. (2014) Effects of natural blend of essential oil on growth performance, blood biochemistry, cecal morphology, and carcass quality of broiler chickens. *Poultry Science*, **93**: 132–137.

KHOSRAVINIA H. (2013) Productive performance, litter characteristics and carcass defects of the broiler chickens given drinking water supplemented with Saturejakhuzistanica essential oils. *Journal of Medicinal Plants Research*, **7**: 1754-1760.

KIZIL, S. & TURK M. (2010) Microelement contents and fatty acid compositions of Rhuscoriaria L. and Pistacia terebinthus L. fruits spread commonly in the south eastern Anatolia region of Turkey. *Natural Product Research*, **24**: 92–98

KUCUKYILMAZ, K., CATLI, A.U. & CINAR, M. (2012) The effect of dietary essential oil mixture supplementation on the broiler performance, carcass yield and some internal organ weight. *The Journal of the Faculty of Veterinary Medicine, University of Kafkas*, **18**: 291-296.

KUSMENOGLU, S., BASER, K.H.C. & OZEK, T. (1995) Constituents of the essential oil from the hulls of Pistaciavera L. *Journal of Essential Oil Research*, **7**: 367-368.

- LEE, K.W., EVERTS, H., KAPPERT, H.J., FREHNER, M., LOSA, R. & BEYNEN, A.C. (2003) Effects of dietary essential oil components on growth performance, digestive enzymes and lipid metabolism in female broiler chickens. *British Poultry Science*, **44**: 450-457.
- MATTHAUS, B. & OZCAN, M.M. (2006) Quantitation of fatty acids, sterols, and tocopherols in turpentine (*Pistacia terebinthus* Chia) growing wild in Turkey. *Journal of Agricultural Food Chemistry*, **54**: 7667-7671.
- N.R.C (National Research Council) (1994) *Nutrient Requirements of Poultry* 9th rev. ed. National Academy Press, Washington, DC.
- OZCAN, M. (2004) Characteristics of fruit and oil of terebinth (*Pistacia terebinthus* L) growing wild in Turkey. *Journal of the Science of Food and Agriculture*, **84**: 517-520.
- OZCAN, M.M., TZAKOU, O. & COULADIS, M. (2009) Essential oil composition of the turpentine tree (*Pistacia terebinthus* L.) fruits growing wild in Turkey. *Food Chemistry*, **114**: 282-285.
- PAQUOT, C. (1979) *Standart Methods for the Analyses of Oils, Fats and Derivates*. 6th edn. Centre Nationale de la Recherche Scientifique, Thiais, France.
- PAPAGEORGIOU., V.P., ASSIMOPOULOU, A.N. & YANNOVITS-ARGIRIADIS, N. (1999) Chemical composition of the essential oil of Chios turpentine. *Journal of Essential Oil Research*, **11**: 367-368.
- TOPCU, G., AY, M., BILICI, A., SARIKURKCU, C., OZTURK, M. & ULUBELEN, A. (2007) A new flavone from antioxidant extracts of *Pistacia terebinthus*. *Food Chemistry*, **103**: 816–822.
- TZAKOU, O., PITAROKILI, D, CHINO, I.B. & HARVALA C. (2001) Composition and antimicrobial activity of the essential oil of *Salvia ringens*. *Planta Medica*, **67**: 181-183.
- VICHI, S., ZITTERL-EGLSEER, K., JUGI, M. & FRAZ, C. (2001) Determination of the presence of antioxidants deriving from sage and oregano extracts added to animal fat by means of assessment of the radical scavenging capacity by photochemiluminescence analyses. *Nahrung*, **45**: 101-104.
- YEE, Y.B. (1996) *An Update and Review of Soybean Oil in Health and Medical Research*. American Soybean Association, Singapore.

ICENS

INTERNATIONAL CONFERENCE ON
ENGINEERING AND NATURAL SCIENCE

May 15 - 19 Skopje

www.icens2015.com



**TURKISH
AIRLINES** 

**EUROPE
CONGRESS**
www.europecongress.org

ZENITH GROUP
CONSULTING | TRADE | TOURISM